QUANTITATIVE SEISMOLOGY

SECOND EDITION

Keiiti Aki

Formerly with Observatoire Volcanologique du Piton de la Fournaise

Paul G. Richards

Lamont-Doherty Earth Observatory of Columbia University

University Science Books

Mill Valley, California

University Science Books
www.uscibooks.com

Editor: *Jane Ellis*
Production Manager: *Ann Knight*
Manuscript Editor: *Lee A. Young*
Designer: *Robert Ishi*
Compositor: *Windfall Software*
Illustrators: *John and Judy Waller*
Printer and Binder: *Integrated Book Technology*

This book is printed on acid-free paper.

Library of Congress Cataloging-in-Publication Data

Aki, Keiiti, 1930–
Quantitative Seismology / Keiiti Aki, Paul G. Richards.—2nd ed.
p. cm.
Includes bibliographical references and index.
ISBN 978-1-891389-63-4, Paperback
1. Seismology—Mathematics. I. Richards, Paul G., 1943– II. Title.
QE539.2.M37 A45 2002
551.22—dc21 2002071360

Printed in the United States of America
10 9 8 7 6 5 4 3

Preface
TO THE FIRST EDITION

In the past decade, seismology has matured as a quantitative science through an extensive interplay between theoretical and experimental workers. Several specialized journals recorded this progress in thousands of pages of research papers, yet such a forum does not bring out key concepts systematically. Because many graduate students have expressed their need for a textbook on this subject and because many methods of seismogram analysis now used almost routinely by small groups of seismologists have never been adequately explained to the wider audience of scientists and engineers who work in the peripheral areas of seismology, we have here attempted to give a unified treatment of those methods of seismology which are currently used in interpreting actual data.

We develop the theory of seismic wave propagation in realistic Earth models. We study specialized theories of fracture and rupture propagation as models of an earthquake, and we supplement these theoretical subjects with practical descriptions of how seismographs work and how data are analyzed and inverted.

Our text is arranged in two volumes. Volume I gives a systematic development of the theory of seismic-wave propagation in classical Earth models, in which material properties vary only with depth. It concludes with a chapter on seismometry. This volume is intended to be used as a textbook in basic courses for advanced students of seismology. Volume II summarizes progress made in the major frontiers of seismology during the past decade. It covers a wide range of special subjects, including chapters on data analysis and inversion, on successful methods for quantifying wave propagation in media varying laterally (as well as with depth), and on the kinematic and dynamic aspects of motions near a fault plane undergoing rupture. The second volume may be used as a textbook in graduate courses on tectonophysics, earthquake mechanics, inverse problems in geophysics, and geophysical data processing.

Many people have helped us. Armando Cisternas worked on the original plan for the book, suggesting part of the sequence of subjects we eventually adopted. Frank Press's encouragement was a major factor in getting this project started. Chapter 12, on inverse problems, grew out of a course given at MIT by one of the authors and Theodore R. Madden, to whom we are grateful for many helpful discussions. Our students' Ph.D. theses have taught us much of what we know, and have been freely raided. We drew upon the explicit ideas and results of several hundred people, many of them colleagues, and hope

their contributions are correctly acknowledged in the text. Here, we express our sincere thanks.

Critical readings of all or part of the manuscript were undertaken by Roger Bilham, Jack Boatwright, David Boore, Roger Borcherdt, Michel Bouchon, Arthur Cheng, Tom Chen, Wang-Ping Chen, Bernard Chouet, George Choy, Vernon Cormier, Allan Cox, Shamita Das, Jim Dewey, Bill Ellsworth, Mike Fehler, Neil Frazer, Freeman Gilbert, Neal Goins, Anton Hales, David Harkrider, Lane Johnson, Bruce Julian, Colum Keith, Gerry LaTorraca, Wook Lee, Dale Morgan, Bill Menke, Gerhard Müller, Albert Ng, Howard Patton, Steve Roecker, Tony Shakal, Euan Smith, Teng-Fong Wong, Mai Yang, and George Zandt. We appreciate their attention, their advice, and their encouragement.

About fifteen different secretaries typed for us over the four years during which we prepared this text. Linda Murphy at Lamont-Doherty carried the major burden, helping us to salvage some self-respect in the way we handled deadlines. We also thank our manuscript editor, Dick Johnson, for his sustained efforts and skill in clarifying the original typescript.

We acknowledge support from the Alfred P. Sloan Foundation and the John Simon Guggenheim Memorial Foundation (P.G.R.). This book could not have been written without the support given to our research projects over the years by several funding agencies: The U.S. Geological Survey and the Department of Energy (K.A.); the Advanced Research Projects Agency, monitored through the Air Force Office of Scientific Research (K.A. and P.G.R.); and the National Science Foundation (K.A. and P.G.R.).

Keiiti Aki
Paul G. Richards
June 1979

Preface

TO THE PAPERBACK VERSION OF THE SECOND EDITION

In 1975 I received a surprising letter from Kei Aki, beginning "I wonder if you would be interested in coauthoring a text book on theoretical seismology with me . . . "

We had both taught advanced seismology courses at our respective institutions, the Massachusetts Institute of Technology and Columbia University. But his were informed by many years as a leading researcher. He had worked on everything from the practical study of noise to theoretical frameworks for interpreting free oscillation signals. I was in my fourth year as an assistant professor, knew nothing about vast areas of seismology, and had focussed on some details in source theory and wave propagation that he knew a great deal more about than I did. But I said yes to his invitation, and thus began a wonderful four-year period of being forced to learn about seismology well enough to write explanations of the underlying theory.

At that time, in the mid to late 1970s, the concept of quantifying seismic sources with a moment tensor had just begun to take hold. Film chips of analog data from the Worldwide Standardized Seismographic Network were the best source of seismograms for most geophysicists in academia, but their narrow band and limited dynamic range were problematic (the seismograms, not the geophysicists). Broadband instruments and digital methods of recording were only beginning to show their potential.

Kei sent me 300 pages of his teaching notes. We quickly drafted a sequence of chapter titles and began writing. In 1978 we sent our first draft to the publisher. It was promptly rejected as being three times longer than planned, and unmarketable. I was devastated. But Kei calmly responded with the suggestion that we could do a little re-organization and offer the material as two volumes. The original publishers agreed, and after two more years of editing and figure preparation the first edition appeared in February 1980.

The IRIS Consortium and the Federation of Digital Seismographic Networks emerged in the 1980s to meet growing needs for high-quality broadband seismic data. Global, national, regional, and local networks of broadband seismometers have since been deployed at thousands of locations, and quantitative seismology is conducted today on a scale that could hardly be imagined in the 1970s and 1980s. Every generation of seismologists correctly knows that it is working at new levels of excellence. As always, the rationale for support to seismology is multi-faceted: to study the Earth's internal structure, to conduct research in the physics of earthquakes, to quantify and mitigate earthquake hazard, and

to monitor explosions both to evaluate the weapons development programs of a potential adversary and to support initiatives in nuclear arms control.

These different applications of seismology are illustrated by our own careers. In 1984 Kei Aki moved from MIT to the University of Southern California, and promoted integration of scientific information about earthquakes and its public transfer as the founding science director of the Southern California Earthquake Center. At the Center, for example, input from earthquake geologists was used together with the fault model of quantitative seismology, to generate output useful for earthquake engineers. In this work, the concept of seismic moment was central to unifying information from plate tectonics, geology, geodesy, and historical and instrumental seismology. The public transfer of the integrated information was made in the form of probabilistic estimates of earthquake hazards. The Center is still alive and well, long after Kei left for an on-site prediction of volcanic eruptions using seismic signals from an active volcano (Réunion) in the Indian Ocean. In the mid-1980s, I also changed my interests to applied aspects of seismology and began work on practical problems of monitoring compliance with nuclear test ban treaties. At first the main issue was estimating the size of the largest underground nuclear explosions, in the context of assessing compliance with the 150 kiloton limit of the Threshold Test Ban Treaty. Later the focus changed to a series of technical issues in detection, location, and identification of small explosions, in the context of verification of the Comprehensive Nuclear-Test-Ban Treaty. This latter treaty became a reality in 1996, and is now associated with an International Data Centre in Vienna and an International Monitoring System currently being built with stations at hundreds of new sites around the world. In early 1996, Xiaodong Song and I working at Columbia's Lamont-Doherty Earth Observatory discovered small changes in the travel time with which seismic waves traverse the Earth's inner core—evidence that we interpreted as due to inner core motion with respect to the rest of the solid Earth.

These developments in understanding earthquake hazard, explosion monitoring, and Earth's internal structure and processes, directly show that people do seismology for utterly different reasons. The common thread is interpretation of seismograms. The quality of data and ease of data access have greatly improved since 1980, but the fundamentals of seismogram interpretation are little changed. Progress in applications of seismology relies upon sophisticated methods of analysis, often incorporated into software that students must learn to use soon after beginning graduate school. The purpose of this book is to provide students and other researchers with the underlying theory essential to understanding these methods—and their pitfalls, and possibilities for improvement.

We received numerous requests to keep the 1980 edition in print, and it would have been easy to accept invitations simply to republish. But I decided in late 1994 to rewrite rather than republish, because the emergence of new methods for detecting and recording seismic motions meant that much of the instrumentation chapter would have to be completely reworked, and rewriting could accommodate new problems, up-to-date references, and thousands of small changes as well as major revision of some sections. The new publisher, University Science Books, working with Windfall Software, enabled this second edition with modern methods of design and typesetting. Numerous typographical errors have been corrected for this paperback edition. I thank many people for finding them, especially Koji Uenishi, who worked on the Japanese edition.

Dropped from the first edition are chapters on inverse theory, methods of data analysis, and seismic wave propagation in media with general heterogeneity. (Note that whole books

have been published since 1980 on these subjects.) Parts of our discarded chapters have been reworked into the chapters that remain. Numerous sections elsewhere are brought up-to-date (for example, an explanation of the centroid moment tensor). The revised and rewritten material emphasizes basic methods that have turned out to be most important in practice.

In May 2005 we received the news of Kei Aki's untimely death in his home town on Réunion Island. In the pages of *Seismological Review Letters* (**76**, 551–553, issue of Sept/Oct 2005) I have described some of his many accomplishments. I am so fortunate to have been among the more than one hundred people who worked as co-authors with him. He was a gentle leader, informal and approachable, who provided the quantitative methods that now guide the work of thousands of Earth scientists around the world.

Books like this are more than scaled-up versions of research papers—teams of people have to work together for years to turn concepts into reality. I thank Jane Ellis, my editor at University Science Books, for encouragement, tact, patience, help, and stamina since we began this project in 1994. The help of the first edition publisher, W. H. Freeman and Co., in allowing us to use original figures where possible, is gratefully acknowledged. I thank Paul Anagnostopoulos of Windfall Software who introduced me to ZzTEX and solved electronic design and typesetting problems on this second edition over more than ten years; Kathy Falato and Violeta Tomsa who took care of my office at Lamont; and Kathy Falato, Elizabeth Jackson, MaryEllen Oliver, and Gillian Richards for entering text and equations to recreate something like the original edition electronically, thus giving me an entity that could be revised. (How else could piles of notes for revision be merged with a text generated in the 1970s with IBM Selectrics?)

I received support during the rewriting from Los Alamos National Laboratory in 1997, and from several federal agencies back at Lamont. Many people helped with comments on the first edition, with suggestions for new material, critical reading, supplying references and figures, and checking the new problems. It is a pleasure here to acknowledge such contributions to the second edition from Duncan Agnew, Joe Andrews, Yehuda Ben-Zion, Phil Cummins, Steve Day, Tony Dahlen, Wen-xuan Du, Göran Ekström, Karen Fischer, Steve Grand, John Granville, David Harkrider, Klaus Jacob, Bruce Julian, Richard Katz, Vitaly Khalturin, Debi Kilb, Won-Young Kim (who selected the broadband seismogram shown in red on the cover, and the filtered versions with all their different character as shown also in Figure 12.1), Boris Kostrov, Anyi Li, Wenyi Li, Gerhard Müller, Jeffrey Park, Mike Ritzwoller, Peter Shearer, Jinghua Shi, Bob Smith, Stan Whitcomb, Rüdi Widmer, Bob Woodward, and Jian Zhang.

To facilitate commentary on the second edition (both hard copy and this paperback), and to provide supplementary material as it may accumulate in future years, a website is maintained at http://www.LDEO.columbia.edu/~richards/Aki_Richards.html

Jody Richards has stayed with all this, and with me, since the very beginning. I owe her more than thanks, and am so glad we can still dance together.

Paul G. Richards
February 2009

Contents

CHAPTER 1

Introduction

Seismology is the scientific study of mechanical vibrations of the Earth. Quantitative seismology is based on data called seismograms, which are recordings of the vibrations, which in turn may be caused artificially by man-made explosions, or caused naturally by earthquakes and volcanic eruptions. Such phenomena have strongly attracted the attention of humankind for centuries, even today arousing feelings of fear and mystery as well as our intellectual curiosity.

The great progress made in seismology since the 1880s—when instruments called seismometers were first deployed that could record the vibrations (seismic waves) generated by an earthquake on the other side of the world—has been stimulated principally by the availability of better and better data, which can still be expected to improve in future decades. The major steps in this progress have been initiated by scientists well grounded in the methods of mathematical physics.

Each generation of seismologists has worked toward quantitative results, with barriers to computation pushed back first by mechanical hand calculators and later by advances in digital microprocessing. Since the 1960s, combined improvements in instrumentation, our understanding of the Earth and the theory of seismic waves, and computation have become effective to handle a large fraction of the information contained in seismograms. These improvements extend even to the interpretation of the detailed shape of waveforms recorded in seismograms, as well as their times of arrival. The quantitative picture of seismology today involves a massive interplay between high-quality data, detailed models of seismic source mechanisms, models of the Earth's internal structure, theories of wave propagation and theories of data inversion, and the largest modern computers.

Today seismology is used in mineral prospecting and exploration for oil and natural gas, and in structural engineering to aid in the design of earthquake-resistant buildings. Other uses arise generally in far-ranging political, economic, and social problems associated with the reduction of seismic hazards, and in the detection of nuclear explosions. Thus, since the 1970s there have been great efforts to mitigate earthquake hazards by improving probabilistic estimates of the location and timing of damaging earthquakes. There is great pressure on seismologists to pursue this aspect of their subject, as can be seen by noting that earthquakes from 1985 to 2001 have killed about 200,000 people, injured about 500,000, made about 2.5 million homeless, and have caused more than $330 billion in economic

losses. The next great earthquake in a major metropolitan region could cause damage at the multi-trillion dollar level. Figures such as these make accurate assessment of earthquake hazards, hazard mitigation, and the general goal of earthquake prediction all so important that seismology is likely to continue to change and grow, just as it grew in the 1960s in response to the need to monitor nuclear explosions, then occurring on average a few times a week. (The first global network of calibrated seismographs as well as several large-aperture arrays was set up initially to improve the capability of seismology to detect and identify underground nuclear tests.) The Comprehensive Nuclear-Test-Ban Treaty of 1996 will drive many improvements in global seismic monitoring. Even though this treaty has yet to enter into force—the United States Senate in October 1999 denied its advice and consent to ratification, and certain key countries had not signed this treaty as of late 2001—there is still the need for global programs of nuclear explosion monitoring. The reading list at the end of this chapter includes books and papers that cover this wide range of applications of modern seismological techniques.

Seismology is at an extreme of the whole spectrum of Earth sciences. First, it is concerned only with mechanical properties and dynamics of the Earth. Second, it offers a means by which investigation of the Earth's interior can be carried out to the greatest depths, with resolution and accuracy higher than are attainable in any other branch of geophysics. Resolution and accuracy are good because seismic waves have the shortest wavelength of any wave that can be observed after modulation by passing through structures inside the Earth. Seismic waves undergo the least distortion in waveform and/or the least attenuation in amplitude, as compared with other geophysical observables, such as heat flow, static displacement, strain, gravity, or electromagnetic phenomena.

A third unique characteristic of seismology is that it contributes to our knowledge of only the *present* state of the Earth's interior. Because of its emphasis on *current* tectonic activity, seismology attracts a rather direct public interest.

The methods of seismology, like other geophysical methods, are applicable to tremendous ranges of scale. These ranges may be classified according to the size of the seismic source (both man-made and natural) and according to the size of the seismograph network and to the signals it may record. The explosive charges used in seismological investigations range in size from less than a gram to more than a megaton (a factor greater than 10^{12}). From the smallest detectable microearthquake to such great events as the Chilean earthquake of 1960 May 22, the range of natural earthquakes is even greater, amounting to a factor of about 10^{18} in terms of the equivalent point-source strength (seismic moment). The linear dimensions of seismograph networks range from tens of meters for an engineering foundation survey to 10,000 km for the global array of seismological observatories, or a factor of 10^6. The signals of ground displacement range down to 10^{-10} m (comparable to the diameter of a hydrogen atom), detectable in good conditions, and up to tens of meters for the slip on a major fault during a great earthquake. It became routine in the 1990s for seismometers to use 24-bit recording (amplitude ranging over tens of millions), but still it is necessary to use different sensors to span the range from the smallest detectable signal in the presence of Earth noise up to the largest reported signals.

The interpretation of seismograms has progressed in the usual scientific manner, starting with an initial guess that is later supported or corrected after testing its consequences against new data. We simplify the problem of interpreting seismograms by artificially sep-

arating the effect of the source from the effect of the medium. Historically, our knowledge of the seismic source and our knowledge of the Earth medium have advanced in a see-saw fashion. For example, at one stage the source may be better known than the medium, in which case new data are used to improve the knowledge of the medium, assuming that the source is known. In the next stage, new data are combined with the improved knowledge of the medium to revise our knowledge of the source.

Many of the concepts developed by geophysicists to interpret seismograms are now being applied, not to the study of the Earth, but rather to the study of the Sun and other stars (helioseismology, asteroseismology), to medical imaging (sonography), and to nondestructive testing of factory-made objects both large and small (aircraft wings, semiconductor chips). In these nongeophysical fields, one finds the basic phenomena of body waves and surface waves being used to explore depth-dependent and three-dimensional structures, and to search for cracks and other defects.

As in all other branches of geophysics, the effects of source and medium are strongly coupled in seismology. Double errors, one in the source and another in the medium, can produce a prediction consistent with observation. A deep understanding of physical principles is required to avoid being lured by an apparent consistency. A fascinating story of such double errors concerns the identification of *P*- and *S*-waves. In the early days of seismology, it was controversial whether the main motion of a local earthquake is due to compressional waves or shear waves. The main motion was called the *S*-phase because it was the secondary arrival, preceded by the smaller *P*-phase, so called because it was the primary, i.e., first, arrival. In 1906, F. Omori, the founder of seismology in Japan, investigated this problem using the seismograms of an earthquake observed at what was then the world's best local station network. Using his own formula relating the time between *S* and *P* arrivals to the distance between seismometer and earthquake epicenter, and using also the relative arrival times at several stations, he located the epicenter at about 500 km south of the coast of Honshu. Then he found that the particle motion of the *S*-phase is mainly in the north–south direction—that is, the *S*-phase is apparently longitudinally polarized. If, at this point, he had insisted that the *S*-phase should be shear waves, having a particle motion perpendicular to the direction of wave propagation, then he could have correctly put the focal depth of the earthquake about 500 km *beneath* Honshu to resolve the inconsistency. Instead, he erroneously concluded that the *S*-phase does not consist of shear waves. This double error was actually in harmony with then dominating ideas about earthquake foci and seismic waves. At that time, the concept of isostasy was already well known to explain gravity observations, and nobody dreamed of earthquake foci deep in what was then thought to be a ductile part of the Earth. The conclusion about the *S*-phase was also in harmony with the so-called Mallet's doctrine, which held that the main motion in the epicentral area is due to longitudinal waves. Robert Mallet, who was also the first person to measure seismic velocity in the field using explosives, arrived at this doctrine from the first scientific field study of earthquake-damaged structures, which he examined in the epicentral area of the Neapolitan earthquake of 1857.

In 1906, the existence of compressional waves and shear waves in solids was well known. Since the discovery of Hooke's law in 1660, major advances in elasticity theory were made by Navier's study in 1821 on the general equation of equilibrium and vibration, as well as by Young's and Fresnel's interpretations showing that light consists of

transversely polarized waves. Before these interpretations, it was generally considered that only longitudinal waves could propagate through an unbounded continuum. Progress in the theory of elastic wave propagation continued with Cauchy (who by 1822 had developed the concept of six independent components of stress, and six of strain) and with Poisson (who used a Newtonian concept of intermolecular forces within a solid, so that the force between any pair of molecules is assumed to be proportional to the distance away from their equilibrium separation). Poisson found theoretically the two types of waves we now know as P and S, and concluded for his restricted model that the P-wave speed is $\sqrt{3}$ times the S-wave speed. A firmer foundation for the theory was given by Green, who invoked the existence of a strain–energy function with 21 independent coefficients for an arbitrary anisotropic body. The number of coefficients reduces to two for an isotropic body.

Love gave an excellent historical sketch of the development of elasticity theory in the introduction to his classic textbook (Love, 1892; reprinted 1944). The early history of observational seismology is well described by Dewey and Byerly (1969).

The explanation of Rayleigh waves (Rayleigh, 1887), which can propagate over the free surface of an elastic body, postdated the first recording of earthquake waves. The first theoretical seismogram was constructed by Lamb (1904) for a point impulsive source buried in a homogeneous half-space. The resultant seismogram at the surface consists of a sequence of three pulses corresponding to P-, S-, and Rayleigh waves—much too simple as compared with observed records.

When the first earthquake seismogram was recorded in the early 1880s, seismologists were puzzled why the oscillations lasted so long. We shall find that Rayleigh waves can be dispersed (meaning that waves having different frequencies travel at different speeds), and this is one reason for long-lasting oscillation. But there are also oscillations after the arrival of P- and S-waves and before the arrival of surface (e.g., Rayleigh) waves. Jeffreys (1931) examined and rejected a host of explanations, concluding that "the only suggestion which survives is that the oscillations are due to reflexions of the original pulse within the surface layers." When the first seismogram for the Moon was obtained in 1969, seismologists were again puzzled by the great length of time for which oscillations continued. Again, the explanation appears to lie in the scattering of waves by heterogeneities.

The application of Lamb's methods to actual earthquakes and explosions in the Earth had to be postponed to about 1960, when high-quality data on long-period seismic waves became available through the efforts of Hugo Benioff, Maurice Ewing, Frank Press, and others. Long-period waves average out the small-scale heterogeneity of the Earth, and the Earth then behaves as if it were an equivalent homogeneous body. The process at the earthquake source is also simpler at long periods. For this reason, the extremely simple model of Lamb's problem can be of practical use in the interpretation of long-period seismograms.

The Earth models considered in this book are very simple. In most cases, the medium is homogeneous or heterogeneous only in one direction, such as the layered half-space or sphere, in which material properties change only vertically or radially.

Models in seismology are mathematical frameworks within which observed seismograms are related to the Earth's interior via model parameters. For example, if a homogeneous, unbounded, isotropic elastic body is used as the model of the Earth in interpreting seismograms, the parameters obtainable from such interpretations are, at best, Lamé's

moduli, λ and μ, and a constant density, ρ. On the other hand, when the model is vertically heterogeneous, we can determine λ, μ, and ρ as functions of depth z. Of course, a three-dimensionally heterogeneous and arbitrarily anisotropic medium is the most desirable model, but the numerical effort to deal with it on a large scale becomes too great to be practical. Also it has more parameters than we can expect to elucidate from data presently available. Despite progress made in three-dimensional tomographic studies as well as in scattering studies using random media models, the most productive model so far in seismology has been a vertically heterogeneous half-space or sphere. The heart of this book is devoted to surface waves (Chapter 7), free oscillations (Chapter 8), and body waves (Chapter 9) in such models.

To prepare the reader for these chapters, we start with basic and practically useful theorems applicable to general problems of elastodynamics, such as the reciprocity theorem and a representation theorem (Chapter 2). In Chapter 3 we formulate the representation of localized internal seismic sources as the starting point for developing the theory of seismic motions in the Earth. The most productive source representation for an earthquake has been the displacement discontinuity across an internal surface, called the dislocation model. In Chapter 3 we also consider a volume source in which transformational strain is prescribed within a volume. Additional aspects of seismic source mechanisms are postponed to Chapters 10 and 11.

A complete description of seismic motion from a point dislocation source in a homogeneous medium is given in Chapter 4. The analysis is extended to a smoothly varying medium, using curvilinear coordinates fixed by the geometrical ray paths. This chapter, among other things, offers the basis for determining the fault plane solution of an earthquake from body waves.

The properties of plane waves, such as reflections and transmissions at a plane interface, phase shifts, inhomogeneous (evanescent) waves, attenuation, and physical dispersion, are extensively studied in Chapter 5. In Chapter 6 we solve Lamb's problem, in which a spherical wave from a point source interacts with a plane surface. Three major types of waves emerge from this interaction: waves that are directly reflected from, or transmitted through, the boundary; waves that travel from source to receiver along the boundary (head waves); and waves of the Rayleigh, or Stoneley type, with amplitude decaying exponentially with distance from the interface. We study these waves using the Cagniard method, as well as Fourier transform methods, to prepare the ground for Chapters 7 through 9, giving practical methods for calculating seismograms in vertically heterogeneous structures.

The ordering of the three chapters on vertically heterogeneous media (surface waves, free oscillations, and body waves) reflects the historical development of wave-theoretical analysis of seismograms, as well as the degree of difficulty of the analysis. The fundamental modes of Love and Rayleigh waves are the first waves whose entire records were understood quantitatively in terms of the parameters of realistic models of the Earth and earthquakes. The analysis of body waves is more difficult, partly because we cannot set up the seismograph station at any desired position along the wave path, but only at its endpoint. A complete analysis of free oscillations is also more difficult than that of surface waves, but in this case the reason is the work involved in manipulating the long records, which can contain thousands of modes. The methods of calculating seismograms for one-dimensionally heterogeneous Earth models described in Chapters 7 through 9 are now well established.

The models in seismology are essentially mathematical. The physics involved is usually rather simple, mostly contained in the equation of motion, Hooke's law, and a few other constitutive relations. The challenge to the seismologist is in reducing the observed complex vector-wave phenomenon in three space dimensions with wiggly temporal variation in an orderly manner to a description of the wave source and the propagation medium. It is therefore very important to have an adequate model of the source of seismic waves. Chapters 10 and 11 are devoted, respectively, to the kinematic and dynamic models of an earthquake fault. In the kinematic model, we study the relation between the fault-slip function and seismic radiation in the far field and near field. We find that sources of finite spatial extent can in practice have seismic radiation differing from that emanating from a point source, even for receivers at great distances from the source. In the dynamic model, the slip function is derived from the initial condition of tectonic stress and from frictional and cohesive properties of the fault zone. These models are important for the study of earthquake source mechanisms and current tectonic activities in the Earth. They are also useful for the practical purpose of predicting earthquake strong motions for an active fault.

Our final subject is the problem of how seismic data may be acquired. Thus, in Chapter 12, we describe principles of seismometry, together with a survey of seismic signals and noises for a wide range of frequencies, sources, and source–receiver distances to help in designing instrumentation for a given experiment. This concluding chapter is accessible to anyone with some knowledge of classical physics (properties of pendulums and elementary electronic circuit theory).

This book is intended to be a self-contained description of the basic elements of modern seismology. Additional material, usually more specialized, is covered in a number of books and monographs listed below, that complement our coverage of quantitative seismology.

Suggestions for Further Reading

EARTHQUAKE ENGINEERING

Chopra, A. K. *Dynamics of Structures: Theory and Applications to Earthquake Engineering.* Englewood Cliffs, New Jersey: Prentice-Hall, 1995.

Kanai, K. *Engineering Seismology.* University of Tokyo Press, 1983.

Paz, M. *International Handbook of Earthquake Engineering: Codes, Programs, and Examples.* London/NewYork: Chapman & Hall, 1994.

Priestley, M. J. N., F. Seible, and G. M. Calvi. *Seismic Design and Retrofit of Bridges.* New York: John Wiley & Sons, 1996.

SEISMIC PROSPECTING

Sheriff, R. E., and L. P. Geldart. *Exploration Seismology.* 2nd ed. Cambridge University Press, 1995.

Telford, W. M., L. P. Geldart, and R. E. Sheriff. *Applied Geophysics.* 2nd ed. Cambridge University Press, 1990.

Yilmaz, O. *Seismic Data Processing.* Tulsa: Society of Exploration Geophysicists, 1987.

SEISMIC DETECTION AND DISCRIMINATION OF NUCLEAR EXPLOSIONS

Bolt, B. A. *Nuclear Explosions and Earthquakes: The Parted Veil.* San Francisco: W. H. Freeman, 1976.

Dahlman, O., and H. Israelson. *Monitoring Underground Nuclear Explosions.* Amsterdam: Elsevier Scientific Publishing Co., 1977.

Husebye, E. S., and A. M. Dainty, eds. *Monitoring a Comprehensive Test Ban Treaty.* Dordrecht: Kluwer, 1996.

National Academy of Sciences. *Technical Issues Related to Ratification of the Comprehensive Nuclear-Test-Ban Treaty.* Washington, D.C.: National Academy Press, 2002.

Panel of the Committee on Seismology, National Research Council. *Research Required to Support Comprehensive Nuclear Test Ban Treaty Monitoring.* Washington, D.C.: National Academy Press, 1997.

Richards, P. G., and W.-Y. Kim. Testing the nuclear test-ban treaty. *Nature,* **389**, 781–782, 1997.

Thirlaway, H. I. S. Forensic seismology. *Quarterly Journal of the Royal Astronomical Society,* **14**, 297–310, 1973.

U.S. Congress, Office of Technology Assessment. *Seismic Verification of Nuclear Testing Treaties.* OTA-ISC-361, Washington, D.C.: U.S. Government Printing Office, 1988.

EARTHQUAKE PREDICTION AND HAZARD REDUCTION

Andrew, C., and R. J. S. Spence. *Earthquake Protection.* New York: John Wiley & Sons, 1992.

Hanks, T. C. Imperfect science: Uncertainty, diversity, and experts. *EOS, Transactions, American Geophysical Union,* **78**, 369, 373 & 377, 1997.

Lomnitz, C. *Fundamentals of Earthquake Prediction.* New York: John Wiley & Sons, 1994.

Papers from Colloquium on Earthquake Prediction: The Scientific Challenge. *Proceedings of the National Academy of Sciences*, **93**, 3719–3837, 1996.

Reiter, L. *Earthquake Hazard Analysis: Issues and Insights.* New York: Columbia University Press, 1991.

Scawthorn, C. *Seismic Risk: Analysis and Mitigation.* New York: John Wiley & Sons, 1998.

Simpson, D. W., and P. G. Richards, eds. *Earthquake Prediction, an International Review.* Maurice Ewing Series, vol. 4. Washington, D.C.: American Geophysical Union, 1981.

U.S. Congress, Office of Technology Assessment. *Reducing Earthquake Losses.* OTA-ETI-623. Washington, D.C.: U.S. Government Printing Office, 1995.

Wyss, M., and R. Dmowska, eds. *Earthquake Prediction—State of the Art.* Basel: Birkhauser, 1997.

SEISMOLOGY AND EARTHQUAKE FAULTING

Ben-Menahem, A. and S. J. Singh. *Seismic Waves and Sources.* New York: Springer-Verlag, 1980.

Bullen, K. E., and B. A. Bolt. *An Introduction to the Theory of Seismology.* Cambridge University Press, 1985.

Dahlen, F. A., and J. Tromp. *Theoretical Global Seismology*. Princeton, New Jersey: Princeton University Press, 1998.

Das, S., J. Boatwright, and C. H. Scholz. *Earthquake Source Mechanics*. Maurice Ewing Series, vol. 6. Washington, D.C.: American Geophysical Union, 1986.

Hudson, J. A. *The Excitation and Propagation of Elastic Waves*. Cambridge University Press, 1980.

Kennett, B. L. N. *Seismic Wave Propagation in Stratified Media*. Cambridge University Press, 1983.

Kostrov, B. V., and S. Das. *Principles of Earthquake Source Mechanics*. Cambridge University Press, 1988.

Lay, T., and T. C. Wallace. *Modern Global Seismology*. San Diego: Academic Press, 1995.

Scherbaum, F. *Of Poles and Zeros: Fundamentals of Digital Seismology*. Modern Approaches in Geophysics, vol. 15, Kluwer Academic, 1995.

Sato, H., and M. C. Fehler. *Seismic Wave Propagation and Scattering in the Heterogeneous Earth*. New York: Springer-Verlag, 1997.

Scholz, C. H. *The Mechanics of Earthquakes and Faulting*. 2nd ed. Cambridge University Press, 2002.

Shearer, P.M. *Introduction to Seismology*. Cambridge University Press, 1999.

Yeats, R. S., K. Sieh, and C. R. Allen. *The Geology of Earthquakes*. Cambridge University Press, 1996.

OTHER APPLICATIONS OF SEISMOLOGY AND OF SEISMOLOGICAL METHODS

Bertagne, A., *et al.* Special section on Borehole Seismology. *Leading Edge*, **17**, 925–959, 1998.

Gibowicz, S. J., and A. Kijko. *An Introduction to Mining Seismology*. San Diego: Academic Press, 1994.

Gubbins, D. Portable broadband seismology: Results from an experiment in New Zealand. In *Seismic Modelling of Earth Structure*, edited by E. Boschi, G. Ekström, and A. Morelli, Istituto Nazionale di Geofisica, Editrice Compositori, 305–398, 1996.

Gubbins, D. *Seismology and Plate Tectonics*. Cambridge University Press, 1990.

Gupta, H. K., and R. K. Chadha, eds. *Induced Seismicity*. Birkhauser, 1995.

Hebenstreit, G., ed. *Perspectives on Tsunami Hazard Reduction: Observations, Theory and Planning*. Advances in Natural and Technological Hazards Research, vol. 9, Kluwer Academic, 1997.

Iyer, H. M., and K. Hirahara, eds. *Seismic Tomography: Theory and Practice*. New York: Chapman & Hall, 1993.

Neuberg, J., R. Luckett, M. Ripepe, and T. Braun. Highlights from a seismic broadband array on Stromboli volcano. *Geophysical Research Letters*, **21**, 749–752, 1994.

Oliver, J. *Shocks and Rocks: Seismology in the Plate Tectonics Revolution*. Washington, D.C.: American Geophysical Union, 1996.

Provost, J., and F.-X. Schmider, eds. *Sounding Solar and Stellar Interiors*. International Astronomical Union Symposia, vol. 81, Kluwer Academic, 1997.

Sanders, R. C., and N. S. Miner, eds. *Clinical Sonography: A Practical Guide.* Lippincott-Raven, 1998.

Webb, S. C. Broadband seismology and noise under the ocean. *Reviews of Geophysics*, **36**, 105–142, 1998.

ADDRESSES FOR INFORMATION ON SEISMOLOGY AVAILABLE ELECTRONICALLY

Surfing the net for seismological information,
http://www.geophys.washington.edu/seismosurfing.html

International Seismological Centre, http://www.isc.ac.uk

The GEOSCOPE Data Center, France,
http://geoscope.ipgp.jussieu.fr

Comprehensive Nuclear-Test-Ban Treaty Organization (Vienna),
http://www.ctbto.org/ http://www.pidc.org

ORFEUS Data Center (Royal Netherlands Meteorological Institute),
http://orfeus.knmi.nl

Swiss Seismological Service, http://seismo.ethz.ch

British Geological Survey, Global Seismology Research Group,
http://www.gsrg.nmh.ac.uk/gsrg.html

Earthquake Research Institute at the University of Tokyo,
http://www.eri.u-tokyo.ac.jp

US Geological Survey National Earthquake Information Center (NEIC),
http://wwwneic.cr.usgs.gov

US Geological Survey, Menlo Park (Northern California),
http://quake.wr.usgs.gov

US Geological Survey, Albuquerque Seismological Laboratory, examples of current seismic data,
http://aslwww.cr.usgs.gov/Seismic_Data

Treaty Monitoring by the US Air Force,
http://www.tt.aftac.gov

General tsunami information and resources,
http://www.geophys.washington.edu/tsunami/intro.html

The IRIS Consortium, http://www.iris.edu

IDA/IRIS programs at the University of California at San Diego,
http://quakeinfo.ucsd.edu/idaweb

Southern California Earthquake Center,
http://www.scecdc.scec.org

Seismological Laboratory of the California Institute of Technology,
http://www.gps.caltech.edu/seismo/seismo.page.html

University of California, Berkeley, Seismograph Stations,
http://www.seismo.berkeley.edu/seismo/Homepage.html

Lamont-Doherty Earth Observatory of Columbia University,
http://www.ldeo.columbia.edu/LCSN

Earth Resources Laboratory of the Massachusetts Institute of Technology, http://eaps.mit.edu/erl

International Association of Seismology and Physics of the Earth's Interior, http://www.iaspei.org

Seismological Society of America, http://www.seismosoc.org

American Geophysical Union, http://www.agu.org/

Earthquake Engineering Research Institute (EERI), http://www.eeri.org

CHAPTER 2

Basic Theorems in Dynamic Elasticity

An analytical framework for studying seismic motions in the Earth must incorporate, at the very least, the following three components: a description of seismic sources, equations for the motions that can propagate once motion has somewhere been initiated, and a theory coupling the source description into the particular solution sought for the equations of motion. It will be useful if the theory can be simplified by taking full advantage of our conjectures about seismic motion (though such a theory may mislead the user if the conjectures are invalid). For example, there is the conjecture that two sets of small motions may be superimposed without interfering with each other. Another conjecture is that the seismic motions set up by some physical source should be uniquely determined by the combined properties of that source and the medium in which the waves propagate. These conjectures, and many others that are generally assumed by seismologists to be true, are properties of infinitesimal motion in classical continuum mechanics for an elastic medium with a linear stress–strain relation; such a theory will provide the mathematical framework for almost all of this text.

Seismology is largely an observational science, so the ability to interpret seismograms is fundamental to progress. For this reason, there is a need to know what information about the motion in one part of a medium is enough to determine uniquely the motion that may be observed in another part. As a practical example, we often need to know how to characterize a seismic source (an explosion or a spontaneous fault motion) and how to allow for boundary conditions at the Earth's free surface in order to determine the resulting motion at a network of receivers. Fortunately, for a linear elastic medium, this problem has a definite solution, in that prescribed source conditions (in terms of body forces) and boundary conditions can readily be stated in forms that do enforce uniqueness for the resulting motions. After giving a formulation of the problem (i.e., establishing notation; defining displacement, strain, traction, body force, and stress; and stating constraints on the motion), we prove the two fundamental theorems of uniqueness and reciprocity. Reciprocity is used together with a Green function to obtain a representation of motion at a general point in the medium in terms of body forces and information on boundaries. This method of representation in elastodynamics is due to Knopoff (1956) and de Hoop (1958). It has many familiar parallels in complex number theory, in potential theory, and in the theory of the scalar wave equation for a homogeneous medium.

BOX 2.1
Examples of representation theorems

1. If $f(z)$ is an analytic function of the complex variable z, then

$$f(z) = \frac{1}{2\pi i} \oint \frac{f(\zeta)d\zeta}{\zeta - z},$$

where the contour integral is taken counterclockwise on any path C around the point z. (No singularities of f are allowed inside C.) This formula is then a *representation* of the function f, which allows f to be evaluated everywhere inside C provided the values of f are known on C itself.

2. If $\phi(x, y, z)$ satisfies the Poisson equation $\nabla^2\phi = -4\pi\rho$, then

$$\phi(\mathbf{x}) = \iiint_V \frac{\rho(\xi)\, dV(\xi)}{|\mathbf{x} - \xi|},$$

where V is a volume including all of the density distribution ρ that contributes to ϕ. This too is a *representation* of ϕ, but one that does not involve values of ϕ itself.

The elastodynamic representation theorem involves both the above types of representation, and also incorporates time dependence.

It is often useful to have the equations of elastic motion referred to general orthogonal curvilinear coordinate systems, since, in many instances, the (curved) coordinate surfaces are just those on which it is natural to apply a boundary condition. We derive the displacement–stress equations and the strain–displacement equations, using the physical components of displacement, stress, and strain in a general orthogonal system.

This chapter may seem at first sight to consist mainly of formal results—of proofs that must be established once, by one person, to legitimize the specific problem-solving methods expounded in later chapters. However, the reader who wishes to develop the ability to solve problems in theoretical or applied seismology on his or her own will soon face the question of how a problem is "set up." That is, how does one translate the physical description of a seismic source—and the general problem of calculating the ensuing motions at nearby and/or distant receivers—into a specific mathematical problem? In large part, the ability to set up such problems will stem from mastery of the representation theorem, given in various forms by equations (2.41)–(2.43) and (3.1)–(3.3). We shall frequently refer to these equations in later chapters.

2.1 Formulation

Two different methods are widely used to describe the motions and the mechanics of motion in a continuum. These are the Lagrangian description, which emphasizes the study of a particular particle that is specified by its original position at some reference time, and the Eulerian description, which emphasizes the study of whatever particle happens to occupy a particular spatial location. For most applications in seismology, the linear theory of

elasticity is conceptually simpler to develop with the Lagrangian description, and this is the framework we shall almost always adopt. Note that a seismogram is the record of motion of a particular part of the Earth (namely, the particles to which the seismometer was attached during installation), so it is directly a record of Lagrangian motion.

We shall work in this chapter with a Cartesian coordinate system (x_1, x_2, x_3), and all tensors here are Cartesian tensors. We use the term *displacement*, regarded as a function of space and time, and written as $\mathbf{u} = \mathbf{u}(\mathbf{x}, t)$, to denote the vector distance of a particle at time t from the position $\mathbf{x}$ that it occupies at some reference time t_0, often taken as $t = 0$. Since $\mathbf{x}$ does not change with time, it follows that the *particle velocity* is $\partial\mathbf{u}/\partial t$ and that the *particle acceleration* is $\partial^2\mathbf{u}/\partial t^2$.

To analyze the distortion of a medium, whether it be solid or fluid, elastic or inelastic, we use the *strain tensor*. If a particle initially at position $\mathbf{x}$ is moved to position $\mathbf{x} + \mathbf{u}$, then the relation $\mathbf{u} = \mathbf{u}(\mathbf{x})$ is used to describe the displacement field. To examine the distortion of the part of the medium that was initially in the vicinity of $\mathbf{x}$, we need to know the new position of the particle that was initially at $\mathbf{x} + \delta\mathbf{x}$. This new position is $\mathbf{x} + \delta\mathbf{x} + \mathbf{u}(\mathbf{x} + \delta\mathbf{x})$. Any distortion is liable to change the relative position of the ends of the line-element $\delta\mathbf{x}$. If this change is $\delta\mathbf{u}$, then $\delta\mathbf{x} + \delta\mathbf{u}$ is the new vector line-element, and by writing down the difference between its end points we obtain

$$\delta\mathbf{x} + \delta\mathbf{u} = \mathbf{x} + \delta\mathbf{x} + \mathbf{u}(\mathbf{x} + \delta\mathbf{x}) - (\mathbf{x} + \mathbf{u}(\mathbf{x})).$$

Since $|\delta\mathbf{x}|$ is arbitrarily small, we can expand $\mathbf{u}(\mathbf{x} + \delta\mathbf{x})$ as $\mathbf{u} + (\delta\mathbf{x} \cdot \nabla)\mathbf{u}$ plus negligible terms of order $|\delta\mathbf{x}|^2$. It follows that $\delta\mathbf{u}$ is related to gradients of $\mathbf{u}$ and to the original line-element $\delta\mathbf{x}$ via

$$\delta\mathbf{u} = (\delta\mathbf{x} \cdot \nabla)\mathbf{u}, \qquad \text{or} \qquad \delta u_i = \frac{\partial u_i}{\partial x_j}\,\delta x_j. \tag{2.1}$$

However, we do not need all of the nine independent components of the tensor $u_{i,j}$ to specify true distortion in the vicinity of $\mathbf{x}$, since part of the motion is due merely to an infinitesimal rigid-body rotation of the neighborhood of $\mathbf{x}$. This can be seen from the identity $(u_{i,j} - u_{j,i})\delta x_j = \varepsilon_{ijk}\varepsilon_{jlm}u_{m,l}\delta x_k$ (see Box 2.2 and Problem 2.2), so that equation (2.1) can be rewritten as

$$\delta u_i = \tfrac{1}{2}(u_{i,j} + u_{j,i})\delta x_j + \tfrac{1}{2}(\operatorname{curl}\mathbf{u} \times \delta\mathbf{x})_i, \tag{2.2}$$

and the rigid-body rotation is of amount $\frac{1}{2}\operatorname{curl}\mathbf{u}$. The interpretation of the last term in (2.2) as a rigid-body rotation is valid if $|u_{i,j}| \ll 1$. If displacement gradients were not "infinitesimal" in the sense of this inequality, then we should instead have to analyze the contribution to $\delta\mathbf{u}$ from a *finite* rotation—a much more difficult matter, since finite rotations do not commute and cannot be expressed as vectors.

In terms of the infinitesimal strain tensor, defined to have components

$$e_{ij} \equiv \tfrac{1}{2}(u_{i,j} + u_{j,i}), \tag{2.3}$$

BOX 2.2
Notation

We shall use boldface symbols (e.g., $\mathbf{u}$, $\boldsymbol{\tau}$) for vector and tensor fields, and subscripts (e.g., u_i, τ_{kl}) to designate vector and tensor components in a Cartesian coordinate system. Useful references for the properties of Cartesian tensors are Jeffreys (1965) and Chapter 3 of Jeffreys and Jeffreys (1972).

For unit vectors (other than $\boldsymbol{\nu}$, $\mathbf{l}$, $\mathbf{n}$, $\mathbf{b}$), the circumflex is used (e.g., $\hat{\mathbf{x}}$). Scalar products are written as $\mathbf{a} \cdot \mathbf{b}$, and vector products are written as $\mathbf{a} \times \mathbf{b}$.

Overdots are used to indicate time derivatives (e.g., $\dot{\mathbf{u}} = \partial \mathbf{u}/\partial t$, $\ddot{\mathbf{u}} = \partial^2 \mathbf{u}/\partial t^2$), and a comma between subscripts is used for spatial derivatives (e.g., $u_{i,j} = \partial u_i/\partial x_j$).

The summation convention for repeated subscripts is followed throughout (e.g., $a_i b_i = a_1 b_1 + a_2 b_2 + a_3 b_3 = \mathbf{a} \cdot \mathbf{b}$), and frequent use is made of the Kronecker symbol δ_{ij} and the alternating tensor with components ε_{ijk}:

$$\delta_{ij} = 0 \quad \text{for} \quad i \neq j, \quad \text{and} \quad \delta_{ij} = 1 \quad \text{for} \quad i = j;$$

$$\varepsilon_{ijk} = 0 \quad \text{if any of } i, j, k \text{ are equal,}$$

otherwise

$$\varepsilon_{123} = \varepsilon_{312} = \varepsilon_{231} = -\varepsilon_{213} = -\varepsilon_{321} = -\varepsilon_{132} = 1.$$

The most important properties of these symbols are then

$$a_i = \delta_{ij} a_j, \qquad \varepsilon_{ijk} a_j b_k = (\mathbf{a} \times \mathbf{b})_i;$$

and they are linked by the properties

$$\varepsilon_{ijk}\varepsilon_{ilm} = \delta_{jl}\delta_{km} - \delta_{jm}\delta_{kl} \quad \text{and} \quad \varepsilon_{ijk}\varepsilon_{lmn} = \begin{vmatrix} \delta_{il} & \delta_{jl} & \delta_{kl} \\ \delta_{im} & \delta_{jm} & \delta_{km} \\ \delta_{in} & \delta_{jn} & \delta_{kn} \end{vmatrix}.$$

The second-order tensor $\mathbf{t}$ is symmetric if and only if $\varepsilon_{ijk} t_{jk} = 0$.

the effect of true distortion on any line-element δx_i is to change the relative position of its end points by $e_{ij}\delta x_j$. Rotation does not affect the length of the element, and the new length is

$$\begin{aligned} |\delta\mathbf{x} + \delta\mathbf{u}| &= \sqrt{\delta\mathbf{x} \cdot \delta\mathbf{x} + 2\delta\mathbf{u} \cdot \delta\mathbf{x}} && \text{(neglecting } \delta\mathbf{u} \cdot \delta\mathbf{u}) \\ &= \sqrt{\delta x_i \delta x_i + 2 e_{ij} \delta x_i \delta x_j} && \text{(from (2.2), and using (curl } \mathbf{u} \times \delta\mathbf{x}) \cdot \delta\mathbf{x} = 0) \\ &= |\delta\mathbf{x}|\,(1 + e_{ij}\nu_i\nu_j) && \text{(to first order, if } |\, e_{ij} \,| \ll 1), \end{aligned}$$

where $\boldsymbol{\nu}$ is the unit vector $\delta\mathbf{x}/|\delta\mathbf{x}|$. It follows that the extensional strain of a line-element originally in the $\boldsymbol{\nu}$ direction is $e_{ij}\nu_i\nu_j$.

To analyze the internal forces acting mutually between adjacent particles within a continuum, we use the concepts of *traction* and *stress tensor*. Traction is a vector, being the

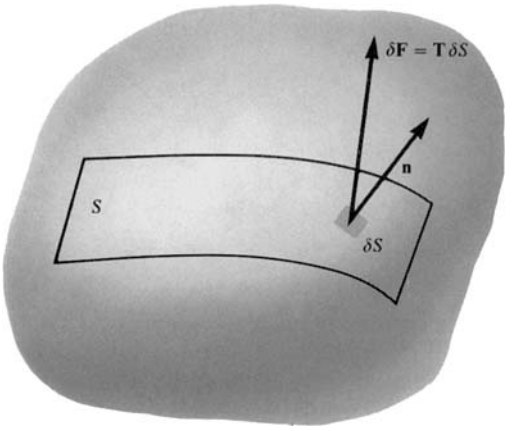

FIGURE **2.1**
The definition of traction $\mathbf{T}$ acting at a point across the internal surface S with normal $\mathbf{n}$. The choice of sign is such that traction is a pulling force. Pushing is in the opposite direction, so for a fluid medium, the pressure would be $-\mathbf{n} \cdot \mathbf{T}$.

force acting per unit area across an internal surface within the continuum, and quantifies the contact force (per unit area) with which particles on one side of the surface act upon particles on the other side. For a given point of the internal surface, traction is defined (see Fig. 2.1) by considering the infinitesimal force $\delta\mathbf{F}$ acting across an infinitesimal area δS of the surface, and taking the limit of $\delta\mathbf{F}/\delta S$ as $\delta S \to 0$. With a unit normal $\mathbf{n}$ to the surface S, the convention is adopted that $\delta\mathbf{F}$ has the direction of force due to material on the side to which $\mathbf{n}$ points and acting upon material on the side from which $\mathbf{n}$ is pointing; the resulting traction is denoted as $\mathbf{T}(\mathbf{n})$. If $\delta\mathbf{F}$ acts in the direction shown in Fig. 2.1, traction is a pulling force, opposite to a pushing force such as pressure. Thus, in a fluid, the (scalar) pressure is $-\mathbf{n} \cdot \mathbf{T}(\mathbf{n})$. For a solid, shearing forces can act across internal surfaces, and so $\mathbf{T}$ need not be parallel to $\mathbf{n}$. Furthermore, the magnitude and direction of traction depend on the orientation of the surface element δS across which contact forces are taken (whereas pressure at a point in a fluid is the same in all directions). To appreciate this orientation-dependence of traction at a point, consider a point P, as shown in Figure 2.2, on the exterior surface of a house. For an element of area on the surface of the wall at P, the traction $\mathbf{T}(\mathbf{n}_1)$ is zero (neglecting atmospheric pressure and winds); but for a horizontal element of area within the wall at P, the traction $\mathbf{T}(\mathbf{n}_2)$ may be large (and negative).

The forces acting upon particles in a solid or fluid medium consist not only of the contact forces between adjacent particles, but also of (i) forces between particles that are

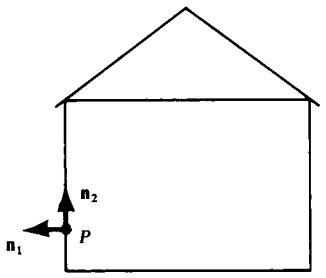

FIGURE **2.2**
$\mathbf{T}(\mathbf{n}_1) \neq \mathbf{T}(\mathbf{n}_2)$.

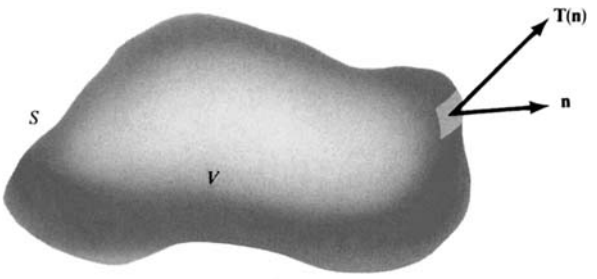

FIGURE **2.3**
A material volume V of the continuum, with surface S.

not adjacent, and (ii) forces due to the application of physical processes external to the medium itself. An example of type (i) would be the mutual gravitational forces acting between particles of the Earth. Type (ii) is illustrated by the forces on buried particles of iron when a magnet is moved around outside the medium in which the iron is contained. To these noncontact forces, we give the name *body forces*, and use the notation $\mathbf{f}(\mathbf{x}, t)$ to denote the body force acting per unit volume on the particle originally at position $\mathbf{x}$ at some reference time. It will often be useful to consider the special case of a force applied impulsively to one particular particle at $\mathbf{x} = \boldsymbol{\xi}$ and time $t = \tau$. If this force is in the direction of the x_n-axis, it follows that $f_i(\mathbf{x}, t)$ is proportional to the three-dimensional Dirac delta function $\delta(\mathbf{x} - \boldsymbol{\xi})$, specifying the spatial location; to the one-dimensional Dirac delta function $\delta(t - \tau)$, specifying the timing of the impulse; and to the Kronecker delta function δ_{in}, signifying the directional property that $f_i = 0$ for $i \neq n$. Thus the body-force distribution in this case is given by

$$f_i(\mathbf{x}, t) = A\, \delta(\mathbf{x} - \boldsymbol{\xi})\, \delta(t - \tau)\, \delta_{in}, \tag{2.4}$$

where A is a constant giving the strength of the impulse. Note that the dimensions of f_i, $\delta(\mathbf{x} - \boldsymbol{\xi})$, and $\delta(t - \tau)$ are, respectively, force per unit volume, 1/unit volume, and 1/unit time. The Kronecker delta is dimensionless, so A does have the correct physical dimension for an impulse (force $\times$ time).

We are now in a position to place a constraint on the accelerations, body forces, and tractions acting throughout a volume V with surface S (see Fig. 2.3). By equating the rate of change of momentum of particles constituting V to the forces acting on these particles, we find

$$\frac{\partial}{\partial t} \iiint_V \rho \frac{\partial \mathbf{u}}{\partial t}\, dV = \iiint_V \mathbf{f}\, dV + \iint_S \mathbf{T}(\mathbf{n})\, dS. \tag{2.5}$$

This relation is based on a Lagrangian description, and V and S move with the particles. The left-hand side can thus be written as $\iiint_V \rho(\partial^2 \mathbf{u}/\partial t^2)\, dV$, since the particle mass $\rho\, dV$ is constant in time.

Our first use of (2.5) is to obtain an explicit form for the functional relationship $\mathbf{T} = \mathbf{T}(\mathbf{n})$ and to introduce the stress tensor. Consider a particle P within the medium for which the acceleration, the body force, and the tractions are all nonsingular. Surround this particle by a small volume ΔV, and consider the relative magnitude of the three terms in

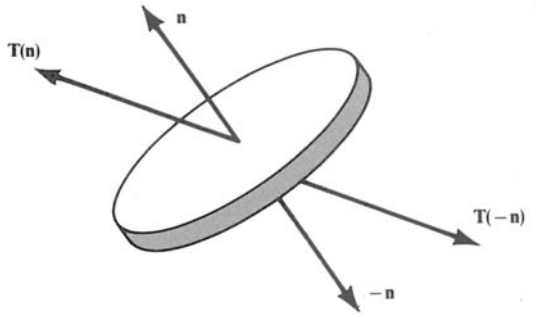

FIGURE **2.4**
A small disc within a stressed medium.

(2.5) as ΔV shrinks down onto P. The volume integrals will be of order ΔV, but the surface integral is of order $\iint_S dS$ taken over the surface of ΔV. In general such integrals are of order $(\Delta V)^{2/3}$, tending to zero more slowly than ΔV. After dividing (2.5) through by $\iint_S dS$, it follows that

$$\frac{\left|\iint \mathbf{T}\, dS\right|}{\iint dS} = O(\Delta V^{1/3}) \to 0 \quad \text{as} \quad \Delta V \to 0. \tag{2.6}$$

Now suppose that ΔV is a disc, with opposite faces having outward normals $\mathbf{n}$ and $-\mathbf{n}$ (see Fig. 2.4) and the edge having insignificant area. Equation (2.6) then implies the result

$$\mathbf{T}(-\mathbf{n}) = -\mathbf{T}(\mathbf{n}). \tag{2.7}$$

Next, take ΔV to be a small tetrahedron, with three of its faces in the coordinate planes (see Fig. 2.5) and the fourth having $\mathbf{n}$ as its outward normal. Equation (2.6) then implies

$$\frac{\mathbf{T}(\mathbf{n})ABC + \mathbf{T}(-\hat{\mathbf{x}}_1)OBC + \mathbf{T}(-\hat{\mathbf{x}}_2)OCA + \mathbf{T}(-\hat{\mathbf{x}}_3)OAB}{ABC + OBC + OCA + OAB} \to \mathbf{0} \tag{2.8}$$

as $\Delta V \to 0$. Here, the symbols ABC etc. denote areas of triangles, and one can show geometrically that the components of $\mathbf{n}$ are given by $(n_1, n_2, n_3) = (OBC, OCA, OAB)/ABC$. Then (2.8) and (2.7) yield

$$\mathbf{T}(\mathbf{n}) = \mathbf{T}(\hat{\mathbf{x}}_j)n_j, \tag{2.9}$$

which is a specific and important relationship between traction $\mathbf{T}(\mathbf{n})$ and $\mathbf{n}$ in terms of three tractions acting across coordinate planes. The properties (2.7) and (2.9) are trivial for a static medium, but we have shown them to be true even during acceleration.

The stress tensor is introduced by defining the nine quantities

$$\tau_{kl} = T_l(\hat{\mathbf{x}}_k),$$

so that τ_{kl} is the lth component of the traction acting across the plane normal to the kth axis due to material with greater x_k acting upon material with lesser x_k. Thus

$$T_i = \tau_{ji}n_j. \tag{2.10}$$

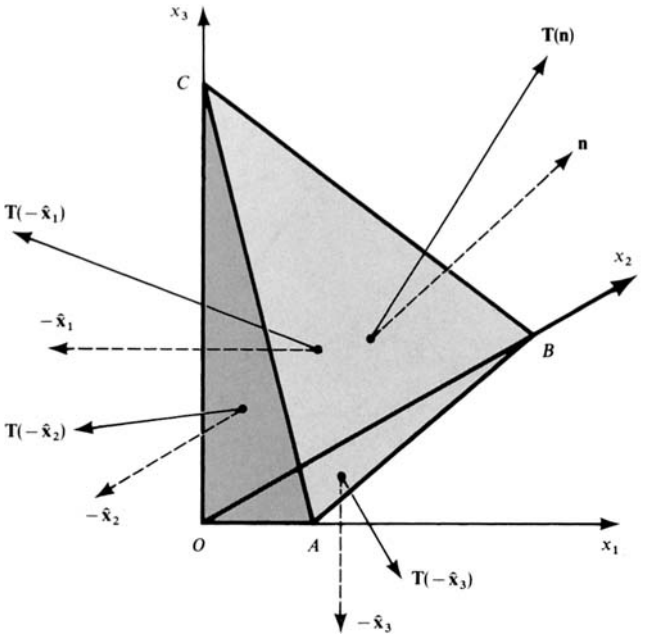

FIGURE **2.5**
The small tetrahedron *OABC* has three of its faces in the coordinate planes, with outward normals $-\hat{\mathbf{x}}_j (j = 1, 2, 3)$, and the fourth face has normal $\mathbf{n}$.

Our second use of (2.5) is to obtain the equation of motion of a general particle. Applying (2.10) and Gauss's divergence theorem to give

$$\iint_S T_i \, dS = \iint_S \tau_{ji} n_j \, dS = \iiint_V \tau_{ji,j} \, dV, \tag{2.11}$$

we find for a general volume V that

$$\iiint_V (\rho \ddot{u}_i - f_i - \tau_{ji,j}) \, dV = 0. \tag{2.12}$$

This integrand must be zero wherever it is continuous, otherwise a volume V could be found that violates (2.12), hence

$$\rho \ddot{u}_i = f_i + \tau_{ji,j}, \tag{2.13}$$

which is our first form for the equation of motion.

Another constraint upon the mechanics of motion is given by equating the rate of change of angular momentum about the origin of coordinates to the moment of forces acting on the particles in V. Thus

$$\frac{\partial}{\partial t} \iiint_V \mathbf{X} \times \rho \dot{\mathbf{u}} \, dV = \iiint_V \mathbf{X} \times \mathbf{f} \, dV + \iint_S \mathbf{X} \times \mathbf{T} \, dS, \tag{2.14}$$

where $\mathbf{X} = \mathbf{x} + \mathbf{u}$. Since $\partial \mathbf{x}/\partial t$, $\dot{\mathbf{u}} \times \dot{\mathbf{u}}$, and $\partial(\rho \, dV)/\partial t$ are all zero, the left-hand side here is $\iiint_V \mathbf{X} \times \rho \ddot{\mathbf{u}} \, dV$. Using the strict interpretation of (2.13) developed in Box 2.3,

BOX **2.3**
Euler or Lagrange?

A closer look at the application of Gauss's theorem in (2.11) shows that our Lagrangian approach is inappropriate for the spatial differentiations in (2.11)–(2.13). The particles constituting S at time t have, in general, moved from their position at the reference time t_0, so that

$$\iint_S \tau_{ji} n_j \, dS = \iiint_V \frac{\partial}{\partial X_j} \tau_{ji} \, dV,$$

where $\mathbf{X} = \mathbf{x} + \mathbf{u}$, and the spatial differentiation that must be conducted on points throughout V at time t is $\partial/\partial X_j$. For finite motions, the exact equation for motion in the continuum is therefore, in our notation,

$$\rho \frac{\partial^2 u_i}{\partial t^2} = f_i + \frac{\partial \tau_{ji}}{\partial X_j}. \qquad \text{(2.13, strict form)}$$

The Eulerian approach instead discusses field variables directly as a function of $\mathbf{X}$ and t (taking $\mathbf{u}$ to be the displacement of the particle at $\mathbf{X}$ and time t from its position $\mathbf{x}$ at time t_0), and τ_{ji} would be a stress component at $(\mathbf{X}, t)$. This offers the advantage of allowing one to work with independent variables that are natural for interpreting the right-hand side of the equation of motion, but has the disadvantage of cumbersome expressions for the rate of change of properties carried by the particles. For example, particle velocity $\mathbf{v}$ at $(\mathbf{X}, t)$ is difficult to express in terms of the displacement field $\mathbf{u} = \mathbf{u}(\mathbf{X}, t)$. The equation for $\mathbf{v}$ is given by seeing that the particle at $\mathbf{X}$ at time t has moved to $\mathbf{X} + \delta\mathbf{X}$ at time $t + \delta t$, so

$$\mathbf{v}\, \delta t = \mathbf{u}(\mathbf{X} + \delta\mathbf{X}, t + \delta t) - \mathbf{u}(\mathbf{X}, t).$$

Since $\mathbf{v}$ = limit of $\delta\mathbf{X}/\delta t$ for a fixed particle,

$$v_i = \left(\frac{\partial u_i}{\partial t}\right)_{\text{fixed position}} + v_j \left(\frac{\partial u_i}{\partial X_j}\right)_{\text{fixed time}}$$

is the implicit equation to be solved for $\mathbf{v}$ in terms of $\mathbf{u}$ (implicit, because components of $\mathbf{v}$ appear on both sides of the equation). Once the particle velocity is found, the acceleration of the particle at $(\mathbf{X}, t)$ is easily given by the material derivative $\partial\mathbf{v}/\partial t + (\mathbf{v} \cdot \nabla)\mathbf{v}$, where ∇ is the Eulerian spatial derivative, i.e., in $\mathbf{X}$ coordinates.

In seismology, the distinction between Lagrangian and Eulerian approaches rarely needs to be made, since spatial fluctuations in the displacements, strains, accelerations, and stresses have wavelengths much greater than the amplitude of particle displacements. In this case, it makes no practical difference whether a spatial gradient is evaluated at a fixed position (Euler) or for a particular particle (Lagrange). In this book we emphasize the Lagrangian approach because there is then a simple exact relationship between particle velocity and particle displacement, $\mathbf{v} = \partial\mathbf{u}(\mathbf{x}, t)/\partial t$, and because a seismometer measures the motion of the fixed particles to which it was originally attached. In fluid mechanics, where particle displacements may not be small, there is little interest in particle displacement as a field variable and the Eulerian approach is more useful.

A final acknowledgment: the "Eulerian" and "Lagrangian" approaches were both developed by Leonhard Euler.

it follows that

$$\begin{aligned}\iiint_V \varepsilon_{ijk} X_j \frac{\partial}{\partial X_l} \tau_{lk}\, dV &= \iiint_V \varepsilon_{ijk} X_j (\rho \ddot{u}_k - f_k)\, dV \\ &= \iint_S \varepsilon_{ijk} X_j T_k\, dS \qquad \text{(from (2.14))} \\ &= \iint_S \varepsilon_{ijk} X_j \tau_{lk} n_l\, dS \qquad \text{(from (2.10))}.\end{aligned}$$

Applying the divergence theorem to this surface integral and using $\partial X_j / \partial X_l = \delta_{jl}$, one obtains

$$\iiint_V \varepsilon_{ijk} \tau_{jk}\, dV = 0 \qquad \text{for any volume } V,$$

implying $\varepsilon_{ijk}\tau_{jk} = 0$ everywhere, and hence that the stress tensor is symmetric:

$$\tau_{kj} = \tau_{jk}. \tag{2.15}$$

With this fundamental result, we can finally state the formula for traction components as

$$T_i = \tau_{ij} n_j \tag{2.16}$$

and the equation of motion as

$$\rho \ddot{u}_i = f_i + \tau_{ij,j}. \tag{2.17}$$

The spatial derivative here should be carried out with respect to X_j, but (as discussed in Box 2.3) differentiation with respect to x_j is usually adequate in seismology, and will henceforth be assumed.

2.2 Stress–Strain Relations and the Strain–Energy Function

A medium is said to be *elastic* if it possesses a natural state (in which strains and stresses are zero) to which it will revert when applied forces are removed. Under the influence of applied loads, stress and strain will change together, and the relation between them, called the constitutive relation, is an important characteristic of the medium. That there is such a relation we prove below by thermodynamic arguments. The relation itself is a proper subject for experimental determination, and Robert Hooke's measurements of "springy bodies" led him, over 300 years ago, to the conclusion that stress is proportional to strain. His statements on this matter were somewhat enigmatic, as today's concepts of traction and tensor were then unavailable. Augustin Cauchy, in the early nineteenth century, was the first to develop many of our modern ideas of traction, and it is clear that he understood many results that today are more easily communicated in terms of tensors, which did not come into general use until the twentieth century. The modern generalization of Hooke's law is that each component

of the stress tensor is a linear combination of all components of the strain tensor, i.e., that there exist constants c_{ijkl} such that

$$\tau_{ij} = c_{ijpq} e_{pq}. \tag{2.18}$$

A body that obeys the constitutive relation (2.18) is said to be *linearly elastic*. The quantities c_{ijkl} are components of a fourth-order tensor, and have the symmetries

$$c_{jipq} = c_{ijpq} \qquad (\text{due to } \tau_{ji} = \tau_{ij}) \tag{2.19}$$

and

$$c_{ijqp} = c_{ijpq} \qquad (\text{due to } e_{qp} = e_{pq}). \tag{2.20}$$

It is also true from a thermodynamic argument that $c_{pqij} = c_{ijpq}$, as we now shall show.

Suppose that an elastic body occupies the volume V with surface S. The first law of thermodynamics states that the body possesses an internal (or, intrinsic) energy, which may change with deformations of the body, and the energy balance for work done on the body is:

$$\begin{aligned} &\text{Rate of doing mechanical work + Rate of heating} \\ &\quad = \text{Rate of increase of (kinetic + internal energies).} \end{aligned} \tag{2.21}$$

Let us analyze each of these terms separately.

(1) The rate of mechanical work is given by

$$\begin{aligned} &\iiint_V \mathbf{f} \cdot \dot{\mathbf{u}}\, dV + \iint_S \mathbf{T} \cdot \dot{\mathbf{u}}\, dS \\ &= \iiint_V \left[f_i \dot{u}_i + (\tau_{ij}\dot{u}_i)_{,j} \right] dV \qquad \text{(from (2.16) and Gauss's divergence theorem)} \\ &= \iiint_V (\rho \dot{u}_i \ddot{u}_i + \tau_{ij}\dot{u}_{i,j})\, dV \qquad \text{(from (2.17))} \\ &= \frac{\partial}{\partial t} \iiint_V \frac{1}{2}\rho \dot{u}_i \dot{u}_i\, dV + \iiint_V \tau_{ij}\dot{e}_{ij}\, dV \quad \text{(symmetry of } \tau_{ij} \text{ and definition of } e_{ij}). \end{aligned} \tag{2.22}$$

(2) Let $\mathbf{h}(\mathbf{x}, t)$ be the heat flux, such that $\mathbf{h} \cdot \mathbf{n}$ is the rate at which heat is transmitted (per unit area) in the $\mathbf{n}$ direction across area elements normal to $\mathbf{n}$. Let $\mathcal{Q}(\mathbf{x}, t)$ be the heat per unit volume due to input through the boundary, so that the rate of heating is given by

$$\frac{\partial}{\partial t} \iiint_V \mathcal{Q}\, dV = -\iint_S \mathbf{h} \cdot \mathbf{n}\, dS. \tag{2.23}$$

Then clearly $\dot{\mathcal{Q}} = -\nabla \cdot \mathbf{h}$.

(3) The rate of increase of kinetic energy is given by

$$\frac{\partial}{\partial t} \iiint_V \frac{1}{2}\rho \dot{u}_i \dot{u}_i\, dV. \tag{2.24}$$

(4) Let $\mathcal{U}$ be the internal energy per unit volume. Then from (2.21)–(2.24) we conclude that

$$\dot{\mathcal{U}} = -h_{i,i} + \tau_{ij}\dot{e}_{ij}, \qquad \text{or} \qquad \dot{\mathcal{U}} = \dot{\mathcal{Q}} + \tau_{ij}\dot{e}_{ij}. \tag{2.25}$$

If $\mathcal{U}$, $\mathcal{Q}$, and e_{ij} are measured as small perturbations away from a state of thermodynamic equilibrium, then (2.25) is equivalent to

$$\begin{aligned} d\mathcal{U} &= d\mathcal{Q} + \tau_{ij}\, de_{ij} \\ &= \mathcal{T}\, d\mathcal{S} + \tau_{ij}\, de_{ij} \qquad \text{(for reversible processes)}, \end{aligned} \tag{2.26}$$

in which $\mathcal{S}$ is the entropy per unit volume and $\mathcal{T}$ is the absolute temperature. Equation (2.26) implies that entropy and strain components are the state variables in terms of which internal energy is completely and uniquely specified. In particular, internal energy does not depend on the time history of strain.

It is often useful to work with a function $\mathcal{W}$ of the strain components that allows the stresses to be generated via

$$\tau_{ij} = \frac{\partial \mathcal{W}}{\partial e_{ij}}. \tag{2.27}$$

A function with this property is called a *strain–energy function*.

Note from (2.26) the formal result

$$\tau_{ij} = \left(\frac{\partial \mathcal{U}}{\partial e_{ij}}\right)_{\mathcal{S}}. \tag{2.28}$$

If the processes of deformation are adiabatic, so that $\mathbf{h} = \mathbf{0}$ and $\dot{\mathcal{Q}} = 0$, then the actual changes in $\mathcal{U}$ associated with changes in strain do occur at constant entropy, and we can choose $\mathcal{W} = \mathcal{U}$ and use (2.28). This is the situation in seismology, since the time constant of thermal diffusion in rock ((distance)^2/diffusivity) is very much longer than the period of seismic waves (wavelength/velocity).

It is also true that $\tau_{ij} = (\partial \mathcal{F}/\partial e_{ij})_{\mathcal{T}}$, where $\mathcal{F} = \mathcal{U} - \mathcal{T}\mathcal{S}$ is the *free energy* per unit volume (for which $d\mathcal{F} = -\mathcal{S}\, d\mathcal{T} + \tau_{ij}\, de_{ij}$). For deformation processes that take place so slowly as to be isothermal, as in some tectonic processes, it is then natural to form τ_{ij} from changes in the free energy, and one would choose $\mathcal{W} = \mathcal{F}$.

For all deformations such that the strain–energy function exists, we may combine its properties with Hooke's law and find

$$\frac{\partial \mathcal{W}}{\partial e_{ij}} = \tau_{ij} = c_{ijpq}e_{pq}, \tag{2.29}$$

which implies

$$c_{pqij} = c_{ijpq} \qquad \left(\text{from} \qquad \frac{\partial^2 \mathcal{W}}{\partial e_{ij}\partial e_{pq}} = \frac{\partial^2 \mathcal{W}}{\partial e_{pq}\partial e_{ij}}\right). \tag{2.30}$$

Since all the first derivatives of $\mathcal{W}$ are homogeneous (of order one) in strain components, and $\mathcal{W}$ can be taken as zero in the natural state, $\mathcal{W}$ itself must be homogeneous (of order two) in the form

$$\mathcal{W} = d_{ijpq} e_{ij} e_{pq}. \tag{2.31}$$

This quadratic is the same as $\frac{1}{2}(d_{ijpq} + d_{pqij}) e_{ij} e_{pq}$, but differentiation of (2.31) to give τ_{ij} shows that $(d_{ijpq} + d_{pqij}) = c_{ijpq}$, hence the strain–energy function is, explicitly,

$$\mathcal{W} = \tfrac{1}{2} c_{ijkl} e_{ij} e_{kl} = \tfrac{1}{2} \tau_{ij} e_{ij}. \tag{2.32}$$

Under adiabatic or isothermal conditions, the strain–energy function is positive except for the natural state (where $\mathcal{W} = 0$), so that $\frac{1}{2} c_{ijkl} e_{ij} e_{kl}$ is a positive definite quadratic form. ($\mathcal{W} \geq 0$, because we assume the natural state is stable.)

The c_{ijkl} are independent of strain, which is why they are sometimes called "elastic constants," although they are varying functions of position in the Earth. The elasticity theory used in seismology is to a large extent characterized by a preoccupation with inhomogeneous media, particularly with a spherically symmetric medium that is everywhere isotropic. In general, the symmetries (2.19), (2.20), and (2.30) reduce the number of independent components in c_{ijkl} from 81 to 21. There is considerable simplification in the case of an isotropic medium, since $\mathbf{c}$ must be isotropic. It can be shown (Jeffreys and Jeffreys, 1972) that the most general isotropic fourth-order tensor, having the symmetries of $\mathbf{c}$, has the form

$$c_{ijkl} = \lambda \delta_{ij} \delta_{kl} + \mu(\delta_{ik} \delta_{jl} + \delta_{il} \delta_{jk}). \tag{2.33}$$

This involves only two independent constants, λ and μ, known as the Lamé moduli.

Note that the results we have obtained in the present section are specialized to the case of small perturbations away from a reference state in which strain and stress are both zero. In the Earth's interior, self-gravitation is responsible for pressures of up to around 1 megabar. Even if one postulates a state of zero stress and strain for Earth materials, it is clear that the results of this section cannot directly be applied in seismology, since strains due to such pressures are not small. Using such a reference state, one must work with a theory of finite strain, in which the stress–strain relation is nonlinear. Alternatively, one can choose the static equilibrium configuration of the Earth, prior to an earthquake, as a reference state. This is the usual procedure in seismology. By definition, the reference state is one of zero strain, but now the initial stress is nonzero, and seismic motions are studied in terms of a linear relationship between strains and *incremental stresses*. Thus the stress is $\boldsymbol{\sigma}^0$ at zero strain, and is $\boldsymbol{\sigma}^0 + \boldsymbol{\tau}$ at nonzero strain, where $\tau_{ij} = c_{ijkl} e_{kl}$, and components σ^0_{ij} can be of the same order as components c_{ijkl} ($\sim$ 1 megabar).

For the present, we shall continue to neglect the effects of initial stress $\boldsymbol{\sigma}^0$. This simplification is justified in Chapter 8, where initial stresses are correctly taken into account and where a brief review is given of those aspects of the theory that need revision (Box 8.5). To quantify the effects of self-gravitation, we shall in Chapter 8 adopt an Eulerian approach.

2.3 Theorems of Uniqueness and Reciprocity

It is natural to introduce the discussion of uniqueness (for the displacement field **u** throughout a body with volume V and surface S) with some general remarks concerning the ways in which motion can be set up. Because the displacement is constrained to satisfy (2.17) throughout V, the application of body forces will generate a displacement field, as will the application of tractions on the surface S. We shall show that specification of the body forces throughout V, and tractions over all of S, is enough to determine uniquely the displacement field that will develop throughout V from given initial conditions. An alternative way to specify the influence of S on the displacement field is to give a boundary condition (on S) for the displacement itself, instead of for the traction. For example, S might be rigid. It might seem at first that the traction on S and the displacement on S are independent properties of the displacement field throughout V. This is not so, however, and it is important for an intuitive understanding of Sections 2.3–2.5 to appreciate that traction over S determines the displacement over S, and vice versa.

2.3.1 UNIQUENESS THEOREM

The displacement $\mathbf{u} = \mathbf{u}(\mathbf{x}, t)$ throughout the volume V with surface S is uniquely determined after time t_0 by the initial values of displacement and particle velocity at t_0 throughout V; and by values at all times $t \geq t_0$ of (i) the body forces **f** and the heat Q supplied throughout V; (ii) the tractions **T** over any part S_1 of S; and (iii) the displacement over the remainder S_2 of S, with $S_1 + S_2 = S$. (Either of S_1 or S_2 can be the whole of S.)

PROOF

Suppose $\mathbf{u}_1$ and $\mathbf{u}_2$ are any solutions for **u** that satisfy the same initial conditions and are set up by the same values for (i)–(iii). Then, using linearity, the difference $\mathbf{U} \equiv \mathbf{u}_1 - \mathbf{u}_2$ is a displacement field having zero initial conditions, and is set up by zero body forces, zero heating, zero traction on S_1, and $\mathbf{U} = \mathbf{0}$ on S_2. It remains to prove that $\mathbf{U} = \mathbf{0}$ throughout V for $t > t_0$.

From (2.22), the rate of doing mechanical work in the displacement field **U** is clearly zero throughout V and S_1 and S_2 for $t \geq t_0$. The last equality in (2.22) can be integrated from t_0 to t, and, together with the zero initial conditions and the use of a strain–energy function (**U** involves adiabatic changes), it follows that

$$\iiint_V \frac{1}{2}\rho \dot{U}_i \dot{U}_i \, dV + \iiint_V \frac{1}{2} c_{ijkl} U_{i,j} U_{k,l} \, dV = 0.$$

Both the kinetic and strain energies are positive definite, so that $\dot{U}_i = 0$ for $t \geq t_0$. But $U_i = 0$ at $t = t_0$, and hence $\mathbf{U} = \mathbf{0}$ throughout V for $t \geq t_0$.

2.3.2 RECIPROCITY THEOREMS

We shall state and prove several general relationships between a pair of solutions for the displacement throughout an elastic body V.

BOX **2.4**

Use of the term "homogeneous" as applied to equations and boundary conditions

The equation for elastic displacement is $\mathbf{L}(\mathbf{u}) = \mathbf{f}$, where $\mathbf{L}$ is the vector differential operator defined on the components of $\mathbf{u}$ by

$$(\mathbf{L}(\mathbf{u}))_i \equiv \rho \ddot{u}_i - (c_{ijkl} u_{k,l})_{,j}.$$

If body forces are absent, then the equation $\mathbf{L}(\mathbf{u}) = \mathbf{0}$ for $\mathbf{u}$ is said to be *homogeneous*. A *homogeneous boundary condition* on the surface S is one for which *either* the displacement *or* the traction vanishes at every point of the surface. If a solution to the homogeneous equation is multiplied by a constant, the result is still a solution (unlike the outcome of multiplying a solution to the inhomogeneous equation, $\mathbf{L}(\mathbf{u}) = \mathbf{f}$ with $\mathbf{f} \neq \mathbf{0}$, by a constant).

This terminology is reminiscent of linear algebra, for which a system of n equations in n unknowns, in the form $\mathbf{Ax} = \mathbf{0}$, is also said to be homogeneous. Here, $\mathbf{x}$ is a column vector and $\mathbf{A}$ is some $n \times n$ matrix. It is well known that nontrivial solutions ($\mathbf{x} \neq \mathbf{0}$) can exist, but only if $\mathbf{A}$ has a special property (namely, a zero determinant). The corresponding result in dynamic elasticity is that motions can occur throughout a finite elastic volume V without any body forces and with a homogeneous boundary condition over the surface of V. These are the *free oscillations* or *normal modes* of the body, which can occur only at certain frequencies. See Chapter 8.

Suppose that $\mathbf{u} = \mathbf{u}(\mathbf{x}, t)$ is one of these displacement fields, and that $\mathbf{u}$ is due to body forces $\mathbf{f}$ and boundary conditions on S and initial conditions at time $t = 0$. Let $\mathbf{v} = \mathbf{v}(\mathbf{x}, t)$ be another displacement field due to body forces $\mathbf{g}$ and to boundary conditions and initial conditions (at $t = 0$) which in general are different from the conditions for $\mathbf{u}$. To distinguish the tractions on surfaces normal to $\mathbf{n}$ in these two cases, we shall use the notation $\mathbf{T}(\mathbf{u}, \mathbf{n})$ for the traction due to the displacement $\mathbf{u}$ and, similarly, $\mathbf{T}(\mathbf{v}, \mathbf{n})$ for the traction due to $\mathbf{v}$.

The first reciprocal relation to note between $\mathbf{u}$ and $\mathbf{v}$ is

$$\begin{aligned} &\iiint_V (\mathbf{f} - \rho\ddot{\mathbf{u}}) \cdot \mathbf{v}\, dV + \iint_S \mathbf{T}(\mathbf{u}, \mathbf{n}) \cdot \mathbf{v}\, dS \\ &\quad = \iiint_V (\mathbf{g} - \rho\ddot{\mathbf{v}}) \cdot \mathbf{u}\, dV + \iint_S \mathbf{T}(\mathbf{v}, \mathbf{n}) \cdot \mathbf{u}\, dS. \end{aligned} \tag{2.34}$$

This result is due to Betti. It can easily be proved by substitution from (2.17) and (2.16) and then applying the divergence theorem to reduce the left side to $\iiint_V c_{ijkl} v_{i,j} u_{k,l}\, dV$. Similarly, the right-hand side reduces to $\iiint_V c_{ijkl} u_{i,j} v_{k,l}\, dV$, and (2.34) follows from the symmetry $c_{ijkl} = c_{klij}$.

Note that Betti's theorem does not involve initial conditions for $\mathbf{u}$ or $\mathbf{v}$. Furthermore, it remains true even if the quantities $\mathbf{u}, \ddot{\mathbf{u}}, \mathbf{T}(\mathbf{u}, \mathbf{n})$, and $\mathbf{f}$ are evaluated at time t_1 but $\mathbf{v}, \ddot{\mathbf{v}}, \mathbf{T}(\mathbf{v}, \mathbf{n})$, and $\mathbf{g}$ are evaluated at a different time t_2. If we choose $t_1 = t$ and $t_2 = \tau - t$

BOX **2.5**
Parallels

A rearrangement of Betti's relation (2.34) gives

$$\iiint_V \{v_i(c_{ijkl}u_{k,l})_{,j} - u_i(c_{ijkl}v_{k,l})_{,j}\}\, dV = \iint_S \{v_i T_i(\mathbf{u},\mathbf{n}) - u_i T_i(\mathbf{v},\mathbf{n})\}\, dS.$$

This is a vector theorem for the second-order spatial derivatives occurring in the wave equation of elasticity, which is analogous to Green's theorem

$$\iiint_V (\psi\nabla^2\phi - \phi\nabla^2\psi)\, dV = \iint_S \left(\psi\frac{\partial\phi}{\partial n} - \phi\frac{\partial\psi}{\partial n}\right) dS$$

for scalars and the Laplacian operator. Green's theorem is a working tool for studying inhomogeneous equations, such as $\nabla^2\phi = -4\pi\rho$, and we shall use Betti's theorem for the elastic wave equation, in which the inhomogeneity is the body-force term.

There are many further analogies between Dirichlet problems (for potentials that are zero on S) and elasticity problems with rigid boundaries; and between Neumann problems ($\partial\phi/\partial n = 0$ on S) and traction-free boundaries.

and integrate (2.34) over the temporal range 0 to τ, then the acceleration terms reduce to terms that depend only on the initial and final values, since

$$\begin{aligned}\int_0^\tau &\rho\{\ddot{\mathbf{u}}(t)\cdot\mathbf{v}(\tau-t) - \mathbf{u}(t)\cdot\ddot{\mathbf{v}}(\tau-t)\}\, dt \\ &= \rho\int_0^\tau \frac{\partial}{\partial t}\{\dot{\mathbf{u}}(t)\cdot\mathbf{v}(\tau-t) + \mathbf{u}(t)\cdot\dot{\mathbf{v}}(\tau-t)\}\, dt \\ &= \rho\,\{\dot{\mathbf{u}}(\tau)\cdot\mathbf{v}(0) - \dot{\mathbf{u}}(0)\cdot\mathbf{v}(\tau) + \mathbf{u}(\tau)\cdot\dot{\mathbf{v}}(0) - \mathbf{u}(0)\cdot\dot{\mathbf{v}}(\tau)\}\,.\end{aligned}$$

If there is some time τ_0 before which $\mathbf{u}$ and $\mathbf{v}$ are everywhere zero throughout V (and hence $\dot{\mathbf{u}} = \dot{\mathbf{v}} = 0$ for $\tau \le \tau_0$), then it follows that the convolution

$$\int_{-\infty}^{\infty} \rho\{\ddot{\mathbf{u}}(t)\cdot\mathbf{v}(\tau-t) - \mathbf{u}(t)\cdot\ddot{\mathbf{v}}(\tau-t)\}\, dt$$

is zero. We deduce from Betti's theorem the important result, for displacement fields with a quiescent past, that

$$\begin{aligned}&\int_{-\infty}^{\infty} dt \iiint_V \{\mathbf{u}(\mathbf{x},t)\cdot\mathbf{g}(\mathbf{x},\tau-t) - \mathbf{v}(\mathbf{x},\tau-t)\cdot\mathbf{f}(\mathbf{x},t)\}\, dV \\ &= \int_{-\infty}^{\infty} dt \iint_S \{\mathbf{v}(\mathbf{x},\tau-t)\cdot\mathbf{T}(\mathbf{u}(\mathbf{x},t),\mathbf{n}) - \mathbf{u}(\mathbf{x},t)\cdot\mathbf{T}(\mathbf{v}(\mathbf{x},\tau-t),\mathbf{n})\}\, dS.\end{aligned} \tag{2.35}$$

2.4 Introducing Green's Function for Elastodynamics

A major aim of this chapter and the next is the development of a representation for the displacements that typically occur in seismology. The representation will be a formula for the displacement (at a general point in space and time) in terms of the quantities that originated the motion, and we have seen (in the uniqueness theorem) that these are body forces and applied tractions or displacements over the surface of the elastic body under discussion. For earthquake faulting, the seismic source is complicated in that it extends over a finite fault plane (or a finite volume) and over a finite amount of time, and in general involves motions (at the source) that have varying direction and magnitude. We shall find that the representation theorem is really nothing but a bookkeeping device by which the displacement from realistic source models is synthesized from the displacement produced by the simplest of sources—namely, the unidirectional unit impulse, which is localized precisely in both space and time.

The displacement field from such a simple source is the elastodynamic Green function. If the unit impulse is applied at $\mathbf{x} = \boldsymbol{\xi}$ and $t = \tau$ and in the n-direction (see (2.4), taking A = unit constant with dimensions of impulse), then we denote the ith component of displacement at general $(\mathbf{x}, t)$ by $G_{in}(\mathbf{x}, t; \boldsymbol{\xi}, \tau)$. Clearly, this Green function is a tensor (we shall work throughout with Cartesian tensors, and therefore do not distinguish between tensors and dyadics). It depends on both receiver and source coordinates, and satisfies the equation

$$\rho \frac{\partial^2}{\partial t^2} G_{in} = \delta_{in}\, \delta(\mathbf{x} - \boldsymbol{\xi})\, \delta(t - \tau) + \frac{\partial}{\partial x_j}\left(c_{ijkl} \frac{\partial}{\partial x_l} G_{kn} \right) \tag{2.36}$$

throughout V. We shall invariably use the initial conditions that $\mathbf{G}(\mathbf{x}, t; \boldsymbol{\xi}, \tau)$ and $\partial\{\mathbf{G}(\mathbf{x}, t; \boldsymbol{\xi}, \tau)\}/\partial t$ are zero for $t \leq \tau$ and $\mathbf{x} \neq \boldsymbol{\xi}$. To specify $\mathbf{G}$ uniquely it remains to state the boundary conditions on S, and we shall use a variety of different boundary conditions in different applications.

If the boundary conditions are independent of time (e.g., S always rigid), then the time origin can be shifted at will, and we see from (2.36) that $\mathbf{G}$ depends on t and τ only via the combination $t - \tau$. Hence

$$\mathbf{G}(\mathbf{x}, t; \boldsymbol{\xi}, \tau) = \mathbf{G}(\mathbf{x}, t - \tau; \boldsymbol{\xi}, 0) = \mathbf{G}(\mathbf{x}, -\tau; \boldsymbol{\xi}, -t), \tag{2.37}$$

which is a reciprocal relation for source and receiver times.

If $\mathbf{G}$ satisfies homogeneous boundary conditions on S, then (2.35) can be used to obtain an important reciprocal relation for source and receiver positions. One takes $\mathbf{f}$ to be a unit impulse applied in the m-direction at $\mathbf{x} = \boldsymbol{\xi}_1$ and time $t = \tau_1$, and $\mathbf{g}$ to be a unit impulse applied in the n-direction at $\mathbf{x} = \boldsymbol{\xi}_2$ and time $t = -\tau_2$. Then $u_i = G_{im}(\mathbf{x}, t; \boldsymbol{\xi}_1, \tau_1)$ and $v_i = G_{in}(\mathbf{x}, t; \boldsymbol{\xi}_2, -\tau_2)$, so that (2.35) directly yields

$$G_{nm}(\boldsymbol{\xi}_2, \tau + \tau_2; \boldsymbol{\xi}_1, \tau_1) = G_{mn}(\boldsymbol{\xi}_1, \tau - \tau_1; \boldsymbol{\xi}_2, -\tau_2). \tag{2.38}$$

Choosing $\tau_1 = \tau_2 = 0$, this becomes

$$G_{nm}(\xi_2, \tau; \xi_1, 0) = G_{mn}(\xi_1, \tau; \xi_2, 0), \tag{2.39}$$

which specifies a purely spatial reciprocity. Choosing $\tau = 0$ in (2.38) gives

$$G_{nm}(\xi_2, \tau_2; \xi_1, \tau_1) = G_{mn}(\xi_1, -\tau_1; \xi_2, -\tau_2), \tag{2.40}$$

which specifies a space–time reciprocity.

The actual computation of an elastodynamic Green function can itself be a complicated problem. We shall take up this subject in later chapters, beginning in Chapter 4 with the simplest of elastic solids (homogeneous, isotropic, infinite) and moving on to the case of large separation between source and receiver in inhomogeneous media.

2.5 Representation Theorems

If the integrated form of Betti's theorem, our equation (2.35), is used with a Green function for one of the displacement fields, then a representation for the other displacement field becomes available.

Specifically, suppose we are interested in finding an expression for the displacement $\mathbf{u}$ due both to body forces $\mathbf{f}$ throughout V and to boundary conditions on S. We substitute into (2.35) the body force $g_i(\mathbf{x}, t) = \delta_{in}\,\delta(\mathbf{x} - \xi)\,\delta(t)$, for which the corresponding solution is $v_i(\mathbf{x}, t) = G_{in}(\mathbf{x}, t; \xi, 0)$, and find

$$\begin{aligned} u_n(\xi, \tau) = &\int_{-\infty}^{\infty} dt \iiint_V f_i(\mathbf{x}, t) G_{in}(\mathbf{x}, \tau - t; \xi, 0)\, dV \\ &+ \int_{-\infty}^{\infty} dt \iint_S \{G_{in}(\mathbf{x}, \tau - t; \xi, 0) T_i(\mathbf{u}(\mathbf{x}, t), \mathbf{n}) \\ &\qquad - u_i(\mathbf{x}, t) c_{ijkl} n_j G_{kn,l}(\mathbf{x}, \tau - t; \xi, 0)\}\, dS. \end{aligned}$$

Before giving a physical interpretation of this equation, it is helpful to interchange the symbols $\mathbf{x}$ and ξ and the symbols t and τ. This permits $(\mathbf{x}, t)$ to be the general position and time at which a displacement is to be evaluated, regarded as an integral over volume and surface elements at varying ξ with a temporal convolution. The result is

$$\begin{aligned} u_n(\mathbf{x}, t) = &\int_{-\infty}^{\infty} d\tau \iiint_V f_i(\xi, \tau) G_{in}(\xi, t - \tau; \mathbf{x}, 0)\, dV(\xi) \\ &+ \int_{-\infty}^{\infty} d\tau \iint_S \{G_{in}(\xi, t - \tau; \mathbf{x}, 0) T_i(\mathbf{u}(\xi, \tau), \mathbf{n}) \\ &\qquad - u_i(\xi, \tau) c_{ijkl} n_j G_{kn,l}(\xi, t - \tau; \mathbf{x}, 0)\}\, dS(\xi). \end{aligned} \tag{2.41}$$

This is our first representation theorem. It states a way in which the displacement $\mathbf{u}$ at a certain point is made up from contributions due to the force $\mathbf{f}$ throughout V, plus

contributions due to the traction $\mathbf{T}(\mathbf{u}, \mathbf{n})$ and to the displacement $\mathbf{u}$ itself on S. However, the way in which each of these three contributions is weighted is unsatisfactory, since each involves a Green function with source at $\mathbf{x}$ and observation point at ξ. (Note that the last term in (2.41) involves differentiation with respect to ξ_l.) We want $\mathbf{x}$ to be the observation point, so that the total displacement obtained there can be regarded as the sum (integral) of contributing displacements at $\mathbf{x}$ due to each volume element and surface element. The reciprocal theorem for $\mathbf{G}$ must be invoked, but this will require extra conditions on Green's function itself, since the equation $G_{in}(\xi, t-\tau; \mathbf{x}, 0) = G_{ni}(\mathbf{x}, t-\tau; \xi, 0)$ (see (2.39)) was proved only if $\mathbf{G}$ satisfies homogeneous boundary conditions on S, whereas (2.41) is valid for *any* Green function set up by an impulsive force in the n-direction at $\xi = \mathbf{x}$ and $\tau = t$.

We shall examine two different cases. Suppose, first, that Green's function is determined with S as a rigid boundary. We write $\mathbf{G}^{\text{rigid}}$ for this function and $G_{in}^{\text{rigid}}(\xi, t-\tau; \mathbf{x}, 0) = 0$ for ξ in S. Then (2.41) becomes

$$\begin{aligned} u_n(\mathbf{x}, t) = &\int_{-\infty}^{\infty} d\tau \iiint_V f_i(\xi, \tau) G_{ni}^{\text{rigid}}(\mathbf{x}, t-\tau; \xi, 0)\, dV \\ &- \int_{-\infty}^{\infty} d\tau \iint_S u_i(\xi, \tau) c_{ijkl} n_j \frac{\partial}{\partial \xi_l} G_{nk}^{\text{rigid}}(\mathbf{x}, t-\tau; \xi, 0)\, dS. \end{aligned} \tag{2.42}$$

Alternatively, we can use $\mathbf{G}^{\text{free}}$ as Green's function, so that the traction $c_{ijkl} n_j (\partial/\partial \xi_l) G_{kn}^{\text{free}}(\xi, t-\tau; \mathbf{x}, 0)$ is zero for ξ in S, finding

$$\begin{aligned} u_n(\mathbf{x}, t) = &\int_{-\infty}^{\infty} d\tau \iiint_V f_i(\xi, \tau) G_{in}^{\text{free}}(\mathbf{x}, t-\tau; \xi, 0)\, dV \\ &+ \int_{-\infty}^{\infty} d\tau \iint_S G_{ni}^{\text{free}}(\mathbf{x}, t-\tau; \xi, 0) T_i(\mathbf{u}(\xi, \tau), \mathbf{n})\, dS. \end{aligned} \tag{2.43}$$

Equations (2.41)–(2.43) are all different forms of the representation theorem and each has its special uses. Taken together, they seem to imply a contradiction to the question of whether $\mathbf{u}(\mathbf{x}, t)$ depends upon displacement on S (see (2.42)) or traction (see (2.43)) or both (see (2.41)). But since traction and displacement cannot be specified independently on the surface of an elastic medium, there is no contradiction. In (2.41), the Green function is not completely defined.

The surface on which values of traction (or displacement) are explicitly required has been taken, in this chapter, as external to the volume V. It is often useful instead to take this surface to include two adjacent internal surfaces, being the opposite faces of a buried fault. Specialized forms of the representation theorem can then be developed, which enable one to analyze the earthquakes set up by activity on a buried fault. This subject is central to earthquake source theory, taken up in Chapter 3 and developed much further in Chapters 10 and 11.

So far, we have considered only Cartesian coordinate systems. In practice, the seismologist is often required to use non-Cartesian coordinates that allow the physical relationship between components of displacement, stress, and strain to be simplified for the geometry of

a particular problem. We do this because it is often found that a boundary condition must be applied on a surface on which a general curvilinear coordinate is constant. Many texts derive formulas in general orthogonal coordinates for vector operations such as grad, div, curl, and ∇^2, but rather more is needed to analyze the vector operations required in elasticity, as we next discuss.

2.6 Strain–Displacement Relations and Displacement–Stress Relations in General Orthogonal Curvilinear Coordinates

Continuing with the notation developed in Box 2.6, we shall first obtain relations between strain components e^{pq} and displacement components u^r that generalize the usual Cartesian result $e_{ij} = \frac{1}{2}(\partial u_i/\partial x_j + \partial u_j/\partial x_i)$. By e^{pq}, we merely mean the components of the Cartesian second-order tensor $\mathbf{e}$, referred to rotated Cartesian axes, which are defined (at the point of interest) to lie along the directions $\mathbf{n}^1, \mathbf{n}^2, \mathbf{n}^3$. Thus we emphasize the physical components of strain, rather than the general tensor components (which may not even have the dimensions of strain). Our problem is to express e^{pq} in terms of derivatives (with respect to c^1, c^2, c^3) of the physical components of displacement also resolved along $\mathbf{n}^1, \mathbf{n}^2, \mathbf{n}^3$: the difficulties that arise are due (a) to spatial changes in the scaling functions h^1, h^2, h^3, and (b) to spatial changes in the directions $\mathbf{n}^1, \mathbf{n}^2, \mathbf{n}^3$.

Direction cosines of the rotated Cartesian axis along $\mathbf{n}^p$ are (n_1^p, n_2^p, n_3^p), referred to the Cartesian axes $\hat{\mathbf{x}}_1, \hat{\mathbf{x}}_2, \hat{\mathbf{x}}_3$ (which are in the same fixed direction at every point). Therefore, from the fundamental transformation property of Cartesian vector and tensor components,

$$u^p = n_i^p u_i \quad \text{(the summation convention is retained for repeated subscripts)} \tag{2.44}$$

$$e^{pq} = n_i^p n_j^q e_{ij}$$

$$= \frac{1}{h^p h^q}\frac{\partial x_i}{\partial c^p}\frac{\partial x_j}{\partial c^q}\frac{1}{2}\left(\frac{\partial u_i}{\partial x_j} + \frac{\partial u_j}{\partial x_i}\right) \quad \text{(from (3) in Box 2.6; no summation over superscripts)}$$

$$= \frac{1}{2h^p h^q}\left(\frac{\partial x_i}{\partial c^p}\frac{\partial u_i}{\partial c^q} + \frac{\partial x_i}{\partial c^q}\frac{\partial u_i}{\partial c^p}\right) \quad \text{(reversing the chain rule in the previous line)}$$

$$= \frac{1}{2h^q}\left[\frac{\partial}{\partial c^q}\left(\frac{u_i}{h^p}\frac{\partial x_i}{\partial c^p}\right) - u_i\frac{\partial}{\partial c^q}\left(\frac{1}{h^p}\frac{\partial x_i}{\partial c^p}\right)\right]$$

$$+ \frac{1}{2h^p}\left[\frac{\partial}{\partial c^p}\left(\frac{u_i}{h^q}\frac{\partial x_i}{\partial c^q}\right) - u_i\frac{\partial}{\partial c^p}\left(\frac{1}{h^q}\frac{\partial x_i}{\partial c^q}\right)\right]$$

$$= \frac{1}{2h^q}\frac{\partial u^p}{\partial c^q} + \frac{1}{2h^p}\frac{\partial u^q}{\partial c^p} - \frac{1}{2}u_i\left[\frac{1}{h^q}\frac{\partial}{\partial c^q}n_i^p + \frac{1}{h^p}\frac{\partial}{\partial c^p}n_i^q\right] \quad \text{(from (3) in Box 2.6, and (2.44))}$$

$$= \frac{1}{2h^q}\frac{\partial u^p}{\partial c^q} + \frac{1}{2h^p}\frac{\partial u^q}{\partial c^p} - \frac{1}{2}\mathbf{u}\cdot\left[\frac{1}{h^q}\frac{\partial \mathbf{n}^p}{\partial c^q} + \frac{1}{h^p}\frac{\partial \mathbf{n}^q}{\partial c^p}\right].$$

BOX **2.6**

General properties of orthogonal curvilinear coordinates

Consider a point at the vector position $\mathbf{x}$ to be specified by three parameters, c^1, c^2, c^3. That is, each of the three components of $\mathbf{x}$ (in some Cartesian coordinate system) is a scalar function of the c^p:

$$x_i = x_i(c^1, c^2, c^3) \qquad (i = 1, 2, 3).$$

We suppose that these functions x_i have continuous derivatives and that there are inverse functions

$$c^p = c^p(x_1, x_2, x_3) \qquad (p = 1, 2, 3) \qquad \text{or} \qquad c^p = c^p(\mathbf{x}),$$

so that the equation $c^p =$ constant can be thought of as a coordinate surface for each p, and these three surfaces intersect in pairs on lines along which only one of the c^1, c^2, c^3 is varying. We use superscripts for quantities identified with the general curvilinear system.

Let $\mathbf{n}^p$ be the unit normal to the coordinate surface $c^p =$ constant, and suppose $\mathbf{x}$ and $\mathbf{x} + d\mathbf{x}$ both lie in this surface. Then $c^p(\mathbf{x}) = c^p(\mathbf{x} + d\mathbf{x})$, and hence $d\mathbf{x} \cdot \nabla c^p = 0$, using the Taylor expansion of $c^p(\mathbf{x} + d\mathbf{x})$. Since $d\mathbf{x}$ is *any* line element within the surface, it follows that ∇c^p is normal to $c^p =$ constant, and ∇c^p must be parallel to $\mathbf{n}^p$.

Let the length of vector ∇c^p be $1/h^p$ (a scaling factor). Then

$$\mathbf{n}^p = h^p \nabla c^p. \tag{1}$$

(We drop the summation convention for superscripts, but retain it for subscripts, these being related to the original Cartesian system.)

We shall assume that c^1, c^2, c^3 form a *right-handed orthogonal system*, i.e., that

$$\mathbf{n}^p \cdot \mathbf{n}^q = \delta^{pq} \qquad \text{(the Kronecker delta)}, \tag{2}$$

and that $\mathbf{n}^3 = \mathbf{n}^1 \times \mathbf{n}^2$.

Using n_i^p for the ith Cartesian component of $\mathbf{n}^p$, we can now obtain an important relation between $\mathbf{n}^p$ and $\partial \mathbf{x}/\partial c^p$, as follows:

$$\mathbf{n}^p = n_i^p \hat{\mathbf{x}}_i = n_i^p \frac{\partial \mathbf{x}}{\partial x_i} = \sum_q n_i^p \frac{\partial \mathbf{x}}{\partial c^q} \frac{\partial c^q}{\partial x_i} \qquad \text{(the chain rule)}$$

$$= \sum_q n_i^p \frac{n_i^q}{h^q} \frac{\partial \mathbf{x}}{\partial c^q} \qquad \text{(from (1))} \qquad = \sum_q \frac{\delta^{pq}}{h^q} \frac{\partial \mathbf{x}}{\partial c^q} \qquad \text{(from (2))}$$

and hence

$$\mathbf{n}^p = \frac{1}{h^p} \frac{\partial \mathbf{x}}{\partial c^p}. \tag{3}$$

A small change $d\mathbf{x}$ in position is associated with a small change in each of coordinates c^1, c^2, c^3 by $d\mathbf{x} = \sum_p (\partial \mathbf{x}/\partial c^p) dc^p$, and the magnitude of this change is given by

$$(ds)^2 = d\mathbf{x} \cdot d\mathbf{x} = \sum_p \frac{\partial \mathbf{x}}{\partial c^p} dc^p \cdot \sum_q \frac{\partial \mathbf{x}}{\partial c^q} dc^q$$

$$= (h^1\, dc^1)^2 + (h^2\, dc^2)^2 + (h^3\, dc^3)^2 \qquad \text{(from (3) and (2))}. \tag{4}$$

(continued)

BOX **2.6** *(continued)*

This result leads to one of the quickest ways of actually finding the scaling functions: the Euclidean distance associated with increment dc^1 along $\mathbf{n}^1$ is $h^1 dc^1$; and similarly for h^2 and h^3.

In Section 2.6, we need formulas for derivatives of the type $\partial \mathbf{n}^p / \partial c^q$ in terms of the undifferentiated normals. From (2) and (3), the equations to be satisfied are

$$\begin{aligned} &\mathbf{n}^p \cdot \frac{\partial \mathbf{n}^q}{\partial c^r} + \mathbf{n}^q \cdot \frac{\partial \mathbf{n}^p}{\partial c^r} = 0 \qquad \text{(18 different scalar equations)} \\ &\frac{\partial}{\partial c^q}(h^p \mathbf{n}^p) = \frac{\partial}{\partial c^p}(h^q \mathbf{n}^q) \qquad \text{(3 nontrivial vector equations).} \end{aligned} \tag{5}$$

The above are 27 different scalar equations for the 27 scalar unknowns in $\partial \mathbf{n}^p / \partial c^q$, and hence are exactly enough to determine the solution. In vector form, this solution is

$$\frac{\partial \mathbf{n}^p}{\partial c^q} = \frac{\mathbf{n}^q}{h^p} \frac{\partial h^q}{\partial c^p} - \delta^{pq} \left[\frac{\mathbf{n}^1}{h^1} \frac{\partial h^p}{\partial c^1} + \frac{\mathbf{n}^2}{h^2} \frac{\partial h^p}{\partial c^2} + \frac{\mathbf{n}^3}{h^3} \frac{\partial h^p}{\partial c^3} \right], \tag{6}$$

as may be verified by direct substitution back into (5).

In this form, we can use the final equation of Box 2.6 to obtain

$$e^{pq} = \frac{1}{2} \left[\frac{h^p}{h^q} \frac{\partial}{\partial c^q} \left(\frac{u^p}{h^p} \right) + \frac{h^q}{h^p} \frac{\partial}{\partial c^p} \left(\frac{u^q}{h^q} \right) \right] + \frac{\delta^{pq}}{h^q} \left[\frac{u^1}{h^1} \frac{\partial h^p}{\partial c^1} + \frac{u^2}{h^2} \frac{\partial h^p}{\partial c^2} + \frac{u^3}{h^3} \frac{\partial h^p}{\partial c^3} \right], \tag{2.45}$$

in which all reference to the Cartesian system (x_1, x_2, x_3) has at last been eliminated. Only the first square bracket is required for the off-diagonal components ($p \neq q$), but for a typical diagonal component (2.45) reduces to, e.g.,

$$e^{11} = \frac{1}{h^1} \frac{\partial u^1}{\partial c^1} + \frac{u^2}{h^1 h^2} \frac{\partial h^1}{\partial c^2} + \frac{u^3}{h^3 h^1} \frac{\partial h^1}{\partial c^3}. \tag{2.46}$$

To obtain the displacement–stress relations for general orthogonal components of $\mathbf{u}$ and $\boldsymbol{\tau}$, we follow steps similar to the derivation of $\rho \ddot{u}_i = \tau_{ij,j}$ given in Section 2.1 for fixed Cartesian directions. The principal difficulty lies in interpreting $\iint_S \mathbf{T}\, dS$, the integral of traction acting across the surface S with volume V. With ν as the outward normal on dS,

$$\begin{aligned} T_i(\nu)\, dS &= \tau_{ij} \nu_j \, dS \\ &= \sum_{p,q} \tau^{pq} n_i^p n_j^q \nu_j dS \qquad \text{(transformation to components in rotated Cartesians)} \\ &= \sum_{p,q} \tau^{pq} n_i^p \nu^q \, dS, \end{aligned}$$

where ν^q is the component of the normal to dS, resolved along $\mathbf{n}^q$.

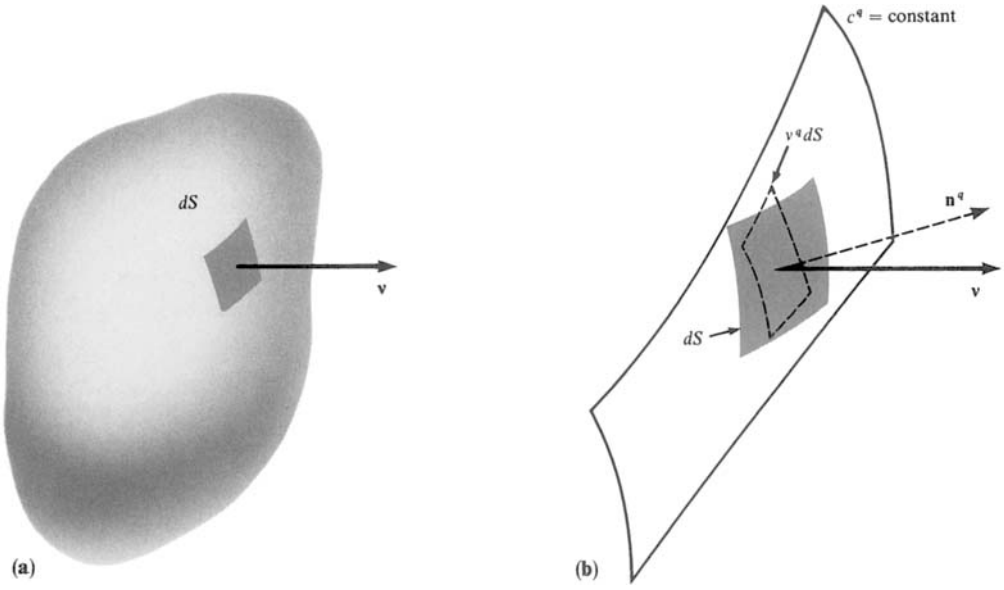

FIGURE **2.6**
The projection of dS onto the surface c^q = constant. The resulting area on the coordinate surface is $v^q\, dS$. (**a**) Shown here is dS as part of the surface of V. (**b**) The projection of dS, in broken outline, onto the coordinate surface c^q = constant.

Now $v^q\, dS$ is the projection of dS onto the surface c^q = constant (see Fig. 2.6), so that $v^1\, dS = h^2h^3\, dc^2\, dc^3$; similarly for $v^2\, dS$ and $v^3\, dS$. It follows that

$$\begin{aligned}\iint_S T_i\, dS &= \sum_p \iint_S [\tau^{p1} n_i^p h^2 h^3\, dc^2\, dc^3 + \tau^{p2} n_i^p h^3 h^1\, dc^3\, dc^1 \\ &\qquad + \tau^{p3} n_i^p h^1 h^2\, dc^1\, dc^2] \\ &= \sum_p \iiint_V \left[\frac{\partial}{\partial c^1}(\tau^{p1} n_i^p h^2 h^3) + \frac{\partial}{\partial c^2}(\tau^{p2} n_i^p h^3 h^1)\right. \\ &\qquad \left. + \frac{\partial}{\partial c^3}(\tau^{p3} n_i^p h^1 h^2)\right] dc^1\, dc^2\, dc^3.\end{aligned}$$

But the physical volume element dV is $h^1h^2h^3\, dc^1\, dc^2\, dc^3$, so from steps parallel to the derivation of the equation of motion given in Section 2.1, we find here that

$$\rho \frac{\partial^2 \mathbf{u}}{\partial t^2} = \mathbf{f} + \frac{1}{h^1h^2h^3} \sum_{p,q} \frac{\partial}{\partial c^q} \left(\tau^{pq}\, \mathbf{n}^p\, \frac{h^1h^2h^3}{h^q}\right). \tag{2.47}$$

Again, the derivative $\partial \mathbf{n}^p / \partial c^q$ is needed (see (6) in Box 2.6), and by resolving (2.47) along direction $\mathbf{n}^1$ we find

$$\rho \frac{\partial^2 u^1}{\partial t^2} = f^1 + \frac{1}{h^1 h^2 h^3}\left[\frac{\partial}{\partial c^1}(\tau^{11} h^2 h^3) + \frac{\partial}{\partial c^2}(\tau^{12} h^3 h^1) + \frac{\partial}{\partial c^3}(\tau^{31} h^1 h^2)\right] + \frac{\tau^{12}}{h^1 h^2}\frac{\partial h^1}{\partial c^2} + \frac{\tau^{31}}{h^3 h^1}\frac{\partial h^1}{\partial c^3} - \frac{\tau^{22}}{h^1 h^2}\frac{\partial h^2}{\partial c^1} - \frac{\tau^{33}}{h^3 h^1}\frac{\partial h^3}{\partial c^1}. \tag{2.48}$$

Similar results for $\rho \ddot{u}^2$ and $\rho \ddot{u}^3$ can be found from a permutation of superscripts in (2.48).

The stress–strain relation, $\tau_{ij} = c_{ijkl} e_{kl}$, becomes

$$\tau_{ij} = \lambda \delta_{ij} e_{kk} + 2\mu e_{ij} \tag{2.49}$$

in isotropic media. We have used (2.33) here: λ and μ are (in general) functions of position, and $e_{kk} = e_{11} + e_{22} + e_{33}$ is the volumetric strain. Equation (2.49) is expressed in terms of components in the fixed-direction Cartesian system, but the corresponding result for physical components in the general orthogonal system has the same form. It is

$$\tau^{pq} = \lambda \delta^{pq} \sum_r e^{rr} + 2\mu e^{pq}, \tag{2.50}$$

since isotropy of the medium implies $c^{pqrs} = c_{pqrs}$, and we can again use (2.33). The only difference in the form of (2.49) and (2.50) is due to our using a summation convention for subscripts but not for superscripts.

Applications of (2.46), (2.48), and (2.50) are common in spherical polars (r, θ, ϕ), for which the scaling functions h^1, h^2, h^3 become, respectively, $1, r, r \sin\theta$; and, in cylindrical polars, (r, ϕ, z) with scaling functions $1, r, 1$. In Chapter 4 we shall use orthogonal curvilinear coordinates associated with the wavefronts and rays that emanate from a point source in an inhomogeneous isotropic medium. Our convention of superscripts is convenient for the derivation of (2.45)–(2.50), but in applications the superscripts are usually replaced by subscripts that directly indicate the coordinate of interest. Thus, if (c^1, c^2, c^3) are the spherical polars (r, θ, ϕ), one refers to e^{12} as $e_{r\theta}$, to u^3 as u_ϕ, and to $\mathbf{n}^2$ as $\hat{\boldsymbol{\theta}}$.

Suggestions for Further Reading

Achenbach, J. D. *Wave Propagation in Elastic Solids*. Amsterdam: North-Holland, 1973.

Fung, Y. C. *Foundations of Solid Mechanics*. Englewood Cliffs, New Jersey: Prentice-Hall, 1965.

Jeffreys, H. *Cartesian Tensors*. Cambridge University Press, 1965.

Love, A. E. H. *A Treatise on the Mathematical Theory of Elasticity*. New York: Dover Publications, 1944.

Malvern, L. E. *Introduction to the Mechanics of a Continuous Medium*. Englewood Cliffs, New Jersey: Prentice-Hall, 1969.

Problems

2.1 Show that the displacement equation for infinitesimal motion in an elastic anisotropic medium is

$$\rho \ddot{u}_i = f_i + (c_{ijkl} u_{k,l})_{,j}.$$

If the medium is homogeneous and isotropic, show that this displacement equation becomes

$$\rho \ddot{u}_i = f_i + (\lambda + \mu) u_{j,ji} + \mu u_{i,jj}.$$

The above two equations are the ith Cartesian component of a vector equation. Show that this vector equation, for the homogeneous isotropic medium, is

$$\rho \ddot{\mathbf{u}} = \mathbf{f} + (\lambda + 2\mu)\nabla(\nabla \cdot \mathbf{u}) - \mu \nabla \times (\nabla \times \mathbf{u}).$$

2.2 From the expression for $\varepsilon_{ijk}\varepsilon_{lmn}$ in Box 2.2, show that

$$\varepsilon_{ijk}\varepsilon_{ilm} = \delta_{jl}\delta_{km} - \delta_{jm}\delta_{kl} \quad \text{and} \quad \varepsilon_{ijk}\varepsilon_{jlm} = \delta_{im}\delta_{kl} - \delta_{il}\delta_{km}.$$

2.3 For an isotropic elastic solid in which the stress–strain relation is $\tau_{ij} = \lambda e_{kk}\delta_{ij} + 2\mu e_{ij}$, show that the strain–stress relation is

$$2\mu e_{ij} = -\frac{\lambda}{3\lambda + 2\mu}\tau_{kk}\delta_{ij} + \tau_{ij}.$$

2.4 What happens to the stress in a body if temperature is raised at fixed strain? Does the stress obey Hooke's law (2.18) or must this be modified in some way? (Recall that seismological applications of (2.18) are usually for adiabatic loading.)

2.5 We have shown how the displacement field $\mathbf{u}(\mathbf{x}, t)$ for an elastic body is given uniquely (e.g., by applied body forces and tractions). Show that body forces and tractions are given uniquely once $\mathbf{u}(\mathbf{x}, t)$ is known everywhere. (A proof "by construction" is very quick and simple.)

2.6 Do the relations (2.21)–(2.25) change if stress depends on strain rate (e.g., for a viscous medium)?

2.7 Obtain the traction due to displacement field $\mathbf{u}$ acting on area elements normal to $\mathbf{n}$, in the form

$$\mathbf{T}(\mathbf{u}, \mathbf{n}) = \lambda(\nabla \cdot \mathbf{u})\mathbf{n} + \mu\left(2\frac{\partial \mathbf{u}}{\partial n} + \mathbf{n} \times (\nabla \times \mathbf{u})\right).$$

Here

$$\frac{\partial \mathbf{u}}{\partial n} = (\mathbf{n} \cdot \nabla)\mathbf{u}.$$

2.8 The traction $\mathbf{T}$ in the previous question is a function of position $\mathbf{x}$, in the sense that $\mathbf{T} = \mathbf{T}(\mathbf{u}(\mathbf{x}), \mathbf{n})$.

a) Modify our derivation of (2.7) to show that traction is a continuous function of position, in the sense that

$$\mathbf{T}(\mathbf{x} + \delta\mathbf{x}) - \mathbf{T}(\mathbf{x}) \to \mathbf{0} \quad \text{as} \quad \delta\mathbf{x} \to \mathbf{0},$$

provided $\delta\mathbf{x}$ is taken parallel to the direction $\mathbf{n}$ that defines the orientation of area elements on which traction is evaluated.

b) Consider a book resting on a flat table. Is it true that traction is a continuous function of position on the surface of the table?

c) Check that your answers to a) and b) are not in conflict.

d) Show that τ_{yz}, τ_{zx}, τ_{zz} are continuous functions of z in any medium, but that τ_{zz} need not be continuous in the x- or y-directions; and that τ_{xx}, τ_{yy}, and τ_{xy} need not be continuous in the z-direction.

2.9 For a point at pressure P in a fluid, the stress tensor is isotropic and has components $\tau_{ij} = -P\delta_{ij}$. To emphasize the differences between stresses that are possible in a solid and those that are present in a fluid, it is convenient to define *deviatoric stresses* τ'_{ij} by $\tau_{ij} = \frac{1}{3}\tau_{kk}\delta_{ij} + \tau'_{ij}$ and *deviatoric strains* by $e_{ij} = \frac{1}{3}e_{kk}\delta_{ij} + e'_{ij}$. Show then that the strain energy $\mathcal{U}$ in an isotropic elastic medium is given by

$$\mathcal{U} = \tfrac{1}{2}[(\lambda + \tfrac{2}{3}\mu)e_{ii}e_{kk} + 2\mu e'_{ij}e'_{ij}].$$

Show that e_{ii} is the change in volume per unit volume (i.e., the volumetric strain). Hence $\mathcal{U}$ can be regarded as a sum of dilatational energy, $\frac{1}{2}(\lambda + \frac{2}{3}\mu)e_{ii}e_{kk}$, and shear strain energy $\mu e'_{ij}e'_{ij}$. Why must $\lambda + \frac{2}{3}\mu$ (often called the *bulk modulus*, denoted by κ) and μ be positive? Is it natural to call κ the *compressibility* or the *incompressibility*?

2.10 Consider two points, $\mathbf{x}$ and $\boldsymbol{\xi}$, in an elastic medium, and let the unit vectors $\mathbf{n}$ and $\boldsymbol{\nu}$ specify particular directions at $\mathbf{x}$ and $\boldsymbol{\xi}$, respectively. Show first that a unit impulse in the $\boldsymbol{\nu}$ direction at $\boldsymbol{\xi}$ leads to a displacement at $\mathbf{x}$ whose component in the $\mathbf{n}$ direction is given by $n_i G_{ip}(\mathbf{x}, t; \boldsymbol{\xi}, 0)\nu_p$. Then show that this displacement component equals the displacement component in the $\boldsymbol{\nu}$ direction at $\boldsymbol{\xi}$ caused by a unit impulse in the $\mathbf{n}$ direction at $\mathbf{x}$. (This result generalizes the reciprocity result given in (2.39), which was for an impulse taken along one of the coordinate axes and a displacement component also along a coordinate axis. The reciprocity is true for arbitrary directions $\mathbf{n}$ and $\boldsymbol{\nu}$.)

CHAPTER 3

Representation of Seismic Sources

Seismic waves are set up by winds, ocean waves, meteorite impacts, rocket launchings, and atmospheric explosions—even by people walking around in the vicinity of seismometers. These, however, are examples of sources external to the solid Earth, and they can usually be analyzed within the simple framework of time-varying tractions applied to the Earth's surface. Other sources that, for many practical purposes, are also external, include volcanic eruptions, vented explosions, and spalling (free fall of a surface layer thrown upward by an underground explosion). For internal sources, such as earthquakes and underground explosions, the analytical framework is more difficult to develop, because the equations governing elastic motion (2.17)–(2.18) do not hold throughout the solid Earth. This chapter is about internal sources, and we shall distinguish two different categories: faulting sources and volume sources.

A faulting source is an event associated with an internal surface, such as slip across a fracture plane. A volume source is an event associated with an internal volume, such as a sudden (explosive) expansion throughout a volumetric source region. We shall find that a unified treatment of both source types is possible, the common link being the concept of an internal surface across which discontinuities can occur in displacement (for the faulting source) or in strain (for the volume source).

The mathematical description of internal seismic sources has classically been pursued along two different lines: first, in terms of a body force applied to certain elements of the medium containing the source; and second, by some discontinuity in displacement or strain (e.g., across a rupturing fault surface or across the surface of a volume source). The second approach can usefully be incorporated into the first if we can find body-force equivalents to discontinuities in displacement and strain. We begin our analysis by developing body-force equivalents in some detail for simple shearing across a fault surface, showing that radically different systems of forces can be equivalent to exactly the same displacement discontinuity. We then develop the general theory for faulting sources, following Burridge and Knopoff (1964), and finally we outline the theory for a volume source.

The motions recorded in a seismogram are a result both of propagation effects and of source effects. Thus a major reason for seeking a better understanding of the source mechanism has been to isolate the propagation effects, since these bear information on the Earth's internal structure. Since the pioneering work of Sykes (1967), earthquake source

mechanisms have been studied to chart the motions of tectonic plates. Source theory can elucidate physical processes such as those taking place in volcanoes. It continues to be developed with a view to predicting earthquake hazards at engineering sites, on the basis of geological and geophysical data on the properties of nearby faults and the distribution of regional stresses.

3.1 Representation Theorems for an Internal Surface; Body-Force Equivalents for Discontinuities in Traction and Displacement

The representation theorems obtained in Chapter 2 can be a powerful aid in seismic source theory if the surface S is chosen to include two adjacent surfaces internal to the volume V. The motivation here comes from the work of H. F. Reid, whose study of the San Andreas fault before and after the 1906 San Francisco earthquake led to general recognition that earthquake motion is due to waves radiated from spontaneous slippage on active geological faults. We shall discuss this source mechanism in more detail in Sections 3.2 and 3.3, and the dynamical processes involved (and other source mechanisms) in Chapter 11. Our present concern is simply to show how the process of slip on a buried fault, and the waves radiated from it, can naturally be analyzed by our representation theorems.

For applications of (2.41)–(2.43), we shall take the surface of V to consist of an external surface labeled S (see Fig. 3.1) and two adjacent internal surfaces, labeled Σ^+ and Σ^-, which are opposite faces of the fault. If slip occurs across Σ, then the displacement field is discontinuous there and the equation of motion is no longer satisfied throughout the interior of S. However, it *is* satisfied throughout the "interior" of the surface $S + \Sigma^+ + \Sigma^-$, and to this we can apply our previous representation results.

The surface S is no longer of direct interest (it may be the surface of the Earth), and we shall assume that both $\mathbf{u}$ and $\mathbf{G}$ satisfy the same homogeneous boundary conditions on

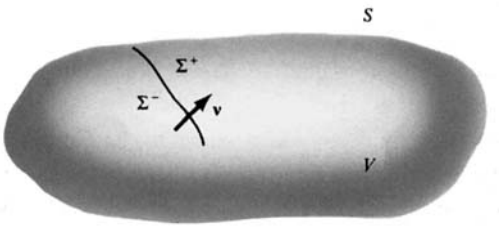

FIGURE **3.1**
A finite elastic body, with volume V and external surface S, and an internal surface Σ (modeling a buried fault) across which discontinuities may arise. That is, displacements on the Σ^- side of Σ may differ from displacements on the Σ^+ side of Σ. The normal to Σ is $\boldsymbol{\nu}$ (pointing from Σ^- to Σ^+), and the displacement discontinuity is denoted by $[\mathbf{u}(\boldsymbol{\xi}, \tau)]$ for $\boldsymbol{\xi}$ on Σ, with square brackets referring to the difference $\mathbf{u}(\boldsymbol{\xi}, \tau)|_{\Sigma^+} - \mathbf{u}(\boldsymbol{\xi}, \tau)|_{\Sigma^-}$. In general, a similar difference may be formed for the tractions (due to external applied forces on Σ), but for spontaneous rupture the tractions must be continuous, and then $\left[\mathbf{T}(\mathbf{u}, \boldsymbol{\nu})\right] = \mathbf{0}$.

S—though not on Σ (see below). Then from (2.41), using (2.39) and renaming some variables and indices,

$$u_n(\mathbf{x},t) = \int_{-\infty}^{\infty} d\tau \iiint_V f_p(\boldsymbol{\eta},\tau) G_{np}(\mathbf{x},t-\tau;\boldsymbol{\eta},0)\, dV(\boldsymbol{\eta}) + \int_{-\infty}^{\infty} d\tau \iint_\Sigma \left\{ \left[u_i(\boldsymbol{\xi},\tau) c_{ijpq} \nu_j \partial G_{np}(\mathbf{x},t-\tau;\boldsymbol{\xi},0)/\partial \xi_q \right] - \left[G_{np}(\mathbf{x},t-\tau;\boldsymbol{\xi},0) T_p(\mathbf{u}(\boldsymbol{\xi},\tau),\boldsymbol{\nu}) \right] \right\} d\Sigma. \tag{3.1}$$

This formula uses $\boldsymbol{\eta}$ as the general position within V, and $\boldsymbol{\xi}$ as the general position on Σ. Square brackets are used for the difference between values on Σ^+ and Σ^- (see caption for Fig. 3.1).

As yet, nothing has been assumed for the boundary conditions on Σ. Although the choice for $\mathbf{u}$ must conform to actual properties of displacement and traction across a rupturing fault surface, the choice for $\mathbf{G}$ can be made in any fashion that turns out to be useful. Thus, for $\mathbf{u}$, the slip on a fault leads to a nonzero value for $[\mathbf{u}]$, but the continuity of traction (see the proof of (2.7), and Problem 2.8) implies $[\mathbf{T}(\mathbf{u},\boldsymbol{\nu})] = \mathbf{0}$. The simplest and most commonly used way to establish a defining property of $\mathbf{G}$ on Σ is to take Σ as an artificial surface across which $\mathbf{G}$ and its derivatives are continuous, so that $\mathbf{G}$ satisfies the equation of motion (2.36) even on Σ. This is by far the easiest Green function to compute for the volume V, and (in the absence of body forces for $\mathbf{u}$) it gives the representation

$$u_n(\mathbf{x},t) = \int_{-\infty}^{\infty} d\tau \iint_\Sigma \left[u_i(\boldsymbol{\xi},\tau) \right] c_{ijpq} \nu_j \frac{\partial}{\partial \xi_q} G_{np}(\mathbf{x},t-\tau;\boldsymbol{\xi},0)\, d\Sigma. \tag{3.2}$$

It is not surprising that displacement on the fault is enough to determine displacement everywhere: this feature of (3.2) might have been expected from the uniqueness theorem. Nevertheless, it *is* at first sight surprising that no boundary conditions on Σ are needed for the Green function that describes waves propagating from the source. One might expect that motions occurring on the fault would set up waves that are themselves diffracted in some fashion by the fault surface. But although this interaction complicates the determination of the slip function $[\mathbf{u}(\boldsymbol{\xi},\tau)]$, it does not enter into the determination of the Green function used in (3.2), and many seismologists have used this formula to compute the motions set up by some assumed model of the slip function. We shall describe examples of such integrations in Chapter 10.

3.1.1 BODY-FORCE EQUIVALENTS

The earthquake model we have just described does not directly involve any body forces, though the representation (3.2) does give displacement at $(\mathbf{x},t)$ as an integral over contributing Green functions, each of which is the same as if it had been set up by a body force. Thus there must be some sense in which an active fault surface can be regarded as a surface distribution of body forces.

To determine this body-force equivalent, we start with (3.1) and assume still that Σ is transparent to $\mathbf{G}$. Making no assumptions about $[\mathbf{u}]$ and $[\mathbf{T}(\mathbf{u}, \mathbf{n})]$ across Σ (so that sources of traction are also allowed), we find

$$u_n(x,t) = \int_{-\infty}^{\infty} d\tau \iiint_V f_p(\eta,\tau) G_{np}(\mathbf{x}, t-\tau; \eta, 0)\, dV(\eta)$$
$$+ \int_{-\infty}^{\infty} d\tau \iint_\Sigma \Big\{ \big[u_i(\xi,\tau)\big] c_{ijpq} \nu_j G_{np,q}(\mathbf{x}, t-\tau; \xi, 0)$$
$$- \big[T_p(\mathbf{u}(\xi,\tau), \nu)\big] G_{np}(\mathbf{x}, t-\tau; \xi, 0) \Big\}\, d\Sigma(\xi). \tag{3.3}$$

The discontinuities on Σ can be localized within V by using the delta function $\delta(\eta - \xi)$. For example, $[\mathbf{T}]\, d\Sigma(\xi)$ has the dimensions of force, and its body-force distribution (i.e., force/unit volume) is $[\mathbf{T}]\, \delta(\eta - \xi) d\Sigma$ as η varies throughout V. The traction discontinuity in (3.3) therefore contributes the displacement

$$\int_{-\infty}^{\infty} d\tau \iiint_V \left\{ - \iint_\Sigma \big[T_p(\mathbf{u}(\xi,\tau), \nu)\big]\, \delta(\eta - \xi)\, d\Sigma \right\} G_{np}(\mathbf{x}, t-\tau; \eta, 0)\, dV.$$

Since this expression has precisely the form of a body-force contribution (see the first term in the right-hand side of (3.3)), the body-force equivalent of a traction discontinuity on Σ is given by $\mathbf{f}^{[\mathbf{T}]}$, where

$$\mathbf{f}^{[\mathbf{T}]}(\eta,\tau) = - \iint_\Sigma [\mathbf{T}(\mathbf{u}(\xi,\tau), \nu)]\, \delta(\eta - \xi)\, d\Sigma(\xi). \tag{3.4}$$

The displacement discontinuity is harder to interpret, displacement being less simply related to force than is traction. We use the delta-function derivative $\partial\delta(\eta - \xi)/\partial\eta_q$ to localize points of Σ within V. This function has the property

$$\frac{\partial}{\partial \xi_q} G_{np}(\mathbf{x}, t-\tau; \xi, 0) = - \iiint_V \frac{\partial}{\partial \eta_q} \delta(\eta - \xi) G_{np}(\mathbf{x}, t-\tau; \eta, 0)\, dV(\eta),$$

so that the displacement discontinuity in (3.3) contributes the displacement

$$\int_{-\infty}^{\infty} d\tau \iiint_V \left\{ - \iint_\Sigma \big[u_i(\xi,\tau)\big] c_{ijpq} \nu_j \frac{\partial}{\partial \eta_q} \delta(\eta - \xi)\, d\Sigma \right\} G_{np}(\mathbf{x}, t-\tau; \eta, 0)\, dV$$

at position $\mathbf{x}$ and time t. The body-force equivalent $\mathbf{f}^{[\mathbf{u}]}$ of a displacement discontinuity on Σ can now be recognized from this expression as

$$f_p^{[\mathbf{u}]}(\eta,\tau) = - \iint_\Sigma \big[u_i(\xi,\tau)\big] c_{ijpq} \nu_j \frac{\partial}{\partial \eta_q} \delta(\eta - \xi)\, d\Sigma. \tag{3.5}$$

BOX **3.1**

On the use of effective slip and effective elastic moduli in the source region

We are using the words "fault plane" and "fault surface," symbolized by Σ, as mathematical entities that have no thickness. Yet there are many places in the world where Earth scientists have direct access to fault regions, and one often finds there a zone of crushed and deformed rock, perhaps several meters thick, so that geologists often speak of "fault gouge" and a "fault zone." What, then, is meant by our claim that body-force equivalents depend only on elastic moduli at the fault surface?

The fault zone itself may be as wide as 200 meters, which for most but not all purposes is far less than the wavelengths of detectable seismic radiation, in which case it is the displacement change across the whole fault zone that is the apparent displacement discontinuity, initiating waves which propagate out of the source region. Therefore, in almost all practical cases, the elastic moduli for equations (3.2), (3.3), and (3.5) are the constants appropriate for the competent (unaltered) rock adjoining the fault zone. Exceptions may arise with fault zone effects that may be significant for seismic wave excitation at frequencies of interest to strong motion seismology (Aki, 1996).

Although the integrand here involves 27 terms (summation over i, j, q), which are different for each p, we shall find important examples in which only two or three terms are nonzero. The body-force equivalents (3.4) and (3.5) hold for a general inhomogeneous anisotropic medium, and they are remarkable in their dependence on properties of the elastic medium only at the fault surface itself.

Since faulting within the volume V is an internal process, the total momentum and total angular momentum must be conserved. It follows that the total force due to $\mathbf{f}^{[\mathbf{u}]}$, and the total moment of $\mathbf{f}^{[\mathbf{u}]}$ about any fixed point, must be zero. Thus

$$\iiint_V \mathbf{f}^{[\mathbf{u}]}(\boldsymbol{\eta}, \tau)\, dV(\boldsymbol{\eta}) = \mathbf{0} \qquad \text{for all } \tau, \tag{3.6}$$

and

$$\iiint_V (\boldsymbol{\eta} - \boldsymbol{\eta}_0) \times \mathbf{f}^{[\mathbf{u}]}(\boldsymbol{\eta}, \tau)\, dV(\boldsymbol{\eta}) = \mathbf{0} \qquad \text{for all } \tau \text{ and any fixed } \boldsymbol{\eta}_0. \tag{3.7}$$

To verify (3.6), note that the p-component of the left-hand side is $-\iint_\Sigma [u_i]\, c_{ijpq} \nu_j \left\{ \iiint_V \partial\delta(\boldsymbol{\eta} - \boldsymbol{\xi})/\partial\eta_q dV \right\} d\Sigma(\boldsymbol{\xi})$. The volume integral here is $\iint_S \delta(\boldsymbol{\eta} - \boldsymbol{\xi}) n_q\, dS(\boldsymbol{\eta})$, which vanishes because $\boldsymbol{\eta}$ on S can never equal $\boldsymbol{\xi}$ (S and Σ having no common point).

To verify (3.7), write the m-component of the left-hand side as

$$\iiint_V \varepsilon_{mnp}(\eta_n - \eta_{0n}) f_p^{[\mathbf{u}]} dV$$

$$= -\iint_\Sigma c_{ijpq}\nu_j [u_i] \left\{ \iiint_V \varepsilon_{mnp}(\eta_n - \eta_{0n}) \frac{\partial}{\partial \eta_q} \delta(\boldsymbol{\eta} - \boldsymbol{\xi})\, dV \right\} d\Sigma \quad \text{(from (3.5))}$$

$$= +\iint_\Sigma \varepsilon_{mqp} c_{ijpq} \nu_j [u_i]\, d\Sigma \qquad \left(\text{using } \frac{\partial}{\partial \eta_q}(\eta_n - \eta_{0n}) = \delta_{nq} \right)$$

$$= 0 \qquad \text{(using the symmetry } c_{ijpq} = c_{ijqp}).$$

As a simple example of a body force that is equivalent to a field discontinuity, consider the case of a body force applied at just one point, and in a particular direction (e.g., the body force for a Green function, given by (2.4)). This can instead be regarded as a discontinuity in a component of stress. To obtain the equivalence, take x_3 as the depth direction and consider a vertical point force, with magnitude F, applied at $(0, 0, h)$ and time $\tau = 0$ and held steady. Then

$$\mathbf{f}(\boldsymbol{\eta}, \tau) = (0, 0, F)\delta(\eta_1)\delta(\eta_2)\delta(\eta_3 - h)H(\tau). \tag{3.8}$$

This source can instead be regarded as a discontinuity in traction across one point of the plane $\xi_3 = h$, with

$$\left[\mathbf{T}(\boldsymbol{\xi}, \tau)\right]_{\xi=(\xi_1,\xi_2,h^-)}^{\xi=(\xi_1,\xi_2,h^+)} = -(0, 0, F)\delta(\xi_1)\delta(\xi_2)H(\tau), \tag{3.9}$$

i.e., τ_{13}, τ_{23} are continuous, and the jump is in τ_{33}. The equivalence of (3.8) and (3.9) can be shown by a straightforward application of (3.4).

The most important example of a body-force equivalent in seismology is found in shear faulting, and we next take up this subject in some detail.

3.2 A Simple Example of Slip on a Buried Fault

The seismic waves set up by fault slip are the same as those set up by a distribution on the fault of certain forces with canceling moment. The distribution (for given fault slip) is not unique, but in an isotropic medium it can always be chosen as a surface distribution of double couples. This conclusion was unexpected, in view of arguments used in a long-lasting debate on the question of whether earthquakes should be modeled by a single couple or by a double couple. Those who advocated the single-couple theory did believe that earthquakes were due to slip on a fault, but they intuitively thought for many years that such slip was equivalent to a single couple (composed of two forces corresponding to the motions on opposite sides of the fault). An intuitive approach is often dangerous in elastodynamics. On the other hand, some of those who advocated the double-couple theory thought that an earthquake must be voluminal collapse under pre-existing shear stress. The fault theory of earthquake sources (now recognized as the equivalent of a double couple) has gained strong

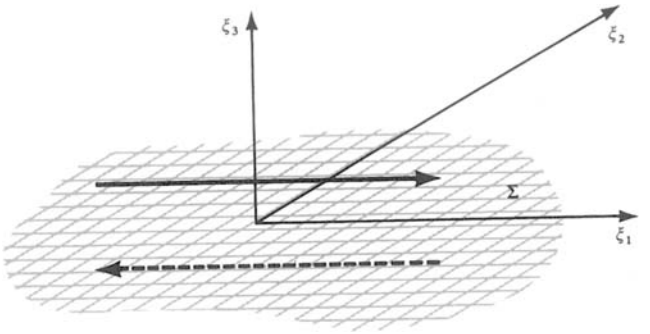

FIGURE **3.2**
A fault surface Σ within an isotropic medium is shown lying in the $\xi_3 = 0$ plane. Slip is presumed to take place in the ξ_1-direction across Σ, as shown by the heavy arrows. Motion on the side Σ^+ (i.e., $\xi_3 = 0^+$) is along the direction of ξ_1 increasing, and on the side Σ^- is along ξ_1 decreasing.

support from increasing amounts of data obtained very close to the source region, as well as support from the radiation patterns observed at great distances.

As shown in Figure 3.2, we shall take the fault Σ to lie in the plane $\xi_3 = 0$, so that $\nu_1 = \nu_2 = 0$. For the case that we are calling "fault slip", $[\mathbf{u}]$ is parallel to Σ and so $[\mathbf{u}]$ has no component in the ξ_3-direction. Let ξ_1 be the direction of slip, so that $[u_2] = [u_3] = 0$. Then the body-force equivalent, from (3.5), reduces to

$$f_p(\eta, \tau) = -\iint_\Sigma [u_1(\xi, \tau)]\, c_{13pq} \frac{\partial}{\partial \eta_q} \delta(\eta - \xi)\, d\xi_1\, d\xi_2.$$

In isotropic (though still possibly inhomogeneous) media, we can find from (2.33) that all c_{13pq} vanish, except $c_{1313} = c_{1331} = \mu$. Hence

$$\begin{aligned} f_1(\eta, \tau) &= -\iint_\Sigma \mu(\xi)\, [u_1(\xi, \tau)]\, \delta(\eta_1 - \xi_1)\delta(\eta_2 - \xi_2) \frac{\partial}{\partial \eta_3} \delta(\eta_3)\, d\xi_1\, d\xi_2, \\ f_2(\eta, \tau) &= 0, \\ f_3(\eta, \tau) &= -\iint_\Sigma \mu\, [u_1]\, \frac{\partial}{\partial \eta_1} \delta(\eta_1 - \xi_1)\delta(\eta_2 - \xi_2)\delta(\eta_3)\, d\xi_1\, d\xi_2. \end{aligned} \tag{3.10}$$

First, let us look at f_1, which we shall find represents a system of single couples (forces in $\pm\eta_1$-direction, arm along η_3-direction, moment along η_2-direction) distributed over Σ. The integral above yields

$$f_1(\eta, \tau) = -\mu(\eta)\, [u_1(\eta, \tau)]\, \frac{\partial}{\partial \eta_3} \delta(\eta_3). \tag{3.11}$$

As shown in Figure 3.3, this component may be thought of as point forces distributed over the plane $\eta_3 = 0^+$ and opposed forces distributed over the plane $\eta_3 = 0^-$.

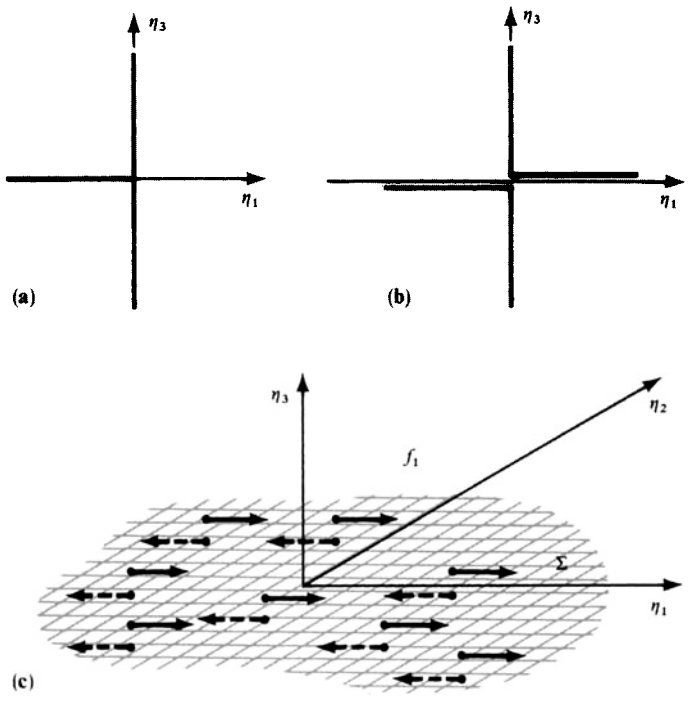

FIGURE **3.3**
Interpretive diagrams for the first component, f_1, of the body-force equivalent to fault slip of the type shown in Figure 3.2. (**a**) The spike $\left(-\delta(\eta_3), 0, 0\right)$ is plotted against η_3. (That is, a spike in the $-\eta_1$-direction, acting at $\eta_3 = 0$.) (**b**) The derivative $\left((-\partial/\partial\eta_3)\delta(\eta_3), 0, 0\right)$ is plotted against η_3. The body force $(f_1, 0, 0)$ is proportional to this quantity (see equation (3.11)). (**c**) Heavy arrows show the distribution of f_1 over the Σ^+ side of Σ and over the Σ^- side (broken arrows). This is the body-force component that would intuitively be expected in any body-force model of the motions shown in Figure 3.2.

The total force due to f_1 vanishes (see discussion of (3.6)), but the moment of this force component alone does not. The total moment about the η_2-axis is

$$\iiint_V \eta_3 f_1 \, dV = -\iiint_V \eta_3 \mu \left[u_1\right] \frac{\partial}{\partial \eta_3} \delta(\eta_3) \, d\eta_1 \, d\eta_2 \, d\eta_3 = \iint_\Sigma \mu \left[u_1(\xi, \tau)\right] \, d\Sigma.$$

If slip is averaged over Σ to define the quantity

$$\overline{u}(\tau) = \frac{\iint_\Sigma \left[u_1(\xi, \tau)\right] \, d\Sigma}{A},$$

where $A = \iint_\Sigma \, d\Sigma$ is the fault area, and if the fault region is homogeneous (so that μ is constant), then the total moment about the η_2-axis due to $f_1(\xi, \tau)$ is simply $\mu \overline{u} A$ along the direction of η_2 increasing.

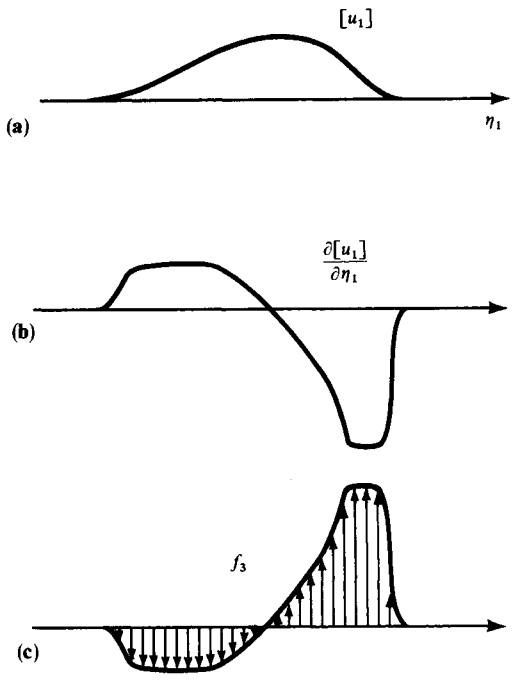

FIGURE **3.4**
Interpretive diagrams for the third component, f_3, of the body-force equivalent to fault slip $[u_1]$. (**a**) An assumed variation of slip $[u_1]$ with η_1, at fixed η_2 and τ. (**b**) The corresponding derivative $\partial [u_1] / \partial \eta_1$. (**c**) The distribution of single forces f_3 with varying η_1 (see equation (3.12)). This distribution will clearly yield a net couple, with moment in the $-\eta_2$-direction.

The body-force equivalent, given in (3.10), also involves f_3, and we shall find that this represents a system of single forces. Taking the η_1-derivative outside the integration, we find

$$f_3(\boldsymbol{\eta}, \tau) = -\frac{\partial}{\partial \eta_1} \{\mu [u_1(\boldsymbol{\eta}, \tau)]\} \delta(\eta_3). \tag{3.12}$$

Although this component is not itself a couple at each point on Σ, in the sense that we have shown f_1 to be a couple, the whole distribution of f_3 across Σ does have a net moment. Figure 3.4 shows how f_3 can reverse direction at different points of Σ. The total moment about the η_2-axis is

$$\begin{aligned} \iiint_V \varepsilon_{213} \eta_1 f_3 \, dV &= \iiint_V \eta_1 \frac{\partial}{\partial \eta_1} \{\mu [u_1]\} \delta(\eta_3) \, d\eta_1 \, d\eta_2 \, d\eta_3 \\ &= \iint_\Sigma \xi_1 \frac{\partial}{\partial \xi_1} \{\mu [u_1]\} \, d\xi_1 \, d\xi_2 = - \iint_\Sigma \mu [u_1] \, d\xi_1 \, d\xi_2. \end{aligned}$$

(This last equality follows from an integration by parts, using a fault surface Σ defined to have $[\mathbf{u}] = \mathbf{0}$ around its perimeter.) In a homogeneous source region, it follows that the total moment due to f_3 is $-\mu \bar{u} A$, which is equal in magnitude to the total moment of f_1, but acts in the opposite direction. We obtained this result in more general form in (3.7), but have found here the two canceling contributions that arise.

We have now shown that fault slip is equivalent to a distribution of single couples (f_1), plus a distribution of single forces (f_3) that have the net effect of an opposing couple. Yet the classical force equivalent for fault slip is a double-couple distribution over Σ, as was first shown for a finite fault by Maruyama in 1963. The fact is that force equivalents to a given fault slip are not unique. A direct way to see this, and to obtain the double-couple density as well as the single-couple/single-force density, is to write out representation (3.2) for the fault slip described in Figure 3.2. The result is

$$u_n(\mathbf{x}, t) = \int_{-\infty}^{\infty} d\tau \iint_{\Sigma} \mu \, [u_1] \left\{ \frac{\partial G_{n1}}{\partial \xi_3} + \frac{\partial G_{n3}}{\partial \xi_1} \right\} d\Sigma. \tag{3.13}$$

The first term here in curly brackets, $\partial G_{n1}(\mathbf{x}, t - \tau; \boldsymbol{\xi}, 0)/\partial \xi_3$, is the limit of

$$\frac{G_{n1}(\mathbf{x}, t - \tau; \boldsymbol{\xi} + \varepsilon \hat{\boldsymbol{\xi}}_3, 0) - G_{n1}(\mathbf{x}, t - \tau; \boldsymbol{\xi} - \varepsilon \hat{\boldsymbol{\xi}}_3, 0)}{2\varepsilon}$$

as $\varepsilon \to 0$. (We take $\hat{\boldsymbol{\xi}}_i$ as a unit vector in the ξ_i-direction.) This is the single-couple distribution shown in Figure 3.5a. The second term in (3.13) involves the limit of

$$\frac{G_{n3}(\mathbf{x}, t - \tau; \boldsymbol{\xi} + \varepsilon \hat{\boldsymbol{\xi}}_1, 0) - G_{n3}(\mathbf{x}, t - \tau; \boldsymbol{\xi} - \varepsilon \hat{\boldsymbol{\xi}}_1, 0)}{2\varepsilon},$$

and this single-couple distribution is shown in Figure 3.5b. These two systems form a double-couple distribution, and we must ask why the earlier set of body-force equivalents we derived, (3.10), made up a single couple plus a single force. The answer can be seen if one term in (3.13) is integrated by parts, giving

$$u_n(\mathbf{x}, t) = \int_{-\infty}^{\infty} d\tau \iint_{\Sigma} \mu \left([u_1] \frac{\partial G_{n1}}{\partial \xi_3} - \left[\frac{\partial u_1}{\partial \xi_1} \right] G_{n3} \right) d\Sigma. \tag{3.14}$$

This force system is illustrated in Figure 3.6; clearly it is the same as the system we found first of all, shown in Figures 3.3 and 3.4. There is always a single couple (f_1, Figs. 3.3, 3.5a, and 3.6a) made up of forces in the same direction as fault-surface displacements (Fig. 3.2). But a complete equivalent to fault slip has another part, which may be regarded as a distribution of single forces (f_3, Figs. 3.4 and 3.6b), a distribution of single couples (Fig. 3.5b), or an appropriate linear combination of these alternative extremes. For a given element of area $d\Sigma$ on the fault, these force systems are physically quite different: from the integrand in representation (3.13), there appears to be no force or moment acting on $d\Sigma$; but from (3.14), there does appear to be both force and moment acting on $d\Sigma$, although we showed earlier that f_1 and f_3 integrate to give zero net force and zero net moment on the whole of Σ.

We have brought out these results in some detail, because they show the limited utility of force equivalents for studying the actual forces occurring in dynamic processes of fault slip. Whereas the body-force equivalent to fault slip *is* unique (see Box 3.3), force equivalents in the sense of this section are *not* unique (force equivalents in this case being force/unit area on a finite fault). It is the whole fault surface that is radiating seismic waves, and we cannot

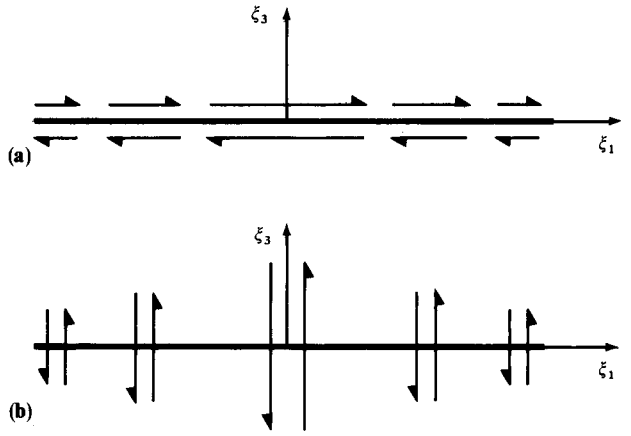

FIGURE **3.5**
The radiation from these two distributions is the same as the radiation from slip on a fault. In this sense, these two single-couple distributions, taken together, are equivalent to fault slip. Note that there is no net couple, and no net force, acting on any element of area in the fault plane ($\xi_3 = 0$).

assess from (3.13) or (3.14) the actual contribution made to the radiation by individual elements of fault area. This makes sense in physical terms, because individual elements of fault area do not move dynamically in isolation from neighboring parts of the source region. Force equivalents (usually chosen as the double-couple distribution) find their main use only when the slip function $[\mathbf{u}(\boldsymbol{\xi}, \tau)]$ has been determined (or guessed), and then they are important because they enable one to compute the radiation by weighting Green functions.

At great distance from a rupturing fault, it often occurs that the only waves observed are those with wavelengths much greater than linear dimensions of Σ, the causative fault.

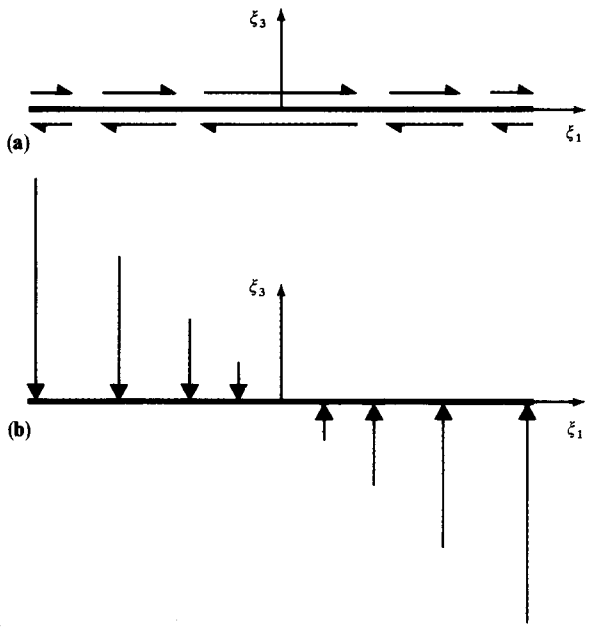

FIGURE **3.6**
Another force system that is equivalent to fault slip (compare with Fig. 3.5). (**a**) and (**b**) here constitute a single-couple plus single-force system, which has zero total couple and zero total force for the whole fault surface. But individual elements of area are acted on by a couple and a force.

(Higher frequency components are relatively weak even at the source—see Chapter 11—and are more effectively attenuated during propagation.) In such cases Σ acts as a point source, and if we also assume that the only waves observed have periods much longer than the source duration then the slip is localized by replacing $[\mathbf{u}(\xi_1, \xi_2, \tau)]$ by the concentrated distribution $\bar{\mathbf{u}} A \delta(\xi_1)\delta(\xi_2)H(\tau)$. Then f_3, as well as f_1, becomes a single couple, and the double-couple point source equivalent to fault slip is

$$\begin{aligned} f_1(\boldsymbol{\eta}, \tau) &= -M_0 \delta(\eta_1)\delta(\eta_2)\frac{\partial}{\partial \eta_3}\delta(\eta_3)H(\tau) \\ f_2(\boldsymbol{\eta}, \tau) &= 0 \\ f_3(\boldsymbol{\eta}, \tau) &= -M_0 \frac{\partial}{\partial \eta_1}\delta(\eta_1)\delta(\eta_2)\delta(\eta_3)H(\tau), \end{aligned} \tag{3.15}$$

where

$$M_0 = \mu \bar{u} A = \mu \times \text{ average slip } \times \text{ fault area.} \tag{3.16}$$

We call M_0 the *seismic moment*. It is perhaps the most fundamental parameter we can use to measure the strength of an earthquake caused by fault slip. Measured values of M_0 range from about 10^{30} dyn-cm (1960 Chilean earthquake, 1964 Alaskan earthquake) down to around 10^{12} dyn-cm for microearthquakes, and 10^5 dyn-cm for microfractures in laboratory experiments on loaded rock samples. Even for geophysics, twenty-five orders of magnitude is an exceptionally large range to be spanned by a single physical variable. The first person to obtain the double-couple equivalence for an effective point source of slip was Vvedenskaya (1956). The first estimate of seismic moment was made by Aki (1966) for the Niigata earthquake of 1964, using long-period Love waves observed by the World-Wide Standard Seismograph Network. Moment estimates are now made routinely within hours, or even minutes, after the occurrence of significant earthquakes. The limiting factors are the time taken for seismic waves to travel through the Earth's interior to the stations whose data are used; and the time taken for the recorded waveform data to be passed to the processing site where the estimate is made.

Kanamori (1977) introduced the concept of *moment magnitude* to seismology. This is simply a magnitude scale based on the seismic moment of an earthquake, which must first be estimated. His definition of the moment magnitude, denoted as M_w, is

$$\log M_0 = 1.5 M_w + 16.1 \tag{3.17}$$

in which the constants were chosen so that M_w is approximately the same as the surface wave magnitude (see Appendix 2) for a certain class of earthquakes. Magnitude scales in seismology have traditionally been defined empirically, usually as some type of distance-corrected measure of the strength of ground shaking. However, the moment magnitude, being derived from a physical characteristic of the source (namely, M_0), is fundamentally different from these empirical magnitudes.

We have defined M_0 as a constant, but for some purposes it is useful to evaluate the seismic moment as a function of time, given by $\mu\overline{u}(t)A$, in which $\overline{u}$ is averaged at time t. In these cases, $M_0H(\tau)$ in (3.15) is replaced by $M_0(\tau)$, and (in the terminology of Chapter 10) we speak of the "rise time" being different from zero.

Note that there is a fundamental ambiguity in identifying the fault plane associated with the point-source double couple (3.15). We have worked in this section with a fault surface normal to the x_3-direction and slip parallel to the x_1-direction. If the fault surface instead is taken normal to the x_1-direction and slip is taken parallel to the x_3-direction in a faulting episode with the same moment, then the equivalent body force is again (3.15). It follows that there can be no information in the seismic radiation or static displacement field from an effective point-source of slip that will enable one to distinguish between the fault plane and its *auxiliary plane* (i.e., the plane perpendicular to both the fault and the slip).

3.3 General Analysis of Displacement Discontinuities across an Internal Surface Σ

In this section we introduce the seismic *moment tensor*, **M**. This is a quantity that depends on source strength and fault orientation, and it characterizes all the information about the source that can be learned from observing waves whose wavelengths are much longer than the linear dimensions of Σ. In this case, the source is effectively a point source with an associated radiation pattern, and the moment tensor can often be estimated in practice for a given earthquake by using long-period teleseismic data. In practice, seismologists usually use moment tensors that are confined to sources having a body-force equivalent given by pairs of forces alone (couples, vector dipoles). Such sources include geologic faults (shearing) and explosions (expansion), with **M** as a second-order tensor. For forces differentiated more than once, sources can be characterized by higher order moment tensors (see Julian *et al.*, 1998).

For sources of finite extent, we shall introduce the seismic *moment density tensor*, **m**, which can often be thought of as $d\mathbf{M}/d\Sigma$, or as $d\mathbf{M}/dV$ for a volume source.

There are two ways in which this section generalizes Section 3.2. First, the coordinate axes are not taken in directions related to directionalities of the source. (This generality is important, because the direction of slip and the orientation of the fault plane are not usually known *a priori*, but must be deduced from the radiated seismic waves.) Second, discontinuities are to be allowed in the displacement component normal to the fault plane, so that expansions or contractions can be simulated.

Our starting point for the general analysis of displacement discontinuities is the representation (3.2), but using now the convolution symbol $*$ so that

$$u_n(\mathbf{x}, t) = \iint_\Sigma [u_i]\, \nu_j c_{ijpq} * \frac{\partial}{\partial \xi_q} G_{np}\, d\Sigma. \tag{3.18}$$

Note that $f * g = \int_0^t f(\tau)g(t-\tau)\,d\tau = \int_0^t f(t-\tau)g(\tau)\,d\tau = \int_{-\infty}^{\infty} f(\tau)g(t-\tau)\,d\tau$ if $f(t)$ and $g(t)$ are zero for $t < 0$. If X_0 is the amplitude of a force applied in the p-direction at $\boldsymbol{\xi}$ with general time variation, then the convolution $X_0 * G_{np}$ gives the n-component of displacement at $(\mathbf{x}, t)$ due to the varying point force at $\boldsymbol{\xi}$. More generally, if the force

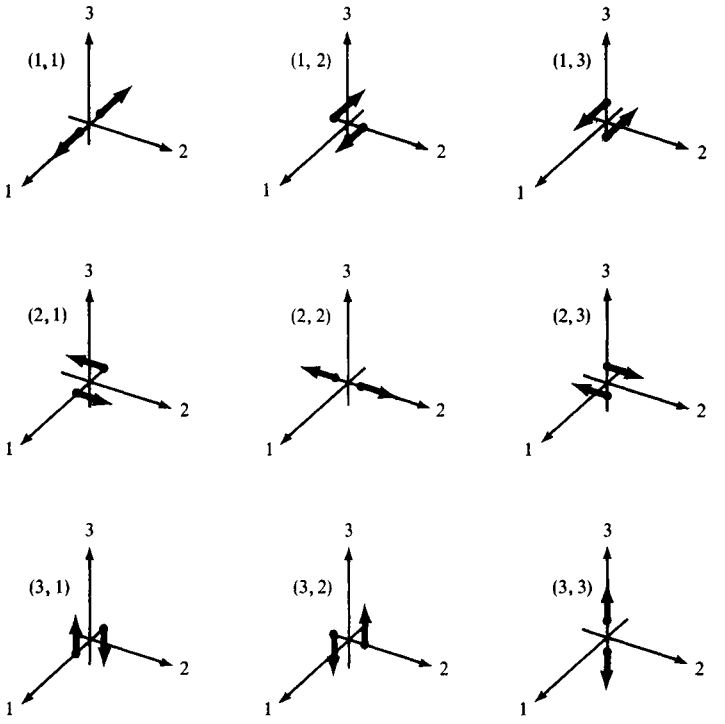

FIGURE **3.7**
The nine possible couples that are required to obtain equivalent forces for a generally oriented displacement discontinuity in anisotropic media.

applied at ξ is $\mathbf{F}(\xi, \tau)$, then we can sum over p and write $F_p * G_{np}$ for the n-component of displacement at $(\mathbf{x}, t)$. For displacement discontinuities as in (3.18), there are instead derivatives of G_{np} with respect to the source coordinates ξ_q. Such a derivative, we saw in Section 3.2, can be thought of physically as the equivalent of having a single couple (with arm in the ξ_q-direction) on Σ at ξ. The sum over q in (3.18) is then telling us that each displacement component at $\mathbf{x}$ is equivalent to the effect of a sum of couples distributed over Σ.

For three components of force and three possible arm directions, there are nine generalized couples, as shown in Figure 3.7. Thus the equivalent surface force corresponding to an infinitesimal surface element $d\Sigma(\xi)$ can be represented as a combination of nine couples. In general, we need "couples" with force and arm in the same direction (cases (1, 1), (2, 2), (3, 3) of Fig. 3.7), and these are sometimes called *vector dipoles.*

Since $[u_i]\, \nu_j c_{ijpq} * \partial G_{np}/\partial \xi_q$ in (3.18) is the n-component of the field at $\mathbf{x}$ due to couples at ξ, it follows that $[u_i]\, \nu_j c_{ijpq}$ is the strength of the (p, q) couple. The dimensions of $[u_i]\, \nu_j c_{ijpq}$ are moment per unit area, and this makes sense because the contribution from ξ has to be a surface density, weighted by the infinitesimal area element $d\Sigma$ to give a moment contribution. We define

$$m_{pq} = [u_i]\, \nu_j c_{ijpq} \tag{3.19}$$

to be the components of the *moment density tensor*, **m**. In terms of this symmetric tensor, which is time dependent, the representation theorem for displacement at **x** due to general displacement discontinuity $[\mathbf{u}(\boldsymbol{\xi}, \tau)]$ across Σ is

$$u_n(\mathbf{x}, t) = \iint_\Sigma m_{pq} * G_{np,q}\, d\Sigma. \tag{3.20}$$

When we have learned more about the Green function (in Chapter 4), we shall find that the time dependence of the integrand in (3.20) is quite simple, because if **x** is many wavelengths away from $\boldsymbol{\xi}$, then convolution with **G** gives a field at $(\mathbf{x}, t)$ that depends on what occurs at $\boldsymbol{\xi}$ only at "retarded time," i.e., t minus some propagation time between $\boldsymbol{\xi}$ and **x**.

For an isotropic body, it follows from (2.33) and (3.19) that

$$m_{pq} = \lambda \nu_k \left[u_k(\boldsymbol{\xi}, \tau)\right] \delta_{pq} + \mu \left(\nu_p \left[u_q(\boldsymbol{\xi}, \tau)\right] + \nu_q \left[u_p(\boldsymbol{\xi}, \tau)\right]\right). \tag{3.21}$$

Further, if the displacement discontinuity (or slip) is parallel to Σ at $\boldsymbol{\xi}$, the scalar product $\nu \cdot [\mathbf{u}]$ is zero and

$$m_{pq} = \mu \left(\nu_p \left[u_q\right] + \nu_q \left[u_p\right]\right). \tag{3.22}$$

In the case of Σ lying in the plane $\xi_3 = 0$, with slip only in the ξ_1-direction, we have the source model considered in Section 3.2, and for this the moment density tensor is

$$\mathbf{m} = \begin{pmatrix} 0 & 0 & \mu\left[u_1(\boldsymbol{\xi}, \tau)\right] \\ 0 & 0 & 0 \\ \mu\left[u_1(\boldsymbol{\xi}, \tau)\right] & 0 & 0 \end{pmatrix},$$

which is the now familiar double couple.

In the case of a tension crack in the $\xi_3 = 0$ plane, only the slip component $[u_3]$ is nonzero, and from (3.21) we find

$$\mathbf{m} = \begin{pmatrix} \lambda\left[u_3(\boldsymbol{\xi}, \tau)\right] & 0 & 0 \\ 0 & \lambda\left[u_3(\boldsymbol{\xi}, \tau)\right] & 0 \\ 0 & 0 & (\lambda + 2\mu)\left[u_3(\boldsymbol{\xi}, \tau)\right] \end{pmatrix}.$$

Thus a tension crack is equivalent to a superposition of three vector dipoles with magnitudes in the ratio $1 : 1 : (\lambda + 2\mu)/\lambda$ (see Fig. 3.8).

The above results have been developed for a fault plane Σ of finite extent, but in practice the seismologist often has data that are good only at periods for which the whole of Σ is effectively a point source. For these waves, the contributions from different surface elements $d\Sigma$ are all approximately in phase, and the whole surface Σ can be considered as a system of couples located at a point, say the center of Σ, with *moment tensor* equal to the integral of moment density over Σ. Thus, for an effective point source,

$$u_n(\mathbf{x}, t) = M_{pq} * G_{np,q}\,, \tag{3.23}$$

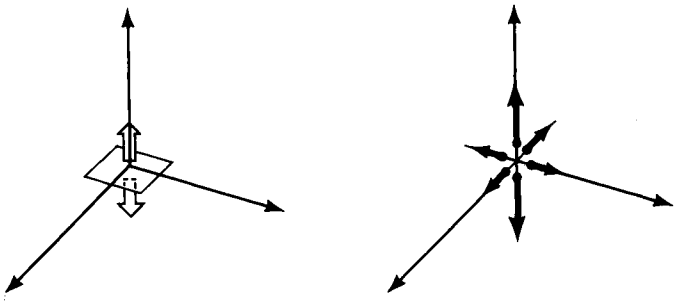

FIGURE **3.8**
The body-force equivalent for a tension crack in an isotropic medium.

where the moment tensor components are

$$M_{pq} = \iint_{\Sigma} m_{pq}\, d\Sigma = \iint_{\Sigma} [u_i]\, \nu_j c_{ijpq}\, d\Sigma, \qquad \text{i.e.,} \qquad m_{pq} = \frac{dM_{pq}}{d\Sigma}. \tag{3.24}$$

In (3.23) we have one of the most important equations of this chapter. Later in this book, we shall evaluate the Green function and the different waves it contains. Thus in Chapter 4 we shall use ray theory for **G** and interpret (3.23) in terms of body waves excited by given **M** (equation (4.96)). In Chapter 7, we shall find the surface waves excited by **M** (equations (7.148)–(7.151)), and in Chapter 8 the normal modes of the whole Earth (8.38).

In terms of seismic moment M_0, and with the choice of coordinate axes made in Section 3.2, the moment tensor for an effective point source of slip is

$$\mathbf{M} = \begin{pmatrix} 0 & 0 & M_0 \\ 0 & 0 & 0 \\ M_0 & 0 & 0 \end{pmatrix}. \tag{3.25}$$

Equations (3.24) justify the name "moment tensor density" for **m**. In the case of a finite source, we can now interpret the representation (3.20) as an areal distribution of point sources, each point having the moment tensor $\mathbf{m}\, d\Sigma$.

We conclude this section with an interesting use of "seismic moment," suggested by Brune (1968), involving the kinematic motions of tectonic plates. Such motions lead frequently to a type of regional seismicity in which many different earthquakes share the same fault plane (although any one event will involve slip over only a part of the whole fault area). If M_0^i is the seismic moment of the ith earthquake in a series of N earthquakes in time interval ΔT, it follows from the definition of M_0^i that the total slip due to the whole series is

$$\Delta U = \frac{\sum_{i=1}^{N} M_0^i}{\mu S}, \tag{3.26}$$

BOX **3.2**

On uses of the word "moment" in seismic source theory

In rotational mechanics, it is often enough to speak of a couple possessing the qualities of magnitude and a single direction. The magnitude of a couple is then a scalar quantity called the moment. In our study of displacement discontinuities, however, and body-force equivalents, we imply more directional qualities behind the word "couple" than is the case in rigid-body rotational mechanics. For us, "couple" involves the directions of both force and lever arm. A result of this is that the quantity "moment" jumps up from scalar to tensor.

Second-order Cartesian tensors in mathematical physics are usually quantities that relate one physical vector to another. One example is given by equation (2.16), in which the stress tensor is a device for obtaining traction from the vector orientation of an area element. Another example is the inertia tensor **I**, which gives angular momentum **h** from angular velocity $\boldsymbol{\omega}$ via $h_i = I_{ij}\omega_j$. In seismic source theory, however, the moment tensor is an input rather than a filter, and it is operated on by a third-order tensor to yield vector displacement (see (3.20) and (3.23)).

where S is the total area broken in the series. ΔU is averaged over all of S, and all the terms in the right-hand side of (3.26) can be estimated. If all the plate motion occurs seismically, and if the seismicity during ΔT is representative of the activity on that plate margin for longer time scales, then $\Delta U/\Delta T$ is an estimate of the relative velocity of the plates, regarded as slow-moving rigid bodies, and it can be obtained from seismic data alone.

3.4 Volume Sources: Outline of the Theory and Some Simple Examples

In order to develop equations for seismic waves from buried explosions or from rapid phase transformations, it is necessary to introduce the concept of a volume source. We shall describe such a source in terms of a transformational (or stress-free) strain introduced in the source volume, and shall develop properties of an associated seismic moment tensor.

Let us illustrate this concept by a set of imaginary cutting, straining, and welding operations described by Eshelby (1957). First, we separate the source material by cutting along a closed surface Σ that surrounds the source, and we remove the source volume (the "inclusion") from its surroundings (the "matrix"). We suppose that the material removed is held in its original shape by tractions having the same value over Σ as the tractions imposed across Σ by the matrix before the cutting operation. Second, we let the source material undergo transformational strain Δe_{rs}. By this, we mean that Δe_{rs} occurs without changing the stress within the inclusion, hence the name "stress-free strain." It is this strain that characterizes the seismic source. Processes that can be described by stress-free strain include phase transformation, thermal expansion, and some plastic deformations. Stress-free strain is a static concept. Third, we apply extra surface tractions that will restore the source volume to its original shape: this will result in an additional stress field $-c_{pqrs}\,\Delta e_{rs} = -\Delta\tau_{pq}$ throughout the inclusion, and the additional tractions applied on its surface Σ are $-c_{pqrs}\,\Delta e_{rs}\nu_q$, where ν_q is the outward normal on Σ. Since $\Delta\tau_{pq}$ is a static field, $\Delta\tau_{pq,q} = 0$. The stress in the matrix is still unchanged, being held at its original value

BOX **3.3**

Body-force equivalents and the seismic moment tensor

For a general displacement discontinuity across Σ, it follows from (3.5) that

$$f_p = -\frac{\partial}{\partial \eta_q}\left\{[u_i]\nu_j c_{ijpq}\delta(\Sigma)\right\},$$

where, by $\delta(\Sigma)$, we mean a one-dimensional spatial Dirac delta function that is zero off Σ. Thus, if Σ lies in the plane $\eta_3 = 0$, $\delta(\Sigma) = \delta(\eta_3)$ for points (η_1, η_2) on Σ.

It must be emphasized that $\mathbf{f}$ is a force *per unit volume*, and it is unique. (Once $[u_i]$ is given on Σ, then $\mathbf{u}$ is determined everywhere, and $\mathbf{f} = \mathbf{L}(\mathbf{u})$, where $\mathbf{L}$ is given in Box 2.4.) The ambiguities mentioned in Section 3.2 arise only when equivalent *surface* forces are sought. Thus the above formula for f_p does not give a distribution of couples and dipoles. Such a distribution arises only after the displacement representation $\iiint_V G_{np}\{f_p\}\, dV$ has been integrated by parts and the η_3 integration completed to give (3.18), which may then be interpreted in terms of equivalent surface forces. These are nonunique—see (3.13) and (3.14)—but a surface distribution of couples and vector dipoles is always possible.

We have introduced the seismic moment tensor in the form $M_{pq} = \iint_\Sigma [u_i]\, \nu_j c_{ijpq}\, d\Sigma$, but from the above formula for body force it is easy to show that

$$M_{pq} = \iiint_V f_p \eta_q \, dV(\eta).$$

This result can be used to extend the definition of $\mathbf{M}$, since it can be used for any body-force distribution, and not just for the body-force equivalent to a displacement discontinuity. With this definition, the moment (in the ordinary sense of rotational mechanics) of body-forces $\mathbf{f}$ about the ith axis is $\iiint_V \varepsilon_{ijk}\eta_j f_k \, dV = \varepsilon_{ijk} M_{kj}$, which is zero whenever the moment tensor is symmetric (e.g., in (3.24)).

by tractions imposed across the internal surface Σ, and having the same value as tractions imposed on the matrix by the inclusion before it was cut out. Fourth, we put the inclusion back in its hole (which is exactly the correct shape) and weld the material across the cut. The traction on Σ^- is now an amount $-c_{pqrs}\, \Delta e_{rs} \nu_q$ greater than that on Σ^+, leading to a traction discontinuity (in the ν-direction) of amount $+c_{pqrs}\, \Delta e_{rs} \nu_q$. This traction is due to applied surface forces that are external to the source and which act on the inclusion to maintain its correct shape. Fifth, we release the applied surface forces over Σ^-. Since traction is actually continuous across Σ, this amounts to imposing an apparent traction discontinuity of $-(c_{pqrs}\, \Delta e_{rs})\nu_q$. The elastic field produced in the matrix by the whole process is that due to the apparent traction discontinuity across Σ.

The above procedure can be extended to a dynamic case of seismic wave generation, since, at any given time, a transformational strain Δe_{rs} can be defined for the unrestrained material. For each instant, it is still true that $\Delta \tau_{pq,q} = 0$ because stress-free strain (and the stress derived from it) is a static concept. The seismic displacement generated by the

BOX **3.4**

The strain energy released by earthquake faulting

Within a medium that initially has a static stress field σ^0, we suppose that a displacement discontinuity develops across an internal surface Σ. This leads to a displacement field $\mathbf{u}(\mathbf{x}, t)$, measured with reference to the initial configuration, and from $\mathbf{u}$ we can determine the additional time-dependent strain and the additional stress τ. Then the total stress is $\sigma = \sigma^0 + \tau$, and after all motions have died down the new static stress field is σ^1. If ΔE is defined as the change in strain energy throughout the medium, from its initial static configuration to its final static configuration, it can be shown that

$$\Delta E = -\tfrac{1}{2} \int_\Sigma [u_i] \, (\sigma_{ij}^0 + \sigma_{ij}^1) \nu_j \, d\Sigma, \tag{1}$$

where $[\mathbf{u}]$ is the final offset. (See Fig. 3.1 for definitions of [ ] and ν.) Equation (1) is known as the Volterra relation (Steketee, 1958; Savage, 1969a).

This result (which we derive below) can be simply restated in terms of work apparently done by tractions on the fault surface. We can say from (1) that the drop in strain energy throughout the medium, $-\Delta E$, is the positive quantity obtained by imagining a quasi-static growth of traction that is linear with offset:

$$T = T^0 + (T^1 - T^0)\frac{U}{[u]} \qquad \text{for} \qquad 0 \le U \le [u] \tag{2}$$

(for each component of traction T and displacement U). Integrating from 0 to $[u]$ to get the total work done on Σ then gives (1).

Several points now need to be made about this relation between ΔE and the average stress.

The liberated energy, $-\Delta E$, supplies the work actually done on the two faces Σ^+ and Σ^- as they grind past each other, plus the work done in initiating the process of fracture. We discuss these two types of work in Chapter 11. Moreover, $-\Delta E$ supplies the seismic energy E_s that is radiated away from the source region. It is natural to introduce the *seismic efficiency*, η, as the ratio $E_s/(-\Delta E)$. Then

$$E_s = -\eta \, \Delta E = \tfrac{1}{2}\eta \int_\Sigma [u_i] \, (\sigma_{ij}^0 + \sigma_{ij}^1) \nu_j \, d\Sigma. \tag{3}$$

If the average of the two static tractions does not vary strongly over Σ, then for the type of tangential slip shown in Figure 3.2 we see that (3) can be expressed in terms of the moment $M_0 = \mu \int_\Sigma [u_1] \, d\Sigma$. This gives

$$E_s = \eta M_0 \bar{\sigma} / \mu, \tag{4}$$

where $\bar{\sigma} = \frac{1}{2}(\sigma_{13}^0 + \sigma_{13}^1)$.

From estimates that can be made of E_s, M_0, and μ, it thus becomes possible from (4) to estimate the product $\eta\bar{\sigma}$, called the *apparent stress* by Wyss and Brune (1968, 1971). The reason for this name is that $\eta\bar{\sigma}$ would be the stress that *appears* to be acting on the fault, if we make the assumption that the observed radiated energy is equal to the liberated strain energy. (The assumption here is not a good one. The seismic efficiency is at most a few percent, so that only a small fraction of the liberated energy is radiated as seismic waves.)

(continued)

BOX **3.4** *(continued)*

Since the slip function $[\mathbf{u}(\xi, t)]$ in (3.18) determines all displacements (and hence strain and stress increments) throughout the medium, it also determines the stress drop, $\boldsymbol{\sigma}^0 - \boldsymbol{\sigma}^1$. But there is no way one can work purely from observations of the radiated field $\mathbf{u}(\mathbf{x}, t)$ and learn anything about the absolute level of stress in the source region. Putting this another way, and using (1), one can make the following statement. If the same slip function $[\mathbf{u}(\xi, t)]$ occurs on Σ in two different faulting events with different initial stresses, then all the seismic displacements will be the same for the two events: but the strain energies liberated for the two events may be quite different.

It remains, then, to prove our main result (1). This is a formula of great generality, and a correct derivation can be given by considering the quasi-static deformation we described in (2). We shall give an explicit proof for the special case in which the internal strain energy $\mathcal{U}$ is given by a strain–energy function $\mathcal{W}$ (see Section 2.2). Further, we assume there is an accessible reference state of zero stress and zero strain. The initial stresses and strains just prior to faulting are σ_{ij}^0 and e_{ij}^0, and $\mathbf{u}$ is measured from this state.

From (2.32) applied to the total stresses and strains, we get

$$\begin{aligned}\mathcal{W} &= \tfrac{1}{2}(\sigma_{ij}^0 + \tau_{ij})(e_{ij}^0 + u_{i,j}) \qquad \text{(using symmetry of } \sigma_{ij}) \\ &= \mathcal{W}^0 + \tfrac{1}{2}\sigma_{ij}u_{i,j} + \tfrac{1}{2}c_{ijkl}u_{k,l}e_{ij}^0 \\ &= \mathcal{W}^0 + \tfrac{1}{2}\sigma_{ij}u_{i,j} + \tfrac{1}{2}\sigma_{kl}^0 u_{k,l} \qquad \text{(using (2.30)).}\end{aligned}$$

Thus the increase in internal energy in the new static configuration is

$$\Delta E = \int_V (\mathcal{W}^1 - \mathcal{W}^0)\, dV = \tfrac{1}{2}\int_V (\sigma_{ij}^1 + \sigma_{ij}^0)u_{i,j}\, dV, \tag{5}$$

where V is the whole elastic volume containing Σ (see Fig. 3.1). Since σ_{ij}^0 and σ_{ij}^1 are static stress fields, (2.17) implies $\sigma_{ij,j}^0 = \sigma_{ij,j}^1 = 0$ (we assume there are no body forces). From (5), we obtain

$$\Delta E = \tfrac{1}{2}\int_V \{(\sigma_{ij}^0 + \sigma_{ij}^1)u_i\}_{,j}\, dV,$$

to which we can apply Gauss's divergence theorem, regarding V as the interior of $S + \Sigma^+ + \Sigma^-$. This does give (1) if S is a rigid surface, or if, like the surface of the Earth, it is free.

discontinuity in traction was given by (3.3). Putting $[T_p] = -(c_{pqrs}\ \Delta e_{rs})\nu_q$ in (3.3), we get

$$u_n(\mathbf{x}, t) = \int_{-\infty}^{\infty} d\tau \iint_\Sigma c_{pqrs}\ \Delta e_{rs}\nu_q G_{np}(\mathbf{x}, t - \tau; \xi, 0)\, d\Sigma(\xi). \tag{3.27}$$

If the integrand and its derivatives with respect to ξ are continuous, we can apply the Gauss theorem to obtain

$$u_n(\mathbf{x}, t) = \int_{-\infty}^{\infty} d\tau \iiint_V \frac{\partial}{\partial \xi_q}\left\{c_{pqrs}\ \Delta e_{rs}G_{np}(\mathbf{x}, t - \tau; \xi, 0)\right\} dV(\xi) \tag{3.28}$$

(V here refers only to the volume of the inclusion, i.e., the source volume). Using $\partial(c_{pqrs}\,\Delta e_{rs})/\partial\xi_q = \Delta\tau_{pq,q} = 0$, we can rewrite (3.28) and obtain

$$u_n(\mathbf{x}, t) = \iiint_V c_{pqrs}\,\Delta e_{rs} * \frac{\partial G_{np}}{\partial \xi_q}\,dV. \tag{3.29}$$

Comparing this volume integral with the surface integral in (3.18), one sees that it is natural to introduce a moment-density tensor

$$\frac{dM_{pq}}{dV} = c_{pqrs}\,\Delta e_{rs} \tag{3.30}$$

with the dimensions of moment per unit volume (compare also with (3.24)). Then

$$u_n(\mathbf{x}, t) = \iiint_V \frac{dM_{pq}}{dV} * \frac{\partial G_{np}}{\partial \xi_q}\,dV. \tag{3.31}$$

Note that $\Delta\tau_{pq} = dM_{pq}/dV$ is not the stress drop (the difference between the initial equilibrium stress and the final equilibrium stress in the source region), as is clear from its definition. The stress drop is not limited to the source volume, but $\Delta\tau_{pq}$ vanishes outside the source volume. $\Delta\tau_{pq}$ is called the "stress glut" by Backus and Mulcahy (1976).

For long waves, for which the whole of V is effectively a point source, the whole volume V can be considered a system of couples located at a point, say the center of V, with moment tensor equal to the integral of moment density over V. Thus, for an effective point source, (3.23) applies, with the moment tensor components

$$M_{pq} = \iiint_V c_{pqrs}\,\Delta e_{rs}\,dV. \tag{3.32}$$

For example, if a shear collapse occurs in a homogeneous isotropic body of volume V with the nonzero transformational strain components $\Delta e_{13} = \Delta e_{31}$, say, the moment tensor is

$$\mathbf{M} = 2\mu V \begin{pmatrix} 0 & 0 & \Delta e_{13} \\ 0 & 0 & 0 \\ \Delta e_{13} & 0 & 0 \end{pmatrix}. \tag{3.33}$$

The seismic radiation is identical to the point source equivalent to a fault slip, except that the seismic moment M_0 is given by $2\mu\,\Delta e_{13}V$. For a group of earthquakes in an intraplate seismic zone, a cumulative strain may be more meaningful than a cumulative slip given by (3.26). Kostrov (1974) suggested summing moments for a group of earthquakes sharing the same source mechanism in a given volume to find the total strain in the volume. From (3.33), the total strain ΔE_{13} may be estimated as

$$\Delta E_{13} = \frac{\sum_{i=1}^{N} M_0^i}{2\mu V}, \tag{3.34}$$

where M_0^i is the moment of the ith earthquake.

Finally, let us consider a spherical volume with radius a undergoing a transformational expansion. The stress-free strain components in this case are $\Delta e_{12} = \Delta e_{13} = \Delta e_{23} = 0$ and $\Delta e_{11} = \Delta e_{22} = \Delta e_{33} = \frac{1}{3}\,\Delta V/V$, where $\Delta V/V$ is the fractional change in volume and $V = \frac{4}{3}\pi a^3$. For this expansion in an isotropic medium, $c_{pqrs}\,\Delta e_{rs} = (\lambda + \frac{2}{3}\mu)\delta_{pq}\,\Delta V/V$ and from (3.32) we have

$$\mathbf{M} = \begin{pmatrix} (\lambda + \frac{2}{3}\mu)\Delta V & 0 & 0 \\ 0 & (\lambda + \frac{2}{3}\mu)\Delta V & 0 \\ 0 & 0 & (\lambda + \frac{2}{3}\mu)\Delta V \end{pmatrix}. \tag{3.35}$$

Thus a spherical source with transformational volume expansion is equivalent to three mutually perpendicular dipoles, as shown in Figure 3.7. In the above equation, ΔV is the stress-free volume change and should not be confused with the volume change δV of a confined source region, as discussed in Problem 3.8.

Suggestions for Further Reading

Backus, G., and M. Mulcahy. Moment tensors and other phenomenological descriptions of seismic sources—I. Continuous displacements. *Geophysical Journal of the Royal Astronomical Society*, **46**, 341–361, 1976.

Backus, G., and M. Mulcahy. Moment tensors and other phenomenological descriptions of seismic sources—II. Discontinuous displacements. *Geophysical Journal of the Royal Astronomical Society*, **47**, 301–329, 1976.

Bowers, D., and J. A. Hudson. Defining the scalar moment of a seismic source with a general moment tensor. *Bulletin of the Seismological Society of America*, **89**, 1390–1394, 1999.

Burridge, R., and L. Knopoff. Body force equivalents for seismic dislocations. *Bulletin of the Seismological Society of America*, **54**, 1875–1888, 1964.

Ekström, G. Anomalous earthquakes on volcano ring-fault structures. *Earth and Planetary Science Letters*, **128**, 707–712, 1994.

Eshelby, J. D. The determination of the elastic field of an ellipsoidal inclusion and related problems. *Proceedings of the Royal Society*, **A241**, 376–396, 1957.

Heaton, T. H., and R. E. Heaton. Static deformations from point forces and force couples located in welded elastic Poissonian half-spaces: Implications for seismic moment tensors. *Bulletin of the Seismological Society of America*, **79**, 813–841, 1989.

Jost, M., and R. B. Herrmann. A student's guide to and review of moment tensors. *Seismological Research Letters*, **60**, 37–57, 1989.

Julian, B. R., A. D. Miller, and G. R. Foulger. Non-double-couple earthquakes 1. Theory. *Reviews of Geophysics*, **36**, 525–549, 1998.

Kostrov, B. V. Seismic moment and energy of earthquakes and seismic flow of rock. *Izvestia, Physics of the Solid Earth*, 13–21, January 1974.

Kostrov, B. V., and S. Das. *Principles of earthquake source mechanics*, New York: Cambridge University Press, 1988.

Maruyama, T. On force equivalents of dynamic elastic dislocations with reference to the earthquake mechanism. *Bulletin of the Earthquake Research Institute, Tokyo University*, **41**, 467–486, 1963.

Press, F., and C. Archambeau. Release of tectonic strain by underground nuclear explosions. *Journal of Geophysical Research*, **67**, 337–342, 1962.

Pujol, J., and R. B. Herrmann. A student's guide to point sources in homogeneous media. *Seismological Research Letters*, **61**, 209–224, 1990.

Savage, J. C. Steketee's paradox. *Bulletin of the Seismological Society of America*, **59**, 381, 1969.

Steketee, J. A. Some geophysical applications of the theory of dislocations. *Canadian Journal of Physics*, **36**, 1168–1198, 1958.

Stump, B. W., and L. R. Johnson. Higher-degree moment tensors—the importance of source finiteness and rupture propagation on seismograms. *Geophysical Journal of the Royal Astronomical Society*, **69**, 721–743, 1982.

Problems

3.1 Equations (3.26) and (3.34) are written as scalar equations, because in their derivation it has been assumed that earthquakes in a given region (on S, or within V) all have moment tensors with the same orientations.

Generalize (3.26) to a vector equation and (3.34) to a tensor equation in cases where earthquakes in the series (on S or in V) have moment tensors of arbitrary orientation. (For (3.26), however, continue to assume that the displacement discontinuity for each event is a shear and that S is planar.)

3.2 In our derivation of (3.2), we have assumed that the elastic moduli are continuous across Σ and that G_{np} and $\partial G_{np}/\partial \xi_q$ are continuous. If the elastic moduli are *not* continuous across Σ, interpret part of the integrand in (3.2) as a traction, and show that this representation is still valid, although $\partial G_{np}/\partial \xi_q$ may not be continuous across the surface. (*Note:* For purposes of defining $\mathbf{G}$, assume Σ^+ and Σ^- have been glued together. These surfaces—which can still move—then do not have relative motion.)

3.3 In the discussion following equations (3.15) and (3.16), we introduced the time-dependent seismic moment given by $M_0(t) = \mu \overline{u}(t) A$. Is $\overline{u}(t)$ here averaged over the area $A(t)$ that has ruptured at time t, or is it averaged over $A(\infty)$, the area that ultimately is ruptured during the seismic event under consideration? (*Hint:* Does it matter?)

3.4 Show that the moment tensor $\mathbf{M}$ described in terms of a double couple in Section 3.2 and equation (3.25), i.e.,

$$\mathbf{M} = \begin{pmatrix} 0 & 0 & M_0 \\ 0 & 0 & 0 \\ M_0 & 0 & 0 \end{pmatrix},$$

can equivalently be described by

$$\mathbf{M} = \begin{pmatrix} M_0 & 0 & 0 \\ 0 & 0 & 0 \\ 0 & 0 & -M_0 \end{pmatrix}$$

where components of **M** are now referred to the principal axes of **M** as coordinate axes. (By definition, the principal axes of a symmetric tensor are such that the off-diagonal components of the tensor, referred to these axes, are all zero.)

In terms of body-force equivalents, this result is illustrated by the following diagram:

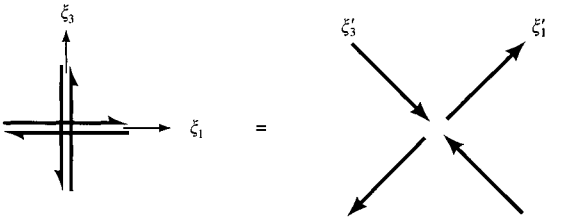

This shows that a double couple is equivalent to a pair of vector dipoles, equal in magnitude but opposite in sign.

3.5 Show that a seismic point source described by a symmetric second-order moment tensor **M** can be thought of as an isotropic point source $\mathbf{M}_{\mathrm{I}}$ plus two double couples. Is this a unique decomposition of such a point source?

Show that **M** can also be written in the form

$$\mathbf{M} = \mathbf{M}_{\mathrm{I}} + (M_1 - M_2)\begin{pmatrix} 0 & 0 & 0 \\ 0 & -1 & 0 \\ 0 & 0 & 1 \end{pmatrix} + M^{\mathrm{CLVD}}\begin{pmatrix} -\frac{1}{2} & 0 & 0 \\ 0 & -\frac{1}{2} & 0 \\ 0 & 0 & 1 \end{pmatrix},$$

in which M_i $(i = 1, 2, 3)$ are the principal moments. The last term here is called a "compensated linear vector dipole," having axial symmetry and no volume change. If $M_1 - M_2$ is the largest difference between principal moments, then M^{CLVD} quantifies the extent to which the deviatoric part of the moment tensor differs from a pure double couple.

3.6 Show that the body-force equivalent to a point source at $\boldsymbol{\xi}$ with moment tensor M_{pq} is given by

$$f_p(\mathbf{x}, t) = -M_{pq}(t)\frac{\partial}{\partial x_q}\delta(\mathbf{x} - \boldsymbol{\xi}).$$

3.7 Consider a spherical cavity with radius a inside a homogeneous isotropic body. When a uniform step in pressure, $\delta p H(t)$, is applied at the surface of the cavity, spherically symmetric waves will be generated, which have displacement only in the radial direction. After the waves have passed, displacement everywhere tends to its final static value, which characterizes the final outward expansion due to the applied pressure in the cavity.

a) Use the vector wave equation of Problem 2.1 to show that this static displacement satisfies $\nabla(\nabla \cdot \mathbf{u}) = \mathbf{0}$.

b) Hence, in this problem with spherical symmetry, show that the radial displacement is proportional to $1/r^2$ (for $a \leq r$, so that this is a so-called external solution).

c) Show from equations (2.50) and (2.46) that for this problem the radial stress is given by

$$\tau_{rr} = (\lambda + 2\mu)\frac{\partial u_r}{\partial r} + \frac{2\lambda}{r}u_r.$$

d) The walls of the cavity will oscillate at first, after the constant step in pressure is applied, but will eventually be displaced outward a constant amount. Let this final static displacement be δa. Show that

$$\delta p = 4\mu\frac{\delta a}{a}.$$

3.8 Suppose that a spherical volume with radius a, inside a homogeneous isotropic unbounded medium, undergoes expansion with stress-free volumetric strain given by $\Delta V/V$ where $V = \frac{4}{3}\pi a^3$. The moment tensor is given by equation (3.35), but now we shall consider the effects of the rest of the medium, which prevents the actual strain from attaining its stress-free value.

The confinement of the source region means that instead of radius a expanding to $a + \Delta a$ (where ΔV is given to first order by $4\pi a^2 \Delta a$), and being subjected to zero pressure, the final static radius is given by $a + \delta a$, subjected to pressure δp. We can build upon the results of Problem 3.7 to obtain relationships between the stress-free changes characterized by Δa and ΔV (see equation (3.35)) and the actual final static changes, δa and δV.

a) Use the method of Problem 3.7 to show that within the source region the final static radial displacement is proportional to r. (This is the so-called internal solution.) If A is the constant of proportionality such that the static radial displacement is Ar, show that the associated radial stress τ_{rr} is a constant and the final static value of pressure throughout the source region is

$$\delta p = -(3\lambda + 2\mu)A.$$

b) For this problem we can evaluate key steps in the series of cutting and welding operations first described by Eshelby and covered in Section 3.4. The static displacement of the surface of the source region, due to the effects of confinement, is from Δa to δa as pressure changes from the stress-free value (which is zero, by definition) to the final actual static value, δp. Show then that

$$\delta p = \frac{3\lambda + 2\mu}{a}(\Delta a - \delta a)$$

and hence, from a relationship given in Problem 3.7, that

$$\Delta a = \frac{\lambda + 2\mu}{\lambda + \frac{2}{3}\mu}\delta a.$$

c) As indicated in equation (3.35), the moment tensor is isotropic. In general $M_{pq} = M_0(t)\delta_{pq}$ is a function of time that depends on details of the process by which the source region undergoes its change in properties. The final static value from (3.35) is given by

$$M_0(\infty) = (\lambda + \tfrac{2}{3}\mu)\,\Delta V$$

where ΔV is the final value of the stress-free volume change. Show that it is also given in terms of the actual final (static) volume change δV by

$$M_0(\infty) = (\lambda + 2\mu)\,\delta V.$$

d) Show that the actual volume change δV is independent of a, in the sense that having proved $M_0(\infty) = (\lambda + 2\mu)\delta V$ as above for some small value of a, we can choose a larger value of a and evaluate the outward actual static displacement for this new surface. But δV is unchanged in value. (*Hint:* Use the exterior solution, mentioned in Problem 3.7.)

[We shall find in later chapters that the time-dependent moment is an important property of the seismic source, which can often be obtained from seismograms, and that the final value $M_0(\infty)$ is related simply to the long-period spectrum of observed signals. Our equations relating moment to ΔV and δV enable measurements of $M_0(\infty)$ to be interpreted in terms of volume change at the source, for isotropic sources. We see that the actual volume change of a source that wants to expand, δV in the present problem, is approximately half the size of the stress-free volume change (since $(\lambda + 2\mu)/(\lambda + \frac{2}{3}\mu) \sim 2$), as noted by Müller (2001). Earlier, Müller (1973b) showed that for isotropic sources the scalar moment is $(\lambda + 2\mu) \times$ area $\times$ outward displacement. In the notation used here, area $\times$ outward displacement $= 4\pi a^2 \times \delta a = \delta V$. Explosive sources are sometimes quantified by this volume change. We are free to take the value of a large enough to confine all nonelastic processes to the interior region, and as noted above the actual volume increment δV has meaning independent of any value of a. The actual volume increment δV represents the expansion that the nonlinear source region applies to the external linearly elastic region. Müller's 1973 result complements the fact that for shear faulting the double couple is based on a scalar moment given by $\mu \times$ area $\times$ slip. This too can be thought of as the output from the nonlinear region, where rocks are fracturing and shearing, applied to the external elastic region. The product given by area $\times$ slip is called the *potency*. Heaton and Heaton (1989) and Ben-Zion (2001) recommend that the potency be used to quantify earthquake (shear dislocation) sources, instead of the seismic moment ($\mu \times$ potency). Like δV, potency has the dimensions of volume change. The potency, δV, and seismic moment all provide ways to characterize quantitative attributes of the nonlinear source, which are needed to interpret measurements made in the linearly elastic region.]

CHAPTER 4

Elastic Waves from a Point Dislocation Source

We now begin a series of six chapters that develop the basic features of seismic wave propagation. So far, in Chapters 2 and 3, we have found that seismic motions can be represented by an integration over the spatial and temporal region within which the seismic source is acting. The integration (e.g., equation (3.2)) is a synthesis from the displacement field of a certain Green function, introduced in Section 2.4. In this first chapter on wave propagation we are concerned with properties of Green's function itself, and we shall derive a specific formula (4.23) for the displacement within a homogeneous, isotropic, unbounded medium due to a unidirectional force acting with general time-varying strength at a particular point of the medium. The formula is obtained by using the device of potentials for elastic displacement, and P-waves and S-waves are identified.

For many purposes, a body force acting at a point is an adequate source model for the seismic displacements observed from an earthquake. But, for fault slip, the point body force itself is a double couple (see (3.15)) rather than a unidirectional force. We obtain the displacement field for a double couple in (4.32) and discuss its radiation pattern at large distances (the "far field") and at small distances (the "near field") from the source point.

In order to adapt these exact results for practical applications, a method is needed to assess the focusing and defocusing of seismic waves by systematic inhomogeneities in the Earth. Classical ray theory can be used to obtain an approximate solution to this problem in the far field, and the chapter concludes with some general results for the amplitude and radiation patterns (both P and S) due to a double couple that models slip in a specified direction on a fault surface with specified strike and dip.

4.1 Formulation: Introduction of Potentials

The first major problem before us is to solve for the displacement $\mathbf{u}(\mathbf{x}, t)$ set up by a unidirectional point body force acting with time-varying magnitude at a fixed point O in a homogeneous, unbounded, isotropic, elastic medium. Without loss of generality, we take O as the origin of Cartesian coordinates and the x_1-axis as the body-force direction. The equation to be solved for $\mathbf{u}$ is given in Problem 2.1, for any body force, as

$$\rho \ddot{u}_i = f_i + (\lambda + \mu) u_{j,ji} + \mu u_{i,jj}$$

or

$$\rho\ddot{\mathbf{u}} = \mathbf{f} + (\lambda + 2\mu)\nabla(\nabla \cdot \mathbf{u}) - \mu\nabla \times (\nabla \times \mathbf{u}). \tag{4.1}$$

In the present case, the body force $\mathbf{f}$ is given by $f_i = X_0(t)\delta(\mathbf{x})\delta_{i1}$, and we have the initial conditions $\mathbf{u}(\mathbf{x}, 0) = \mathbf{0}$ and $\dot{\mathbf{u}}(\mathbf{x}, 0) = \mathbf{0}$ for $\mathbf{x} \neq \mathbf{0}$.

In the notation of earlier chapters, this displacement field has components

$$u_n(\mathbf{x}, t) = X_0 * G_{n1},$$

and the problem has every appearance of being complicated by details of directionality at the source ($\hat{\mathbf{x}}_1$ at O) and receiver ($\mathbf{u}$ at $\mathbf{x}$). What, then, is a similar scalar problem—but without such distracting complications—in whose terms we can begin to study the general properties of waves propagating in three dimensions away from a point source? To avoid directionality at the source, the scalar problem must be spherically symmetric, hence the problem that suggests itself is to find $g = g(\mathbf{x}, t)$ such that

$$\ddot{g} = \delta(\mathbf{x})\delta(t) + c^2\nabla^2 g, \tag{4.2}$$

with zero initial conditions.

The solution of (4.2) is

$$g(\mathbf{x}, t) = \frac{1}{4\pi c^2}\frac{\delta(t - |\mathbf{x}|/c)}{|\mathbf{x}|}. \tag{4.3}$$

This amazingly simple result, proved in Box 4.1, is very informative as to the nature of three-dimensional waves, and from it we shall construct a hierarchy of ever-more-useful Green functions for elastodynamic problems. Solution (4.3) is the first explicit wave solution we have given in this book, and three major properties should be remembered for future use. First, the solution is the product of one factor (the delta function) whose spatial fluctuation is rapid and another factor (the reciprocal distance function) whose fluctuation is relatively slow, at least away from the source. In general, there would be a radiation-pattern factor, dependent on the direction of $\mathbf{x}$ from the source, but that factor is constant in this case because of the spherical symmetry. Second, the rapidly varying function depends, at any given $|\mathbf{x}|$, only on time relative to an "arrival time," here $|\mathbf{x}|/c$, at which motion begins. Clearly, c is the velocity of wave propagation. Third, the wave shape is the same in time (at any fixed receiver) as the time history of the inhomogeneous term in (4.2). This turns out to be true only for cases in which the spatial singularity at the source is like $\delta(\mathbf{x})$ (and not, for example, a dipole), but the elastodynamic problem (4.1) is just such a case and we shall find there too that particle displacements are often dominated by the same pulse shape as is present in the applied body force. A related property for (4.2) and (4.3) is that g returns to zero at a given receiver after the wave (in this case, with shape $\delta(t - |\mathbf{x}|/c)$) has gone by.

BOX **4.1**

Proof that

$$g(\mathbf{x},t)=\frac{1}{4\pi c^2|\mathbf{x}|}\delta\left(t-\frac{|\mathbf{x}|}{c}\right)$$

is the outgoing solution of $\ddot{g}=\delta(\mathbf{x})\delta(t)+c^2\nabla^2 g$ *with zero initial conditions*

By symmetry, the spatial dependence of the solution can be only on the distance $r=|\mathbf{x}|$ from the source, so we seek the functional form of $g=g(r,t)$. Expressing ∇^2 as a differential operator in spherical polar coordinates, it follows that

$$\nabla^2 g=\frac{1}{r^2}\frac{\partial}{\partial r}\left(r^2\frac{\partial g}{\partial r}\right)=\frac{1}{r}\frac{\partial^2}{\partial r^2}(rg).$$

Therefore, everywhere except at $r=0$, rg satisfies the one-dimensional wave equation $(rg)''=r\ddot{g}/c^2$ (a prime here denoting $\partial/\partial r$), and this has the well-known general solution $rg=f(t-r/c)+h(t+r/c)$. We know that $h\equiv 0$ because the required solution is outgoing, hence it remains to prove that $f(\tau)=\delta(\tau)/(4\pi c^2)$, i.e., that $4\pi c^2 f(\tau)$ has the same properties as $\delta(\tau)$ when integrated over ranges of time.

We can establish this required result by investigating the function

$$F(r,\varepsilon_1,\varepsilon_2)\equiv 4\pi c^2\int_{r/c-\varepsilon_1}^{r/c+\varepsilon_2} g(r,t)\,dt=\frac{4\pi c^2}{r}\int_{-\varepsilon_1}^{\varepsilon_2} f(\tau)\,d\tau.$$

Operating with ∇^2 on F, we have to differentiate the limits and the integrand g with respect to r, finding

$$\nabla^2 F=4\pi c\left[2g'(r,t)+\frac{2}{r}g(r,t)+\frac{\dot{g}}{c}(r,t)\right]_{t=r/c-\varepsilon_1}^{t=r/c+\varepsilon_2}+4\pi c^2\int_{r/c-\varepsilon_1}^{r/c+\varepsilon_2}\nabla^2 g(r,t)\,dt.$$

Substituting $c^2\nabla^2 g=\ddot{g}-\delta(\mathbf{x})\delta(t)$, one can carry out the above integral of $\ddot{g}$ to give another term in $\dot{g}/c$ in the square bracket above. All these terms then cancel out, since $rg=f(t-r/c)$ implies $g'=-g/r-\dot{g}/c$, which leaves

$$\nabla^2 F=-4\pi\delta(\mathbf{x})\int_{r/c-\varepsilon_1}^{r/c+\varepsilon_2}\delta(t)\,dt.$$

When the right-hand side is integrated over any volume V, whether the origin is in V or not, it yields the same result as the volume integral of $-4\pi\delta(\mathbf{x})\int_{-\varepsilon_1}^{\varepsilon_2}\delta(t)\,dt$. Using the property $\nabla^2(1/r)=-4\pi\delta(\mathbf{x})$, it follows that

$$F(r,\varepsilon_1,\varepsilon_2)=\frac{1}{r}\int_{-\varepsilon_1}^{\varepsilon_2}\delta(t)\,dt.$$

(F does not involve an additional harmonic function, since such a function would either add another singularity at $r=0$ or violate the property $F\to 0$ as $r\to\infty$.) From the second equality given in the definition of F, we can now see that $4\pi c^2\int_{-\varepsilon_1}^{\varepsilon_2} f(\tau)\,dt=\int_{-\varepsilon_1}^{\varepsilon_2}\delta(t)\,dt$ for all $(\varepsilon_1,\varepsilon_2)$, and hence $f(\tau)$ is the required delta function.

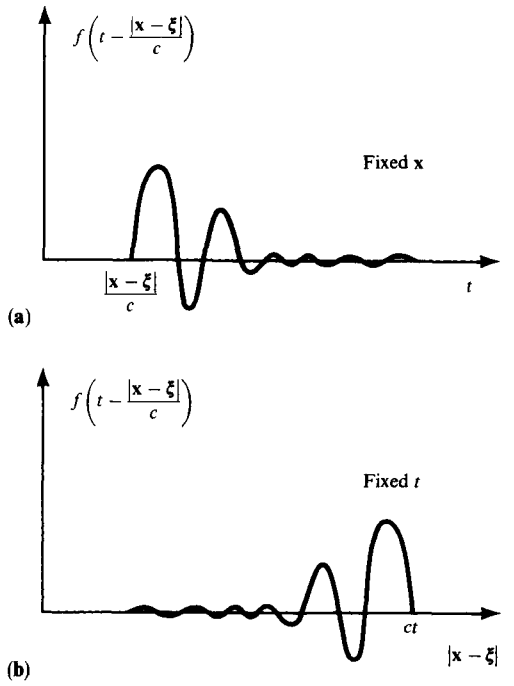

FIGURE **4.1**
In its simplest form, a wave is a propagating quantity that is a function only of a particular linear combination of spatial coordinates and time. (**a**) For some purposes, we are interested in the wave as a function of time at a fixed distance $|\mathbf{x}-\boldsymbol{\xi}|$ from the source at $\boldsymbol{\xi}$. This is the case in a seismogram. (**b**) For other purposes, we are interested in the wave as a function of position at fixed time. This is the case in a photograph.

At this stage, the following three problems can be stated and solved (zero initial conditions are assumed throughout):

(i) If $\ddot{g}_1 = \delta(\mathbf{x}-\boldsymbol{\xi})\delta(t-\tau) + c^2\nabla^2 g_1$ then a shift of the origin used in the previous solution gives here

$$g_1(\mathbf{x},t) = \frac{1}{4\pi c^2}\frac{\delta\left(t-\tau-\dfrac{|\mathbf{x}-\boldsymbol{\xi}|}{c}\right)}{|\mathbf{x}-\boldsymbol{\xi}|}.$$

(ii) If $\ddot{g}_2 = \delta(\mathbf{x}-\boldsymbol{\xi})f(t) + c^2\nabla^2 g_2$, we note that $f(t) = \int_{-\infty}^{\infty} f(\tau)\delta(t-\tau)\,d\tau$ so that we can use a superposition of solutions g_1 above to get the following exact result

$$g_2(\mathbf{x},t) = \int_{-\infty}^{\infty} f(\tau)g_1(\mathbf{x},t)\,d\tau = \frac{1}{4\pi c^2}\frac{f\left(t-\dfrac{|\mathbf{x}-\boldsymbol{\xi}|}{c}\right)}{|\mathbf{x}-\boldsymbol{\xi}|}. \tag{4.4}$$

We shall later find solutions in a form similar to (4.4), but for wave propagation in inhomogeneous media. These, however, will be only approximations, accurate only at great distance from the point source.

(iii) If the source is extended throughout a volume V as well as in time, say

$$\frac{\partial^2 \phi}{\partial t^2} = \frac{\Phi(\mathbf{x}, t)}{\rho} + \alpha^2 \nabla^2 \phi \tag{4.5}$$

(using ϕ now rather than g_3, to anticipate future needs), then the source is

$$\Phi(\mathbf{x}, t) = \int_{-\infty}^{\infty} d\tau \iiint_V \Phi(\xi, \tau)\, \delta(\mathbf{x} - \xi)\, \delta(t - \tau)\, dV(\xi).$$

From superposition of g_2 solutions, the solution of (4.5) is

$$\phi(\mathbf{x}, t) = \frac{1}{4\pi\alpha^2\rho} \iiint_V \frac{\Phi\left(\xi, t - \dfrac{|\mathbf{x} - \xi|}{\alpha}\right)}{|\mathbf{x} - \xi|}\, dV, \tag{4.6}$$

which has the important property that the field at $(\mathbf{x}, t)$ is sensitive to source activity in the element δV (at ξ) only at the so-called *retarded time*, $t - |\mathbf{x} - \xi|/\alpha$. With this understood, it should again be emphasized that the solution (4.6) is remarkably simple, in view of the equation that it solves, (4.5). This equation is a second-order partial differential equation in four variables (three of space, one of time), and has a general inhomogeneous term.

The equation

$$\nabla^2 \phi = -\frac{\Phi(\mathbf{x})}{\alpha^2 \rho} \tag{4.7}$$

is a special example of (4.5), called a Poisson equation, and it has no time dependence. From (4.6), we see that it has the time-independent solution

$$\phi(\mathbf{x}) = \frac{1}{4\pi\alpha^2\rho} \iiint_V \frac{\Phi(\xi)}{|\mathbf{x} - \xi|}\, dV. \tag{4.8}$$

The problem now facing us is to find a way of breaking up the elastodynamic equation (4.1) into soluble equations of the type (4.5). In what follows, we shall state a way in which this breakup can be achieved (Lamé's theorem), and in Box 4.2 we give some perspective on what is actually a rather subtle result.

4.1.1 LAMÉ'S THEOREM

If the displacement field $\mathbf{u} = \mathbf{u}(\mathbf{x}, t)$ satisfies

$$\rho \ddot{\mathbf{u}} = \mathbf{f} + (\lambda + 2\mu)\nabla(\nabla \cdot \mathbf{u}) - \mu \nabla \times (\nabla \times \mathbf{u}), \tag{4.1 again}$$

and if the body force and initial values of $\dot{\mathbf{u}}$ and $\mathbf{u}$ are expressed in terms of Helmholtz potentials via

$$\mathbf{f} = \nabla\Phi + \nabla \times \Psi; \qquad \dot{\mathbf{u}}(\mathbf{x}, 0) = \nabla A + \nabla \times \mathbf{B}; \qquad \mathbf{u}(\mathbf{x}, 0) = \nabla C + \nabla \times \mathbf{D}, \tag{4.9}$$

with

$$\nabla \cdot \Psi, \quad \nabla \cdot \mathbf{B}, \quad \nabla \cdot \mathbf{D} \qquad \text{all zero}, \tag{4.10}$$

then there exist potentials ϕ and $\boldsymbol{\psi}$ for $\mathbf{u}$ with all of the following four properties:

(i)

$$\mathbf{u} = \nabla\phi + \nabla \times \boldsymbol{\psi} \tag{4.11}$$

(ii)

$$\nabla \cdot \boldsymbol{\psi} = 0, \tag{4.12}$$

(iii)

$$\ddot{\phi} = \frac{\Phi}{\rho} + \alpha^2 \nabla^2 \phi \qquad \left(\text{with } \alpha^2 = \frac{\lambda + 2\mu}{\rho}\right), \tag{4.5 again}$$

(iv)

$$\ddot{\boldsymbol{\psi}} = \frac{\boldsymbol{\Psi}}{\rho} + \beta^2 \nabla^2 \boldsymbol{\psi} \qquad \left(\text{with } \beta^2 = \frac{\mu}{\rho}\right) \tag{4.13}$$

($\nabla\phi$ and $\nabla \times \boldsymbol{\psi}$ are called the *P-wave* and *S-wave components* of $\mathbf{u}$, respectively).

The proof entails constructing ϕ and $\boldsymbol{\psi}$ by integrations of $\ddot{\phi}$ and $\ddot{\boldsymbol{\psi}}$ as follows:

$$\phi(\mathbf{x}, t) = \rho^{-1} \int_0^t (t - \tau)\{\Phi(\mathbf{x}, \tau) + (\lambda + 2\mu)\nabla \cdot \mathbf{u}(\mathbf{x}, \tau)\}\, d\tau + tA + C \tag{4.14}$$

$$\boldsymbol{\psi}(\mathbf{x}, t) = \rho^{-1} \int_0^t (t - \tau)\{\boldsymbol{\Psi}(\mathbf{x}, \tau) - \mu\nabla \times \mathbf{u}(\mathbf{x}, \tau)\}\, d\tau + t\mathbf{B} + \mathbf{D}, \tag{4.15}$$

and verifying that all the properties (i)–(iv) are indeed satisfied if we use (4.14) and (4.15) to *define* ϕ and $\boldsymbol{\psi}$. Properties (i) and (ii) are easy to verify. To obtain (iii), note from (4.14) that the left-hand side of (iii) is $\{\Phi + (\lambda + 2\mu)\nabla \cdot \mathbf{u}\}/\rho$. This does equal the right-hand side of (iii), because from (i) it follows that $\nabla^2\phi = \nabla \cdot \mathbf{u}$. The final property (iv) follows in a similar fashion, making repeated use of the vector identities

$$\nabla^2 \mathbf{V} \equiv \nabla(\nabla \cdot \mathbf{V}) - \nabla \times (\nabla \times \mathbf{V}), \qquad \nabla \times (\nabla\Phi) \equiv \mathbf{0}, \qquad \nabla \cdot (\nabla \times \mathbf{V}) \equiv 0.$$

Now that we have found the solution for the scalar wave equation and have found how to turn the elastic wave equation into simpler equations for potentials, we can return to the main theme of this chapter.

4.2 Solution for the Elastodynamic Green Function in a Homogeneous, Isotropic, Unbounded Medium

Recall that we are seeking to solve for the displacement $\mathbf{u}(\mathbf{x}, t)$ that satisfies the elastic-wave equation (4.1) with a body force $\mathbf{f}$, which is $X_0(t)$ applied in the x_1-direction (i.e., $\hat{\mathbf{x}}_1$) at the origin.

BOX **4.2**
On potentials

Helmholtz potentials for the vector field $\mathbf{Z} = \mathbf{Z}(\mathbf{x})$ are fields $X, \mathbf{Y}$ such that $\mathbf{Z} = \nabla X + \nabla \times \mathbf{Y}$, with $\nabla \cdot \mathbf{Y} = 0$. To construct X and $\mathbf{Y}$ (given $\mathbf{Z}$), it is enough to solve the vector Poisson equation $\nabla^2 \mathbf{W} = \mathbf{Z}$, since then the identity $\nabla^2 \mathbf{W} \equiv \nabla(\nabla \cdot \mathbf{W}) - \nabla \times (\nabla \times \mathbf{W})$ tells us that we can choose potentials $X = \nabla \cdot \mathbf{W}$ and $\mathbf{Y} = -\nabla \times \mathbf{W}$. The solution for the vector Poisson equation is a simple extension of (4.8) and (4.7), giving here

$$\mathbf{W}(\mathbf{x}) = -\iiint_V \frac{\mathbf{Z}(\xi)}{4\pi|\mathbf{x} - \xi|} dV(\xi).$$

Why, then, do we not define elastic potentials ϕ and ψ to be Helmholtz potentials for $\mathbf{u}$? The reason is that a substitution of (4.11) and (4.12) into the elastic-wave equation (4.1) yields a *third*-order partial differential equation in ϕ and ψ. This has to be operated on with $\nabla \cdot (\ )$ and $\nabla \times (\ )$ to give separated equations for the potentials, which then satisfy *fourth*-order wave equations,

$$\nabla^2\{\rho\ddot{\phi} - \Phi - (\lambda + 2\mu)\nabla^2\phi\} = 0, \qquad \nabla^2\{\rho\ddot{\psi} - \Psi - \mu\nabla^2\psi\} = \mathbf{0}.$$

Lamé's theorem gives us a much better result, to the effect that we need seek potentials satisfying only *second*-order wave equations.

Finally, two remarkable facts: Lamé's theorem was conjectured and used for almost 100 years before a proof such as the one here, based on equations (4.14) and (4.15), was ever given; and the theorem remains true even for static fields $\mathbf{u} = \mathbf{u}(\mathbf{x})$. In this case, ϕ and ψ are still functions of $(\mathbf{x}, t)$, and they still satisfy wave equations. The static displacement is still the sum of the P-wave and the S-wave, although the time dependence cancels out for the combination $\nabla\phi + \nabla \times \psi$.

The first step is to find body-force potentials Φ and Ψ such that

$$X_0(t)\,\delta(\mathbf{x})\,\hat{\mathbf{x}}_1 = \mathbf{f} = \nabla\Phi + \nabla \times \Psi \qquad \text{and} \qquad \nabla \cdot \Psi = 0. \tag{4.16}$$

This is a problem of the type solved in Box 4.2, since Φ and Ψ are Helmholtz potentials for $\mathbf{f}(\mathbf{x}, t)$ at each fixed moment of time. One first constructs

$$\mathbf{W} = -\frac{X_0(t)}{4\pi} \iiint_V (1, 0, 0) \frac{\delta(\xi)\, dV}{|\mathbf{x} - \xi|} = -\frac{X_0(t)}{4\pi|\mathbf{x}|}\hat{\mathbf{x}}_1,$$

which then gives

$$\Phi(\mathbf{x}, t) = \nabla \cdot \mathbf{W} = -\frac{X_0(t)}{4\pi} \frac{\partial}{\partial x_1} \frac{1}{|\mathbf{x}|}$$

$$\Psi(\mathbf{x}, t) = -\nabla \times \mathbf{W} = \frac{X_0(t)}{4\pi} \left(0, \frac{\partial}{\partial x_3} \frac{1}{|\mathbf{x}|}, -\frac{\partial}{\partial x_2} \frac{1}{|\mathbf{x}|}\right). \tag{4.17}$$

At first sight, it is somewhat surprising that our spatially concentrated body force (proportional to $\delta(\mathbf{x})$) has potentials (4.17) that are nonzero outside the source region. This often happens in elasticity, and it brings out the artificiality of the potential method.

The second step in finding displacements is to solve wave equations for the Lamé potentials ϕ and $\boldsymbol{\psi}$. From (4.5), (4.13), and (4.17), we get

$$\ddot{\phi} = -\frac{X_0(t)}{4\pi\rho}\frac{\partial}{\partial x_1}\frac{1}{|\mathbf{x}|} + \alpha^2\nabla^2\phi \tag{4.18}$$

and

$$\ddot{\boldsymbol{\psi}} = \frac{X_0(t)}{4\pi\rho}\left(0, \frac{\partial}{\partial x_3}\frac{1}{|\mathbf{x}|}, -\frac{\partial}{\partial x_2}\frac{1}{|\mathbf{x}|}\right) + \beta^2\nabla^2\boldsymbol{\psi}. \tag{4.19}$$

The solution of (4.18) follows by comparison with (4.5) and (4.6), so that here

$$\phi(\mathbf{x}, t) = -\frac{1}{(4\pi\alpha)^2\rho}\iiint_V \frac{X_0\left(t - \dfrac{|\mathbf{x}-\boldsymbol{\xi}|}{\alpha}\right)}{|\mathbf{x}-\boldsymbol{\xi}|}\frac{\partial}{\partial\xi_1}\frac{1}{|\boldsymbol{\xi}|}dV(\boldsymbol{\xi}). \tag{4.20}$$

Fortunately, this integral can be simplified by integrating over the volume V via the system of concentric spherical shells centered on $\mathbf{x}$. If $\alpha\tau$ is the radius of a typical shell S, so that $|\mathbf{x}-\boldsymbol{\xi}| = \alpha\tau$ and the shell thickness is $\alpha\, d\tau$, then

$$\phi(\mathbf{x}, t) = -\frac{1}{(4\pi\alpha)^2\rho}\int_0^\infty \frac{X_0(t-\tau)}{\tau}\left(\iint_S \frac{\partial}{\partial\xi_1}\frac{1}{|\boldsymbol{\xi}|}dS\right)d\tau.$$

In Box 4.3, it is shown that the integral over S is a simple explicit function of $\mathbf{x}$ and τ, and it follows that

$$\phi(\mathbf{x}, t) = -\frac{1}{4\pi\rho}\left(\frac{\partial}{\partial x_1}\frac{1}{|\mathbf{x}|}\right)\int_0^{|\mathbf{x}|/\alpha} \tau X_0(t-\tau)\, d\tau. \tag{4.21}$$

Similarly, for the vector Lamé potential, one finds

$$\boldsymbol{\psi}(\mathbf{x}, t) = \frac{1}{4\pi\rho}\left(0, \frac{\partial}{\partial x_3}\frac{1}{|\mathbf{x}|}, -\frac{\partial}{\partial x_2}\frac{1}{|\mathbf{x}|}\right)\int_0^{|\mathbf{x}|/\beta} \tau X_0(t-\tau)\, d\tau. \tag{4.22}$$

The third and final step in obtaining the displacement due to body force $X_0(t)$ applied in the x_1-direction at the origin is to form $\nabla\phi + \nabla\times\boldsymbol{\psi}$ from (4.21) and (4.22). Using $r = |\mathbf{x}|$, this gives

$$u_i(\mathbf{x}, t) = \frac{1}{4\pi\rho}\left(\frac{\partial^2}{\partial x_i\partial x_1}\frac{1}{r}\right)\int_{r/\alpha}^{r/\beta} \tau X_0(t-\tau)\, d\tau$$
$$+ \frac{1}{4\pi\rho\alpha^2 r}\left(\frac{\partial r}{\partial x_i}\frac{\partial r}{\partial x_1}\right)X_0\left(t - \frac{r}{\alpha}\right) + \frac{1}{4\pi\rho\beta^2 r}\left(\delta_{i1} - \frac{\partial r}{\partial x_i}\frac{\partial r}{\partial x_1}\right)X_0\left(t - \frac{r}{\beta}\right).$$

BOX **4.3**

Evaluation of a surface integral

We define

$$h(\mathbf{x}, \tau) \equiv \iint_{|\mathbf{x}-\boldsymbol{\xi}|=\alpha\tau} \frac{\partial}{\partial \xi_1} \frac{1}{|\boldsymbol{\xi}|} dS(\boldsymbol{\xi})$$

and show here that

$$h(\mathbf{x}, \tau) = 0 \qquad \text{for} \qquad |\mathbf{x}|/\alpha < \tau,$$

but

$$h(\mathbf{x}, \tau) = 4\pi\alpha^2\tau^2 \frac{\partial}{\partial x_1} \frac{1}{|\mathbf{x}|} \qquad \text{for} \qquad \tau < |\mathbf{x}|/\alpha.$$

1. Note the physical meaning of the result: suppose there is a uniform surface density on S. Then $|\boldsymbol{\xi}|^{-1} dS$ is proportional to the gravitational potential of dS at O, and $\partial|\boldsymbol{\xi}|^{-1}/\partial\xi_1 dS$ is the component of the force in the $\hat{\mathbf{x}}_1$ direction. The desired result follows from finding the total potential at O due to the shell and then differentiating to get the total force component along $\hat{\mathbf{x}}_1$. The potential inside a spherical shell is constant, and outside the spherical shell one can find the potential by lumping all the mass into a point at the center, i.e., at $\mathbf{x}$.

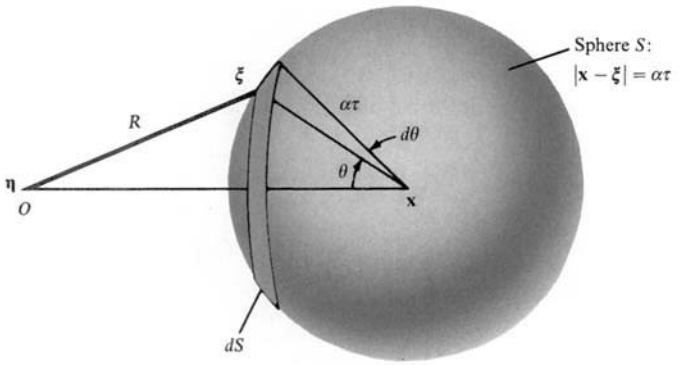

2. Detailed proof: Suppose that O is at $\boldsymbol{\eta}$, so that we can differentiate with respect to varying $\boldsymbol{\eta}$ and subsequently set $\boldsymbol{\eta} = \mathbf{0}$. Also take $r = |\mathbf{x} - \boldsymbol{\eta}|$, $R = |\boldsymbol{\xi} - \boldsymbol{\eta}|$, and θ as the angle between $\mathbf{x} - \boldsymbol{\eta}$ and $\mathbf{x} - \boldsymbol{\xi}$. Then

$$h = -\frac{\partial}{\partial \eta_1} \iint_S \frac{dS}{R} \qquad \text{(since } \boldsymbol{\eta} \text{ is fixed for all } \boldsymbol{\xi} \text{ on } S\text{)}.$$

Now choose $dS = 2\pi\alpha^2\tau^2 \sin\theta \, d\theta$:

$$\iint_S \frac{dS}{R} = 2\pi\alpha^2\tau^2 \int_0^\pi \frac{\sin\theta \, d\theta}{R}.$$

(continued)

BOX **4.3** *(continued)*

But $R^2 = r^2 + \alpha^2\tau^2 - 2r\alpha\tau\cos\theta$, so that $2R\,dR = 2r\alpha\tau\sin\theta\,d\theta$, and

$$\iint_S \frac{dS}{R} = \frac{2\pi\alpha\tau}{r}\int_{R(\theta=0)}^{R(\theta=\pi)} dR = \frac{2\pi\alpha\tau}{r}\int_{|\alpha\tau-r|}^{\alpha\tau+r} dR = \begin{cases} 4\pi\alpha\tau & \text{if } O \text{ is inside } S \quad (r/\alpha < \tau) \\ \dfrac{4\pi\alpha^2\tau^2}{r} & \text{if } O \text{ is outside } S \quad (\tau < r/\alpha). \end{cases}$$

Hence, if O is inside S,

$$h = -\frac{\partial}{\partial\eta_1}4\pi\alpha\tau = 0 \qquad (r/\alpha < \tau),$$

and if O is outside S,

$$h = -\frac{\partial}{\partial\eta_1}\frac{4\pi\alpha^2\tau^2}{r} = 4\pi\alpha^2\tau^2\frac{\partial}{\partial x_1}\frac{1}{r} \qquad (\tau < r/\alpha).$$

If we change the subscript 1 to j throughout this formula, the result corresponds to the displacement set up by a point force in the x_j- direction. Using direction cosines γ_i for the vector $\mathbf{x}$, so that $\gamma_i = x_i/r = \partial r/\partial x_i$, we can write

$$\frac{\partial^2}{\partial x_i\,\partial x_j}\frac{1}{r} = \frac{3\gamma_i\gamma_j - \delta_{ij}}{r^3}.$$

Then for a point force $X_0(t)$ in the x_j-direction at the origin, we have

$$\begin{aligned} u_i(\mathbf{x},t) &= X_0 * G_{ij} \qquad \text{(in the notation of Chapter 3)} \\ &= \frac{1}{4\pi\rho}\left(3\gamma_i\gamma_j - \delta_{ij}\right)\frac{1}{r^3}\int_{r/\alpha}^{r/\beta}\tau X_0(t-\tau)\,d\tau \\ &\quad + \frac{1}{4\pi\rho\alpha^2}\gamma_i\gamma_j\frac{1}{r}X_0\left(t-\frac{r}{\alpha}\right) - \frac{1}{4\pi\rho\beta^2}\left(\gamma_i\gamma_j - \delta_{ij}\right)\frac{1}{r}X_0\left(t-\frac{r}{\beta}\right). \end{aligned} \tag{4.23}$$

This is the formula we wanted to find; an equivalent version was first given by Stokes in 1849. It is one of the most important solutions in elastic wave radiation, and we next examine its main properties.

The relative magnitude of different terms in the Green function depends upon the source–receiver distance r. Note that $r^{-3}\int_{r/\alpha}^{r/\beta}\tau X_0(t-\tau)\,d\tau$ behaves like r^{-2} for sources in which X_0 is nonzero for times that are short compared to $r/\beta - r/\alpha$ (e.g., for the impulsive source of Green's function itself, with $X_0(t) = \delta(t)$). The remaining terms in (4.23) behave like r^{-1}, becoming dominant (over r^{-2}) as $r \to \infty$. The terms including $r^{-1}X_0(t - r/\alpha)$ and $r^{-1}X_0(t - r/\beta)$ are therefore called *far-field* terms. But since r^{-2} dominates r^{-1} as $r \to 0$, the term including $r^{-3}\int \tau X_0(t-\tau)\,d\tau$ is called a *near-field* term. Almost all seismic data used in geophysics are collected in the far field (i.e., at a distance at which far-field terms in (4.23) are dominant). There are important exceptions, however, such as observations of the final static offset due to faulting, which is a near-field effect. The seismic data used in earthquake engineering are occasionally collected in the near field. But when one takes up

in more detail the question of where the near field ends and where the far field begins, it becomes apparent that far-field terms also can be big enough to cause earthquake damage to engineering structures. (See Problem 4.1.)

4.2.1 PROPERTIES OF THE FAR-FIELD P-WAVE

We introduce here the *far-field P-wave*, which for (4.23) has the displacement $\mathbf{u}^P$ given by

$$u_i^P(\mathbf{x}, t) = \frac{1}{4\pi\rho\alpha^2}\gamma_i\gamma_j\frac{1}{r}X_0\left(t - \frac{r}{\alpha}\right). \tag{4.24}$$

As in (4.23), this is for a point force $X_0(t)$ in the x_j-direction at the origin. Along a given direction $\boldsymbol{\gamma}$ from the source, it follows from (4.24) that this wave

(i) attenuates as r^{-1};

(ii) has a waveform that depends on the time–space combination $t - r/\alpha$, and therefore propagates with speed α (recall that $\alpha^2 = (\lambda + 2\mu)/\rho$);

(iii) has a displacement waveform that is proportional to the applied force at retarded time; and

(iv) has a direction of displacement at $\mathbf{x}$ that is parallel to the direction $\boldsymbol{\gamma}$ from the source. This follows from the property $u_i^P \propto \gamma_i$ (see (4.24)). The far-field P-wave is therefore *longitudinal* (sometimes called *radial*) in that its direction of particle motion is the same as the direction of propagation. If $t = 0$ is chosen as the time at which $X_0(t)$ first becomes nonzero, then r/α is the *arrival time* of the P-wave at r.

4.2.2 PROPERTIES OF THE FAR-FIELD S-WAVE

The *far-field S-wave* in (4.23) has displacement $\mathbf{u}^S$ given by

$$u_i^S(x, t) = \frac{1}{4\pi\rho\beta^2}(\delta_{ij} - \gamma_i\gamma_j)\frac{1}{r}X_0\left(t - \frac{r}{\beta}\right). \tag{4.25}$$

As in (4.23), this is for a point force $X_0(t)$ in the x_j-direction at the origin. Recall that $\boldsymbol{\gamma}$ is the unit vector directed from the source to the receiver. Along a given direction $\boldsymbol{\gamma}$, this wave

(i) attenuates as r^{-1};

(ii) propagates with speed β and has arrival time r/β at $\mathbf{x}$;

(iii) has a displacement waveform that is proportional to the applied force at retarded time; and

(iv) has a direction of displacement $\mathbf{u}^S$ at $\mathbf{x}$ that is perpendicular to the direction $\boldsymbol{\gamma}$ from the source. (From (4.25) it is easy to show that $\mathbf{u}^S \cdot \boldsymbol{\gamma} = 0$.) The far-field S-wave is therefore a *transverse* wave, because its direction of particle motion is normal to the direction of propagation.

Radiation patterns for $\mathbf{u}^P$ and $\mathbf{u}^S$ are given in Figure 4.2.

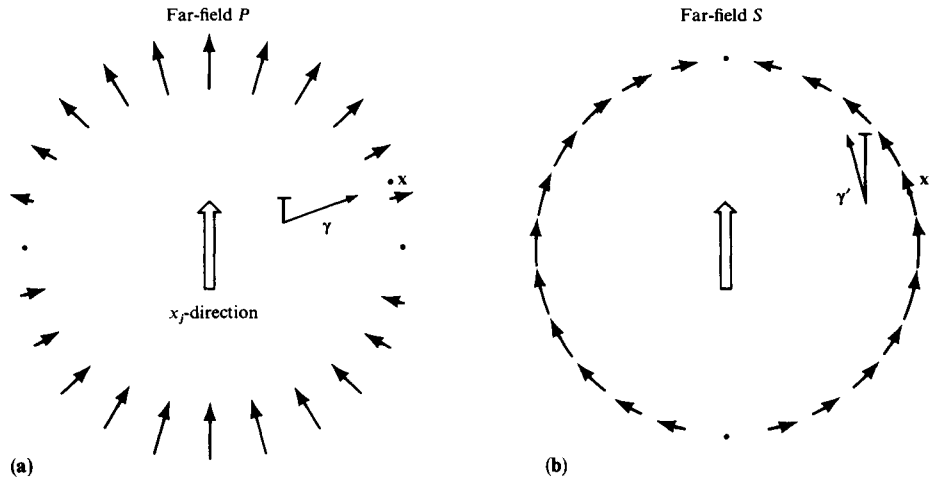

FIGURE **4.2**
Radiation patterns showing the amplitude and direction of P and S motions in the far field, for a point force $\Uparrow$ in the x_j-direction within an infinite homogeneous isotropic medium. Directions for P and S are given by properties (iv) for each wave (see text), the particular choice of transverse direction $\boldsymbol{\gamma}'$ for S being determined by requiring axial symmetry. (**a**) The magnitude of $\mathbf{u}^P$ is given by $\mathbf{u}^P \cdot \boldsymbol{\gamma} \propto \gamma_j$, where γ_j is the cosine of the angle between the force direction and the direction of $\mathbf{u}^P$. (**b**) The magnitude of $\mathbf{u}^S$ is given by $\mathbf{u}^S \cdot \boldsymbol{\gamma}' \propto \gamma'_j$, where γ'_j is the cosine of the angle between the force direction and the direction of $\mathbf{u}^S$.

4.2.3 PROPERTIES OF THE NEAR-FIELD TERM

We define the near-field displacement $\mathbf{u}^N$ in (4.23) by

$$u_i^N(\mathbf{x}, t) = \frac{1}{4\pi\rho}(3\gamma_i\gamma_j - \delta_{ij})\frac{1}{r^3}\int_{r/\alpha}^{r/\beta} \tau X_0(t-\tau)\, d\tau. \tag{4.26}$$

As in (4.23), this is for a point force $X_0(t)$ in the x_j-direction at the origin.

In our derivation (see above) of this near-field component, we see that there are contributions both from the gradient of the P-wave potential (ϕ) and from the curl of the S-wave potential (ψ). In this sense, $\mathbf{u}^N$ is composed of both P-wave and S-wave motions. It is neither irrotational (i.e., having zero curl), nor solenoidal (i.e., having zero divergence), and this indicates that it is not always fruitful to decompose an elastic displacement field into its P-wave and S-wave components. Furthermore, $\mathbf{u}^N$ has both longitudinal and transverse motions, since the longitudinal component is

$$\mathbf{u}^N \cdot \boldsymbol{\gamma} = \gamma_j \frac{1}{2\pi\rho r^3}\int_{r/\alpha}^{r/\beta} \tau X_0(t-\tau)\, d\tau$$

and the transverse component is

$$\mathbf{u}^N \cdot \boldsymbol{\gamma}' = -\gamma'_j \frac{1}{4\pi\rho r^3}\int_{r/\alpha}^{r/\beta} \tau X_0(t-\tau)\, d\tau$$

(see Fig. 4.2 for definitions of $\boldsymbol{\gamma}$ and $\boldsymbol{\gamma}'$).

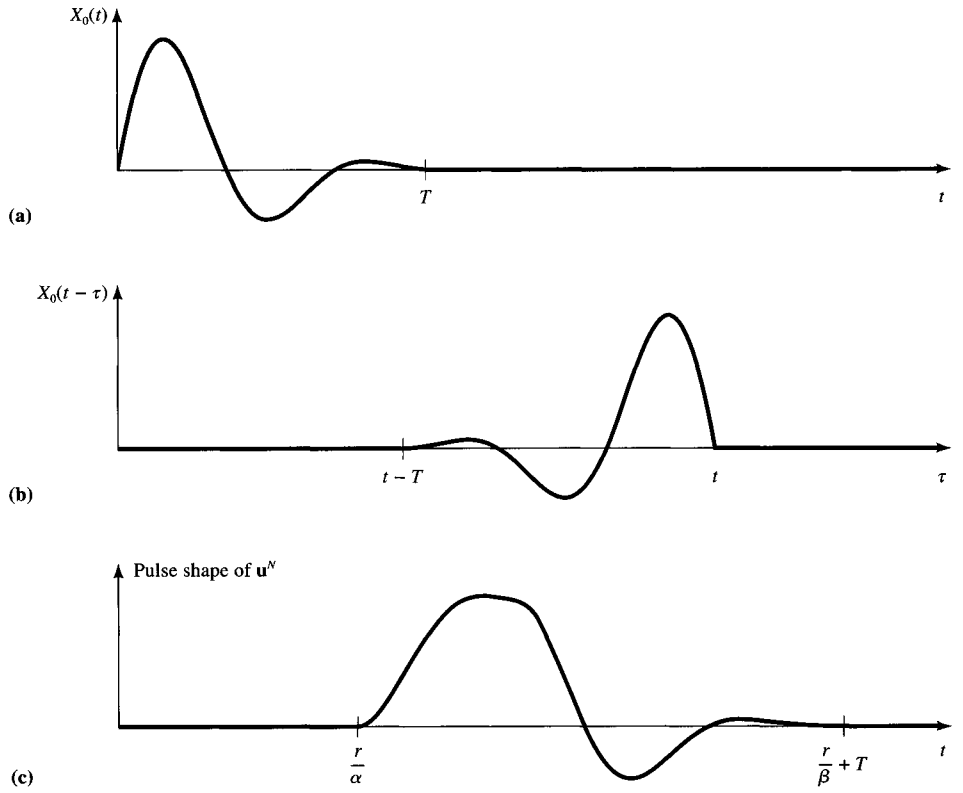

FIGURE **4.3**
Diagrams to interpret the "arrival time" and "duration" of the near-field motion, $\mathbf{u}^N$. (**a**) Body-force time function, nonzero only for t between 0 and T. (**b**) Variation of $X_0(t-\tau)$ against τ for fixed t. This function is nonzero for τ in the range r/α to r/β only if t lies between r/α and $r/\beta + T$. (**c**) Variation of $\int_{r/\alpha}^{r/\beta} \tau X_0(t-\tau)\, d\tau$ with time. At great distance, $r/\alpha \gg T$, $X_0(t-\tau)$ in the integrand for $\mathbf{u}^N$ is effectively a delta function, and $\mathbf{u}^N$ has nonzero values only between r/α and r/β, with height proportional to time. At such distances, however, $\mathbf{u}^N$ is usually negligible compared to the far-field terms.

For the near-field displacement, it is not possible to identify the simple properties corresponding to (i)–(iv) found for the far field. Nevertheless we can identify the arrival time and the duration of displacement $\mathbf{u}^N$ at a fixed receiver. If $t = 0$ is chosen as the time when $X_0(t)$ first becomes nonzero, let us suppose that $X_0(t)$ returns again to zero for all times $t \geq T$. A function of this type is shown in Figure 4.3a, and $X_0(t-\tau)$ is shown (against τ) in Figure 4.3b. It then follows from (4.26) that $\mathbf{u}^N$ is a motion that arrives at $\mathbf{x}$ at the P-wave arrival time (r/α) and which is active until the time $r/\beta + T$, so that it has duration $(r/\beta - r/\alpha) + T$. If $X_0(t)$ never does return permanently to zero (i.e., if T is not finite), then the near-field term persists indefinitely. Several further properties of $X_0 * \mathbf{G}$ are brought out in Problems 4.1 and 4.2.

We have seen in Chapters 2 and 3 that in seismology the Green function is more appropriately studied in the form $G_{np,q}$, with an active couple at the source, rather than a single force. We now develop some special properties of this more directly relevant displacement field.

4.3 The Double-Couple Solution in an Infinite Homogeneous Medium

This section describes one more step in the sequence of wave solutions that we initiated in Box 4.1 with a scalar wave, spreading in spherically symmetric fashion from a point source. We have seen how to synthesize vector waves and second-order tensor fields G_{ij}. Now we wish to study the third-order tensor field $G_{np,q}$ so that we may understand the radiation pattern (in both near field and far field) for the waves set up by a displacement discontinuity (see (3.18), or, for a point source, (3.23)). We shall conclude with remarkably straightforward formulas (4.32)–(4.33) for the displacement due to a moment tensor **M** corresponding to a point shear dislocation. These formulas describe the far-field radiation pattern that has actually been observed in many thousands of earthquakes. Since this double-couple source is of such practical interest, it might be thought that we should restrict our analysis to a particular combination such as $M_0 * (\partial G_{n1}/\partial \xi_3) + M_0 * (\partial G_{n3}/\partial \xi_1)$ (see (3.23) and (3.25)). Instead, with less effort and using the summation convention we shall work with the fully general nine couples in $M_{pq} * G_{np,q}$.

Our principal findings will be that far-field displacements still attenuate as r^{-1} and are proportional to particle velocity at the source; that certain remarkable similarities are found between far-field and near-field radiation patterns; and that the final static displacement, set up throughout the medium by a displacement dislocation that eventually reaches a final fixed offset, attenuates as r^{-2}.

We start with an application of Stokes' solution, (4.23), to obtain the n-component of displacement due to a body-force distribution $\mathbf{f}(\mathbf{x}, t) = \mathbf{F}(t)\delta(\mathbf{x} - \boldsymbol{\xi})$, i.e., the force $\mathbf{F}(t)$ applied at $\boldsymbol{\xi}$. This displacement, at $(\mathbf{x}, t)$, is

$$F_p * G_{np} = \frac{1}{4\pi\rho}(3\gamma_n\gamma_p - \delta_{np})\frac{1}{r^3}\int_{r/\alpha}^{r/\beta} \tau F_p(t-\tau)\, d\tau + \frac{1}{4\pi\rho\alpha^2}\gamma_n\gamma_p\frac{1}{r}F_p\left(t - \frac{r}{\alpha}\right) - \frac{1}{4\pi\rho\beta^2}(\gamma_n\gamma_p - \delta_{np})\frac{1}{r}F_p\left(t - \frac{r}{\beta}\right), \quad (4.27)$$

in which $r = |\mathbf{x} - \boldsymbol{\xi}|$ is the source–receiver distance and direction cosines $\gamma_i = (x_i - \xi_i)/r$ are referred to a source at $\boldsymbol{\xi}$. Formula (4.27) has the same apparent form as (4.23), but now a summation over p is present, since **F** in general is not along a particular coordinate direction.

In order to obtain the total effect of nine couples, of the type shown in Figure 3.7, we can evaluate (4.27) for $\mathbf{F}(t)$ applied at $\boldsymbol{\xi} + \Delta\mathbf{l}_q$ (where $\Delta\mathbf{l}_q$ is a small distance in the ξ_q-direction) and subtract the value of (4.27) for $\mathbf{F}(t)$ applied at $\boldsymbol{\xi}$. This difference gives the displacement field (at $\mathbf{x}$) due to a couple with the moment $|\Delta l_q|\,|\mathbf{F}|$, and it is a difference which, to first order in Δl_q, is given directly by the calculus operation $\Delta l_q(\partial/\partial\xi_q)$. (This is a dimensionless operation, so the result is still a displacement. The sum over q gives the outcome for all of the three possible "arm" directions.) The final step is to equate the product $\Delta l_q F_p(t)$, in which $\Delta l_q \to 0$ and $F_p \to \infty$ such that the product remains finite, with the moment tensor component $M_{pq}(t)$.

The above procedure is expressed by the equality

$$M_{pq} * G_{np,q} = \left(\begin{array}{c} \text{limit} \\ {\scriptstyle \Delta l_q \to 0} \\ {\scriptstyle F_p \to \infty} \\ {\scriptstyle \Delta l_q F_p = M_{pq}} \end{array} \right) \Delta l_q F_p * \frac{\partial}{\partial \xi_q} G_{np}. \tag{4.28}$$

The summation is over both p and q. The operation given in (4.28) is straightforward to apply to (4.27), using the two rules

$$\frac{\partial r}{\partial \xi_q} = -\gamma_q \qquad \text{and} \qquad \frac{\partial \gamma_j}{\partial \xi_q} = \frac{\gamma_j \gamma_q - \delta_{jq}}{r},$$

and the outcome is a displacement field (see (3.23)) having the nth component

$$\begin{aligned} M_{pq} * G_{np,q} = & \left(\frac{15\gamma_n\gamma_p\gamma_q - 3\gamma_n\delta_{pq} - 3\gamma_p\delta_{nq} - 3\gamma_q\delta_{np}}{4\pi\rho} \right) \frac{1}{r^4} \int_{r/\alpha}^{r/\beta} \tau M_{pq}(t-\tau)\, d\tau \\ & + \left(\frac{6\gamma_n\gamma_p\gamma_q - \gamma_n\delta_{pq} - \gamma_p\delta_{nq} - \gamma_q\delta_{np}}{4\pi\rho\alpha^2} \right) \frac{1}{r^2} M_{pq}\left(t - \frac{r}{\alpha}\right) \\ & - \left(\frac{6\gamma_n\gamma_p\gamma_q - \gamma_n\delta_{pq} - \gamma_p\delta_{nq} - 2\gamma_q\delta_{np}}{4\pi\rho\beta^2} \right) \frac{1}{r^2} M_{pq}\left(t - \frac{r}{\beta}\right) \\ & + \frac{\gamma_n\gamma_p\gamma_q}{4\pi\rho\alpha^3} \frac{1}{r} \dot{M}_{pq}\left(t - \frac{r}{\alpha}\right) - \left(\frac{\gamma_n\gamma_p - \delta_{np}}{4\pi\rho\beta^3} \right) \gamma_q \frac{1}{r} \dot{M}_{pq}\left(t - \frac{r}{\beta}\right). \end{aligned} \tag{4.29}$$

The near-field terms in this displacement field, radiated by a general second-order symmetric moment tensor (point source), are proportional to $r^{-4} \int_{r/\alpha}^{r/\beta} \tau M_{pq}(t-\tau)\, d\tau$, and the far-field terms are proportional to $r^{-1}\dot{M}_{pq}(t - r/\alpha)$ (P-waves) or to $r^{-1}\dot{M}_{pq}(t - r/\beta)$ (S-waves). Recall from Chapter 3 (equation (3.23)) that $M_{pq} * G_{np,q}$ is the n-component of displacement, at $\mathbf{x}$, from a displacement discontinuity over a fault plane with linear dimensions much smaller than the wavelength of radiated waves of interest at the receiver, so that components of the moment tensor $\mathbf{M}$ are proportional to particle displacements averaged over the fault plane. It follows that $\dot{M}_{pq}(t - r/\alpha)$ and $\dot{M}_{pq}(t - r/\beta)$, giving the pulse shape of displacement in the far field, are proportional to particle *velocities* at the source, averaged over the fault plane.

Present in (4.29) are some terms proportional to $r^{-2}M_{pq}(t - r/\alpha)$ and $r^{-2}M_{pq}(t - r/\beta)$. Since their asymptotic properties, at small and large values of r, are intermediate to the asymptotic properties of the near-field and far-field displacements, we can naturally call these the *intermediate-field terms*. This is, however, a slightly misleading name, since there is no intermediate range of distances in which these terms dominate, so it is common to include them with the near-field terms. Vidale *et al.* (1995) pointed out an unusual example where an effect of these intermediate terms is observable at great distance from a very large deep earthquake (see also Problem 4.11).

From the generality of formula (4.29), which gives the radiation from any moment tensor $\mathbf{M}$, we shall often specialize to cases where $\mathbf{M}$ arises from a shear dislocation. The averaged displacement discontinuity, $\overline{\mathbf{u}}$, is then parallel to the fault surface: $\overline{\mathbf{u}} \cdot \boldsymbol{\nu} = 0$, where $\boldsymbol{\nu}$ is normal to the fault surface. And from (3.24) and (3.21), we see that $M_{pq} = \mu(\overline{u}_p \nu_q + \overline{u}_q \nu_p)A$ for a fault with area A. Then

$$
\begin{aligned}
&\mu(\overline{u}_p \nu_q + \overline{u}_q \nu_p)A * G_{np,q} \\
&= \left(\frac{30\gamma_n\gamma_p\gamma_q\nu_q - 6\nu_n\gamma_p - 6\delta_{np}\gamma_q\nu_q}{4\pi\rho r^4}\right)\mu A \int_{r/\alpha}^{r/\beta} \tau \overline{u}_p(t-\tau)\, d\tau \\
&\quad + \left(\frac{12\gamma_n\gamma_p\gamma_q\nu_q - 2\nu_n\gamma_p - 2\delta_{np}\gamma_q\nu_q}{4\pi\rho\alpha^2 r^2}\right)\mu A \overline{u}_p\left(t - \frac{r}{\alpha}\right) \\
&\quad - \left(\frac{12\gamma_n\gamma_p\gamma_q\nu_q - 3\nu_n\gamma_p - 3\delta_{np}\gamma_q\nu_q}{4\pi\rho\beta^2 r^2}\right)\mu A \overline{u}_p\left(t - \frac{r}{\beta}\right) \\
&\quad + \frac{2\gamma_n\gamma_p\gamma_q\nu_q}{4\pi\rho\alpha^3 r}\mu A \dot{\overline{u}}_p\left(t - \frac{r}{\alpha}\right) - \left(\frac{2\gamma_n\gamma_p\gamma_q\nu_q - \nu_n\gamma_p - \delta_{np}\gamma_q\nu_q}{4\pi\rho\beta^3 r}\right)\mu A \dot{\overline{u}}_p\left(t - \frac{r}{\beta}\right).
\end{aligned}
\tag{4.30}
$$

Our next goal is to turn this expression, for the displacement field radiated by a shear dislocation, from its Cartesian form into a form that naturally brings out the radial and transverse components of motion. This goal can be accomplished by choosing axes so that the fault lies in the (x_1, x_2) plane, i.e., $\boldsymbol{\nu} = (0, 0, 1)$, with $\boldsymbol{\xi} = \mathbf{0}$, and introducing spherical polar coordinates r, θ, and ϕ centered on the source. We measure θ from the x_3-direction (see Fig. 4.4); choose the x_1-axis to be the direction of slip, so that $\overline{\mathbf{u}} = (\overline{u}, 0, 0)$; and take $\phi = 0$ as the plane containing $\boldsymbol{\nu}$ and $\overline{\mathbf{u}}$. Unit vectors $\hat{\mathbf{r}}, \hat{\boldsymbol{\theta}}, \hat{\boldsymbol{\phi}}$ are in the directions of r, θ, ϕ increasing (respectively) so that the "radial" direction is along $\hat{\mathbf{r}}$, and $\hat{\boldsymbol{\theta}}$ and $\hat{\boldsymbol{\phi}}$ are both "transverse" directions.

We seek to express the displacement vector at $\mathbf{x}$, for which the nth Cartesian component is given in (4.30), as a sum of vectors in the three directions $\hat{\mathbf{r}}$, $\hat{\boldsymbol{\theta}}$, and $\hat{\boldsymbol{\phi}}$. Fortunately, (4.30) is composed of vectors of only three types—namely, $\gamma_n\gamma_p\overline{u}_p\gamma_q\nu_q$, $\nu_n\gamma_p\overline{u}_p$, and $\delta_{np}\overline{u}_p\gamma_q\nu_q$. These three types can be recognized, respectively, as follows:

$$
\begin{aligned}
2\gamma_n\gamma_p\overline{u}_p\gamma_q\nu_q \quad &\text{is the } n\text{th component of } \overline{u}\ \sin 2\theta \cos\phi\ \hat{\mathbf{r}}, \\
2\nu_n\gamma_p\overline{u}_p \quad &\text{is the } n\text{th component of } \overline{u}\ \sin 2\theta \cos\phi\ \hat{\mathbf{r}} - \overline{u}\, 2\sin^2\theta \cos\phi\ \hat{\boldsymbol{\theta}}, \\
2\delta_{np}\overline{u}_p\gamma_q\nu_q \quad &\text{is the } n\text{th component of } \overline{u}\ \sin 2\theta \cos\phi\ \hat{\mathbf{r}} + \overline{u}\, 2\cos^2\theta \cos\phi\ \hat{\boldsymbol{\theta}} \\
&\qquad - \overline{u}\, 2\cos\theta \sin\phi\ \hat{\boldsymbol{\phi}}.
\end{aligned}
\tag{4.31}
$$

These results follow from relations $\hat{\mathbf{r}} = \boldsymbol{\gamma} = (\sin\theta\cos\phi, \sin\theta\sin\phi, \cos\theta)$, $\hat{\boldsymbol{\theta}} = (\cos\theta\cos\phi, \cos\theta\sin\phi, -\sin\theta)$, and $\hat{\boldsymbol{\phi}} = (-\sin\phi, \cos\phi, 0)$.

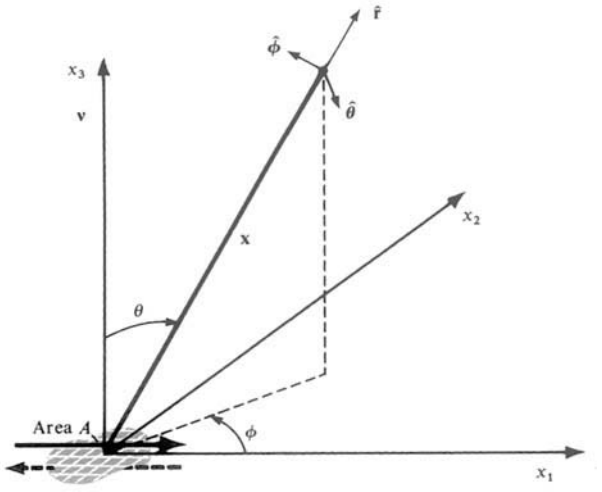

FIGURE **4.4**
Cartesian and spherical polar coordinates for analysis of radial and transverse components of displacement radiated by a shear dislocation of area A and average slip $\bar{\mathbf{u}}$. See (4.31).

With the identification of vector components in (4.31), it now becomes possible to write our displacement field $u_n = M_{pq} * G_{np,q}$ in a concise vector form, using the time-dependent seismic moment $M_0(t) = \mu\bar{u}(t)A$. We find

$$\begin{aligned}\mathbf{u}(\mathbf{x},t) = {} & \frac{1}{4\pi\rho}\mathbf{A}^N\frac{1}{r^4}\int_{r/\alpha}^{r/\beta}\tau M_0(t-\tau)\,d\tau \\ & + \frac{1}{4\pi\rho\alpha^2}\mathbf{A}^{IP}\frac{1}{r^2}M_0\left(t-\frac{r}{\alpha}\right) + \frac{1}{4\pi\rho\beta^2}\mathbf{A}^{IS}\frac{1}{r^2}M_0\left(t-\frac{r}{\beta}\right) \\ & + \frac{1}{4\pi\rho\alpha^3}\mathbf{A}^{FP}\frac{1}{r}\dot{M}_0\left(t-\frac{r}{\alpha}\right) + \frac{1}{4\pi\rho\beta^3}\mathbf{A}^{FS}\frac{1}{r}\dot{M}_0\left(t-\frac{r}{\beta}\right),\end{aligned} \tag{4.32}$$

in which the near-field, the intermediate-field P and S, and the far-field P and S have radiation patterns given, respectively, by

$$\begin{aligned}\mathbf{A}^N &= 9\sin 2\theta\cos\phi\,\hat{\mathbf{r}} - 6(\cos 2\theta\cos\phi\,\hat{\boldsymbol{\theta}} - \cos\theta\sin\phi\,\hat{\boldsymbol{\phi}}) \\ \mathbf{A}^{IP} &= 4\sin 2\theta\cos\phi\,\hat{\mathbf{r}} - 2(\cos 2\theta\cos\phi\,\hat{\boldsymbol{\theta}} - \cos\theta\sin\phi\,\hat{\boldsymbol{\phi}}) \\ \mathbf{A}^{IS} &= -3\sin 2\theta\cos\phi\,\hat{\mathbf{r}} + 3(\cos 2\theta\cos\phi\,\hat{\boldsymbol{\theta}} - \cos\theta\sin\phi\,\hat{\boldsymbol{\phi}}) \\ \mathbf{A}^{FP} &= \sin 2\theta\cos\phi\,\hat{\mathbf{r}} \\ \mathbf{A}^{FS} &= \cos 2\theta\cos\phi\,\hat{\boldsymbol{\theta}} - \cos\theta\sin\phi\,\hat{\boldsymbol{\phi}}.\end{aligned} \tag{4.33}$$

These radiation patterns explicitly display a radial component, proportional to $\sin 2\theta\cos\phi\,\hat{\mathbf{r}}$, and a transverse component, proportional to $(\cos 2\theta\cos\phi\,\hat{\boldsymbol{\theta}} - \cos\theta\sin\phi\,\hat{\boldsymbol{\phi}})$. The important property brought out by (4.33) is that these are the only two radiation patterns needed to obtain a complete picture of all the different terms in the displacement field radiated from a shear dislocation (double couple). Figure 4.5 shows the way in which

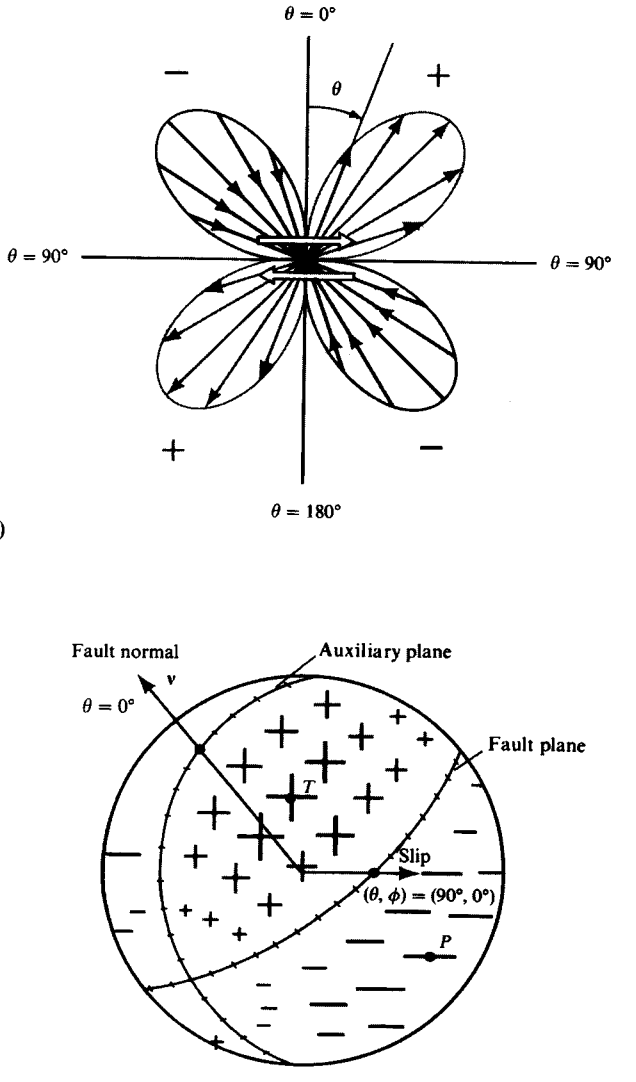

FIGURE **4.5**
Diagrams for the radiation pattern of the radial component of displacement due to a double couple, i.e., $\sin 2\theta \cos\phi\, \hat{\mathbf{r}}$. (**a**) The lobes are a locus of points having a distance from the origin that is proportional to $\sin 2\theta$. The diagram is for a plane of constant azimuth, and the pair of arrows at the center denotes the shear dislocation. Note the alternating quadrants of inward and outward directions. In terms of far-field P-wave displacement, plus signs denote outward displacement (if $\dot{M}_0(t - r/\alpha)$ is positive), and minus signs denote inward displacement. (**b**) View of the radiation pattern over a sphere centered on the origin. Plus and minus signs of various sizes denote variation (with θ, ϕ) of outward and inward motions. The fault plane and the auxiliary plane are nodal lines (on which $\sin 2\theta \cos\phi = 0$). An equal-area projection has been used (see Fig. 4.17). Point P marks the pressure axis, and T the tension axis.

the radial component varies in magnitude for different directions (θ, ϕ), and Figure 4.6 shows how the transverse component varies in both magnitude and direction. Only the radial component is present for the far-field P-wave, and only the transverse component is present for the far-field S-wave. However, the intermediate-field displacements, both P and S, involve both radial and transverse components, as does the near-field displacement.

The surprisingly simple dependence on (θ, ϕ), which we have found in (4.32) and (4.33) and shown in Figures 4.5 and 4.6, prompts one to ask if a more direct method can be used in the derivation. Indeed this is the case, vector surface harmonics (see Chapter 8) providing the necessary analytical framework and demonstrating the simple dependence on (θ, ϕ) from the outset, but the associated algebraic manipulations for this more sophisticated method are

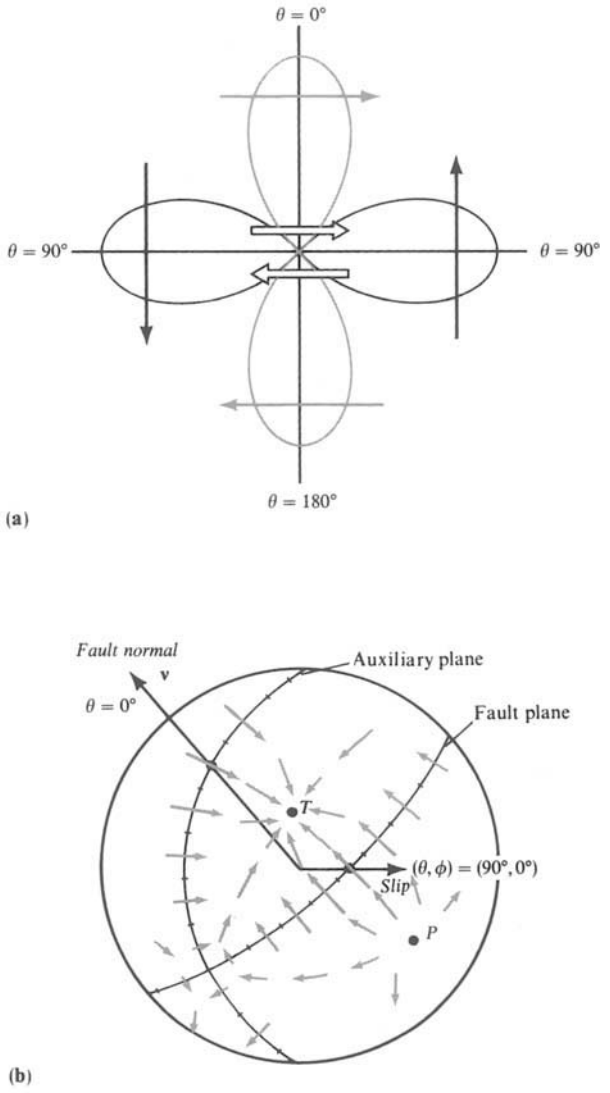

FIGURE **4.6**

Diagrams for the radiation pattern of the transverse component of displacement due to a double couple, i.e., $\cos 2\theta \cos\phi\, \hat{\boldsymbol{\theta}} - \cos\theta \sin\phi\, \hat{\boldsymbol{\phi}}$. (**a**) The four-lobed pattern in plane $\{\phi = 0, \phi = \pi\}$. The central pair of arrows shows the sense of shear dislocation, and arrows imposed on each lobe show the direction of particle displacement associated with the lobe. If applied to the far-field S-wave displacement, it is assumed that $\dot{M}_0(t - r/\beta)$ is positive. (**b**) Off the two planes $\theta = \pi/2$ and $\{\phi = 0, \phi = \pi\}$, the $\hat{\boldsymbol{\phi}}$ component is nonzero, hence (a) is of limited use. This diagram is a view of the radiation pattern over a whole sphere centered on the origin, and arrows (with varying size and direction) in the spherical surface denote the variation (with θ, ϕ) of the transverse motions. There are no nodal lines (where there is zero motion), but nodal points do occur. Note that the nodal point for transverse motion at $(\theta, \phi) = (45°, 0)$ is a maximum in the radiation pattern for longitudinal motion (Fig. 4.5b). But the maximum transverse motion (e.g., at $\theta = 0$) occurs on a nodal line for the longitudinal motion. The stereographic projection has been used (see Fig. 4.16). It is a conformal projection, meaning that it preserves the angles at which curves intersect and the shapes of small regions, but it does not preserve relative areas.

(in our opinion) as laborious as the Cartesian analysis we have chosen to use. In Section 4.4, we shall develop properties of the far-field displacement for a medium that, like the Earth, is inhomogeneous. In Section 4.5 we shall reexamine the radiation patterns (4.33), showing how they may be used in practice to obtain (from seismic data) the fault-plane orientation and the direction of slip.

To conclude the present section, we obtain from (4.32) the final static displacement field for a shear dislocation of strength M_0. This involves taking the limit of $\dot{M}_0(t-\tau)$, $M_0(t-\tau)$, and $\int_{r/\alpha}^{r/\beta} \tau M_0(t-\tau)\, d\tau$ as $t \to \infty$, assuming that the seismic moment itself has a final constant value, $M_0(\infty)$. The result is

$$\begin{aligned}\mathbf{u}(\mathbf{x},\infty) &= \frac{M_0(\infty)}{4\pi\rho r^2}\left[\mathbf{A}^N\left(\frac{1}{2\beta^2}-\frac{1}{2\alpha^2}\right)+\frac{\mathbf{A}^{IP}}{\alpha^2}+\frac{\mathbf{A}^{IS}}{\beta^2}\right] \\ &= \frac{M_0(\infty)}{4\pi\rho r^2}\left[\frac{1}{2}\left(\frac{3}{\beta^2}-\frac{1}{\alpha^2}\right)\sin 2\theta\cos\phi\,\hat{\mathbf{r}}\right. \\ &\qquad \left. +\frac{1}{\alpha^2}(\cos 2\theta\cos\phi\,\hat{\boldsymbol{\theta}}-\cos\theta\sin\phi\,\hat{\boldsymbol{\phi}})\right],\end{aligned} \tag{4.34}$$

which attenuates (along any given direction (θ,ϕ)) as r^{-2}.

4.4 Ray Theory for Far-Field *P*-waves and *S*-waves from a Point Source

Books and papers on the theory of elastic wave propagation are for the most part concerned with homogeneous media. Seismologists often require a good grasp of the properties of waves in such simple media and of the exact solutions that may be obtained (e.g., Chapters 5 and 6). However, the practical analysis of seismograms requires also a good grasp of approximate solutions for the waves that propagate in inhomogeneous media. Not only does the Earth have material boundaries across which the elastic properties are discontinuous, but also it contains vast regions within which there is a systematic and continuous change of bulk modulus, rigidity, and density. Thus P-wave and S-wave velocities both increase by a factor of about two from the top to the bottom of the mantle, and this is enough to distort beyond recognition the radiation patterns we have described above, unless the effects of inhomogeneity are accounted for. In this section and the next, we show how to remove the distortion, and demonstrate how amplitudes of body waves can be substantially changed by focusing or defocusing effects of the type exhibited by light propagating in media of varying refractive index. The approximate solution we shall obtain, called the geometric ray solution, provides a guide to more sophisticated methods, should they be necessary.

Ray theory can perhaps best be remembered as a collection of verifiable intuitive ideas and approximations. Thus body waves travel with a local propagation speed along "ray paths" determined by Snell's law, arriving (as a "wavefront") with an amplitude determined by the geometrical spreading of rays from the source to the receiver. These are statements that we shall prove, but intuition enters strongly at the initial stage of setting up a trial form for the solution.

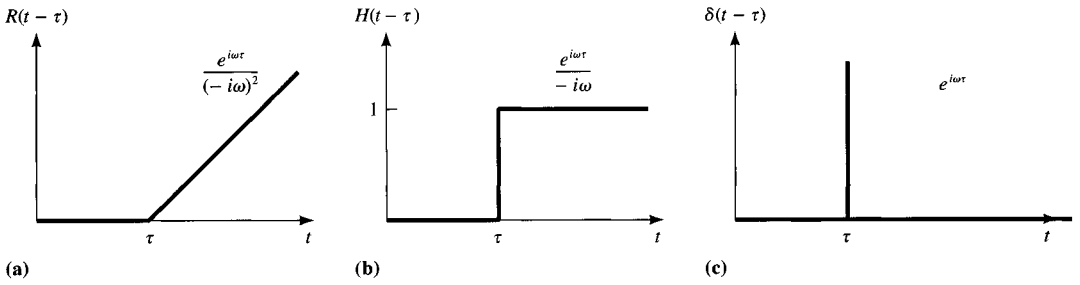

FIGURE **4.7**
A hierarchy of discontinuous functions, with formulas for their associated high-frequency spectra. The ramp values are given by $R(t) = tH(t)$.

Our approach will be to generalize the form of the far-field solution we have already found for P- and S-waves, and to use a system of coordinates that provides a natural way to describe the spreading of a wavefront due to a point source in an isotropic inhomogeneous medium. For spherically symmetric media, orthogonal coordinates based on the rays have the property that P and two different components of S (known as SV and SH) are separated out. These three different motions are parallel to three different coordinate directions.

A *wavefront* is a propagating discontinuity in some dependent variable of physical interest (such as the particle acceleration). In this context, the word "discontinuity" is taken to mean "discontinuity in the variable or one of its derivatives." Thus the ramp shown in Figure 4.7a is actually continuous at $t = T$, but such a function is an eligible candidate for describing the behavior near a wavefront, since the ramp has a discontinuous derivative. Where necessary, one speaks of a function whose $(n-1)$th derivative is discontinuous at $t = T$ (but with all lower-order derivatives continuous there) as having an *nth order discontinuity* at $t = T$. A review of the Green function solution (4.23) will show that a (temporal) discontinuity in the body force $X_0(t)$ leads to a propagating discontinuity in the far-field terms which has the same order as that occurring in the body force. That is, $X_0(t)$ acting at $r = 0$ leads to displacement pulse shapes $X_0(t - r/\alpha)$ and $X_0(t - r/\beta)$ at large r. (There has to be a discontinuity of some order at the source, otherwise $X_0(t)$ and all its derivatives are zero for all time and no waves are generated.) There is also a propagating discontinuity in the near-field terms, $\int_{r/\alpha}^{r/\beta} \tau X_0(t-\tau)\, d\tau$, but it is less severe. For example, if $X_0(t) \propto H(t)$ (the Heaviside step function, which has a first-order discontinuity), then propagating steps in displacement are radiated to the far field, but the near-field terms carry second-order discontinuities, since $\int_{r/\alpha}^{r/\beta} \tau H(t-\tau)\, d\tau$ is continuous at $t = r/\alpha$ and $t = r/\beta$ but has discontinuous first derivatives there (see Fig. 4.8).

This observation, that the strongest discontinuities are carried by what we have called the far-field terms, is of fundamental importance. In fact, it is sometimes better to use it as the defining property of these terms, since the commonly used labels "far-field" and "near-field" can be misleading. At *any* fixed distance r, whether large or small, the behavior of the radiated wave at times sufficiently near r/α and r/β will be dominated by the strongest discontinuity (strongest wavefront) arriving at these times, and in general this is contained in

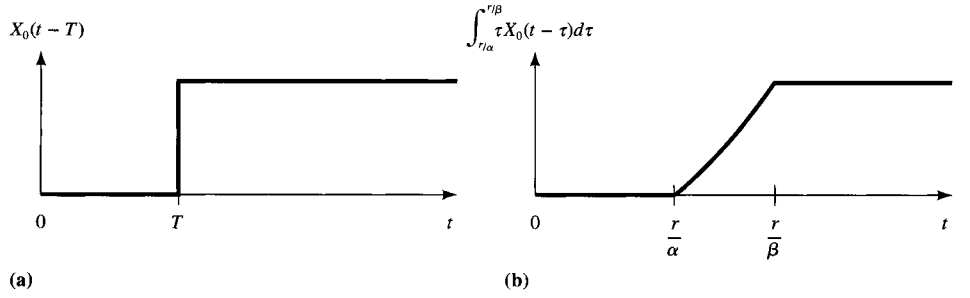

FIGURE **4.8**
Comparison of far-field and near-field displacement pulse shapes for the Green function convolved with $X_0(t) \propto H(t)$. **(a)** The far field: there is a first-order discontinuity at time $t = T$, where T is either r/α or r/β. **(b)** The near field: the displacement is continuous at all times and grows parabolically between times r/α and r/β, but particle velocity is discontinuous at both these wavefronts.

a far-field term. At large enough r, there are therefore two reasons for the far-field terms to dominate: strength of discontinuity and relatively weak attenuation (geometrically) with distance. At fixed small r, however, the far-field terms will dominate or not dominate according as the strength of their discontinuity is more or less important than the weakness of the singularity in r^{-1}.

Fortunately, by turning to the frequency domain, a simpler way can be found to compare the displacements that we have labeled as near-field and far-field. Throughout this book, we shall use the notation and conventions

$$f(\omega) = \int_{-\infty}^{\infty} f(t)e^{+i\omega t}dt, \qquad f(t) = \frac{1}{2\pi}\int_{-\infty}^{\infty} f(\omega)e^{-i\omega t}d\omega$$

for a Fourier transform on functions of time and frequency, letting the context determine whether f is evaluated in the time or frequency domain. (See Box 5.2 for our reasons in choosing this convention.) Then $X_0(t - r/\alpha)$ transforms to $e^{+i\omega r/\alpha}X_0(\omega)$, and $\int_{r/\alpha}^{r/\beta} \tau X_0(t-\tau)\,d\tau$ can be seen as the convolution of $X_0(t)$ with a function shaped like

in which the sloping part would pass through the origin at time $t = 0$ if it were projected back to earlier times. The convolution therefore transforms to the product

$$X_0(\omega)\int_{r/\alpha}^{r/\beta} te^{+i\omega t}dt = X_0(\omega)\left[-\left(\frac{r}{\alpha}-\frac{1}{i\omega}\right)\frac{e^{+i\omega r/\alpha}}{i\omega} + \left(\frac{r}{\beta}-\frac{1}{i\omega}\right)\frac{e^{+i\omega r/\beta}}{i\omega}\right],$$

and from (4.23) we obtain the Fourier transform of $X_0(t) * G_{ij}(t)$ as

$$X_0(\omega)G_{ij}(\omega) = \frac{X_0(\omega)e^{+i\omega r/\alpha}}{4\pi\rho\alpha^2 r}\left[\gamma_i\gamma_j + (3\gamma_i\gamma_j - \delta_{ij})\left(-\frac{\alpha}{i\omega r}\right) + (3\gamma_i\gamma_j - \delta_{ij})\left(-\frac{\alpha}{i\omega r}\right)^2\right]$$
$$-\frac{X_0(\omega)e^{+i\omega r/\beta}}{4\pi\rho\beta^2 r}\left[(\gamma_i\gamma_j - \delta_{ij}) + (3\gamma_i\gamma_j - \delta_{ij})\left(-\frac{\beta}{i\omega r}\right) + (3\gamma_i\gamma_j - \delta_{ij})\left(-\frac{\beta}{i\omega r}\right)^2\right]. \tag{4.35}$$

The dimensionless terms within the square brackets of (4.35) give relative magnitudes of different far-field and near-field displacements. Of importance here are the dimensionless ratios $\omega r/\alpha$, $\omega r/\beta$ and we note that

$\omega r/\alpha = 2\pi \times$ (number of wavelengths, for a *P*-wave of frequency ω, between source and receiver), and

$\omega r/\beta = 2\pi \times$ (number of wavelengths, for an *S*-wave of frequency ω, between source and receiver).

With this interpretation, we can at last get a clear picture of where different terms of the Green function dominate. The far field is simply "all positions that are more than a few wavelengths away from the source," and the near field is "all positions within a small fraction of a wavelength from the source." At near and intermediate distances, one must assess the relative magnitude of each term in (4.35), perhaps concluding that no single term is dominant (see Problem 4.1).

Our above discussion of the discontinuities that can propagate in the time domain translates formally to properties of the high-frequency spectra. If $g(t)$ has a unit jump at the origin, then the spectrum $g(\omega)$ has a term behaving asymptotically like $(-i\omega)^{-1}$ as $\omega \to \infty$ (Bracewell, 1965). Integrating this result repeatedly and applying the shift theorem,

$$g(t - T) \to g(\omega)e^{i\omega T},$$

we obtain the following: if $f(t)$ has an nth-order discontinuity at $t = T$, such that

$$\frac{\partial^{n-1} f(t)}{\partial t^{n-1}}\bigg|_{t=T^-}^{t=T^+} = A \qquad \text{(where } A \text{ is a constant)},$$

then the Fourier transform $f(\omega)$ behaves asymptotically like $A(-i\omega)^{-n}e^{+i\omega T}$ as $\omega \to \infty$. This does enable us to see how the different terms in (4.35) are associated correctly with different discontinuities in the time domain, but it can be a misleading result, since the behavior of $f(\omega)$ may be like that of $A(-i\omega)^{-n}e^{+i\omega T}$ only at frequencies much higher than can be observed. Putting it in another way: the observed trend of a physical variable $f(\omega)$ at high frequencies may not be indicative of the properties of any underlying wavefront, since the latter might require kilohertz or megahertz frequencies to be observed; and these frequencies are usually unavailable in seismology. We can separate near-field and far-field terms, even at seismic frequencies, on the basis of the different frequency dependencies shown in (4.35), although the abstract qualities "wavefront" and "strength of discontinuity" may be unobservable.

These results are brought out in some detail because formal texts on ray theory tend to emphasize the analysis of different levels of discontinuity, and we cannot appeal to this method in seismology. Rather, we shall adopt a less rigorous approach, though with clearly stated assumptions, in which the derivative $\dot{X}_0(t - r/\alpha)$ is presumed to dominate over $(\alpha/r)X_0(t - r/\alpha)$, because this would be true at the high frequencies we commonly observe in far-field body waves (i.e., $\omega r/\alpha \gg 1$).

An elegant way to study the longitudinal and two transverse components of body-wave displacement is to set up a system of curvilinear coordinates in which these three components lie either along a coordinate axis or within a coordinate plane. Suppose a point source at position $\boldsymbol{\xi}$ becomes active at a time chosen to be the origin, $t = 0$. In a homogeneous medium, wavefronts emanate from the source as ever-expanding spheres, with radii αt (for P-waves) and βt (for S), arriving at the general position $\mathbf{x}$ at times r/α and r/β, where $r = |\mathbf{x} - \boldsymbol{\xi}|$. We generalize this for inhomogeneous media by introducing $T(\mathbf{x}, \boldsymbol{\xi})$ as the position-dependent travel time required for the wavefront to reach $\mathbf{x}$ from $\boldsymbol{\xi}$. If more than one wavefront can exist for the particular source in question, as will be the case if both longitudinal and transverse waves are present, then more than one travel-time function will be needed. Often, however, it is enough to refer to $T(\mathbf{x})$ and let the context indicate which wavefront and which point source are of interest.

Our first *ansatz* (i.e., trial form of solution) for displacement in the vicinity of a wavefront is therefore

$$\mathbf{u}(\mathbf{x}, t) = f(\mathbf{x})\mathbf{U}(t - T), \tag{4.36}$$

in which $\mathbf{U}$ is the vector waveform (pulse shape) in the vicinity of the wavefront, and f gives the spatial variability of the amplitude of this waveform. We shall examine (4.36) as an approximate solution for the wave equation $\rho\ddot{u}_i = \tau_{ij,j}$ (valid everywhere except at the source singularity $\mathbf{x} = \boldsymbol{\xi}$). The stress-displacement relations for a general anisotropic inhomogeneous medium are $\tau_{ij} = c_{ijkl}(\mathbf{x})u_{k,l}(\mathbf{x}, t)$, and direct substitution yields

$$\rho\ddot{U}_i f = [c_{ijkl}(U_k f)_{,l}]_{,j}. \tag{4.37}$$

Near a wavefront, we assume that $\mathbf{U}$ is fluctuating much more rapidly than f or c_{ijkl}; and that the successive derivatives $\dot{U}$ and $\ddot{U}$ are fluctuating still more rapidly. Equation (4.37) contains both temporal and spatial derivatives of U_k, but the dependence of $\mathbf{U}$ on the space–time combination $(t - T(\mathbf{x}))$ makes possible such relations as

$$U_{k,lj} = \ddot{U}_k \frac{\partial T}{\partial x_l}\frac{\partial T}{\partial x_j} - \dot{U}_k \frac{\partial^2 T}{\partial x_l \partial x_j},$$

so that the second derivatives in (4.37) can be gathered together as

$$\left(\rho\delta_{ik} - c_{ijkl}\frac{\partial T}{\partial x_j}\frac{\partial T}{\partial x_l}\right)\ddot{U}_k f = E_i(\mathbf{U}f), \tag{4.38}$$

where $\mathbf{E}$ includes merely (i) first-order derivatives of $\mathbf{U}$, (ii) $\mathbf{U}$ itself, and (iii) the elastic moduli and amplitude function $f(\mathbf{x})$ and gradients of these. Thus $\mathbf{E}$ must be

much smaller than $\ddot{\mathbf{U}}$, so we conclude that the matrix of coefficients of $\ddot{U}_k f$ must be singular:

$$\det\left|\rho\delta_{ik} - c_{ijkl}\frac{\partial T}{\partial x_j}\frac{\partial T}{\partial x_l}\right| = 0. \tag{4.39}$$

It is this equation which determines the possible wavefronts in an elastic medium, since it gives a constraint on the function $T(\mathbf{x})$.

In an inhomogeneous isotropic medium, the special form of c_{ijkl} (see (2.33)) allows (4.39) to be factorized in the form

$$\left(\nabla T \cdot \nabla T - \frac{\rho}{\lambda + 2\mu}\right)\left(\nabla T \cdot \nabla T - \frac{\rho}{\mu}\right)^2 = 0. \tag{4.40}$$

That is, T satisfies the *eikonal equation*

$$(\nabla T)^2 = \frac{1}{c^2}, \tag{4.41}$$

where c is either the local P-wave speed $\sqrt{(\lambda(\mathbf{x}) + 2\mu(\mathbf{x}))/\rho(\mathbf{x})} = \alpha(\mathbf{x})$, or the local S-wave speed, $\sqrt{\mu(\mathbf{x})/\rho(\mathbf{x})} = \beta(\mathbf{x})$.

We next develop the consequences of T satisfying an eikonal equation with velocity c, and derive an equation from which rays can be introduced.

4.4.1 PROPERTIES OF THE TRAVEL-TIME FUNCTION $T(\mathbf{x})$ ASSOCIATED WITH VELOCITY FIELD $c(\mathbf{x})$

Suppose that a wavefront S is given by $t = T(\mathbf{x})$ and that S reaches the point $\mathbf{x} + d\mathbf{x}$ at a time dt later than it reaches the point $\mathbf{x}$. Then $t + dt = T(\mathbf{x} + d\mathbf{x})$, so that $dt = \nabla T \cdot d\mathbf{x}$. If $\mathbf{V}$ is the velocity of the advancing wavefront, in the direction $d\mathbf{x}$, it follows that $\mathbf{V} = d\mathbf{x}/dt$, and $\nabla T \cdot \mathbf{V} = 1$. Hence

$$V^2 \geq \frac{1}{(\nabla T)^2} = c^2 \qquad \text{(using (4.41))},$$

with equality only when vectors $\mathbf{V}$ and ∇T are parallel, i.e., when $d\mathbf{x}$ is perpendicular to S. It follows that c is the velocity of S, normal (perpendicular) to itself.

For a given wavefront S, we introduce *rays* as the normals to S as the wavefront propagates. If a ray is parameterized in the form $\mathbf{x} = \mathbf{x}(\zeta)$, with ζ changing monotonically along the ray, it follows that $d\mathbf{x}/d\zeta = g(\mathbf{x})\nabla T$ is the equation of the ray, where g, a scalar function relating parallel vectors, is determined by the particular choice one makes for ζ.

For example, choosing

$$\frac{d\mathbf{x}}{d\zeta} = c^2\nabla T = (c\nabla T)c \tag{4.42}$$

and noting that $c\nabla T$ is the unit normal to S and that c is the velocity of S normal to itself, it follows that ζ has the interpretation of travel time along the ray. As S propagates normal

to a particular ray R, the intersection of S and R will occur at different values of T. To examine the relation between this T and the ζ of (4.42), we note that

$$\frac{dT}{d\zeta} = \nabla T \cdot \frac{d\mathbf{x}}{d\zeta} = \nabla T \cdot (c^2 \nabla T) = 1,$$

and hence T and ζ increase in precisely the same manner along the ray direction. The ray itself may thus be parameterized by T, and T has the physical interpretation of travel time along the ray.

In working with the equation of the ray path, it is sometimes convenient to use as a parameter the distance s, measured along the ray from some reference point. It follows that

$$\frac{d\mathbf{x}}{ds} = c\nabla T \tag{4.43}$$

(since $d\mathbf{x}/ds$ and ∇T are parallel, but the left-hand side of (4.43) is a unit vector).

The rays themselves are fixed curves in space, and so to examine their geometrical properties we often need to eliminate the time quantity T in (4.43), in this way obtaining an equation for $\mathbf{x} = \mathbf{x}(s)$ that involves only $c(\mathbf{x})$. Several stages are needed in such an elimination (which uses the eikonal equation), and step by step we have

$$\frac{d}{ds}\left(\frac{1}{c}\frac{d\mathbf{x}}{ds}\right) = \frac{d}{ds}\nabla T = \left(\frac{d\mathbf{x}}{ds} \cdot \nabla\right)\nabla T = (c\nabla T \cdot \nabla)\nabla T$$

$$= \frac{1}{2}c\nabla[(\nabla T)^2] = \frac{1}{2}c\nabla\left(\frac{1}{c^2}\right) = -\frac{1}{c^2}\nabla c.$$

The differential equation for a ray, in spatial coordinates only, is thus

$$\frac{d}{ds}\left(\frac{1}{c}\frac{d\mathbf{x}}{ds}\right) = \nabla\left(\frac{1}{c}\right). \tag{4.44}$$

This equation is conceptually simple to solve by finite differences, to obtain the path of a ray whose starting point and initial direction are known in a medium for which c and $\nabla(1/c)$ may be computed at each point. In a homogeneous region, (4.44) reduces to $d^2\mathbf{x}/ds^2 = \mathbf{0}$, with the general solution $\mathbf{x} = \boldsymbol{\gamma} s + \boldsymbol{\xi}$ ($\boldsymbol{\gamma}$ and $\boldsymbol{\xi}$ here are vector constants), which is a straight line in the $\boldsymbol{\gamma}$ direction, and passing through the point $\mathbf{x} = \boldsymbol{\xi}$.

In a medium where c depends only on depth z (in a Cartesian coordinate system), the quantity

$$\hat{\mathbf{z}} \times \frac{1}{c}\frac{d\mathbf{x}}{ds} \equiv \mathbf{Q} \tag{4.45a}$$

is constant along a ray, since

$$\frac{d\mathbf{Q}}{ds} = \hat{\mathbf{z}} \times \frac{d}{ds}\left(\frac{1}{c}\frac{d\mathbf{x}}{ds}\right) = \hat{\mathbf{z}} \times \nabla\left(\frac{1}{c}\right) = \mathbf{0}$$

($\hat{\mathbf{z}}$ being parallel to $\nabla(1/c)$). It follows that rays are confined to planes parallel to the z-axis and that $|\mathbf{Q}| = \sin i(z)/c(z) \equiv p$ is constant along a ray, where i is the angle between the

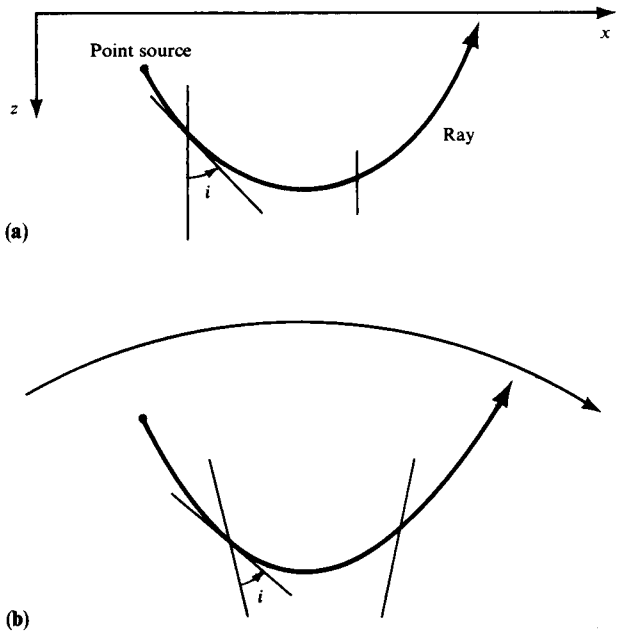

FIGURE **4.9**
(**a**) A ray path in a medium where velocity depends only on depth: $\sin i(z)/c(z)$ is constant, and the ray is confined to a vertical plane. (**b**) A ray path in a spherically symmetric medium where velocity depends only on the distance r from the center of symmetry: $r \sin i(r)/c(r)$ is constant, and the ray stays in a vertical plane. The angle i evaluated at the source is known as the *take-off angle*.

increasing z-direction and the ray (see Fig. 4.9a). This is *Snell's law*, and p is known as the *ray parameter*.

In a spherically symmetric medium, $c = c(r)$, it is the quantity

$$\mathbf{r} \times \frac{1}{c}\frac{d\mathbf{r}}{ds} \equiv \mathbf{Q} \tag{4.45b}$$

that is constant along a ray. (Here we are using $\mathbf{r} = (r, \theta, \phi)$ and spherical polars with origin at the center of symmetry.) This result again uses (4.44), as

$$\frac{d\mathbf{Q}}{ds} = \frac{d\mathbf{r}}{ds} \times \frac{1}{c}\frac{d\mathbf{r}}{ds} + \mathbf{r} \times \frac{d}{ds}\left(\frac{1}{c}\frac{d\mathbf{r}}{ds}\right) = \mathbf{0} + \mathbf{r} \times \nabla\left(\frac{1}{c}\right) = \mathbf{0}.$$

Rays stay in a vertical plane, and now the quantity $r \sin i(r)/c(r) \equiv p$ (still called the ray parameter) is constant along a ray path (see Fig. 4.9b). This is Snell's law for spherically symmetric media. We shall make frequent use of the quantity p in later chapters, often treating it as a variable, with different values corresponding to different rays from a point source. Note that p has a different physical dimension in depth-dependent media (4.45a) than is the case in spherically symmetric media (4.45b).

There is one more general property of rays to be brought out before returning to the study of amplitudes of radiated particle displacement. This result is known as Fermat's Principle, which states that for two points A and B on a ray R, the ray itself is a path along which, in the velocity field $c(\mathbf{x})$, the travel time from A to B is stationary. We can prove this by using further properties of the parameter ζ in the ray equation $d\mathbf{x}/d\zeta = g(\mathbf{x})\nabla T = g(\zeta)\nabla T$ (recall that we have already used ζ for travel time and for

distance). The quantities $g(\zeta)$ and ζ are constrained by the eikonal equation (4.41), which implies

$$\frac{d\mathbf{x}}{d\zeta} \cdot \frac{d\mathbf{x}}{d\zeta} = \left(\frac{g}{c}\right)^2 .$$

Given ζ, we then require for the associated g that

$$g = c\left(\frac{d\mathbf{x}}{d\zeta} \cdot \frac{d\mathbf{x}}{d\zeta}\right)^{1/2} . \tag{4.46}$$

In general $d/ds = (c/g)\, d/d\zeta$, hence from (4.44) we have the ray equation for any choice of ζ as

$$\frac{c}{g}\frac{d}{d\zeta}\left[\frac{1}{g}\frac{d\mathbf{x}}{d\zeta}\right] = \nabla\left(\frac{1}{c}\right).$$

This form can be identified with the Euler equations of variational calculus by first eliminating g via (4.46) to obtain

$$\frac{d}{d\zeta}\left[\frac{1}{c(\mathbf{x})}\frac{\dfrac{d\mathbf{x}}{d\zeta}}{\left(\dfrac{d\mathbf{x}}{d\zeta}\cdot\dfrac{d\mathbf{x}}{d\zeta}\right)^{1/2}}\right] = \left(\frac{d\mathbf{x}}{d\zeta}\cdot\frac{d\mathbf{x}}{d\zeta}\right)^{1/2}\nabla\left(\frac{1}{c}\right).$$

This in turn can be written as three scalar equations ($i = 1, 2, 3$):

$$\frac{d}{d\zeta}\left\{\frac{\partial}{\partial\left(\dfrac{\partial x_i}{\partial\zeta}\right)}\left[\frac{\left(\dfrac{d\mathbf{x}}{d\zeta}\cdot\dfrac{d\mathbf{x}}{d\zeta}\right)^{1/2}}{c(\mathbf{x})}\right]\right\} = \frac{\partial}{\partial x_i}\left[\frac{1}{c(\mathbf{x})}\left(\frac{d\mathbf{x}}{d\zeta}\cdot\frac{d\mathbf{x}}{d\zeta}\right)^{1/2}\right].$$

These are the Euler equations we seek, since they tell us the travel time is stationary for a ray path. In other words,

$$T(B, A) = \int_A^B \frac{|d\mathbf{x}|}{c(\mathbf{x})} = \int_A^B \frac{1}{c(\mathbf{x})}\left(\frac{d\mathbf{x}}{d\zeta}\cdot\frac{d\mathbf{x}}{d\zeta}\right)^{1/2} d\zeta \tag{4.47}$$

is an integral that, for all possible paths connecting A and B, is stationary if and only if $\mathbf{x} = \mathbf{x}(\zeta)$ is a ray path.

4.4.2 RAY COORDINATES

The wavefront S is orthogonal to its associated rays, and we have shown how points along a ray are parameterized by values of T. We now introduce (c^2, c^3) as some coordinate system within the wavefront itself (or, equivalently, recognize that rays associated with a point source form a two-parameter family), and then each point reached by rays in the velocity field $c(\mathbf{x})$ ($c = \alpha$ or β) is described by values in a ray coordinate system (T, c^2, c^3).

Our notation for curvilinear coordinates is introduced in Box 2.6. The T-direction (which is along the ray) is orthogonal to the c^2 and c^3 directions at every point, but in general inhomogeneous media it is not possible to choose coordinates so that the c^2 and c^3 directions are always orthogonal. Fortunately, the special case of a spherically symmetric medium does permit a choice for orthogonal c^2 and c^3, allowing us then to apply directly the results for general orthogonal systems developed in Chapter 2. Note here that the scale factor $h_T = h^1 = c$, since a distance increment ds along the ray is $c\,dT$.

In homogeneous media, we found that far-field P-waves are longitudinal and S-waves are transverse. The same holds true for general inhomogeneous (but still isotropic) media, as may be seen from taking the vector product and the scalar product of equation (4.38) with ∇T. In isotropic media, the results are

$$[\rho - \mu \nabla T \cdot \nabla T]\ddot{\mathbf{U}} \times \nabla T = \mathbf{E}(\mathbf{U}) \times \nabla T \tag{4.48}$$

and

$$[\rho - (\lambda + 2\mu)\nabla T \cdot \nabla T]\ddot{\mathbf{U}} \cdot \nabla T = \mathbf{E}(\mathbf{U}) \cdot \nabla T. \tag{4.49}$$

Since $|\mathbf{E}|$ is of order $|\dot{\mathbf{U}}|$, and terms of order $|\ddot{\mathbf{U}}|$ are much greater than terms of order $|\dot{\mathbf{U}}|$, it follows that either

$$\ddot{\mathbf{U}} \times \nabla T = \mathbf{0}, \qquad \text{in which case} \qquad (\nabla T)^2 = \frac{\rho}{\lambda + 2\mu} = \frac{1}{\alpha(\mathbf{x})^2}, \tag{4.50}$$

or

$$\ddot{\mathbf{U}} \cdot \nabla T = 0, \qquad \text{in which case} \qquad (\nabla T)^2 = \frac{\rho}{\mu} = \frac{1}{\beta(\mathbf{x})^2}. \tag{4.51}$$

The ray direction is given by ∇T, so that equation (4.50) describes a longitudinal wave propagating along rays defined by the local P-wave speed, and (4.51) describes a transverse wave propagating along rays defined by the local S-wave speed.

Our next goal is to find the amplitude variation of P- and S-waves as they propagate along rays in an inhomogeneous medium. From our results (4.50) and (4.51), we shall assume that

(i) if (T, c^2, c^3) are defined in terms of the P-wave speed $\alpha(\mathbf{x})$, then the equations of motion have solutions in which u^1 is dominant and can be factorized into a pulse shape times an amplitude factor. This is the longitudinal solution, with ansatz

$$\mathbf{u}(\mathbf{x}, t) = \left(u^1(\mathbf{x}, t), 0, 0\right) + (0, \Delta u^2, \Delta u^3) \tag{4.52}$$

and

$$u^1(\mathbf{x}, t) = f^1(\mathbf{x}) U^1(t - T), \tag{4.53}$$

in which $|u^1| \gg |\Delta u^2|$ and $|u^1| \gg |\Delta u^3|$, and the pulse shape U^1 stays the same along the ray, merely being shifted in time by the amount $T(\mathbf{x})$ at position $\mathbf{x}$, i.e., by the

travel time along the ray. Within this framework, we want to find the explicit form of the amplitude factor $f^1(\mathbf{x})$. Examples of f^1 are obtained in Section 4.4.3.

For the transverse solutions (S-waves), we assume that

(ii) if (T, c^2, c^3) are defined in terms of the S-wave speed $\beta(\mathbf{x})$, then the displacements u^2 and u^3 are dominant. This is the transverse solution, with ansatz

$$\mathbf{u}(\mathbf{x}, t) = \Big(0, u^2(\mathbf{x}, t), u^3(\mathbf{x}, t)\Big) + (\Delta u^1, 0, 0) \tag{4.54}$$

and

$$u^2(\mathbf{x}, t) = f^2(\mathbf{x})U^2(t - T), \qquad u^3(\mathbf{x}, t) = f^3(\mathbf{x})U^3(t - T), \tag{4.55}$$

in which $|u^2| \gg |\Delta u^1|$ and $|u^3| \gg |\Delta u^1|$, and we want to find the explicit forms of the amplitude factors f^2 and f^3.

We shall first examine the special case of a spherically symmetric medium, this being a good approximation to the Earth's structure. For this case, described in Section 4.4.4, c^2 and c^3 are chosen as the orthogonal coordinates p and ϕ described in Figure 4.10. We shall find that the amplitude functions f^1, f^2, and f^3 of (4.53) and (4.55) can be obtained quickly, and two independent components of the S-wave are identified. A more general solution is given in Section 4.4.5.

4.4.3 THE GEOMETRICAL SOLUTION FOR P-WAVES IN SPHERICALLY SYMMETRIC MEDIA

The exact equation satisfied by $u^1(\mathbf{x}, t)$ is now

$$\begin{aligned}\rho\frac{\partial^2 u^1}{\partial t^2} = \frac{1}{\alpha h^2 h^3}\left[\frac{\partial}{\partial T}(h^2h^3\tau^{11}) + \frac{\partial}{\partial c^2}(h^3\alpha\tau^{12}) + \frac{\partial}{\partial c^3}(\alpha h^2\tau^{31})\right] \\ + \frac{\tau^{12}}{\alpha h^2}\frac{\partial \alpha}{\partial c^2} + \frac{\tau^{31}}{h^3\alpha}\frac{\partial \alpha}{\partial c^3} - \frac{\tau^{22}}{\alpha h^2}\frac{\partial h^2}{\partial T} - \frac{\tau^{33}}{h^3\alpha}\frac{\partial h^3}{\partial T}\end{aligned} \tag{4.56}$$

(see (2.48) and Figure 4.10), except at the source $\mathbf{x} = \boldsymbol{\xi}$. The right-hand-side terms in (4.56) are of different magnitude, depending on how many derivatives of the wavefunction in the T-direction they contain. We can simplify this scalar wave equation by assuming that

(iii) wavefunction derivatives perpendicular to the wavefront are much greater than derivatives parallel to the wavefront.

Our approach is to apply the formulas (2.50), (2.45), and (2.46) relating stress to strain and thence to displacement derivatives. We shall retain in (4.56) only the strongest terms such as $\ddot{u}^1$ and $\partial^2 u^1/\partial T^2$, together with terms at the next level such as $\partial u^1/\partial T$. We ignore terms of order u^1 which are two levels smaller than the main terms.

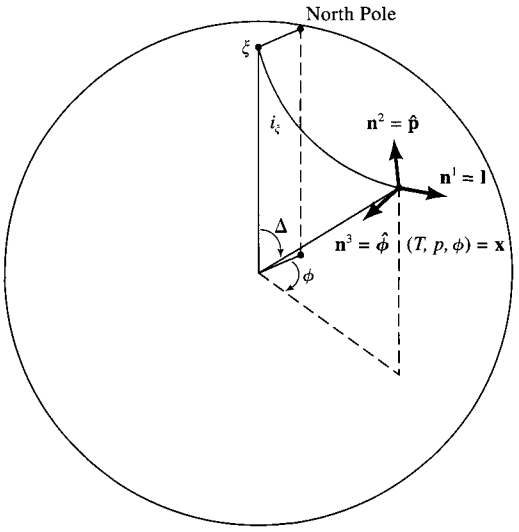

FIGURE **4.10**
General orthogonal ray coordinates for a spherically symmetric medium. We choose $(c^1, c^2, c^3) = (T, p, \phi)$, where T is the travel time taken for a wavefront to go from $\boldsymbol{\xi}$ to $\mathbf{x}$ along the ray path, p is the ray parameter $r \sin i(r)/c(r)$ (which is constant along a given ray), and ϕ is the geographical azimuth angle. Thus, assigning a value to the pair (p, ϕ) specifies a particular ray leaving the source, and T specifies a particular point along the ray. Associated normals at $\mathbf{x}$ are $\mathbf{n}^1$ (along the ray), $\mathbf{n}^2$ (transverse and in a vertical plane), and $\mathbf{n}^3$ (transverse and horizontal). We use the symbols $\mathbf{l}, \hat{\mathbf{p}}, \hat{\boldsymbol{\phi}}$ for these respective unit normals.

Another possible choice for c^2 is i_ξ, often called the take-off angle: in this case i_ξ and ϕ would be the angles for a system of spherical polar coordinates centered on the source, with direction $i_\xi = 0$ taken downward and the direction $\phi = 0$ being due North from the source. The reason for taking $i_\xi = 0$ as the *downward* vertical is that a right-handed coordinated system is then obtained with ϕ measured *clockwise* round from North, which is the usual way to specify azimuth angles.

Contributing strains are

$$e^{11} = \frac{1}{\alpha}\frac{\partial u^1}{\partial T}, \qquad e^{22} = \frac{u^1}{\alpha h^2}\frac{\partial h^2}{\partial T}, \qquad e^{33} = \frac{u^1}{\alpha h^3}\frac{\partial h^3}{\partial T}, \tag{4.57}$$

leading to stresses

$$\tau^{11} = \frac{\lambda + 2\mu}{\alpha}\frac{\partial u^1}{\partial T} + \frac{\lambda u^1}{\alpha}\left(\frac{1}{h^2}\frac{\partial h^2}{\partial T} + \frac{1}{h^3}\frac{\partial h^3}{\partial T}\right), \qquad \tau^{22} = \tau^{33} = \frac{\lambda}{\alpha}\frac{\partial u^1}{\partial T}. \tag{4.58}$$

Shear strains and shear stresses are not needed since they contribute to (4.56) only at the u^1 level, not at the $\ddot{u}^1$ or $\dot{u}^1$ levels. Substituting from (4.58) into (4.56) gives the approximate form

$$\rho\frac{\partial^2 u^1}{\partial t^2} = \frac{1}{\alpha h^2 h^3}\left[\frac{\partial}{\partial T}\left(h^2 h^3 \frac{\lambda + 2\mu}{\alpha}\frac{\partial u^1}{\partial T}\right)\right].$$

To the same order of approximation (i.e., retaining strongest terms such as $\ddot{u}^1$ and $\partial^2 u^1/\partial T^2$, and terms at the next level such as $\partial u^1/\partial T$), this is equivalent to

$$\frac{\partial^2}{\partial t^2}\left(\sqrt{\rho\alpha h^2 h^3}\, u^1\right) = \frac{\partial^2}{\partial T^2}\left(\sqrt{\rho\alpha h^2 h^3}\, u^1\right), \tag{4.59}$$

which is merely a one-dimensional wave equation for a wave propagating along the direction of varying T. The general solution for $\sqrt{\rho\alpha h^2 h^3}\, u^1$ is therefore a function of $t - T$ plus a function of $t + T$. The P-wave solution for longitudinal motion that propagates in the direction of *increasing* T must therefore be of the form

$$\mathbf{u}^P(\mathbf{x}, t) = (u^1, 0, 0) = \sqrt{\frac{1}{\rho\alpha h^2 h^3}}\, \mathcal{F}^P(c^2, c^3)\left(U^1(t - T(\mathbf{x}))\, 0, 0\right), \tag{4.60}$$

and at last we have obtained an explicit form of the amplitude function appearing in (4.53).

The factors in the right-hand side of this expression have several of the properties that were noted in Section 4.1 (following (4.3)) for the elementary solution of a wave spreading from a point source in a homogeneous medium. The quantity $(h^2 h^3)^{-1/2}$ describes the attenuation of the wave due to geometrical spreading (see Fig. 4.11); the factor $\mathcal{F}^P(c^2, c^3)$ describes the radiation pattern of P-waves emanating in different directions (c^2, c^3) from the source; and we can expect that the function $U^1(t - T(\mathbf{x}))$, giving the displacement pulse shape in the longitudinal direction, must be related to the time function of the operative body force at the source.

The most cryptic factor in (4.60) is $(h^2 h^3)^{-1/2}$, which in Figure 4.11 we have associated with geometrical spreading, and which in homogeneous media is simply $1/|\mathbf{x} - \boldsymbol{\xi}|$. The geometrical spreading factor in inhomogeneous media is of great practical importance, since it describes the focusing and defocusing of rays. We therefore introduce a new function, $\mathcal{R}^P(\mathbf{x}, \boldsymbol{\xi})$, described in the following specific way: the pencil of P-wave rays spreading from the source $\boldsymbol{\xi}$ within solid angle $d\Omega$ has, on the wavefront coinciding with $\mathbf{x}$, the area dA given by $[\mathcal{R}^P(\mathbf{x}, \boldsymbol{\xi})]^2\, d\Omega$. It follows that

$$\mathcal{R}^P(\mathbf{x}, \boldsymbol{\xi}) = \sqrt{\frac{dA}{d\Omega}}. \tag{4.61}$$

If the rays are straight lines, then $\mathcal{R}^P(\mathbf{x}, \boldsymbol{\xi}) = |\mathbf{x} - \boldsymbol{\xi}|$. But in the more general case of curved rays shown in Figure 4.11, with $\mathbf{x}$ varying along a particular ray tube, $\mathcal{R}^P(\mathbf{x}, \boldsymbol{\xi}) \propto (h^2 h^3)^{1/2}$. The constant of proportionality here can depend only on $\boldsymbol{\xi}$ and on the ray direction at $\boldsymbol{\xi}$ specified by (c^2, c^3). Since it is merely a scale factor, it can be absorbed within $\mathcal{F}^P$ and U^1 to give

$$\mathbf{u}^P(\mathbf{x}, t) = \sqrt{\frac{1}{\rho(\mathbf{x})\alpha(\mathbf{x})}}\, \frac{1}{\mathcal{R}^P(\mathbf{x}, \boldsymbol{\xi})}\, \mathcal{F}^P(c^2, c^3)\left(U^1(t - T^P(\mathbf{x}, \boldsymbol{\xi})), 0, 0\right) \tag{4.62}$$

for the geometrical ray solution of P-wave displacement. A superscript is also used here for the travel time, and $T^P(\mathbf{x}, \boldsymbol{\xi}) = \int_{\boldsymbol{\xi}}^{\mathbf{x}} |ds|/\alpha$, in which the integral (see (4.47)) is taken along the ray. In Section 4.5 we shall evaluate $\mathcal{F}(c^2, c^3)$ and $U^1(t)$ explicitly for a point shear dislocation of arbitrary orientation.

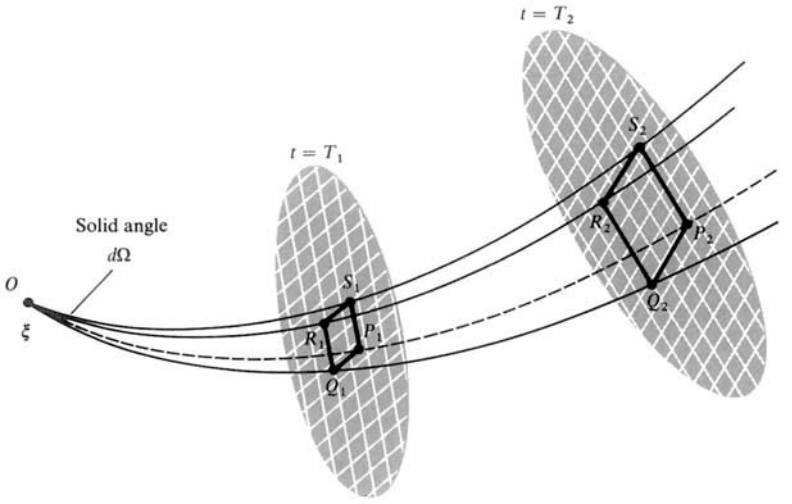

FIGURE **4.11**
Geometrical spreading of four rays. Suppose OP_1P_2 is the ray with coordinates (c^2, c^3) in the general orthogonal system (T, c^2, c^3), and that T_1 and T_2 give the position of the same wavefront at successive times $t = T_1, t = T_2$. Suppose that rays OQ_1Q_2, OR_1R_2, OS_1S_2 have coordinates $(c^2, c^3 + dc^3)$, $(c^2 + dc^2, c^3 + dc^3)$, and $(c^2 + dc^2, c^3)$, respectively, and that the solid angle of this pencil at O is $d\Omega$. Then the area of $P_1Q_1R_1S_1$ is $h^2h^3dc^2dc^3$, with (h^2, h^3) evaluated at $T = T_1$, and $P_2Q_2R_2S_2$ is $h^2h^3dc^2dc^3$, with (h^2h^3) evaluated at $T = T_2$. In this sense, h^2h^3 is proportional to the areal cross section of a pencil of rays emanating from the point source.

If coordinates c^2 and c^3 are not orthogonal (this is the case for general inhomogeneous media), then the areas $P_1Q_1R_1S_1$ and $P_2Q_2R_2S_2$ are not rectangles, but are given by $|(\partial \mathbf{x}/\partial c^2) \times (\partial \mathbf{x}/\partial c^3)|dc^2\,dc^3$. Such areas are still proportional to $d\Omega$ on any given wavefront, and we define a geometrical spreading function $\mathcal{R}(\mathbf{x}, \boldsymbol{\xi})$ by equating the ray-tube cross-sectional area at $\mathbf{x}$ to $\mathcal{R}^2(\mathbf{x}, \boldsymbol{\xi})\, d\Omega$.

4.4.4 THE GEOMETRICAL SOLUTION FOR *S*-WAVES IN SPHERICALLY SYMMETRIC MEDIA: INTRODUCTION OF THE COMPONENTS

The ray coordinates of Figure 4.10, with travel time T defined for the shear-wave speed $\beta(\mathbf{x}) = \beta(r)$, are also appropriate for analyzing transverse motions, $\mathbf{u} = (0, u^2, u^3)$. Using assumptions (ii) and (iii) above and the stress–strain and strain–displacement formulas of Section 2.6, we find that all stress components are negligible, except for the shearing stresses

$$\tau^{12} = \frac{\mu}{\beta}\frac{\partial u^2}{\partial T}, \qquad \tau^{31} = \frac{\mu}{\beta}\frac{\partial u^3}{\partial T}.$$

These may be substituted into the equations for $\ddot{u}^2$ and $\ddot{u}^3$ (see (2.48)), and by steps similar to the derivation of (4.59) we now find

$$\frac{\partial^2}{\partial t^2}\left(\sqrt{\rho\alpha h^2h^3}\,u^2\right) = \frac{\partial^2}{\partial T^2}\left(\sqrt{\rho\alpha h^2h^3}\,u^2\right) \tag{4.63}$$

$$\frac{\partial^2}{\partial t^2}\left(\sqrt{\rho\alpha h^2h^3}\,u^3\right) = \frac{\partial^2}{\partial T^2}\left(\sqrt{\rho\alpha h^2h^3}\,u^3\right). \tag{4.64}$$

Again, these are one-dimensional wave equations for which we know the general solution; equations (4.63) and (4.64) also tell us that u^2 and u^3 propagate independently. Referring to Figure 4.10, we see that u^3 is a motion in the horizontal direction at $\mathbf{x}$, hence it is called the SH-component in seismology. The motion u^2 is also transverse to the ray, but is in the vertical plane, hence it is called the SV-component. Note that in general the SV-component is not in the vertical direction.

The geometrical S-wave solutions in spherically symmetric media can now be stated as

$$\mathbf{u}^{SV}(\mathbf{x},t) = \sqrt{\frac{1}{\rho(\mathbf{x})\beta(\mathbf{x})}}\,\frac{1}{\mathcal{R}^S(\mathbf{x},\boldsymbol{\xi})}\,\mathcal{F}^{SV}(p,\phi)\left(0, U^3(t - T^S(\mathbf{x},\boldsymbol{\xi})), 0\right) \tag{4.65}$$

and

$$\mathbf{u}^{SH}(\mathbf{x},t) = \sqrt{\frac{1}{\rho(\mathbf{x})\beta(\mathbf{x})}}\,\frac{1}{\mathcal{R}^S(\mathbf{x},\boldsymbol{\xi})}\,\mathcal{F}^{SH}(p,\phi)\left(0, 0, U^3(t - T^S(\mathbf{x},\boldsymbol{\xi}))\right). \tag{4.66}$$

Although the radiation patterns $\mathcal{F}^{SV}$ and $\mathcal{F}^{SH}$ may be different, the two components of S in an isotropic medium share the same geometrical spreading factor $\mathcal{R}^S(\mathbf{x},\boldsymbol{\xi})$ and the same travel-time function T^S. The pulse shapes U^2 and U^3 may, in general, be different, although we shall find in the next section that they are the same for far-field S-waves from a point shear dislocation. The relative amount of motion partitioned into SV and SH is known as the *polarization* of the S-wave, and it does not change along a given ray in a continuously varying medium: this is a property of great importance in interpreting body-wave seismograms.

4.4.5 THE GEOMETRICAL RAY SOLUTIONS IN GENERAL INHOMOGENEOUS MEDIA

The precision of modern seismology makes apparent the fact that the Earth's internal structure is not quite spherically symmetric. Thus travel-time curves (plots of the time T against distance over the Earth's surface) for body waves from a surface source show systematic differences in different regions. Part of the departure from symmetry is due to the Earth's ellipticity, but corrections for this are now well understood (Bullen, 1937; Kennett and Gudmundsson, 1996). In studies such as that by Dziewonski (1984), significant differences of a few tenths of a second (in travel times amounting to several minutes), remaining after corrections for ellipticity, have been used to estimate the departure from homogeneity in the deep mantle. Van der Hilst *et al.* (1997) used travel-time anomalies for paths in the upper and lower mantle to identify major laterally varying structures such as descending slabs of lithosphere, some of which appear to reach all the way down to the Earth's core. For inhomogeneous media, there are effects on body waves that may sometimes be interpreted in terms of reflection and refraction at oblique (i.e., nonhorizontal) boundaries, but our present concern is with ray theory for media that vary smoothly, i.e., without discontinuities in the structure.

If the assumption of spherical symmetry is dropped, then the principal complication is that a given ray is no longer confined to lie in a plane. At worst, it may twist around like a

bent corkscrew, and it is therefore surprising that the results (4.62), (4.65), (4.66), already obtained for spherical symmetry, require very little adaptation to the general case. In fact, the geometrical ray solution (4.62) for P-waves is unchanged in general isotropic media. For S-waves, the displacement amplitude still changes like $1/[\sqrt{\rho\beta}\,\mathcal{R}^S(\mathbf{x},\boldsymbol{\xi})]$ (cf. (4.65), (4.66)), and there is still a sense in which the polarization is unchanged along the ray path. But because it is no longer possible to find coordinates (c^2, c^3) that are orthogonal in every wavefront, the results we have just stated require a different and more intricate method of proof.

Thus, for P-waves, we can try the ansatz

$$\mathbf{u}^P(\mathbf{x},t) = f(\mathbf{x})\,U(t - T(\mathbf{x}))\,\alpha\nabla T, \tag{4.67}$$

which is suggested by (4.50). Here $\alpha\nabla T$ is a unit vector in the direction of longitudinal particle motion, and to find $f(\mathbf{x})$ we substitute (4.67) into the general displacement equation for inhomogeneous isotropic media,

$$\rho\frac{\partial^2 u_i}{\partial t^2} = \frac{\partial}{\partial x_j}[\lambda\delta_{ij}u_{k,k} + \mu(u_{i,j} + u_{j,i})], \tag{4.68}$$

obtained from (2.17), (2.49), and (2.3). The terms of order $\ddot{U}$ all cancel, because $(\nabla T)^2 = 1/\alpha^2$, and if we require the terms of order $\dot{U}$ also to vanish, we do indeed obtain an equation for the P-wave amplitude function, $f(\mathbf{x})$. Taking the scalar product with ∇T (cf. (4.49)), this equation is obtained after some manipulation in the form

$$(\lambda + 2\mu)[2\nabla T\cdot\nabla(\alpha f) + 2\alpha^3 f T_{,k}T_{,ik}T_{,i} + \alpha f\nabla^2 T] + \alpha f\nabla(\lambda + 2\mu)\cdot\nabla T = 0. \tag{4.69}$$

Most of these terms can immediately be converted to spatial derivatives with respect to distance s along the ray, since $\alpha(\partial T/\partial x_i)(\partial/\partial x_i) = \partial/\partial s$. For example,

$$T_{,k}T_{,ik}T_{,i} = \frac{\partial T}{\partial x_k}\frac{1}{\alpha}\frac{\partial}{\partial s}\frac{\partial T}{\partial x_k} = \frac{1}{2\alpha}\frac{\partial}{\partial s}\left(\frac{\partial T}{\partial x_k}\frac{\partial T}{\partial x_k}\right) = \frac{1}{2\alpha}\frac{\partial}{\partial s}\left(\frac{1}{\alpha^2}\right).$$

The effect of geometrical spreading is present in (4.69) in the term $\nabla^2 T$. This is the divergence of ∇T, and using an elementary volume with corners at $T \pm \frac{1}{2}\delta T$, $c^2 \pm \frac{1}{2}\delta c^2$, $c^3 \pm \frac{1}{2}\delta c^3$, we see that the flux of ∇T out of the volume is nonzero only for the two sides with area $\mathcal{R}^2(\mathbf{x},\boldsymbol{\xi})\,d\Omega$. (See Fig. 4.11 and its legend.) It follows from the fundamental definition of divergence (flux per unit volume) that

$$\nabla^2 T = \frac{1}{\mathcal{R}^2(\mathbf{x},\boldsymbol{\xi})\,d\Omega\,\alpha\,\delta T}\frac{\partial}{\partial T}\left(\frac{\mathcal{R}^2(\mathbf{x},\boldsymbol{\xi})\,d\Omega}{\alpha}\right)\delta T = \frac{1}{\mathcal{R}^2}\frac{\partial}{\partial s}\left(\frac{\mathcal{R}^2}{\alpha}\right), \tag{4.70}$$

and (4.69) reduces to

$$\frac{1}{f}\frac{\partial f}{\partial s} + \frac{1}{2\rho}\frac{\partial\rho}{\partial s} + \frac{1}{2\alpha}\frac{\partial\alpha}{\partial s} + \frac{1}{\mathcal{R}}\frac{\partial\mathcal{R}}{\partial s} = 0. \tag{4.71}$$

This integrates to give $f(\mathbf{x}) \propto 1/[\sqrt{\rho(\mathbf{x})\alpha(\mathbf{x})}\,\mathcal{R}(\mathbf{x}, \xi)]$, in which the constant of proportionality depends on the particular ray, i.e., on (c^2, c^3). The ansatz (4.67) therefore leads to exactly the same geometrical solution for P-waves, as we found in (4.62) for spherically symmetric media.

For S-waves, we know from (4.51) that particle displacement is still, in general, transverse to the ray, but there is now a phenomenon that cannot be quantified from experience in the study of homogeneous or spherically symmetric media. The new phenomenon is that the direction of particle motion may rotate around the ray as the wavefront propagates.

Our ansatz for S-wave motion is

$$\mathbf{u}^S(\mathbf{x}, t) = f(\mathbf{x})U(t - T(\mathbf{x}))\nu(\mathbf{x}), \tag{4.72}$$

where $f(\mathbf{x})$ is the amplitude, $U(t)$ the pulse shape, and unit vector ν is the direction of (transverse) particle motion, so that $\nu \cdot \nabla T = 0$. Again, we substitute our ansatz into the displacement equation (4.68), but this time form the vector product with ∇T. The largest terms in $\ddot{U}$ cancel in view of the property $(\nabla T)^2 = 1/\beta^2$, and by requiring the terms in $\dot{U}$ to vanish we obtain

$$\begin{aligned}\mu[2(\nabla f \cdot \nabla T)\nu \times \nabla T + 2f((\nabla T \cdot \nabla)\nu) \times \nabla T + f(\nabla^2 T)\nu \times \nabla T] \\ + f(\nabla \mu \cdot \nabla T)\nu \times \nabla T = \mathbf{0}.\end{aligned} \tag{4.73}$$

Using the rule $\beta(\partial T/\partial x_i)(\partial/\partial x_i) = \partial/\partial s$ to convert to derivatives with respect to distance s along the ray, and also $\nabla^2 T = (1/\mathcal{R}^2)(\partial/\partial s)(\mathcal{R}^2/\beta)$, where $\mathcal{R}$ is the geometrical spreading factor for S-waves (cf. (4.70)), (4.73) becomes

$$\left(\frac{1}{f}\frac{\partial f}{\partial s} + \frac{1}{2\rho}\frac{\partial \rho}{\partial s} + \frac{1}{2\beta}\frac{\partial \beta}{\partial s} + \frac{1}{\mathcal{R}}\frac{\partial \mathcal{R}}{\partial s}\right)(\nu \times \nabla T) + \left(\frac{\partial \nu}{\partial s} \times \nabla T\right) = \mathbf{0}. \tag{4.74}$$

However, the two vector directions here, $\nu \times \nabla T$ and $\partial\nu/\partial s \times \nabla T$, are orthogonal. (This follows from the mutual orthogonality of ∇T, ν, and $\nu \times \nabla T$; and from the fact that $0 = \partial/\partial s(\nu \cdot \nu) = 2\nu \cdot \partial\nu/\partial s$, so that $\partial\nu/\partial s$ lies in the plane of ∇T and $\nu \times \nabla T$.) Hence the amplitude function f is constrained by

$$\frac{1}{f}\frac{\partial f}{\partial s} + \frac{1}{2\rho}\frac{\partial \rho}{\partial s} + \frac{1}{2\beta}\frac{\partial \beta}{\partial s} + \frac{1}{\mathcal{R}}\frac{\partial \mathcal{R}}{\partial s} = 0, \tag{4.75}$$

and also

$$\partial\nu/\partial s \times \nabla T = \mathbf{0}, \tag{4.76}$$

implying that $\partial\nu/\partial s$ must be along the longitudinal direction, ∇T.

From (4.75) we see that $f(\mathbf{x}) \propto 1/[\sqrt{\rho(\mathbf{x})\beta(\mathbf{x})}\,\mathcal{R}(\mathbf{x}, \xi)]$, and the amplitude has the same property previously found for both the SV- and SH-components in spherically symmetric media (cf. (4.65), (4.66)).

From (4.76) we can show that there is a sense in which the S-wave retains the same polarization at different points along the ray, even in general inhomogeneous media. This

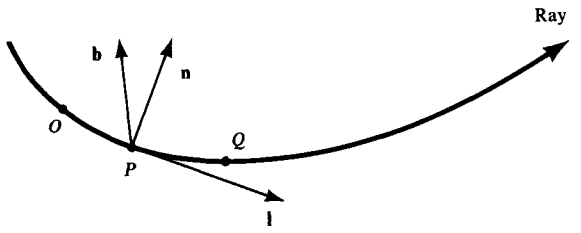

FIGURE **4.12**
The system of three mutually orthogonal unit vectors at point P, intrinsic to the geometry of a twisting ray: $\mathbf{l}$ is along the ray; $\mathbf{n}$ is normal to the ray and lies in the plane in which the ray is changing direction ($d\mathbf{l}/ds$). (This is the osculating plane, defined as the limiting plane containing points OPQ lying on the curved ray, as O and Q tend to P.) The unit binormal $\mathbf{b}$ is taken in the direction that makes ($\mathbf{l}$, $\mathbf{n}$, $\mathbf{b}$) a right-handed triple. If the ray does not twist, but merely curves in a plane, then $\mathbf{b}$ is normal to that plane.

effect may be analyzed using the intrinsic system of unit vectors associated with each point along a ray. These are the unit tangent $\mathbf{l} = \beta \nabla T$, the unit normal $\mathbf{n} = (d\mathbf{l}/ds)/|d\mathbf{l}/ds|$, and the unit binormal $\mathbf{b} = \mathbf{l} \times \mathbf{n}$. The local curvature of the ray, $\kappa(s)$, measures the tendency to change direction, and is simply $|d\mathbf{l}/ds|$. Note that this direction change, which is normal to $\mathbf{l}$, is related to $\mathbf{n}$ by

$$\frac{d\mathbf{l}}{ds} = \kappa(s)\mathbf{n}. \tag{4.77}$$

For each point on the ray, the vectors $\mathbf{l}$ and $\mathbf{n}$ determine a plane known as the *osculating plane* (see Fig. 4.12), which coincides with the plane of the ray in cases where the ray is confined to one plane (e.g., rays in a spherically symmetric Earth). More generally, the osculating plane (which is normal to $\mathbf{b}$) changes direction along the ray, and the derivative $d\mathbf{b}/ds$ gives a measure of the tendency of the ray to "twist" out of the osculating plane.

Writing $d\mathbf{b}/ds = c_1\mathbf{l} + c_2\mathbf{n} + c_3\mathbf{b}$, it is simple to show from the fixed length of $\mathbf{b}$ that $c_3 = 0$, and from the definitions of $\mathbf{b}$ and $\mathbf{n}$ that $c_1 = 0$. Thus $d\mathbf{b}/ds$ is in direction $\mathbf{n}$, and the local torsion $\mathcal{T}$ of the ray, or second curvature, is defined by

$$\frac{d\mathbf{b}}{ds} = -\mathcal{T}\,\mathbf{n}. \tag{4.78}$$

This equation means that the axes ($\mathbf{n}$, $\mathbf{b}$) rotate around the ray in a right-handed fashion at rate $\mathcal{T}$ per unit distance.

Since $\mathbf{n} = \mathbf{b} \times \mathbf{l}$, it follows that

$$\frac{d\mathbf{n}}{ds} = -\kappa\,\mathbf{l} + \mathcal{T}\,\mathbf{b}. \tag{4.79}$$

Equations (4.77)–(4.79) are known as the Frénet formulas, and we now return to the problem of finding out how the direction of transverse motion changes during propagation.

At distance s along the ray, suppose that the transverse direction $\boldsymbol{\nu}$ of S-wave motion makes an angle γ with the local normal:

$$\boldsymbol{\nu} = \cos\gamma\ \mathbf{n} + \sin\gamma\ \mathbf{b}. \tag{4.80}$$

Then, from (4.78) and (4.79),

$$\frac{\partial \boldsymbol{\nu}}{\partial s} = -\kappa\cos\gamma\ \mathbf{l} - \left(\frac{d\gamma}{ds} + \mathcal{T}\right)(\sin\gamma\ \mathbf{n} - \cos\gamma\ \mathbf{b}). \tag{4.81}$$

But we already concluded from (4.76) that $\partial\boldsymbol{\nu}/\partial s$ is directed along ∇T, i.e., along $\mathbf{l}$, hence the coefficients of $\mathbf{n}$ and $\mathbf{b}$ in (4.81) must vanish, and

$$\frac{d\gamma}{ds} = -\mathcal{T}. \tag{4.82}$$

This means that the S-wave motion $\mathbf{u}^S$, as referred to the $(\mathbf{n}, \mathbf{b})$ directions, rotates around the ray at exactly the same rate $\mathcal{T}$ as the axes themselves rotate (see (4.78)), *but in the opposite direction*. Because of this cancellation, the S-wave may be said to retain its polarization in isotropic media. (This contrasts with the behavior of S-waves in anisotropic media, where splitting can occur due to differences in propagation speed associated with different polarizations. See Box 5.9.) Though it might appear that spatial gradients of the S-wave speed in inhomogeneous isotropic media often vary (both vertically and horizontally) in such a way as to require full 3-D ray tracing for the analysis of travel times and radiation patterns from a particular point source, it is difficult to accumulate much of a change in practice in the $SH : SV$ ratio for 3-D structures (see Cormier, 1984). A change begins to accumulate in high gradient zones, but the ray will quickly turn out of such zones.

These results conclude our present development of geometrical ray theory in isotropic media. In Chapter 5, we shall relate the above results to the conservation of energy in ray tubes; and in Chapter 9 we shall develop further properties of rays in a spherically symmetric medium (finding for caustics, where $\mathcal{R}(\mathbf{x}, \boldsymbol{\xi}) = 0$, and for shadows that the results of this section must be modified).

The methods of this section have been carried much further by V. M. Babich and by J. B. Keller and their colleagues, using trial solutions such as

$$\mathbf{u}(\mathbf{x}, \omega) = \exp(i\omega T)\sum_{n=0}^{\infty} \mathbf{A}_n(\mathbf{x})(i\omega)^{-n}. \tag{4.83}$$

Recursion relations between the $\mathbf{A}_n$ can be found that make it possible to find as many terms in the infinite series as may be required (Karal and Keller, 1959). Our work above is for $\mathbf{A}_0$, which dominates at sufficiently high frequencies. Occasionally, $\mathbf{A}_1$ is useful. (For example, if material boundaries are present, and the source–receiver geometry is such as to permit head waves, then their dominant effect is contained within $\mathbf{A}_1$.) More commonly, it may be said that where $\mathbf{A}_0$ alone is inadequate, then one must either take many more terms in the series (4.83) (which is impractical), or use a different form of trial solution. (In the time domain, $\mathbf{A}_n$ in (4.83) weights a term proportional to $(t - T(x))^{n-1}$, so that this solution "blows up" away from wavefronts; see Okal and Mechler, 1973.)

4.5 The Radiation Pattern of Body Waves in the Far Field for a Point Shear Dislocation of Arbitrary Orientation in a Spherically Symmetric Medium

A thorough understanding of this subject title has played a major role in the discovery and measurement of lithospheric plate motions (Sykes, 1967; Isacks, Oliver, and Sykes, 1968). This radiation pattern, once it has been recognized and its orientation obtained for a given earthquake, gives information about the direction of block motions caused by episodes of faulting.

We have already given a description of the radiation pattern in source coordinates in Section 4.3 (see Figs. 4.5b, 4.6b). For P-waves, there are two nodal planes. These are orthogonal, and one of them is the fault plane. This source-coordinate system, however, is unavailable to us until we have learned the orientation of the causative fault and the direction of the slip on that fault. Fault orientation is specified by *strike* and *dip*, and then either the *rake* or the *plunge* is used to specify the direction of slip (see Fig. 4.13). A fault has two surfaces, and the one illustrated is the surface of the *foot wall*. The other surface is known as the *hanging wall*. The strike direction is that one of the two horizontal directions in the fault plane for which the block containing the hanging wall is on the right, as viewed by an observer looking along strike. Slip $\bar{\mathbf{u}}$ is taken as the direction of the hanging wall, relative to the foot wall. Rake λ is the angle between strike direction and slip: $-\pi < \lambda \leq \pi$. If δ is neither 0 nor $\pi/2$ and λ is within the range $(0, \pi)$, the fault is termed a *reverse fault* or a *thrust fault*. However, if λ is within the range $(-\pi, 0)$, the fault is termed a *normal fault*.

Instead of the rake (which is measured within the fault plane), some authors use the *plunge*, which is measured in the vertical plane. Measuring the plunge from the horizontal down to the direction of $\bar{\mathbf{u}}$, we find the sine of the plunge is equal to $-\sin\lambda \sin\delta$.

A *strike-slip fault* is one for which the slip is horizontal ($\lambda = 0$ or π). For a vertical strike-slip fault ($\delta = \pi/2$ in addition to $\lambda = 0$ or π), there are two possible choices of

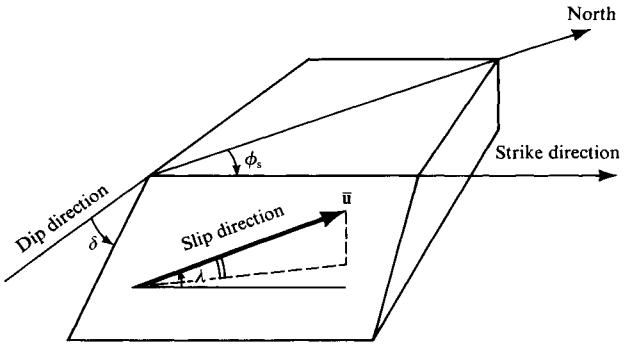

FIGURE **4.13**
Definition of the fault-orientation parameters (strike ϕ_s, dip δ) and the slip-direction parameter (rake λ). ϕ_s is measured clockwise round from North, with the fault dipping down to the right of the strike direction: $0 \leq \phi_s < 2\pi$. The dip angle δ is measured down from the horizontal: $0 \leq \delta \leq \pi/2$. The slip direction is specified by the rake λ, measured in the fault plane as the angle between the directions of strike and slip.

strike direction and the one we choose determines which of the two fault surfaces is the hanging wall (it is the fault surface of the block on the right, when looking in the along-strike direction). Then right-lateral and left-lateral strike-slip faults can immediately be distinguished by λ values alone. (A *right-lateral fault* is one for which an observer standing on one block sees the other block as having moved to the right.) $\lambda = 0$ is a left-lateral strike-slip fault and $\lambda = \pi$ is right-lateral.

A *dip-slip fault* is one for which slip is perpendicular to the strike direction ($\lambda = \pi/2$ or $-\pi/2$). For a vertical dip-slip fault ($\delta = \pi/2$), again there is ambiguity in strike direction. We take the foot wall to lie in the down-dropped block, and the strike direction as again that for which the hanging wall is on the right, when looking in the strike direction. Then a vertical dip-slip fault always has $\lambda = \pi/2$.

In this section, we introduce the *focal sphere* (see Fig. 4.14) as a surface on which to describe the radiation pattern, and shall show how nodal planes are obtained from global observation of far-field body waves. We augment this descriptive approach by deriving specific formulas for the radiation pattern of P-, SV-, and SH-waves as a function of general strike, dip, and rake, and also as a function of ray parameter p and azimuth ϕ from source to receiver. Such formulas are required for an accurate estimation (from body waves) of seismic moment M_0.

4.5.1 A METHOD FOR OBTAINING THE FAULT-PLANE ORIENTATION OF AN EARTHQUAKE AND THE DIRECTION OF SLIP USING TELESEISMIC BODY-WAVE OBSERVATIONS

The radiation pattern of a shear dislocation is characterized, for P-waves (see Fig. 4.5), by a quadrantal distribution. This feature is most commonly studied in terms of the first motion of P-wave displacement. For a given receiver, the longitudinal particle motion is either toward or away from the source: the first-arriving waves at a seismometer often provide the most unambiguous and most easily interpreted part of the record of ground displacement. The radiation pattern can conveniently be understood in terms of the focal sphere, defined in Figure 4.14. Thus, for a given observation of a P-wave at $\mathbf{x}$, we trace the ray back to the source at ξ, transferring information obtained at $\mathbf{x}$ onto the corresponding point on the focal sphere (i.e., the point with coordinates (i_ξ, ϕ)).

To illustrate the distortion such a mapping can make, Figure 4.15 shows an outline of the major continents as mapped by P-waves on the lower half of a focal sphere centered on a point 42 km below the Kurile Islands (a part of the North Pacific). Because the P-wave speed increases with depth throughout the mantle (in the Earth model used to obtain this figure), very strong areal distortion occurs in mapping the Earth's surface onto the focal sphere.

Note that another mapping is required to show the focal sphere on a plane surface (such as the printed page). The two most commonly used are the stereographic projection (Fig. 4.16) and the zenithal equal-area projection (sometimes called the Schmidt–Lambert equal-area projection; see Fig. 4.17).

The process of obtaining a fault-plane solution from P-wave motions involves (a) marking particular positions on the focal sphere that correspond to P-wave rays for which one has data, using a different symbol depending on whether the longitudinal motion, trav-

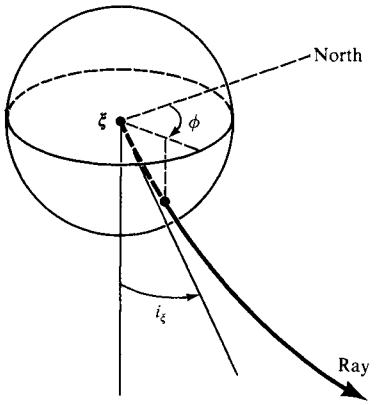

FIGURE **4.14**
The focal sphere for a seismic point source is a sphere centered on the source and having arbitrarily small radius. It is a convenient device for displaying radiation patterns, since information recorded by seismometers (distributed over the Earth's surface) may be transferred to the focal sphere; this involves tracing the ray back from each receiver to the source and seeing where the ray intersects the focal sphere. Equivalently, one may specify a point on the focal sphere by angular ray coordinates (i_ξ, ϕ), used now in a spherical polar system centered on the source. ($i_\xi = 0$ is the downward vertical; ϕ is azimuth round from North. The radius of the focal sphere is then immaterial, and usually taken as unity.) The radiation patterns of Figures 4.5b and 4.6b are shown as patterns on the focal sphere.

Since the focal sphere lies within the near field of the source, it is not obvious that far-field radiation patterns mapped onto the focal sphere would directly indicate the displacements actually occurring in the source region. However, for a shear dislocation with final offset in the same direction as averaged particle velocity, confusion does not occur. This is because the far-field radiation pattern (the terms $\mathbf{A}^{FP}$ and $\mathbf{A}^{FS}$ in (4.32) and (4.33)) is then the same as the radiation pattern for static displacements (4.34) at all distances from the source (and, in particular, on the focal sphere).

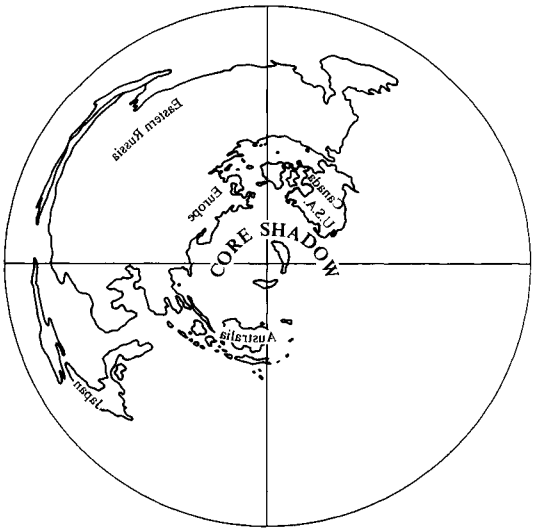

FIGURE **4.15**
The focal sphere is shown, in equal area projection, for a point beneath the Kurile Islands (43°26′N, 147°03′E, depth 42 km). For seismological purposes, eastern Russia could contribute more information than all other continental areas combined. The lack of coverage in the Pacific Ocean would make it very difficult to obtain a fault-plane solution. [Adapted from Davies and McKenzie, 1969.]

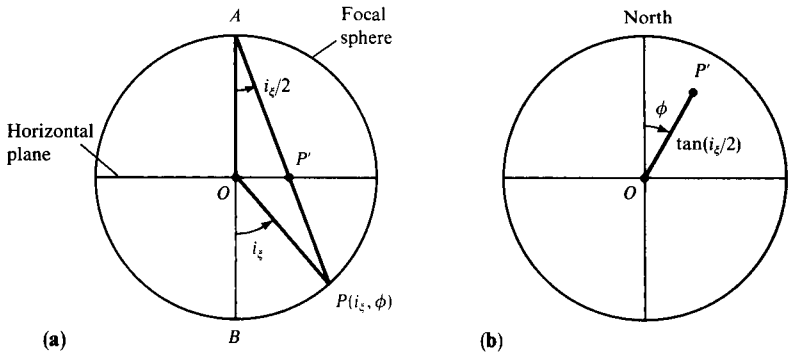

FIGURE **4.16**

The stereographic projection of the focal sphere maps point P on the lower hemisphere to the point P' as shown in the horizontal plane that separates upper and lower halves of the focal sphere. **(a)** Shown here is a vertical plane through the center of the focal sphere and the point P. **(b)** A plan view of the horizontal plane viewed on edge in (a). This is the plane of the projection, and point P' is at distance $\tan \frac{1}{2} i_\xi$ from the point O. The figure shows projection only of the lower half of the focal sphere, but by projecting from B instead of A, the upper half of the focal sphere can also be mapped inside a circle of unit radius.

Since this projection preserves the shapes of small regions, the scale is locally the same in all directions at position P'. However, this scale at P' is proportional to $\sec^2 \frac{1}{2} i_\xi$, so that area elements at P are scaled at P' by a factor $\sec^4 \frac{1}{2} i_\xi$. This is highly undesirable, since it gives a large amplification of areas for points on the focal sphere that are not near A and B. The effect appears in (b) mainly as a relative compression of the area associated with downgoing rays (i.e., with small i_ξ).

The stereographic projection is used in association with a Wulff net, which provides a template for drawing in (b) the possible curves that in (a) represent the intersection of the focal sphere with fault planes of arbitrary orientation.

eling along the ray from the focal sphere to the recording station, is *outward* or *inward*; and (b) partitioning the focal sphere by two perpendicular great circles, with each quadrant having either all outward or all inward arrivals. An example is given in Figure 4.18. (Instead of characterizing the P-wave motion as outward or inward, the alternative terms *compressional* and *dilatational* are often used. Demonstrating the linkage between these descriptions is set as Problem 5.9.)

There are two principal points to note. The first is the ambiguity in choosing which of two nodal planes is the fault plane. This difficulty was foreseen in Section 3.2, from the symmetry between the two components of the double-couple body-force equivalent (3.15). For the event shown in Figure 4.18, a surface break was observed whose strike differed by only 8° from that of one of the two nodal planes, hence the choice $\phi_s = 301°$, $\delta = 67°$ can be made with confidence. The second is that a so-called *pressure axis* is located in the center of the dilatational quadrant and a *tension axis* in the center of the compressional quadrant (outward motions). These are principal axes of the moment tensor (see Problem 4.3), and are also principal stress axes if the fault plane is a plane of maximum shear. The fault plane for a given earthquake, however, is established by tectonic processes extending back into geologic time. Rather than a plane of maximum shear stress, it is often

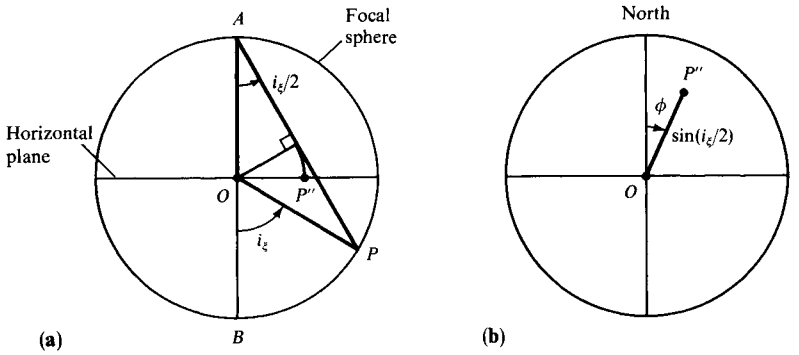

FIGURE **4.17**
The zenithal equal-area projection of the focal sphere maps point P to the point P''. The azimuthal angle ϕ is unchanged (this is a property of all zenithal projections), and distance OP'' is $\sin(\frac{1}{2}i_\xi)$. (**a**) Shown here is a vertical plane through the center of the focal sphere and the point P. (**b**) A plan view of the horizontal plane that is viewed on edge in (a). If the area element $\sin i_\xi \, di_\xi \, d\phi$ at P is mapped into an element at P'', its new area is

$$\sin(\tfrac{1}{2}i_\xi)\, d\phi[\sin(\tfrac{1}{2}i_\xi + \tfrac{1}{2}di_\xi) - \sin(\tfrac{1}{2}i_\xi)] = \tfrac{1}{4} \sin i_\xi \, di_\xi \, d\phi,$$

i.e., a reduction by the constant factor $\frac{1}{4}$. The whole focal sphere (area 4π) maps into the unit circle (area π), but it is conventional to plot the upper half (projected from B, i.e., using $\sin(\frac{1}{2}\pi - \frac{1}{2}i_\xi)$) separately from the lower half in order to avoid the large angle-distortions of the upper focal sphere that would otherwise occur. Again, a system of templates is needed to draw possible fault-plane positions in (b). Differences between the equal-angle and the equal-area projections are apparent in Figures 4.5b and 4.6b, which show the fault plane and the auxiliary plane (for the same focal mechanism) in the two different ways.

a pre-existing fault plane that is reactivated in a given earthquake. Even for new fractures, the angle between the greatest compressive stress and the fault plane is typically about 30°, not 45°. McKenzie (1969) showed in general that the only restriction on the direction of greatest compressive stress is that it must lie in a dilatational (inward) quadrant of the focal sphere.

The use of S-wave radiation patterns entails considerably greater effort than for P-waves, since more than one instrument must be used at each receiving station to obtain the polarization; moreover, a correction must be made for the effect of observation at the Earth's free surface (see Problem 5.6). The principal features of S-wave radiation are shown in the example of Figure 4.19: particle motion diverges from the pressure axis, converges on the tension axis, and is perpendicular to the P-wave nodal planes.

Once the strike, dip, and rake have been determined, it is possible to set up the system of spherical polar (source) coordinates used in Figures 4.5 and 4.6 to analyze amplitude dependence within the radiation pattern in detail. However, in i_ξ and ϕ (Figs. 4.10 and 4.14) we already have a system of spherical polar angles at the source. Furthermore, these are the natural source coordinates to use since we know their properties also as ray coordinates for SV- and SH-waves (see Section 4.4). Our next goal is therefore to obtain the radiation

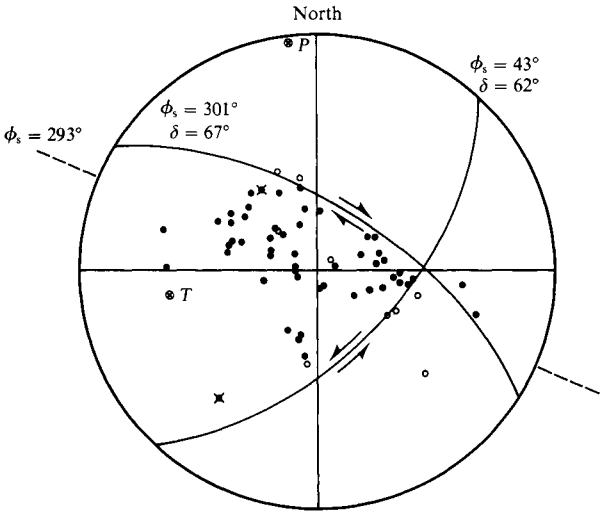

FIGURE **4.18**
P-wave first motions obtained by McKenzie for the shock of 1966 August 19 in eastern Turkey. The diagram is an equal-area projection of the lower hemisphere of the focal sphere. Solid circles represent compressions, open circles dilatations; crosses indicate stations near a nodal plane. ϕ_s and δ are the strike and dip of the nodal planes, and arrows indicate the sense of motion. The broken line shows the strike of the major right-lateral surface break that accompanied the earthquake. [From McKenzie, 1969.]

pattern of *P*-, *SV*-, and *SH*-waves as a function of i_ξ and ϕ, and also as a function of general strike, dip, and rake.

Two different steps may be distinguished in achieving this goal. The first step is to identify *P*, *SV*, and *SH* in the far field for a source within a homogeneous medium. The second step is to adapt this result to the case of a spherically symmetric medium, like the Earth.

4.5.2 ARBITRARY ORIENTATION OF THE DOUBLE COUPLE IN A HOMOGENEOUS MEDIUM

From the Cartesian components of displacement given in (4.30) for an effective point source with moment tensor M_{pq} appropriate for a shear dislocation, we can identify the far-field *P*-wave in vector form as

$$\mathbf{u}^P(\mathbf{x}, t) = \frac{2(\boldsymbol{\gamma} \cdot \boldsymbol{\nu})(\boldsymbol{\gamma} \cdot \dot{\bar{\mathbf{u}}})\mu A \boldsymbol{\gamma}}{4\pi\rho\alpha^3 r}. \tag{4.84}$$

Here $\boldsymbol{\gamma}$ is the longitudinal direction from the source at $\boldsymbol{\xi}$ to the receiver at $\mathbf{x}$; $\boldsymbol{\nu}$ is the fault normal; $\dot{\bar{\mathbf{u}}}$ is the particle velocity at the source, averaged over fault area A and evaluated at retarded time $t - r/\alpha$; and r is the distance $|\mathbf{x} - \boldsymbol{\xi}|$. The corresponding result for the far-field *S*-wave is

$$\mathbf{u}^S(\mathbf{x}, t) = \frac{[(\boldsymbol{\gamma} \cdot \boldsymbol{\nu})\dot{\bar{\mathbf{u}}} + (\boldsymbol{\gamma} \cdot \dot{\bar{\mathbf{u}}})\boldsymbol{\nu} - 2(\boldsymbol{\gamma} \cdot \boldsymbol{\nu})(\boldsymbol{\gamma} \cdot \dot{\bar{\mathbf{u}}})\boldsymbol{\gamma}]\mu A}{4\pi\rho\beta^3 r}, \tag{4.85}$$

in which $\dot{\bar{\mathbf{u}}}$ is evaluated at $t - r/\beta$.

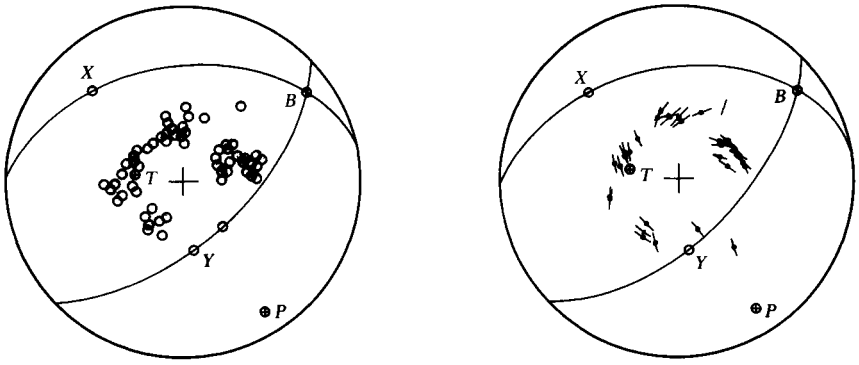

1966, May 15, 14 hr 46 min 06 sec

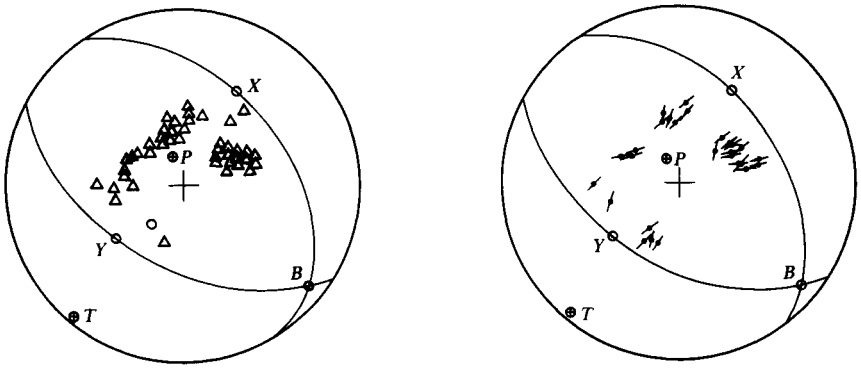

1966, June 2, 03 hr 27 min 53 sec

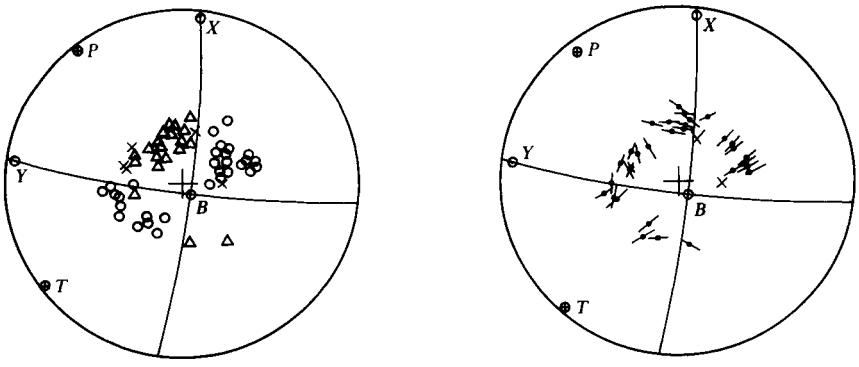

1966, July 4, 18 hr 33 min 36 sec

FIGURE **4.19**
Individual focal mechanism diagrams are shown, using the equal-area projection. In the P-wave diagrams (the left figure of each pair) the triangles represent dilatational first motions, circles represent compressions, and crosses represent P-wave arrivals that appear to be near nodal lines. (Such arrivals are identified by their emergent nature.) Symbols P, T, B are the axes of the moment tensor, and X and Y are the poles of the nodal planes. S-wave diagrams are on the right. [From Stauder, 1968; copyright by American Geophysical Union.]

Since γ is a unit vector at the source, directed along the ray to $\mathbf{x}$, the problem of obtaining the radiation pattern of the P-wave is simply a matter of expressing $\gamma \cdot \nu$ and $\gamma \cdot \dot{\bar{\mathbf{u}}}$ in terms of strike ϕ_s, dip δ, rake λ, take-off angle i_ξ, and source–receiver azimuth ϕ. The radiation patterns for SV and SH are slightly more complicated because the separation into SV and SH is not immediately apparent in (4.85). Clearly, this formula does indicate that $\mathbf{u}^S$ is a transverse motion, because $\mathbf{u}^S \cdot \gamma = 0$. It follows that SV and SH motions, which are (respectively) in the directions $\hat{\mathbf{p}}$ and $\hat{\boldsymbol{\phi}}$ of Figure 4.10, are given by

$$\mathbf{u}^{SV}(\mathbf{x}, t) = (\mathbf{u}^S \cdot \hat{\mathbf{p}})\, \hat{\mathbf{p}} = \frac{[(\gamma \cdot \nu)(\dot{\bar{\mathbf{u}}} \cdot \hat{\mathbf{p}}) + (\gamma \cdot \dot{\bar{\mathbf{u}}})(\nu \cdot \hat{\mathbf{p}})]\mu A\, \hat{\mathbf{p}}}{4\pi\rho\beta^3 r} \tag{4.86}$$

and

$$\mathbf{u}^{SH}(\mathbf{x}, t) = (\mathbf{u}^S \cdot \hat{\boldsymbol{\phi}})\, \hat{\boldsymbol{\phi}} = \frac{[(\gamma \cdot \nu)(\dot{\bar{\mathbf{u}}} \cdot \hat{\boldsymbol{\phi}}) + (\gamma \cdot \dot{\bar{\mathbf{u}}})(\nu \cdot \hat{\boldsymbol{\phi}})]\mu A\, \hat{\boldsymbol{\phi}}}{4\pi\rho\beta^3 r}. \tag{4.87}$$

To obtain all three radiation patterns in terms of $(\phi_s, \delta, \lambda, i_\xi, \phi)$, we introduce Cartesian coordinate directions $\hat{\mathbf{x}}, \hat{\mathbf{y}}, \hat{\mathbf{z}}$ at the epicenter. Our choice is $\hat{\mathbf{x}}$ = North, $\hat{\mathbf{y}}$ = East, and $\hat{\mathbf{z}}$ = vertically downward, as shown in Figure 4.20. In terms of these three unit vectors,

$$\begin{aligned}
\text{slip } \bar{\mathbf{u}} &= \bar{u}\,(\cos\lambda\cos\phi_s + \cos\delta\sin\lambda\sin\phi_s)\,\hat{\mathbf{x}} \\
&\quad + \bar{u}\,(\cos\lambda\sin\phi_s - \cos\delta\sin\lambda\cos\phi_s)\,\hat{\mathbf{y}} \\
&\quad - \bar{u}\sin\lambda\sin\delta\,\hat{\mathbf{z}}, \\
\text{fault normal } \nu &= -\sin\delta\sin\phi_s\,\hat{\mathbf{x}} + \sin\delta\cos\phi_s\,\hat{\mathbf{y}} - \cos\delta\,\hat{\mathbf{z}}, \\
P\text{-wave direction } \mathbf{l} = \gamma &= \sin i_\xi\cos\phi\,\hat{\mathbf{x}} + \sin i_\xi\sin\phi\,\hat{\mathbf{y}} + \cos i_\xi\,\hat{\mathbf{z}}, \\
SV\text{-wave direction } \hat{\mathbf{p}} &= \cos i_\xi\cos\phi\,\hat{\mathbf{x}} + \cos i_\xi\sin\phi\,\hat{\mathbf{y}} - \sin i_\xi\,\hat{\mathbf{z}}, \\
SH\text{-wave direction } \hat{\boldsymbol{\phi}} &= -\sin\phi\,\hat{\mathbf{x}} + \cos\phi\,\hat{\mathbf{y}}.
\end{aligned} \tag{4.88}$$

Six different scalar products are needed in the radiation pattern formulas (4.84), (4.86), (4.87), and these can readily be obtained from (4.88). In dimensionless form, the radiation patterns $\mathcal{F}^P$, $\mathcal{F}^{SV}$, and $\mathcal{F}^{SH}$ are given by

$$\begin{aligned}
\mathcal{F}^P &= 2(\gamma \cdot \nu)(\gamma \cdot \dot{\bar{\mathbf{u}}})/\dot{\bar{u}} \\
&= \cos\lambda\sin\delta\sin^2 i_\xi\sin 2(\phi - \phi_s) - \cos\lambda\cos\delta\sin 2i_\xi\cos(\phi - \phi_s) \\
&\quad + \sin\lambda\sin 2\delta(\cos^2 i_\xi - \sin^2 i_\xi\,\sin^2(\phi - \phi_s)) \\
&\quad + \sin\lambda\cos 2\delta\sin 2i_\xi\sin(\phi - \phi_s),
\end{aligned} \tag{4.89}$$

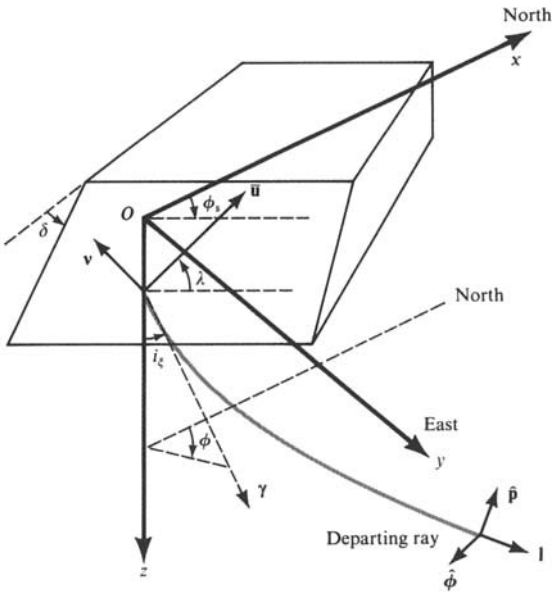

FIGURE **4.20**
Definition of Cartesian coordinates (x, y, z) used to obtain the explicit dependence of P, SV, and SH radiation patterns on $(\phi_s, \delta, \lambda, i_\xi, \phi)$. The origin is taken at the *epicenter* (the point of the Earth's surface vertically above the seismic source of interest). Advantages of this coordinate system are that z follows convention in being the depth direction, and azimuthal angles ϕ, measured clockwise round from North (the x-axis), follow the geographical convention. The horizontal components of $\bar{\mathbf{u}}$ can easily be resolved into $\bar{u}\cos\lambda$ (along strike) and $\bar{u}\cos\delta\sin\lambda$ (in the negative dip direction). Components given in the text (4.88) are for North (x) and East (y). This is a natural coordinate system in which to give components of a moment tensor (Box 4.4). The take-off angle i_ξ can be used interchangeably with ray parameter p as a ray coordinate. Since $\mathbf{l}$ is the longitudinal direction along the ray, $\mathbf{l} = \boldsymbol{\gamma}$ for a homogeneous medium.

$$
\begin{aligned}
\mathcal{F}^{SV} &= \left[(\boldsymbol{\gamma}\cdot\boldsymbol{\nu})(\dot{\bar{\mathbf{u}}}\cdot\hat{\mathbf{p}}) + (\boldsymbol{\gamma}\cdot\dot{\bar{\mathbf{u}}})(\boldsymbol{\nu}\cdot\hat{\mathbf{p}})\right]/\dot{\bar{u}} \\
&= \sin\lambda\cos 2\delta\cos 2i_\xi\sin(\phi-\phi_s) - \cos\lambda\cos\delta\cos 2i_\xi\cos(\phi-\phi_s) \\
&\quad + \tfrac{1}{2}\cos\lambda\sin\delta\sin 2i_\xi\sin 2(\phi-\phi_s) \\
&\quad - \tfrac{1}{2}\sin\lambda\sin 2\delta\sin 2i_\xi(1+\sin^2(\phi-\phi_s)),
\end{aligned}
\tag{4.90}
$$

$$
\begin{aligned}
\mathcal{F}^{SH} &= \left[(\boldsymbol{\gamma}\cdot\boldsymbol{\nu})(\dot{\bar{\mathbf{u}}}\cdot\hat{\boldsymbol{\phi}}) + (\boldsymbol{\gamma}\cdot\dot{\bar{\mathbf{u}}})(\boldsymbol{\nu}\cdot\hat{\boldsymbol{\phi}})\right]/\dot{\bar{u}} \\
&= \cos\lambda\cos\delta\cos i_\xi\sin(\phi-\phi_s) + \cos\lambda\sin\delta\sin i_\xi\cos 2(\phi-\phi_s) \\
&\quad + \sin\lambda\cos 2\delta\cos i_\xi\cos(\phi-\phi_s) \\
&\quad - \tfrac{1}{2}\sin\lambda\sin 2\delta\sin i_\xi\sin 2(\phi-\phi_s).
\end{aligned}
\tag{4.91}
$$

Associated far-field displacements are then

$$\mathbf{u}^P(\mathbf{x},t) = \frac{\mathcal{F}^P\,\mu A}{4\pi\rho\alpha^3 r}\,\dot{\bar{u}}\left(t-\frac{r}{\alpha}\right)\mathbf{l},$$

$$\mathbf{u}^{SV}(\mathbf{x},t) = \frac{\mathcal{F}^{SV}\,\mu A}{4\pi\rho\beta^3 r}\,\dot{\bar{u}}\left(t-\frac{r}{\beta}\right)\hat{\mathbf{p}}, \tag{4.92}$$

$$\mathbf{u}^{SH}(\mathbf{x},t) = \frac{\mathcal{F}^{SH}\,\mu A}{4\pi\rho\beta^3 r}\,\dot{\bar{u}}\left(t-\frac{r}{\alpha}\right)\hat{\boldsymbol{\phi}}.$$

4.5.3 ADAPTING THE RADIATION PATTERN TO THE CASE OF A SPHERICALLY SYMMETRIC MEDIUM

We have taken care to obtain P, SV, and SH displacements (4.92) in a form comparable with the geometric ray solutions derived in Section 4.4 (see (4.62), (4.65), (4.66)). To complete the comparison for P-waves, it remains only to identify and generalize r/α as the ray travel time T^P, $1/r$ as the geometrical spreading factor $1/\mathcal{R}^P(\mathbf{x},\boldsymbol{\xi})$, and $\mu/(\rho\alpha^3)$ as the factor $\mu(\boldsymbol{\xi})/\left[\sqrt{\rho(\boldsymbol{\xi})\,\rho(\mathbf{x})\,\alpha(\boldsymbol{\xi})\,\alpha(\mathbf{x})}\,\alpha^2(\boldsymbol{\xi})\right]$. This last result follows from generalizing $\mu/(\rho\alpha^3)$ to a term proportional to $1/\sqrt{\rho(\mathbf{x})\alpha(\mathbf{x})}$ (as required by (4.62)), in which the constant of proportionality can depend only on properties at the source. Then

$$\mathbf{u}^P(\mathbf{x},t) = \frac{\mathcal{F}^P\,\mu(\boldsymbol{\xi})\,A\,\dot{\bar{u}}(t-T^P)\,\mathbf{l}}{4\pi\,\sqrt{\rho(\boldsymbol{\xi})\,\rho(\mathbf{x})\,\alpha(\boldsymbol{\xi})\,\alpha(\mathbf{x})}\,\alpha^2(\boldsymbol{\xi})\,\mathcal{R}^P(\mathbf{x},\boldsymbol{\xi})}, \tag{4.93}$$

and similarly

$$\mathbf{u}^{SV}(\mathbf{x},t) = \frac{\mathcal{F}^{SV}\,\mu(\boldsymbol{\xi})\,A\,\dot{\bar{u}}(t-T^S)\,\hat{\mathbf{p}}}{4\pi\,\sqrt{\rho(\boldsymbol{\xi})\,\rho(\mathbf{x})\,\beta(\boldsymbol{\xi})\,\beta(\mathbf{x})}\,\beta^2(\boldsymbol{\xi})\,\mathcal{R}^S(\mathbf{x},\boldsymbol{\xi})}, \tag{4.94}$$

$$\mathbf{u}^{SH}(\mathbf{x},t) = \frac{\mathcal{F}^{SH}\,\mu(\boldsymbol{\xi})\,A\,\dot{\bar{u}}(t-T^S)\,\hat{\boldsymbol{\phi}}}{4\pi\,\sqrt{\rho(\boldsymbol{\xi})\,\rho(\mathbf{x})\,\beta(\boldsymbol{\xi})\,\beta(\mathbf{x})}\,\beta^2(\boldsymbol{\xi})\,\mathcal{R}^S(\mathbf{x},\boldsymbol{\xi})}. \tag{4.95}$$

The radiation patterns here are exactly the same as for a homogeneous medium, and are given in (4.89)–(4.91). The only noteworthy symmetry is a reversal in sign of $\mathcal{F}^P$, $\mathcal{F}^{SV}$, $\mathcal{F}^{SH}$ if the rake is changed by 180°. Particularly, one should note that there is no symmetry to changes of 180° in strike ϕ_s, or takeoff azimuth ϕ, so that care must be taken to follow the definitions given in Figures 4.13 and 4.20, in which these angles increase clockwise round from North.

The principal use of our final formulas (4.93)–(4.95) lies in estimating the seismic moment. From a far-field observation of the displacement, one can obtain $\mu A\dot{\bar{u}}(t-T)$ after correction for the radiation pattern, geometrical spreading, and scaling factors at source and receiver. (In practice, correction is typically required also for the effects of transmission across material boundaries, attenuation, and instrument response.) It often occurs that the

duration of faulting is much shorter than the periods at which body waves are observed, yet these periods are still short enough to use ray theory. In this case, the averaged particle displacement $\overline{u}$ at the source is effectively a step function, $M_0(t) = M_0(\infty)H(t)$, hence the spectrum of the observed displacement pulse shape, $\mu(\xi)\, A\overline{u}$, is just $M_0(\infty)$ at long periods. Section 10.1 goes into the effects on far-field waveforms when the duration of faulting is comparable to, or longer than, the periods in the observed waveform.

For point sources specified by a general moment tensor (i.e., nine couples with symmetry $M_{pq} = M_{qp}$), the far-field body waves are given in terms of the six independent components of $\mathbf{M}$ by generalizing (4.84) and (4.86)–(4.87). We use the far-field terms in (4.29), and for homogeneous media it follows that

$$\begin{aligned}
\mathbf{u}^P(\mathbf{x},t) &= \left(\frac{\gamma \cdot \dot{\mathbf{M}}\left(t - \dfrac{r}{\alpha}\right) \cdot \gamma}{4\pi\rho\alpha^3 r} \right) \mathbf{l}, \\
\mathbf{u}^{SV}(\mathbf{x},t) &= \left(\frac{\hat{\mathbf{p}} \cdot \dot{\mathbf{M}}\left(t - \dfrac{r}{\beta}\right) \cdot \gamma}{4\pi\rho\beta^3 r} \right) \hat{\mathbf{p}}, \\
\mathbf{u}^{SH}(\mathbf{x},t) &= \left(\frac{\hat{\boldsymbol{\phi}} \cdot \dot{\mathbf{M}}\left(t - \dfrac{r}{\beta}\right) \cdot \gamma}{4\pi\rho\beta^3 r} \right) \hat{\boldsymbol{\phi}},
\end{aligned} \tag{4.96}$$

which are easily adapted to inhomogeneous media by using ray theory. First, the denominators in (4.96) are replaced by those of (4.93)–(4.95). Second, we must be careful to distinguish where the unit vectors $\hat{\mathbf{p}}$ and $\hat{\boldsymbol{\phi}}$ are evaluated—whether at the source (at ξ) or at the receiver (at $\mathbf{x}$). In (4.96) the contraction of the transverse directions $\hat{\mathbf{p}}$ and $\hat{\boldsymbol{\phi}}$ with $\dot{\mathbf{M}}$ takes place at the *source*, whereas $\hat{\mathbf{p}}$ and $\hat{\boldsymbol{\phi}}$ at the *receiver* are the appropriate directions for identifying SV- and SH-components in the radiated particle motion. The adaptation to inhomogeneous media is then

$$\begin{aligned}
\mathbf{u}^P(\mathbf{x},t) &= \left(\frac{\gamma \cdot \dot{\mathbf{M}}\left(t - T^P\right) \cdot \gamma}{4\pi \sqrt{\rho(\xi)\,\rho(\mathbf{x})\,\alpha(\xi)\,\alpha(\mathbf{x})}\,\alpha^2(\xi)\,\mathcal{R}^P(\mathbf{x},\xi)} \right) \mathbf{l}, \\
\mathbf{u}^{SV}(\mathbf{x},t) &= \left(\frac{\hat{\mathbf{p}}(\xi) \cdot \dot{\mathbf{M}}\left(t - T^S\right) \cdot \gamma}{4\pi \sqrt{\rho(\xi)\,\rho(\mathbf{x})\,\beta(\xi)\,\beta(\mathbf{x})}\,\beta^2(\xi)\,\mathcal{R}^S(\mathbf{x},\xi)} \right) \hat{\mathbf{p}}(\mathbf{x}), \\
\mathbf{u}^{SH}(\mathbf{x},t) &= \left(\frac{\hat{\boldsymbol{\phi}}(\xi) \cdot \dot{\mathbf{M}}\left(t - T^S\right) \cdot \gamma}{4\pi \sqrt{\rho(\xi)\,\rho(\mathbf{x})\,\beta(\xi)\,\beta(\mathbf{x})}\,\beta^2(\xi)\,\mathcal{R}^S(\mathbf{x},\xi)} \right) \hat{\boldsymbol{\phi}}(\mathbf{x}).
\end{aligned} \tag{4.97}$$

BOX **4.4**

Cartesian components of the moment tensor for a shear dislocation of arbitrary orientation

In our final formulas for the body-wave radiation pattern from a shear dislocation, we have combined properties of the moment tensor with properties of the Green function. If it is surface waves we wish to study, or free oscillations in a more complicated medium, then we must develop further theories of wave propagation to evaluate the appropriate Green function. But the moment tensor is unchanged, even if the medium is inhomogeneous and anisotropic. We here obtain the Cartesian components of $\mathbf{M}$ for a shear fault described by strike ϕ_s, rake λ, dip δ, and moment M_0.

Referring to Figure 4.20, in which the x-direction is taken as North, the Cartesian components of fault slip $\bar{\mathbf{u}}$ and fault normal ν have already been given in (4.88). Recall from Chapter 3 that the moment M_0 of a shear dislocation is $\mu A\bar{u}$, where μ is the rigidity in the source region (Box 3.1) and A is the area over which the displacement discontinuity has been averaged. From (2.21) and (2.23), it follows that $M_{pq} = \mu A(\bar{u}_p \nu_q + \bar{u}_q \nu_p)$, and hence the Cartesian components of moment tensor $\mathbf{M}$ are

$$\begin{aligned}
M_{xx} &= -M_0(\sin\delta\cos\lambda\sin 2\phi_s + \sin 2\delta\sin\lambda\sin^2\phi_s),\\
M_{xy} &= +M_0(\sin\delta\cos\lambda\cos 2\phi_s + \tfrac{1}{2}\sin 2\delta\sin\lambda\sin 2\phi_s) = M_{yx},\\
M_{xz} &= -M_0(\cos\delta\cos\lambda\cos\phi_s + \cos 2\delta\sin\lambda\sin\phi_s) = M_{zx},\\
M_{yy} &= +M_0(\sin\delta\cos\lambda\sin 2\phi_s - \sin 2\delta\sin\lambda\cos^2\phi_s),\\
M_{yz} &= -M_0(\cos\delta\cos\lambda\sin\phi_s - \cos 2\delta\sin\lambda\cos\phi_s) = M_{zy},\\
M_{zz} &= +M_0\sin 2\delta\sin\lambda.
\end{aligned} \tag{1}$$

This general result can be recognized as a weighted sum of four elementary moment tensors,

$$\mathbf{M} = \cos\delta\cos\lambda\,\mathbf{M}^{(1)} + \sin\delta\cos\lambda\,\mathbf{M}^{(2)} - \cos 2\delta\sin\lambda\,\mathbf{M}^{(3)} + \sin 2\delta\sin\lambda\,\mathbf{M}^{(4)} \tag{2}$$

where

$$\begin{aligned}
\mathbf{M}^{(1)} &= M_0\begin{pmatrix} 0 & 0 & -\cos\phi_s \\ 0 & 0 & -\sin\phi_s \\ -\cos\phi_s & -\sin\phi_s & 0 \end{pmatrix}, \mathbf{M}^{(2)} = M_0\begin{pmatrix} -\sin 2\phi_s & \cos 2\phi_s & 0 \\ \cos 2\phi_s & \sin 2\phi_s & 0 \\ 0 & 0 & 0 \end{pmatrix},\\
\mathbf{M}^{(3)} &= M_0\begin{pmatrix} 0 & 0 & \sin\phi_s \\ 0 & 0 & -\cos\phi_s \\ \sin\phi_s & -\cos\phi_s & 0 \end{pmatrix}, \mathbf{M}^{(4)} = M_0\begin{pmatrix} -\sin^2\phi_s & \tfrac{1}{2}\sin 2\phi_s & 0 \\ \tfrac{1}{2}\sin 2\phi_s & -\cos^2\phi_s & 0 \\ 0 & 0 & 1 \end{pmatrix}.
\end{aligned} \tag{3}$$

Each of $\mathbf{M}^{(i)}(i = 1, 2, 3, 4)$ has eigenvalues M_0, $-M_0$, and zero, so that each is the moment tensor for a shear dislocation. In fact (from (2)), $\mathbf{M}^{(1)}$ is given by $\mathbf{M}$ in the case of $\delta = 0$, $\lambda = 0$, so $\mathbf{M}^{(1)}$ is appropriate for a horizontal fault plane, with slip direction defining the strike. Similarly, $\mathbf{M}^{(2)}$ is the moment tensor for a pure strike-slip fault ($\delta = \pi/2,\ \lambda = 0$), $\mathbf{M}^{(3)}$ is for a pure dip-slip fault ($\delta = \pi/2,\ \lambda = \pi/2$) and $\mathbf{M}^{(4)}$ is for a thrust fault dipping at 45° with slip being purely up-dip ($\delta = \pi/4,\ \lambda = \pi/2$).

(continued)

BOX **4.4** *(continued)*

Although our formulas for the Green function may involve some approximations, the decomposition of the radiation field implied by (2) is exact. That is, the waves radiated from a shear dislocation of arbitrary orientation can always be written as the sum of waves radiated from four different elementary shear dislocations, all sharing the same strike. Only *three* elementary shear dislocations need be studied, if one drops the requirement that they share a common strike. This follows by replacing $\mathbf{M}^{(1)}$ in (2) by $\mathbf{M}^{(3)}$ evaluated at strike $\phi_s - \pi/2$.

In the above presentation, we have taken coordinates (x, y, z) at the source as (North, East, Down). Another convention, more natural in the context of normal-mode studies for the whole Earth, is based on coordinates (r, Δ, ϕ), where Δ measures epicentral distance and ϕ is the epicentral longitude ($\phi = 0$ is South). Cartesian components of the moment tensor are then M_{rr}, $M_{r\Delta}$, etc., where these components are referred to a Cartesian system at the source with directions (Up, South, East). It follows that components of $\mathbf{M}$ in the two systems are related by

$$\begin{pmatrix} M_{rr} & M_{r\Delta} & M_{r\phi} \\ M_{\Delta r} & M_{\Delta\Delta} & M_{\Delta\phi} \\ M_{\phi r} & M_{\phi\Delta} & M_{\phi\phi} \end{pmatrix} = \begin{pmatrix} M_{zz} & M_{zx} & -M_{zy} \\ M_{xz} & M_{xx} & -M_{xy} \\ -M_{yz} & -M_{yx} & M_{yy} \end{pmatrix}. \tag{4}$$

Note, in this normal-mode convention, that the source–receiver azimuth becomes $\pi - \phi$.

Suggestions for Further Reading

Červený, V., and F. Hron. The ray series method and dynamic ray tracing system for three-dimensional inhomogeneous media. *Bulletin of the Seismological Society of America*, **70**, 47–77, 1980.

Červený, V., I. A. Molotkov, and I. Pšenčik. *The Ray Method in Seismology.* Prague: Charles University Press, 1978.

Julian, B. R., A. D. Miller, and G. R. Foulger. Non-double couple earthquakes 1. Theory. *Reviews of Geophysics*, **36**, 525–549, 1998.

Kravtsov, Y., and Y. Orlov. *Geometrical Optics of Inhomogeneous Media.* New York: Springer-Verlag, 1990.

Love, A. E. H. *A Treatise on the Mathematical Theory of Elasticity.* New York: Dover Publications, 1944.

Morse, P. M., and H. Feshbach. *Methods of Theoretical Physics* (Chap. 13 for Green's functions in elasticity). New York: McGraw-Hill, 1953.

Moser, T. Shortest path calculation of seismic rays. *Geophysics*, **56**, 59–67, 1991.

Pulliam, J., and R. Snieder. Ray perturbation theory, dynamic ray tracing and the determination of Fresnel zones. *Geophysical Journal International*, **135**, 463–469, 1998.

Steinberg, E. On the integration of the equations of motion in the classical theory of elasticity. *Archive for Rational Mechanics and Analysis*, **6**, 34–50, 1960.

Problems

4.1 Sketch the "seismogram" for Green's function G_{ij} itself. That is, draw the relative positions and pulse shapes of the three different terms in (4.23) when X_0 is an impulse. Then show that the area under each one of the three pulses has a distance dependence proportional to $1/r$. The area under a pulse is equal to the limit (as $\omega \to 0$) of the Fourier transform of the pulse, and from the frequency dependence of (4.35) it therefore appears that the area is unbounded. Show that in fact there is a cancellation of the terms in $1/(\omega^2 r^3)$, $1/(\omega r^2)$ in (4.35), and that the distance dependence as $\omega \to 0$ is indeed like $1/r$.

For a seismometer that is sensitive only to periods much longer than the $S - P$ time, i.e., $(r/\beta - r/\alpha)$, note then that the near-field term of the Green function is effectively an impulse, as well as the far-field terms. To study near-field effects (such as the strong ground motion near a rupturing fault), it also follows that the so-called "far-field" and "near-field" terms are equally important in the near field, in the sense that the source time function X_0 will be nonzero for times that are long compared to $(r/\beta - r/\alpha)$, so the first term in (4.23) is also of order $1/r$.

To summarize: "far-field" terms dominate in the far field, but "near-field" and "far-field" terms are of equal importance in the near field after they have been convolved with a source time function.

4.2 If a constant force X_0 is applied in the j-direction at the origin within an infinite homogeneous isotropic medium, show from (4.23) that the static solution for the i-component of displacement at $\mathbf{x}$ is

$$\frac{X_0}{8\pi\rho r}\left[\left(\frac{1}{\beta^2}-\frac{1}{\alpha^2}\right)\gamma_i\gamma_j+\left(\frac{1}{\beta^2}+\frac{1}{\alpha^2}\right)\delta_{ij}\right].$$

(This expression is sometimes known as the Somigliana tensor.)

4.3 Which of the principal axes ξ_1', ξ_3' of the moment tensor shown in Problem 3.4 marks the pressure axis (P), and which the tension axis (T)?

Note from Figures 4.5 and 4.6 that the P and T axes correspond to directions of maximum radiated P-wave amplitude out of the focal sphere—and to zero radiated S-waves. Which of these axes corresponds to maximum *outward* particle motion (motion away from the source) in the radiated waves, and which to maximum *inward* motion (motion toward the source)?

4.4 To evaluate the geometrical spreading function $\mathcal{R}(\mathbf{x}, \boldsymbol{\xi})$ between two points $\boldsymbol{\xi}$ and $\mathbf{x}$ in a spherically symmetric Earth, consider two rays departing from $\boldsymbol{\xi}$ with the same azimuth and with takeoff angles i_ξ and $i_\xi + \delta i_\xi$ (see Figure 4.10, and take $\mathbf{x} = \mathbf{0}$ as the center of the Earth).

Consider also two rays obtained from the previous two by making an azimuth increment $\delta\phi_0$. The solid angle made at $\boldsymbol{\xi}$ by the four rays is $\sin i_\xi \, \delta i_\xi \, \delta\phi_0$. Show that the cross-sectional area of the ray tube at $\mathbf{x}$ is $-|\mathbf{x}|^2 \cos i_x \sin\Delta \, \delta\Delta \, \delta\phi_0$. Then use ray parameter

$$p = \frac{|\boldsymbol{\xi}| \sin i_\xi}{c(\xi)} = \frac{|\mathbf{x}| \sin i_x}{c(\mathbf{x})}$$

(see (4.45b)) to obtain

$$\mathcal{R}(\mathbf{x}, \xi) c(\xi) = |\mathbf{x}|\, |\boldsymbol{\xi}| \left[\frac{\cos i_x \cos i_\xi \sin \Delta}{p} \left| \frac{\partial \Delta}{\partial p} \right| \right]^{1/2}.$$

Because of the symmetry of the right-hand side, we immediately find the reciprocity $\mathcal{R}(\mathbf{x}, \xi) c(\xi) = \mathcal{R}(\xi, \mathbf{x}) c(\mathbf{x})$, proved here for spherically symmetric media only.

4.5 Obtain the ray theory solution

$$\frac{l_i(\mathbf{x}) l_j(\xi)\, \delta(t - T(\mathbf{x}, \xi))}{4\pi \rho^{1/2}(\mathbf{x}) \rho^{1/2}(\xi) \alpha^{3/2}(\xi) \alpha^{1/2}(\mathbf{x}) \mathcal{R}(\mathbf{x}, \xi)}$$

for the far-field P-wave contribution to $G_{ij}(\mathbf{x}, t; \xi, 0)$. (Use the far-field P-wave term in (4.23), given also in (4.24), to get the ray theory approximation for G_{ij} in a homogeneous medium, then discuss how each factor generalizes for an inhomogeneous medium.) Then apply the reciprocity theorem (2.39) to prove that

$$\mathcal{R}(\mathbf{x}, \xi) \alpha(\xi) = \mathcal{R}(\xi, \mathbf{x}) \alpha(\mathbf{x})$$

in general inhomogeneous isotropic media. [This reciprocity for geometrical spreading is a remarkable result in the differential geometry of rays. A direct proof due to George Backus is given by Richards (1971).]

4.6 Show that the root-mean-square value for the radiation pattern of far-field P-wave amplitudes from a point source of fault slip, averaged over the focal sphere, is $\sqrt{\frac{4}{15}}$; for S-waves, show that the corresponding result is $\sqrt{\frac{2}{5}}$. (*Hint:* Start from the radiation patterns defined in (4.33).)

Show from these results, and the discussion of energy in Section 5.1, that the energy in a homogeneous whole space radiated seismically from a double-couple point source as P-waves is E_P and as S-waves is E_S where

$$E_P = \frac{\int_0^\infty [\ddot{M}_0]^2\, dt}{15\pi\rho\alpha^5} \quad \text{and} \quad E_S = \frac{\int_0^\infty [\ddot{M}_0]^2\, dt}{10\pi\rho\beta^5},$$

and $M_0(t)$ is the moment as a function of time. (Since $\beta^5/\alpha^5 \ll 1$, note that E_P is only a few percent the size of E_S.)

Discuss whether these are "far-field" results, or simply statements about the source. How are the formulas changed if the source $M_0(t)$ acts as a double couple in an *inhomogeneous* medium?

4.7 For the spherical polar coordinates used in (4.31)–(4.33) to describe the radiation pattern for a double couple, show that the far-field components of $F_j * G_{ij}$ are

$$\frac{1}{4\pi\rho\alpha^2} \frac{\hat{r}_i \hat{r}_j}{r} F_j\left(t - \frac{r}{\alpha}\right) + \frac{1}{4\pi\rho\beta^2} \frac{(\hat{\theta}_i \hat{\theta}_j + \hat{\phi}_i \hat{\phi}_j)}{r} F_j\left(t - \frac{r}{\beta}\right).$$

(This gives the i-component of displacement at (r, θ, ϕ) in terms of the Cartesian components of unit vectors $\hat{\mathbf{r}}, \hat{\boldsymbol{\theta}}, \hat{\boldsymbol{\phi}}$ for a force $\mathbf{F}(t)$ applied at the origin.)

4.8 Show that the problem of solving for the path of a ray in an inhomogeneous medium with wavespeed $c = c(\mathbf{x})$ is equivalent to solving for the motion of a particle moving in a force field with potential proportional to $1/c^2$. (*Hint:* Choose a scalar variable σ to define position along a ray, with σ having the property that $d\mathbf{x}/d\sigma = \nabla T$.)

4.9 For parts of an isotropic medium within which the body-wave speed c is a linear function of depth z, show that ray paths are arcs of circles. Specifically, for a region within which $c(z) = az + b$ for some constants a and b, show that the path with ray parameter p is a circular arc whose center lies at the depth $z = -b/a$ and whose radius is $(pa)^{-1}$.

For a spherically symmetric medium in which the body-wave speed c depends only on the radius r from the center of symmetry, show that ray paths are circular arcs in regions for which $c(r) = a - br^2$.

4.10 In terms of the unit tangent $\mathbf{l}$ along a ray in an isotropic medium (see Figure 4.12), the gradient of the body-wave travel time is $\nabla T = \mathbf{l}/c$, where $c = c(\mathbf{x})$ is the body-wave speed in an inhomogeneous medium (see (4.43)). Show then that

a) $\nabla \times \left(\dfrac{\mathbf{l}}{c}\right) = \mathbf{0}$,

b) $\nabla \times \mathbf{l} = c\mathbf{l} \times \nabla\left(\dfrac{1}{c}\right) = \left(\dfrac{\nabla c}{c}\right) \times \mathbf{l}$,

c) $(\nabla \times \mathbf{l}) \times \mathbf{l} = \dfrac{d\mathbf{l}}{ds}$ where s is distance along the ray from a fixed point,

d) $\dfrac{d\mathbf{l}}{ds} = c\nabla\left(\dfrac{1}{c}\right) - \left[c\mathbf{l} \cdot \nabla\left(\dfrac{1}{c}\right)\right]\mathbf{l} = \left[\mathbf{l} \cdot \nabla(\log c)\right]\mathbf{l} - \nabla(\log c)$.

e) This last result is useful in setting up a finite difference computation for ray paths in an inhomogeneous medium. Starting at position $\mathbf{x}_0$ where s is set to zero, and choosing an initial take-off direction $\mathbf{l}_0$ at $\mathbf{x}_0$, show that the ray position at discrete points measured by $\Delta s, 2\Delta s, 3\Delta s, \ldots$ along the ray is given by $\mathbf{x}_1, \mathbf{x}_2, \mathbf{x}_3$ etc., where

$$\mathbf{x}_{m+1} = \mathbf{x}_m + \Delta s\, \mathbf{l}_m$$

$$\mathbf{l}_{m+1} = \mathbf{l}_m + \Delta s \left.\frac{d\mathbf{l}}{ds}\right|_{\mathbf{x}=\mathbf{x}_m}$$

$$= \mathbf{l}_m + \Delta s\, [(\mathbf{l}_m \cdot \mathbf{g}_m)\mathbf{l}_m - \mathbf{g}_m] \qquad \text{where} \qquad \mathbf{g}_m = \nabla(\log c)\big|_{\mathbf{x}=\mathbf{x}_m}$$

for $m = 0, 1, 2, 3, \ldots$

f) Show that $\mathbf{l}$ does not change direction along the ray, at points where it is parallel to the gradient of the body-wave velocity; and that the directions of $\mathbf{l}$ for which the ray changes direction at the maximum rate, are those for which $\mathbf{l}$ is perpendicular to the gradient of c.

4.11 Show that for times near the P-wave arrival, the P-wave in the far field of a shear dislocation with time-dependent scalar moment $M_0(t)$ has a displacement pulse shape proportional to

$$\dot{M}_0(t - T^P) + \frac{4}{T^P} M_0(t - T^P)$$

in a homogeneous medium. [For a sufficiently large dislocation, the additional term here, $(4/T^P)M_0(t - T^P)$, can be seen even in the far field (see Vidale *et al.*, 1995)].

4.12 Using a homogeneous sphere as a model, find rays whose travel times are stationary, but not minima.

4.13 This set of questions is based upon use of a Cartesian coordinate system with x-, y-, and z-directions in the North, East, and Down directions, respectively.

a) Give the orientation of the fault plane, and direction of slip, for an example of shear faulting that is modeled by a moment tensor $\mathbf{M}$ in which all components are zero except $M_{zx} = M_{xz} \neq 0$.

b) What is a different example of shear faulting that has the same moment tensor as a)?

c) If $M_{ij} = 0$ except for $M_{zx} = M_{xz} \neq 0$ *and* $M_{zy} = M_{yz} \neq 0$, what then are the orientations of faulting, and directions of slip, represented by $\mathbf{M}$, that generalize a) and b)? (*Hint:* Define an angle by $\phi = \tan^{-1}(M_{zy}/M_{zx}$.)

d) Using Hooke's Law for an isotropic solid elastic medium, what can be said about the shear strains e_{zx} and e_{zy} at the surface $z = 0$, if this surface is taken as the stress-free surface of the Earth?

4.14 With the notation of Box 4.4, show that the elementary matrices $\mathbf{M}^{(2)}$ and $\mathbf{M}^{(4)}$ are related by

$$\tfrac{1}{2}\mathbf{M}^{(2)} = \mathbf{M}^{(4)} + M_0 \begin{pmatrix} \frac{1}{2} & 0 & 0 \\ 0 & \frac{1}{2} & 0 \\ 0 & 0 & -1 \end{pmatrix}$$

if the strike of the $\mathbf{M}^{(4)}$ dislocation is $\pi/4$ greater than the strike of the $\mathbf{M}^{(2)}$ dislocation. Hence show that the SH waves due to a vertical strike-slip fault in a spherically symmetric Earth are the same (at all azimuths and all distances) as the SH waves from a thrust fault dipping at 45° with pure up-dip slip, but having a strike angle that is 45° greater and a seismic moment that is a factor of two smaller, than the strike and moment of the strike-slip fault.

Is this result unchanged if the sources are in an isotropic but laterally inhomogeneous Earth?

CHAPTER 5

Plane Waves in Homogeneous Media and Their Reflection and Transmission at a Plane Boundary

So far, we have investigated the details of seismic wave generation by various point sources in a homogeneous, infinite, isotropic, elastic medium, and we have begun to look at transmission problems by developing geometrical ray theory for smoothly varying inhomogeneous media. We now continue to develop the theory of wave transmission, looking at basic problems involving a discontinuity of elastic properties in the medium within which waves are propagating. We analyze here only the simplest type of discontinuity, in which two homogeneous isotropic elastic media are in welded contact on a plane boundary. Details of the seismic source are avoided by considering only the case of a plane wave incident on the boundary.

The first analysis of such problems is due to George Green (1839); it appeared in the same classic paper that introduced a strain–energy function. Green was attempting to explain reflection and refraction of light in terms of elastic waves, and his work is similar in some detail to a modern analysis of P, SV, and SH plane waves. He did not, however, complete all the algebra necessary for the case in which the two half-spaces have entirely different elastic constants (moduli) and densities. This generalization was obtained by Knott (in 1899), using potentials, and independently by Zoeppritz (in 1907).

The assumption of an *incident plane wave* may be quite good in practice for investigating waves at great distances from their source (see Fig. 5.1a). But if the reflection and refraction take place near the source (Fig. 5.1b), phenomena are observed that cannot be explained directly by Knott's theory. An outstanding example is the P_n-wave, discovered by Mohorovičić in 1909. Although this wave is of a type that can propagate in a medium composed of two welded homogeneous half-spaces (see Box 6.4), it involves a point source radiating *spherical waves*. We mention this point in order to bring out an important indirect application of Knott's theory: a method of studying spherical waves is to decompose them into a sum (or integral) of plane waves, then to apply Knott's theory to each plane wave, and finally to synthesize the required result by superimposing the results for each plane wave.

In this chapter, we shall summarize the basic properties of plane waves, which are required in many of the following chapters. After showing how to set up P, SV, SH problems with three scalar potentials, we obtain specific formulas for reflection/conversion/transmission coefficients, and relate these to unitary scattering matrices. We describe inhomogeneous waves and the associated phase shift of scattering coefficients.

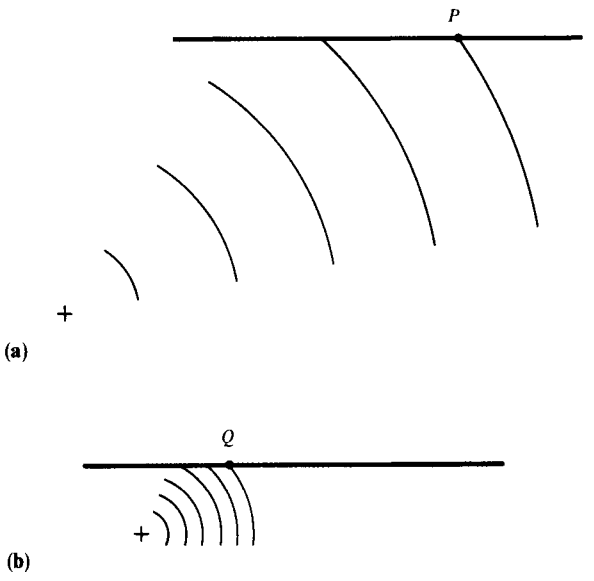

FIGURE **5.1**
(**a**) If the point P on some boundary within the Earth is sufficiently far from the localized source of waves under study, then wavefronts arriving at P may effectively be treated as incoming plane waves. (**b**) If Q is sufficiently close to the source, then curvature of the wavefronts at Q may have to be taken into account (see Chapter 6). Note that by "sufficiently far" and "sufficiently close" we refer to the number of wavelengths between the point of interest (P or Q) and the source. Thus, even for the source/receiver geometry in (b), it may be possible to use plane wave theory for the very high frequencies.

The Earth is an imperfect elastic medium, in the sense that small particle motions initiated by a propagating wave lead to irreversible loss of energy from the wave due to a wide variety of dissipative mechanisms. From the point of view of the effect on the propagating wave, such attenuation is summarized conveniently by the parameter Q. We continue the chapter with a brief description of the effect on the pulse shape of propagation in an attenuating medium like the Earth, in which Q is nearly constant over the frequency range of observed seismic waves. Finally, we outline the basic theory for plane-wave propagation in anisotropic media.

5.1 Basic Properties of Plane Waves in Elastic Media

A physical quantity (such as particle acceleration or a stress component) propagates as a *plane wave* in direction $\mathbf{l}$ with speed c if

(i) at a fixed time, the quantity is spatially unchanged over each plane normal to the unit vector $\mathbf{l}$, and if

(ii) the plane associated with a particular value of the quantity moves with speed c in direction $\mathbf{l}$.

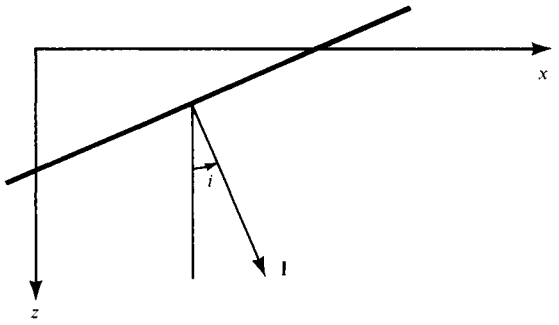

FIGURE **5.2**
For a quantity propagating with speed c in the $\mathbf{l}$ direction, the heavy oblique line marks a plane on which values of the quantity are all equal. Conventionally in seismology we take positive z as the depth direction and define the x-axis to be the direction that lies along the horizontal component of $\mathbf{l}$. We often use the angle i, between the z-axis and direction $\mathbf{l}$, to specify the direction of wave propagation. Then the apparent speed of propagation along the x-axis is $c/\sin i$, which exceeds c if $0 \leq i < 90°$. This apparent speed is often measured in seismology by using instruments arrayed over part of the Earth's surface. Its reciprocal is the horizontal slowness, or ray parameter.

It follows that physical quantities propagating with these two properties must have a functional dependence on space and time only via the combination $t - (\mathbf{l} \cdot \mathbf{x})/c$. We call $\mathbf{l}/c$ the *slowness vector* $\mathbf{s}$. An advantage of using slowness (rather than velocity) to summarize the speed and direction of propagation of a wave is that slownesses may be added vectorially (but velocities, in this context, may not). Thus, using Cartesian coordinates (x, y, z), the slowness of a given wave is the vectorial sum of its components s_x, s_y, s_z along each coordinate direction: $\mathbf{s} = s_x\hat{\mathbf{x}} + s_y\hat{\mathbf{y}} + s_z\hat{\mathbf{z}}$ and the slowness in direction $\mathbf{n}$ is simply $\mathbf{s} \cdot \mathbf{n}$. In contrast, the velocity with which a plane wave advances in a particular direction is, in general, faster than its velocity in the direction of propagation (see Fig. 5.2).

BOX **5.1**
Notation

The advantage of using subscripts to denote vector and tensor components is considerably reduced if one is interested in the detailed properties of a particular component. In this chapter, we shall often use the notation $\mathbf{u} = (u, v, w)$ for the three Cartesian components of displacement, with $\mathbf{x} = (x, y, z)$ as the coordinates. We shall find that P- and SV-waves are coupled by boundary conditions on horizontal planes and that P and SV plane waves can each be analyzed in terms of displacement components $u = u(x, z, t)$, $w = w(x, z, t)$. SH plane waves involve $v = v(x, z, t)$, and they do not couple to P or SV.

Where the subscript notation is still convenient (equations (5.1), (5.2), (5.5)), we retain it with the obvious interpretations, e.g., $e_{23} = \frac{1}{2}(\partial u_2/\partial x_3 + \partial u_3/\partial x_2) = \frac{1}{2}(\partial v/\partial z + \partial w/\partial y) = e_{yz}$.

The two basic types of plane waves in a homogeneous isotropic medium are easily distinguished by substituting the general form $\mathbf{u} = \mathbf{u}(t - \mathbf{s} \cdot \mathbf{x})$ for displacement into the elastic displacement equation,

$$\rho \ddot{u}_i = (\lambda + \mu) u_{j,ji} + \mu u_{i,jj}, \tag{5.1}$$

to give

$$\left[\rho \delta_{ik} - (\lambda + \mu) s_i s_k - \mu s_j s_j \delta_{ik}\right] \ddot{u}_k = 0. \tag{5.2}$$

Forming the vector product and scalar product of (5.2) with $\mathbf{s}$, and using $s^2 = 1/c^2$, we obtain

$$\left(\rho - \frac{\mu}{c^2}\right) \ddot{\mathbf{u}} \times \mathbf{s} = \mathbf{0}, \qquad \left(\rho - \frac{\lambda + 2\mu}{c^2}\right) \ddot{\mathbf{u}} \cdot \mathbf{s} = 0. \tag{5.3}$$

Therefore, either [$\ddot{\mathbf{u}} \times \mathbf{s} = \mathbf{0}$ and $c^2 = (\lambda + 2\mu)/\rho$], or [$\ddot{\mathbf{u}} \cdot \mathbf{s} = 0$ and $c^2 = \mu/\rho$]. It follows that the plane wave is *either* a P-wave, with longitudinal motion (parallel to $\mathbf{s}$) and speed $\sqrt{(\lambda + 2\mu)/\rho} = \alpha$, *or* an S-wave with transverse motion and speed $\sqrt{\mu/\rho} = \beta$. Our analysis here is similar to that of equations (4.48)–(4.51), the difference being now that we do not have to make approximations. The longitudinal or transverse nature of P or S motion is exact, at all frequencies, for plane waves in homogeneous isotropic media.

To describe the energy associated with elastic motion, we developed in Chapter 2 the concept of an elastic strain-energy density. The strain energy of a medium is its capacity to do work by virtue of its configuration, and in (2.32) we found the strain-energy density to be $\frac{1}{2}\tau_{ij}e_{ij}$. For a plane wave $u_i = u_i(t - \mathbf{s} \cdot \mathbf{x})$, the strain tensor is $e_{ij} = -\frac{1}{2}[\dot{u}_i s_j + \dot{u}_j s_i]$, and from the stress–strain relations for an isotropic medium (2.49) it is easy to show that

$$\tfrac{1}{2}\tau_{ij}e_{ij} = \tfrac{1}{2}[(\lambda + \mu)(\mathbf{s} \cdot \dot{\mathbf{u}})^2 + \mu(\dot{\mathbf{u}} \cdot \dot{\mathbf{u}})(\mathbf{s} \cdot \mathbf{s})]. \tag{5.4}$$

In the case of either a P-wave (for which $\mathbf{s}$ is parallel to $\dot{\mathbf{u}}$, and $|\mathbf{s}| = \alpha^{-1}$) or an S-wave ($\mathbf{s}$ perpendicular to $\dot{\mathbf{u}}$, and $|\mathbf{s}| = \beta^{-1}$), it follows from (5.4) that

$$\tfrac{1}{2}\tau_{ij}e_{ij} = \tfrac{1}{2}\rho \dot{u}^2, \tag{5.5}$$

i.e., that the strain-energy density equals the kinetic-energy density. The quantities in (5.5) are all real, and the energy densities depend on t and $\mathbf{x}$ only via the combination $t - \mathbf{s} \cdot \mathbf{x}$. Hence the speed of energy propagation is no different from the speed with which a pulse shape in particle displacement is propagated: either α for P-waves or β for S-waves.

It follows that the flux rate of energy transmission in a plane wave (i.e., the amount of energy transmitted per unit time across unit area normal to the direction of propagation) is $\rho\alpha\dot{u}^2$ for P-waves and $\rho\beta\dot{u}^2$ for S-waves. We have proved this result only for plane waves in homogeneous media, and it is a "local" property, depending on material properties and on the planar nature of the wave only at the point at which the flux rate is evaluated. We can therefore expect that flux rates are still given approximately by $\rho\dot{u}^2$ times the propagation velocity for the case of slightly curved wavefronts in a medium with some spatial fluctuation

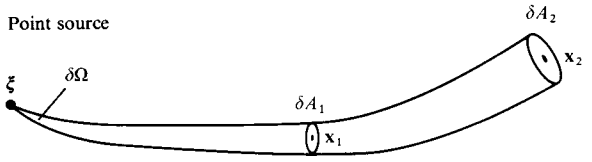

FIGURE **5.3**
Parameters for a ray tube originating on a point source at ξ. The cross-sectional areas of the tube at $\mathbf{x}_1$ and $\mathbf{x}_2$ are given by $\delta A_i = \delta\Omega\, \mathcal{R}^2(\mathbf{x}_i, \xi)(i = 1, 2)$, where $\delta\Omega$ is the solid angle at the source. According to geometrical ray theory, the energy crossing δA_1 in unit time is the same as the energy crossing δA_2 in unit time, after allowing for the time delay in propagation between $\mathbf{x}_1$ and $\mathbf{x}_2$.

in material properties. It follows that there is a physical interpretation of the results of geometrical ray theory for displacement amplitude, which we obtained in Chapter 4. Thus, for P-waves spreading from a point source in an inhomogeneous medium, (4.62) indicates (for a particular ray) that $\sqrt{\rho(\mathbf{x})\alpha(\mathbf{x})}\, \dot{u}^P$ is dependent on receiver position $\mathbf{x}$ only via the geometrical factor $1/\mathcal{R}^P(\mathbf{x}, \xi)$ and the travel time $T^P(\mathbf{x}, \xi)$. Hence the flux rate is controlled only by the ray geometry. Referring to Figure 5.3, the rate at which energy crosses δA_1 is equal to $\rho(\mathbf{x}_1)\alpha(\mathbf{x}_1)\dot{u}^2\, \delta A_1$. But since $\delta A_1 \propto [\mathcal{R}^P(\mathbf{x}_1, \xi)]^2$, it follows from (4.62) that the rate at which energy crosses δA_1 at time T_1 is equal to the rate at which it crosses δA_2 at time T_2 ($T_2 - T_1$ being the time taken for the wave to advance from $\mathbf{x}_1$ to $\mathbf{x}_2$). In this sense we learn from geometrical ray theory that propagating seismic energy is confined within ray tubes. This is only an approximation, becoming accurate at sufficiently high frequencies.

5.1.1 POTENTIALS FOR PLANE WAVES

We saw in Chapter 4 that potentials for elastic displacement can be used to separate P- and S-components, and that this is useful because wave equations for the separate potentials are much simpler (involving only one wave speed) than the wave equation for elastic displacement. The advantages of using potentials (ϕ and $\boldsymbol{\psi}$) appear to be offset by the fact that ϕ and $\boldsymbol{\psi}$ involve *four* unknown functions, whereas the physical quantity we are often interested in, elastic displacement, is a vector with only *three* unknown components. The extra unknown is constrained by an extra equation, usually $\nabla \cdot \boldsymbol{\psi} = 0$. In homogeneous isotropic media we find we can work with only three scalar potential functions, corresponding separately to the P-, SV-, and SH-components of motion.

We shall prove this general result in Box 6.5, but our present interest is in plane waves, and for these there is a special form for the two scalar S-wave potentials. Thus an S-wave in general has displacement $\nabla \times \boldsymbol{\psi}$. If the wave is a plane wave and Cartesian coordinates are chosen as in Figure 5.2, with the x-axis taken in the direction of the horizontal slowness component, then $\boldsymbol{\psi}$ depends only on x, z, and t. It follows from the constraint $\nabla \cdot \boldsymbol{\psi} = 0$ that

$$\frac{\partial \psi_x}{\partial x} + \frac{\partial \psi_z}{\partial z} = 0. \tag{5.6}$$

If the wave is polarized purely as SV, then the y-component of displacement is zero, and

$$\frac{\partial \psi_x}{\partial z} - \frac{\partial \psi_z}{\partial x} = 0. \tag{5.7}$$

In the context of the theory of functions of a complex variable, (5.6) and (5.7) are Cauchy–Riemann equations. It follows that $\psi_z + i\psi_x$ is an analytic function of the variable $x + iz$. By Liouville's theorem, a function that is everywhere analytic and bounded is constant. For a plane wave, $\psi_z + i\psi_x$ is certainly bounded. Furthermore, if the SV-wave is given by $\nabla \times \boldsymbol{\psi}$ only in a restricted depth range, one can conceptually extend this displacement to all depths, so that $\psi_z + i\psi_x$ is analytic everywhere. It follows that $\psi_z + i\psi_x$ is a constant; and since only gradients of ψ_x and ψ_z are of any physical concern, the constant can be taken as zero. We therefore conclude that the most general plane SV-wave, propagating in a vertical plane containing the x-axis, can be expressed in terms of the potential $\boldsymbol{\psi} = (0, \psi, 0)$ with displacement $\nabla \times \boldsymbol{\psi} = (-\partial\psi/\partial z, 0, \partial\psi/\partial x)$. The vector wave equation reduces to the scalar form $\beta^2 \nabla^2 \psi = \ddot{\psi}$.

For a plane SH-wave the use of a vector potential is unnecessary, since the horizontal displacement component is itself a satisfactory scalar function with which to work. For coordinates chosen as in Figure 5.2, the displacement $\mathbf{u} = (u, v, w)$ reduces for SH to $\mathbf{u} = (0, v, 0)$, with $v = v(x, z, t)$ for a plane wave. Already the constraint $\nabla \cdot \mathbf{u} = 0$ for a shear wave is satisfied, and it is easy to show that the elastic displacement equation reduces to $\beta^2 \nabla^2 v = \ddot{v}$.

For P-waves, displacement is $\nabla\phi$ with ϕ satisfying $\alpha^2 \nabla^2 \phi = \ddot{\phi}$. The special case of a plane P-wave propagating as in Figure 5.2 leads to a zero component of displacement in the y-direction, and $\phi = \phi(x, z, t)$ (independent of the y-coordinate). Thus the P-wave displacement may be analyzed via $(\partial\phi/\partial x, 0, \partial\phi/\partial z)$.

5.1.2 SEPARATION OF VARIABLES; STEADY-STATE PLANE WAVES

We shall show briefly that solving the wave equation

$$\alpha^2 \nabla^2 \phi = \ddot{\phi} \tag{5.8}$$

by the method of separation of variables in a Cartesian coordinate system is equivalent to analyzing a type of plane-wave solution.

Thus we shall seek solutions of (5.8) in the form $X(x)Y(y)Z(z)T(t)$, each factor being a function of only one variable. It follows from (5.8) that

$$\frac{\alpha^2}{X}\frac{d^2X}{dx^2} + \frac{\alpha^2}{Y}\frac{d^2Y}{dy^2} + \frac{\alpha^2}{Z}\frac{d^2Z}{dz^2} = \frac{1}{T}\frac{d^2T}{dt^2} \tag{5.9}$$

implying that $(1/T)\, d^2T/dt^2$ is constant (differentiate (5.9) with respect to t in order to see this). For example,

$$\frac{d^2T}{dt^2} + \omega^2 T = 0, \qquad \text{and thus} \qquad T \propto \exp(\pm i\omega t).$$

BOX 5.2

The sign convention for Fourier transforms used in solving wave-propagation problems

Using a Cartesian coordinate system in which z increases with depth, we shall often carry out Fourier transforms of the two horizontal variables, x transforming to k_x, and y to k_y. Our convention for spatial transforms here is

$$f(x) \rightarrow f(k_x) = \int_{-\infty}^{\infty} f(x) e^{-ik_x x} dx,$$

and similarly for functions of y. Note that we shall usually avoid special symbols (such as $\tilde{f}$ or $\bar{f}$ or F) to denote that f has been transformed. Whenever it is not clear from the context whether f denotes $f(x)$ or the transformed function, we shall write f with its specific argument, $f(x)$ or $f(k_x)$.

We shall also be transforming the time dependence, either with a Laplace transform from t to s and the convention

$$f(t) \rightarrow f(s) = \int_{0}^{\infty} f(t) e^{-st} dt$$

or with a Fourier transform from t to ω. Although these transforms are essentially the same, if the transform variable assumes complex values, it is still useful to distinguish between them, since some methods of analysis work with real ω, so that Fourier transformation is appropriate, whereas some methods work with real s (i.e., imaginary ω), in which case the Laplace transform is more convenient.

For Fourier transformation of time dependence, our sign convention for the exponent is

$$f(t) \rightarrow f(\omega) = \int_{-\infty}^{\infty} f(t) \exp(+i\omega t)\, dt.$$

Note that this differs from the convention adopted above in this Box for spatial Fourier transformations. Of course, one would like to avoid using a mixed convention, but there are three good reasons why it is appropriate in solving wave-propagation problems relevant to seismology.

First, it permits a convenient interpretation of the inverse Fourier transforms. If $f(x, y, z, t)$ is some propagating physical variable of interest, it is often possible to obtain the triply transformed function $f(k_x, k_y, z, \omega)$. Then the required solution is

$$f(x, y, z, t) = \frac{1}{8\pi^3} \int_{-\infty}^{\infty} dk_x \int_{-\infty}^{\infty} dk_y \int_{-\infty}^{\infty} d\omega\, f(k_x, k_y, z, \omega) \exp[i(k_x x + k_y y - \omega t)].$$

For our choice of sign convention, this integrand can be interpreted in the case of positive k_x, k_y, and ω, as a wave propagating in the directions of *increasing* x and y.

Second, if $f(x, y, z, t)$ satisfies a wave equation of type $c^2 \nabla^2 f = \ddot{f}$, then $f(k_x, k_y, z, \omega)$ satisfies

$$\frac{\partial^2 f}{\partial z^2} = \left(k_x^2 + k_y^2 - \frac{\omega^2}{c^2}\right) f.$$

(continued)

BOX **5.2** *(continued)*

If the medium is homogeneous (i.e., c is constant), then

$$f(k_x, k_y, z, \omega) \propto e^{\pm i\omega\xi z}, \tag{1}$$

where $\omega\xi = (\omega^2/c^2 - k_x^2 - k_y^2)^{1/2}$. The choice of sign in (1) indicates whether f is a downgoing wave (+) or an upcoming wave (−). However, if $\omega^2/c^2 < k_x^2 + k_y^2$, we shall find almost always that we wish to work with the *positive* imaginary value of $\omega\xi$, for then the wave $e^{+i\omega\xi z}$ attenuates correctly with depth ($z \to \infty$) if $\omega > 0$, and the wave $e^{-i\omega\xi z}$ attenuates correctly with height ($z \to -\infty$).

Third, anticipating our need in later chapters to use Hankel functions, we use what physicists have almost universally adopted, i.e., the convention that Hankel functions of type 1 represent outgoing waves and those of type 2 represent incoming waves. As propagating (steady-state) waves, these must then be associated with the factor $e^{-i\omega t}$. Integration (with respect to ω) over terms with this factor constitutes the inverse Fourier transform back to the time domain, and hence our sign convention is indeed correct for the standard Hankel function convention.

Similarly,

$$\frac{d^2X}{dx^2} + k_x^2 X = 0, \qquad \text{and} \qquad X \propto \exp(\pm i k_x x)$$

$$\frac{d^2Y}{dy^2} + k_y^2 Y = 0, \qquad \text{and} \qquad Y \propto \exp(\pm i k_y y)$$

for some constants k_x, k_y. The z-dependence, however, is constrained in that

$$\frac{d^2Z}{dz^2} + k_z^2 Z = 0 \qquad (\text{with solutions } Z \propto \exp(\pm i k_z z))$$

where the separation constant is given by

$$k_z^2 = \frac{\omega^2}{\alpha^2} - k_x^2 - k_y^2, \tag{5.10}$$

so that the solution is characterized by only three independent numbers (ω, k_x, k_y), not four.

Separated solutions are therefore of the type

$$\exp[i(\mathbf{k} \cdot \mathbf{x} - \omega t)],$$

in which $\mathbf{k} = (k_x, k_y, k_z)$, and $|\mathbf{k}| = |\omega/\alpha|$. Clearly, this is a plane wave with a particularly simple time dependence, a steady oscillation at a fixed frequency ω. The vector $\mathbf{k}$, of three separation constraints, is known as the *wavenumber vector*, and it is just ω times the slowness.

General solutions of (5.8) are obtained by superposition of the separated solutions, and

$$\phi(x, y, z, t) = \int_{-\infty}^{\infty} d\omega \int_{-\infty}^{\infty} dk_x \int_{-\infty}^{\infty} dk_y \, \Phi(k_x, k_y, \omega) \times \exp\left\{ i \left[k_x x + k_y y + \sqrt{\frac{\omega^2}{\alpha^2} - k_x^2 - k_y^2}\; z - \omega t \right] \right\}. \quad (5.11)$$

Here, $\Phi(k_x, k_y, \omega)$ is acting merely as some weighting function, giving the amount of plane wave characterized by (k_x, k_y, ω) that is present in the superposition for the required solution $\phi(\mathbf{x}, t)$.

The result we have obtained in (5.11) is essentially the same as that stated by using inverse Fourier transforms in Box 5.2. Here we have used Cartesian coordinates, but for other coordinate systems it is also true that a solution given by inverse transforms can be thought of as a superposition of separated solutions.

Plane waves are directly of importance in seismology, because body waves from a distant source will often behave locally like plane waves. Representation (5.11) also indicates the indirect importance of steady-state plane waves, showing that they are a basis for synthesizing more general solutions. The details of this synthesis have been extensively studied, and they form the subject of Chapter 6 and parts of 7 and 9. Since these details determine the properties of plane waves that we shall need to develop, it is useful to list here the following comments on representation (5.11).

(i) Because of the dependence on k_x, k_y, it will be important to study plane waves as a function of their horizontal wavenumber—or, often more conveniently, as a function of their horizontal slowness.

(ii) Part of the process of solving a wave-propagation problem via (5.11) will be the determination of the function $\Phi(k_x, k_y, \omega)$ that is appropriate for the particular source under study. In the context of an integration over elements $d\omega\, dk_x\, dk_y$, Φ can be thought of as a *density function* in (ω, k_x, k_y) space. In the context of Fourier transform theory, it is related to the *triple transform* of ϕ with respect to t, x, and y. In the context of superposition, it is the *excitation function*, indicating how much of a particular plane wave is excited by the source under study.

(iii) It is often useful to study waves propagating in only two spatial dimensions, x and z, in which case the y-dependence and the k_y integral are absent in (5.11).

(iv) A decision must be made as to the sign of a square root appearing in the integrand in (5.11). Also, if the horizontal wavenumber is great enough, the square root of a negative number must be taken, and exponential growth or decay will occur in the z-direction. We take up this subject in Section 5.3.

(v) Once the various factors appearing in the integrand of (5.11) have all been obtained, a method is required for evaluating the triple integral. We shall find that many different methods are in use, and that they often involve making approximations. In a few cases, the integrals can be inverted exactly to give a closed-form expression for ϕ. For the elastic media that are studied in problems relevant to seismology, it often

occurs that a part of the evaluation of the integrals must be carried out numerically. The most fruitful methods of this type all emphasize manipulations of the integral over horizontal slowness.

With this justification for a thorough analysis of plane waves, we return to the main theme of the chapter.

5.2 Elementary Formulas for Reflection/Conversion/Transmission Coefficients

We have seen that steady-state plane wave solutions to equations of type $\alpha^2\nabla^2\phi = \ddot{\phi}$ in a homogeneous medium take the form $A\exp[i\omega(\mathbf{s}\cdot\mathbf{x} - t)]$, where A is the amplitude, and $(\partial\phi/\partial x, 0, \partial\phi/\partial z)$ is the associated P-wave displacement for propagation in a direction normal to the y-axis. In this section, we shall study the effect of the boundary between two half-spaces that are in contact along the plane $z = 0$. If the half-spaces consist of a solid, a fluid, or a vacuum, then there are five nontrivial cases to consider: solid/solid, solid/fluid, solid/vacuum, fluid/fluid, and fluid/vacuum.

5.2.1 BOUNDARY CONDITIONS

Consideration of basic physical principles governing displacement and traction, in the vicinity of the boundary between two different half-spaces, results in a number of different constraints on elastic wave solutions. These constraints are called *boundary conditions*. In practice they are used to determine features such as the ratio between a signal that is reflected from an interface, and the incident signal. This particular ratio, called a *reflection coefficient*, in turn can be regarded as a direct consequence of the underlying boundary condition, and different boundary conditions lead to different values for the reflection coefficient.

In practice, two different boundary conditions are commonly considered in seismology: those concerning displacement (often called kinematic boundary conditions) and those concerning traction, or stress components (dynamic boundary conditions).

For two solids in welded contact, the kinematic condition is that all three components of displacement must be continuous through the boundary. There would also be continuity of displacement across the boundary between a solid half-space and a viscous fluid half-space. For a solid half-space in contact with a fluid half-space where the fluid is completely inviscid, slip can occur parallel to the boundary, but the normal component of displacement must be continuous (unless cavitation occurs or the fluid moves into interstices in the solid). For typical wavelengths and periods of seismic waves (kilometers, seconds), it appears that the two fluids of principal importance in seismology, namely the oceans and the Earth's outer core, do behave in an inviscid fashion. That is, their viscosity is so low as to confine kinematic viscous drag in the fluid to only a negligible fraction of a wavelength away from solid/fluid interfaces such as the sea floor or the core–mantle boundary. Under these circumstances, the tangential component of displacement can effectively be discontinuous, and the only candidate for a kinematic boundary condition is the normal component of displacement. The strong compressive stresses prevailing in the Earth's interior will not permit cavitation to occur (since this would entail shock propagation with a

BOX **5.3**

The distinction between kinematics and dynamics

Kinematics is the branch of mechanics that deals purely with motion, without analyzing the underlying forces that cause or participate in the motion. Dynamics is the branch of mechanics that deals directly with force systems, and with the energy balance that governs motion. From these fundamental definitions, two useful conventions have developed for applying the words "kinematic" and "dynamic."

First, in the analysis of displacements alone, kinematic properties are those that may be derived from the eikonal equation (4.41), whereas dynamic properties are those related to displacement amplitudes. Thus the existence of particular wavefronts and ray paths is part of the kinematics of the problem in hand. As an example of a dynamic problem, we might ask if a certain approximation is adequate for the displacements observed at a given receiver at some given distance from a localized source.

Second, in those problems for which we have a direct interest in both the displacement and the associated system of stresses, then kinematic properties are properties of the displacement field and dynamic properties are related to the stresses. For example, if the relative displacement between opposite faces of a fault surface is known as a function of space and time, we say that we have a kinematic description of the fault motion. If the stresses (i.e., traction components) are known on the fault surface, we have a dynamic description. As another example, one refers to boundary conditions as being kinematic or dynamic, in the sense developed in the present section.

stress discontinuity many orders of magnitude greater than the strength of rocks). Moreover, any significant diffusion of fluid into solid would require a time far greater than the period of seismic waves. It is therefore appropriate in seismology to take the kinematic boundary condition for a solid/fluid interface as continuity of normal displacement only.

The dynamic boundary condition is continuity of traction across the interface. This result can be proved along the lines of our discussion of Figure 2.4. The tractions acting across a small thin disc, with its two flat faces in different media, are equal in magnitude but opposite in direction (see (2.7)). Reversing the direction of one of the outward normals of the disc, the traction $\mathbf{T}(\mathbf{n})$ is the same for each face of the disc, and hence is continuous through the interface (see also Problem 2.8). Since traction is a vector, this appears to give three scalar constraints. One or two of these, however, may be satisfied trivially, since a propagating plane wave does not necessarily excite all three components of traction. Note that these traction components, for our choice of the interface as a plane normal to the z-axis, are the stress tensor components $\tau_{zx}, \tau_{zy}, \tau_{zz}$. At an interface with a vacuum, these three stress components are all zero, and this is effectively the case also for the surface of the Earth or the oceans, since the elastic moduli for the atmosphere are several orders of magnitude less than the elastic moduli of rock or the bulk modulus of sea water. (Exceptions can occur for air-coupled surface waves, as described in Appendix 1.) The case $(\tau_{zx}, \tau_{zy}, \tau_{zz}) = (0, 0, 0)$ on $z = 0$ is referred to as the "free-surface boundary condition" on $z = 0$, and this is the first reflection problem we shall examine in detail.

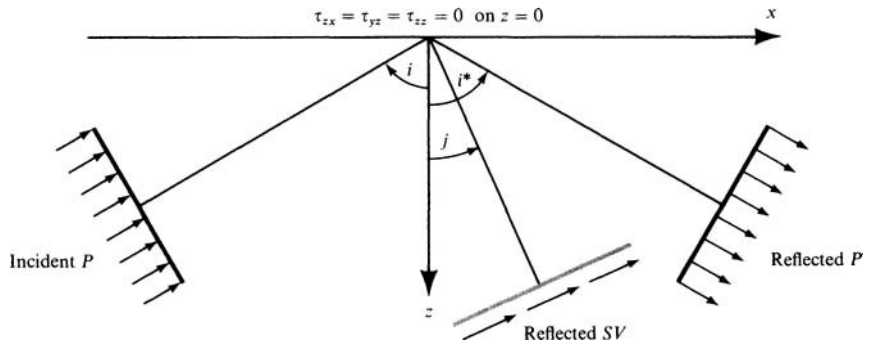

FIGURE **5.4**
The wave system and coordinates for analysis of the reflected waves set up by a plane P-wave incident on the free surface of a solid elastic half-space. Portions of plane waves are shown as heavy line segments, and associated sets of arrows show the direction of particle motion. Angles i and j are defined in terms of the ray trajectories, orthogonal to the plane fronts of P and SV, respectively. Reflection angle i^* equals incident angle i.

5.2.2 REFLECTION OF PLANE P-WAVES AND SV-WAVES AT A FREE SURFACE

Suppose a plane P-wave is traveling with horizontal slowness in the direction of increasing x (see Fig. 5.4). Then, for some potential ϕ, the P-wave displacement is given by $\mathbf{u} = (\partial\phi/\partial x, 0, \partial\phi/\partial z)$ and the associated traction by

$$\mathbf{T}(\mathbf{u}, \hat{\mathbf{z}}) = (\tau_{zx}, \tau_{yz}, \tau_{zz}) = \left(2\mu\frac{\partial^2\phi}{\partial z \partial x}, 0, \lambda\nabla^2\phi + 2\mu\frac{\partial^2\phi}{\partial z^2}\right). \tag{5.12}$$

For completeness, it is convenient to give here the corresponding results for SV- and SH-waves: for SV, there is a scalar potential ψ, the SV-displacement is $\mathbf{u} = (-\partial\psi/\partial z, 0, \partial\psi/\partial x)$ and the traction is

$$\mathbf{T}(\mathbf{u}, \hat{\mathbf{z}}) = (\tau_{zx}, \tau_{yz}, \tau_{zz}) = \left(\mu\left(\frac{\partial^2\psi}{\partial x^2} - \frac{\partial^2\psi}{\partial z^2}\right), 0, 2\mu\frac{\partial^2\psi}{\partial z\,\partial x}\right); \tag{5.13}$$

for SH only one displacement component is needed, so the SH-displacement is $\mathbf{u} = (0, v, 0)$ and the traction is

$$\mathbf{T}(\mathbf{u}, \hat{\mathbf{z}}) = (\tau_{zx}, \tau_{yz}, \tau_{zz}) = \left(0, \mu\frac{\partial v}{\partial z}, 0\right). \tag{5.14}$$

In terms of the incidence angle i (see Fig. 5.4), the slowness of the incident P-wave is

$$\mathbf{s} = \left(\frac{\sin i}{\alpha}, 0, \frac{-\cos i}{\alpha}\right).$$

Since no τ_{yz} component is excited by this wave (see (5.12)), no SH-component is excited (see (5.14)), and the only candidates for reflected waves are P and SV, with respective slownesses

$$\left(\frac{\sin i^*}{\alpha}, 0, \frac{\cos i^*}{\alpha}\right), \left(\frac{\sin j}{\beta}, 0, \frac{\cos j}{\beta}\right).$$

Thus the total ϕ potential is made up from an incident component ϕ^{inc}, and reflected component ϕ^{refl}, with

$$\phi = \phi^{\text{inc}} + \phi^{\text{refl}}, \tag{5.15}$$

$$\phi^{\text{inc}} = A \exp\left[i\omega\left(\frac{\sin i}{\alpha}x - \frac{\cos i}{\alpha}z - t\right)\right], \tag{5.16}$$

$$\phi^{\text{refl}} = B \exp\left[i\omega\left(\frac{\sin i^*}{\alpha}x + \frac{\cos i^*}{\alpha}z - t\right)\right]. \tag{5.17}$$

The amplitudes A and B are constant in each wave, and the total SV-wave is given by

$$\psi = \psi^{\text{refl}} \tag{5.18}$$

where

$$\psi^{\text{refl}} = C \exp\left[i\omega\left(\frac{\sin j}{\beta}x + \frac{\cos j}{\beta}z - t\right)\right]. \tag{5.19}$$

There are no kinematic boundary conditions to concern us, since it is meaningless to speak of displacements above the free surface, and the displacement of the free surface of the solid is not constrained. The nontrivial dynamic boundary conditions are $\tau_{zx} = \tau_{zz} = 0$ on $z = 0$, and from equations (5.12), (5.13), (5.15)–(5.19) we find that each of τ_{zx}, τ_{zz} is a sum of three contributions involving factors of the type

$$\exp\left[i\omega\left(\frac{\sin i}{\alpha}x - t\right)\right] \quad \text{or} \quad \exp\left[i\omega\left(\frac{\sin i^*}{\alpha}x - t\right)\right] \quad \text{or} \quad \exp\left[i\omega\left(\frac{\sin j}{\beta}x - t\right)\right].$$

The boundary conditions hold on $z = 0$ for all x and t, so that these factors, which control the horizontal propagation of the wave system, must all be the same, for all (x, t). Hence

$$i^* = i \qquad \text{and} \qquad \frac{\sin i}{\alpha} = \frac{\sin j}{\beta}. \tag{5.20}$$

The angles of reflected and incident P are equal, but, perhaps even more basic, the horizontal slowness of the incident wave is preserved on reflection, and is preserved also on conversion to SV. If there were transmission into an upper half-space, the horizontal slowness component would again be preserved. These results are all consistent with Snell's law, which we have already proved (see (4.45a)) for media with smoothly varying depth-dependence of

BOX **5.4**
Impedance

The impedance that a given medium presents to a given motion is a measure of the amount of resistance to particle motion. Specifically, impedance in elasticity is a ratio of stress to particle velocity, so that for a given applied stress, the particle velocity is inversely proportional to impedance.

Impedance properties of different wave types can vary considerably, as we now discuss by looking at specific examples.

First, consider an SH-wave with displacement $v = v_0 \exp\{i\omega[px + (\beta^{-1} \cos j)z - t]\}$. Then, for horizontal planes (z = constant), the tangential stress is $\tau_{yz} = i\mu\omega(\beta^{-1} \cos j)v$ and the tangential particle velocity is $\dot{v} = -i\omega v$, so that the impedance is $\tau_{yz}/\dot{v} = -\mu(\beta^{-1} \cos j) = -\rho\beta \cos j$. For the Earth's crust, representative values of density and shear velocity are $\rho = 2.8$ g/cm^3 and $\beta = 3.5$ km/s, so that the impedance is of order 10^6 cgs units. A stress wave with amplitude 100 bars ($= 10^8$ cgs units) therefore corresponds to a ground velocity of about 100 cm/s. For SH waves, however, note that impedance $\tau_{yz}/\dot{v} \to 0$ as $j \to \pi/2$ (grazing incidence).

Second, consider an acoustic wave (i.e., a P-wave in a fluid) in which the pressure is given by $P = P_0 \exp\{i\omega[px + (\alpha^{-1} \cos i)z - t]\}$. Then, since $\rho\ddot{\mathbf{u}} = -\nabla P$, the vertical particle velocity is given by $-i\omega\rho\dot{u}_z = -\partial P/\partial z$, and the impedance is $P/\dot{u}_z = (\rho\alpha)/\cos i$. Note now that the impedance approaches infinity as $i \to \pi/2$ (grazing incidence), in contrast to the behavior of SH-waves.

velocity. We are developing here the important concept that the whole system of waves, set up by reflection and transmission of plane waves in plane-layered media, is characterized by the value of their common horizontal slowness. Often we shall call this value the *ray parameter*, although the name is inadequate since $(\sin i)/\alpha = (\sin j)/\beta = p$ is a parameter of a whole system of rays, not just of one ray.

Simplifying the equations (5.12), (5.13) giving physical variables as a function of potentials ϕ and ψ and writing them now in terms of p, ϕ, ψ, $\partial\phi/\partial z$, and $\partial\psi/\partial z$, we find

$$\text{for } P \begin{cases} \text{displacement} = \left(i\omega p\phi, 0, \dfrac{\partial\phi}{\partial z}\right) \\ \text{traction} \quad\quad = \left(2\rho\beta^2 i\omega p \dfrac{\partial\phi}{\partial z}, 0, -\rho(1 - 2\beta^2 p^2)\omega^2\phi\right) \end{cases} \tag{5.21}$$

$$\text{for } SV \begin{cases} \text{displacement} = \left(-\dfrac{\partial\psi}{\partial z}, 0, i\omega p\psi\right) \\ \text{traction} \quad\quad = \left(\rho(1 - 2\beta^2 p^2)\omega^2\psi, 0, 2\rho\beta^2 i\omega p \dfrac{\partial\psi}{\partial z}\right). \end{cases} \tag{5.22}$$

Our immediate goal is to obtain formulas for the ratios B/A and C/A, giving the amplitude of the potentials for reflected and converted waves as a fraction of the amplitude of the potential for the incident wave. The two equations to determine these ratios are

$$\left.\begin{aligned}\tau_{zx} &= 2\rho\beta^2 i\omega p\left(\frac{\partial\phi^{\text{inc}}}{\partial z}+\frac{\partial\phi^{\text{refl}}}{\partial z}\right)+\rho(1-2\beta^2p^2)\omega^2\psi^{\text{refl}}=0\\ \tau_{zz} &= -\rho(1-2\beta^2p^2)\omega^2(\phi^{\text{inc}}+\phi^{\text{refl}})+2\rho\beta^2 i\omega p\frac{\partial\psi^{\text{refl}}}{\partial z} \quad =0\end{aligned}\right\} \text{ on } z=0.$$

Substituting from (5.16), (5.17), (5.19), these become

$$2\rho\beta^2 p\frac{\cos i}{\alpha}(A-B)+\rho(1-2\beta^2p^2)C=0 \tag{5.23}$$

$$\rho(1-2\beta^2p^2)(A+B)+2\rho\beta^2 p\frac{\cos j}{\beta}C=0 \tag{5.24}$$

with solutions

$$\frac{B}{A}=\frac{4\beta^4p^2\dfrac{\cos i}{\alpha}\dfrac{\cos j}{\beta}-(1-2\beta^2p^2)^2}{4\beta^4p^2\dfrac{\cos i}{\alpha}\dfrac{\cos j}{\beta}+(1-2\beta^2p^2)^2} \tag{5.25}$$

$$\frac{C}{A}=\frac{-4\beta^2p\dfrac{\cos i}{\alpha}(1-2\beta^2p^2)}{4\beta^4p^2\dfrac{\cos i}{\alpha}\dfrac{\cos j}{\beta}+(1-2\beta^2p^2)^2}. \tag{5.26}$$

Using trigonometrical identities and relations between elastic moduli, a large number of different but equivalent forms have been derived for the above two expressions. Note, for example, that $(1-2\beta^2p^2)$ is $\cos 2j$. We have chosen to work with p, $\alpha^{-1}\cos i$, and $\beta^{-1}\cos j$ because these are the components of the slowness vector and in Chapter 9 we shall show that the reflection coefficients (5.25) and (5.26) can then be easily generalized, using horizontal and vertical slownesses, to study media that are vertically heterogeneous.

We have called the ratios B/A and C/A "reflection coefficients," but actually these ratios are amplitude ratios only for potentials. In practice, we are usually interested in amplitude ratios for displacements (and, occasionally, for energy). For a propagating steady-state P-wave, the displacement amplitude is $\omega\times$(potential amplitude)/α, and similarly for SV displacement the amplitude is $\omega\times$(potential amplitude)/β. (5.25) and (5.26) may be adapted to give displacement reflection coefficients, though we still need to establish a sign convention for reflection coefficients. Our choice is described in Figure 5.5.

Many, many different notations have been proposed for reflection/conversion/transmission coefficients. Fortunately, the problems one needs to solve turn out usually to require only a small number (one or two) of particular coefficients. In these cases, a comprehensive notation is unnecessary, since it may be clear from its context that a symbol such as RPP or PP is a reflection coefficient, with no ambiguity as to which particular combination of reflected wave/incident wave is intended. Such is the case in the present problem of a solid half-space with a free surface; only one type of incident P-wave is present, and only one P-wave is derived from it. Nevertheless, we shall shortly have to deal with the solid/solid interface, for which P-waves (and S-waves) can be incident from above and below. Each of the four possible types of incident P–SV waves (P or SV, from above or below) can

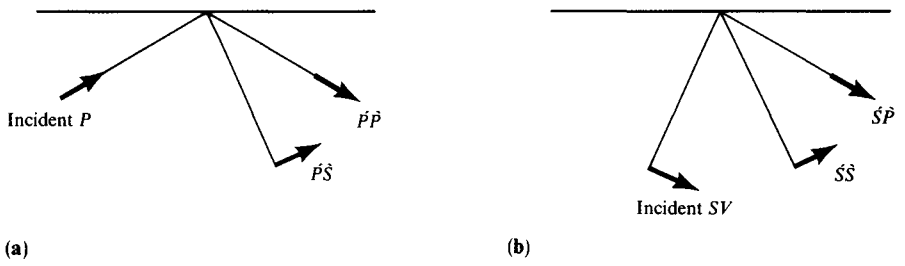

FIGURE **5.5**
Notation and sign convention for coefficients of reflection and transmission due to P or SV incidence on a free surface. A motion is taken as positive if its component to the right (i.e., in the horizontal direction of propagation) has the same phase as the propagation factor, $\exp[i\omega(px - t)]$.

generate all four types of outgoing P–SV waves, hence 16 coefficients are involved for a complete analysis of just this one interface. In the present problem, therefore, it will be convenient to adopt a notation that can easily be extended to more complicated interfaces. We shall take $\acute{P}\grave{P}$ as the $P \rightarrow P$ reflection coefficient for Figure 5.5a and $\acute{P}\grave{S}$ as the $P \rightarrow S$ conversion coefficient. In Figure 5.5b, the $S \rightarrow P$ conversion is given by $\acute{S}\grave{P}$, and $S \rightarrow S$ reflection by $\acute{S}\grave{S}$. This use of acute and grave accents indicates directly the intended sequence of incident wave $\rightarrow$ derived wave, since all waves are moving from left to right. Thus an acute accent (e.g., $\acute{P}$) indicates an upcoming wave, and a grave accent (e.g., $\grave{S}$) a downgoing wave. Combining this notation with the sign convention of Figure 5.5, we specify in Table 5.1 the exact vector form of motions corresponding to the two possible types of incident wave.

Our notation with grave and acute accents has been introduced for displacement amplitude ratios. It can also be applied for particle-velocity amplitude ratios and for particle-acceleration amplitude ratios (since these incident and scattered waves are scaled by the same power of frequency). However, *coefficients are different* for ratios of potentials, or energy fluxes. Where such different ratios are needed (e.g., Box 6.6, and equation (5.43)), we shall retain accented symbols for displacement amplitude ratios, and multiply by appropriate scaling corrections.

It follows from Table 5.1 and equations (5.25)–(5.26) that

$$\acute{P}\grave{P} = \frac{-\left(\frac{1}{\beta^2} - 2p^2\right)^2 + 4p^2 \frac{\cos i}{\alpha}\frac{\cos j}{\beta}}{+\left(\frac{1}{\beta^2} - 2p^2\right)^2 + 4p^2 \frac{\cos i}{\alpha}\frac{\cos j}{\beta}}, \tag{5.27}$$

$$\acute{P}\grave{S} = \frac{4\frac{\alpha}{\beta}p\frac{\cos i}{\alpha}\left(\frac{1}{\beta^2} - 2p^2\right)}{\left(\frac{1}{\beta^2} - 2p^2\right)^2 + 4p^2 \frac{\cos i}{\alpha}\frac{\cos j}{\beta}}. \tag{5.28}$$

In the case of an SV-wave incident on the free surface, we can expect a reflected P-wave ($\acute{S}\grave{P}$) and a reflected SV-wave ($\acute{S}\grave{S}$). For the vector displacements in Table 5.1,

TABLE **5.1**

Explicit expressions for the vector displacements involved in *P–SV* plane-wave problems of the type shown in Figure 5.5. In this Table we use S to denote the amplitude of the incident wave. This amplitude can be thought of in two ways: either as the displacement amplitude of a steady-state wave; or as the amplitude of the Fourier transform of particle velocity, in the case that the incident wave is a step S in displacement.

Incident wave		*Scattered waves*	
Type	Displacement	Type	Displacement
Upgoing P	$S(\sin i, 0, -\cos i) \exp\left[i\omega\left(\frac{\sin i}{\alpha}x - \frac{\cos i}{\alpha}z - t\right)\right]$	Downgoing P	$S(\sin i, 0, \cos i)\acute{P}\grave{P} \exp\left[i\omega\left(\frac{\sin i}{\alpha}x + \frac{\cos i}{\alpha}z - t\right)\right]$
		Downgoing SV	$S(\cos j, 0, -\sin j)\acute{P}\grave{S} \exp\left[i\omega\left(\frac{\sin j}{\beta}x + \frac{\cos j}{\beta}z - t\right)\right]$
Upgoing SV	$S(\cos j, 0, \sin j) \exp\left[i\omega\left(\frac{\sin j}{\beta}x - \frac{\cos j}{\beta}z - t\right)\right]$	Downgoing P	$S(\sin i, 0, \cos i)\acute{S}\grave{P} \exp\left[i\omega\left(\frac{\sin i}{\alpha}x + \frac{\cos i}{\alpha}z - t\right)\right]$
		Downgoing SV	$S(\cos j, 0, -\sin j)\acute{S}\grave{S} \exp\left[i\omega\left(\frac{\sin j}{\beta}x + \frac{\cos j}{\beta}z - t\right)\right]$

we find that the condition $\tau_{zx} = 0$ on $z = 0$ reduces to the equation

$$-2p\alpha\beta\frac{\cos i}{\alpha}\acute{S}\grave{P} + (1 - 2\beta^2p^2)(1 - \acute{S}\grave{S}) = 0, \tag{5.29}$$

and the condition $\tau_{zz} = 0$ on $z = 0$ reduces to

$$-(1 - 2\beta^2p^2)\acute{S}\grave{P} + \frac{2\beta^3p}{\alpha}\frac{\cos j}{\beta}(1 + \acute{S}\grave{S}) = 0. \tag{5.30}$$

Solving (5.29) and (5.30), we obtain

$$\acute{S}\grave{P} = \frac{4\frac{\beta}{\alpha}p\frac{\cos j}{\beta}\left(\frac{1}{\beta^2} - 2p^2\right)}{\left(\frac{1}{\beta^2} - 2p^2\right)^2 + 4p^2\frac{\cos i}{\alpha}\frac{\cos j}{\beta}}, \tag{5.31}$$

$$\acute{S}\grave{S} = \frac{\left(\frac{1}{\beta^2} - 2p^2\right)^2 - 4p^2\frac{\cos i}{\alpha}\frac{\cos j}{\beta}}{\left(\frac{1}{\beta^2} - 2p^2\right)^2 + 4p^2\frac{\cos i}{\alpha}\frac{\cos j}{\beta}}. \tag{5.32}$$

In this simple example of reflection from the free surface of a solid half-space, we have now obtained specific formulas for each component of the matrix

$$\begin{pmatrix} \acute{P}\grave{P} & \acute{S}\grave{P} \\ \acute{P}\grave{S} & \acute{S}\grave{S} \end{pmatrix}.$$

This matrix, summarizing all possible reflection coefficients for the problem at hand, is an example of a *scattering matrix.* Each of its components is plotted against slowness in Figure 5.6, and even for this very simple interface, the components are found to vary quite strongly. Only the range $0 \leq p \leq 1/\alpha$ is shown. For slowness in the range 0.14 to 0.195 s/km, note that the reflected motion is almost all opposite in type from the incident motion. That is, incident P is converted almost totally to reflected SV, and incident SV to reflected P. Far more complicated behavior can occur in other interface problems (solid/fluid, etc.), and seismologists often have to analyze this behavior in great detail in order to interpret a particular piece of data. For convenience, therefore, we shall give the coefficient formulas for two other interfaces of importance in seismology. Unfortunately, there is a long history of published misprints in these formulas (see Hales and Roberts, 1974, or Young and Braile, 1976, for a review). In order for an individual to have confidence in his or her evaluation of a particular coefficient, we conclude Section 5.2.5 with a useful check to verify that the formulas have been correctly transcribed.

5.2.3 REFLECTION AND TRANSMISSION OF SH-WAVES

To consider the scattering of a plane SH-wave at the interface between two solid half-spaces we use the notation of Figure 5.7 and Table 5.2. Stress components τ_{zx} and τ_{zz}

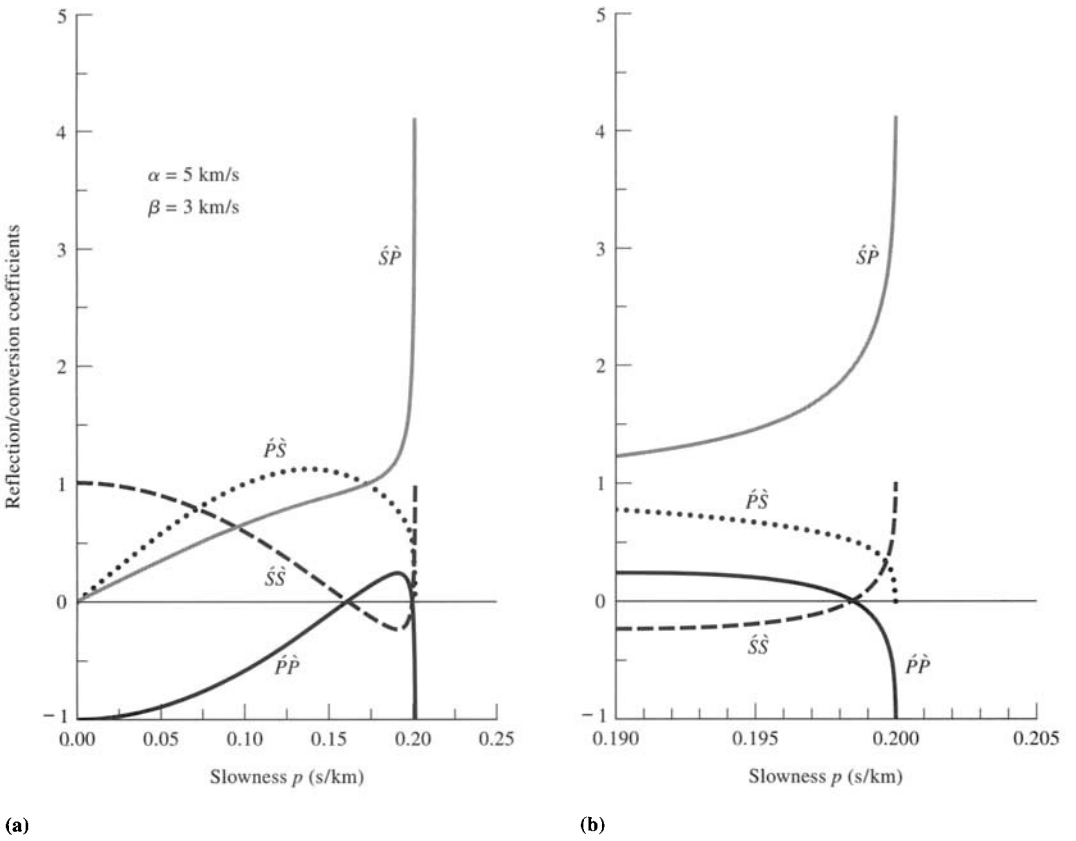

FIGURE **5.6**
The four possible *P–SV* reflection/conversion coefficients (displacement amplitude ratios) for a free surface are shown against horizontal slowness p. See Figure 5.5. In this case, $\alpha = 5$ km/s and $\beta = 3$ km/s, and we restrict p to lie in the range $0 \leq p \leq 1/\alpha$ so that incidence angle i is always real. For $i = 90°$, $\acute{S}\grave{P}$ is quite large (~ 4.1). The left panel shows the whole range of p. The right panel shows an expanded view of the range just less than $p = 1/\alpha$.

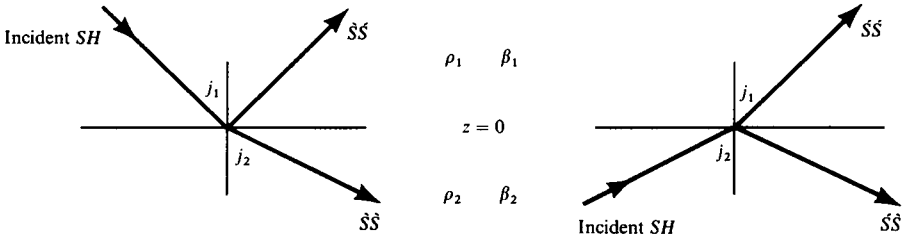

FIGURE **5.7**
Notation for the four possible reflection/transmission coefficients arising for problems of incident SH-waves.

TABLE **5.2**
Vector displacements for the SH plane wave problems shown in Figure 5.7.

Incident wave		*Scattered waves*	
Type	Displacement	Type	Displacement
Downgoing SH	$(0, S, 0) \exp\left[i\omega\left(px + \frac{\cos j_1}{\beta_1} z - t\right)\right]$	Upgoing SH	$(0, S, 0)\grave{S}\acute{S} \exp\left[i\omega\left(px - \frac{\cos j_1}{\beta_1} z - t\right)\right]$
		Downgoing SH	$(0, S, 0)\grave{S}\grave{S} \exp\left[i\omega\left(px + \frac{\cos j_2}{\beta_2} z - t\right)\right]$
Upgoing SH	$(0, S, 0) \exp\left[i\omega\left(px - \frac{\cos j_2}{\beta_2} z - t\right)\right]$	Upgoing SH	$(0, S, 0)\acute{S}\acute{S} \exp\left[i\omega\left(px - \frac{\cos j_1}{\beta_1} z - t\right)\right]$
		Downgoing SH	$(0, S, 0)\acute{S}\grave{S} \exp\left[i\omega\left(px + \frac{\cos j_2}{\beta_2} z - t\right)\right]$

are not excited by any of the incident/reflected/transmitted SH displacements, so that the only nontrivial dynamic boundary condition is continuity of τ_{yz} across $z = 0$. The y-component of displacement is also continuous, and we find from (5.14) that the elements of the scattering matrix

$$\begin{pmatrix} \grave{S}\acute{S} & \acute{S}\acute{S} \\ \grave{S}\grave{S} & \acute{S}\grave{S} \end{pmatrix}$$

are

$$\begin{aligned} \grave{S}\acute{S} &= \frac{\rho_1\beta_1 \cos j_1 - \rho_2\beta_2 \cos j_2}{\Delta}, & \acute{S}\acute{S} &= \frac{2\rho_2\beta_2 \cos j_2}{\Delta}, \\ \grave{S}\grave{S} &= \frac{2\rho_1\beta_1 \cos j_1}{\Delta}, & \acute{S}\grave{S} &= -\grave{S}\acute{S}, \end{aligned} \tag{5.33}$$

where

$$\Delta = \rho_1\beta_1 \cos j_1 + \rho_2\beta_2 \cos j_2.$$

5.2.4 REFLECTION AND TRANSMISSION OF *P–SV* ACROSS A SOLID–SOLID INTERFACE

The scattering matrix now is

$$\begin{pmatrix} \grave{P}\acute{P} & \grave{S}\acute{P} & \acute{P}\acute{P} & \acute{S}\acute{P} \\ \grave{P}\acute{S} & \grave{S}\acute{S} & \acute{P}\acute{S} & \acute{S}\acute{S} \\ \grave{P}\grave{P} & \grave{S}\grave{P} & \acute{P}\grave{P} & \acute{S}\grave{P} \\ \grave{P}\grave{S} & \grave{S}\grave{S} & \acute{P}\grave{S} & \acute{S}\grave{S} \end{pmatrix},$$

and it may be obtained from continuity of the x- and z-components of both displacement and traction. Each column of the scattering matrix represents the four waves scattered away from the interface by a particular type of incident wave. Hence, to evaluate all columns, it appears that we must set up four systems of four equations in four unknowns to solve for scattered waves from all the different incident waves shown in Figure 5.8 and described in Table 5.3. Unless some care is taken to use all available symmetries in the problem, a complete statement of all 16 coefficients can involve extensive algebraic manipulation. This manipulation is minimized in the method we now describe, which is based on the work of Nafe (1957).

We shall assume that all four possible incident waves are present together and have the same horizontal slowness, as shown in Figure 5.9, with respective displacement amplitudes $\grave{P}_1, \grave{S}_1, \acute{P}_2, \acute{S}_2$. Subscripts are now necessary in order to identify the medium in which the wave is traveling. The four scattered waves have displacement amplitudes $\acute{P}_1, \acute{S}_1, \grave{P}_2, \grave{S}_2$.

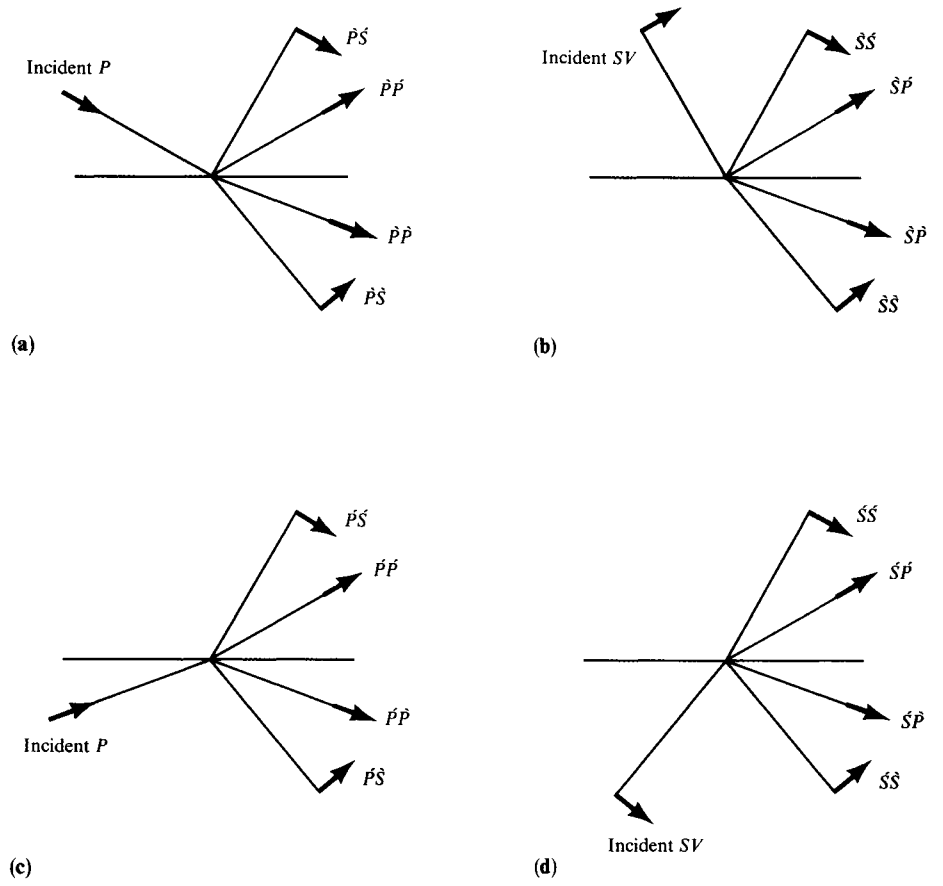

FIGURE **5.8**
Notation for the sixteen possible reflection/transmission coefficients arising for problems of *P–SV* waves at the welded interface between two different solid half-spaces. Short arrows show the direction of particle motion.

From continuity of $u_x, u_z, \tau_{zx}, \tau_{zz}$, we obtain the four equations

$$
\begin{aligned}
&\sin i_1(\grave{P}_1 + \acute{P}_1) + \cos j_1(\grave{S}_1 + \acute{S}_1) = \sin i_2(\grave{P}_2 + \acute{P}_2) + \cos j_2(\grave{S}_2 + \acute{S}_2),\\
&\cos i_1(\grave{P}_1 - \acute{P}_1) - \sin j_1(\grave{S}_1 - \acute{S}_1) = \cos i_2(\grave{P}_2 - \acute{P}_2) - \sin j_2(\grave{S}_2 - \acute{S}_2),\\
&2\rho_1\beta_1^2 p \cos i_1(\grave{P}_1 - \acute{P}_1) + \rho_1\beta_1(1 - 2\beta_1^2 p^2)(\grave{S}_1 - \acute{S}_1)\\
&\qquad = 2\rho_2\beta_2^2 p \cos i_2(\grave{P}_2 - \acute{P}_2) + \rho_2\beta_2(1 - 2\beta_2^2 p^2)(\grave{S}_2 - \acute{S}_2),\\
&\rho_1\alpha_1(1 - 2\beta_1^2 p^2)(\grave{P}_1 + \acute{P}_1) - 2\rho_1\beta_1^2 p \cos j_1(\grave{S}_1 + \acute{S}_1)\\
&\qquad = \rho_2\alpha_2(1 - 2\beta_2^2 p^2)(\grave{P}_2 + \acute{P}_2) - 2\rho_2\beta_2^2 p \cos j_2(\grave{S}_2 + \acute{S}_2),
\end{aligned}
\tag{5.34}
$$

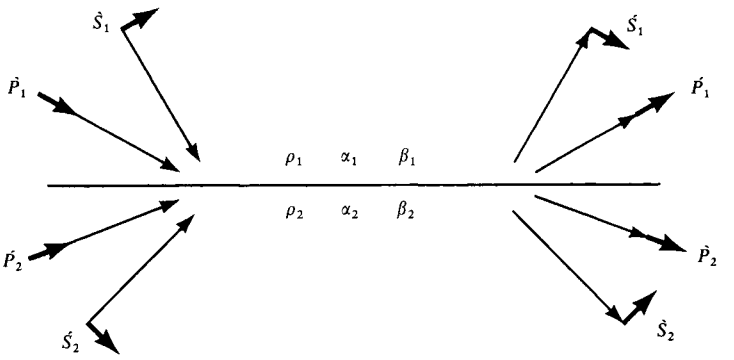

FIGURE **5.9**
The complete system of incident and scattered plane *P–SV* waves, in terms of which the scattering matrix can quickly be found. Short arrows show the direction of particle motion; long arrows show the direction of propagation.

respectively. Rearranging these equations so that scattered waves are all on the left-hand side and incident waves all on the right, we find

$$\mathbf{M}\begin{pmatrix} \acute{P}_1 \\ \acute{S}_1 \\ \grave{P}_2 \\ \grave{S}_2 \end{pmatrix} = \mathbf{N}\begin{pmatrix} \grave{P}_1 \\ \grave{S}_1 \\ \acute{P}_2 \\ \acute{S}_2 \end{pmatrix}, \tag{5.35}$$

in which the coefficient matrices are

$$\mathbf{M} = \begin{pmatrix} -\alpha_1 p & -\cos j_1 & \alpha_2 p & \cos j_2 \\ \cos i_1 & -\beta_1 p & \cos i_2 & -\beta_2 p \\ 2\rho_1\beta_1^2 p\cos i_1 & \rho_1\beta_1(1-2\beta_1^2p^2) & 2\rho_2\beta_2^2 p\cos i_2 & \rho_2\beta_2(1-2\beta_2^2p^2) \\ -\rho_1\alpha_1(1-2\beta_1^2p^2) & 2\rho_1\beta_1^2 p\cos j_1 & \rho_2\alpha_2(1-2\beta_2^2p^2) & -2\rho_2\beta_2^2 p\cos j_2 \end{pmatrix}, \tag{5.36}$$

$$\mathbf{N} = \begin{pmatrix} \alpha_1 p & \cos j_1 & -\alpha_2 p & -\cos j_2 \\ \cos i_1 & -\beta_1 p & \cos i_2 & -\beta_2 p \\ 2\rho_1\beta_1^2 p\cos i_1 & \rho_1\beta_1(1-2\beta_1^2p^2) & 2\rho_2\beta_2^2 p\cos i_2 & \rho_2\beta_2(1-2\beta_2^2p^2) \\ \rho_1\alpha_1(1-2\beta_1^2p^2) & -2\rho_1\beta_1^2 p\cos j_1 & -\rho_2\alpha_2(1-2\beta_2^2p^2) & 2\rho_2\beta_2^2 p\cos j_2 \end{pmatrix}. \tag{5.37}$$

In the case that $\grave{P}_1 = 1$ and $\grave{S}_1 = \acute{P}_2 = \acute{S}_2 = 0$, the first column of the scattering matrix becomes simply $(\acute{P}_1, \acute{S}_1, \grave{P}_2, \grave{S}_2)^T$, i.e., the first column of $\mathbf{M}^{-1}\mathbf{N}$. There are similar results for

TABLE **5.3**
Vector displacements for the *P–SV* plane wave problems shown in Figure 5.8 (solid over solid).

Incident wave		*Scattered waves*	
Type	Displacement	Type	Displacement
Downgoing P	$S(\sin i_1, 0, \cos i_1) \exp\left[i\omega\left(px + \frac{\cos i_1}{\alpha_1}z - t\right)\right]$	Upgoing P	$S(\sin i_1, 0, -\cos i_1)\grave{P}\acute{P} \exp\left[i\omega\left(px - \frac{\cos i_1}{\alpha_1}z - t\right)\right]$
		Upgoing SV	$S(\cos j_1, 0, \sin j_1)\grave{P}\acute{S} \exp\left[i\omega\left(px - \frac{\cos j_1}{\beta_1}z - t\right)\right]$
		Downgoing P	$S(\sin i_2, 0, \cos i_2)\grave{P}\grave{P} \exp\left[i\omega\left(px + \frac{\cos i_2}{\alpha_2}z - t\right)\right]$
		Downgoing SV	$S(\cos j_2, 0, -\sin j_2)\grave{P}\grave{S} \exp\left[i\omega\left(px + \frac{\cos j_2}{\beta_2}z - t\right)\right]$
Downgoing SV	$S(\cos j_1, 0, -\sin j_1) \exp\left[i\omega\left(px + \frac{\cos j_1}{\beta_1}z - t\right)\right]$	Upgoing P	$S(\sin i_1, 0, -\cos i_1)\grave{S}\acute{P} \exp\left[i\omega\left(px - \frac{\cos i_1}{\alpha_1}z - t\right)\right]$
		Upgoing SV	$S(\cos j_1, 0, \sin j_1)\grave{S}\acute{S} \exp\left[i\omega\left(px - \frac{\cos j_1}{\beta_1}z - t\right)\right]$
		Downgoing P	$S(\sin i_2, 0, \cos i_2)\grave{S}\grave{P} \exp\left[i\omega\left(px + \frac{\cos i_2}{\alpha_2}z - t\right)\right]$
		Downgoing SV	$S(\cos j_2, 0, -\sin j_2)\grave{S}\grave{S} \exp\left[i\omega\left(px + \frac{\cos j_2}{\beta_2}z - t\right)\right]$

TABLE **5.3**
Continued

Incident wave		*Scattered waves*	
Type	Displacement	Type	Displacement
Upgoing P	$S(\sin i_2, 0, -\cos i_2) \exp\left[i\omega\left(px - \frac{\cos i_2}{\alpha_2}z - t\right)\right]$	Upgoing P	$S(\sin i_1, 0, -\cos i_1)\acute{P}\acute{P} \exp\left[i\omega\left(px - \frac{\cos i_1}{\alpha_1}z - t\right)\right]$
		Upgoing SV	$S(\cos j_1, 0, \sin j_1)\acute{P}\acute{S} \exp\left[i\omega\left(px - \frac{\cos j_1}{\beta_1}z - t\right)\right]$
		Downgoing P	$S(\sin i_2, 0, \cos i_2)\acute{P}\grave{P} \exp\left[i\omega\left(px + \frac{\cos i_2}{\alpha_2}z - t\right)\right]$
		Downgoing SV	$S(\cos j_2, 0, -\sin j_2)\acute{P}\grave{S} \exp\left[i\omega\left(px + \frac{\cos j_2}{\beta_2}z - t\right)\right]$
Upgoing SV	$S(\cos j_2, 0, \sin j_2) \exp\left[i\omega\left(px - \frac{\cos j_2}{\beta_2}z - t\right)\right]$	Upgoing P	$S(\sin i_1, 0, -\cos i_1)\acute{S}\acute{P} \exp\left[i\omega\left(px - \frac{\cos i_1}{\alpha_1}z - t\right)\right]$
		Upgoing SV	$S(\cos j_1, 0, \sin j_1)\acute{S}\acute{S} \exp\left[i\omega\left(px - \frac{\cos j_1}{\beta_1}z - t\right)\right]$
		Downgoing P	$S(\sin i_2, 0, \cos i_2)\acute{S}\grave{P} \exp\left[i\omega\left(px + \frac{\cos i_2}{\alpha_2}z - t\right)\right]$
		Downgoing SV	$S(\cos j_2, 0, -\sin j_2)\acute{S}\grave{S} \exp\left[i\omega\left(px + \frac{\cos j_2}{\beta_2}z - t\right)\right]$

the other three columns, and it follows that the complete scattering matrix is given directly by

$$\begin{pmatrix} \grave{P}\acute{P} & \grave{S}\acute{P} & \acute{P}\acute{P} & \acute{S}\acute{P} \\ \grave{P}\acute{S} & \grave{S}\acute{S} & \acute{P}\acute{S} & \acute{S}\acute{S} \\ \grave{P}\grave{P} & \grave{S}\grave{P} & \acute{P}\grave{P} & \acute{S}\grave{P} \\ \grave{P}\grave{S} & \grave{S}\grave{S} & \acute{P}\grave{S} & \acute{S}\grave{S} \end{pmatrix} = \mathbf{M}^{-1}\mathbf{N}. \tag{5.38}$$

Fortunately, the many similarities between matrices **M** and **N** lead to quite simple formulas for each component of the scattering matrix. In detail, these formulas make repeated use of the variables

$$a = \rho_2(1 - 2\beta_2^2 p^2) - \rho_1(1 - 2\beta_1^2 p^2), \quad b = \rho_2(1 - 2\beta_2^2 p^2) + 2\rho_1\beta_1^2 p^2,$$
$$c = \rho_1(1 - 2\beta_1^2 p^2) + 2\rho_2\beta_2^2 p^2, \quad d = 2(\rho_2\beta_2^2 - \rho_1\beta_1^2),$$

and repeated use also of the cosine-dependent terms

$$E = b\frac{\cos i_1}{\alpha_1} + c\frac{\cos i_2}{\alpha_2}, \quad F = b\frac{\cos j_1}{\beta_1} + c\frac{\cos j_2}{\beta_2},$$
$$G = a - d\frac{\cos i_1}{\alpha_1}\frac{\cos j_2}{\beta_2}, \quad H = a - d\frac{\cos i_2}{\alpha_2}\frac{\cos j_1}{\beta_1}, \tag{5.39}$$
$$\mathsf{D} = EF + GHp^2 = (\det \mathbf{M})/(\alpha_1\alpha_2\beta_1\beta_2).$$

The main formulas are

$$\grave{P}\acute{P} = \left[\left(b\frac{\cos i_1}{\alpha_1} - c\frac{\cos i_2}{\alpha_2}\right)F - \left(a + d\frac{\cos i_1}{\alpha_1}\frac{\cos j_2}{\beta_2}\right)Hp^2\right] \Big/ \mathsf{D},$$

$$\grave{P}\acute{S} = -2\frac{\cos i_1}{\alpha_1}\left(ab + cd\frac{\cos i_2}{\alpha_2}\frac{\cos j_2}{\beta_2}\right)p\alpha_1/(\beta_1\mathsf{D}),$$

$$\grave{P}\grave{P} = 2\rho_1\frac{\cos i_1}{\alpha_1}F\alpha_1/(\alpha_2\mathsf{D}),$$

$$\grave{P}\grave{S} = 2\rho_1\frac{\cos i_1}{\alpha_1}Hp\alpha_1/(\beta_2\mathsf{D}),$$

$$\grave{S}\acute{P} = -2\frac{\cos j_1}{\beta_1}\left(ab + cd\frac{\cos i_2}{\alpha_2}\frac{\cos j_2}{\beta_2}\right)p\beta_1/(\alpha_1\mathsf{D}),$$

$$\grave{S}\acute{S} = -\left[\left(b\frac{\cos j_1}{\beta_1} - c\frac{\cos j_2}{\beta_2}\right)E - \left(a + d\frac{\cos i_2}{\alpha_2}\frac{\cos j_1}{\beta_1}\right)Gp^2\right] \Big/ \mathsf{D},$$

$$\grave{S}\grave{P} = -2\rho_1 \frac{\cos j_1}{\beta_1} Gp\beta_1/(\alpha_2 \mathsf{D}),$$

$$\grave{S}\grave{S} = 2\rho_1 \frac{\cos j_1}{\beta_1} E\beta_1/(\beta_2 \mathsf{D}),$$

$$\acute{P}\acute{P} = 2\rho_2 \frac{\cos i_2}{\alpha_2} F\alpha_2/(\alpha_1 \mathsf{D}),$$

$$\acute{P}\acute{S} = -2\rho_2 \frac{\cos i_2}{\alpha_2} Gp\alpha_2/(\beta_1 \mathsf{D}),$$

$$\acute{P}\grave{P} = -\left[\left(b\frac{\cos i_1}{\alpha_1} - c\frac{\cos i_2}{\alpha_2}\right) F + \left(a + d\frac{\cos i_2}{\alpha_2}\frac{\cos j_1}{\beta_1}\right) Gp^2\right] \Big/ \mathsf{D},$$

$$\acute{P}\grave{S} = 2\frac{\cos i_2}{\alpha_2}\left(ac + bd\frac{\cos i_1}{\alpha_1}\frac{\cos j_1}{\beta_1}\right) p\alpha_2/(\beta_2 \mathsf{D}),$$

$$\acute{S}\acute{P} = 2\rho_2 \frac{\cos j_2}{\beta_2} Hp\beta_2/(\alpha_1 \mathsf{D}),$$

$$\acute{S}\acute{S} = 2\rho_2 \frac{\cos j_2}{\beta_2} E\beta_2/(\beta_1 \mathsf{D}),$$

$$\acute{S}\grave{P} = 2\frac{\cos j_2}{\beta_2}\left(ac + bd\frac{\cos i_1}{\alpha_1}\frac{\cos j_1}{\beta_1}\right) p\beta_2/(\alpha_2 \mathsf{D}),$$

$$\acute{S}\grave{S} = \left[\left(b\frac{\cos j_1}{\beta_1} - c\frac{\cos j_2}{\beta_2}\right) E + \left(a + d\frac{\cos i_1}{\alpha_1}\frac{\cos j_2}{\beta_2}\right) Hp^2\right] \Big/ \mathsf{D}. \tag{5.40}$$

For two different solids that meet at a planar interface, but are not in welded contact, then traction is still continuous but by implication sliding can take place. Chaisri and Krebes (2000) consider displacement discontinuities on $z = 0$ such that

$$\begin{aligned} \tau_{zx1} &= \tau_{zx2}, \qquad & u_{x2} - u_{x1} &= c_x \tau_{zx}, \\ \tau_{zz1} &= \tau_{zz2}, \qquad & u_{z2} - u_{z1} &= c_z \tau_{zz}, \end{aligned} \tag{5.41}$$

where c_x and c_z are constants and subscripts 1 and 2 refer to the upper and lower media. They obtained 16 coefficients of the same general form as (5.40). But in their more general case (i.e., with c_x and c_z not equal to zero), there is an explicit dependence on frequency, absent in (5.40).

5.2.5 ENERGY FLUX

For a steady-state plane wave incident on the boundary between two homogeneous half-spaces, there is no possibility of trapping energy at the interface (otherwise amplitudes

would increase indefinitely). Hence the flux of energy leaving the boundary must equal that in the incident wave.

For a steady-state displacement P-wave having amplitude S and propagation factor $\exp[i\omega(\mathbf{s}\cdot\mathbf{x}-t)]$, the actual (real) displacement amplitude is $S\cos[\omega(\mathbf{s}\cdot\mathbf{x}-t)]$. Then $\rho\alpha S^2\omega^2\sin^2[\omega(\mathbf{s}\cdot\mathbf{x}-t)]$ is the rate of energy transmission across unit area of wavefront (see Section 5.1). One must multiply this result by $\cos i$ to obtain the energy flux across unit area of a horizontal boundary upon which the wave is incident at angle i, since only $\cos i$ of wavefront area is involved. Similarly, for S-waves the energy flux is $\rho\beta\cos j\, S^2\omega^2\sin^2[\omega(\mathbf{s}\cdot\mathbf{x}-t)]$. Since the reflection/transmission coefficients we have found above were for displacements, it follows that the equality of incoming and outgoing energy flux will give, for example,

$$\begin{aligned}\rho_1\alpha_1\cos i_1 = {}& \rho_1\alpha_1\cos i_1(\grave{P}\acute{P})^2 + \rho_1\beta_1\cos j_1(\grave{P}\acute{S})^2 \\ & + \rho_2\alpha_2\cos i_2(\grave{P}\grave{P})^2 + \rho_2\beta_2\cos j_2(\grave{P}\grave{S})^2\end{aligned} \tag{5.42}$$

for the scattered wave system shown in Figure 5.8a.

Equation (5.42) is a constraint on the first column of the scattering matrix for a solid/solid interface. It can be simplified by working with new dependent variables: namely, displacement $\times\sqrt{\text{density}\times\text{wave speed}\times\text{cosine of angle of incidence}}$. In terms of these scaled displacements (which are proportional to the square root of energy flux), the scattering matrix $\mathbf{S}$ is a unitary Hermitian matrix. This property can be shown from equations given by Frasier (1970), and has been extensively studied by Kennett *et al.* (1978).

For example, the new reflection coefficient corresponding to the previous $\acute{P}\grave{S}$ is

$$\frac{\text{displacement amplitude of downgoing } SV\text{-wave}\times\sqrt{\rho_2\beta_2\cos j_2}}{\text{displacement amplitude of incident upgoing } P\text{-wave}\times\sqrt{\rho_2\alpha_2\cos i_2}}$$

(see Figure 5.8c), which is $\acute{P}\grave{S}\sqrt{(\beta_2\cos j_2)/(\alpha_2\cos i_2)}$. The complete form of this scattering matrix is

$$\mathbf{S}=\begin{pmatrix} \grave{P}\acute{P} & \grave{S}\acute{P}\sqrt{\dfrac{\alpha_1\cos i_1}{\beta_1\cos j_1}} & \acute{P}\acute{P}\sqrt{\dfrac{\rho_1\alpha_1\cos i_1}{\rho_2\alpha_2\cos i_2}} & \acute{S}\acute{P}\sqrt{\dfrac{\rho_1\alpha_1\cos i_1}{\rho_2\beta_2\cos j_2}} \\ \grave{P}\acute{S}\sqrt{\dfrac{\beta_1\cos j_1}{\alpha_1\cos i_1}} & \grave{S}\acute{S} & \acute{P}\acute{S}\sqrt{\dfrac{\rho_1\beta_1\cos j_1}{\rho_2\alpha_2\cos i_2}} & \acute{S}\acute{S}\sqrt{\dfrac{\rho_1\beta_1\cos j_1}{\rho_2\beta_2\cos j_2}} \\ \grave{P}\grave{P}\sqrt{\dfrac{\rho_2\alpha_2\cos i_2}{\rho_1\alpha_1\cos i_1}} & \grave{S}\grave{P}\sqrt{\dfrac{\rho_2\alpha_2\cos i_2}{\rho_1\beta_1\cos j_1}} & \acute{P}\grave{P} & \acute{S}\grave{P}\sqrt{\dfrac{\alpha_2\cos i_2}{\beta_2\cos j_2}} \\ \grave{P}\grave{S}\sqrt{\dfrac{\rho_2\beta_2\cos j_2}{\rho_1\alpha_1\cos i_1}} & \grave{S}\grave{S}\sqrt{\dfrac{\rho_2\beta_2\cos j_2}{\rho_1\beta_1\cos j_1}} & \acute{P}\grave{S}\sqrt{\dfrac{\beta_2\cos j_2}{\alpha_2\cos i_2}} & \acute{S}\grave{S} \end{pmatrix} \tag{5.43}$$

and

$$\mathbf{S} = \mathbf{S}^H = \mathbf{S}^{-1}. \tag{5.44}$$

(By $\mathbf{S}^H$ we mean the complex conjugate of the transpose of $\mathbf{S}$.)

Once the 16 coefficients $\grave{P}\acute{P}$, $\grave{P}\acute{S}$, etc. have been obtained from (5.38) or (5.40), they can be checked by verifying that $\mathbf{S}$ satisfies (5.44). In fact, provided that the slowness is low enough for all the angles i_1, j_1, i_2, j_2 to be real, the entries of $\mathbf{S}$ (as we have defined them) are all real, so that the transpose of $\mathbf{S}$ is also the inverse of $\mathbf{S}$. As a specific example, we find that

$$\mathbf{S} = \begin{pmatrix} 0.1065 & -0.1766 & 0.9701 & -0.1277 \\ -0.1766 & -0.0807 & 0.1326 & 0.9720 \\ 0.9701 & 0.1326 & -0.0567 & 0.1950 \\ -0.1277 & 0.9720 & 0.1950 & 0.0309 \end{pmatrix}$$

in the case $(\rho_1, \alpha_1, \beta_1, \rho_2, \alpha_2, \beta_2, p) = (3, 6, 3.5, 4, 7, 4.2, 0.1)$, and this particular matrix does indeed have the properties $\mathbf{S} = \mathbf{S}^T = \mathbf{S}^{-1}$.

A matrix $\mathbf{S}$ with complex entries would be obtained if, in forming the 16 coefficients, reference levels $z_1 < 0$ in the upper half-space and $z_2 > 0$ in the lower half-space were used. Extra phase factors must then be introduced to account for the shift in vertical reference. In this case, it is the complex conjugate transpose of $\mathbf{S}$ (i.e., $\mathbf{S}^H$), which is also the inverse of $\mathbf{S}$. Finally, we remark that if there is some more complicated transition zone in the range $z_1 < z < z_2$ (e.g., a continuous variation of elastic properties or a stack of welded homogeneous layers having different elastic moduli), but with the regions above z_1 and below z_2 still homogeneous, then a scattering matrix $\mathbf{S}$ can still be defined for the whole transition zone, and $\mathbf{S}$ is still Hermitian and unitary. These properties are a consequence of energy conservation, reciprocity, and causality.

5.2.6 A USEFUL APPROXIMATION FOR REFLECTION/TRANSMISSION COEFFICIENTS BETWEEN TWO SIMILAR HALF-SPACES

If the two half-spaces under consideration have similar properties, then one may expect that transmission coefficients will be large for waves that retain the same mode of propagation (e.g., $\grave{P}\grave{P}$, in which the mode of both the incident and the transmitted wave is downgoing P), but all other types of scattering coefficient will be small. Thus, if there is a jump in properties amounting to $\Delta\rho = \rho_2 - \rho_1$, $\Delta\alpha = \alpha_2 - \alpha_1$, $\Delta\beta = \beta_2 - \beta_1$, and the ratios $\Delta\rho/\rho$, $\Delta\alpha/\alpha$, $\Delta\beta/\beta$ have magnitudes much less than one (where ρ, α, β are the mean values of density and velocities for the two half-spaces), we may expect that quantities such as $\grave{S}\acute{P}$, $\acute{P}\grave{S}$ will be small, but that transmissions $\grave{P}\grave{P}$ and $\acute{S}\acute{S}$ will be of order one. We shall here derive the first-order effect of small jumps in density and velocities for the P-SV problem of two solid half-spaces, since the resulting approximate formulas (5.46) are often remarkably accurate. They give some insight into the separate contributions made by $\Delta\rho$, $\Delta\alpha$, $\Delta\beta$. Chapman (1976a), Stolt and Weglein (1985), and many others have shown that these formulas are important in the analysis of waves in inhomogeneous media.

We shall assume that all angles i_1, i_2, j_1, j_2 are real and that none of these angles is near 90°. Then from Snell's law relating i_1 and i_2, j_1 and j_2, it follows that

$$\Delta i = i_2 - i_1 = \tan i(\Delta\alpha/\alpha), \qquad \Delta j = j_2 - j_1 = \tan j(\Delta\beta/\beta) \tag{5.45}$$

(correct to first order in the velocity jumps). After expanding the terms defined in (5.39), correct to first order in the jumps $\Delta\rho$, $\Delta\alpha$, $\Delta\beta$, we can substitute into (5.40), finding that

$$\begin{aligned}
\grave{P}\acute{P} &= \tfrac{1}{2}(1 - 4\beta^2 p^2)\frac{\Delta\rho}{\rho} + \frac{1}{2\cos^2 i}\frac{\Delta\alpha}{\alpha} - 4\beta^2 p^2 \frac{\Delta\beta}{\beta}, \\
\grave{P}\acute{S} &= \frac{-p\alpha}{2\cos j}\left[\left(1 - 2\beta^2 p^2 + 2\beta^2 \frac{\cos i}{\alpha}\frac{\cos j}{\beta}\right)\frac{\Delta\rho}{\rho} - 4\beta^2\left(p^2 - \frac{\cos i}{\alpha}\frac{\cos j}{\beta}\right)\frac{\Delta\beta}{\beta}\right], \\
\grave{P}\grave{P} &= 1 - \tfrac{1}{2}\frac{\Delta\rho}{\rho} + \left(\frac{1}{2\cos^2 i} - 1\right)\frac{\Delta\alpha}{\alpha}, \\
\grave{P}\grave{S} &= \frac{p\alpha}{2\cos j}\left[\left(1 - 2\beta^2 p^2 - 2\beta^2 \frac{\cos i}{\alpha}\frac{\cos j}{\beta}\right)\frac{\Delta\rho}{\rho} - 4\beta^2\left(p^2 + \frac{\cos i}{\alpha}\frac{\cos j}{\beta}\right)\frac{\Delta\beta}{\beta}\right], \\
\grave{S}\acute{P} &= \frac{\cos j}{\alpha}\frac{\beta}{\cos i}\grave{P}\acute{S}, \\
\grave{S}\acute{S} &= -\tfrac{1}{2}(1 - 4\beta^2 p^2)\frac{\Delta\rho}{\rho} - \left(\frac{1}{2\cos^2 j} - 4\beta^2 p^2\right)\frac{\Delta\beta}{\beta}, \\
\grave{S}\grave{P} &= \frac{-\cos j}{\alpha}\frac{\beta}{\cos i}\grave{P}\grave{S}, \\
\grave{S}\grave{S} &= 1 - \tfrac{1}{2}\frac{\Delta\rho}{\rho} + \left(\frac{1}{2\cos^2 j} - 1\right)\frac{\Delta\beta}{\beta}.
\end{aligned} \tag{5.46}$$

The remaining eight coefficients are easily deduced from the eight given above, merely by making a change in sign in the jumps $\Delta\rho$, $\Delta\alpha$, $\Delta\beta$. A generalization of (5.46) to handle weakly anisotropic media is given by Vavryčuk and Pšenčík (1998).

There is a tendency for the coefficients of $\Delta\beta/\beta$ in (5.46) to be larger than the coefficients of $\Delta\rho/\rho$ and $\Delta\alpha/\alpha$, implying that fluctuations in shear velocity are relatively more efficient in scattering elastic waves. It is interesting that all of the conversions between P and S ($\grave{P}\grave{S}$, $\acute{S}\grave{P}$, etc.) are insensitive to first-order changes in the P-wave speed.

The approximate formulas (5.46) will fail if angles i (or j) are near 90°, since then only a small jump in velocity can lead to a large change in i (or j). It can even happen that the wave undergoes total internal reflection. Uses of the first-order approximations (5.46) are given by Bortfeld (1961) and Richards and Frasier (1976). The approximations are important for interpreting "amplitude variation with offset" (known as AVO in geophysical exploration), i.e., the variability of reflection amplitudes with source–receiver distance, as noted in Problem 5.8 and discussed by Russell (1993). Chapman (1976a), in a major study of the waves set up by a point source in media with depth-dependent properties, showed how to handle the singularities in (5.46) at $i = 90°$ and $j = 90°$.

5.2.7 FREQUENCY INDEPENDENCE OF PLANE-WAVE REFLECTION/TRANSMISSION COEFFICIENTS

So far in this section, we have analyzed only steady-state plane waves with frequency ω (see Tables 5.1–5.3), so that reflection and transmission coefficients have been obtained in the frequency domain. But in formulas for the coefficients (e.g., (5.27), (5.33), (5.40)), there does not appear to be any frequency dependence. We phrase this cautiously, using the word "appear," because in Section 5.3 we shall find that there can be a type of frequency dependence (involving sign-dependent phase shifts) in the coefficients we have obtained. However, the coefficients *are* frequency independent when the angles of incidence (referred to above variously as i, j, j_1, j_2, i_1, i_2) are all real. In this case, p^{-1}, the horizontal phase velocity, is greater than propagation speeds α and β of P- and S-waves. The reflection/transmission coefficients are then all real, and the fact that they are independent of frequency means that waves leaving the boundary must have the same pulse shape (but with different amplitudes) as the incident wave. This is a very special property, and it is not true in general if the boundary is not plane or if the waves are not plane waves. One of the important phenomena we shall describe later is the way in which the pulse shape of a reflected or transmitted wave can differ from that of an incident wave when the incident wavefront is curved (Chapter 6) or if the boundary is slightly curved (Chapter 9).

5.3 Inhomogeneous Waves, Phase Shifts, and Interface Waves

For the plane waves we have described so far, it has been implied that the direction $\mathbf{l}$ of propagation is a vector (parallel to slowness $\mathbf{s}$) that has real Cartesian components. In this section, we investigate the consequences of allowing the components of $\mathbf{l}$ (or $\mathbf{s}$) in the depth direction to be imaginary. We shall find that waves of this type are possible, and that their amplitude grows or decays exponentially with depth. They are examples of inhomogeneous waves (formally defined, following (5.98)), and again we shall use their horizontal slowness p as an independent variable to study their properties.

Previously, we found for P-waves that

$$\mathbf{s} = (\alpha^{-1} \sin i, 0, \pm\alpha^{-1} \cos i) = (p, 0, \pm\sqrt{1/\alpha^2 - p^2}).$$

If the depth component of $\mathbf{s}$ is imaginary, then $p > 1/\alpha$. That is, the horizontal phase velocity, p^{-1}, is less than the propagation speed of P-waves. The quantity we have previously called "sin i", equal to αp, is still real but is now greater than unity, so that angle i is no longer real. If p is even greater, so that $p > 1/\beta > 1/\alpha$, then the associated S-wave is also an inhomogeneous wave, its slowness $\mathbf{s}$ being $(p, 0, \pm\sqrt{1/\beta^2 - p^2})$. Previously, we studied steady-state plane waves with phase factor $\exp[i\omega(\mathbf{s} \cdot \mathbf{x} - t)]$, it being understood that the actual fluctuation of the wave, in space and time, is given by the real part of this phase factor, i.e., $\cos[\omega(\mathbf{s} \cdot \mathbf{x} - t)]$. Now, however, with imaginary s_z, the actual fluctuation of the wave is expressed by a factor like $\exp(i\omega s_z z)\cos[\omega(px - t)]$, in which the real quantity $\exp(i\omega s_z z)$ gives exponential growth or decay with depth, according as ωs_z is negative or positive imaginary. Previously, we found that the requirement of satisfying a wave

equation reduced to the requirement that $s^2 = 1/c^2$, where $c = \alpha = \sqrt{(\lambda + 2\mu)/\rho}$ for P-waves and $c = \beta = \sqrt{\mu/\rho}$ for S. This requirement still holds for inhomogeneous waves, and since now $p = s_x > 1/c$ and $s^2 = s_x^2 + s_z^2 = 1/c^2$, we see that the wave equation provides the fundamental reason for having an imaginary vertical slowness component when the horizontal component of slowness is sufficiently large.

Before going into further detail, let us step back and see that the physically distinctive features of inhomogeneous waves are (i) that their phase velocity is slower than the underlying body-wave speed, and (ii) that they have amplitudes that grow or decay exponentially in directions of constant phase. These two properties are linked, because the wave equation shows that exponentially growing amplitudes are associated with low phase velocities, and *vice versa*. The slower the phase (below the body-wave velocity), the greater the exponential rate of change of amplitude with distance. For an inhomogeneous wave in an elastic isotropic medium, the surfaces of constant phase are perpendicular to surfaces of constant amplitude.

As an example of the need for considering inhomogeneous waves in seismology, consider again the problem shown in Figure 5.5b of a plane SV-wave incident upon a free surface. We obtained formulas in (5.31) and (5.32) for conversion coefficient $\acute{S}\grave{P}$ and reflection coefficient $\acute{S}\grave{S}$ and showed values of these in Figure 5.6 as functions of p in the range $0 \le p \le 1/\alpha$. But what happens when $1/\alpha < p$? If p becomes so great that $1/\beta < p$, then even the SV-wave is inhomogeneous and it is not clear what we mean by an "incident wave." However in the range $1/\alpha < p < 1/\beta$, the SV-wave does have a real angle of incidence $j = \sin^{-1}(\beta p)$. In this range, we must regard $\cos j$ as real and positive, but $\alpha^{-1} \cos i = \sqrt{1/\alpha^2 - p^2}$ is pure imaginary. Since the entry in Table 5.1 involving $\acute{S}\grave{P}$ gives the P-wave displacement as

$$S(\sin i, 0, \cos i)\, \acute{S}\grave{P} \exp\left(i\omega \frac{\cos i}{\alpha} z\right) \exp\left[i\omega\left(\frac{\sin i}{\alpha} x - t\right)\right], \tag{5.47}$$

and since we cannot allow the P-wave to grow exponentially with depth, it follows that

$$\frac{\cos i}{\alpha} = \pm i \sqrt{p^2 - \frac{1}{\alpha^2}}, \qquad \text{according as } \omega \gtrless 0. \tag{5.48}$$

Thus, for positive frequencies, we find that (5.47) becomes

$$S\left(\alpha p, 0, i\sqrt{\alpha^2 p^2 - 1}\right)\, \acute{S}\grave{P} \exp\left(-\omega \sqrt{p^2 - \frac{1}{\alpha^2}}\, z\right) \exp\left[i\omega\,(px - t)\right]. \tag{5.49}$$

The steps taken in (5.29)–(5.32) to derive $\acute{S}\grave{P}$ and $\acute{S}\grave{S}$ are unchanged, provided we interpret "cos i" as an imaginary quantity given by (5.48), so that now the coefficients $\acute{S}\grave{P}$ and $\acute{S}\grave{S}$ are no longer real. Consequently, when the real part is taken of the vector components in (5.49) to obtain the physical displacement, we find there is a phase shift of amount ϕ, where ϕ = phase ($\acute{S}\grave{P}$) for the horizontal component and $\phi = \pi/2 +$ phase ($\acute{S}\grave{P}$) for the vertical. At fixed p, the phase shift is the same for all positive frequencies, and it is easy to see that the shift is in the opposite direction for all negative frequencies.

BOX **5.5**

Phase shifts: phase delay and phase advance

Phase shifts in a propagating wave are caused by a variety of mechanisms. Thus, in the phase factor $\exp[i\omega(\mathbf{s}\cdot\mathbf{x}-t)]$, we can define a phase shift due to propagation as $\phi(\omega)=\omega\mathbf{s}\cdot\mathbf{x}$. Such a shift is termed a *phase delay*, since it is the equivalent of evaluating the basic time variation $\exp(-i\omega t)$ at a time delayed by $\mathbf{s}\cdot\mathbf{x}$, i.e., as $\exp[-i\omega(t-\mathbf{s}\cdot\mathbf{x})]$.

Another example of a phase shift occurs in equation (5.49), showing that the downward vertical component of motion in an inhomogeneous P-wave has a phase that is $\pi/2$ greater than the phase of the horizontal component in the direction of propagation. This too is an example of phase delay: the maximum downward displacement is delayed a time $\pi/(2\omega)$ with respect to the maximum horizontal component (in the direction of propagation). The time delay is a quarter of a period, leading to prograde particle motion (see Problem 5.4).

In contrast, the phase shift occurring in $\acute{S}\grave{S}$, due to an SV-wave incident on a free surface at angle j greater than $\sin^{-1}(\beta/\alpha)$, is a *phase advance*. This can be seen from (5.32) with $\cos i$ having a positive imaginary part, so that the phase of $\acute{S}\grave{S}$ is negative (see also Fig. 5.10), corresponding to an evaluation of $\exp(-i\omega t)$ at an *earlier* time.

Our overall point here is that the sign of a phase shift can depend on the sign of frequency (see (5.48)) and on our convention of signs in the Fourier time transform, but the designations "phase delay" and "phase advance" are more fundamental, and give a better indication of the physical significance of the phenomenon causing the phase shift. Thus, in Section 5.5, we shall discuss the phase delay due to attenuation, and in Chapter 9 we shall find that a phase advance occurs when a body wave touches a caustic.

Although the derived P-wave (5.49) is an inhomogeneous wave, the reflected S-wave does not decay with depth. From Table 5.1, with $\cos j$ real and equal to $\sqrt{1-\beta^2p^2}$, the reflected S-wave displacement is

$$S\left(\sqrt{1-\beta^2p^2},0,-\beta p\right)\ \acute{S}\grave{S}\ \exp\left[i\omega\left(px+\sqrt{\frac{1}{\beta^2}-p^2}\,z-t\right)\right]. \tag{5.50}$$

But because of the phase shift in $\acute{S}\grave{S}$, it is no longer true that the pulse shape of the reflected S-wave is the same as that of the incident wave. From the argument in Box 5.6, the reflected pulse shape is a linear combination of the incident shape and its Hilbert transform.

In Figure 5.10, we show $\acute{S}\grave{P}$ and $\acute{S}\grave{S}$ as functions of p in the range $0\le p\le 1/\beta$, giving both amplitude and phase.

As another example of the need for using inhomogeneous waves, consider the reflection and transmission of SH-waves, as described in Figure 5.7 and equations (5.33). Inhomogeneous waves will be present in the upper medium if $1/\beta_1 < p$, and then this wave attenuates away from the interface, provided that we again choose

$$\frac{\cos j_1}{\beta_1}=+i\sqrt{p^2-\frac{1}{\beta_1^2}}\qquad\text{(in the case }\omega>0\text{)}, \tag{5.51}$$

BOX **5.6**

The Hilbert transform and the frequency-independent phase advance

If the Fourier components of a function $f = f(t)$ are all advanced in phase by $\pi/2$, then the resulting phase-distorted function in the time domain is

$$\begin{aligned}
&\frac{1}{2\pi}\int_{-\infty}^{\infty} f(\omega)\exp\left[-i\omega\left(t+\left|\frac{\pi}{2\omega}\right|\right)\right]d\omega \\
&\quad=\frac{1}{2\pi}\int_{-\infty}^{\infty} f(\omega)\exp\left(-i\frac{\pi}{2}\mathrm{sgn}(\omega)\right)\exp(-i\omega t)\,d\omega \qquad (1)\\
&\quad=\frac{1}{2\pi}\int_{-\infty}^{\infty}(-i\,\mathrm{sgn}(\omega))f(\omega)\exp(-i\omega t)\,d\omega
\end{aligned}$$

where $\mathrm{sgn}(\omega) = \pm 1$ according as $\omega \gtrless 0$. Substituting $f(\omega) = \int_{-\infty}^{\infty} f(\tau)\exp(i\omega\tau)\,d\tau$ in (1), we obtain the equivalent formula

$$\frac{1}{\pi}\int_0^{\infty} d\omega\int_{-\infty}^{\infty} f(\tau)\sin[\omega(\tau-t)]\,d\tau, \qquad (2)$$

sometimes called the *allied function* of $f(t)$. Integrating over ω in (2), one finds also the form

$$\frac{1}{\pi}\int_{-\infty}^{\infty}\frac{f(\tau)}{\tau-t}\,d\tau, \qquad (3)$$

in which the singularity at $\tau = t$ is handled by taking the principal value of the integral, i.e., by cancelling out the singular contributions from τ just greater and just less than t.

The form (3) is one common definition of the Hilbert transform of $f(t)$, which we symbolize by $\mathcal{H}[f(t)]$. It can also be seen as a convolution (denoted by $*$), so that the final equivalent form for the distorted signal is

$$f(t) * (-1/\pi t). \qquad (4)$$

We shall loosely refer to any one of the versions (1)–(4) as the Hilbert transform of $f(t)$. In practice, when this transform is to be computed, the original form (1) is the most straightforward: one Fourier transform gives $f(\omega)$, and the $\pi/2$ phase advance reduces to an interchange of real and imaginary parts of $f(\omega)$ (with a sign change in the resulting imaginary part). An inverse Fourier transform then returns the required $\mathcal{H}[f(t)]$.

Note that

$$\mathcal{H}[f(t)] = \frac{1}{\pi}\int_0^{\infty} d\omega\int_{-\infty}^{\infty} f(\tau)\sin[\omega(\tau-t)]\,d\tau,$$

whereas

$$f(t) = \frac{1}{\pi}\int_0^{\infty} d\omega\int_{-\infty}^{\infty} f(\tau)\cos[\omega(\tau-t)]\,d\tau.$$

If the Hilbert transform pair, $f(t)$ and $\mathcal{H}[f(t)]$, is itself Hilbert-transformed, the resulting pair is $\mathcal{H}[f(t)]$ and $-f(t)$. This polarity reversal is simply a result of two $\pi/2$ phase advances.

(continued)

BOX **5.6** *(continued)*

Arons and Yennie (1950) pointed out that if a function $f(t)$ undergoes a phase advance ε, then the resulting function may be calculated from a linear combination of $f(t)$ and its Hilbert transform. The large class of seismological examples of such phase shifts includes all plane waves that are supercritically reflected or transmitted at a discontinuity such as the Earth's free surface, ocean bottom, crust–mantle boundary, or core–mantle boundary. Choy and Richards (1975) pointed out several examples in seismograms of SH-waves and SV-waves. Constants in the linear combination may be derived as follows:

$$\begin{aligned}&\frac{1}{2\pi}\int_{-\infty}^{\infty} f(\omega)\exp[-i\varepsilon\ \mathrm{sgn}(\omega)]\exp(-i\omega t)\,d\omega\\&\quad=\frac{1}{2\pi}\int_{-\infty}^{\infty} f(\omega)[\cos\varepsilon - i\ \mathrm{sgn}(\omega)\sin\varepsilon]\exp(-i\omega t)\,d\omega\\&\quad=\cos\varepsilon\ f(t)+\sin\varepsilon\ \mathcal{H}[f(t)].\end{aligned}\tag{5}$$

The most important Hilbert transform is that of the Dirac delta function $\delta(t)$, which is $(-1/\pi t)$. A box function that is unity for $0 < t < T$ and zero elsewhere has the Hilbert transform $(-1/\pi)(\log|t| - \log|t - T|)$. If $t \ll T$, the box function approaches the Heaviside function $H(t)$, and its Hilbert transform approaches $(-1/\pi)\log|t/T|$.

Note that a Hilbert-transformed function has the same Fourier amplitude spectrum as the original function.

for then $\exp[-i\omega(\beta^{-1}\cos j)z] \to 0$ as $z \to -\infty$, when $1/\beta < p$. The phenomenon of *total internal reflection* can occur if the lower medium (velocity β_2) has slower S-waves than the upper medium (i.e., $\beta_2 < \beta_1$), and an SH-wave is incident upward from below. For slowness in the range $1/\beta_1 < p < 1/\beta_2$, the incident wave is an ordinary traveling plane wave, and the scattered waves are still correctly given by Table 5.2 and formulas (5.33), provided that $\cos j_1$ is interpreted by (5.51). In particular, note that $|\acute{S}\grave{S}| = 1$, but there is a phase shift in the reflection. (See J.A. Hudson (1962) for an analysis of energy flux in this problem.) Since the behavior for p in the range $0 \le p < 1/\beta_1$ is so different, it is natural to refer to $p = 1/\beta_1$ as a *critical value* and $j_2 = \sin^{-1}(\beta_2/\beta_1)$ as the *critical angle of incidence*. We shall refer to a wave whose slowness components are all real as a *homogeneous* wave, so that in this SH example, the transmitted wave is homogeneous or inhomogeneous according as p is less than or greater than a critical value.

As a general rule, *all* the reflection/transmission coefficients associated with a particular interface will become complex if *at least one* of the waves set up at the interface by an incident wave is an inhomogeneous wave. So far, we have looked at examples in which the incident wave is homogeneous, in which case at least one of the scattered waves must also be a homogeneous wave; the overall picture is still one of energy propagating toward the boundary, then interacting with the other half-space and finally propagating away from the interface.

The next possibility we must consider is that *all* the plane waves interacting with the boundary are inhomogeneous waves. Thus, for inhomogeneous plane P- and SV-waves at the free surface of a half-space (Fig. 5.5, Table 5.1), we consider slowness in the range

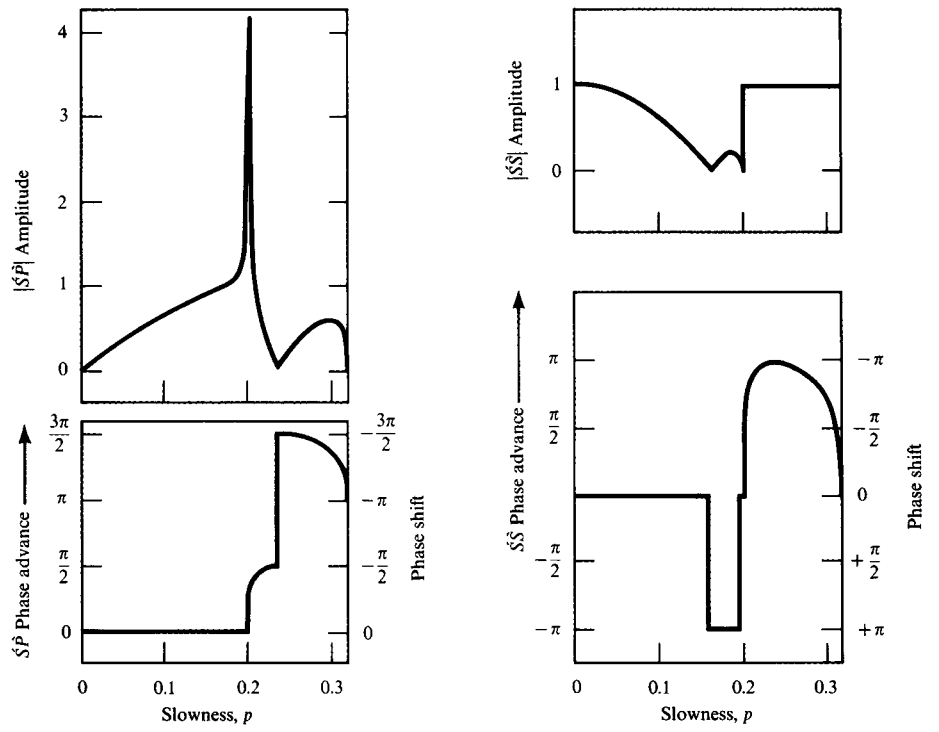

FIGURE **5.10**
The amplitude and phase of two reflection coefficients are shown as a function of p, the horizontal slowness. The coefficients are $\acute{S}\grave{P}$ and $\acute{S}\grave{S}$ for an SV-wave incident on the free surface, and we have taken $\alpha = 5$ km/s, $\beta = 3$ km/s, so that these coefficients have already been shown in Figure 5.6 for the range $0 \leq p \leq 1/\alpha$. Here we extend the range to $0 \leq p \leq 1/\beta$, so that an inhomogeneous P-wave is present for the range $1/\alpha < p \leq 1/\beta$. We have chosen to emphasize phase advance rather than phase shift, since the former is independent of the sign of frequency and independent of our Fourier sign convention. The phases actually plotted are those of $\acute{S}\grave{P}$ and $\acute{S}\grave{S}$ as determined by (5.31) and (5.32). Note that zeros in the coefficients are now associated with jumps of amount π in phase.

$1/\alpha < 1/\beta < p$. In this case, we have a very different overall picture from that considered so far, since now the energy is no longer transmitted toward the boundary and scattered from it. Rather, it can be channelled only along the boundary itself. For a half-space we cannot permit unbounded waves, so that the only permissible wave types are those which exponentially decay with distance from the surface:

$$\grave{P}\left(\alpha p, 0, i\sqrt{\alpha^2 p^2 - 1}\right) \exp\left(-\omega\sqrt{p^2 - \frac{1}{\alpha^2}}\, z\right) \exp[i\omega(px - t)] \qquad (5.52)$$

for the inhomogeneous P-wave, and

$$\grave{S}\left(i\sqrt{\beta^2 p^2 - 1}, 0, -\beta p\right) \exp\left(-\omega\sqrt{p^2 - \frac{1}{\beta^2}}\, z\right) \exp[i\omega(px - t)] \qquad (5.53)$$

for the inhomogeneous SV-wave. In each of (5.52) and (5.53), the first factor ($\grave{P}$ or $\grave{S}$) gives the displacement amplitude at $z = 0$. The second factor is a unit vector (in the sense that $l_x^2 + l_z^2 = 1$ implies $\mathbf{l}$ is a unit vector, even though $l_x > 1$). The third factor gives the amplitude decay with depth (which is different for P- and S-waves), and the final factor gives the phase due to horizontal propagation and time. These two waves are coupled by boundary conditions ($\tau_{zx} = \tau_{zz} = 0$ on $z = 0$), and, just as we found previously for homogeneous waves, the amplitude ratio of these two inhomogeneous waves is determined by these two conditions. The difference this time is that we have not identified a specific incident wave in the coupled system, so that there is one less amplitude ratio to be determined, with no reduction in the number of boundary conditions. The free surface boundary condition requires that

$$2p\alpha\beta i\sqrt{p^2 - 1/\alpha^2}\,\grave{P} + (1 - 2\beta^2 p^2)\,\grave{S} = 0 \qquad (\text{from } \tau_{zx} = 0 \text{ on } z = 0) \tag{5.54}$$

and

$$(1 - 2\beta^2 p^2)\,\grave{P} - 2(\beta^3 p/\alpha)i\sqrt{p^2 - 1/\beta^2}\,\grave{S} = 0 \qquad (\text{from } \tau_{zz} = 0 \text{ on } z = 0). \tag{5.55}$$

Since these are two equations for the same amplitude ratio ($\grave{S}/\grave{P}$), the determinant of coefficients must vanish and p must satisfy $\mathsf{R}(p) = 0$, where

$$\begin{aligned} \mathsf{R}(p) &\equiv \left(\frac{1}{\beta^2} - 2p^2\right)^2 - 4p^2\sqrt{p^2 - \frac{1}{\alpha^2}}\sqrt{p^2 - \frac{1}{\beta^2}} \\ &= \left(\frac{1}{\beta^2} - 2p^2\right)^2 + 4p^2\frac{\cos i}{\alpha}\frac{\cos j}{\beta}. \end{aligned} \tag{5.56}$$

This function of p^2 has just one zero (for positive imaginary "cosines"), which is real and positive. Since the corresponding positive value of p is slightly (4–14%) greater than $1/\beta$ for all elastic solids, it is indeed possible for a coupled pair of inhomogeneous waves, P and SV, to propagate along the surface of a half-space. The surface wave is named for Rayleigh, who described its properties in 1886, and $\mathsf{R}(p)$ defined in (5.56) is known as the *Rayleigh function*. Note that the Rayleigh function is just the denominator of the plane-wave coefficients given in (5.27), (5.28), (5.31), (5.32). Rayleigh waves are widely observed in seismology, and as a surface wave for a homogeneous half-space we note the following main properties:

(i) their propagation speed c_R, where $\mathsf{R}(1/c_R) = 0$, is a few percent less than the shear-wave speed;

(ii) c_R is independent of frequency, hence the wave does not disperse (this property arises physically because there is no intrinsic length scale in a homogeneous half-space, though we shall find in Chapter 7 that surface waves in media with depth-dependent properties are necessarily dispersed);

(iii) the particles move in an elliptical trajectory (see Fig. 5.11) that is retrograde at the free surface (this result, developed in Problems 5.4 and 5.5, is remarkable in that for each

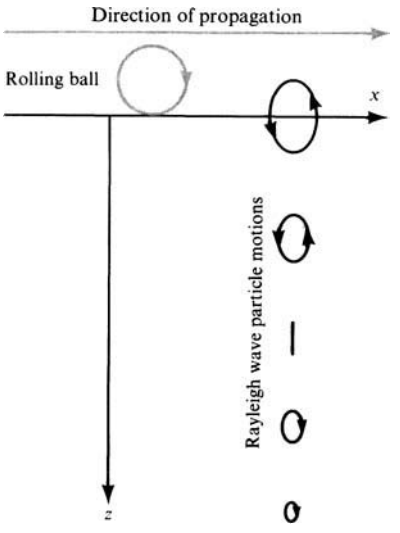

FIGURE **5.11**
The sense of particle motion in a Rayleigh wave as a function of depth. The convention for distinguishing between prograde and retrograde motion can be remembered in terms of a ball rolling along the top of the half-space from source to receiver. The sense of rotation of the ball is prograde, which is the direction of motion for inhomogeneous P- and SV-waves, and also for the Rayleigh wave at sufficient depth. However, the particle motion for the Rayleigh wave at the surface is retrograde.

of the component inhomogeneous waves, P and SV, the particle motion is prograde elliptical);

(iv) below a certain depth, which depends on frequency, the particle motion in a Rayleigh wave is dominated by the SV-component, and hence becomes prograde elliptical.

Once the above theory for Rayleigh waves is thoroughly grasped, the generalization to interface waves ($P - SV$) for two homogeneous half-spaces can be readily obtained. Such a wave is composed of inhomogeneous waves decaying upward in the upper medium and decaying downward in the lower medium, so that particle motions are effectively confined to the vicinity of the interface. In terms of the "scattered" waves listed in Table 5.3, we therefore make the following interpretations (for positive frequency):

$$\begin{aligned} \frac{\cos i_1}{\alpha_1} &\to +i\sqrt{p^2 - \frac{1}{\alpha_1^2}}; & \frac{\cos j_1}{\beta_1} &\to +i\sqrt{p^2 - \frac{1}{\beta_1^2}}, \\ \frac{\cos i_2}{\alpha_2} &\to +i\sqrt{p^2 - \frac{1}{\alpha_2^2}}; & \frac{\cos j_2}{\beta_2} &\to +i\sqrt{p^2 - \frac{1}{\beta_2^2}}, \end{aligned} \tag{5.57}$$

(compare with (5.51) and (5.48)), and the possible values of horizontal slowness p are determined by the requirement that $\mathsf{D}(p) = 0$, where D is defined in (5.39). Of course, we are interested only in real roots, for which p is greater than the largest of $(1/\alpha_1, 1/\beta_1, 1/\alpha_2, 1/\beta_2)$, so that all the "cosines" in (5.57) are pure imaginary. It was shown by Scholte (1947) that $\mathsf{D}(p) = 0$ always has four roots (i.e., two values of p^2, with four roots for p), but that these are real and appropriately large only when the ratios ρ_1/ρ_2 and β_1/β_2 lie in certain ranges. These waves are named for Stoneley, who discovered their main properties in 1924. As a special case, Stoneley waves can always exist at the interface between a fluid and a solid.

Note that frequency does not enter the definition of D, so Stoneley waves, like Rayleigh waves, are not dispersive (for homogeneous half-spaces).

In this section, we have chosen to emphasize the differences between homogeneous and inhomogeneous waves, although we have unified the theory by studying these waves as a function of their horizontal slowness. In later work, we shall refer to both these wave types as "plane waves," finding that both types are required to synthesize the wave system set up by a localized source. We shall find in Chapter 6 how the Hilbert transform arises in wide-angle reflections, and in Chapter 7 how surface waves are associated with poles of reflection coefficients. To prepare for these later chapters, it is helpful now to introduce a systematic matrix method for working with the fundamental (plane wave) solutions.

5.4 A Matrix Method for Analyzing Plane Waves in Homogeneous Media

For all the plane waves that were considered in Section 5.3, the equations of motion and the constitutive relation can be combined in such a way that only first-order depth derivatives of stress and displacement are needed. By this statement, we mean that plane waves in homogeneous media can be studied in terms of an equation of the type

$$\frac{d\mathbf{f}}{dz} = \mathbf{A}\mathbf{f}, \tag{5.58}$$

in which $\mathbf{f} = \mathbf{f}(z)$ is a column-vector giving the depth dependence of particle displacement and stress. $\mathbf{A}$ is a constant matrix (i.e., independent of z), with entries depending on elastic properties of the (homogeneous) medium and on horizontal slowness p and frequency ω.

For example, the SH-waves considered in Table 5.2 are all a result of analyzing the displacement $u_y = v = v(x, z, t)$ in which the dependence on (x, t) is only via a factor $\exp[i\omega(px - t)]$. The equation of motion is $\rho\ddot{v} = \tau_{yz,z} + \tau_{yx,x}$, and the constitutive relation (2.18) becomes merely $\tau_{yz} = \mu\partial v/\partial z$, $\tau_{yx} = \mu\partial v/\partial x$. It follows that such SH problems can be discussed in terms of the vector $\mathbf{f}$ given by

$$\mathbf{f}(z)\exp[i\omega(px - t)] = \begin{pmatrix} v \\ \tau_{yz} \end{pmatrix}, \tag{5.59}$$

and the depth dependence of $\mathbf{f}$ is given by solving the standard equation (5.58) with coefficient matrix

$$\mathbf{A} = \begin{pmatrix} 0 & \mu^{-1} \\ \omega^2(\mu p^2 - \rho) & 0 \end{pmatrix}. \tag{5.60}$$

For acoustic waves (see Box 5.4), with pressure P and vertical particle displacement u_z, we take

$$\mathbf{f}(z)\exp[i\omega(px - t)] = \begin{pmatrix} u_z \\ P \end{pmatrix} \quad \text{and} \quad \mathbf{A} = \begin{pmatrix} 0 & \dfrac{p^2}{\rho} - \dfrac{1}{\rho\alpha^2} \\ \rho\omega^2 & 0 \end{pmatrix}. \tag{5.61}$$

For *P–SV* waves, we take

$$\mathbf{f}(z)\exp[i\omega(px-t)]=\begin{pmatrix} u_x \\ u_z \\ \tau_{zx} \\ \tau_{zz} \end{pmatrix} \quad \text{and}$$

$$\mathbf{A}=\begin{pmatrix} 0 & -i\omega p & \frac{1}{\mu} & 0 \\ \frac{-i\omega p\lambda}{\lambda+2\mu} & 0 & 0 & \frac{1}{\lambda+2\mu} \\ \frac{4\omega^2 p^2\mu(\lambda+\mu)}{\lambda+2\mu}-\rho\omega^2 & 0 & 0 & \frac{-i\omega p\lambda}{\lambda+2\mu} \\ 0 & -\rho\omega^2 & -i\omega p & 0 \end{pmatrix}. \tag{5.62}$$

A great deal is known about the solutions of coupled first-order differential equations like $d\mathbf{f}/dz = \mathbf{A}\mathbf{f}$ (see, e.g., Coddington and Levinson, 1955; Gantmacher, 1959), and we shall make extensive use of this theory in Chapters 7–9 to study wave propagation in inhomogeneous media. Our present discussion, however, concerns homogeneous media, for which $\mathbf{A}$ is independent of z.

The first property to notice is that, if $\mathbf{v}^\alpha$ is an eigenvector of $\mathbf{A}$ and λ^α is the associated eigenvalue, a solution to (5.58) is given by

$$\mathbf{f}=\mathbf{v}^\alpha \exp[\lambda^\alpha(z-z_{\text{ref}})] \tag{5.63}$$

(no summation over superscript α), where z_{ref} is a reference level for the exponential.

Now let $\mathbf{F}$ be the matrix whose columns consist of different solutions of type (5.63). Thus, if $\mathbf{A}$ is an $n \times n$ matrix, we can find n eigenvalues and n linearly independent eigenvectors ($\alpha = 1, \ldots, n$), so that $\mathbf{F}$ is also an $n \times n$ matrix, with the αth column given by $\mathbf{v}^\alpha \exp[\lambda^\alpha(z - z_{\text{ref}})]$. It follows that the most general solution $\mathbf{f}$ to the equation $d\mathbf{f}/dz = \mathbf{A}\mathbf{f}$ is some linear combination of the columns of $\mathbf{F}$, i.e.,

$$\mathbf{f}=\mathbf{F}\mathbf{w}, \tag{5.64}$$

where $\mathbf{w}$ is a vector of constants, weighting the columns of $\mathbf{F}$ that appear in solution $\mathbf{f}$.

The reason why an analysis of plane waves in terms of such eigenvalues and eigenvectors can be powerful lies in the physical interpretation of (5.63) and (5.64). Thus consider the case of *SH*-waves, for which $d\mathbf{f}/dz = \mathbf{A}\mathbf{f}$, with $\mathbf{f}$ and $\mathbf{A}$ given in (5.59) and (5.60). The two eigenvalues of $\mathbf{A}$ are $\pm i\omega\sqrt{1/\beta^2 - p^2} = \pm i\omega\beta^{-1}\cos j$, which are merely i times the vertical wavenumbers for downward and upward traveling *SH*-waves. The quantity $\beta^{-1}\cos j$ is the vertical slowness for *S* waves, and we introduce the notation

$$\eta=\frac{\cos j}{\beta}=\sqrt{\frac{1}{\beta^2}-p^2}. \tag{5.65}$$

Corresponding to eigenvalues $\pm i\omega\eta$ are the eigenvectors

$$\begin{pmatrix} 1 \\ \pm i\omega\mu\eta \end{pmatrix}.$$

Hence, following (5.63), the basic solutions for SH motion are either of type

$$\begin{pmatrix} 1 \\ i\omega\mu\eta \end{pmatrix} \exp[i\omega\eta(z - z_{\text{ref}})]$$

or of type

$$\begin{pmatrix} 1 \\ -i\omega\mu\eta \end{pmatrix} \exp[-i\omega\eta(z - z_{\text{ref}})].$$

Clearly, the first of these gives particle displacement and shearing stress for a downgoing SH-wave, and the second is for an upgoing wave. The most general type of plane SH-wave is a linear combination of these, so that the interpretation of vector $\mathbf{w}$ (appearing in (5.64)) is that its first component gives the amount of downgoing wave, and its second component gives the amount of upgoing wave, present in the total wave system $\mathbf{f}$.

Note that the matrix $\mathbf{F}$ for SH-waves can be explicitly stated as

$$\begin{aligned} \mathbf{F} &= \begin{pmatrix} 1 & 1 \\ i\omega\mu\eta & -i\omega\mu\eta \end{pmatrix} \begin{pmatrix} \exp[i\omega\eta(z - z_{\text{ref}})] & 0 \\ 0 & \exp[-i\omega\eta(z - z_{\text{ref}})] \end{pmatrix} \\ &= \mathbf{E}\Lambda, \end{aligned} \tag{5.66}$$

and $\mathbf{F}$ itself has been factored into a matrix $\mathbf{E}$, made up from eigenvectors of $\mathbf{A}$, times a diagonal matrix Λ containing the vertical phase factors, which have been referred to the level z_{ref}. $\mathbf{F}$ is known as the *solution matrix*, or (within the context in which it has been most used in seismology) the *layer matrix*. The inverse of $\mathbf{F}$ for SH-waves is

$$\mathbf{F}^{-1} = \Lambda^{-1}\mathbf{E}^{-1} = \begin{pmatrix} \exp[-i\omega\eta(z - z_{\text{ref}})] & 0 \\ 0 & \exp[i\omega\eta(z - z_{\text{ref}})] \end{pmatrix} \begin{pmatrix} \frac{1}{2} & \frac{-i}{2\omega\mu\eta} \\ \frac{1}{2} & \frac{i}{2\omega\mu\eta} \end{pmatrix}. \tag{5.67}$$

For P–SV waves, the four eigenvalues of $\mathbf{A}$ are $\pm i\omega\xi$, where

$$\xi = \frac{\cos i}{\alpha} = \sqrt{\frac{1}{\alpha^2} - p^2}, \tag{5.68}$$

and $\pm i\omega\eta$, where η is given by (5.65). The general solution of $d\mathbf{f}/dz = \mathbf{A}\mathbf{f}$ (with $\mathbf{f}$, $\mathbf{A}$ given in (5.62)) is again $\mathbf{f} = \mathbf{F}\mathbf{w}$, with $\mathbf{F}$ factored into $\mathbf{E}\Lambda$, and

$$\mathbf{E} = \begin{pmatrix} \alpha p & \beta\eta & \alpha p & \beta\eta \\ \alpha\xi & -\beta p & -\alpha\xi & \beta p \\ 2i\omega\rho\alpha\beta^2 p\xi & i\omega\rho\beta(1-2\beta^2p^2) & -2i\omega\rho\alpha\beta^2 p\xi & -i\omega\rho\beta(1-2\beta^2p^2) \\ i\omega\rho\alpha(1-2\beta^2p^2) & -2i\omega\rho\beta^3 p\eta & i\omega\rho\alpha(1-2\beta^2p^2) & -2i\omega\rho\beta^3 p\eta \end{pmatrix}, \tag{5.69}$$

$$\Lambda = \begin{pmatrix} \exp[i\omega\xi(z-z_{\text{ref}})] & 0 & 0 & 0 \\ 0 & \exp[i\omega\eta(z-z_{\text{ref}})] & 0 & 0 \\ 0 & 0 & \exp[-i\omega\xi(z-z_{\text{ref}})] & 0 \\ 0 & 0 & 0 & \exp[-i\omega\eta(z-z_{\text{ref}})] \end{pmatrix}.$$

Note that components of $\mathbf{f}$ are just those physical quantities that are continuous across a welded interface. Thus, for $P-SV$ problems, we have seen that $u_x, u_z, \tau_{zx}, \tau_{zz}$ are continuous across a horizontal boundary ($z = 0$, say) between two different half-spaces. Hence, from (5.62), $\mathbf{f}$ is continuous, although $\mathbf{A}$ is not.

The matrix method we are developing plays a major role in the study of plane waves propagating in a stack of homogeneous layers. As a very simple example, we shall indicate a derivation of formulas (5.33) that gives all reflection/transmission coefficients for SH-waves incident on the boundary between two half-spaces.

Going back to Figure 5.7, we have $\mathbf{f} = \mathbf{F}_1(z)\mathbf{w}_1$ in the upper medium ($z < 0$), where $\mathbf{F}_1$ is given by (5.66) with values of ρ, β, j appropriate to the upper medium, and $\mathbf{w}_1$ is a vector giving the amounts of downgoing and upgoing wave in the upper medium. Similarly, in the lower medium ($z > 0$), $\mathbf{f} = \mathbf{F}_2(z)\mathbf{w}_2$. Then

$$\mathbf{F}_1(0)\mathbf{w}_1 = \mathbf{F}_2(0)\mathbf{w}_2, \tag{5.70}$$

since $\mathbf{f}$ is continuous across $z = 0$, giving a general relation between the upgoing and downgoing wave systems in the two media, whatever these systems may be.

To solve for $\grave{S}\acute{S}$, etc., we apply (5.70) to the two cases shown in Figure 5.7. Thus, for SH incident from above, we have

$$\mathbf{w}_1 = \begin{pmatrix} 1 \\ \grave{S}\acute{S} \end{pmatrix} \quad \text{and} \quad \mathbf{w}_2 = \begin{pmatrix} \grave{S}\grave{S} \\ 0 \end{pmatrix}.$$

Substitution of these into (5.70) gives two scalar equations in the two unknowns $\grave{S}\acute{S}$ and $\grave{S}\grave{S}$. For SH incident from below, we have

$$\mathbf{w}_1 = \begin{pmatrix} 0 \\ \acute{S}\acute{S} \end{pmatrix} \quad \text{and} \quad \mathbf{w}_2 = \begin{pmatrix} \acute{S}\grave{S} \\ 1 \end{pmatrix},$$

which again we can substitute into (5.70), to obtain two scalar equations for $\acute{S}\acute{S}$ and $\acute{S}\grave{S}$.

In practice, it is often worthwhile to normalize the eigenvectors $\mathbf{v}^\alpha$ so that the associated particle displacement has unit amplitude. We did this above, for our discussion both of SH and $P-SV$. In order to keep frequency as a common factor for all terms in $\mathbf{E}$, some authors

use components of particle velocity and traction to define the solution vector $\mathbf{f}$, rather than components of displacement and traction as we have done in (5.59) and (5.62).

As we shall find in Chapters 7 and 9, a major reason why these matrix methods are important is that they permit computation of the waves that interact with numerous homogeneous layers and with the interfaces between them. Computations are facilitated by the fact that the matrix $\mathbf{F}(z)$ has an inverse $\mathbf{F}^{-1} = \mathbf{\Lambda}^{-1}\mathbf{E}^{-1}$ that can be stated in closed form. For example, for $P - SV$ waves the matrix $\mathbf{E}$ of (5.69) has inverse

$$\mathbf{E}^{-1} = \begin{pmatrix} \dfrac{\beta^2 p}{\alpha} & \dfrac{1-2\beta^2 p^2}{2\alpha\xi} & \dfrac{-ip}{2\omega\rho\alpha\xi} & \dfrac{-i}{2\omega\rho\alpha} \\ \dfrac{1-2\beta^2 p^2}{2\beta\eta} & -\beta p & \dfrac{-i}{2\omega\rho\beta} & \dfrac{ip}{2\omega\rho\beta\eta} \\ \dfrac{\beta^2 p}{\alpha} & \dfrac{-(1-2\beta^2 p^2)}{2\alpha\xi} & \dfrac{ip}{2\omega\rho\alpha\xi} & \dfrac{-i}{2\omega\rho\alpha} \\ \dfrac{1-2\beta^2 p^2}{2\beta\eta} & \beta p & \dfrac{i}{2\omega\rho\beta} & \dfrac{ip}{2\omega\rho\beta\eta} \end{pmatrix}. \tag{5.71}$$

5.5 Wave Propagation in an Attenuating Medium: Basic Theory for Plane Waves

For the adiabatic wave propagation we have so far been describing, wave motion will continue indefinitely, once it has been initiated by some specific source. Thus the wave motion may be spatially attenuated, as waves spread away from a localized source region, but the total energy of particle motion (i.e., the volume integral of kinetic energy and elastic strain energy throughout the medium) has been held constant. This follows from the discussion in Section 2.2. In contrast to such idealized behavior, however, it is common experience that as a wave is propagated through real materials, wave amplitudes attenuate as a result of a variety of processes, which we can summarize macroscopically as "internal friction."

To give but two examples: the strains and stresses occurring within a propagating wave can lead to irreversible changes in the crystal defect structures of the medium, and work may also be done on grain boundaries within the medium if adjacent material grains are not elastically bonded. Such media are said to be *anelastic*, since the configuration of material particles is to some extent dependent on the history of applied stress. The gross effect of internal friction is summarized by the dimensionless quantity Q, defined in various ways (for slightly anelastic media) in Box 5.7.

The general subject of wave attenuation by internal friction (sometimes called intrinsic attenuation) is very large, as can be seen from identifying three different aspects:

(i) As a branch of materials science, studies are made of the fundamental (microscopic) processes that cause attenuation. The effects of a variety of crystal defects, grain-boundary processes, and some thermoelastic processes have been reviewed by Mason (1958), Jackson and Anderson (1970), and Nowick and Berry (1972).

(ii) The frequency dependence of Q is studied as a macroscopic phenomenon in a variety of materials. From observations of the frequency dependence of Q in seismic waves

BOX **5.7**
Different definitions of Q

If a volume of material is cycled in stress at a frequency ω, then a dimensionless measure of the internal friction (or the anelasticity) is given by

$$\frac{1}{Q(\omega)} = -\frac{\Delta E}{2\pi E}, \tag{1}$$

where E is the peak strain energy stored in the volume and $-\Delta E$ is the energy lost in each cycle because of imperfections in the elasticity of the material.

The definition is rarely of direct use, since only in special experiments is it possible to drive a material element with stress waves of unchanging amplitude and period. More commonly, one observes either (i) the temporal decay of amplitude in a standing wave at fixed wavenumber or (ii) the spatial decay of amplitude in a propagating wave at fixed frequency. The commonest situation in seismology involves attenuation of a signal composed of a range of frequencies, and we shall make the strong assumption (which must be checked later) that attenuation is a linear phenomenon, in the sense that a wave may be resolved into its Fourier components, each of which can be studied in terms of (i) or (ii), and that subsequent Fourier synthesis gives the correct effect of attenuation on actual seismic signals.

In the case of either (i) or (ii), for a medium with linear stress–strain relation, wave amplitude A is proportional to $E^{1/2}$. (For example, A may represent a maximum particle velocity, or a stress component in the wave. We assume also that $Q \gg 1$, so that successive peaks have almost the same strain energy.) Hence

$$\frac{1}{Q(\omega)} = -\frac{1}{\pi}\frac{\Delta A}{A}, \tag{2}$$

from which we can obtain the amplitude fluctuations due to attenuation.

Thus, in case (i), we ask: What is $A = A(t)$, given that initially $A = A_0$ and A decreases a fraction π/Q at successive times $2\pi/\omega, 4\pi/\omega, \ldots, 2n\pi/\omega \ldots$? Clearly,

$$A(t) = A_0(1 - \pi/Q)^n \qquad (\text{for } t = 2n\pi/\omega).$$

Thus, using the definition $\exp(x) = \lim_{n\to\infty} (1 + x/n)^n$,

$$A(t) = A_0\left[1 - \frac{\omega t}{2Qn}\right]^n \to A_0 \exp\left[-\frac{\omega t}{2Q}\right] \qquad (\text{for large } n;\ \text{i.e., for large times}). \tag{3}$$

From observations of exponentially decaying values of $A(t)$, we use (3) to define the value of a *temporal* Q. It is this value that is used in describing the attenuation of the Earth's free oscillations (see Chapter 8).

We were forced to obtain the above result (3) by using discrete times, since this is the nature of experiments based on case (i). For case (ii), however, the derivation of the form $A = A(x)$ for distance x is easier, since a particular wave peak can be followed along a distance dx, and the gradual spatial decay of A can be observed. (We assume here that the direction of maximum attenuation is along the x-axis, which is also the direction of propagation.) Then $\Delta A = (dA/dx)\lambda$, where λ is the wavelength given in terms of ω and

(continued)

BOX **5.7** *(continued)*

phase velocity c by $\lambda = 2\pi c/\omega$. Equation (2) becomes $dA/dx = -(\omega/2cQ)A$, with the exponentially decaying solution

$$A(x) = A_0 \exp\left[-\frac{\omega x}{2cQ}\right]. \tag{4}$$

From observations of exponentially decaying values of $A(x)$, we use (4) to define the value of a *spatial* Q. Of course, any spatial decay due to geometrical spreading effects must be studied too. In Section 5.5, we shall avoid this problem by confining our attention to plane waves propagating in homogeneous media. Such simple problems also avoid the complication of geometric dispersion due to material heterogeneity, which involves differences between Q measured via (3) and Q measured by (4). These additional effects of dispersion (which are present even in perfectly elastic media) are taken up in Section 7.3.4, in connection with surface waves.

Note that to obtain the effect of attenuation on a wave solution such as $e^{i(kx-\omega t)}$, an experiment to measure temporal Q can be thought of as replacing ω by a complex-valued frequency, and an experiment to measure spatial Q can be thought of as replacing k by a complex-valued wavenumber. In the first case, ω acquires an imaginary part, $-i\omega/2Q^{\text{temporal}}$; in the second case, k acquires an imaginary part, $ik/2Q^{\text{spatial}}$.

(Archambeau *et al.*, 1969; Solomon, 1972, 1973), one may then constrain the possibilities for Earth composition. Solomon used this method to estimate the extent of partial melting in the upper mantle.

(iii) Many authors have developed macroscopic stress–strain relations to replace Hooke's law, and hence (with $\rho\ddot{u}_i = \tau_{ij,j}$) have obtained equations of motion for materials with some particular $Q = Q(\omega)$. Critical here is the use of a causality constraint, which leads to the phenomenon of dispersion for an attenuating medium.

In the remainder of this chapter, we shall cover some of the ground mentioned in (iii), since pulse shapes observed in seismology are certainly influenced by internal friction. The principal result is that, if Q is effectively constant over the range of frequencies observed in seismology, then wave propagation in the attenuating Earth can be studied by considering body-wave velocity (α and/or β, which we have hitherto regarded as real and independent of frequency) as the complex-valued and frequency-dependent quantity defined in (5.94). But if Q varies significantly with frequency in the seismic range, then (5.94) may be inadequate.

5.5.1 THE NECESSITY FOR MATERIAL DISPERSION IN AN ATTENUATING MEDIUM

Consider a plane wave having the impulsive shape $\delta(t - x/c)$, propagating with speed c along the positive x-direction in a perfectly elastic homogeneous medium. As we have

shown in earlier sections of this chapter, such a wave retains its shape exactly, and all frequency components travel coherently with the same velocity c.

Now consider such a wave as the input at $x = 0$ to an attenuating medium. Knopoff (1964a) has summarized the experimental measurements of attenuation by concluding that $Q(\omega) \propto \omega^{-1}$ for a variety of fluids, but that Q is approximately constant for the frequency range of observation in solids. It is this type of behavior with which we are most concerned in seismology: Q is taken to be constant, or only weakly dependent on frequency.

Each Fourier component of the impulse,

$$\int_{-\infty}^{\infty} \delta(t - x/c)e^{i\omega t}\, dt = \exp[i\omega x/c],$$

will now be attenuated by a factor $\exp[-\alpha(\omega)x]$, and from equation (4) of Box 5.7 we find that this attenuation rate is $\alpha = \omega/(2cQ)$.

At distance x, what will be the pulse shape $p(x, t)$ (say) of the attenuated wave? As a first attempt at an answer, let us suppose that no dispersion is present, so that the pulse is a synthesis from its Fourier components, all having the same speed c. Then

$$p(x,t) = \frac{1}{2\pi}\int_{-\infty}^{\infty} \exp\left[\frac{-\omega x}{2cQ}\right] \exp\left[i\omega\left(\frac{x}{c} - t\right)\right] d\omega \tag{5.72}$$

(here $x > 0$, and Q is interpreted as an odd function of ω in order to evaluate attenuation for negative frequencies: see Problem 5.12). If Q is constant (for $\omega > 0$), the integral here is easily shown to be

$$p(x,t) = \frac{1}{\pi}\left[\frac{\dfrac{x}{2cQ}}{\left(\dfrac{x}{2cQ}\right)^2 + \left(\dfrac{x}{c} - t\right)^2}\right], \tag{5.73}$$

and this pulse shape is plotted against time at fixed distance x in Figure 5.12.

Unfortunately, Figure 5.12 shows this pulse shape to have several unacceptable features. It shows a (small) arrival at positions $x > 0$ *even before time* $t = 0$, which violates our most elementary notions of causality. It shows a rise time (see figure caption) that is too large (Stacey *et al.*, 1975, report that the measured rate of increase of τ with distance is

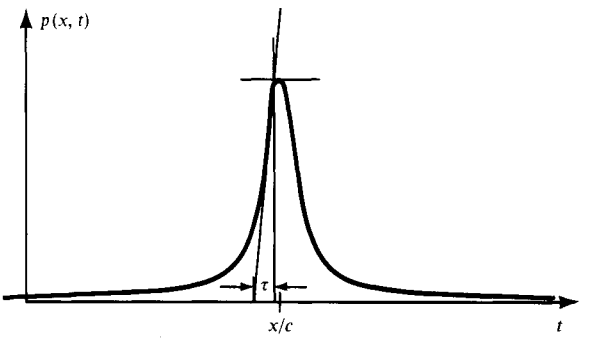

FIGURE **5.12**
The pulse shape $p(x, t)$ given by (5.73) is shown against time at a fixed distance. The rise time τ, defined by extrapolating the tangent to $p(x, t)$ at the point with maximum gradient, can be found in terms of x, c, Q as $\tau = 4x/(3\sqrt{3}cQ)$ for this pulse whereas the experimental rise time is found to be considerably shorter.

only $(2cQ)^{-1}$, but Fig. 5.12 and equation (5.73) imply about 1.5 times this rate); and the symmetrical shape of the pulse also disagrees with experiments, which show an asymmetric shape having a decay time much greater than the rise time.

In questioning the three assumptions that went into our derivation of this pulse shape (5.73), i.e., linearity, constant Q, and no dispersion, it is natural to try to retain the first two and relax the third. (The indirect evidence for retaining linearity is simply that it has led to self-consistent results in so many careful analyses of seismic data. Nowhere is this more clear than in studies of the Earth's normal modes, which are excited to observational levels by hundreds of earthquakes each year, with periods of oscillation that, to a high degree of precision, are found to be unchanged for different sources and different seismographs.) Although we shall shortly drop the assumption of constant Q, one of our points here is that we *must* permit some dispersion, since the symmetry of an attenuated impulse is otherwise unavoidable (Problem 5.12).

5.5.2 SOME SUGGESTED VALUES FOR MATERIAL DISPERSION IN AN ATTENUATING MEDIUM

Our first attempts at quantifying material dispersion will invoke the concept of a wavefront for anelastic media. We shall assume that a plane wave $u(x, t)$ propagates in the direction of increasing x and that the wavefront first arrives at position $x = 0$ at time $t = 0$. Thus

$$u(0, t) = 0 \qquad \text{for} \qquad t < 0. \tag{5.74}$$

At $x > 0$, each Fourier component of u can be factored as

$$u(x, \omega) = u(0, \omega) \exp(iKx),$$

where the complex wavenumber K is now given in terms of phase velocity $c(\omega)$ and attenuation factor $\alpha(\omega)$ by

$$K = \frac{\omega}{c(\omega)} + i\alpha(\omega). \tag{5.75}$$

With the assumption of linear superposition, the wave at (x, t) is

$$u(x, t) = \frac{1}{2\pi} \int_{-\infty}^{\infty} u(0, \omega) \exp[i(Kx - \omega t)]\, d\omega,$$

which is equivalent to the convolution of $u(0, t)$ with

$$p(x, t) = \frac{1}{2\pi} \int_{-\infty}^{\infty} \exp[i(Kx - \omega t)]\, d\omega, \tag{5.76}$$

$p(x, t)$ being the attenuated response to an impulse that was described earlier in (5.72). Now, however, we are allowing c to be frequency dependent, and in Box 5.8 we show that

requiring $p(x,t)$ to be zero until an arrival time x/c_∞ implies

$$\frac{\omega}{c(\omega)} = \frac{\omega}{c_\infty} + \mathcal{H}[\alpha(\omega)]. \tag{5.77}$$

Here, c_∞ is the limit of $c(\omega)$ as $\omega \to \infty$, and $\mathcal{H}[\alpha(\omega)]$ is the Hilbert transform of the attenuation factor.

It appears at this stage that the problem of finding values of $c(\omega)$ is essentially solved. We merely have to take the Hilbert transform of a constant-Q attenuation factor and then use (5.77). However, from equation (4) of Box 5.7, we require

$$\frac{\omega}{c_\infty} + \mathcal{H}[\alpha(\omega)] = 2Q\alpha(\omega), \tag{5.78}$$

and there is no Hilbert transform pair for which this relation is satisfied with constant Q. (If it *were* satisfied, we could Hilbert-transform (5.78). But this cannot be done, since the transform for ω/c_∞ is a divergent integral.) Instead, we must tolerate a frequency-dependent Q, satisfying (5.78), but with an attenuation chosen to make Q effectively constant over the seismic frequency range. This approach has been taken by Azimi *et al.* (1968), and one of the Hilbert transform pairs they have suggested using is

$$\alpha(\omega) = \frac{\alpha_0\omega}{1+\alpha_1\omega}, \qquad \mathcal{H}[\alpha(\omega)] = \frac{2\alpha_0\omega}{\pi(1-\alpha_1^2\omega^2)} \log\left(\frac{1}{\alpha_1\omega}\right), \tag{5.79}$$

in which α_0, α_1 are constants and log is the natural logarithm.

In Figure 5.13, we show the pulse shape (5.76) that results from Azimi's attenuation law (5.79). Note the asymmetry of the pulse and its delay with respect to the nondispersed pulse shape described earlier. Stacey *et al.* (1975) found that the rise time for Azimi's pulse shape does change with distance at the rate determined from measurement in a variety of solid materials, so that the dispersion corresponding to (5.79) is likely to be a good approximation for our needs in seismology. The presumption behind (5.79) is that $1 \gg \alpha_1\omega$ for all seismic

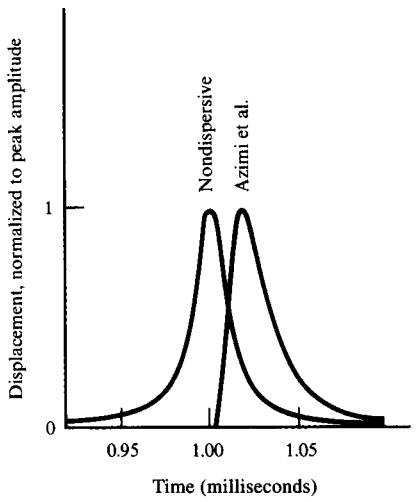

FIGURE **5.13**
Comparison of two attenuated pulse shapes $p(x,t)$, each for x fixed at 5 m. In the nondispersive case, $c = 5$ km/s and $Q = 50$ at all frequencies. In the dispersive case (using Azimi's attenuation law (5.79)), with $c(\omega)$ and $Q(\omega)$ given by (5.77)–(5.79), $c_\infty = 5$ km/s and $(2\alpha_0 c_\infty)^{-1} = 50$. [After Gladwin and Stacey, 1974.]

BOX 5.8

Relations between the amplitude spectrum and phase spectrum of a causal propagating pulse shape

We assume that the propagating pulse shape $p(x,t)$ has the Fourier transform e^{iKx} with real and imaginary parts of K given by

$$K = \frac{\omega}{c(\omega)} + i\alpha(\omega). \tag{1}$$

Then if

$$p(x,t) = 0 \qquad \text{for} \qquad t < x/c_\infty, \tag{2}$$

we shall show that

$$\frac{\omega}{c(\omega)} = \frac{\omega}{c_\infty} + \mathcal{H}[\alpha(\omega)]. \tag{3}$$

First, we note that the causality described in (2) is completely equivalent to the statement that

$$\begin{aligned} &F(\omega), \text{ defined by } F(\omega) = \exp[i(K - \omega/c_\infty)x], \text{ is analytic} \\ &\text{in the upper half-plane (i.e., for Im } \omega \geq 0). \end{aligned} \tag{4}$$

For, if (2) is true, then

$$F(\omega) = p(x,\omega)\exp(-i\omega x/c_\infty) = \int_{x/c_\infty}^{\infty} p(x,t)\exp[i\omega(t - x/c_\infty)]\,dt, \tag{5}$$

which, by Jordan's Lemma (see Box 6.8), does indeed converge in the upper half-plane. F and all its derivatives exist, hence (4) is obtained. On the other hand, if (4) is true, we write

$$p(x,t) = \frac{1}{2\pi}\int_{-\infty}^{\infty} F(\omega)\exp[-i\omega(t - x/c_\infty)]\,d\omega \tag{6}$$

and add a semicircular path at infinity in the upper half-plane (from which there is no contribution if $t < x/c_\infty$, since the exponential vanishes). The integrand in (6) is then analytic everywhere inside a closed contour, and so (2) is obtained.

Second, we show also that $\log F(\omega)$ is analytic in the upper half-plane. To prove this, we need show only that $F(\omega)$ has no zeros for which ω has a nonnegative imaginary part. Suppose, in fact, that $F(\omega_0) = 0$ for Im $\omega_0 \geq 0$. Then $F(\omega) = (\omega - \omega_0)^\lambda f(\omega)$ for some $\lambda > 0$ and some f with $f(\omega_0) \neq 0$. However, if x is increased to $x + \Delta x$, it follows from (4) that

$$(\omega - \omega_0)^{\lambda(1+\Delta x/x)} f(\omega)^{1+\Delta x/x}$$

is analytic in the upper half-plane—which is impossible, because in this form it is seen to have a branch point at ω_0.

(continued)

BOX **5.8** *(continued)*

Third, we note a special form of Cauchy's theorem: if $g(z)$ is analytic on and inside a closed circuit C, then for a point x *on* C *itself*, we have

$$g(x) = \frac{1}{\pi i} P \int_C \frac{g(z)\, dz}{z - x} \tag{7}$$

(where P indicates the process of taking Cauchy's principal value).

Finally, we apply (7) to the analytic function

$$\begin{aligned} \log F(\omega) &= \log|F(\omega)| + i \text{ phase } F(\omega) \\ &= -\alpha(\omega)x + i\omega \left(\frac{1}{c(\omega)} - \frac{1}{c_\infty} \right) x, \end{aligned} \tag{8}$$

using for C the infinite semicircle encompassing the upper half of the complex ω plane, with diameter as the real ω-axis. We find for a real value of ω that

$$\log F(\omega) = \frac{1}{\pi i} P \int_{-\infty}^{\infty} \frac{\log F(\zeta)\, d\zeta}{\zeta - \omega} \tag{9}$$

(unless there is a contribution from the arc of the semicircle; see below). Substituting from (8) into (9), and separating real and imaginary parts, we find

$$\alpha(\omega) = -\frac{1}{\pi} P \int_{-\infty}^{\infty} \zeta \left(\frac{1}{c(\zeta)} - \frac{1}{c_\infty} \right) \frac{d\zeta}{\zeta - \omega} = -\mathcal{H}\left[\omega \left(\frac{1}{c(\omega)} - \frac{1}{c_\infty} \right) \right] \tag{10}$$

and

$$\omega \left(\frac{1}{c(\omega)} - \frac{1}{c_\infty} \right) = \frac{1}{\pi} P \int_{-\infty}^{\infty} \frac{\alpha(\zeta)\, d\zeta}{\zeta - \omega} = \mathcal{H}[\alpha(\omega)], \qquad \text{(3) again}$$

which is the required result. A result equivalent to (3) in electromagnetic theory is known as the Kramers–Krönig relation.

It can happen that $\log F(\omega)$ for large $|\omega|$ does not behave in a fashion that permits (9) to be valid, because of a contribution from the semicircular arc (see e.g., Problem 5.14). However, one can modify the above analysis by applying (7) to the function $\log F(\omega)/\omega$. The same infinite semicircle is used, leading now to two semiresidues; at $\zeta = 0$ and $\zeta = \omega$,

$$\frac{\log F(0)}{-\omega} + \frac{\log F(\omega)}{\omega} = \frac{1}{\pi i} P \int_{-\infty}^{\infty} \frac{\log F(\zeta)}{\zeta(\zeta - \omega)}\, d\zeta. \tag{11}$$

[There is no contribution from the large arc if, for example,

$$\log F(\omega) = O(\log \omega) \qquad \text{as } |\omega| \to \infty. \tag{12}$$

An nth order discontinuity of $p(x, t)$ at the wavefront $t = x/c_\infty$ will lead to $F(\omega) = O(\omega^{-n})$, and hence to (12) and (11).]

(continued)

BOX **5.8** *(continued)*

It follows from (11) and (8) that

$$\frac{1}{c(\omega)} = \frac{1}{c_\infty} + \mathcal{H}\left[\frac{\alpha(\omega)}{\omega}\right] \quad \text{and} \quad \frac{\alpha(\omega) - \alpha(0)}{\omega} = -\mathcal{H}\left[\frac{1}{c(\omega)} - \frac{1}{c_\infty}\right]. \tag{13}$$

This is a simple example of a more general result called a *dispersion relation with one subtraction*, and $\alpha(0)$ is called the *subtraction constant* (Nussenzveig, 1972).

There are circumstances in which it may be known that a function $f(t)$ is such that $f(t) = 0$ for $t < 0$, and hence that $f(\omega)$ is analytic in the upper half-plane, but nothing else is known about $f(\omega)$. (In the special problem above, a specific formula given in (4) is available for the function in the frequency domain.) In the general case, we cannot reject the possibility that $f(\omega)$ has zeros.

Suppose, then, that $f(\omega)$ has zeros at $\omega = \omega_i$ $(i = 1, 2, \ldots, n)$ in the upper half-plane. We construct a function $f_0(\omega)$ via

$$f(\omega) = f_0(\omega) \prod_{i=1}^{n} \frac{\omega - \omega_i}{\omega - \omega_i^*}. \tag{14}$$

Since $f_0(\omega)$ has no zeros, its amplitude and phase $\phi_0(\omega)$ are related by

$$\phi_0(\omega) = \mathcal{H}[\log|f(\omega)|] \tag{15}$$

(proved by steps parallel to the derivation of (3) above; note that f and f_0 have the same amplitude spectra). But, from (14), the phase $\phi(\omega)$ of $f(\omega)$ is related to $\phi_0(\omega)$ by

$$\phi(\omega) = \phi_0(\omega) - \sum_{i=1}^{n} 2\tan^{-1}\left(\frac{\operatorname{Im}\omega_i}{\omega - \operatorname{Re}\omega_i}\right).$$

Now, given the various possible pulse shapes in the time domain that have the same amplitude spectrum $|f(\omega)|$, the pulse shape associated with the phase spectrum $\phi_0(\omega)$ is known as the *minimum-delay* pulse shape, because the group delay due to the zeros,

$$\frac{d}{d\omega}\{\phi(\omega) - \phi_0(\omega)\} = +2\sum_{i=1}^{n} \frac{\operatorname{Im}\omega_i}{\{(\operatorname{Im}\omega_i)^2 + (\omega - \operatorname{Re}\omega_i)^2\}},$$

is always positive (since $\operatorname{Im}\omega_i > 0$).

The special pulse shape considered above, in equation (6), which is due to attenuation after propagation a distance x, is therefore a minimum-delay pulse shape after the arrival time x/c_∞.

frequencies, so that the departure of attenuation from a law $\alpha(\omega) \propto \omega$ is not apparent until ω is very large. We can then neglect $\alpha_1^2\omega^2$ in the expression for $\mathcal{H}[\alpha(\omega)]$, finding from (5.77) that the phase velocity is given effectively by

$$\frac{1}{c(\omega)} = \frac{1}{c_\infty} + \frac{2\alpha_0}{\pi}\log\left(\frac{1}{\alpha_1\omega}\right). \tag{5.80}$$

From (5.78) and (5.79), Q has approximately the value $(2c_\infty\alpha_0)^{-1}$, enabling us to obtain from (5.80) the ratio of phase velocities at two different seismic frequencies ω_1 and ω_2:

$$\frac{c(\omega_1)}{c(\omega_2)} = 1 + \frac{1}{\pi Q}\log\left(\frac{\omega_1}{\omega_2}\right). \tag{5.81}$$

This is an important result, since it appears to be a good approximation for a variety of attenuation laws in which Q is effectively constant over the seismic frequency range (see Problem 5.13 for other examples). However, specific attenuation laws have been proposed that do have an effectively constant Q, but for which the dispersion is *not* given accurately by (5.81) (see, e.g., Strick, 1970, and Problem 5.14). To see how this can happen, note from (5.77) that the phase delay at frequency ω, i.e., $x/c(\omega)$, is x/c_∞ plus an amount $x\omega^{-1}\,\mathcal{H}[\alpha(\omega)]$. Thus the phase delay at a *specific* frequency depends on an integral (the Hilbert transform) of the attenuation spectrum over *all* frequencies. If the asymptotic behavior of $\alpha(\omega)$ as $\omega \to 0$ and $\omega \to \infty$ is chosen so that the integral converges slowly, a very large phase delay can occur at seismic frequencies. In this circumstance, it is advisable for us to constrain the attenuation factor $\alpha(\omega)$ at very high and very low frequencies by returning to a discussion of the physical nature of anelasticity.

Suppose that a step-function stress $\sigma = \sigma_0 H(t)$ is applied to a solid that is initially in a state of zero stress and zero strain. For a linear medium, the resulting strain $\varepsilon(t)$ can be written as

$$M_U\varepsilon(t) = \sigma_0[1 + \phi(t)], \tag{5.82}$$

where M_U is an elastic modulus and $\phi(t)$ is known as the *creep function* for this modulus. (We shall discuss (5.82) as a relation between scalars, since in this section we are interested only in one-dimensional wave propagation.) For an isotropic elastic medium, $\phi = 0$ with $M_U = \mu$ for transverse waves, and $M_U = \lambda + 2\mu$ for longitudinal waves. For anelastic materials, there is an instantaneous strain σ_0/M_U in response to the applied stress (note that $\phi(t) = 0$ for $t \leq 0$). This is the reason for our use of a subscript U on the modulus: U stands for *unrelaxed* in the sense that M_U gives the proportionality between stress and strain as soon as the stress has been applied, before the material has started to relax (via creep) to some new configuration.

The stress–strain relation (5.82) is easily generalized to the case of general loading $\sigma = \sigma(t)$, to give

$$M_U\varepsilon(t) = \left[\sigma(t) + \int_{-\infty}^{t} \sigma(\tau)\dot{\phi}(t-\tau)\,d\tau\right],$$

as shown by Boltzmann in 1876. Since $\dot{\phi}(t) = 0$ for $t \leq 0$, the above can conveniently be written as a convolution,

$$M_U\varepsilon(t) = \sigma(t) + \sigma(t) * \dot{\phi}(t). \tag{5.83}$$

Consider now the situation in which σ and ε are due to a plane wave propagating with fixed frequency ω in the x-direction: $\sigma = \sigma_0 \exp i(Kx - \omega t)$, with complex wavenumber K

related to the phase velocity $c(\omega)$ and the attenuation factor $\alpha(\omega)$ by (5.75). The stress–strain relation then becomes

$$M_U \varepsilon(t) = \sigma(t)\left[1 + \int_0^\infty \dot{\phi}(\tau)\exp(i\omega\tau)\,d\tau\right] \tag{5.84}$$

(using the special form of $\sigma(t) \propto \exp(-i\omega t)$ and $\dot{\phi}(t) = 0$ for $t \leq 0$). It follows that stress is proportional to strain via a complex modulus $M(\omega)$, where

$$M(\omega) = M_U \Big/ \left[1 + \int_0^\infty \dot{\phi}(\tau)\exp(i\omega\tau)\,d\tau\right]. \tag{5.85}$$

The continuity of ϕ at the origin implies that the integral here tends to zero as $\omega \to \infty$, showing that $M(\omega) \to M_U$ as $\omega \to \infty$.

From the equation of motion $\rho\ddot{u} = \partial\sigma/\partial x = M\partial^2 u/\partial x^2$, we obtain $\rho\omega^2 = K^2 M(\omega)$, from which follow the relations

$$\begin{aligned} \frac{\omega}{c(\omega)} + i\alpha(\omega) &= \omega\sqrt{\frac{\rho}{M(\omega)}} = \frac{\omega}{c_\infty}\left[1 + \int_0^\infty \dot{\phi}(t)\exp(i\omega t)\,dt\right]^{1/2}, \\ \frac{1}{Q(\omega)} &= \frac{2c(\omega)\alpha(\omega)}{\omega} = -\frac{\mathrm{Im}M(\omega)}{\mathrm{Re}M(\omega)} = \frac{\mathrm{Im}\left\{\int_0^\infty \dot{\phi}(t)\exp(i\omega t)\,dt\right\}}{1 + \mathrm{Re}\left\{\int_0^\infty \dot{\phi}(t)\exp(i\omega\tau)\,dt\right\}}. \end{aligned} \tag{5.86}$$

We have here identified a velocity c_∞ in terms of the unrelaxed modulus via $c_\infty = \sqrt{M_U/\rho}$, and (5.86) is now in a form that permits us to translate various creep laws into laws of attenuation and dispersion.

Thus Lomnitz (1956, 1957) summarized his laboratory observations of creep in rocks by the logarithmic law

$$\phi(t) = \begin{cases} 0 & t \leq 0 \\ q\log(1+at) & t \geq 0 \end{cases}$$

in which the fundamental frequency a may be as high as the vibration frequency of a vacancy in the crystal lattice (i.e., of the order of 10^{10} Hz; see Savage and O'Neill, 1975). The Fourier transform of $\dot{\phi}$ is then

$$aq\int_0^\infty \frac{\exp(i\omega t)}{1+at}dt \sim -q\left[\gamma + \log\left(\frac{\omega}{a}\right) - \frac{i\pi}{2}\right]e^{-i\omega/a} \tag{5.87}$$

for $\omega \ll a$, where $\gamma = 0.577\ldots$ is Euler's constant. Since $q \ll 1$, we find from (5.86) and (5.87) that

$$\frac{\omega}{c(\omega)} + i\alpha(\omega) = \frac{\omega}{c_\infty}\left\{1 - \frac{q}{2}\left[\gamma + \log\left(\frac{\omega}{a}\right)\right] + \frac{i\pi q}{4}\right\} \tag{5.88}$$

(correct to first order). The imaginary part of this expression yields

$$q = \frac{2}{\pi Q}\frac{c_\infty}{c(\omega)} \sim \frac{2}{\pi Q}$$

for one of Lomnitz' constants. From this result and the real part of (5.88), the frequency dependence of c is found via

$$\frac{1}{c(\omega)} = \frac{1}{c_\infty}\left\{1 - \frac{1}{\pi Q}\left[\gamma + \log\left(\frac{\omega}{a}\right)\right]\right\},$$

which is in agreement with the relation

$$\frac{c(\omega_1)}{c(\omega_2)} = 1 + \frac{1}{\pi Q}\log\left(\frac{\omega_1}{\omega_2}\right) \qquad \text{(5.81 again)}$$

established above for Azimi's attenuation law.

We have now obtained logarithmic dispersion in the form (5.81) for media with almost constant Q, via two completely different methods—namely, from an attenuation law (5.79), and from laboratory observations of creep. Further support for logarithmic dispersion is provided, as we show next, by Boltzmann's approach using a creep function that is synthesized from well-understood mechanisms so as to give an effectively constant Q over seismic frequencies (Liu *et al.*, 1976). Thus, from what follows, a physical basis for (5.81) is available directly from the observation of constant Q.

The assumption made by Liu *et al.* is that attenuation is due to a superposition of different relaxation phenomena, each one of which (if it acted alone) would be represented by the stress–strain relation

$$\sigma + \tau_\sigma \dot{\sigma} = M_R(\varepsilon + \tau_\varepsilon \dot{\varepsilon}). \tag{5.89}$$

(Many of the physical mechanisms proposed to explain attenuation appear to satisfy this relation, which is the stress–strain law for a *standard linear solid*, first studied in detail by Zener, 1948.) Here τ_ε is the characteristic relaxation time of strain under an applied step in stress, and τ_σ is the relaxation time for stress corresponding to a step change in strain. M_R is an elastic modulus, and (5.89) can be solved for the response to a step-function load $\sigma(t) = \sigma_0 H(t)$ to give

$$\varepsilon(t) = \frac{\sigma_0}{M_R}\left[1 - \left(1 - \frac{\tau_\sigma}{\tau_\varepsilon}\right)e^{-t/\tau_\varepsilon}\right]. \tag{5.90}$$

Comparing this with (5.82) and giving special consideration to the instantaneous response at $t = 0$, we can identify

$$M_R = M_U \frac{\tau_\sigma}{\tau_\varepsilon}$$

and

$$\phi(t) = \left(\frac{\tau_\varepsilon}{\tau_\sigma} - 1\right)(1 - e^{-t/\tau_\varepsilon}). \tag{5.91}$$

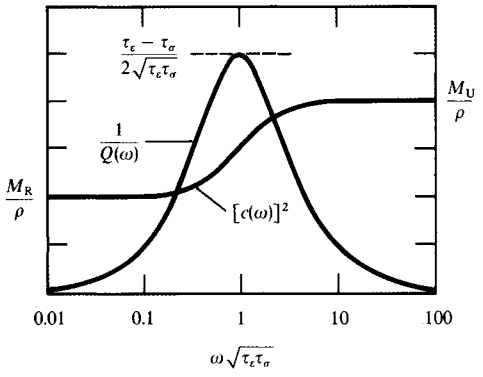

FIGURE **5.14**
The internal friction, Q^{-1}, and the square of the phase velocity, $[c(\omega)]^2$, as a function of frequency in a standard linear solid (i.e., a solid with a single relaxation mechanism). [After Liu *et al.*, 1976.]

M_R is known as the *relaxed modulus*, since (from (5.90)) it gives the ratio of stress to strain in the limit as $t \to \infty$. The transform

$$\int_0^\infty \dot{\phi}(t) \exp(i\omega t)\, dt$$

is needed in (5.86) to obtain Q values and the dispersion, and it is simple to show from the creep function (5.91) that

$$\frac{1}{Q} = \frac{\omega(\tau_\varepsilon - \tau_\sigma)}{1 + \omega^2 \tau_\sigma \tau_\varepsilon}$$

and

$$[c(\omega)]^2 = \frac{M_U}{\rho}\left[1 + \left(\frac{M_U}{M_R} - 1\right)\frac{1}{1 + \omega^2 \tau_\varepsilon^2}\right]^{-1}.$$

These two quantities are plotted in Figure 5.14, and note that attenuation is concentrated near the frequency $(\tau_\sigma \tau_\varepsilon)^{-1/2}$, with Q^{-1} behaving like ω for frequencies below this central peak and like ω^{-1} for frequencies above it. Moreover, the phase velocity $c(\omega)$ increases monotonically with frequency, the lower limit at $\omega = 0$ being $\sqrt{M_R/\rho}$.

In order to reproduce the effectively constant Q values observed at seismic frequencies, Liu *et al.* (1976) used a discrete superposition of twelve relaxation peaks of the type shown in Figure 5.14, all sharing the same relaxed modulus M_R. They chose the 24 available anelastic parameters (τ_ε and τ_σ for each mechanism) to give Q^{-1} and phase velocity as shown in Figure 5.15. Over the range 0.0001–10 Hz, note that Q^{-1} is effectively constant within 1% and that phase velocity has a linear dependence on log ω. Carrying the analysis one stage further, they considered a continuous superposition of relaxations, specified by a density function, and again found the linear dependence of $c(\omega)$ on log ω to be like that shown in Figure 5.15. In fact, they found the gradient of $c(\omega)$ analytically, and showed that the ratio $c(\omega_1)/c(\omega_2)$ has the now-familiar value from (5.81), namely $1 + (\pi Q)^{-1} \log(\omega_1/\omega_2)$.

This logarithmic dispersion now has ample justification for materials in which Q is observed to be constant, so that it is clear how to solve problems of wave propagation in

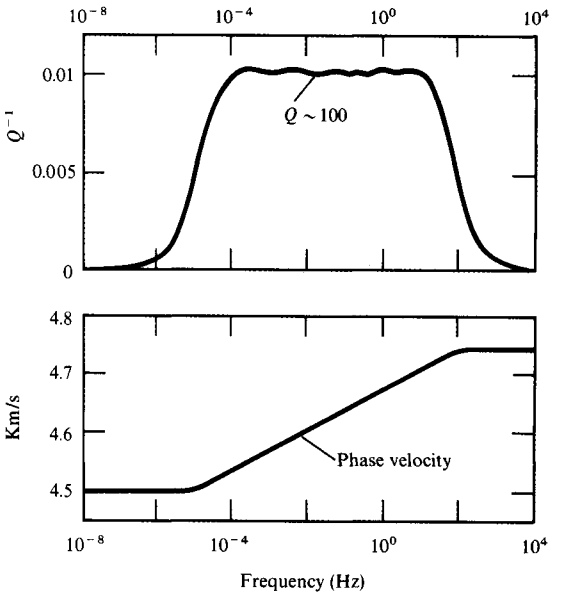

FIGURE **5.15**
Top. Internal friction values. Bottom. Phase velocities obtained (via (5.86)) from a superposition of 12 different relaxation peaks. [After Liu *et al.*, 1976.]

anelastic media once the parallel problem for an elastic medium has been solved. We have seen that the propagation factor

$$\exp[i(kx - \omega t)] = \exp[i\omega(x/c - t)]$$

for elastic media is to be replaced by

$$\exp i(Kx - \omega t) = \exp\left[\frac{-\omega x}{2c(\omega)Q(\omega)}\right] \exp\left[i\omega\left(\frac{x}{c(\omega)} - t\right)\right].$$

Although c appears as a frequency-independent constant in the elastic solution, $c = c_e$, that solution will be an analytic function of c_e. It then follows by analytic continuation that the anelastic solution is given by replacing c_e via the rule

$$\frac{1}{c_e} \to \frac{1}{c(\omega)}\left(1 + \frac{i}{2Q(\omega)}\right), \tag{5.92}$$

which is equivalent, to first order, to

$$c_e \to c(\omega)\left(1 - \frac{i}{2Q(\omega)}\right). \tag{5.93}$$

If Q is effectively constant, then we can expect to be able to use the logarithmic dispersion law (5.81) relating values of c at two different frequencies, in order to evaluate the frequency-dependence of c appearing in (5.93). We need here to fix a reference frequency—say, ω_0—against which dispersion can be recognized. For example, a frequency of 1 Hz

corresponds to $\omega_0 = 2\pi$. Then the elastic wave speed c_e is replaced via the rule

$$c_e \to c(\omega_0)\left[1 + \frac{1}{\pi Q}\log\left(\frac{\omega}{\omega_0}\right) - \frac{i}{2Q}\right] \tag{5.94}$$

(correct to first order in Q), where the constant $c(\omega_0)$ is the body-wave phase velocity at the reference frequency ω_0.

Throughout this section, we have so far assumed that the attenuating plane wave of interest is a one-dimensional wave. Thus, for a propagating wave described by $\exp(-\alpha x)\exp[i\omega(x/c(\omega) - t)]$, the direction of maximum attenuation is also the direction of increasing phase delay. For plane waves in general, these two directions are different. In what follows, we shall explore the way in which phase velocity depends on Q for two-dimensional wave propagation, showing that it is still fruitful to analyze plane waves in terms of their horizontal slowness, even when the wave is attenuating.

We consider solutions to

$$\nabla^2\psi + K^2\psi = 0, \tag{5.95}$$

where $K^2 = \omega^2\rho/\mu$ is complex because the shear modulus μ is complex. In general, the steady-state plane wave solution to (5.95) is a constant times

$$\exp(-\mathbf{A}\cdot\mathbf{x})\exp\left[i(\mathbf{P}\cdot\mathbf{x} - \omega t)\right], \tag{5.96}$$

where **A** and **P** are vectors with real Cartesian components. **A** is the direction of maximum attenuation, and **P** is the direction of wave propagation (i.e., of increasing phase delay). Substituting (5.96) into (5.95) yields

$$P^2 - A^2 = \mathrm{Re}\{K^2\}, \tag{5.97}$$

$$PA\cos\gamma = \tfrac{1}{2}\,\mathrm{Im}\{K^2\}, \tag{5.98}$$

where P and A are the amplitudes of **P** and **A**, and γ is the angle between **P** and **A**. The wave is said to be *homogeneous* or *inhomogeneous* according to whether $\gamma = 0$ or $\gamma \neq 0$. We met these terms before in Section 5.3 in the context of elastic media. As shown by Buchen (1971) and Borcherdt (1973), for elastic media one must either have $A = 0$ or $\gamma = \pi/2$. This follows from (5.98), with $\mathrm{Im}\{K^2\} = 0$. But, for anelastic media, necessarily $A \neq 0$ and $\gamma \neq \pi/2$. Previously in this section, we have considered only $A \neq 0$ and $\gamma = 0$, which is a homogeneous attenuating wave. But to handle the effect of an interface between anelastic half-spaces, we must consider inhomogeneous plane waves, with $0 < \gamma < \pi/2$.

Fortunately, these more general plane waves can still be studied as a function of the independent variable p, because

$$\exp\left[i\omega px + i\sqrt{K^2 - \omega^2 p^2}\,z - i\omega t\right] \tag{5.99}$$

is also a general plane-wave solution to the wave equation. Solutions (5.99) and (5.96) are equivalent, with the y-axis perpendicular to **P** and **A**. The Cartesian components of **P** and **A** are

$$\begin{aligned} \mathbf{P} &= \left(\mathrm{Re}\{\omega p\}, 0, \mathrm{Re}\left\{\sqrt{K^2 - \omega^2 p^2}\right\}\right), \\ \mathbf{A} &= \left(\mathrm{Im}\{\omega p\}, 0, \mathrm{Im}\left\{\sqrt{K^2 - \omega^2 p^2}\right\}\right). \end{aligned} \tag{5.100}$$

These expressions allow for the possibility that p might be complex, and this we shall find is desirable in Chapters 6–9. The (physical) horizontal slowness is $\mathrm{Re}\{p\}$.

Buchen (1971), Borcherdt (1973, 1977), and Richards (1984) have extensively studied the properties of plane waves in terms of the vectors **P** and **A**. Physical properties of individual plane waves are then easy to identify. For example, the angle of incidence to the vertical is simply θ, where

$$\mathbf{P} \cdot \hat{\mathbf{z}} = P \cos\theta. \tag{5.101}$$

The phase velocity is ω/P, and it follows from $K^2 = \omega^2\rho/\mu$ and (5.97)–(5.98) that this velocity is exactly

$$\sqrt{\frac{\mathrm{Re}\{\mu\}}{\rho}}\sqrt{\frac{2(1+Q^{-2})}{1+\sqrt{1+\sec^2\gamma\, Q^{-2}}}}. \tag{5.102}$$

Note that (5.102) is based on a Q defined by $Q^{-1} = -\mathrm{Im}\{\mu\}/\mathrm{Re}\{\mu\}$; see (5.86). This is probably the best of several different definitions that scientists have used for Q (see O'Connell and Budiansky, 1978). In Box 5.7, we noted several properties, derived when $Q \gg 1$, that can be used as the definition of Q. But these definitions will disagree with each other if they are applied for strongly attenuating media.

Because two angles (θ and γ) are now needed to characterize a plane wave incident upon an interface, Snell's law takes an extremely complicated form in terms of physical quantities such as **P** and **A** for each wave at the interface (Borcherdt, 1977). But in terms of plane waves expressed via (5.99), with K taking different (complex) values on either side of the interface, Snell's law reduces to the familiar rule that parameter p is the same for all plane waves coupled by the interface. This allows us very quickly to generalize all the formulas we previously obtained for reflection/conversion/transmission coefficients in elastic media, making them applicable in the anelastic case. Thus, to obtain the $\grave{S}\grave{S}$ transmission coefficient for SH-waves crossing between two anelastic half-spaces (see Fig. 5.7, left), we must first interpret the angles j_1 and j_2 in terms of the independent parameter p:

$$\frac{\sin j_1}{\beta_1} = p = \frac{\sin j_2}{\beta_2},$$
$$\frac{\cos j_1}{\beta_1} = \sqrt{\frac{1}{\beta_1^2} - p^2} = \eta_1, \tag{5.103}$$
$$\frac{\cos j_2}{\beta_2} = \sqrt{\frac{1}{\beta_2^2} - p^2} = \eta_2.$$

The incident wave here is proportional to $\exp[i\omega(px + \eta_1 z - t)]$, and the algebra that led to (5.33) gives us here

$$\grave{S}\grave{S} = \frac{2\rho_1\beta_1^2\eta_1}{\rho_1\beta_1^2\eta_1 + \rho_2\beta_2^2\eta_2} = \frac{2\mu_1\eta_1}{\mu_1\eta_1 + \mu_2\eta_2}. \tag{5.104}$$

Care must be taken in working out the angles of incidence and emergence of the transmitted wave $\grave{S}\grave{S}\exp[i\omega(px + \eta_2 z - t)]$. For this we must use (5.100) and the angle θ in (5.101), determined for each individual plane wave. Note in general that the angles of incidence and emergence will not be j_1 and j_2, since these angles have meaning only via (5.103), and we have chosen to use p as the independent variable (rather than, say, j_1). Richards (1984) showed that the square roots in (5.103) may need to be chosen such that amplitude *increases* with distance from the interface (though decreasing along the direction **P** of wave propagation).

Inspection will show that our coefficient $\grave{S}\grave{S}$ in (5.104) depends directly upon complex body-wave velocities β_1 and β_2 (or upon μ_1 and μ_2) and p. For example, β_1 and β_2 must be evaluated via rules such as (5.93) (or (5.94) if Q is nearly independent of frequency). Our earlier description of attenuation was limited to one-dimensional homogeneous waves. It is satisfying that the complex elastic moduli we introduced for these simple waves are all that we need to evaluate two-dimensional plane waves, even though the latter may be inhomogeneous waves. Thus reflection/transmission/conversion coefficients for an interface in attenuating media may be obtained from the analogue in elastic media (e.g., (5.33)) merely by substituting complex elastic moduli, provided we are careful to interpret such concepts as "angle of incidence" and "angle of emergence."

5.6 Wave Propagation in an Elastic Anisotropic Medium: Basic Theory for Plane Waves

Steady-state plane waves in a homogeneous anisotropic medium can propagate with constant slowness **s**, provided that the displacement $\mathbf{u} = \mathbf{U}\exp[-i\omega(t - \mathbf{s}\cdot\mathbf{x})]$ satisfies the wave equation, $\rho\ddot{u}_i = c_{ijpq}u_{p,qj}$. **U** is a constant, the polarization vector, giving the direction of particle motion. Therefore we require that

$$c_{ijpq}s_j s_q U_p = \rho U_i. \tag{5.105}$$

We need to understand the conditions under which values of the slowness and polarization vectors can be found, that satisfy this equation.

By defining $M_{ip} = c_{ijpq} l_j l_q$ where $\mathbf{l}$ is the unit vector in the slowness direction (so that $\mathbf{s} = |\mathbf{s}|\mathbf{l}$), we find that (5.105) becomes

$$M_{ip} U_p = (\rho/|\mathbf{s}|^2) U_i. \tag{5.106}$$

Since $\mathbf{M}$ is symmetric, it follows from (5.106) that in general there are three mutually orthogonal eigenvectors for the polarization $\mathbf{U}$, each one of them associated with an eigenvalue. The equation for the three eigenvalues is

$$\det[\mathbf{M} - (\rho/|\mathbf{s}|^2)\mathbf{I}] = 0, \qquad \text{equivalent to} \qquad \det|\rho\delta_{ip} - c_{ijpq} s_j s_q| = 0. \tag{5.107}$$

In isotropic media, (5.107) factors into three separate equations for slowness amplitudes, namely $|\mathbf{s}|^2 = \rho/(\lambda + 2\mu)$, $|\mathbf{s}|^2 = \rho/\mu$, and $|\mathbf{s}|^2 = \rho/\mu$ again, corresponding to P-waves and two types of S-wave (see (4.36)–(4.39) and (5.2)). It is the nature of an isotropic medium that these slowness amplitudes are independent of the slowness direction. But for the general anisotropic case it is not possible to solve analytically for slowness amplitudes, and furthermore the three different values for $|\mathbf{s}|^2$ are dependent on $\mathbf{l}$.

In practice the three separate types of body waves in an anisotropic medium have properties that are often strongly similar to those of body waves in an isotropic medium. For example, a wave typically exists with particle motion that is dominantly longitudinal and that is much faster than the other two waves—which are dominantly transverse. In such cases it is common to refer to the quasi P-wave, or the quasi shear waves.

A useful aid in visualizing the allowed slowness of wavefronts is the *slowness surface*, S. Using Cartesian axes (s_1, s_2, s_3) for points in slowness space, S is composed of points that satisfy (5.107). For isotropic media, S consists of three concentric spheres: one with radius $\sqrt{\rho/(\lambda + 2\mu)}$; and two, which are coincident, with radius $\sqrt{\rho/\mu}$. But for an anisotropic medium, S has three sheets that are separate and nonspherical. For a given unit direction $\mathbf{l}$ of slowness, there are three different values of the magnitude $|\mathbf{s}|$ that make $\mathbf{s} = |\mathbf{s}|\mathbf{l}$ lie on the slowness surface (see Fig. 5.16). They correspond to three different body waves with mutually perpendicular particle motions, and the magnitudes of their slowness are found by solving the eigenvalue problem (5.107).

From the slowness surface, it is possible to construct another three-sheeted surface, $W(t)$, for the position (at a given time t) of the wavefronts associated with a point source. Clearly, W is related to the solutions (x_1, x_2, x_3) that satisfy $t = \mathbf{s} \cdot \mathbf{x}$. The problem here is that, for each $\mathbf{x}$ in the wavefront, there will be a different $\mathbf{s}$ on the slowness surface. We define W to be the envelope of planes $t = \mathbf{s} \cdot \mathbf{x}$, as $\mathbf{s}$ varies over the slowness surface. Geometrical relationships between a point $\mathbf{s}$ on S and the corresponding point $\mathbf{x}$ on W are described by Musgrave (1970). The normal to S at $\mathbf{s}$ is parallel to $\mathbf{x}$. From this a graphical construction of W can be devised (since the direction of $\mathbf{x}$ is now known, and $|\mathbf{x}|$ is determined by $t = \mathbf{s} \cdot \mathbf{x}$). The reciprocal relation also holds, and perhaps this is more important from the seismological point of view: the normal to W at $\mathbf{x}$ is parallel to $\mathbf{s}$. The simplest observable quality of a wavefront is likely to be the direction (normal to itself) in which it advances, and this is

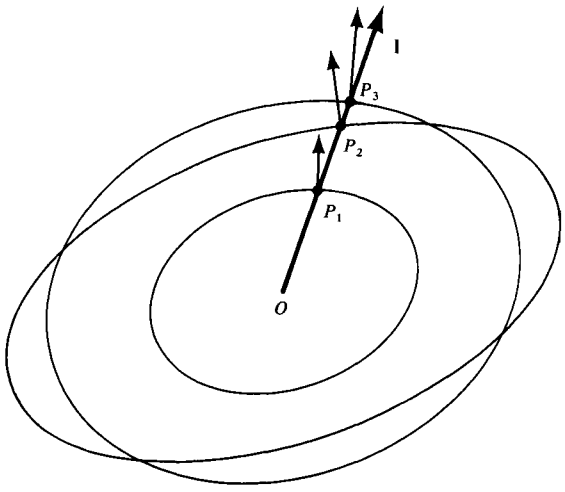

FIGURE **5.16**
The three-sheeted slowness surface S. There are three possible slownesses in the **l** direction, with magnitudes OP_1, OP_2, and OP_3. Normals to S at P_1, P_2, P_3 give the directions of energy propagation (rays) for each of the three slownesses.

given by **s**. However, as described by Vlaar (1968), the ray direction, which is the direction of energy transport, is not in general along **s**, but lies along the normal to the slowness surface at **s**. A general method for computing the geometrical spreading for wavefronts in anisotropic inhomogeneous media is given by Červený (1972).

To analyze the effects of horizontal interfaces between homogeneous half-spaces, we have previously (i.e., for isotropic media) taken an x_2-direction so that $\mathbf{s} = (p, 0, s_3)$. Snell's law for interfaces normal to x_3 reduces to $s_1 = p$, $s_2 = 0$ for all plane waves coupled at the interface, and s_3 is different for each wave. The same approach is helpful in anisotropic media, and Figure 5.18 gives a construction for the s_3-components for plane waves on either side of a horizontal interface between two half-spaces. The plane portrayed in Figure 5.18, containing all the coupled slowness vectors, is known as the *sagittal plane*. This also is the plane of incidence, and if it is varied then one may rotate the (x_1, x_2) axes to keep $s_2 = 0$. The penalty for this is that Cartesian components of **c** must be transformed to the new coordinate system.

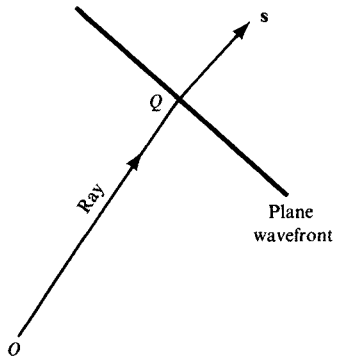

FIGURE **5.17**
For a plane wavefront, the ray direction (given by the energy flux) is not, in general, perpendicular to the wavefront, nor does it necessarily lie in the sagittal plane.

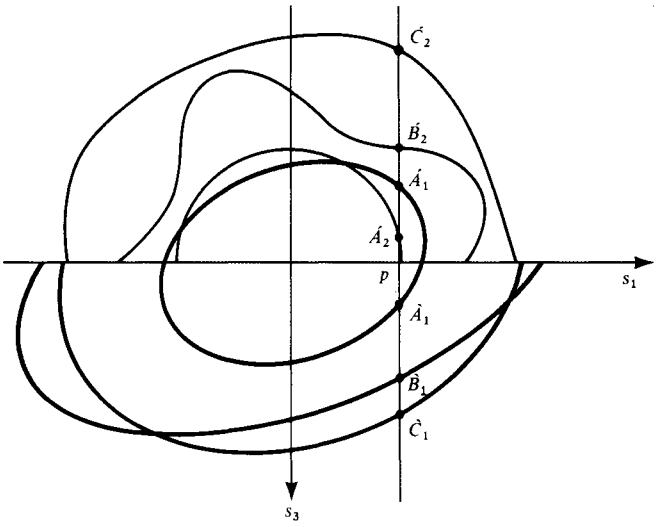

FIGURE **5.18**
Graphical method for determining the vector slowness for each plane wave scattered from a horizontal interface between two anisotropic half-spaces. Heavy curves are part of the three-sheeted slowness surface for the lower medium, and an incident wave (propagating upward) has slowness coordinates given by the point $\acute{A}_1$. The six scattered waves all share the same horizontal slowness p. Positive values of s_3 are for downgoing waves in the lower medium, and negative values (lying on medium-weight curves, which are part of the slowness surface for the upper medium) are for the transmitted waves. If p is large enough for some or all of the s_3 values to be imaginary, then corresponding plane waves are exponentially growing or decaying with depth.

A good way to quantify the reflection and transmission properties for an interface is to develop the equations of motion (on either side of the interface) in the form $d\mathbf{f}/dz = \mathbf{A}\mathbf{f}$ as in Section 5.4, where now

$$\mathbf{f} \exp[i\omega(px - t)] = (u_x, u_y, u_z, \tau_{zx}, \tau_{yz}, \tau_{zz})^T. \tag{5.108}$$

$\mathbf{A}$ is a 6×6 matrix, and one finds its six eigenvalues are the six values of $i\omega s_3$ where roots s_3 are shown graphically (for given p and a given half-space) in Figure 5.18. We form a matrix $\mathbf{E}$ whose columns are eigenvectors of $\mathbf{A}$ and a phase matrix $\mathbf{\Lambda}$ that is diagonal with six entries $\exp(i\omega s_3 z)$ for the six different s_3. With an appropriate ordering of columns of $\mathbf{E}$ and $\mathbf{\Lambda}$, the general plane wave solution in each homogeneous medium is given by $\mathbf{f} = \mathbf{E}\mathbf{\Lambda}\mathbf{w}$, where $\mathbf{w}$ is a 6-vector of weighting coefficients. The methods of Section 5.4 can now be used to obtain the 36 different reflection/transmission coefficients as a function both of p and the orientation of the sagittal plane. (The matrix $\mathbf{A}$ depends in general upon this orientation.) Some numerical examples are given by Keith and Crampin (1977).

There are several special types of anisotropy that are important in seismology. The simplest departure from isotropy is that for which the tensor of elasticity ($\mathbf{c}$) is isotropic in all directions normal to one particular direction, x_3. Such a medium is said to be *transversely*

BOX **5.9**

Shear-wave splitting due to anisotropy

In a weakly anisotropic medium, elastic waves can propagate with properties similar to the P- and S-waves of isotropic media. But certain distinctive differences, between wave properties in anisotropic and isotropic media, provide information on the extent of the anisotropy. The best example is that of the so-called quasi shear wave in an anisotropic medium, which can show features associated with the fact that the two components of the particle motion, resolved in the directions of fastest and slowest propagation, will become spatially separated because they propagate with different speeds. Such shear-wave splitting is measurable, and has been widely used to quantify the departure from isotropy.

In the simplest example of such a phenomenon, suppose that a quasi shear wave is propagating in the z direction, with particle motion $\mathbf{U}$ in the (x, y) plane; and that the x-axis is taken as the direction of particle motion for which such shear waves propagate fastest. From the discussion of (5.107), the y-axis will then be the direction of particle motion associated with the slowest propagation. Suppose the velocity of propagation is β for shear waves with particle motion polarized purely along the y-axis, and is $\beta + \Delta\beta$ for the x-axis.

Now consider a plane quasi shear wave in this anisotropic medium, propagating in the z-direction with general polarization. Let P be a spatial reference point which is passed by the wave, and let the pulse shape be $f(t)$ at P. If the particle displacements of this transverse wave make an angle ϕ with the x-axis at P, then the (x, y) components of the wave at P are

$$\mathbf{U}(P, t) = (f(t) \cos\phi, f(t) \sin\phi) .$$

What then are the components of the wave after it has propagated to the point Q, a distance z away from P? The (x, y) components will be

$$\mathbf{U}(Q, t) = \left(f\left(t - \frac{z}{\beta + \Delta\beta}\right) \cos\phi, f\left(t - \frac{z}{\beta}\right) \sin\phi \right) .$$

The component of this wave at Q in the original direction of polarized particle motion is then

$$f\left(t - \frac{z}{\beta + \Delta\beta}\right) \cos^2\phi + f\left(t - \frac{z}{\beta}\right) \sin^2\phi = f\left(t - \frac{z}{\beta}\right) + \frac{df}{dt} \cdot \frac{\Delta\beta}{\beta} \cdot \frac{z}{\beta} \cdot \cos^2\phi$$

to first order. This particle motion differs from what would be observed in an isotropic medium by only a small amount—the last term, above.

More interesting is the component of the wave at Q in the direction perpendicular to the original direction of polarized particle motion at P. This component is

$$\left[f\left(t - \frac{z}{\beta + \Delta\beta}\right) - f\left(t - \frac{z}{\beta}\right) \right] \cos\phi \sin\phi = \left. \frac{df}{dt} \right|_{t - \frac{z}{\beta}} \cdot \frac{\Delta\beta}{\beta} \cdot \frac{z}{\beta} \cdot \cos\phi \sin\phi$$

to first order. In an isotropic medium, $\Delta\beta = 0$ and this component would be zero. But for the anisotropic case, we see that the "perpendicular" component has a pulse shape that is proportional to the derivative, df/dt, of the dominant pulse shape in the main direction

(continued)

BOX **5.9** *(continued)*

of polarization. By comparing the shape and amplitude of the "perpendicular" component with the time derivative of the dominant pulse shape in the main direction, and seeing how this comparison changes for waves coming in with different initial polarities at P, it is possible to estimate both the fast direction ($\phi = 0$) and the time $\Delta T = \frac{\Delta\beta}{\beta} \cdot \frac{z}{\beta}$ by which the component in the slow direction is delayed.

The basic idea of shear-wave splitting, first described in the geophysical context by Kosarev *et al.* (1979), has been widely applied (Vinnik *et al.*, 1989; Silver and Chan, 1991). The values of ΔT, obtained from seismic data, indicate the amount of anisotropy present along the path of propagation. One of the most important examples of shear wave splitting in the Earth that appears to be quantified approximately by the above model of anisotropy, is the near-vertical propagation of *SKS* waves. S-waves, when they leave the source, in general consisting of mixed SH and SV, are converted to P-waves in the core, and are then polarized as SV at the point on the core–mantle boundary that begins their upward path through the mantle. But observations of *SKS* at the Earth's surface often show an S-wave signal, in the horizontal direction perpendicular to SV, with pulse shape that is approximately the derivative of the SV pulse shape.

Anisotropy can also be studied with observations of SH-waves that have been converted from P, as described by Kosarev *et al.* (1984) and Vinnik and Montagner (1996).

isotropic, and it is characterized by five independent moduli. The coefficient matrix for $d\mathbf{f}/dz = \mathbf{A}\mathbf{f}$ in transversely isotropic material has been extensively analyzed by Takeuchi and Saito (1972) with the anomalous direction x_3 taken as vertical. In this case there is remarkably little difference from isotropic media. SH decouples from quasi P and quasi SV, which are often written qP and qSV, and the symmetry about a vertical axis means that wave solutions do not depend upon the orientation of the sagittal plane. This major simplification is not possible for any other type of anisotropy.

Where anisotropy is weak but otherwise quite general, Backus (1965) has shown that the velocity of body waves propagating within a particular plane has a simple dependence upon direction of propagation within that plane. For example, qP waves propagating in the (x_1, x_2) plane with slowness $(\cos\phi, \sin\phi, 0)/\alpha$ have phase velocity $\alpha(\phi)$ given approximately by

$$\rho\alpha^2 = A + B\cos 2\phi + C\sin 2\phi + D\cos 4\phi + E\sin 4\phi. \tag{5.109}$$

Backus's discovery of this form for $\alpha = \alpha(\phi)$ was prompted by Hess's (1964) observation from published data that P-waves refracted along the underside of the Moho beneath oceans appeared to have several percent velocity anisotropy. In turn, the specific form (5.109) has stimulated attempts (e.g., Crampin and Bamford, 1977) to invert observations of α in terms of five other elastic parameters (the coefficients A, B, C, D, E, which themselves are linear combinations of components of $\mathbf{c}$).

Suggestions for Further Reading

Auld, B. A. *Acoustic Fields and Waves in Solids*. 2 vols. 2nd ed. Malabon, Florida: Krieger Pub. Co., 1990.

Babuska, V., and M. Cara. *Seismic Anisotropy in the Earth*. Boston: Kluwer Academic, 1991.

Coddington, E. A., and N. Levinson. *Theory of Ordinary Differential Equations* (Chap. 6). New York: McGraw-Hill, 1955.

Gantmacher, F. R. *The Theory of Matrices*. 2 vols. New York: Chelsea Publishing Co., 1959.

Liu, H.-P, D. L. Anderson, and H. Kanamori. Velocity dispersion due to anelasticity; implications for seismology and mantle composition. *Geophysical Journal of the Royal Astronomical Society*, **47**, 41–58, 1976.

Randall, M. J. Attenuative dispersion and frequency shifts of the earth's free oscillations. *Physics of the Earth and Planetary Interiors*, **12**, 1–4, 1976.

Silver, P. G. Seismic Anisotropy. *Annual Reviews of Earth and Planetary Sciences*, **24**, 38–432, 1996.

Silver, P. G., and M. L. Savage. The interpretation of shear-wave splitting parameters in the presence of two anisotropic layers. *Geophysical Journal International*, **119**, 949–963, 1994.

Tsvankin, I.D. *Seismic Signatures and Analysis of Reflection Data in Anisotropic Media*. Amsterdam; New York: Pergamon, 2001.

Problems

5.1 If the surface of a solid elastic half-space is traction-free, we found that there can exist a surface wave of displacement (the Rayleigh wave). If the surface is rigid, show that there can be no corresponding surface wave of tractions. (*Hint:* Find a determinant that does not vanish for appropriate values of p.)

5.2 Why can there be no interface SH-wave at the boundary between two homogeneous half-spaces?

5.3 For a solid half-space $z > 0$ (see Fig. 5.5 and Table 5.1), obtain the P–SV scattering matrices

$$\begin{pmatrix} \acute{P}\grave{P} & \acute{S}\grave{P} \\ \acute{P}\grave{S} & \acute{S}\grave{S} \end{pmatrix}$$

when the boundary condition on $z = 0$ is given (a) by $u_z = 0$ and $\tau_{zx} = 0$, and (b) by $u_x = 0$ and $\tau_{zz} = 0$. (You can reduce the algebra by working from equations (5.34).)

If a combination of P-wave and SV-wave energy is propagating toward the surface $z = 0$, show that by adding the reflections derived from boundary conditions (a) to the reflections corresponding to (b) all downward reflections are eliminated. (Smith, 1974, 1975, showed that this is a useful way to eliminate

unwanted reflections from grid boundaries in numerical work with the Finite Element and Finite Difference methods.)

5.4 This problem concerns the particle motion in Rayleigh waves (see Fig. 5.11).

a) Show briefly that the inhomogeneous P-wave (5.52) and the inhomogeneous SV-wave (5.53) each have *prograde* elliptical particle motion.

b) From (5.52)–(5.56), show for Rayleigh waves that the particle displacement vector at the free surface ($z = 0$) is proportional to the vector

$$\left(\frac{2i}{c_R}\sqrt{\frac{1}{c_R^2}-\frac{1}{\beta^2}}, 0, \frac{2}{c_R^2}-\frac{1}{\beta^2}\right).$$

c) Show then that particle motion for the free surface is *retrograde* elliptical.

d) Give a brief argument to show that particle motion at sufficient depth is again prograde elliptical.

5.5 Show that it is the *horizontal* (and not the *vertical*) component of the Rayleigh wave that goes through zero as depth increases, as shown in Figure 5.11.

5.6 Since seismometers are often placed on (or very near to) the traction-free surface of the Earth, it is of interest to obtain the total displacement of the free surface of a half-space due to a P, SV, or SH plane wave incident from below. Using the notation of Table 5.1 and Figure 5.5, show that this total displacement at the surface is

$$\frac{\acute{P}\left[\frac{4\alpha p}{\beta^2}\frac{\cos i}{\alpha}\frac{\cos j}{\beta}, 0, \frac{-2\alpha}{\beta^2}\frac{\cos i}{\alpha}\left(\frac{1}{\beta^2}-2p^2\right)\right]\exp[i\omega(px-t)]}{\left(\frac{1}{\beta^2}-2p^2\right)^2+4p^2\frac{\cos i}{\alpha}\frac{\cos j}{\beta}}$$

for a P-wave (of amplitude $\acute{P}$) incident from below; and is

$$\frac{\acute{S}\left[\frac{2}{\beta}\frac{\cos j}{\beta}\left(\frac{1}{\beta^2}-2p^2\right), 0, \frac{4p}{\beta}\frac{\cos i}{\alpha}\frac{\cos j}{\beta}\right]\exp[i\omega(px-t)]}{\left(\frac{1}{\beta^2}-2p^2\right)^2+4p^2\frac{\cos i}{\alpha}\frac{\cos j}{\beta}}$$

for an SV-wave (of amplitude $\acute{S}$) incident from below. (In the range $1/\alpha < p < 1/\beta$, this last formula can be used with the positive imaginary value $\alpha^{-1}\cos i = i\sqrt{p^2 - 1/\alpha^2}$ to give the phase shift in the surface displacement when SV is incident at a supercritical angle $j > j_c = \sin^{-1}(\beta/\alpha)$.)

For incident SH, show that particle motion in the free surface is simply double the particle motion in the incident wave.

5.7 Suppose that we have accurate three-component recordings $(Z(t), N(t), E(t))$ of the free-surface motions described in Problem 5.6 for the incident SV-wave, which comes in to the recording station from azimuth ϕ with pulse shape $\acute{S}(t)$ in the

time domain. Then the horizontal particle motion $R(t)$ is given from the data by combining the North and East components via $R(t) = -N(t)\cos\phi - E(t)\sin\phi$. The data R and Z record the total free-surface motion (noting that Z is measured as positive upward, though depth is positive downward—see Box 7.10).

Show then that we can estimate the incident waveform from the data via

$$\acute{S}(t) = \frac{\cos 2j}{2\cos j}\cdot R(t) - \sin j \cdot Z(t) = \frac{1-2\beta^2p^2}{2\sqrt{1-\beta^2p^2}}\cdot R(t) - \beta p \cdot Z(t)$$

provided we can estimate the horizontal slowness p and the shear-wave speed β.

This formula in a sense provides a "free-surface correction," enabling the effects of reflected waves, present in the recorded data, to be removed. See House and Boatwright (1980), Kennett (1991), and Kim *et al.* (1997).

For the case of a P-wave incident as in Problem 5.6, with pulse shape $\acute{P}(t)$ and slowness p, show that $\acute{P}$ can be recovered from the data via

$$\acute{P}(t) = \frac{\cos 2j}{2\cos i}\cdot Z(t) + \frac{\beta}{\alpha}\sin j \cdot R(t) = \frac{1-2\beta^2p^2}{2\sqrt{1-\alpha^2p^2}}\cdot Z(t) + \frac{\beta^2 p}{\alpha}\cdot R(t)$$

and that a Hilbert transform of the Z-component is needed here if $p > 1/\alpha$.

5.8 Show that the $\grave{P}\acute{P}$ coefficient of Section 5.2.6 has (to first order) the form $\grave{P}\acute{P}_0 + B\sin^2 i$, where $\grave{P}\acute{P}_0$ is the reflection coefficient at normal incidence ($i = 0$), and B is a constant. (This formula for $\grave{P}\acute{P}$ is important because it indicates how to estimate S-wave properties and changes in rigidity, from knowledge of the variability of P-wave reflection amplitudes as a function of the angle of incidence. See Shuey, 1985, and Russell, 1993.)

5.9 Show that the longitudinal first motion of a compressional P-wave is outward, and that for a dilatational P-wave is inward.

5.10 Given the form of $\mathbf{f}$ defined in (5.62), show that indeed $d\mathbf{f}/dz = \mathbf{A}\mathbf{f}$ for P–SV waves, provided that $\mathbf{A}$ has the form given in (5.62). Show that $\mathbf{A}$ still has this form when ρ, λ, and μ are functions of z, but that (5.63) does not then in general solve (5.58).

5.11 Consider the P-wave potential $\phi = A\exp[i\omega(px + \xi z - t)]$, which, for a homogeneous medium, satisfies $\alpha^2\nabla^2\phi = \ddot{\phi}$ provided that $\xi = \sqrt{\alpha^{-2} - p^2}$. Show that $u_x, u_z, \tau_{zx}, \tau_{zz}$ constructed from this potential forms essentially the first column of $\mathbf{F} = \mathbf{E}\mathbf{\Lambda}$, given in (5.69). (The difference is due only to a different normalization of this downgoing P-wave.)

Repeat the discussion for SV-potential $B\exp[i\omega(px + \eta z - t)]$ (with $\eta = \sqrt{\beta^{-2} - p^2}$), P-potential $C\exp[i\omega(px - \xi z - t)]$, and SV-potential $D\exp[i\omega(px - \eta z - t)]$. (The point here is that different columns of $\mathbf{F}$ in (5.69) are downgoing and upgoing P- and SV-waves in which the displacement and stress components are given explicitly for each wave.)

Show that these four waves, described by potentials, are equivalent to the wave system $\mathbf{f} = \mathbf{F}\mathbf{w}$, in which $\mathbf{w}$ is the column vector

$$\mathbf{w} = \left(\frac{i\omega A}{\alpha}, -\frac{i\omega B}{\beta}, \frac{i\omega C}{\alpha}, \frac{i\omega D}{\beta} \right)^T .$$

5.12 Show that Q is in general an odd function of ω (i.e., $Q(-\omega) = -Q(\omega)$). Then show that the attenuated impulse described by (5.72) is always symmetric about $t = x/c$ if there is no dispersion.

5.13 Obtain the approximation (5.81) in the cases

a) $\alpha(\omega) = \dfrac{\alpha_0 \omega}{1 + \alpha_2 \omega^2}$ and

b) $\alpha(\omega) = \alpha_0 \omega \{ H(\omega - \omega_l) - H(\omega - \omega_h) \}$

(ω_l and ω_h being low- and high-frequency cutoffs and H the Heaviside step function); use $0 < \omega_l \ll \omega \ll \omega_h$ in deriving (5.81). Hilbert transforms of the above two attenuation functions will be needed. Definitions above are for $\omega > 0$. Corresponding $\mathcal{H}[\alpha(\omega)]$ are then

$$\frac{\alpha_0}{\pi} \frac{\omega}{1 + \alpha_2 \omega^2} \log \left(\frac{1}{\alpha_2 \omega^2} \right) \qquad \text{for (a)}$$

and

$$\frac{\alpha_0 \omega}{\pi} \log \left\{ \frac{\omega_h^2 - \omega^2}{\omega_l^2 - \omega^2} \right\} \qquad \text{for (b).}$$

5.14 Azimi *et al.* (1968) and Strick (1970) examined the attenuation law $\alpha(\omega) = \alpha_0 |\omega|^s$ for s just less than one. This can give an effectively linear dependence of $\alpha(\omega)$ on ω over observed frequencies (i.e., $Q =$ constant). From relation (13) of Box 5.8 and the Hilbert transform $\mathcal{H}[\operatorname{sgn} \omega |\omega|^{s-1}] = |\omega|^{s-1} \tan s\pi/2$, show here that

$$\frac{1}{c(\omega)} = \frac{1}{c_\infty} + \frac{\alpha(\omega)}{|\omega|} \tan \frac{s\pi}{2} .$$

Show then that relative dispersion between different frequency components over the seismic frequency range might be small, and hence hard to detect, though absolute dispersion (with respect to the phase velocity c_∞) may be large for s only just less than one. (This curious result is due to the slow convergence of the Hilbert transform integral. The amplitude spectrum at megahertz frequencies and higher is controlling the phase delay at seismic frequencies. This implausible behavior here is associated with a medium for which $Q \to \infty$ as $\omega \to \infty$. Real materials have finite Q as $\omega \to \infty$.)

5.15 If $Q^{-1} \ll 1$ and (5.102) is expanded by the binomial theorem, we find that the phase velocity in general for an attenuating plane S-wave is $\sqrt{\operatorname{Re}\{\mu\}/\rho} \times (1 +$ term of

order $1/Q^2$). Does this violate an important conclusion of Section 5.5; namely, that attenuation in a causal medium has an effect on velocity that introduces a correction of order $1/Q$?

5.16 An attenuating medium that has all its losses confined to shear and none to pure compression can be characterized as having a complex rigidity, but a bulk modulus that is purely real. Show for such a medium that the ratio of Q for P-waves to Q for S-waves is $3\alpha^2/(4\beta^2)$, where α and β are the two wave speeds (assume $Q \gg 1$).

If there are losses also in pure compression, show more generally that

$$\frac{1}{Q_P} = \frac{1}{Q_\kappa} + \frac{4\beta^2}{3\alpha^2}\left(\frac{1}{Q_S} - \frac{1}{Q_\kappa}\right),$$

where $-Q_\kappa$ is the ratio of the real and imaginary parts of the bulk modulus.

5.17 For times t such that $|t - T| \ll T$, show that one can regard the Heaviside function $H(t - T)$ as having the Hilbert transform $(-1/\pi)\log\left|\dfrac{t-T}{T}\right|$.

5.18 Consider an anelastic medium cycled at frequency ω. Show that there is a phase difference between stress and strain, amounting to $1/(\omega Q)$ seconds. [You may assume $Q \gg 1$, and the discussions in Box 5.5 and following equation (5.82).]

Does the stress lead the strain, or the strain lead the stress?

On a plot of strain against stress, there will be a hysteresis loop. Evaluate its area, and show that this is consistent with the first definition of Q given in Box 5.5.

CHAPTER 6

Reflection and Refraction of Spherical Waves; Lamb's Problem

The elementary theory needed to explain seismic data usually falls into one or the other of two categories: one studies either the asymptotic approximations for the waves that propagate in realistic models of the Earth, or the exact form of waves that propagate in highly idealized media. Thus the first category includes geometric ray theory (Chapter 4), and the second includes all of our work in Chapter 5 on plane waves and homogeneous half-spaces. As we develop more sophisticated methods, these two categories gradually merge, in the sense that we shall aim to calculate quite accurately the waves that propagate in fairly realistic Earth models.

The present chapter is mainly a contribution to the second category of theoretical development referred to above, for we shall be concerned with the calculation of waves emanating from a point source in a medium consisting of only two homogeneous half-spaces. In 1904, Horace Lamb gave the exact solution for a problem of this type, in which the source acted as an impulse applied normal to a point on the free surface of a solid half-space. However, since his paper contained so much more, the term "Lamb's problem" has come to refer to more general source/medium geometries with a single interface, in which one is principally interested in the exact calculation (in the time domain) of waves emanating from an impulsive line source or point source.

We introduce this subject by expressing the spherical wave emanating from a point source as a superposition of plane waves (the Weyl integral) and then as a superposition of conical waves (the Sommerfeld integral). When the spherical wave interacts with a plane boundary between two different half-spaces, the resulting wave systems can naturally be divided into three major types: (i) waves that are directly reflected from or transmitted through the boundary; (ii) waves that travel from source to receiver via a path involving refraction along the boundary at a body-wave speed (head waves); and (iii) waves of Rayleigh or Stoneley type, with amplitude decaying exponentially with distance from the interface. These results are derived by manipulation of integration paths in the complex ray-parameter plane. After giving a general outline of the three major wave types, using the frequency domain, we develop exact methods of solution based on the work of Cagniard and de Hoop. These methods employ the Laplace transform of time, although final solutions are stated in the time domain. The basic division into three different wave types is again

apparent, together with minor contributions from a leaking mode (another type of interface wave).

At the outset, we must emphasize that the best way to solve Lamb's problem is via Laplace transformation and the inversion methods of Cagniard. The discussion of integration paths in the complex ray-parameter plane is then relatively simple; and the actual inversion of the Laplace transform, to obtain pulse shapes in the time domain, is made trivial. A self-contained description of these methods is given here in Sections 6.4 and 6.5. We introduce this material, however, with a Fourier transform. In part, this is an acknowledgment to the vast literature on the subject, including books by Ewing *et al.* (1957), Brekhovskikh (1960), and Červený and Ravindra (1971), and many hundreds of papers. But the major reason for developing Fourier-transform methods in connection with Lamb's problem is to prepare the ground for Chapter 9, which gives practical methods for calculating seismograms in realistic structures. We shall find there that the reflectivity method for layered media and powerful solution methods for problems of grazing incidence are based on numerical work with the Fourier transform rather than analytic inversion of the Laplace transform.

6.1 Spherical Waves as a Superposition of Plane Waves and Conical Waves

Consider an inhomogeneous wave equation with source at the origin and time dependence $\exp(-i\omega t)$:

$$\frac{\partial^2 \phi}{\partial t^2} - c^2 \nabla^2 \phi = 4\pi c^2 \delta(\mathbf{x}) \exp(-i\omega t). \tag{6.1}$$

The solution of this equation (in an infinite homogeneous space) is obtained from (4.4) as

$$\phi(\mathbf{x}, t) = \frac{1}{R} \exp\left[i\omega\left(\frac{R}{c} - t\right)\right], \tag{6.2}$$

where $R = \sqrt{x^2 + y^2 + z^2}$.

Equation (6.1) can also be solved by recognizing the time dependence of $\phi(\mathbf{x}, t)$ as the steady oscillation $\exp(-i\omega t)$ and then using Fourier-transform methods to derive the spatial dependence. From transformation of (6.1) we find that

$$\phi(\mathbf{k}, t) = [4\pi c^2/(k^2 c^2 - \omega^2)] \exp(-i\omega t),$$

where $k^2 = k_x^2 + k_y^2 + k_z^2$. Then from (6.2) and the triple inverse transform of $\phi(\mathbf{k}, t)$,

$$\frac{1}{R} \exp\left[i\omega\left(\frac{R}{c} - t\right)\right] = \frac{\exp(-i\omega t)}{2\pi^2} \iiint_{-\infty}^{\infty} \frac{\exp(i\mathbf{k} \cdot \mathbf{x})}{k^2 - \dfrac{\omega^2}{c^2}} dk_x\, dk_y\, dk_z. \tag{6.3}$$

The left-hand side of (6.3) is a spherical wave propagating from the origin with speed c. Its amplitude is a function only of radial distance and has no directional variation. The right-hand side of (6.3) is a superposition of plane waves $\exp[i(\mathbf{k} \cdot \mathbf{x} - \omega t)]$ over the entire range of k_x, k_y, k_z, weighted by $[2\pi^2(k^2 - \omega^2/c^2)]^{-1}$. It therefore appears that we have

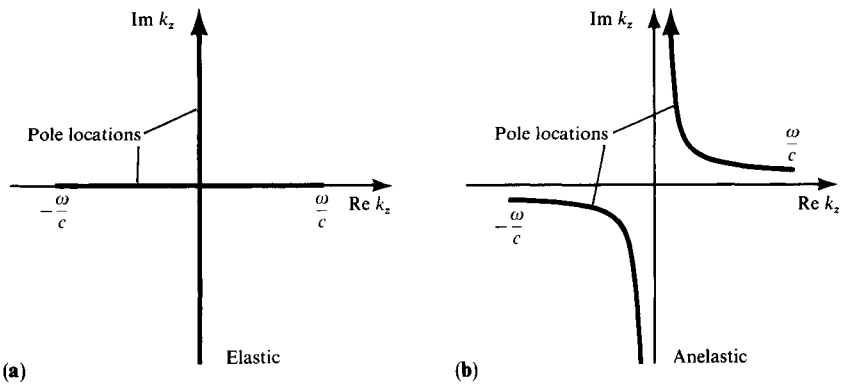

FIGURE **6.1**
Pole locations in the complex k_z-plane for different real values of k_x, k_y, and fixed $\omega > 0$. (**a**) Elastic medium. (**b**) Attenuating medium.

already accomplished our aim of representing the spherical wave by superposing plane waves. However, a closer look at the plane waves in (6.3) shows that they have arbitrary velocity ($= \omega/k$), from $-\infty$ to ∞, so that they do not yet have the form of plane waves in a medium with given velocity c.

In order to obtain the Weyl integral (see Box 6.1), we must carry out an integration with respect to one of the wavenumber components. We shall do this for k_z, so that the integrals that remain will be over horizontal wavenumbers.

The integration over k_z in (6.3) is simple if we extend k_z to complex values and apply residue theory. For given k_x and k_y, the integrand has poles at $k_z = \pm\sqrt{(\omega^2/c^2) - k_x^2 - k_y^2}$, and the only difficulty is that (for a certain range of values of k_x and k_y) these poles lie on the real k_z-axis, interfering with the integration path (see Fig. 6.1a). For convenience, we introduce a small attenuation by making $1/c$ complex. As we have seen in Chapter 5 (equations (5.92), (5.94)), the proper way of doing this is to regard $1/c$ as the sum of a certain reference value, plus a small complex correction that has a *positive* imaginary part. Thus $\mathrm{Im}\{1/c\} = \varepsilon$ and $\varepsilon > 0$ (for $\omega > 0$). The immediate result is to change the pole locations into the first and third quadrants (see Fig. 6.1b), removing the interference with the integration path.

We define the location of the pole in the first quadrant as

$$k_z = i\gamma = +\sqrt{\omega^2/c^2 - k_x^2 - k_y^2}.$$

Then the position of the other pole (third quadrant) is

$$k_z = -i\gamma = -\sqrt{\omega^2/c^2 - k_x^2 - k_y^2}.$$

In both cases, we find that $\mathrm{Re}\{\gamma\}$ is positive and $\mathrm{Im}\{\gamma\}$ is negative.

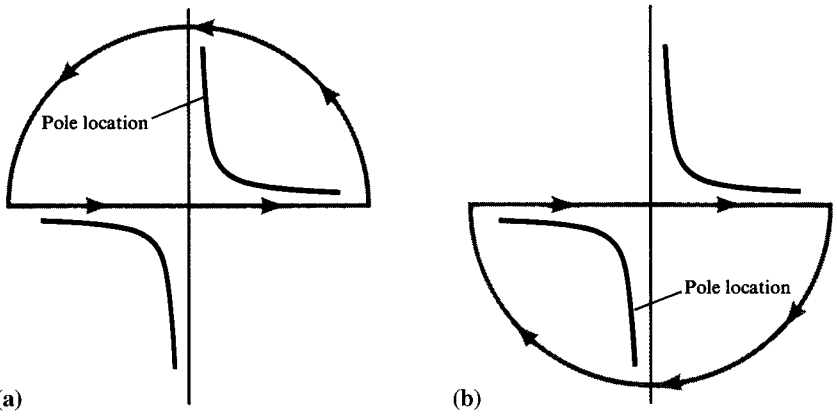

FIGURE **6.2**
Paths of integration in the complex k_z-plane for obtaining the Weyl integral. (**a**) The path when $z > 0$. (**b**) $z < 0$.

The residue evaluation is now straightforward. For $z > 0$ the factor $\exp(ik_z z)$ suppresses the integrand in (6.3) if it is taken around a sufficiently large semicircle in the upper half-plane (see Fig. 6.2a). Adding this semicircle to the integration path along the real axis, we have a closed path going in the positive direction around a pole at $k_z = i\gamma$ in the first quadrant, so that

$$\phi = 2\pi i \times \text{residue} = \frac{\exp(-i\omega t)}{2\pi} \int\int_{-\infty}^{\infty} \frac{\exp(ik_x x + ik_y y - \gamma z)}{\gamma} dk_x\, dk_y.$$

For $z < 0$, we add a sufficiently large semicircle in the lower half-plane (Fig. 6.2b) to obtain a closed path in the negative (i.e., clockwise) direction, which picks up a pole at $k_z = -i\gamma$ in the third quadrant:

$$\phi = -2\pi i \times \text{residue} = \frac{\exp(-i\omega t)}{2\pi} \int\int_{-\infty}^{\infty} \frac{\exp(ik_x x + ik_y y + \gamma z)}{\gamma} dk_x\, dk_y.$$

Combining these results for $z > 0$ and $z < 0$, we obtain the Weyl integral

$$\frac{1}{R} \exp\left(i\omega \frac{R}{c}\right) = \frac{1}{2\pi} \int\int_{-\infty}^{\infty} \frac{\exp(ik_x x + ik_y y - \gamma |z|)}{\gamma} dk_x\, dk_y, \tag{6.4}$$

where $\gamma = \sqrt{k_x^2 + k_y^2 - \omega^2/c^2}$ and the sign of γ is chosen so that $\text{Re}\ \gamma > 0$. In the limiting case of zero attenuation, this becomes $\text{Re}\ \gamma \geq 0$.

In the above expression, the plane waves in the integrand do satisfy the wave equation with velocity c, so that the spherical wave is indeed represented by a superposition of such plane waves. Note that for some parts of the (k_x, k_y) integration, the plane waves are inhomogeneous. This occurs for $\omega^2/c^2 < k_x^2 + k_y^2$, so that γ becomes positive real

BOX 6.1

Fundamental significance of Weyl and Sommerfeld integrals

The totality of solutions to a wave equation with particular homogeneous boundary conditions is a vector space, and for various coordinate systems one may establish a basis of vectors to span this space. The Weyl integral uses plane waves as a basis, summing them to give the solution for a point source. The Sommerfeld integral is the analogous result for conical waves. Often we refer to the basis vectors as eigenvectors or eigenfunctions, appropriate for a particular coordinate system. Plane waves and conical waves are seen to be eigenfunctions, in the context of studying solutions to the wave equation by the method of separation of variables (e.g., see Chapter 5, equations (5.9) and (5.10)).

These ideas will recur repeatedly in later chapters, where the eigenfunctions may be surface wave modes of vector displacement, where the source may have a complicated radiation pattern, where the coordinate system may involve spherical polars with origin at the center of the Earth, and where a discrete sum over eigenfunctions may be appropriate, rather than the integrations over horizontal wavenumber that we have used here.

The problem of finding the particular integral (or sum) of eigenfunctions appropriate for a particular source is then the problem of finding the coefficient of each (suitably normalized) eigenfunction in the expansion. This coefficient is a measure of the degree to which a particular eigenfunction has been excited.

A property common to all these source expansions, true for the Weyl integral as well as the more complicated expressions for surface waves and normal modes described in Chapters 7 and 8, is that the integrand (or each term in the sum) can be factored into a vertical eigenfunction evaluated at the source, a vertical eigenfunction evaluated at the receiver, and a transverse wavefunction that is dependent on the horizontal separation of source and receiver. (In our case, e.g., (6.4) and (6.9), vertical eigenfunctions at source and receiver are waves traveling in opposite directions, so that only the difference phase appears, proportional to the vertical separation.) The independent variable describing different terms in the integral is essentially the horizontal slowness, and a function of this variable provides a weighting factor for the integrand.

and the corresponding inhomogeneous waves propagate parallel to the xy-plane, changing amplitude most rapidly in the z-direction.

As suggested above, a different wavenumber component could have been used for the integration instead of k_z. If we had used k_x, we should find inhomogeneous waves propagating parallel to the yz-plane, equally representing the spherical wave. We chose to work with the depth component of wavenumber, for then the result (6.4) is appropriate for analyzing boundary conditions on horizontal surfaces.

To obtain the Sommerfeld integral (see Box 6.1), we change integration variables from (k_x, k_y) to (k_r, ϕ') via

$$k_x = k_r \cos\phi', \qquad k_y = k_r \sin\phi'. \tag{6.5}$$

Thus $i\gamma = \sqrt{\omega^2/c^2 - k_r^2}$, and the area element $dk_x\, dk_y$ is replaced by the element $k_r dk_r\, d\phi'$, with the whole horizontal wavenumber plane $(-\infty < k_x < \infty; -\infty < k_y < \infty)$ being covered by the ranges $0 \le k_r < \infty, 0 \le \phi' < 2\pi$. The integral (6.4) becomes

$$\frac{1}{R}\exp\left(i\omega\frac{R}{c}\right)=\frac{1}{2\pi}\int_0^\infty dk_r\int_0^{2\pi}d\phi'\frac{k_r}{\gamma}\exp[ik_r r\cos(\phi-\phi')-\gamma|z|], \quad (6.6)$$

where we have introduced (r, ϕ) as the polar coordinates related to (x, y) via $x = r\cos\phi$, $y = r\sin\phi$. We often call r the *offset* or the *horizontal range*, or simply the *range*, and ϕ is the azimuthal coordinate of cylindrical or spherical polars. Since z is measured downward, note that ϕ increases clockwise when the horizontal plane is viewed from above.

The integral over ϕ' in (6.6) can be given explicitly, using the relation $2\pi J_0(k_r r) = \int_0^{2\pi}\exp(ik_r r\cos\Phi)\,d\Phi$ to obtain the Sommerfeld integral

$$\frac{1}{R}\exp\left(i\omega\frac{R}{c}\right)=\int_0^\infty\frac{k_r J_0(k_r r)\exp(-\gamma|z|)}{\gamma}\,dk_r \quad (6.7)$$

where $i\gamma=\sqrt{\omega^2/c^2-k_r^2}$ and $\mathrm{Re}\{\gamma\}>0$. The integrand here is a new kind of fundamental wave, the conical wave (with symmetry about a vertical axis). The dependence on r and on z appears via separate factors.

In Chapter 5, we found it convenient to analyze plane waves by choosing a y-axis normal to the direction of propagation, and then identifying k_x with ray parameter p via $k_x = \omega\sin i/c = \omega p$ (e.g., equation (5.16)). Now, however, for a point source, the system of plane waves *departing from the source* involves all possible horizontal directions of propagation, as shown directly in (6.6) by the integration over ϕ'. The relation between horizontal wavenumber and ray parameter therefore becomes

$$k_x=\omega\sin i\cos\phi'/c=\omega p\cos\phi', \qquad k_y=\omega\sin i\sin\phi'/c=\omega p\sin\phi'.$$

By comparison with (6.5) we see that

$$k_r=\omega p. \quad (6.8)$$

Hence, from (6.7), we can express the spherical wave as an integral over all ray parameters in the form

$$\frac{1}{R}\exp\left(i\omega\frac{R}{c}\right)=i\omega\int_0^\infty\frac{p}{\xi}J_0(\omega pr)\exp(i\omega\xi|z|)\,dp. \quad (6.9)$$

Here we have taken $i\gamma = \omega\xi$. Recall too that $\mathrm{Re}\{\gamma\} > 0$. Hence

$$\xi=\sqrt{\frac{1}{c^2}-p^2}, \quad (6.10)$$

and we must choose the branch $\mathrm{Im}\{\xi\} > 0$,which becomes $\mathrm{Im}\{\xi\}\geq 0$ for perfectly elastic media. With this definition of the square root, the vertical wave function in (6.9) can readily be identified with the formulas of Chapter 5: it is $\exp[i\omega(c^{-1}\cos i)|z|]$, with $(c^{-1}\cos i) = \sqrt{c^{-2}-p^2}=\xi$ being positive imaginary if $1/c < p$. Note that ξ is the vertical slowness (compare with (5.65)) and $i\gamma$ the corresponding vertical wavenumber, whereas p is the horizontal slowness.

In terms of slownesses s_x, s_y, ξ related to wavenumber components by $k_x = \omega s_x$, $k_y = \omega s_y$, $\omega\xi = i\gamma$, the Weyl integral (6.4) can be written as

$$\frac{1}{R}\exp\left[i\omega\left(\frac{R}{c}-t\right)\right] = \frac{i\omega}{2\pi}\iint_{-\infty}^{\infty}\frac{\exp[i\omega(s_x x + s_y y + \xi|z| - t)]}{\xi}ds_x\, ds_y, \qquad (6.11)$$

in which the integrand is particularly easy to recognize as a plane wave. The horizontal slowness is $\sqrt{s_x^2 + s_y^2} = p$, and ξ is given by (6.10).

For a solid medium, we shall use ξ for the P-wave vertical slowness so that $\xi^2 + p^2 = 1/\alpha^2$. For S-waves, we shall use η as the vertical slowness (as in (5.65)) and $i\nu$ for the vertical wavenumber. Thus $\eta^2 + p^2 = 1/\beta^2$. Because this chapter is predominantly about body waves and nondispersive surface waves, it is convenient in practice to work with slownesses p, ξ, η. Therefore, we shall consistently work here with (6.9) rather than (6.7). For the surface waves described in Chapter 7, when strong dispersion can be present and the vertical wavenumber is imaginary, we shall revert to using variables such as k_r, γ, and ν.

6.2 Reflection of Spherical Waves at a Plane Boundary: Acoustic Waves

In this section and the next, we shall examine the basic phenomena that arise when a curved wavefront is incident upon the boundary between two different media. For this initial work we shall use waves at fixed frequency, since so many of the observations in seismology can be physically interpreted as a synthesis (the inverse Fourier transform) of such waves. In later work, to obtain exact wave solutions in the time domain, we shall turn to a method that is more conveniently developed via the Laplace transform.

The first problem we shall solve (see Fig. 6.3) involves acoustic waves in a body consisting of two different homogeneous semi-infinite liquids in contact along the plane $z = 0$. The source is in medium 1 (density ρ_1, velocity α_1) at depth $z_0 < 0$, and we shall also take the observation point (x, y, z) in medium 1. The source–receiver distance is given by

$$R = \sqrt{x^2 + y^2 + (z - z_0)^2},$$

and we shall assume that the source generates waves of pressure P in the form

$$P = P^{\text{inc}} \equiv A\frac{1}{R}\exp\left[i\omega\left(\frac{R}{\alpha_1}-t\right)\right]$$

for some constant A.

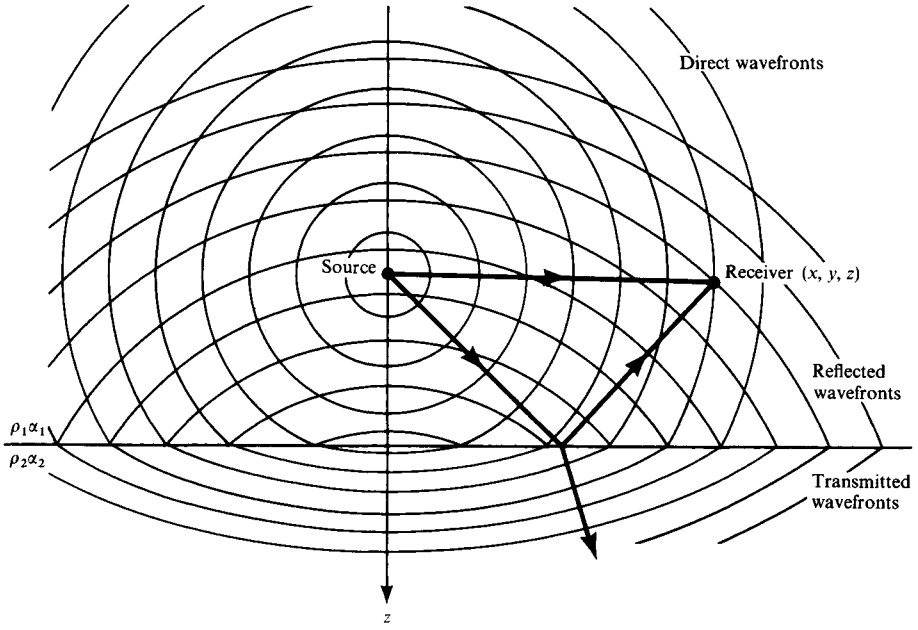

FIGURE **6.3**
Configuration of source and receiver in a fluid half-space $z < 0$ with density ρ_1 and velocity α_1. A different fluid half-space (ρ_2, α_2) occupies $z > 0$, and pressure and vertical displacement are continuous across the interface. It is because of the complexity of wavefront systems that we shall usually use rays alone.

Using the results of Section 6.1, we shall express P^{inc} as a superposition of conical waves. Then we apply the theory of Chapter 5 to find reflected and transmitted plane waves, which must again be superposed. Thus

$$\begin{aligned} P^{\text{inc}} &= \frac{A}{R}\exp\left[i\omega\left(\frac{R}{\alpha_1} - t\right)\right] \\ &= i\omega\exp(-i\omega t)\int_0^\infty \frac{Ap}{\xi_1} J_0(\omega p r)\exp(i\omega\xi_1|z - z_0|)\,dp \end{aligned} \tag{6.12}$$

where $\xi_1 = \alpha_1^{-1}\cos i_1 = \sqrt{\alpha_1^{-2} - p^2}$ is positive imaginary if $1/\alpha_1 < p$. Seeing the integrand here as an azimuthal integral over plane waves (compare with equation (6.6)), it is natural to attempt a solution for the reflection and transmission fields as

$$P^{\text{refl}} = i\omega\exp(-i\omega t)\int_0^\infty \frac{Bp}{\xi_1} J_0(\omega p r)\exp[-i\omega\xi_1(z + z_0)]\,dp \quad \text{in } z < 0 \tag{6.13}$$

and

$$P^{\text{trans}} = i\omega\exp(-i\omega t)\int_0^\infty \frac{Cp}{\xi_1} J_0(\omega p r)\exp(-i\omega\xi_1 z_0 + i\omega\xi_2 z)\,dp \quad \text{in } z > 0. \tag{6.14}$$

BOX 6.2

Determining the branch cuts of $\sqrt{\alpha^{-2} - p^2} = \xi$ *in the complex p-plane, so that* $\operatorname{Im} \xi \geq 0$ *for a whole plane.*

We wish to make ξ a single-valued analytic function of p, and the ambiguity of sign for a square root requires us to consider two p-planes (Riemann sheets) to describe ξ completely. We speak of a *top sheet* and a *bottom sheet*, according as $\operatorname{Im} \xi > 0$ and $\operatorname{Im} \xi < 0$, connected along lines (branch cuts) determined by $\operatorname{Im} \xi = 0$. Clearly the cuts include points where $\xi = 0$ (branch points), and these are $p = \pm 1/\alpha$. We shall need to understand how to take closed paths around a branch point in such a way that ξ varies smoothly with p for the whole path.

Since branch cuts are determined by $\operatorname{Im} \xi = 0$, it follows that $\alpha^{-2} - p^2$ is real and nonnegative on the cut itself, and hence that

$$1/\alpha^2 - (\operatorname{Re} p)^2 + (\operatorname{Im} p)^2 - 2i(\operatorname{Re} p)(\operatorname{Im} p) \geq 0. \tag{1}$$

But since $\operatorname{Im} (1/\alpha^2)$ is (small and) positive, the requirement that the left-hand side of (1) is real implies

$$(\operatorname{Re} p)(\operatorname{Im} p) = \varepsilon \qquad \text{for some } \varepsilon = \tfrac{1}{2}\operatorname{Im} (1/\alpha^2) > 0, \qquad \text{with } \varepsilon \to 0$$

in the limiting case of perfect elasticity. Hence the branch cuts lie on a hyperbola in the first and third quadrants. A further restriction, from (1), is that $(\operatorname{Im} p)^2 \geq (\operatorname{Re} p)^2 - \operatorname{Re} (1/\alpha^2)$, limiting the branch cuts to positions shown schematically in Figure 6.4.

In order to see how the devices of branch cuts and Riemann sheets make a single-valued analytic function out of what ordinarily is considered a double-valued function $\xi = \xi(p)$, consider the three circuits shown below:

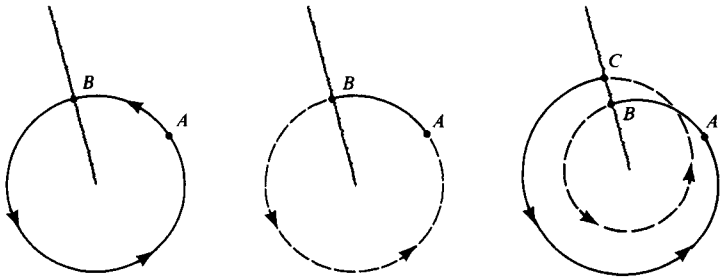

Starting from point A, the closed circuit Γ_1 is drawn entirely on the same sheet: ξ is single valued, but is discontinuous on crossing the branch cut at B. For the circuit Γ_2, ξ is analytic at B, requiring Γ_2 to go on to a different sheet (broken line); but then Γ_2 does not return ξ to the same value at A as it had initially. Finally, Γ_3 shows a path going *twice* around the branch point, with ξ varying analytically all the way and returning to its original value at A.

Continuity of pressure across $z = 0$ requires that $A + B = C$. From Box 5.4, continuity of vertical displacement across $z = 0$ leads to continuity of $(1/\rho)\partial P/\partial z$. Hence $(\xi_1/\rho_1)(A - B) = (\xi_2/\rho_2)C$, and we now have two equations determining plane-wave reflection/transmission coefficients, solved as

$$\frac{B}{A} = -\frac{\rho_1\xi_2 - \rho_2\xi_1}{\rho_1\xi_2 + \rho_2\xi_1} = -\frac{\rho_1\dfrac{\cos i_2}{\alpha_2} - \rho_2\dfrac{\cos i_1}{\alpha_1}}{\rho_1\dfrac{\cos i_2}{\alpha_2} + \rho_2\dfrac{\cos i_1}{\alpha_1}} \tag{6.15}$$

and

$$\frac{C}{A} = \frac{2\rho_2\xi_1}{\rho_1\xi_2 + \rho_2\xi_1} = \frac{2\rho_2\dfrac{\cos i_1}{\alpha_1}}{\rho_1\dfrac{\cos i_2}{\alpha_2} + \rho_2\dfrac{\cos i_1}{\alpha_1}}.$$

Note also that $\alpha_2^{-1}\cos i_2 = \xi_2 = \sqrt{\alpha_2^{-2} - p^2}$ is positive imaginary if $1/\alpha_2 < p$, to ensure exponential decay of (6.14) with depth.

In the remainder of this section, we shall concentrate on an approximate evaluation of the reflected wave (6.13), using the standard method of saddle-point integration and beginning with the case that $\alpha_1 > \alpha_2$.

The first step is to rewrite (6.13) using the Hankel function $H_0^{(1)}$ instead of J_0. Since $J_0(x) = \frac{1}{2}[H_0^{(1)}(x) + H_0^{(2)}(x)]$ and $H_0^{(2)}(x) = -H_0^{(1)}(-x)$, we find

$$P^{\text{refl}} = \frac{i\omega}{2}\exp(-i\omega t)\int_{-\infty}^{\infty}\frac{Bp}{\xi_1}H_0^{(1)}(\omega pr)\exp[-i\omega\xi_1(z + z_0)]\,dp \tag{6.16}$$

(using the fact that B is even in p).

Secondly, let us assume that the range r is many wavelengths, so that pr is large and we can approximate $H_0^{(1)}(\omega pr)$ by its asymptotic expansion

$$H_0^{(1)}(\omega pr) = \sqrt{\frac{2}{\pi\omega pr}}\exp[i(\omega pr - \pi/4)]\left[1 - \frac{i}{8\omega pr} + O\left(\frac{1}{\omega^2 p^2 r^2}\right)\right]. \tag{6.17}$$

(The above expansion is inaccurate for p-values near zero, but we shall later distort the integration path in a way that avoids $p = 0$. It would be more correct to substitute from (6.17) after the distortion.) The approximate result is now

$$P^{\text{refl}} = \sqrt{\frac{\omega}{2\pi r}}\exp[-i(\omega t - \pi/4)]\int_{-\infty}^{\infty}\frac{B\sqrt{p}}{\xi_1}\exp[i\omega(pr - \xi_1 z - \xi_1 z_0)]\,dp, \tag{6.18}$$

in which terms of order $1/\omega$ have been neglected in the integrand; and $B = B(p)$, involving both ξ_1 and ξ_2, is given in (6.15).

The location of branch cuts for ξ_1 and ξ_2 is described in Box 6.2, and the cuts for P^{refl} are shown in Figure 6.4. Our goal now is to distort the path of integration in such a way that

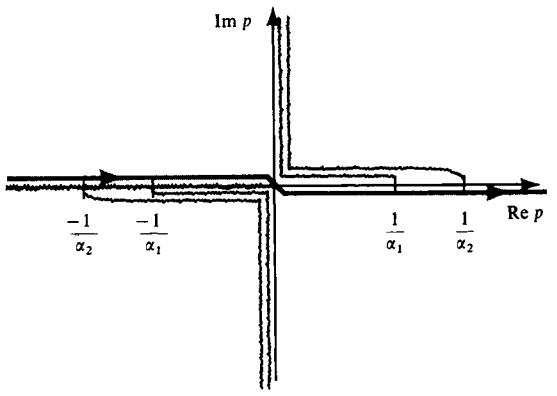

FIGURE **6.4**
Branch cuts for ξ_1, ξ_2, and $\sqrt{p}$ in the complex p-plane. The cuts are given by Im $\xi_1 = 0$, Im $\xi_2 = 0$; and Re $\sqrt{p} = 0$ (this being the cut assumed in (6.17); in fact, it is directly a branch cut for $H_0^{(1)}(\omega pr)$). The integration path for P^{refl} (see (6.18)) lies on the negative real axis just above three cuts, and lies on the positive real axis just below two cuts.

only a limited range of p-values makes any significant contribution, and then to evaluate the integral itself. To this end, we use standard methods of saddle-point analysis to obtain an asymptotic approximation to P^{refl}, valid for sufficiently large frequencies.

Following the notation of Box 6.3, with $x = \omega$, $\zeta = p$, we see that

$$\begin{aligned} f(p) &= i(pr + \xi_1|z + z_0|) \qquad (\text{recall } z < 0, z_0 < 0), \\ f'(p) &= i(r - p|z + z_0|/\xi_1), \\ f''(p) &= -i|z + z_0|/(\alpha_1^2 \xi_1^3), \end{aligned} \tag{6.19}$$

indicating a saddle point $p = p_s$ such that $r\xi_1 = p|z + z_0|$. In terms of an angle, $p_s = \alpha_1^{-1} \sin i_s$. Then $\xi_1 = \alpha_1^{-1} \cos i_s$, so that $r \cos i_s = |z + z_0| \sin i_s$. From Figure 6.5 it is now apparent that the saddle occurs precisely for that value of p which gives the reflected ray between source and receiver. Following through with the approximation (1) of Box 6.3, a little algebra and trigonometry give the asymptotic result

$$P^{\text{refl}} \sim \frac{B(p_s)}{R_0} \exp\left[i\omega\left(\frac{R_0}{\alpha_1} - t\right)\right] \qquad \text{as } \omega \to \infty, \tag{6.20}$$

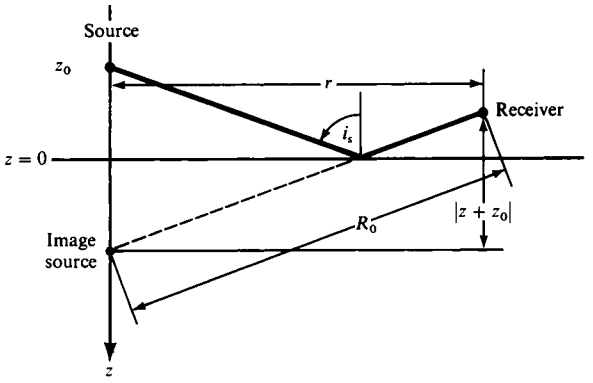

FIGURE **6.5**
Geometry for the ray reflected at the interface between source and receiver. It has the special ray parameter $p_s = \alpha_1^{-1} \sin i_s$. R_0 is the distance between image source (at $z = -z_0$) and receiver. Note the trigonometrical relationships $r = R_0 p_s \alpha_1$, $pr + \alpha_1^{-1} \cos i_s |z + z_0| = R_0/\alpha_1$, and $r \cos i_s = |z + z_0| \sin i_s$.

BOX **6.3**

The evaluation of $I(x) = \int_C F(\zeta) \exp[xf(\zeta)]\, d\zeta$ *by the method of steepest descents*

We presume the reader has some acquaintance with this method (see, e.g., Jeffreys and Jeffreys, 1972). Our purpose here is to state notation and review the main concepts. F and f are complex functions of ζ, and x is large and positive.

To begin, suppose $f(\zeta)$ has a saddle point at $\zeta = \zeta_0$. Where f is analytic, contours of Re f = constant and contours of Im f = constant are orthogonal to each other. Near ζ_0, these contours are hyperbolas, as shown in the figure here. (The angle χ is shown having a value about $-30°$. In general, it can lie anywhere in the range $-\pi/2 \leq \chi \leq \pi/2$.)

The designations "valley" and "ridge" and the directions of rising and falling describe topography of the surface with height given by Re f, evaluated near ζ_0. The integrand for $I(x)$ is primarily controlled (in magnitude) by $\exp(x \text{ Re } f)$; therefore, since x is large and positive, the terms "valley" and "ridge" apply *a fortiori* to this integrand. By taking the integration path up one valley, across the ridge at its lowest point, and down the opposite valley, one often achieves the desirable goal of minimizing the range of integration that is significant for evaluation of $I(x)$. Details of how contour C is deformed—in order to cross the saddle from valley to valley—will depend on singularities and branch cuts of the integrand and on the end points of C. We shall assume that C has been deformed to the path of ascent and descent as described above, the path making an angle χ with the positive real ζ-axis. Making a Taylor series expansion of $f(\zeta)$ about ζ_0, it is easy to show that $f''(\zeta_0)e^{2i\chi}$ is real and negative if the integrand is to behave like a gaussian function near ζ_0. If f'' has phase ϕ, then $\chi = \frac{1}{2}(\pi - \phi)$ or $\frac{1}{2}(-\pi - \phi)$. By ignoring $O[(\zeta - \zeta_0)^3]$ in the expansion for $f(\zeta)$, one finds that the contribution to $I(x)$ from the saddle is asymptotically

$$\sqrt{\left|\frac{2\pi}{xf''(\zeta_0)}\right|} F(\zeta_0)e^{i\chi} \exp[xf(\zeta_0)] \qquad \text{as} \qquad x \to \infty. \tag{1}$$

(continued)

provided only that the real path of integration in (6.18) can be deformed onto the steepest descents path over $p = p_s$, without picking up any further contributions from singularities or branch cuts of the integrand. The saddle itself lies on two branch cuts, so that at first sight it does not seem possible to use the steepest descents path. Indeed, it is not possible if the path is confined only to the Riemann sheet with Im $\xi_1 \geq 0$, Im $\xi_2 \geq 0$. But, by using (in the first quadrant) the sheet with Im $\xi_1 < 0$, Im $\xi_2 < 0$, the path Γ shown in Figure 6.6 is obtained with the following properties:

(i) the quantity $i(pr + \xi_1|z + z_0|)$ is an analytic function, taking the value iR_0/α_1 at the saddle point;

(ii) elsewhere on Γ, $i(pr + \xi_1|z + z_0|) - iR_0/\alpha_1$ is a negative real number;

(iii) the asymptotes of Γ are lines, as shown in Figure 6.6, making angles i_s with the negative and positive real p-axis.

These three properties arise from the solution of $i(pr + \xi_1|z + z_0|) = -X^2 + iR_0/\alpha_1$ for p as a function of the real number X. We shall give further details of such solutions later

BOX **6.3** *(continued)*

This formula, however, is only of passing interest in seismology, since we shall find that it gives nothing more than the answer we would obtain by using geometrical ray theory. More important are the numerical methods of integrating over the saddle *without* making crude approximations to $f(\zeta)$. Often we shall follow the "valleys" of Re f out to some distance from the saddle itself (see, e.g., Fig. 6.6), in which case the trend of the valleys may not be orthogonal to the trend of the ridges at the saddle itself.

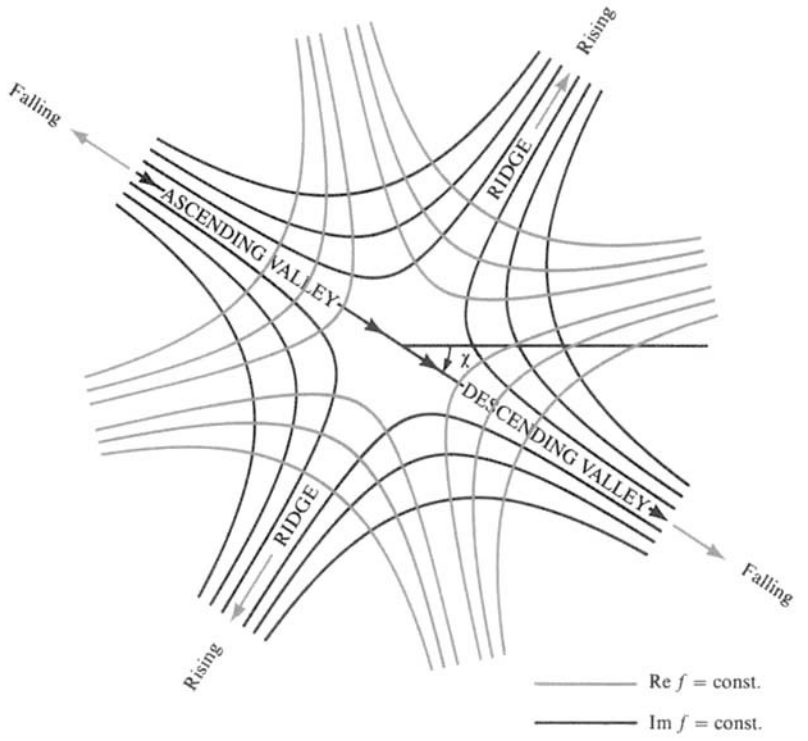

(in the legend of Fig. 6.12c, and also for related paths in the context of Cagniard theory). The remaining point to make here is that when $\alpha_1 > \alpha_2$, there is no difficulty in deforming from the real-axis path of (6.18) to the path Γ of Figure 6.6. Connecting arcs C_1 and C_2 are required in the first and second quadrants, but on these the integrand vanishes exponentially. At point B, the path Γ must leave the top Riemann sheet if it is to avoid discontinuities in the integrand. On reaching the top of the saddle, Γ reappears on the top sheet, where it remains for the rest of the path. Having satisfied ourselves that branch cuts and singularities make no contribution, we return to a discussion of the asymptotic solution (6.20).

We note first that the geometrical spreading factor for the reflected wave would be just $1/R_0$, and its travel time would be R_0/α_1. The expectation from geometrical ray theory would then be that $P^{\text{refl}} \sim A(1/R_0)\exp[i\omega(R_0/\alpha_1 - t)]$ multiplied by a factor representing the ratio of reflected/incident pressures for the interface. We have obtained such ratios in

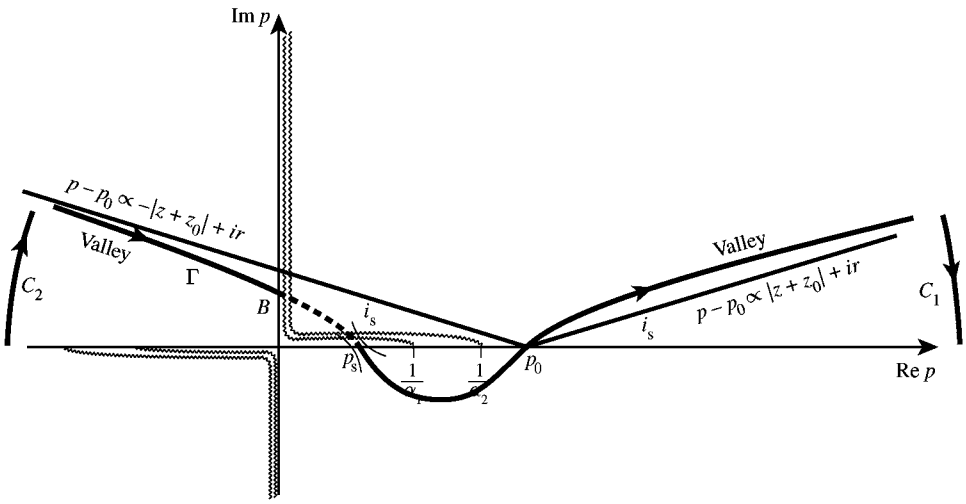

FIGURE **6.6**
The steepest descents path Γ in the complex ray-parameter plane for obtaining P^{refl} (see (6.18)), when $\alpha_1 > \alpha_2$. We have indicated the path Γ for its whole length, using the rule that $\omega f(p) - \omega f(p_s)$ is negative real, so that $\exp[\omega f(p)]$ decays exponentially away from the saddle point. Near the saddle point itself, ridges and valleys are as shown in Box 6.3, with $\chi = -\pi/4$. The dotted path is on a lower Riemann sheet, for which Im ξ_1 and Im ξ_2 are negative. $p_0 = 1/(\alpha_1 \sin i_s)$; see also Figure 6.12.

Chapter 5 for plane waves, but here the incident wave has a spherical wavefront. Nevertheless, the plane-wave reflection coefficient B/A given in (6.15) will be adequate if the radius of curvature is sufficiently large, provided that $B = B(p)$ is evaluated at the ray-parameter value p_s (corresponding to the actual angle of reflection, i_s). It is satisfying that we have now given a physical interpretation of the solution (6.20) in terms of geometrical ray theory and plane-wave reflection coefficients. We shall find that such explanations are still available as we advance our theoretical methods to handle ever more realistic Earth models. However, if these were all we could achieve with integrations in the complex ray-parameter plane, the effort would hardly be worthwhile. Going over the derivation of (6.20), we see that several different approximations were made, beginning with the neglect of higher-order terms in (6.17) and continuing in Box 6.3 with the approximation of $f(p)$ by $f(p_s) + \frac{1}{2}(p - p_s)^2 f''(p_s)$. This last approximation is particularly poor, since it is valid only in the vicinity of the saddle, yet is applied for the whole p-plane. As we shall find later in this chapter and also in Chapter 9, modern methods of quantitative seismology often make the approximation (6.17), keeping only the first term, and then finding a numerical way to obtain the steepest descents path Γ, evaluating $f(p)$ exactly on this path.

By keeping additional terms in the approximations used to derive (6.20), it can formally be shown for $\alpha_1 > \alpha_2$ that

$$P^{\text{refl}} = \frac{B(p_s)}{R_0}\left[1 + \sum_{n=1}^{\infty} a_n \left(\frac{i}{\omega}\right)^n\right] \exp\left[i\omega\left(\frac{R_0}{\alpha_1} - t\right)\right] \tag{6.21}$$

as $\omega \to \infty$, in which the constants $a_1, a_2, \ldots$ depend on source–receiver geometry. In the time domain, P^{refl} becomes

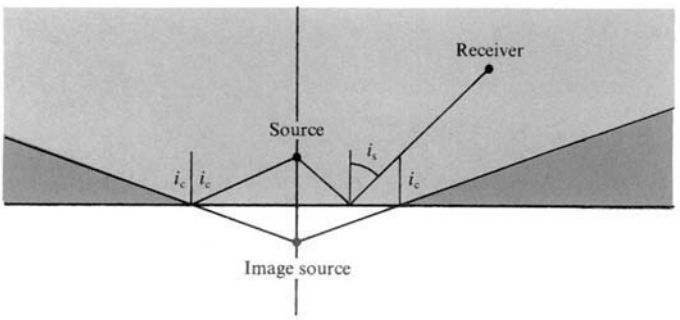

FIGURE **6.7**
For receivers in the light gray region, the reflected ray has angle of incidence $i_s < i_c$, as shown. We define $i_c = \sin^{-1}(\alpha_1/\alpha_2)$, so that, by Snell's law, rays incident at this angle emerge in the lower half-space with $i_2 = \pi/2$, i.e., in the horizontal direction. Receivers in the dark gray region would have $i_s > i_c$, so that $p_s = \alpha_1^{-1} \sin i_s > 1/\alpha_2$. Then plane waves in the lower medium with this ray parameter would be inhomogeneous waves. It is for receivers in the dark gray region that head waves may be observed.

$$\frac{B(p_s)}{R_0}\left\{\delta\left(t-\frac{R_0}{\alpha_1}\right)+H\left(t-\frac{R_0}{\alpha_1}\right)\left[a_1+a_2\left(t-\frac{R_0}{\alpha_1}\right)+a_3\left(t-\frac{R_0}{\alpha_1}\right)^2+\cdots\right]\right\} \tag{6.22}$$

as $t \to R_0/\alpha_1$, so that the reflected wave has a longer tail than the incident wave in the time domain ($P^{\text{inc}} = (A/R)\delta(t - R/\alpha_1)$). The equivalent expressions in (6.21) and (6.22) are *wavefront expansions*. As we indicated in Chapter 4 (following (4.83)), their use in seismology is limited, although the first term can be of interest in giving geometrical ray theory.

To continue our analysis of acoustic waves in two different half-spaces, we next discuss the case $\alpha_1 < \alpha_2$, which permits head waves (see Box 6.4) to exist. Equation (6.18) is still valid, and the branch cuts are as we found them in Figure 6.4 but with $1/\alpha_1$ now to the right of $1/\alpha_2$. As before, there is a saddle point $p_s = \alpha_1^{-1} \sin i_s$, which must lie between 0 and $1/\alpha_1$, but now there is the possibility that p_s lies to the right of $1/\alpha_2$. In Figure 6.7, a critical angle $i_c = \sin^{-1}(\alpha_1/\alpha_2)$ is defined, and the spatial regions corresponding to $p_s = \alpha_1^{-1} \sin i_s < 1/\alpha_2$ and $p_s = \alpha_1^{-1} \sin i_s > 1/\alpha_2$, are identified.

First, we shall consider the case of a receiver in the light gray region of Figure 6.7, i.e., $p_s < 1/\alpha_2$. Then the reflected wave P^{refl} can be analyzed in detail by exactly the same type of steepest descents path Γ as we found earlier. The path is shown in Figure 6.8, and again it must be taken on to the sheet $\text{Im}\,\xi_1 < 0$, $\text{Im}\,\xi_2 < 0$ in the first quadrant. Our discussion above of the geometrical ray solution (6.20) is unchanged.

Second, we consider the case of a receiver in the dark gray region of Figure 6.7, i.e., $p_s > 1/\alpha_2$. Although p_s is still a saddle point of $i(pr + \xi_1|z + z_0|)$, the problem now is that the valley of approach in the first quadrant lies on the sheet $\text{Im}\,\xi_1 < 0$, $\text{Im}\,\xi_2 > 0$. From this sheet, how is it possible to circumvent branch cuts and cross from one sheet to another with a path that begins (as required) in the second quadrant on the sheet $\text{Im}\,\xi_1 > 0$, $\text{Im}\,\xi_2 > 0$? A solution is shown in detail in Figure 6.9.

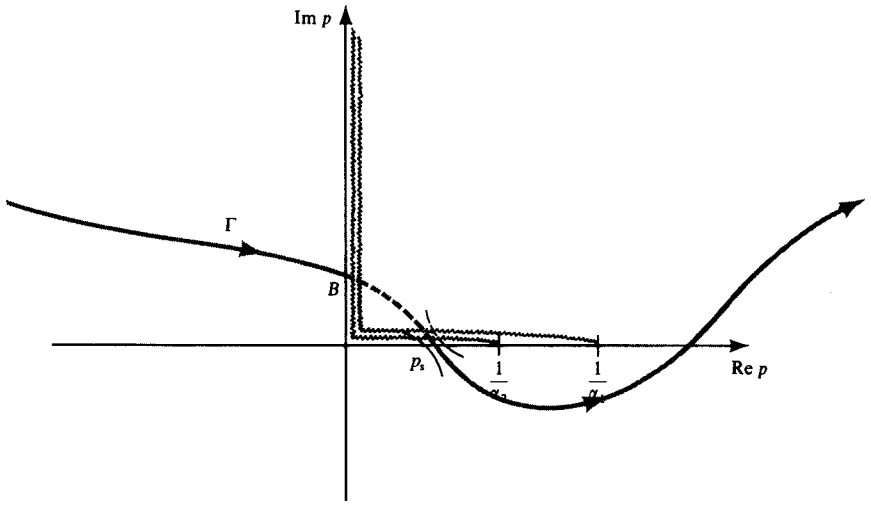

FIGURE **6.8**
The steepest descents path Γ in the complex ray parameter plane for obtaining P^{refl} (see (6.18)), when $\alpha_1 < \alpha_2$ but $p_s < 1/\alpha_2$. The path is similar to that of Figure 6.6.

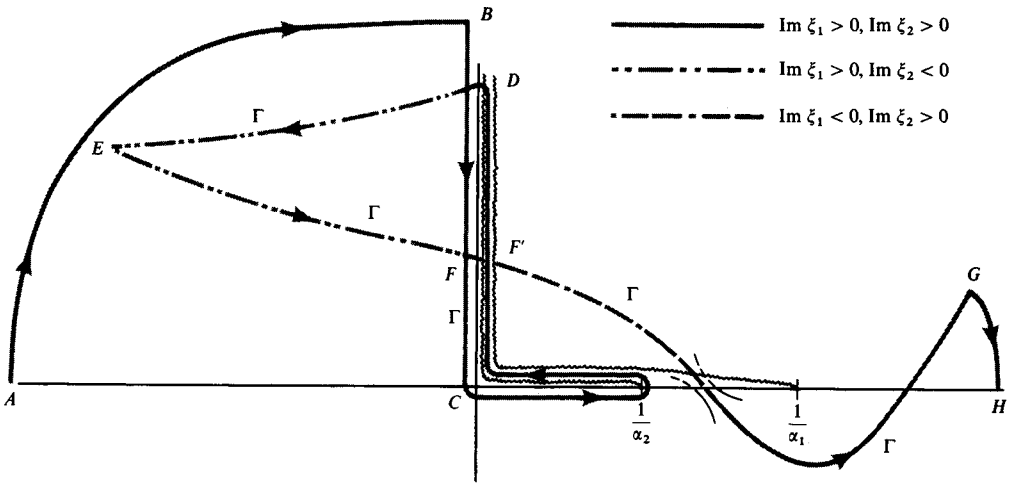

FIGURE **6.9**
The integration path Γ in the complex ray-parameter plane for obtaining P^{refl} (see (6.18)) when $\alpha_1 < \alpha_2$ but $p_s > 1/\alpha_2$. Note that three Riemann sheets are needed as shown at the upper right. Starting at point A, there is no contribution from arc AB. For BC, C to $1/\alpha_2$, and around the cut Im $\xi_2 = 0$, the path stays on the top sheet to D, which is some point sufficiently far up to give a negligible integrand. Crossing the cut at D, the path must descend to Im $\xi_1 > 0$, Im $\xi_2 < 0$ in order to keep the integrand analytic. From E to the saddle point and on to G is exactly the path of steepest descents; at F, the path crosses to Im $\xi_1 < 0$, Im $\xi_2 > 0$, and crosses back to the top sheet at saddle. A large arc GH contributes nothing.

BOX **6.4**

Outstanding features of head waves

1. Amplitude attenuates with distance as $r^{-1/2}L^{-3/2}$, which will be approximately r^{-2} for $r \gg |z + z_0|$, so that the attenuation is much stronger than for the incident spherical wave P^{inc} or for the wide-angle reflection.
2. The factor i/ω corresponds to an integration in the time domain, making the wave form smoother, with a more emergent onset and longer tail as compared to the waveform of P^{inc}.
3. Near the critical distance at which head waves formally can exist, L is small (see Fig. 6.10), and our approximate formula (6.26) blows up as $L \to 0$, i.e., as $i_1 \to i_c$ from above. A corresponding failure can be shown for the reflection formula (6.21), in that $a_1 \to \infty$ as $i_1 \to i_c$ from below, so that our asymptotic formulas will fail completely at the critical distance. Different asymptotic formulas can be developed that apply specifically in the critical range $i_1 \sim i_c$ (Brekhovskikh, 1960, para. 22), but for practical purposes it is imperative to develop numerical methods applicable for all distance ranges.

Head waves are also known in the seismological literature as "conical waves" or "lateral waves," and their propagation path was first recognized by Mohorovičić during his studies of the arrival time of certain waves from a European earthquake of 1909. These waves, which we now call P_n, are refracted along the top of the mantle. They have a linear relationship between arrival time and horizontal range, unlike the travel-time curve for a reflected or direct arrival, as shown in Figures A and B. At sufficient distance, the head wave is the first-arriving wave (see receiver A_4), but this is offset by the amplitude decay noted above in item 1. Jeffreys (1926) originated the theory of head waves as recognizably distinct arrivals. The method we have used in Section 6.2 has been extended by Berry and West (1966) for an elastic layered medium, and applied by them to interpret the waves P_g, P_n, P^*, $P_M P$, $P_I P$ that had earlier been recorded on the Colorado Plateau by the U.S. Geological Survey. Figure C gives propagation paths for these waves: P_g, P^* and P_n are head waves; $P_I P$ and $P_M P$ are reflections. Observations are shown in Figure D, and there is general agreement with amplitudes calculated for a particular crustal model, shown in Figure E. [Figures D and E here are taken from Berry and West (1966), copyright by American Geophysical Union.] The low amplitude of head waves makes them difficult to detect, except when they arrive ahead of *all* reflected waves. The major discrepancy is in reflected wave amplitudes, which are observed to be much smaller than those calculated. The effect is attributed by Berry and West to roughness of the Conrad and Moho discontinuities.

A better flat-layered approximation to Earth's crustal structure and upper mantle may require consideration of layers in which there are velocity gradients, rather than homogeneous layers as described here. Any velocity gradient, whether positive or negative, will destroy the pure head wave, since the refracted wave on the faster side of the interface cannot continue to propagate horizontally unless the material is homogeneous. A seismic wave with essentially the travel-time curve of P_n is often still observed (a straight line), even when there is a velocity gradient in the mantle just below the Moho, but this "P_n" wave may have an amplitude very different from that predicted by our theory here for head waves at an interface between homogeneous layers. We return to this subject in Chapter 9.

(continued)

BOX **6.4** *(continued)*

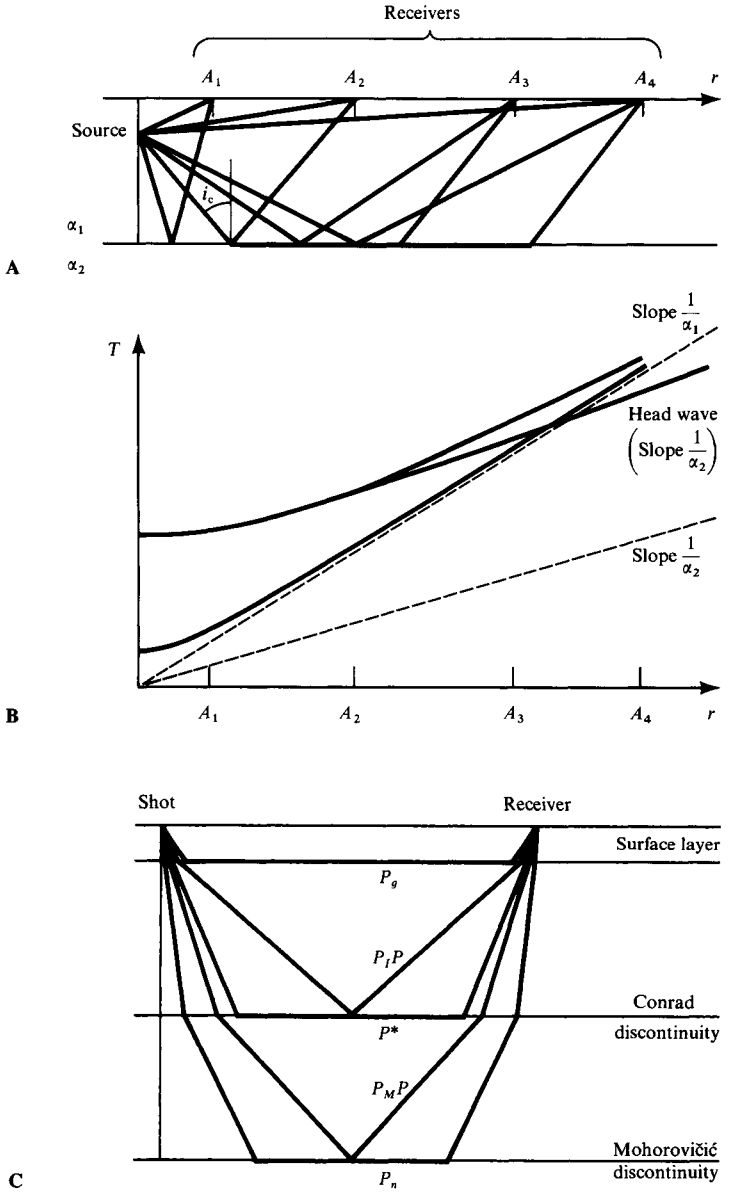

BOX **6.4** *(continued)*

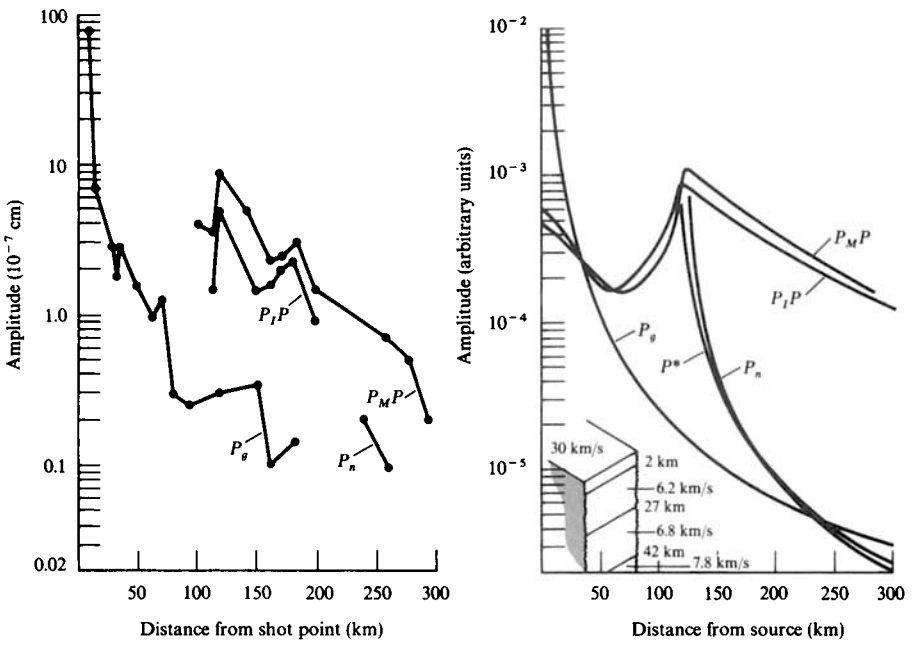

In considering the complicated path of integration shown in Figure 6.9, note that the integrand is exponentially small, and hence negligible, for all points except those near the real axis. Integration over the saddle again gives a term that is approximately

$$\frac{B(p_s)}{R_0} \exp\left[i\omega\left(\frac{R_0}{\alpha_1} - t\right)\right], \tag{6.23}$$

although now the reflection coefficient has a phase shift due to inhomogeneous waves in the lower medium associated with $1/\alpha_2 < p_s$. For reasons that are apparent in Figure 6.7, the wave approximated by (6.23) is known in seismology as a *wide-angle reflection* (note $i_s > i_c$). Because of the phase shift in $B(p_s)$, the reflected pulse shape is distorted in a fashion described in Section 5.3 and Box 5.6.

The other contribution from path Γ of Figure 6.9 comes from integration around the branch cut of ξ_2. On the positive real axis just below this cut, ξ_2 is positive real, equal to

$\alpha_2^{-1} \cos i_2$; just above the cut, $\xi_2 = -\alpha_2^{-1} \cos i_2$. It follows from (6.18) and (6.15) that this contribution is

$$A\sqrt{\frac{\omega}{2\pi r}} \exp[-i(\omega t - \pi/4)] \left(\int_{i\infty}^{0} + \int_{0}^{1/\alpha_2} \right) \frac{\alpha_1 \sqrt{p}}{\cos i_1} \exp[\omega f(p)] \times \left[\frac{-\rho_1 \alpha_1 \cos i_2 + \rho_2 \alpha_2 \cos i_1}{+\rho_1 \alpha_1 \cos i_2 + \rho_2 \alpha_2 \cos i_1} - \frac{+\rho_1 \alpha_1 \cos i_2 + \rho_2 \alpha_2 \cos i_1}{-\rho_1 \alpha_1 \cos i_2 + \rho_2 \alpha_2 \cos i_1} \right] dp, \tag{6.24}$$

where the exponent function $f(p)$ is given in (6.19). Between $p = 0$ and $p = 1/\alpha_2$, $f(p)$ is imaginary, so that the integrand in (6.24) has rapid oscillations. The main contributions come from p-values for which $\mathrm{Im}\{f'(p)\}$ is smallest, and from (6.19) one finds this smallest value occurs right at $p = 1/\alpha_2$. Hence, to obtain an approximation for the branch-cut integral (6.24), we can make a Taylor expansion that is valid near the right-hand end of the branch cut, namely

$$f(p) = f(1/\alpha_2) + (p - 1/\alpha_2) f'(1/\alpha_2).$$

We evaluate $\cos i_1$ and $\sqrt{p}$ at $p = 1/\alpha_2$, and take $\cos i_2 = \sqrt{2\alpha_2(1/\alpha_2 - p)}$. From (6.19) and the trigonometry of Figure 6.10, we find $f(1/\alpha_2) = it_h$, where $t_h = |z + z_0|/(\alpha_1 \cos i_c) + L/\alpha_2$ is the arrival time of head waves and $f'(1/\alpha_2) = iL$. The approximation for (6.24) then becomes

$$-4A\sqrt{\frac{\omega}{\pi r}} \frac{\exp[i\omega(t_h - t)] e^{i\pi/4} \rho_1 \alpha_1^2}{(1 - \alpha_1^2/\alpha_2^2)\rho_2 \alpha_2} \int_0^{1/\alpha_2} \sqrt{\frac{1}{\alpha_2} - p} \exp\left[i\omega L \left(p - \frac{1}{\alpha_2} \right) \right] dp. \tag{6.25}$$

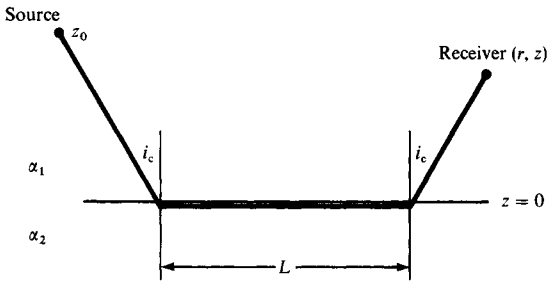

FIGURE **6.10**
Head waves have a travel time t_h corresponding to a leg of length $|z_0|$ sec i_c in the upper medium, a leg of length L in the lower medium (traveling horizontally), and a leg of length $|z|$ sec i_c back in the upper medium. Thus

$$t_h = (\alpha_1^{-1} \sec i_c)|z + z_0| + \alpha_2^{-1} L,$$

which can be shown to equal $r/\alpha_2 + (\alpha_1^{-1} \cos i_c)|z + z_0|$. Distance L is clearly $r - |z + z_0| \tan i_c$.

Putting $(p - 1/\alpha_2) = iy^2$ and using $\int_0^\infty y^2 e^{-\alpha y^2}\, dy = (1/4)\sqrt{\pi}/\alpha^{3/2}$, we finally get the asymptotic approximation

$$\frac{2i}{\omega} A \frac{\rho_1 \alpha_1^2}{\rho_2 \alpha_2 (1 - \alpha_1^2/\alpha_2^2)} \frac{1}{\sqrt{r} L^{3/2}} \exp[i\omega(t_h - t)] \qquad \text{as } \omega \to \infty. \tag{6.26}$$

Identification of the whole branch-cut integral (6.24) as head waves (see Box 6.4) is made on the basis of the approximate result we have just obtained. Again, we emphasize that numerical methods (without approximating the integrand) give more accurate results.

6.3 Spherical Waves in an Elastic Half-Space: The Rayleigh Pole

In Section 5.2, we saw that a free surface can lead to very strong interactions between P and S plane waves. For example, at some angles of incidence for an incident P-wave, the reflected system consists entirely of S-waves (see Fig. 5.6). With spherical waves now recognized as an integral over plane waves, it may thus be expected that a detailed discussion of elastic waves from a point source in a half-space will require a careful study of coupling between P and S at the boundary.

This problem was first solved by Lamb (1904), and subsequently re-examined by many others. We shall here follow Lapwood (1949) in decomposing the elastic wave field into several component waves, each with a simple physical interpretation. In particular, we shall study the generation of Rayleigh waves, which are the dominant part of seismograms written at a distant observation point on the free surface. Later we shall solve the problem by Cagniard–de Hoop methods, giving the exact solution for the total field.

We assume that a homogeneous, isotropic, elastic body, with body-wave velocities α and β and density ρ, occupies the half-space $z > 0$. A point source is located at $z = h, x = y = 0$. We shall work through a P–SV problem (see Box 6.5) that has been simplified in that axial symmetry is imposed about the vertical line through the source. In this sense the problem is two-dimensional, with solutions dependent only on (r, z), where $r = \sqrt{x^2 + y^2}$. We shall use both Cartesian and cylindrical coordinates, (x, y, z) and (r, ϕ, z), sharing the same depth direction. Thus displacement is represented as

$$\mathbf{u} = \nabla\phi + \nabla \times \nabla \times (0, 0, \psi),$$

with P-potential ϕ satisfying

$$\ddot{\phi} = \frac{\Phi}{\rho} + \alpha^2 \nabla^2 \phi, \tag{6.27}$$

and SV-potential ψ satisfying

$$\ddot{\psi} = \frac{\Psi}{\rho} + \beta^2 \nabla^2 \psi,$$

BOX **6.5**

Independence of P–SV *and SH motions for piecewise homogeneous media in which the material discontinuities are horizontal*

A piecewise homogeneous medium is one composed of different regions, each of which is homogeneous. We have already seen in Chapter 5 that a horizontal plane interface between two homogeneous media leads to coupling between P and SV plane waves, and that SH waves propagate independently. Here, we generalize this result.

Beginning with Lamé's theorem (Section 4.1), we note that wave equations

$$\ddot{\phi} = \Phi/\rho + \alpha^2\nabla^2\phi, \qquad \ddot{\boldsymbol{\psi}} = \boldsymbol{\Psi}/\rho + \beta^2\nabla^2\boldsymbol{\psi} \tag{1}$$

are satisfied by potentials related to displacement $\mathbf{u}$ and body force $\mathbf{f}$ via

$$\mathbf{u} = \nabla\phi + \nabla\times\boldsymbol{\psi}, \qquad \mathbf{f} = \nabla\Phi + \nabla\times\boldsymbol{\Psi}, \quad \text{with} \qquad \nabla\cdot\boldsymbol{\psi} = 0, \qquad \nabla\cdot\boldsymbol{\Psi} = 0.$$

The wave equations (1) are equivalent to three scalar equations

$$\begin{aligned} \ddot{\phi} &= \Phi/\rho + \alpha^2\nabla^2\phi, \\ \frac{d^2}{dt^2}(\nabla\times\boldsymbol{\psi})_z &= \frac{1}{\rho}(\nabla\times\boldsymbol{\Psi})_z + \beta^2\nabla^2[(\nabla\times\boldsymbol{\psi})_z], \\ \ddot{\psi}_z &= \Psi_z/\rho + \beta^2\nabla^2\psi_z. \end{aligned} \tag{2}$$

In the absence of body forces. it is clear from (2) that any motion can be decomposed into three kinds of motion; namely, those in which two out of the three functions ϕ, $(\nabla\times\boldsymbol{\psi})_z$, ψ_z, vanish everywhere.

1. Motions of the first kind, with $(\nabla\times\boldsymbol{\psi})_z$ and ψ_z being zero, are clearly P-waves. They are characterized by nonzero $\nabla\cdot\mathbf{u}$, but $\nabla\times\mathbf{u} = \mathbf{0}$.
2. Motions of the second kind involve $\phi = 0$ and $\psi_z = 0$. Since also $\nabla\cdot\boldsymbol{\psi} = 0$, we know $\partial\psi_x/\partial x + \partial\psi_y/\partial y = 0$. This is the condition for existence of some function M such that $\psi_x = \partial M/\partial y$, $\psi_y = -\partial M/\partial x$, i.e., $\boldsymbol{\psi} = \nabla\times(0, 0, M)$. We can choose to write M as the scalar ψ. Then

$$\mathbf{u} = \nabla\times\nabla\times(0, 0, \psi) = \left(\frac{\partial^2\psi}{\partial z\,\partial x}, \frac{\partial^2\psi}{\partial z\,\partial y}, -\frac{\partial^2\psi}{\partial x^2} - \frac{\partial^2\psi}{\partial y^2}\right).$$

   For these motions, $\nabla\cdot\mathbf{u}$ and $(\nabla\times\mathbf{u})_z$ are zero, hence SV waves fall into this category.
3. Motions of the third kind involve $\phi = 0$ and $(\nabla\times\boldsymbol{\psi})_z = 0$. Then $\nabla\cdot\mathbf{u} = 0$ and $u_z = 0$, so that displacement here is like $\boldsymbol{\psi}$ in item 2: there exists a function χ such that $\mathbf{u} = \nabla\times(0, 0, \chi)$. This motion is clearly like SH, being characterized by $(\nabla\times\mathbf{u})_z \neq 0, u_z = 0, \nabla\cdot\mathbf{u} = 0$.

   Similarly, the three types of body force in (2) can each be described by a scalar potential, and $\mathbf{f} = \nabla\Phi + \nabla\times\nabla\times(0, 0, \Psi) + \nabla\times(0, 0, \mathrm{X})$, with P-, SV-, SH-wave equations being, respectively,

$$\ddot{\phi} = \Phi/\rho + \alpha^2\nabla^2\phi, \qquad \ddot{\psi} = \Psi/\rho + \beta^2\nabla^2\psi, \qquad \ddot{\chi} = \mathrm{X}/\rho + \beta^2\nabla^2\chi. \tag{3}$$

(continued)

BOX **6.5** *(continued)*

For a horizontal discontinuity in material properties, the three scalar conditions of continuity of components of $\mathbf{u}$ can be differentiated in horizontal directions. The three conditions are then equivalent to continuity of

$$\frac{\partial u_y}{\partial x} - \frac{\partial u_x}{\partial y}, \qquad \frac{\partial u_x}{\partial x} + \frac{\partial u_y}{\partial y}, \qquad u_z,$$

i.e., continuity of

$$(\nabla \times \mathbf{u})_z, \qquad \nabla \cdot \mathbf{u} - \partial u_z/\partial z, \qquad u_z. \tag{4}$$

Similarly, continuity of traction implies continuity of

$$\mu \frac{\partial}{\partial z}[(\nabla \times \mathbf{u})_z], \qquad \mu\left[\frac{\partial}{\partial z}\nabla \cdot \mathbf{u} - 2\frac{\partial^2 u_z}{\partial z^2} + \nabla^2 u_z\right], \qquad \lambda \nabla \cdot \mathbf{u} + 2\mu \frac{\partial u_z}{\partial z}. \tag{5}$$

For an SH-wave, with $(\nabla \times \mathbf{u})_z \neq 0$ but $u_z = 0$ and $\nabla \cdot \mathbf{u} = 0$, it follows that four of the six continuity conditions in (4) and (5) are satisfied trivially, and that u_z and $\nabla \cdot \mathbf{u}$ remain zero after interaction with the boundary, so that SH-waves remain SH.

Similarly, for an incident wave with $(\nabla \times \mathbf{u})_z = 0$ but with nonzero u_z and $\nabla \cdot \mathbf{u}$, there is no coupling to SH at a boundary. However, the coupling between u_z and $\nabla \cdot \mathbf{u}$ implies that P and SV are coupled.

In media whose density and Lamé parameters are depth-dependent, there is again decoupling between SH and $P + SV$ motions: the coupling between P and SV is directly apparent in the wave equations, which do not separate into the form (2). Instead, one finds two equations, each involving ϕ and $(\nabla \times \psi)_z$.

where Φ and Ψ are potentials for the body force $\mathbf{f}$ via

$$\mathbf{f} = \rho \ddot{\mathbf{u}} - (\lambda + 2\mu)\nabla(\nabla \cdot \mathbf{u}) + \mu \nabla \times (\nabla \times \mathbf{u}) = \nabla \Phi + \nabla \times \nabla \times (0, 0, \Psi). \tag{6.28}$$

We shall consider a point source of P-waves, as shown in Figure 6.11. (The figure also describes a simple point source of SV. Point sources that are more relevant for seismology are described in terms of cylindrical coordinates in the next chapter. A line source of SV is described in Section 6.4.) Thus we take here

$$\Phi = A 4\pi\rho\alpha^2\, \delta(x)\, \delta(y)\, \delta(z - h) \exp(-i\omega t); \qquad \Psi = 0. \tag{6.29}$$

Via the wave equation (6.27) for potential, this source generates a spherical wave

$$\phi^{\text{inc}}(\mathbf{x}, t) = \frac{A}{R} \exp\left[i\omega\left(\frac{R}{\alpha} - t\right)\right] \qquad \text{with} \qquad R = \sqrt{x^2 + y^2 + (z - h)^2}, \tag{6.30}$$

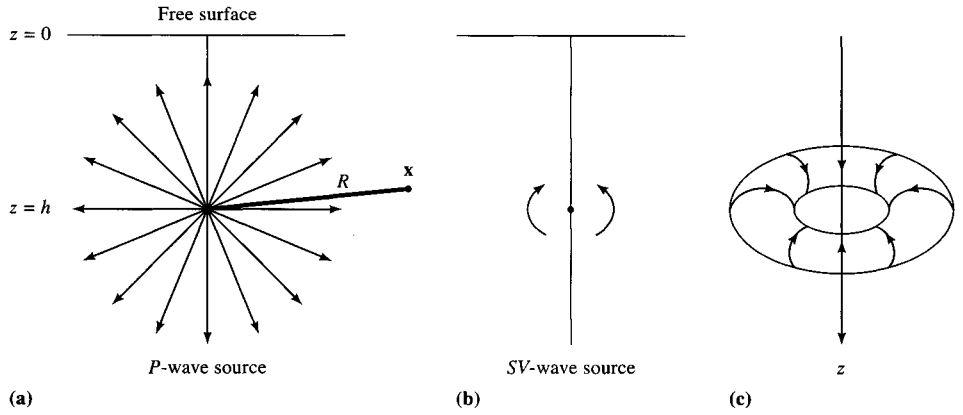

FIGURE **6.11**
Two different point sources are shown at depth h in an elastic half-space. (**a**) The P-wave source, leading to the spherical wave $\phi^{\text{inc}} = (A/R)\exp i\omega(R/\alpha - t)$, where R is the straight-line source–receiver distance. This source is a simple model of an explosion. (**b**) The SV-wave source, leading to $\psi^{\text{inc}} = (A/R)\exp i\omega(R/\beta - t)$. (**c**) To visualize this SV source, consider a small torus (doughnut) with its axis vertical and an axisymmetric motion in which particles of the torus "roll," as shown by the arrows, so that particle motions are confined to vertical planes. It is clear that SV-waves are radiated by such a torus, and it can be shown that a source of this type, in the limit as the torus tends to a point, does have a spherically symmetric ψ^{inc} as given above.

which then is incident on the free surface at $z = 0$. The total potentials are

$$\begin{aligned}\phi = {} & Ai\omega \exp(-i\omega t)\int_0^\infty \frac{p}{\xi} J_0(\omega p r)\exp[i\omega\xi|z-h|]\,dp \qquad \text{(incident wave)} \\ & + Ai\omega \exp(-i\omega t)\int_0^\infty \acute{P}\grave{P}\frac{p}{\xi} J_0(\omega p r)\exp[i\omega\xi(z+h)]\,dp \\ & \qquad\qquad \text{(generalized } \acute{P}\grave{P} \text{ reflection),}\end{aligned} \tag{6.31}$$

$$\begin{aligned}\psi = {} & Ai\omega \exp(-i\omega t)\int_0^\infty \left(\frac{1}{i\omega p}\frac{\beta}{\alpha}\acute{P}\grave{S}\right)\frac{p}{\xi} J_0(\omega p r)\exp[i\omega(\xi h + \eta z)]\,dp \\ & \qquad\qquad \text{(generalized } \acute{P}\grave{S} \text{ reflection)}\end{aligned} \tag{6.32}$$

(see Box 6.6), in which $\acute{P}\grave{P}$ and $\acute{P}\grave{S}$ are the p-dependent coefficients described for the free surface in Chapter 5 (equations (5.27) and (5.28)).

We focus attention on the generalized $\acute{P}\grave{P}$ reflection in (6.31), showing how it separates out into three different types of P-waves as range r is increased.

First we split J_0 into its traveling-wave components to obtain the generalized $\acute{P}\grave{P}$ reflection:

$$\begin{aligned}&\frac{Ai\omega}{2}\exp(-i\omega t)\int_{-\infty}^{\infty} \acute{P}\grave{P}\frac{p}{\xi} H_0^{(1)}(\omega p r)\exp\left[i\omega\xi(z+h)\right]\,dp \\ &\qquad \sim A\sqrt{\frac{\omega}{2\pi r}}e^{-i(\omega t-\pi/4)}\int_{-\infty}^{\infty}\acute{P}\grave{P}\frac{\sqrt{p}}{\xi}\exp\left[i\omega(pr+\xi z+\xi h)\right]\,dp\end{aligned} \tag{6.33}$$

as $\omega \to \infty$ (compare with the derivation of (6.16) and (6.18)). Recall that $\operatorname{Im}\xi \geq 0$, $\operatorname{Im}\eta \geq 0$.

BOX **6.6**
On cylindrical coordinates

Formulas (6.31) and (6.32) can be obtained using the theory of plane waves in Cartesian coordinates, the Weyl integral (6.4), and subsequent conversion to cylindrical coordinates, parallel to our derivation of (6.9). Much quicker, however, is the following method due to Lamb (1904), using cylindrical geometry throughout.

Axisymmetric solutions of the homogeneous wave equations for potentials are

$$J_0(\omega p r)\exp(\pm i\omega\xi z - i\omega t) \quad \text{for } \phi \quad \text{and} \quad J_0(\omega p r)\exp(\pm i\omega\eta z - i\omega t) \quad \text{for } \psi,$$

where $\xi = \sqrt{\alpha^{-2} - p^2}$ and $\eta = \sqrt{\beta^{-2} - p^2}$. Suppose an incident upgoing P-wave and its reflections are expressed by the total fields

$$\phi = J_0(\omega p r)[Ae^{-i\omega\xi z} + Be^{i\omega\xi z}]\exp(-i\omega t),$$
$$\psi = J_0(\omega p r)Ce^{i\omega\eta z}\exp(-i\omega t).$$

Then, from $\mathbf{u} = \nabla\phi + \nabla \times \nabla \times (0, 0, \psi)$ and $dJ_0(x)/dx = -J_1(x)$, we find

$$u_r = \frac{\partial\phi}{\partial r} + \frac{\partial^2\psi}{\partial r\,\partial z} = -\omega p J_1(\omega p r)[Ae^{-i\omega\xi z} + Be^{i\omega\xi z} + i\omega\eta Ce^{i\omega\eta z}]\exp(-i\omega t),$$
$$u_z = \frac{\partial\phi}{\partial z} - \frac{1}{r}\frac{\partial}{\partial r}\left(r\frac{\partial\psi}{\partial r}\right) = J_0(\omega p r)[-i\omega\xi Ae^{-i\omega\xi z} + i\omega\xi Be^{i\omega\xi z} + \omega^2 p^2 Ce^{i\omega\eta z}]\exp(-i\omega t).$$

From Section 2.6, with axisymmetry,

$$\tau_{zr} = 2\mu e_{zr} = \mu\left(\frac{\partial u_r}{\partial z} + \frac{\partial u_z}{\partial r}\right) \tag{1}$$
$$= i\omega^2 J_1(\omega p r)[2\rho\beta^2 p\xi(A - B) + \rho(1 - 2\beta^2 p^2)(-i\omega p C)]\exp(-i\omega t) \qquad \text{on } z = 0,$$

$$\tau_{zz} = \lambda\,\mathrm{div}\,\mathbf{u} + 2\mu\frac{\partial u_z}{\partial z} = -\frac{\lambda\omega^2}{\alpha^2}\phi + 2\mu\frac{\partial u_z}{\partial z} \tag{2}$$
$$= -\omega^2 J_0(\omega p r)[\rho(1 - 2\beta^2 p^2)(A + B) + 2\rho\beta^2 p\eta(-i\omega p C)]\exp(-i\omega t) \qquad \text{on } z = 0.$$

Equating (1) and (2) above to zero (the free-surface boundary conditions), we find equations that differ from those obtained in our study of plane waves only in the substitution of $-i\omega pC$ for the C appearing in (5.23) and (5.24). It follows that

$$B = A\acute{P}\grave{P} \quad \text{and} \quad C = \frac{A}{i\omega p}\frac{\beta}{\alpha}\acute{P}\grave{S}. \tag{3}$$

where $\acute{P}\grave{P}$ and $\acute{P}\grave{S}$ are the reflection/conversion coefficients for displacement given in (5.27) and (5.28). Formulas (6.31) and (6.32) follow immediately from the Sommerfeld integral for the incident wave and from superposition of reflections.

Second, we inspect the branch cuts and steepest descents paths of the exponent in (6.33). On the top Riemann sheet (Im $\xi \geq 0$, Im $\eta \geq 0$), as shown in Figure 6.12, there is a saddle point at $p_s = \alpha^{-1}\sin i_s$ and a pole where $p = 1/c_R$ (c_R being the Rayleigh wave speed and a zero of the denominator of $\acute{P}\grave{P}$). If we compare the steepest descents path Γ

of Figure 6.12c with the singularities of Figure 6.12b, we see that there is little interference from singularities, provided the reflection angle is small. This is the case in Figure 6.12d, and the saddle point contribution alone is important. However, if i_s becomes large (i.e., if $r \gg z + h$), a strong interference takes place, as shown in Figure 6.12e, leading to three identifiable contributions: (i) from Γ_α, the main contribution is still from the saddle point, and can be interpreted as the surface P reflection shown in Figure 6.12a; (ii) from Γ_β, the main contribution comes from the vicinity of the branch point $p = 1/\beta$. This propagation path is identifiable as an inhomogeneous P-wave decaying upward from the source to the free surface, followed by horizontal propagation along the free surface as an SV-wave and ending as an inhomogeneous P-wave decaying downward from free surface to receiver. It is called the *surface S-wave*. Finally, (iii) from Γ_R, the P-wave component of the Rayleigh wave is obtained, with amplitude given simply by the residue of the integrand (6.33). Since

$$\acute{P}\grave{P} \sim -\left(\frac{1}{p - 1/c_R}\right) \frac{8\sqrt{c_R^{-2} - \alpha^{-2}}\sqrt{c_R^{-2} - \beta^{-2}}}{c_R^2 \mathsf{R}'(1/c_R)}$$

as $p \to 1/c_R$, where $\mathsf{R}(p) = 4p^2\xi\eta + (1/\beta^2 - 2p^2)^2$ and $\mathsf{R}' = d\mathsf{R}/dp$, we find from (6.33) that the Rayleigh wave has P-wave component

$$\phi_R \sim -8A\sqrt{\frac{2\pi\omega}{rc_R}}\sqrt{\frac{1}{c_R^2} - \frac{1}{\beta^2}}\frac{e^{i\pi/4}}{c_R^2 \mathsf{R}'(1/c_R)} \times \exp\left[i\omega\left(\frac{r}{c_R} - t\right)\right]\exp\left[-\omega\sqrt{\frac{1}{c_R^2} - \frac{1}{\alpha^2}}(z + h)\right] \tag{6.34}$$

as $\omega \to \infty$. An estimate of the distance range at which this residue is *not* picked up is given by seeing when the steepest descents path Γ (Fig. 6.12c) still lies below the Rayleigh pole. Roughly, this occurs where

$$\frac{1}{\alpha \sin i_s} > \frac{1}{c_R},$$

or, equivalently, for

$$\tan i_s = \frac{r}{z + h} < \frac{c_R}{\sqrt{\alpha^2 - c_R^2}}. \tag{6.35}$$

The inequality (6.35) was first obtained by Nakano, and interpreted as the distance range for which Rayleigh waves have not yet built up. If

$$\frac{r}{z + h} \gg \frac{c_R}{\sqrt{\alpha^2 - c_R^2}} \sim 0.6,$$

then the pole contribution is well isolated from branch cuts and the steepest descents path, and (6.34) will be significant.

We can analyze the SV-wave (6.32) along similar lines, generalizing $\acute{P}\grave{S}$ and finding that an ordinary downgoing S-wave is reflected from the incident spherical P-wave. Also present, at sufficient range, is a wave with horizontal slowness $1/\beta$. Known as the *secondary S-wave*, this leaves the source as an inhomogeneous P-wave, decaying upward and then propagating horizontally as S to the receiver. A Rayleigh pole is again present, and the residue gives

$$\psi_R \sim 4A\sqrt{\frac{2\pi\omega}{rc_R}}\frac{e^{i\pi/4}}{\omega \mathsf{R}'(1/c_R)}\left(\frac{1}{\beta^2}-\frac{2}{c_R^2}\right) \times \exp\left[i\omega\left(\frac{r}{c_R}-t\right)\right]\exp\left[-\omega\sqrt{\frac{1}{c_R^2}-\frac{1}{\alpha^2}}\,h-\omega\sqrt{\frac{1}{c_R^2}-\frac{1}{\beta^2}}\,z\right] \tag{6.36}$$

as $\omega \to \infty$.

Corresponding displacements can be calculated from

$$u = u_r = \frac{\partial\phi}{\partial r}+\frac{\partial^2\psi}{\partial r\,\partial z}, \qquad w = u_z = \frac{\partial\phi}{\partial z}-\frac{1}{r}\frac{\partial}{\partial r}\left(\frac{r\partial\psi}{\partial r}\right).$$

(We adhere to the common convention of u for horizontal displacement, though now meaning the radial component rather than the horizontal Cartesian component in the x-direction.) The Rayleigh wave displacement at the surface ($z = 0$) is then

$$u_R \sim -2iFe^{i\pi/4}\left[\frac{2}{c_R}\sqrt{\frac{1}{c_R^2}-\frac{1}{\beta^2}}\right]\exp\left[i\omega\left(\frac{r}{c_R}-t\right)\right]\exp\left[-\omega\sqrt{\frac{1}{c_R^2}-\frac{1}{\alpha^2}}\,h\right], \tag{6.37}$$

$$w_R \sim -2Fe^{i\pi/4}\left[\frac{2}{c_R^2}-\frac{1}{\beta^2}\right]\exp\left[i\omega\left(\frac{r}{c_R}-t\right)\right]\exp\left[-\omega\sqrt{\frac{1}{c_R^2}-\frac{1}{\alpha^2}}\,h\right],$$

where

$$F = A\sqrt{\frac{2\pi\omega}{rc_R}}\frac{\omega}{\beta^2\mathsf{R}'(1/c_R)}.$$

Although the pole at $p = 1/c_R$ is a predominant feature of half-space problems, we shall find in the next section that other zeros of the Rayleigh function, occurring on different Riemann sheets, can also be significant. The main properties of Rayleigh waves are summarized in Box 6.7.

In our analysis of spherical waves incident on plane boundaries, we have now seen two phenomena, head waves and Rayleigh waves, that are not manifested when the incident wavefront is plane. Our asymptotic formulas that evaluate these phenomena have enabled us quickly to assess many of their properties, but now we turn to an alternative approach that, for Lamb's problem, can be made exact.

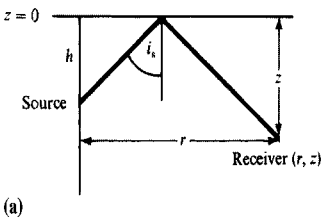
z = 0
h
i_s
z
Source
r
Receiver (r, z)

(a)

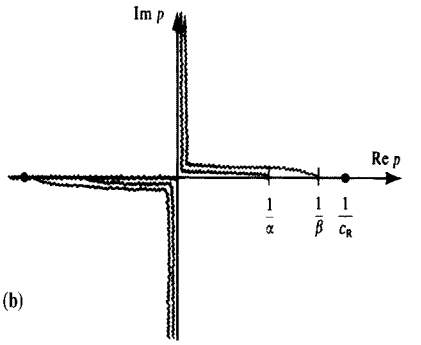
Im p
Re p
$\frac{1}{\alpha}$
$\frac{1}{\beta}$
$\frac{1}{c_R}$

(b)

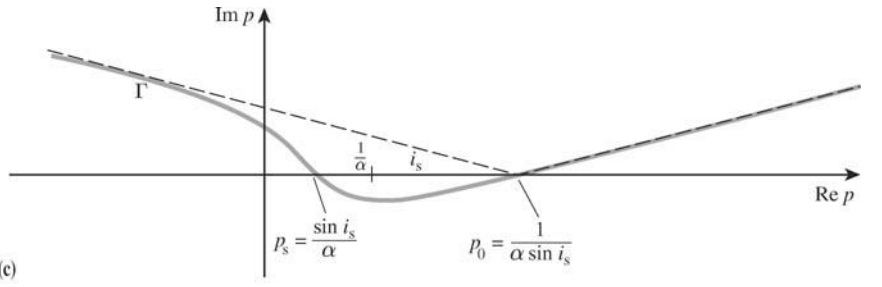
Im p
Γ
$\frac{1}{\alpha}$
i_s
Re p
$p_s = \frac{\sin i_s}{\alpha}$
$p_0 = \frac{1}{\alpha \sin i_s}$

(c)

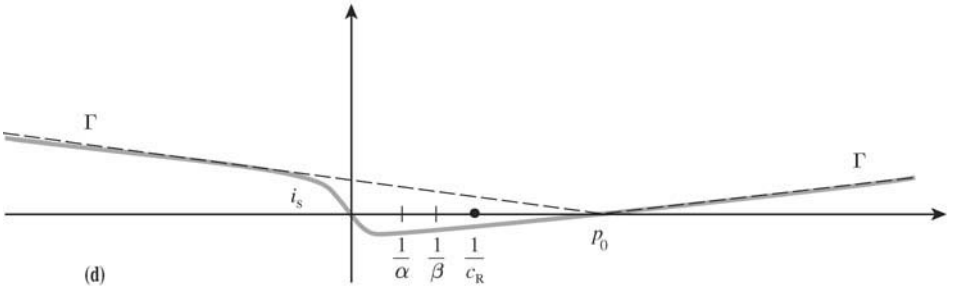
Γ
Γ
i_s
p_0
$\frac{1}{\alpha}$
$\frac{1}{\beta}$
$\frac{1}{c_R}$

(d)

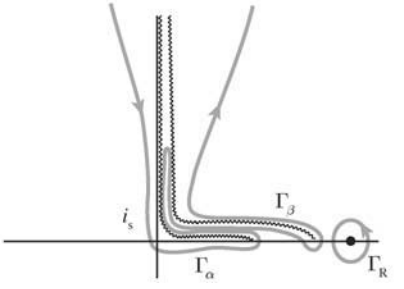
i_s
Γ_β
Γ_α
Γ_R

(e)

FIGURE **6.12**
Diagrams for interpretation of the generalized reflection for a point source in an elastic half-space. (**a**) The source–receiver geometry and a reflected P-wave defining the reflection angle i_s. (**b**) Branch cuts for ξ and η in the complex p-plane, together with a pole at $p = 1/c_R$. (*Note:* For attenuating media, the branch cuts and pole on the positive real axis move up into the first quadrant.) (**c**) The steepest descents path Γ for the exponent in (6.33), this being the path such that $pr + \xi z + \xi h = R_0/\alpha +$ positive imaginary quantity $= R_0/\alpha + iX^2$. One may solve for p to find

$$R_0^2 p = r(iX^2 + R_0/\alpha) \pm \sqrt{X^4 - 2iX^2 R_0/\alpha}\,(z+h)$$

on Γ, crossing the real axis at $p = p_s = \alpha^{-1}\sin i_s$ and also at $p_0 = 1/(\alpha \sin i_s)$. (**d**) For small i_s, p_s is just to the right of the origin and the steepest descents path can be taken as in Fig. 6.8 for a small part of the first quadrant. (**e**) For large i_s, p_s and p_0 are slightly to the left and the right of $1/\alpha$, and the integration path can be thought of as a sum of two branch-cut integrals, Γ_α and Γ_β, plus a circuit Γ_R picking up the residue from the Rayleigh pole.

BOX **6.7**
Outstanding features of Rayleigh waves from a buried point source

1. Attenuation behaves like $r^{-1/2}$ with distance, as compared with body waves ($\sim r^{-1}$) and head waves (r^{-2}), so that Rayleigh waves must dominate the ground motion at sufficient range. Note that the ratio between horizontal and vertical motions in the *cylindrical* Rayleigh wave (6.37) is just that found for a *plane* Rayleigh wave in Problem 5.4b.
2. Phase delay is given by $\omega r/c_R$, and is independent of depth h, so that the travel time curve is a straight line.
3. Amplitude is an exponentially decaying function of h and ω:

$$\exp[-\omega\sqrt{c_R^{-2} - \alpha^{-2}}\,h] \sim \exp[-\sqrt{0.9}\,\omega h/\beta].$$

   For an S-wave source, this becomes

$$\exp[-\omega\sqrt{c_R^{-2} - \beta^{-2}}\,h] \sim \exp[-\sqrt{0.2}\,\omega h/\beta].$$

4. Particle motion is retrograde elliptical (w has a phase shift of $-\pi/2$ with respect to u, and hence a phase advance of $+\pi/2$; see Box 5.5), and the ellipticity is the same as for the free Rayleigh waves described in Section 5.3.
5. From items 2 and 3 above, the slope of the phase spectrum is a function of range but not of depth, and the shape of the amplitude spectrum is a function of depth but not of range. Therefore, the amplitude and phase are independent of each other. This is a common feature of what we generally call *normal modes*, to be investigated in more detail for a layered medium in Chapter 7. This independence, of course, violates causality (see Box 5.8), hence it is meaningless to speak of the "first motion" of Rayleigh waves or individual normal modes.

6.4 Cagniard–De Hoop Methods for Line Sources

The time-dependence of sources we have considered so far in this chapter has been $\exp(-i\omega t)$, and we have been seeking a way to express the response (i.e., some physical variable, evaluated at a receiver) in the form $\tilde{r}(\omega)\exp(-i\omega t)$. Written in input–output form,

$$\exp(-i\omega t) \rightarrow \text{Elastic medium} \rightarrow \tilde{r}(\omega)\exp(-i\omega t).$$

For many purposes, the goal is to find the response $r(t)$ to an input $\delta(t)$. Then

$$\delta(t) = \frac{1}{2\pi}\int_{-\infty}^{\infty}\exp(-i\omega t)d\omega \rightarrow \text{Elastic medium} \rightarrow \frac{1}{2\pi}\int_{-\infty}^{\infty}\tilde{r}(\omega)\exp(-i\omega t)d\omega = r(t),$$

and we see that $r(t)$ is the inverse Fourier transform of $\tilde{r}(\omega)$. The physical causality requires $r(t) = 0$ for $t < 0$, and note that so far we have been looking at details of the Fourier transform of $r(t)$ primarily for real positive ω. Knowing $r(t)$, we can express the response to an arbitrary input $x(t)$ by the convolution

$$x(t) = \int_{-\infty}^{\infty} x(t-\tau)\delta(\tau)\,d\tau \rightarrow \text{Elastic medium} \rightarrow \int_{0}^{\infty} x(t-\tau)r(\tau)\,d\tau. \quad (6.38)$$

(Integration can be restricted to positive τ, because r is causal.)

Using Cagniard's method, we shall work with the Laplace transform of $r(t)$:

$$\bar{r}(s) = \int_{0}^{\infty} r(t)e^{-st}\,dt \qquad \text{(in which } s \text{ is } \textit{real} \text{ and } \textit{positive}\text{)}. \quad (6.39)$$

Supposing that an explicit solution for $\bar{r}(s)$ can be found, the use of Cagniard's method entails manipulation of the expression for $\bar{r}(s)$ until it is in the form of (6.39). Then, whatever appears as the integrand factor $r(t)$ can be identified as the impulse response in the time domain. (The contribution of de Hoop was to simplify the methods of manipulation. It should be noted that Cagniard attributes his method to Carson. It was developed also by Smirnov and Sobolev; Pekeris; Sauter; Garvin; and Gilbert.) Once the impulse response is known, the problem is regarded as solved, because the response to an arbitrary input can be obtained by convolution.

It is not obvious, however, that the impulse response $r(t)$ is uniquely determined by the above procedure from $\bar{r}(s)$ known only for real positive s. After all, the inverse transform of (6.39) is

$$r(t) = \frac{1}{2\pi i}\int_{c-i\infty}^{c+i\infty}\bar{r}(s)e^{st}\,ds$$

(in which the line of integration lies to the right of all singularities of $\bar{r}(s)$), requiring the analysis of $\bar{r}(s)$ for complex s. Fortunately for us, Cagniard (1962, Chapter 3) proved that identifying $r(t)$ from the integrand of $\bar{r}(s)$ written in the form (6.39) does indeed uniquely determine the required impulse response under fairly minor constraints on the

differentiability and boundedness of $r(t)$. This is known as Lerch's lemma (or theorem). The proof is intricate and long, and is omitted here.

It is clear that $\bar{r}(s)$ can be obtained from formal substitution of $\omega = is$ in the expressions for $\tilde{r}(\omega)$ in our Sections 6.1–6.3. It is convenient, however, to derive $\bar{r}(s)$ directly from Laplace transformation of the output when the source is $\delta(t)$. For example, in two-dimensional problems involving propagation normal to the Cartesian y-direction, we seek to obtain the functional form of $r = r(x, z, t)$. With an input $\delta(t)$, we shall find it convenient to take a spatial Fourier transform over x and a Laplace transform over t, obtaining an algebraic expression for the double transform $\bar{\tilde{r}} = \bar{\tilde{r}}(k_x, z, s)$. The inverse Fourier transform is then

$$\bar{r}(x, z, s) = \frac{1}{2\pi} \int_{-\infty}^{\infty} \bar{\tilde{r}}(k_x, z, s) \exp(ik_x x)\, dk_x.$$

Since k_x here is the horizontal component of wavenumber, we extract a factor is and identify $k_x/(is) = p$ as the ray parameter. Then

$$\bar{r}(x, z, s) = -\frac{is}{2\pi} \int_{-i\infty}^{i\infty} \bar{\tilde{r}}(isp, z, s) e^{-spx}\, dp. \tag{6.40}$$

Regarding p here as a dummy variable of integration, it remains to manipulate (6.40) into the form of the integral in (6.39). The resulting integrand then permits $r(x, z, t)$ to be recognized immediately, without ever having to carry out an integration.

The surprising and most important feature of Cagniard's method is that by obtaining and then manipulating an explicit expression $\bar{\tilde{r}}$ for the doubly transformed solution, we can end up with the solution $r(x, z, t)$ where we want it, namely in the space–time domain, *without actually having to carry out either one of the two inverse transform integrals.*

Note that s appears in the integral (6.39) in only one position, as a factor of the exponent. The manipulation of (6.40) often leads to a form

$$\bar{r} = s^n \int_0^{\infty} g(t) e^{-st}\, dt, \tag{6.41}$$

in which case the impulse response can be calculated from

$$r(t) = \frac{d^n}{dt^n} g(t)$$

in which $g(t)$ is known explicitly. Alternatively, taking as input a delta function that has been integrated n times, the response is directly recognized as $g(t)$.

In the remainder of this section we shall investigate the above method for line sources of SH-waves, and for a line source of P-SV waves in an elastic half-space. We shall find the medium response can be given exactly by algebraic expressions. Extension of the method to point sources is given in the next section, and we conclude the chapter with some overall comparisons between the Cagniard–de Hoop approach, and the Fourier transform methods discussed in Section 6.1–6.3.

We begin with a simple SH problem. Using Cartesians (x, y, z), we suppose that a line source in an infinite elastic medium acts along the y-axis and consists of a body force acting

impulsively in the y-direction. Thus the body force is

$$\mathbf{f} = (0, A\,\delta(x)\,\delta(z)\,\delta(t), 0),$$

where A is a constant having the dimensions of impulse per unit length. Only the y-component of displacement is excited by this source, so that displacement $\mathbf{u}$ is $(0, v(x, z, t), 0)$. The equation for v is

$$\rho\ddot{v} = A\,\delta(x)\,\delta(z)\,\delta(t) + \mu\nabla^2 v, \tag{6.42}$$

and both v and $\dot{v}$ are zero for $t < 0$.

To solve for v at later times, the simplest method is to take the point-source solution of Box 4.1 and integrate for sources all along the y-axis:

$$v(x, z, t) = \frac{1}{4\pi\beta^2}\int_{-\infty}^{\infty} \frac{A}{\rho}\frac{1}{R_3}\delta\left(t - \frac{R_3}{\beta}\right) dy,$$

where $R_3 = \sqrt{x^2 + y^2 + z^2}$. Since $dy/R_3 = dR_3/y$ and R_3 is even in y,

$$v(x, z, t) = \frac{A}{2\pi\rho\beta^2}\int_R^{\infty} \frac{1}{y}\delta\left(t - \frac{R_3}{\beta}\right) dR_3 = \begin{cases} 0 & \text{for } t < \dfrac{R}{\beta}, \\ \dfrac{A}{2\pi\rho\beta^2}\dfrac{1}{\sqrt{t^2 - \dfrac{R^2}{\beta^2}}} & \text{for } t > \dfrac{R}{\beta}, \end{cases} \tag{6.43}$$

where $R = \sqrt{x^2 + z^2}$ is the distance function for two-dimensional problems.

Let us now derive (6.43) again, using the Cagniard–de Hoop approach.

Taking the double transform

$$\int_{-\infty}^{\infty} \exp(-ik_x x)dx \int_0^{\infty} e^{-st}\,dt,$$

we find

$$\frac{\partial^2}{\partial z^2}v(k_x, z, s) = -\frac{A}{\rho\beta^2}\delta(z) + n^2 v(k_x, z, s), \qquad \text{where } n^2 = k_x^2 + \frac{s^2}{\beta^2}. \tag{6.44}$$

Thus everywhere except at $z = 0$, we know $\partial^2 v/\partial z^2 = n^2 v$, with solutions

$$v(k_x, z, s) = ae^{nz} + be^{-nz} \qquad \text{(fixing the choice of root by } n > 0)$$

for some constants a and b. Considering separately the two regions $z \gtrless 0$ and requiring v to be bounded as $z \to \pm\infty$, we see that $a = 0$ for $z > 0$ and $b = 0$ for $z < 0$. But (6.44) implies

that v is continuous across $z = 0$, and $\partial v/\partial z$ has a step jump down of amount $A/\rho\beta^2$. It follows that $v \propto e^{-n|z|}$, and knowing the magnitude of the step in $\partial v/\partial z$ we finally find

$$v(k_x, z, s) = \frac{A}{2\rho\beta^2 n} e^{-n|z|}. \tag{6.45}$$

(Alternatively, we can obtain (6.45) by transforming the z-dependence in (6.44) and using poles in the k_z plane, just as we did in deriving the Weyl integral, (6.4).) In (6.45), we have obtained the necessary explicit form of the double-transformed solution, needed as part of the Cagniard method.

The Laplace transform of the space–time solution we seek is now

$$v(x, z, s) = \frac{A}{4\pi\rho\beta^2} \int_{-\infty}^{\infty} \frac{\exp(ik_x x - n|z|)}{n} dk_x \tag{6.46}$$

with $\operatorname{Re} n = \operatorname{Re}(\sqrt{k_x^2 + s^2/\beta^2}) > 0$, generalized from the previous $n > 0$ to allow discussion of complex values. Observe in (6.46) that k_x is a dummy variable of integration, and write it instead as $k_x = isp$. Then

$$v(x, z, s) = \frac{A}{4\pi\rho\beta^2} \int_{-i\infty}^{i\infty} \frac{-ie^{-s(px+\eta|z|)}}{\eta} dp \tag{6.47}$$

where $\eta = \sqrt{\beta^{-2} - p^2}$, and $\operatorname{Re} \eta > 0$.

Already we have isolated s to just one position in the integrand (6.47); we now continue the manipulations to force (6.47) into the form of a forward Laplace transform. To this end, we write the real and imaginary parts of $(1/\eta)e^{-s(px+\eta|z|)}$ as $E(p)$ and $O(p)$, respectively, noting that E is even and O is odd for imaginary values of p. Then

$$\int_{-i\infty}^{i\infty} -i(E + iO)dp = -2i \int_0^{i\infty} E\, dp = 2 \operatorname{Im} \left\{ \int_0^{i\infty} (E + iO)\, dp \right\},$$

and hence

$$v(x, z, s) = \frac{A}{2\pi\rho\beta^2} \operatorname{Im} \left\{ \int_0^{i\infty} \frac{e^{-s(px+\eta|z|)}}{\eta} dp \right\}. \tag{6.48}$$

Titchmarsh (1939) gives a result similar to our derivation of (6.48) from (6.47), and calls it "the principle of reflection." The branch cuts for η are determined now by $\operatorname{Re} \eta \geq 0$, and are shown in Figure 6.13. (To analyze Fourier transforms, note that we chose $\operatorname{Im} \eta \geq 0$, for which branch cuts were much more complicated, involving parts of the real and imaginary p-axes.)

If we are to force (6.48) into the form of a forward Laplace transform, we must investigate the path C in the complex p-plane for which the quantity $px + \eta|z|$ is real. It is natural to label this quantity as t, so that the exponential in (6.48) becomes e^{-st}, and then we shall use

$$t = px + \eta|z| \tag{6.49}$$

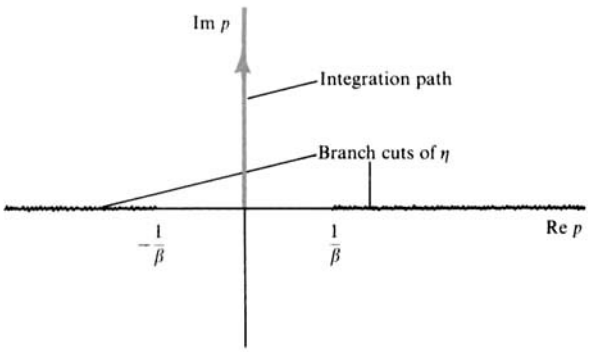

FIGURE **6.13**
Branch cuts and integration path in the complex p-plane for the Laplace transform (6.48).

as an independent variable of integration, instead of p. We call the path C, given by $p = p(t)$ where t is real and positive, the *Cagniard path*. Our next step is to find how this path is parameterized by real values of t increasing from zero to infinity.

Solving (6.49) for p as a function of t merely requires solving a quadratic equation, and one of the roots is

$$p = \begin{cases} \dfrac{xt - |z|\sqrt{\dfrac{R^2}{\beta^2} - t^2}}{R^2} & \text{for } t \le \dfrac{R}{\beta} \\[2ex] \dfrac{xt + i|z|\sqrt{t^2 - \dfrac{R^2}{\beta^2}}}{R^2} & \text{for } t \ge \dfrac{R}{\beta}. \end{cases} \tag{6.50}$$

In Figure 6.14, we show the path $p = p(t)$ given by (6.50) in the complex p-plane for different real values of t. We have taken $x > 0$. If $x < 0$, the mirror image

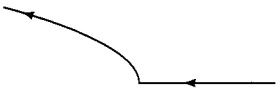

can be used for C.

The next stage is to see if the integral (6.48) up the positive imaginary p-axis can instead be taken over the Cagniard path, on which t increases from zero to infinity. If we can do this, then $v(x, z, s)$ will look like an explicit Laplace transform from whose integrand we can identify our desired solution in the space–time domain. In fact, there is no contribution from the integrand in (6.48) along that part of C between $t = 0$ and $t = R/\beta$, since the integrand and the small increments dp are purely real. Neither is there a contribution from the large arc C in the first quadrant (see Box 6.8). Since there are no singularities between C and the positive imaginary p-axis, we conclude that

$$v(x, z, s) = \frac{A}{2\pi\rho\beta^2} \operatorname{Im} \left\{ \int_C \frac{e^{-s(px + \eta|z|)}}{\eta} dp \right\}. \tag{6.51}$$

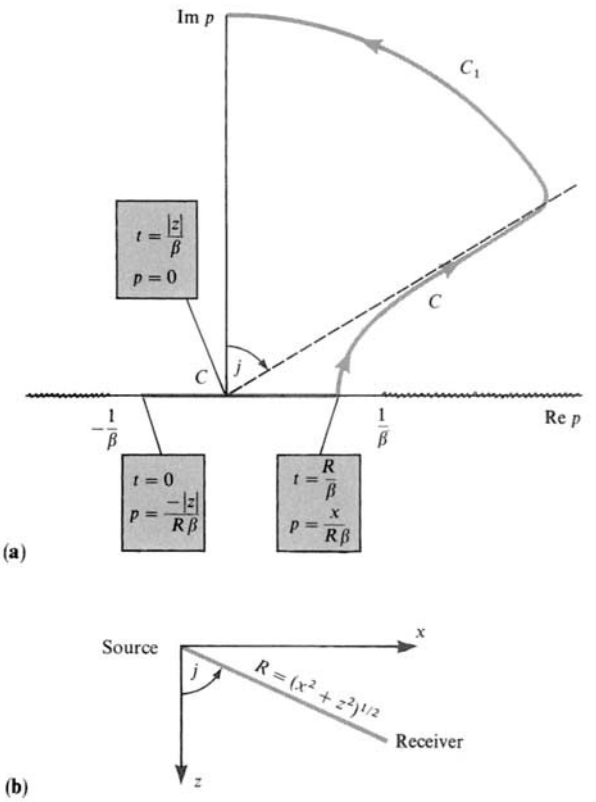

FIGURE **6.14**
(**a**) The Cagniard path C given by (6.50) is shown in the complex p-plane, beginning at $t = 0$ on the negative real p-axis, turning on to a branch of a hyperbola at $t = R/\beta$, and continuing into the first quadrant along a path with asymptote making the angle $j = \tan^{-1} x/|z|$ with the positive imaginary p-axis. Note that on the real p-axis, C cannot lie on the branch cuts. Also shown is part of a large arc in the first quadrant, connecting the imaginary p-axis and C. (**b**) Angle j is identified as the angle of incidence of the ray from source to receiver.

It remains only to convert to using t as the variable of integration. From (6.49) and (6.50), one can show that

$$\frac{dp}{dt} = \frac{i\eta}{\sqrt{t^2 - R^2/\beta^2}} \qquad \text{on } C, \text{ for } t > R/\beta,$$

which gives

$$v(x, z, s) = \frac{A}{2\pi\rho\beta^2} \int_{R/\beta}^{\infty} \frac{e^{-st}}{\sqrt{t^2 - R^2/\beta^2}} dt. \tag{6.52}$$

From this expression we can at last identify the time-domain solution as

$$v(x, z, t) = \frac{A}{2\pi\rho\beta^2} \frac{H(t - R/\beta)}{\sqrt{t^2 - R^2/\beta^2}}. \tag{6.43 again}$$

This concludes our rederivation of the delta-function response. Note that the pulse shape (6.43) has the arrival time $t = R/\beta$, which we should expect. There is a singularity in v at $t = R/\beta$, but it is integrable, so that there is no difficulty in obtaining by convolution the response to a body force $\mathbf{f}$ with general time dependence.

BOX **6.8**

An example of Jordan's Lemma

We shall show that

$$\int_{C_1} \frac{e^{-s(px+\eta|z|)}}{\eta} dp \to 0$$

as the radius of large arc C_1 (shown in Fig. 6.14) tends to ∞.

On C_1, $p = Le^{i\theta}$ for some large L, and $0 \le \pi/2 - j \le \theta \le \pi/2$. Then $\eta \sim -ip$ (since Re $\eta > 0$), and $\eta \sim L \sin\theta - iL\cos\theta$, hence

$$\left| \int_{C_1} \right| \le \int_{\pi/2-j}^{\pi/2} 2\exp[-s(L\cos\theta x + L\sin\theta|z|)]\, d\theta \tag{1}$$

(provided L is large enough; the "2" is inserted to ensure correctness of $\le$). If neither x nor z is zero, the exponent here is vanishingly small for all θ. If x is zero, then $j = 0$ and the Cagniard path is just the imaginary axis, so there is nothing to prove. But if z is zero, then $j = \pi/2$ and we must check that the integral in (1) still tends to zero for large L, even though the integrand in (1) does not tend to zero as $\theta \to \pi/2$. We use the inequality $1 - 2\theta/\pi < \cos\theta$ for $0 < \theta < \pi/2$. Then from (1), with $|z| = 0$,

$$\left| \int_{C_1} \right| \le \int_0^{\pi/2} 2e^{-sL(1-2\theta/\pi)x} d\theta = \frac{\pi}{sLx}(1 - e^{-sLx}) \to 0 \qquad \text{as } L \to \infty.$$

More generally, it is true that $\int_\Gamma e^{-\lambda p} f(p) dp \to 0$ as $L \to \infty$, where λ is real and positive, Γ is the semicircle $p = Le^{i\theta}(-\pi/2 \le \theta \le \pi/2)$, and $|f(p)| \to 0$ as $|p| \to \infty$ on Γ. This general result is Jordan's Lemma, often stated for negative imaginary λ, and with Γ as the upper semicircle with $0 \le \theta \le \pi$.

Next we examine a simple SH problem in which head waves can arise. We suppose that a line source given by $\mathbf{f} = (0, A\,\delta(x)\,\delta(z - z_0)\,\delta(t), 0)$ acts in a homogeneous half-space $z < 0$, so that $z_0 < 0$, with another half-space in $z > 0$ and welded contact along $z = 0$. Density and shear speed are ρ_1 and β_1 for the upper medium, ρ_2 and β_2 for the lower (see Figure 6.15). Taking the double transform $(x, t) \to (k_x, s)$, it follows from (6.45) that the incident wave in the upper medium is

$$v^{\text{inc}}(k_x, z, s) = \frac{A}{2\rho_1\beta_1^2 s\eta_1} \exp(-s\eta_1|z - z_0|), \tag{6.53}$$

where $\eta_1 = \sqrt{1/\beta_1^2 - p^2}$. Continuity of v and $\tau_{yz} = \mu\ \partial v/\partial z$ across $z = 0$ determines reflection and transmission coefficients $\grave{S}\acute{S}$ and $\grave{S}\grave{S}$, and from (5.33) these are

$$\grave{S}\acute{S} = \frac{\mu_1\eta_1 - \mu_2\eta_2}{\mu_1\eta_2 + \mu_2\eta_2}, \qquad \grave{S}\grave{S} = \frac{2\mu_1\eta_1}{\mu_1\eta_1 + \mu_2\eta_2}.$$

The total fields are then

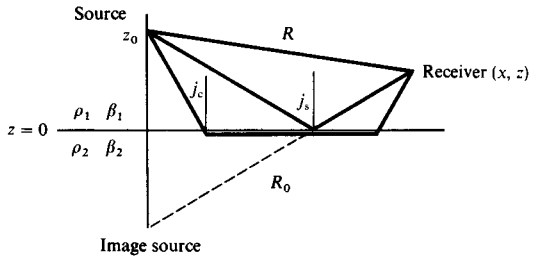

(a)

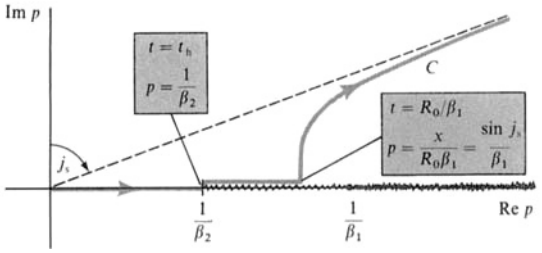

(b)

FIGURE **6.15**
(**a**) Parameters for a line source of SH at $x = 0, z = z_0 < 0$, in a medium consisting of two half-spaces in welded contact along $z = 0$. $R_0 = \sqrt{x^2 + (z + z_0)^2}$ is the distance of the receiver from an image source in the lower medium. We presume $\beta_2 > \beta_1$, and the critical angle $j_c = \sin^{-1}(\beta_1/\beta_2)$. The wide-angle reflection has an angle of incidence j_s, and $j_s > j_c$. (**b**) Features of the complex ray-parameter plane for evaluation of the generalized reflection (6.56) at a receiver beyond the critical distance, so that $j_s > j_c$ (see (a)), and head waves can occur beginning at $t = t_h$.

$$\text{in } z < 0, \quad v(k_x, z, s) = \frac{A}{2\mu_1 s\eta_1}\{\exp(-s\eta_1|z - z_0|) + \grave{S}\acute{S}\exp[-s\eta_1|z + z_0|]\}, \tag{6.54}$$

$$\text{in } z > 0, \quad v(k_x, z, s) = \frac{A}{2\mu_1 s\eta_1}\grave{S}\grave{S}\exp[-s(\eta_2 z + \eta_1|z_0|)]. \tag{6.55}$$

These are the algebraic expressions needed to start the Cagniard–de Hoop inversion. We have already examined the first term in (6.54). We shall now examine the second term, which we can call v^{refl}, giving the generalized reflection response in the upper medium. Following the steps that led to (6.48), we know that

$$v^{\text{refl}}(x, z, s) = \frac{A}{2\pi\rho_1\beta_1^2}\text{Im}\left\{\int_0^{i\infty}\frac{1}{\eta_1}\left(\frac{\mu_1\eta_1 - \mu_2\eta_2}{\mu_1\eta_1 + \mu_2\eta_2}\right)\exp[-s(px + \eta_1|z + z_0|)]\,dp\right\} \tag{6.56}$$

involving branches defined by $\text{Re}\,\eta_1 \geq 0, \text{Re}\,\eta_2 \geq 0$.

The Cagniard path C for the reflection is a solution $p = p(t)$ of

$$t = px + \eta_1|z + z_0|, \tag{6.57}$$

that is,

$$p = \begin{cases} \dfrac{xt - |z+z_0|\sqrt{\dfrac{R_0^2}{\beta_1^2} - t^2}}{R_0^2} & t \le \dfrac{R_0}{\beta_1} \qquad (6.57a) \\ \dfrac{xt + i|z+z_0|\sqrt{t^2 - \dfrac{R_0^2}{\beta_1^2}}}{R_0^2} & t \ge \dfrac{R_0}{\beta_1} \qquad (6.57b) \end{cases}$$

where $R_0 = \sqrt{x^2 + (z+z_0)^2}$ is the distance between receiver and image source (see Fig. 6.15b). It is interesting to compare this Cagniard path with the steepest descents path of integration for (6.56). To find this latter path, we adopt the terminology of Box 6.3 with $x = s$, $\zeta = p$, and $f = -(px + \eta_1|z+z_0|)$. A saddle point $p = p_s$ must be such that $f'(p_s) = 0$, i.e., $x \cos j_s = |z+z_0| \sin j_s$, where $p_s = \beta_1^{-1} \sin j_s$, so that p_s is just the ray parameter for the reflected ray between source and receiver, having j_s as the angle of incidence in the upper medium (Fig. 6.15a). Note that some close parallels with Section 6.2 are beginning to emerge (see (6.19)). In that section, we analyzed a P-wave problem, used a Fourier transform, and considered a point source. Yet here we find essentially the same saddle-point position. A difference now is that the steepest descents path is perpendicular to the real p-axis; i.e., angle $\chi = \pi/2$ (see Box 6.3), whereas previously we found $\chi = -\pi/4$. In fact, where the Cagniard path lies on the real axis (6.57a), it lies on a "ridge" of the integrand, the ridge descending to a saddle point at $p_s = x/(R_0\beta_1) = \beta_1^{-1} \sin j_s$ as t increases to R_0/β_1. There the Cagniard path turns through $\pi/2$ and follows a "valley" of the integrand, which is the ordinary steepest descents path for t increasing from R_0/β_1 (see (6.57b)).

If the receiver is in a position such that $x/R_0 < \beta_1/\beta_2$, then the point of departure of the Cagniard path from the real p-axis lies to the left of branch cuts emanating from $p = 1/\beta_1$ and $p = 1/\beta_2$. (The inequality implies that x is less than the critical distance at which head waves begin to be observable.) No interference with the branch cuts can occur, and since

$$dp/dt = i\eta_1 \Big/ \sqrt{t^2 - R_0^2/\beta_1^2} \qquad \text{on } C \text{ (for } t > R_0/\beta_1),$$

it follows that

$$v^{\text{refl}}(x,z,t) = \frac{A}{2\pi\rho_1\beta_1^2} \text{Re}\left\{\frac{\mu_1\eta_1 - \mu_2\eta_2}{\mu_1\eta_1 + \mu_2\eta_2}\right\} \frac{H(t - R_0/\beta_1)}{\sqrt{t^2 - R_0^2/\beta_1^2}}. \qquad (6.58)$$

(There is no contribution for $t < R_0/\beta_1$, since then $p(t)$ is real (see (6.57a)), and the integrand (6.56) has zero imaginary part.) This algebraic formula (6.58) is exact, and is evaluated for $t > R_0/\beta_1$ by first using (6.57b) to obtain a corresponding point on the Cagniard path, then finding $\eta_i = \sqrt{\beta_i^{-2} - p^2}$ $(i = 1, 2)$; and finally, substituting into (6.58). This an example of what we can naturally call a *narrow-angle* reflection.

If the receiver is beyond the critical distance, so that $\beta_1/\beta_2 < x/R_0 < 1$ and we expect a *wide-angle* reflection (see discussion of (6.23)), then the Cagniard path departs from the real p-axis at a point $p = p_s$ between $1/\beta_2$ and $1/\beta_1$, as shown in Figure 6.15b. The deformation

from the positive imaginary p-axis (6.56) to the Cagniard path proceeds just as before, but now there can be a contribution from that part of the path which lies on the real p-axis. This is the head-wave contribution, which arises in the evaluation of (6.56) along the Cagniard path for real p-values between $1/\beta_2$ and $\beta_1^{-1} \sin j_s$; then η_2 is pure imaginary, so that the integrand has a nonzero imaginary part. Corresponding values of time are found from (6.57):

$$\text{at } p = 1/\beta_2, \qquad t = t_h = x/\beta_2 + |z + z_0|\sqrt{\beta_1^{-2} - \beta_2^{-2}},$$

t_h being the arrival time at (x, z) of head waves from $(0, z_0)$;

$$\text{at } p = \beta_1^{-1} \sin j_s, \qquad t = R_0/\beta_1,$$

the arrival time of the wide-angle reflection. Between times t_h and R_0/β_1, η_2 is a negative pure imaginary quantity. It follows that an exact formula for the generalized reflection is

$$\begin{aligned} v^{\text{refl}}(x, z, t) = {} & \frac{A}{2\pi\rho_1\beta_1^2} \operatorname{Im} \left\{ \frac{\mu_1\eta_1 - \mu_2\eta_2}{\mu_1\eta_1 + \mu_2\eta_2} \right\} \frac{H(t - t_h) - H(t - R_0/\beta_1)}{\sqrt{R_0^2/\beta_1^2 - t^2}} \\ & + \frac{A}{2\pi\rho_1\beta_1^2} \operatorname{Re} \left\{ \frac{\mu_1\eta_1 - \mu_2\eta_2}{\mu_1\eta_1 + \mu_2\eta_2} \right\} \frac{H(t - R_0/\beta_1)}{\sqrt{t^2 - R_0^2/\beta_1^2}}. \end{aligned} \tag{6.59}$$

The last term here evaluates the shape of the wide-angle reflection at time $t > R_0/\beta_1$. However, there is a phase shift, because associated waves in the lower medium are inhomogeneous ($p > 1/\beta_2$). As we showed in Box 5.6 and in Section 6.2, the pulse shape of the wide-angle reflection is a linear sum of the incident pulse shape and its Hilbert transform. The latter involves motions often called the head-wave term. In this sense, one can speak of the wide-angle reflection as "emerging from the tail of the head wave." Note, however, that the attempt to separate the head-wave and reflection contributions will fail whenever there is a breakdown of the approximate (asymptotic) theory for each contribution (e.g., (6.26), if the receiver is near the critical distance, so that L is very small). Although this is a breakdown of terminology, (6.59) continues to give the exact total effect of "head wave" plus "reflection" even when L is small.

The final problem we shall consider in this section on the exact impulse response for two-dimensional problems is that of a line source of *P–SV* waves in a half-space taken as the region $z < 0$, with a free surface at $z = 0$ so that a Rayleigh wave is generated. We closely follow Chapman (1972), obtaining exact results that have many points of similarity with Section 6.3 above. One new idea is introduced: the concept of a "leaking mode," associated with zeros of the Rayleigh function lying in the Riemann sheet $\{\operatorname{Re} \xi < 0; \operatorname{Re} \eta > 0\}$.

We shall consider *P–SV* motions with displacement only in the x- and z-directions. Then, from an argument given in Section 5.1, it is sufficient to work with scalar potentials ϕ and ψ related to displacement via

$$\mathbf{u} = \nabla\phi + \nabla \times (0, \psi, 0) = (\partial\phi/\partial x - \partial\psi/\partial z, 0, \partial\phi/\partial z + \partial\psi/\partial x). \tag{6.60}$$

The source of such motions is a body force $\mathbf{f}$, which (without loss of generality) is given by $\mathbf{f} = \nabla\Phi + \nabla \times (0, \Psi, 0)$. From Lamé's theorem, potentials satisfy

$$\ddot{\phi} = \alpha^2\nabla^2\phi + \Phi/\rho \qquad \text{and} \qquad \ddot{\psi} = \beta^2\nabla^2\psi + \Psi/\rho, \tag{6.61}$$

and to specialize to a line source at depth h, we take

$$\begin{aligned} \Phi(x,z,t) &= L_0(t)\,\delta(x)\,\delta(z-h) \qquad (P\text{-wave source}), \\ \Psi(x,z,t) &= M_0(t)\,\delta(x)\,\delta(z-h) \qquad (SV\text{-wave source}). \end{aligned} \tag{6.62}$$

Each of these two sources generates a wave incident on the free surface, and after the transformation $(x,t) \to (k_x, s)$ we see by comparison with (6.53) that the incident waves have potentials

$$\phi^{\text{inc}}(k_x,z,s) = \frac{L_0(s)}{2\rho\alpha^2 s\xi}e^{-s\xi|z-h|}, \qquad \psi^{\text{inc}}(k_x,z,s) = \frac{M_0(s)e^{-s\xi|z-h|}}{2\rho\beta^2 s\eta}. \tag{6.63}$$

As usual, we have here used $\xi = (\alpha^{-2} - p^2)^{1/2}$, $\eta = (\beta^{-2} - p^2)^{1/2}$ and chosen the roots $\operatorname{Re}\xi > 0, \operatorname{Re}\eta > 0$ to satisfy radiation conditions. When waves (6.63) reach the free surface, they will generate P and S reflections with amplitude determined by satisfaction of boundary conditions $\tau_{zx} = \tau_{zz} = 0$ on $z = 0$. By transforming to the (k_x, z, s) domain, we have essentially reduced the calculation of reflections to a problem in plane-wave theory, so that the total potentials are just

$$\begin{aligned} \phi(k_x,z,s) = {} & \frac{L_0(s)}{2\rho\alpha^2 s\xi}\{\exp(-s\xi|z-h|) + \acute{P}\grave{P}\exp[-s\xi(z+h)]\} \\ & + \frac{M_0(s)}{2\rho\beta^2 s\eta}\cdot\frac{\alpha}{\beta}\acute{S}\grave{P}\exp[-s(\xi z + \eta h)], \\ \psi(k_x,z,s) = {} & -\frac{L_0(s)}{2\rho\alpha^2 s\xi}\cdot\frac{\beta}{\alpha}\acute{P}\grave{S}\exp[-s(\eta z + \xi h)] \\ & + \frac{M_0(s)}{2\rho\beta^2 s\eta}\{\exp(-s\eta|z-h|) - \acute{S}\grave{S}\exp[-s\eta(z+h)]\}, \end{aligned} \tag{6.64}$$

where reflection/conversion coefficients (see (5.27)–(5.28); (5.31)–(5.32)) are

$$\begin{aligned} \acute{P}\grave{P} &= \frac{4p^2\xi\eta - (\beta^{-2} - 2p^2)^2}{\mathsf{R}(p)}, & \acute{S}\grave{P} &= \frac{4\beta p\eta(\beta^{-2} - 2p^2)/\alpha}{\mathsf{R}(p)}, \\ \acute{P}\grave{S} &= \frac{4\alpha p\xi(\beta^{-2} - 2p^2)/\beta}{\mathsf{R}(p)}, & \acute{S}\grave{S} &= \frac{-4p^2\xi\eta + (\beta^{-2} - 2p^2)^2}{\mathsf{R}(p)}, \end{aligned} \tag{6.65}$$

and

$$\mathsf{R}(p) = 4p^2\xi\eta + (\beta^{-2} - 2p^2)^2 \tag{6.66}$$

is the Rayleigh function.

BOX **6.9**

On writing down the multitransformed solution, (6.64)

The only difficulty that prevents one from immediately writing down the formulas (6.64) concerns the detail of our sign convention and normalization of reflection/conversion coefficients. Beginning in Chapter 5, we adopted the convention of writing these coefficients for displacement-amplitude ratios, with a positive sign for motion in the increasing x-direction (see Fig. 5.5). Since (6.64) is for potentials, minus signs are introduced for $\acute{P}\grave{S}$ and $\acute{S}\grave{S}$; and factors α/β and β/α for $\acute{S}\grave{P}$ and $\acute{P}\grave{S}$, respectively.

In practice, one does not carry out the inversion of potentials to the time domain and then use (6.60) for displacement components. Rather, one obtains the transformed displacement components equivalent to (6.64), inverting these directly to the time domain. Using $\mathbf{u} = (u, 0, w)$ and recognizing that operation $\partial/\partial x$ becomes multiplication by $(-sp)$ in the transformed domain, it follows from (6.60) that, for $0 \leq z \leq h$,

$$\begin{aligned}\begin{pmatrix} u(k_x, z, s) \\ w(k_x, z, s) \end{pmatrix} = \frac{L_0(s)}{2\rho\alpha^2\xi}\left[\begin{pmatrix} -p \\ \xi \end{pmatrix}\exp[s\xi(z-h)] + \acute{P}\grave{P}\begin{pmatrix} -p \\ -\xi \end{pmatrix}\exp[-s\xi(z+h)]\right] \\ + \frac{M_0(s)}{2\rho\beta^2\eta}\frac{\alpha}{\beta}\acute{S}\grave{P}\begin{pmatrix} -p \\ -\xi \end{pmatrix}\exp[-s(\xi z + \eta h)] \\ + \frac{L_0(s)}{2\rho\alpha^2\xi}\frac{\beta}{\alpha}\acute{P}\grave{S}\begin{pmatrix} -\eta \\ p \end{pmatrix}\exp[-s(\eta z + \xi h)] \\ + \frac{M_0(s)}{2\rho\beta^2\eta}\left[\begin{pmatrix} -\eta \\ -p \end{pmatrix}\exp[s\eta(z-h)] + \acute{S}\grave{S}\begin{pmatrix} -\eta \\ p \end{pmatrix}\exp[-s\eta(z+h)]\right].\end{aligned} \tag{1}$$

Since the vectors

$$\begin{pmatrix} -p \\ \xi \end{pmatrix} \quad \text{and} \quad \begin{pmatrix} -\eta \\ -p \end{pmatrix}$$

have amplitude $1/\alpha$ and $1/\beta$, respectively, a factor α/β precedes $\acute{S}\grave{P}$ (and β/α precedes $\acute{P}\grave{S}$) in order for conversion coefficients to retain their standard definition in terms of displacement-amplitude ratios.

In the remainder of this section, to establish some general methods and obtain specific results, we shall restrict ourselves to the inversion of just one wave to the time domain. (A total of six waves is indicated by (6.64), but two of these are incident waves, which are trivial to evaluate.) We choose to evaluate the generalized $\acute{S}\grave{S}$ reflection in the case that $M_0(t) = M_0 H(t)$ (i.e., a step of constant height M_0 for which the Laplace transform is M_0/s). From the last term in (1) of Box 6.9, the horizontal component of displacement in this wave is u_{SS}, where

$$u_{SS}(k_x, z, s) = -\frac{M_0}{2\rho\beta^2 s}\acute{S}\grave{S}\exp[-s\eta(z+h)]. \tag{6.67}$$

Since $\acute{S}\grave{S}$ is even in p, the inverse k_x-transform can be written as

$$u_{SS}(x,z,s) = -\frac{M_0}{2\pi\rho\beta^2}\mathrm{Im}\left\{\int_0^{i\infty} \acute{S}\grave{S}(p)\exp[-spx - s\eta(z+h)]\,dp\right\} \tag{6.68}$$

(recall that $k_x = isp$). Defining a Cagniard path by $t = px + \eta(z+h)$, i.e.,

$$p(t) = \begin{cases} \dfrac{xt - (z+h)\sqrt{\dfrac{R_0^2}{\beta^2} - t^2}}{R_0^2} & t \le \dfrac{R_0}{\beta} \\[2ex] \dfrac{xt + i(z+h)\sqrt{t^2 - \dfrac{R_0^2}{\beta^2}}}{R_0^2} & t \ge \dfrac{R_0}{\beta}, \end{cases} \tag{6.69}$$

with $R_0 = \sqrt{x^2 + (z+h)^2}$ as the distance between receiver and image source, we obtain

$$u_{SS}(x,z,s) = -\frac{M_0}{2\pi\rho\beta^2}\mathrm{Im}\left\{\int_0^{i\infty} \acute{S}\grave{S}(p)e^{-st}\frac{dp}{dt}dt\right\},$$

and hence the exact solution in the time domain is

$$\begin{aligned} u_{SS}(x,z,t) &= -\frac{M_0}{2\pi\rho\beta^2}\mathrm{Im}\left\{\acute{S}\grave{S}(p)\frac{dp}{dt}\right\} \\ &= \frac{M_0}{2\pi\rho\beta^2}\mathrm{Im}\left\{\frac{4p^2\xi\eta - (\beta^{-2} - 2p^2)^2}{4p^2\xi\eta + (\beta^{-2} - 2p^2)^2}\frac{dp}{dt}\right\}\Bigg|_{p=p(t)}. \end{aligned} \tag{6.70}$$

In this expression,

$$\frac{dp}{dt} = \begin{cases} \dfrac{\eta}{\sqrt{\dfrac{R_0^2}{\beta^2} - t^2}} & 0 < t < \dfrac{R_0}{\beta}, \\[2ex] \dfrac{i\eta}{\sqrt{t^2 - \dfrac{R_0^2}{\beta^2}}} & \dfrac{R_0}{\beta} < t, \end{cases}$$

so that an integrable singularity is present in (6.70) at the ray arrival time of reflected waves, $t = R_0/\beta$.

Despite the simplicity of the exact solution (6.70) it is worthwhile to go further, since insight is acquired by identifying various features in the associated complex p-plane (Fig. 6.16b) and the approximate properties of waves that are controlled by these features. Thus, the first arrival at the receiver (if it is sufficiently distant from the source) is a head wave, having ray parameter $1/\alpha$ and arrival time $t_h = x/\alpha + (z+h)\sqrt{\beta^{-2} - \alpha^{-2}}$. Its pulse shape is determined by evaluation of (6.70) in the vicinity of $t = t_h$, $p = 1/\alpha$, values for which the Cagniard path lies on a branch cut beginning at $p = 1/\alpha$. Another major arrival is the reflection associated with a saddle point of (6.68). This occurs on the Cagniard path

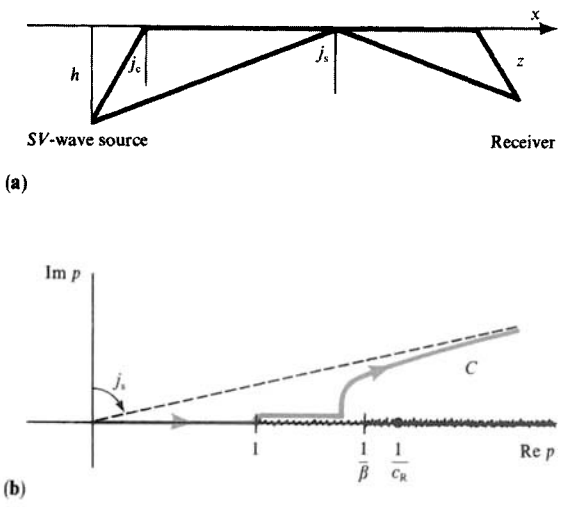

FIGURE **6.16**
The generalized $\acute{S}\grave{S}$ reflection for a line source buried in a homogeneous half-space. (**a**) The source–receiver geometry in the case $j_s > j_c$, showing both reflection and head-wave paths. (**b**) The complex p-plane, with Cagniard path on the Riemann sheet $\{\text{Re}\,\xi > 0; \text{Re}\,\eta > 0\}$. The Rayleigh pole at $p = 1/c_R$ now lies on two branch cuts.

at $t = R_0/\beta$ and has properties similar to those we investigated in (6.58) and (6.59). The two new phenomena that occur are due to poles of the integrand in (6.68), i.e., zeros of the Rayleigh function

$$\mathsf{R}(p) = 4p^2\xi\eta + (\beta^{-2} - 2p^2)^2.$$

From Section 5.3, we know that $\mathsf{R}(p)$ has zeros at $p = \pm 1/c_R$ near $p = \pm 1/\beta$ on the sheet $\{\text{Re}\,\xi \geq 0; \text{Re}\,\eta \geq 0\}$, where ξ and η are in fact pure imaginary. $\mathsf{R}(p) = 0$ also has zeros near $p = \pm 1/\alpha$ on the sheet $\{\text{Re}\,\xi < 0; \text{Re}\,\eta \geq 0\}$. Such a sheet is often called "forbidden" or "unphysical," in the sense that an integrand evaluated at a point on this sheet would tend to infinity as $z \to \infty$, in violation of the radiation condition. However, we shall find that poles of $\acute{S}\grave{S}$ at zeros of $\mathsf{R}(p)$ that are on a forbidden sheet can yet make an identifiable contribution on a seismogram.

We shall assess first the effect of the Rayleigh pole at $p = 1/c_R$. As the source–receiver distance increases, the angle j_s increases (Fig. 6.16a) and the Cagniard-path asymptote becomes closer to the real p-axis (Fig. 6.16b). The Cagniard path itself therefore passes closer to the Rayleigh pole. If one were to contour the magnitude of $\acute{S}\grave{S}(p)$ in the vicinity of $p = 1/c_R$, as shown in Figure 6.17, it is apparent that the large values of $\acute{S}\grave{S}(p)$ in the vicinity of the pole would lead to an identifiable Rayleigh wave, provided the Cagniard path lies sufficiently close to $p = 1/c_R$. To get an estimate of when the Rayleigh pulse is well developed, we can see if, at its "arrival time" x/c_R, the Cagniard path lies closer to the Rayleigh pole than does the next-nearest feature of $\acute{S}\grave{S}$ and dp/dt that might influence u_{SS} in (6.70). Since this next-nearest feature is a branch point at $p = 1/\beta$, it follows that the Rayleigh wave is likely to be well developed if

$$\left| p\left(\frac{x}{c_R}\right) \right| < \frac{1}{c_R} - \frac{1}{\beta} \tag{6.71}$$

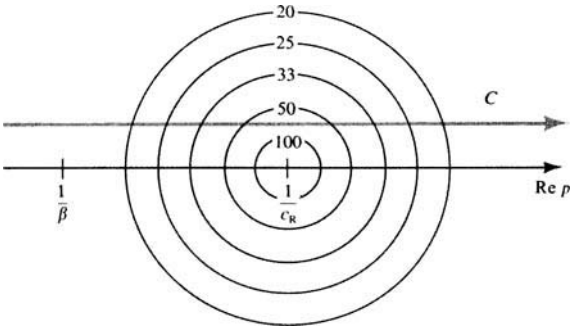

FIGURE **6.17**
The magnitude of $\dot{S}\grave{S}(p)$ is contoured in the complex p-plane for values near the Rayleigh pole. Then $\grave{S}\dot{S}(p) \propto (p - 1/c_R)^{-1}$, so that contours are essentially a system of concentric circles centered on the pole. The numbers shown are in the ratio $1 : \frac{1}{2} : \frac{1}{3} : \frac{1}{4} : \frac{1}{5} : \ldots$, which is appropriate for equal increments of radius. For a large value of j_s (see Fig. 6.16ab), the Cagniard path C is shown cutting across the contours close to the pole: associated values of u_{SS} given by (6.70) will clearly be large at these times. Such values constitute the Rayleigh-wave pulse shape (i.e., its shear wave component). There is another contribution from generalized $\dot{S}\dot{P}$, giving the P-wave component.

since then the p-value gives a point on the Cagniard path whose distance to the pole is less than the distance from the pole to the branch point, and the effect of the pole will be likely to dominate for that point on C. In this inequality, we can evaluate p at time x/c_R from (6.69) and find that a completely equivalent inequality is the geometrical relation

$$\tan j_s > \sqrt{\frac{2c_R}{\beta - c_R}}. \tag{6.72}$$

In practice, this result appears to be rather better than Nakano's inequality (6.35), which we developed for a P-wave source (the inequality there being reversed, since it designated the range for which Rayleigh waves had *not* developed). Since $c_R \sim 0.92\beta$ for many rocks, we conclude from (6.72) that the range must be at least five times greater than the source + receiver depths in order for the Rayleigh pulse to be developed as an identifiable feature in the seismogram.

Gilbert and Laster (1962) labeled the pole at $p = 1/c_R$ the $\overline{S}$-pole, and the associated Rayleigh wave as the $\overline{S}$-pulse. This label was chosen because, in general terms, the Rayleigh wave is a phenomenon of diffraction associated with a nearby S-wave wavefront, which interacts with the free surface. Similarly, there is an effect associated with poles of $\mathsf{R}(p)$ which usually lie near $p = 1/\alpha$, moving away from this branch point only for values of Poisson's ratio greater than about 0.4. These poles, called $\overline{P}$-poles by Gilbert and Laster, do not lie on the physical Riemann sheet. Introducing the notation of Phinney (1961), we designate the physical sheet {Re $\xi > 0$; Re $\eta > 0$} as the (++) sheet, and similarly for the three unphysical sheets: (+−); (−+), and (−−). Whereas the Rayleigh pole ($\overline{S}$) lies on the (++) sheet, $\overline{P}$-poles lie on the (−+) sheet.

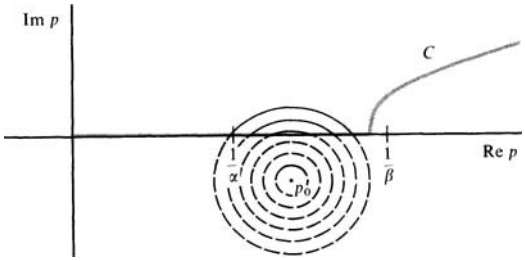

FIGURE **6.18**
Contours showing the magnitude of $\acute{S}\grave{S}(p)$ in the vicinity of a $\overline{P}$-pole $p = p_0$ lying on an "unphysical" Riemann sheet. This is the $(-+)$ sheet, and $\mathsf{R}(p_0) = 0$, where still $\mathsf{R}(p) = 4p^2\xi\eta + (\beta^{-2} - 2p^2)^2$. Although the contours close to p_0 are concentric circles lying entirely in the fourth quadrant of the $(-+)$ sheet, contours with larger radius must run into the branch cut running to the right from $p = 1/\alpha$. Such contours will then extend on to the first quadrant of the *physical* Riemann sheet, since this is the way $\acute{S}\grave{S}(p)$ is kept analytic across a branch cut (see Box 6.2). On the $(-+)$ sheet, contours are shown as broken lines. The extension of contours onto the $(++)$ sheet is shown by solid lines. Note that the Cagniard path lies on the real p-axis for part of the segment between $1/\alpha$ and $1/\beta$.

It might reasonably be thought that poles of $\acute{S}\grave{S}(p)$ lying on unphysical sheets cannot influence the generalized reflection u_{SS} in (6.70), since the Cagniard path lies entirely on the $(++)$ sheet. Shown schematically in Figure 6.18, however, is a system of contours of $\acute{S}\grave{S}$ in the vicinity of a $\overline{P}$-pole. Since we are interested in values of $\acute{S}\grave{S}$ in the first quadrant of the $(++)$ sheet (this is the region in which our Cagniard path lies), it is just this sheet that is contoured for the first quadrant in Figure 6.18. Analytic continuation of $\acute{S}\grave{S}$ into the fourth quadrant (i.e., across the real p-axis for $1/\alpha < p$) then requires going on to a different Riemann sheet, the fourth quadrant of the $(-+)$ sheet, and in this region there *is* a pole of $\acute{S}\grave{S}$. The pole shown is in fact in the appropriate location for a Poisson's ratio of around 0.4, and the important point is that contours associated with this pole do appear on the physical sheet. For a receiver at sufficient range, so that the Cagniard path lies on or close to the real p-axis, these solid-line contours of Figure 6.18 will be crossed in the evaluation of (6.70), and a rather broad pulse shape will be the result. This is the $\overline{P}$-pulse described in detail by Gilbert, Laster, Backus, and Schell (1962). It occurs for ray parameters lying between $1/\alpha$ and $1/\beta$, and its place in the seismogram is between the head-wave arrival and the wide-angle reflection. An example is shown in Figure 6.19a.

Values of Poisson's ratio up around 0.4 are abnormal. For values decreasing from 0.4 to around 0.263 (which is physically more plausible), $\overline{P}$-poles migrate to the real p-axis just to the left of $p = 1/\alpha$ (but still on the $(-+)$ sheet). As Poisson's ratio decreases still further, from 0.263 to zero, $\overline{P}$-poles remain on the real p-axis, one pole actually tending to the branch point itself, at $p = 1/\alpha$ (see Problem 6.4). The presence of a pole near that point of the Cagniard path at which head waves originate (also at $p = 1/\alpha$, but on the $(++)$ sheet) has the effect of distorting the head-wave arrival from its usual shape. In Figure 6.19b, we show an example of u_{SS} for an ordinary value of Poisson's ratio (0.25), and in Figure 6.19c we show the theoretical seismogram for a very low Poisson's ratio (0.1).

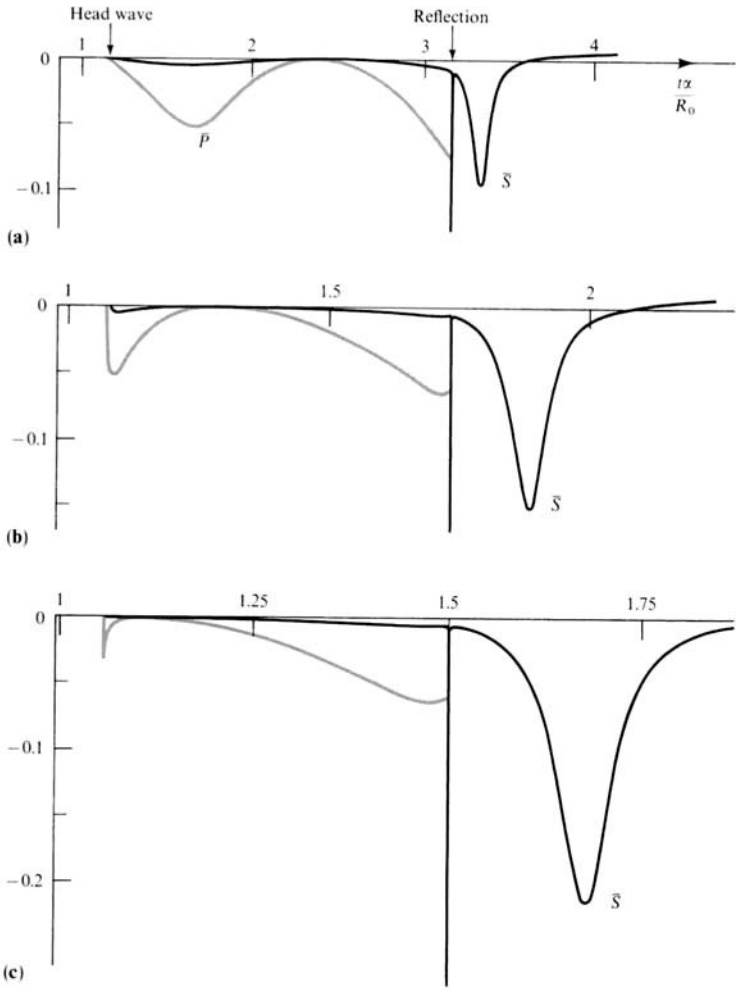

FIGURE **6.19**

The horizontal component of the generalized $\acute{S}\grave{S}$ reflection given by (6.70) is shown as a function of time for three different values of Poisson's ratio. We use dimensionless time, $t\alpha/R_0$, where R_0 is the distance between receiver and image source: $(h, x, z) = (1, 20, 0.1)$ units. Since the head wave is traveling at the P-wave speed for most of its path, it arrives just after $t\alpha/R_0 = 1$. Time scales have been chosen so that head-wave and reflection times are aligned on the three traces. To bring out the detailed pulse shapes between head-wave and reflection arrival times, a tenfold increase in amplitude scale is also used for this part of the seismogram (shown in gray). (**a**) Poisson's ratio $= \frac{4}{9}$. There is a $\overline{P}$ pole away from the real p-axis, of the type shown in Figure 6.18, leading to a $\overline{P}$-wave between the head-wave arrival time and the wide-angle reflection. (**b**) Poisson's ratio $= \frac{1}{4}$. The head-wave and the wide-angle reflection are clearly separated pulses. (**c**) Poisson's ratio $= \frac{1}{10}$. A $\overline{P}$-pole lies on the real p-axis, close to the branch point $p = 1/\alpha$, although not on the $(++)$ sheet. Its principal effect is to influence the shape of the head wave, giving here an impulsive arrival. There is an integrable singularity at the reflection arrival time, but there is insignificant area under this part of the pulse for all three cases shown, since $x \gg h + z$.

The $\overline{P}$-pulse is a simple example of a *leaking mode*. The adjective "leaking" is appropriate, because, for that part of the Cagniard path which is influenced by the $\overline{P}$-pole, η is either purely real or, for times just after the reflection arrival, has only a small imaginary part. This implies that energy is radiated downward, away from the free surface, as SV motion. Such a radiation leakage of energy does not occur for $\overline{S}$, for which both ξ and η are imaginary. We shall look further at leaking modes in Chapter 7.

6.5 Cagniard–De Hoop Methods for Point Sources

The attractive feature of Cagniard–de Hoop analysis for two-dimensional problems (line sources) was found above to be that exact algebraic solutions are possible. For three-dimensional problems, we shall find here that exact solutions in the time domain cannot usually be stated as algebraic expressions, but rather as single integrals. It is common to manipulate these integrals so that they are carried out over a finite segment of the Cagniard path itself. For many three-dimensional problems of practical interest, an adequate approximate form of solution can be found (see (6.95), (6.96)), in which the integral is readily computed because it is a convolution.

We begin again with a simple SH problem, using both Cartesian coordinates (x, y, z) and related cylindrical coordinates (r, ϕ, z). We suppose that a point source in an infinite elastic medium acts as a point torque at the origin, so that the body force is

$$\mathbf{f} = \nabla \times (0, 0, \mathrm{X}) \tag{6.73}$$

in which the body-force potential X is axisymmetric, so that $\mathrm{X} = \mathrm{X}(r, z, t)$, independent of ϕ. Only the azimuthal component of displacement $\mathbf{u}$ is excited by this source, and it is independent of ϕ. Thus, in cylindrical coordinates,

$$\mathbf{u} = \nabla \times (0, 0, \chi) = (0, -\partial\chi/\partial r, 0), \tag{6.74}$$

and the equation of motion reduces to

$$\rho\ddot{\chi} = \mathrm{X} + \mu\nabla^2\chi. \tag{6.75}$$

For a point source at the origin, with a step-like time dependence,

$$\mathrm{X} = N_0 H(t)\, \delta(x)\, \delta(y)\, \delta(z) = N_0 H(t) \frac{\delta(r)}{2\pi r} \delta(z) \tag{6.76}$$

for some constant N_0, and from (4.4) it is clear that the solution for SH-potential χ is exactly

$$\chi(x, y, z, t) = \frac{N_0}{4\pi\rho\beta^2} \frac{H(t - R/\beta)}{R}, \tag{6.77}$$

using $R = |\mathbf{x}|$.

Let us now derive this result again, using instead the Cagniard–de Hoop approach for three-dimensional problems.

We start by taking the triple transform

$$\int_{-\infty}^{\infty} \exp(-ik_x x)\, dx \int_{-\infty}^{\infty} \exp(-ik_y y)\, dy \int_{-\infty}^{\infty} \exp(-st)\, dt$$

operating on (6.75) and (6.76):

$$\frac{\partial^2}{\partial z^2}\chi(k_x, k_y, z, s) = -\frac{N_0}{\rho\beta^2 s}\delta(z) + n^2\chi(k_x, k_y, z, s),$$

where $n^2 = k_x^2 + k_y^2 + s^2/\beta^2$. Comparing with (6.44) and (6.45), it follows that

$$\chi(k_x, k_y, z, s) = \frac{N_0}{2\rho\beta^2 sn} e^{-n|z|}, \tag{6.78}$$

choosing the root of n^2 for which Re $n > 0$.

The Laplace transform of the desired solution is given by two inverse Fourier transform of (6.78):

$$\chi(\mathbf{x}, s) = \frac{N_0}{8\pi^2\rho\beta^2 s}\int_{-\infty}^{\infty} dk_x \int_{-\infty}^{\infty} dk_y \frac{\exp(ik_x x + ik_y y - n|z|)}{n}, \tag{6.79}$$

and our goal is to rearrange this into the form of a forward Laplace transform, from which the integrand can be recognized as χ in the time domain.

To this end, we investigate the (k_x, k_y)-plane by using new variables (w, q) defined by

$$k_x = s(w\cos\phi - q\sin\phi), \qquad k_y = s(w\sin\phi + q\cos\phi). \tag{6.80}$$

This is the de Hoop transformation (de Hoop, 1960): it involves the azimuthal coordinate ϕ, and consists of a rotation and stretch of the whole horizontal-wavenumber plane. Since $x = r\cos\phi$, $y = r\sin\phi$, and the area element $dk_x\, dk_y$ is replaced by $s^2 dw\, dq$, we find from (6.79) that

$$\chi(\mathbf{x}, s) = \frac{N_0}{8\pi^2\rho\beta^2}\int_{-\infty}^{\infty} dw \int_{-\infty}^{\infty} dq \frac{\exp(iswr - s\eta|z|)}{\eta}, \tag{6.81}$$

where $\eta = \sqrt{\beta^{-2} + q^2 + w^2}$ and Re $\eta > 0$.

One standard method of inverting (6.81) to the time domain is to convert the q-integral to a forward Laplace transform of the w-integral. This approach is often taken in the applied mechanics literature, and is used for a solution quoted in our Chapter 11 (see equations (11.31) and (11.32), in which an extra factor $1/\alpha$ has been removed from q and w to make these variables dimensionless). The resulting solution for $\chi(\mathbf{x}, t)$ is an integral over a finite range of w-values.

Another method of inverting (6.81) is to exploit the similarities with line-source problems. To bring the integrand (6.81) into a form familiar in the two-dimensional case (e.g., see (6.47)), we change the w-variable via $p = -iw$, giving

$$\chi(\mathbf{x},s)=\frac{N_0}{2\pi^2\rho\beta^2}\int_0^\infty dq\ \mathrm{Im}\left[\int_0^{i\infty}\frac{\exp(-s(pr+\eta|z|))}{\eta}dp\right], \tag{6.82}$$

where $\eta=\sqrt{\beta^{-2}+q^2-p^2}$. (To obtain (6.82) from (6.81), we also used half-ranges of integration and properties of evenness in q; and evenness and oddness in w for the real and imaginary parts of the integrand.)

Strong similarities are now apparent between the integrands of (6.48) and (6.82). Note here that the horizontal variable is r, rather than x, and $1/\beta^2+q^2$ replaces $1/\beta^2$ in the definition of η. Previously, we found that

$$\mathrm{Im}\left[\int_0^{i\infty}\frac{\exp(-s(px+\eta|z|))}{\eta}dp\right]\qquad\left(\text{with }\eta=\sqrt{\beta^{-2}-p^2}\right)$$

is the Laplace transform of

$$\frac{H\left(t-\dfrac{\sqrt{x^2+z^2}}{\beta}\right)}{\sqrt{t^2-\dfrac{x^2+z^2}{\beta^2}}},$$

and this enables us now to write (6.82) as

$$\chi(\mathbf{x},s)=\frac{N_0}{2\pi^2\rho\beta^2}\int_0^\infty dq\int_0^\infty\frac{H[t-R\sqrt{\beta^{-2}+q^2}]}{\sqrt{t^2-R^2(\beta^{-2}+q^2)}}e^{-st}\,dt. \tag{6.83}$$

Here we are using $R=\sqrt{x^2+y^2+z^2}=\sqrt{r^2+z^2}$ as the three-dimensional distance function. If we integrate with respect to q first, and then with respect to t, we find

$$\chi(\mathbf{x},s)=\frac{N_0}{2\pi^2\rho\beta^2}\int_0^\infty dt\,e^{-st}\left\{H\left(t-\frac{R}{\beta}\right)\int_0^{\sqrt{t^2/R^2-1/\beta^2}}\frac{dq}{\sqrt{t^2-R^2(\beta^{-2}+q^2)}}\right\} \tag{6.84}$$

(as explained in Fig. 6.20). But now from this integrand we can recognize the required solution as

$$\chi(\mathbf{x},t)=\frac{N_0}{2\pi^2\rho\beta^2}H\left(t-\frac{R}{\beta}\right)\int_0^{\sqrt{t^2/R^2-1/\beta^2}}\frac{dq}{\sqrt{t^2-R^2(\beta^{-2}+q^2)}}. \tag{6.85}$$

This is essentially the method of de Hoop (1960), and we list the following comments on (6.85):

(i) The solution has the typical form for point-source problems, in that the exact solution is a single finite integral.

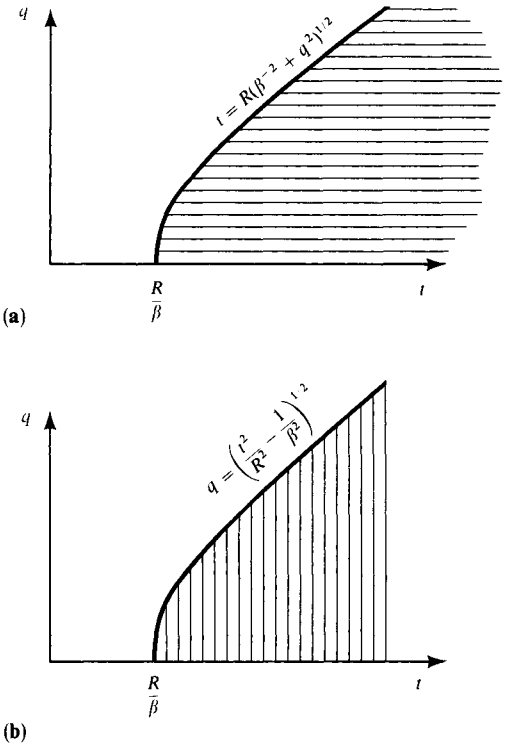

FIGURE **6.20**
Diagrams to explain equivalent integrations in the $t - q$ plane. (**a**) The t-integration at fixed q is conducted first, as in (6.83), with the lower limit as a function of q. (**b**) The q-integration at fixed t is conducted first, as in (6.84), with the upper limit as a function of t.

(ii) In our particular case, the integral in (6.85) is easy to evaluate analytically. The substitution $q = \sqrt{t^2/R^2 - 1/\beta^2}\ \sin\theta$ immediately gives $\pi/(2R)$ for the integral, and solution (6.77) is recovered.

(iii) Going back to (6.84), we find $\chi(\mathbf{x}, s) = (N_0 e^{-sR/\beta})/(4\pi\rho\beta^2 sR)$. For a general time dependence $N_0(t)$, rather than the step function we have so far assumed,

$$\chi(\mathbf{x}, s) = \frac{N_0(s)}{4\pi\rho\beta^2 R} e^{-sR/\beta} \qquad \text{and} \qquad \chi(\mathbf{x}, t) = \frac{N_0(t - R/\beta)}{4\pi\rho\beta^2 R}.$$

The physical displacement, from (6.74), is

$$u_\phi = -\left[\frac{\partial}{\partial r}\frac{N_0(t - R/\beta)}{4\pi\rho\beta^2 R}\right].$$

(iv) When an interface is present, with its attendant head waves and interface waves, the above method is changed only in that the t-integral of (6.83) is more complicated (again, it can be written down from prior study of the corresponding two-dimensional problem).

Although the above method of solution is a brilliantly conceived and successful approach, it does not fully exploit the properties of ray parameter and of integration in the complex ray-parameter plane, which educated our intuition in Section 6.4. Therefore, modern

methods of solving Lamb's problem for a point source have often taken the approach initiated by Strick (1959), and later extended by Helmberger (1968) and Gilbert and Helmberger (1972), in which the complex ray-parameter plane again plays a central role. These methods require familiarity with the Hankel transform and related results for modified Bessel functions, which are reviewed in Box 6.10. By way of illustration, we again turn to the problem (6.75)–(6.76), operating this time with the double transform $\int_0^\infty r I_0(\lambda r)\, dr \int_0^\infty e^{-st}\, dt$ to find

$$\frac{\partial^2}{\partial z^2}\chi(\lambda, z, s) = \frac{-N_0}{2\pi\rho\beta^2 s}\delta(z) + \left(\frac{s^2}{\beta^2} - \lambda^2\right)\chi(\lambda, z, s).$$

The doubly transformed solution is therefore (compare (6.45) and (6.44))

$$\chi(\lambda, z, s) = \frac{N_0}{4\pi\rho\beta^2 s^2 \eta} e^{-s\eta|z|}, \tag{6.86}$$

where $\eta = \sqrt{1/\beta^2 - \lambda^2/s^2}$ and $\operatorname{Re}\eta > 0$. Using $\lambda = sp$ (a factorization we have now done several times in one form or another) and the inverse transform (Box 6.10, equation (4)), we see that

$$\chi(r, z, s) = \frac{N_0}{4\pi^2\rho\beta^2 i}\int_{-i\infty}^{i\infty} \frac{p}{\eta} K_0(spr) e^{-s\eta|z|}\, dp, \tag{6.87}$$

in which $\eta = (\beta^{-2} - p^2)^{1/2}$ and s, r, η are all real and positive.

Noting that $K_0(\zeta^*) = [K_0(\zeta)]^*$ where * denotes taking a complex conjugate, we can see that (6.87) gives

$$\chi(\mathbf{x}, s) = \frac{N_0}{2\pi^2\rho\beta^2}\operatorname{Im}\left\{\int_0^{i\infty} \frac{p}{\eta} K_0(spr) e^{-s\eta|z|}\, dp\right\}. \tag{6.88}$$

In view of the asymptotic result

$$K_0(spr) = \sqrt{\frac{\pi}{2spr}}\, e^{-spr}\left(1 + O\left(\frac{1}{spr}\right)\right) \tag{6.89}$$

for large argument, (6.88) bears a very strong similarity to the line-source formula (6.48). Both integrands involve the complex ray-parameter plane, but now r replaces x as the horizontal variable. We define

$$t' = pr + \eta|z|$$

and then solve for a Cagniard path $p = p(t')$ in the first quadrant (see Fig. 6.21). Deforming the path of integration in (6.88) to the Cagniard path gives

$$\chi(\mathbf{x}, s) = \frac{N_0}{2\pi^2\rho\beta^2}\operatorname{Im}\int_{p(t')} \frac{p}{\eta} K_0(spr) e^{-s\eta|z|}\, dp, \tag{6.90}$$

and at last we are in a position to invert to the time domain.

BOX 6.10

Horizontal transforms for functions symmetric about a vertical axis

Consider a function $f = f(x, y)$ in which the dependence is really only on $\sqrt{x^2 + y^2} = r$. The transformed function,

$$f(k_x, k_y) = \int\int_{-\infty}^{\infty} f(x, y) \exp[-i(k_x x + k_y y)]\, dx\, dy,$$

may be evaluated in terms of k_r, and ϕ', just as we did in (6.5) to develop the Sommerfeld integral. Following the method that led to (6.7), we find now that

$$f(k_x, k_y) = 2\pi \int_0^{\infty} r f(r) J_0(k_r r)\, dr,$$

which is a function only of k_r, and not ϕ'. It is conventional to use $f(r) = f(x, y)$, but $f(k_r) = f(k_x, k_y)/2\pi$. We then find from the above and a similar treatment of the inverse transform that

$$\left.\begin{aligned} f(k_r) &= \int_0^{\infty} r f(r) J_0(k_r r)\, dr \\ f(r) &= \int_0^{\infty} k_r f(k_r) J_0(k_r r)\, dk_r \end{aligned}\right\} \text{ which is the Hankel transform pair of order zero.} \tag{1}$$

More generally it can be shown that there is a Hankel transform pair of order n:

$$\left.\begin{aligned} f^{(n)}(k_r) &= \int_0^{\infty} r f(r) J_n(k_r r)\, dr \\ f(r) &= \int_0^{\infty} k_r f^{(n)}(k_r) J_n(k_r r)\, dk_r. \end{aligned}\right\} \tag{2}$$

(We use the superscript (n) when it is necessary to emphasize the order of the Bessel function used in the transform. The proof of (2) entails showing that if the general result is true for some integer $n \geq 0$, it is true for the integer $n + 1$. But it is true for $n = 0$, and hence must be true in general.)

The order of Hankel transform to choose in any particular wave problem is the one for which, in the wave equation under discussion, operations with the variable r are reduced to scalar multiplication in the transform domain. For example, the derivatives in (6.75) are written

$$\rho \ddot{\chi} = \mathrm{X} + \mu \left[\frac{1}{r} \frac{\partial}{\partial r} \left(\frac{r\, \partial \chi}{\partial r} \right) + \frac{\partial^2 \chi}{\partial z^2} \right].$$

Here it is appropriate to use the zero-order Hankel transform, since

$$\int_0^{\infty} r \left[\frac{1}{r} \frac{\partial}{\partial r} \left(\frac{r\, \partial \chi}{\partial r} \right) \right] J_0(k_r r)\, dr = -k_r^2 \chi(k_r, z, t).$$

(continued)

BOX **6.10** *(continued)*

(This equality follows from integrating by parts twice, then using the differential equation satisfied by J_0.) However, the wave equation satisfied by $u_\phi = -\partial\chi/\partial r$ is

$$\rho\ddot{u}_\phi = f_\phi + \mu(\nabla^2\mathbf{u})_\phi = f_\phi + \mu\left(\nabla^2 u_\phi - \frac{u_\phi}{r^2}\right), \tag{3}$$

and the extra last term here indicates that the zero-order Hankel transform would be unsuccessful. Instead, the first-order transform is the one that reduces all operations with r and $\partial/\partial r$ in (3) to scalar multiplication in the k_r-domain. In P-SV problems with a point source on $r = 0$, use of the zero-order transform is appropriate for u_z and τ_{zz}. The first-order transform is needed for u_r and τ_{zr}. These results are apparent from Box 6.6, which treats waves in the wavenumber–frequency domain.

In solving two-dimensional problems via the Cagniard–de Hoop method, we made early use of a relation $k_x = isp$ between horizontal wavenumber and ray parameter (see (6.40)). For point-source problems, this relation clearly becomes $k_r = isp$ (compare with (6.8) for the Fourier time transform), hence it will be important to examine (2) for pure imaginary values of k_r. We shall use $k_r = i\lambda$ and then (2) can be rewritten as

$$\left.\begin{aligned} f^{(n)}(\lambda) &= \int_0^\infty rf(r)I_n(\lambda r)\,dr \\ f(r) &= \frac{1}{\pi i}\int_{-i\infty}^{i\infty} \lambda f^{(n)}(\lambda)K_n(\lambda r)\,d\lambda. \end{aligned}\right\} \tag{4}$$

Here, I_n and K_n are modified Bessel functions. The transform pair (4) bears the same relationship to (2) as the Laplace transform does to the Fourier transform.

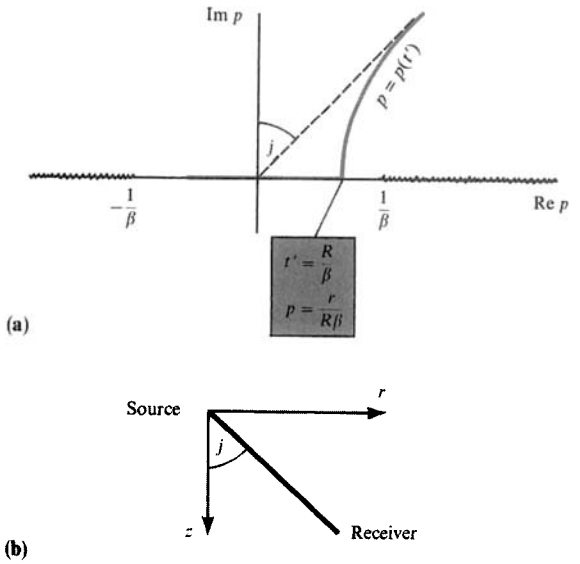

FIGURE **6.21**
The complex ray-parameter plane and features for the evaluation of (6.90)–(6.92). Note the similarity to Figure 6.14.

From tables, we know that $K_0(s\sigma_1)$ is the Laplace transform of

$$H(t-\sigma_1)/\sqrt{t^2-\sigma_1^2},$$

and hence $K_0(s\sigma_1)\, e^{-s\sigma_2}$ is the Laplace transform of

$$H(t-\sigma_1-\sigma_2)/\sqrt{(t-\sigma_2)^2-\sigma_1^2}.$$

Therefore, (6.90) implies

$$\chi(\mathbf{x},t)=\frac{N_0}{2\pi^2\rho\beta^2}\mathrm{Im}\int_{p(t')}\frac{p}{\eta}\frac{H(t-pr-\eta|z|)}{\sqrt{(t-\eta|z|)^2-p^2r^2}}dp. \tag{6.91}$$

The contribution to this integral comes only from values $R/\beta < t' < t$ (at the lower limit, the integrand begins to have an imaginary part: the upper limit is the cutoff from the step function), so that

$$\chi(\mathbf{x},t)=\frac{N_0}{2\pi^2\rho\beta^2}\mathrm{Im}\int_{R/\beta}^{t}\frac{p}{\eta}\frac{1}{\sqrt{t-t'}\sqrt{t-t'+2pr}}\frac{dp}{dt'}dt', \tag{6.92}$$

in which

$$p=p(t')=\frac{rt'+i|z|\sqrt{t'^2-R^2/\beta^2}}{R^2},$$

$$\frac{dp}{dt'}=\frac{i\eta}{\sqrt{t'^2-R^2/\beta^2}},\qquad\text{and}\qquad\eta=\sqrt{\frac{1}{\beta^2}-p^2}\qquad\text{with Re}\,\eta>0.$$

Although it is not obvious that the imaginary part of the integral in (6.92) reduces to $\pi/(2R)$, the integral is simple to evaluate numerically after taking account of integrable singularities at both upper and lower limits. So the result is (6.77) again.

Once the derivation of (6.92) has been mastered, almost all the features of practical Cagniard–de Hoop applications are relatively simple. Thus, suppose two half-spaces are in welded contact along $z=0$, as shown in Figure 6.15, with a *point* source of SH-waves acting at $z_0<0$ in the upper medium. The SH-potential in the upper medium is just the incident wave

$$\chi^{\mathrm{inc}}(\mathbf{x},t)=\frac{N_0}{4\pi\rho_1\beta_1^2}\frac{H(t-R/\beta_1)}{R}$$

using $R=\sqrt{r^2+(z-z_0)^2}$ (see (6.77)), together with a generalized reflection potential. By analogy with the line-source problem and (6.92), the reflection is exactly

$$\chi^{\mathrm{refl}}(\mathbf{x},t)=\frac{N_0}{2\pi^2\rho_1\beta_1^2}\mathrm{Im}\int_0^t\frac{p}{\eta_1}\left[\frac{\mu_1\eta_1-\mu_2\eta_2}{\mu_1\eta_1+\mu_2\eta_2}\right]\frac{1}{\sqrt{t-t'}\sqrt{t-t'+2pr}}\frac{dp}{dt'}dt' \tag{6.93}$$

in which $p(t')$ is given by (6.57), but now of course with r in place of x and t' in place of t. The integral in (6.93) is extended down to zero to pick up possible head waves in the case that $\beta_2 > \beta_1$.

We have made no approximations in deriving (6.93), but for many practical purposes an important approximation can often be made that vastly reduces the computational effort, with little sacrifice in accuracy. Thus, suppose $|pr| \gg t - t'$ throughout the range of integration. Then we can make the approximation

$$\sqrt{t - t' + 2pr} \sim \sqrt{2pr} \tag{6.94}$$

and recognize (6.92) and (6.93) as convolutions of a function of time with $1/\sqrt{t}$. That is, if we wish to calculate χ^{refl} from (6.93) for the whole interval $0 \leq t \leq T$, we first calculate the function

$$\psi(t) = \frac{1}{2\pi^2 \rho_1 \beta_1^2} \text{Im} \left\{ \frac{p(t)}{\eta_1} \left[\frac{\mu_1\eta_1 - \mu_2\eta_2}{\mu_1\eta_1 + \mu_2\eta_2} \right] \frac{1}{\sqrt{2pr}} \frac{dp}{dt} \right\} \tag{6.95}$$

for $0 \leq t \leq T$. Then

$$\chi(\mathbf{x}, t) = N_0 \int_0^t \frac{\psi(t')}{\sqrt{t - t'}} dt' = N_0 \psi(t) * \frac{1}{\sqrt{t}}, \tag{6.96}$$

and the theoretical seismogram for $0 \leq t \leq T$ can be generated in just one convolution operation—a very efficient and fast computational process. By comparison, the exact result (6.93) requires a different numerical integration for each single point in the desired time series.

Note that the approximation (6.94) is good for large ranges, but fails even then for sufficiently long times. It is equivalent to using $\sqrt{\pi/(2spr)}e^{-spr}$ for $K_0(spr)$ in (6.88), and hence is the same approximation we made at (6.18) in Section 6.2 for a point-source problem discussed in the frequency domain. Further terms can be kept in the expansion for K_0, and are equivalent to approximating $1/\sqrt{t - t' + 2pr}$ by the binomial expansion

$$\sqrt{\frac{1}{2pr}} \left[1 - \frac{t - t'}{4pr} + \frac{3}{32} \left(\frac{t - t'}{pr} \right)^2 + \cdots \right].$$

Provided $|2pr| > t - t'$, these further terms may be expected to give improved accuracy, though the effort is rarely worthwhile. Since they depend on t only via factors of type $(t - t')^n$, they too yield simple convolutions (Helmberger and Harkrider, 1978).

The solutions (6.92) and (6.93) are for the case of a step-function time dependence of the force. Other time dependences can clearly be obtained by convolution, but there is one time dependence that in effect "cancels out" the convolution (6.96). Suppose, for example, that

$$X(r, z, t) = N_0(t) \frac{\delta(r)}{2\pi r} \delta(z) \qquad \text{with} \qquad N_0(t) = \frac{H(t)}{\pi\sqrt{t}}.$$

Then it is an elementary exercise in convolutions to show that

$$\chi(\mathbf{x}, t) = \frac{d\psi}{dt} * \frac{1}{\sqrt{t}} * \frac{1}{\pi\sqrt{t}} = \psi(t),$$

and in this sense we can actually get a useful *algebraic* expression for the seismogram, given by (6.95).

The approximation (6.94) and the resulting convolution (6.96) are now very much a part of modern seismology, as we shall find in Chapter 9 when looking at the effects of multiple layering.

6.6 Summary of Main Results and Comparison between Different Methods

We have described two methods for solving problems of a spherical wave interacting with a plane boundary. The first method (Sections 6.1–6.3) uses the Fourier transform of time dependence, and leads to solutions for displacement, pressure, etc. as a function of frequency. The second method (Sections 6.4–6.5) uses a Laplace transform, but (by manipulations due to Cagniard, de Hoop, and others) leads to solutions directly in the time domain. In this section we list some similarities and differences between the two methods and briefly discuss their merits and disadvantages.

First, we list the similarities. Both the Fourier method and the Cagniard method entail integrations in the complex ray-parameter plane: ray paths in the physical problem correspond to saddle points in the integrand under consideration; head waves correspond to branch cuts; interface waves (e.g., Rayleigh, Stoneley) correspond to poles; and leaking modes (e.g., $\overline{P}$) correspond to poles on Riemann sheets other than that on which the radiation condition is satisfied.

Second, there are several superficial differences. (i) To obtain results in the time domain via the Fourier method, a numerical inverse transform is required. But, in practice, the Cagniard solution must be convolved with a source function and with the instrument response, and these operations are essentially equivalent to numerical Fourier transformations. (ii) We characterized the Cagniard methods as being exact, whereas early in the development of the Fourier method, we made an approximation to certain Hankel functions (see (6.16)–(6.18)). In practice, an equivalent approximation (6.94) is often made in the Cagniard approach. (iii) Branch cuts in the Cagniard method were chosen to make $\{\text{Re } \xi \geq 0; \text{Re } \eta \geq 0\}$, and it was found possible to keep the path of integration on this same physical Riemann sheet, without crossing branch cuts. However, we developed the Fourier theory with branch cuts fixed by $\{\text{Im } \xi \geq 0; \text{Im } \eta \geq 0\}$, in which case we found it necessary to develop complicated paths of integration (e.g., Fig. 6.9) that had segments on nonphysical sheets. Many authors have taken this approach, and a correct discussion of the effect of leaking modes can be highly involved. Fortunately, the choice of branch cuts is quite flexible in the Fourier method, and a path of integration can in fact be chosen that does lie close to the steepest descents path, yet also stays on the same Riemann sheet. The main constraint, the radiation condition, requires that the integrand (e.g., (6.33)) tend to zero as $|z| \to 0$ only for values of p on the original path of integration. Thus, in (6.33), we really require $\text{Im } \xi \geq 0$ only for p-values on the real p-axis, and do *not* need to use branch cuts

for which Im $\xi \geq 0$ on the whole plane. In Figure 6.22 are shown some different choices for branch cuts, which enable one to take integration paths that are more successful for numerical applications of the Fourier method.

Finally, we point out some of the differences between our two methods in order to show the appropriateness of each for certain circumstances. (i) The Cagniard path must be found exactly for each generalized ray, but the path of integration in the Fourier method need only approximately follow a steepest descents path: as we shall see in Chapter 9, two or three straight-line segments are often adequate. This difference between the two methods is particularly important when theoretical seismograms are required for a large suite of source depths or source–receiver distances. Then, in the Fourier method, the same integration path can be used several times to generate different seismograms by changing only one factor (e.g., $e^{i\omega pr}$, to look at different ranges). The various Cagniard paths we have described have all been obtained by solving a quadratic equation, but in practice the equation to be solved is often of higher order. For example, the $\acute{S}\grave{P}$ reflection (6.64) entails solving $t = px + \eta z + \xi h$, which is a quartic in p. Fortunately, as Helmberger (1968) has shown, there is no difficulty in determining a numerical solution, even for multilayered media. (ii) The success of the Cagniard method depends on a certain property of the Laplace transform of the required solution—namely, that it can be written as a function of s times a factor in the form $\int_0^\infty g(t)e^{-st}\,dt$ (see (6.41)). Unfortunately, this property is quite easily destroyed. For example, if attenuation is introduced, then, as we saw in Chapter 5, the body-wave velocity becomes frequency dependent. The Laplace transform of the response takes a form $\int_0^\infty g(s,t)e^{-st}\,dt$, and it is not possible to factor g in a way that permits the time-domain solution to be identified directly. The same difficulty arises for media in which elastic properties vary continuously with depth, but with occasional discontinuities, as we shall see in Chapter 9. (If WKBJ theory—see Box 9.6—can be applied to obtain the depth-dependence of the solution in the transform domain, then Cagniard–de Hoop methods may be suitable for the inversion back to time and space: see Verweij and de Hoop, 1990.)

In summary, it is clear that the Cagniard–de Hoop solution has great advantages for solving Lamb's problem with a point source or a line source. The impulse response is obtained directly and with a minimum of computational effort. The Fourier method also has merit, giving some complementary insight in that the behavior of different frequency components is studied directly and being more flexible than the Cagniard method in applications beyond Lamb's problem.

Suggestions for Further Reading

Brekhovskikh, L. M. *Waves in Layered Media.* New York: Academic Press, 1960.

Červený, V., and R. Ravindra. *Theory of Seismic Head Waves.* University of Toronto Press, 1971.

Chapman, C. H. Lamb's problem and comments on the paper 'On leaking modes' by Usha Gupta. *Pure and Applied Geophysics*, **94**, 233–247, 1972.

de Hoop, A. T. Modification of Cagniard's method for solving seismic pulse problems. *Applied Science Research*, **B8**, 349–356, 1960.

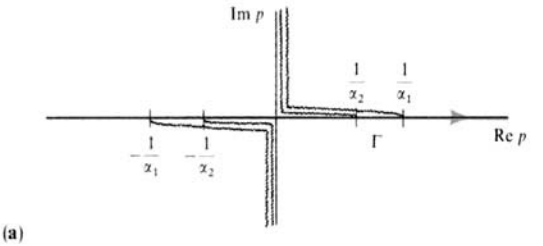

(a)

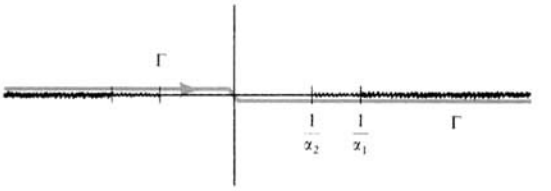

(b)

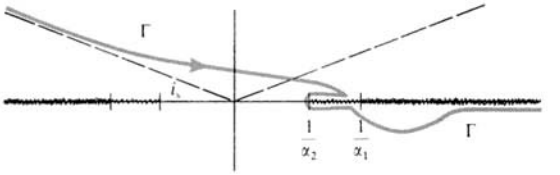

(c)

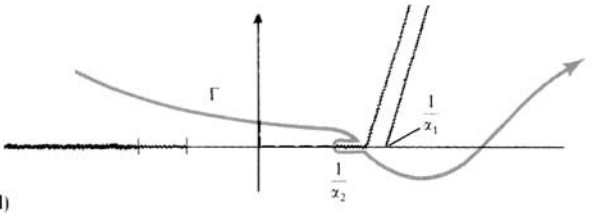

(d)

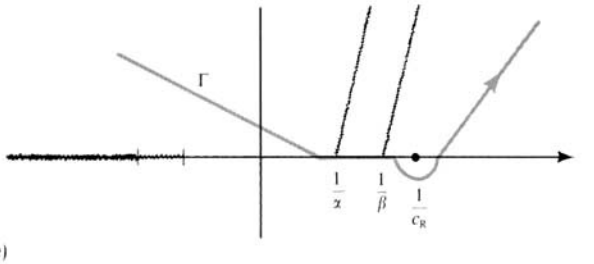

(e)

FIGURE **6.22** *(continued)*
Various branch cuts and integration paths in the complex p-plane, showing the flexibility of choice. (a)–(d) are relevant to the problem solved in Section 6.2 of a point source of pressure in a medium consisting of two fluid half-spaces. (**a**) Branch cuts are chosen so that $\text{Im}\ \xi_1 > 0, \text{Im}\ \xi_2 > 0$ for the whole plane. Γ lies on the real axis, just above cuts in the third quadrant, and below cuts in the first. Compare with Figure 6.4. (**b**) For the same problem, we have changed branch cuts to $\text{Re}\ \xi_1 > 0, \text{Re}\ \xi_2 > 0$. The solution is unchanged, because Γ is unchanged and the value of an integrand (e.g., (6.18)) at any point on Γ is unchanged from (a). (**c**) Γ is distorted from the position shown in (b) to lie on a steepest descents path in a case where head waves are possible. The path around the cut is now much simpler than that shown in Figure 6.9, although there is still a problem in that the steepest descents path runs into the cuts at $p = 1/(\alpha_1 \sin i_s)$, hence Γ is subsequently drawn below the cut. (**d**) For cuts like those shown here, there is no difficulty in keeping Γ everywhere on the steepest descents path (except around the branch point at $p = 1/\alpha_2$). To see that these cuts are possible, note that they can be moved from the position shown in (a) *before* Γ is distorted from the real axis. In subsequent distortion of Γ to the path shown here, $\text{Im}\ \xi_1$ and $\text{Im}\ \xi_2$ do become negative in the first quadrant to the left of the cuts shown. This is allowed because no singularities are present between this part of Γ and a path (shown as a broken line) on which $\text{Im}\ \xi_1$ and $\text{Im}\ \xi_2$ are positive. (**e**) This shows the p-plane for a solid half-space problem, e.g., for evaluating the generalized $\acute{P}\grave{P}$ reflection (see Fig. 6.12 for comparison). Branch cuts are drawn upward into the first quadrant, and a path Γ favorable for computations is made up from straight-line segments and a semicircle around $p = 1/c_R$. Branch cuts of this type have properties similar to the lines of poles found in Chapter 9 in generating theoretical seismograms when the Earth's spherical geometry is taken into account.

Gilbert, F., and L. Knopoff. The directivity problem for a buried line source. *Geophysics*, **26**, 626–634, 1961.

Johnson, L. R. Green's function for Lamb's problem. *Geophysical Journal of the Royal Astronomical Society*, **37**, 99–131, 1974.

Lamb, H. On the propagation of tremors over the surface of an elastic solid. *Philosophical Transactions of the Royal Society of London*, **A203**, 1–42, 1904.

Lapwood, E. R. The disturbance due to a line source in a semi-infinite elastic medium. *Philosophical Transactions of the Royal Society of London*, **A242**, 63–100, 1949.

Pekeris, C. L. The seismic buried pulse. *Proceedings of the National Academy of Sciences*, **41**, 629–639, 1955.

Richards, P. G. Elementary solutions to Lamb's problem for a point source and their relevance to three-dimensional studies of spontaneous crack propagation. *Bulletin of the Seismological Society of America*, **69**, 947–956, 1979.

Verweij, M. D. Reflection of transient acoustic waves by a continuously layered halfspace with depth-dependent attenuation. *Journal of Computational Acoustics*, **5**, 265–276, 1997.

Wilson, C. R. The Abel-Fourier method of Hankel transformation: Applications to seismic data. *Geophysical Prospecting*, **34**, 545–568, 1986.

Problems

6.1 When head waves can occur in the solution (6.93), arriving at time t_h, show that (6.94) is equivalent to requiring

$$\frac{r}{\beta_2} \gg t - t_h.$$

When $\beta_2 < \beta_1$, show that (6.94) is equivalent to requiring

$$\frac{r^2}{R_0\beta_1} \gg t - \frac{R_0}{\beta_1}.$$

The above constraints on the applicability of our convolution solution (6.96) might at first sight make it seem that (6.96) is nothing more than a wavefront approximation (e.g., (6.22)). In fact, (6.96) is much more powerful than a wavefront approximation. Show briefly that this is so by considering expressions for the seismograms at distances near critical, where the head wave and wide-angle reflection are superimposed.

6.2 Use a body-force equivalent like (3.8) of Chapter 3 to show that the discontinuity in $\partial v/\partial z$, used to obtain (6.45), is physically due to a discontinuity in stress.

6.3 Show from (6.14) that the transmitted wave in Figure 6.3 is given approximately by

$$P^{\text{trans}} = \sqrt{\frac{\omega}{2\pi r}}\, e^{-i(\omega t - \pi/4)} \int_{-\infty}^{\infty} \frac{C(p)\sqrt{p}}{\xi_1} \exp[i\omega(pr + \xi_1|z_0| + \xi_2 z)]\, dp.$$

Find an equation for the value of p at which this integrand is stationary, and show that the stationary point is given by the horizontal slowness corresponding to the transmitted ray from source to receiver.

6.4 Show that the zero crossings of $\acute{P}\grave{P}$ and $\acute{S}\grave{S}$ in Figure 5.6 occur precisely at values of p for which the Rayleigh function has zeros on nonphysical Riemann sheets. (It is the right-most zero crossing of Fig. 5.6, near $p = 1/\alpha$, that can affect the head-wave arrival contained in expression (6.70), evaluated in Fig. 6.18.)

6.5 Give an algebraic solution for the classical Lamb problem with a line source. That is, give the surface displacements (u, w) when a line source along the y-axis acts on the surface of an elastic half-space, so that there is an impulse I (per unit length) applied downward at the origin $(x = 0, t = 0)$ on the free surface $z = 0$. Obtain a simple approximation for the shape of the Rayleigh wave.

6.6 In setting up P-SV problems with the method of potentials, note that in general the SV-displacement is represented by $\nabla \times \nabla \times (0, 0, \psi)$. See Box 6.5. Reconcile this with a conclusion reached in Section 5.1, in which the SV-displacement was represented by $\nabla \times (0, \psi, 0)$ for plane waves. (By a synthesis from such waves, $\nabla \times (0, \psi, 0)$ is appropriate for SV in all problems with fields independent of the y-coordinate.)

6.7 In Figure 6.9, is the result of integrating along the total path Γ (as shown) any different from using the path $A \to B \to C \to$ (around $1/\alpha_2$) $\to F' \to$ (saddle) $\to G \to H$? (That is, omitting $F' \to D \to E \to F'$.)

6.8 Show that the motion u_{SS} obtained in (6.70), and illustrated in Figure 6.19, diverges to infinity as $t \to \infty$. Show (without developing full algebraic details) that this behavior is cancelled out by a similar divergent expression arising from the P-wave component of particle motion (generalized $\acute{S}\grave{P}$).

CHAPTER 7

Surface Waves in a Vertically Heterogeneous Medium

Surface waves are propagated in directions parallel to the surface of the Earth. Their amplitude distribution over depth is stationary with horizontal position (apart from an overall multiplicative factor describing the horizontal spreading). Therefore, the geometrical spreading effect is much less for surface waves than for body waves (for which the energy spreads both horizontally and vertically down into the Earth's interior). In fact, surface waves are usually the dominant feature of seismograms in the period range 10–200 s, and much of the reliable information on the long-period part of seismic source spectra is obtained from surface waves. Surface-wave phase velocities, group velocities, and attenuation characteristics have been useful in delineating the structure of the crust and upper mantle in various regions of the Earth. Surface-wave source spectra and radiation patterns have contributed to determination of seismic moments, focal mechanisms, and focal depths of remote events. Surface waves also supply crucial data for distinguishing earthquakes from underground explosions.

The main purpose of this chapter is to describe the basic properties of surface waves in a vertically heterogeneous medium bounded by a free surface, and to derive formulas for their amplitude and phase spectra due to arbitrary point sources. In the final section, to complete the modal approach, we shall represent the total wave field as a sum of normal modes and leaky modes.

7.1 Basic Properties of Surface Waves

Let the z-axis be vertical, with the positive direction downward. Our vertically heterogeneous medium occupies the lower half-space, $z > 0$. As we saw in Sections 5.1 and 5.2, it is worthwhile to consider waves in which the dependence on spatial coordinates and time is given by the method of separation of variables. Thus, beginning with the simplest of problems, we shall consider Cartesian coordinates and a surface wave propagating in the horizontal direction of increasing x, with frequency ω:

$$\mathbf{u}(x, y, z, t) = \mathbf{Z}(z) \exp[i(kx - \omega t)]. \tag{7.1}$$

BOX **7.1**
Initial assumptions

As we begin to discuss surface waves, note that a double meaning is attached to the very first equation here, (7.1). In the main text, this basic wave is introduced as a steady-state wave, having fixed horizontal wavenumber. (For brevity, we shall use k where in previous chapters we used k_x or k_r.) This permits a clear physical picture of the wave, and obviously

$$\frac{\partial}{\partial t}\mathbf{u}(x,z,t) = -i\omega\mathbf{u}(x,z,t),$$
$$\frac{\partial}{\partial x}\mathbf{u}(x,z,t) = ik\mathbf{u}(x,z,t).$$

But the surface waves in seismology are actually a synthesis of such basic waves, so it is appropriate for us to think of the displacement field as a function of (k, z, ω), being the double Fourier transform (over x and t) of the nonseparable surface wave $\mathbf{u}(\mathbf{x}, t)$. In this context, the double transforms of $\partial\mathbf{u}(\mathbf{x}, t)/\partial t$ and $\partial\mathbf{u}(\mathbf{x}, t)/\partial x$ are, respectively, $-i\omega\mathbf{u}(k, z, \omega)$ and $+ik\mathbf{u}(k, z, \omega)$. By two different but related approaches, we have thus reduced partial derivatives (with respect to x and t) to scalar multiplications.

The all-important consequences of this equation are that only z-derivatives remain in the wave equation and boundary conditions, and such one-dimensional problems are relatively simple to solve.

In fact, the problem is to evaluate (7.1) under three general conditions. These waves must satisfy the free surface condition at $z = 0$, where the traction vanishes. At the other boundary, $z = \infty$, their amplitude must vanish because no energy is supplied at infinity. In addition, they must, of course, satisfy the equation of motion. Under such restrictive conditions, a nontrivial solution of the form (7.1) does not exist for arbitrary values of both frequency ω and wavenumber k. It *can* exist, however, if ω is given an arbitrary value, and k takes a special value that depends on ω. We write the special value as $k_n(\omega)$. This is an eigenvalue problem, and we use a subscript n because it can often happen that more than one value of k provides a surface wave (7.1) with given ω. Here $k_n(\omega)$ is an eigenvalue, and the corresponding solution $\mathbf{u}_n(z)$ is the eigenfunction. Thus, for a given frequency ω, surface waves (if they exist) have uniquely determined wavenumbers $k_0(\omega), k_1(\omega), k_2(\omega) \ldots$. The largest eigenvalue is designated as k_0, with others ordered as $k_0 > k_1 > k_2 \ldots$. Then phase velocities $c_n = \omega/k_n$ must also take discrete values at any fixed ω, and $c_0 < c_1 < c_2 \ldots$. The z-dependence of the eigenfunction is fixed, independent of the horizontal location.

To illustrate these general concepts, we shall first study the simplest case of plane Love waves in a single homogeneous layer overlying a homogeneous half-space (Fig. 7.1). Putting the rigidities of the layer and half-space as μ_1, μ_2 and their densities as ρ_1, ρ_2 respectively, the y-component of displacement (v) satisfies the wave equation

$$\frac{\partial^2 v}{\partial t^2} = \frac{\mu_1}{\rho_1}\left(\frac{\partial^2 v}{\partial x^2} + \frac{\partial^2 v}{\partial z^2}\right) \qquad \text{in the layer } 0 < z < H$$

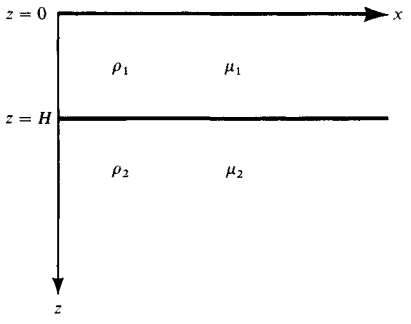

FIGURE **7.1**
A homogeneous layer over a homogeneous half-space, the simplest medium in which Love waves can be generated.

and

$$\frac{\partial^2 v}{\partial t^2} = \frac{\mu_2}{\rho_2}\left(\frac{\partial^2 v}{\partial x^2} + \frac{\partial^2 v}{\partial z^2}\right) \qquad \text{in the half-space } H < z.$$

Using trial solutions of the form (7.1), we find

$$v = \left[\grave{S}_1 e^{-\nu_1 z} + \acute{S}_1 e^{\nu_1 z}\right] \exp\left[i(kx - \omega t)\right] \qquad 0 \le z \le H$$

and

$$v = \left[\grave{S}_2 e^{-\nu_2 z} + \acute{S}_2 e^{\nu_2 z}\right] \exp\left[i(kx - \omega t)\right] \qquad H \le z, \tag{7.2}$$

where

$$\nu_i = \sqrt{k^2 - \omega^2/\beta_i^2}, \qquad \text{Re } \nu_i \ge 0, \qquad \text{and} \qquad \beta_i = \sqrt{\mu_i/\rho_i}$$

for $i = 1$ and 2. Then Im $\nu_i \le 0$ (cf. properties of γ in (6.4)). $\grave{S}_1$, $\acute{S}_1$, $\grave{S}_2$, and $\acute{S}_2$ are constants, as yet unknown.

We shall assume that the velocity β_1 of the layer is lower than the velocity β_2 of the half-space. From the boundary conditions as $z \to \infty$, we know (if the wave is homogeneous, i.e., if ν_2 is negative imaginary) that there can be no upcoming wave, so that $\acute{S}_2 = 0$, and it is also just this wave that must vanish if ν_2 is positive real, to avoid exponential growth with depth. (The sign of the root for ν_1 and ν_2 gives $i\nu_1$ and $i\nu_2$ the property of vertical wavenumber, having real and imaginary parts that are either positive or zero if k, ω, and β_i are real-valued.) Since the free surface condition is satisfied if $\partial v/\partial z = 0$ at $z = 0$, we must have $\grave{S}_1 = \acute{S}_1$. Thus we are left with two unknowns, $\grave{S}_1$ and $\grave{S}_2$, which must satisfy the following equations, required for continuity of displacement and traction across $z = H$:

$$\begin{aligned} 2\grave{S}_1 \cos(i\nu_1 H) &= \grave{S}_2 e^{-\nu_2 H} \\ 2i\mu_1\nu_1\grave{S}_1 \sin(i\nu_1 H) &= \mu_2\nu_2\grave{S}_2 e^{-\nu_2 H} \end{aligned} \tag{7.3}$$

or

$$\frac{\grave{S}_2}{\grave{S}_1} = \frac{2\cos(i\nu_1 H)}{e^{-\nu_2 H}} = \frac{2i\mu_1\nu_1 \sin(i\nu_1 H)}{\mu_2\nu_2 e^{-\nu_2 H}}. \tag{7.4}$$

This gives wavenumber eigenvalues k_n as the solutions of $F(k) = 0$, where

$$F(k) \equiv \tan(i\nu_1 H) - \frac{\mu_2\nu_2}{i\mu_1\nu_1}, \tag{7.5}$$

or phase-velocity eigenvalues $c_n = \omega/k_n$ as the solutions of

$$\tan \omega H \sqrt{\frac{1}{\beta_1^2} - \frac{1}{c^2}} = \frac{\mu_2}{\mu_1} \frac{\sqrt{\dfrac{1}{c^2} - \dfrac{1}{\beta_2^2}}}{\sqrt{\dfrac{1}{\beta_1^2} - \dfrac{1}{c^2}}}. \tag{7.6}$$

The corresponding eigenfunctions ν_n are obtained by putting (7.4), $\grave{S}_1 = \acute{S}_1$, and $\acute{S}_2 = 0$ into (7.2):

$$\begin{aligned} \nu_n(x, z, t) &= 2\grave{S}_1 \cos\left[\omega\sqrt{\frac{1}{\beta_1^2} - \frac{1}{c_n^2}}\, z\right] \exp[i(k_n x - \omega t)] \qquad \text{for } 0 \le z \le H \\ &= 2\grave{S}_1 \cos\left[\omega\sqrt{\frac{1}{\beta_1^2} - \frac{1}{c_n^2}}\, H\right] \exp\left[-\omega\sqrt{\frac{1}{c_n^2} - \frac{1}{\beta_2^2}}\,(z - H)\right] \\ &\quad \times \exp[i(k_n x - \omega t)] \qquad \text{for } H \le z, \end{aligned} \tag{7.7}$$

which shows a sinusoidal oscillation with depth in the layer and an exponential decay with depth in the half-space.

Solutions to (7.6) may be shown graphically, to illustrate properties of the phase-velocity values. Figure 7.2 shows the right side of (7.6) as a broken line and the left side as a solid line, both as functions of $(H/\beta_1)\sqrt{1 - \beta_1^2/c^2} = X$, say, so that the right-hand side of (7.6) is proportional to $\sqrt{(\text{constant})^2 - X^2}/X$. The roots are given by line intersections. From the figure, it is clear that the real roots for c are limited to lie between β_1 and β_2 (we assumed $\beta_1 < \beta_2$). We see that there are only a finite number of real roots for a given frequency ω. When $\omega = 0$ there is only one root, which is a point on the fundamental mode that corresponds to the extreme left branch of the tangent curves. If we increase ω, the tangent curve marked as $n = 1$ enters the range from the right. It enters when π/ω is equal to $(H/\beta_1)\sqrt{1 - \beta_1^2/\beta_2^2}$. If we further increase ω, more tangent curves will enter the range from the right. The nth curve enters there when ω is equal to

$$\omega_{cn} = \frac{n\pi\beta_1}{H} \Big/ \sqrt{1 - \frac{\beta_1^2}{\beta_2^2}}, \tag{7.8}$$

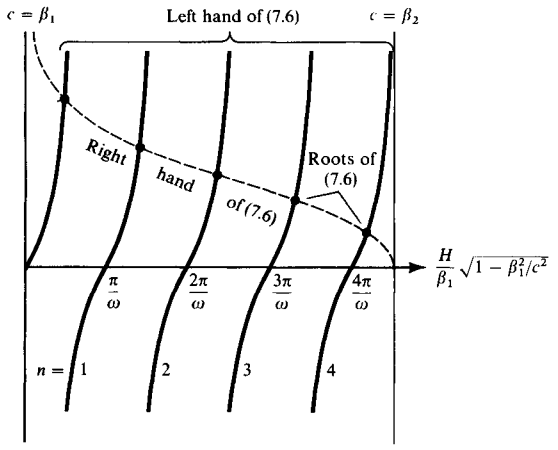

FIGURE **7.2**
Graphic solution of equation (7.6) for the dispersion of Love waves in a single layer over a half-space.

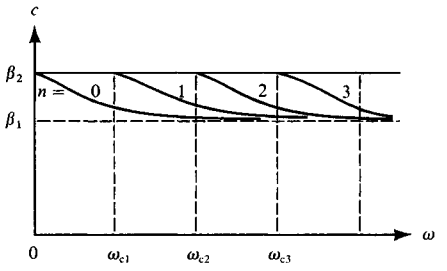

FIGURE **7.3**
Schematic diagram of phase velocities for the fundamental mode ($n = 0$) and the next three higher modes, plotted against frequency.

which is called the *cut-off frequency of the* nth *higher mode*, because, as shown in Figure 7.3, the nth mode exists only for $\omega > \omega_{cn}$. For example, in the case of a typical crust–mantle structure in a continent, taking $H = 35$ km, $\beta_1 = 3.5$ km/s, and $\beta_2 = 4.5$ km/s, the cut-off frequency of the first higher mode is 0.08 Hz (a period of 13 s).

Thus the nth-higher mode appears at $\omega = \omega_{cn}$ and exists for frequencies higher than ω_{cn}. At the cut-off frequency, all the modes have a phase velocity of $c = \beta_2$. As $\omega \to \infty$, the phase velocity approaches β_1 for all modes. We can draw schematic phase-velocity curves as shown in Figure 7.3. It is now clear that for a given frequency ω, there are only a finite number of modes. The eigenfunction corresponding to each mode can be calculated by (7.7), once the phase velocity is determined.

The relative excitation of different modes depends on the depth and nature of the seismic source. For example, long-period waves from a shallow source are in general predominantly of the fundamental mode, which we have designated as $n = 0$. One way of separating different modes is to record them at a great distance, where they arrive at different times due to propagation with different group velocities. The group velocity for a given frequency ω_0 is the velocity of transport of a wave packet consisting of contributions from a band of frequencies around ω_0. The peaks, troughs, and zeros of the wave packet are propagated at the phase velocity, which is in general different from the group velocity.

Since the group velocity is a concept attached to a wave packet having a continuous spectrum instead of a discrete line spectrum, it is best explained by constructing a waveform in the time domain from integrating the single-mode solution (with unit amplitude and zero initial phase) over a finite frequency band around a given frequency ω_0. Using a cosine transform, this construction for the nth mode is

$$f_0(x,t) = \frac{1}{\pi} \int_{\omega_0 - 1/2\ \Delta\omega}^{\omega_0 + 1/2\ \Delta\omega} \cos[\omega t - k_n(\omega)x]\, d\omega. \tag{7.9}$$

For small $\Delta\omega$, we can expand $k_n(\omega)$ in a Taylor series,

$$k_n(\omega) = k_n(\omega_0) + \left(\frac{dk_n}{d\omega}\right)_0 (\omega - \omega_0) + \cdots. \tag{7.10}$$

Neglecting terms higher than $(\omega - \omega_0)$, we put (7.10) into (7.9) and integrate to obtain

$$f_0(x,t) \sim \frac{\Delta\omega}{\pi} \frac{\sin Y}{Y} \cos[\omega_0 t - k_n(\omega_0)x], \tag{7.11}$$

where

$$Y = \frac{\Delta\omega}{2}\left[t - \left(\frac{dk_n}{d\omega}\right)_0 x\right].$$

The waveform (7.11) is a sinusoidal oscillation of frequency ω_0 modulated by an envelope $\sin Y/Y$, which is peaked at $Y = 0$ or $x = (d\omega/dk_n)_0 t$. For fixed x, this peak arrives at a particular time. We therefore see that the envelope is transported with the group velocity $(d\omega/dk_n)_0$, and the phase (marked by a peak, trough, or zero of the cosine function) is moving with the phase velocity $\omega_0/k_n(\omega_0)$.

A wave packet with a given spectral density $|F(\omega)|$ and initial phase $\phi(\omega)$ composed of a single mode may be expressed as

$$f(x,t) = \frac{1}{2\pi} \int_{-\infty}^{\infty} |F(\omega)| \exp\left[-i\omega t + ik_n x + i\phi(\omega)\right]\, d\omega. \tag{7.12}$$

This integral may be evaluated by dividing the ω-axis into consecutive sections of width $\Delta\omega_i$ and summing up the approximate solutions, such as (7.11). See Problem 7.8 to find how the effect of $d|F(\omega)|/d\omega$ is included for all the sections.

When a surface wave is nondispersive, such as Rayleigh waves in a half-space, the waveform does not change with propagation, because c_n does not change with frequency and so

$$\begin{aligned} f(x,t) &= \frac{1}{2\pi} \int F(\omega) \exp\left[-i\omega(t - x/c_n)\right]\, d\omega \\ &= f(t - x/c_n). \end{aligned} \tag{7.13}$$

When a surface wave is strongly dispersive, we can use the stationary phase method to approximate the waveform. Similar to the steepest descents method, integration by the stationary phase method also exploits behavior of an integrand near its saddle point. In the steepest descent (see Box 6.3), integration is taken along a path for which the phase is constant and the amplitude has the most rapid change. In the stationary phase method applied to (7.12), the path is along the real axis of ω, along which the phase $(-\omega t + k_n x)$ varies most rapidly. Then for large x and/or t, the real and imaginary parts of the integrand in general are very rapidly oscillating functions of ω, with a self-canceling effect on the integral. Only at and near the saddle point, where the phase is stationary or varies slowly with ω, will there be an appreciable contribution to the integral. The saddle point, or the point of stationary phase, is given by the frequency value for which

$$\frac{d}{d\omega}(-\omega t + k_n x) = 0$$

or

$$\frac{x}{t} = \frac{d\omega}{dk_n}. \tag{7.14}$$

This equation determines the frequency $\omega_s = \omega_s(x, t)$ that can be expected to dominate at time t for a given distance x; and ω_s is the frequency for which the group velocity is equal to x/t. As discussed with a particular example in Box 7.2, there may be zero or 1 or 2 ω_s values that satisfy (7.14) for given values of x and t. The practical details of how many $\omega_s(x, t)$ values there are, as t varies for fixed x, determine the overall character of a surface-wave seismogram at position x.

Expanding the phase as a Taylor series in the vicinity of the point of stationary phase and neglecting terms of order higher than $(\omega - \omega_s)^2$, we have

$$-\omega t + k_n x \sim -\omega_s t + k_n(\omega_s)x + \frac{x}{2}\frac{d^2 k_n}{d\omega^2}(\omega - \omega_s)^2. \tag{7.15}$$

For large x, a small departure of ω from ω_s will generate a rapid oscillation of the integrand, leading to a self-canceling effect. Therefore, the integration limit can be extended beyond the limit for Taylor expansion. Taking twice the real contribution from positive frequencies only, to account for a contribution from negative frequencies, we then have

$$f(x,t) = \frac{1}{2\pi} 2\mathrm{Re}\left\{\exp[-i\omega_s t + ik_n(\omega_s)x]|F(\omega_s)|\int_{-\infty}^{\infty}\exp\left[\frac{x}{2}i\frac{d^2 k_n}{d\omega^2}(\omega - \omega_s)^2\right]d\omega\right\}. \tag{7.16}$$

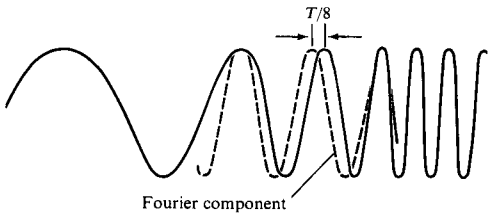

FIGURE **7.4**
The misalignment (by $T/8$) between a peak with period T in a dispersed wave train and the peak of the corresponding Fourier component. This example is for *normal* dispersion, in which the longer periods have greater velocity and hence arrive earlier. The opposite phenomenon, in which longer periods travel slower, is called *anomalous* dispersion.

Since integral tables give

$$\int_0^\infty \sin\left(\frac{1}{2}a\omega^2\right)\, d\omega = \int_0^\infty \cos\left(\frac{1}{2}a\omega^2\right)\, d\omega = \frac{1}{2}\sqrt{\frac{\pi}{a}}, \tag{7.17}$$

we have

$$f(x,t) \sim \frac{|F(\omega_s)|}{\pi}\sqrt{\frac{2\pi}{x\left|\dfrac{d^2k_n}{d\omega^2}\right|}}\cos\left[-\omega_s t + k_n(\omega_s)x \pm \frac{\pi}{4}\right], \tag{7.18}$$

in which $\pm$ corresponds to $d^2k_n/d\omega^2 \gtrless 0$, respectively. For a given x and t, ω_s is obtained by solving (7.14). The above formula gives the waveform of dispersive surface waves when the phase velocity $c_n = \omega/k_n$, group velocity $U_n = d\omega/dk_n$, and $dU_n^{-1}/d\omega$ are known. The sign of a phase shift by $\pi/4$ (a time shift by $\frac{1}{8}$ of a period) implies a *delay* when the group velocity increases with period. A visual Fourier analysis of waves with such a dispersive property, called normal dispersion and shown in Fig. 7.4, gives an intuitive explanation of the apparent phase delay for $f(x,t)$ relative to the Fourier component (Brune *et al.*, 1960). As shown in Box 7.2, there may be two different points of stationary phase for some values of x and t, in which case the seismogram is approximated by summing two applications of (7.18), one for each value of ω_s.

When the group velocity is stationary with respect to frequency, the denominator in (7.18) vanishes and this formula is no longer valid. Inclusion of higher-order terms in the Taylor expansion of phase gives a result in terms of the Airy function (see Savage, 1969b). For this reason, the arrivals associated with the group velocity maxima and minima are called Airy phases. The evaluation of an Airy phase is also easily done by a straightforward numerical integration of (7.12), because the group velocity is slowly varying and the total duration of the phase is short.

BOX 7.2

Analysis of a simple surface-wave seismogram

The best way to appreciate the concepts of dispersion relation, group velocity, and Airy phase—and to see how surface waves begin and end in a seismogram—is to work through the details of a particular example. Here, we examine the fundamental Love wave in the single layer over a half-space with parameters as given in Figure A.

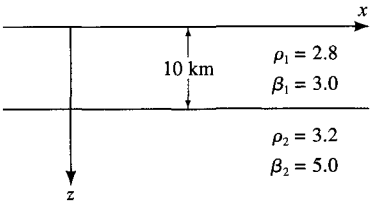

A

The structure used here to analyse fundamental Love waves.

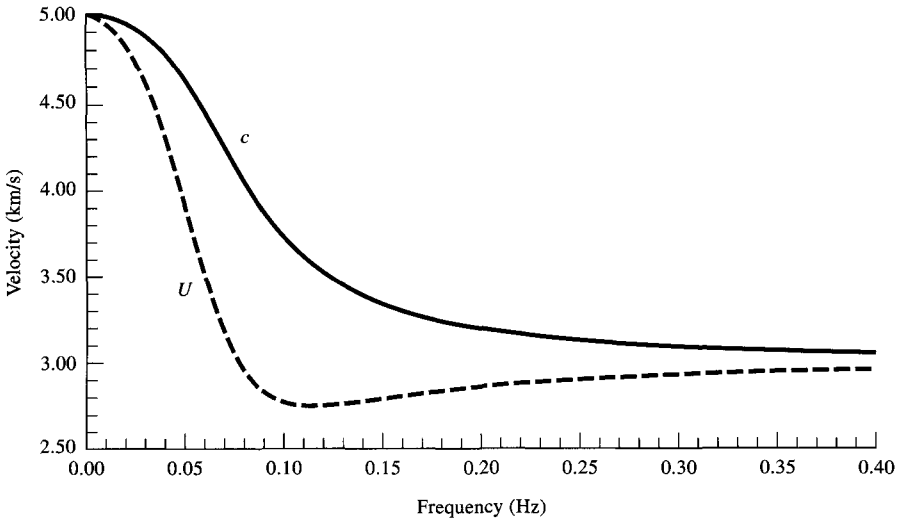

B

Phase velocity (c) and group velocity (U) as a function of frequency.

Figure B shows the phase velocity dispersion relation, $c = c(\omega)$, of the fundamental mode. It is obtained by finding the lowest value of c that solves (7.6), at 41 frequencies from 0 to 0.4 Hz. From $c = c(\omega) = \omega/k$ we can obtain the horizontal wavenumber k at different frequencies. Figure B also shows values of the group velocity U as a function of frequency, obtained from finite differences as the ratio $\Delta\omega/\Delta k$.

(continued)

BOX **7.2** *(continued)*

Let us now use these values of c and U to analyse the seismogram at a particular distance $x = 500$ km, assuming it is given by

$$f(500, t) = \frac{1}{2\pi} \int_{-\infty}^{\infty} \exp\left[i(500k - \omega t)\right] d\omega. \tag{1}$$

This assumes a unit amplitude spectrum, and all frequencies leave the source at $x = 0$ with the same zero initial phase.

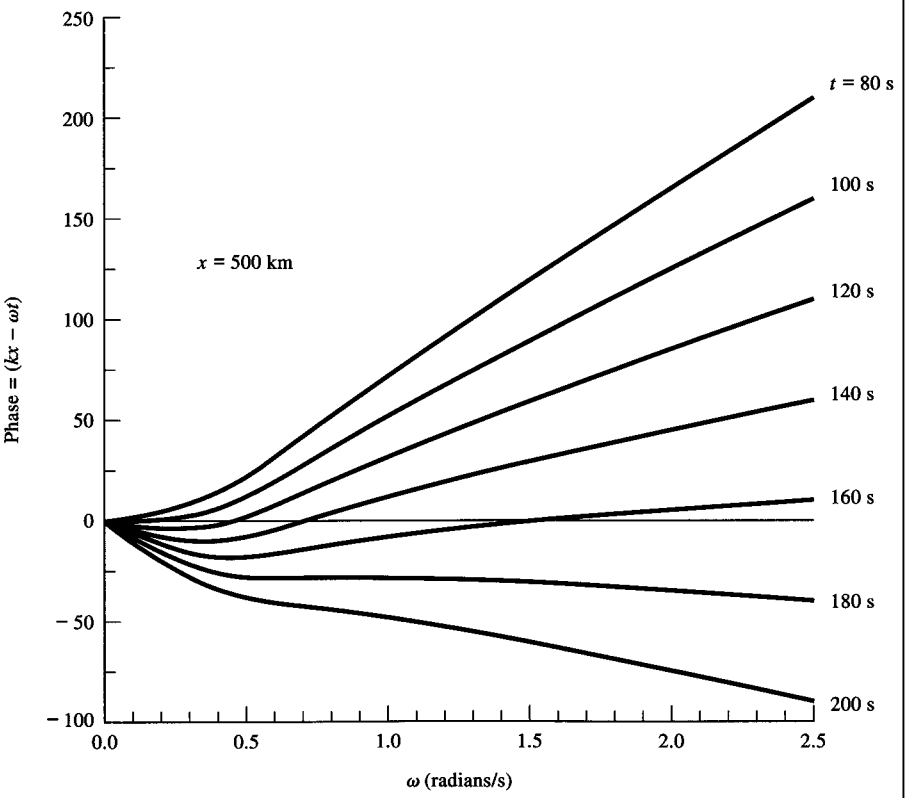

C

The phase of (1) at seven different times, giving examples where ω_s has 0, 1, or 2 values.

Figure C shows the phase of (1), plotted as a function of ω at 20 s increments from $t = 80$ to 200 s. It can be seen that the phase at times $t = 80$ and 200 s does not have stationary values—that is, there is no solution of $d(kx - \omega t)/d\omega = 0$ for $(x, t) = (500, 80)$ or $(500, 200)$. For $t = 100$, 120, and 160 s there is only one stationary value, a solution ω_s of equation (7.14). And for $t = 180$ s, there are two solutions ω_s.

BOX **7.2** *(continued)*

It is apparent from Figure B that double solutions occur at times just after $t = 500/3 = 166.67$ s, since this time corresponds to the arrival, at $x = 500$ km, of the signal with group velocity 3 km/s, appropriate for infinite frequency. For each group velocity in the range from about 2.748 to 3 km/s, i.e., for each time from about 166.67 to 182 s, there are two values ω_s at which the phase of (1) is stationary. Further detail is given in Figure D, showing the phase of (1) at 4 s increments from $t = 166$ to 190 s. At time $t = 166$ s there is one stationary value—i.e., one solution ω_s; at $t = 170$, 174, and 178 s there are two solutions ω_s; and at $t = 182$ s there is an inflection corresponding to the minimum in the group velocity curve at frequency about 0.11 Hz. At $t = 186$ and 190 s there are no stationary values.

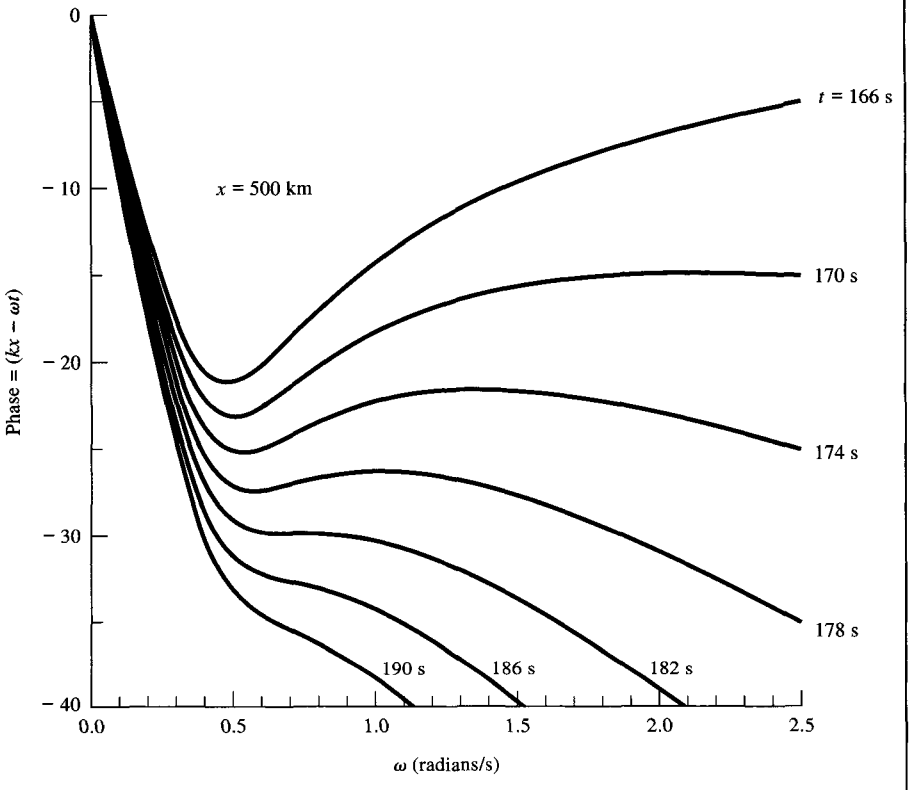

D

Further examples of the phase of (1) at different times, including the inflection at 0.11 Hz corresponding to the Airy phase.

(continued)

BOX **7.2** *(continued)*

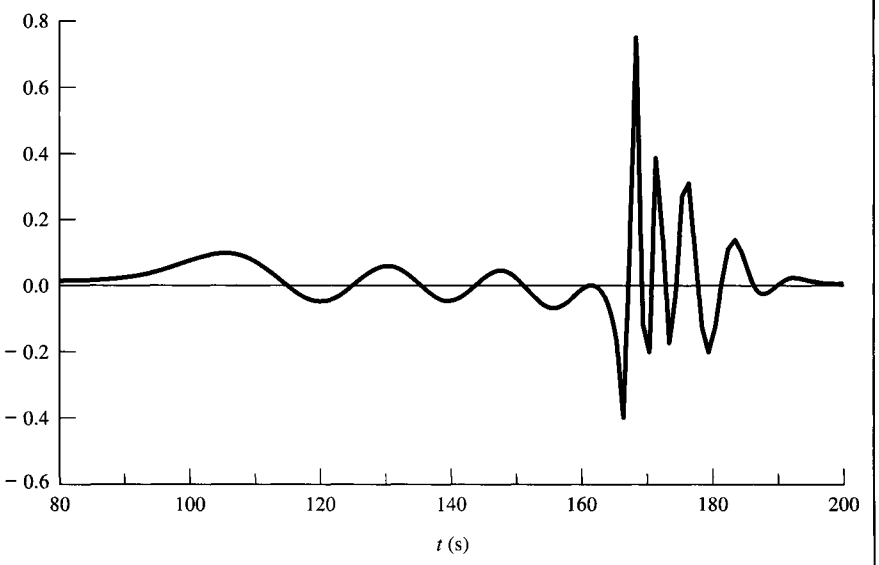

E

The seismogram obtained from (1) by summing contributions such as (7.11) from frequency intervals of width 0.01 Hz, from 0 to 1 Hz.

These results allow us to interpret in general terms the seismogram given in (1). It is shown in Figure E, obtained by the procedure described following (7.12). At times less than 100 s there is no stationary value of frequency and the seismogram begins gradually with a long period component (ω is near zero in Figure B for group velocity near 5 km/s, corresponding to $t = 100$ s at $x = 500$ km). As time in the seismogram increases from 100 s, the group velocity decreases from 5 km/s and there is just one frequency (ω_s) for which the phase is stationary. This frequency increases as time increases (normal dispersion), until time $t = 166.67$ s is reached. At this point, corresponding to $U = 3$ km/s, and shortly thereafter, a wide range of high frequencies arrive—leading to the appearance of a quite sharp pulse, followed by signal with anomalous dispersion superimposed upon the normally dispersed wavetrain. The normal and anomalous wavetrains, where they are superimposed, correspond to the two ω_s values. Where they merge, at around $t = 182$ s, there is an Airy phase. It corresponds to the minimum in the group velocity at about 0.11 Hz, and very shortly thereafter the surface wave seismogram ends (i.e., returns to negligible amplitude).

BOX **7.2** *(continued)*

In this analysis, the key step is being able to go backwards and forwards between time t in the seismogram, and the corresponding value or values of frequency

$$\omega_s = \omega_s(x, t)|_{x=500 \text{ km}}$$

which dominate the wavetrain by virtue of being stationary values of the phase of (1). We also make frequent use of the 1:1 relationship between time and group velocity (given here by $500/t$). Indeed, seismologists sometimes replace the time scale on seismograms by a scale based on group velocity, which systematically decreases from first to last arriving signal.

Finally, Figure F shows the approximation (7.18), applied to each of the two solutions $\omega_s = \omega_s(500, t)$ in the time range for which (7.18) has some validity. The approximations fail as the Airy phase is approached. Though (7.18) is helpful in showing the normal and anomalous contributions separately, in practice a direct evaluation of (1) by the method given in Problem 7.8 is reliable for all times in the seismogram.

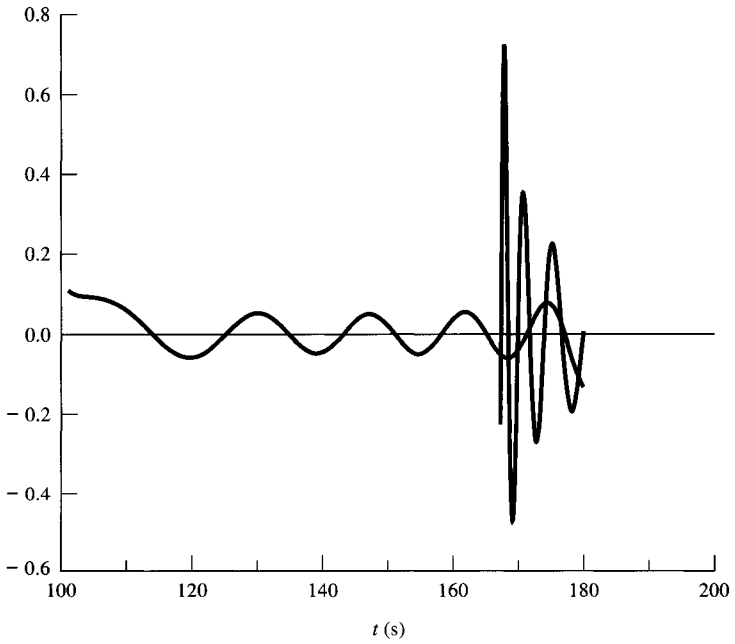

F

7.2 Eigenvalue Problem for the Displacement–Stress Vector

Let us now consider surface waves in a vertically heterogeneous, isotropic, elastic medium occupying a half-space $z > 0$ in which elastic moduli $\lambda(z)$, $\mu(z)$ and density $\rho(z)$ are arbitrary functions of z. In this section, we shall work on plane surface waves propagating

in the x-direction. It will be shown later that their z-dependence is the same as that of cylindrical surface waves spreading from a point.

In some aspects, this section duplicates parts of an earlier discussion of body waves, Section 5.4. However, our notation here is more suited to surface waves in that $\pi/2$ phase shifts between various displacement and stress components are recognized explicitly. Moreover, because of dispersion, the frequency dependence of horizontal wavenumber k is here more complicated, so that k is left as an explicit symbol and is not factored into $\omega \times$ horizontal slowness.

For Love waves, we shall seek a solution for the equation of motion (2.13) of the form

$$\begin{aligned} u &= 0 \\ v &= l_1(k, z, \omega) \exp\left[i(kx - \omega t)\right], \\ w &= 0. \end{aligned} \tag{7.19}$$

The stress components associated with the above displacement are

$$\begin{aligned} \tau_{xx} &= \tau_{yy} = \tau_{zz} = \tau_{zx} = 0, \\ \tau_{yz} &= \mu \frac{dl_1}{dz} \exp\left[i(kx - \omega t)\right], \\ \tau_{xy} &= ik\mu l_1 \exp\left[i(kx - \omega t)\right]. \end{aligned} \tag{7.20}$$

If we substitute (7.19) and (7.20) into (2.13), we obtain the equation of motion for $l_1(k, z, \omega)$:

$$-\omega^2 \rho(z) l_1 = \frac{d}{dz}\left[\mu(z)\frac{dl_1}{dz}\right] - k^2 \mu(z) l_1. \tag{7.21}$$

As described in the preceding section, such Love waves are a solution of the equation of motion that satisfies the source-free condition everywhere (no body force). The traction must vanish at the free surface $z = 0$, and no source exists at infinity. In addition to these conditions, the displacement and traction must be continuous at any interfaces where the elastic moduli have a discontinuity, because otherwise the discontinuities in displacement and traction would act as a seismic source (Section 3.1). Since in this chapter we are considering media for which discontinuities occur only across horizontal planes, the stress component τ_{yz} is required to be continuous for Love waves. Here we shall introduce a new function to describe the z-dependence of τ_{yz} by

$$\tau_{yz} = l_2(k, z, \omega) \exp\left[i(kx - \omega t)\right]. \tag{7.22}$$

Then (7.20) and (7.21) can be rewritten as a set of first-order ordinary differential equations,

$$\begin{aligned} \frac{dl_1}{dz} &= \frac{l_2}{\mu(z)}, \\ \frac{dl_2}{dz} &= \left(k^2\mu(z) - \omega^2\rho(z)\right) l_1, \end{aligned} \tag{7.23}$$

or in a matrix form,

$$\frac{d}{dz}\begin{pmatrix} l_1 \\ l_2 \end{pmatrix} = \begin{pmatrix} 0 & \mu(z)^{-1} \\ k^2\mu(z) - \omega^2\rho(z) & 0 \end{pmatrix}\begin{pmatrix} l_1 \\ l_2 \end{pmatrix}. \tag{7.24}$$

It is often a convenience to write the column vector in (7.24) as the transpose of a row vector, $(l_1, l_2)^T$, where $(\ldots)^T$ is used to denote a transpose. We shall refer to the vector in (7.24) as the *motion-stress vector for Love waves* and note (Box 7.1) that it is also the double transform of the (x, t) dependence of $(u_y, \tau_{yz})^T$ for general SH particle motion along the y-direction.

The *motion-stress vector for Rayleigh waves* can be obtained in a similar manner. We start with the following form for the displacements:

$$\begin{aligned} u &= r_1(k, z, \omega) \exp\left[i(kx - \omega t)\right], \\ v &= 0, \\ w &= ir_2(k, z, \omega) \exp\left[i(kx - \omega t)\right]. \end{aligned} \tag{7.25}$$

(For real positive r_1 and r_2, the above combination of u, w represents a prograde motion. In practice r_1 and r_2 may have different signs, giving a retrograde motion.) The stress components corresponding to (7.25) are given by

$$\begin{aligned} \tau_{yz} &= \tau_{xy} = 0, \\ \tau_{xx} &= i\left[\lambda\frac{dr_2}{dz} + k(\lambda + 2\mu)r_1\right] \exp\left[i(kx - \omega t)\right], \\ \tau_{yy} &= i\left(\lambda\frac{dr_2}{dz} + k\lambda r_1\right) \exp\left[i(kx - \omega t)\right], \\ \tau_{zz} &= i\left[(\lambda + 2\mu)\frac{dr_2}{dz} + k\lambda r_1\right] \exp\left[i(kx - \omega t)\right], \\ \tau_{zx} &= \mu\left(\frac{dr_1}{dz} - kr_2\right) \exp\left[i(kx - \omega t)\right]. \end{aligned} \tag{7.26}$$

The stress components τ_{zx} and τ_{zz} are continuous in z. We write them as

$$\begin{aligned} \tau_{zx} &= r_3(k, z, \omega) \exp\left[i(kx - \omega t)\right], \\ \tau_{zz} &= ir_4(k, z, \omega) \exp\left[i(kx - \omega t)\right]. \end{aligned} \tag{7.27}$$

BOX 7.3

Measurement of surface wave phase velocity

The measurement of phase velocity conventionally presupposes that the wave group under consideration consists purely of a single surface-wave mode, possessing a propagation velocity determined only by frequency. In other words, we assume that the wave group propagating along the x-axis can be expressed as

$$f(x,t) = \frac{1}{2\pi}\int_{-\infty}^{\infty} |f(x,\omega)| \exp\left[-i\omega\left(t - \frac{x}{c(\omega)}\right) + i\phi(\omega)\right] d\omega, \qquad (1)$$

where $|f(x,\omega)|$ is the amplitude spectral density, $\phi(\omega)$ is the phase term due to factors other than propagation, and $c(\omega)$ is the phase velocity. The phase delay $\omega x/c(\omega)$ due to propagation can be obtained by Fourier analysis of the seismogram. The Fourier transform of the above equation can be written as

$$\int_{-\infty}^{\infty} f(x,t)\exp(i\omega t)\,dt = |f(x,\omega)| \exp\left[i\phi(\omega) + i\frac{\omega x}{c(\omega)}\right].$$

By measuring the difference in phase spectra between two stations at distance x_1 and x_2, which is $[\omega/c(\omega)](x_1 - x_2) \pm 2n\pi$, we can obtain the phase velocity $c(\omega)$. The unknown integer n can be determined by an approximate *a priori* knowledge of $c(\omega)$, by measurement at more than two stations, or by evaluating c as a continuous function of frequency, beginning at low frequencies (for which n is usually unambiguous) and choosing n so that c is continuous as frequency increases.

To consider the effect of noise on the accuracy of phase-velocity measurement, suppose that the seismogram $d(t)$ consists of signal $s(t)$ and noise $n(t)$. Then

$$d(t) = s(t) + n(t).$$

Let us write the Fourier transform of $s(t)$ as $|s(\omega)| \exp[i\phi_s(\omega)]$ and that of $n(t)$ (for the duration $2T$ of signal) as $|n_T(\omega)| \exp[i\phi_n(\omega)]$. The Fourier transform $d(\omega)$ of the seismogram can be written as

$$|d(\omega)| \exp[i\phi_d(\omega)] = |s(\omega)| \exp[i\phi_s(\omega)] + |n_T(\omega)| \exp[i\phi_n(\omega)].$$

For small $|n_T(\omega)|/|s(\omega)|$, we can write

$$\phi_d(\omega) \sim \phi_s(\omega) + \frac{|n_T(\omega)|}{|s(\omega)|} \sin[\phi_n(\omega) - \phi_s(\omega)].$$

The second term is the fluctuation of phase due to the noise. If $n(t)$ is uncorrelated with $s(t)$, and $\phi_n - \phi_s$ is randomly and uniformly distributed from 0 to 2π, the RMS fluctuation of $\phi_d(\omega)$ will be equal to

$$\Delta\phi_{\text{RMS}} = \frac{1}{\sqrt{2}} \frac{|n_T(\omega)|}{|s(\omega)|}.$$

(continued)

BOX **7.3** *(continued)*

The RMS error of the phase difference between two stations that share the same signal and noise level will be $|n_T(\omega)|/|s(\omega)|$. Therefore, the RMS error of the phase-velocity measurement will be

$$\frac{\Delta c_{\text{RMS}}}{c} = \frac{1}{2\pi} \frac{|n_T(\omega)|}{|s(\omega)|} \frac{\lambda}{\Delta x}, \tag{2}$$

where λ is the wavelength and Δx is the distance over which the phase difference is measured. The error in measurement of the phase velocity decreases inversely in proportion to the signal-to-noise ratio.

Equation (2) indicates two ways to improve the measurement of surface-wave phase velocity: either the signal-to-noise ratio must be increased, or the wavelength relative to the distance between stations must be decreased.

The most straightforward way of improving the accuracy may seem to be to increase the signal amplitude by studying larger seismic sources. However, the noise may also increase with the strength of the source. [As mentioned above, we presume that the signal is a single surface-wave mode. Therefore, if other waves from the same source coexist in the data, they must be considered noise. If our signal is the fundamental mode of Rayleigh waves, then all the higher modes of Rayleigh waves, body waves, and even the fundamental-mode Rayleigh waves which approach from different propagation directions because of lateral heterogeneity must be considered as noise. Obviously such noise increases with the source strength. Therefore, if the main part of the noise consists of such signal-generated noise, no further improvement in accuracy in possible by studying larger sources.] Note also that larger sources tend to have a finite spatial extent rather than radiating in effect from a point, indicating that measurement of phase velocity may actually become more inaccurate as the size of the source increases.

Further improvement of the signal-to-noise ratio is possible by increasing the number of measurements for an appropriate arrangement of sources and receivers. If the signal-generated noise can be made uncorrelated among these measurements, the error of the velocity measurement will decrease inversely in proportion to the square root of the number of measurements.

The phase-velocity method was first applied to the California area by Press (1956), using a large earthquake in Samoa with the path to California lying entirely in the deep ocean and showing little evidence of multipath interference effects. He used a tripartite method, in which phase-delay times measured at three stations are combined to give the phase velocity and azimuth of wave approach. Although the ratio of wavelength to the distance between sensors was small, around 1, a good signal-to-noise ratio allowed an accuracy of about 1%.

Taking advantage of what, for its time, was a dense network of seismographic stations, operating in Japan, Aki (1961) found a significant variation of phase velocity within Japan. About 50 stations were divided into several geographic groups. A large number of stations made possible an accuracy of about 1.5% for each group, although the wavelength was comparable to or greater than the station distance.

The accuracy of velocity measurement may be improved by increasing the travel distance Δx at the expense of the spatial resolution. For a relatively uniform area, such as shield and deep ocean floor, a long travel distance has been effectively used to attain an accurate average phase-velocity measurement. For example, Brune and Dorman (1963) obtained

(continued)

BOX **7.3** *(continued)*

a good result for the Canadian shield using the two-station method, in which the phase velocity was obtained from the records of earthquakes whose epicenters lie within 4° of the great-circle path connecting two receivers. The wavelength λ ranged from 80 to 300 km, and the station distance, Δx, was about 3000 km. Thus the ratio $\lambda/\Delta x$ ranged from 1/40 to 1/10. Equation (2) gives the corresponding range of velocity error:

$$\frac{\Delta c}{c} = \frac{|n_T(\omega)|}{|s(\omega)|}(0.004 - 0.015). \tag{3}$$

From the scatter of measured phase velocities about a mean smooth curve, Brune and Dorman estimated an RMS error of about 0.5%, roughly independent of wavelength. From (3), we find for this phase-velocity error that the signal-to-noise ratio must have been about 1 for the shortest waves and about 3 for the longest waves.

In a tripartite measurement of the phase velocity, if the propagation direction is parallel to one leg of the tripartite net, the magnitude of phase velocity is determined by the time difference between the two stations of the leg, and is unaffected by a small fluctuation in the measured time at the third station. Recognizing this fact, Knopoff *et al.* (1967) showed experimentally that the two-station method does a better job of minimizing errors in phase shifts in the presence of lateral inhomogeneity than does the tripartite method. Theoretical support for this result comes from Chernov (1960), who showed that the phase fluctuation of waves propagating in a random medium has much greater correlation distance (smoother variation) in the direction parallel to the propagation path, than perpendicular to it.

In some cases, the single-station method gives even better results than the two-station method. The single-station method is applicable to earthquakes with known source parameters needed for calculating the term $\phi(\omega)$ in equation (1). This term essentially is governed by the phase of the surface wave as it leaves the source, and it can be obtained from formulas we derive in Section 7.4. The single-station method has been successfully applied to many earthquakes in numerous regions. For example, Weidner (1974) showed that the phase velocities across the Atlantic Ocean determined by the two-station method using a Greek earthquake and a Nicaraguan earthquake agree well with those by the single-station method using a mid-Atlantic ridge earthquake recorded at both sides of the ocean, but the former showed a somewhat greater interference effect than the latter.

The differential equations for the motion-stress vector $(r_1, r_2, r_3, r_4)^T$ are then obtained from (7.26) and (2.13) as

$$\frac{d}{dz}\begin{pmatrix} r_1 \\ r_2 \\ r_3 \\ r_4 \end{pmatrix} = \begin{pmatrix} 0 & k & \mu^{-1}(z) & 0 \\ -k\lambda(z)\,[\lambda(z)+2\mu(z)]^{-1} & 0 & 0 & [\lambda(z)+2\mu(z)]^{-1} \\ k^2\zeta(z) - \omega^2\rho(z) & 0 & 0 & k\lambda(z)\,[\lambda(z)+2\mu(z)]^{-1} \\ 0 & -\omega^2\rho(z) & -k & 0 \end{pmatrix}\begin{pmatrix} r_1 \\ r_2 \\ r_3 \\ r_4 \end{pmatrix} \tag{7.28}$$

where $\zeta(z) = 4\mu(z)\,[\lambda(z)+\mu(z)]\,/\,[\lambda(z)+2\mu(z)]$. The matrices in (7.24) and (7.28) look very simple, and in essence are the same as those obtained in Section 5.4 for a homogeneous

medium. They do not contain spatial gradients of medium parameters explicitly, although $\lambda(z)$, $\mu(z)$, and $\rho(z)$ are functions of z.

The boundary conditions for surface waves—i.e., vanishing traction at the free surface $z = 0$ and no motion at infinity—require that

$$\begin{aligned} &r_1 \to 0,\ r_2 \to 0, \qquad \text{and} \qquad l_1 \to 0 \qquad \text{as } z \to \infty; \\ &r_3 = r_4 = l_2 = 0 \qquad \text{at the free surface } (z = z_0). \end{aligned} \tag{7.29}$$

For a given ω, nonvanishing solutions of (7.24) or (7.28) under the condition (7.29) exist only for certain $k = k_n(\omega)$. In exactly the same manner as for Love waves in a single-layered half-space studied in Section 7.1, $\omega/k_n(\omega)$ gives the phase velocity, and the corresponding solution of (7.24) or (7.28) gives the z-dependence of the mode.

There are many ways to solve this eigenvalue-eigenvector problem. We shall start with the numerical integration method and the propagator matrix method. Explicit results are obtained by the Thomson–Haskell method (which is a special case of what we shall later be calling the propagator matrix method), applicable to a stack of homogeneous layers overlying a half-space.

7.2.1 NUMERICAL INTEGRATION

The eigenvalue problem for the motion-stress vector may be solved by a direct integration of (7.24) and (7.28) using numerical methods such as that of Runge–Kutta. Takeuchi and Saito (1972) advocate this approach because it models the Earth more smoothly than does the typical matrix method in which the Earth is approximated by a stack of homogeneous layers.

To illustrate how to solve the eigenvalue problem by a numerical integration, let us first suppose that the displacement is forced to be zero at a great depth z_n (i.e., a rigid boundary).

In the case of Love waves, we can start by integrating the equation system (7.24) upward from $z = z_n$, with the initial value for $l_1(z_n)$ chosen as zero. Since our equations are homogeneous in the sense of Box 2.4, any nonzero starting value of $l_2(z_n)$ can be chosen, so we may as well choose $l_2(z_n) = 1$. The resulting solution, once obtained for other depths, can later be scaled by an overall multiplicative constant. A trial value of k has to be chosen for a given ω, and the process of numerical integration gives us a vector (l_1, l_2) that is a function of (k, z, ω). [Note that the numerical solution will in practice be valid for the upper regions of an infinite half-space, provided we use it only at frequencies high enough that the actual amplitudes of $l_2(k, z_n, \omega)$ are negligible compared to typical values in the shallower depth range where the solution is needed. If we started with both l_1 and l_2 equal to zero at $z = z_n$ then (7.24) implies the solution is zero throughout $0 \le z \le z_n$.]

The result of integration should give $l_2 = 0$ at $z = z_0$ if k is the eigenvalue, but in general one finds $l_2(z_0) \neq 0$ for the trial value. But the whole process of numerical integration can be iterated, correcting k until $l_2(z_0)$ vanishes, and then an eigenvalue $k = k(\omega)$ has been found, and the corresponding eigenfunction (l_1, l_2) for this combination of (k, ω).

In the case of Rayleigh waves with a rigid boundary at great depth, we integrate equation (7.28) upwards for two different sets of initial values at $z = z_n$; $r_1 = r_2 = 0$ in both sets, but $r_3 = 1$ and $r_4 = 0$ in set 1, and $r_3 = 0$ and $r_4 = 1$ in set 2. Writing the solutions for set 1 and

set 2 as $\mathbf{r}^{(1)}$ and $\mathbf{r}^{(2)}$, respectively, a general solution of (7.28) can be expressed as

$$\mathbf{r} = A\mathbf{r}^{(1)} + B\mathbf{r}^{(2)}. \tag{7.30}$$

If $\mathbf{r}$ is an eigenvector, its stress components $r_3(z_0)$ and $r_4(z_0)$ must vanish, i.e.,

$$\begin{aligned} Ar_3^{(1)}(z_0) + Br_3^{(2)}(z_0) &= 0, \\ Ar_4^{(1)}(z_0) + Br_4^{(2)}(z_0) &= 0. \end{aligned} \tag{7.31}$$

Thus a nontrivial solution of (7.30) is possible only when

$$\begin{vmatrix} r_3^{(1)}(z_0) & r_3^{(2)}(z_0) \\ r_4^{(1)}(z_0) & r_4^{(2)}(z_0) \end{vmatrix} = 0. \tag{7.32}$$

The eigenvalue is searched for by trial and correction until (7.32) is met. Once the eigenvalue is found, A/B can be determined from (7.31), and then the eigenvector from (7.30).

A better approximation of the lower boundary condition than infinite rigidity is to replace the Earth below z_n by a homogeneous half-space. The solutions in the homogeneous half-space that involve exponential decay with depth are well known. For Love waves, we use the following initial values:

$$\begin{aligned} l_1(z_n) &= \exp(-\nu_{n+1}z_n), \\ l_2(z_n) &= \mu_{n+1}\frac{dl_1}{dz} = -\nu_{n+1}\mu_{n+1}\exp(-\nu_{n+1}z_n), \end{aligned} \tag{7.33}$$

where $\nu_{n+1} = \sqrt{k^2 - \omega^2/\beta_{n+1}^2}$, chosen so that Re $\nu_{n+1} \geq 0$ (and hence Im $\nu_{n+1} \leq 0$). The subscript $n+1$ applies to the properties of the lower half-space. For Rayleigh waves, the required two sets of initial values may be calculated using potentials given by

$$\phi = \exp(-\gamma_{n+1}z), \qquad \psi = 0 \tag{7.34}$$

for the first set and

$$\phi = 0, \qquad \psi = \exp(-\nu_{n+1}z) \tag{7.35}$$

for the second set, where $\gamma_{n+1} = \sqrt{k^2 - \omega/\alpha_{n+1}^2}$ and $\nu_{n+1} = \sqrt{k^2 - \omega^2/\beta_{n+1}^2}$. The corresponding motion-stress vectors $\mathbf{r}^{(1)}(z)$ and $\mathbf{r}^{(2)}(z)$ throughout $z_0 \leq z \leq z_n$ can be calculated by putting (7.34) and (7.35) into (6.60) to get starting values at $z = z_n$, then using (7.25) and (7.28). The upward numerical integration is carried out for each of the two sets of initial values $\mathbf{r}^{(1)}(z_n)$ and $\mathbf{r}^{(2)}(z_n)$, and the result is iterated over k-values until (7.32) is satisfied to find the eigenvalue. For small ω/k, the two sets of initial values become numerically indistinguishable. In such cases, the sum and difference of the two solutions may be used as the initial values.

BOX **7.4**
Runge–Kutta methods

There are many numerical methods for solving the first-order differential equation

$$\frac{dy}{dx} = f(x, y). \tag{1}$$

To give a simple example: if we approximate dy/dx at x_i by the so-called forward difference formula $(y_{i+1} - y_i)/(x_{i+1} - x_i)$, the finite difference equation corresponding to (1) is written as

$$\begin{aligned} y_{i+1} &= y_i + (x_{i+1} - x_i) f_i, \\ f_i &= f(x_i, y_i). \end{aligned} \tag{2}$$

Repeated application of (2) gives y at discrete points if the initial value y_0 is known. This is Euler's method, but it uses only the first two terms in the Taylor series for y_{i+1}, so (2) has a truncation error of order h^2, where $h = x_{i+1} - x_i$. The Runge–Kutta method of nth order is usually an improvement, in that it is designed to give a truncation error of order h^{n+1}. This method starts with defining a location $(\bar{x}, \bar{y})$ in the xy-plane by

$$\begin{aligned} \bar{x} &= x_i + \alpha h \\ \bar{y} &= y_i + \beta h. \end{aligned} \tag{3}$$

We wish to determine α and β such that

$$\overline{\Delta y_i} \equiv h f(\bar{x}, \bar{y}) \tag{4}$$

is identical with the increment

$$\Delta y_i = h y_i' + \frac{h^2}{2} y_i'' + \cdots + \frac{h^n}{n!} \frac{d^n y_i}{dx^n},$$

where primes denote derivatives with respect to x, and such derivatives are evaluated at x_i.

If α and β can be found with this property, then the solution can be carried forward one step, by (4), with the same accuracy as if derivatives of y up to nth order were available at the start of the step, i.e. the same accuracy as if the nth-order Taylor series were available.

For example, if $n = 2$, α and β are determined such that

$$\Delta y_i = h y_i' + \tfrac{1}{2} h^2 y_i'' = \overline{\Delta y_i}. \tag{5}$$

(continued)

7.2.2 PROPAGATOR MATRIX METHOD

The matrix method due to Thomson (1950) and corrected by Haskell (1953) has been extensively used in surface-wave analysis since the advent of large-scale computers. In their method, the vertically heterogeneous medium is replaced by a stack of homogeneous layers overlying a homogeneous half-space, as shown in Figure 7.5. The Thomson–Haskell method is a special case of the propagator matrix method introduced to seismology by Gilbert and Backus (1966).

BOX **7.4** *(continued)*

Expanding (4) around (x_i, y_i), we have

$$\overline{\Delta y_i} = f(x_i + \alpha h, y_i + \beta h) \cdot h \sim \left[f_i + \alpha h \left(\frac{\partial f}{\partial x} \right)_i + \beta h \left(\frac{\partial f}{\partial y} \right)_i \right] h. \tag{6}$$

On the other hand, since

$$y'' = \frac{df}{dx} = \frac{\partial f}{\partial x} + \frac{\partial f}{\partial y} \frac{dy}{dx}$$

we obtain

$$hy_i' + \tfrac{1}{2}h^2 y_i'' = hf_i + \tfrac{1}{2}h^2 \left[\left(\frac{\partial f}{\partial x} \right)_i + \left(\frac{\partial f}{\partial y} \right)_i f_i \right]. \tag{7}$$

Putting (6) and (7) into (5), we find (5) is satisfied if we choose $\alpha = \frac{1}{2}$ and $\beta = \frac{1}{2} f_i$, or

$$\bar{x} = x_i + \tfrac{1}{2}h, \quad \bar{y} = y_i + \tfrac{1}{2}hf_i. \tag{8}$$

Thus, in the second-order Runge–Kutta method, the solution is given by

$$\begin{aligned} y_{i+1} &= y_i + \overline{\Delta y_i}, \\ \overline{\Delta y_i} &= hf(\bar{x}, \bar{y}) = hf(x_i + \tfrac{1}{2}h, y_i + \tfrac{1}{2}hf_i). \end{aligned} \tag{9}$$

In the case of simultaneous equations

$$\frac{dy}{dx} = f(x, y, z), \quad \frac{dz}{dx} = g(x, y, z), \tag{10}$$

the solution by the second-order Runge–Kutta method is given by

$$\begin{aligned} y_{i+1} &= y_i + \overline{\Delta y_i}, \\ z_{i+1} &= z_i + \overline{\Delta z_i}, \\ \overline{\Delta y_i} &= hf(x_i + \tfrac{1}{2}h, y_i + \tfrac{1}{2}hf_i, z_i + \tfrac{1}{2}hg_i), \\ \overline{\Delta z_i} &= hg(x_i + \tfrac{1}{2}h, y_i + \tfrac{1}{2}hf_i, z_i + \tfrac{1}{2}hg_i). \end{aligned} \tag{11}$$

We first generalize the differential equations (7.24) and (7.28) for the motion-stress vector to a matrix form,

$$\frac{d\mathbf{f}(z)}{dz} = \mathbf{A}(z)\mathbf{f}(z), \tag{7.36}$$

where $\mathbf{f}(z)$ is an $n \times 1$ column vector and $\mathbf{A}(z)$ is an $n \times n$ matrix; $n = 2$ for Love waves, and $n = 4$ for Rayleigh waves.

The *propagator matrix* (sometimes called the *matrizant*) is defined as

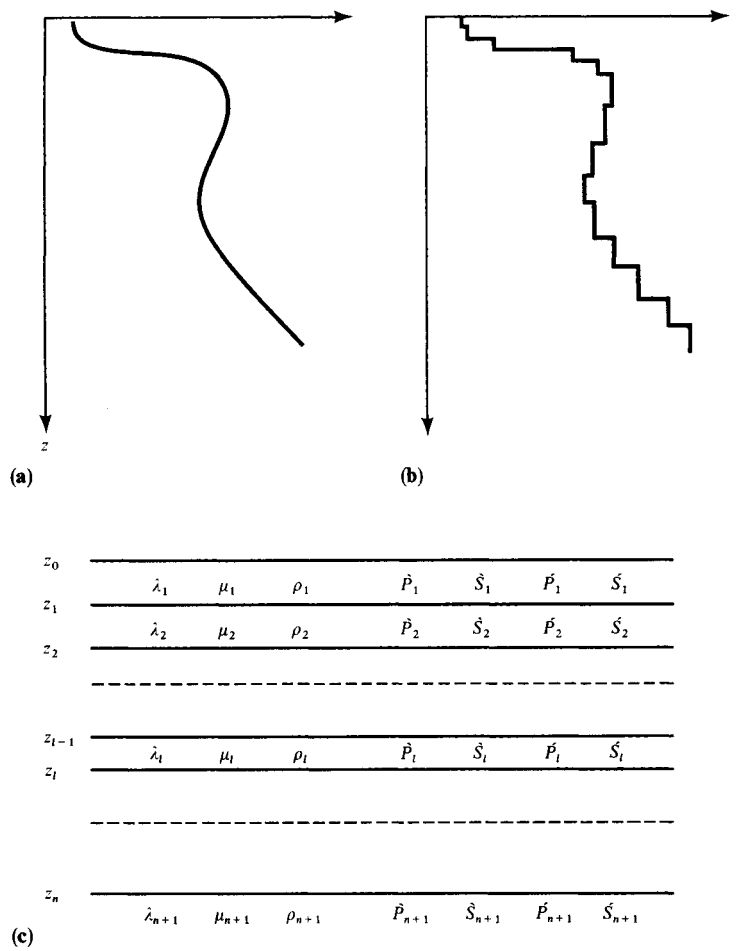

FIGURE **7.5**
(**a**) A continuous variation of properties (one of $\rho, \lambda, \mu, \alpha$, or β) with depth. (**b**) A piecewise constant approximation to (a). This may be regarded as a stack of homogeneous welded plates. (**c**) Numbering system for elastic moduli, layers, and upgoing and downgoing waves.

$$\mathbf{P}(z, z_0) = \mathbf{I} + \int_{z_0}^{z} \mathbf{A}(\zeta_1)\, d\zeta_1 + \int_{z_0}^{z} \mathbf{A}(\zeta_1) \int_{z_0}^{\zeta_1} \mathbf{A}(\zeta_2)\, d\zeta_2\, d\zeta_1 + \cdots, \tag{7.37}$$

where $\mathbf{I}$ is the identity matrix of order n. Obviously, $\mathbf{P}(z, z_0)$ satisfies the differential equation (7.36):

$$\frac{d}{dz}\mathbf{P}(z, z_0) = \mathbf{A}(z)\mathbf{P}(z, z_0). \tag{7.38}$$

Further, from (7.37), $\mathbf{P}(z_0, z_0) = \mathbf{I}$. Hence we obtain the most important property of the propagator matrix, namely

$$\mathbf{f}(z) = \mathbf{P}(z, z_0)\mathbf{f}(z_0), \tag{7.39}$$

since the right-hand side here satisfies the differential equation (7.36) and does give $\mathbf{f}(z_0)$ at $z = z_0$. Thus $\mathbf{P}(z, z_0)$ generates the motion-stress vector at z by operating on the vector at z_0.

An interesting property of $\mathbf{P}(z, z_0)$ can be found by observing that

$$\begin{aligned}\mathbf{f}(z_2) &= \mathbf{P}(z_2, z_1)\mathbf{f}(z_1) \\ &= \mathbf{P}(z_2, z_1)\mathbf{P}(z_1, z_0)\mathbf{f}(z_0).\end{aligned}$$

Choosing $z_2 = z_0$ and applying the above chain rule for any $\mathbf{f}(z_0)$, it follows that

$$\mathbf{I} = \mathbf{P}(z_0, z_1)\mathbf{P}(z_1, z_0), \tag{7.40}$$

so that the inverse of $\mathbf{P}(z_1, z_0)$ is $\mathbf{P}(z_0, z_1)$.

When $\mathbf{A}(z)$ is constant (i.e., is independent of z), as assumed within a given layer by Thomson and Haskell, the propagator matrix takes a simple form. From (7.37)

$$\begin{aligned}\mathbf{P}(z, z_0) &= \mathbf{I} + (z - z_0)\mathbf{A} + \tfrac{1}{2}(z - z_0)^2\mathbf{A}\mathbf{A} + \cdots \\ &= \exp\left[(z - z_0)\mathbf{A}\right].\end{aligned} \tag{7.41}$$

For a square matrix $\mathbf{A}$ with distinct eigenvalues λ_k ($k = 1, 2, \ldots n$), a function of the matrix $\mathbf{A}$ can be expanded by Sylvester's formula (e.g., Hildebrand, 1952):

$$F(\mathbf{A}) = \sum_{k=1}^{n} F(\lambda_k) \frac{\prod_{r \neq k} (\mathbf{A} - \lambda_r \mathbf{I})}{\prod_{r \neq k} (\lambda_k - \lambda_r)}. \tag{7.42}$$

It is this relation that assigns meaning to the last part of (7.41). For Love waves, $\mathbf{A}$ is given in (7.24). To find eigenvalues, we set

$$|\mathbf{A} - \lambda\mathbf{I}| = \begin{vmatrix} -\lambda & \mu^{-1} \\ k^2\mu - \omega^2\rho & -\lambda \end{vmatrix} = 0$$

and obtain $\lambda = \pm\sqrt{k^2 - \omega^2/\beta^2} = \pm\nu$. Putting these results into (7.42), we find

$$\mathbf{P}(z, z_0) = \exp\left[(z - z_0)\mathbf{A}\right] = \begin{pmatrix} \cosh \nu(z - z_0) & (\nu\mu)^{-1} \sinh \nu(z - z_0) \\ \nu\mu \sinh \nu(z - z_0) & \cosh \nu(z - z_0) \end{pmatrix}. \tag{7.43}$$

This matrix generates the motion-stress vector $\mathbf{l}(z)$ by operating on $\mathbf{l}(z_0)$ when both z and z_0 are in the same layer. For a layered medium as shown in Figure 7.5, the propagator matrix $\mathbf{P}(z, z_0)$ for $z_{k-1} < z < z_k$ is found from

$$\mathbf{f}(z) = \mathbf{P}(z, z_{k-1})\mathbf{P}(z_{k-1}, z_{k-2}) \cdots \mathbf{P}(z_1, z_0)\mathbf{f}(z_0) = \mathbf{P}(z, z_0)\mathbf{f}(z_0),$$

and hence

$$\mathbf{P}(z, z_0) = \exp\left[(z - z_{k-1})\mathbf{A}_k\right] \prod_{l=1}^{k-1} \exp\left[(z_l - z_{l-1})\mathbf{A}_l\right]. \tag{7.44}$$

Similarly, the layer matrix for Rayleigh waves can be obtained by putting $\mathbf{A}$ given in (7.28) into (7.41). In this case, the eigenvalues of $\mathbf{A}$ are $\pm\gamma = \pm\sqrt{k^2 - \omega^2/\alpha^2}$ and $\pm\nu = \pm\sqrt{k^2 - \omega^2/\beta^2}$. The resulting elements of $\mathbf{P}(z, z_0)$ are given below (with z and z_0 in the same layer):

$$\begin{aligned}
P_{11} &= P_{33} = 1 + \frac{2\mu}{\omega^2\rho}\left[2k^2 \sinh^2\frac{\gamma(z - z_0)}{2} - (k^2 + \nu^2)\sinh^2\frac{\nu(z - z_0)}{2}\right],\\
P_{12} &= -P_{43} = \frac{k\mu}{\omega^2\rho}\left[(k^2 + \nu^2)\frac{\sinh\gamma(z - z_0)}{\gamma} - 2\nu\sinh\nu(z - z_0)\right],\\
P_{13} &= \frac{1}{\omega^2\rho}\left[k^2\frac{\sinh\gamma(z - z_0)}{\gamma} - \nu\sinh\nu(z - z_0)\right],\\
P_{14} &= -P_{23} = \frac{2k}{\omega^2\rho}\left[\sinh^2\frac{\gamma(z - z_0)}{2} - \sinh^2\frac{\nu(z - z_0)}{2}\right],\\
P_{21} &= -P_{34} = \frac{k\mu}{\omega^2\rho}\left[(k^2 + \nu^2)\frac{\sinh\nu(z - z_0)}{\nu} - 2\gamma\sinh\gamma(z - z_0)\right],\\
P_{22} &= P_{44} = 1 + \frac{2\mu}{\omega^2\rho}\left[2k^2\sinh^2\frac{\nu(z - z_0)}{2} - (k^2 + \nu^2)\sinh^2\frac{\gamma(z - z_0)}{2}\right],\\
P_{24} &= \frac{1}{\omega^2\rho}\left[k^2\frac{\sinh\nu(z - z_0)}{\nu} - \gamma\sinh\gamma(z - z_0)\right],\\
P_{31} &= \frac{\mu^2}{\omega^2\rho}\left[4k^2\gamma\sinh\gamma(z - z_0) - (k^2 + \nu^2)^2\frac{\sinh\nu(z - z_0)}{\nu}\right],\\
P_{32} &= -P_{41} = 2\mu^2(k^2 + \nu^2)P_{14},\\
P_{42} &= \frac{\mu^2}{\omega^2\rho}\left[4k^2\nu\sinh\nu(z - z_0) - (k^2 + \nu^2)^2\frac{\sinh\gamma(z - z_0)}{\gamma}\right].
\end{aligned} \tag{7.45}$$

Equations (7.43), (7.44), and (7.45) give the propagator matrix in the Thomson–Haskell method.

The propagator matrix can also be used to solve the system with a source term,

$$\frac{d\mathbf{f}(z)}{dz} = \mathbf{A}(z)\mathbf{f}(z) + \mathbf{g}(z), \tag{7.46}$$

where $\mathbf{g}(z)$ is a known $n \times 1$ matrix function of z. The solution is

$$\mathbf{f}(z) = \mathbf{P}(z, z_0)\left[\int_{z_0}^{z} \mathbf{P}^{-1}(\zeta, z_0)\,\mathbf{g}(\zeta)\,d\zeta + \mathbf{f}(z_0)\right]. \tag{7.47}$$

To verify this result, we use (7.38) to get

$$\frac{d\mathbf{f}}{dz} = \frac{d\mathbf{P}}{dz}\left[\int_{z_0}^{z} \mathbf{P}^{-1}(\zeta, z_0)\,\mathbf{g}(\zeta)\,d\zeta + \mathbf{f}(z_0)\right] + \mathbf{P}(z, z_0)\mathbf{P}^{-1}(z, z_0)\,\mathbf{g}(z)$$
$$= \mathbf{A}(z)\mathbf{P}(z, z_0)\mathbf{P}^{-1}(z, z_0)\mathbf{f}(z) + \mathbf{g}(z)$$
$$= \mathbf{A}(z)\mathbf{f}(z) + \mathbf{g}(z).$$

Thus (7.47) satisfies (7.46). From (7.40), $\mathbf{P}(z, z_0)\mathbf{P}^{-1}(\zeta, z_0) = \mathbf{P}(z, z_0)\mathbf{P}(z_0, \zeta) = \mathbf{P}(z, \zeta)$, so the solution (7.47) simplifies to

$$\mathbf{f}(z) = \int_{z_0}^{z} \mathbf{P}(z, \zeta)\,\mathbf{g}(\zeta)\,d\zeta + \mathbf{P}(z, z_0)\mathbf{f}(z_0). \tag{7.48}$$

Let us now discuss some of the practical problems encountered in the application of Thomson–Haskell methods. One problem is that the radiation condition is imposed by suppressing certain waves at infinity, rather than by a constraint on the motion-stress vector directly, so we need to relate the motion-stress vector to the presence (or absence) of upgoing and downgoing wave types in the bottom half-space. Of course, for large enough k, these wave types become respectively growing or decaying exponentially with depth. From (5.64) and (5.66), with vertical wavenumber $i\nu$ replacing $\omega\eta$, the relation for SH-waves in a homogeneous body is

$$\begin{pmatrix} l_1 \\ l_2 \end{pmatrix} = \begin{pmatrix} e^{-\nu z} & e^{\nu z} \\ -\nu\mu e^{-\nu z} & \nu\mu e^{\nu z} \end{pmatrix} \begin{pmatrix} \grave{S} \\ \acute{S} \end{pmatrix} \tag{7.49}$$

or $\mathbf{l} = \mathbf{F}\mathbf{w}$, where $\nu = \sqrt{k^2 - \omega^2/\beta^2}$ and $\beta = \sqrt{\mu/\rho}$. $\grave{S}$ and $\acute{S}$ are constants giving the displacement amplitudes of downgoing and upgoing waves, respectively. The inverse of the relationship in (7.49) is

$$\mathbf{w} = \begin{pmatrix} \grave{S} \\ \acute{S} \end{pmatrix} = \frac{1}{2\nu\mu} \begin{pmatrix} \nu\mu e^{\nu z} & -e^{\nu z} \\ \nu\mu e^{-\nu z} & e^{-\nu z} \end{pmatrix} \begin{pmatrix} l_1 \\ l_2 \end{pmatrix} \tag{7.50}$$

or $\mathbf{w} = \mathbf{F}^{-1}\mathbf{l}$.

Applying this latter relation to the motion-stress vector at $z = z_n$, the amplitudes of upgoing and downgoing waves in the lower half-space are expressed in terms of the motion-stress vector at the free surface $z = z_0$:

$$\mathbf{w}_{n+1} = \mathbf{F}_{n+1}^{-1}\mathbf{P}(z_n, z_0)\mathbf{l}(z_0) = \mathbf{B}\mathbf{l}(z_0). \tag{7.51}$$

BOX **7.5**
On avoiding potentials

In contrast to the methods of Haskell (1953, 1960, 1962) for wave propagation in layered media, we have minimized the use of potentials for P, SV, and SH-waves in this chapter. Although it is true that potentials can clarify certain steps in the theory of elastic waves in homogeneous isotropic media, matrix methods for discussing solutions to $d\mathbf{f}/dz = \mathbf{A}(z)\mathbf{f}$ are usually far more powerful. Potentials are of no direct interest, and are awkward to use in imposing boundary conditions, whereas $\mathbf{f}$ is made up from the components of particle motion and stress, which are the physical quantities for which we wish to solve.

The reader may note that the first reflection coefficient discussed in Chapter 5 was derived by using potentials, but that we quickly turned to work with displacements directly. Potentials recur in Chapter 6, because their scalar wave equations appear simpler than vector equations containing P- and S-motions, since we had not then put wave equations into the form $d\mathbf{f}/dz = \mathbf{A}\mathbf{f}$. However, in Box 6.9 we did discuss the first two entries of the motion-stress vector $\mathbf{f}$ for P-SV waves, and did develop a result that equates $\mathbf{f}$ to a sum of the basic waves possible, i.e., $\mathbf{f} = \mathbf{F}\mathbf{w}$ (in the notation of this chapter).

Radiation conditions are easy to impose by setting appropriate components of $\mathbf{w}$ equal to zero.

To summarize: understanding elastic wave potentials, and solving for them, is an important learning process. But it is better to move on to the use of matrix methods for solving the relevant wave equations. We shall occasionally use potentials in the pages that follow, but for the most part we shall emphasize an understanding of $\mathbf{f}(z) = \mathbf{P}(z, z_0)\mathbf{f}(z_0)$ and $\mathbf{f}(z) = \mathbf{F}(z)\mathbf{w}$. A connection between potentials and the layer matrix $\mathbf{F}$ is developed in Problem 5.11.

Since $\acute{S}_{n+1} = 0$ and $l_2(z_0) = 0$ from the radiation/boundary conditions, we have

$$\begin{pmatrix} \grave{S}_{n+1} \\ 0 \end{pmatrix} = \begin{pmatrix} B_{11} & B_{12} \\ B_{21} & B_{22} \end{pmatrix} \begin{pmatrix} l_1(z_0) \\ 0 \end{pmatrix}. \tag{7.52}$$

For a nontrivial solution $\mathbf{l}$, we see from the above equation that B_{21} must vanish. Thus the eigenvalue is determined by

$$B_{21} = 0. \tag{7.53}$$

To find the root of this equation for a given ω, we start with a trial value of k. For known ω and k, one can calculate the value of B_{21} by the matrix multiplication (7.51), using the layer parameters of the medium. Then k is changed slightly, and the resulting change in B_{21} is monitored. Once the eigenvalue is found, the eigenfunction can be calculated via (7.44).

The above method is easily extended to Rayleigh waves by finding a relation between the motion-stress vector (r_1, r_2, r_3, r_4) and the numbers $(\grave{P}, \grave{S}, \acute{P}, \acute{S})$ describing how much of each of the four possible wave types is present in each layer. Just as we developed $\mathbf{f} = \mathbf{F}\mathbf{w}$ to solve $d\mathbf{f}/dz = \mathbf{A}\mathbf{f}$ in Section 5.4, with $\mathbf{F}$ factored into a matrix made up from eigenvectors

of **A** times a diagonal matrix containing the vertical phase factors (see (5.69)), so here we have

$$\begin{pmatrix} r_1 \\ r_2 \\ r_3 \\ r_4 \end{pmatrix} = \mathbf{Fw} = \mathbf{F} \begin{pmatrix} \grave{P} \\ \grave{S} \\ \acute{P} \\ \acute{S} \end{pmatrix}. \tag{7.54}$$

The matrix **F** is factored as

$$\begin{aligned} \mathbf{F} = \omega^{-1} &\begin{pmatrix} \alpha k & \beta\nu & \alpha k & \beta\nu \\ \alpha\gamma & \beta k & -\alpha\gamma & -\beta k \\ -2\alpha\mu k\gamma & -\beta\mu(k^2+\nu^2) & 2\alpha\mu k\gamma & \beta\mu(k^2+\nu^2) \\ -\alpha\mu(k^2+\nu^2) & -2\beta\mu k\nu & -\alpha\mu(k^2+\nu^2) & -2\beta\mu k\nu \end{pmatrix} \\ &\times \begin{pmatrix} e^{-\gamma z} & 0 & 0 & 0 \\ 0 & e^{-\nu z} & 0 & 0 \\ 0 & 0 & e^{\gamma z} & 0 \\ 0 & 0 & 0 & e^{\nu z} \end{pmatrix}. \end{aligned} \tag{7.55}$$

We are free to choose any suitable normalization for the eigenvectors of the coefficient matrix appearing in (7.28), and for the specific forms of (7.54) and (7.55) we have been guided by two requirements. The first is that the four component waves contained in **Fw** do have displacement amplitudes given by $(\grave{P}, \grave{S}, \acute{P}, \acute{S})$ for homogeneous waves (i.e., when γ and ν are negative imaginary). The second is that for surface waves (when γ and ν are positive real), the entries in **F** are all real numbers.

A specific inverse can be written down for each of the matrix factors of **F** in (7.55), and

$$\begin{aligned} \mathbf{F}^{-1} = &\begin{pmatrix} e^{\gamma z} & 0 & 0 & 0 \\ 0 & e^{\nu z} & 0 & 0 \\ 0 & 0 & e^{-\gamma z} & 0 \\ 0 & 0 & 0 & e^{-\nu z} \end{pmatrix} \times \frac{\beta}{2\alpha\mu\gamma\nu\omega} \\ &\times \begin{pmatrix} 2\beta\mu k\gamma\nu & -\beta\mu\nu(k^2+\nu^2) & -\beta k\nu & \beta\gamma\nu \\ -\alpha\mu\gamma(k^2+\nu^2) & 2\alpha\mu k\gamma\nu & \alpha\gamma\nu & -\alpha k\gamma \\ 2\beta\mu k\gamma\nu & \beta\mu\nu(k^2+\nu^2) & \beta k\nu & \beta\gamma\nu \\ -\alpha\mu\gamma(k^2+\nu^2) & -2\alpha\mu k\gamma\nu & -\alpha\gamma\nu & -\alpha k\gamma \end{pmatrix}. \end{aligned} \tag{7.56}$$

Each of $\mathbf{w}, \mathbf{F}, \mathbf{F}^{-1}$ is layer dependent, and we can relate the amplitude of different wave-types in the lowermost half-space to the motion-stress vector at the free surface:

$$\mathbf{w}_{n+1} = \mathbf{F}_{n+1}^{-1}\mathbf{P}(z_n, z_0)\mathbf{r}(z_0) = \mathbf{Br}(z_0). \tag{7.57}$$

Corresponding to our treatment of Love waves, (7.51)–(7.52), we find here that

$$\begin{pmatrix} \grave{P}_{n+1} \\ \grave{S}_{n+1} \\ 0 \\ 0 \end{pmatrix} = \begin{pmatrix} B_{11} & B_{12} & B_{13} & B_{14} \\ B_{21} & B_{22} & B_{23} & B_{24} \\ B_{31} & B_{32} & B_{33} & B_{34} \\ B_{41} & B_{42} & B_{43} & B_{44} \end{pmatrix} \begin{pmatrix} r_1(z_0) \\ r_2(z_0) \\ 0 \\ 0 \end{pmatrix}. \tag{7.58}$$

BOX 7.6
Mixture of solid and liquid layers

A liquid layer in seismology may be (i) at the top, as in an oceanic structure; (ii) sandwiched between solid layers, as in an ice-covered ocean or a volcanic area with a magma lens; or (iii) at the bottom, as in a mantle underlain by a liquid core. We shall consider here an ideal liquid with zero viscosity, for which the shear stress must vanish at the liquid–solid interface, but a discontinuity in horizontal displacements is allowed (see Section 5.2).

In the case of Love waves, a liquid–solid interface becomes a free surface, and the liquid layers behave like a vacuum.

In the case of Rayleigh waves, the shear stress vanishes, but the normal stress and normal displacement do not vanish, and must be continuous across the liquid–solid interface. Thus the layer matrix $\mathbf{F}$ for a liquid layer becomes singular, and its inverse does not exist. We need to find a method that works as if the inverse *did* exist.

Consider the case of a liquid layer lying between the depths $z_{f-1} < z < z_f$ in a solid layered half-space, as shown in the figure. Within the layer, only compressional waves exist. To determine the motion-stress vector through this mixed-layered medium, we shall start from the free surface $z = z_0$. The motion-stress vector $\mathbf{r}(z)$ at $z = z_{f-1}$ can be expressed in terms of $\mathbf{r}(z_0)$ using the layers matrices $\mathbf{F}$ given in the text (see Problem 7.3). Since the traction vanishes, $r_3 = r_4 = 0$ at z_0, and $\mathbf{r}(z_{f-1})$ is determined completely as a linear combination of two unknowns $r_1(z_0)$ and $r_2(z_0)$. On the other hand, $z = z_{f-1}$ is a liquid–solid interface, and the shear traction $r_3(z_{f-1})$ vanishes. This imposes a linear relation between $r_1(z_0)$ and $r_2(z_0)$. Using this relation, one can eliminate $r_1(z_0)$ from the expression for $\mathbf{r}(z_{f-1})$, which is now completely determined by one unknown, $r_2(z_0)$ alone. Then $r_2(z_f)$ and $r_4(z_f)$ can be determined from $r_2(z_{f-1})$ and $r_4(z_{f-1})$ through the upgoing and downgoing compressional waves $\acute{P}_f$ and $\grave{P}_f$. At $z = z_f$, $r_3(z_f)$ is known to be zero, so that the only unknown component of $\mathbf{r}(z_f)$ is $r_1(z_f)$. The motion-stress vector below z_f can therefore be expressed as a linear combination of two unknowns $r_1(z_f)$ and $r_2(z_0)$.

(continued)

Thus the eigenvalue is determined by

$$\begin{vmatrix} B_{31} & B_{32} \\ B_{41} & B_{42} \end{vmatrix} = 0. \tag{7.59}$$

To find the root of this determinant for a given ω, we start again with a trial value of k and iterate on values of k until (7.59) is met. In calculating the subdeterminant on the left side of (7.59) for a trial value of k, a numerical problem arises if the wavelength λ of surface waves becomes shorter than a certain limit. According to Schwab and Knopoff (1970), when using 16 decimal digits in the computations, this limit is approximated by

$$H/\lambda = 3 \times 10^{(14.3-\sigma)/12.4}, \tag{7.60}$$

where H is the depth to the homogeneous half-space and σ is the required accuracy in phase velocity given in significant figures. This limit does not exist for Love waves. The reason

BOX **7.6** *(continued)*

It follows that the radiation condition on waves in the half-space leads to an equation similar to (7.58), where $r_1(z_0)$ is replaced by $r_1(z_f)$, and $r_2(z_0)$ by $r_2(z_f)$.

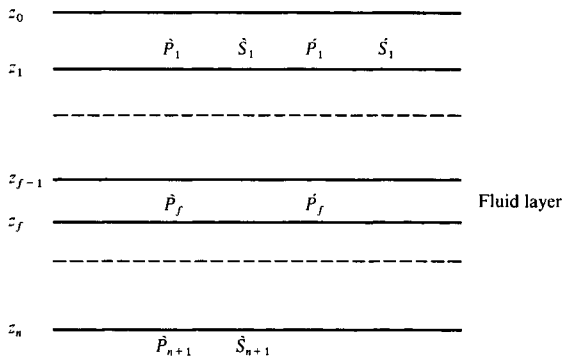

In the case of a liquid layer overlying a solid medium, the unknown component of $\mathbf{r}(z_0)$ will be only $r_1(z_0)$ to start with, and therefore the steps to be taken are identical to the preceding case in which overlying solid layers are eliminated. In the case of a liquid half-space, the condition of vanishing $r_3(z_n)$ will replace that of vanishing $\acute{S}_{n+1}$.

Although, as we have shown above, a mix of solid and fluid layers can still be handled by matrix methods, the necessary matrices are not easily obtained simply by taking the limit for solid/solid layers as the rigidity for one layer tends to zero, because the underlying 4×4 system becomes singular. Gilbert (1998) has given two approximate methods that remove the singularity.

why it exists for Rayleigh waves is due to the following matrix $\Lambda_l(z)$, present in the layer matrix (7.55):

$$\Lambda_l(z) = \begin{pmatrix} \exp(-\gamma_l z) & 0 & 0 & 0 \\ 0 & \exp(-\nu_l z) & 0 & 0 \\ 0 & 0 & \exp(\gamma_l z) & 0 \\ 0 & 0 & 0 & \exp(\nu_l z) \end{pmatrix}. \tag{7.61}$$

When H/λ is large, some of the diagonal elements of Λ_l will be very large. Lumping the matrix products in $\mathbf{B}$ before and after Λ_l as $\mathbf{L}$ and $\mathbf{R}$, we write

$$\mathbf{B} = \mathbf{L}\Lambda_l\mathbf{R}. \tag{7.62}$$

The subdeterminant of $\mathbf{B}$ corresponding to (7.59) will contain terms like

$$\exp(2\gamma_l z)(l_{33}r_{31}l_{43}r_{32} - l_{43}r_{31}l_{33}r_{32}),$$

BOX **7.7**

Surface waves in the Gutenberg Earth model

As an example of surface waves evaluated by the methods of Section 7.2, we show in Figures A to E the phase velocity c, group velocity U, and eigenfunctions for Love and Rayleigh waves in Gutenberg's classic Earth model for a continent. The model consists of a stack of 24 homogeneous layers, for each of which the depth to bottom, density, and compressional and shear wave velocities are listed in the table below.

Gutenberg's layered model of continental structure.

Layer number	Depth to bottom (km)	density(g/cm^3)	v_p (km/s)	v_s (km/s)
1	19	2.74	6.14	3.55
2	38	3.00	6.58	3.80
3	50	3.32	8.20	4.65
4	60	3.34	8.17	4.62
5	70	3.35	8.14	4.57
6	80	3.36	8.10	4.51
7	90	3.37	8.07	4.46
8	100	3.38	8.02	4.41
9	125	3.39	7.93	4.37
10	150	3.41	7.85	4.35
11	175	3.43	7.89	4.36
12	200	3.46	7.98	4.38
13	225	3.48	8.10	4.42
14	250	3.50	8.21	4.46
15	300	3.53	8.38	4.54
16	350	3.58	8.62	4.68
17	400	3.62	8.87	4.85
18	450	3.69	9.15	5.04
19	500	3.82	9.45	5.21
20	600	4.01	9.88	5.45
21	700	4.21	10.30	5.76
22	800	4.40	10.71	6.03
23	900	4.56	11.10	6.23
24	1000	4.63	11.35	6.32

(continued)

BOX **7.7** *(continued)*

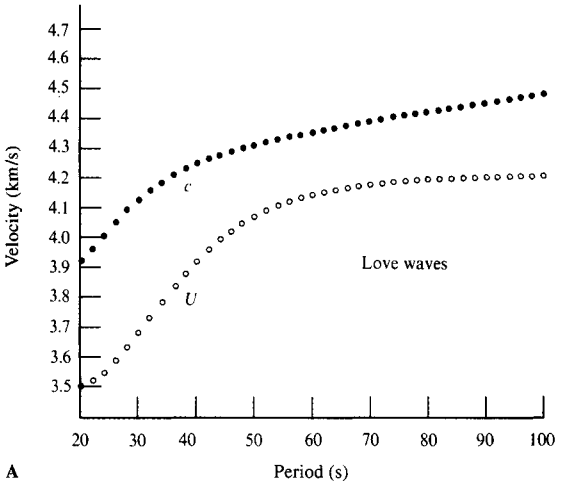

A

Phase and group velocity of the fundamental-mode Love waves for the Gutenberg Earth model.

(continued)

which is identically zero, but which will be obtained as a difference of two large numbers in the process of computation if $\exp(\gamma_l z)$ is large, causing a loss of significant figures. This problem was pointed out by Dunkin (1965) and remedied by him and Knopoff (1964b) by the use of Laplace's development by minors. It can be remedied also by the layer-reduction method (Schwab and Knopoff, 1970), in which the lower part of the medium is replaced by a homogeneous half-space at increasingly shallower depths for waves of shorter period. The layer-reduction method, however, should be avoided for cases with deep wave guides and be used only at depths for which all the layers below contain only inhomogeneous P- and SV-waves. Another approach is to use propagator-matrix methods for the second-order minors from solutions $\mathbf{r}^{(1)}$ and $\mathbf{r}^{(2)}$ (see (7.30)). These six minors are:

$$R_1 = r_1^{(1)} r_2^{(2)} - r_2^{(1)} r_1^{(2)}, \qquad R_2 = r_1^{(1)} r_3^{(2)} - r_3^{(1)} r_1^{(2)},$$

$$R_3 = r_1^{(1)} r_4^{(2)} - r_4^{(1)} r_1^{(2)}, \qquad R_4 = r_2^{(1)} r_3^{(2)} - r_3^{(1)} r_2^{(2)},$$

$$R_5 = r_2^{(1)} r_4^{(2)} - r_4^{(1)} r_2^{(2)}, \qquad R_6 = r_3^{(1)} r_4^{(2)} - r_4^{(1)} r_3^{(2)}.$$

Takeuchi and Saito (1972) showed that $\mathbf{f} = (R_1, R_2, R_3, R_4, R_5, R_6)^T$ satisfies an equation of type $d\mathbf{f}/dz = \mathbf{C}\mathbf{f}$, which we have already shown how to solve. This time, however, the dispersion relation (7.32) reduces to requiring one scalar component of $\mathbf{f}$ (namely, R_6) to vanish at the free surface $z = z_0$.

BOX **7.7** *(continued)*

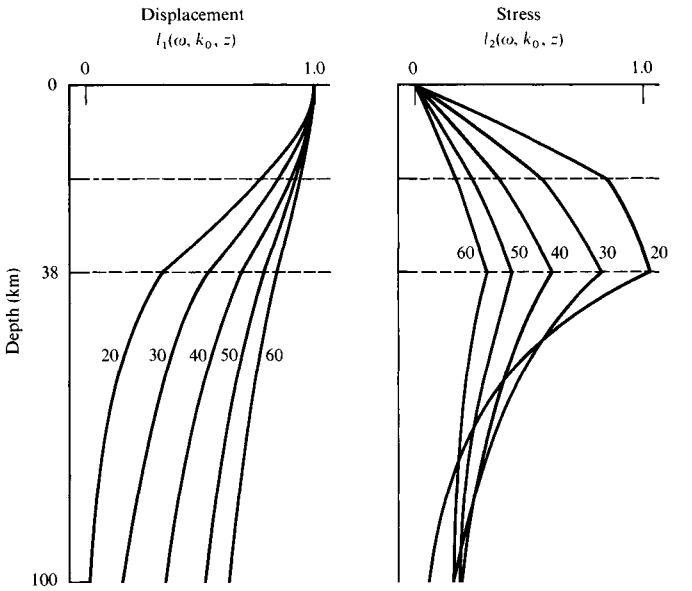

B

The eigenfunctions for the fundamental-mode Love waves for various periods. The amplitude is normalized to the displacement at $z = 0$.

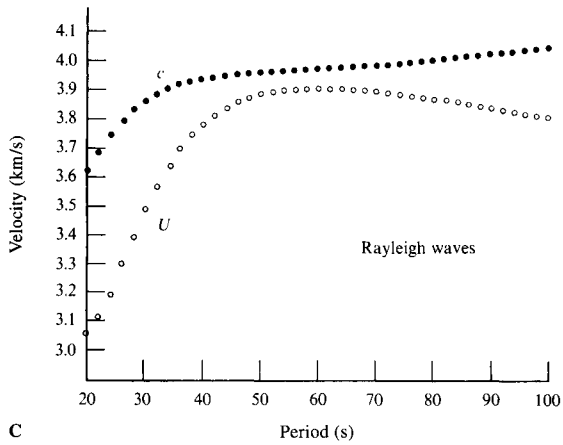

C

Phase and group velocity of the fundamental-mode Rayleigh waves for the Gutenberg Earth model.

(continued)

BOX **7.7** *(continued)*

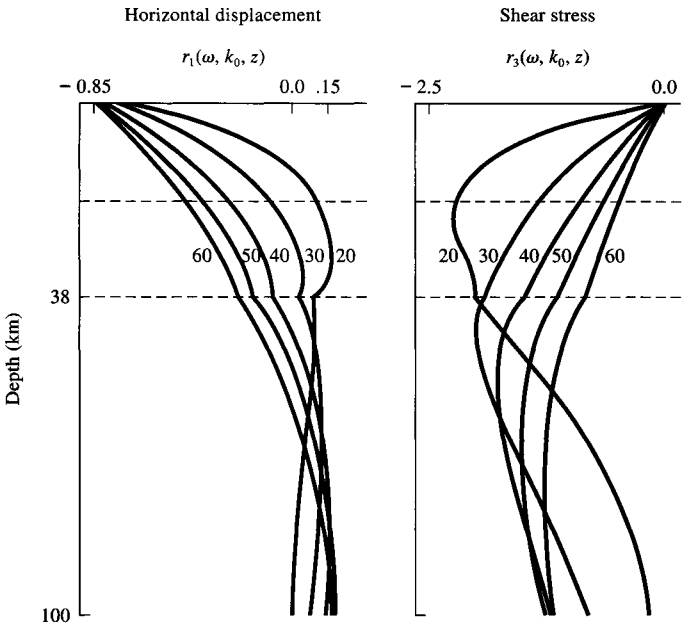

The horizontal eigenfunctions for the fundamental-mode Rayleigh waves for various periods. The amplitude is normalized to the vertical displacement r_2 at $z = 0$.

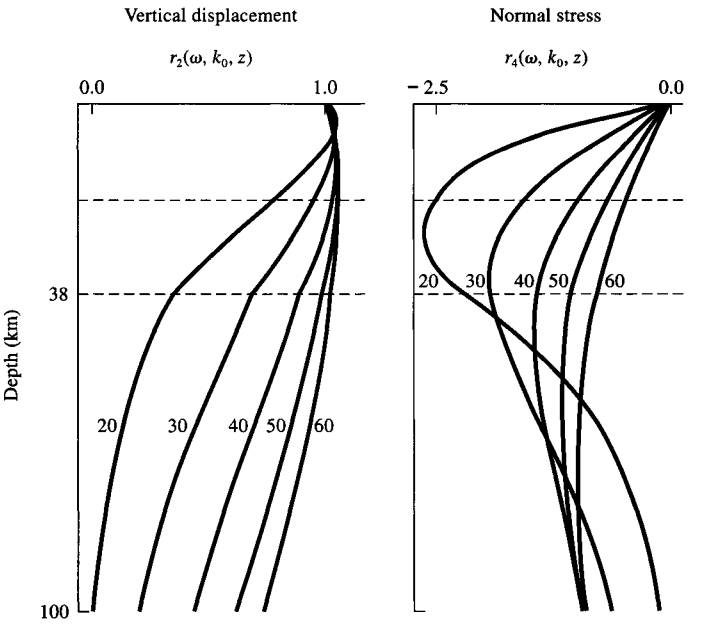

The vertical eigenfunctions for the fundamental-mode Rayleigh waves for various periods. Again, the amplitude is normalized to the vertical displacement r_2 at $z = 0$.

7.3 Variational Principle for Love and Rayleigh Waves

We show here that the eigenvalue–eigenfunction problem discussed above can be solved by the Rayleigh–Ritz method. We shall also use variational techniques for finding several important formulas to calculate group velocity, attenuation, and partial derivatives of phase velocity with respect to medium parameters.

Let us find expressions for the Lagrangian densities L for Love and Rayleigh waves in isotropic vertically inhomogeneous media. For a linear elastic body, the Lagrangian density is the kinetic energy minus the elastic strain energy (2.32). For an isotropic body,

$$L = \tfrac{1}{2}\rho \dot{u}_i \dot{u}_i - \left[\tfrac{1}{2}\lambda (e_{kk})^2 + \mu e_{ij} e_{ij}\right]. \tag{7.63}$$

In the case of plane Love waves given by (7.19), since $e_{ij} = \frac{1}{2}(u_{i,j} + u_{j,i})$, we have

$$\langle L \rangle = \tfrac{1}{4}\rho\omega^2 l_1^2 - \tfrac{1}{4}\mu \left[k^2 l_1^2 + \left(\frac{dl_1}{dz}\right)^2\right]. \tag{7.64}$$

The brackets $\langle\ \rangle$ here denote an averaging process, so that terms like $\cos^2(kx - \omega t)$ and $\sin^2(kx - \omega t)$, present in (7.63), have been replaced by $\frac{1}{2}$ in the derivation of (7.64).

In the case of plane Rayleigh waves given by (7.25),

$$\begin{aligned}\langle L \rangle = \tfrac{1}{4}\rho\omega^2 (r_1^2 + r_2^2) - \tfrac{1}{4}\Bigg[&\lambda \left(k r_1 + \frac{dr_2}{dz}\right)^2 + \mu \left(\frac{dr_1}{dz} - k r_2\right)^2 \\ &+ 2\mu k^2 r_1^2 + 2\mu \left(\frac{dr_2}{dz}\right)^2\Bigg].\end{aligned} \tag{7.65}$$

7.3.1 LOVE WAVES

For these surface waves we define the energy integrals

$$I_1 = \tfrac{1}{2}\int_0^\infty \rho l_1^2\, dz, \qquad I_2 = \tfrac{1}{2}\int_0^\infty \mu l_1^2\, dz, \qquad I_3 = \tfrac{1}{2}\int_0^\infty \mu \left(\frac{dl_1}{dz}\right)^2 dz. \tag{7.66}$$

When there are no body forces and no surface tractions, Hamilton's principle tells us that the integral of $\langle L \rangle$ must be stationary for any first-order perturbation of l_1 about the actual motion. To verify this, we examine the perturbation in the integral of $\langle L \rangle$, which is just one-half of

$$\begin{aligned}&\omega^2\, \delta I_1 - k^2\, \delta I_2 - \delta I_3 \\ &\quad = \omega^2 \int_0^\infty \rho l_1\, \delta l_1\, dz - k^2 \int_0^\infty \mu l_1\, \delta l_1\, dz - \int_0^\infty \mu \frac{dl_1}{dz}\frac{d\,\delta l_1}{dz}\, dz \\ &\quad = \int_0^\infty \left\{\omega^2 \rho l_1 - k^2 \mu l_1 + \frac{d}{dz}\left(\mu \frac{dl_1}{dz}\right)\right\} \delta l_1\, dz - \mu \frac{dl_1}{dz}\delta l_1 \Big|_0^\infty.\end{aligned}$$

If (i) the equation of motion (7.21), (ii) the free surface condition $dl_1/dz = 0$ at $z = 0$, (iii) vanishing δl_1 at $z = \infty$ and (iv) continuity of l_1 and $\mu\, dl_1/dz$ (which was used above, in the integration by parts) are all satisfied, we do indeed find that

$$\omega^2\, \delta I_1 - k^2\, \delta I_2 - \delta I_3 = 0. \tag{7.67}$$

The l_1 that satisfies these four conditions is nothing but an eigenfunction. Thus we have verified that $\omega^2 I_1 - k^2 I_2 - I_3$ is stationary for perturbation of l_1 around an eigenfunction. Furthermore, we can show that the Lagrangian integral $\omega^2 I_1 - k^2 I_2 - I_3$ vanishes at its stationary point by multiplying the equation of motion (7.21) by l_1 and integrating it with respect to z from 0 to ∞:

$$\begin{aligned} 0 &= \int_0^\infty \left\{ \omega^2 \rho l_1^2 - k^2 \mu l_1^2 + l_1 \frac{d}{dz}\left(\mu \frac{dl_1}{dz}\right) \right\} dz \\ &= 2\omega^2 I_1 - 2k^2 I_2 - 2I_3 + l_1 \mu \frac{dl_1}{dz}\bigg|_0^\infty, \end{aligned} \tag{7.68}$$

and when l_1 is an eigenfunction, $l_1 = 0$ at $z = \infty$ and $\mu dl_1/dz = 0$ at $z = 0$, so that the last term in (7.68) vanishes. Thus, for an eigenfunction,

$$\omega^2 I_1 = k^2 I_2 + I_3. \tag{7.69}$$

In other words, averaged over a cycle, the total elastic energy contained in a normal mode is equal to the total kinetic energy.

There are three particularly important applications of the two relations $\omega^2\, \delta I_1 = k^2\, \delta I_2 + \delta I_3$ and $\omega^2 I_1 = k^2 I_2 + I_3$ for us to examine. Different quantities are perturbed in each application, and the subtlety and power of variational methods are well illustrated by the fact that three such different results all stem from the same root.

First, we shall suppose that in a numerical attempt to evaluate a true eigenfunction $l_1(z)$, we have made errors and have in fact obtained $l_1 + \delta l_1$. From this, we would numerically obtain $I_1 + \delta I_1$, $I_2 + \delta I_2$, and $I_3 + \delta I_3$ by using $l_1 + \delta l_1$ in (7.66). However, addition of the two relations (7.67) and (7.69) tells us that ω^2 is related to k^2 via

$$k^2 = \frac{\omega^2(I_1 + \delta I_1) - (I_3 + \delta I_3)}{I_2 + \delta I_2}.$$

It follows that k can be determined accurately as a function of ω if the l_1 are approximately known, since first-order errors in l_1 do not lead to first-order errors in the eigenvalue.

Second, we shall obtain a useful formula for group velocity U without having to perform a numerical derivative. We suppose that $l_1(k, \omega)$ and $l_1 + \delta l_1 = l_1(k + \delta k, \omega + \delta\omega)$ are both eigenfunctions. Using this $l_1 + \delta l_1$ to evaluate energy integrals, it follows from (7.69) that

$$(\omega + \delta\omega)^2 (I_1 + \delta I_1) = (k + \delta k)^2 (I_2 + \delta I_2) + (I_3 + \delta I_3).$$

Subtracting (7.69), we find, to first order, that

$$\omega^2\, \delta I_1 + 2\omega\, \delta\omega I_1 = k^2\, \delta I_2 + 2k\, \delta k I_2 + \delta I_3.$$

However, using this $l_1 + \delta l_1$ does constitute a perturbation to l_1 for which (7.67) applies. Therefore $2\omega\,\delta\omega I_1 = 2k\,\delta k I_2$, and

$$U = \frac{\delta\omega}{\delta k} = \frac{k}{\omega}\frac{I_2}{I_1} = \frac{I_2}{cI_1}. \tag{7.70}$$

This exact formula gives the group velocity in terms of integrals, and the result is numerically more stable than differentiation.

Third, we shall evaluate the changes in phase velocity and group velocity that arise (at fixed frequency) when small perturbations in rigidity μ and density ρ are made in the structure. Suppose that $l_1(k, \omega)$ is the eigenfunction in structure $(\rho(z), \mu(z))$. We write this as $l_1 = l_1(\rho, \mu, k, \omega)$ and consider a perturbation $l_1 + \delta l_1 = l_1(\rho + \delta\rho, \mu + \delta\mu, k + \delta k, \omega)$ that is also an eigenfunction, but in a slightly different structure. Applying (7.69) to the new eigenfunction gives

$$\omega^2 \int_0^\infty (\rho + \delta\rho)(l_1 + \delta l_1)^2\,dz = (k + \delta k)^2 \int_0^\infty (\mu + \delta\mu)(l_1 + \delta l_1)^2\,dz + \int_0^\infty (\mu + \delta\mu)\left[\frac{d}{dz}(l_1 + \delta l_1)\right]^2 dz,$$

and subtracting (7.69) for the original eigenfunction gives (to first order)

$$\omega^2 \int_0^\infty (l_1^2\,\delta\rho + 2\rho l_1\,\delta l_1)\,dz = k^2 \int_0^\infty (l_1^2\,\delta\mu + 2\mu l_1\,\delta l_1)\,dz + 2k\,\delta k \int_0^\infty \mu l_1^2\,dz + \int_0^\infty \left(\frac{dl_1}{dz}\right)^2 \delta\mu\,dz + \int_0^\infty 2\mu \frac{dl_1}{dz}\frac{d\,\delta l_1}{dz}\,dz.$$

But from (7.67) we can cancel out all integrals here that contain the terms in δl_1 and $d(\delta l_1)/dz$. We are left with a relation between δk and integrals over $\delta\rho$ and $\delta\mu$. It remains to relate δc and δk, and the final result is

$$\left(\frac{\delta c}{c}\right)_\omega = -\frac{\delta k}{k} = \frac{\displaystyle\int_0^\infty \left[k^2 l_1^2 + \left(\frac{dl_1}{dz}\right)^2\right]\delta\mu\,dz - \int_0^\infty \omega^2 l_1^2\,\delta\rho\,dz}{\displaystyle 2k^2 \int_0^\infty \mu l_1^2\,dz}. \tag{7.71}$$

This formula shows a linear relation between the fractional change $\delta c/c$ in phase velocity and the perturbation in model parameters, and it plays a central role in the inversion of phase-velocity data. (In the language of inversion theory, (7.71) solves the forward problem of seeing how phase velocity is changed by perturbation of the model. The inverse problem, is to find the model that makes the phase velocity fit a particular data set. The procedure for inverting commonly uses a trial model, for which the forward problem is solved, and then finds the model perturbation needed to make a change in the derived data from the trial model, so that the perturbed model fits the observed phase velocity data. The change is given by (7.71). Because (7.71) is correct only to first order, iteration is generally needed to achieve an accurate fit to observations.) The weight, or kernel, function for $(\delta\mu/\mu)$ is proportional to the strain-energy density and that for $(\delta\rho/\rho)$ to the kinetic-energy density,

BOX **7.8**

"Partial derivatives" of phase velocity

The small change in phase velocity of Love waves, due to small perturbations $\delta\rho$ and $\delta\mu$ in the structure, can naturally be written in the form

$$\left(\frac{\delta c}{c}\right)_\omega = \int_0^\infty \frac{\rho}{c}\left[\frac{\partial c}{\partial \rho}\right]_{\omega,\mu} \frac{\delta\rho}{\rho} dz + \int_0^\infty \frac{\mu}{c}\left[\frac{\partial c}{\partial \mu}\right]_{\omega,\rho} \frac{\delta\mu}{\mu} dz. \tag{1}$$

The symbols appearing here in square brackets are known as partial derivatives of phase velocity with respect to density (or rigidity) at a particular depth. Comparing with (7.71), we have

$$\frac{\rho}{c}\left[\frac{\partial c}{\partial \rho}\right]_{\omega,\mu} = -\frac{\rho\omega^2 l_1^2}{2k^2 \int_0^\infty \mu l_1^2\, dz} \tag{2}$$

and

$$\frac{\mu}{c}\left[\frac{\partial c}{\partial \mu}\right]_{\omega,\rho} = \frac{\mu\left\{k^2 l_1^2 + \left(\frac{dl_1}{dz}\right)^2\right\}}{2k^2 \int_0^\infty \mu l_1^2\, dz}. \tag{3}$$

The notation here is deceptive, in that the left-hand sides of (2) and (3) appear to be dimensionless. As is made clear from the right-hand sides, the unit is in fact reciprocal length (this is apparent directly from (1)).

The first computations of partial derivatives of phase velocity were conducted by Dorman and Ewing (1962) and Brune and Dorman (1963), who simply found the phase velocities for two slightly different structures and then took the numerical difference. The variational approach for both Love and Rayleigh waves was suggested by Jeffreys (1961). A practical scheme for obtaining partial derivatives of group velocity was given by Rodi *et al.* (1975). Zeng and Anderson (1995) showed how to compute differential seismograms efficiently with respect to a velocity change in a layered elastic solid.

showing that perturbations in μ and ρ at depths where the energy densities are larger affect the phase velocity more strongly.

The change in group velocity at fixed frequency, due to small perturbations in rigidity and density, is obtained from (7.70) as

$$\frac{\delta U}{U} = \frac{\delta I_2}{I_2} - \frac{\delta c}{c} - \frac{\delta I_1}{I_1}, \tag{7.72}$$

but in this case δl_1 must be computed before δI_1 and δI_2 are found, since integrals involving δl_1 and $d(\delta l_1)/dz$ do not cancel out in a manner similar to (7.71).

7.3.2 RAYLEIGH WAVES

Using the Lagrangian density given in (7.65), Hamilton's principle for Rayleigh waves can be written as

$$\omega^2\, \delta I_1 - k^2\, \delta I_2 - k\, \delta I_3 - \delta I_4 = 0, \tag{7.73}$$

where

$$I_1 = \tfrac{1}{2}\int_0^\infty \rho(r_1^2 + r_2^2)\,dz, \qquad I_2 = \tfrac{1}{2}\int_0^\infty \left[(\lambda + 2\mu)r_1^2 + \mu r_2^2\right] dz, \tag{7.74}$$

$$I_3 = \int_0^\infty \left(\lambda r_1 \frac{dr_2}{dz} - \mu r_2 \frac{dr_1}{dz}\right) dz, \qquad I_4 = \tfrac{1}{2}\int_0^\infty \left[(\lambda + 2\mu)\left(\frac{dr_2}{dz}\right)^2 + \mu\left(\frac{dr_1}{dz}\right)^2\right] dz.$$

It can be shown that (7.73) is equivalent to the equation of motion (7.28), boundary conditions (7.29), and continuity of r_1, r_2, r_3, and r_4. Since r_1, r_2, which satisfy these conditions, are eigenfunctions for Rayleigh waves, (7.73) shows that the integral $\omega^2 I_1 - k^2 I_2 - kI_3 - I_4$ is stationary for perturbation of eigenfunctions. As is true for Love waves, we find that this integral vanishes at the stationary point:

$$\omega^2 I_1 - k^2 I_2 - kI_3 - I_4 = 0. \tag{7.75}$$

So this equation can be used as a check on the eigenvalue and eigenfunction calculations for Rayleigh waves, using the methods discussed earlier for Love waves.

By perturbing k and ω in (7.75) and using (7.73), we find that

$$I_1\,\delta(\omega^2) = I_2\,\delta(k^2) + I_3\,\delta k$$

and hence the formula for group velocity is

$$U = \frac{\delta\omega}{\delta k} = \frac{I_2 + \dfrac{I_3}{2k}}{cI_1} \tag{7.76}$$

where c is the phase velocity.

The change in phase velocity due to small perturbations in λ, μ, and ρ can also be obtained from (7.75). For a given ω, again using (7.73), we have

$$\begin{aligned}\delta k(2kI_2 + I_3) = {} & \tfrac{1}{2}\int_0^\infty \omega^2(r_1^2 + r_2^2)\,\delta\rho\,dz - \tfrac{1}{2}\int_0^\infty \left(kr_1 + \frac{dr_2}{dz}\right)^2 \delta\lambda\,dz \\ & - \tfrac{1}{2}\int_0^\infty \left[2k^2 r_1^2 + 2\left(\frac{dr_2}{dz}\right)^2 + \left(kr_2 - \frac{dr_1}{dz}\right)^2\right]\delta\mu\,dz.\end{aligned} \tag{7.77}$$

The corresponding fractional change in phase velocity can be written as

$$\begin{aligned}\left(\frac{\delta c}{c}\right)_\omega = -\frac{\delta k}{k} = {} & \frac{1}{4k^2 U c I_1}\left\{\int_0^\infty \left(kr_1 + \frac{dr_2}{dz}\right)^2 \delta\lambda\,dz + \int_0^\infty \left[2k^2 r_1^2\right.\right. \\ & \left.\left. + 2\left(\frac{dr_2}{dz}\right)^2 + \left(kr_2 - \frac{dr_1}{dz}\right)^2\right]\delta\mu\,dz - \int_0^\infty \omega^2(r_1^2 + r_2^2)\,\delta\rho\,dz\right\},\end{aligned} \tag{7.78}$$

where (7.76) was used in simplifying the denominator on the right-hand side. The weight function for $\delta\rho/\rho$ is again the kinetic energy, and that for $\delta\lambda$ is proportional to the dilatational

strain energy. By rewriting (7.78) in terms of $\delta(\lambda + \frac{2}{3}\mu)$ and $\delta\mu$, we would find weight functions proportional to dilatational- and shear-strain energies (see Problem 2.9; note that $\lambda + \frac{2}{3}\mu$ is the bulk modulus).

7.3.3 RAYLEIGH–RITZ METHOD

The variational principle, such as given in (7.67) and (7.73) for Love and Rayleigh waves, is used in the Rayleigh–Ritz method to find eigenvalues and eigenfunctions. In this approach, we approximate the eigenfunction by a linear combination of basis functions $\phi_i(z)$,

$$l_1(z) = \sum_{i=1}^{n} c_i \phi_i(z), \tag{7.79}$$

which are chosen usually to satisfy boundary conditions at $z = 0$ and $z = \infty$. If we substitute this form into the energy integrals in (7.66), we find

$$I_1 = \mathbf{c}^T \mathbf{A}_1 \mathbf{c}, \qquad I_2 = \mathbf{c}^T \mathbf{A}_2 \mathbf{c}, \qquad I_3 = \mathbf{c}^T \mathbf{A}_3 \mathbf{c}, \tag{7.80}$$

where $\mathbf{c} = (c_1, c_2, \ldots, c_n)^T$ and the symmetric matrices $\mathbf{A}_1$, $\mathbf{A}_2$, and $\mathbf{A}_3$ have elements

$$\begin{aligned} A_{1ij} &= \tfrac{1}{2} \int_0^\infty \rho \phi_i \phi_j \, dz, \\ A_{2ij} &= \tfrac{1}{2} \int_0^\infty \mu \phi_i \phi_j \, dz, \\ A_{3ij} &= \tfrac{1}{2} \int_0^\infty \mu \frac{d\phi_i}{dz} \frac{d\phi_j}{dz} \, dz. \end{aligned} \tag{7.81}$$

The coefficient vector $\mathbf{c}$ that minimizes the Lagrangian integral $\omega^2 I_1 - k^2 I_2 - I_3$ is obtained by setting the derivative of the integral with respect to $c_i (i = 1, 2, \ldots, n)$ equal to zero. The result is given by

$$(\omega^2 \mathbf{A}_1 - k^2 \mathbf{A}_2 - \mathbf{A}_3)\mathbf{c} = \mathbf{0}. \tag{7.82}$$

This equation defines an eigenvalue–eigenvector problem for $\mathbf{c}$. Nontrivial solutions $\mathbf{c}$ exist only when k is an eigenvalue that satisfies

$$|\omega^2 \mathbf{A}_1 - k^2 \mathbf{A}_2 - \mathbf{A}_3| = 0 \tag{7.83}$$

for a given ω. Once an eigenvalue is determined, the corresponding eigenvector is obtained by solving (7.82).

Since the eigenvalue is stationary with respect to any perturbation in the eigenfunction, the approximate eigenvector determined by solving (7.82) can be used to find a more accurate eigenvalue using (7.69).

Takeuchi and Kobayashi (1959) used exponentially decaying functions as the basis functions and determined the Love-wave dispersion in a half-space in which rigidity increases linearly with depth. They demonstrated the power of Rayleigh–Ritz methods by obtaining essentially the same results as the numerical integration method of Satô (1959), but with far less computational effort. Wiggins (1976b) used cubic polynomials, as shown in Figure 7.6, for the basis functions. Their values and derivatives are unity or vanish at the end points, which is convenient for constructing a trial eigenfunction satisfying prescribed boundary conditions. Wiggins concluded that the Rayleigh–Ritz method using these basis functions is competitive with the most efficient propagator matrix method. A similar approach was taken also by Buland and Gilbert (1976).

In the early 1990s, a series of papers by Robert Geller and colleagues developed elastodynamic solutions with a source term (Geller *et al.*, 1990a, b; Hara *et al.*, 1991; Cummins *et al.*, 1994a, b). For general (k, ω) and using our present notation, these solutions satisfy

$$(\omega^2 \mathbf{A}_1 - k^2 \mathbf{A}_2 - \mathbf{A}_3)\mathbf{c} = \mathbf{g} \tag{7.84}$$

where $\mathbf{g}(k, \omega)$ is a source term, known explicitly for a given moment tensor. The solution in the time domain is obtained by numerically solving (7.84) for $\mathbf{c} = \mathbf{c}(k, \omega)$ and then numerically carrying out the inverse transforms over (k, ω)—a process of summation. Various different basis functions have been tried, including the following system of linear splines as the basis functions:

$$\phi_i(z) = \begin{cases} (z - z_{i-1})/(z_i - z_{i-1}) & z_{i-1} < z \leq z_i \\ (z_{i+1} - z)/(z_{i+1} - z_i) & z_i \leq z < z_{i+1} \\ 0 & \text{otherwise.} \end{cases}$$

Note that the matrix $\omega^2 \mathbf{A}_1 - k^2 \mathbf{A}_2 - \mathbf{A}_3$ in (7.84) is singular at (k, ω) values corresponding to a surface-wave eigenvalue. But such singularities are avoided in attenuating media using real (k, ω). We return to some of these issues in Section 7.4.2 (obtaining surface waves for a given source, using integration over continuous real k) and Section 9.2 (obtaining the complete seismogram in the time domain, again by summation over (k, ω) contributions).

7.3.4 ATTENUATION OF SURFACE WAVES

In Chapter 5, we introduced spatial $Q(\omega)$ to describe the attenuation of plane body waves with increasing travel distance and discussed the associated dispersion. We found that the propagation factor $\exp\left[i(kx - \omega t)\right] = \exp\left[i\omega(x/c - t)\right]$ for elastic media is to be replaced by

$$\exp\left[i(Kx - \omega t)\right] = \exp\left[\frac{(-\omega x)}{2c(\omega)Q(\omega)}\right] \exp\left\{i\omega\left[\frac{x}{c(\omega)} - t\right]\right\}.$$

When the solution of an elastic-wave problem is given in terms of $c = c_e$, the corresponding anelastic solution is given by replacing c_e via the rule

$$\frac{1}{c_e} \to \frac{1}{c(\omega)}\left(1 + \frac{i}{2Q(\omega)}\right). \tag{5.92 again}$$

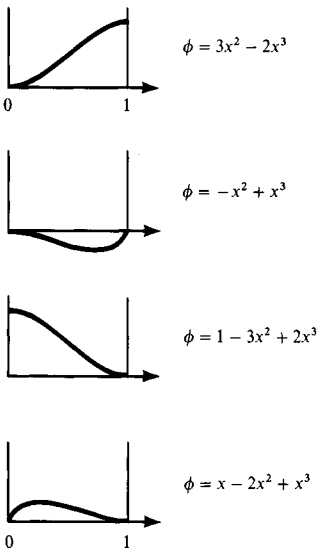

FIGURE **7.6**
Basis functions used by Wiggins (1976b) to find eigenfunctions via the Rayleigh–Ritz method. Many inhomogeneous layers may be present in the medium; shown here are the four normalized functions used for each layer ($x = 0$ and $x = 1$ correspond to layer boundaries). For each of the four functions shown, ϕ or $d\phi/dx$ is zero or one at $x = 0$ and 1.

In particular, if Q is effectively constant, we found that dispersion is logarithmic, and is given by

$$\frac{c(\omega_1)}{c(\omega_2)} = 1 + \frac{1}{\pi Q} \ln\left(\frac{\omega_1}{\omega_2}\right).$$

For a lossy medium with high Q, the rule (5.92) can be considered to introduce a small perturbation to the velocity c_e (Anderson and Archambeau, 1964; Anderson *et al.*, 1965). The change δc, which is made at fixed frequency, will have real and imaginary components:

$$\left(\frac{\delta c}{c}\right)_\omega = \left(\frac{c}{c_e} - 1\right) - \frac{i}{2Q^{\text{spatial}}}. \tag{7.85}$$

Let us first consider the change in phase velocity of Love waves due to perturbations in S-wave speed at each depth. Since $\delta\beta/\beta = \frac{1}{2}(\delta\mu/\mu - \delta\rho/\rho)$, we have from (7.71), neglecting density perturbation,

$$\left(\frac{\delta c}{c}\right)_\omega = \frac{\displaystyle\int_0^\infty \left[k^2 l_1^2 + \left(\frac{dl_1}{dz}\right)^2\right] 2\mu \frac{\delta\beta}{\beta}\, dz}{\displaystyle k^2 \int_0^\infty 2\mu l_1^2\, dz}. \tag{7.86}$$

Substituting the form (7.85) for $\delta\beta/\beta$ in the above equation, we obtain $(\delta c/c)$, with real and imaginary parts. The real part will introduce material dispersion for Love waves due to anelasticity in addition to geometric dispersion due to vertical heterogeneity of the medium.

The imaginary part will cause attenuation of Love-wave amplitudes, and from (7.85) we define the spatial Q_L of Love waves by

$$\text{spatial } Q_L^{-1} = -2\text{Im}\,(\delta c/c)_\omega. \tag{7.87}$$

Putting $\text{Im}\,(\delta\beta/\beta) = -1/(2Q_\beta)$ in (7.86), we obtain

$$\text{spatial } Q_L^{-1} = \frac{\displaystyle\int_0^\infty \left[k^2 l_1^2 + \left(\frac{dl_1}{dz}\right)^2\right] \mu Q_\beta^{-1}\, dz}{\displaystyle k^2 \int_0^\infty \mu l_1^2\, dz}. \tag{7.88}$$

This formula shows that Q_L^{-1} for Love waves is expressed as an integral of Q_β^{-1} for shear waves, weighted by the strain-energy density of the particular mode.

For Rayleigh waves, the perturbations in λ and μ are replaced by those in α and β, and recognizing the term $\delta(\lambda + 2\mu)/(\lambda + 2\mu) = 2\delta\alpha/\alpha + \delta\rho/\rho$ in (7.78), we obtain

$$\begin{aligned}\left(\frac{\delta c}{c}\right)_\omega = \frac{1}{4k^2 U c I_1} \Bigg\{ &\int_0^\infty \left(kr_1 + \frac{dr_2}{dz}\right)^2 (\lambda + 2\mu) 2 \left(\frac{\delta\alpha}{\alpha}\right) dz \\ &+ \int_0^\infty \left[\left(kr_2 - \frac{dr_1}{dz}\right)^2 - 4kr_1 \frac{dr_2}{dz}\right] 2\mu \left(\frac{\delta\beta}{\beta}\right) dz \Bigg\}.\end{aligned} \tag{7.89}$$

Defining the spatial Q_R of Rayleigh waves in a manner similar to that of (7.87), we put $\text{Im}(\delta\alpha/\alpha) = -1/(2Q_\alpha)$. From (7.89), we then get

$$\begin{aligned}\text{spatial } Q_R^{-1} = \frac{1}{4k^2 U c I_1} \Bigg\{ &\int_0^\infty \left(kr_1 + \frac{dr_2}{dz}\right)^2 (\lambda + 2\mu) 2 Q_\alpha^{-1}\, dz \\ &+ \int_0^\infty \left[\left(kr_2 - \frac{dr_1}{dz}\right)^2 - 4kr_1 \frac{dr_2}{dz}\right] 2\mu Q_\beta^{-1}\, dz \Bigg\}.\end{aligned} \tag{7.90}$$

Again, Q_R^{-1} for Rayleigh waves is expressed as an integral of Q^{-1} for P- and S-waves with appropriate weight functions.

So far, we have considered the spatial Q defined for attenuation with travel distance (Box 5.7). This definition is suitable for measurement on propagating waves. However, there are several cases of seismic measurements in which the temporal Q is directly observed. The most important case is the attenuation of a particular free oscillation of the whole Earth. In this case k is fixed, whereas in a propagating-wave experiment ω is fixed. The change of phase velocity due to model-parameter perturbation is different between experiments with fixed ω and fixed k. Thus the phase function $\exp[i(kx - \omega t)]$ is replaced by

$$\exp\,[i(kx - \Omega t)] = \exp\left[-\frac{\omega t}{2Q(\omega)}\right] \exp\,[ik(x - ct)]\,.$$

BOX **7.9**
Some effects of anisotropy

The general theory of surface-wave propagation in anisotropic media with vertical inhomogeneity is conceptually a simple extension of the propagator matrix techniques given in Section 7.2. The displacement–stress vector (see (7.36)) is now of length 6, and in general we cannot speak of Love and Rayleigh waves as separate families of surface waves. Rather, there exists one generalized family of surface waves, which, in weakly anisotropic media, can be broken down into quasi-Love and quasi-Rayleigh motions.

If anisotropy is weak, then the phase velocity c of surface waves can be shown to have dependence on the azimuthal direction ϕ of propagation via

$$c(\phi, \omega) = A(\omega) + B(\omega) \cos 2\phi + C(\omega) \sin 2\phi + E(\omega) \cos 4\phi + F(\omega) \sin 4\phi \quad (1)$$

(Smith and Dahlen, 1973; detailed discussion is given by Auld, 1990). This formula is approximate, and is similar to the body-wave result (5.109). Forsyth (1975) applied (1) to surface-wave data for the Pacific, though he did not include the 4ϕ terms because in practice (with his data) their effect was minor.

For an anisotropic half-space composed of a welded stack of homogeneous layers, a detailed discussion of surface-wave dispersion has been given by Crampin (1970, 1971), 1975, 1977). If anisotropy is present in the Earth because of some preferential alignment of anisotropic crystals (e.g., of olivine) that originally solidified near a spreading center such as a midoceanic ridge, then horizontal planes through the anisotropy are likely to be planes of symmetry. Taking x_3 as the depth direction, Love (1944) showed that there is symmetry about horizontal planes if and only if $c_{ijkl} = 0$ when either one or three of the subscripts is the number 3. Crampin (1975) described a surface-wave particle motion characteristic of this type of anistropy. Called *Inclined-Rayleigh* motion, it consists of elliptical particle motion with vertical and horizontal axes, but the plane of the ellipse is inclined to the sagittal plane (see Section 5.6). Thus particle motion has a component transverse to the slowness direction in which the wave is propagating. The horizontal components are in phase, but are $\pm\pi/2$ out of phase with the vertical component. Crampin and King (1977) described several observations of this particle motion at an array of seismometers in Norway (NORSAR), for surface waves that have travelled across Eurasia.

The replacement of an elastic velocity c_e is now made via the rule

$$c_e \to c\left(1 - \frac{i}{2Q^{\text{temporal}}}\right);$$

that is,

$$\left(\frac{\delta c}{c}\right)_k = \left(\frac{c}{c_e} - 1\right) - \frac{i}{2Q^{\text{temporal}}}. \quad (7.91)$$

Since both $(\omega, k + \delta k)$ and $(\omega + \delta\omega, k)$ are pairs of eigenvalues for the perturbed medium, the slope of the line connecting the two points in an ω–k diagram will give group velocity U for the perturbed medium:

$$U = \frac{\omega - (\omega + \delta\omega)}{(k + \delta k) - k} = -\frac{\delta\omega}{\delta k}. \quad (7.92)$$

But in the one case we have $k + \delta k = K = k(1 + i/2Q^{\text{spatial}})$, and in the other we have $\omega + \delta\omega = \Omega = \omega(1 - i/2Q^{\text{temporal}})$. From these we construct $-\delta\omega/\delta k$ and obtain the general rule

$$\text{temporal } Q^{-1} = \frac{U}{c} \times \text{spatial } Q^{-1}. \tag{7.93}$$

These two kinds of Q were first distinguished by Brune (1962) in a study of surface waves. The above formula is important when we compare Q of dispersive waves determined by a standing-wave experiment and by a propagating-wave experiment. For nondispersive waves, $c = U$ and there is no distinction between the two Q's.

Equation (7.93) can be easily understood if we measure the attenuation of dispersed waves using the stationary-phase approximation (7.18). At a given x and t, the frequency ω that dominates the record is given by the solution to $x/t = U(\omega)$. Since the wave with frequency ω has existed in the medium over the time period $t = x/(U(\omega))$, it must have been attenuated by a factor

$$\exp\left[\frac{-\omega t}{2 \text{ temporal } Q(\omega)}\right] = \exp\left[\frac{-\omega x}{2U(\omega) \text{ temporal } Q(\omega)}\right]. \tag{7.94}$$

Since, by definition, this is equal to

$$\exp\left[\frac{-\omega x}{2c(\omega) \text{ spatial } Q(\omega)}\right]$$

we again obtain (7.93).

7.4 Surface-Wave Terms of Green's Function for a Vertically Heterogeneous Medium

In this section, we shall obtain a simple compact solution for surface waves generated by a point force with time dependence $e^{-i\omega t}$ buried in a vertically heterogeneous medium. We shall first express the general solution for the equations of motion in cylindrical coordinates (r, ϕ, z), using the motion-stress vector introduced in previous sections and a set of vectors that are functions of r, ϕ alone to describe the horizontal propagation. A stress discontinuity equivalent to a point source is expanded in a series of these horizontally varying vector functions. We then find a solution with the prescribed discontinuity that also satisfies the boundary conditions at the free surface and at infinite depth. This approach was used by Haskell (1964), Harkrider (1964b), Ben-Menahem *et al.* (1970), and Hudson (1969a). A compact result is obtained by applying the variational principle to the residue evaluated at poles in the k-plane. This last step was taken by Keilis-Borok and Yanovskaya (1962), Harkrider and Anderson (1966), Vlaar (1966) and Saito (1967).

We shall first describe a simple method that works for two-dimensional cases, using a reciprocal theorem of Herrera (1964) that, unfortunately, does not apply in three dimensions. We shall then follow Saito (1967) to find the solution in three dimensions.

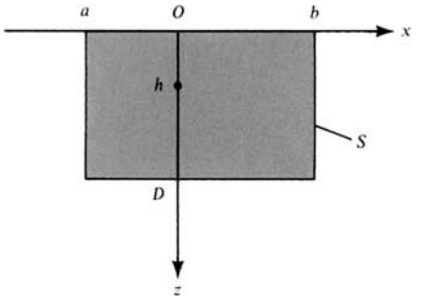

FIGURE **7.7**
Integration in (7.95) is taken over the surface S enclosing the shaded slab.

7.4.1 TWO-DIMENSIONAL CASE

Let us first find orthogonality relations for eigenfunctions of Love and Rayleigh waves by the use of our reciprocal theorem (2.35). Neglecting body forces, the Fourier transform of (2.35) becomes

$$0 = \int\int_S \{\mathbf{v}(\mathbf{x}, \omega) \cdot \mathbf{T}(\mathbf{u}(\mathbf{x}, \omega), \mathbf{n}) - \mathbf{u}(\mathbf{x}, \omega) \cdot \mathbf{T}(\mathbf{v}(\mathbf{x}, \omega), \mathbf{n})\}\, dS \tag{7.95}$$

(in which the original convolution has become a product of transforms). This equation holds for any pair of solutions **u** and **v** of the equation of motion for a given medium without body forces. We take two different modes of Love waves propagating in the x-direction as **u** and **v** and define S as the surface enclosing the shaded slab with corners at $(a, 0)$, $(b, 0)$, (a, D), and (b, D), as shown in Figure 7.7.

For Love waves, the traction **T** vanishes at the free surface $z = 0$, and the displacement vanishes at $z = \infty$. The displacement and traction components along the *vertical* plane are

$$\begin{aligned} u_y &= l_1(k_n, z, \omega) \exp(ik_n x) \\ T_y &= \tau_{xy} = \mu \frac{\partial u_y}{\partial x} = ik_n \mu l_1 \exp(ik_n x) \end{aligned} \tag{7.96}$$

for the first solution and

$$\begin{aligned} v_y &= l_1(k_m, z, \omega) \exp(ik_m x) \\ T_y &= ik_m \mu l_1 \exp(ik_m x) \end{aligned} \tag{7.97}$$

for the second. Other components do not contribute to the integral (7.95). Substituting (7.96) and (7.97) in (7.95), we find as $D \to \infty$ that

$$\begin{aligned} &\exp\left[i(k_n + k_m)a\right] \int_0^\infty i(k_n - k_m)\mu(z) l_1(k_m, z, \omega) l_1(k_n, z, \omega)\, dz \\ &\qquad = \exp\left[i(k_n + k_m)b\right] \int_0^\infty i(k_n - k_m)\mu(z) l_1(k_m, z, \omega) l_1(k_n, z, \omega)\, dz. \end{aligned}$$

This equality holds for arbitrary a and b, if and only if

$$\int_0^\infty \mu(z) l_1(k_m, z, \omega) l_1(k_n, z, \omega)\, dz = 0 \qquad \text{for } k_n \neq k_m. \tag{7.98}$$

The eigenfunctions of different modes of Love waves, for fixed ω, are therefore orthogonal to each other with the rigidity $\mu(z)$ as a weight function.

For Rayleigh waves, we similarly take the nth mode as $\mathbf{u}$, and displacement and traction components along the vertical plane are then

$$\begin{aligned}
u_x &= r_1(k_n, z, \omega) \exp(ik_n x), \\
u_z &= i r_2(k_n, z, \omega) \exp(ik_n x), \\
\tau_{xx} &= i T_1(k_n, z, \omega) \exp(ik_n x) = i \left\{ \lambda \frac{dr_2}{dz} + (\lambda + 2\mu) k_n r_1 \right\} \exp(ik_n x), \\
\tau_{zx} &= T_2(k_n, z, \omega) \exp(ik_n x) = \left(\mu \frac{dr_1}{dz} - \mu k_n r_2 \right) \exp(ik_n x).
\end{aligned} \tag{7.99}$$

Those for $\mathbf{v}$ are obtained by replacing k_n by k_m. The orthogonality relation for Rayleigh waves is then obtained as

$$\sum_{i=1}^{2} \int_0^\infty \left[r_i(k_n, z, \omega) T_i(k_m, z, \omega) - r_i(k_m, z, \omega) T_i(k_n, z, \omega) \right] dz = 0$$

or

$$\begin{aligned}
\int_0^\infty \Big\{ & (\lambda + 2\mu)(k_m - k_n) r_1(k_n, z, \omega) r_1(k_m, z, \omega) - \mu(k_m - k_n) r_2(k_n, z, \omega) r_2(k_m, z, \omega) \\
& + \lambda \left[r_1(k_n, z, \omega) \frac{dr_2(k_m, z, \omega)}{dz} - r_1(k_m, z, \omega) \frac{dr_2(k_n, z, \omega)}{dz} \right] \\
& + \mu \left[r_2(k_n, z, \omega) \frac{dr_1(k_m, z, \omega)}{dz} - r_2(k_m, z, \omega) \frac{dr_1(k_n, z, \omega)}{dz} \right] \Big\} \, dz = 0.
\end{aligned} \tag{7.100}$$

With these orthogonality relations in hand, we shall proceed to find surface-wave terms of Green's function, using the reciprocal theorem again. We use the same solution for $\mathbf{u}$ as defined in (7.96) and (7.99) for Love and Rayleigh waves, respectively, but for $\mathbf{v}$ we use a two-dimensional Green function $\mathbf{G}_k \exp(-i\omega t)$, taken here to be the response to a line force with time dependence $\exp(-i\omega t)$ having unit strength per unit distance in the y-direction, and located at $x = 0, z = h$. The line is parallel to the y-axis (i.e., the x_2-axis), and the force acts in the x_k-direction (i.e., x or y or z), so that

$$-\rho\omega^2 G_{ik}(x, z; 0, h; \omega) = \frac{\partial}{\partial x_j} \tau_{ij}(\mathbf{G}_k) + \delta_{ik}\, \delta(x)\, \delta(z - h). \tag{7.101}$$

Following the same steps as taken from (2.35) to the representation theorem (2.41), we find that

$$u_k(0,h) = \int_S \left\{ G_{ik}(x,z;0,h;\omega) T_i(\mathbf{u},\mathbf{n}) - u_i(x,z) T_i(\mathbf{G}_k,\mathbf{n}) \right\} \, dS. \tag{7.102}$$

Now we choose again the same integration surface S as shown in Figure 7.7, but this time make not only $D \to \infty$, but also $a \to -\infty$ and $b \to +\infty$. Since surface waves from a line source suffer no geometric spreading but body waves do, we expect that the Green function at a large distance will consist entirely of surface waves propagating outward from the source. Thus for a large x, the y-component of Green's function is given by a sum of Love waves,

$$G_{yy}(x,z;0,h;\omega) \sim \begin{cases} \sum_m b^+_{m2}(h) l_1(k_m,z,\omega) \exp(ik_m x) & x \gg 0 \\ \sum_m b^-_{m2}(h) l_1(k_m,z,\omega) \exp(-ik_m x) & x \ll 0. \end{cases} \tag{7.103}$$

The x- and z-components are composed of Rayleigh waves,

$$\begin{aligned} G_{xk}(x,z;0,h;\omega) &\sim \begin{cases} \sum_m a^+_{mk}(h) r_1(k_m,z,\omega) \exp(ik_m x) & x \gg 0 \\ \sum_m a^-_{mk}(h) r_1(k_m,z,\omega) \exp(-ik_m x) & x \ll 0, \end{cases} \\ G_{zk}(x,z;0,h;\omega) &\sim \begin{cases} \sum_m i a^+_{mk}(h) r_2(k_m,z,\omega) \exp(ik_m x) & x \gg 0 \\ \sum_m i a^-_{mk}(h) r_2(k_m,z,\omega) \exp(-ik_m x) & x \ll 0. \end{cases} \end{aligned} \tag{7.104}$$

Substituting (7.103) and (7.96) into (7.102), we find the y-component of displacement is given by

$$\begin{aligned} u_y(0,h) = &\sum_m b^+_{m2}(h) \int_0^\infty i(k_n - k_m)\mu(z) l_1(k_n,z,\omega) l_1(k_m,z,\omega) \exp\left[i(k_n + k_m)b\right] \, dz \\ &- \sum_m b^-_{m2}(h) \int_0^\infty i(k_n + k_m)\mu(z) l_1(k_n,z,\omega) l_1(k_m,z,\omega) \exp\left[i(k_m - k_n)a\right] \, dz. \end{aligned}$$

Using the orthogonality relation (7.98), this reduces to

$$u_y(0,h) = l_1(k_n,h,\omega) = -2ik_n b^-_{n2}(h) \int_0^\infty \mu(z) l_1^2(k_n,z,\omega) \, dz$$

or

$$b^-_{n2}(h) = \frac{l_1(k_n,h,\omega)}{-4ik_n I_2}, \tag{7.105}$$

where I_2 was defined in (7.66). Similarly, using $u_y = l_1 \exp(-ik_n x)$ instead of (7.96), we obtain

$$b^+_{n2}(h) = b^-_{n2}(h). \tag{7.106}$$

Putting (7.105) and (7.106) into (7.103), we obtain the Love-wave terms of Green's function due to a line force oriented in the y-direction,

$$G_{yy}(x,z;0,h;\omega) \sim \sum_n \frac{l_1(k_n,h,\omega)l_1(k_n,z,\omega)}{4k_nI_2} \exp\left(ik_nx + i\frac{\pi}{2}\right) \quad x \gg 0, \quad (7.107)$$

or using (7.70),

$$G_{yy}(x,z;0,h;\omega) \sim \sum_n \frac{l_1(k_n,h,\omega)l_1(k_n,z,\omega)}{4k_ncUI_1} \exp\left(ik_nx + i\frac{\pi}{2}\right) \quad x \gg 0,$$

where I_1 and I_2 are given in (7.66).

The above equation shows the remarkable simplicity of Love-wave terms of Green's function. The effect of source depth h, receiver depth z, travel distance x, and medium properties expressed by c, U, and I_1 are separated for each mode. Once the eigenvalue–eigenfunction problem is solved, the calculation of the Love-wave amplitude generated by a line force is extremely simple. We shall show later that this formula with only minor modification applies to Love waves from a point force.

The Rayleigh-wave terms of Green's function can be obtained similarly by substituting (7.104) and (7.99) into (7.102) and applying the orthogonal relation (7.100). For example, putting subscript $k = 1$ (the x-direction) in (7.102), we obtain

$$\begin{aligned} u_x(0,h) &= r_1(k_n,h,\omega) \\ &= -ia_{n1}^-(h)\int_0^\infty \left\{2k_n\left[(\lambda+2\mu)r_1^2(k_n,z,\omega) + \mu r_2^2(k_n,z,\omega)\right]\right. \\ &\quad \left. +2\left[\lambda r_1(k_n,z,\omega)\frac{dr_2(k_n,z,\omega)}{dz} - \mu r_2(k_n,z,\omega)\frac{dr_1(k_n,z,\omega)}{dz}\right]\right\} dz \end{aligned}$$

or

$$a_{n1}^-(h) = \frac{r_1(k_n,h,\omega)}{-i4k_n\left(I_2 + \dfrac{I_3}{2k_n}\right)} = \frac{r_1(k_n,h,\omega)}{-i4k_ncUI_1} \quad (7.108)$$

where I_1, I_2, I_3 are given in (7.74). Again, we have $a_{n1}^+(h) = a_{n1}^-(h)$. Substituting them into (7.104), we obtain Rayleigh-wave terms of Green's function due to a line force acting in the x-direction:

$$\begin{aligned} G_{xx}(x,z;0,h;\omega) &\sim \sum_n \frac{r_1(k_n,h,\omega)r_1(k_n,z,\omega)}{4k_ncUI_1} \exp\left(ik_nx + i\frac{\pi}{2}\right) \quad x \gg 0, \\ G_{zx}(x,z;0,h;\omega) &\sim \sum_n \frac{r_1(k_n,h,\omega)r_2(k_n,z,\omega)}{4k_ncUI_1} \exp(ik_nx + i\pi) \quad x \gg 0, \end{aligned} \quad (7.109)$$

BOX 7.10
Sign convention on vertical motion

Since x_3, or the z-axis, is directed downward, one might expect that the positive direction for the vertical displacement would be chosen as downward. But practice has not usually followed this logic. Seismologists have naturally considered the depth to be positive downward, but have then inconsistently chosen the vertical component of seismic motion to be positive upward. In this book, we have chosen that the z-axis be positive downward for both displacement and depth wherever we develop results with (x, y, z) or (r, ϕ, z) coordinates. Whenever we make explicit reference to the seismologist's "Z-component of motion", i.e., in the upward vertical direction, as in Problem 5.7, a sign change must then be introduced. Of course, in spherical polars, with $r = 0$ at the center of the Earth and r as a vertical coordinate, the vertically upward direction is naturally positive, as we shall assume in Chapter 8 and relevant parts of Chapter 9.

Again, this is an extremely simple form that separates the source, receiver, and path effects. Green's function for a line force oriented in the z-direction can be obtained likewise as

$$G_{xz}(x, z; 0, h; \omega) \sim \sum_n \frac{r_2(k_n, h, \omega) r_1(k_n, z, \omega)}{4 k_n c U I_1} \exp(i k_n x) \qquad x \gg 0, \quad (7.110)$$

$$G_{zz}(x, z; 0, h; \omega) \sim \sum_n \frac{r_2(k_n, h, \omega) r_2(k_n, z, \omega)}{4 k_n c U I_1} \exp\left(i k_n x + i \frac{\pi}{2}\right) \qquad x \gg 0, \quad (7.111)$$

Note that the phase shifts appearing in G_{xx}, G_{yy}, and G_{zz} are all $\frac{1}{2}\pi$ phase delay.

A cursory glance at the form of these solutions, with k_n in the denominator, suggests the amplitude spectrum behaves like ω^{-1}. However, I_1 (with normalized r_1 and r_2) depends on ω in such a way that $k_n I_1$ is only a weakly varying function of ω. See Problem 7.7.

7.4.2 THREE-DIMENSIONAL CASE

A natural framework in which to study Green's function for a point source is the cylindrical system (r, ϕ, z) defined in Figure 7.8. Let us go back to Box 6.5 and start with the three scalar potentials ϕ, ψ, χ representing P-, SV-, and SH-waves, respectively. (Our use of standard symbols unfortunately leads us here to a double use of ϕ—to represent both azimuth angle and P-wave potential. But the context in each use makes clear which of these very different quantities is symbolized by ϕ.) We showed in Box 6.5 that the elastic displacement in a homogeneous body can be expressed as

$$\mathbf{u} = \nabla\phi + \nabla \times \nabla \times (0, 0, \psi) + \nabla \times (0, 0, \chi), \qquad (7.112)$$

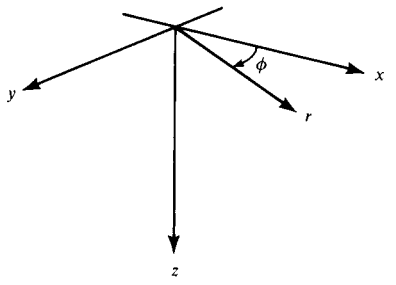

FIGURE **7.8**
Orientations of Cartesian and cylindrical polar coordinates used to analyze waves from a point source in a vertically heterogeneous medium.

the potentials here satisfying wave equations (3) of Box 6.5. It follows by the methods of separation of variables that general solutions can be obtained by a superposition of the basic solutions

$$\begin{aligned}\phi(\mathbf{x},\omega) &= J_m(kr)e^{im\phi}(Ae^{-\gamma z} + Be^{\gamma z})\exp(-i\omega t),\\ \psi(\mathbf{x},\omega) &= J_m(kr)e^{im\phi}(Ce^{-\nu z} + De^{\nu z})\exp(-i\omega t),\\ \chi(\mathbf{x},\omega) &= J_m(kr)e^{im\phi}(Ee^{-\nu z} + Fe^{\nu z})\exp(-i\omega t),\end{aligned} \tag{7.113}$$

where $J_m(kr)$ is the mth-order Bessel function; m is an integer; A, B, C, D, E, F are constants; and $\gamma = \sqrt{k^2 - \omega^2/\alpha^2}$, $\nu = \sqrt{k^2 - \omega^2/\beta^2}$. (Compare (7.113) with the axisymmetric solutions in Box 6.6.) We shall find it useful to lump together the r, ϕ dependence as

$$Y_k^m(r,\phi) = J_m(kr)e^{im\phi}, \tag{7.114}$$

a scalar expression that can naturally be called the basic *horizontal wavefunction*, since it alone characterizes the horizontal propagation for potentials.

An apparent barrier to our continuing with the method of potentials lies in the fact that our present interest is in vertically heterogeneous media, whereas the solutions (7.113) require homogeneity. Potentials can, however, help sort out the different horizontal wavefunctions that are appropriate for different physical variables, since this aspect of the problem is unchanged by vertical heterogeneity. Continuing, then, with a homogeneous medium, we can construct (u_r, u_ϕ, u_z) from potentials via (7.112). The P-wave component, $\nabla\phi$, is easily obtained, and for SV and SH we have

$$\begin{aligned}\mathbf{u}^{SV} &= \left(\frac{\partial^2\psi}{\partial r\partial z}, \frac{1}{r}\frac{\partial^2\psi}{\partial z\,\partial\phi}, -\frac{1}{r}\frac{\partial}{\partial r}\left(r\frac{\partial\psi}{\partial r}\right) - \frac{1}{r^2}\frac{\partial^2\psi}{\partial\phi^2}\right),\\ \mathbf{u}^{SH} &= \left(\frac{1}{r}\frac{\partial\chi}{\partial\phi}, -\frac{\partial\chi}{\partial r}, 0\right).\end{aligned} \tag{7.115}$$

In Section 2.6 we found the stress–displacement relations for general orthogonal curvilinear coordinates, and from (2.50) and (2.45) we can give the traction acting on horizontal planes in terms of displacement components:

$$\tau_{rz} = \mu\left(\frac{\partial u_z}{\partial r} + \frac{\partial u_r}{\partial z}\right), \quad \tau_{z\phi} = \mu\left(\frac{1}{r}\frac{\partial u_z}{\partial\phi} + \frac{\partial u_\phi}{\partial z}\right), \quad \tau_{zz} = \lambda\nabla\cdot\mathbf{u} + 2\mu\frac{\partial u_z}{\partial z}. \tag{7.116}$$

If we substitute potentials (7.113) into (7.112) and (7.116), we find that the displacement $\mathbf{u}$ and the traction $\mathbf{T}$ acting on the horizontal plane at depth z have the following form:

$$\begin{aligned}\mathbf{u} &= \left[l_1(k,z,\omega)\mathbf{T}_k^m(r,\phi) + r_1(k,z,\omega)\mathbf{S}_k^m(r,\phi) + r_2(k,z,\omega)\mathbf{R}_k^m(r,\phi)\right]\exp(-i\omega t),\\ \mathbf{T} &= \left[l_2(k,z,\omega)\mathbf{T}_k^m(r,\phi) + r_3(k,z,\omega)\mathbf{S}_k^m(r,\phi) + r_4(k,z,\omega)\mathbf{R}_k^m(r,\phi)\right]\exp(-i\omega t),\end{aligned} \tag{7.117}$$

in which, to describe the r,ϕ dependence of $\mathbf{u}$ and $\mathbf{T}$, we have introduced three orthogonal vector functions defined by

$$\begin{aligned}\mathbf{T}_k^m(r,\phi) &= \frac{1}{kr}\frac{\partial Y_k^m}{\partial\phi}\hat{\mathbf{r}} - \frac{1}{k}\frac{\partial Y_k^m}{\partial r}\hat{\boldsymbol{\phi}},\\ \mathbf{S}_k^m(r,\phi) &= \frac{1}{k}\frac{\partial Y_k^m}{\partial r}\hat{\mathbf{r}} + \frac{1}{kr}\frac{\partial Y_k^m}{\partial\phi}\hat{\boldsymbol{\phi}},\\ \mathbf{R}_k^m(r,\phi) &= -Y_k^m(r,\phi)\hat{\mathbf{z}},\end{aligned} \tag{7.118}$$

where $\hat{\mathbf{r}}$, $\hat{\boldsymbol{\phi}}$, and $\hat{\mathbf{z}}$ are unit vectors in directions r,ϕ,z. The z-dependence of $\mathbf{u}$ and $\mathbf{T}$ is described by six scalar functions l_1, l_2, r_1, r_2, r_3, and r_4. It can be verified that these functions (derived here from z-dependent terms in the potentials (7.113)) do satisfy the familiar equation $\partial\mathbf{f}/\partial z = \mathbf{A}\mathbf{f}$ discussed in Section 7.2, first with $\mathbf{f} = (l_1, l_2)^T$ to give (7.24), and then $\mathbf{f} = (r_1, r_2, r_3, r_4)^T$ to give (7.28).

This result for homogeneous media motivates us to *start* with the form (7.117), even in vertically *heterogeneous* media, substituting it into the equations of motion and the stress–strain relation. By this route we arrive *directly* at the first-order simultaneous differential equations (7.24) and (7.28), finding that the z-dependence for the motion-stress vector in cylindrical waves is exactly the same as the z-dependence in plane-wave problems.

We have just given a precise reason why cylindrical waves and plane waves share a common z-dependence. The result becomes intuitively reasonable if we make r large in the vector functions (7.118). First, we replace $J_m(kr)$ by $\frac{1}{2}[H_m^{(1)}(kr) + H_m^{(2)}(kr)]$, as we did in (6.16), and use the asymptotic expansion for outgoing waves

$$H_m^{(1)}(kr) \sim \sqrt{\frac{2}{\pi kr}}\exp\left[i\left(kr - \frac{2m+1}{4}\pi\right)\right].$$

We also neglect terms attenuating with distance more rapidly than $1/\sqrt{r}$. Then

$$\begin{aligned}\text{outgoing } \mathbf{T}_k^m(r,\phi) &\sim -i\sqrt{\frac{1}{2\pi kr}}\exp\left(ikr - i\frac{2m+1}{4}\pi + im\phi\right)\hat{\boldsymbol{\phi}},\\ \text{outgoing } \mathbf{S}_k^m(r,\phi) &\sim +i\sqrt{\frac{1}{2\pi kr}}\exp\left(ikr - i\frac{2m+1}{4}\pi + im\phi\right)\hat{\mathbf{r}},\\ \text{outgoing } \mathbf{R}_k^m(r,\phi) &\sim -\sqrt{\frac{1}{2\pi kr}}\exp\left(ikr - i\frac{2m+1}{4}\pi + im\phi\right)\hat{\mathbf{z}},\end{aligned} \tag{7.119}$$

showing that at a large distance, these waves do behave locally like plane Love and Rayleigh waves with appropriate polarization. Therefore, their z-dependence can be obtained by

studying plane waves. To solve the cylindrical wave problem, we can use all the results obtained previously on motion-stress vectors for plane waves.

Let us now consider surface waves generated by a point force $\mathbf{F}\exp(-i\omega t)$ in a vertically heterogeneous medium. Taking the point of application as $r = 0$, $z = h$, the corresponding body force (force per unit volume) is $\mathbf{F}\exp(-i\omega t)[\delta(r)/(2\pi r)]\delta(z-h)$. In the following we shall make frequent use of Cartesian coordinates (x, y, z), related to (r, ϕ, z) via $x = r\cos\phi$, $y = r\sin\phi$, and note then that $\delta(r)/(2\pi r) = \delta(x)\delta(y)$ (since each side of this equality has the same effect when integrated over horizontal planes). By equation (3.4), the applied body force is equivalent to a discontinuity in traction on horizontal planes at $z = h$, given by

$$\mathbf{T}(h+0) - \mathbf{T}(h-0) = -\mathbf{F}\exp(-i\omega t)\,\delta(x)\,\delta(y). \tag{7.120}$$

Our method of solution will be (i) to decompose this discontinuity into its (k, m) components; (ii) to solve the equation $\partial\mathbf{f}/\partial z = \mathbf{A}\mathbf{f}$ for each (k, m), where $\mathbf{f}$ is the z-dependent motion-stress vector with known discontinuity across $z = h$; and then (iii) to construct the solution as a function of (r, ϕ, z) by superposition of its (k, m) components.

Thus, we first want to obtain the coefficients f_T, f_S, f_R in

$$-\mathbf{F}\exp(-i\omega t)\,\delta(x)\,\delta(y) = \frac{\exp(-i\omega t)}{2\pi}\sum_m \int_0^\infty k\left[f_T(k,m)\mathbf{T}_k^m + f_S(k,m)\mathbf{S}_k^m + f_R(k,m)\mathbf{R}_k^m\right] dk. \tag{7.121}$$

We use the fact that $\mathbf{T}_k^m$, $\mathbf{S}_k^m$, and $\mathbf{R}_k^m$ are mutually orthogonal, and also that each of these three types of horizontal wavefunction satisfies an orthogonality relation (for different k and m) in the form

$$\int_0^{2\pi}\int_0^\infty \mathbf{T}_k^m(r,\phi)\cdot\left[\mathbf{T}_{k'}^{m'}(r,\phi)\right]^* r\,dr\,d\phi = \frac{2\pi\delta_{mm'}\delta(k-k')}{\sqrt{kk'}}, \tag{7.122}$$

where * indicates the complex conjugate. It follows that the expansion coefficients in (7.121) are given by

$$f_T(k,m) = -\int_0^{2\pi}\int_0^\infty \mathbf{F}\cdot\left[\mathbf{T}_k^m(r,\phi)\right]^*\,\delta(x)\,\delta(y) r\,dr\,d\phi, \tag{7.123}$$

with similar results for f_S and f_R.

Evaluation of the double integral in (7.123) is simplified by using Cartesians, recognizing $\int_0^{2\pi}\int_0^\infty(\ \ ) r\,dr\,d\phi = \int_{-\infty}^\infty\int_{-\infty}^\infty(\ \ )\,dx\,dy$ and the useful property

$$\mathbf{T}_k^m(r,\phi) = k^{-1}\nabla\times(0,0,Y_k^m). \tag{7.124}$$

BOX 7.11
On horizontal wavefunctions

The horizontal wavefunction for plane waves described in Chapters 6 and 7 is e^{ikx}. It is a unique feature of plane waves that this same phase factor is common to all the physical field variables of interest (such as displacement, dilatation, strain, and stress). For non-Cartesian coordinates, there is first the problem that separable solutions may not even exist. However, separable solutions *do* exist for cylindrical and spherical polars, which are the most important cases to examine for wave propagation in geophysics.

The second problem is that horizontal wavefunctions in (for example) cylindrical coordinates may differ from one physical variable to another. We saw a simple example of this in Box 6.6, where for u_z and τ_{zz} it was J_0 but for u_r and τ_{zr} it was J_1, in an example where potentials were axisymmetric ($m = 0$). To handle the general axisymmetric case, there is a dependence on azimuthal order number m as well as on k, and in (7.117) and (7.118) the solution we found was to work with three different horizontal wavefunctions, each of which is a vector.

With the plane-wave horizontal wavefunction, it is possible to synthesize functions of the horizontal spatial variable x by the Fourier inverse transform,

$$f(x) = \frac{1}{2\pi} \int_{-\infty}^{\infty} f(k) e^{+ikx}\, dk. \tag{1}$$

In Box 6.10 we developed similar results (the inverse Hankel transform) for the horizontal phase function J_m. It is then possible to combine these with the Fourier series

$$\begin{aligned} f(\phi) &= \frac{1}{2\pi} \sum_{m=-\infty}^{\infty} f(m) e^{im\phi} \\ f(m) &= \int_0^{2\pi} f(\phi) e^{-im\phi}\, d\phi \end{aligned} \tag{2}$$

to obtain an expansion for vector functions of (r, ϕ). This expansion is

$$\mathbf{f}(r,\phi) = \frac{1}{2\pi} \sum_{m=-\infty}^{\infty} \int_0^{\infty} \left[f_T(k,m)\mathbf{T}_k^m(r,\phi) + f_S(k,m)\mathbf{S}_k^m(r,\phi) + f_R(k,m)\mathbf{R}_k^m(r,\phi) \right] k\, dk, \tag{3}$$

in which $\mathbf{T}_k^m, \mathbf{S}_k^m, \mathbf{R}_k^m$ are the horizontal wavefunctions given in (7.118). For the Cartesian case, scalar horizontal wavefunctions have an orthogonality expressed as $\delta(k - k') = 1/(2\pi) \int_{-\infty}^{\infty} \exp\left[i(k - k')x\right]\, dx$. Our vector horizontal wavefunctions are orthogonal too, and an example for $\mathbf{T}_k^m$ is stated in (7.122). It follows that the coefficients in (3) are given by

$$\begin{aligned} f_T(k,m) &= \int_0^{2\pi} \int_0^{\infty} \mathbf{f}(r,\phi) \cdot \left[\mathbf{T}_k^m(r,\phi)\right]^* r\, dr\, d\phi, \\ f_S(k,m) &= \int_0^{2\pi} \int_0^{\infty} \mathbf{f}(r,\phi) \cdot \left[\mathbf{S}_k^m(r,\phi)\right]^* r\, dr\, d\phi, \\ f_R(k,m) &= \int_0^{2\pi} \int_0^{\infty} \mathbf{f}(r,\phi) \cdot \left[\mathbf{R}_k^m(r,\phi)\right]^* r\, dr\, d\phi. \end{aligned} \tag{4}$$

Interpreting (7.124) in Cartesians, we find from (7.123) that

$$\begin{aligned} f_T(k,m) &= -\int_{-\infty}^{\infty}\int_{-\infty}^{\infty}\frac{1}{k}\left(F_x\frac{\partial Y_k^{-m}}{\partial y}-F_y\frac{\partial Y_k^{-m}}{\partial x}\right)\delta(x)\,\delta(y)\,dx\,dy \\ &= -F_x e^{-im\pi/2}\frac{\partial}{\partial(ky)}J_m(ky)\bigg|_{y=0}+F_y\frac{\partial}{\partial(kx)}J_m(kx)\bigg|_{x=0}. \end{aligned} \tag{7.125}$$

Since J_m has a zero derivative at the origin except for $m=\pm1$, $f_T(k,m)=0$ unless $m=\pm1$. And $(d/d\zeta)J_{\pm1}(\zeta)=\pm\frac{1}{2}$ at $\zeta=0$, so that

$$\begin{aligned} f_T(k,1) &= \tfrac{1}{2}(F_y+iF_x), \\ f_T(k,-1) &= \tfrac{1}{2}(-F_y+iF_x). \end{aligned} \tag{7.126}$$

A similar method works for $f_S(k,m)$, using

$$\mathbf{S}_k^m(r,\phi)=k^{-1}\nabla Y_k^m(r,\phi) \tag{7.127}$$

and working in Cartesians to find $f_S(k,m)=0$ unless $m=\pm1$, and then

$$\begin{aligned} f_S(k,1) &= \tfrac{1}{2}(-F_x+iF_y), \\ f_S(k,-1) &= \tfrac{1}{2}(F_x+iF_y). \end{aligned} \tag{7.128}$$

For $f_R(k,m)$ we work directly in cylindrical coordinates:

$$f_R(k,m)=\int_0^{2\pi}\int_0^{\infty}F_z\frac{\delta(r)}{2\pi r}e^{-im\phi}J_m(kr)\,r\,dr\,d\phi,$$

so that $f_R(k,m)=0$ unless $m=0$, and then

$$f_R(k,0)=J_0(0)F_z=F_z. \tag{7.129}$$

All the expansion coefficients for our traction discontinuity have now been found, the only contributing terms being those with $m=0, m=\pm1$.

Our next step is to find the motion-stress vector $(l_1,l_2,r_1,r_2,r_3,r_4)$ that has prescribed discontinuities f_T, f_S, f_R in traction components l_2, r_3, r_4 (respectively). Of course, our solution must satisfy the equations of motion and the free surface condition

$$l_2=r_3=r_4=0 \qquad \text{on } z=0. \tag{7.130}$$

It must also satisfy the radiation condition, requiring that l_1, r_1, and r_2 must contain only downward-traveling waves as $z\to\infty$, or, if the wavenumber is large enough so that $\gamma=\sqrt{k^2-\omega^2/\alpha^2}$ and $\nu=\sqrt{k^2-\omega^2/\beta^2}$ become real (positive), then all of

$$l_1, r_1, r_2 \to 0 \qquad \text{as } z\to\infty. \tag{7.131}$$

When the surface-wave eigenvalue problem was introduced in Section 7.2, we found that a continuous solution of the equations of motion did not satisfy the homogeneous boundary conditions (7.130) and (7.131) unless, for given ω, k took on special discrete values. It is therefore interesting to find that when a traction discontinuity at the source depth is added to the problem, it becomes possible to find a solution for *every* value of k. We give this solution below, noting here that once the motion-stress vector problem is solved as a function of (k, m, z, ω) it becomes possible to write the steady-state displacement due to point force $\mathbf{F}\exp(-i\omega t)$ in the form

$$\mathbf{u}(r,\phi,z,t) = \exp(-i\omega t)\frac{1}{2\pi}\sum_{m=-\infty}^{\infty}\int_0^{\infty} k\left[l_1(k,m,z,\omega)\mathbf{T}_k^m(r,\phi) + r_1(k,m,z,\omega)\mathbf{S}_k^m(r,\phi) + r_2(k,m,z,\omega)\mathbf{R}_k^m(r,\phi)\right] dk. \tag{7.132}$$

Let us first find the solution $l_1(k, m, z, \omega)$, recapitulating that

$$\mathbf{l} = \begin{pmatrix} l_1 \\ l_2 \end{pmatrix}$$

satisfies

$$\frac{\partial \mathbf{l}}{\partial z} = \begin{pmatrix} 0 & \mu^{-1} \\ -\omega^2\rho + k^2\mu & 0 \end{pmatrix}\mathbf{l}, \tag{7.24 again}$$

with $l_2 = 0$ on $z = 0$. As $z \to \infty$ we have a radiation condition, which is that:

$$\begin{aligned} &\textit{either } \mathbf{l} \text{ becomes a downgoing wave (a homogeneous body wave)} \\ &\textit{or} \quad \mathbf{l} \to \mathbf{0} \text{ (an inhomogeneous wave),} \end{aligned} \tag{7.133}$$

depending on the value of k/ω (the horizontal slowness). Finally

$$\mathbf{l}\Big|_{z=h^+} - \mathbf{l}\Big|_{z=h^-} = \begin{pmatrix} 0 \\ f_T(k,m) \end{pmatrix}. \tag{7.134}$$

We shall construct a discontinuous solution $\mathbf{l}'$ that satisfies (7.134) and then construct a continuous solution $\mathbf{l}''$ such that a linear combination

$$\mathbf{l} = \mathbf{l}' + \frac{\mathbf{l}''}{\Delta(k)} \tag{7.135}$$

satisfies *all* the required conditions. Both $\mathbf{l}'$ and $\mathbf{l}''$ solve the equation of motion, and boundary conditions are

$$\begin{aligned} &l_1' = 0 \quad \text{and} \quad l_2' = 0 \qquad \text{for all } z > h, \\ &l_1' = 0 \quad \text{and} \quad l_2' = -f_T \quad \text{at } z = h - 0, \end{aligned} \tag{7.136}$$

$$\begin{aligned} &l_1'' \to \text{downgoing} \quad \text{or} \quad l_1'' \to 0 \qquad \text{as } z \to \infty, \\ &l_2'' = -\Delta(k) l_2' \quad \text{at } z = 0. \end{aligned} \tag{7.137}$$

It can readily be verified that $\mathbf{l}$ given by (7.135), with $\mathbf{l}'$ and $\mathbf{l}''$ as defined above, does satisfy all the required conditions (7.133) and (7.134). The radiation condition for l_1'' in (7.137), as $z \to \infty$, takes two forms, depending on the value of the horizontal slowness k/ω. If this value is small enough, then l_1'' at great depth is a homogeneous downward-traveling body wave. But if $(k/\omega) > \lim_{z\to\infty}(1/\beta(z))$, then l_1'' is an inhomogeneous wave tending to zero as $z \to \infty$. The function $\Delta(k)$ is defined so that the surface shear stress in the discontinuous solution $\mathbf{l}'$, when multiplied by $-\Delta(k)$, exactly equals the surface shear stress in the continuous solution. But if k happens to be a surface-wave eigenvalue, the surface stress vanishes in the continuous solution $\mathbf{l}''$. It follows that $\Delta(k)$ must be zero when k is an eigenvalue and $\mathbf{l}''$ is a surface-wave eigenfunction. No downgoing wave (as $z \to \infty$) is allowed in this case, since $\mathbf{l}''$ satisfies a wave equation with homogeneous boundary conditions and no source term. Eigenvalues of k must therefore be large enough so that $l_1'' \to 0$ as $z \to \infty$, to prevent the downward loss of energy that would be carried by a body wave.

In Figure 7.9 we give more detail on obtaining $\mathbf{l}'$ and $\mathbf{l}''$. Constructing $\mathbf{l}$ via (7.135), we can now use (7.132) to synthesize displacement as

$$\mathbf{u}(r,\phi,z,t) = \exp(-i\omega t)\frac{1}{2\pi}\sum_m \int_0^\infty k\left[l_1' + \frac{l_1''}{\Delta(k)}\right]\mathbf{T}_k^m(r,\phi)\,dk. \tag{7.138}$$

This solution includes the body waves, head waves, etc., as well as the surface waves—in fact, it is the complete synthetic seismogram for a point source $\mathbf{F}\exp(-i\omega t)$. For a point source $\mathbf{F}(t)$ in the time domain we can then obtain the time domain displacement by summing the solution (7.138) over frequency. This is the overall approach adopted in the "Direct Solution Method" of Geller and others (Cummins *et al.*, 1994a, b), who obtain the integrand factor [. . .] of (7.138) by use of basis functions whose coefficients (see (7.79)) are determined by an equation of the type (7.84). But it is instructive to identify the surface-wave contributions in the complete displacement (7.138), since they turn out to have a simple form, and this will be our next goal. Recall from (7.125) that contributions come only from $m = \pm 1$ if the source is a point force.

The integrand in (7.138) has poles at $\Delta(k) = 0$. Since we have chosen for Δ a function that vanishes when k is an eigenvalue, the contribution from these poles will give the normal modes, or Love waves in this case. Our evaluation of the integral will follow some of the steps taken in the discussion of (6.12)–(6.16) and (6.31). Thus we replace $J_m(kr)$ by $\frac{1}{2}[H_m^{(1)}(kr) + H_m^{(2)}(kr)]$, converting the integral of $H_m^{(2)}$ over positive k to an integral of $H_m^{(1)}$ over negative k so that (7.138) becomes an integral over the whole real k-axis. We write $\mathbf{T}_k^m$ with J_m replaced by $\frac{1}{2}H_m^{(1)}$ as $\mathbf{T}_k^{m(1)}$, and then the pole contributions will be

$$\mathbf{u}^{\text{LOVE}} = \exp(-i\omega t)\sum_m\sum_n ik_n \frac{l_1''(k_n, m, z, \omega)}{\left(\dfrac{\partial\Delta}{\partial k}\right)_{k=k_n}}\mathbf{T}_{k_n}^{m(1)}(r,\phi), \tag{7.139}$$

where $k_n (n = 0, 1, 2, \ldots)$ are the positive real roots of $\Delta(k) = 0$. (Negative real roots do not contribute, by an argument based on the effect of slight anelasticity. Poles on the negative real axis move down into the third quadrant, and are outside a closed contour formed

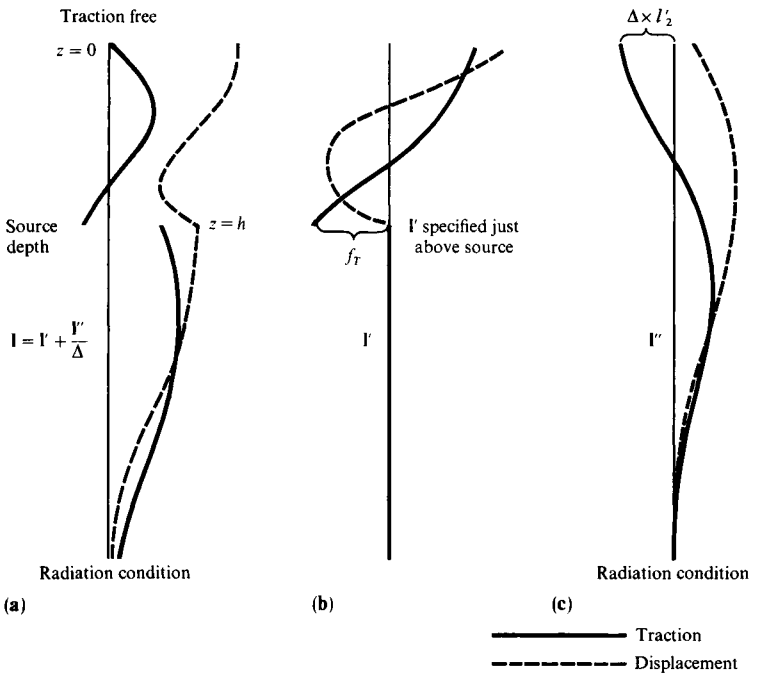

FIGURE **7.9**

(**a**) Diagrammatic representation of properties of the SH-wave with a traction discontinuity at $z = h$. This wave is $\mathbf{l}$, satisfying homogeneous conditions at $z = 0$ and $z = \infty$. (**b**) The solution $\mathbf{l}'$ is zero below $z = h$. For given k, $\mathbf{l}'$ can be obtained above the source by taking initial values

$$\mathbf{l}'\Big|_{z=h^-} = \begin{pmatrix} 0 \\ -f_T \end{pmatrix}$$

and integrating $d\mathbf{l}'/dz = \mathbf{A}\mathbf{l}'$ upward to $z = 0$. However, for surface-wave excitation, we shall find that $\mathbf{l}'$ does not actually have to be evaluated. (**c**) The solution $\mathbf{l}''$ is continuous. It can be found (for given k) by taking a solution that satisfies the radiation condition at great depth and integrating the equation of motion upward to $z = 0$. This solution is multiplied (at all depths) by a scalar constant, chosen so that the surface traction becomes $-\Delta(k) \times$ surface traction in $\mathbf{l}' = -\Delta(k)l'_2$.

Note that $\mathbf{l} = \mathbf{l}' + \Delta^{-1}\mathbf{l}''$ is defined for all choices of k. For small enough wavenumbers, downward radiation of energy is possible (body waves). With large enough wavenumber, however, there is exponential decay of $\mathbf{l}$ (and $\mathbf{l}''$) with depth. It is this situation that is shown in the figure.

in the upper half plane, whereas poles on the positive real k-axis move up into the first quadrant, and their residues *are* picked up. We shall discuss these integration paths further, and associated branch cuts and body waves, in Sections 7.6 and 9.3.)

The evaluation of $(\partial\Delta/\partial k)_{k=k_n}$ can be done very simply by using the variational principles of Section 7.3. From (7.68), we find for a continuous solution $\mathbf{l}''$ of the equations of motion that

$$\frac{1}{2}[l''_1 l''_2]_0^\infty = -\omega^2 I_1 + k^2 I_2 + I_3.$$

Then, from boundary conditions (7.137),

$$\frac{1}{2}\Delta(k)(l_2'l_1'')_{z=0} = -\omega^2 I_1 + k^2 I_2 + I_3.$$

If k is nearly an eigenvalue, then $\mathbf{l}''$ is nearly an eigenfunction. Because of the stationarity of $(-\omega^2 I_1 + k^2 I_2 + I_3)$ for slight departures of $\mathbf{l}''$ from a true eigenfunction (see (7.67)), it follows that the change in Δ due to a perturbation in k can be written as

$$\left(\frac{\partial \Delta}{\partial k}\right)_{k=k_n} (l_2'l_1'')_{z=0} = 4k_n I_2 = 4k_n c U I_1, \tag{7.140}$$

where c and U are the phase and group velocity corresponding to ω and k_n (see (7.70)). We can even eliminate l_2' at $z = 0$ from the above equation, because it is easy to show from the equations of motion that $(d/dz)(l_1'l_2'' - l_1''l_2') = 0$. Evaluating the constant $l_1'l_2'' - l_1''l_2'$ at $z = 0$ and $z = h - 0$, and using (7.136) and (7.137), we find

$$l_1''l_2'|_{z=0} = -f_T(k_n, m) l_1''|_{z=h}. \tag{7.141}$$

Assembling (7.139)–(7.141), we now find

$$\mathbf{u}^{\text{LOVE}} = -i \exp(-i\omega t) \sum_m \sum_n \frac{f_T(k_n, m) l_1''(h) l_1''(z)}{4cUI_1} \mathbf{T}_{k_n}^{m(1)}. \tag{7.142}$$

The sum over m is easy to carry out, because $f_T = 0$ unless $m = \pm 1$ (see (7.126)). Since l_1'' in (7.142) is merely a particular Love-wave mode, we shall drop the primes and use l_1; i.e., we revert to our original notation for individual modes. We also replace $\mathbf{T}_k^{m(1)}$ by the asymptotic form given in (7.119). Our final result, giving the excitation of Love modes by a point force $\mathbf{F} \exp(-i\omega t)$ applied at $r = 0, z = h$, is then

$$\begin{aligned} \mathbf{u}^{\text{LOVE}} = \exp(-i\omega t) \sum_n & \frac{(F_y \cos\phi - F_x \sin\phi) l_1(k_n, h, \omega)}{8cUI_1} \\ & \times \sqrt{\frac{2}{\pi k_n r}} \left[l_1(k_n, z, \omega)\hat{\boldsymbol{\phi}}\right] \exp\left[i\left(k_n r + \frac{\pi}{4}\right)\right], \end{aligned} \tag{7.143}$$

where $I_1 = \frac{1}{2}\int_0^\infty \rho \left[l_1(k_n, z, \omega)\right]^2 dz$ and $l_1(k_n, z, \omega)$ is a continuous eigenfunction.

For Rayleigh waves, following similar steps, the final result is

$$\begin{aligned} \mathbf{u}^{\text{RAYLEIGH}} = \exp(-i\omega t) \sum_n & \frac{F_z r_2(k_n, h, \omega) + i(F_x \cos\phi + F_y \sin\phi) r_1(k_n, h, \omega)}{8cUI_1} \\ & \times \sqrt{\frac{2}{\pi k_n r}} \left[r_1(k_n, z, \omega) e^{-i\pi/4} \hat{\mathbf{r}} + r_2(k_n, z, \omega) e^{i\pi/4} \hat{\mathbf{z}}\right] \exp(ik_n r), \end{aligned} \tag{7.144}$$

where $I_1 = \frac{1}{2}\int_0^\infty \rho(r_1^2 + r_2^2)\, dz$.

The compact result, i.e., the pole residue in terms of $1/(cUI_1)$ in equations (7.143) and (7.144), was given for Love waves by Keilis-Borok and Yanovskaya (1962). The corresponding result for Rayleigh waves was guessed at by Harkrider and Anderson (1966) and verified by them numerically. Saito (1967) was the first to obtain the same compact form for the excitation of free oscillations of the whole Earth by a point source (a subject we take up in the next chapter).

Comparison with the line-source solutions given in (7.107), (7.109), and (7.110) shows a remarkable similarity between the two- and three-dimensional solutions. The solution for a point source is advanced in phase by $\pi/4$ and contains more high frequencies by a factor proportional to $\omega^{1/2}$, as compared to the line source. This is easily understood because a line source may be considered as a superposition (and hence spatial smoothing) of the point source. The basic simplicity of the solutions, i.e., the separation of source, medium, and receiver factors, applies to both cases (see also Box 6.1).

To coordinate these results for steady-state displacements with our notation for the Green function, note that we can drop an $\exp(-i\omega t)$ factor in (7.143) and (7.144), and then regard the left-hand side as displacement in the frequency domain due to a point force $\mathbf{F}(\omega)$ acting at $\xi = (0, 0, h)$. It follows that

$$u_i(\mathbf{x}, \omega) = F_p(\omega) G_{ip}(\mathbf{x}; \xi; \omega). \tag{7.145}$$

By $\mathbf{G}(\mathbf{x}; \xi; \omega)$ we mean the Fourier transform of the t-dependent $\mathbf{G}(\mathbf{x}, t; \xi, \tau)$, with τ fixed at zero. Convolutions equivalent to (7.145) appeared frequently in Chapters 3 and 4. Comparisons with (7.143) and (7.144) now show that surface-wave excitation is described by Love and Rayleigh wave terms in the Green function. Specifically, these are

$$\mathbf{G}^{\text{LOVE}} = \sum_n \frac{l_1(z) l_1(h)}{8cUI_1} \begin{pmatrix} \sin^2\phi & -\sin\phi\cos\phi & 0 \\ -\sin\phi\cos\phi & \cos^2\phi & 0 \\ 0 & 0 & 0 \end{pmatrix} \sqrt{\frac{2}{\pi k_n r}} \exp\left[i\left(k_n r + \frac{\pi}{4}\right)\right] \tag{7.146}$$

and

$$\mathbf{G}^{\text{RAYLEIGH}} = \sum_n \frac{1}{8cUI_1} \begin{pmatrix} r_1(z)r_1(h)\cos^2\phi & r_1(z)r_1(h)\cos\phi\sin\phi & -ir_1(z)r_2(h)\cos\phi \\ r_1(z)r_1(h)\sin\phi\cos\phi & r_1(z)r_1(h)\sin^2\phi & -ir_1(z)r_2(h)\sin\phi \\ ir_2(z)r_1(h)\cos\phi & ir_2(z)r_1(h)\sin\phi & r_2(z)r_2(h) \end{pmatrix} \times \sqrt{\frac{2}{\pi k_n r}} \exp\left[i\left(k_n r + \frac{\pi}{4}\right)\right]. \tag{7.147}$$

7.5 Love and Rayleigh Waves from a Point Source with Arbitrary Seismic Moment

If surface waves are excited by a point source described only by its moment tensor $\mathbf{M}$, then one way to study the excitation is in terms of the equivalent body force, for which we can use the methods of the previous section. This is Saito's (1967) approach, and the (k, m) expansion of the traction discontinuity (7.121) is now found to have nonzero terms from

$m = \pm 2$. However, we have already obtained the Love and Rayleigh components of Green's function, so that a quicker route is simply to use the formula

$$u_i(\mathbf{x}, \omega) = M_{pq}(\omega) \frac{\partial}{\partial \xi_q} G_{ip}(\mathbf{x}; \boldsymbol{\xi}; \omega). \qquad \text{(3.23 again)}$$

In differentiating $\mathbf{G}^{\text{LOVE}}$ and $\mathbf{G}^{\text{RAYLEIGH}}$, we shall retain only the largest terms, namely, those that involve depth derivatives of the vertical eigenfunctions or horizontal derivatives of $\exp(ik_n r)$. Using $\partial r/\partial \xi_1 = -\cos\phi$, $\partial r/\partial \xi_2 = -\sin\phi$, we find, for example, that

$$\begin{aligned} u_x^{\text{LOVE}}(\mathbf{x}, \omega) = & -\sum_n \sin\phi \frac{l_1(z)}{8cUI_1} \sqrt{\frac{2}{\pi k_n r}} \exp\left[i\left(k_n r + \frac{\pi}{4}\right)\right] \\ & \times \left\{ ik_n l_1(h)[M_{xx} \sin\phi \cos\phi - M_{yx} \cos^2\phi + M_{xy} \sin^2\phi \right. \\ & \left. - M_{yy} \sin\phi \cos\phi] - \left.\frac{dl_1}{dz}\right|_h [M_{xz} \sin\phi - M_{yz} \cos\phi] \right\}. \end{aligned} \qquad (7.148)$$

The derivation of (7.148) is similar to our derivation of (4.29) via (4.28), although we are now keeping only the far-field terms. A similar expression can be found for u_y^{LOVE}, and it is clear that $u_z^{\text{LOVE}} = 0$, so that a vector formula can be given as

$$\mathbf{u}^{\text{LOVE}}(\mathbf{x}, \omega) = \sum_n \frac{l_1(z)}{8cUI_1} \sqrt{\frac{2}{\pi k_n r}} \exp\left[i\left(k_n r + \frac{\pi}{4}\right)\right] \{\quad\} \hat{\boldsymbol{\phi}}, \qquad (7.149)$$

where { } is the same as the bracket { } of (7.148).

For Rayleigh waves, we find from the last row of components in (7.147) that

$$\begin{aligned} u_z^{\text{RAYLEIGH}} = & \sum_n \frac{r_2(z)}{8cUI_1} \sqrt{\frac{2}{\pi k_n r}} \exp\left[i\left(k_n r + \frac{\pi}{4}\right)\right] \times \left\{ k_n r_1(h)[M_{xx} \cos^2\phi \right. \\ & + (M_{xy} + M_{yx}) \sin\phi \cos\phi + M_{yy} \sin^2\phi] + i \left.\frac{dr_1}{dz}\right|_h [M_{xz} \cos\phi \\ & \left. + M_{yz} \sin\phi] - ik_n r_2(h)[M_{zx} \cos\phi + M_{zy} \sin\phi] + \left.\frac{dr_2}{dz}\right|_h M_{zz} \right\}. \end{aligned} \qquad (7.150)$$

For the radial (i.e., horizontal) component of Rayleigh-wave motion, one finds

$$u_r^{\text{RAYLEIGH}} = \sum_n \frac{r_1(z)}{8cUI_1} \sqrt{\frac{2}{\pi k_n r}} \exp\left[i\left(k_n r - \frac{\pi}{4}\right)\right] \{\quad\}, \qquad (7.151)$$

where { } is the same as the bracket { } of (7.150). It follows from the phase shift between (7.150) and (7.151), and accounting for the different signs of $r_1(z)$ and $r_2(z)$ at shallow

depths (see Box 7.7), that the Rayleigh wave here has retrograde particle motion, as we expect.

Note that these formulas for surface-wave excitation in terms of the moment tensor are appropriate not only for small dislocation sources, but also for small volume sources. To see this, consider a volume source with moment density $m_{pq} = \partial M_{pq}/\partial V$. This is the moment density per unit volume described in Section 3.4, and we start with an equation equivalent to (3.31) for the x_i-component of displacement:

$$u_i(\mathbf{x}, \omega) = \int_V m_{pq}(\eta, \omega) \frac{\partial}{\partial \eta_q} G_{ip}(\mathbf{x}; \eta; \omega)\, dV(\eta).$$

If the moment density is concentrated at a point ξ, then

$$m_{pq}(\eta, \omega) = M_{pq}(\omega)\, \delta(\eta - \xi)$$

as η varies within V, and the above representation does indeed give $u_i = M_{pq} G_{ip,q}$ again.

As an example, let us first consider the case of an explosive source. Regarded as a point source, the moment tensor for this isotropic source is a diagonal matrix with equal elements $M_{xx} = M_{yy} = M_{zz} = M_{\mathrm{I}}$. In this case it is apparent that Love waves are not excited. Rayleigh waves are azimuthally isotropic, and the vertical displacement is given by (7.150) as

$$u_z(\mathbf{x}, \omega) = \sum_n \frac{r_2(z)}{8cUI_1} \sqrt{\frac{2}{\pi k_n r}} \left(\frac{-1}{i\omega}\right) \exp\left[i\left(k_n r + \frac{\pi}{4}\right)\right] \left\{k_n r_1(h) + \left.\frac{dr_2}{dz}\right|_h\right\}, \quad (7.152)$$

where we have assumed that $M_{\mathrm{I}}(t)$ is a unit-valued step with the physical units of moment (often taken as dyn-cm), so that $M_{\mathrm{I}}(\omega) = -1/i\omega$.

Using the phase velocity, group velocity, and eigenfunctions obtained earlier for Gutenberg's continental Earth model (see Box 7.7), it is a simple matter to compute the amplitude of fundamental Rayleigh waves from an explosive source buried at various depths. Only the first term (i.e., $n = 0$) is taken in (7.152), which has units of cm-s if $M_{\mathrm{I}}(t) = H(t)$ dyn-cm. Numerical results at an epicentral distance of 2000 km are shown in Figure 7.10, and it is clear that Rayleigh-wave excitation from an explosive source decreases smoothly with depth.

On the other hand, an earthquake source with the moment tensor of double-couple symmetry (3.20) generates a Rayleigh-wave spectrum with complicated dependences on source mechanism and focal depth. The case of pure strike–slip motion on a vertical fault and the case of a pure dip–slip motion along a fault plane with dip angle 45° are shown in Figures 7.11 and 7.12, respectively. In both cases, the receiver is located at an epicentral distance of 2000 km and azimuth 30° from the fault strike, and a steplike change of double-couple moment by 1 dyn-cm is assumed for both Rayleigh and Love waves. The Cartesian components of $\mathbf{M}$, needed in (7.149)–(7.150), are obtained from Box 4.4. Although the Love-wave spectrum decreases with focal depth smoothly in both cases, the Rayleigh-wave spectrum shows strong dependence on both the source mechanism and the focal depth, offering a powerful method for determining these source parameters.

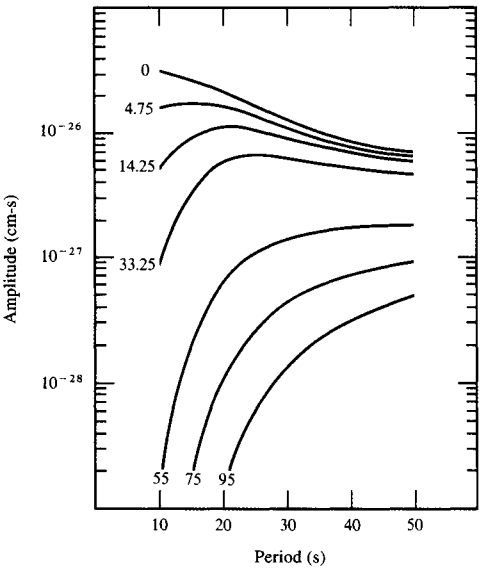

FIGURE **7.10**
Amplitude spectra of Rayleigh waves (vertical displacement) at $\Delta = 2000$ km for an underground explosion with unit seismic moment (each diagonal element). The number attached to each curve represents the source depth in kilometers. [Reproduced from Tsai and Aki (1971); copyright by the American Geophysical Union.]

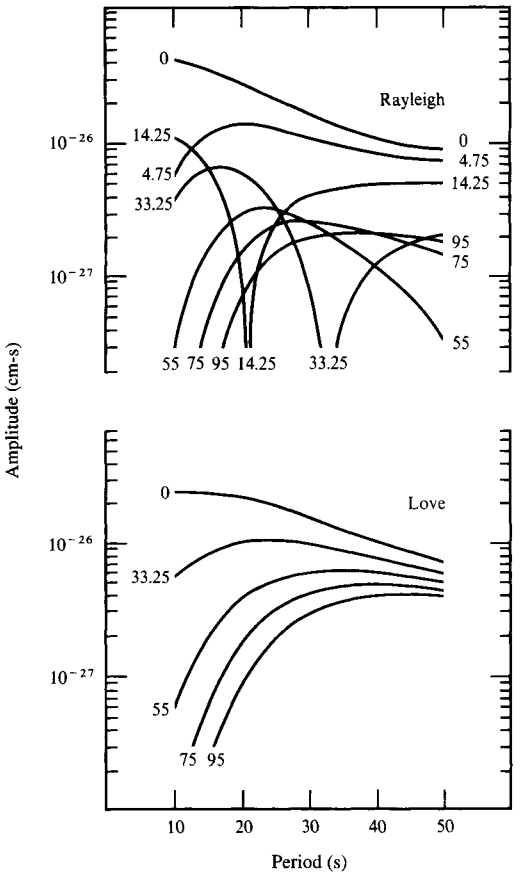

FIGURE **7.11**
Amplitude spectra of Rayleigh (vertical) and Love waves at $\Delta = 2000$ km and $\phi = 30°$ from the fault strike for a vertical strike–slip earthquake with unit step-function seismic moment. The number attached to each curve represents the source depth in kilometers. [Reproduced from Tsai and Aki (1971); copyright by the American Geophysical Union.]

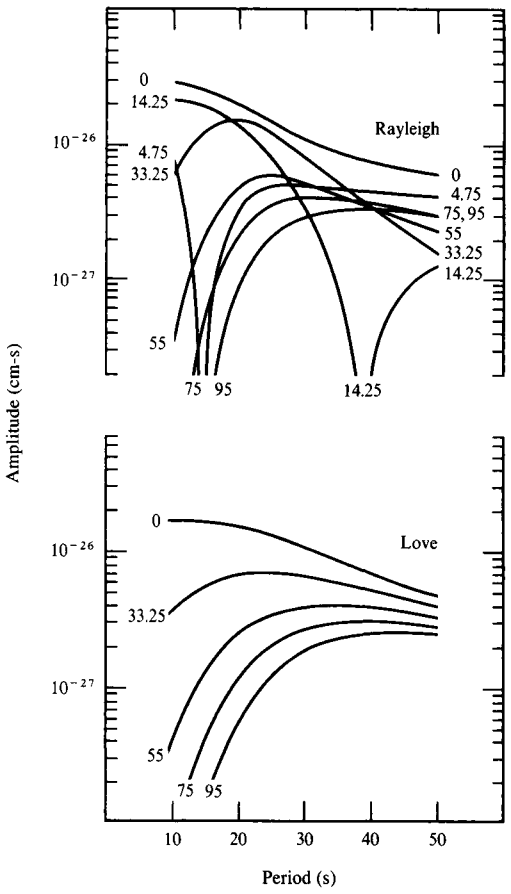

FIGURE **7.12**
Amplitude spectra of Rayleigh (vertical) and Love waves at $\Delta = 2000$ km and $\phi = 30°$ from the fault strike for a dip–slip fault with dip angle 45° and unit step-function seismic moment. The number by each curve gives the source depth in kilometers. [Reproduced from Tsai and Aki (1971); copyright by the American Geophysical Union.]

7.6 Leaky Modes

So far in this chapter, we have considered only surface waves or normal modes that arise as residue contributions at poles in the wavenumber plane. The solution for the normal mode vanishes at and beyond the cut-off frequency, because the poles move from the "top" Riemann sheet (where the imaginary part of vertical wavenumber is chosen positive to assure the radiation condition at an infinite depth) to lower sheets. A complete analytic or asymptotic solution requires evaluation of additional integrals around branch cuts, such as those shown in Figure 6.12 for a half-space problem. In this section, we shall show that the branch-cut integrals may be transformed into a sum of residue contributions from poles in the lower sheets, which, unlike the normal modes, attenuate exponentially with time because of leakage to the underlying half-space. For this reason, they are called leaky modes.

We shall study leaky modes for the simplest layered medium, namely, a liquid layer overlying a liquid half-space. Wave generation and propagation in this medium were extensively studied by Pekeris (1948) in order to explain observations on ocean acoustics obtained by Ewing and Worzel (1948). Here we shall follow Rosenbaum (1960) in deriving a complete representation of the total wave field as a sum of normal modes and leaky modes. The result is useful to obtain simple approximate formulas valid for a large lapse of time.

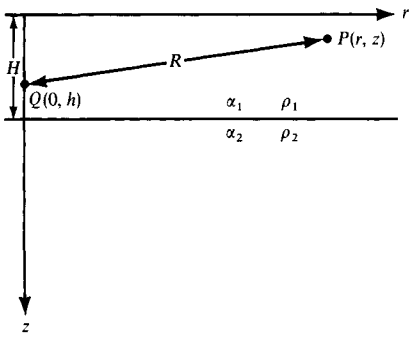

FIGURE **7.13**
Parameters for a point source at Q in a fluid layer over a fluid half-space.

Consider a liquid layer with thickness H, density ρ_1, and acoustic wave velocity α_1 overlying a liquid half-space with density ρ_2 and velocity α_2 (Fig. 7.13). We shall assume a spherical pressure source located at a depth h within the layer. We shall use the same coordinates and start with the same source expressions as in the problem of two liquid half-spaces in contact, studied in Section 6.2. We shall first write the primary pressure waves in the form (6.12),

$$P^{\text{inc}} = \frac{A}{R} \exp\left[i\omega\left(\frac{R}{\alpha_1} - t\right)\right], \tag{7.153}$$

where R is the distance between the source point Q and the receiver point P. We use a trial form of solution similar to (6.13) and (6.14), with additional terms representing waves going both ways in the layer, and determine the unknown factor in integrands to meet the boundary conditions. The boundary conditions are (i) vanishing pressure at $z = 0$, (ii) continuity of pressure and vertical displacement across the interface at $z = H$, and (iii) no waves coming from $z = +\infty$. Then (for $0 \le z \le h$) the total pressure field in the layer can be written as

$$2\exp(-i\omega t)\int_0^\infty J_0(kr)k\frac{\sinh \gamma_1 z}{\gamma_1}F_1(k,\omega)\,dk, \tag{7.154}$$

where

$$F_1(k,\omega) = A\frac{\rho_2\gamma_1\cosh\left[\gamma_1(H-h)\right] + \rho_1\gamma_2\sinh\left[\gamma_1(H-h)\right]}{\rho_2\gamma_1\cosh(\gamma_1 H) + \rho_1\gamma_2\sinh(\gamma_1 H)}. \tag{7.155}$$

Here $\gamma_i = \sqrt{k^2 - \omega^2/\alpha_i^2}$, and the signs of γ_1 and γ_2 are chosen so that $\text{Re}\,\gamma_1 \ge 0$, $\text{Re}\,\gamma_2 \ge 0$. A convenient rule to remember is that $i\gamma_2$ has real and imaginary parts that are positive or zero if the radiation condition is satisfied.

In order to derive the modal solution for frequencies below the cut-off frequency, it is necessary to consider a transient source with a continuous spectrum. Let us consider primary pressure waves of the form

$$\begin{aligned} P^{\text{inc}}(t) &= \frac{A}{R}\exp\left[i\omega\left(\frac{R}{\alpha_1} - t\right)\right], \qquad t > \frac{R}{\alpha_1}, \\ &= 0, \qquad t < \frac{R}{\alpha_1}. \end{aligned} \tag{7.156}$$

Since the above source can be expressed as a Fourier inverse integral via

$$P^{\text{inc}}(t) = \frac{A}{2\pi R}\int_{-\infty}^{\infty} \frac{\exp\left[-i\omega\left(t - \dfrac{R}{\alpha_1}\right)\right]}{\sigma - i\omega}\, d\omega, \tag{7.157}$$

the corresponding total pressure field can be obtained by an integral of (7.154) with respect to ω:

$$P^{\text{total}}(t) = \frac{1}{\pi}\int_{-\infty}^{\infty} \frac{\exp(-i\omega t)}{\sigma - i\omega}\, d\omega \int_0^{\infty} J_0(kr)k\frac{\sinh \gamma_1 z}{\gamma_1} F_1(k,\omega)\, dk. \tag{7.158}$$

Since $P^{\text{total}}(t)$ is real, its Fourier transforms for $\pm\omega$ are complex conjugate, and we can rewrite (7.158) as

$$P^{\text{total}}(t) = \frac{2}{\pi}\text{Re}\int_0^{\infty} \frac{\exp(-i\omega t)}{\sigma - i\omega}\, d\omega \int_0^{\infty} J_0(kr)k\frac{\sinh \gamma_1 z}{\gamma_1} F_1(k,\omega)\, dk. \tag{7.159}$$

Now let us change the order of integration and first evaluate the integral with respect to ω by deforming the path of integration in the complex ω-plane. Since the integrand is an even function of γ_1, $\omega = \pm\alpha_1 k$ is not a branch point, and the only branch cuts in the problem are those associated with γ_2. The branch cuts around $\omega = \pm\alpha_2 k$ are made along Re $\gamma_2 = 0$, which corresponds to that part of the real ω-axis for which $|\text{Re }\omega| > \alpha_2 k$, as shown in Figure 7.14.

Because of the radiation condition, our original integration path lies on the top sheet, for which Re $\gamma_2 > 0$. We next show that only a finite number of real roots of

$$f_1(k,\omega) \equiv \rho_2\gamma_1 \cosh \gamma_1 H + \rho_1\gamma_2 \sinh \gamma_1 H = 0 \tag{7.160}$$

exist on the top sheet. Putting

$$i\gamma_1 H = p_1 + iq_1, \qquad i\gamma_2 H = p_2 + iq_2,$$

where p_1, p_2, q_1, q_2 are real, substituting them into $f_1(\omega, k)$, and taking its imaginary part, we find that

$$\frac{\sinh q_1 \cosh q_1}{\cos^2 p_1 \cosh^2 q_1 + \sin^2 p_1 \sinh^2 q_1} + \frac{\rho_2}{\rho_1}\frac{p_1p_2 + q_1q_2}{p_2^2 + q_2^2} = 0 \tag{7.161}$$

if (7.160) holds. Since $\gamma_1^2 - \gamma_2^2 = \omega^2/\alpha_2^2 - \omega^2/\alpha_1^2$ is real, $p_1q_1 = p_2q_2$. Therefore,

$$\frac{p_1p_2 + q_1q_2}{p_2^2 + q_2^2} = \frac{q_1}{q_2}\cdot\frac{p_1^2 + q_2^2}{p_2^2 + q_2^2}.$$

Substituting this into (7.161), we see that the first and second terms of (7.161) have the same sign if $q_2 > 0$. Thus the root of $f_1(\omega, k)$ cannot exist on the top sheet, where

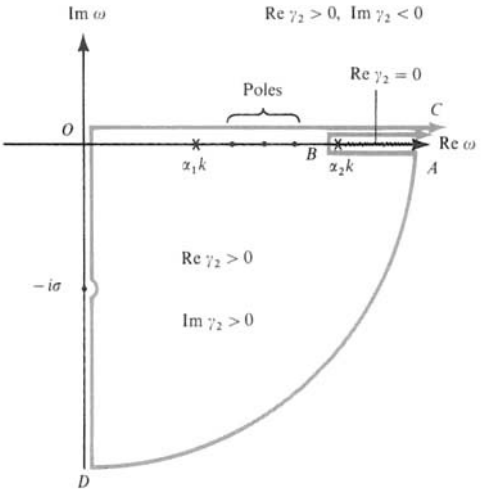

FIGURE **7.14**
Poles (closed circles) and branch points (crosses) in the ω-plane.

$q_2 = \text{Re}\ \gamma_2 H > 0$, except when $q_1 = \text{Re}\ \gamma_1 H = 0$. When $\text{Re}\ \gamma_1 = 0$, the roots are real and the corresponding phase velocity c is given by the formula

$$\tan\ \omega H \sqrt{\frac{1}{\alpha_1^2} - \frac{1}{c^2}} = -\frac{\rho_2 \sqrt{\dfrac{1}{\alpha_1^2} - \dfrac{1}{c^2}}}{\rho_1 \sqrt{\dfrac{1}{c^2} - \dfrac{1}{\alpha_2^2}}}. \tag{7.162}$$

This is similar to the dispersion equation (7.6) for Love waves but with an important difference. Because of the negative sign on the right side, the zeroth-order tangent curve does not contribute a root (see Fig. 7.2). Thus *all* the modes in a layered acoustic medium have finite cut-off frequencies, and we shall take $n = 1$ as the lowest mode (rather than $n = 0$). The cut-off frequency ω_{cn} for the nth mode is given by setting $c = \alpha_2$ in (7.162):

$$\omega_{cn} = \frac{\pi(n - \frac{1}{2})}{H \sqrt{\dfrac{1}{\alpha_1^2} - \dfrac{1}{\alpha_2^2}}}. \tag{7.163}$$

The corresponding cut-off wavenumber is given by

$$k_{cn} = \frac{\omega_{cn}}{\alpha_2}. \tag{7.164}$$

For a given k, there are only a finite number of roots with $k_{cn} \leq k$ that appear on the top sheet, as shown in Figure 7.14. In addition to these poles on the real axis, another pole due to the source-time function exists at $-i\sigma$ on the negative imaginary axis.

Now let us deform the initial integration path OC into $ODABC$, as shown in Figure 7.14, in such a way that

$$\int_{OC} = \int_{OD} + \int_{DA} + \int_{ABC} - 2\pi i \sum \text{residues at poles.}$$

For a large t, because of the factor $\exp(-i\omega t)$, the integrand of (7.159) vanishes on DA as the radius of the arc approaches infinity. On the other hand, along the path OD, the integrand is purely imaginary except along the small semicircle around $-i\sigma$, and its only contribution is minus half the residue at $-i\sigma$ times $2\pi i$. We shall write this as

$$P_L = \int_{OD} = 2e^{-\sigma t} \int_0^\infty J_0(kr) k \frac{\sinh \gamma_1(\sigma) z}{\gamma_1(\sigma)} F_1(k, -i\sigma)\, dk \tag{7.165}$$

where $\gamma_1(\sigma) = \sqrt{\sigma^2/\alpha_1^2 + k^2}$. This represents nonoscillatory motion with time dependence identical to the source function. Although this expression violates the notion of causality associated with solutions to the acoustic equation (motion starts before the arrival of primary waves), the result is valid for the large times t in which we are primarily interested.

The normal-mode solution is a sum of residues from poles on the real axis, given by

$$\begin{aligned} P_N &= -2\pi i \sum \text{residues} \\ &= 4 \operatorname{Re} \sum_n \int_{k_{cn}}^\infty J_0(kr) k \sinh(\gamma_1 z) \frac{\exp(-i\gamma_n t)}{\omega_n + i\sigma} F_2(k, \omega_n)\, dk, \end{aligned} \tag{7.166}$$

where

$$F_2(k, \omega_n) = \frac{A\rho_2 \sinh(\gamma_1 h)}{\sinh(\gamma_1 H) \left[\dfrac{\partial}{\partial \omega} f_1(k, \omega)\right]_{\omega=\omega_n}}. \tag{7.167}$$

Here ω_n are the roots of $f_1(k, \omega_n) = 0$, and k_{cn} is the cut-off wavenumber defined in (7.164). The integration limit is imposed because, for $k < k_{cn}$, the nth pole does not exist on the top sheet.

We are now left with the integral along the path ABC. If the integrand is continuous across the real axis between AB and BC, this integral of course vanishes. It does not vanish, because γ_2 is discontinuous, having opposite signs across the branch cut. In fact, Im γ_2 is negative along BC and positive along AB. To show this, using $r_1, r_2, \theta_1, \theta_2$ defined in Figure 7.15, we write

$$\alpha_2\gamma_2 = -i\sqrt{\omega^2 - \alpha_2^2 k^2} = -i\sqrt{r_1 r_2}\left(\cos\frac{\theta_1 + \theta_2}{2} + i \sin\frac{\theta_1 + \theta_2}{2}\right).$$

The first quadrant may be defined by $0 < \theta_1 + \theta_2 < \pi$. Thus, on the top sheet, where Re $\gamma_2 > 0$, Im γ_2 is negative. Likewise, we can show that Im γ_2 is positive in the fourth

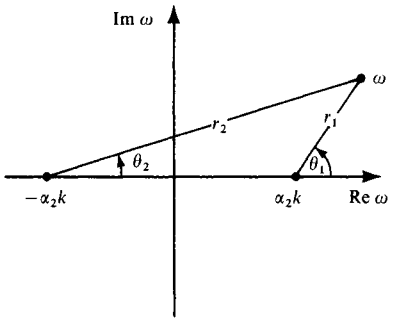

FIGURE **7.15**
Definition of the root chosen for γ_2 in Figure 7.14. Use $0 \le \theta_1 < 2\pi$, $-\pi < \theta_2 \le \pi$, and

$$\alpha_2\gamma_2 = \sqrt{r_1 r_2}\exp[i(\theta_1 + \theta_2 - \pi)/2].$$

quadrant of the top sheet of the ω-plane. (On the bottom sheet, the first quadrant is defined by $2\pi < \theta_1 + \theta_2 < 3\pi$.)

With the sign of γ_2 clearly defined, we can rewrite the integral along ABC as

$$\begin{aligned}\int_{ABC} &= \int_{BC} - \int_{BA} \\ &= \frac{4}{\pi}\mathrm{Im}\int_0^\infty J_0(kr)k\,dk\int_{\alpha_2 k}^\infty \frac{\exp(-i\omega t)}{\omega + i\sigma}\sinh\gamma_1 z F_3(k,\omega)\,d\omega,\end{aligned} \tag{7.168}$$

where

$$F_3(k,\omega) = \frac{A\rho_1\rho_2\gamma_2\sinh\gamma_1 h}{(\rho_2\gamma_1\cosh\gamma_1 H + \rho_1\gamma_2\sinh\gamma_1 H)(\rho_2\gamma_1\cosh\gamma_1 H - \rho_1\gamma_2\sinh\gamma_1 H)}. \tag{7.169}$$

To evaluate the above integral, we further deform the integration path from BC to BC', as shown in Figure 7.16. This time we shall keep the integrand of (7.168) analytic. It follows that we are forced to take the path into the fourth quadrant, where $\mathrm{Re}\,\gamma_2 < 0$; i.e., we descend to a lower Riemann sheet. The integral along a quarter-circle CC' vanishes as the radius tends to infinity. This deformation replaces the branch-line integral partially by the residue contribution from poles located in the area swept by the deformation. Thus

$$\int_{ABC} = P_{B1} + P_{B2}$$

where

$$P_{B1} = \frac{4}{\pi}\mathrm{Im}\int_0^\infty J_0(kr)k\,dk\int_{\alpha_2 k}^{\alpha_2 k - i\infty}\frac{\exp(-i\omega t)}{\omega + i\sigma}\sinh\gamma_1 z\,F_3(k,\omega)\,d\omega \tag{7.170}$$

and

$$P_{B2} = -2\pi i \sum \text{residues}$$
$$= 4 \text{ Re} \sum_n \int_0^{k_{0n}} J_0(kr) k \, dk \frac{\exp(-i\omega_n t)}{\omega_n + i\sigma} \sinh \gamma_1 z \, F_2(k, \omega_n) \, dk. \tag{7.171}$$

In evaluating the residues, note that all the poles of F_3 encountered in the lower sheet are the roots of

$$\rho_2 \gamma_1 \cosh \gamma_1 H + \rho_1 \gamma_2 \sinh \gamma_1 H = 0,$$

i.e., of $f_1(k, \omega) = 0$. This follows from our discussion of (7.160), which implies here that $\rho_2\gamma_1 \cosh \gamma_1 H - \rho_1\gamma_2 \sinh \gamma_1 H$ cannot have complex roots if Re $\gamma_2 < 0$. The expression (7.171) is identical to the normal-mode solution (7.166) except for the integration limits. These limits arise because the poles exist in the area on the right of BC' only for $0 < k < k_{0n}$. To explain this result, we shall trace the movement of poles in the ω-plane as k increases from zero to infinity.

Thus, let us pretend that k represents time. At $k = 0, i\gamma_1 = \omega/\alpha_1, i\gamma_2 = \omega/\alpha_2$, and the roots of $f_1(0, \omega) = 0$ are given by

$$\omega_n = \frac{\alpha_1(n - \frac{1}{2})\pi}{H} - i\frac{\alpha_1}{2H} \ln \frac{\alpha_2\rho_2 - \alpha_1\rho_1}{\alpha_2\rho_2 + \alpha_1\rho_1}. \tag{7.172}$$

The poles are located in the lower sheet of the ω-plane, as shown in Figure 7.16 (we assume $\rho_2\alpha_2 > \alpha_1\rho_1$). At $k = 0$, initial velocity and acceleration in the ω-plane are, respectively,

$$\frac{d\omega_n}{dk} = 0,$$
$$\frac{d^2\omega_n}{dk^2} = \frac{\alpha_1^2}{\omega_n}\left[1 + i\frac{\rho_1\alpha_2}{\rho_2\omega_n H}\left(1 - \frac{\alpha_1^2}{\alpha_2^2}\right) \Big/ \left(1 - \frac{\rho_1^2\alpha_1^2}{\rho_2^2\alpha_2^2}\right)\right]. \tag{7.173}$$

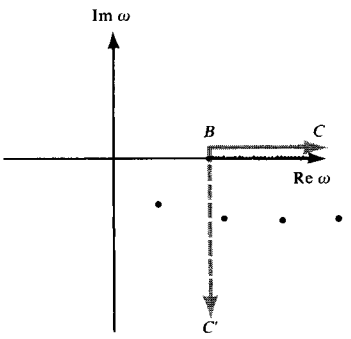

FIGURE **7.16**
Poles on the lower Riemann sheet (Re $\gamma_2 < 0$) of the complex ω-plane.

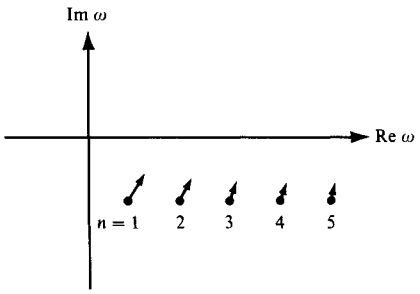

FIGURE **7.17**
Initial position (i.e., at $k = 0$) of poles on the lower Riemann sheet. Arrows show the direction and relative magnitude of "acceleration" of pole positions.

Examining the real and imaginary parts of acceleration, we find that the poles are accelerated in the direction shown by arrows in Figure 7.17. The lowest order pole is accelerated most.

At $k = 0$, on the other hand, the integration path BC' is located on the negative imaginary axis. The path BC' moves to the right at a constant velocity α_2, which is higher than that of the poles in the initial stage. Thus BC' passes poles one by one as k increases. The integration limit k_{0n} introduced in (7.171) is the value of k at the instant when the nth pole is caught up by BC'. For $k < k_{0n}$, the nth pole is on the right of BC', hence the residue contribution. The location ω_{0n} of the nth pole at $k = k_{0n}$ satisfies the following equation:

$$\text{Re } \omega_{0n} = \alpha_2 k_{0n}. \tag{7.174}$$

After being passed by BC', a pole proceeds to the right and upward to the real ω-axis. At the real axis, it meets the other pole coming from the first quadrant (double roots). Then one of the roots moves to the left, the other to the right, both along the real axis. The root that moves to the right is now accelerated and catches up with BC' again at $k = k_{cn}$, where the pole jumps up to the top sheet at the cut-off frequency $\omega_{cn} = \alpha_2 k_{cn}$. Thereafter, it slows down to reach $\alpha_1 k$ as k goes to infinity.

We must now evaluate the integral P_{B1} along path BC' given in (7.170). To do this, we shall change the order of integration again and return to the k-plane. At the same time, we change the variable ω to q by

$$q = i(\omega - \alpha_2 k). \tag{7.175}$$

Rewriting (7.170), we have

$$P_{B1} = \frac{4}{\pi}\text{Im} \int_0^\infty e^{-qt}\, dq \int_0^\infty J_0(kr)k \frac{e^{-i\alpha_2 kt}}{q - \sigma + i\alpha_2 k} \sinh \gamma_1 z\, F_3(k, \omega)\, dk. \tag{7.176}$$

Since $\gamma_2 = \sqrt{iq/\alpha_2}\sqrt{2k - iq/\alpha_2}$, the branch point is located at $k = i(q/2\alpha_2)$, as shown in Figure 7.18. The cut is made from the branch point to $-i\infty$. This choice of branch cut and the original integration path BC' lying on the lower sheet (Fig. 7.16) give the signs of real and imaginary parts of γ_2, as indicated in Figure 7.18.

We change the integration path from the positive real k-axis to the negative imaginary axis so that the factor $e^{-i\alpha_2 kt}$ in the integrand will attenuate rapidly along the latter path. By

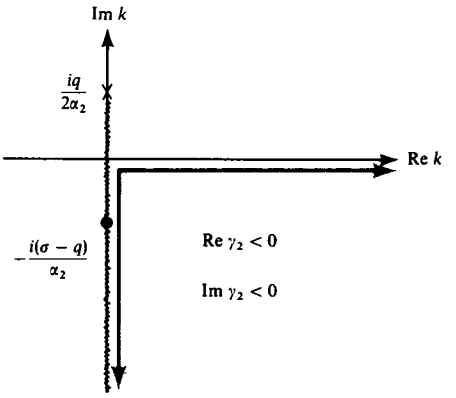

FIGURE **7.18**
A pole (closed circle) and a branch point (cross) in the k-plane.

this deformation, we pick up contributions from the complex poles in the fourth quadrant. Since Re $\gamma_2 < 0$ there, $\rho_2\gamma_1 \cosh \gamma_1 H - \rho_1\gamma_2 \sinh \gamma_1 H = 0$ cannot have complex roots. Therefore, the poles are the roots of $\rho_2\gamma_1 \cosh \gamma_1 H + \rho_1\gamma_2 \sinh \gamma_1 H = 0$. Thus we have

$$P_{B1} = P_{BL} + P_{B3}$$
$$P_{BL} = \frac{4}{\pi}\text{Im}\int_0^{\infty} e^{-qt}\,dq \int_0^{-i\infty} J_0(kr)k\frac{e^{-i\alpha_2 kt}}{q - \sigma + i\alpha_2 k}\sinh \gamma_1 z\, F_3(k,\omega)\,dk \tag{7.177}$$

and

$$P_{B3} = -2\pi i \sum \text{residues}$$
$$= 4\,\text{Re}\sum_n \int_0^{q_{0n}} e^{-qt} J_0(k_n r)k_n \frac{\exp(-i\alpha_2 k_n t)}{q - \sigma + i\alpha_2 k_n}\sinh \gamma_1 z\, F_4(k,q)\,dq, \tag{7.178}$$

where

$$F_4(k,q) = \frac{A\rho_2 \sinh \gamma_1 h}{\sinh \gamma_1 H\left[\dfrac{\partial}{\partial k}(\rho_2\gamma_1 \cosh \gamma_1 H + \rho_1\gamma_2 \sinh \gamma_1 H)\right]_{k=k_n}}. \tag{7.179}$$

The integral with respect to k in (7.177) vanishes if $\sigma < q$, because the pole $i(q - \sigma)/\alpha_2$ will not be on the integration path. Therefore, the integration range for q is $0 < q < \sigma$. Hence P_{BL} vanishes if $\sigma = 0$ (i.e., a step-function source), and it cannot be an important term to us.

The integration limit q_{0n} for P_{B3} requires an explanation. As mentioned before, for real positive k there are only two values of k, namely k_{0n} and k_{cn}, at which the real part of ω becomes equal to $\alpha_2 k$. In other words, for real positive k and real positive q, there are two roots of $f_1(k,\omega) = 0$ that have the form

$$\omega = \alpha_2 k - iq. \tag{7.180}$$

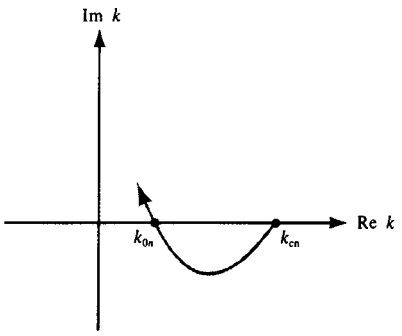

FIGURE **7.19**
Path of a pole in the k-plane.

One root corresponds to k_{cn}, at which $q = 0$, and the other root corresponds to k_{0n} at which $q = q_{0n}$. For real positive q, there are no other roots of $f_1(k, \omega) = 0$ on the real positive k-axis.

Now, near $q = 0$, it can be shown that $\text{Im}(dk/dq)_{f_1=0} < 0$. Therefore, a pole moves to the fourth quadrant as q increases from zero, as shown in Figure 7.19. Since the pole crosses the real k-axis only once more at $q = q_{0n}$, it will not exist in the fourth quadrant for $q > q_{0n}$. For this reason, the integration limits for P_{B3} are $0 < q < q_{0n}$.

Finally, we change the integration variable from q to k, by the following relation:

$$f_1(k, q) = \rho_2 \gamma_1 \cosh \gamma_1 H + \rho_1 \gamma_2 \sinh \gamma_1 H = 0.$$

Then

$$\frac{dq}{dk} = -\frac{(\partial f_1/\partial k)_{q=\text{const.}}}{(\partial f_1/\partial q)_{k=\text{const.}}} = \frac{(\partial f_1/\partial k)_{q=\text{const.}}}{i(\partial f_1/\partial \omega)_{k=\text{const.}}}$$

Substituting this into (7.178), we have

$$P_{B3} = 4 \text{ Re} \sum_n \int_{k_{0n}}^{k_{cn}} \frac{J_0(kr) k \exp(-i\omega_n t)}{\omega_n + i\sigma} \sinh \gamma_1 z \; F_2(k, \omega_n) \, dk, \qquad (7.181)$$

which has the integrand identical to P_N and P_{B2} in (7.166) and (7.171). Putting all the terms together, we finally have

$$P^{\text{total}} = 4 \text{ Re} \sum_n \int_0^{\infty} \frac{J_0(kr) k \exp(-i\omega_n t)}{\omega_n + i\sigma} \sinh \gamma_1 z \; F_2(k, \omega_n) \, dk, \qquad (7.182)$$

where nonoscillatory terms P_L and P_{BL} are neglected. The integration path deviates from the real k-axis between k_{0n} and k_{cn}, as shown in Figure 7.19.

7.6.1 ORGAN-PIPE MODE

We first consider the case in which the receiver is located above the source, at $r = 0$, as may be encountered in a reflection survey. The integral (7.182) then takes a form considered in Box 6.3, with the exponent $-i\omega_n t$, and the integral may be evaluated by the steepest

descents method for large t. Since, as shown in (7.173), $d\omega_n/dk = 0$ at $k = 0$, the saddle point is located at $k = 0$ in this case. Assuming the main contribution to come from the vicinity of $k = 0$, we expand the integrand phase factor $\exp(-i\omega_n t)$ as a power series in k, keeping only the first two terms. Values of ω_n and $d^2\omega_n/dk^2$ at $k = 0$ are given in (7.172) and (7.173), respectively. The steepest descents path is determined by

$$-\frac{it}{2}\omega_n''(0)k^2 = -i\frac{t}{2}k^2\left[\frac{d^2\omega_n}{dk^2}\right]_{k=0} = -x^2,$$

where x is real. Changing the variable from k to x by the above equation, we obtain

$$P^{\text{total}} = -4\,\text{Re}\sum_n \frac{F_2(0,\omega_n)}{\omega_n(0)+i\sigma}\sin(\omega_n z/\alpha_1)\exp(-i\omega_n(0)t)\frac{2}{\omega_n''(0)t}\int_0^\infty xe^{-x^2}\,dx.$$

Substituting $F_2(0,\omega_n)$, $\omega_n(0)$ from (7.167) and (7.172), and recognizing that $\int_0^\infty xe^{-x^2}\,dx = \frac{1}{2}$, the above formula can be rewritten as

$$\begin{aligned} P^{\text{total}} = 4A\frac{\alpha_1^2}{Ht}\sum_n &\left|\frac{\sin(\omega_n h/\alpha_1)\sin(\omega_n z/\alpha_1)}{\omega_n(-i\omega_n+\sigma)\omega_n}\right|_{k=0} \\ &\times\left(\frac{\alpha_2\rho_2-\alpha_1\rho_1}{\alpha_2\rho_2+\alpha_1\rho_1}\right)^{-\alpha_1 t/2H}\cos\left[\frac{\alpha_1}{H}(n-\tfrac{1}{2})\pi t+\psi\right], \end{aligned} \tag{7.183}$$

where ψ is the phase angle of the quantity inside the absolute value symbol.

The above formula shows a damped oscillation, with period $4H/\left[(2n-1)\alpha_1\right]$. The lowest order mode ($n = 1$) has wavelength equal to four times the layer thickness H: a quarter-wavelength oscillator. The damping is such that the corresponding temporal Q (Box 5.7) is given by

$$Q = \frac{(n-\frac{1}{2})\pi}{\ln\left(\dfrac{\alpha_2\rho_2+\alpha_1\rho_1}{\alpha_2\rho_2-\alpha_1\rho_1}\right)}. \tag{7.184}$$

If the impedance contrast is large, i.e., $\alpha_2\rho_2 \gg \alpha_1\rho_1$, the logarithm approaches 0 and Q becomes large, resulting in a long-lasting reverberation. This type of reverberation is called an organ-pipe mode, because it is essentially a one-dimensional oscillation in the vertical direction.

7.6.2 PHASE VELOCITY AND ATTENUATION

Let us consider the case in which the receiver is located far from the source, so that we can use the asymptotic expansion of the Bessel function $J_0(kr)$. Substituting (6.17) into (7.182) and retaining only the leading term, we have

$$P^{\text{total}} \sim \frac{4}{\pi r}\text{Re}\sum_n \int_{-\infty}^{\infty}\sqrt{k}\frac{\exp\left(-i\omega_n t+ikr-i\pi/4\right)}{\omega_n+i\sigma}F_2(k,\omega_n)\,dk. \tag{7.185}$$

In this case, the saddle point is determined by

$$\frac{d(-i\omega_n t + ikr)}{dk} = 0$$

or

$$\frac{d\omega_n}{dk} = \frac{r}{t}. \tag{7.186}$$

Since r/t is real, we see that the group velocity $d\omega_n/dk$ is real at the saddle point. To locate the saddle point, we must find the (k_n, ω_n) that satisfies (7.186) and $f_1(k_n, \omega_n) = 0$ (7.160) simultaneously. Once we find the saddle point, say k_{sn}, and the corresponding ω_{sn}, the steepest descents path is determined by

$$\begin{aligned} -i\omega_n t + ikr &\sim -i\omega_{sn} t + ik_{sn} r - \tfrac{1}{2} i\omega''_{sn}(k - k_{sn})^2 t \\ &= -i\omega_{sn} t + ik_{sn} r - x^2 \end{aligned}$$

with real x. Carrying out the integration along the steepest descents path, we obtain

$$P^{\text{total}} \sim \frac{4}{\sqrt{rt}} \sum_n |Q_n| \exp(-L_n t) \cos(\text{Re}\ \omega_{sn} t - \text{Re}\ k_{sn} r + \psi), \tag{7.187}$$

where $L_n = -\text{Im}\ \omega_{sn} + \text{Im}\ k_{sn} r/t$,

$$Q_n = \frac{\sqrt{k_{sn}} F_2(k_{sn}, \omega_{sn})}{(i\omega_{sn} + \sigma)\sqrt{\omega''_{sn}}},$$

and ψ is the phase angle of Q_n. These formulas give the phase velocity and attenuation associated with each leaky mode.

Rosenbaum (1960) gives some numerical results. For example, Figure 7.20 shows the relation between group velocity $d\omega_n/dk = r/t$ and phase velocity $\text{Re}(\omega_{sn})/\text{Re}(k_{sn}) = c$ for the lowest mode ($n = 1$) in the case $\alpha_2/\alpha_1 = 4$ and $\rho_2/\rho_1 = 2.7$. Figure 7.21 shows the corresponding attenuation factor L. The acoustic leaking mode has lower group velocity for higher phase velocity, and its group velocity is always lower than that of the normal mode. The relation between group and phase velocity for a normal mode in a layer overlying a rigid surface is shown by a broken line in Figure 7.20. For an elastic body, on the other hand, leaky modes arriving earlier than normal modes do exist. A decaying oscillatory long-period motion following P-waves, called the PL-wave, is often observed at short distances. Such motions are interpreted as leaky modes by Oliver and Major (1960). Haddon (1984) gives leaking mode theory for solid-layered models, showing that leaking mode poles are simply analytic extensions of Rayleigh mode poles and can be used naturally to include all of the various body-wave phases which result from wave/boundary interactions in the model.

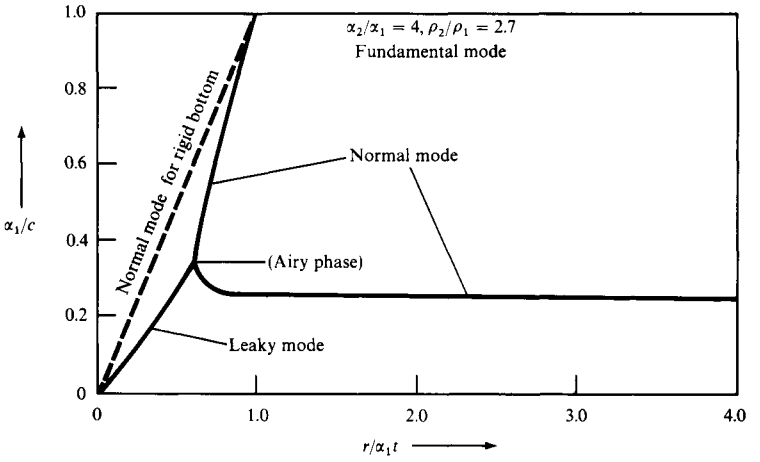

FIGURE **7.20**
Relation between group velocity and phase velocity for the fundamental normal mode and leaky mode in the case $\alpha_2/\alpha_1 = 4$ and $\rho_2/\rho_1 = 2.7$. The relation for the leaky mode is similar to that for the normal mode when the half-space is rigid. [From Rosenbaum (1960); copyright by the American Geophysical Union.]

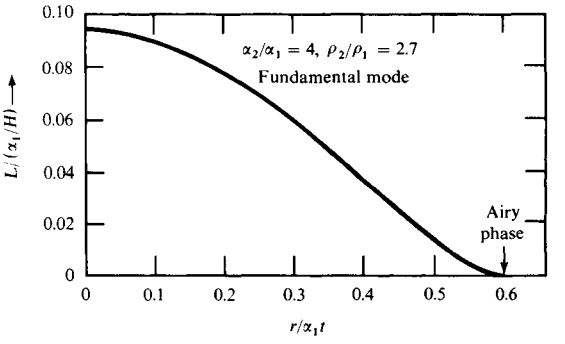

FIGURE **7.21**
The attenuation factor of a leaky mode. [From Rosenbaum (1960); copyright by the American Geophysical Union.]

Suggestions for Further Reading

Bamford, D., S. Crampin, *et al.* Special edition on anisotropy. *Geophysical Journal of the Royal Astronomical Society*, **49**, 1–243, 1977.

Brune, J. N., J. E. Nafe, and J. E. Oliver. A simplified method for the analysis and synthesis of dispersed wave trains. *Journal of Geophysical Research*, **65**, 287–304, 1960.

Ekström, G., and P. G. Richards. Empirical measurements of tectonic moment release in nuclear explosions from teleseismic surface waves and body waves. *Geophysical Journal International*, **117**, 120–140, 1994.

Ewing, M., J. L. Worzel, and C. L. Pekeris. *Propagation of Sound in the Ocean.* Geological Society of America, Memoir 27, 1948.

Gantmacher, F. R. *The Theory of Matrices.* 2 vols. New York: Chelsea Publishing Co., 1959.

Gilbert, F., and G. E. Backus. Propagator matrices in elastic wave and vibration problems. *Geophysics,* **31**, 326–332, 1966.

Haddon, R. A. W. Computation of synthetic seismograms in layered Earth models using leaking modes. *Bulletin of the Seismological Society of America,* **74**, 1225–1248, 1984.

Kennett, B. L. N. *Seismic wave propagation in stratified media.* Cambridge University Press, 1983.

Lighthill, M. J. Group velocity. *Journal of the Institute of Mathematics and Its Applications,* **1**, 1–28, 1965.

Schultz, M. H. *Spline Analysis.* Engelwood Cliffs, New Jersey: Prentice-Hall, 1973.

Oliver, J., and M. Major. Leaking modes and the PL phase. *Bulletin of the Seismological Society of America,* **50**, 165–180, 1960.

Problems

7.1 We develop here an alternative view of Love waves in a single layer over a half-space. A physical mechanism for such a surface wave (with frequency ω and phase velocity $c(\omega)$) is provided by body waves that are reflected supercritically within the upper layer ($\beta_1 < \beta_2$). For two points A and B at the same depth and separated by a distance X along the direction of propagation of the surface wave, the phase at B must be shifted from that at A by $X\omega/c$.

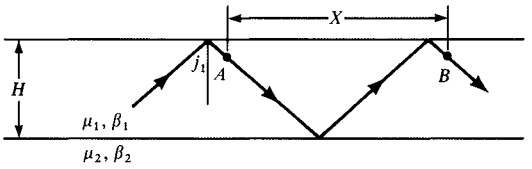

a) For the body wave between A and B, show that this phase shift is

$$\psi = \frac{2H\omega}{\beta_1} \sec j_1 - 2 \tan^{-1} \left[\frac{\mu_2 \sqrt{\frac{1}{c^2} - \frac{1}{\beta_2^2}}}{\mu_1 \sqrt{\frac{1}{\beta_1^2} - \frac{1}{c^2}}} \right].$$

(*Hint:* Equation (5.33) is useful here.)

b) For a surface wave to exist, show that ψ and $X\omega/c$ can differ only by an integer multiple of 2π. From this requirement, obtain the dispersion relation (7.6).

c) Why is it that Love waves cannot exist if $\beta_1 > \beta_2$?

7.2 Show that the propagator matrix for SH-waves in a homogeneous layer is given by a matrix multiplication of (7.50) (evaluated at $z = z_0$) substituted in (7.49). Obtain the corresponding result for P-SV waves from (7.55) and (7.56). (In essence, this is the way in which Thomson and Haskell originally obtained the propagator, rather than from (7.41).)

7.3 Generalize the idea expressed in the previous question by relating both $\mathbf{f}(z_l)$ and $\mathbf{f}(z_{l-1})$ to $\mathbf{w}_l$ and then showing that

$$\mathbf{f}(z_l) = \mathbf{F}_l(z_l)\mathbf{F}_l^{-1}(z_{l-1})\mathbf{f}(z_{l-1}).$$

Hence show that the propagator from z_0 to z_k is

$$\mathbf{P}(z_k, z_0) = \left[\mathbf{F}_k(z_k)\mathbf{F}_k^{-1}(z_{k-1})\right]\left[\mathbf{F}_{k-1}(z_{k-1})\mathbf{F}_{k-1}^{-1}(z_{k-2})\right]\cdots\left[\mathbf{F}_1(z_1)\mathbf{F}_1^{-1}(z_0)\right].$$

(*Note:* These results are still true if the medium consists of a stack of inhomogeneous layers, provided $\mathbf{F}_l(z)$ is a matrix whose columns are linearly independent solutions of $\partial\mathbf{f}/\partial z = \mathbf{A}(z)\mathbf{f}$ in the lth layer.)

7.4 In Sections 5.4 and 7.2, we showed that $\mathbf{Fw}$ can be thought of as a sum of all the possible wave types that solve $\partial\mathbf{f}/\partial z = \mathbf{Af}$; that each of the columns of $\mathbf{F}$ is separately a basic solution of $\partial\mathbf{f}/\partial z = \mathbf{Af}$; and that $\mathbf{w}$ is a vector of constants that give the weight of each basic solution present in the sum $\mathbf{Fw}$. Consider the first column of $\mathbf{F}$ in (7.55) when $k > \omega/\alpha$, and show that the corresponding wave in the sum $\mathbf{Fw}$ of (7.54) is an inhomogeneous P-wave with displacement amplitude

$$\grave{P}e^{-\gamma z}\sqrt{\alpha^2k^2/\omega^2 - \sin^2(kx - \omega t)}.$$

7.5 Show by redefining the origin that one way to construct $G_{np}(0, 0, h; x, y, z; \omega)$ is by making the switches $(r \to r; \phi \to \phi + \pi; z \to h; h \to z)$ in formulas for $G_{np}(x, y, z; 0, 0, h; \omega)$. Use this approach to verify that the reciprocity

$$G_{np}(0, 0, h; x, y, z; \omega) = G_{pn}(x, y, z; 0, 0, h; \omega)$$

is satisfied for surface-wave components (7.146) and (7.147).

7.6 Show that the change in phase velocity of Love waves at fixed wavenumber, which will result from a perturbation $(\delta\rho, \delta\mu)$ in the structure, is

$$\left(\frac{\delta c}{c}\right)_k = \frac{\displaystyle\int_0^\infty \left[k^2l_1^2 + \left(\frac{dl_1}{dz}\right)^2\right]\delta\mu\, dz - \int_0^\infty \omega^2 l_1^2\, \delta\rho\, dz}{\displaystyle 2\omega^2\int_0^\infty \rho l_1^2\, dz}.$$

7.7 Show that the Rayleigh-wave eigenfunction for a half-space with Poisson's ratio 0.25 is given by

$$r_1 = e^{-0.8475kz} - 0.5773\, e^{-0.3933kz},$$

$$r_2 = 0.8475\, e^{-0.8475kz} - 1.4679\, e^{-0.3933kz},$$

and that the energy integral I_1 is equal to $0.6205\rho/k$ (k is the horizontal wavenumber and ρ is the density). Then, using (7.150), obtain an explicit formula for

Rayleigh waves due to a point source with arbitrary moment tensor located at depth h.

7.8 The waveform of a dispersed wave train given by

$$f(t) = \frac{1}{2\pi}\int_{-\infty}^{\infty} |F(\omega)|e^{-i\omega t + i\phi(\omega)}\, d\omega$$
$$= \frac{1}{\pi}\int_{0}^{\infty} |F(\omega)| \cos\left[\omega t - \phi(\omega)\right]\, d\omega$$

can be computed easily and accurately if the group delay time $t_g = d\phi/d\omega$ and $d|F(\omega)|/d\omega$ are known at discrete frequencies ω_i. Show that

$$f(t) = \sum \frac{1}{\pi}\int_{\omega_i - \Delta\omega_i/2}^{\omega_i + \Delta\omega_i/2} |F(\omega)| \cos(\omega t - \phi(\omega))\, d\omega$$
$$\sim \sum_i \frac{\Delta\omega_i}{\pi}\left[|F(\omega_i)| \cos\omega_i(t - t_{pi}) \frac{\sin\left[(\Delta\omega_i/2)(t - t_{gi})\right]}{(\Delta\omega_i/2)(t - t_{gi})}\right.$$
$$\left. - \frac{d|F(\omega_i)|}{d\omega} \frac{\sin\omega_i(t - t_{pi})}{t - t_{gi}} \left\{\frac{\sin\left[(\Delta\omega_i/2)(t - t_{gi})\right]}{(\Delta\omega_i/2)(t - t_{gi})} - \cos\left[\frac{\Delta\omega_i}{2}(t - t_{gi})\right]\right\}\right],$$

where $t_{pi} = \phi(\omega_i)/\omega_i$ is the phase delay time at ω_i.

7.9 Determine the phase velocity as a function of frequency for surface waves that are observed with all of the following properties:

a) their group velocity is 4.4 km/s independent of frequency;

b) their wave shape changes with the travel distance, but comes back to the same shape every 8800 km (and not at shorter distances);

c) their phase velocity increases with period.

(*Note:* Long-period Love waves in the period range 40–200 s are characterized approximately by the above properties. They show an impulsive form because of the frequency-independent group velocity, and are sometimes called G waves, honoring Beno Gutenberg.)

7.10 Show that the phase velocity of a Love-wave mode, at a particular frequency, exceeds the group velocity at the same frequency. (*Hint:* Try eliminating I_1 between (7.69) and (7.70).)

7.11 In structures that support surface wave higher modes as well as the fundamental mode, show that the rate of decay of amplitude with depth is greater for the fundamental mode than for the higher modes. (Show that this result is true, either if frequency ω is fixed and different modes are specified with different horizontal wavenumbers k; or if k is fixed and different modes are specified with different ω.)

7.12 This problem explores some practical issues associated with surface waves from sources that are shallow—including the case of underground nuclear explosions. Though such explosions may be approximated by an isotropic moment tensor with components $M_{ij} = M_I \delta_{ij}$, it has been widely observed that explosions often generate Love waves and that occasionally the polarity of explosion-generated Rayleigh waves is reversed. The part of the seismic radiation that is not directly due to the explosive source is generally thought to be due to a release of tectonic stress, which can often be modeled by slip on a fault. Therefore, in addition to $M_I \delta_{ij}$, there are moment tensor components given by the first equations of Box 4.4, for faulting specified by the double couple moment M_0, and the strike, dip, and rake angles ϕ_s, δ, λ. We shall find the special form of the surface wave radiation patterns for shallow sources, and explore constraints on the five parameters $(M_I, M_0, \phi_s, \delta, \lambda)$ if the radiation patterns are known from observations.

The formulas (7.149) and (7.151) for excitation of Love waves and Rayleigh waves by a source with symmetric moment tensor **M** can be simplified if the source is very shallow (or, equivalently, at very long wavelength), since then

$$l_2(h) = \mu \frac{dl_1}{dz}\bigg|_h = 0, \qquad r_3(h) = \mu \left(\frac{dr_1}{dz} - kr_2 \right)_h = 0,$$

and

$$r_4(h) = 0 \qquad \text{implies} \qquad \frac{dr_2}{dz}\bigg|_h = \left(\frac{2\beta^2}{\alpha^2} - 1 \right) kr_1(h).$$

With this background:

a) show for a shallow source specified by **M** that

$$\mathbf{u}^{\text{LOVE}}(\mathbf{x}, \omega) = \mathbf{G}^{\text{L}} \left[U_2 \sin 2\phi - U_3 \cos 2\phi \right] \qquad \text{and}$$

$$\mathbf{u}^{\text{RAYLEIGH}}(\mathbf{x}, \omega) = \mathbf{G}^{\text{R}} \left[U_1 + U_2 \cos 2\phi + U_3 \sin 2\phi \right],$$

where the vectors $\mathbf{G}^{\text{L}}$ and $\mathbf{G}^{\text{R}}$ are given by

$$\mathbf{G}^{\text{L}}(\mathbf{x}; h, \omega) = \sum_n \frac{ik_n l_1(h)}{8cUI_1} \sqrt{\frac{2}{\pi k_n r}} \exp\left[i \left(k_n r - \frac{\pi}{4} \right) \right] l_1(z)\, \hat{\boldsymbol{\phi}} \qquad \text{and}$$

$$\mathbf{G}^{\text{R}}(\mathbf{x}; h, \omega) = \sum_n \frac{k_n r_1(h)}{8cUI_1} \sqrt{\frac{2}{\pi k_n r}} \exp\left[i \left(k_n r - \frac{\pi}{4} \right) \right] \left[r_1(z)\, \hat{\mathbf{r}} + i r_2(z)\, \hat{\mathbf{z}} \right],$$

and the radiation pattern coefficients (U_1, U_2, U_3) are given by

$$U_1 = \tfrac{1}{2}(M_{xx} + M_{yy}) - (1 - 2\beta^2/\alpha^2) M_{zz},$$

$$U_2 = \tfrac{1}{2}(M_{xx} - M_{yy}),$$

$$U_3 = M_{xy}.$$

b) Show that long-period surface waves are not excited by a shallow vertical dip–slip fault (dip $\delta = 90°$, rake $\lambda = 0°$).

Note the implication, that M_{xz} and M_{yz} components of the moment tensor cannot be estimated from surface waves alone if the source is very shallow.

c) Given an explosion with isotropic moment M_I and an associated tectonic release characterized by $M_0, \phi_s, \delta, \lambda$, show that

$$U_1 = \frac{2\beta^2}{\alpha^2} M_I - \frac{3\alpha^2 - 4\beta^2}{\alpha^2} DS,$$

$$U_2 = DS \cos 2\phi_s - SS \sin 2\phi_s,$$

$$U_3 = SS \cos 2\phi_s + DS \sin 2\phi_s$$

where

$$SS = M_0 \sin \delta \cos \lambda \qquad \text{and} \qquad DS = \tfrac{1}{2} M_0 \sin 2\delta \sin \lambda$$

and hence that the surface wave excitation is

$$\mathbf{u}^{\text{LOVE}} = \mathbf{G}^{\text{L}} [DS \sin 2(\phi - \phi_s) - SS \cos 2(\phi - \phi_s)] \quad \text{and}$$

$$\mathbf{u}^{\text{RAYLEIGH}} = \mathbf{G}^{\text{R}} [(2\beta^2/\alpha^2) M_I - (3 - 4\beta^2/\alpha^2) DS + DS \cos 2(\phi - \phi_s) + SS \sin 2(\phi - \phi_s)].$$

We can think of SS as the strength of the strike–slip component of the double couple, and DS as the strength of the dip–slip component. (If $\delta = 90°$ and $\lambda = 0$ then $SS = M_0$ and $DS = 0$; if $\delta = 45°$ and $\lambda = 90°$, then $SS = 0$ and $DS = \frac{1}{2} M_0$.)

d) Suppose that surface waves from a nuclear explosion are observed with enough detail, and that $\mathbf{G}^{\text{L}}$ and $\mathbf{G}^{\text{R}}$ are sufficiently well known, that we can estimate the three coefficients U_1, U_2, U_3 of the radiation.

If it turns out that U_2 and U_3 are much smaller than U_1, then $SS \sim 0$ and $DS \sim 0$. The Love waves are small, the Rayleigh waves have an isotropic pattern with standard polarity, and the isotropic moment (and hence the explosion yield) can be estimated from U_1. But if the explosion generates significant Love waves and the Rayleigh waves are not isotropic, the tectonic release is presumably significant and yield estimation based upon surface waves is problematic.

Show that if the tectonic release is associated with thrusting, then DS is positive and the estimate of M_I (based on measurement of U_1) must increase as estimates of DS increase.

e) If $SS = 0$, how big does DS have to be, for the Rayleigh wave to have reverse polarity at some azimuths? How big must DS be, for reverse Rayleigh polarity at all azimuths?

f) Suppose an explosion ($M_I > 0$) occurs with tectonic release specified by values of DS, SS, and ϕ_s. (Note that the same values of DS and SS can result from different values of M_0, δ, λ.) Show in general that the Love waves and Rayleigh

waves are the same as those resulting from either (i) an explosion of different M_{I} ($M_{\mathrm{I}}^{(1)}$, say, which may be negative in which case this would be an implosion), and tectonic release that is purely left-lateral strike slip with strength $SS^{(1)} = +\sqrt{DS^2 + SS^2}$ on a fault with strike $\phi_s^{(1)} = \phi_s - \frac{1}{2}\tan^{-1}(DS/SS)$; or (ii) an explosion of different M_{I} ($M_{\mathrm{I}}^{(2)}$, say), and tectonic release that is purely dip slip thrusting with strength $DS = +\sqrt{DS^2 + SS^2}$ on a fault with strike $\phi_s^{(2)} = \phi_s + \frac{1}{2}\tan^{-1}(SS/DS) = \phi_s^{(1)} + 45°$.

Show further that the same Love waves and Rayleigh waves are generated, either if the strike slip described in (i) is replaced by right-lateral strike slip $SS^{(1)} = -\sqrt{DS^2 + SS^2}$ and the strike angle is increased 90°, or if the thrusting in (ii) is replaced by normal faulting $DS^{(2)} = -\sqrt{DS^2 + SS^2}$ with the strike increased from that in (ii) by 90°. In the latter case, show that the isotropic moment must be given yet another value, $M_{\mathrm{I}}^{(3)}$ (say), to obtain the same observations of surface waves.

Since different types of tectonic release, associated with different isotropic moments, can fit the same surface wave radiation patterns, it follows in general that additional information (for example, the orientation of local faulting) is needed to determine the parameters of the tectonic release in order to use surface waves to estimate the isotropic moment—and hence the yield—of nuclear explosions.

CHAPTER 8

Free Oscillations of the Earth

Long-period surface waves generated by a large earthquake may be recorded several times at a given station as they continue to travel around the world. The flat Earth model studied in Chapter 7 is obviously inadequate for analyzing these long-period waves. Even for periods as short as 20 s, the effect of the Earth's curvature on surface-wave dispersion cannot be ignored, especially when a pronounced low-velocity layer in the upper mantle traps a large part of the energy and effectively reduces the travel distance. Furthermore, the dispersion can be so strong that long-period surface waves that have traveled $N + 1$ times around the Earth can interfere with slower, short-period waves that have traveled N times around and with waves that have traveled in the opposite direction. It is therefore important, just to complete the surface-wave analysis, that we study the spherical Earth model. But our main goal in this chapter is to understand that surface waves and body waves (and head waves and leaking modes) are phenomena that can be expressed in terms of more basic motions, the Earth's free oscillations.

Because the Earth is a body of finite size, it can resonate as a whole only at certain discrete frequencies. Let us first understand why this must be so.

In the previous chapter, wave systems were characterized by their horizontal wavenumber (k) and frequency (ω). Because these waves were propagating in media that extend indefinitely in the lateral (horizontal) direction, k in that case was a continuous variable. We emphasized an approach in which, for each ω, only certain wavenumbers $k = k_n(\omega)$ ($n = 0, 1, 2, \ldots$) are possible. But we could instead have taken k as the independent variable, finding that only a certain number of eigenfrequencies $\omega = {}_n\omega(k)$ are possible for surface wave modes—though, for each n, ${}_n\omega(k)$ varies continuously as a function of k. It is this latter form of the dispersion relation that connects naturally to a discussion of free oscillations in the spherical Earth. This follows because in spherical geometry the "horizontal wavenumber" is fixed at certain discrete values by the finite lateral extent of the medium ($0 \leq \Delta < 2\pi$, where Δ, shown in Fig. 8.1, is the standard variable used in seismology to measure horizontal distance over a spherical Earth). Because the horizontal wavenumber takes discrete values, ${}_n\omega$ must take discrete values at fixed n. In fact, we shall work with horizontal *angular* wavenumber l, instead of k, and find in Box 8.1 that l must be zero or a positive integer. Rather than ${}_n\omega(l)$, we write ${}_n\omega_l$, and one of our first goals must be to obtain the possible eigenfrequencies ${}_n\omega_l$ ($n = 0, 1, 2, \ldots$) for given l.

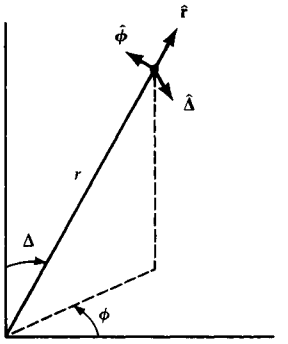

FIGURE **8.1**
Spherical polar coordinates (r, Δ, ϕ), with origin at the center of the Earth. The line $\Delta = 0$ is often taken to pass through a seismic source, in which case (r, Δ, ϕ) are known as *epicentral coordinates.*

We shall start this analysis with a discussion of the "dispersion relation" $\omega = {}_n\omega_l$ for a homogeneous liquid sphere—that is, we need to know how ω depends on l for the fundamental ($n = 0$) and overtones ($n > 0$) in such a medium. We shall neglect self-gravitation, so that we shall be working with an unrealistic but simple model that is very useful for introducing many of the concepts (such as horizontal and radial wave functions) that are needed in the analysis of any spherical model. We shall then describe the excitation of free oscillations by a point source with emphasis on the effect of the Earth's sphericity on the propagation of surface waves. For waves with periods longer than about 500 s, the effect of gravity becomes important, and we shall show how self-gravitation can be taken into account. We shall describe how the normal mode framework is used to interpret body-wave and surface-wave observations in terms of a moment tensor, now routinely estimated for several hundreds of earthquakes each year. Finally, we shall discuss the splitting of spectral lines due to the Earth's rotation, and analyze the splitting due to lateral variation of structure in the Earth.

8.1 Free Oscillations of a Homogeneous Liquid Sphere

Perhaps the simplest of all free-oscillation systems that shares some major aspects with free oscillations of the Earth is the "violin-string" problem. The transverse motion of the string, as a function of position x and time t, satisfies a one-dimensional wave equation $c^2\partial^2 y/\partial x^2 = \partial^2 y/\partial t^2$, and $y(x, t) = 0$ at $x = 0$ and $x = L$. We shall expect the reader to have some familiarity with the associated Sturm–Liouville theory. The most important result is that *any* solution $y(x, t)$ satisfying the above wave equation and boundary conditions can be expanded as

$$y = \sum_n a_n y_n(x, t),$$

where the a_n are constants and the y_n are free oscillations; $y_n = \sin({}_n\omega x/c)\cos({}_n\omega t)$ with eigenfrequencies ${}_n\omega = (n + 1)\pi c/L$.

To develop some familiarity with the special properties of a *spherical* medium, we shall imagine a homogeneous compressible fluid sphere of radius r_0, with elastic properties specified by bulk modulus κ and density ρ. No body forces will be allowed to act within

this medium, and we shall examine the free oscillations of small pressure perturbations P about the equilibrium pressure field. The usual equation of motion (2.17) simplifies to

$$\rho\ddot{\mathbf{u}} = -\nabla P, \tag{8.1}$$

because stress τ_{ij} is merely $-P\delta_{ij}$; and Hooke's law (2.18) reduces to

$$P = -\kappa\nabla \cdot \mathbf{u}. \tag{8.2}$$

Therefore, since ρ and κ are constants,

$$c^2\nabla^2 P = \partial^2 P/\partial t^2, \tag{8.3}$$

where $c^2 = \kappa/\rho$.

We shall assume a "stress free" boundary condition—namely, that $P(\mathbf{x}, t) = 0$ on the surface with radius r_0—and shall obtain solutions to the homogeneous wave equation (8.3). Choosing spherical polar coordinates (r, Δ, ϕ), as in Figure 8.1, it is natural to try to find special solutions in which the dependence upon (r, Δ, ϕ, t) is separated into four different factors: $P = R(r)\Theta(\Delta)\Phi(\phi)T(t)$. Our discussion of (5.8) indicates that $T = \exp(\pm i\omega t)$ for some constant ω, and in order to separate spatial dependences we need to use the explicit form of ∇^2 in spherical polars, which is

$$\nabla^2 P = \frac{1}{r^2}\frac{\partial}{\partial r}\left(r^2\frac{\partial P}{\partial r}\right) + \frac{1}{r^2\sin\Delta}\frac{\partial}{\partial\Delta}\left(\sin\Delta\frac{\partial P}{\partial\Delta}\right) + \frac{1}{r^2\sin^2\Delta}\frac{\partial^2 p}{\partial\phi^2}. \tag{8.4}$$

In Box 8.1, we find that

$$\Theta(\Delta)\Phi(\phi) = Y_l^m(\Delta,\phi) \equiv (-1)^m\left[\frac{2l+1}{4\pi}\frac{(l-m)!}{(l+m)!}\right]^{1/2} P_l^m(\cos\Delta)e^{im\phi}, \tag{8.5}$$

where l and m are integers, $-l \le m \le l$, and $P_l^m(\cos\Delta)$ is the associated Legendre function. Although the Δ and ϕ dependences have been separated, it is common practice to write $Y_l^m(\Delta,\phi)$ for the product $\Theta\Phi$ in (8.5).

Next we must examine the radial wave function $R = R(r)$, and this must satisfy

$$\frac{1}{r^2}\frac{d}{dr}\left(r^2\frac{dR}{dr}\right) + \left[\frac{\omega^2}{c^2} - \frac{l(l+1)}{r^2}\right]R = 0. \tag{8.6}$$

Since c here is constant, (8.6) is a standard equation that is known to have spherical Hankel functions as its solutions. Furthermore, since we are interested in solutions that have no singularity in pressure anywhere in the range $0 \le r \le r_0$, the solution of (8.6) must be $R(r) \propto j_l(\omega r/c)$, where j_l is the spherical Bessel function of order l. Because l is an integer, we can take advantage of the relation

$$j_l(x) = x^l\left(-\frac{1}{x}\frac{d}{dx}\right)^l\left(\frac{\sin x}{x}\right) \tag{8.7}$$

BOX **8.1**

Spherical surface harmonics

A long list of important properties can be derived for the special functions $\Theta(\Delta)\Phi(\phi)$ that separate the horizontal variation of solutions to $c^2\nabla^2 P = \partial^2 P/\partial t^2$ in spherical geometry. We here outline the formal derivation of some of these properties, which are needed frequently in geophysics because of the need to define continuous bounded functions over spherical surfaces within the Earth.

Trying a solution $P(\mathbf{x}, t) = R(r)\Theta(\Delta)\Phi(\phi)\exp(-i\omega t)$, we find from (8.3) and (8.4) that

$$\frac{\sin^2\Delta}{R}\frac{d}{dr}\left(r^2\frac{dR}{dr}\right) + \frac{\sin\Delta}{\Theta}\frac{d}{d\Delta}\left(\sin\Delta\frac{d\Theta}{d\Delta}\right) + \frac{\omega^2 r^2}{c^2}\sin^2\Delta = -\frac{1}{\Phi}\frac{d^2\Phi}{d\phi^2}.$$

The left-hand side is independent of ϕ, hence $(1/\Phi)(d^2\Phi/d\phi^2)$ is a constant. Solving for Φ and noting that $\Phi(\phi)$ must be periodic with period 2π if $P(\mathbf{x}, t)$ is to be a single-valued function of position, we find that the eigenfunctions associated with the azimuthal coordinate are

$$\Phi = e^{im\phi} \qquad m = 0, \pm 1, \pm 2, \pm 3, \ldots \tag{1}$$

The equation in (r, Δ) for R and Θ is now

$$\frac{1}{R}\frac{d}{dr}\left(r^2\frac{dR}{dr}\right) + \frac{\omega^2 r^2}{c^2} = \frac{m^2}{\sin^2\Delta} - \frac{1}{\Theta\sin\Delta}\frac{d}{d\Delta}\left(\sin\Delta\frac{d\Theta}{d\Delta}\right),$$

where it has been arranged that the left-hand side depends only on r and the right-hand side only on Δ. The equation can thus be satisfied for all (r, Δ) only if there is some constant K for which

$$\frac{d}{dr}\left(r^2\frac{dR}{dr}\right) + \left(\frac{\omega^2 r^2}{c^2} - K\right)R = 0 \tag{2}$$

and

$$\frac{d}{d\Delta}\left(\sin\Delta\frac{d\Theta}{d\Delta}\right) = \left(\frac{m^2}{\sin^2\Delta} - K\right)\Theta\sin\Delta \tag{3}$$

We continue with an analysis of the Θ-equation, beginning with:

THE CASE $m = 0$

The function $\Phi(\phi)$ is constant, and the solution $P(\mathbf{x}, t)$ has axial symmetry. Θ satisfies $d/d\Delta(\sin\Delta\, d\Theta/d\Delta) = -K\Theta\sin\Delta$, and it is convenient to get away from the angle Δ and use instead the variable $x = \cos\Delta$, since then the trigonometric terms in the Θ-equation are suppressed. We find

$$(1 - x^2)\frac{d^2\Theta}{dx^2} - 2x\frac{d\Theta}{dx} + K\Theta = 0, \tag{4}$$

known as the *Legendre equation*. For general values of the constant K, the solutions have singularities at the end points of the range $-1 \le x \le 1$. This is the range corresponding to $0 \le \Delta \le \pi$, which is needed to describe position in the Earth. But for certain special values of K, there are nonsingular solutions Θ that turn out to be polynomials in x.

(continued)

BOX **8.1** *(continued)*

To prove these statements, one assumes a power series solution exists in the form

$$\Theta(x) = x^k \sum_{i=0}^{\infty} b_i x^i \qquad (b_0 \neq 0). \tag{5}$$

Substituting (5) into (4) and equating the coefficient of each power of x to zero, we find

$$b_0 k(k-1) = 0, \tag{6}$$

$$b_1 (k+1)k = 0, \tag{7}$$

and, in general,

$$b_{i+2} = b_i \left[\frac{(k+i)(k+i+1) - K}{(k+i+1)(k+i+2)} \right]. \tag{8}$$

From (8) we see in general that $|b_{i+2}/b_i| \to 1$ as $i \to \infty$. Thus, by comparison with a geometric series, there is convergence of (5) provided $-1 < x < 1$. But what happens at $x = \pm 1$ ($\Delta = 0$ or π)? It can be shown, for such x values, that the infinite series for $\Theta(x)$ will *diverge*, unless one of the even-suffix b_i is zero and one of the odd-suffix b_i is zero. (For then all further b_i are zero, so that the infinite series is reduced to a polynomial, which clearly does "converge" for all values including the special values $x = \pm 1$.)

Given that $b_0 \neq 0$, (6) requires $k = 0$ or 1.

Looking at (8) with $k = 0$, we see that the only way to stop the even power series from having an infinite number of terms is if $K = i(i+1)$ for some even integer i. Then $b_i \neq 0$ but $b_{i+2} = b_{i+4} = \ldots = 0$. The only way to stop the odd power series is to require that $b_1 = 0$, which via (8) means that all coefficients of odd powers vanish, and also (7) is satisfied.

Looking at (8) with $k = 1$, we see that the power series for Θ starts with the term $b_0 x$. The only way to stop the odd power series is to require that $K = (i+1)(i+2)$ for some even integer i. If $k = 1$, then (7) requires that $b_1 = 0$, and it follows from (8) that there are no even terms.

We have obtained the important result that the constant K, which was introduced to separate the radial equation from the Θ-equation, must in general be the product of two successive integers. Otherwise, the Θ-equation does not have a solution valid throughout the range $0 \leq \Delta \leq \pi$.

Furthermore, if $K = l(l+1)$ and l is even, then it is the even powers of x that make up the solution. Similarly, if $K = l(l+1)$ and l is odd, then the solution consists only of odd powers of x. In either case, the solution for Θ is a polynomial of order l, with other terms of order $l-2, l-4, \ldots$, with a lowest order term of order 1 (if l is odd) or 0 (if l is even). The customary choice for b_0 is made by requiring

$$\Theta(x) = 1 \qquad \text{for } x = 1. \tag{9}$$

The polynomials that result are the *Legendre polynomials*. Writing them out as a sum of descending powers, a great deal of manipulation gives, for l either even or odd, the expression

$$\Theta = P_l(x) = \frac{(2l)!}{2^l (l!)^2} \left[x^l - \frac{l(l-1)x^{l-2}}{2(2l-1)} + \frac{l(l-1)(l-2)(l-3)x^{l-4}}{2 \cdot 4 \cdot (2l-1)(2l-3)} - \cdots \right], \tag{10}$$

(continued)

BOX **8.1** *(continued)*

stopping at either x or 1 (times a constant) as the last term. The first few Legendre polynomials are

$$P_0(x) = 1, \qquad P_1(x) = x, \qquad P_2 = \tfrac{1}{2}(3x^2 - 1),$$
$$P_3(x) = \tfrac{1}{2}(5x^3 - 3x), \qquad P_4(x) = \tfrac{1}{8}(35x^4 - 30x^2 + 3),$$

and, in general,

$$P_l(x) = \frac{1}{2^l\, l!}\frac{d^l}{dx^l}(x^2 - 1)^l,$$

which is known as *Rodrigues' formula.*

The figure shows some examples of Legendre functions, plotted as (large scale, axially symmetric) topography on a sphere. $P_l(\cos \Delta)$ has l oscillations around the circumference. Note from the figure (e.g., with $l = 5, 10, 14$) that these oscillations are not quite evenly spaced: there is an increase in wavelength and amplitude for the peaks (or troughs) at $\Delta = 0$ and $\Delta = \pi$.

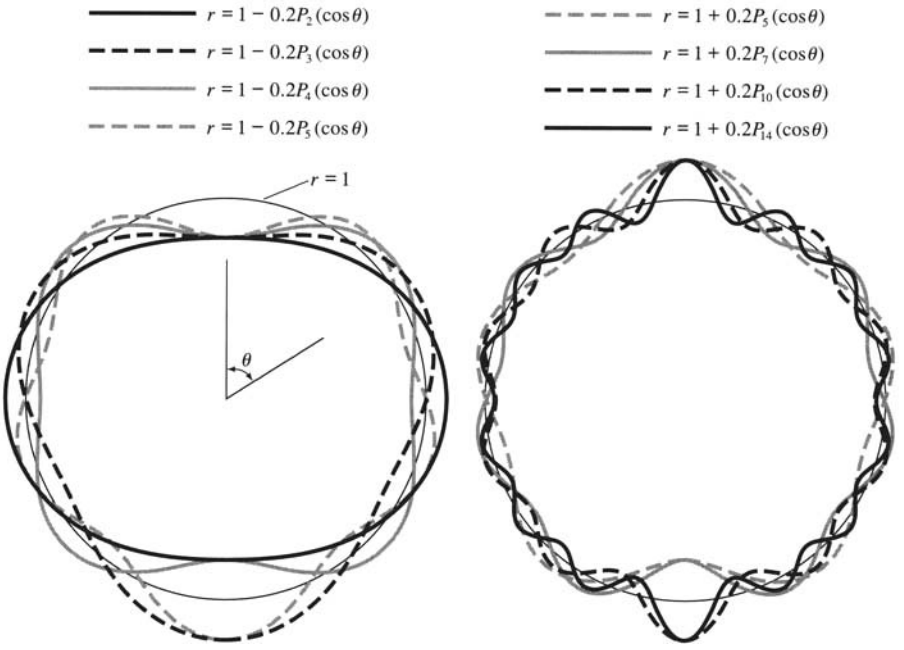

THE CASES $m \neq 0$

We shall initially assume the integer m is positive. Then with $x = \cos \Delta$ in (3), we find

$$\frac{d}{dx}\left[(1 - x^2)\frac{d\Theta}{dx}\right] = \frac{m^2\Theta}{1 - x^2} - K\Theta. \tag{11}$$

We might attempt a power-series solution like (5). However, this approach becomes difficult because the formula for b_{i+2} turns out to involve not just b_i (as it did before for Θ

(continued)

BOX **8.1** *(continued)*

with $m = 0$), but also b_{i+1}, and the general solution of such a three-term recursion relation is quite complicated. To guess at an alternative approach, we recall that for $m = 0$ the properties of Θ near $x = \pm 1$ are important. They may also be expected to be important for $m > 0$, by inspection of the coefficients in (11). We thus turn to a brief examination of Θ near $x = \pm 1$. With $\varepsilon = x \pm 1$ and ε small, (11) is approximately

$$\varepsilon \frac{d^2\Theta}{d\varepsilon^2} + \frac{d\Theta}{d\varepsilon} - \frac{m^2\Theta}{4\varepsilon} = 0,$$

which has solutions $\Theta = \varepsilon^{m/2}$ and $\varepsilon^{-m/2}$. The second solution is not well-behaved at $\varepsilon = 0$, and can be rejected. It seems then that Θ should have zeros of order $m/2$ at $x = \pm 1$. They can both be factored out by writing

$$\Theta(x) = (1 - x^2)^{m/2} A(x),$$

and we can hope to study Θ by studying $A(x)$.

This approach turns out to be fruitful, because A satisfies the ordinary differential equation

$$(1 - x^2)\frac{d^2A}{dx^2} - 2(m + 1)x\frac{dA}{dx} + [K - m(m + 1)]A = 0, \tag{12}$$

which *does* have just a two-term recursion formula for the coefficients in an expansion of the form $A(x) = x^k \sum_{i=0}^{\infty} c_i x^i$. The recursion formula turns out to be

$$c_{i+2} = \frac{[(i + m)(i + m + 1) - K]}{(i + 1)(i + 2)} c_i.$$

In general, this formula will generate two series solutions for $A(x)$ (one of even powers of x, and one of odd powers). If these series were not terminated at some power x^r, they would behave like $(1 - x^2)^{-m}$. The requirement that Θ have no singularities in $-1 \leq x \leq 1$ ($0 \leq \Delta \leq \pi$) thus leads to the result $c_{r+2} = 0$ for some r. The series ends with the power x^r. It begins with the power x^0 (i.e., a constant) if r is even, and with the power x if r is odd. Thus

$$(r + m)(r + m + 1) = K,$$

and K has eigenvalues that again (i.e., as for $m = 0$) are the product of consecutive integers; $r \geq 0, m \geq 0$, hence we take $K = l(l + 1)$ for some integer $l \geq 0$. Since $r \geq 0$, we find also the important result $m \leq l$.

Since K takes the same eigenvalues if $m = 0$ or $m > 0$, the radial function $R(r)$, determined from (2), is unchanged by dropping the requirement of axial symmetry. So the radial functions are independent of m.

We have shown that $\Theta(x) = (1 - x^2)^{m/2} A(x)$ where A is now a polynomial in x. There is no difficulty in finding the coefficients of this polynomial. However, a quick way to get an explicit formula for A is available, since, if the equation satisfied by Legendre polynomial P_l (see (4)) is differentiated m times, the result is

$$(1 - x^2)\frac{d^{m+2}}{dx^{m+2}}P_l - 2(m + 1)x\frac{d^{m+1}}{dx^{m+1}}P_l + [l(l + 1) - m(m + 1)]\frac{d^m}{dx^m}P_l = 0.$$

(continued)

BOX **8.1** *(continued)*

Comparing this with the equation (12) satisfied by $A(x)$, we see that a solution for A is $A(x) = d^m P_l(x)/dx^m$. Since $P_l(x)$ is a polynomial involving nonnegative powers of x, there is no danger of $A(x)$ blowing up anywhere in $-1 \le x \le 1$.

The product $(1 - x^2)^{m/2} d^m P_l(x)/dx^m$ is therefore a solution for the angular function $\Theta(x)$. It is called the *associated Legendre function*, denoted by $P_l^m(x)$.

The equation (11) for Θ depends upon m only via m^2. Therefore, if $m < 0$, the nonsingular solution must be proportional to $P_l^{|m|}(\cos \Delta)$. We adopt the convention

$$P_l^{-m}(x) = (-1)^m \frac{(l-m)!}{(l+m)!} P_l^m(x), \tag{13}$$

in which the constant of proportionality has been chosen so that

$$P_l^m(x) = \frac{(1-x^2)^{m/2}}{2^l l!} \frac{d^{l+m}}{dx^{l+m}} (x^2 - 1)^l \tag{14}$$

applies for all (l, m) such that $-l \le m \le l$.

Several books have been written on properties of P_l and P_l^m (e.g., Robin 1957; Hobson, 1955), and Wiggins and Saito (1971) and Masters and Richards-Dinger (1998) showed how to compute these functions efficiently. Summarizing the most important formulas, it is known that

$$\frac{1}{(1 + r^2 - 2r \cos \Delta)^{1/2}} = \sum_{l=0}^{\infty} r^l P_l(\cos \Delta) \quad 0 < r < 1 \tag{15}$$

$$(l - m + 1) P_{l+1}^m(x) - (2l + 1) x P_l^m(x) + (l + m) P_{l-1}^m(x) = 0 \tag{16}$$

$$(1 - x^2) \frac{d}{dx} P_l^m(x) = (l + 1) x P_l^m(x) - (l - m + 1) P_{l+1}^m(x). \tag{17}$$

It is convenient to define fully normalized surface harmonics

$$Y_l^m(\Delta, \phi) = (-1)^m \left[\frac{2l+1}{4\pi} \frac{(l-m)!}{(l+m)!} \right]^{1/2} P_l^m(\cos \Delta) e^{im\phi} \tag{18}$$

for integers $l \ge 0$ and integers m such that $-l \le m \le l$. Then

$$Y_l^{-m}(\Delta, \phi) = (-1)^m [Y_l^m(\Delta, \phi)]^*,$$

the * denoting a complex conjugate.

The Legendre functions are orthogonal, as are the azimuthal functions $e^{im\phi}$, and the normalizing factor in (18) has been chosen so that the orthogonality of the $Y_l^m(\Delta, \phi)$ takes a simple form, namely

$$\int_0^{2\pi} d\phi \int_0^{\pi} [Y_l^m(\Delta, \phi)]^* Y_{l'}^{m'}(\Delta, \phi) \sin \Delta \, d\Delta = \delta_{ll'} \delta_{mm'}. \tag{19}$$

(*Note:* This is an integration over the surface of a sphere of unit radius.)

If ψ is the angle between the two directions out from the center of coordinates to the points specified by (Δ, ϕ) and (Δ', ϕ') in spherical polars, then $\cos \psi = \cos \Delta \cos \Delta' + \sin \Delta \sin \Delta' \cos(\phi - \phi')$, and

$$P_l(\cos \psi) = \frac{4\pi}{2l+1} \sum_{-l \le m \le l} Y_l^m(\Delta, \phi) [Y_l^m(\Delta', \phi')]^*. \tag{20}$$

(continued)

BOX **8.1** *(continued)*

In the theory for excitation of normal modes by a point source, we need values of Y_l^m and some of its derivatives at $\Delta = 0$. A key result is

$$P_l^m(\cos\Delta) \to \frac{1}{2^m m!}\frac{(l+m)!}{(l-m)!}\Delta^m \qquad \text{as } \Delta \to 0, \qquad \text{for } m \geq 0.$$

Finally, we comment that surface harmonics provide the horizontal wavefunctions needed to study wave propagation in spherical coordinates, and in this sense play roles similar to those of $\cos(k_x x + k_y y)$ and $J_m(kr)e^{im\phi}$ in earlier chapters for Cartesian and cylindrical coordinates.

so that, for $l = 0$,

$$R(r) \propto \frac{c}{\omega r}\sin\left(\frac{\omega r}{c}\right); \tag{8.8}$$

for $l = 1$,

$$R(r) \propto \frac{c^2}{\omega^2 r^2}\sin\left(\frac{\omega r}{c}\right) - \frac{c}{\omega r}\cos\left(\frac{\omega r}{c}\right); \tag{8.9}$$

and for $l = 2$,

$$R(r) \propto \left(\frac{3c^3}{\omega^3 r^3} - \frac{c}{\omega r}\right)\sin\left(\frac{\omega r}{c}\right) - \frac{3c^2}{\omega^2 r^2}\cos\left(\frac{\omega r}{c}\right). \tag{8.10}$$

It remains to take account of the "free" boundary condition on $r = r_0$, which requires $R(r_0) = 0$. It is this condition that gives the permissible eigenfrequencies ${}_n\omega_l$. Thus, from (8.8), we find for $l = 0$ that $\sin(\omega r_0/c) = 0$. It follows that

$${}_n\omega_0 = \frac{(n+1)\pi c}{r_0} \qquad (n = 0, 1, 2, \ldots). \tag{8.11}$$

$n = 0$ gives the *fundamental* mode, and $n \geq 1$ constitute the *overtones,* or higher modes. Motions with $l = 0$ are purely *radial modes,* because the associated u_Δ and u_ϕ are zero. In the case that $r_0 = 6000$ km and $c = 5$ km/s, the periods (in seconds) corresponding to (8.11) are $2\pi/{}_n\omega_0 = (2400)/(n+1)$, with the fundamental ($n = 0$) being 40 min. For $l = 2$, the first zero of $j_l(x)$ occurs where $x \sim 1.8\pi$, hence the period for the mode with $n = 0$ and $l = 2$ is about 22 min. In Figure 8.2 we show the eigenfunctions ${}_nR_0 \propto j_0({}_n\omega_0 r/c)$ for $n = 0, 1, 2$; and ${}_nR_2 \propto j_2({}_n\omega_2 r/c)$ for $n = 0, 1, 2$.

Important properties of the free oscillations of our homogeneous fluid sphere are their *orthogonality,* and their *degeneracy* with respect to azimuthal order number m. Thus, for the vector space of steady-state $[\exp(-i\omega t)]$ solutions to $c^2\nabla^2 P = \partial^2 P/\partial t^2$ within $|\mathbf{x}| < r_0$, and

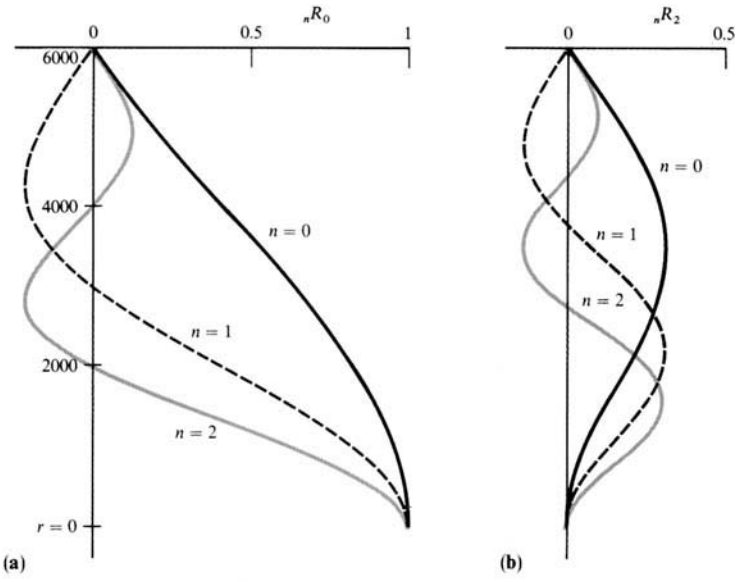

FIGURE **8.2**
Eigenfunctions ${}_nR_l$ of pressure within a fluid sphere of radius 6000 km are shown as a function of radius. (**a**) ${}_nR_0(r)$ for $n = 0, 1, 2$. (**b**) ${}_nR_2(r)$ for $n = 0, 1, 2$.

satisfying $P(\mathbf{x}, t) = 0$ for $|\mathbf{x}| = r_0$, we define an inner product. If f and g are two members of this vector space, we define

$$\{f, g\} = \iiint_{|\mathbf{X}| \le r_0} \rho f^* g \, dV. \tag{8.12}$$

Suppose further that f and g are normal modes, with eigenfrequencies ω_f and ω_g, respectively. Then some algebra yields

$$[\omega_g^2 - (\omega_f^*)^2]\{f, g\} = 0.$$

Putting $f = g$ here, it follows that ω_f^2 must be real. Since equilibrium is stable and motion does not grow exponentially, the eigenfrequencies themselves are real. With $f \neq g$ and $\omega_f \neq \omega_g$, it also follows that f and g are *orthogonal* in the sense that $\{f, g\} = 0$. Thus, in our present problem,

$$\{j_l({}_n\omega_l r/c) Y_l^m(\Delta, \phi), \, j_{l'}({}_{n'}\omega_{l'} r/c) Y_{l'}^{m'}(\Delta, \phi)\} = 0 \tag{8.13}$$

unless $l = l'$ and $m = m'$ and $n = n'$. Previously, we have seen orthogonality results for vertical wavefunctions (for example, (7.98) or (7.100)), or for horizontal wavefunctions (for example, $\delta(k - k') = 1/(2\pi) \int_{-\infty}^{\infty} [\exp(ikx)][\exp(ik'x)]^* \, dx$, or (7.122), or equation (19) of Box 8.1). The result given in (8.13) is a compact statement of the orthogonality of wavefunctions in all three dimensions.

For each choice of integers $l \geq 0, n \geq 0$, there are $(2l + 1)$ free oscillations sharing the same eigenfrequency ${}_n\omega_l$ and the same radial eigenfunctions $j_l({}_n\omega_l r/c)$. This degeneracy arises because the one-dimensional wave equation (8.6) is independent of m, and each m in the range $-l \leq m \leq l$ provides a different normal mode, via pressure $={}_nP_l^m(\mathbf{x}, t) = j_l({}_n\omega_l r/c)Y_l^m(\Delta, \phi)\exp(-i_n\omega_l t)$.

It is possible to extend the analysis of free oscillations to spherical media that are considerably better models of Earth than our homogeneous fluid sphere, and still retain the same features of orthogonality and degeneracy and the same numbering scheme for the modes in terms of (l, m, n). A significant improvement over the fluid model is the homogeneous elastic solid sphere, which in 1882 was thoroughly studied by Horace Lamb. This is the simplest compressible medium that exhibits two independent families of modes, spheroidal and toroidal, which differ in their properties precisely in the way that we have found *P–SV* motions to differ from *SH* in a flat Earth model (Chapter 7). Just as we introduced vector surface harmonics for cylindrical geometry (7.118), so now we can introduce such vectors for spherical geometry. We define

$$\begin{aligned}
\mathbf{R}_l^m(\Delta, \phi) &= Y_l^m \hat{\mathbf{r}}, \\
\mathbf{S}_l^m(\Delta, \phi) &= \frac{1}{\sqrt{l(l+1)}}\left(\frac{\partial Y_l^m}{\partial \Delta}\,\hat{\boldsymbol{\Delta}} + \frac{1}{\sin\Delta}\frac{\partial Y_l^m}{\partial \phi}\,\hat{\boldsymbol{\phi}}\right), \\
\mathbf{T}_l^m(\Delta, \phi) &= \frac{1}{\sqrt{l(l+1)}}\left(\frac{1}{\sin\Delta}\frac{\partial Y_l^m}{\partial \phi}\,\hat{\boldsymbol{\Delta}} - \frac{\partial Y_l^m}{\partial \Delta}\,\hat{\boldsymbol{\phi}}\right),
\end{aligned} \tag{8.14}$$

where $Y_l^m(\Delta, \phi)$ is the fully normalized surface harmonic defined in (8.5) and $\hat{\mathbf{r}}$, $\hat{\boldsymbol{\Delta}}$, $\hat{\boldsymbol{\phi}}$ are unit vectors in directions r, Δ, ϕ, respectively (Fig. 8.1). It is easy to see that $\mathbf{R}$, $\mathbf{S}$, and $\mathbf{T}$ are perpendicular to each other. Because $Y_l^m(\Delta, \phi)$ is fully normalized, the vector functions satisfy the following orthogonal relations:

$$\begin{aligned}
\int_0^{\pi} \sin\Delta\, d\Delta \int_0^{2\pi} d\phi\, \mathbf{R}_l^{m*} \cdot \mathbf{R}_{l'}^{m'} &= \delta_{mm'}\delta_{ll'}, \\
\int_0^{\pi} \sin\Delta\, d\Delta \int_0^{2\pi} d\phi\, \mathbf{S}_l^{m*} \cdot \mathbf{S}_{l'}^{m'} &= \delta_{mm'}\delta_{ll'}, \\
\int_0^{\pi} \sin\Delta\, d\Delta \int_0^{2\pi} d\phi\, \mathbf{T}_l^{m*} \cdot \mathbf{T}_{l'}^{m'} &= \delta_{mm'}\delta_{ll'},
\end{aligned}$$

A *spheroidal* motion is one for which the radial component of $\nabla \times \mathbf{u}$ is zero; and a *toroidal* motion has both $u_r = 0$ and $\nabla \cdot \mathbf{u} = 0$. The homogeneous fluid sphere clearly can support only spheroidal motions. If a normal mode in this medium has the pressure field proportional to $j_l({}_n\omega_l r/c)Y_l^m(\Delta, \phi)\exp(-i_n\omega_l t)$, then, from (8.1), the corresponding displacement field is proportional to

$$\left\{\left(\frac{dj_l}{dr}\right)\mathbf{R}_l^m(\Delta, \phi) + \frac{\sqrt{l(l+1)}}{r}\, j_l\, \mathbf{S}_l^m(\Delta, \phi)\right\}\frac{\exp(-i_n\omega_l t)}{\rho({}_n\omega_l)^2}. \tag{8.15}$$

It is apparent from this result, and directly from (8.14), that $\mathbf{R}_l^m$ and $\mathbf{S}_l^m$ are required to describe vector fields associated with spheroidal motion, and $\mathbf{T}_l^m$ for toroidal motion.

Provided we consider Earth models that are spherically symmetric and that do not rotate, we shall find it possible to describe spheroidal modes by generalizing the radial functions appearing in (8.15). But the modes will still display the same horizontal wave functions, the same degeneracy, and an orthogonality similar to that of (8.13). The symbol ${}_nS_l$ is often used to identify a spheroidal mode, and ${}_nT_l$ a toroidal mode.

In a sense, the spherical Earth model is easier to investigate than a flat Earth model, because any motion within a sphere can be expressed by a superposition of normal modes. The leaky mode, for which we allocated considerable space in Chapter 7, does not exist for a sphere. As shown in the next section, the formulas for excitation of free oscillations by a point source can be derived more simply than those for surface waves.

8.2 Excitation of Free Oscillations by a Point Source

Since a sphere is a finite body, any disturbance can be expressed as superposition of normal modes. Following Gilbert (1971), we shall go back to the nineteenth century and start with the vibration of a system of N particles as studied by Rayleigh and Routh.

Consider N particles initially in stable equilibrium. A set of external forces is then applied with $\mathbf{f}_\alpha(t)$ acting on the αth particle ($\alpha = 1, \ldots, N$), putting all the particles in motion. Let the mass of the αth particle be m_α and the displacement of the αth particle from its equilibrium position be $\mathbf{u}_\alpha$. For small displacements, we may assume that the change in internal force between particles is a linear sum of displacements. The equation of motion for the αth particle can then be written as

$$m_\alpha \frac{d^2\mathbf{u}_\alpha(t)}{dt^2} + \sum_{\beta=1}^{N} c_{\alpha\beta}\mathbf{u}_\beta(t) = \mathbf{f}_\alpha(t) \qquad t > 0 \ (\alpha = 1, 2, \ldots, N), \tag{8.16}$$

where the initial conditions are

$$\mathbf{u}_\alpha(0) = \mathbf{0} \qquad \text{and} \qquad \frac{d}{dt}\mathbf{u}_\alpha(0) = \mathbf{0}$$

and $\mathbf{c}$ is symmetric and positive definite since equilibrium is stable (cf. (2.32)).

The normal modes of the system are given by nontrivial solutions of (8.16) for $\mathbf{f}_\alpha = \mathbf{0}$. Early on, we noted similarities between normal modes and solutions to linear homogeneous algebraic equations (see Box 2.4). Since there are now three scalar equations for each particle, there are $3N$ eigenfrequencies ω_i and $3N$ eigenvectors (normal modes) for the total system. The normal modes are denoted by ${}_i\mathbf{u}_\alpha \exp(-i\omega_i t)$, this being the displacement of the αth particle in the ith normal mode. (The use of "i" here, to denote the mode index, is not to be confused with use of the same symbol for $\sqrt{-1}$.) For each index i, the motion of all the particles ($\alpha = 1, \ldots, N$) is needed to describe the mode. The motion of the αth particle in the ith normal mode is obtained by solving

$$-\omega_i^2 m_\alpha({}_i\mathbf{u}_\alpha) + \sum_{\beta} c_{\alpha\beta}({}_i\mathbf{u}_\beta) = \mathbf{0} \qquad (\alpha = 1, \ldots, N). \tag{8.17}$$

By forming $\sum_\alpha [{}_j\mathbf{u}_\alpha^* \cdot$ (8.17 for mode i) $-$ (8.17 for mode j)$^* \cdot {}_i\mathbf{u}_\alpha]$ and using $c_{\beta\alpha} = c_{\alpha\beta}$, we can show that the eigenvectors ${}_i\mathbf{u}_\alpha$ are orthogonal, in the sense that

$$\sum_\alpha m_\alpha ({}_j\mathbf{u}_\alpha^*) \cdot ({}_i\mathbf{u}_\alpha) = 0$$

unless $i = j$, but their amplitudes are not determined by (8.17). We choose to normalize them by

$$\sum_\alpha m_\alpha ({}_j\mathbf{u}_\alpha^*) \cdot ({}_i\mathbf{u}_\alpha) = \delta_{ij}. \tag{8.18}$$

Taking the scalar product of (8.16) with ${}_j\mathbf{u}_\alpha^*$, summing over α, and using (8.18), we obtain

$$\sum_{\alpha\beta} c_{\alpha\beta} ({}_j\mathbf{u}_\alpha^*) \cdot ({}_i\mathbf{u}_\beta) = \omega_i^2 \delta_{ij}. \tag{8.19}$$

Returning to the problem of solving the inhomogeneous equation (8.16), we write the solution as a superposition of normal modes. We then need to find the coefficients a_i in the expansion

$$\mathbf{u}_\alpha(t) = \sum_i a_i ({}_i\mathbf{u}_\alpha) \exp(-i\omega_i t) \qquad (t > 0). \tag{8.20}$$

(It is the real part of (8.20) that we use in practice for real $\mathbf{u}_\alpha(t)$.) We work with the Laplace transform, $\mathbf{u}_\alpha(t) \to \mathbf{u}_\alpha(s)$, finding from (8.20) that

$$\mathbf{u}_\alpha(s) = \sum_i \frac{a_i}{s + i\omega_i} {}_i\mathbf{u}_\alpha. \tag{8.21}$$

To find the coefficients a_i, we substitute from (8.21) into the Laplace transform of (8.16):

$$m_\alpha s^2 \sum_i \left(\frac{a_i}{s + i\omega_i} \right) {}_i\mathbf{u}_\alpha + \sum_\beta c_{\alpha\beta} \sum_i \left(\frac{a_i}{s + i\omega_i} \right) {}_i\mathbf{u}_\beta = \mathbf{f}_\alpha(s). \tag{8.22}$$

From (8.18), (8.19), and (8.22), it is then easy to show that

$$\frac{a_j}{s + i\omega_j} = \frac{\sum_\alpha {}_j\mathbf{u}_\alpha^* \cdot \mathbf{f}_\alpha(s)}{s^2 + \omega_j^2},$$

so that from (8.21) we have

$$\mathbf{u}_\alpha(s) = \sum_i \left[\frac{\sum_\beta {}_i\mathbf{u}_\beta^* \cdot \mathbf{f}_\beta(s)}{s^2 + \omega_i^2} \right] {}_i\mathbf{u}_\alpha, \tag{8.23}$$

which is simple to invert to the time domain. Assuming that the forces vary as a temporal step function, $\mathbf{f}_\alpha(t) = \mathbf{F}_\alpha H(t)$, we find that $\mathbf{f}_\beta(s) = s^{-1}\mathbf{F}_\beta$ in (8.23). The Laplace inverse

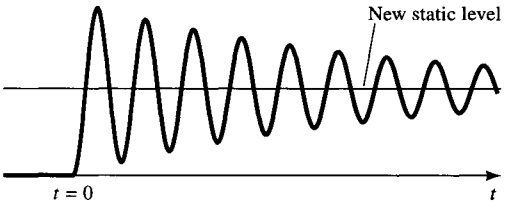

FIGURE **8.3**
Record of ground motion in a given normal mode due to a source that acts as a step function in time at $t = 0$.

of $[s(s^2 + \omega_i^2)]^{-1}$ is $H(t)(1 - \cos \omega_i t)/\omega_i^2$, so that for $t > 0$ we obtain

$$\mathbf{u}_\alpha(t) = \sum_i \left(\sum_\beta {}_i\mathbf{u}_\beta^* \cdot \mathbf{F}_\beta \right) {}_i\mathbf{u}_\alpha \frac{1 - \cos \omega_i t}{\omega_i^2}. \tag{8.24}$$

When the medium is dissipative, we find, using the temporal Q (Box 5.7), that

$$\mathbf{u}_\alpha(t) = \sum_i \left(\sum_\beta {}_i\mathbf{u}_\beta^* \cdot \mathbf{F}_\beta \right) {}_i\mathbf{u}_\alpha \frac{1 - \exp[-(\omega_i t/2Q_i)] \cos \omega_i t}{\omega_i^2}. \tag{8.25}$$

The structure of this solution has some very interesting properties. First, we note that the static displacement $\mathbf{u}_\alpha(t \to \infty)$ is easily obtained from (8.25) as a sum of the normal modes. In fact, (8.25) indicates that the motion in each mode can be thought of as a decaying oscillation about a new reference level, this new level being initiated at $t = 0$, as shown in Figure 8.3. Second, the form of the normal mode summation (8.25) tells us what can be learned about the source from observations of the displacement of just one particle. Suppose we know all the normal modes of the system. If we observe the αth particle and its displacement $\mathbf{u}_\alpha(t)$, we can hope to infer the excitation coefficients

$$\sum_\beta {}_i\mathbf{u}_\beta^* \cdot \mathbf{F}_\beta$$

for $i = 1, 2, \ldots, 3N$. (This is not possible for those modes that have a node at the αth particle. In these cases, ${}_i\mathbf{u}_\alpha = \mathbf{0}$, and the excitation coefficient of the ith mode cannot be determined from knowledge of $\mathbf{u}_\alpha(t)$ because the mode is not observed there. The process of obtaining the excitation coefficients involves looking at the Fourier spectrum of $\mathbf{u}_\alpha(t)$ and measuring the height of spectral peaks centered on each ω_i. Again, there is difficulty in determining excitation coefficients for two modes that have nearly the same frequency.) It is interesting that, by observing just one particle and obtaining the excitation coefficients, it is then possible to use (8.25) with different α and predict the motion of all other particles in the system. Even if some of the excitation coefficients are not determined (for reasons noted above), it may still be possible to predict major parts of the spectrum of $\mathbf{u}_\alpha(t)$ for all α.

We have made these comments on the solution (8.25) because it can easily be modified to apply to the Earth. We consider increasing the number of particles so that they approach a continuum. In the limit, a sum over particles such as $\sum_{\beta=1}^{N} {}_i\mathbf{u}_\beta^* \cdot \mathbf{F}_\beta$ is replaced by a volume

integral such as $\int_i \mathbf{u}^*(\xi) \cdot \mathbf{f}(\xi)\, dV(\xi)$, where $\mathbf{f}(\xi)$ is now the body force per unit volume. We shall continue to assume that this body force acts as a step function in time. From (8.25) we immediately obtain

$$\mathbf{u}(\mathbf{x}, t) = \sum_i \left(\int_V {}_i\mathbf{u}^*(\xi) \cdot \mathbf{f}(\xi)\, dV \right) {}_i\mathbf{u}(\mathbf{x}) \frac{1 - \exp[-(\omega_i t/2Q_i)] \cos\, \omega_i t}{\omega_i^2}. \quad (8.26)$$

Our use of i here denotes the ith normal mode of the whole Earth. That is, each i corresponds to some value for the triplet of integers (l, m, n) that we found in Section 8.1 were necessary for characterizing individual modes. The sum in (8.25) is thus an infinite sum, but, as shown by Rayleigh in his classic text "The Theory of Sound" (reprinted 1945, paragraph 101), it does converge because of the factor ω_i^{-2}. The normal modes in (8.26) have been normalized (cf. (8.18)) by

$$\int_V \rho(\xi)\, {}_j\mathbf{u}^*(\xi) \cdot {}_i\mathbf{u}(\xi)\, dV = \delta_{ij}, \quad (8.27)$$

where $\rho(\xi)$ is the density, and the volume integrals above are taken over the whole Earth.

We shall now find the vibration of a spherical Earth model due to a point source that is specified by a moment tensor. Using a result that was previously given as an exercise (Problem 3.6), the body force becomes

$$f_p(\xi, t) = -M_{pq}(t) \frac{\partial}{\partial \xi_q} \delta(\xi - \mathbf{x}_s). \quad (8.28)$$

We shall assume that $\mathbf{M}$ acts as a step function in time at $\mathbf{x}_s$, so that the body force is also a step function, and (8.26) is directly applicable. The ith excitation coefficient is now

$$\begin{aligned} \int_V {}_i\mathbf{u}^*(\xi) \cdot \mathbf{f}(\xi)\, dV &= -M_{pq} \int_V {}_i\mathbf{u}_p^*(\xi) \frac{\partial}{\partial \xi_q} \delta(\xi - \mathbf{x}_s) dV(\xi) \\ &= {}_iu_{p,q}^*(\mathbf{x}_s) M_{pq} = {}_ie_{pq}^*(\mathbf{x}_s) M_{pq}, \end{aligned} \quad (8.29)$$

where ${}_ie_{pq}$ is the (pq) strain component in the ith normal mode. To obtain the last equality in (8.29), we used the symmetry $M_{pq} = M_{qp}$. Putting (8.29) into (8.26), we finally obtain the displacement for an arbitrary point source $\mathbf{M}H(t)$ acting at $\mathbf{x}_s$:

$$\mathbf{u}(\mathbf{x}, t) = \sum_i [{}_ie_{pq}^*(\mathbf{x}_s) M_{pq}]\, {}_i\mathbf{u}(\mathbf{x}) \frac{1 - \exp(-\omega_i t/2Q_i) \cos \omega_i t}{\omega_i^2}. \quad (8.30)$$

Thus, once the normal modes ${}_i\mathbf{u}$ of the Earth are known, it is conceptually a simple matter to calculate the response of the Earth to a point source with arbitrary moment tensor.

To find explicit forms for the normal modes, we must be more specific about the Earth model. We shall consider here a nonrotating spherically symmetric Earth in which the density ρ and Lamé parameters λ and μ depend only on the distance r from the center of symmetry. The equations of motion (2.47)–(2.50) for this model can fruitfully be studied by the motion-stress vector approach that we adopted in Chapter 7. In spherical polar

coordinates, the appropriate ansatz for displacement in the mode (l, m, n) is

$$[{}_nU_l(r)\mathbf{R}_l^m(\Delta,\phi) + {}_nV_l(r)\mathbf{S}_l^m(\Delta,\phi) + {}_nW_l(r)\mathbf{T}_l^m(\Delta,\phi)]\exp(-i_n\omega_l t). \quad (8.31)$$

The associated traction working on spherical surfaces $r =$ constant is

$$[{}_nR_l(r)\mathbf{R}_l^m(\Delta,\phi) + {}_nS_l(r)\mathbf{S}_l^m(\Delta,\phi) + {}_nT_l(r)\mathbf{T}_l^m(\Delta,\phi)]\exp(-i_n\omega_l t) \quad (8.32)$$

and we can write the equations for the radial function in the following separate forms:

$$\frac{d}{dr}\begin{pmatrix} V \\ U \\ S \\ R \end{pmatrix} = \begin{pmatrix} \frac{1}{r} & -\frac{\sqrt{l(l+1)}}{r} & \frac{1}{\mu} & 0 \\ \frac{\lambda\sqrt{l(l+1)}}{r(\lambda+2\mu)} & -\frac{2\lambda}{r(\lambda+2\mu)} & 0 & \frac{1}{\lambda+2\mu} \\ \frac{4l(l+1)\mu(\lambda+\mu)}{r^2(\lambda+2\mu)} - \rho\omega^2 - \frac{2\mu}{r^2} & -\frac{2\mu(3\lambda+2\mu)\sqrt{l(l+1)}}{r^2(\lambda+2\mu)} & -\frac{3}{r} & -\frac{\lambda\sqrt{l(l+1)}}{r(\lambda+2\mu)} \\ -\frac{2\mu(3\lambda+2\mu)\sqrt{l(l+1)}}{r^2(\lambda+2\mu)} & -\rho\omega^2 + \frac{4\mu(3\lambda+2\mu)}{r^2(\lambda+2\mu)} & \frac{\sqrt{l(l+1)}}{r} & -\frac{4\mu}{r(\lambda+2\mu)} \end{pmatrix}\begin{pmatrix} V \\ U \\ S \\ R \end{pmatrix} \quad (8.33)$$

and

$$\frac{d}{dr}\begin{pmatrix} W \\ T \end{pmatrix} = \begin{pmatrix} \frac{1}{r} & \frac{1}{\mu} \\ \frac{\mu(l-1)(l+2)}{r^2} - \rho\omega^2 & -\frac{3}{r} \end{pmatrix}\begin{pmatrix} W \\ T \end{pmatrix}. \quad (8.34)$$

(We have dropped subscripts l and n from the dependent variables and from ω. Note that m does not enter the matrix equations.)

Thus the vibrations of a spherically symmetric Earth without rotation can be separated into two type of modes. One is the spheroidal mode with horizontal wave functions $\mathbf{R}_l^m$ and $\mathbf{S}_l^m$ and radial wavefunctions determined by (8.33). The other is the toroidal or torsional mode with horizontal wavefunction $\mathbf{T}_l^m$ and radial wavefunctions determined by (8.34). It is clear from a comparison of matrices in (8.33) and (7.28) that the spheroidal modes include Rayleigh waves. Comparing (8.34) and (7.24), we see that the toroidal modes include Love waves. Such comparisons require that the horizontal wave number k of surface waves be identified with $\sqrt{l(l+1)}/r$ for free oscillations. We shall present a more detailed comparison of surface waves and free oscillations in the next section.

To find the normal modes, we must solve the eigenvalue–eigenvector problems (8.33) and (8.34) under the boundary conditions that the solutions are regular at $r = 0$ and the tractions vanish at the Earth's surface ($r = r_\oplus$). The numerical method and the Rayleigh–Ritz method described in Chapter 7 can be adapted to solve these problems. One method of handling the condition at $r = 0$ (Takeuchi and Saito, 1972) is to assume that the Earth is uniform in $r < r_1$ and solve the differential equations in powers of r. The power series are then evaluated at $r = r_1$, and numerical integration is initiated from these values and taken upward. For each integer l, there are eigenvalues ${}_n\omega_l (n = 0, 1, 2, \ldots)$ that make the stress wavefunctions (R_l, S_l, T_l) all zero at $r = r_\oplus$, and for each ${}_n\omega_l$ there is an eigenfunction for the motion-stress vector. Again we note a degeneracy, in that eigenfrequency and radial eigenfunction are independent of m.

The normalization formula (8.27) for normal modes together with that for horizontal wave functions leads to the following normalization for radial functions:

$$\int_0^{r_\oplus} \rho(r)\{[{}_nU_l(r)]^2 + [{}_nV_l(r)]^2\}r^2\,dr = 1 \tag{8.35}$$

and

$$\int_0^{r_\oplus} \rho(r)[{}_nW_l(r)]^2 r^2\,dr = 1, \tag{8.36}$$

where $r_\oplus$ is the radius of the Earth.

With the normal-mode solution thus completely defined, our next step toward computing the point-source response is to evaluate the strain tensor for the normal-mode displacement at the source point, since this is needed in (8.30). For the spherical coordinates (r, Δ, ϕ), we obtain the strain components from (2.45) by putting $h^r = 1, h^\Delta = r$, and $h^\phi = r \sin \Delta$:

$$\begin{aligned}
e_{rr} &= \frac{\partial u_r}{\partial r}, \\
e_{\Delta\Delta} &= \frac{1}{r}\frac{\partial u_\Delta}{\partial \Delta} + \frac{u_r}{r}, \\
e_{\phi\phi} &= \frac{1}{r \sin \Delta}\frac{\partial u_\phi}{\partial \phi} + \frac{u_\Delta}{r}\cot \Delta + \frac{u_r}{r}, \\
e_{\Delta\phi} = e_{\phi\Delta} &= \frac{1}{2}\left[\frac{1}{r}\left(\frac{\partial u_\phi}{\partial \Delta} - u_\phi \cot \Delta\right) + \frac{1}{r \sin \Delta}\frac{\partial u_\Delta}{\partial \phi}\right], \\
e_{\phi r} = e_{r\phi} &= \frac{1}{2}\left[\frac{1}{r \sin \Delta}\frac{\partial u_r}{\partial \phi} + \frac{\partial u_\phi}{\partial r} - \frac{u_\phi}{r}\right], \\
e_{r\Delta} = e_{\Delta r} &= \frac{1}{2}\left[\frac{\partial u_\Delta}{\partial r} - \frac{u_\Delta}{r} + \frac{1}{r}\frac{\partial u_r}{\partial \Delta}\right],
\end{aligned} \tag{8.37}$$

where u_r, u_Δ, and u_ϕ are the r, Δ, ϕ components of the displacement given in (8.31).

Following Gilbert and Dziewonski (1975), we shall put the source point at the pole ($\Delta = 0$) and evaluate normal-mode strain components as $\lim_{\Delta \to 0} \mathbf{e}(\Delta)$. We then find that all the components vanish for $|m| > 2$. The strain components for a spheroidal mode are shown in Table 8.1. Corresponding results for a toroidal mode are shown in Table 8.2. The constant b_0 appearing in these tables is $\sqrt{(2l+1)/4\pi}$. Evaluating the strain components at the source level $r = r_s$ and substituting them into (8.30), we find the response of the Earth to a point source with an arbitrary moment tensor that varies as a step function in time. For general time dependence we can use $M_{pq}(t) = \int_{-\infty}^{\infty} \dot{M}_{pq}(\tau)H(t-\tau)\,d\tau$. Interpreting this integrand as a step-function source acting at $t = \tau$, we find from (8.30) that

$$\mathbf{u}(\mathbf{x}, t) = \sum_i [{}_ie^*_{pq}(\mathbf{x}_s)\dot{M}_{pq}(t)] * {}_i\mathbf{u}(\mathbf{x}) \left(\frac{1 - \exp(-\omega_i t/2Q_i)\cos \omega_i t}{\omega_i^2}\right). \tag{8.38}$$

TABLE **8.1**
Strain components for a spheroidal mode.

	$m = 0$	$m = \pm 1$	$m = \pm 2$
e_{rr}	$b_0 \dfrac{dU}{dr}$	0	0
$e_{\Delta\Delta}$	$\dfrac{b_0}{r}[U - \frac{1}{2}\sqrt{l(l+1)}V]$	0	$\dfrac{b_0\sqrt{(l+2)(l-1)}}{4}\dfrac{V}{r}$
$e_{\phi\phi}$	$e_{\Delta\Delta}$	0	$-e_{\Delta\Delta}$
$2e_{r\Delta}$	0	$\dfrac{-b_0 m}{2}\left[\dfrac{\sqrt{l(l+1)}}{r}U + \dfrac{dV}{dr} - \dfrac{V}{r}\right]$	0
$2e_{r\phi}$	0	$2ie_{r\Delta}$	0
$2e_{\Delta\phi}$	0	0	$ime_{\Delta\Delta}$

TABLE **8.2**
Strain components for a toroidal mode.

	$m = 0$	$m = \pm 1$	$m = \pm 2$
e_{rr}	0	0	0
$e_{\Delta\Delta}$	0	0	$\dfrac{imb_0}{8}\sqrt{(l+2)(l-1)}\dfrac{W}{r}$
$e_{\phi\phi}$	0	0	$-e_{\Delta\Delta}$
$2e_{r\Delta}$	0	$\dfrac{-ib_0}{2}\left[\dfrac{dW}{dr} - \dfrac{W}{r}\right]$	0
$2e_{r\phi}$	0	$\dfrac{b_0 m}{2}\left[\dfrac{dW}{dr} - \dfrac{W}{r}\right]$	0
$2e_{\Delta\phi}$	0	0	$\dfrac{-b_0\sqrt{(l+2)(l-1)}}{2}\dfrac{W}{r}$

The asterisk in (8.38) following $\dot{M}_{pq}$ indicates convolution, and (8.38) indicates that the point source is naturally characterized by its moment-rate tensor, $\dot{\mathbf{M}}(t)$.

In this section we have followed the simple and straightforward steps due to Gilbert (1971) and Gilbert and Dziewonski (1975) in deriving the formula for excitation of free oscillations. Earlier, Saito (1967) solved the same problem using a method similar to the one we described for surface-wave excitation in Chapter 7, and he obtained a formula equivalent to (8.30). Figure 8.4 shows a comparison between observed and calculated spectral peaks at several WWSSN stations for a large deep earthquake in Colombia. The continuous lines indicate the observed radial displacement spectrum, and the vertical bars show the theoretical amplitudes of free oscillations calculated by Mendiguren (1973a) using Saito's formula and a focal mechanism determined from the observed P-wave first-motion pattern. Saito's results were used by Mendiguren (1973b) in devising a stacking technique for high-resolution identification of spectral peaks, as described in Box 8.2.

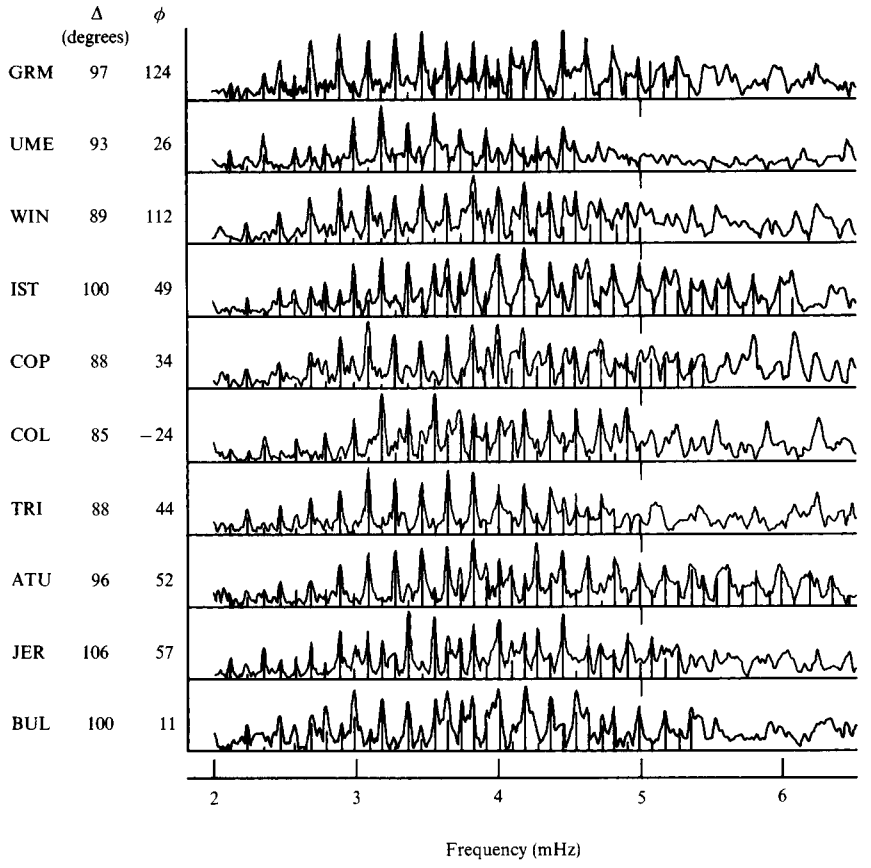

FIGURE **8.4**
Continuous lines indicate the observe radial displacement spectrum. Vertical bars are the theoretical spectral lines for the fundamental spheroidal mode. Δ is the epicentral distance. ϕ is the azimuth at the epicenter measured clockwise from North. [From Mendiguren, 1973a.]

BOX **8.2**
Identification of free-oscillation peaks when the earthquake source mechanism is known

When seismic motions are excited in a spherically symmetric nonrotating Earth by an earthquake, we have found that the oscillation consists of normal modes with distinct frequencies, expressed by spherical harmonics as different angular (l) and azimuthal (m) order numbers and depth-dependent eigenfunctions specified by another order number (n). If we know the epicenter, focal depth, and source mechanism of the earthquake, we can calculate the motion due to a normal mode of a given frequency by methods developed in this chapter. Assuming a point source of slip on a fault, the shape of the time function for each mode will be common at all the stations on the Earth, but the amplitude and sign will change from one station to another, as determined by the value of the excitation coefficient. For example, if the source is the moment tensor $\mathbf{M}(t) = \mathbf{M}H(t)$ acting at $\mathbf{x}_s$, then the excitation coefficient for the ith mode, from (8.30), is given by ${}_ie^*_{pq}(\mathbf{x}_s)M_{pq}$.

(continued)

BOX **8.2** *(continued)*

Suppose that we collect many seismograms from a good global network for an earthquake with known source parameters, and correct the sign according to the theoretical prediction for a particular mode based on the source parameters. (If the theoretical sign is plus, the record is unchanged. But if it is minus, the sign of the record is reversed.) We then sum all these corrected seismograms algebraically with no time shift. The result will enhance the signal (see Figure 8.3) associated with the particular mode for which we worked out the signs, and will tend to reduce the other modes. The Fourier transform of the stacked record will more clearly show the spectral peak of the wanted mode. The same result is obtained by first making Fourier transforms of the records, correcting the phase by π for a minus sign, and then stacking them.

This method was first applied by Mendiguren (1973b) to global data for a large deep-focus earthquake in Columbia. The method not only improved the resolution of spectral analysis, but also made possible a unique, unambiguous identification of many overtones. As shown in the Figure here, the method enhances the mode with given order number and suppresses neighboring modes. Subsequently, many hundreds of new modes were identified by Gilbert and Dziewonski (1975) using a similar stacking technique.

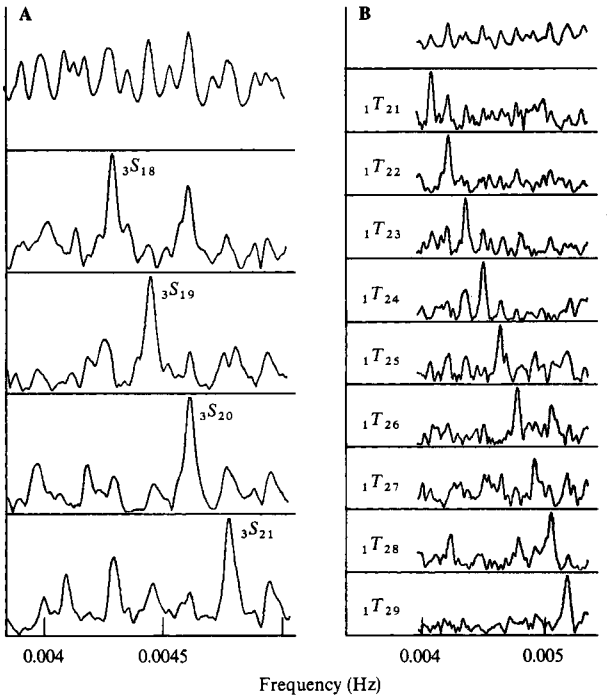

Spectral peaks of free oscillation for (on the left) the third higher spheroidal modes $_3S$ derived from the horizontal ground motion, and (on the right) the first higher torsional modes $_1T$ derived from the transverse horizontal ground motion. The spectra at the top are the sum of the absolute amplitudes of the spectra at all stations. The remaining spectra are the result of stacking with sign correction. [From Mendiguren, 1973b, copyright by the American Association for the Advancement of Science.]

8.3 Surface Waves on the Spherical Earth

In the preceding section, we found that the coefficient matrix for free oscillations ((8.33) or (8.34)) approaches that for surface waves as r tends to infinity provided that the wavenumber k of surface waves is replaced by $\sqrt{l(l+1)}/r$ for free oscillations. For most purposes here, $\sqrt{l(l+1)} \sim l + \frac{1}{2}$, and we can identify surface wave k as $(l+\frac{1}{2})/r$. (In fact, $k \leftrightarrow (l+\frac{1}{2})/r$ is more appropriate than $k \leftrightarrow \sqrt{l(l+1)}/r$, as shown in Box 9.6.) Since the wavelength λ is $2\pi/k$, λ is equal to $2\pi r/(l+\frac{1}{2})$, implying that the circumference is not exactly an integer multiple of this wavelength; it appears that there is an extra half wavelength. In other words, the distance between neighboring nodes of a free oscillation cannot be equal to half a wavelength everywhere. To examine this more closely, we shall consider the simple case of spheroidal modes generated by an explosive point source $M_{rr} = M_{\Delta\Delta} = M_{\phi\phi} = M_0$, with $M_{\Delta\phi} = M_{\phi r} = M_{r\Delta} = 0$. Substituting from Table 8.1 into (8.30), we find that the r-component of displacement is the spheroidal mode sum

$$u_r(\mathbf{x}, t) = \sum_n \sum_l {}_nA_l \cdot P_l(\cos\Delta) \cdot [1 - \exp(-{}_n\omega_l t/2{}_nQ_l)\cos {}_n\omega_l t], \tag{8.39}$$

where

$${}_nA_l = \frac{2l+1}{4\pi({}_n\omega_l)^2}\left[\frac{d}{dr}{}_nU_l + \frac{2\,{}_nU_l}{r} - \frac{\sqrt{l(l+1)}}{r}\,{}_nV_l\right]\Bigg|_{r=r_s} {}_nU_l(r), \tag{8.40}$$

and we have assumed that $M_0(t)$ is a step with unit amplitude (e.g., 1 dyn-cm). In (8.39) we are using $\mathbf{x} = (r, \Delta, \phi)$, and the sum over all modes i has been written as a sum over the fundamental and overtones n and order numbers l. Only $m = 0$ contributes. Thus, (8.39) shows a superposition of standing-wave patterns called *zonal harmonics*, determined by $P_l(\cos\Delta)$. Since $P_l(\cos\Delta)$ has exactly l nodes in the interval $0 < \Delta < \pi$, there are l cycles of oscillation around the great circle. On the other hand, the asymptotic expansion of $P_l(\cos\Delta)$, which is valid for large l except near $\Delta = 0$ or $\Delta = \pi$, is (see Boxes 8.4 and 9.6)

$$P_l(\cos\Delta) \sim \left(\frac{2}{(l+\frac{1}{2})\pi\sin\Delta}\right)^{1/2} \cos[(l+\tfrac{1}{2})\Delta - \pi/4]. \tag{8.41}$$

This shows again that the wavelength is approximately $2\pi r/(l+\frac{1}{2})$ except near $\Delta = 0$ or $\Delta = \pi$. Taking l cycles of such waves, we get $2\pi rl/(l+\frac{1}{2})$ instead of $2\pi r$. This means that the distance between neighboring nodes in the vicinity of $\Delta = 0$ or π is longer than elsewhere (see the figure in Box 8.1), and therefore that the apparent phase velocity is faster in these special regions.

In measuring surface-wave phase velocity, the above effect causes an apparent phase advance amounting to $\pi/2$ at each polar passage, which must be allowed for if the path contains the epicenter or its antipode. (The phase shift $\pi/4$ in (8.41) is doubled for entrance to and exit from the pole.) This is known as the *polar phase shift*, introduced in modern seismology by Brune *et al.* (1961), who showed that it resolved what previously had been inconsistent results for the phase velocities measured over minor arcs, major arcs, and full great circles.

BOX **8.3**

An example of the Poisson sum formula

Given a function $g = g(\nu)$, we shall first prove that

$$\sum_{l=-\infty}^{\infty} g(l+\tfrac{1}{2}) = \sum_{s=-\infty}^{\infty} (-1)^s \int_{-\infty}^{\infty} g(\nu) e^{2i\pi s\nu}\, d\nu. \tag{1}$$

Then, applying (1) to the function $f(\nu)$, where $f = g$ for $\nu \geq 0$ and $f = 0$ for $\nu < 0$, it follows that

$$\sum_{l=0}^{\infty} g(l+\tfrac{1}{2}) = \sum_{s=-\infty}^{\infty} (-1)^s \int_{0}^{\infty} g(\nu) e^{2i\pi s\nu}\, d\nu. \tag{2}$$

To prove (1), define $S = S(x)$ by $S(x) = \sum_{l=-\infty}^{\infty} g(l+\frac{1}{2}+x)$. Then S is periodic with period 1. We can write out the Fourier series expansion for $S(x)$ as

$$S(x) = \sum_{s=-\infty}^{\infty} S_s e^{-2i\pi sx}, \qquad \text{where } S_s = \int_0^1 S(y) e^{2i\pi sy}\, dy.$$

Taking $x = 0$ and substituting for S_s and $S(y)$, we get

$$S(0) = \sum_{s=-\infty}^{\infty} \int_0^1 \sum_{l=-\infty}^{\infty} g(l+\tfrac{1}{2}+y) e^{2i\pi sy}\, dy,$$

and note that $S(0)$ equals the left-hand side of (1). Moreover,

$$e^{2i\pi sy} = (-1)^s e^{2i\pi s(l+1/2+y)}$$

because s and l are integers. Thus

$$\begin{aligned}\sum_{l=-\infty}^{\infty} g(l+\tfrac{1}{2}) &= \sum_{s=-\infty}^{\infty} (-1)^s \int_0^1 \sum_{l=-\infty}^{\infty} g(l+\tfrac{1}{2}+y) e^{2i\pi s(l+1/2+y)}\, dy \\ &= \sum_{s=-\infty}^{\infty} (-1)^s \sum_{l=-\infty}^{\infty} \int_{l+1/2}^{l+3/2} g(\nu) e^{2i\pi s\nu}\, d\nu,\end{aligned}$$

which equals the right-hand side of (1).

For a more quantitative comparison of free oscillations and surface waves, we shall use the Poisson sum formula for each overtone in (8.39). From equation (2) of Box 8.3, we then obtain

$$u_r(\mathbf{x}, t) = \sum_n \int_0^{\infty} d\nu \sum_{s=-\infty}^{\infty} (-1)^s ({}_nA_{\nu-1/2}) P_{\nu-1/2}(\cos\Delta) C(\nu, t) e^{2i\pi s\nu}, \tag{8.42}$$

where

$$C(\nu, t) = H(t)[1 - \cos({}_n\omega_{\nu-1/2} t) \cdot \exp(-{}_n\alpha_{\nu-1/2} t)] \tag{8.43}$$

and α is related to the temporal Q via $\alpha = \omega/2Q$.

Following Gilbert (1976), we rewrite the sum over s in (8.42) using Legendre functions of the second kind, denoted by $Q_l(\cos\Delta)$ (see Box 8.4). Then

$$u_r(\mathbf{x},t) = \sum_n \int_0^\infty {}_nA_{\nu-1/2} \sum_{N=1}^{\infty} R_N(\nu,\Delta)C(\nu,t)\,d\nu, \tag{8.44}$$

where, for N odd,

$$\begin{aligned} R_N = (-1)^{(N-1)/2}\{&P_{\nu-1/2}(\cos\Delta)\cos[(N-1)\pi\nu] \\ &+ \frac{2}{\pi}Q_{\nu-1/2}(\cos\Delta)\sin[(N-1)\pi\nu]\}, \end{aligned} \tag{8.45}$$

and for N even,

$$R_N = (-1)^{N/2}\left\{P_{\nu-1/2}(\cos\Delta)\cos(N\pi\nu) - \frac{2}{\pi}Q_{\nu-1/2}(\cos\Delta)\sin(N\pi\nu)\right\}. \tag{8.46}$$

The equivalence of (8.42) and (8.44) follows from

$$\begin{aligned} &R_1 + R_2 + R_3 + R_4 \cdots \\ &\quad = P_{\nu-1/2}(1 - \cos 2\pi\nu - \cos 2\pi\nu + \cos 4\pi\nu + \cos 4\pi\nu - \cos 6\pi\nu - \cdots) \\ &\quad + \frac{2}{\pi}Q_{\nu-1/2}(0 + \sin 2\pi\nu - \sin 2\pi\nu - \sin 4\pi\nu + \sin 4\pi\nu + \sin 6\pi\nu - \cdots) \\ &\quad = \sum_{s=-\infty}^{\infty}(-1)^s P_{\nu-1/2}e^{2i\pi\nu s}. \end{aligned}$$

The reason for introducing the R_N is that they are the appropriate horizontal wave functions for the Nth orbit of waves around the Earth. The orbit numbering is shown in Figure 8.5. Note, however, that each R_N as defined in (8.45)–(8.46) is still a standing wave, rather than a traveling wave. This is demonstrated in Box 8.4, and our point here is that for purposes of comparison with surface waves we should expect, for each N, to have horizontal

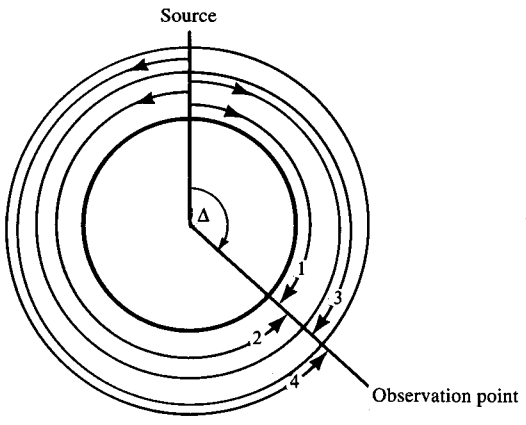

FIGURE **8.5**
Orbit numbering for waves traveling around the Earth. $N = 1$ is the minor arc; $N = 2$ the major arc; $N \geq 3$ involves at least one great-circle path.

BOX **8.4**

Different Legendre functions and their asymptotic approximations

In Box 8.1 we examined Legendre polynomials $P_l(\cos\Delta)$. Although these are the only solutions that are physically allowed near $\Delta = 0$ and $\Delta = 180°$, it is often worthwhile to work with different solutions to the Legendre equation, since these may locally be suitable for representing seismic motions at distances away from $\Delta = 0$ and $\Delta = 180°$.

Quoting from Nussenzveig (1965),

$$P_{\nu-1/2}(\cos\Delta) = \sqrt{\frac{2}{\pi\nu\sin\Delta}}\left[\cos\left(\nu\Delta - \frac{\pi}{4}\right) + \frac{\cot\Delta}{8\nu}\sin\left(\nu\Delta - \frac{\pi}{4}\right) + O\left(\frac{1}{\nu^2}\right)\right] \quad (1)$$

for $0 < \varepsilon \le \Delta \le \pi - \varepsilon$, $|\nu| \gg 1$, and $|\nu|\varepsilon \gg 1$. This solution, behaving like

$$(\sin\Delta)^{-1/2}\cos(\nu\Delta - \tfrac{1}{4}\pi),$$

suggests that a linearly independent solution might exist with asymptotic behavior like $(\sin\Delta)^{-1/2}\sin(\nu\Delta - \frac{1}{4}\pi)$. By summing and subtracting these solutions, one can thus obtain traveling waves. In fact, there are Legendre solutions $Q^{(i)}(i = 1, 2)$ with the following properties:

$$Q^{(1)(2)}_{\nu-1/2}(\cos\Delta) = \frac{e^{\mp i(\nu\Delta - \pi/4)}}{\sqrt{2\pi\nu\sin\Delta}}\left[1 \pm i\frac{\cot\Delta}{8\nu} + O\left(\frac{1}{\nu^2}\right)\right] \quad (2)$$

for $0 < \varepsilon \le \Delta \le \pi - \varepsilon$, $|\nu| \gg 1$, $|\nu|\varepsilon \gg 1$, and $(\nu - \frac{1}{2})$ not near the negative integers, where $Q^{(i)}_{\nu-1/2}$ has poles. These poles cancel in the sum

$$P_l = Q_l^{(1)} + Q_l^{(2)}.$$

The formal definition of $Q_l^{(i)}$ is

$$Q_l^{(1)} = \frac{1}{2}\left(P_l + \frac{2i}{\pi}Q_l\right), \qquad Q_l^{(2)} = \frac{1}{2}\left(P_l - \frac{2i}{\pi}Q_l\right), \quad (3)$$

where Q_l is the Legendre function of the second kind, but the major properties of $Q_l^{(i)}$ are those that follow from (2).

(continued)

phase functions that, for positive wavenumber, are standing waves. This follows because in Chapters 6 and 7 we frequently found solutions

$$u(X, \omega) = \int_0^\infty f(k, \omega)J_0(kX)\,dk \quad (8.47)$$

for flat Earth models. Here we have introduced X as the horizontal distance (the range); k is horizontal wavenumber, and J_0 is the zero-order Bessel function. The integrand of (8.47) is a standing wave, and to obtain a traveling-wave representation we used $f(-k, \omega) = -f(k, \omega)$ and

BOX **8.4** *(continued)*

Two further solutions of Legendre's equation are given by the combinations (8.45) and (8.46). Writing these in terms of $Q^{(1)}$ and $Q^{(2)}$, one obtains, for N odd,

$$R_N = (-1)^{(N-1)/2}[Q^{(1)}_{\nu-1/2}(\cos\Delta)e^{-i(N-1)\pi\nu} + Q^{(2)}_{\nu-1/2}(\cos\Delta)e^{i(N-1)\pi\nu}]$$
$$\sim (-1)^{(N-1)/2}\sqrt{\frac{2}{\pi\nu\sin\Delta}}\cos\left\{\nu[(N-1)\pi+\Delta]-\frac{\pi}{4}\right\}, \tag{4}$$

and for N even,

$$R_N = (-1)^{N/2}[Q^{(2)}_{\nu-1/2}(\cos\Delta)e^{-iN\pi\nu} + Q^{(1)}_{\nu-1/2}(\cos\Delta)e^{iN\pi\nu}]$$
$$\sim (-1)^{N/2}\sqrt{\frac{2}{\pi\nu\sin\Delta}}\cos\left\{\nu[N\pi-\Delta]+\frac{\pi}{4}\right\}. \tag{5}$$

From (4) and (5), it is clear that each R_N is a standing-wave pattern.

A uniformly asymptotic approximation for $P_{\nu-1/2}$, which works even near $\Delta = 0$, is

$$P_{\nu-1/2}(\cos\Delta) = \sqrt{\frac{\Delta}{\sin\Delta}}\left[J_0(\nu\Delta)+\frac{1}{8}(\Delta\cot\Delta-1)\frac{J_1(\nu\Delta)}{\nu\Delta}+O\left(\frac{1}{\nu^2}\right)\right].$$

The effort to identify body waves and surface waves, in some expression that includes these as well as other waves, is primarily an exercise in manipulating the six Legendre functions P, Q, $Q^{(1)}$, $Q^{(2)}$, $R_N(N \text{ even})$, $R_N(N \text{ odd})$. This problem will recur in Chapter 9, where we choose to use a Watson transformation rather than a Poisson sum.

$$u(X,\omega) = \tfrac{1}{2}\int_{-\infty}^{\infty} f(k,\omega)H_0^{(1)}(kX)\,dk \tag{8.48}$$

(see, e.g., (6.16)). It is interesting that the traveling wave functions $H_0^{(1)}$ and $H_0^{(2)}$ for a flat Earth have a branch cut on the negative real-wavenumber axis ($k < 0$), and that the analogous wave functions for a spherical Earth, $Q^{(2)}_{\nu-1/2}$ and $Q^{(1)}_{\nu-1/2}$, have poles on the negative real wavenumber axis ($\nu < 0$). In Chapter 9 we shall find several further examples of strings of poles that, in many ways, behave like branch cuts.

Working only with the first-arriving waves from (8.44), $N = 1$, we write $l + \frac{1}{2} = \nu = kr$, where $r = |\mathbf{x}|$ is the radial position of the receiver (usually $r = r_\oplus$, the Earth's radius). Then

$$u_r(\mathbf{x},t) = \sqrt{\frac{\Delta}{\sin\Delta}}\sum_n \int_0^\infty r\,{}_nA(k)\,J_0(kX)\,C(kr,t)\,dk, \tag{8.49}$$

where we have used

$$R_1(\nu,\Delta) = P_{\nu-1/2}(\cos\Delta) \sim \sqrt{\frac{\Delta}{\sin\Delta}}J_0(kX). \tag{8.50}$$

X is the horizontal range $r\Delta$, so that $\nu\Delta = kX$; and ${}_nA(k) = {}_nA_{\nu-1/2}$.

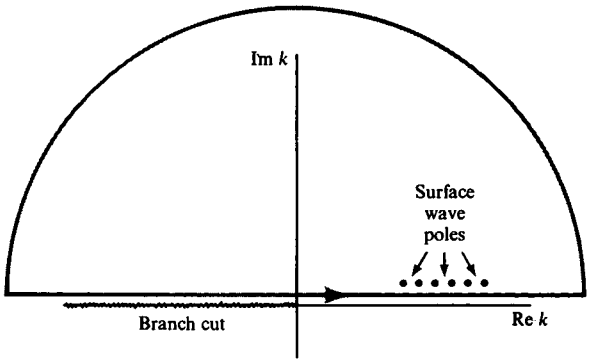

FIGURE **8.6**
Features in the complex wavenumber plane, used to evaluate the surface waves present in (8.51).

Ignoring the static offset term in $C(kr, t)$, we note that the Fourier transform $u_r(\mathbf{x}, \omega)$ is given by substituting

$$\frac{1}{2}\left[\frac{1}{i[\omega + {}_n\omega(k)] - {}_n\alpha(k)} + \frac{1}{i[\omega - {}_n\omega(k)] - {}_n\alpha(k)}\right]$$

for C in (8.49). The coefficient of $J_0(kX)$ in (8.49) is odd in k, hence

$$u_r(\mathbf{x}, \omega) = \frac{1}{4}\sqrt{\frac{\Delta}{\sin\Delta}} \sum_n \int_{-\infty}^{\infty} r\ {}_nA(k)\ H_0^{(1)}(kX) \frac{dk}{i[\omega - {}_n\omega(k)] - {}_n\alpha(k)}. \quad (8.51)$$

The other term, involving $\omega + {}_n\omega(k)$, has been dropped, since it generates a pole in the lower half of the complex k-plane, and our intention is to complete a closed path in the upper half-plane. To locate the pole of the above integrand and evaluate its residue, we can obtain the Taylor series for ${}_n\omega(k)$ as k varies near that value $k_n(\omega)$ which is the eigenvalue for the nth surface-wave mode. Thus

$${}_n\omega(k) = \omega + (k - k_n)U_n(\omega) + \cdots,$$

where $U_n(\omega) = d\omega/dk =$ the group velocity. Almost always the group velocity is positive, so that the pole of (8.51) lies in the first quadrant of the complex k-plane, at $k = k_n(\omega) + i\alpha_n/U_n(\omega)$. Here α_n is based on a temporal Q, so that if we shift to a description of attenuation based on spatial Q we must replace $\alpha_n/U_n = \omega/2Q_n^{\text{temporal}}U_n$ by $\omega/2Q_n^{\text{spatial}}c_n = k_n/2Q_n^{\text{spatial}}$ (see ((7.93)). Using the integration path shown in Figure 8.6, with the far-field approximation to $H_0^{(1)}$, we can evaluate the residue from the poles in the first quadrant (one pole for each n; $n = 0, 1, 2, \ldots$), and obtain

$$u_r(\mathbf{x}, \omega) = i\frac{\pi}{2}\sqrt{\frac{\Delta}{\sin\Delta}} \sum_n \frac{rA(k_n)}{U_n}\sqrt{\frac{2}{\pi k_n X}} \exp\left[i\left(k_n X + \frac{\pi}{4}\right)\right] \exp(-k_n X/2Q_n). \quad (8.52)$$

Here we are writing $A(k_n)$ for ${}_nA(k)$ evaluated at $k = k_n(\omega)$, and we have assumed that factors in (8.51) are slowly varying functions of k near each pole, except for the phase function e^{ikX}. Equation (8.52) gives a representation of surface waves due to an explosive unit step-function source in a spherical Earth.

In order to compare (8.52) with the corresponding formula (7.152) for Rayleigh waves in a plane-stratified medium, we must allow for the differences in normalization of radial/vertical eigenfunctions. In fact, $r\,{}_nU_l(r)$ corresponds to $r_2(z)/\sqrt{2I_1}$; $rd({}_nU_l(r))/dr$ to $-(dr_2(z)/dz)/\sqrt{2I_1}$; and $r\,{}_nV_l(r)$ to $r_1(z)/\sqrt{2I_1}$. Thus $rA(k_n)$ in (8.52) is replaced to first order by

$$-\frac{k_n}{2\pi\omega^2}\left[\frac{dr_2}{dz} + k_n r_1\right]\Bigg|_{\text{source level}} \frac{r_2(z)}{2I_1}.$$

Noting that (8.52) is for *upward* motion, but (7.152) is for the *downward* component (see Box 7.10), it follows that the two formulas are virtually identical. The only differences lie in the spatial attenuation factor, which we have explicitly included in (8.52), and in the factor $\sqrt{\Delta/\sin\Delta}$, which accounts for the azimuthal geometrical spreading over the surface of a sphere as opposed to the spreading over a flat surface.

In summary, the effect of the Earth's sphericity can be taken into account by the use of geometrical spreading factor proportional to $1/\sqrt{\sin\Delta}$ and by appropriate eigenfunctions obtained by solving (8.33) and/or (8.34) for the motion-stress vector in the spherical Earth model.

8.4 Free Oscillations of a Self-Gravitating Earth

Gravity does not affect the torsional modes of free oscillation, because these have no radial component of displacement and are divergence-free, so that the density distribution is unchanged. But vertical motions and density perturbations do occur in spheroidal motions. Since gravity is effectively a body force, its time dependence will influence the overall motion. Self-gravitation cannot be neglected for accurate study of spheroidal modes with periods longer than about 500 seconds, and before giving the necessary theory it is interesting to look at the historical background.

From the theory of free oscillations of a homogeneous solid elastic sphere, published by Lamb in 1882, it is apparent that the mode with the greatest period is ${}_0S_2$. Bromwich (1898) studied the period equation numerically, and was able to incorporate the effect of self-gravitation in the case of an incompressible medium. He showed that for an incompressible sphere having the same size and mass as the Earth, and with rigidity that of steel, the period of ${}_0S_2$ is decreased from about 65 minutes to about 55 minutes by including self-gravitation. Love (1911, reprinted 1967) was able to allow for self-gravitation even in a compressible medium, and by taking Poisson's ratio equal to $\frac{1}{4}$ in an Earth model that was otherwise the same as that considered by Bromwich, he found the period of ${}_0S_2$ would be very close to one hour. Clearly, if this mode were to be observed, instruments would be needed that had sensitivity at periods very much longer than the periods of seismic motion then being routinely recorded.

In the 1940s and 1950s, it became apparent that observed seismic surface waves had properties that to a large extent could be understood in terms of the theory for surface waves within a stack of homogeneous flat-lying plates welded together at the interfaces. The theory for such a medium was extensively studied (Haskell, 1953; Ewing *et al.*, 1957), and in particular the dispersion for such an elastic medium could be calculated. There was clearly a need to design seismometers that were useful at longer and longer periods, because the observed surface-wave dispersion could then be used to infer Earth structure deeper and deeper within the mantle. Hugo Benioff, at the California Institute of Technology, was a leader in instrument design, and for the Kamchatka earthquake of 1952 November 4 his quartz-rod strain seismometer recorded a 57-min oscillation that "may represent free oscillations of the Earth as a whole" (Benioff *et al.*, 1954). Many different individuals were stimulated by this result to develop better seismometers for very long periods, and also to undertake the theoretical and numerical efforts needed to predict the free oscillations of realistic Earth models. Thus Alterman *et al.* (1959) published the theoretical value for the ${}_0S_2$-period in Earth models that had earlier been proposed by Bullen and Bullard: in different models, with and without an inner solid core, the values were always around 53.5–53.7 min. Concurrent improvements in instrumentation had been made, but observational confirmation had to await a large enough earthquake. In 1960 May 22, one of the greatest earthquakes of modern times occurred in Chile. (The magnitude was greater than 8, but this event was so big that it saturated conventional magnitude scales. See Kanamori, 1977.) Amid great excitement, three different groups of investigators reported at the IASPEI (International Association of Seismology and Physics of the Earth's Interior) meeting, held in the summer of 1960 in Helsinki, that they had observed a wide range of normal modes of the whole Earth (Benioff *et al.*, 1961; Ness *et al.*, 1961; Alsop *et al.*, 1961a). Clearly, a whole new branch of seismology had been opened.

In this section we give the theory for spheroidal modes in an Earth model that is spherically symmetric, nonrotating, self-gravitating and elastic, and has an isotropic stress–strain relation and an isotropic initial stress.

The equations of elastic motion that we developed in Chapter 2 were for the most part based upon a Lagrangian formulation in which the particle $\mathbf{x}$ at time t_0 was assumed to move to $\mathbf{x} + \mathbf{u} = \mathbf{X}$ at time t, and we studied $\mathbf{u}$ as the function $\mathbf{u} = \mathbf{u}(\mathbf{x}, t)$. Unfortunately, the Lagrangian formulation does not easily handle variations of density and the consequent effects of a fluctuating gravity field, so we shall here take an Eulerian approach: $\mathbf{x}$, $\mathbf{X}$, and $\mathbf{u}$ are defined as above, but we study quantities such as $\mathbf{u}$ and ρ as functions of $(\mathbf{X}, t)$.

Let us then consider a spherical Earth model that is in hydrostatic equilibrium under the self-gravitation. The equilibrium state is described by its density $\rho_0(r)$, pressure $P_0(r)$, and gravitational potential $V_0(r)$, all of which are functions only of r. Since V_0 is due to the density distribution ρ_0, we can apply Poisson's equation

$$\nabla^2 V_0 = -4\pi\gamma\rho_0, \tag{8.53}$$

where γ is the gravitational constant ($\sim 6.674 \times 10^{-11}\,\mathrm{m^3\,kg^{-1}s^{-2}}$). The equation of equilibrium is given by matching the body force to the pressure gradient. Then

$$-\rho_0 g_0 \hat{\mathbf{r}} = \rho_0 \nabla V_0 = \nabla P_0, \tag{8.54}$$

where $g_0 = g_0(r)$, which is positive, is the magnitude of the unperturbed gravitational force per unit mass.

Superimposed on this initial state, we consider a small displacement perturbation $\mathbf{u}(\mathbf{X})\exp(-i\omega t)$. We shall describe the density and gravitational potential in the perturbed state by $\rho(\mathbf{X}, t)$ and $V_0 + K(\mathbf{X})\exp(-i\omega t)$, respectively, taking here an Eulerian approach.

From conservation of mass, the increase in mass within a volume V (fixed in space) is equal to the influx of mass through the surface S enclosing V, so that

$$\int_V \rho\, dV = \int_V \rho_0\, dV - \int_S \rho_0 \mathbf{u}\exp(-i\omega t)\cdot \mathbf{n}\, dS, \tag{8.55}$$

where $\mathbf{n}$ is the outward unit normal for the surface element dS. (Equation (8.55) is an approximation, in that the density of material crossing S is actually changing with time. We have taken it as ρ_0, which is adequate for a first-order approximation because $\mathbf{u}$ is small.) Changing the surface integral to a volume integral by Gauss's theorem, we obtain

$$\rho(\mathbf{X}, t) = \rho_0 - \nabla\cdot(\rho_0\mathbf{u}\exp(-i\omega t)).$$

Since ρ_0 is a function only of r, we can rewrite the above equation as

$$\rho = \rho_0 - \left(u_r\frac{d\rho_0}{dr} + \rho_0\nabla\cdot\mathbf{u}\right)\exp(-i\omega t). \tag{8.56}$$

The gravitational potential in the perturbed state satisfies the Poisson equation

$$\nabla^2[V_0 + K\exp(-i\omega t)] = -4\pi\gamma\rho,$$

which with (8.53) and (8.56) can be used to show that

$$\nabla^2 K = 4\pi\gamma\left(u_r\frac{d\rho_0}{dr} + \rho_0\nabla\cdot\mathbf{u}\right). \tag{8.57}$$

To obtain the equation of motion, we use Cartesian coordinates (X_1, X_2, X_3) and begin with the relation between rate of change of momentum, body force (gravity), and stress gradient:

$$-\rho\omega^2 u_i\exp(-i\omega t) = \rho[V_0 + K\exp(-i\omega t)]_{,i} + \sigma_{i,jj}. \tag{8.58}$$

(To be exact, the left-hand side here should contain the material acceleration, which is $D^2\mathbf{u}\exp(-i\omega t)/Dt^2$. But $\mathbf{u}$ and the particle velocity are small, so that the acceleration is $-\omega^2\mathbf{u}\exp(-i\omega t)$ to first order.) The stress $\sigma_{ij}(\mathbf{X}, t)$ is evaluated in the perturbed state. Since the particle at $\mathbf{X}$ at time t was initially at $\mathbf{u} = \mathbf{X} - \mathbf{u}\exp(-i\omega t)$, the stress at $\mathbf{X}$ is the initial stress at $\mathbf{X} - \mathbf{u}\exp(-i\omega t)$ together with an additional effect due to the distortion of the

region around the **x**-particle, i.e., due to the strains associated with **u**. For an isotropic body with Lamé's constants λ and μ, we therefore have

$$\begin{aligned}\sigma_{ij}(\mathbf{X},t) &= -P_0\delta_{ij}\Big|_{\mathbf{X}-\mathbf{u}\exp(-i\omega t)} + \text{stress due to } \mathbf{u} \\ &= -P_0(r)\delta_{ij} + \left[u_r\frac{dP_0}{dr}\delta_{ij} + \lambda\nabla\cdot\mathbf{u}\delta_{ij} + \mu(u_{i,j}+u_{j,i})\right]\exp(-i\omega t)\end{aligned} \tag{8.59}$$

Substituting the above form into (8.58) and retaining first-order terms, it follows that

$$\begin{aligned}-\rho_0\omega^2\mathbf{u} = &\left(u_r\frac{d\rho_0}{dr} + \rho_0\nabla\cdot\mathbf{u}\right)g_0\hat{\mathbf{r}} + \rho_0\nabla K - \nabla(\rho_0 u_r g_0) + \Big[(\lambda+2\mu)\nabla\nabla\cdot\mathbf{u} \\ &- \mu\nabla\times(\nabla\times\mathbf{u}) + \frac{d\lambda}{dr}(\nabla\cdot\mathbf{u})\hat{\mathbf{r}} + 2\frac{d\mu}{dr}\frac{\partial\mathbf{u}}{\partial r} + \frac{d\mu}{dr}\hat{\mathbf{r}}\times(\nabla\times\mathbf{u})\Big].\end{aligned} \tag{8.60}$$

The term [ ] here is merely the vector having its ith Cartesian component given by $\{\lambda\nabla\cdot\mathbf{u}\delta_{ij} + \mu(u_{i,j}+u_{j,i})\}_{,j}$, assuming that λ and μ depend only on radius r. The remaining terms on the right-hand side of (8.60) quantify the effect of self-gravitation. When $\rho_0(r)$, $\lambda(r)$, and $\mu(r)$ are known, it is possible to find $g_0(r)$ and then solve (8.57) and (8.60) for K and **u** under appropriate initial and boundary conditions. Note that (8.60) is valid also for toroidal modes, although most of the terms in this equation are then zero.

We have previously found that equations of motion are conveniently handled if they are transformed into $d\mathbf{f}/dr = \mathbf{A}\mathbf{f}$, with **f** continuous across discontinuities in the coefficient matrix $\mathbf{A} = \mathbf{A}(r,\omega)$. This result motivates the following discussion.

When there is a discontinuous jump in some medium property (e.g., ρ_0, λ, or μ) at a certain radius r_d, then displacement and traction components are continuous across r_d and so is the gravitational potential perturbation K. But dK/dr is discontinuous if there is a density jump. We therefore seek a quantity related to dK/dr, which is continuous.

Rewriting (8.57) as $\nabla\cdot(\nabla K - 4\pi\gamma\rho_0\mathbf{u}) = 0$, we apply Gauss's theorem to any volume V with surface S and find $\int_S(\nabla K - 4\pi\gamma\rho_0\mathbf{u})\cdot\mathbf{n}\,dS = 0$. Choosing V as the thin disc with one flat face just above the interface r_d and one just below, it follows that $dK/dr - 4\pi\gamma\rho_0 u_r$ must be the same on either side of the interface. Thus we might choose the continuous quantity $dK/dr - 4\pi\gamma\rho_0 u_r$ as one of the dependent variables.

For a spheroidal mode, we have already seen that the displacement and traction in the mode (l,m,n) are given by

$$\begin{aligned}u_r &= {}_nU_l(r)Y_l^m(\Delta,\phi), \quad u_\Delta = \frac{{}_nV_l(r)}{\sqrt{l(l+1)}}\frac{\partial Y_l^m}{\partial\Delta}, \quad u_\phi = \frac{{}_nV_l(r)}{\sqrt{l(l+1)}}\frac{1}{\sin\Delta}\frac{\partial Y_l^m}{\partial\phi}, \\ \tau_{rr} &= {}_nR_l(r)Y_l^m, \quad \tau_{r\Delta} = \frac{{}_nS_l(r)}{\sqrt{l(l+1)}}\frac{\partial Y_l^m}{\partial\Delta}, \quad \tau_{r\phi} = \frac{{}_nS_l(r)}{\sqrt{l(l+1)}}\frac{1}{\sin\Delta}\frac{\partial Y_l^m}{\partial\phi},\end{aligned} \tag{8.61}$$

where $(\tau_{rr}, \tau_{r\Delta}, \tau_{r\phi})$ is the traction derived from **u**. The gravitational potential can also be separated as

$$K = {}_nK_l(r)Y_l^m(\Delta,\phi), \tag{8.62}$$

and following Takeuchi and Saito (1972) we introduce

$$ {}_nG_l(r) = \frac{d_nK_l}{dr} - 4\pi\gamma\rho_0({}_nU_l) + \frac{l+1}{r}{}_nK_l. \tag{8.63} $$

We have already pointed out that $(dK/dr - 4\pi\gamma\rho_0 u_r)$ and K are continuous across density jumps, so that ${}_nG_l$ is continuous. The additional virtue of ${}_nG_l$ is that ${}_nG_l(r_\oplus) = 0$ (i.e., at the Earth's surface), a result that follows from K satisfying Laplace's equation in $r > r_\oplus$ and hence ${}_nK_l(r) = {}_nK_l(r_\oplus)(r_\oplus/r)^{l+1}$ outside the Earth.

Substituting (8.61)–(8.63) into (8.57) and (8.60), we arrive at a set of six first-order linear differential equations for the radial functions:

$$ \begin{aligned}
\frac{dU}{dr} &= \frac{1}{\lambda+2\mu}\left\{R - \frac{\lambda}{r}[2U - \sqrt{l(l+1)}V]\right\},\\
\frac{dR}{dr} &= -\omega^2\rho_0 U + \frac{2}{r}\left(\lambda\frac{dU}{dr} - R\right) + \frac{1}{r}\left[\frac{2(\lambda+\mu)}{r} - \rho_0 g_0\right][2U - \sqrt{l(l+1)}V]\\
&\quad + \frac{\sqrt{l(l+1)}}{r}S - \rho_0\left(G - \frac{l+1}{r}K + \frac{2g_0}{r}U\right),\\
\frac{dV}{dr} &= \frac{1}{\mu}S + \frac{1}{r}[V - \sqrt{l(l+1)}U],\\
\frac{dS}{dr} &= -\omega^2\rho_0 V - \frac{\lambda}{r}\sqrt{l(l+1)}\frac{dU}{dr} - \frac{\lambda+2\mu}{r^2}[2\sqrt{l(l+1)}U - l(l+1)V]\\
&\quad + 2\frac{\mu}{r^2}[\sqrt{l(l+1)}U - V] - \frac{3}{r}S - \frac{\rho_0}{r}\sqrt{l(l+1)}(K - g_0U),\\
\frac{dK}{dr} &= G + 4\pi\gamma\rho_0 U - \frac{l+1}{r}K,\\
\frac{dG}{dr} &= \frac{l-1}{r}(G + 4\pi\gamma\rho_0 U) + \frac{4\pi\gamma\rho_0}{r}[2U - \sqrt{l(l+1)}V],
\end{aligned} \tag{8.64} $$

where we have dropped the subscripts n and l. The equations (8.64) can be written as $d\mathbf{f}/dr = \mathbf{A}\mathbf{f}$ with $\mathbf{f}$ continuous and $\mathbf{A} = \mathbf{A}(r, \omega)$. The existence of a solution for $\mathbf{f}$ that is regular at $r = 0$, and for which ${}_nR_l(r_\oplus)$, ${}_nS_l(r_\oplus)$, and ${}_nG_l(r_\oplus)$ are zero, requires that ω be an eigenvalue. Because the numerical effort to solve (8.64) for the eigenvalues ${}_n\omega_l$ and eigenvectors $\mathbf{f} = ({}_nV_l, {}_nU_l, {}_nS_l, {}_nR_l, {}_nK_l, {}_nG_l)^T$ is very similar to the effort described in Section 7.2 for surface waves, we shall not give further details. For toroidal modes, (8.60) gives the coupled system (8.34), since gravity has no direct influence.

The variational methods of Section 7.3 also apply to normal modes, with only notational changes. Perturbation in phase velocity (due to small changes in structure) is replaced by perturbation in eigenfrequency. For example, for a toroidal mode (see (8.34) and (8.36)), and using ρ now for the original density distribution (rather that ρ_0),

$$ \left(\frac{\delta\omega}{\omega}\right)_l = \int_0^{r_\oplus}\left[\frac{\rho}{\omega}\left(\frac{\partial\omega}{\partial\rho}\right)_{l,\beta}\frac{\delta\rho}{\rho} + \frac{\beta}{\omega}\left(\frac{\partial\omega}{\partial\beta}\right)_{l,\rho}\frac{\delta\beta}{\beta}\right]dr, \tag{8.65} $$

where

$$\left(\frac{\rho}{\omega}\frac{\partial\omega}{\partial\rho}\right)_{l,\beta} = \frac{1}{2\omega^2}\left[-\omega^2\rho r^2W^2 + \frac{r^2T^2}{\mu} + (l-1)(l+2)\mu W^2\right]$$

and

$$\left(\frac{\beta}{\omega}\frac{\partial\omega}{\partial\beta}\right)_{l,\rho} = \frac{1}{\omega^2}\left[\frac{r^2T^2}{\mu} + (l-1)(l+2)\mu W^2\right]. \tag{8.66}$$

Partial derivatives for toroidal and spheroidal modes in a transversely isotropic Earth model were given by Takeuchi and Saito (1972), and Woodhouse (1976) showed how the perturbation of internal boundaries affects the eigenfrequencies.

We have now given a fairly complete account of normal-mode theory in a spherically symmetric nonrotating Earth model. About 40 different eigenfrequencies were distinguished in 1960 following the Chilean earthquake, and the initial effort of various investigators was simply to identify these modes of oscillation correctly. The data provided by eigenfrequencies were quite clearly of a different nature from travel-time data of body waves, since it was known how to construct Earth models having a given travel-time curve, but it was not clear how normal-mode eigenfrequencies could be used to infer Earth structure other than by trial and error. The importance of this problem was a stimulus to develop new methods of inverting geophysical data, and Backus and Gilbert (1967, 1968, 1970) developed inversion theory using normal-mode data as an example.

It has been possible in recent decades to observe and identify individual normal modes from earthquakes with magnitude (M_s) as low as 6.5 (Block *et al.*, 1970). To determine which normal modes will be favorably excited by a given earthquake, we see from (8.38) that the crucial quantity is the strain in the mode, evaluated at the source. Thus shallow earthquakes favorably excite the fundamental modes (${}_0S_l$ and ${}_0T_l$ for different l), whereas deep earthquakes are best for observing overtones. Using the spectra of 211 WWSSN seismograms from two deep earthquakes, Gilbert and Dziewonski (1975) were able to report 812 eigenfrequencies. The great majority were overtones. Errors were estimated to be as low as 0.05% for many modes, and generally were less than 0.1%.

Figure 8.7 shows 1203 torsional mode frequencies in the band from 0 to 18 mHz for l ranging from 0 to 100. Each mode indicated in the figure is a multiplet (ranging over $-m \le l \le m$) that degenerates to a unique frequency (independent of m) for a nonrotating spherically symmetric isotropic Earth. The figure also shows 380 of these modes (plotted with a larger symbol) that have been identified in seismic data. From the relation $l + \frac{1}{2} = kr$, we can identify the apparent velocity of a given mode, measured at the Earth's surface as $\omega r_\oplus/(l+\frac{1}{2})$ (in km/s). The seismic body wave ScS (the S-wave reflected upward from the core–mantle boundary) has apparent velocities greater than a certain minimum value determined by the apparent velocity of the ScS wave that just grazes the core–mantle boundary. This minimum slope of $\omega/(l+\frac{1}{2})$ is indicated by the oblique line in Figure 8.7. The information about the Earth that is contained in ScS data (polarized as SH) can be expected to be similar to the information in toroidal modes with the same horizontal phase velocity as ScS, i.e., modes to the left of the line. Modes to the right have lower apparent velocity, and correspond to SH-waves in the mantle that do not travel steeply enough to hit the core.

Figure 8.8, for spheroidal modes, is far more complicated because it is equivalent to P–SV phenomena, including Rayleigh and Stoneley waves. This figure shows 2099

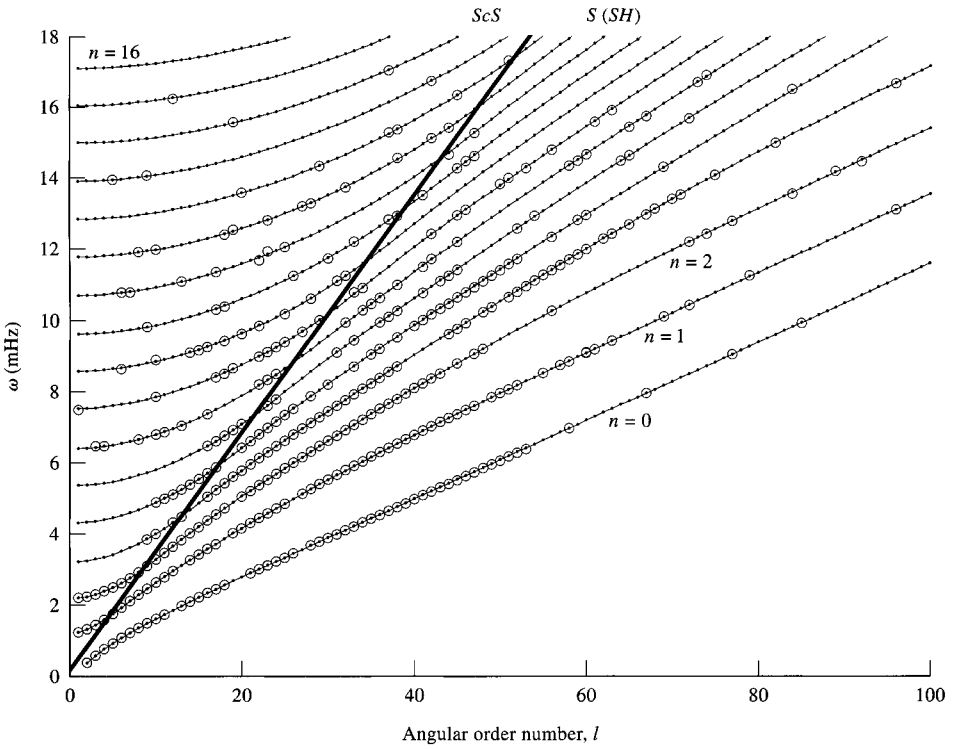

FIGURE **8.7**
Toroidal modes ${}_n\omega_l$ plotted against l for different branches $0 \leq n \leq 17$. The larger symbols indicate 380 observed modes that have been separately identified using data from the Global Seismographic Network. Smaller symbols are theoretical values for ${}_n\omega_l$. [Figure based on information supplied by Rüdi Widmer, 1997.]

degenerate spheroidal eigenfrequencies, with n running from 0 to 50, together with 760 mode frequencies (larger plotting symbol) that have been observed and separately identified in seismic data. Problem 8.4 shows an enlarged version of part of Figure 8.8.

Figures 8.7 and 8.8 show generally good agreement between calculated and identified normal modes at periods greater than about 60 s. The possibility therefore arises of summing all the modes according to (8.38), using some particular model of an earthquake (i.e., its moment rate tensor) and seeing if the resulting theoretical seismograms agree with those actually observed—that is, to make comparisons in the time domain, rather than the frequency domain. Satô *et al.* (1962) were the first to compute seismograms by summing normal modes. A summary of early work in this field is given by Landisman *et al.* (1970), who compared various features of the normal-mode summation (e.g., the amplitude of a particular body wave) with corresponding features in seismic data. The first comparisons in the time domain—whole wave trains (including body waves) from observed seismograms and from normal-mode summation—were done by Luh and Dziewonski (1975) for the deep Colombian earthquake of 1970. Using a previously determined moment rate tensor for this event and a particular Earth model, these authors computed 75 seismograms by superimposing more than a thousand modes in the period range 100–1000 s. Their results are shown in Figure 8.9. Straight lines across the record sections indicate Rayleigh waves,

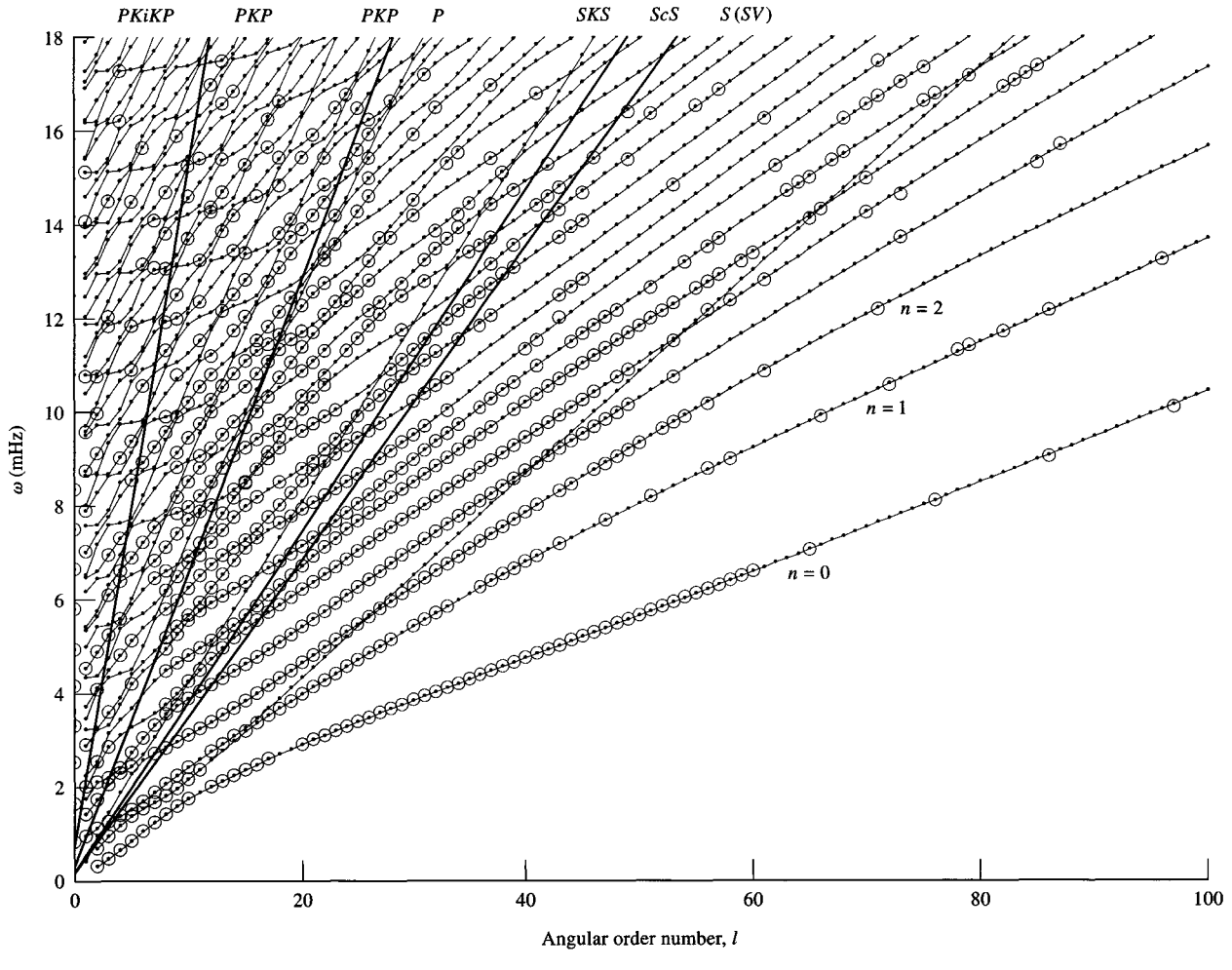

FIGURE **8.8**
Spheroidal modes ${}_n\omega_l$ plotted against l for different branches n. Modes can correspond to marked body-wave phases only if they lie to the left of the appropriate phase-velocity line. The larger symbols indicate 760 observed modes that have been identified in seismic data. [Figure based on information supplied by Rüdi Widmer, 1997.]

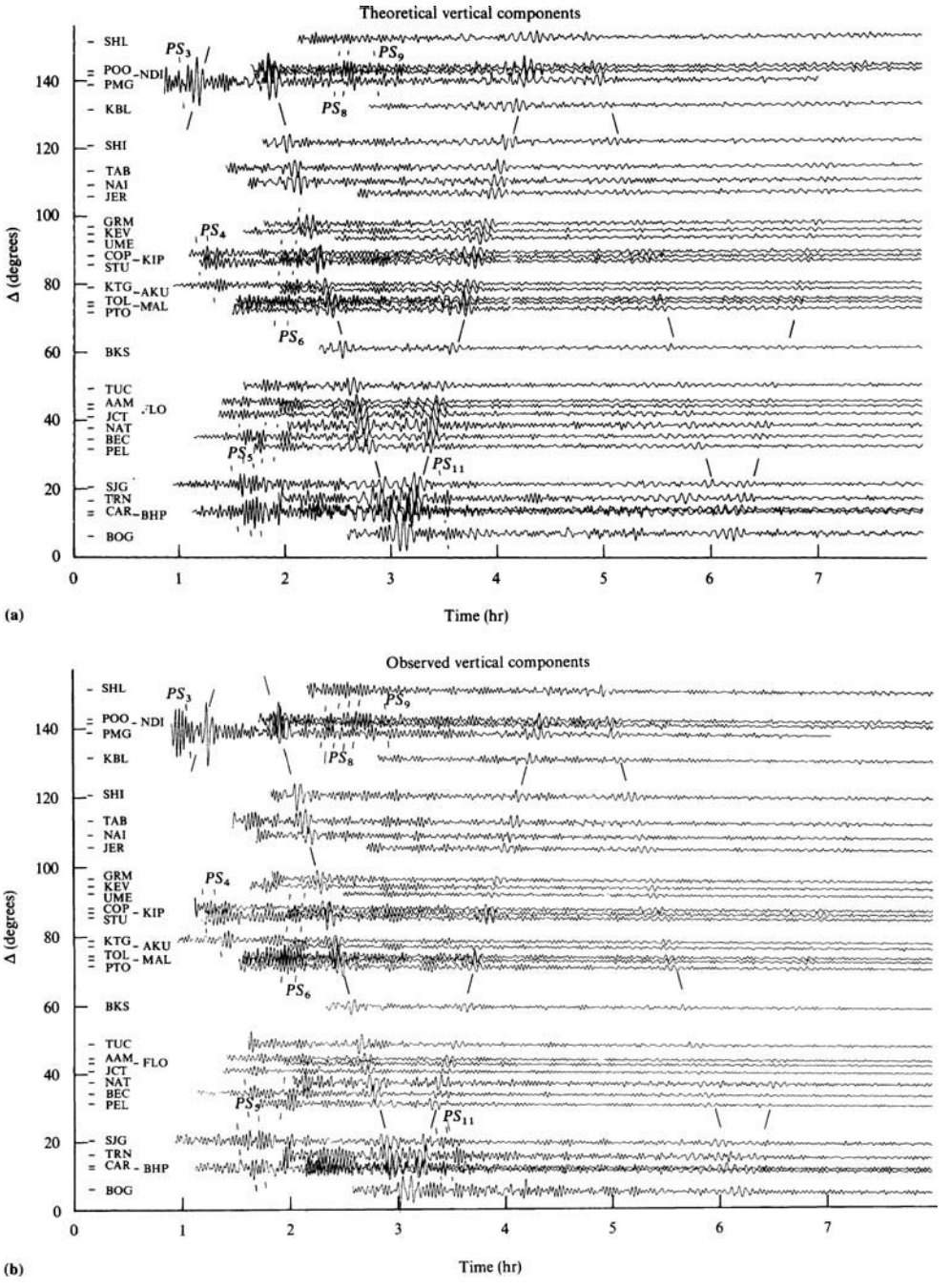

FIGURE **8.9**

Vertical-component seismograms for the deep Colombian earthquake of 31 July 1970. **(a)** Theoretical records for 34 WWSSN stations, with each seismogram plotted at its correct distance Δ from the epicenter. (This method of display is known as a *record section*.) Computation is via (8.38), using modes in the period range 100–1000 s and the source model and Earth model 1066A of Gilbert and Dziewonski (1975). **(b)** Observed vertical ground motion for the same stations and the same earthquake as (a). (These seismograms have been corrected for instrument response and filtered to pass the same frequency range as that used in computing (a).) [From Luh and Dziewonski (1975).]

R_1, R_2, etc., which are prominent at these periods, even for such a deep event (depth assigned as 651 km). Prominent also are body-wave phases in which P- and S-waves traversing the mantle have multiple legs, e.g., *PSPSPS*, the conversion between P and S taking place on reflection at the Earth's surface. The example we have just given is denoted PS_3 and several PS_n are marked on the figure. General characteristics of the data are reproduced by the theoretical record section, and where there is disagreement, Luh and Dziewonski suggest that the inadequacy can be traced to the assumed moment-rate tensor and/or the Q-model. Clearly, this method of interpreting seismograms has great potential. In execution, the principal difficulties lie in adequate computation and storage of the large number of "short-period" normal modes (periods down to about 5 s) that are observed but are not separately identifiable on "broadband" digital seismograms. For toroidal modes, a transformation is known (Box 9.2) that converts the spherical geometry of the Earth to a plane-layered problem. In this case, highly efficient programs have been written that permit modal computations down to periods of about 1 s (Nakanishi *et al.*, 1977; Mantovani *et al.*, 1977). For spheroidal modes, Rayleigh–Ritz methods have been implemented that allow computation of all modes down to periods of about 45 s (Buland and Gilbert, 1976, 1984). At even shorter periods, an accurate asymptotic theory has been developed for each mode (Woodhouse, 1978; Zhao and Dahlen, 1993, 1995a,b). Therefore, it is to be expected that (8.38) may be used to generate comparisons like those shown in Figure 8.9a,b, but for broadband signals, without the drastic filtering of the data.

8.5 The Centroid Moment Tensor

In the early 1980s, a series of developments in theoretical understanding and data acquisition combined to permit components of the moment tensor to be estimated routinely for numerous seismic sources. Thus, moment tensors have been routinely estimated by Adam Dziewonski and colleagues from global network data for an average of about two earthquakes per day. About 15,000 earthquakes had been so analysed by 1998, going back to 1977.

The basis of this work is equation (8.38) in which the source is approximated by a moment tensor acting at a point. Using a moment rate tensor $\dot{M}_{pq}(t) = M_{pq}\delta(t - t_s)$ acting at $\mathbf{x} = \mathbf{x}_s$ and the (Up, South, East) convention for Cartesian components of $\mathbf{M}$ (see Box 4.4, equation (4)), our goal is to estimate the six quantities $(M_{rr}, M_{r\theta}, M_{r\phi}, M_{\theta\theta}, M_{\theta\phi}, M_{\phi\phi})$ which for convenience can be labelled respectively as $M_k, k = 1, 2, \ldots, 6$. The jth component of (8.30) or (8.38) then becomes

$$u_j(\mathbf{x}, t) = \sum_{k=1}^{6} G_{jk}(\mathbf{x}, \mathbf{x}_s, t - t_s)M_k \tag{8.67}$$

in which

$$G_{jk}(\mathbf{x}, \mathbf{x}_s, t) = \text{mode sum for } (j, k) \qquad \text{if } k = 1, 4, 6$$

and

$$G_{jk}(\mathbf{x}, \mathbf{x}_s, t) = 2 \times \text{mode sum for } (j, k) \qquad \text{if } k = 2, 3, 5,$$

where

$$\text{mode sum for } (j, k) \equiv \sum_i {}_ie_k^*(\mathbf{x}_s)\, {}_i\mathbf{u}(\mathbf{x})\Big|_j \left(\frac{1 - \exp(-\omega_i t/2Q_i)\cos\omega_i t}{\omega_i^2}\right) \tag{8.68}$$

BOX **8.5**

Consideration of initial stress

Stresses within the Earth can reach values of the order of megabars. Since the elastic moduli in Hooke's law are also of this order, it follows that strains of order one may be present in the Earth, even in the simple situation where there is a reference state in which strain and stress are both zero, such that the Earth's present configuration can be obtained from this state by linear stress–strain theory. But we have no reason to suppose there is such a reference state; and even if there were, it would not be a suitable reference for studying seismic waves, as wave-propagation theory for finite strains is nonlinear. Instead, we need to work with a theory for small *incremental* stresses, using as reference an initial state in which the stress may be large but strains are defined to be zero.

In seismology, it is natural to take as the initial state the Earth's configuration just before an earthquake. Because the initial stress is predominantly isotropic (being due at any given depth to the gravity field acting on the overburden of material), it turns out that there are virtually no complications introduced in all the formulas we have so far obtained, which altogether ignore the initial stress field. However, the formal development of the theory of elasticity is very much more complicated. The work necessary to check whether formulas based on classical elasticity need modification for Earth models with high initial stress has largely been carried out by Dahlen (1972, 1973, 1976a, 1977).

Some of the complications of working with a general initial stress lie in the fact that incremental stress at a material particle consists of two parts: one depending on local strains, and familiar from the theory given in Chapter 2; the other depending on local rotations, which act to rotate the initial stress field. Thus total stresses in general depend upon $e_{ij} = \frac{1}{2}(u_{i,j} + u_{j,i})$ and $\omega_{ij} = \frac{1}{2}(u_{i,j} - u_{j,i})$. In order to describe the stress and strain fields, Dahlen (1973) advocates a Lagrangian approach. Furthermore, in order to refer boundary conditions (such as a description of faulting) back to the initial configuration, the Cauchy stress tensor used in Chapter 2 is inappropriate. The area elements (in magnitude and orientation) across which traction acts are in the deformed state for definition of the Cauchy stress. Instead, Dahlen (1972, 1973) recommends the use of area elements in the initial state to describe subsequent tractions. Suppose an element of material area centered on $\mathbf{x}$ has, in the initial state, magnitude $dS(\mathbf{x})$ and orientation $\mathbf{n}(\mathbf{x})$. At some later time t, the particle originally at $\mathbf{x}$ has moved to $\mathbf{X} = \mathbf{x} + \mathbf{u}$ and the area element of material has magnitude $dS(\mathbf{X}, t)$ and orientation $\mathbf{n}(\mathbf{X}, t)$. The Cauchy stress tensor $\boldsymbol{\sigma}^{\mathrm{C}}$ has Cartesian components such that the jth component of the traction across the material element is $n_i(\mathbf{X}, t)\sigma_{ij}^{\mathrm{C}}(\mathbf{X}, t)\, dS(\mathbf{X}, t)$. This traction is equated to $n_i(x)\sigma_{ij}^{\mathrm{PK}}(\mathbf{x}, t)\, dS(\mathbf{x})$ to define Cartesian components of the *Piola–Kirchhoff stress tensor,* a tensor that can thus quantify time dependent tractions per unit original area of a deforming surface. Accounting for the initial stress $\boldsymbol{\sigma}^0$, the incremental Piola–Kirchhoff stress tensor $\tilde{\boldsymbol{\tau}}$ and the incremental Cauchy stress $\boldsymbol{\tau}$ are given by

$$\boldsymbol{\sigma}^{\mathrm{PK}} = \boldsymbol{\sigma}^0 + \tilde{\boldsymbol{\tau}} \quad \text{and} \quad \boldsymbol{\sigma}^{\mathrm{C}} = \boldsymbol{\sigma}^0 + \boldsymbol{\tau}. \tag{1}$$

Dahlen (1972) and Malvern (1969) point out that the Piola–Kirchhoff stress tensor is not symmetric. The relation between incremental stress tensors is (to first order in initial stresses and subsequent strains)

$$\tilde{\tau}_{ij} = \tau_{ij} + \sigma_{ij}^0 \frac{\partial u_k}{\partial x_k} - \sigma_{jk}^0 \frac{\partial u_i}{\partial x_k},$$

(continued)

BOX **8.5** *(continued)*

reducing to

$$\tilde{\tau}_{ij} = \tau_{ij} - p_0\,\delta_{ij}\frac{\partial u_k}{\partial x_k} + p_0\frac{\partial u_i}{\partial x_j}$$

for an isotropic initial stress, $\sigma^0_{ij} = -p_0\delta_{ij}$.

For an Earth model that is rotating, self-gravitating, and isotropically elastic for stresses and strains about an isotropically stressed initial state, Dahlen (1972) showed that the body-force equivalent for a shear dislocation (which we derived in Chapters 2 and 3) is still a distribution of double couples. If the initial state has shearing stresses too, then the body-force equivalent for shearing consists of double couples plus extra terms, of order [(initial shearing stresses) ÷ (*in situ* elastic moduli)]. These extra terms are very small, since rocks typically cannot support shear stresses greater than one or two kilobars. For shear faulting in the x_3-plane, Dahlen (1976a) found still the continuity $[\tau_{31}] = [\tau_{32}] = [\tau_{33}] = 0$ for the incremental Cauchy stress tensor, and still the formula

$$\Delta E = -\frac{1}{2}\int_\Sigma [u_i(\mathbf{x}, \infty)](\sigma^0_{ij} + \sigma^1_{ij})v_j\,dS \tag{2}$$

(see Box 3.4) for the changes in strain energy throughout a medium due to faulting across Σ. Formulas for frictional work on Σ, and work needed to create new fault surface, are also unchanged by the presence of an isotropic initial stress. Dahlen (1977) studied the balance of energy in earthquake faulting, taking into account the changes in the Earth's rotation rate and changes in the gravitational field that can occur for a spontaneous internal source in a rotating planet. He showed that (2) still expresses the energy of faulting in a prestressed Earth model (i.e., the sum of changes in rotational energy, gravitational energy, and internal shear-strain energy), even though individual terms in this sum can range up to four orders of magnitude greater than the right-hand side of (2). Chao and Gross (1995) used normal modes to evaluate changes in the Earth's inertia tensor associated with each of more than 11,000 earthquakes from 1977 to 1993, and concluded that earthquakes occur with orientations that tend to increase the Earth's spin energy. Chao *et al.* (1995) showed that the same set of earthquakes has tended to decrease the Earth's gravitational energy. They point out that earthquakes act to transfer energy, in amounts much larger than (2), between the energies associated with the Earth's rotation, elastic field, gravitational field, and internal heat; and they argue that earthquakes may make a significant contribution to global heat flow by converting gravitational energy.

for all $j = r, \theta, \phi$ and all $k = 1, 2, \ldots, 6$. The quantity $G_{jk}(\mathbf{x}, \mathbf{x}_s, t - t_s)$ is essentially a Green function, being the jth component of displacement at $(\mathbf{x}, t)$ for a step in moment values applied at $(\mathbf{x}_s, t_s)$, and associated with sources described by the special tensors

$$\begin{pmatrix} 1 & 0 & 0 \\ 0 & 0 & 0 \\ 0 & 0 & 0 \end{pmatrix}, \begin{pmatrix} 0 & 1 & 0 \\ 1 & 0 & 0 \\ 0 & 0 & 0 \end{pmatrix}, \begin{pmatrix} 0 & 0 & 1 \\ 0 & 0 & 0 \\ 1 & 0 & 0 \end{pmatrix}, \begin{pmatrix} 0 & 0 & 0 \\ 0 & 1 & 0 \\ 0 & 0 & 0 \end{pmatrix}, \begin{pmatrix} 0 & 0 & 0 \\ 0 & 0 & 1 \\ 0 & 1 & 0 \end{pmatrix}, \begin{pmatrix} 0 & 0 & 0 \\ 0 & 0 & 0 \\ 0 & 0 & 1 \end{pmatrix}$$

for $k = 1, 2, \ldots, 6$ respectively.

In application of (8.67), the $G_{jk}(\mathbf{x}, \mathbf{x}_s, t - t_s)$ may be computed from (8.68) at each $(\mathbf{x}, t)$ where there is data, provided $(\mathbf{x}_s, t_s)$ are specified and we have an adequate Earth model. The values of M_k—which are components of the general moment tensor $\mathbf{M}$—are then obtained as the coefficients which best fit the right-hand side of (8.67) to the data on the left.

The process of inversion begins with solving for the six coefficients that best fit (8.67) for some initial choice of $(\mathbf{x}_s, t_s)$. This step is based usually upon hypocentral coordinates that are estimated from P-wave arrival times. The outcome is an initial estimate, $M_k^{(0)}$, of the moment tensor components.

At this stage, it is appropriate to reconsider the choice of $(\mathbf{x}_s, t_s)$. Such reconsideration is an essential feature of estimating what is now known as the *centroid moment tensor*, or CMT. The underlying issue is that the location of the point source which best fits long-period seismograms may differ from an initial choice of $(\mathbf{x}_s, t_s)$ determined from short-period body-wave arrival times. It is clear from representations such as equation (3.2), discussed further in Chapter 10, that it is the whole fault surface which radiates seismic waves, whereas the first-arriving P-waves presumably originate from the point of fault nucleation.

To investigate the possibility of improving the fit to long-period data with a better source location and better origin time, the CMT method is developed as an iterative procedure based upon the first order difference between

$$u_j^{(l)}(\mathbf{x}, t) = \sum_k G_{jk}(\mathbf{x}, \mathbf{x}_s^{(l)}, t - t_s^{(l)})\, M_k^{(l)} \qquad \text{and}$$

$$u_j(\mathbf{x}, t) = \sum_k G_{jk}(\mathbf{x}, \mathbf{x}_s^{(l)} + \Delta\mathbf{x}_s, t - t_s^{(l)} - \Delta t_s)\left(M_k^{(l)} + \Delta M_k\right).$$

This difference is

$$u_j - u_j^{(l)} = b_j \Delta r_s + c_j \Delta\theta_s + d_j \Delta\phi_s + e_j \Delta t_s + \sum_k G_{jk}^{(l)}\, \Delta M_k \tag{8.69}$$

where $u_j^{(l)} = \sum_k G_{jk}^{(0)}\, M_k^{(l)}$ is the theoretical displacement for the lth estimate of the source coordinates and the moment tensor, and the coefficients (b_j, c_j, d_j, e_j) are the partial derivatives with respect to perturbation of each hypocenter coordinate about its lth estimate. Expressions for such derivatives may be obtained via differentiation of (8.68), and (8.69) is used to estimate the refinements $\Delta\mathbf{x}_s = (\Delta r_s, \Delta\theta_s, \Delta\phi_s)$ and $\Delta\mathbf{M}$ for each iteration. The process is started with $l = 0$ and ended when the long-period data are fit according to some appropriate criterion (and/or there is no further improvement in the fit).

The procedure as given above is quite general. The CMT method was introduced by Dziewonski, Chou, and Woodhouse (1981) as a practical way of explaining (modeling, fitting) the long-period body-wave train, with maximum spectral energy in the period range from 50 to 60 s, in a window from the P-wave until the arrival of the fundamental-mode surface waves. They found the lower limit for which the CMT could be estimated from such data was about magnitude 5.5, using a cut-off period of 45 s (for which the number of modes in the summation (8.68) is about 5000). Dziewonski and Woodhouse (1983) extended the CMT method by applying it also to overtones and fundamental modes with period longer than 135 s, finding that such "mantle wave" data were a useful addition (to long-period

body waves) because the signals propagating along minor and major arcs could be used, in effect doubling the network coverage. Another advantage of going to longer period, such as mantle waves, is that the "point source" approximation is even more appropriate. The dominant frequency of mantle wave observations is less than the corner frequency of the source for all but the largest earthquakes, so there is less sensitivity to source finiteness (see Section 10.1.7). In addition to the possible complications of source finiteness, estimation of the CMT using surface wave data at periods shorter than mantle waves requires taking the strong effects of lateral heterogeneity into account. The theory for such effects has been developed (for example by Woodhouse and Dziewonski, 1984—note that (8.68) does not require spherical symmetry of structure), but practical application for the period range where surface waves are strongest (permitting the study of smaller sources, well below magnitude 5.5) must await better knowledge of actual Earth structure and its lateral variability.

The above presentation of the CMT method is based on $u_j = \sum_k G_{jk} * \dot{M}_k$ with $M_k(t) = M_k H(t - t_s)$ and hence $\dot{M}_k = M_k \delta(t - t_s)$. More generally, $\dot{M}_k$ may have finite duration and thus may differ from a δ-function. Then $\dot{M}_k = \dot{M}_k(t)$ and

$$u_j(\mathbf{x}, \omega) = \sum_k G_{jk}(\mathbf{x}, \mathbf{x}_s, \omega) e^{i\omega t_s} \dot{M}_k(\omega). \tag{8.70}$$

The solution here can be obtained for a number of frequency intervals, within each of which $\dot{M}_k(\omega)$ can be modeled as appropriate. Thus, if $\dot{M}_k(t)$ is a box function with duration $2T$, the excitation functions would be multiplied by $(1/\omega T) \sin \omega T$ in computing synthetics. For spatially propagating sources, a variety of different assumptions can be modeled as outlined in Problem 10.7.

For double-couple sources, $M_1 + M_2 + M_3 = 0$. This relation can be added as a constraint in fitting data via (8.67), thus reducing the number of unknowns from six to five. The resulting moment tensor can then be analysed to see how well its principal values conform to those expected of a double couple, namely $\pm M_0$ and zero. The disadvantage of adopting $M_1 + M_2 + M_3 = 0$ as a constraint is that it prevents learning from the data if any volume change is present in the source.

For shallow sources, the dip–slip components of $\mathbf{M}$, corresponding to $k = 2$ and 3, are inefficient in exciting seismic waves. This result, developed further in Problems 7.12 and 8.6, is apparent from (8.68), noting that the free surface boundary condition and Hooke's law imply $e_{r\theta} = e_{r\phi} = 0$ at $r = r_\oplus$. It follows that the $M_{r\theta}$ and $M_{r\phi}$ components of $\mathbf{M}$ may be poorly estimated in some cases where other components are well fit. Nevertheless, the ability to estimate centroid moment tensors routinely and promptly from long-period data, for numerous earthquakes, is well established and has provided one of the strongest rationales for deployment of stations in a global network.

8.6 Splitting of Normal Modes Due to the Earth's Rotation

The worst features of the Earth models we discussed in Section 8.4 are that they did not rotate and were spherically symmetric. We consider here the effect of rotation, and allow for lateral heterogeneity in Section 8.7.

The Earth's daily rotation can be expected to produce quantitative effects upon normal modes that are roughly in the dimensionless ratio (normal mode period)/(24 hours). Clearly,

this can amount to a few percent for low-order fundamental modes, and should be observable. Observations of the 1960 Chilean earthquake indeed indicated that modes such as ${}_0S_2$ did not have a single spectral peak, but were composed of at least two lines with periods of 54.7 and 53.1 minutes (Benioff *et al.*, 1961). The effect was recognized to be mathematically similar to the Zeeman effect (the splitting of degenerate energy levels of a hydrogen atom in a magnetic field). For each l, we found previously that there exist $2l + 1$ modes, i.e., $-l \leq m \leq l$, with the same eigenfrequency and radial eigenfunction. But rotation removes this degeneracy, and instead of a single eigenfrequency ${}_n\omega_l$, we must speak of the multiplet ${}_n\omega_l^m (-l \leq m \leq l)$, each having a different radial eigenfunction. Before giving the relevant theory, it is useful to note some of the practical problems that the Earth's rotation imposes on normal-mode observations.

First, there is the problem of determining the temporal Q of a given mode. A standard method for measuring the decay rate of a given frequency component in a time series is to compute the spectrum and measure the width of the spectral peak at its half-power level. Thus, for a time function $f(t) = H(t)[e^{-\omega_0 t/2Q} \cos \omega_0 t]$, the amplitude spectrum near ω_0 is

$$|f(\omega)| \sim \frac{1}{2}\left[(\omega - \omega_0)^2 + \left(\frac{\omega_0}{2Q}\right)^2\right]^{-1/2}. \tag{8.71}$$

When $\omega = \omega_0 \pm \omega_0/2Q$, the amplitude is down by a factor of $1/\sqrt{2}$ from its peak value, and the associated power spectrum $|f(\omega)|^2$ is down by a factor of $\frac{1}{2}$. Measuring the width $\Delta\omega$ of the peak at its half-power level, it follows that $Q^{-1} = \Delta\omega/\omega_0$. Clearly, this standard method of finding Q will not work, if spectral peaks within a given multiplet overlap. Then individual modes are not resolved, and (8.71) is an inadequate model of the spectrum near ω_0. Alsop *et al.* (1961b) found that another common method of measuring Q could still be made to work. Their approach was to interpret the relative amplitude of spectra determined from carefully chosen time windows (of equal length) along the original seismogram, one spectrum for each window.

The second problem associated with multiplet splitting by rotation is that it obscures the multiplet splitting caused by the Earth's departure from spherical symmetry. Dahlen (1968, 1969) showed that rotation effects to both first and second order must be removed if the lateral heterogeneity of the Earth is to be studied by its splitting effect on normal modes.

With this background, we can now give the first-order perturbation theory for rotational splitting.

Consider a toroidal mode of oscillation, which from (8.60) satisfies

$$\rho_0 \frac{\partial^2 u_i}{\partial t^2} = [\mu(u_{i,j} + u_{j,i})]_{,j}. \tag{8.72}$$

This describes small motions away from a nonrotating equilibrium state in which a fixed inertial coordinate system can be identified. But the Earth has a daily rotation, and it is therefore appropriate to modify (8.72) so that $\mathbf{u}$ describes small motions away from a rotating equilibrium state. To do this, we use a coordinate system rotating with constant angular velocity $\boldsymbol{\Omega} = \Omega\hat{\mathbf{z}}$, where Ω is 2π per 24 hours (actually, per sidereal day) and $\hat{\mathbf{z}}$ is a unit

vector along the Earth's rotation axis. In this noninertial system, particle velocity is given by $\partial \mathbf{u}/\partial t + \boldsymbol{\Omega} \times \mathbf{u}$ and particle acceleration by $\partial^2 \mathbf{u}/\partial t^2 + 2\boldsymbol{\Omega} \times \partial \mathbf{u}/\partial t + \boldsymbol{\Omega} \times (\boldsymbol{\Omega} \times \mathbf{u})$. Since Ω is so small (relative to normal-mode frequencies), we shall neglect terms of order Ω^2, and (8.72) becomes

$$\rho_0 \frac{\partial^2 \mathbf{u}}{\partial t^2} + 2\rho_0 \boldsymbol{\Omega} \times \frac{\partial \mathbf{u}}{\partial t} = \mathbf{X}, \tag{8.73}$$

where $X_i = [\mu(u_{i,j} + u_{j,i})]_{,j}$.

We shall assume that (8.73) without the Coriolis acceleration $2\boldsymbol{\Omega} \times \partial \mathbf{u}/\partial t$ has a degenerate eigenvalue

$$\omega_0 = {}_n\omega_l. \tag{8.74}$$

The toroidal solution $\mathbf{u}$ of (8.73) that we wish to investigate has spatial dependence dominated by ${}_nW_l(r)\mathbf{T}_l^m(\Delta, \phi)$ and an eigenfrequency $\omega = {}_n\omega_l^m$ that is slightly perturbed from (8.74). It can be shown (Backus and Gilbert, 1961) that $\mathbf{u}$ is analytic in Ω for small Ω, so that we may use power series in the form

$$\begin{aligned} \frac{\omega}{\omega_0} &= 1 + \sigma_1 \left(\frac{\Omega}{\omega_0}\right) + \sigma_2 \left(\frac{\Omega}{\omega_0}\right)^2 + \cdots, \\ \mathbf{u} &= \mathbf{u}_0 + \mathbf{u}_1 \left(\frac{\Omega}{\omega_0}\right) + \cdots, \\ \mathbf{X} &= \mathbf{X}_0 + \mathbf{X}_1 \left(\frac{\Omega}{\omega_0}\right) + \cdots, \end{aligned} \tag{8.75}$$

where ω is the eigenvalue of (8.73) (i.e., $\mathbf{u} \propto \exp(-i\omega t)$). Substituting $\boldsymbol{\Omega} = \Omega\hat{\mathbf{z}}$ and (8.75) into (8.73) and equating powers of (Ω/ω_0), we find

$$-\rho_0 \omega_0^2 \mathbf{u}_0 = \mathbf{X}_0 \tag{8.76}$$

$$-\rho_0 \omega_0^2 \mathbf{u}_1 - 2\rho_0 \omega_0^2 [\sigma_1 \mathbf{u}_0 + i\hat{\mathbf{z}} \times \mathbf{u}_0] = \mathbf{X}_1. \tag{8.77}$$

Our goal now is to obtain the first-order perturbation σ_1. Clearly, $\mathbf{u}_1$ must be linearly independent of $\mathbf{u}_0$, so that by redefining $\mathbf{u}_0$ if necessary, we can assume $\mathbf{u}_1$ and $\mathbf{u}_0$ are orthogonal. Pekeris *et al.* (1961) have also shown that $\mathbf{X}_1$ is orthogonal to $\mathbf{u}_0$, hence from (8.77),

$$\int \rho_0 [\sigma_1 \mathbf{u}_0^* \cdot \mathbf{u}_0 + i\mathbf{u}_0^* \cdot (\hat{\mathbf{z}} \times \mathbf{u}_0)]\, dV = 0.$$

This is an equation for σ_1, and can be rewritten (using (8.36)) as

$$\sigma_1 = -i\hat{\mathbf{z}} \cdot \int \rho_0 \mathbf{u}_0 \times \mathbf{u}_0^*\, dV. \tag{8.78}$$

Since $\mathbf{u}_0 = {}_nW_l(r)\mathbf{T}_l^m(\Delta, \phi) \exp[-i\,{}_n\omega_l t]$, the integral in (8.78) gives

$$\sigma_1 = \frac{-m}{l(l+1)}. \tag{8.79}$$

This result is disappointing from a geophysical viewpoint, for it tells us that the first-order splitting of toroidal modes is independent of Earth structure. The perturbed eigenfrequencies are, from (8.75),

$${}_n\omega_l^m = {}_n\omega_l - \frac{m}{l(l+1)}\Omega \qquad \text{for} \qquad -l \le m \le l, \tag{8.80}$$

and the degeneracy has been removed.

Remarkably, equation (8.78) still holds for spheroidal modes, where $\mathbf{u}_0 = [{}_nU_l\mathbf{R}_l^m + {}_nV_l\mathbf{S}_l^m] \exp[-i\,{}_n\omega_l t]$, and the normalization (8.35) is enforced. Again, σ_1 can be evaluated, giving

$${}_n\omega_l^m = {}_n\omega_l - m\,\Omega\,{}_n\beta_l, \tag{8.81}$$

where

$${}_n\beta_l = \int_0^{r_\oplus} \frac{\rho_0({}_nV_l)^2}{l(l+1)} r^2\,dr + 2\int_0^{r_\oplus} \frac{\rho_0({}_nU_l)({}_nV_l)}{\sqrt{l(l+1)}} r^2\,dr.$$

The values of ${}_n\beta_l(\Omega/{}_n\omega_l)$ have been computed by Dahlen (1968), and are largest for the modes ${}_1S_1$ and ${}_0S_2$, amounting to about 0.015.

Perhaps the main use of the theory of rotational splitting lies in modeling part of an observed spectral peak in terms of closely spaced components of a split multiplet so that a method of data analysis can be designed to estimate Q. Stein and Geller (1978) advocate a synthesis of ground motion in the time domain—that is, obtaining the excitation for each mode within the multiplet $-l \le m \le l$ associated with a given (n, l). They sum the modes within the multiplet and compare this synthetic record with the data. (Both synthetics and data are narrow-band filtered to isolate the multiplet of interest.) Figure 8.10 gives an example for ${}_0S_2$ observed after the great Chilean earthquake of 1960, and the 150-hour length of the record shows interference between different modes within the multiplet.

In this section we have outlined only the simplest aspects of rotational splitting. Dahlen and Smith (1975) have given an extended treatment, showing that normal modes for a rotating Earth are no longer orthogonal. When part of the Earth model is fluid (e.g., the outer core), a whole new range of theoretical problems is opened up, even without the complications of rotation, because suites of normal modes with very long periods can exist. They can have periods of many hours, and have been called *undertones* (Pekeris and Accad, 1972).

There are many influences acting upon the Earth with time scales that are long compared to the period of ${}_0S_2$. It might be hoped that a quasistatic treatment of deformation could be given, but unfortunately this is not simple, due to the presence of the fluid core. Longman (1963) pointed out that equations (8.64) become mutually inconsistent in the limit as $\mu \to 0$, and $\omega \to 0$, and many authors have suggested ways to resolve the paradox (Crossley and Gubbins, 1975; and see Box 7.6). In the context of normal modes and Earth rotation, the

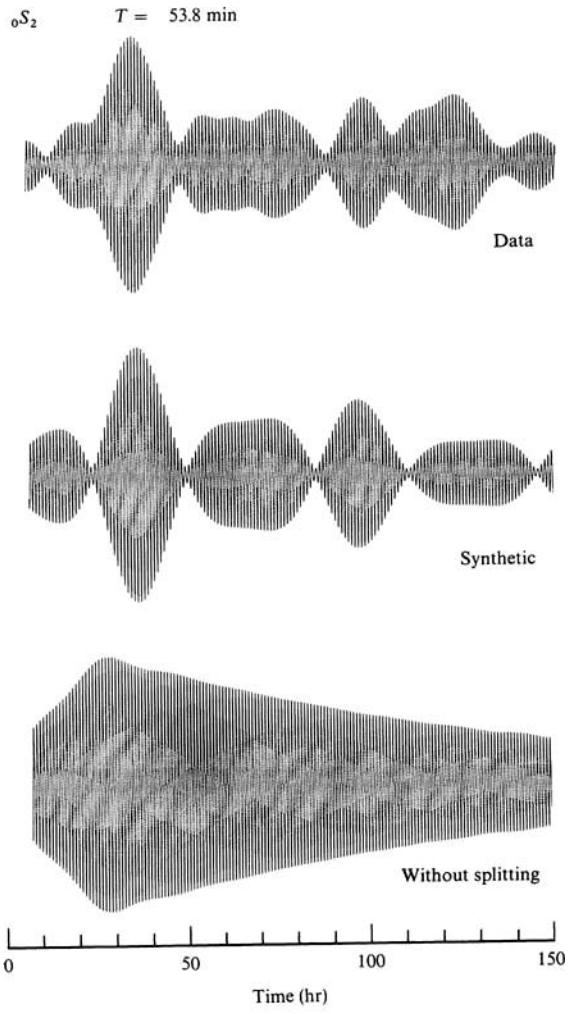

FIGURE **8.10**
Comparison between observations of ${}_0S_2$ in the time domain and a synthesis of this record using methods that include and exclude the effect of rotational splitting. [From Stein and Geller (1978).]

theory of the Chandler wobble is complicated by Longman's paradox. Smith (1977) has avoided a quasistatic treatment, and showed how the dynamic equations for a rotating Earth (with fluid core but without oceans) have the Chandler wobble as a normal mode. He calculated the period to be 405.19 sidereal days for an Earth model with a stably stratified fluid core. The observed period is 434.14 ± 1.02 sidereal days (Currie, 1974), but Dahlen (1976b) and Smith and Dahlen (1981) showed that the world's oceans would act to increase the Chandler period for an Earth model such as Smith's (1977), giving satisfactory agreement between observed and predicted Chandler periods.

8.7 Spectral Splitting of Free Oscillations Due to Lateral Inhomogeneity of the Earth's Structure

Large-scale inhomogeneities are present all around the Earth, such as oceans, continents, mid-ocean ridges, trenches, and mountain ranges. Consider then what happens to surface

waves generated by an earthquake. These waves spread out, sweep the Earth's surface, and converge on the antipode. During this sweep, all the inhomogeneities act as secondary sources and generate scattered waves. These scattered waves will interfere with each other and with the original surface waves making a return trip from the antipode to the epicenter, as well as with scattered waves generated by the returning surface waves. If the Earth were a lossless medium, the above process would go on for ever, and the result would be a very complex, completely coupled pattern of surface waves propagating around the Earth.

What would happen to the free oscillation periods?

To answer this question, we shall introduce small perturbations to the parameters of the laterally homogeneous Earth model, and shall see what is the effect on the free-oscillation solutions obtained earlier in this chapter. We start with the basic equations for an arbitrarily heterogeneous, hydrostatically prestressed medium and follow the steps taken by Madariaga (1972). If the initial stress field is $-P\delta_{ij}$, the equation of motion can be obtained from (8.55)–(8.60) and (8.73) in the form

$$-\rho\omega^2 u_i - 2i\rho\omega(\boldsymbol{\Omega}\times\mathbf{u})_i = (\lambda e_{kk}\delta_{ij} + 2\mu e_{ij})_{,j} + \rho(V_{,j}u_j)_{,i} - P_{,i}e_{kk} + \rho K_{,i} \tag{8.82}$$

where $\mathbf{u}\exp(-i\omega t)$ is the displacement of a small elastic vibration about its equilibrium state, $K\exp(-i\omega t)$ is the variation of gravitational potential about its equilibrium value V, and we are now using ρ rather than ρ_0 to denote the original density distribution (i.e., prior to the occurrence of seismic motion). The second term on the left-hand side is the Coriolis force due to the Earth's rotation $\boldsymbol{\Omega}$. λ and μ are the Lamé elastic moduli, e_{ij} is the strain component associated with $\mathbf{u}$, and $e_{kk} = u_{k,k}$ is dilatation. The gravitational potential K satisfies

$$\nabla^2 K = 4\pi\gamma(\rho u_i)_{,i} \tag{8.83}$$

where γ is the gravitational constant.

Using the spherical coordinates (r,θ,ϕ), we shall separate the elastic constants and density into a spherically symmetric part and a small arbitrarily inhomogeneous part:

$$\begin{aligned}
\rho(r,\theta,\phi) &= \rho_0(r) + \delta\rho(r,\theta,\phi),\\
\lambda(r,\theta,\phi) &= \lambda_0(r) + \delta\lambda(r,\theta,\phi),\\
\mu(r,\theta,\phi) &= \mu_0(r) + \delta\mu(r,\theta,\phi).
\end{aligned} \tag{8.84}$$

Putting (8.84) into (8.82) and (8.83) and keeping only first-order terms of the perturbation, we have the following equations for $\mathbf{u}$ and K:

$$\begin{aligned}
H_i(\mathbf{u},K) &= H_{0i}(\mathbf{u},K) + \delta H_i(\mathbf{u},K) = -\rho_0\omega^2 u_i,\\
\mathcal{L}(\mathbf{u},K) &= \mathcal{L}_0(\mathbf{u},K) + \delta\mathcal{L}(\mathbf{u},K) = 0,
\end{aligned} \tag{8.85}$$

where

$$H_{0i}(\mathbf{u},K) = (\lambda_0 e_{kk}\delta_{ij} + 2\mu_0 e_{ij})_{,j} - \rho_0 V_{0,r}\, e_{kk}\delta_{ir} + \rho_0(V_{0,r}\, u_r)_{,i} + \rho_0 K_{,i}, \tag{8.86}$$

$$\mathcal{L}_0(\mathbf{u},K) = \frac{1}{4\pi\gamma}\nabla^2 K - (\rho_0 u_i)_{,i}, \tag{8.87}$$

so that H_{0i} and $\mathcal{L}_0$ are operators for the radially symmetric problem, with $V = V_0 + \delta V$; and

$$\begin{aligned}\delta H_i(\mathbf{u}, K) = {} & \delta\rho\omega^2 u_i + 2i\rho_0\omega(\boldsymbol{\Omega} \times \mathbf{u})_i + (\delta\lambda e_{kk}\delta_{ij} + 2\delta\mu e_{ij})_{,j} \\ & + \delta\rho[(V_{0,r}\, u_r)_{,i} - V_{0,r}\, \delta_{ri} e_{kk}] + \rho_0[(\delta V_{,j}\, u_j)_{,i} - \delta V_{,j}\, e_{kk}] + \delta\rho\, K_{,i},\end{aligned} \tag{8.88}$$

$$\delta\mathcal{L}(\mathbf{u}, K) = -(\delta\rho\, u_i)_{,i}. \tag{8.89}$$

Here, δV is the perturbation of the gravity field due to the density perturbation. δV satisfies Poisson's equation:

$$\nabla^2 \delta V = -4\pi\gamma\, \delta\rho.$$

Equations (8.85), together with the appropriate homogeneous boundary conditions, define an eigenvalue problem that gives the free-oscillation periods for a laterally inhomogeneous Earth. We shall assume that the eigenfunction of the laterally inhomogeneous Earth can be expressed as a linear combination of the eigenfunctions (sharing the same order numbers (n, l)) of the spherically symmetric Earth.

Let us consider a spheroidal mode ${}_nS_l$ or a torsional mode ${}_nT_l$ in a spherically symmetric Earth. We take the eigenfunctions corresponding to ${}_nS_l$ as

$$\begin{aligned}{}_n\mathbf{u}_l^{0Sm} &= U(r)\mathbf{R}_l^m(\theta, \phi) + V(r)\mathbf{S}_l^m(\theta, \phi), \\ {}_n\phi_l^{0m} &= K(r)Y_l^m(\theta, \phi),\end{aligned} \tag{8.90}$$

and those corresponding to ${}_nT_l$ as

$${}_n\mathbf{u}_l^{0Tm} = W(r)\mathbf{T}_l^m(\theta, \phi), \tag{8.91}$$

using the vector surface harmonics introduced in (8.14). For fixed l and n, all $2l + 1$ spheroidal modes ${}_nS_l^m$ $(-l \le m \le l)$ for a spherically symmetric nonrotating Earth have the same angular eigenfrequency ${}_n\omega_l^S$, and all $2l + 1$ torsional modes ${}_nT_l^m$ have the same angular eigenfrequency ${}_n\omega_l^T$. The lateral inhomogeneities will, in general, remove this degeneracy and split each unperturbed frequency into $2l + 1$ frequencies, which we write as

$${}_n\omega_l^{Si} = {}_n\omega_l^S + \delta_n\omega_l^{Si} \qquad \text{and} \qquad {}_n\omega_l^{Ti} = {}_n\omega_l^T + \delta_n\omega_l^{Ti} \qquad (-l \le i \le l). \tag{8.92}$$

To approximate the corresponding eigenfunctions, we use the following ansatz:

$${}_n\mathbf{u}_l^{Si} = \sum_m c_m^i\, {}_n\mathbf{u}_l^{0Sm} \qquad {}_nK_l^i = \sum_m c_m^i\, {}_nK_l^{0m} \qquad (-l \le i \le l), \tag{8.93}$$

and

$${}_n\mathbf{u}_l^{Ti} = \sum_m D_m^i\, {}_n\mathbf{u}_l^{0Tm} \qquad (-l \le i \le l). \tag{8.94}$$

BOX 8.6
Quasi-degeneracy

The use of the linear combination of unperturbed eigenfunctions with fixed (n, l) as a trial function for the eigenfunction for a perturbed medium, see (8.93) and (8.94), may be allowed if the degenerate eigenfrequencies of multiplets of the unperturbed problem are sufficiently different from each other, so that no coupling occurs to modes with different (n, l). On the other hand, if the degenerate eigenvalues of multiplets of the unperturbed problem are so close to each other that the first-order corrections within any single multiplet due to perturbation are larger than the separation of different multiplets, then the above form of trial function is no longer appropriate. This is the case of *quasi-degeneracy*, which was studied by Dahlen (1969) for a rotating, elliptical Earth and by Luh (1973) for a laterally inhomogeneous Earth.

Putting the above ansatz into (8.85) and omitting the labels S, l, and n, we find for spheroidal modes that

$$\begin{aligned} &\sum_m c_m^i [H_{0j}(\mathbf{u}^{0m}, K^{0m}) + \delta H_j(\mathbf{u}^{0m}, K^{0m})] = -\rho_0 (\omega^i)^2 \sum_m c_m^i \, u_j^{om}, \\ &\sum_m c_m^i [\mathcal{L}_0(\mathbf{u}^{0m}, K^{0m}) + \delta \mathcal{L}(\mathbf{u}^{0m}, K^{0m})] = 0. \end{aligned} \tag{8.95}$$

The eigenfunctions $(\mathbf{u}^{0m}, K^{0m})$ for the unperturbed medium satisfy the equations

$$\begin{aligned} H_{0i}(\mathbf{u}^0, K^0) &= -\rho_0 \omega^2 u_i^0, \\ \mathcal{L}_0(\mathbf{u}^0, K^0) &= 0. \end{aligned} \tag{8.96}$$

Subtracting (8.96) from (8.95), we obtain

$$\begin{aligned} &\sum_m c_m^i \, \delta H_j(\mathbf{u}^{0m}, K^{0m}) = -\rho_0 \, \delta(\omega^i)^2 \sum_m c_m^i \, u_j^{0m}, \\ &\sum_m c_m^i \, \delta \mathcal{L}_0(\mathbf{u}^{0m}, K^{0m}) = 0. \end{aligned} \tag{8.97}$$

Taking the inner product of (8.97) with each eigenfunction for the unperturbed medium, we find

$$\sum_{m=-l}^{l} c_m^i \, \delta H_{m'm} = \delta(\omega^i)^2 c_{m'}^i \qquad (-l \le i \le l) \tag{8.98}$$

where

$$\delta H_{m'm} = \frac{-\int_V [u_j^{0m'*} \delta H_j(\mathbf{u}^{0m}, K^{0m}) + K^{0m'*} \delta \mathcal{L}(\mathbf{u}^{0m}, K^{0m})] \, dV}{\int_V \rho_0 |\mathbf{u}^{0m'}|^2 \, dV}. \tag{8.99}$$

The system of linear equations (8.98) defines an eigenvalue problem. For nonvanishing c_m^i, $\delta(\omega^i)^2$ must be the eigenvalue of matrix $\delta H_{m'm}$. Once the eigenvalue is determined, the corresponding eigenfunction can be obtained by putting the solution c_m^i of (8.98) into (8.93).

For toroidal oscillations, for example, the frequency perturbation is the eigenvalue of matrix $\delta\mathbf{H}$ with elements

$$\delta H_{m'm} = -\frac{\int_V u_i^{0m'*}(2\,\delta\mu e_{ij}^{0m})_{,j}\,dV + \omega^2 \int_V \delta\rho u_i^{0m'*} u_i^{0m}\,dV}{\int_V \rho_0 |\mathbf{u}^{0m'}|^2\,dV}, \tag{8.100}$$

where $\delta\mathbf{H}$ is known explicitly in terms of $\delta\mu$ and $\delta\rho$, as given in (8.88); the effect of the Earth's rotation, discussed in the previous section, is neglected. One can show, by using Gauss's theorem and the traction-free condition on the Earth's surface, that the matrix $\delta H_{m'm}$ is Hermitian:

$$\delta H_{m'm} = \delta H_{mm'}^*. \tag{8.101}$$

Hence the eigenvalues $\delta(\omega^i)^2 \sim 2\omega\,\delta\omega^i$ of (8.98) will be real.

In order to evaluate $\delta H_{m'm}$, one must know eigenfunctions u_i^{0m} for the unperturbed medium. Since their dependences on (θ, ϕ) are given by $Y_l^m(\theta, \phi)$ as in (8.90) and (8.91), it is natural also to expand the medium perturbations $\delta\lambda$, $\delta\mu$, and $\delta\rho$ by spherical harmonics:

$$\begin{aligned}
\delta\lambda(r,\theta,\phi) &= \sum_{s=1}^{\infty}\sum_{t=-s}^{s} \delta\lambda_s^t(r) Y_s^t(\theta,\phi),\\
\delta\mu(r,\theta,\phi) &= \sum_{s=1}^{\infty}\sum_{t=-s}^{s} \delta\mu_s^t(r) Y_s^t(\theta,\phi),\\
\delta\rho(r,\theta,\phi) &= \sum_{s=1}^{\infty}\sum_{t=-s}^{s} \delta\rho_s^t(r) Y_s^t(\theta,\phi).
\end{aligned} \tag{8.102}$$

Writing the volume element as $dV = r^2\,dr \cdot d\Omega$, the terms in (8.100) can be separated into radial and angular integrals. The radial part must be evaluated numerically. The angular part is reduced to the integral of products of three spherical harmonics:

$$I = \int_{\Omega_0} d\Omega\, Y_l^{m'*}(\theta,\phi) Y_s^t(\theta,\phi) Y_l^m(\theta,\phi), \tag{8.103}$$

where Ω_0 is the surface of a sphere of unit radius. The above integral may be expressed in terms of Clebsch–Gordon coefficients, extensively used in the quantum theory of angular momentum (Edmonds, 1960),

$$I = \sqrt{\frac{2s+1}{4\pi}}(stlm|sllm')(s0l0|sll0). \tag{8.104}$$

The bracketed terms are the Clebsch–Gordon coefficients. They can each be expanded in an integer series whose sum is easily computed.

The angular integral I is different from zero only if

$$\begin{aligned} &\text{(i)} && s \text{ is even,} \\ &\text{(ii)} && s < 2l, \\ &\text{and (iii)} && m' = t + m. \end{aligned} \tag{8.105}$$

These three relations between the degree and order of the spherical harmonics are called selection rules. They have important and interesting implications on the effect of lateral heterogeneity on the free-oscillation periods.

Rule (i) shows that the lateral inhomogeneity expressed by spherical harmonics of odd order number does not show an observable effect on free-oscillation periods. Obviously, then, we cannot uncover the odd harmonics of lateral inhomogeneity from observed free-oscillation periods. This is true, however, only when the assumptions used in the perturbation methods are valid. They may break down if two different modes of the unperturbed medium have very close frequencies. In such a case, the method of quasi-degeneracy is applicable (Box 8.6).

Rule (ii) shows that free oscillations of order l are affected only by the lateral inhomogeneity harmonics of orders lower than $2l$. In other words, those inhomogeneities whose scale length is shorter than half the wavelength of the free oscillation do not affect the eigenfrequency. This is a remarkable insensitivity to the effect of shorter wavelength scatterers.

Rule (iii) shows that the coupling between the unperturbed eigenfunctions ${}_n\mathbf{u}_l^m$ and ${}_n\mathbf{u}_l^{m'}$ occurs only through inhomogeneity harmonics whose azimuthal order number t is equal to $m' - m$. This is interesting in the context of known properties of scattering in inhomogeneous media. In general, the wavenumber spectra of incident waves, scattered waves, and inhomogeneity in laterally inhomogeneous media are related by a convolution in k-space. If the inhomogeneity and the incident waves had single wavenumbers k_0 and k_1, respectively, the convolution would give $\delta(k - k_0) * \delta(k - k_1) = \delta(k - k_0 - k_1)$. Therefore, the scattered wave will have the single wavenumber $k_0 + k_1$. This is essentially rule (iii).

From rule (iii), it follows that the diagonal element δH_{mm} contains only $Y_s^0(\theta, \phi)$, and the sum of the diagonal elements will have a factor of the form

$$\int_{\Omega_0} d\Omega\, Y_s^0(\theta, \phi) \sum_{m=-l}^{l} Y_l^{m'*}(\theta, \phi) Y_l^m(\theta, \phi).$$

Then the addition theorem for spherical harmonics (see equation (20) of Box 8.1) gives

$$\sum_{m=-l}^{l} Y_l^{m*}(\theta, \phi) Y_l^m(\theta, \phi) = \frac{2l+1}{4\pi} P_l(0) = \frac{2l+1}{4\pi},$$

and since

$$\int_{\Omega_0} d\Omega\, Y_s^0(\theta, \phi) = 0 \qquad \text{provided } s > 0,$$

we have

$$\sum_{m=-l}^{l} \delta H_{mm} = 0. \tag{8.106}$$

Because of the invariance of the trace of a matrix, we find that the sum of eigenvalues $\delta_n\omega_l^i$ is also zero:

$$\sum_{i=-l}^{l} \delta_n\omega_l^i = 0. \tag{8.107}$$

This is called the *diagonal sum rule*. It was first applied to the perturbation of free oscillations by Gilbert (1971a). Because of this rule, we can be sure that the average of frequencies in a multiplet split by lateral heterogeneity is equal to the frequency for the unperturbed, spherically symmetric Earth model. If we work with observations of free-oscillation frequencies that are averages of the frequencies split by lateral heterogeneity, then these observations are relevant to a spherically symmetric Earth model obtained from the actual Earth by lateral averaging.

Calculations of $\delta\omega^i$ were made by Madariaga (1972) for torsional oscillations, and by Luh (1973) for spheroidal oscillations. Figure 8.11 shows an example of the extent of the splitting, for six different torsional multiplets.

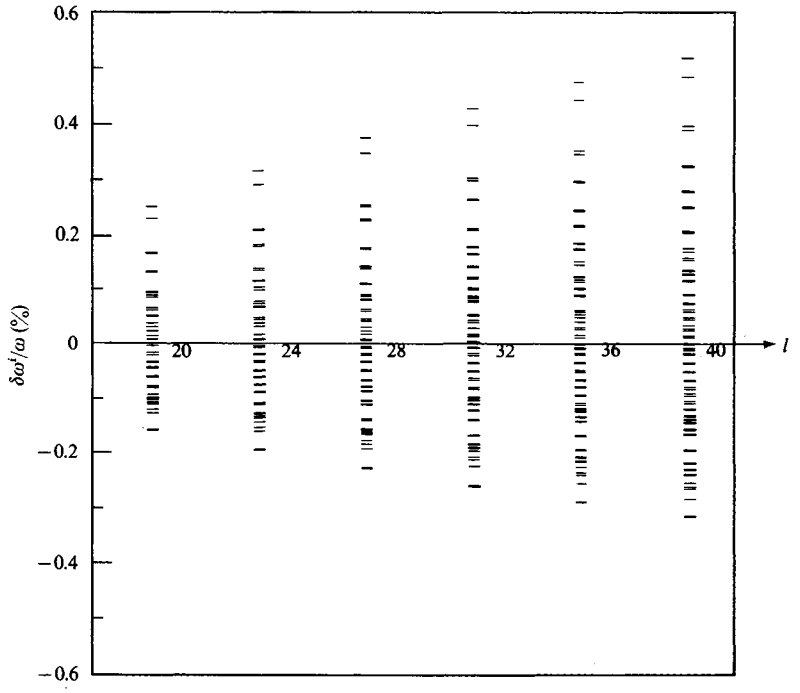

FIGURE **8.11**
Spectral splitting of toroidal modes for several different order numbers for the ocean–continent heterogeneity with the model CANSD under continents (Brune and Dorman, 1963) and 8099 under oceans (Dorman *et al.*, 1960). [From Madariaga and Aki, 1972; copyright by the American Geophysical Union.]

Suggestions for Further Reading

Biot, M. A. *Mechanics of Incremental Deformations*. New York: Wiley, 1965.

Brune, J. N., and F. Gilbert. Torsional overtone dispersion from correlations of S waves to SS waves. *Bulletin of the Seismological Society of America*, **64**, 313–320, 1974.

Cummins, P. R., N. Takeuchi, and R. J. Geller. Computation of complete synthetic seismograms for laterally heterogeneous models using the Direct Solution Method. *Geophysical Journal International*, **130**, 1–16, 1997.

Dahlen, F. A., and J. Tromp. *Theoretical Global Seismology*. Princeton, New Jersey: Princeton University Press, 1998.

Dziewonski, A. M., and J. H. Woodhouse. Studies of the seismic source using normal-mode theory. In *Proceedings of the International School of Physics, "Enrico Fermi,"* Course LXXXV, *Earthquakes: Observation, Theory and Interpretation*, 45–137, 1983.

Friederich, W., and J. Dalkolmo. Complete synthetic seismograms for a spherically symmetric Earth by a numerical computation of the Green's function in the frequency domain. *Geophysical Journal International*, **122**, 537–550, 1995.

Gilbert, F., and A. M. Dziewonski. An application of normal mode theory to the retrieval of structural parameters and source mechanisms from seismic spectra. *Philosophical Transactions of the Royal Society* (Lond.), **A278**, 187–269, 1975.

Kanamori, H. Shaking without quaking. *Science*, **279**, 2063–2064, 1998.

Love, A. E. H. *Some Problems of Geodynamics*. New York: Dover Publications, 1967.

Rayleigh, Baron. *Theory of Sound* (Chapter 5). New York: Dover Publications, 1945.

Satô, Y., T. Usami, and M. Landisman. Theoretical seismograms of spheroidal type on the surface of a gravitating elastic sphere—II. Case of Gutenberg-Bullen A′ earth models. *Bulletin of the Earthquake Research Institute, Tokyo Univ.*, **45**, 601–624, 1967.

Takeuchi, H., and M. Saito. Seismic surface waves. In *Seismology: Surface Waves and Earth Oscillations*. Methods in Computational Physics, vol. 11, edited by B. A. Bolt, 217–295. New York: Academic Press, 1972.

Woodhouse, J. H. Long period seismology and the Earth's free oscillations. In *Seismic Modelling of Earth Structure*, edited by E. Boschi, G. Ekström, and A. Morelli. Istituto Nazionale di Geofisica, Editrice Compositori, 31–80, 1996.

Problems

8.1 Give the normal-mode theory for torsional oscillations of a homogeneous elastic solid sphere, and find the two longest periods. What generally is the most favorable depth for exciting ${}_0T_2$ by (a) a single horizontal force, and (b) by a couple with moment about a vertical axis?

8.2 Show that the temporal Q of a torsional mode is related to the $Q_\beta(r)$ of body waves at radius r by

$$Q^{-1} = \int_0^{r_\oplus} \frac{\beta}{\omega} \left[\frac{\partial \omega}{\partial \beta} \right] Q_\beta^{-1}(r)\, dr,$$

the partial derivative here being given in (8.66).

8.3 What is wrong with the following argument? The Earth's daily rotation is not excited by external forces, and is therefore a free oscillation of the Earth. It must be a torsional oscillation, and corresponds to $l = 1$. For an Earth that is spherically symmetric, it follows that rotation can have no effect on any of the other modes (toroidal and spheroidal), since orthogonal modes in such a model do not interact.

8.4 The figure here is an expanded version of part of Figure 8.8. Use both figures to assign l and n for the identified (i.e., large symbol) spheroidal modes with frequency between 13 and 14 mHz that are associated with *PKP* but not with *PKIKP*.

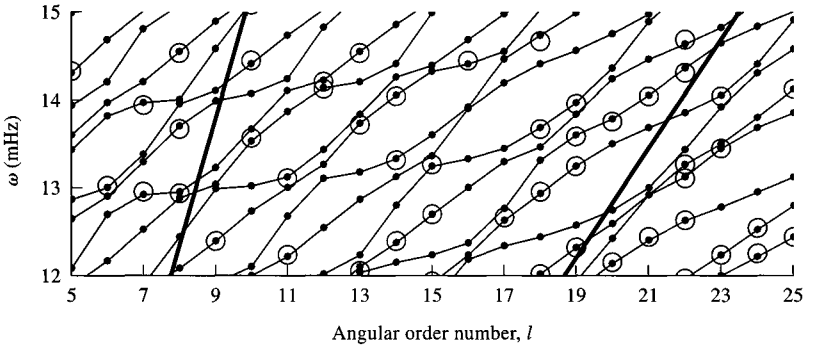

8.5 Consider a sequence of G-waves, $G1, G2, \ldots, Gn$, arriving at a given station after a large earthquake (see Appendix 1). Taking into account the polar phase shift, derive a formula for determining the phase velocity over the great circle from the Fourier transforms of Gn and Gm.

The formula does not include the initial phase due to any source effects if n and m differ by an even number. Otherwise, it requires knowledge of the difference between the initial phases at opposite radiation azimuths. Is there any simple rule relating the initial phases at opposite azimuths from a point source (7.149) that can be used to simplify the formula for the latter case?

Consider the same problem for mantle Rayleigh waves using (7.150).

8.6 This question is based on the concepts and notation presented in equations (8.30) and (8.38), and the answers to Problem 4.13.

a) What is the value of

$$ {}_ie^*_{zx}(\mathbf{x}_s)M_{zx} + {}_ie^*_{xz}(\mathbf{x}_s)M_{xz} + {}_ie^*_{zy}(\mathbf{x}_s)M_{zy} + {}_ie^*_{yz}(\mathbf{x}_s)M_{yz} $$

if the source position $\mathbf{x}_s$ is taken very close to a stress-free surface?

b) Show that a dip–slip earthquake (vertical fault, vertical slip) becomes very inefficient in exciting normal modes if the hypocenter is very shallow.

c) At a fixed depth h, give arguments to show that the strain tensor associated with seismic motion is essentially the same as the strain tensor at the free surface, provided the period of the seismic motion is long enough.

d) For a dip–slip earthquake in the crust, the body waves observed teleseismically include P followed by two near-source surface reflections, pP and sP (see figure); and S followed by two near-source reflections, pS and sS. What can be said about the sum of amplitudes in the P-wave group, and the sum of amplitudes in the S-wave group?

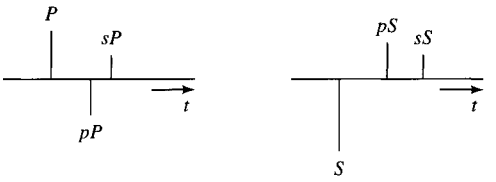

[This figure shows "stick seismograms" for the teleseismic P and S arrivals, each followed by their near-source reflections (i.e., the source acts as an impulse, and the Earth is taken as elastic, with no attenuation). The figure is schematically the same for each of the three components of motion—vertical and two horizontals. In this problem, take the source to be shallow enough that the arrivals within these two groups blend together, at long period.]

e) In general, how many of the components M_{ij} of a moment tensor are independent? Suppose a large shallow earthquake is well-recorded at long period all around the world, and the effort is made (using an interpretation based on normal modes, or Rayleigh and Love waves, or long-period body waves) to analyze these signals to infer independent components of the moment tensor. Point out an intrinsic problem of nonuniqueness, in procedures to determine some of these components.

f) Do your answers to all previous parts of this question depend upon assumptions about whether the Earth is laterally homogeneous?

CHAPTER 9

Body Waves in Media with Depth-Dependent Properties

The most successful single method for using seismic waves to investigate the Earth's internal structure has historically been the application of ray-theory formulas (Section 4.4) to interpret short-period body waves. For example, just from observations of the travel-time function $T(\mathbf{x}, \boldsymbol{\xi})$ for varying receiver position $\mathbf{x}$ and varying source position $\boldsymbol{\xi}$, Beno Gutenberg in 1913 accurately estimated the depth to the core–mantle boundary as 2900 km. Also on the basis of travel times and interpreting picked arrivals in terms of an appropriate path of propagation through the Earth, accurate estimates of crustal thickness began with Mohorovičić in 1909, and the existence of an inner core was recognized by Inge Lehmann in 1936. By 1939, the independent efforts of Gutenberg and Harold Jeffreys in applying ray theory had led to velocity models of the whole Earth which differ from each other by only a few percent. They used the Herglotz–Wiechert formula (given here as equation (9.36)) to infer Earth structure from ray travel times. In the depth range 800–2800 km, there is less than 1% difference between the P-wave velocities in Jeffreys' and Gutenberg's models, and also less than 1% between Jeffreys' model and the more recent Earth model iasp91 of Kennett and Engdahl (1991). However, these early results of Gutenberg and Jeffreys, achieved with ray theory, are not enough to resolve many questions about the composition and state of materials at great depth within the Earth. For example, in the upper mantle there are two depth ranges (around 410 km and 660 km) within which the velocity gradient $(d\alpha/dz)$ is anomalously large. The cause is likely to be either a compositional gradient or a transition between different solid phases of the same mineral, or both, and any generally acceptable resolution of this difficult question will depend heavily on seismologists being able to give very accurate estimates of $d\alpha/dz$ and $d\beta/dz$ with depth. Similarly, to understand the energetics of a dynamo in the Earth's fluid core, it is important to know if the velocity gradient there has values that will either inhibit or promote convection.

It has therefore turned out that one of the most classical aspects of seismology is still an active research field: namely, the deduction of the Earth's internal structure, but now with emphasis on fine detail, such as velocity gradients within restricted depth ranges and the estimation of jumps in properties across recognized discontinuities such as the Moho.

Body waves here have an important role to play, since their relatively short period, and the possibility of isolating them in time from other waves on a seismogram, permit their use in studying highly localized regions within the Earth. One such use is found in the methods

of seismic tomography, in which travel times are analyzed for many different ray paths that to be effective must thoroughly sample a volume of interest. Seismic tomography is widely used today to study three-dimensional structure, and has enabled major discoveries such as the presence of deeply subducted slabs of former lithosphere, which penetrate almost to the core–mantle boundary (van der Hilst *et al.*, 1998). Another use of body-wave travel times has been to study time-varying changes of the Earth's seismic velocity structure. Such temporal changes are seen in exploration geophysics in the context of extraction of oil (He *et al.*, 1998), and in studies of foreshock and aftershock signals associated with shallow earthquakes that may induce changes in crack distribution, and changes in fluid saturation (Schaff, 2001). Changes in travel time have also been used to study features of the Earth's inner core, in particular the possibility that it is rotating at a slightly different speed from the mantle and crust. (Because the inner core is slightly anisotropic and inhomogeneous, the travel time of the phase *PKIKP* as documented at a fixed station will be slightly different from earthquakes at the same place but at different times, if the inner core is rotating or undergoing some other type of internal deformation. See Song, 2000, and Richards, 2000.)

Attempts to use ray theory for the *amplitude* of seismic body-wave arrivals have been summarized by Julian and Anderson (1968), Wesson (1970), Shimshoni and Ben-Menahem (1970), Chapman (1971) and Okal (1992). The geometrical spreading function ($\mathcal{R}(\mathbf{x}, \boldsymbol{\xi})$ in the notation of Chapter 4) can be an exceedingly sensitive function of velocity gradients, which is a desirable feature for purposes of inverting for Earth structure. However, it is at this stage that one can clearly recognize some limitations in applying classical ray theory to the interpretation of data. The problem is a breakdown of the theory itself, for in body-wave data can be seen a variety of frequency-dependent effects that geometrical ray theory cannot quantify. Body waves are seen in "shadow zones" (which could not be penetrated according to Snell's law); they are seen near caustics (a surface that is a weak type of focus, on which $\mathcal{R}(\mathbf{x}, \boldsymbol{\xi}) = 0$), with frequency-dependent amplitudes that do not have the singularity predicted by the geometrical spreading function; and they are seen in situations where a variety of rays between source and receiver all have similar arrival times, so that complicated interference effects are observed. To go beyond the framework of geometrical ray theory in order to model these observations, we need extensions of the methods used in Chapter 6 to solve Lamb's problem, and extensions of the systematic procedures described in Chapter 7 for handling waves in layered media. In fact, we shall distinguish three rather different theoretical methods for successfully studying body waves. Although the methods of calculation are substantially different, each theory is now used in the same way—namely, to generate synthetic seismograms in some given Earth model with a given seismic source. A comparison is then made between theory and observations. Because whole waveforms present in the data are used to judge whether particular models of the Earth and source are successful or not, synthetic seismograms are a major advance over the use merely of ray-theoretical travel-time curves and polarity of first motions.

In this chapter, the concluding one of three that address seismic waves in depth-dependent (one dimensional) structures, a major goal is to develop an understanding of the way in which body waves have their waveforms affected by departures from the predictions of geometrical ray theory—for example, by the presence of caustics, by various types of diffraction, and by tunneling.

The first of the theoretical methods we shall describe is an extension of Cagniard's approach (Section 6.5), used in practice to handle the case of a medium composed of

very many (possibly several hundred) homogeneous plane layers. As shown by Helmberger (1968), the key here is a numerical approach for obtaining the Cagniard path in the complex ray-parameter plane (rather than an evaluation of simple hyperbolas, such as that given following (6.91)). The second theoretical approach, originated by Fuchs (1968, 1970, 1971) and often called the "reflectivity method," again is directed toward the computation of waves within a medium composed of very many homogeneous layers. Based on the matrix methods developed in seismology by Haskell (see Chapter 7), Fuchs' method entails numerical integration over a limited range of real ray parameters, followed by a numerical inverse Fourier transform over frequency to obtain the synthetic seismogram.

The Earth, of course, is not composed of a stack of homogeneous plane layers; therefore, to apply the above two methods to the interpretation of seismograms, it is necessary to note two important results. One, due to a theorem given by Volterra (see Gilbert and Backus, 1966), is that the wave systems in a medium with *continuous* spatial variations of density and wave speeds can indeed be studied by solving for the waves in a *discrete* medium composed of many homogeneous parts. By taking the wave solution for the discrete medium (in the limit as the number of homogeneous regions tends to infinity in such a way as to give the density and wave speeds of the continuous medium), this solution does tend to the wave solution for the continuous medium. In practice, for a medium in which ρ, α, β depend only on depth (i.e., on the Cartesian coordinate z), it is therefore permissible to model a continuous profile with a large number of homogeneous plane layers. Such an approach has been widely adopted, though Chapman (1976a) has extended the Cagniard method to allow a solution directly, for continuously varying $\rho(z)$, $\alpha(z)$, $\beta(z)$.

The second result needed to apply Cagniard's and Fuchs' methods in seismology involves a consideration of the Earth's spherical geometry. (Throughout this chapter, we shall be concerned only with media in which ρ, α, β are functions of r in a spherical polar coordinate system or functions of depth z with z belonging to either a Cartesian system or a cylindrical system with vertical axis of symmetry.) The question, then, is how to transform a wave-propagation problem posed for a medium with spherical symmetry (i.e., radial heterogeneity) into a problem posed for a plane-stratified medium, in which our first two methods of solution are directly applicable. By using such an "Earth-flattening transformation" (see Box 9.2 for details), Andrianova *et al.* (1967) and Biswas and Knopoff (1970) showed that, for *SH*-waves, it is possible to obtain *exact* wave solutions in spherical media from the corresponding solution in plane media. Chapman (1973) showed that an exact transform for *P-SV* problems does not appear possible, but he obtained Earth-flattening transformations that are useful approximations to *P–SV* problems in spherical media.

The third method of solution we shall describe is one in which the Earth model is composed of radially inhomogeneous layers. The seismic motions (as a function of time, at different positions in the Earth) are broken up into signals arriving within different time windows, each signal corresponding basically to some particular type of body-wave ray path. Instead of geometrical ray theory, one uses a more accurate solution for the signal of interest by considering an integral that is conducted over both frequency and ray parameter. Within this general procedure, several different methods have been proposed for executing the double integration. Either the frequency integral or the ray-parameter integral can be done first. The ray-parameter integral can be carried out over real values or over complex values. Many different scientists have contributed toward the underlying theory. A major

contribution was made by Scholte (1956), who used well-established methods for summing partial wave expansions in spherical geometry and showed in some detail how the solution in the frequency domain for specific seismic rays could be identified. The solution involves an integral in the complex plane using a variable that (essentially) is the ray parameter, and Phinney and Alexander (1966) and Phinney and Cathles (1969) showed that this integral can easily be obtained numerically. Taking the approach of complex integration over ray parameter, followed by a real integration over frequency, we shall show some practical applications to several seismic waves that have interacted with the Earth's solid and fluid cores. Chapman (1978a, b) has described several alternative approaches. One that is often very effective entails first an integration over real frequencies (in many cases, this is possible analytically rather than numerically), followed by a fairly simple inversion of the ray parameter integral. This approach, an application of asymptotic methods based on WKBJ theory, is approximate but computationally very fast. Chapman and Orcutt (1985) evaluated such WKBJ synthetics, in comparison to a more accurate but computationally more intensive approach based on Earth flattening and the reflectivity method.

9.1 Cagniard's Method for a Medium with Many Plane Layers: Analysis of a Generalized Ray

This section is a natural extension of Section 6.5, in which we showed how to evaluate the generalized reflection from the interface between two half-spaces. Supposing that the reader is familiar with a derivation of (6.91), and the steps detailed in (6.92)–(6.95), we follow Helmberger (1968) in describing how to evaluate the generalized primary reflection shown in Figure 9.1. Helmberger's original application of this method was to the interpretation of hydrophone records due to a point source of pressure (a charge of TNT, fired at depth d_1 below the surface of the Bering Sea). With a receiver at depth d_2, a major goal was to interpret the response at ranges r of about 30–70 km in terms of the head wave and reflection at the Moho. Therefore, the theory required extensions to handle layering in the crust and possible interference between the head wave and the reflection.

Taking z_0 as the ocean–air interface, and layer 1 as the ocean itself, the source is specified by an incident pressure field in layer 1:

$$P^{\text{inc}}(r,z,t) = \frac{R_s}{\sqrt{r^2+(z-z_0-d_1)^2}} P_0\left(t - \frac{\sqrt{r^2+(z-z_0-d_1)^2}}{\alpha_1}\right). \tag{9.1}$$

That is, the initial pressure pulse has shape $P_0(t - R_s/\alpha_1)$ at a standard (fixed) distance R_s from the source. It follows from our analysis of pressure sources in Chapter 6 that we can immediately write down the Laplace transform for the generalized P-wave primary shown in Figure 9.1b. It is

$$P(r,z,s) = \frac{2s}{\pi} R_s P_0(s) \text{Im} \int_0^{i\infty} \frac{p}{\xi_1} \times K_0(spr)[\text{PRODUCT}(p)]\exp\{-s[\text{SUM}(p)]\}dp, \tag{9.2}$$

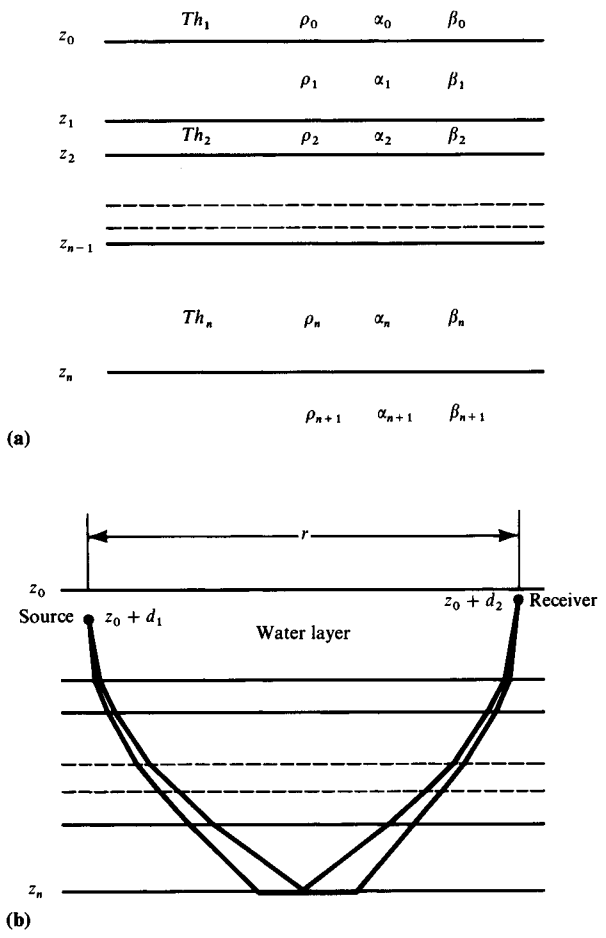

FIGURE **9.1**
(a) Notation for the density (ρ) and two wave speeds (α, β) in a stack of homogeneous layers. The boundary between layers n and $n+1$ is at depth z_n, and the thickness of the nth layer is $Th_n = z_n - z_{n-1}$. (b) Ray interpretation for the two main contributions to the generalized P-wave reflection associated with the nth boundary; source and receiver are in layer 1. We have assumed $\alpha_{n+1} > \alpha_n$, so that a head wave (involving horizontal propagation at the top of the $(n+1)$th layer) can exist, together with a wide-angle reflection, as shown. Because this generalized reflection is associated with only one interface, it is known as a *primary* reflection. No mode conversions (from P to SV) are shown. In practice, for a P-wave source, it is often true that the total P-wave response at the receiver is given quite accurately by summing such primary reflections, one for each interface (i.e., by ignoring multiple internal reflections and conversions from P to SV and back to P).

where K_0 is a modified Bessel function and

$$\begin{aligned}\text{PRODUCT}(p) = {} & (\grave{P}\grave{P})_1 \cdot (\grave{P}\grave{P})_2 \cdot \cdots \cdot (\grave{P}\grave{P})_{n-1} \cdot (\grave{P}\acute{P})_n \\ & \cdot (\acute{P}\acute{P})_{n-1} \cdot \cdots \cdot (\acute{P}\acute{P})_2 \cdot (\acute{P}\acute{P})_1,\end{aligned} \tag{9.3}$$

$$\begin{aligned}\text{SUM}(p) = {} & (Th_1 - d_1)\xi_1 + Th_2\xi_2 + \cdots + Th_n\xi_n \\ & + Th_n\xi_n + \cdots + Th_2\xi_2 + (Th_1 - d_2)\xi_1.\end{aligned} \tag{9.4}$$

Here, $\xi_i = \sqrt{\alpha_i^{-2} - p^2}$ with branch cuts chosen by Re $\xi_i \geq 0$, and $(\grave{P}\grave{P})_{n-1}$ (etc.) is a transmission coefficient for the $(n-1)$th boundary. The product in (9.3), involving plane-wave transmission and reflection coefficients, is easily written down with an eye on Figure 9.1b, following the generalized ray across interfaces. (Although our physical variable

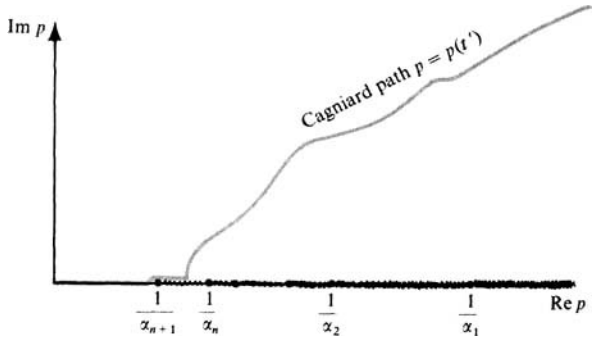

FIGURE **9.2**
The first quadrant of the complex p-plane, showing many branch points on the real axis (with cuts extending to the right), and a Cagniard path solving (9.5) (i.e., for the generalized ray of Figure 9.1). The head-wave contribution arises near $p = 1/\alpha_{n+1}$, and the reflection arises near the departure of the Cagniard path from the real p-axis.

is *pressure*, we have used *displacement* coefficients in this case because source and receiver are in the same layer, and pressure coefficients would give the same product.) Similarly, the sum in (9.4) is the accumulated vertical phase delay along the generalized ray.

The Cagniard path for inversion of (9.2) is now the solution $p = p(t')$ of

$$t' = pr + \text{SUM}(p), \tag{9.5}$$

where t' is real and positive. Although this step must be accomplished numerically, a solution for p as a function of t' can readily be found that has many of the features described for the generalized reflection in Figure 6.15. We show the solution for a multilayered case in Figure 9.2, assuming that P-wave speeds $\alpha_1, \alpha_2, \ldots, \alpha_{n+1}$ increase with depth and that r is great enough so that a head wave from the $(n+1)$th layer is indeed present.

If the source pulse $P_0(t)$ is a unit step at distance R_s, then the time-domain response for the generalized primary is exactly

$$\frac{2}{\pi} R_s \,\text{Im} \int_0^t \frac{p}{\xi_1} \left(\frac{dp}{dt'}\right) \frac{\text{PRODUCT}(p)\, dt'}{\sqrt{t-t'}\sqrt{t-t'+2pr}} \tag{9.6}$$

(compare with (6.92)). In practice, it is often adequate to replace $\sqrt{t-t'+2pr}$ in this denominator by $\sqrt{2pr}$, so that the step function response (9.6) becomes a convolution,

$$\frac{2}{\pi}\psi(t) * \sqrt{\frac{1}{t}}, \qquad \text{where } \psi(t) = R_s \,\text{Im}\left\{\frac{\sqrt{p}}{\xi_1}\frac{dp}{dt}\frac{\text{PRODUCT}(p(t))}{\sqrt{2r}}\right\}. \tag{9.7}$$

To compare this response with the recorded hydrophone signal, we can differentiate it to obtain the impulse response, and then convolve it with what we may call a transfer function, $T(t)$, that includes all the steps remaining in the derivation of the desired synthetic hydrophone record. The transfer function is itself the convolution of a realistic source pulse

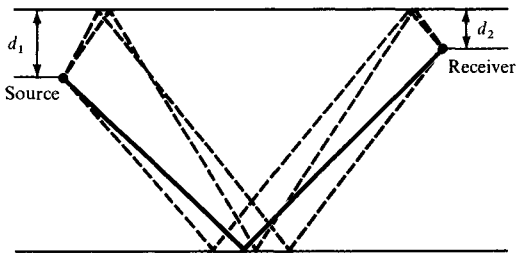

FIGURE **9.3**
The effect of surface reflections, for a near-surface source and receiver, is to add three extra generalized rays to the original ray shown in Figure 9.1b. Thus, for the near-source reflection, a time delay $2d_1/\alpha_1$ is introduced (the ocean sound speed being so much slower than α_{n+1} means that for Moho refraction the ray paths in the ocean are nearly vertical). Since $d_1 \ll Th_1$ and $d_1 \ll r$, this time delay is the only important effect (apart from a sign change on reflection), the remainder of the ray being essentially the same as for the original generalized ray.

$P_0(t)$, the instrument response $I(t)$, and a term that allows for near-source and near-receiver reflections. These effects together are summarized by

$$T(t) = P_0(t) * I(t) * \left[\delta(t) - \delta\left(t - \frac{2d_1}{\alpha_1}\right) - \delta\left(t - \frac{2d_2}{\alpha_1}\right) + \delta\left(t - \frac{2d_1}{\alpha_1} - \frac{2d_2}{\alpha_1}\right)\right]. \quad (9.8)$$

The assumptions behind this choice of three extra delta functions to represent surface reflections are described in Figure 9.3, and Figure 9.4 shows the way in which Helmberger (1968) developed $T(t)$ from its components. The synthetic hydrophone record is then

$$T(t) * \frac{d}{dt}[\text{step-function response given in (9.6)}] = \frac{dT}{dt} * \frac{2}{\pi}\psi(t) * \sqrt{\frac{1}{t}} \quad (9.9)$$

in which the time derivative has been transferred from ψ to T. In practice the derivative can be applied to P_0 or I.

Recall that only the generalized P-wave primary reflection from the interface at z_n has been considered here. For the oceanic crustal model shown in Figure 9.5, there are P-wave primaries to be considered from four other interfaces above the Moho at depth 19 km. However, these can easily be included by summing the appropriate ψ-functions defined in (9.7), each with a different Cagniard path, and then carrying out the two convolutions expressed in (9.9). The result is shown in Figure 9.6, a comparison of synthetic and observed waveforms given by Helmberger (1968) for a refraction experiment conducted in the Bering Sea, about 500 km north of Adak. The figure does show remarkably good agreement between synthetic and observed pulse shapes, although some discrepancies in relative amplitude remain, due possibly to errors in calibration of the source. Further details of the Cagniard path, and the wavefront expansion for head wave and reflection, are described in Problems 9.1 and 9.2.

The ease with which the contribution from each generalized ray can be computed makes it feasible to consider cases in which several hundred generalized rays are summed together.

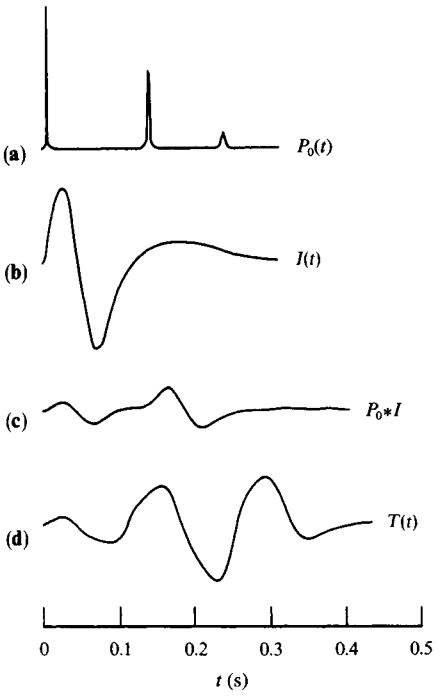

FIGURE **9.4**
Construction of the transfer function. **(a)** Typical source function $P_0(t)$ for a charge of TNT fired at a depth of 160 feet. An oscillating gas bubble is responsible for the later pulses. **(b)** The instrument function (hydrophone plus recording system), which is the response that would be recorded for a delta-function pressure wave passing the receiver. **(c)** Convolution of (a) and (b). **(d)** The transfer function itself, after a typical convolution to describe near-source and near-receiver reflections (see (9.8)). [After Fig. 6 of Helmberger, 1968.]

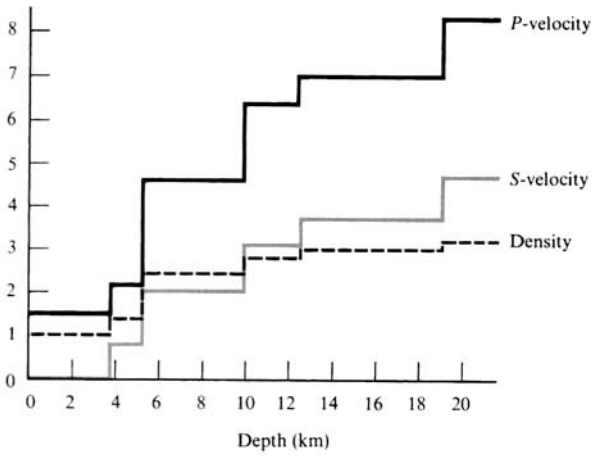

FIGURE **9.5**
A model of the oceanic crust beneath the Northern Aleutian Basin. Moho at depth 19 km, water layer 3.75 km. [After Fig. 10 of Helmberger, 1968.]

A large number of interesting geophysical problems have therefore yielded to analyses based on this extension to Cagniard's theory. Mellman and Helmberger (1974) showed how a thin high-velocity layer can cause attenuation of high-frequency waves; Vared and Ben-Menahem (1974) and Langston and Helmberger (1975) showed how to analyze shear dislocation sources; Helmberger and Malone (1975) matched synthetics and observations of SH waves to show how crustal layering can severely distort the waveforms due to local

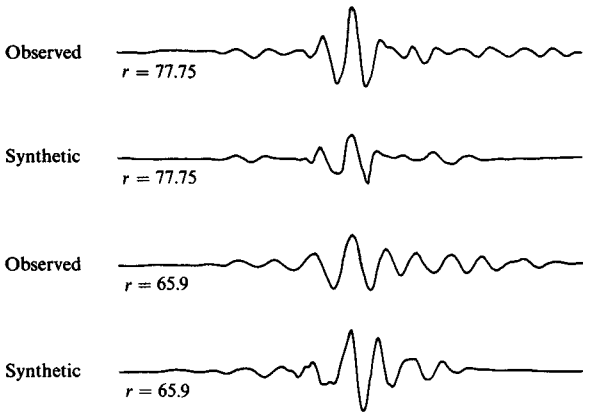

FIGURE **9.6**
Comparison of observed and synthetic hydrophone records for the head wave and wide-angle reflection from the Moho beneath the Northern Aleutian Basin. The reflection is relatively quite strong. Synthetics were computed from the generalized P-wave primary reflections in the model of Figure 9.5. [After Fig. 11 of Helmberger, 1968.]

earthquakes; and Spudich and Helmberger (1979) examined the sedimentary structures that may be expected at the ocean floor, evaluating the practical effect of leaking modes like the $\bar{P}$ wave we have described in Chapter 6 for a half-space. Richards *et al.* (1991) showed that the concept of generalized rays based on (9.3) and (9.4) in plane-layered media could be extended to media with planar but non-parallel interfaces.

Often, however, the number of generalized rays that must be considered is prohibitively large. This will occur for structures having strong velocity gradients and/or synthetics that are to be evaluated for extended times. Because of the importance of such problems, we turn now to an alternative method of computation, in which *all* the multiples are retained.

9.2 The Reflectivity Method for a Medium with Many Plane Layers

In Chapters 6 and 7, we showed how to obtain doubly transformed solutions as a function of (k, z, ω), where k is the horizontal wavenumber. These chapters emphasized manipulations in the complex k-plane (or p-plane, with $k = \omega p$), in order to evaluate an inverse transform giving the solution as a function of (r, z, ω). Fuchs (1968) initiated direct numerical evaluation of this inverse transform, by integrating over real values of k, and then also integrating over real values of ω to obtain the desired solution as a function of (r, z, t). For example, in describing the excitation of Love waves (Section 7.4) we obtained a formula for the multitransformed solution. This can be computed by using the known form of the propagator for SH-waves in a stack of homogeneous layers. The integral over real k is carried out at a sequence of different frequencies, and then a discrete form of $(1/\pi)$ Re $\int_0^\infty s(r, z, \omega) \exp(-i\omega t)\, d\omega$ is used to obtain the synthetic seismogram in the time domain.

A difficulty in execution of the above program is caused by poles in the multitransformed solution that correspond to surface-waves modes. These lie on the real k-axis itself, and hence on the path of integration. The difficulty can be removed by adding a small complex part to the velocity in each layer, accounting for anelasticity (see (5.94)), which moves surface-wave poles off the positive real k-axis and up into the first quadrant of the k-plane. However, Fuchs' approach is often used in body-wave studies to get the response, at the

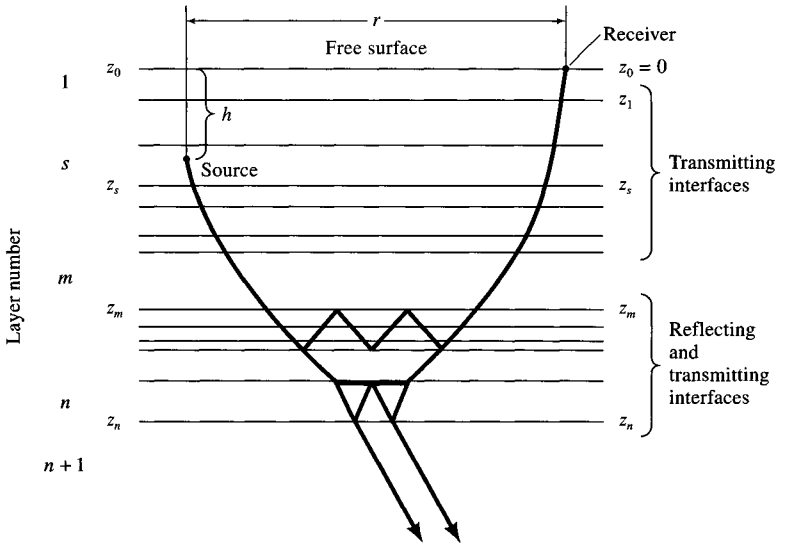

FIGURE **9.7**
The reflectivity method. A point source at depth h is located in layer s. It is desired to synthesize the displacement at range r on the free surface for body waves that have interacted with structure in the medium between depths z_m and z_n . Since the propagator matrix is used between these two depths, all multiples occurring within the structure of interest are retained. For example, a P head wave and S-waves are shown in layer n. Only those waves that depart downward from the source as P-waves and up to the receiver as P-waves are described in the text. The effect of structure above the source is conceptually simple to include.

free surface, of a stack of homogeneous plane layers within which a point source is active. If interest is restricted to body waves, then integration over k can often be limited to a part of the real k-axis that has no surface-wave poles. We now discuss a particular example of this numerical approach, which has come to be known as the *reflectivity method*.

Referring to Figure 9.7, suppose a point source at depth h generates waves that, at the receiver, appear to be reflected from structure between depths z_m and z_n. For example, in the Earth this might be a region of high velocity gradient, modeled here by many thin homogeneous layers.

Using the motion-stress vector approach, we have seen that the source is handled by a discontinuity in $\mathbf{f}(k, z, \omega)$ at $z = h$, where components of $\mathbf{f}$ are multitransformed components of displacement and traction. If the source has azimuthal (ϕ) dependence, then we have seen that a transform from ϕ to m is necessary; that the solution for each m component is obtained; and that $\mathbf{f}(k, \phi, z, \omega)$ contains a sum over m. However, only a few terms are necessary in practice, since $-2 \leq m \leq 2$ for sources described by a second-order moment tensor such as a double couple. The discontinuity in $\mathbf{f}$, for a shear dislocation of general orientation, has been described by Hudson (1969a,b).

If the source were in an infinite homogeneous whole space with the same elastic parameters as layer s, it would not be difficult to obtain the downgoing motion-stress vector below the source. We shall consider only a *P–SV* problem, with an interest in the P-wave

mode of propagation in the region above the reflecting structure. Recall in our notation $\mathbf{f} = \mathbf{F}\mathbf{w}$ that $\mathbf{F} = \mathbf{F}(z)$ is the *layer matrix*, defined in each layer (see (5.69)) and that $\mathbf{w}$ is a vector that weights the columns of $\mathbf{F}$. The four components of $\mathbf{w}$ are constant in general in each layer, and give the amplitude of downgoing P, downgoing SV, upgoing P, upgoing SV (respectively) in the layer. The source layer differs from all others in that $\mathbf{w}_s$ takes two values, one appropriate for $z < h$ (there are extra upgoing waves from the source), and one appropriate for $z > h$ (with extra downgoing waves). It follows from (5.69) that the motion stress for downgoing P-waves from the source alone is given by the first column of the matrix $\mathbf{E}$, times phase factor $\exp[i\omega\xi_s(z-h)]$, times a scalar P^{inc} that is related to the discontinuity in $\mathbf{f}$ at h. It is this vector, $\mathbf{f}^{\text{inc}P}$, that we need to start the propagation part of the problem, and it is

$$\mathbf{f}^{\text{inc}P} = \mathbf{f}^{\text{inc}P}(k, m, z, \omega) = P^{\text{inc}} \begin{pmatrix} \alpha_s p \\ \alpha_s \xi_s \\ 2i\omega\rho_s\alpha_s\beta_s^2 p\xi_s \\ i\omega\rho_s\alpha_s(1-2\beta_s^2 p^2) \end{pmatrix} \exp[i\omega\xi_s(z-h)]. \tag{9.10}$$

The source spectrum, and any azimuthal effects, are contained within the scalar P^{inc}. Since our main interest is in displacement, we shall not continue to write out the last two components of the motion-stress vector.

Carrying the wave on to a downgoing P-wave at the bottom of layer m, we multiply the downgoing wave by transmission coefficients and vertical phase factors, obtaining

$$\begin{pmatrix} \alpha_m p \\ \alpha_m \xi_m \end{pmatrix} \left(\prod_{j=s}^{m-1} \grave{P}\grave{P}_j \right) \exp\left[i\omega \left(\sum_{j=s+1}^{m} \xi_j T h_j \right) \right] P^{\text{inc}} \exp[i\omega\xi_s(z_s - h)]$$

for the motion that is incident on the stack of layers between z_m and z_n in which we are interested.

Let the P–P reflection coefficient for this stack of layers be denoted by $\{\grave{P}\acute{P}\}_n^m$ with similar notation for converted ($P \to S$) and transmitted phases. To obtain this coefficient, we work with the propagator matrix $\mathbf{P}(z_m, z_n)$ which is known explicitly (see Box 9.1) for homogeneous layers. Recalling the property

$$\mathbf{f}(z_m) = \mathbf{P}(z_m, z_n)\mathbf{f}(z_n), \tag{9.11}$$

we substitute

$$\mathbf{f}(z_m) = \mathbf{E}_m \begin{pmatrix} 1 \\ 0 \\ \{\grave{P}\acute{P}\}_n^m \\ \{\grave{P}\acute{S}\}_n^m \end{pmatrix} \quad \text{and} \quad \mathbf{f}(z_n) = \mathbf{E}_{n+1} \begin{pmatrix} \{\grave{P}\grave{P}\}_n^m \\ \{\grave{P}\grave{S}\}_n^m \\ 0 \\ 0 \end{pmatrix}. \tag{9.12}$$

The reference level for phase is here taken as z_m for reflections and z_n for transmission coefficients, so it is the matrices $\mathbf{E}$ that appear in (9.12) (because $\mathbf{E}_m = \mathbf{F}_m(z_m)$ and $\mathbf{E}_{n+1} = \mathbf{F}_{n+1}(z_n)$, from (5.69)). The first of equations (9.12) contains our assumption that the only wave incident on the stack is downgoing P; and the second of (9.12) has no upgoing

waves in the half-space below z_n. Since these forms for the motion-stress vector, substituted in (9.11), give four scalar equations in four unknowns, we can solve for the particular unknown of interest, namely $\{\grave{P}\acute{P}\}_n^m$. Detailed discussion is given by Červený (1974) and Kind (1976) (see also Box 9.9). The upgoing P-wave at the bottom of layer m is

$$\begin{pmatrix} \alpha_m p \\ -\alpha_m \xi_m \end{pmatrix} \left(\prod_{j=s}^{m-1} \grave{P}\grave{P}_j \right) \exp\left[i\omega \left(\sum_{j=s+1}^{m} \xi_j Th_j \right) \right] P^{\text{inc}} \{\grave{P}\acute{P}\}_n^m \exp[i\omega \xi_s (z_s - h)].$$

Next, we carry this motion up to the free surface as a P-wave, obtaining

$$\begin{pmatrix} \alpha_1 p \\ -\alpha_1 \xi_1 \end{pmatrix} (\text{PRODUCT}) \times \exp[i\omega(\text{SUM})] \{\grave{P}\acute{P}\}_n^m P^{\text{inc}}, \tag{9.13}$$

where

$$\begin{aligned} \text{PRODUCT} &= \left(\prod_{j=s}^{m-1} \grave{P}\grave{P}_j \right) \times \left(\prod_{j=1}^{m-1} \acute{P}\acute{P}_j \right), \qquad \text{and} \\ \text{SUM} &= \left(\sum_{j=s+1}^{m} \xi_j Th_j \right) + \left(\sum_{j=1}^{m} \xi_j Th_j \right) + \xi_s (z_s - h). \end{aligned} \tag{9.14}$$

The displacement (9.13) must be corrected for the effect of a free surface by adding the downward-reflected P- and S-waves at $z = 0$ to the upcoming P-wave. The correction is given in Problem 5.6, and at last we can state the displacement components of the motion-stress vector at the receiver. They are

$$\begin{aligned} \begin{pmatrix} u_r(k, m, 0, \omega) \\ u_z(k, m, 0, \omega) \end{pmatrix} &= \begin{pmatrix} 4\alpha_1 \beta_1^2 p \xi_1 \eta_1 \\ -2\alpha_1 \xi_1 (1 - 2\beta_1^2 p^2) \end{pmatrix} \\ &\quad \times \frac{\text{PRODUCT} \times \exp[i\omega\, \text{SUM}] \times \{\grave{P}\acute{P}\}_n^m \times P^{\text{inc}}}{(1 - 2\beta_1^2 p^2)^2 + 4\beta_1^4 p^2 \xi_1 \eta_1}. \end{aligned} \tag{9.15}$$

This is the multitransformed solution, which is to be summed over m (P^{inc} is m-dependent, in general) and integrated over k and ω. Thus, working from (7.132), we find that in the frequency domain the solution is

$$\mathbf{u}(r, \phi, 0, \omega) = \frac{1}{2\pi} \sum_{m=-\infty}^{\infty} \int_0^{\infty} k[u_r(k, m, 0, \omega)\mathbf{S}_k^m - iu_z(k, m, 0, \omega)\mathbf{R}_k^m]\, dk.$$

At body-wave values of k, and with some horizontal separation between source and receiver, the $\hat{\phi}$ component of $\mathbf{S}_k^m$ (see (7.118)) is often negligible, hence (9.15) is integrated via

BOX 9.1

Propagator matrices for SH and for P–SV problems

We introduced propagator matrices in the context of Love and Rayleigh waves (Section 7.2). We noted that particle motion decays with depth, so it was convenient to work with $e^{\pm\gamma z}$, $e^{\pm\nu z}$, in which γ and ν were usually real. Moreover, for P-SV, a $\pi/2$ phase shift was explicitly recognized between vertical and horizontal components of displacement and traction (see (7.25)–(7.27)), so that r_1, r_2, r_3, r_4 were real. Although the resulting equations are correct for body waves too, the notation γ, ν is inconvenient because γ and ν become negative imaginary. Note also that (for homogeneous waves) there is no phase shift between displacement components or between traction components, so that r_1, r_2, r_3, r_4 cannot all be real. In short, it is better to work with the motion-stress vectors introduced (for plane waves) in Section 5.4 and to work with slownesses p, ξ, η rather than horizontal wavenumber k and decay constants γ and ν.

For SH-waves in the far field, we use

$$\mathbf{f} = \mathbf{f}(k, m, z, \omega) = \mathbf{f}(\omega p, m, z, \omega) = \begin{pmatrix} u_\phi(\omega p, m, z, \omega) \\ \tau_{\phi z}(\omega p, m, z, \omega) \end{pmatrix} \tag{1a}$$

for cylindrical coordinates (r, ϕ, z). The underlying horizontal wavefunction is $e^{im\phi}\, d\left[J_m(kr)\right]/dr$. This representation is an approximation, since it neglects a horizontal component of motion perpendicular to the ϕ-direction. An exact approach can be based on displacement $\mathbf{u} = U(k, m, z, \omega)\mathbf{T}_k^m(r, \phi)$ and traction $= T(k, m, z, \omega)\mathbf{T}_k^m(r, \phi)$, where $\mathbf{T}_k^m$ is the vector surface harmonic defined in (7.118). In the exact representation, valid in the near field and for long times, we take

$$\mathbf{f} = \begin{pmatrix} U(\omega p, m, z, \omega) \\ T(\omega p, m, z, \omega) \end{pmatrix}. \tag{1b}$$

In either (1a) or (1b), the associated equations $\mathbf{f} = \mathbf{F}\mathbf{w}$, $\mathbf{F} = \mathbf{E}\boldsymbol{\Lambda}$ are described in Section 5.4, and layer matrix $\mathbf{F}$ and its inverse are given explicitly in (5.66)–(5.67). The propagator is

$$\mathbf{P}(z, z_0) = \mathbf{F}(z)\mathbf{F}^{-1}(z_0) = \begin{pmatrix} \cos[\omega\eta(z - z_0)] & \dfrac{-1}{\omega\mu\eta}\sin[\omega\eta(z - z_0)] \\ \omega\mu\eta\,\sin[\omega\eta(z - z_0)] & \cos[\omega\eta(z - z_0)] \end{pmatrix}, \tag{2}$$

provided z and z_0 are in the same (homogeneous) layer. If these depths are in different layers of a structure composed of homogeneous welded layers, we can use (7.44).

For P-SV in the far field, we use $u_r, u_z, \tau_{rz}, \tau_{zz}$ for the components of $\mathbf{f}$. Then $\mathbf{F}$ is found from (5.69) and its inverse from (5.71). The propagator (for z and z_0 in the same homogeneous layer) is then

(continued)

$$\mathbf{u}(r, \phi, 0, \omega) = \frac{1}{2\pi}\sum_{m=-\infty}^{\infty}\int_0^\infty \omega^2 p\left[u_r\frac{d}{d(\omega p r)}J_m(\omega p r)\hat{\mathbf{r}} + iu_z J_m(\omega p r)\hat{\mathbf{z}}\right]e^{im\phi}\,dp, \tag{9.16}$$

followed by a numerical integral over ω to recover $\mathbf{u}(r, \phi, 0, t)$.

BOX **9.1** *(continued)*

$$\mathbf{P}(z, z_0) = \begin{pmatrix} 2\beta^2 p^2 C_\xi + (1-2\beta^2 p^2) C_\eta & \frac{ip}{\xi}(1-2\beta^2 p^2) S_\xi - 2i\beta^2 p \eta S_\eta \\ 2i\beta^2 p \xi S_\xi - \frac{ip}{\eta}(1-2\beta^2 p^2) S_\eta & (1-2\beta^2 p^2) C_\xi + 2\beta^2 p^2 C_\eta \\ -4\omega\rho\beta^4 p^2 \xi S_\xi - \frac{\omega\rho}{\eta}(1-2\beta^2 p^2)^2 S_\eta & 2i\omega\rho\beta^2 p(1-2\beta^2 p^2)[C_\xi - C_\eta] \\ 2i\omega\rho\beta^2 p(1-2\beta^2 p^2)[C_\xi - C_\eta] & -\frac{\omega\rho}{\xi}(1-2\beta^2 p^2)^2 S_\xi - 4\omega\rho\beta^4 p^2 \eta S_\eta \\ \frac{p^2}{\omega\rho\xi} S_\xi + \frac{\eta}{\omega\rho} S_\eta & -\frac{ip}{\omega\rho}[C_\xi - C_\eta] \\ -\frac{ip}{\omega\rho}[C_\xi - C_\eta] & \frac{\xi}{\omega\rho} S_\xi + \frac{p^2}{\omega\rho\eta} S_\eta \\ 2\beta^2 p^2 C_\xi + (1-2\beta^2 p^2) C_\eta & 2i\beta^2 p \xi S_\xi - \frac{ip}{\eta}(1-2\beta^2 p^2) S_\eta \\ \frac{ip}{\xi}(1-2\beta^2 p^2) S_\xi - 2i\beta^2 p \eta S_\eta & (1-2\beta^2 p^2) C_\xi + 2\beta^2 p^2 C_\eta \end{pmatrix} \tag{3}$$

where columns 1 and 2 are written above columns 3 and 4, $C_\xi = \cos[\omega\xi(z - z_0)]$, $C_\eta = \cos[\omega\eta(z - z_0)]$, $S_\xi = \sin[\omega\xi(z - z_0)]$, and $S_\eta = \sin[\omega\eta(z - z_0)]$.

Note the checkerboard pattern of real and imaginary entries in (3). A product of such matrices has the same pattern, so that it is easy to program the required manipulations of the propagator (e.g., (7.44)) using only real variables if p is real and the medium is elastic. Some of the entries in (2) and (3) are $O(\omega)$, and some are $O(\omega^{-1})$. It is sometimes desirable to remove this frequency dependence algebraically, for example to reduce the number of multiplications when looping over ω. The removal can be done by working with particle velocities and tractions rather than particle displacements and tractions.

In practice, only a finite range of p-values is used in (9.16), and Fuchs and Müller (1971) recommend $0 \le p \le 1/\alpha_{\max}$, where $\alpha_{\max}$ is the fastest P-wave speed in the layers above the reflecting region. It follows that SUM is always real, and inhomogeneous waves are avoided above the reflecting region.

The reflecting region itself appears in the computation only via $\{\grave{P}\acute{P}\}_n^m$ and we shall shortly look at a simple example that shows how all the multireflected rays within the depth range z_m to z_n are automatically accounted for. But first we show a record section of synthetic seismograms obtained by the reflectivity method for an explosive source acting at the surface of a particular crustal structure. The structure is shown in Figure 9.8a, and Fuchs and Müller (1971) have obtained the synthetics shown in Figure 9.8c, using as reflector the lower boundary of the low-velocity channel and the layers below this channel. A guide in the interpretation is given by the *reduced travel-time curve*, Figure 9.8b. (If t were plotted against r instead of the reduced time $t - r/6$ against r, the vertical scale would spread over about 26 s instead of the 6 s shown, and much detail of the temporal separation between arrivals would be lost.) The travel-time curve is a guide to the range of p-values needed in the integration (9.16), since the ray parameter at which prominent waves will arrive at the receiver is the gradient of time against distance (see Problem 9.2(i)). Since this gradient ranges from about 1/8.15 to 1/6, the range of p-values used in the integration for Figure 9.8c was $1/8.15 \le p \le 1/6$. The most time-consuming part of the computation is the evaluation

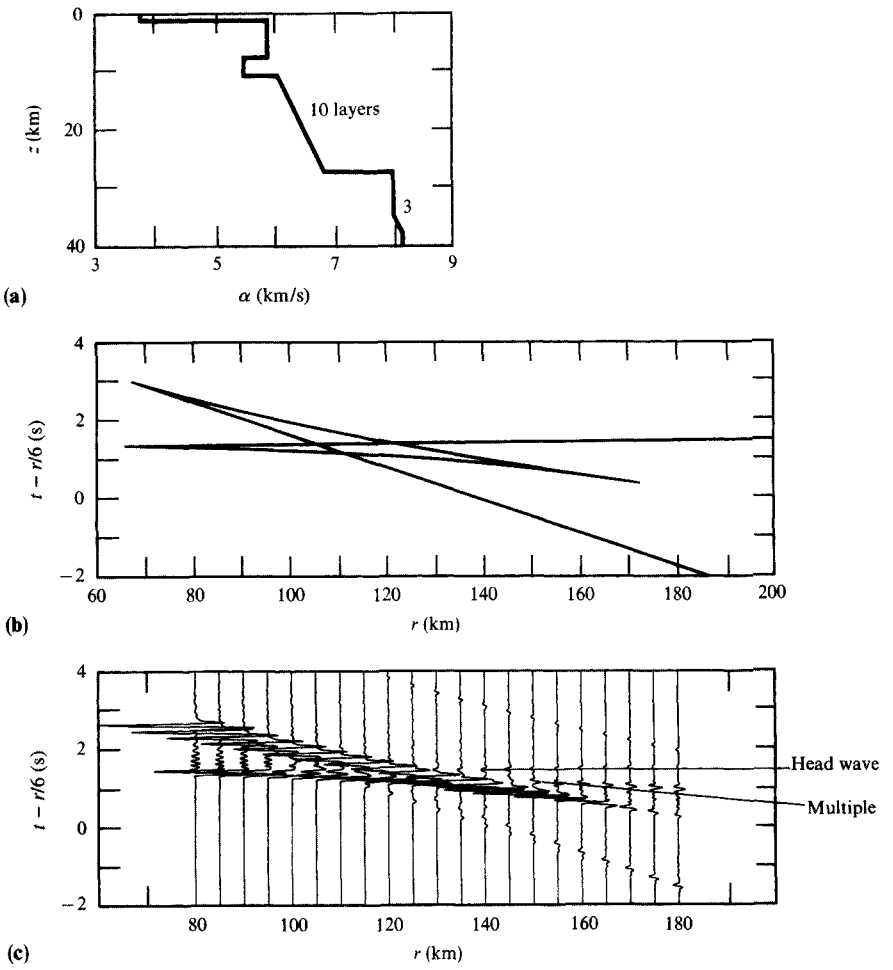

FIGURE **9.8**

An application of the reflectivity method. **(a)** A model of crustal structure. Only the P-wave speed is shown. The linear increase in the lower crust (down to the Moho at depth 27 km) is in fact modeled by 10 homogeneous layers, and a thin linear region below the Moho by 3 layers. **(b)** A reduced travel-time curve for P-waves in (a) that have slowness less than 1/6 s/km. **(c)** Synthetic seismograms (vertical component of displacement) corresponding to (b), obtained via the reflectivity method. Most prominent are the wave that has been turned around once within the velocity gradient in the lowermost crust and the wide-angle reflection at the Moho. P_n is small, but its early arrival beyond 120 km would permit its identification in the Earth if this crustal structure is accurate. In the range 150–180 km is seen a prominent multiple at reduced travel time 1 s that may be identified as a wave turned around twice within the lowermost crust, having also been reflected once from below the low-velocity zone. The "head wave" from just below the lower boundary of the low-velocity zone is very weak beyond about 140 km because of the positive velocity gradient. Latest of all to arrive is a phase with slowness equal to 1/8.15 (like the main head wave, P_n). This is an artifact of truncating the integration in (9.16) to a finite range of p. [After Fig. 7 of Fuchs and Müller 1971.]

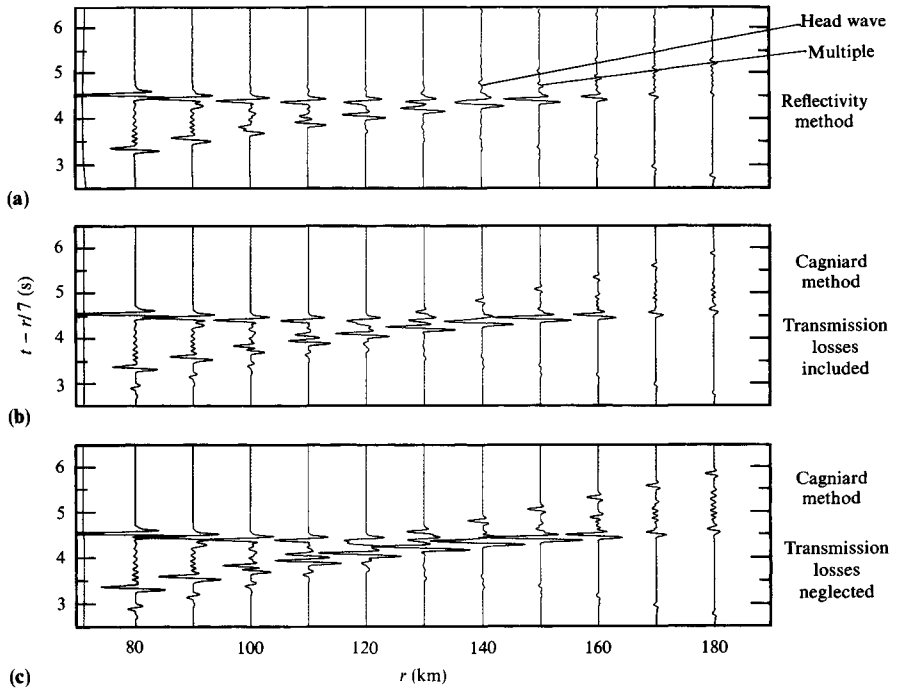

FIGURE **9.9**
A comparison between the reflectivity method and the Cagniard method for crustal structure given in Figure 9.8a. **(a)** Selected seismograms from Figure 9.8c plotted to show detailed pulse shapes obtained by the reflectivity method. Reduced travel time here is based on a slowness of 1/7 s/km. **(b)** The calculation in (a) is repeated, using (9.9) for each of the primary interactions in the stack of layers. **(c)** The calculation in (b) is repeated, equating all transmission factors (down to and up from each reflecting interface) to unity. That is, the term PRODUCT in (9.2) and (9.3) is approximated by $(\grave{P}\acute{P})_n$ only. Also included in calculations (b) and (c) are reflections from the upper crust that have been ignored in (a), which explains some differences in pulse shapes for earlier times, out to about 120 km. Other discrepancies between (a) and (b) are also apparent, particularly at 100 km and 110 km for reduced time around 4 s. This part of the seismogram is controlled mostly by crustal structure just below the low-velocity zone. The increase of velocity with depth in this region causes multiples that have been ignored in (b) but are automatically retained in (a). At greater distances, 140–180 km, the head wave and multiple marked in (a) are quite different in amplitude from the computation shown in (b) (see also Fig. 9.8c). [After Fig. 8 of Fuchs and Müller, 1971.]

of $\{\grave{P}\acute{P}\}_n^m$ at different values of p and ω. However, it is a step that needs to be done only once since this term is independent of r. A fast program was first given by Kind (1976).

The pulse shapes are shown in somewhat more detail in Figure 9.9, using a different time scale. A comparison is given between the reflectivity method and the Cagniard procedure described in Section 9.1, and some differences are apparent. These differences would disappear if enough generalized rays were picked for subsequent Cagniard inversion. Computation times for parts (a), (b), (c) of the figure were found by Fuchs and Müller (1971) to be in the ratio 20 to 5 to 1, so that the reflectivity method can be significantly longer than a method that retains only the primary interactions with each boundary in the stack of layers.

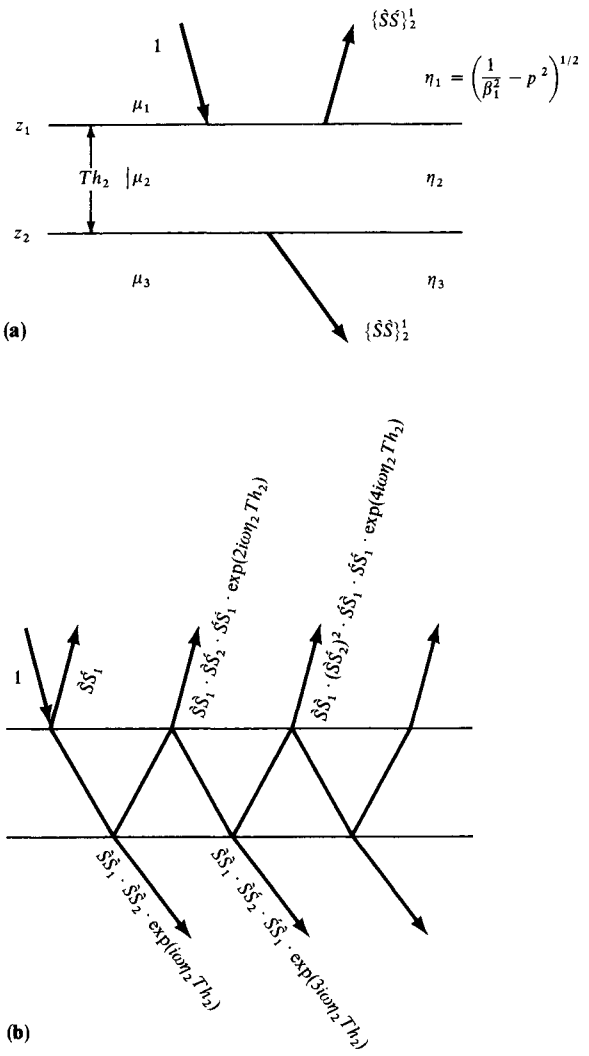

FIGURE **9.10**
The infinite family of generalized SH rays that are equivalent to the reflection/transmission obtained for a single layer between two boundaries via the propagator matrix. **(a)** Parameters for the layer. The complete reflection is contained within $\{\grave{S}\acute{S}\}_2^1$. **(b)** The family of generalized rays, shown in the text to be equivalent to (a).

To conclude this account of the reflectivity method, let us establish the fact that a term like $\{\grave{P}\acute{P}\}_n^m$ includes all multiples between the levels z_m and z_n. Although a demonstration in general can be extremely lengthy, the main idea can be seen with a simple example for SH-waves.

Thus, in Figure 9.10, we show a single layer between two half-spaces. The motion-stress vector for SH is (see Box 9.1)

$$\mathbf{f} = \begin{pmatrix} u_\phi(k, z, \omega) \\ \tau_{\phi z}(k, z, \omega) \end{pmatrix},$$

and equations corresponding to (9.12) for this SH-problem are

$$\mathbf{f}(z_1) = \begin{pmatrix} 1 & 1 \\ i\omega\mu_1\eta_1 & -i\omega\mu_1\eta_1 \end{pmatrix} \begin{pmatrix} 1 \\ \{\grave{S}\acute{S}\}_2^1 \end{pmatrix}, \quad \mathbf{f}(z_2) = \begin{pmatrix} 1 & 1 \\ i\omega\mu_3\eta_3 & -i\omega\mu_3\eta_3 \end{pmatrix} \begin{pmatrix} \{\grave{S}\grave{S}\}_2^1 \\ 0 \end{pmatrix}.$$

Substituting these into $\mathbf{f}(z_1) = \mathbf{P}(z_1, z_2)\mathbf{f}(z_2)$ and using the SH propagator matrix (Box 9.1, equation (2)), we obtain two equations for the two unknowns $\{\grave{S}\acute{S}\}_2^1$ and $\{\grave{S}\grave{S}\}_2^1$. The reflection solution is

$$\{\grave{S}\acute{S}\}_2^1 = \frac{\left(C - \dfrac{i\mu_3\eta_3 S}{\mu_2\eta_2}\right) - \left(\dfrac{\mu_3\eta_3}{\mu_1\eta_1}C - \dfrac{i\mu_2\eta_2 S}{\mu_1\eta_1}\right)}{\left(C - \dfrac{i\mu_3\eta_3 S}{\mu_2\eta_2}\right) + \left(\dfrac{\mu_3\eta_3}{\mu_1\eta_1}C - \dfrac{i\mu_2\eta_2 S}{\mu_1\eta_1}\right)}, \tag{9.17}$$

where $C = \cos(\omega\eta_2 Th_2)$, and $S = \sin(\omega\eta_2 Th_2)$.

Shown in Figure 9.10b is the system of multiples that may be expected from a causal approach to the problem. That is, a reflection $\grave{S}\acute{S}_1$ is expected from the top of the layer, followed by a wave once-reflected from the bottom of the layer, $\grave{S}\grave{S}_1 \cdot \grave{S}\acute{S}_2 \cdot \acute{S}\acute{S}_1 e^{2i\omega\eta_2 Th_2}$, etc. The phase factor allows for vertical propagation, and the total of reflections should be given as

$$\{\grave{S}\acute{S}\}_2^1 = \grave{S}\acute{S}_1 + \grave{S}\grave{S}_1 \left[\sum_{j=1}^{\infty} (\grave{S}\acute{S}_2\, e^{2i\omega\eta_2 Th_2})^j (\acute{S}\grave{S}_1)^{j-1}\right] \acute{S}\acute{S}_1 \tag{9.18}$$

$$= \grave{S}\acute{S}_1 + \frac{\grave{S}\grave{S}_1 \cdot \grave{S}\acute{S}_2 \cdot \acute{S}\acute{S}_1 \cdot e^{2i\omega\eta_2 Th_2}}{1 - \grave{S}\acute{S}_2 \cdot \acute{S}\grave{S}_1 \cdot e^{2i\omega\eta_2 Th_2}}. \tag{9.19}$$

This is the key stage. An infinite geometrical series has been replaced by a single exact expression for the sum. Individual terms of (9.18) correspond to particular rays, and the whole infinite family of multiples is clearly contained in (9.19). To evaluate (9.19), we can use (5.33) for individual reflections/transmissions, finding

$$\{\grave{S}\acute{S}\}_2^1 = \left(\frac{\mu_1\eta_1 - \mu_2\eta_2}{\mu_1\eta_1 + \mu_2\eta_2}\right) + \frac{\dfrac{2\mu_1\eta_1}{\mu_1\eta_1 + \mu_2\eta_2} \cdot \dfrac{\mu_2\eta_2 - \mu_3\eta_3}{\mu_2\eta_2 + \mu_3\eta_3} \cdot \dfrac{2\mu_2\eta_2}{\mu_1\eta_1 + \mu_2\eta_2} \cdot e^{2i\omega\eta_2 Th_2}}{1 - \dfrac{\mu_2\eta_2 - \mu_3\eta_3}{\mu_2\eta_2 + \mu_3\eta_3} \cdot \dfrac{\mu_2\eta_2 - \mu_1\eta_1}{\mu_1\eta_1 + \mu_2\eta_2} \cdot e^{2i\omega\eta_2 Th_2}},$$

which does reduce (after some algebraic manipulation) exactly to (9.17). In this way we have shown that the propagator-derived reflection for the double interface can be written as an infinite set of generalized rays.

If more than two interfaces are present, and with the complication of conversion between P and SV, it is clear that an immensely involved system of generalized rays may be present in the propagator-derived reflection, e.g., in $\{\grave{P}\acute{P}\}_n^m$. Spencer (1960, 1965) pointed out the main virtue of working with generalized rays—namely, that each term in the infinite series has an extremely simple dependence on frequency or on the Laplace transform variable s. For example, in (9.18) we note that $\omega\eta_2 = \omega\sqrt{1/\beta_2^2 - p^2} = is\sqrt{1/\beta_2^2 - p^2}$, and s enters each generalized ray only via the exponent function. A Cagniard method can therefore be used to get the contribution (in the time domain) of each generalized ray. The ω-dependence of (9.15) and (9.17) is far more complicated, and Cagniard methods do not

BOX 9.2

Earth-flattening transformation and approximations

In Section 7.2 and Box 9.1, we showed how to obtain and use the motion-stress vector

$$\begin{pmatrix} u_\phi \\ \tau_{\phi z} \end{pmatrix}$$

that solves

$$\frac{d}{dz}\begin{pmatrix} u_\phi \\ \tau_{\phi z} \end{pmatrix} = \begin{pmatrix} 0 & 1/\mu(z) \\ k^2\mu(z) - \omega^2\rho(z) & 0 \end{pmatrix}\begin{pmatrix} u_\phi \\ \tau_{\phi z} \end{pmatrix}. \tag{1}$$

This is the SH-wave equation, and matrix methods for its solution are highly developed, particularly when the medium is approximated by large numbers of homogeneous plane layers. For example, the reflectivity method makes this approximation.

Our present interest, however, lies in spherically symmetric media and, from (8.34),

$$\frac{d}{dr}\begin{pmatrix} W \\ T \end{pmatrix} = \begin{pmatrix} \frac{1}{r} & \frac{1}{\mu} \\ \frac{\mu(l-1)(l+2)}{r^2} - \omega^2\rho & -\frac{3}{r} \end{pmatrix}\begin{pmatrix} W \\ T \end{pmatrix}, \tag{2}$$

which is the equivalent of (1) in spherical geometry. An outline of the derivation of (2) is also given in (9.79)–(9.82). We are interested in the corresponding *P–SV* equations, too. Fortunately, Andrianova *et al.* (1967) and Biswas and Knopoff (1970) have found a transformation of (2) that gives, exactly, the equation (1). Therefore, the reflectivity method can be applied in spherical geometry for SH problems with no approximations (other than the replacement of depth-dependent $\rho(z)$, $\mu(z)$ by many thin layers and the truncation of integration ranges $\int_0^\infty dk \int_0^\infty d\omega$). For *P–SV* problems, Kiselev *et al.* (1997) have shown that an exact Earth-flattening transformation can still be made between spherical and plane coordinates, but it entails the use of nonlinear equations. The transformation between the linear wave equation using spherical coordinates and the linear wave equation using Cartesians cannot be made exact for *P–SV* problems, and new approximations are introduced.

(continued)

apply directly to the sum of the whole system of multiples. Hron (1971, 1972) showed how subfamilies of generalized rays could be found that all used the same Cagniard path, and Cisternas *et al.* (1973) gave a systematic method for finding out the generalized rays contained within the exact (i.e., propagator-derived) solution.

The reflectivity method was developed by Fuchs and his colleagues for crustal studies. Orcutt *et al.* (1976) applied the method to study the structure of the East Pacific Rise. By using a flat Earth model that has the same travel times as a spherical Earth model (Box 9.2), Müller (1973) used the reflectivity method to interpret long-period body waves that pass through the Earth's core, and Müller and Kind (1976) analyzed long-period body-wave seismograms for the whole Earth. The reflectivity method for spherical problems was given a careful evaluation by Chapman and Orcutt (1985), and it has become a standard technique for obtaining synthetics.

BOX **9.2** *(continued)*

First we shall describe the SH transformation. It is convenient to use a subscript s for quantities relevant to the spherical medium, such as μ_s, ρ_s, β_s, and a subscript f for quantities in the flat-layered (i.e., z-dependent) medium. Given profiles μ_s, ρ_s, and an order number l, we want to transform the equation (2) for

$$\begin{pmatrix} W \\ T \end{pmatrix}$$

into the equation (1) for

$$\begin{pmatrix} u_\phi \\ \tau_{\phi z} \end{pmatrix}.$$

The new depth variable z is defined by

$$e^{-z/a} = \frac{r}{a}, \tag{3}$$

where a is any convenient radius (usually taken as the radius of the whole Earth). New velocity profiles are defined by

$$\alpha_f(z) = \frac{a}{r}\alpha_s(r), \qquad \beta_f(z) = \frac{a}{r}\beta_s(r). \tag{4}$$

New dependent variables and density are defined by

$$\begin{pmatrix} u_\phi(z) \\ \tau_{\phi z}(z) \end{pmatrix} = \begin{pmatrix} (a/r)W \\ -(r/a)^3 T \end{pmatrix}, \qquad \rho_f(z) = \left(\frac{r}{a}\right)^5 \rho_s(r), \tag{5}$$

and it is possible now to show from (2) that

$$\frac{d}{dz}\begin{pmatrix} u_\phi \\ \\ \tau_{\phi z} \end{pmatrix} = \begin{pmatrix} 0 & \dfrac{1}{\mu_f} \\ \dfrac{(l-1)(l+2)}{a^2}\mu_f - \omega^2\rho_f & 0 \end{pmatrix}\begin{pmatrix} u_\phi \\ \\ \tau_{\phi z} \end{pmatrix}. \tag{6}$$

Clearly, the transformation to (1) is complete if the new horizontal wavenumber is defined to be

$$k^2 = (l-1)(l+2)/a^2. \tag{7}$$

A satisfying feature of (3) and (4) is that travel time along a ray in the spherical medium is equal to the travel time in the corresponding flat problem. Thus, from (9.21),

$$\begin{aligned} T_s &= \int \frac{dr}{\beta_s\sqrt{1 - p_s^2\beta_s^2/r^2}} \qquad \left(\text{where } p_s = \frac{r\sin i(r)}{\beta_s(r)}\right) \\ &= \int \frac{dz}{\beta_f\sqrt{1 - p_s^2\dfrac{\beta_f^2}{a^2}}} \qquad \text{(from (3) and (4)).} \end{aligned} \tag{8}$$

(continued)

BOX **9.2** *(continued)*

But, from (9.20),

$$T_f = \int \frac{dz}{\beta_f \sqrt{1 - p_f^2 \beta_f^2}} \qquad \left(\text{where } p_f = \frac{\sin i(z)}{\beta_f(z)}\right)$$
$$= \int \frac{dz}{\beta_f \sqrt{1 - \dfrac{(l-1)(l+2)\beta_f^2}{\omega^2 a^2}}} \qquad (\text{using } k = \omega p_f \text{ and } (7)). \tag{9}$$

It follows that (8) and (9) are *identical* if the ray parameter in the spherical case is given by $\omega^2 p_s^2 = (l+2)(l-1)$. The transformations (3) and (4) preserve the *kinematic* qualities of wave propagation. The transformation (5) exactly preserves the *dynamic* qualities of wave propagation in the two media. Since $(l+2)(l-1) = (l+\frac{1}{2})^2 - 2\frac{1}{4}$, ωp_s is approximately $l + \frac{1}{2}$. A better approximation here is $\omega p_s \approx (l+\frac{1}{2}) - 9/[8(l+\frac{1}{2})]$. In Sections 9.5 and 9.6 we shall frequently equate ωp and $l + \frac{1}{2}$ in the development of asymptotic theories for wave propagation in spherical geometry.

Moving on to the *P–SV* problem, we should like to be able to transform (9.81) exactly into (5.62). Clearly, one uses the same transformations (3) and (4) that worked for *SH*, because these still preserve the kinematic properties for *P–SV* waves. However, Chapman (1973, 1974) showed it is impossible to get a transform for dependent variables and density that will exactly preserve the dynamic properties of *P–SV*. He described the effect of a variety of transformations like (5), and found the asymptotic properties of errors that will arise if the wave solutions for the resulting z-dependent medium are used to generate solutions in the r-dependent medium. In general, these errors are of order ω^{-1}.

Once the kinematic transformations (3) and (4) have been made, Cagniard's and Fuchs' methods replace the z-dependent profiles by a stack of homogeneous layers. It is interesting to see how this layering appears once it has been transformed back into spherical geometry. For the P-wave profile, we find from (4) that

$$\alpha_s(r) = r\alpha_f/a, \tag{10}$$

hence α_s is proportional to r in each layer (α_f is piecewise constant). An example is shown in the figure here, and observe that even where the original velocity profile is homogeneous (e.g., near 1500 km radius), fine layers are still needed in the transformed medium. In fact, the velocity gradient for (10) is precisely that for which the angle between a ray and the local vertical is unchanged. That is, $di/dr = 0$, as can be seen from (9.24) with the special velocity profile (10). The rays will have the same angle to the local vertical throughout any given layer. This is the kinematic quality we might have expected, for it is true also in a stack of homogeneous plane layers. It follows that no turning point is present along rays in the inhomogeneous layering of the figure. All the phenomena which, in Section 9.6, we associate with the properties of wavefunctions near their turning point, must arise in Cagniard's and Fuchs' methods by interference between different rays within the stack of inhomogeneous layers.

(continued)

BOX **9.2** *(continued)*

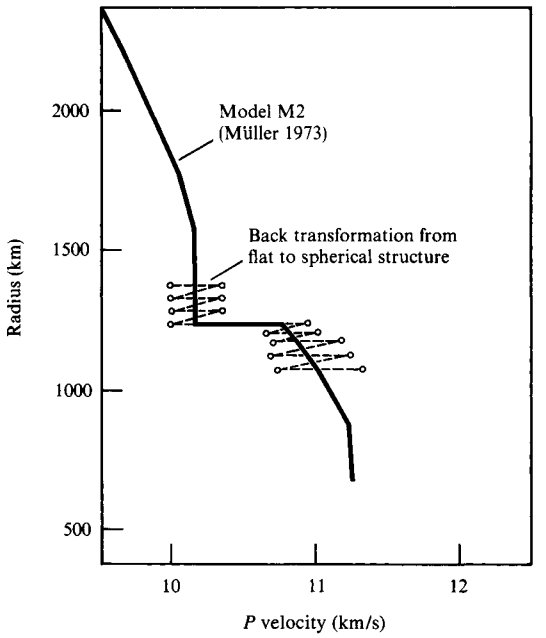

Solid line gives P-velocity near the inner-core/outer-core boundary in the spherical model M2 of Müller (1973). The broken line gives a back-transformed structure that is equivalent to a stack of plane homogeneous layers. [After Müller, 1977; copyright by American Geophysical Union.]

Our description of wave propagation in a stack of homogeneous layers has led us so far to two different numerical procedures. However, whether Cagniard's method is adopted (for many generalized rays) or Fuchs' method (with its double integration), there is one skill that turns out again and again to be useful in acquiring some insight into the waves that propagate within a given structure—namely, the ability to recognize the way in which particular waves in the elastic medium are related to properties of certain wavefunctions in the complex ray-parameter plane. For example, we have examined saddle points, branch cuts, and poles in the p-plane, and have related them to ray paths, head waves, and surface waves. For a stack of homogeneous layers, the analysis of a particular generalized ray is fairly simple in the p-plane. This is largely because the horizontal distance to which a particular ray can propagate is always an *increasing* function of ray parameter (see Problem 9.2). However, in the remainder of this chapter, we shall be looking at waves in media for which there can be a continuous change in seismic velocities and density within each layer. This can lead, first, to the phenomenon of a ray being completely turned around *within* a given layer. An example is shown in Figure 9.11. Second, we shall find that the horizontal distance reached by a particular ray (propagating in a stack of inhomogeneous layers) is very often

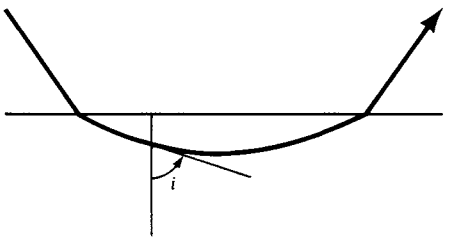

FIGURE **9.11**
A ray is shown that turns around within an inhomogeneous layer. The point at which the ray is traveling horizontally is said to be the *turning point*. Snell's law, $(\sin i)/v = p$ (a constant), applies along the ray. Since $i = 90°$ for a turning point, the equation $1/v(z) = p$ is satisfied if z is the depth of a turning point.

a *decreasing* function of ray parameter. The distance can also increase with p, and (for a given distance Δ) there can exist rays of both types (i.e., some with $d\Delta/dp < 0$, others with $d\Delta/dp > 0$).

These complications will lead us, in Section 9.5, to develop mathematical methods that explore phenomena not present for waves in homogeneous layers. However, properties of wavefunctions in the complex ray-parameter plane will still be of paramount importance. We prepare for this material in the next section, which reviews some elementary ray theory. Section 9.4 describes how elementary ray methods are used in the analysis of travel times to infer Earth structure, and in later sections we return to the main theme of this chapter, which is the development of body-wave propagation theory when geometrical ray theory may be inadequate.

9.3 Classical Ray Theory in Seismology

In Chapter 4 we derived the ray-theory solutions for displacement for high-frequency waves radiated into the far field from a point source. The key concepts of geometrical spreading and travel time along a ray path were well understood by Christiaan Huygens and Pierre de Fermat about 300 years ago. Our interest is in the particular properties of the rays, as receiver position varies, for a medium that is laterally homogeneous. For example, if travel time T is plotted against distance for a particular observed body wave, how might we conclude that the wave is a reflection from some internal discontinuity within the Earth? Or how might we find evidence for a low-velocity zone?

We begin in Figure 9.12 with a look at the S-wave rays that are present for a surface source in a model of the upper mantle. Clearly, several rays might arrive at a given receiver, and the travel-time function (Figure 9.12c) is multivalued for a certain range of distances. However, each point along the travel-time curve has a unique slope, the value decreasing from A to B, B to C, etc. This suggests a useful independent variable. It follows from Figure 5.2 that this slope, $dT/d\Delta$, which is the horizontal slowness for an obliquely propagating wave, is nothing but the ray parameter p. (Horizontal distance is Δ in dimensionless units and is $r\Delta$ in units of length.)

Thus consider how the distance function depends on p. From Figure 9.12c it is clear that distance and slope decrease together for the branch BC, but along AB and CD distance is increasing while slope decreases. This is shown explicitly in Figure 9.13, and some special significance is attached to the points B and C. Note that $d\Delta/dp$ changes sign at these points, and it can happen that $d\Delta/dp$ remains continuous, so that $d\Delta/dp = 0$ at C or at B and C. Since the geometrical spreading function $\mathcal{R}^{-1}$ is proportional to $1/\sqrt{d\Delta/dp}$ (see Problem 4.4),

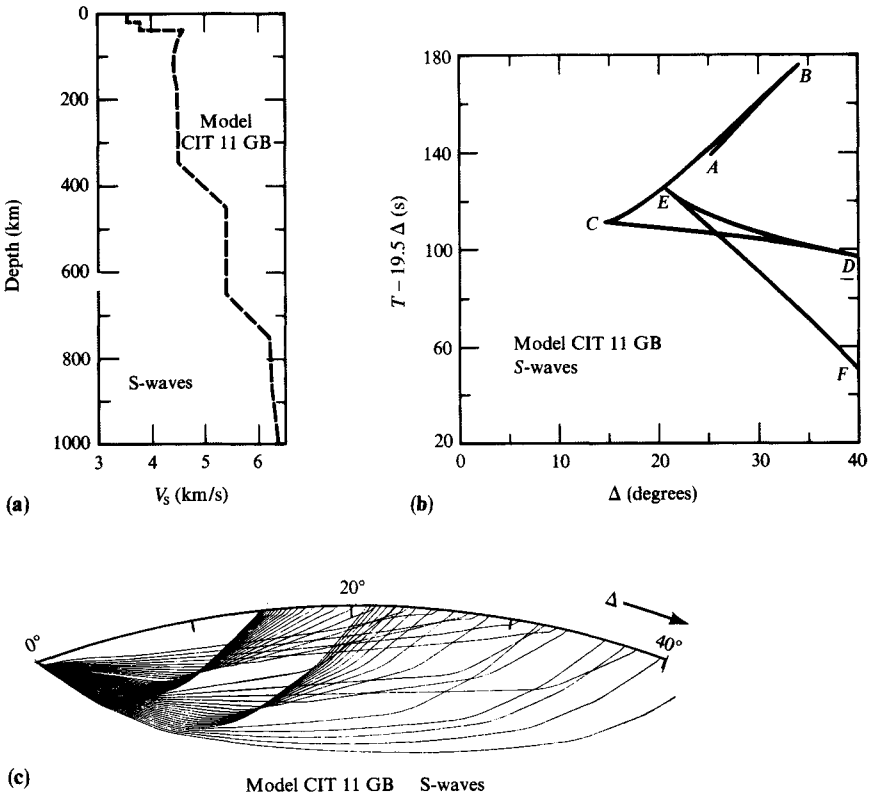

FIGURE **9.12**

(a) The S-wave velocity for the upper mantle, taken from model CIT 11 GB. **(b)** Corresponding S-wave rays for a point source at the surface, calculated for take-off angles increasing from 28° to 50° in $\frac{1}{2}°$ increments. Note that distance between source and receiver in the Earth is measured by the angle Δ subtended at the Earth's center. **(c)** Corresponding reduced travel-time curve. Point C is clearly identified with strong focusing of rays in (b) at Δ near 14°, and amplitudes there will be large. Lines AB, BC, and CD together constitute a *triplication*, as do the lines CD, DE, and EF, and each of these two triplications is associated with a major velocity increase (with depth) in the Earth model. [After Julian and Anderson, 1968.]

ray theory predicts a singular amplitude for the displacement. This is the phenomenon of a *caustic*, and an example is shown in Figure 9.12 at the distance 14°. A caustic is the envelope of a system of rays, and for the source and Earth model of Figure 9.12 the envelope in three dimensional space is a surface inside the Earth, which intersects the Earth's surface at a circle centered on the seismic source. Of course, the prediction of ray theory here is incorrect: there is no singularity at finite frequencies, although amplitudes may be large in the vicinity of a caustic (as shown by the focusing of rays in Figure 9.12b).

In practice, the sensitivity of amplitudes (calculated by ray theory) to the quantity $d\Delta/dp$ leads to some difficulties in computation. The problem is that Earth models are ordinarily specified by giving the values of density (ρ) and P- and S-wave speeds (α and β) at several different radii. But different methods of interpolation between such discrete values can

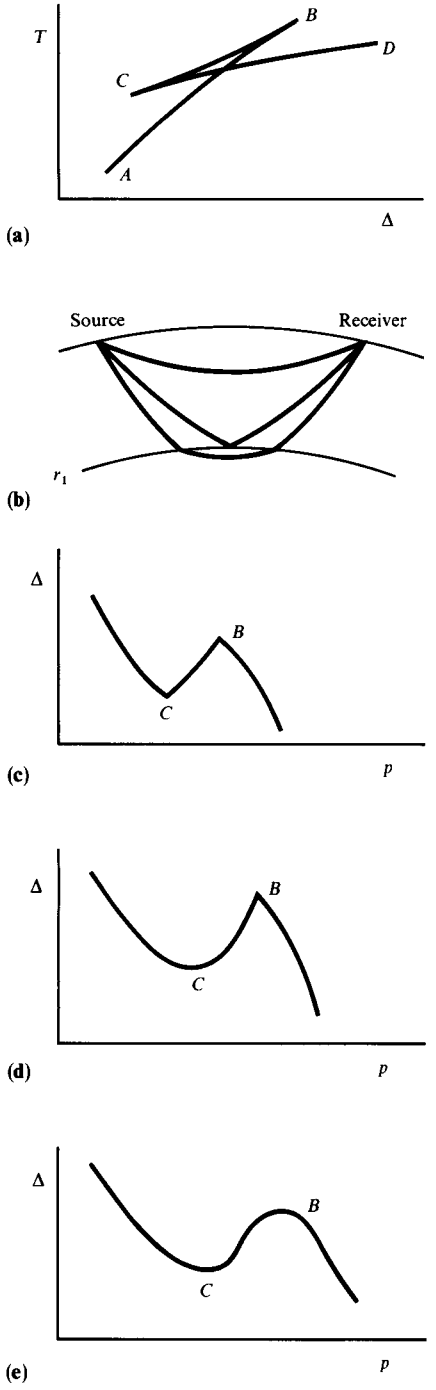

FIGURE **9.13**
The behavior of T, Δ, and p for a velocity increase with depth. **(a)** Nomenclature for a typical triplication. **(b)** Three rays are shown, all having the same Δ. The velocity is assumed to be increasing with depth, and at the level r_1 an anomalous increase of velocity with depth also occurs. The uppermost ray here may be called the direct ray (branch AB); then there is a reflection-like ray (branch BC); and finally a head-wave-like ray (branch CD). The degree of continuity in the velocity profile across r_1 determines whether rays actually change direction when they reach this level or have high curvature. **(c)** $\Delta(p)$ is shown for a discontinuous velocity increase across r_1. Note that $d\Delta/dp$ is discontinuous at B and C, and may never be small. (The quantity $(d\Delta/dp)^{-1/2}$ is a controlling factor in the wave amplitude predicted by ray theory.) **(d)** $\Delta(p)$ is shown for a continuous velocity profile in which the velocity gradient is discontinuous across r_1. Then $d\Delta/dp = 0$ at C, giving a caustic. **(e)** $\Delta(p)$ is shown when both velocity and velocity gradient are continuous. Both B and C are caustics.

often lead to completely different estimates for the geometrical spreading. Chapman (1971) recommends a cubic spline for the velocity interpolation, since the second derivative of velocity with respect to depth can then be made continuous with depth, and this degree of continuity is needed if $d\Delta/dp$ is to be continuous. Bullen (1960) gives some examples of how $d\Delta/dp$ can change character for different kinds of velocity increase with depth, as shown here in Figure 9.13. The effect of caustics is widely observed in seismic waves, and wave-theoretical methods of calculation of amplitudes in the vicinity of caustics are described in Section 9.5.

In Sections 9.1 and 9.2, we have emphasized plane-stratified media in which the ray parameter p is $\sin i/\alpha$ (both i and velocity α being depth dependent). There is frequently a need to express travel time and distance as a function of p (see Problem 9.2). The results for P-waves are

$$\begin{aligned} \text{TIME}(p) &= \int \frac{dz}{\alpha(z)\cos i(z)} = \int \frac{dz}{\alpha^2 \xi}, \\ \text{DISTANCE}(p) &= \int \tan i \, dz = \int \frac{p}{\xi} dz, \end{aligned} \tag{9.20}$$

in which

$$\xi = \xi(p, z) = \sqrt{\frac{1}{\alpha^2(z)} - p^2} = \frac{\cos i}{\alpha}$$

and the integration is carried out over the range of depths traversed by the ray. However, much of this chapter is devoted to spherically stratified media, in which the ray parameter p is $(r \sin i)/\alpha$, since it is for such media that ray theory in seismology is most extensively applied.

The specific formulas for travel time T and distance Δ, as a function of p, are easily derived in spherically symmetric media if we note that an element of ray length ds is related to a change dr in radius by $\cos i \, ds = dr$, where i is the angle between local vertical and the ray direction. Thus, for the P-wave velocity $\alpha = \alpha(r)$,

$$\begin{aligned} T(p) &= \int \frac{ds}{\alpha} = \int \frac{dr}{\alpha(r)\cos i(r)} = \int \left(1 - \frac{p^2\alpha^2}{r^2}\right)^{-1/2} \frac{dr}{\alpha} = \int \frac{dr}{\alpha^2 \xi}, \\ \Delta(p) &= \int \sin i \frac{ds}{r} = \int \frac{p\alpha}{r^2} \left(1 - \frac{p^2\alpha^2}{r^2}\right)^{-1/2} dr = \int \frac{p \, dr}{r^2 \xi}, \end{aligned} \tag{9.21}$$

where we have used $p = (r \sin i)/\alpha$ from (4.45b), and $\xi = \xi(r) = \sqrt{1/\alpha^2 - p^2/r^2} = \cos i/\alpha$ for vertical slowness. The integration is carried out over the range of radii traversed by the ray, so a turning point will often appear as one of the limits in the integration. Using r_p as the turning-point radius corresponding to ray parameter p, it follows that $p = r_p/\alpha(r_p)$, and hence that the integrands in (9.21) can have singularities.

A quantity formed from T and Δ that does not have a singular integrand at a turning point is

$$\tau = \tau(p) \equiv T - p\Delta = \int \frac{\cos i}{\alpha} dr = \int \xi \, dr. \tag{9.22}$$

We shall find that $\tau(p)$ has a surprising number of uses. It appears in inverse theories (Johnson and Gilbert, 1972; Bessonova *et al.*, 1976) and in theories of wave propagation. However, even in the restricted context of ray theory it has remarkable properties due to the relation

$$\frac{d\tau}{dp} = -\Delta(p) \tag{9.23}$$

(which is proved by differentiating $\int \xi \, dr$ and comparing with Δ in (9.21)). It follows that τ is a monotonically decreasing function of p, unlike $\Delta(p)$, so that it is an even better function than $\Delta(p)$ for unfolding triplications in travel-time curves. Note that SUM(p) of (9.4) is effectively the new variable $\tau(p)$ that we have just defined in (9.22), and a Cagniard path $p = p(t)$ is the set of points p such that $t = pr + \tau(p)$ where t is real and positive.

We have seen in Figures 9.12 and 9.13 that triplications are associated with velocity increasing with depth. If velocity *decreases* sufficiently rapidly with depth (i.e., $d\alpha/dr$ is positive and sufficiently large), then another characteristic feature appears in the travel-time curve. This is the phenomenon of a *shadow zone*, illustrated in Figure 9.14. Within the low-velocity zone, there is a range of depths in which no turning point is present. When a turning point is present at the bottom of a ray, it is achieved by the angle i (between ray and vertical) being an increasing function of decreasing radius along the ray. Thus a shadow zone occurs whenever the velocity gradient in the low-velocity zone is such as to make $di/dr > 0$, for then i can never increase to the turning-point value (90°) as r is decreased. Since $(r \sin i)/\alpha$ is constant, we find that

$$r\frac{di}{dr} = -[1 - \zeta(r)] \tan i, \tag{9.24}$$

where ζ is the normalized velocity gradient $(r/\alpha)(d\alpha/dr)$. The condition $di/dr > 0$, under which a shadow is generated, therefore translates to $\zeta(r) > 1$, or $d\alpha/dr > \alpha/r$. Comparing Figures 9.14c and 9.14d, note that there are two or one or no values of Δ corresponding to a given value of p, whereas $\tau = T - p\Delta$ has just one value almost everywhere.

To conclude this brief review of ray theory, a few remarks are needed to augment our Chapter 4 formulas for pulse shapes. Recall that we found (e.g., (4.57)) that amplitudes at $\mathbf{x}$ are controlled by the factor $1/\mathcal{R}(\mathbf{x}, \boldsymbol{\xi})$ for a point source at $\boldsymbol{\xi}$. However, in the course of propagation along the ray from $\boldsymbol{\xi}$ to $\mathbf{x}$, there are several effects that can introduce a frequency-independent phase advance to the waves received in the far field, thus introducing a distortion into the pulse shape that can often be seen in seismic data. One example is that of a wave incident upon a discontinuity in the Earth at an angle of incidence great enough to excite an inhomogeneous wave. As described in Chapter 5, the resulting phase shift leads to a change in the incident pulse shape that can be calculated via the Hilbert transform. Another example is that of a ray between $\boldsymbol{\xi}$ and $\mathbf{x}$ that, though stationary, is not a minimum time path. Some of the rays most important to seismology in which this arises are direct P- and S-waves that depart downward from the source and are received on a branch of the travel-time curve for which $d^2T/d\Delta^2 = 1/(d\Delta/dp) > 0$; PP and SS; and $SKKS$. Thus SS has

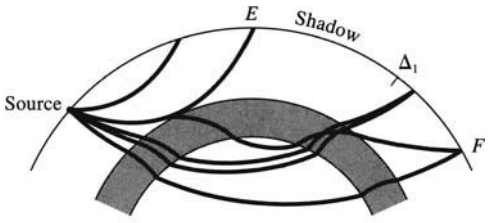

(a)

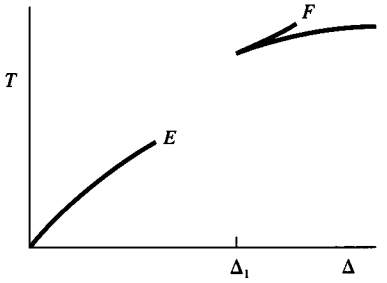

(b)

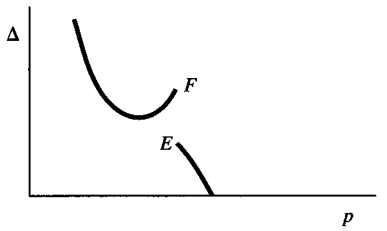

(c)

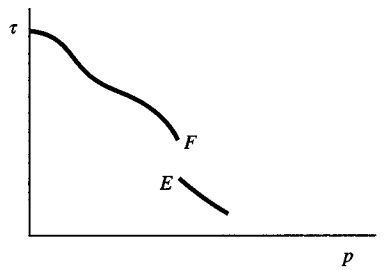

(d)

FIGURE **9.14**

The behavior of T, Δ, and τ as functions of p for a velocity decrease with depth. **(a)** A low-velocity zone (within which $d\alpha/dr > \alpha/r$ and there are no turning points) is shown shaded, and a shadow within which no rays are received is observed at the surface. **(b)** The travel-time curve. The upper boundary of the low-velocity zone is the turning point for the ray emerging at point E. Point F has the same ray parameter, but lies on a ray going through the low-velocity zone itself. As ray parameter decreases slightly from its value at F, distance Δ *decreases* until a caustic is reached at Δ_1. **(c)** The values of $\Delta = \Delta(p)$. These show that the further boundary of the shadow is in fact a caustic. **(d)** Upper and lower boundaries of the low-velocity zone are turning points for rays that differ infinitesimally in their ray parameter. The turning-point radius is therefore a discontinuous function of p. This is also a discontinuity in $\tau(p) = T - p\Delta$ and in the gradient $d\tau/dp = -\Delta(p)$.

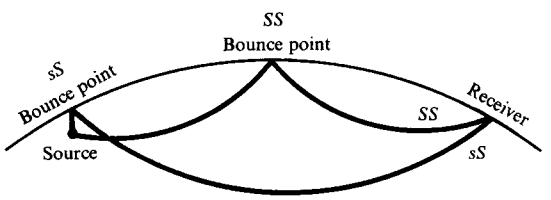

FIGURE **9.15**
An S-wave departing downward from the source and reflected once at the Earth's surface between source and receiver is known as SS, whereas sS departs upward from the source and is reflected near the source.

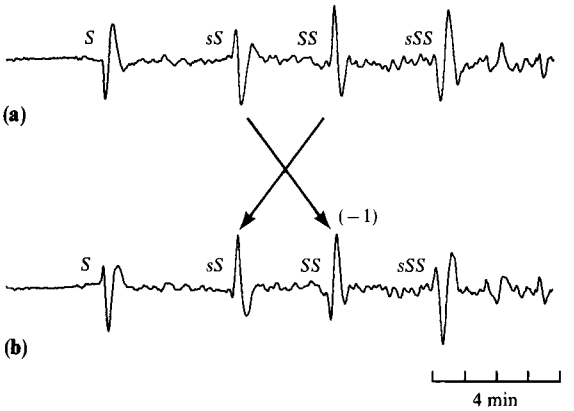

FIGURE **9.16**
(a) Original EW seismogram (orientation is for SH-waves) of a deep earthquake (608 km) below the Sea of Japan on 1960 October 8. Recorded at PAL, $\Delta = 96.3°$. **(b)** The Hilbert transform of (a). For convenience, the four main phases are still labeled with the original names. One arrow indicates that SS in (a) is the same shape as the Hilbert transform of sS, shown in (b). The second arrow indicates that sS in (a) is the same shape (after a polarity reversal) as the Hilbert transform of SS, shown in (b). [After Choy and Richards, 1975.]

a minimax time path (see Fig. 9.15), because a perturbation of the " bounce point" to points on the Earth's surface in the same plane as the source and receiver will actually decrease the travel time (and perturbation perpendicular to this direction will increase the travel time). On the other hand, sS is a true minimum time path, and Choy and Richards (1975) showed observations of SS that were quite accurately the Hilbert transform of sS (see Fig. 9.16).

Although we have emphasized spherically symmetric media in this section, all the ideas and formulas have analogues in plane-stratified media provided the two types of structure are related by the Earth-flattening transformation (see Box 9.2). We call upon this result when developing the Earth-flattening approximation to apply Cagniard's and Fuchs' methods to teleseismic waves in the Earth.

9.4 Inversion of Travel-Time Data to Infer Earth Structure

Most of this chapter is about wave propagation, and we shall go on in Sections 9.5–9.7 to improve upon the classical ray theory results of Section 9.3. But here we take a break from

wave propagation theory, and show how to infer the variation of seismic velocities with depth inside the Earth, if travel-time data are interpreted in terms of ray theory.

One of the main objectives of seismology is to determine the Earth's interior structure from data obtained at the Earth's surface. Ultimately we want to find a method that will give structure and source parameters by processing all the information in seismograms—that is, by processing whole waveforms. Mostly in this book, we concentrate on developing solutions to the "forward problem." That is, for specific models of Earth structure and seismic source we find out how to compute properties of seismic motion that are observable, such as travel times, dispersion curves, spectra of near-field strong ground motion, free-oscillation periods, far-field seismograms, and complete seismograms. The "inverse problem" is to start with one or more of these observables and to derive information about Earth structure and seismic sources. Whenever the solution to the forward problem is known, then trial and error provides one method of inversion: the parameters of a model are readjusted on some *ad hoc* basis until some acceptable agreement between observables and data is discovered. Such an approach immediately brings out the main features we must consider in any inverse method: Is the model *adequate* to explain the data? Is it *unique*? And, if not unique, what knowledge about the model do we gain from a particular data set? Books by Menke (1984), Tarantola (1987) and Parker (1994) address these three questions, and describe methods and applications of modern inverse theory in geophysics. Here, we shall consider the classic problem of travel-time inversion for body waves propagated through an Earth model in which the seismic velocity depends only on depth or distance from the Earth's center. In this case, the velocity distribution with depth can be uniquely determined by the formula due to Herglotz (1907) and Wiechert (1910) in the absence of a low-velocity layer. It is unusual for a dataset to permit construction of a unique inverse—but such a desirable objective is attainable within the framework of ray theory. We shall also derive formulas applying to structures that include low-velocity layers, following Gerver and Markushevitch (1966).

This section, then, is a self-contained presentation of classical results, some of them more than a hundred years old, that are a major reason why seismology has been the most successful geophysical technique for learning about the Earth's deep interior.

9.4.1 THE HERGLOTZ–WIECHERT FORMULA

Travel-time data in seismology are derived from sets of arrival times giving the onset of body-wave signals as a function of distance X between the seismic source and receiver, with X measured along the Earth's surface. The travel-time data $T = T(X)$ are obtained by subtracting origin time from arrival time. Our results will apply to both P- and S-wave data. To obtain fundamental results we first consider the case of a flat Earth in which the generic body-wave velocity $c(z)$ varies only with depth z. From (4.45a), we know that the ray parameter p defined by

$$p = \frac{\sin i}{c(z)} \tag{9.25}$$

is a constant along a given ray path (i is the angle between the ray path and the vertical (see Figure 9.17)). The maximum depth $Z(p)$ penetrated by the ray with parameter p is given by $c(Z(p)) = 1/p$, because $i = \pi/2$ at the deepest point. The horizontal distance $X(p)$ that

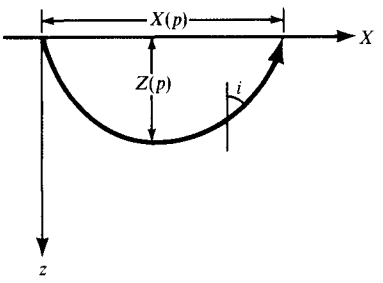

FIGURE **9.17**
Ray path in a flat Earth model.

the ray with parameter p travels before coming back up to the surface (see Figure 9.17) is given by

$$X(p) = 2\int_0^{Z(p)} \tan i \, dz = 2\int_0^{Z(p)} \frac{\sin i}{\cos i}\, dz = 2\int_0^{Z(p)} \frac{p\, dz}{\sqrt{(c(z))^{-2} - p^2}}, \tag{9.26}$$

where we have used (9.25). Likewise, the travel time $T(p)$ for the ray with parameter p is given by

$$T(p) = 2\int_0^{Z(p)} \frac{(c(z))^{-2}\, dz}{\sqrt{(c(z))^{-2} - p^2}}. \tag{9.27}$$

Since $dT/dX = \sin i_0/c(0)$, where $c(0)$ and i_0 are the values of $c(z)$ and i, respectively, at the surface, the ray parameter p can be determined directly from the travel-time data $T(X)$ as

$$p = \frac{dT}{dX}. \tag{9.28}$$

Thus the relationships $X = X(p)$ and $T = T(p)$ are observable quantities at the Earth's surface. The travel-time inverse problem is to find $c(z)$ from observed $X(p)$ or $T(p)$.

In the case of a spherically symmetric Earth, the ray parameter is no longer related to the horizontal phase velocity but to the angular velocity. As shown in (4.45b), the ray parameter p defined by

$$p = \frac{r \sin i}{c(r)} \tag{9.29}$$

is constant along a ray path for a spherically symmetric Earth, where i is the angle between the ray path and the radial direction from the Earth's center (Fig. 9.18). For both the source and the receiver on the surface, the angular distance $\Delta(p)$ can be written as

$$\Delta(p) = 2\int_{r_p}^{r_\oplus} \tan i \frac{dr}{r} = 2\int_{r_p}^{r_\oplus} \frac{p}{\sqrt{(r/c)^2 - p^2}} \frac{dr}{r}, \tag{9.30}$$

where $r_\oplus$ is the Earth's radius and r_p is the radial distance to the deepest point of the ray (Fig. 9.18). The corresponding travel time $T(p)$ is given by

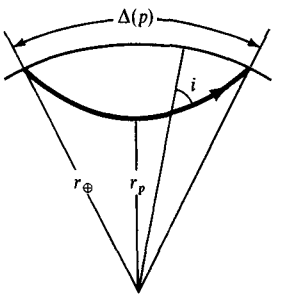

FIGURE **9.18**
Ray path in a spherical Earth model.

$$T(p) = 2\int_{r_p}^{r_\oplus} \frac{(r/c)^2}{\sqrt{(r/c)^2 - p^2}} \frac{dr}{r}. \tag{9.31}$$

Corresponding to the relation (9.28) for flat-lying structures, we have

$$p = \frac{dT}{d\Delta} \tag{9.32}$$

for the spherical Earth.

The above equations, (9.29) through (9.32) for the spherical Earth, can be obtained from the corresponding ones (9.25) to (9.28) for the flat Earth simply by replacing $X(p)$ by $r_\oplus \Delta(p)$, depth z by $r_\oplus \ln(r_\oplus/r)$, $c(z)$ by $c(r)r_\oplus/r$, and the ray parameter p by $p/r_\oplus$ (see Box 9.2, equations (3) and (4)). It therefore suffices to solve the inverse problem for the flat Earth. The solution for spherical Earth problems can be obtained immediately by the above changes of variables.

The formulas expressing the travel distance in terms of the velocity–depth function, (9.26) and (9.30), can be reduced to the form of Abel's integral equation, for which the inverse problem has been solved (see Box 9.3).

We shall first rewrite equation (9.26) using $(c(z))^{-2}$ as the integration variable:

$$\frac{X(p)}{2p} = \int_0^{Z(p)} \frac{dz}{\sqrt{(c(z))^{-2} - p^2}} = \int_{c_0^{-2}}^{p^2} \frac{dz/d(c^{-2})}{\sqrt{c^{-2} - p^2}} d(c^{-2}), \tag{9.33}$$

where c_0 is the velocity at $z = 0$. The upper limit of integration $c^{-2} = p^2$ follows from the fact that $Z(p)$ is the depth of a ray's deepest point, at which the velocity c is the reciprocal of ray parameter p. Equation (9.33) is identical to (9) of Box 9.3 if we replace $X(p)/2p$ by $t(x)$, p^2 by x, and $(c(z))^{-2}$ by ξ. Therefore, the solution of the inverse problem corresponding to equation (10) of Box 9.3 can be rewritten as

$$z(c) = -\frac{1}{\pi}\int_{c_0^{-2}}^{c^{-2}} \frac{X(p)/2p}{\sqrt{p^2 - c^{-2}}} d(p^2) = -\frac{1}{\pi}\int_{c_0^{-1}}^{c^{-1}} \frac{X(p)}{\sqrt{p^2 - c^{-2}}} dp, \tag{9.34}$$

where we have dropped the derivative with respect to c^{-2} from both sides. Equation (9.34) gives the depth for a given velocity c from observed travel-time data $X = X(p)$. It can be

BOX 9.3
Abel's problem

The classical problem solved by Abel in 1826 was to determine the shape of a hill when the time taken by a particle to go up and return is known as a function of the particle's initial velocity. The particle is constrained to slide over the surface of the hill without friction and moves under the force of gravity.

From conservation of energy, the maximum height x it reaches with the initial velocity v_0 is given by $gx = \frac{1}{2}v_0^2$. Consider the movement along a path from the point of maximum height $P(x, y)$ down to the starting point O, as shown in Figure A. The potential energy of the particle at height ξ is equal to $-mg(x - \xi)$, and the kinetic energy is $\frac{1}{2}m(ds/dt)^2$, where m is the particle mass and s is the distance measured along the path. Since there is no frictional loss, we have

$$\left(\frac{ds}{dt}\right)^2 = 2g(x - \xi). \tag{1}$$

Taking the square root of both sides and integrating, we have

$$t(x) = \int_0^x \frac{ds/d\xi}{\sqrt{2g(x - \xi)}} d\xi. \tag{2}$$

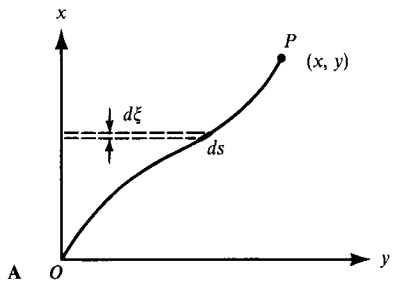

Rewriting this in the standard form of Abel's integral equation,

$$t(x) = \int_0^x \frac{f(\xi)}{\sqrt{(x - \xi)}} d\xi, \tag{3}$$

our inverse problem is to find $f(\xi)$ when $t(x)$ is known.

The solution is obtained by the following steps. First, multiply both sides of (3) by $dx/\sqrt{\eta - x}$ and integrate with respect to x from 0 to η:

$$\begin{aligned} \int_0^\eta \frac{t(x)\,dx}{\sqrt{\eta - x}} &= \int_0^\eta \frac{dx}{\sqrt{\eta - x}} \int_0^x \frac{f(\xi)}{\sqrt{x - \xi}} d\xi \\ &= \int_0^\eta f(\xi)\,d\xi \int_\xi^\eta \frac{dx}{\sqrt{\eta - x}\sqrt{x - \xi}} \end{aligned} \tag{4}$$

(continued)

BOX **9.3** *(continued)*

by changing the order of integration. The integration limits are also changed to cover the shaded area (Figure C), which is the original area of integration (Figure B), but made up of strips with different orientation. The integral with respect to x in (4) is seen to be a constant by making the variable change $x = \xi \cos^2 \theta + \eta \sin^2 \theta$, giving

$$\int_{\xi}^{\eta} \frac{dx}{\sqrt{\eta - x}\sqrt{x - \xi}} = \int_{0}^{\pi/2} 2\, d\theta = \pi. \tag{5}$$

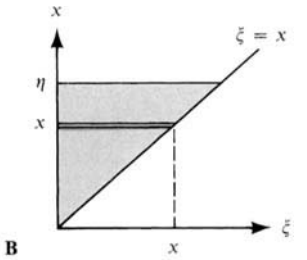

B

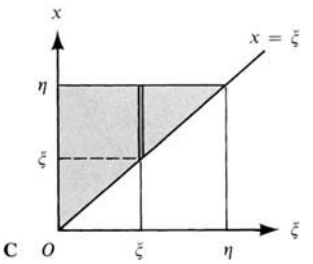

Then equation (4) can be written as

$$\int_{0}^{\eta} \frac{t(x)\, dx}{\sqrt{\eta - x}} = \pi \int_{0}^{\eta} f(\xi)\, d\xi. \tag{6}$$

Differentiating (6) with respect to η, we obtain

$$\frac{d}{d\eta} \int_{0}^{\eta} \frac{t(x)\, dx}{\sqrt{\eta - x}} = \pi f(\eta). \tag{7}$$

(continued)

BOX **9.3** *(continued)*

Replacing η by ξ, we have the standard form

$$f(\xi) = \frac{1}{\pi}\frac{d}{d\xi}\int_0^{\xi} \frac{t(x)\,dx}{\sqrt{\xi - x}} \tag{8}$$

as the solution of Abel's integral equation (3).

According to Bôcher (1909), the necessary and sufficient conditions that Abel's integral equation (3) has the continuous solution (8) are the following:

1. $t(x)$ must be continuous,
2. $t(0) = 0$, and
3. $t(x)$ has a derivative that is finite with at most a finite number of discontinuities.

The most serious restriction is the exclusion of a discontinuity in $t(x)$, to avoid having two different return times for a given velocity at O. This happens if the hill is undulating with peaks and troughs—corresponding to the presence of low-velocity channels, in the case of travel-time inversion.

Finally, changing the variables in (3) and (8) such that $\xi \to a - \xi$ and $x \to a - x$, we obtain formulas more suited to our problem of travel-time inversion:

$$t(x) = \int_x^a \frac{f(\xi)}{\sqrt{\xi - x}} d\xi \tag{9}$$

and

$$f(\xi) = -\frac{1}{\pi}\frac{d}{d\xi}\int_{\xi}^{a} \frac{t(x)\,dx}{\sqrt{x - \xi}}. \tag{10}$$

rewritten in the following forms by integration by parts:

$$z(c) = -\frac{1}{\pi}\int_{\cosh^{-1}(c/c_0)}^{0} X(p)d(\cosh^{-1}(pc)) = \frac{1}{\pi}\int_0^{X(c^{-1})} \cosh^{-1}(pc)\,dX, \tag{9.35}$$

where we have used $X(c_0^{-1}) = 0$. The result for a spherical Earth is obtained from (9.35) by variable changes mentioned earlier, giving

$$\log[r_\oplus / r(c)] = \frac{1}{\pi}\int_0^{\Delta(r/c)} \cosh^{-1}(pc/r)\,d\Delta. \tag{9.36}$$

In applications, a particular value of the ratio $r/c(r)$ is selected. Via the $\Delta = \Delta(p)$ curve, the upper limit of integration in (9.36) is then known, and the integral itself is carried out (using general values $p \geq r/c$) to give a value of $\log(r_\oplus/r)$. Hence r is known for a value of $r/c(r)$, leading to the determination of one point in the velocity profile $c = c(r)$. Equations (9.34) through (9.36) are called Herglotz–Wiechert formulas.

The conditions for the validity of Herglotz–Wiechert formulas may be obtained from Bôcher's conditions, discussed in Box 9.3. Translating them for the travel-time problem, we find that the formulas are applicable to cases in which the derivative of $X(p)$ is discontinuous, but not to cases in which $X(p)$ itself is discontinuous. Cases of the latter type occur when velocity decreases with depth (for a spherical Earth, an increase in $c(r)/r$ with r). Thus the Herglotz–Wiechert method of inversion cannot be used in cases involving low-velocity channels. It can be applied, however, to the case of a rapid velocity increase that causes a triplication in the travel-time curve.

Figure 9.19 shows an example of the triplication. For ray paths bottoming above the zone of rapid velocity increase, the rays penetrating deeper usually emerge farther away from the source point (i.e., $dX/dp < 0$). However, the strong refraction by a transition zone can cause the ray to emerge closer to the source, as depicted in Figure 9.19 for some of the rays arriving between X_1 and X_2 ($dX/dp > 0$). If the ray bottoms below the transition zone, the behavior of the travel-time curve returns to normal. The travel time $T(X)$ and ray parameter $p = dT/dX$ are also shown schematically as functions of X. The travel-time curve is downward concave on the normal branches, but upward concave along the receding branch because $d^2T/dX^2 = dp/dX > 0$ there. As shown at the bottom of Figure 9.19, $X(p)$ is a single-valued continuous function of p, and therefore the Herglotz–Wiechert formula (9.34) is applicable in this case.

Let us apply the formula to an extreme example due to Slichter (1932), consisting of a homogeneous layer overlying a homogeneous half-space, in which velocity increases discontinuously as shown in Figure 9.20. The direct waves traveling with velocity c_0 in the upper layer are designated as P. The refracted and reflected waves from the half-space are designated as P_n and $P_M P$, respectively. The corresponding travel-time branches meet at a distance where the total reflection first shows up at the critical angle i_n, which satisfies $\sin i_n = c_0/c_1$. The corresponding relationship between p and X is shown at the bottom of the figure.

Since the travel time $T(X)$ for the reflection branch $P_M P$ is given by

$$T(X) = \frac{2}{c_0}\sqrt{h^2 + \left(\frac{X}{2}\right)^2},$$

we can easily obtain the explicit form of $X(p)$ as

$$X(p) = \frac{2hp}{\sqrt{1/c^2 - p^2}} \qquad \text{for } c_1^{-1} < p < c_0^{-1}$$

for that branch. Inserting this result into the inversion formula (9.34), we find that

$$\begin{aligned} z(c) &= -\frac{1}{\pi}\int_{c_0^{-1}}^{c^{-1}} \frac{2hp\,dp}{\sqrt{c_0^{-2} - p^2}\sqrt{p^2 - c^{-2}}} \\ &= h \qquad \text{for } c_0^{-1} > c^{-1} > c_1^{-1}. \end{aligned} \tag{9.37}$$

Thus the correct depth h is recovered for all velocities in the range from c_0 to c_1.

For a successful inversion of travel-time data with a triplication, it is necessary to identify the normal and receding branches correctly. This requires the correct identification

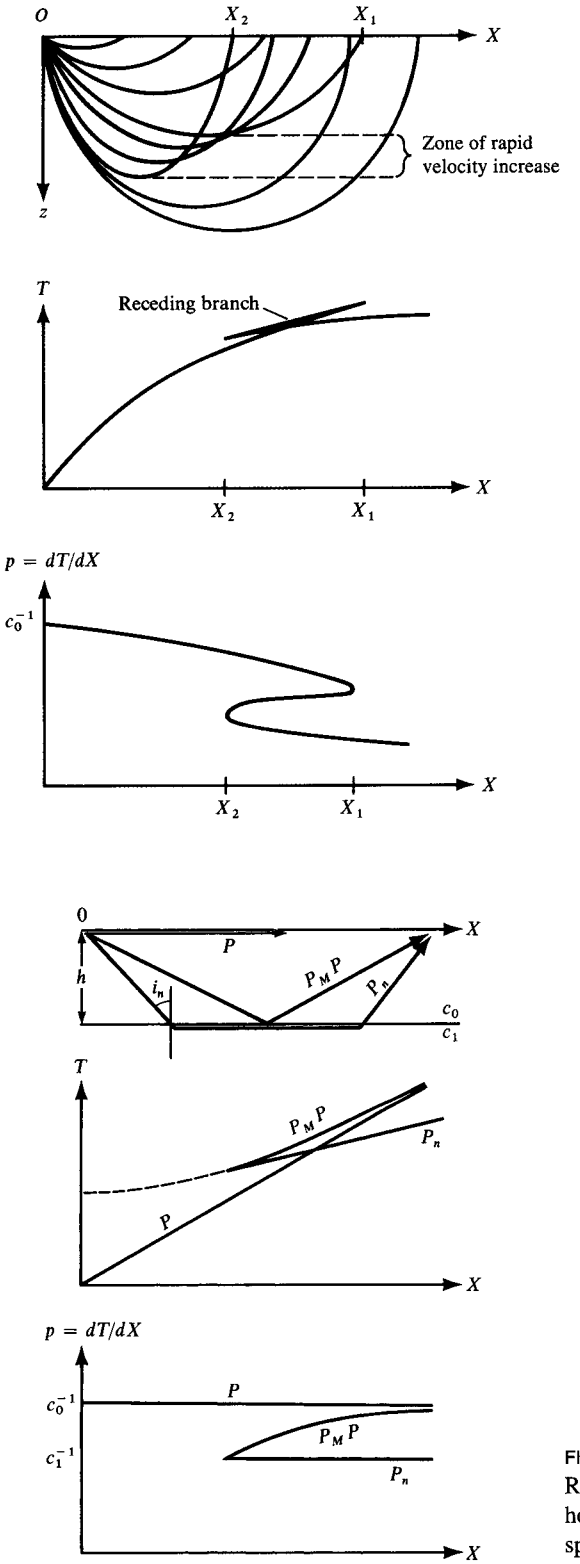

FIGURE **9.19**
Triplication of the travel-time curve due to a rapid increase in velocity with depth. $X = X(p)$ is single valued.

FIGURE **9.20**
Ray paths and travel times for a homogeneous layer over a half-space.

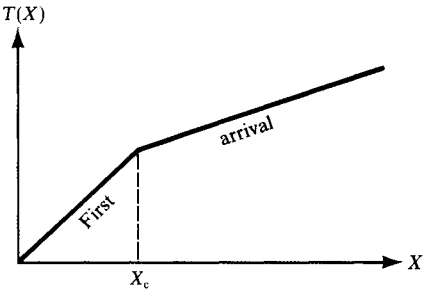

FIGURE **9.21**
Travel times of the first arrival are known as shown here, but those of later arrivals are unknown. The nonuniqueness problem in this case is demonstrated in Figure 9.22.

of not only the first arrivals but also later arrivals. In practice, correct readings of arrival times of later phases are often difficult because of interference from the coda of earlier arrivals. In this situation the use of an array can be helpful, for then the relationship between X and $p = dT/dX$ can be measured directly for different branches having the same arrival time T.

Suppose that only the first arrival is correctly identified, and is found to consist of two line segments, as shown in Figure 9.21. Then there are an infinite number of structures that will give the same first arrival. In a study of crustal structure along the coast of California, Healy (1963) considered n-layered structures, for various n, which give the identical first arrival, while forcing all the arrivals from "masked layers" to pass through the intersection of the two first-arrival lines. The result is reproduced for $n = 1, 2$, and 50 in Figure 9.22. The 50-layer case approaches the formula $c(z) = c_0 \cosh \pi z / X_c$, obtained by Slichter (1932) for a continuous structure for which all rays emerge at the intersection point (X_c is the horizontal distance to this point). Thus Figure 9.22 illustrates the nonuniqueness of interpreting the travel-time data when only the first arrivals are known.

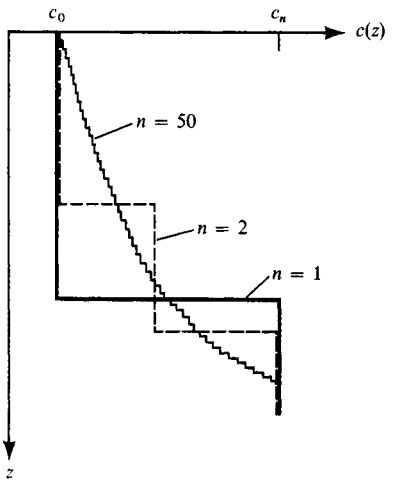

FIGURE **9.22**
Velocity distributions that give the same first-arrival times as shown in Figure 9.21 (n is the number of layers). [After Healy, 1963.]

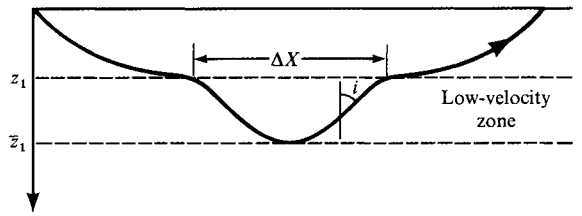

FIGURE **9.23**
Ray paths and travel times for an Earth model containing a low-velocity layer.

9.4.2 TRAVEL-TIME INVERSION FOR STRUCTURES INCLUDING LOW-VELOCITY LAYERS

If the velocity $c(z)$ starts decreasing with depth z at a certain depth z_1 in the flat Earth model (or if the ratio of velocity to radius, $c(r)/r$, starts to decrease with decreasing r in the case of the spherical Earth model), then no ray can have its deepest point below this depth until the velocity comes back to the value it had at z_1, as illustrated in Figures 9.23 and 9.14. In this case, a shadow zone occurs with a gap in the travel-time curve, and a discontinuity appears in the $X = X(p)$ relation, violating a condition for applicability of the Herglotz–Wiechert inversion method. In such cases, what can we learn about the Earth's structure from discontinuous travel-time curves?

Slichter (1932) analysed this problem and drew several interesting conclusions. Since there are no rays bottoming within the low-velocity zone (LVZ), the velocity distribution throughout the LVZ affects the travel time, which is always integrated over this zone. Suppose we simulate the velocity distribution in the LVZ by a stack of playing cards. The cards may be shuffled without changing the integrated travel time. Thus, the ordering of the cards cannot be determined from the travel-time data.

However, Slichter found an upper bound for the thickness of the LVZ from observed gaps ΔX and ΔT in the travel-time curve (see Fig. 9.24). Defining upper and lower boundaries of the LVZ as shown in Figure 9.23, we find

$$\frac{\Delta X}{2} = \int_{z_1}^{\bar{z}_1} \tan i \, dz \tag{9.38}$$

and

$$\frac{\Delta T}{2} = \int_{z_1}^{\bar{z}_1} \frac{dz}{c(z)\cos i} = \int_{z_1}^{\bar{z}_1} \frac{p_1 \, dz}{\sin i \cos i} = p_1 \frac{\Delta X}{2} + p_1 \int_{z_1}^{\bar{z}_1} \cot i \, dz, \tag{9.39}$$

where p_1 is the ray parameter of the ray that grazes both the upper and lower boundaries of the LVZ, so that $p_1 = c^{-1}(z_1) = c^{-1}(\bar{z}_1)$. For given ΔT and ΔX, the integrals of both $\tan i$ and $\cot i$ over the range $z_1 < z < \bar{z}_1$ are fixed. If the LVZ has a uniform velocity, i will be constant and the integrals will become αh and h/α, where $\alpha = \tan i$. On the other hand, if the LVZ consists of a stack of homogeneous layers, the corresponding integrals will be $\Sigma \alpha_n h_n$ and $\Sigma h_n/\alpha_n$, where h_n is the thickness and α_n is $\tan i$ for the nth layer. For a given ΔT and ΔX, these integrals are given and their product is therefore the same for the two cases,

$$\alpha h \cdot h/\alpha = h^2 = (\Sigma h_n/\alpha_n)(\Sigma \alpha_n h_n).$$

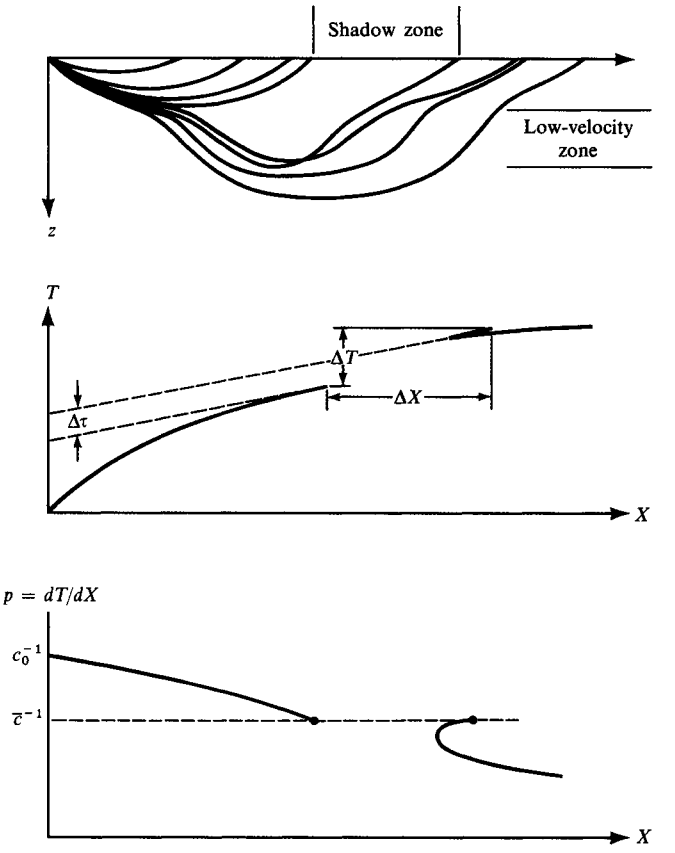

FIGURE **9.24**
Ray paths and travel times for a structure including a low-velocity layer.

Since the right-hand side is greater than $(\Sigma h_n)^2$ unless the layers all have the same value α_n, we conclude that the thickness of the LVZ is maximum for a uniform velocity. This bound on the LVZ thickness can be obtained by putting $c(z) = c_L$, for $z_1 < z < \bar{z}_1$, in (9.38) and (9.39):

$$\begin{aligned} \frac{\Delta X}{2} &= \frac{p_1(\bar{z}_1 - z_1)_{\max}}{(c_L^{-2} - p_1^2)^{1/2}} \\ \frac{\Delta T}{2} &= \frac{c_L^{-2}(\bar{z}_1 - z_1)_{\max}}{(c_L^{-2} - p_1^2)^{1/2}}. \end{aligned} \tag{9.40}$$

By eliminating c_L from the above equations, we can find the maximum estimate of the thickness of the LVZ from observed gaps in the travel-time curve.

A more general and complete analysis of low-velocity layer problems was made by Gerver and Markushevitch (1966), whose approach made use of the function $\tau(p)$ defined by

$$\tau(p) = T(p) - pX(p), \tag{9.41}$$

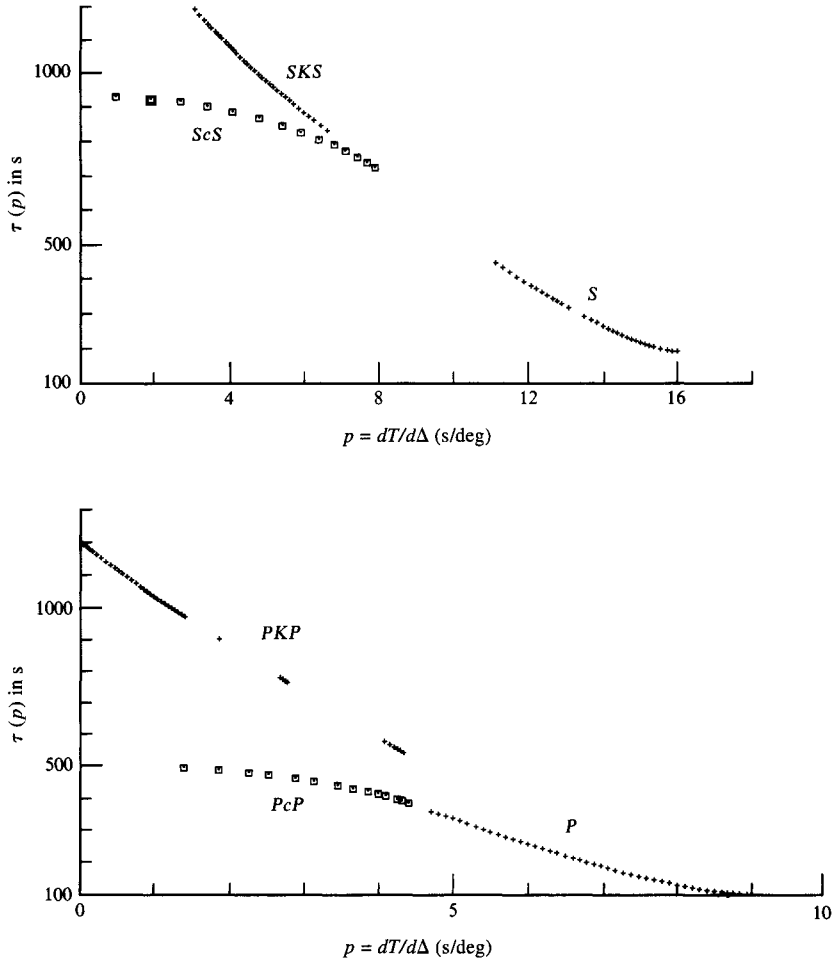

FIGURE **9.25**
Top: $\tau(p)$ for S, SKS, and ScS. Bottom: $\tau(p)$ for P, PKP, and PcP. [From Johnson and Gilbert, 1972.]

which was introduced (for spherical Earth problems) in (9.22). The physical meaning of $\tau(p)$ is clear: $\tau(p)$ is the intercept with $X = 0$ of the tangent to the travel-time curve $T = T(X)$, since p is the slope of that line. From (9.26) and (9.27), we have

$$\tau(p) = 2\int_0^{Z(p)} \sqrt{c^{-2}(z) - p^2}\, dz, \tag{9.42}$$

which monotonically increases with $Z(p)$ and decreases with p. The observed $\tau(p)$ for P- and S-waves in the Earth are shown in Figure 9.25.

The jump in $\tau(p)$ due to a low-velocity layer can be written as

$$\Delta\tau = \Delta T - p_1 \Delta X. \tag{9.43}$$

BOX 9.4
Measurement of $\tau(p)$

Bessonova *et al.* (1974) used a simple and reliable method of obtaining $\tau(p)$ from a set of travel-time data (T_i, X_i). The method is based on an extremum property of $T(p_0) - pX(p_0)$ as p_0 is varied with p fixed.

First, we note that $[T(p_0) - pX(p_0)]$ at $p_0 = p$ is just $\tau(p)$. Second, note that $\partial/\partial p_0[T(p_0) - pX(p_0)] = (p_0 - p)dX/dp_0$, so that $[T(p_0) - pX(p_0)]$ has an extremum at $p_0 = p$.

The method of Bessonova *et al.* proceeds as follows. For a given set of travel-time data (T_i, X_i), plot $T_i - pX_i$ for a fixed p as a function of X_i, as shown in the figure. It will take an extreme value at $X(p)$, and the extreme value of $T_i - pX_i$ is equal to $\tau(p)$.

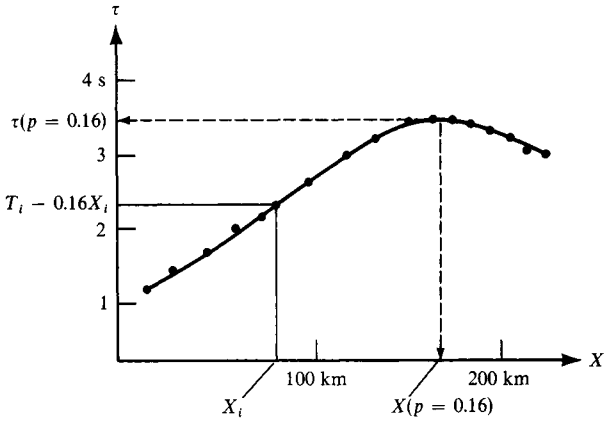

The inversion formulas based upon data in the form $X = X(p)$ can be rewritten to apply to data in the form $\tau = \tau(p)$, by using the relation $d\tau = -X\,dp$. For example, equation (9.34) becomes simply

$$Z(p) = \frac{1}{\pi}\int_0^{\tau(p)} \frac{d\tau}{\sqrt{v^2(\tau) - p^2}},$$

where $v(\tau)$ and $\tau(p)$ are mutually inverse functions and $z(c) = Z(p)|_{p=1/c}$.

Note that $\tau(p)$ alone contains all the information available from the travel-time data. Since $dT/dX = p$,

$$\frac{d\tau}{dp} = \frac{dT}{dp} - p\frac{dX}{dp} - X(p) = -X(p). \tag{9.44}$$

We can therefore solve the forward problems of determining $X = X(p)$, and then $T = T(p)$, if $\tau = \tau(p)$ alone is known (note that $T(p) = \tau(p) + pX(p)$). The gaps ΔT and ΔX in the travel-time curve due to a LVZ can also be found if $\tau(p)$ alone is known, because the

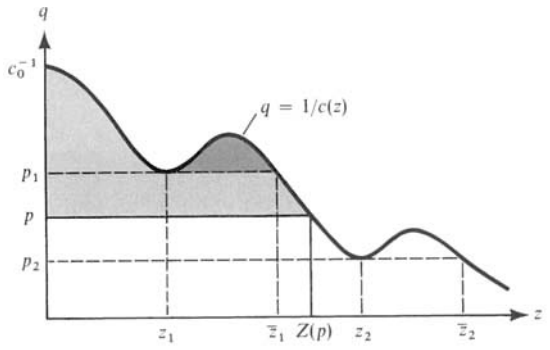

FIGURE **9.26**
Area of integration for (9.45).

difference in $d\tau/dp$ between $p_1 - 0$ and $p_1 + 0$ gives ΔX. Then ΔT can be determined by putting known ΔX and $\Delta\tau$ into (9.43).

Let us now turn to the inversion problems associated with a velocity–depth distribution that includes low-velocity zones. We shall start with the following identity:

$$Z(p) = \int_0^{Z(p)} dz \cdot \frac{1}{\pi} \int_{p^2}^{[c(z)]^{-2}} \frac{d(q^2)}{\sqrt{[c(z)^{-2} - q^2](q^2 - p^2)}}. \tag{9.45}$$

This is easily verified by substituting $q^2 = p^2 \cos^2\theta + c^{-2}\sin^2\theta$.

The area of the above integration is shown by a shaded region in the $q = q(z)$ diagram in Figure 9.26. The integral is taken for a fixed z with respect to q from p to $1/c(z)$, and then the result is integrated with respect to z from 0 to $Z(p)$. The kth low-velocity zone is specified by the ray parameter p_k at two depths z_k and $\bar{z}_k$, corresponding to the top and bottom of the zone, respectively.

Since $Z(p)$ is the depth at which a ray with ray parameter p bottoms and p is equal to the reciprocal velocity at the bottom, $Z(p)$ as a function of p is equivalent to $1/c(z)$ as a function of z except within the low-velocity zone, where there are no turning points. For the kth low-velocity zone, we shall assume that the curve $Z(p)$ is a straight line connecting the two points (p_k, z_k) and $(p_k, \bar{z}_k)$. By this definition, $Z(p)$ does not increase with p.

Changing the order of integration, we can rewrite (9.45) as

$$Z(p) = \frac{2}{\pi} \int_p^{1/c_0} \frac{q\,dq}{\sqrt{q^2 - p^2}} \int_0^{Z(q)} \frac{dz}{\sqrt{[1/c(z)]^2 - q^2}} + I(p), \tag{9.46}$$

where $I(p)$ is the integral over the densely shaded area in Figure 9.26. From (9.26)

$$X(q) = 2\int_0^{Z(q)} \frac{q\,dz}{\sqrt{[1/c(z)]^2 - q^2}},$$

so we can rewrite (9.46):

$$Z(p) = \frac{1}{\pi} \int_p^{1/c_0} \frac{X(q)\, dq}{\sqrt{q^2 - p^2}} + I(p). \tag{9.47}$$

The first term of the right-hand side of the above equation is nothing but the Herglotz–Wiechert formula, and is determined uniquely from the observed travel-time data. The contribution $I(p)$ from the low-velocity layers can be obtained as

$$\begin{aligned} I(p) &= \sum_{i=1}^{k} \frac{2}{\pi} \int_{z_i}^{\bar{z}_i} dz \int_{p_i}^{1/c(z)} \frac{q\, dq}{\sqrt{\left[1/c(z)\right]^2 - q^2}\sqrt{q^2 - p^2}} \\ &= \sum_{i=1}^{k} \frac{2}{\pi} \int_{z_i}^{\bar{z}_i} \tan^{-1} \sqrt{\frac{\left[1/c(z)\right]^2 - p_i^2}{p_i^2 - p^2}}\, dz \qquad \text{for } p_k > p > p_{k+1}. \end{aligned} \tag{9.48}$$

The above equations (9.47) and (9.48), obtained by Gerver and Markushevitch (1966), represent the extension of the Herglotz–Wiechert formula to include low-velocity layers.

For $p > p_1$, $I(p) = 0$. Therefore, the Herglotz–Wiechert term gives the solution $Z(p)$, which gives the velocity–depth function uniquely for $z < z_1$.

For $p < p_1$, the Herglotz–Wiechert term is determined from the observed travel-time data. However, through the second term $I(p)$, an arbitrary velocity–depth function $v(z)$ may be assigned to the low-velocity layer subject to some constraints described below. Except for the upper boundary of the first low-velocity layer, the boundary depths z_k, $\bar{z}_k$ are also unknown.

The first constraint from observations, on $c(z)$, z_k, and $\bar{z}_k$, is given by the discontinuity in $\tau(p)$:

$$\Delta\tau_k = 2 \int_{z_k}^{\bar{z}_k} \sqrt{\left[1/c(z)\right]^2 - p_k^2}\, dz. \tag{9.49}$$

The second is, by definition, that the calculated $Z(p)$ should not increase with p. The third is that $Z(p_k + 0)$ and $Z(p_k - 0)$ must agree, respectively, with the depths of the lower and upper boundaries, z_k and $\bar{z}_k$, of the kth layer. As shown in Figure 9.27, Gerver and Markushevitch gave a "giraffe-like" area in which the plots of all possible solutions $c(z)$ must lie for the case of two low-velocity layers. The upper bound for $c(z)$ corresponds to the Herglotz–Wiechert term. Figure 9.27 also shows the existence of an upper bound for the thickness of the LVZ given earlier by (9.40).

The special methods we have described in this section, for inverting travel-time data, are closely associated with the special properties of the Abel integral equation. These methods are unusual in that a method of *construction* is known for obtaining the inverse. More general methods of inversion, applied to travel times, are described by Johnson and Gilbert (1972).

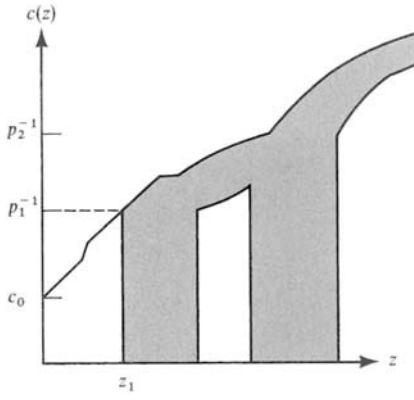

FIGURE **9.27**
A solution obtained by Gerver and Markushevitch (1966).

9.5 Wave Propagation in Media Having Smoothly Varying Depth-Dependent Velocity Profiles within Which Turning Points Are Present

When a ray departs downward from some point source within the Earth, it can be observed again at a surface receiver only after it is reflected back upward from some internal discontinuity, or after it gradually changes from "down-going" to "upgoing" simply by passing through a turning point. We have mentioned turning points in Section 9.3, in the context of ray theory, but our present aim is to understand turning points in the context of a frequency-dependent wave theory for inhomogeneous media. The importance of this is that it avoids the artificiality of using large numbers of layers to model the inhomogeneity.

The key elements of elastic-wave theory in homogeneous media include Lamé's theorem, the analysis of plane waves, the Sommerfeld integral, and ways to evaluate such integrals by manipulations in the complex ray-parameter plane. Each of these elements is generalized in this section, and we shall find that WKBJ theory (reviewed in Box 9.6) has great utility. In fact, in situations where WKBJ approximations are accurate, our computation of body waves will merge classical ray theory with some of the methods used to solve Lamb's problem. But new features emerge where WKBJ approximations are inaccurate (this is the case if a turning point is present at a depth close to some discontinuity within the Earth).

In studying homogeneous elastic media, we found it convenient to move from a study of potentials to a method based on the motion-stress vector. A similar development is convenient in inhomogeneous media, because potentials display the properties of scalar wave solutions in their simplest form. Beginning, then, with potentials, and deferring to Section 9.6 a discussion of the motion-stress vector approach (which enables one more easily to handle boundary conditions and to do the necessary bookkeeping for physical quantities), we find in Box 9.5 that displacement $\mathbf{u}$ in a spherically symmetric medium can be written as a sum of three vector terms

$$\mathbf{u} = \rho^{-1/2}[\nabla P + \nabla \times \nabla \times (rV, 0, 0)] + \mu^{-1/2}\nabla \times (rH, 0, 0). \qquad (9.50a)$$

Here, the three vectors on the right-hand side are, respectively, the P-, SV-, and SH-components of displacement, with scalar potentials P, V, H satisfying (in the frequency domain) the decoupled wave equations

$$\nabla^2 P + \frac{\omega^2}{\alpha^2} P = 0, \qquad \nabla^2 V + \frac{\omega^2}{\beta^2} V = 0, \qquad \nabla^2 H + \frac{\omega^2}{\beta^2} H = 0. \tag{9.50b}$$

In (9.50a) and (9.50b), the quantities ρ, μ, α, and β are each functions only of radius r in the spherical polar system (r, Δ, ϕ). Thus each of the wave equations has the form of a Helmholtz equation with radially varying wavenumber.

Suppose next that a point source is introduced into the medium. We first obtain a representation of the source that plays a role similar to the Sommerfeld integral for waves in homogeneous media. The simplest source to consider is a delta function introduced into the wave equation for $P(\mathbf{r}, \omega)$:

$$\nabla^2 P + \frac{\omega^2}{\alpha^2(r)} P = K_s \, \delta(\mathbf{r} - \mathbf{r}_s), \tag{9.51}$$

where the source is at $\mathbf{r}_s$ and K_s is a constant (subscript s refers throughout this discussion to constants determined by the source).

The solution of (9.51) for an outgoing wave in an infinite homogeneous medium is

$$P(\mathbf{r}, \omega) = -\frac{K_s \exp(i\omega|\mathbf{r} - \mathbf{r}_s|/\alpha_s)}{4\pi|\mathbf{r} - \mathbf{r}_s|}, \tag{9.52}$$

which has a well-known partial wave expansion in terms of spherical Hankel functions and Legendre polynomials:

$$P(\mathbf{r}, \omega) = -\frac{iK_s\omega}{4\pi\alpha_s} \sum_{l=0}^{\infty} (l + \tfrac{1}{2}) h_l^{(1)}\left(\frac{\omega r}{\alpha_s}\right)\left[h_l^{(1)}\left(\frac{\omega r_s}{\alpha_s}\right) + h_l^{(2)}\left(\frac{\omega r_s}{\alpha_s}\right)\right] P_l(\cos\Delta) \tag{9.53}$$

(for $r > r_s$), where α_s is the P-wave velocity, constant throughout the medium as well as being the value at the source in this case.

This last expansion must be generalized if we are to progress in our study of *inhomogeneous* media. Fortunately, the method of separation of variables shows that horizontal wave functions are still Legendre polynomials, and all the complications are confined to the vertical (now, radial) wavefunction. Thus we shall try to solve (9.51) by a sum of separated solutions in the form

$$P(\mathbf{r}, \omega) = \sum_{l=0}^{\infty} a(r, l) P_l(\cos\Delta). \tag{9.54}$$

Then $a(r, l) = (l + \frac{1}{2}) \int_0^{\pi} P(\mathbf{r}, \omega) P_l(\cos\Delta) \sin\Delta \, d\Delta$, and substitution of (9.54) in the wave equation gives

$$\frac{d^2}{dr^2}[ra(r, l)] + \left[\frac{\omega^2}{\alpha^2(r)} - \frac{l(l+1)}{r^2}\right] ra(r, l) = K_s \, \delta(r - r_s) \frac{(2l+1)}{4\pi r}. \tag{9.55}$$

BOX **9.5**

Scalar potentials for P-, SV-, and SH-waves in spherically symmetric media

We now use spherical coordinates (r, Δ, ϕ) in which $r = 0$ is the center of symmetry in the medium and the direction $\Delta = 0$ is taken to lie on some point source. A second-order vector wave equation for displacement $\mathbf{u} = (u_r, u_\Delta, u_\phi)$ can then be obtained from relations between acceleration and stress (2.47), stress and strain (2.50), and strain and displacement (2.45). The equation is

$$\begin{aligned}\rho\omega^2\mathbf{u} = &-(\lambda+2\mu)\nabla\nabla\cdot\mathbf{u}+\mu\nabla\times(\nabla\times\mathbf{u})-\lambda'(\nabla\cdot\mathbf{u},0,0)\\ &-2\mu'\frac{\partial\mathbf{u}}{\partial r}+\mu'(0,\ \mathrm{curl}_\phi\mathbf{u},-\mathrm{curl}_\Delta\mathbf{u})-\mathbf{f}.\end{aligned} \tag{1}$$

Here, and below, a prime denotes radial differentiation, and $\mathrm{curl}_\alpha\mathbf{u}$ is the α-coordinate of $\nabla\times\mathbf{u}$ $(\alpha = r, \Delta, \phi)$. We shall here consider free solutions, i.e., taking the body force $\mathbf{f}$ equal to $\mathbf{0}$.

In deriving potentials for $\mathbf{u}$, we shall follow in outline the same method used in Section 4.1. (Further details for the present problem are given by Richards, 1974.) Thus we seek to turn (1) directly into the required representation by giving a specific construction for the potentials.

This construction is

$$\begin{aligned}P &\equiv \frac{-(\lambda+2\mu)}{\rho^{1/2}\omega^2}\left[\nabla\cdot\mathbf{u}+\frac{\mu}{\lambda+\mu}\left(\frac{2\mu'}{\mu}-\frac{\rho'}{\rho}\right)u_r\right],\\ \mathbf{S} &\equiv \frac{\mu}{\rho^{1/2}\omega^2}\left[\nabla\times\mathbf{u}+\frac{\lambda+2\mu}{\lambda+\mu}\left(\frac{\rho'}{\rho}-\frac{2\mu'}{\lambda+2\mu}\right)(0,-u_\phi,u_\Delta)\right].\end{aligned} \tag{2}$$

After dividing (1) through by $\rho\omega^2$, the equation of motion can be written in the form

$$\mathbf{u} = \rho^{-1/2}(\nabla P+\nabla\times\mathbf{S}) + \text{ terms of order } |\mathbf{u}|/\omega. \tag{3}$$

For the body waves we shall be studying, these last terms are negligible. They are typically of order $(\beta'/\omega)|\mathbf{u}|$, which reaches about 2% of $|\mathbf{u}|$ for 20-s waves in the upper mantle of Earth models with a fairly high shear-velocity gradient (0.005 km/s per km).

The definitions (2) are now to be turned into wave equations, substituting for $\mathbf{u}$ from (3). In this way, it is found that

$$\begin{aligned}\nabla^2 P+\frac{\rho\omega^2}{\lambda+2\mu}P &= \text{terms of order } \frac{|\mathbf{u}|}{\omega},\\ \nabla^2\mathbf{S}+\frac{\rho\omega^2}{\mu}\mathbf{S} &= \text{terms of order } \frac{|\mathbf{u}|}{\omega},\end{aligned} \tag{4}$$

But each separate term on the left-hand side in (4) is of order $\omega|\mathbf{u}|$, so that terms on the right-hand side are negligible for most purposes, being two orders lower in frequency.

It remains only to find scalar potentials separately for SV and SH. This entails an inversion of the Beltrami operator B, where

$$Bf \equiv \frac{1}{\sin\Delta}\frac{\partial}{\partial\Delta}\left(\sin\Delta\,\frac{\partial f}{\partial\Delta}\right)+\frac{1}{\sin^2\Delta}\frac{\partial^2 f}{\partial\phi^2}.$$

(continued)

BOX **9.5** *(continued)*

Note that B contains the horizontal derivatives present in the Laplacian operator, so that $BY_l^m = -l(l+1)Y_l^m$ for any surface harmonic Y_l^m. The inverse B^{-1} of B has been discussed by Backus (1958): if $g = g(r, \Delta, \phi)$ can be expressed as a sum $g = \sum_{l=1}^{\infty} \sum_{m=-l}^{l} g_l^m(r) Y_l^m$, then we invert $Bf = g$ to obtain $f = B^{-1}g = -\sum_{l=1}^{\infty} \sum_{m=-l}^{l} [l(l+1)]^{-1} g_l^m Y_l^m$.

SV-POTENTIAL

For spheroidal motion, $\text{curl}_r \mathbf{u} = 0$, and then $S_r = 0$ and $\nabla \cdot \mathbf{S} = 0$ both follow from (2). Thus $\partial(\sin \Delta S_\Delta)/\partial\Delta + \partial S_\phi/\partial\phi = 0$, which is a condition that there exists a function V such that $S_\Delta = (1/\sin\Delta)\,\partial V/\partial\phi$, $S_\phi = -\partial V/\partial\Delta$. Hence

$$\mathbf{S} = \nabla \times (rV, 0, 0) \qquad \text{for } SV \text{ waves.} \tag{5}$$

To construct V, we form $\text{curl}_r \mathbf{S}$ and note that $-r\ \text{curl}_r \mathbf{S} = BV$, an operator we have already found how to invert. Richards (1974) shows that

$$\nabla^2 V + \frac{\rho\omega^2}{\mu} V = \text{terms of order } \frac{|\mathbf{u}|}{\omega^2}. \tag{6}$$

SH-POTENTIAL

For toroidal motion, $u_r = 0$ and $\nabla \cdot \mathbf{u} = 0$. We can therefore follow the same stages as discussed above for $\mathbf{S}$, introducing a potential H_0 via $H_0 = -B^{-1}(r\ \text{curl}_r \mathbf{u})$. To get the canonical form of the wave equation for SH-potential, it is convenient to work with $H = \mu^{1/2} H_0$. Then

$$\mathbf{u} = \mu^{-1/2} \nabla \times (rH, 0, 0) \qquad \text{for } SH\text{-waves,}$$

and

$$\nabla^2 H + \frac{\rho\omega^2}{\mu} H = \text{terms of order } \frac{|\mathbf{u}|}{\omega}. \tag{7}$$

Equations (9.50a) and (9.50b) are obtained by ignoring small terms in (3)–(7). (All these terms are zero in homogeneous media.)

Following Seckler and Keller (1959) and Friedman (1951), we introduce three particular solutions of the homogeneous equation related to (9.55). Let $f_l(r)$ be that solution for (r, l) which is regular at the central point $r = 0$. For very large values of r, the wave equation becomes roughly $d^2a/dr^2 = -\omega^2 a/\alpha^2$. By analogy with the solutions $e^{\pm i\omega r/\alpha}$ when α is constant, we expect that two independent solutions of our wave equation can be chosen, one with a phase that increases with r, and another with a phase that decreases. We label these solutions $g_l^{(1)}(r)$ and $g_l^{(2)}(r)$, respectively. In association with the factor $\exp(-i\omega t)$, $g^{(1)}$ is an outgoing wave and $g^{(2)}$ is ingoing. Apart from a normalization, the three solutions are completely defined and we may take

$$a(r, l) = \begin{cases} c_1 g_l^{(1)}(r) & r_s \le r \\ c_2 f_l(r) & \text{for } 0 \le r \le r_s. \end{cases} \tag{9.56}$$

The constants c_1 and c_2 are determined by noting that (9.55) implies continuity of $a(r,l)$ as r increases through r_s, and also implies a step of height $K_s(2l+1)/(4\pi r_s^2)$ in $d(a(r,l))/dr$. It follows that

$$c_1 = -\frac{K_s(2l+1)}{4\pi r_s^2}\frac{f_l(r_s)}{W(r_s)}, \qquad c_2 = -\frac{K_s(2l+1)}{4\pi r_s^2}\frac{g_l^{(1)}(r_s)}{W(r_s)}, \tag{9.57}$$

where $W(r) = g_l^{(1)}(r)df_l/dr - f_l(r)\,dg_l^{(1)}/dr$ is the Wronskian of $g_l^{(1)}$ and f_l. But $W(r)$ is proportional to $1/r^2$, since the wave equations satisfied by $g_l^{(1)}$ and f_l can be used to show $d(r^2W)/dr = 0$. The constant of proportionality depends on the normalization of our wave functions, and at this stage we appeal to WKBJ theory. From Box 9.6 (equation 11), it follows for large ω that

$$rg_l^{(2)}(r) \sim \frac{K^{(2)}}{\left[\dfrac{1}{\alpha^2(r)} - \left(\dfrac{l+\frac{1}{2}}{\omega r}\right)^2\right]^{1/4}} \exp\left\{\pm i\omega \int_{r_p}^{r} \sqrt{\frac{1}{\alpha^2(r')} - \left(\frac{l+\frac{1}{2}}{\omega r'}\right)^2}\, dr'\right\}, \tag{9.58}$$

where $K^{(1)}$ and $K^{(2)}$ are constants and r_p is that radius at which the integrand vanishes.

Taking

$$p = \frac{l+\frac{1}{2}}{\omega}, \qquad \text{we have} \qquad p = \frac{r_p}{\alpha(r_p)}. \tag{9.59}$$

Since the ray parameter in spherical geometry is $(r \sin i)/\alpha$, it follows that r_p has a physical interpretation as the radius to the turning point along the ray with ray parameter p.

Our normalization for $g_l^{(j)}$ is made after comparison with the Debye approximation to spherical Hankel functions (see discussion in Box 9.6). This is appropriate, for we shall assume $g_l^{(j)}$ actually equals $h_l^{(j)}(\omega r/\alpha_s)$ if the medium is homogeneous with constant velocity α_s. $K^{(1)}$ and $K^{(2)}$ are now determined, and

$$g_l^{(2)}(r) \sim e^{\mp i\pi/4}\frac{\sqrt{\alpha_s}}{\omega r} \cdot \frac{1}{\left[\dfrac{1}{\alpha^2(r)} - \dfrac{p^2}{r^2}\right]^{1/4}} \cdot \exp\left\{\pm i\omega \int_{r_p}^{r} \sqrt{\frac{1}{\alpha^2(r')} - \frac{p^2}{(r')^2}}\, dr'\right\}$$

in the region for which $r/\alpha(r) > p$ (i.e., above the depth of deepest penetration of the ray with parameter p). Pursuing this link with ray theory even further, we recognize $\sqrt{1/\alpha^2 - p^2/r^2}$ as $\alpha^{-1}\cos i$, which is the P-wave vertical slowness we have previously labeled as ξ. Thus

$$g_l^{(2)}(r) \sim \frac{e^{\mp i\pi/4}}{\omega r} \cdot \sqrt{\frac{\alpha_s}{\xi(r)}} \cdot \exp\left[\pm i\omega \int_{r_p}^{r} \xi(r')\, dr'\right]. \tag{9.60}$$

BOX **9.6**
WKBJ theory

We are concerned here with finding approximate solutions to the second-order equation

$$\frac{d^2\phi}{dx^2} + \omega^2 s^2 \phi = 0, \tag{1}$$

where ω is large and positive and where $s = s(x)$ is such that s^2 is a monotonically increasing function of x for a range of x-values. The method we are about to describe has great generality, because any linear homogeneous equation of second order can be transformed into (1), often with the special properties of ω and s^2 mentioned above. Many authors have rediscovered the method (including Wentzel, Kramers, Brillouin, and Jeffreys—hence the name). The main ideas certainly go back to Green and Liouville, and were used by Rayleigh (1912).

We shall suppose that s^2 has a zero, called a *turning point*, at $x = x_p$, so that $s^2 \gtrless 0$ according as $x \gtrless x_p$. It follows from (1) that the curvature of a solution $\phi = \phi(x)$ has the opposite or the same sign as ϕ, according as $x \gtrless x_p$. This fact alone suggests the main character of the solutions, which is oscillatory above the turning point x_p, and exponential below.

Where $s(x)$ is constant, solutions are $\phi = e^{\pm i\omega s x}$, and this suggests that we try the form $\phi = e^{i\omega\tau(x)}$. From (1),

$$i\omega\tau'' - \omega^2(\tau')^2 + \omega^2 s^2 = 0,$$

where a prime denotes d/dx. As a first approximation, we neglect $\omega\tau''$ here, giving $\tau' \sim \pm s(x)$ and $\tau(x) \sim \pm \int s(x)\,dx$. This would give $\tau'' \sim \pm s'$, so that the second approximation for τ satisfies $(\tau')^2 = s^2 \pm is'/\omega$, i.e., $\tau' = \pm s + is'/2s\omega$, and then $\tau(x) = \pm \int s(x)dx + (i/2\omega)\log s$. Corresponding general WKBJ solutions for ϕ in the region above the turning point ($x > x_p, s^2 > 0$) are therefore

$$\phi(x) \sim \frac{A}{\sqrt{s(x)}} \exp\left(i\omega \int_{x_p}^{x} s\,dx\right) + \frac{B}{\sqrt{s(x)}} \exp\left(-i\omega \int_{x_p}^{x} s\,dx\right) \tag{2}$$

(A and B are constants). This is valid provided $|s'/\omega| \ll |s^2|$. Since, very crudely, $\omega s \times$ wavelength $= 2\pi$, the validity condition amounts to $|s' \times$ wavelength$| \ll 2\pi|s|$, and the change in $s(x)$ in one wavelength must be much less than s itself. Clearly, (2) will be invalid near $x = x_p$ where s is zero.

Note that s is imaginary in the exponential region ($x < x_p$), so that an appropriate notation for the general WKBJ solution below the turning point ($x < x_p, s^2 < 0$) is

$$\phi(x) \sim \frac{C}{(-s^2)^{1/4}} \exp\left[\omega \int_{x}^{x_p} \sqrt{-s^2}\,dx\right] + \frac{D}{(-s^2)^{1/4}} \exp\left[-\omega \int_{x}^{x_p} \sqrt{-s^2}\,dx\right]. \tag{3}$$

If C is nonzero, then there is an exponentially growing component in the solution as x decreases below x_p, and in practice it dominates in this region, whatever the value of D. To remove this growing solution we require $C = 0$, leaving only the special solution that exponentially decays as x decreases below x_p. Given a value of D, this special solution is

(continued)

BOX **9.6** *(continued)*

defined by (1) in all ranges of x, and we seek to find its asymptotic expression in the form (2) for the region above the turning point. What then are the special values of A and B, in terms of D, for the special solution such that $C = 0$ below the turning point? We cannot simply carry (3) up to the turning point, equate it there to (2), and then continue upward, because both these formulas are invalid near the turning point, having singularities at $x = x_p$ that are absent from the actual solution $\phi(x)$. Instead we have to find the connection between the exponentially decaying solution and the two propagating solutions summed in (2), using a method that avoids use of (2) and (3) near the turning point itself. We shall use the method suggested by Rayleigh (1912), based on Airy functions.

We note that $Ai(-y)$ is a solution of $d^2w/dy^2 + yw = 0$, which is a special example of our equation (1). The following results are known (Abramowitz and Stegun, 1964, formulas 10.4.59–60):

$$\begin{aligned} Ai(-y) &\sim \pi^{-1/2} y^{-1/4} \cos[\tfrac{2}{3}y^{3/2} - \pi/4] \qquad \text{as } y \to \infty, \\ Ai(-y) &\sim \tfrac{1}{2}\pi^{-1/2}(-y)^{-1/4} \exp[-\tfrac{2}{3}(-y)^{3/2}] \qquad \text{as } y \to -\infty. \end{aligned} \tag{4}$$

Thus $Ai(-y)$ is the special solution that has exponential decay below the turning point.

Near $x = x_p$, we approximate $s^2(x)$ by $s^2 = \lambda(x - x_p)$, where $\lambda = ds^2/dx$ at $x = x_p$. Then the decaying solution in (3) is

$$\frac{D}{\lambda^{1/4}(x_p - x)^{1/4}} \exp[-\tfrac{2}{3}\omega\lambda^{1/2}(x_p - x)^{3/2}]$$

for very large ω and x just below x_p. Comparing with the second of (4), this is

$$2D\pi^{1/2}(\omega/\lambda)^{1/6}\, Ai(-\omega^{2/3}\lambda^{1/3}(x - x_p)). \tag{5}$$

But now we can use the *first* of (4) to find how this solution behaves just above the turning point. It must be like

$$\frac{2D}{\lambda^{1/4}(x - x_p)^{1/4}} \cos[\tfrac{2}{3}\omega\lambda^{1/2}(x - x_p)^{3/2} - \pi/4]. \tag{6}$$

However, in this region, it is given by (2) as

$$\frac{1}{\lambda^{1/4}(x - x_p)^{1/4}}\{A \exp[i\tfrac{2}{3}\omega\lambda^{1/2}(x - x_p)^{3/2}] + B \exp[-i\tfrac{2}{3}\omega\lambda^{1/2}(x - x_p)^{3/2}]\}. \tag{7}$$

Comparing (6) and (7), we conclude that

$$A = De^{-i\pi/4}, \qquad B = De^{+i\pi/4}, \tag{8}$$

and we have finally found the asymptotic behavior above the turning point for the solution that decays below.

Actually, the equation to which we wish to apply this method is

$$\frac{d^2}{dr^2}(ra) + \left(\frac{\omega^2}{\alpha^2} - \frac{l(l+1)}{r^2}\right) ra = 0. \qquad \text{(cf. 9.55)} \tag{9}$$

(continued)

BOX **9.6** *(continued)*

There is a singularity at $r = 0$ that we remove by working with x via $r = r_0 e^{x/x_0}$ (the Earth-flattening transformation again; r_0 and x_0 are constants). Then $\sqrt{r}a(r,l) = \phi$ satisfies

$$\frac{d^2\phi}{dx^2} + \frac{r_0^2}{x_0^2} e^{2x/x_0} \left[\frac{\omega^2}{\alpha^2} - \left(\frac{l+\frac{1}{2}}{r_0 e^{x/x_0}} \right)^2 \right] \phi = 0,$$

which *is* in the form (1). Terms like $\omega \int_{x_p}^{x} s\, dx$ become

$$\omega \int_{r_p}^{r} \sqrt{\frac{1}{\alpha^2} - \left(\frac{l+\frac{1}{2}}{\omega r'} \right)^2}\, dr',$$

and the exponentially decaying solution for $a(r,l)$ is approximately given by

$$ra(r,l) = \sqrt{r}\phi \sim \frac{D}{\left[\left(\frac{l+\frac{1}{2}}{\omega r} \right)^2 - \frac{1}{\alpha^2} \right]^{1/4}} \exp \left\{ -\omega \int_{r}^{r_p} \sqrt{\left(\frac{l+\frac{1}{2}}{\omega r'} \right)^2 - \frac{1}{\alpha^2}}\, dr' \right\} \quad (10)$$

in the region $r < r_p$. This same solution $a(r,l)$ is given, above the turning point ($r > r_p$), by

$$ra(r,l) = \sqrt{r}\phi \sim \frac{D}{\left[\frac{1}{\alpha^2} - \left(\frac{l+\frac{1}{2}}{\omega r} \right)^2 \right]^{1/4}} \left[\exp\left(i\omega\tau - i\frac{\pi}{4} \right) + \exp\left(-i\omega\tau + i\frac{\pi}{4} \right) \right], \quad (11)$$

where

$$\tau = \int_{r_p}^{r} \sqrt{\frac{1}{\alpha^2} - \left(\frac{l+\frac{1}{2}}{\omega r'} \right)^2}\, dr'.$$

Several of the special functions used in applied mathematics have widely used approximations that are particular examples of (2) and (3). An example has already been given in (4) for the Airy function. Others include spherical Hankel functions $h_l^{(1)}(\omega r/\alpha)$ and $h_l^{(2)}(\omega r/\alpha)$ (in which α is constant), for which the corresponding WKBJ formula (10), known in this case as the Debye approximation to $h_l^{(1)} + h_l^{(2)}$, has the normalization $D = \sqrt{\alpha}/\omega$. Since α in this case is constant, τ in (11) can be integrated to

$$\sqrt{\frac{r^2}{\alpha^2} - \left(\frac{l+\frac{1}{2}}{\omega} \right)^2} + \frac{(l+\frac{1}{2})}{\omega} \sin^{-1}\left[\frac{(l+\frac{1}{2})\,\alpha}{\omega r} \right].$$

The spherical Bessel function $j_l(\omega r/\alpha)$ is approximated by (10), with $D = \sqrt{\alpha}/2\omega$ when $r < r_p = p\alpha$.

(continued)

BOX **9.6** *(continued)*

The WKBJ approximation to Legendre's equation gives

$$P_l(\cos\Delta) \sim \sqrt{\frac{1}{2\pi l \sin\Delta}} \left\{ \exp\left[-i(l+\tfrac{1}{2})\Delta + \frac{i\pi}{4}\right] + \exp\left[+i(l+\tfrac{1}{2})\Delta - \frac{i\pi}{4}\right] \right\}, \quad (12)$$

and in this case the "turning point" (where (12) breaks down) occurs for $\sin\Delta = 0$, e.g., $\Delta = 0$ and π. Note that (12) is a standing wave, proportional to $\cos[(l+\frac{1}{2})\Delta - \pi/4]$, although it has been written in traveling-wave components (cf. (9.64)).

Similarly, from WKBJ theory, we have

$$f_l(r) \sim \frac{\sqrt{\alpha_s}}{2\omega r} \cdot \frac{1}{\left[\dfrac{p^2}{r^2} - \dfrac{1}{\alpha^2}\right]^{1/4}} \cdot \exp\left\{ -\omega \int_r^{r_p} \sqrt{\frac{p^2}{(r')^2} - \frac{1}{\alpha^2(r')}}\, dr' \right\} \quad (9.61)$$

in the region for which $r/\alpha(r) < p$, (i.e., $r < r_p$), so that $f_l(r)$ is exponentially decaying with depth below the turning point. The normalization implied by (9.61) is such as to make $f_l(r) = j_l(\omega r/\alpha_s)$ (the spherical Bessel function) in a homogeneous medium.

The three functions $f_l, g_l^{(1)}, g_l^{(2)}$ are solutions in all ranges of radius, and it is important to obtain and to understand the connection formula between them. From Box 9.6, we find it is the same relation as that for spherical Bessel/Hankel functions, i.e., the connection formula is simply

$$f_l(r) = \tfrac{1}{2}[g_l^{(1)}(r) + g_l^{(2)}(r)]. \quad (9.62)$$

The physical interpretation is that amplitudes decay below the turning point. But above, there is a standing wave composed of downgoing and upgoing components, just as the ray first goes down to the turning point and then up. Below the turning point, each of $g_l^{(1)}$ and $g_l^{(2)}$ will grow exponentially with depth.

With the normalization above, it is now possible to evaluate the Wronskian. We find $W(r) = -i\alpha_s/(\omega r^2)$ exactly. Thus, from (9.54), (9.56), (9.57), and (9.62) we finally obtain

$$P(\mathbf{r}, \omega) = -\frac{iK_s\omega}{4\pi\alpha_s} \sum_{l=0}^{\infty} (l+\tfrac{1}{2}) g_l^{(1)}(r_>)[g_l^{(1)}(r_<) + g_l^{(2)}(r_<)] P_l(\cos\Delta) \quad (9.63)$$

where $r_>$ = greater of (r, r_s), and $r_<$ = lessor of (r, r_s).

It is often useful to split the Legendre function into its traveling-wave components,

$$P_l = Q_l^{(1)} + Q_l^{(2)}, \qquad \text{where } Q_l^{(1)}_{(2)}(\cos\Delta) \sim \frac{\exp\{\mp i[(l+\frac{1}{2})\Delta - \pi/4]\}}{\sqrt{2\pi l \sin\Delta}} \quad (9.64)$$

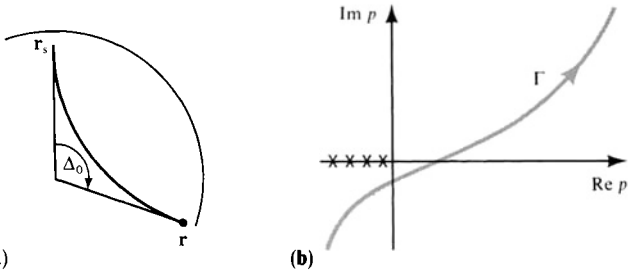

FIGURE **9.28**
(a) Parameters for a ray departing downward from source to receiver. A turning point is present. **(b)** Associated integration path Γ. See equation (9.65). [From Richards, 1973a.]

for large l (provided that l is not near a negative integer and that Δ is not near 0 or 180°). Recall for Cartesian coordinates that the horizontal wavefunction is $e^{i\omega px}$, in which p is the horizontal slowness/ray parameter. Similarly, from (9.64), we can recognize $(l + \frac{1}{2})/\omega$ as the ray parameter in spherical geometry, as indicated already in (9.59).

The result (9.63) is conceptually similar to the Sommerfeld integral, in the sense that it shows how the waves from a simple point source can be expanded in vertical and horizontal wavefunctions appropriate to the coordinate system in which boundary conditions can easily be analyzed. However, although the partial wave expansion (9.63) is a convergent series, the individual terms do not significantly decrease until l is large enough to make $g_l^{(1)}(r_<) + g_l^{(2)}(r_<)$ exponentially decaying. This requires l greater than $\omega r_< \div \alpha(r_<)$. Since $r_<$ is usually several thousand kilometers and $\alpha(r_<)$ is about 10 km/s, several thousand terms in (9.63) would have to be summed to study short-period (1- or 2-s) body waves! Such numerical difficulty is effectively avoided by converting the summation over l into an integral (the Watson or Poisson transform), and then direct integration is simple to carry out after a suitable contour is found in the (complex) order plane. A rigorous derivation of the suitable contour is not easy (Nussenzveig, 1965; Ansell, 1978), since (9.63) is essentially a sum of four different types of waves. Each is of type $g_l^{(j)}(r_<)Q_l^{(k)}$, with $j = 1$ or 2, $k = 1$ or 2, and can be recognized in terms of downward or upward departure from $r_<$ to $r_>$ and of arrival toward or away from the source. But if the series (9.63) is separated into four series, one for each wave type, each series *diverges*. Some intricate manipulations of the series and integration paths are needed to avoid the divergence, and in Box 9.7 we give an example for the most important case, that illustrated in Figure 9.28, in which a turning point is present.

Although the rigorous manipulation of partial wave expansions is laborious, the results make sense in that the physical traveling wave of interest can still be identified in the partial wave expansion. The effect of using complex integration paths is twofold: to eliminate all unwanted traveling waves; and to obtain a computationally attractive integral for the remainder. Thus, for source and receiver as shown in Figure 9.28a, the result (2) of Box 9.7 identifies precisely the traveling wave one should expect. We obtain

$$P(\mathbf{r}, \omega) = \frac{-iK_s\omega^3}{4\pi\alpha_s} \int_\Gamma p g^{(1)}_{\omega p - \frac{1}{2}}(r) g^{(1)}_{\omega p - \frac{1}{2}}(r_s) Q^{(2)}_{\omega p - \frac{1}{2}}(\cos\Delta)\, dp, \qquad (9.65)$$

in which p is ray parameter ($\nu = l + \frac{1}{2} = \omega p$), and Γ, shown in Figure 9.28b, can be deformed to cross any convenient point or points of the positive real p-axis.

BOX **9.7**

A sample application of the Watson transform

This is a device for converting sums to integrals. Using poles of sec $\nu\pi$ at $\nu = \frac{1}{2}, 1\frac{1}{2}, 2\frac{1}{2}, \ldots$, the transform is

$$\sum_{l=0}^{\infty} f(l+\tfrac{1}{2}) = \tfrac{1}{2}\int_C f(\nu)e^{-i\nu\pi}\sec\nu\pi\, d\nu, \tag{1}$$

where C is taken around the positive real ν-axis as shown in the first figure.

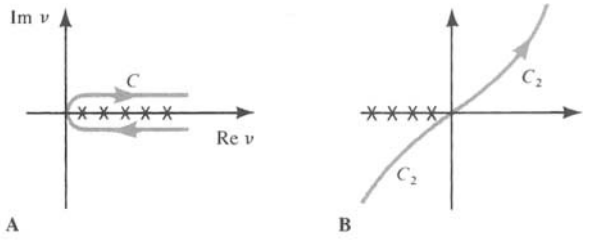

Figure A shows the path for Watson transformation. Poles occur all along the real axis and are shown for positive ν at $\nu = l + \frac{1}{2}; l = 0, 1, 2, \ldots$. Figure B shows a deformation of C for the direct ray with a turning point, after the $Q^{(2)}_{-\nu-\frac{1}{2}}$ integration is reflected in the origin.

We shall apply (1) to the partial wave expansion (9.63) in the case that the ray from source $\mathbf{r}_s$ to receiver $\mathbf{r}$ has a turning point. This configuration is shown in Figure 9.28a, and using $P_l(\cos\Delta) = e^{il\pi}P_l(-\cos\Delta)$ we find

$$P(\mathbf{r},\omega) = -\frac{K_s\omega}{4\pi\alpha_s}\int_C \nu g^{(1)}_{\nu-\frac{1}{2}}(r) f_{\nu-\frac{1}{2}}(r_s) P_{\nu-\frac{1}{2}}(-\cos\Delta)\sec\nu\pi\, d\nu.$$

To manipulate this integrand and integration path into a more useful form, many special properties of the vertical and horizontal wavefunctions must be deployed to avoid divergent integrals at intermediate steps. Thus it follows from Nussenzveig (1965) that C may be deformed across the fourth quadrant, and parts of the first and third, into the path C_2, which is symmetric about the origin (see figure). At this stage, the integrand still has poles on the positive real ν-axis. Writing

$$P_{\nu-\frac{1}{2}}(-\cos\Delta)\sec\nu\pi = [-e^{-i\nu\pi}Q^{(2)}_{\nu-\frac{1}{2}}(\cos\Delta) + e^{i\nu\pi}Q^{(2)}_{-\nu-\frac{1}{2}}(\cos\Delta)]\csc\nu\pi$$

allows the integral along C_2 to be split into two terms. Replacing ν by $-\nu$ in the integral containing $Q^{(2)}_{-\nu-\frac{1}{2}}$, and using $g^{(1)}_{-\nu-\frac{1}{2}}(r_s)e^{-i\nu\pi} = g^{(1)}_{\nu-\frac{1}{2}}(r_s)$ and

$$f_{-\nu-\frac{1}{2}}(r_s) = f_{\nu-\frac{1}{2}}(r_s)e^{-i\nu\pi} + i\sin\nu\pi\, g^{(1)}_{\nu-\frac{1}{2}}(r_s),$$

we get

$$P(\mathbf{r},\omega) = -\frac{iK_s\omega}{4\pi\alpha_s}\int_{C_2}\nu g^{(1)}_{\nu-\frac{1}{2}}(r) g^{(1)}_{\nu-\frac{1}{2}}(r_s) Q^{(2)}_{\nu-\frac{1}{2}}(\cos\Delta)\, d\nu. \tag{2}$$

(continued)

BOX **9.7** *(continued)*

We note that (i) the final integral here can be identified with just one of the four traveling-wave terms present in the partial wave expansion (9.63); (ii) the factor $Q^{(2)}_{\nu-\frac{1}{2}}(\cos\Delta)$ in (2) has poles only on the negative real axis, so that C_2 can now be distorted to cross the positive real ν-axis wherever convenient; (iii) if there is no turning point present between $\mathbf{r}_s$ and $\mathbf{r}$, e.g., if the ray is everywhere going upward, then the expected traveling-wave term in (9.63) is $g_l^{(1)}(r)g_l^{(2)}(r_s)Q_l^{(2)}(\cos\Delta)$.

The effect of discontinuities in the Earth, such as the core–mantle boundary, is examined in the next section. We shall find it necessary to include reflection and transmission coefficients in the integrand of (9.65). However, the effect of multipathing between source and receiver, of the type shown in Figure 9.12b,c, is already included in (9.65). Implicit in our definition of $g_l^{(j)}$ is the assumption that just one turning point r_p solves $p = r/\alpha(r)$, hence low-velocity zones have been excluded. (WKBJ expressions may be modified to permit a relaxation of this assumption.) Because the $T - \Delta$ curve has no gaps, the branches of the travel-time curve are such as to give one ray, three rays, or, in general, some odd number of rays between source and receiver.

The uses made of (9.65) have included the computation of the vertical wavefunctions directly (by integration of the equations of motion), followed by integration as in (9.65) over a path Γ chosen near a steepest descents path (Chapman and Phinney, 1972). However, approximations for the wavefunctions are often adequate, and this permits much more rapid computation. We shall first discuss WKBJ approximations, applied to the radial displacement derived from (9.65) for a receiver at distance Δ_0 from the source. Then, from (9.50a), (9.60), and (9.64),

$$u_r(r, \Delta_0, \omega) = \sqrt{\frac{1}{\rho(r)}\frac{\partial P}{\partial r}} = \frac{K_s e^{-3i\pi/4}\omega^{3/2}}{\sqrt{2\pi\rho(r)\sin\Delta_0}}\frac{1}{4\pi r r_s}\int_\Gamma \sqrt{\frac{p\xi(r)}{\xi(r_s)}}e^{i\omega J}\,dp, \quad (9.66)$$

where the phase-delay integral is

$$J = J(p) = p\Delta_0 + \int_{r_p}^{r_s} \xi\,dr + \int_{r_p}^{r} \xi\,dr.$$

As pointed out in (9.22), $\int \xi\,dr$ is related to the travel-time and distance integrals, so that

$$J = p\Delta_0 + T(p) - p\,\Delta(p) = p\Delta_0 + \tau(p), \quad (9.67)$$

where $T(p)$ and $\Delta(p)$ are the time and distance at which the ray with ray parameter p arrives at radius r from the source at level r_s. Since $\partial J/\partial p = \Delta_0 - \Delta(p)$ (see (9.23)), it follows that the integrand for u_r has saddle points at values of p such that $\Delta(p) = \Delta_0$, i.e., at just the ray parameters for which there is a ray between source and receiver. Near such a

saddle point p_0 (say), Taylor series expansion gives

$$J(p) = T(p_0) + \tfrac{1}{2}(p - p_0)^2(-\partial\Delta/\partial p). \tag{9.68}$$

If there is just one real ray between $\mathbf{r}$ and $\mathbf{r}_s$, then $\partial\Delta/\partial p$ is negative (the AB branch in Fig. 9.13), and the saddle is oriented favorably for Γ to be taken as the path of steepest descent, leading to the approximation of (9.66) by

$$u_r(r, \Delta_0, \omega) \sim \frac{-iK_s\omega}{4\pi}\sqrt{\frac{\alpha_s}{\rho\alpha}}\frac{e^{i\omega T}}{rr_s}\left[\frac{\cos i_s \sin\Delta_0}{p_0 \cos i}\left(-\frac{\partial\Delta}{\partial p}\right)\right]^{-1/2}.$$

Identifying the geometrical spreading via

$$\alpha_s\mathcal{R}(\mathbf{r}, \mathbf{r}_s) = rr_s\sqrt{\cos i \cos i_s \sin\Delta_0 |\partial\Delta/\partial p|/p_0} \tag{9.69}$$

(see Problem 4.4), we have

$$u_r(r, \Delta_0, \omega) \sim \frac{-iK_s\omega}{4\pi\sqrt{\rho\alpha\alpha_s}}\frac{e^{i\omega T}}{\mathcal{R}(\mathbf{r}, \mathbf{r}_s)}\cos i(r). \tag{9.70}$$

We have described the source strength by K_s. If the P-wave source is described instead by its moment tensor $M_{ij}(t) = M_I(t)\delta_{ij}$, then the body force is $f_i(\mathbf{x}, t) = -M_I(t)\,\partial\delta(\mathbf{x} - \mathbf{r}_s)/\partial x_i$. To relate K_s and M_I when gradients of material properties in the source region are small, note that dominant terms in the vector wave equation (Box 9.5, equation (1)) become $\rho\omega^2\mathbf{u} + \nabla(\rho\alpha^2\nabla\cdot\mathbf{u}) = \nabla[M_I(\omega)\delta(\mathbf{x} - \mathbf{r}_s)]$, and with $\mathbf{u} = \rho^{-1/2}\nabla P$ this gives (comparing with (9.51)) $K_s = M_I(\omega)/(\sqrt{\rho_s}\alpha_s^2)$. In the time domain we therefore find from (9.70) that

$$u_r(r, \Delta_0, t) \sim \frac{\cos i(r)\dot{M}_I(t - T)}{4\pi\sqrt{\rho(r)\rho_s\alpha(r)\alpha_s^5}\,\mathcal{R}(\mathbf{r}, \mathbf{r}_s)}, \tag{9.71}$$

which is exactly what geometrical ray theory would predict.

A more complex configuration is shown in Figure 9.29, where for the distance Δ_0 there are five ray parameters that solve the equation $\Delta(p) = \Delta_0$. The second derivative of the phase integral, $-\omega\,\partial\Delta/\partial p$, is alternately positive and negative, giving saddles with the orientation shown in Figure 9.29b. Γ may be chosen to cross each saddle by the steepest descents path to give approximations of the type (9.71) for the first, third, and fifth saddles. For the second and fourth, the approximation is of type (9.71) times $(-i)$, i.e., with a $\pi/2$ phase advance. Inverting to the time domain, arrivals corresponding to even-numbered saddles have pulse shapes that are the Hilbert transform of those for odd numbers. The phenomenon of a caustic occurs at special distances Δ_c for which the equation $\Delta_c = \Delta(p)$ has a double root (at p_c, say), so that $\partial\Delta/\partial p$ is zero at $p = p_c$. Figure 9.30 describes wavefunction properties in this case, and the point to emphasize is that (9.66) is still quite easily evaluated numerically, after generalizing programs to compute T and Δ for complex ray parameter. In this way, Richards (1973a) described the effect of the caustic in *PKKP* on amplitudes near 240°.

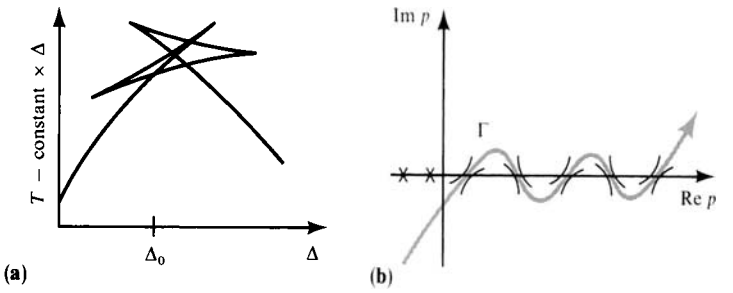

FIGURE **9.29**
(a) A reduced travel-time curve, with two overlapping triplications. **(b)** Integration path in the complex ray-parameter plane crossing five saddles, each at a value of p satisfying $\Delta(r, p) = \Delta_0$. [From Richards, 1973a.]

Chapman (1976b) has described how representations like (9.66) can be written in the time domain as a sum of convolutions. The result is important, because it leads to perhaps the simplest useful method of synthesizing seismograms when multiple arrivals and caustics can be present. Remarkably, the method has close links to the Cagniard technique, although it works even when turning points are present. We begin with (9.66), but using an isotropic moment tensor $M_{ij} = M_{\mathrm{I}}(\omega)\delta_{ij}$ so that

$$u_r(r, \Delta_0, \omega) = \frac{-i\omega M_{\mathrm{I}}(\omega)\, e^{-i\pi/4}\omega^{1/2}}{\sqrt{2\pi\rho\rho_{\mathrm{s}} \sin \Delta_0\, 4\pi r r_{\mathrm{s}}\alpha_{\mathrm{s}}^2}} \int_\Gamma B(p) e^{i\omega J(p)}\, dp, \tag{9.72}$$

where

$$B(p) = \sqrt{\frac{p\xi(r)}{\xi_{\mathrm{s}}}} = \sqrt{p}\left(\frac{1}{\alpha^2} - \frac{p^2}{r^2}\right)^{1/4} \Big/ \left(\frac{1}{\alpha_{\mathrm{s}}^2} - \frac{p^2}{r_{\mathrm{s}}^2}\right)^{1/4}.$$

In the time domain, this becomes (see Box 9.8)

$$u_r(r, \Delta_0, t) = \frac{\dot{M}_{\mathrm{I}}}{\sqrt{2\pi\rho\rho_{\mathrm{s}} \sin \Delta_0\, 4\pi r r_{\mathrm{s}}\alpha_{\mathrm{s}}^2}} * \frac{d}{dt}\frac{H(t)}{\sqrt{\pi t}} * \frac{1}{\pi}\mathrm{Re}\int_0^\infty \int_\Gamma B(p) e^{i\omega(J-t)} dp\, d\omega. \tag{9.73}$$

But the last of the three functions of time convolved here, given as an inverse Fourier integral, can be recognized in the time domain as $f(t)$ with

$$f(t) = \mathrm{Re}\int_\Gamma B(p)\, \delta[J(p) - t]\, dp. \tag{9.74}$$

Therefore, the integrand makes a contribution precisely from p-values for which $J(p)$ is equal to t. Such p-values are parameterized by real t, and are, in part, identical to values on a Cagniard path. To see this, we consider first a simple case where just one ray parameter p_0 solves $\Delta(p) = \Delta_0$, with travel time t_0 between $\mathbf{r}_{\mathrm{s}}$ and $\mathbf{r}$ (Fig. 9.28). The

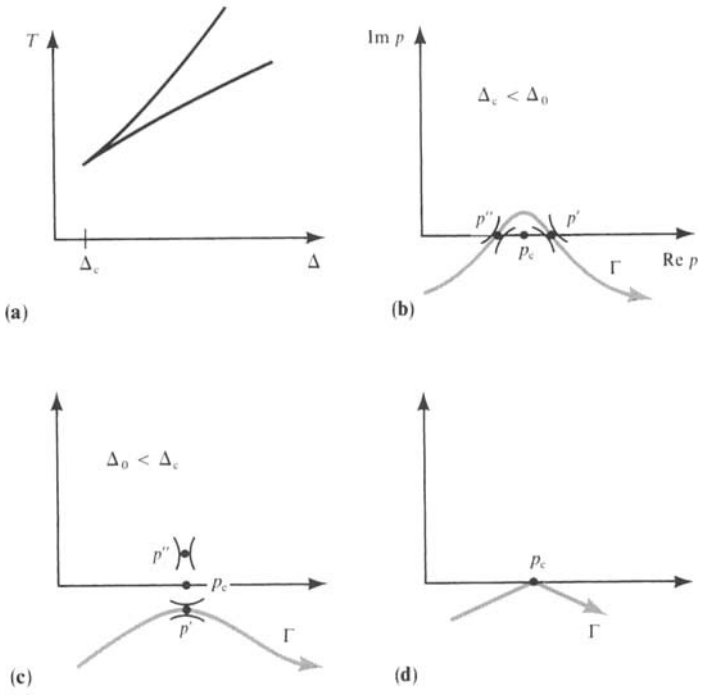

FIGURE **9.30**
Behavior of saddle points near a caustic. **(a)** Two branches of $T = T(\Delta)$ touch at the distance Δ_c, where there is a caustic. **(b)** For distances Δ_0 just greater than Δ_c, two real solutions of $\Delta(p) = \Delta_0$ are present, each giving a saddle point on the real p-axis. As Δ_0 moves through Δ_c, these two saddles merge at p_c, and then **(c)** for distances Δ_0 just less than Δ_c, two complex conjugate solutions of $\Delta(p) = \Delta_0$ are present, one parallel to and below the real p-axis, and the latter solution gives the steepest descents path. **(d)** Two straight-line segments are shown, which are adequate for numerical evaluation of (9.66) in both cases $\Delta_0 \gtrless \Delta_c$. [After Richards, 1973a.]

quantity $J(p) = p\Delta_0 + T(p) - p\Delta(p)$ is shown in Figure 9.31a, and its slope $\Delta_0 - \Delta(p)$ is zero at p_0, where $J(p) = t_0$. For times greater than t_0, the equation

$$t = J(p) \tag{9.75}$$

has two roots, which Chapman (1976b) labels $\pi_1(t)$ and $\pi_2(t)$. In fact, equation (9.75) is just like an equation for a Cagniard path, $t = p\Delta_0 + \tau(p)$. Previously, we have had an interest in just one root, and we have followed it off the real p-axis for times later than some ray-arrival time. Here we shall keep both roots and hold Γ only to the real p-axis (in the vicinity of p_0) so that complex ray-parameter values are avoided. The paths $\pi_1(t)$ and $\pi_2(t)$, shown in Figure 9.31b, have real values only for $t \geq t_0$. Note that the direction taken along $\pi_1(t)$ as t increases is opposite to the direction familiar from Chapter 6 and Section 9.1. The reason is that $\partial\Delta/\partial p$ is now negative at p_0, and values along $\pi_j(t)$ near p_0 are given via the Taylor expansion

$$t = t_0 + \tfrac{1}{2}(\pi_j - p_0)^2 \frac{\partial^2 J}{\partial p^2} = t_0 - \tfrac{1}{2}(\partial\Delta/\partial p)|_{p_0}(\pi_j - p_0)^2. \tag{9.76}$$

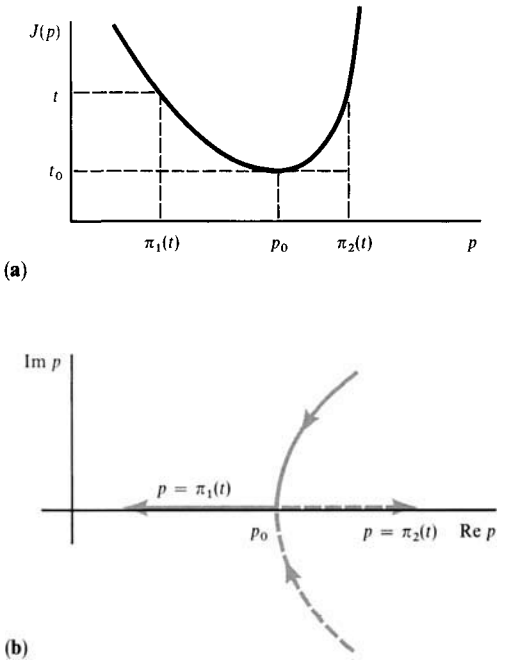

FIGURE **9.31**
(a) The function $J(p)$ is obtained from $\tau(p)$ (Fig 9.14d) by adding a linear term $p\Delta_0$. A minimum at p_0 corresponds to time $t_0 = J(p_0)$. **(b)** The paths $p = \pi_j(t)$ of solutions to $t = J(p)$, *which lie on the real p-axis* for $t > t_0$.

Once the real solutions $\pi_j = \pi_j(t)$ of (9.75) are known, we can approximate the delta-function argument in (9.74) by

$$J(p) - t = (p - \pi_j)\frac{\partial J}{\partial p}\bigg|_{\pi_j} = (p - \pi_j)[\Delta_0 - \Delta(\pi_j)]$$

near each $\pi_j(t)$. There is no basis for including higher order terms here, since the expression being approximated is itself the outcome of a WKBJ approximation. Thus, (9.73) becomes

$$u_r(r, \Delta_0, t) = \frac{\dot{M}_I}{\sqrt{2\rho\rho_s \sin\Delta_0}\, 4\pi^2 r r_s \alpha_s^2} * \frac{d}{dt}\frac{H(t)}{\sqrt{t}} * \sum_j \frac{B(\pi_j)}{|\Delta_0 - \Delta(\pi_j)|}. \quad (9.77)$$

To work with, this result is similar to our earlier Cagniard-derived solutions, but without the complex arithmetic. To be reassured that geometrical ray theory is contained in (9.77), we expand $\Delta_0 - \Delta(\pi_j)$ near p_0 as $(-\partial\Delta/\partial p)_{p_0}(\pi_j - p_0)$ and then use (9.76) to write

$$\Delta_0 - \Delta(\pi_j) \sim \sqrt{-2\,\partial\Delta/\partial p|_{p_0}}\,\sqrt{t - t_0}. \quad (9.78)$$

From convolutions in (9.77) and Box 9.8, it follows that each of the two terms ($j = 1, 2$) contributes just half the geometrical approximation (9.71).

BOX 9.8
Useful transform pairs

Because our time series are real, their Fourier transforms have real parts that are even in frequency and imaginary parts that are odd. With this understood, we write formulas only for positive real frequencies: $f(t) = (1/\pi)\ \mathrm{Re}\ \int_0^\infty f(\omega)\exp(-i\omega t)\,d\omega$. The connections between convolutions with $t^{-1/2}$ and multiplication by $\omega^{-1/2}$ are then based on the following transform pairs:

Frequency	*Time*
$e^{i\pi/4}\sqrt{\dfrac{\pi}{\omega}}$	$\dfrac{H(t)}{\sqrt{t}}$
$e^{-i\pi/4}\sqrt{\dfrac{\pi}{\omega}}$	$\dfrac{H(-t)}{\sqrt{-t}}$
$e^{-i\pi/4}\sqrt{\pi\omega}$	$\dfrac{d}{dt}\dfrac{H(t)}{\sqrt{t}}$
$e^{i\pi/4}\sqrt{\pi\omega}$	$-\dfrac{d}{dt}\dfrac{H(-t)}{\sqrt{-t}}$.

The Hilbert transform of $H(t)/\sqrt{t}$ is $H(-t)/\sqrt{-t}$, and a basic transform to remember is

$$\frac{H(t)}{\sqrt{t}} * \frac{H(t-T)}{\sqrt{t-T}} = \pi H(t-T).$$

Convolutions that contain the Hilbert transform operator and the operator d/dt can be written in many different forms by using commutative properties and associating these operators with different functions. Thus

$$\frac{d\psi}{dt} * \frac{H(t)}{\sqrt{t}} * \frac{H(t-T)}{\sqrt{t-T}} = \psi * \frac{d}{dt}[\pi H(t-T)] = \pi\psi(t-T),$$

and

$$\psi(t) * \left[-\frac{d}{dt}\frac{H(-t)}{\sqrt{-t}} * \frac{H(T-t)}{\sqrt{T-t}}\right] = \left(-\frac{d\psi}{dt}\right) * (-\pi H(t-T)) = \pi\psi(t-T).$$

To get geometrical ray theory out of (9.77)–(9.78), we use

$$\frac{d}{dt}\frac{H(t)}{\sqrt{t}} * \frac{H(t-t_0)}{\sqrt{t-t_0}} = \pi\delta(t-t_0).$$

The main virtue of (9.77) is that multipathing and caustics are handled straightforwardly. Thus, in Figure 9.32 is shown a more complicated travel-time curve, with three solutions p_1, p_2, p_3 to $\Delta(p) = \Delta_0$. There are four solutions to $t = J(p)$, and it is fairly clear how to apply (9.77). The caustics at B and C are inflections in $J = J(p)$, and if Δ_0 is a caustic then the corresponding inflection in Figure 9.32d is horizontal. Instead of (9.78) one now finds that $\Delta_0 - \Delta(\pi_j) \propto (t - t_0)^{2/3}$, which gives strong amplitudes via (9.77).

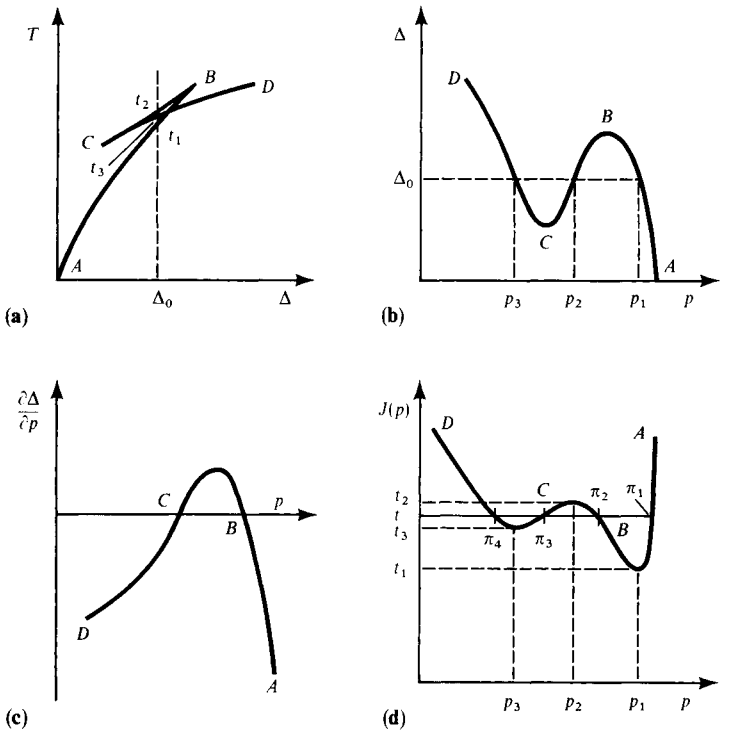

FIGURE **9.32**
A travel-time curve with caustics at B and C, and derived curves. Geometrical ray quantities are indicated for a distance Δ_0 in the triplication. **(a)** Travel-time curve with arrivals at t_1, t_3, t_2. **(b)** $\Delta = \Delta(p)$, with three solutions p_1, p_2, p_3 to $\Delta(p) = \Delta_0$. **(c)** Zeros in $\partial\Delta/\partial p$ occur at B and C. **(d)** The construction of solutions $\pi_j(t)$ to $t = J(p)$ is shown for a particular distance Δ_0. [After Chapman, 1976b; copyright by the American Geophysical Union.]

It is interesting that (9.77) was discovered by methods quite different from the one we have followed. Thus, Chapman (1976a) investigated Cagniard's method for large numbers of homogeneous plane layers, and was able to obtain an expression for the generalized primary reflection (see (9.6)). He summed over all interfaces and took the limit as the layer thicknesses all shrank to zero. Near wavefronts, the expression was $\pi/3$ times that given in (9.77) (but adapted for plane layering). For turning-point rays, this implies the surprising result that fine layering and large numbers of primary reflections do not, in the limit, give the geometrical ray theory formula at wavefronts. Rather, the total effect of primaries is about 5% too large. However, tertiary reflections (triply reflected waves) tend in the limit to $-\pi^3/648$ times (9.77) near wavefronts, and Chapman showed from $(2l + 1)$th order reflections that the wavefront approximation was $2(-1)^l(\pi/6)^{2l+1}/(2l + 1)!$ times (9.77). Adding successive orders of reflection does then give a rapidly converging series, which does converge to (9.77) because

$$\frac{\pi}{3} - \frac{\pi^3}{648} + \cdots = 2 \sin \frac{\pi}{6} = 1.$$

Wiggins (1976a) formulated another approach, identifying $J(p)$ as the arrival time at Δ_0 of a wavefront (or "disc") with slowness p. By picking equal time increments along the $J(p)$ curve, he obtained a discrete version of (9.77) and called this *disc-ray theory*. Chapman (1978a) suggested that an appropriate name for the solution (9.77) is the *WKBJ seismogram*. This is appropriate, because it is an expression in the space/time domain that is equivalent to WKBJ approximations in the ray-parameter/frequency domain. The WKBJ seismogram is quickly computed, and in many cases it is probably the method that should be preferred for investigating waveforms. We have obtained it as a special example of what Chapman (1978a,b) has called the *slowness method*, i.e., intermediate results (after the frequency integration) are obtained in the slowness (ray parameter) domain. However, in the next section we shall find that there are important examples in which WKBJ approximations are inaccurate, so that alternatives to (9.77) must be explored.

Throughout this section we have assumed a smoothly varying velocity profile. If discontinuities are to be allowed for, such as the Earth's free surface, then the associated reflections and transmission coefficients must be introduced. For the WKBJ seismogram, it turns out that these are simply plane-wave coefficients. Going beyond WKBJ theory, the principal techniques are well known (Scholte, 1956) for simple Earth models consisting of a few homogeneous shells, since in these the vertical wavefunctions are made up from spherical Hankel functions. It is found in such models that the wave path of interest (for example, *SKKP*) can be analyzed by isolating its partial wave series in an expression for the total response. This is conceptually the same exercise as identifying a particular generalized ray within an expression that quantifies an infinite family of rays (see Fig. 9.10). A Watson transform can still be used, but any path deformation in the complex p-plane must now take account of poles in the reflection/transmission coefficients for the ray path of interest. Most of these poles are located by studying properties of the WKBJ approximation to spherical Hankel functions, hence in more realistic Earth models, with radial variation of elastic properties between depths of discontinuity, we may still expect to locate relevant poles by using WKBJ formulas (9.60)–(9.61) for the generalized vertical wavefunctions $g^{(j)}_{\omega p-\frac{1}{2}}$. The rigorous analysis of path deformations needed to change the Watson path into paths such as Γ (Fig. 9.28) is a formidable project for realistic Earth models. However, several different canonical problems in wave propagation can be identified, and these are now well understood. In what follows, we shall emphasize *spectral methods*, in which intermediate results are obtained in the frequency domain (after an integration over complex ray parameter).

9.6 Body-Wave Problems for Spherically Symmetric Earth Models in Which Discontinuities are Present between Inhomogeneous Layers

A systematic treatment of the reflections and transmissions at discontinuities within the Earth is simplified if we develop an approach based on the motion-stress vector. Without this device, an *ad hoc* approach based (usually) on potentials must be used, and detailed algebraic manipulation must be carried out for each particular application. In this section, we shall develop the motion-stress vector for *P–SV* motion in spherically symmetric media, using a notation similar to that we have developed for homogeneous plane layers. The scattering matrix is easy to write down, and we shall go on to study several different body

waves including three canonical problems that illustrate the most important examples of departures from geometrical ray theory.

The appropriate horizontal wavefunctions to use are the vector surface harmonics introduced in Chapter 8. Our notation is based on the fully normalized surface harmonic $Y_l^m(\Delta, \phi)$ (see (8.5)), and

$$\begin{aligned}
\mathbf{R}_l^m(\Delta, \phi) &= Y_l^m \hat{\mathbf{r}}, \\
\mathbf{S}_l^m(\Delta, \phi) &= \frac{1}{\sqrt{l(l+1)}} \left(\frac{\partial Y_l^m}{\partial \Delta} \hat{\Delta} + \frac{1}{\sin \Delta} \frac{\partial Y_l^m}{\partial \phi} \hat{\boldsymbol{\phi}} \right), \\
\mathbf{T}_l^m(\Delta, \phi) &= \frac{1}{\sqrt{l(l+1)}} \left(\frac{1}{\sin \Delta} \frac{\partial Y_l^m}{\partial \phi} \hat{\Delta} - \frac{\partial Y_l^m}{\partial \Delta} \hat{\boldsymbol{\phi}} \right).
\end{aligned} \tag{9.79}$$

With these we make the expansions

$$\mathbf{u} = \mathbf{u}(r, \Delta, \phi, \omega) = (u_r, u_\Delta, u_\phi) = \sum_{l=0}^{\infty} \sum_{m=-l}^{l} [U_l^m \mathbf{R}_l^m + V_l^m \mathbf{S}_l^m + W_l^m \mathbf{T}_l^m], \tag{9.80}$$

and

$$\text{traction vector} = (\tau_{rr}, \tau_{r\Delta}, \tau_{r\phi}) = \sum_{l=0}^{\infty} \sum_{m=-l}^{l} [R_l^m \mathbf{R}_l^m + S_l^m \mathbf{S}_l^m + T_l^m \mathbf{T}_l^m].$$

We wish to solve for the six quantities U_l^m, V_l^m, W_l^m, R_l^m, S_l^m, T_l^m. Each is a function of (r, l, m, ω), and in this sense is the triple transform of a solution in the domain (r, Δ, ϕ, t), in which we are interested. For each inhomogeneous layer, only radial derivatives remain in the multitransformed equations of motion (2.47)–(2.50), and these separate into two groups, namely

$$\frac{d}{dr} \begin{pmatrix} V \\ U \\ S \\ R \end{pmatrix} = \begin{pmatrix} \frac{1}{r} & -\frac{\sqrt{l(l+1)}}{r} & \frac{1}{\mu} & 0 \\ \frac{\lambda\sqrt{l(l+1)}}{r(\lambda+2\mu)} & -\frac{2\lambda}{r(\lambda+2\mu)} & 0 & \frac{1}{\lambda+1\mu} \\ \frac{4l(l+1)\mu(\lambda+\mu)}{r^2(\lambda+2\mu)} - \rho\omega^2 - \frac{2\mu}{r^2} & \frac{-2\mu(3\lambda+2\mu)\sqrt{l(l+1)}}{r^2(\lambda+2\mu)} & -\frac{3}{r} & -\frac{\lambda\sqrt{l(l+1)}}{r(\lambda+2\mu)} \\ \frac{-2\mu(3\lambda+2\mu)\sqrt{l(l+1)}}{r^2(\lambda+2\mu)} & -\rho\omega^2 + \frac{4\mu(3\lambda+2\mu)}{r^2(\lambda+2\mu)} & \frac{\sqrt{l(l+1)}}{r} & \frac{-4}{r(\lambda+2\mu)} \end{pmatrix} \begin{pmatrix} V \\ U \\ S \\ R \end{pmatrix} \tag{9.81}$$

and

$$\frac{d}{dr} \begin{pmatrix} W \\ T \end{pmatrix} = \begin{pmatrix} \frac{1}{r} & \frac{1}{\mu} \\ \frac{\mu(l-1)(l+2)}{r^2} - \rho\omega^2 & \frac{3}{r} \end{pmatrix} \begin{pmatrix} W \\ T \end{pmatrix}. \tag{9.82}$$

We have dropped subscript l and superscript m from the dependent variables. Note that m does not even enter the equations, but we must remember that an m-dependence is present,

in general, because of the m-dependence of the source expansion. In Chapter 8, we also associated an overtone number, n, with the radial functions. Overtones do not arise in our present approach, because we do not now seek the special solutions subject to regularity at $r = 0$ and zero traction at $r = r_\oplus$ (the Earth's surface). Rather, we shall work with a complete set of linearly independent solutions without (yet) imposing boundary conditions.

Clearly, (9.81) describes P-SV motion (cf. (5.62)), and (9.82) describes SH (cf. (5.60)), and these two groups of equations are in the standard form $d\mathbf{f}/dr = \mathbf{A}(r)\mathbf{f}$. Our next goal is to find how $\mathbf{f}$ can be written as $\mathbf{f} = \mathbf{F}\mathbf{w} = \mathbf{E}\Lambda\mathbf{w}$, where the layer matrix $\mathbf{F}$ has been factored into a term $\mathbf{E}$ describing the amplitude of displacement and stress components for waves in each layer and a term Λ (a diagonal matrix) giving vertical wavefunctions for downgoing and upgoing P and SV. The simplest way to generate $\mathbf{F}$ and its factors $\mathbf{E}$ and Λ is via the potentials (9.50a) appropriate to spherical geometry, since each column of $\mathbf{F}$ is derivable from an identifiable vertical wavefunction (Problem 5.11). Another way is to invert transformations given by Chapman (1973, 1974). The final result is quite remarkably similar to plane-wave theory (5.69). For P-SV problems, it is

$$\mathbf{f}(r) = \begin{pmatrix} V \\ U \\ S \\ R \end{pmatrix} = \mathbf{E}\Lambda\mathbf{w}, \qquad \text{where } \Lambda = \begin{pmatrix} \pi^{(2)}(r) & 0 & 0 & 0 \\ 0 & \sigma^{(2)}(r) & 0 & 0 \\ 0 & 0 & \pi^{(1)}(r) & 0 \\ 0 & 0 & 0 & \sigma^{(1)}(r) \end{pmatrix} \tag{9.83}$$

and

$$\mathbf{E} = \begin{pmatrix} -\frac{i\alpha p}{r} & -i\beta\grave{\eta} & -\frac{i\alpha p}{r} & -i\beta\acute{\eta} \\ -\alpha\grave{\xi} & \frac{\beta p}{r} & \alpha\acute{\xi} & -\frac{\beta p}{r} \\ -2\omega\rho\alpha\beta^2\frac{p}{r}\grave{\xi} & -\omega\rho\beta\left(1-2\beta^2\frac{p^2}{r^2}\right) & 2\omega\rho\alpha\beta^2\frac{p}{r}\acute{\xi} & \omega\rho\beta\left(1-2\beta^2\frac{p^2}{r^2}\right) \\ i\omega\rho\alpha\left(1-2\beta^2\frac{p^2}{r^2}\right) & -2i\omega\rho\beta^3\frac{p}{r}\grave{\eta} & i\omega\rho\alpha\left(1-2\beta^2\frac{p^2}{r^2}\right) & -2i\omega\rho\beta^3\frac{p}{r}\acute{\eta} \end{pmatrix}. \tag{9.84}$$

The wavefunctions $\pi^{(j)}$ are for P-waves, and are related to our previous $g_l^{(j)}$ via

$$\overset{(1)}{\pi}{}^{(2)}(r, p, \omega) \equiv \sqrt{\frac{\rho_s}{\rho}}\frac{\alpha_s}{\alpha}\overset{(1)}{g}{}_l^{(2)} \sim e^{\mp i\pi/4}\sqrt{\frac{\rho_s\alpha_s}{\rho\alpha\cos i}}\frac{\alpha_s}{\omega r}\exp\left[\pm i\omega\int_{r_p}^{r}\xi(r')\,dr'\right]. \tag{9.85}$$

Wavefunctions $\sigma^{(j)}$ for SV are defined from the shear-velocity profile $\beta(r)$, and similarly

$$\overset{(1)}{\sigma}{}^{(2)}(r, p, \omega) \sim e^{\mp i\pi/4}\sqrt{\frac{\rho_s\beta_s}{\rho\beta\cos j}}\frac{\beta_s}{\omega r}\exp\left[\pm i\omega\int_{r_p}^{r}\eta(r')\,dr'\right] \tag{9.86}$$

(r_p here is the S-wave turning point, where $\eta = \sqrt{1/\beta^2 - p^2/r^2} = \beta^{-1}\cos j$ is zero). Accented vertical slownesses in (9.84) are defined by

$$\grave{\xi} \equiv \frac{1}{-i\omega\pi^{(2)}}\frac{d\pi^{(2)}}{dr}, \quad \acute{\xi} \equiv \frac{1}{i\omega\pi^{(1)}}\frac{d\pi^{(1)}}{dr}, \quad \grave{\eta} \equiv \frac{1}{-i\omega\sigma^{(2)}}\frac{d\sigma^{(2)}}{dr}, \quad \acute{\eta} \equiv \frac{1}{i\omega\sigma^{(2)}}\frac{d\sigma^{(2)}}{dr}, \tag{9.87}$$

and to first order it follows from WKBJ theory that, above the turning points, $\grave{\xi} \sim \acute{\xi} \sim \alpha^{-1} \cos i$ and $\grave{\eta} \sim \acute{\eta} \sim \beta^{-1} \cos j$. However, below the turning points, $\grave{\xi} \sim -\acute{\xi} \sim -i\sqrt{p^2/r^2 - 1/\alpha^2}$ and $\grave{\eta} \sim -\acute{\eta} \sim -i\sqrt{p^2/r^2 - 1/\beta^2}$. Our use of the accents, as $\grave{\xi}$ and $\acute{\xi}$, is intended to bring out the origin of $\grave{\xi}$ (read as "xi-down") from a downgoing wave and $\acute{\xi}$ ("xi-up") from an upgoing wave.

The sequence of columns in $\mathbf{F}$, $\mathbf{E}$, and $\mathbf{\Lambda}$ is taken in the order downgoing P, downgoing SV, upgoing P, upgoing SV, and the amount in which each wave is present is controlled by $\mathbf{w}$. These three matrices are defined for each inhomogeneous layer in the Earth, but in applications there is a major difference in the way they are used compared with those for homogeneous layers, simply because so few "layers" are now needed. For example, it is often adequate to use just one layer for the inner core, one layer for the fluid core, and one layer for the lower mantle from a depth around 650 km all the way down to the core–mantle boundary.

Because the method of potentials as given in (9.50a)–(9.50b) is only approximate, it must be recognized that the formulas we give for $\mathbf{\Lambda}$ and its wavefunctions are only approximate. However, we shall be able to improve upon the WKBJ approximations. The formula (9.84) for $\mathbf{E}$ is also approximate, even in a homogeneous spherical layer. Nevertheless, errors are only of order $\alpha/\omega r$ and $\beta/\omega r$ for most depth ranges, and at worst are of order $(\alpha/\omega r)^{2/3}$ and $(\beta/\omega r)^{2/3}$, which are still insignificant at body-wave frequencies.

Although we have developed a motion-stress vector approach containing nothing that was not already implied by potentials, recall that our purpose was to get a systematic method of bookkeeping when boundary conditions at a discontinuity are encountered. We use the layer numbering shown in Figure 9.33. A scattering matrix like that given in (5.38) can be set up for each interface. For reference purposes, we give specific formulas in Box 9.9 for all sixteen P-SV reflection/conversion/transmission coefficients for an interface at r_1.

At last we are in a position to apply our theory to some problems of seismic body waves. For our first canonical problem we shall investigate the basic properties of P, PcP, and P_{diff} waves associated with the core–mantle boundary. The faster medium lies above

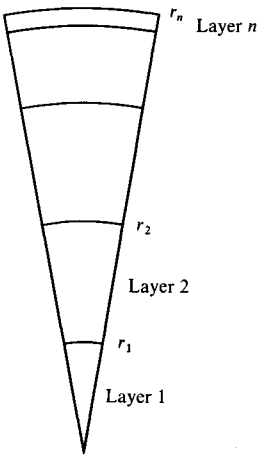

FIGURE **9.33**
Layer/boundary numbering in spherical geometry. Since each layer may be inhomogeneous, only a few layers (about 10) are needed to investigate long-period body waves in the whole Earth.

BOX **9.9**

Generalized scattering from a stack of inhomogeneous layers; and the special example of one spherical interface between two radially inhomogeneous layers

We suppose that for a stack of inhomogeneous layers it is desired to find the scattering from all interfaces between the Mth and $(N+1)$th layers. The interfaces themselves lie at radii $r_M, r_{M+1}, r_{M+2}, \ldots, r_{N-1}, r_N$, and layer $N+1$ is above r_N.

In the Mth layer, the system of upgoing and downgoing P–SV waves is described by the vector of constants

$$\mathbf{w}_M = (\grave{P}_M, \grave{S}_M, \acute{P}_M, \acute{S}_M)^T,$$

and, from $\mathbf{f} = \mathbf{F}\mathbf{w}$ in each layer,

$$\mathbf{w}_M = \mathbf{F}_M^{-1}(r_M)\mathbf{f}(r_M).$$

Thus,

$$\begin{aligned}\mathbf{w}_M &= \mathbf{F}_M^{-1}(r_M)\mathbf{F}_{M+1}(r_M)\mathbf{w}_{M+1} \\ &= \{\mathbf{F}_M^{-1}(r_M)\mathbf{F}_{M+1}(r_M)\} \cdot \cdots \cdot \{\mathbf{F}_N^{-1}(r_N)\mathbf{F}_{N+1}(r_N)\}\mathbf{w}_{N+1} \\ &= \mathbf{H}\mathbf{w}_{N+1}, \qquad \text{where } \mathbf{H} \text{ is a matrix product.}\end{aligned} \tag{1}$$

It follows that

$$(\grave{P}_M, \grave{S}_M, \acute{P}_M, \acute{S}_M)^T = \mathbf{H}(\grave{P}_{N+1}, \grave{S}_{N+1}, \acute{P}_{N+1}, \acute{S}_{N+1})^T, \tag{2}$$

and $\mathbf{H}$ can be obtained explicitly if all the layer matrices $\mathbf{F}$ and their inverses $\mathbf{F}^{-1}$ are known. For many applications, $\mathbf{F}$ in a radially inhomogeneous layer is given by (9.83)–(9.84), with inverse

$$\mathbf{F}^{-1} = \frac{ir^2\omega}{2\rho_s}\begin{pmatrix} F_{33}/\alpha_s^3 & F_{43}/\alpha_s^3 & -F_{13}/\alpha_s^3 & -F_{23}/\alpha_s^3 \\ F_{34}/\beta_s^3 & F_{44}/\beta_s^3 & -F_{14}/\beta_s^3 & -F_{24}/\beta_s^3 \\ -F_{31}/\alpha_s^3 & -F_{41}/\alpha_s^3 & F_{11}/\alpha_s^3 & F_{21}/\alpha_s^3 \\ -F_{32}/\beta_s^3 & -F_{42}/\beta_s^3 & F_{12}/\beta_s^3 & F_{22}/\beta_s^3 \end{pmatrix}. \tag{3}$$

Subscript s here refers to properties at some reference level (see (9.60)). This formula for $\mathbf{F}^{-1}$ in terms of elements of $\mathbf{F}$ is a consequence of properties of the Wronskian for $(\pi^{(1)}, \pi^{(2)})$ and $(\sigma^{(1)}, \sigma^{(2)})$.

We define a scattering matrix $\mathbf{S}$ by

$$(\acute{P}_{N+1}, \acute{S}_{N+1}, \grave{P}_M, \grave{S}_M)^T = \mathbf{S}(\grave{P}_{N+1}, \grave{S}_{N+1}, \acute{P}_M, \acute{S}_M)^T, \tag{4}$$

where

$$\mathbf{S} = \begin{pmatrix} \grave{P}\acute{P} & \grave{S}\acute{P} & \acute{P}\acute{P} & \acute{S}\acute{P} \\ \grave{P}\acute{S} & \grave{S}\acute{S} & \acute{P}\acute{S} & \acute{S}\acute{S} \\ \grave{P}\grave{P} & \grave{S}\grave{P} & \acute{P}\grave{P} & \acute{S}\grave{P} \\ \grave{P}\grave{S} & \grave{S}\grave{S} & \acute{P}\grave{S} & \acute{S}\grave{S} \end{pmatrix}. \tag{5}$$

(Compare with (5.35)–(5.38) for one interface between two homogeneous half-spaces. The left-hand side of (4) represents the scattered waves, and $\mathbf{S}$ operates on the incident waves.)

(continued)

BOX **9.9** *(continued)*

Entries in **S** now refer to generalized scattering coefficients, so that, for example, $\grave{P}\grave{S}$ denotes the phase and amplitude of an SV-wave transmitted downward in inhomogeneous layer number M due to downward P in layer $N+1$. Thus $\grave{P}\grave{S}$ contains all the multiples within the stack of layers between interfaces M and N. To obtain **S** explicitly in terms of entries of **H**, manipulate (2) into the form (4) to find

$$\begin{aligned}\mathbf{S} &= -\begin{pmatrix} H_{13} & H_{14} & -1 & 0 \\ H_{23} & H_{24} & 0 & -1 \\ H_{33} & H_{34} & 0 & 0 \\ H_{43} & H_{44} & 0 & 0 \end{pmatrix}^{-1} \begin{pmatrix} H_{11} & H_{12} & 0 & 0 \\ H_{21} & H_{22} & 0 & 0 \\ H_{31} & H_{32} & -1 & 0 \\ H_{41} & H_{42} & 0 & -1 \end{pmatrix} \\ &= \frac{1}{\mathsf{D}} \begin{pmatrix} 0 & 0 & -H_{44} & H_{34} \\ 0 & 0 & H_{43} & -H_{33} \\ \mathsf{D} & 0 & H_{14}H_{43} - H_{13}H_{44} & H_{13}H_{34} - H_{14}H_{33} \\ 0 & \mathsf{D} & H_{24}H_{43} - H_{23}H_{44} & H_{23}H_{34} - H_{24}H_{33} \end{pmatrix} \begin{pmatrix} H_{11} & H_{12} & 0 & 0 \\ H_{21} & H_{22} & 0 & 0 \\ H_{31} & H_{32} & -1 & 0 \\ H_{41} & H_{42} & 0 & -1 \end{pmatrix}, \end{aligned} \tag{6}$$

where $\mathsf{D} = H_{33}H_{44} - H_{34}H_{43}$.

Multiplying out the two matrices in (6), one can find any desired entry in **S**. The method we have given here is due to Červený (1974), who also showed how to avoid numerical difficulties by working with the 6×6 matrix of 2×2 minors of **H** (the so-called *delta matrix*). The delta matrix method, reduced to manipulations with 5×5 matrices, has been described in detail by Kind (1976) for homogeneous layers.

It is often important to obtain **S** in the special case of a single interface between two inhomogeneous layers. Matrix **H** is then obtained from (1). The method in (5.35)–(5.37) leads us to define

$$a = \rho_2(1 - 2\beta_2^2 p^2/r_1^2) - \rho_1(1 - 2\beta_1^2 p^2/r_1^2), \quad b = \rho_2(1 - 2\beta_2^2 p^2/r_1^2) + 2\rho_1\beta_1^2 p^2/r_1^2,$$

$$c = \rho_1(1 - 2\beta_1^2 p^2/r_1^2) + 2\rho_2\beta_2^2 p^2/r_1^2, \quad d = 2(\rho_2\beta_2^2 - \rho_1\beta_1^2), \quad E = b\grave{\xi}_1 + c\acute{\xi}_2,$$

$$F = b\grave{\eta}_1 + c\acute{\eta}_2, \quad G = a - d\grave{\xi}_1\acute{\eta}_2, \quad H = a - d\acute{\xi}_2\grave{\eta}_1, \quad \text{and} \quad \mathsf{D} = EF + GHp^2/r_1^2,$$

where subscript 1 is for the lower layer and subscript 2 for the upper. The interface itself is at r_1, and the *P–SV* coefficients themselves are

$$\grave{P}\acute{P} = -\left\{\left[(b\grave{\xi}_1 - c\grave{\xi}_2)F + (a + d\grave{\xi}_2\grave{\eta}_1)Gp^2/r_1^2\right]/\mathsf{D}\right\}(\pi_2^{(2)}/\pi_2^{(1)}),$$

$$\grave{P}\acute{S} = \left\{(\acute{\xi}_2 + \grave{\xi}_2)(ac + bd\grave{\xi}_1\grave{\eta}_1)p\alpha_2/(r_1\beta_2\mathsf{D})\right\}(\pi_2^{(2)}/\sigma_2^{(1)}),$$

$$\grave{P}\grave{P} = \left\{\rho_2(\acute{\xi}_2 + \grave{\xi}_2)F\alpha_2/(\alpha_1\mathsf{D})\right\}(\pi_2^{(2)}/\pi_1^{(2)}),$$

$$\grave{P}\grave{S} = -\left\{\rho_2(\acute{\xi}_2 + \grave{\xi}_2)Gp\alpha_2/(r_1\beta_1\mathsf{D})\right\}(\pi_2^{(2)}/\sigma_1^{(2)}),$$

$$\grave{S}\acute{P} = \left\{(\acute{\eta}_2 + \grave{\eta}_2)(ac + bd\grave{\xi}_1\grave{\eta}_1)p\beta_2/(r_1\alpha_2\mathsf{D})\right\}(\sigma_2^{(2)}/\pi_2^{(1)}),$$

$$\grave{S}\acute{S} = \left\{\left[(b\grave{\eta}_1 - c\grave{\eta}_2)E + (a + d\grave{\xi}_1\grave{\eta}_2)Hp^2/r_1^2\right]/\mathsf{D}\right\}(\sigma_2^{(2)}/\sigma_2^{(1)}),$$

$$\grave{S}\grave{P} = \left\{\rho_2(\acute{\eta}_2 + \grave{\eta}_2)Hp\beta_2/(r_1\alpha_1\mathsf{D})\right\}(\sigma_2^{(2)}/\pi_1^{(2)}),$$

$$\grave{S}\grave{S} = \left\{\rho_2(\acute{\eta}_2 + \grave{\eta}_2)E\beta_2/(\beta_1\mathsf{D})\right\}(\sigma_2^{(2)}/\sigma_1^{(2)}),$$

(continued)

BOX **9.9** *(continued)*

$$\acute{P}\acute{P} = \left\{\rho_1(\dot{\xi}_1 + \acute{\xi}_1)F\alpha_1/(\alpha_2\mathsf{D})\right\}(\pi_1^{(1)}/\pi_2^{(1)}),$$

$$\acute{P}\acute{S} = \left\{\rho_1(\dot{\xi}_1 + \acute{\xi}_1)Hp\alpha_1/(r_1\beta_2\mathsf{D})\right\}(\pi_1^{(1)}/\sigma_2^{(1)}),$$

$$\acute{P}\grave{P} = \left\{\left[(b\acute{\xi}_1 - c\xi_2)F - (a + d\acute{\xi}_1\acute{\eta}_2)Hp^2/r_1^2\right]/\mathsf{D}\right\}(\pi_1^{(1)}/\pi_1^{(2)}),$$

$$\acute{P}\grave{S} = -\left\{(\dot{\xi}_1 + \acute{\xi}_1)(ab + cd\xi_2\acute{\eta}_2)p\alpha_1/(r_1\beta_1\mathsf{D})\right\}(\pi_1^{(1)}/\sigma_1^{(2)}),$$

$$\acute{S}\acute{P} = -\left\{\rho_1(\dot{\eta}_1 + \acute{\eta}_1)Gp\beta_1/(r_1\alpha_2\mathsf{D})\right\}(\sigma_1^{(1)}/\pi_2^{(1)}),$$

$$\acute{S}\acute{S} = \left\{\rho_1(\dot{\eta}_1 + \acute{\eta}_1)E\beta_1/(\beta_2\mathsf{D})\right\}(\sigma_1^{(1)}/\sigma_2^{(1)}),$$

$$\acute{S}\grave{P} = -\left\{(\dot{\eta}_1 + \acute{\eta}_1)(ab + cd\xi_2\acute{\eta}_2)p\beta_1/(r_1\alpha_1\mathsf{D})\right\}(\sigma_1^{(1)}/\pi_1^{(2)}),$$

$$\acute{S}\grave{S} = -\left\{\left[(b\acute{\eta}_1 - c\acute{\eta}_2)E - (a + d\xi_2\acute{\eta}_1)Gp^2/r_1^2\right]/\mathsf{D}\right\}(\sigma_1^{(1)}/\sigma_1^{(2)}).$$

The last factor in each coefficient, a ratio of wavefunctions, is evaluated at r_1.

Our sign convention here is geared to the dependent variables in (9.83). For example, if

$$\mathbf{w}_2 = \left(0, 1, \grave{S}\acute{P}, \grave{S}\acute{S}\right)^T \qquad \text{then} \qquad \mathbf{w}_1 = \left(\grave{S}\grave{P}, \grave{S}\grave{S}, 0, 0\right)^T.$$

If one of the two layers is a fluid, then only nine of the sixteen coefficients have meaning. They can easily be found from those given here by a limiting procedure. For example, if layer 1 is the fluid core, use $\beta_1 \to 0$, $\eta_1 \to \infty$, and $bc - adp^2/r_1^2 = \rho_1\rho_2$. In this way, coefficients $\grave{P}\grave{P}$, $\acute{P}\grave{P}$, $\acute{P}\acute{S}$ defined above are used for the core–mantle boundary to derive $\grave{P}\grave{K}$, $\acute{K}\grave{K}$, $\acute{K}\acute{S}$, respectively, using the traditional notation for a P-wave in the fluid core, in which P is replaced by K (derived from the German word "Kern," meaning "core").

Corresponding results for SH and a single interface are

$$\grave{S}\acute{S} = \left[(\mu_2\dot{\eta}_2 - \mu_1\dot{\eta}_1)/\mathsf{D}\right]\sigma_2^{(2)}/\sigma_2^{(1)}, \qquad \grave{S}\grave{S} = \left[(\mu_2(\dot{\eta}_2 + \acute{\eta}_2))/\mathsf{D}\right]\sigma_2^{(2)}/\sigma_1^{(2)},$$

$$\acute{S}\acute{S} = \left[(\mu_1(\acute{\eta}_1 + \dot{\eta}_1))/\mathsf{D}\right]\sigma_1^{(1)}/\sigma_2^{(1)}, \qquad \acute{S}\grave{S} = \left[(\mu_1\acute{\eta}_1 - \mu_2\acute{\eta}_2)/\mathsf{D}\right]\sigma_1^{(1)}/\sigma_1^{(2)},$$

where $\mathsf{D} = \mu_1\dot{\eta}_1 + \mu_2\acute{\eta}_2$ and μ_1, μ_2 are, respectively, the rigidities below and above the interface.

the slower medium, and the travel-time curves are illustrated generically by rays 1, 2, and 3 in Figure 9.34. Our interest is in the distance range around $X = X_1$, where interference phenomena for $X < X_1$ change to diffraction phenomena for $X_1 < X$.

Using the spherical coordinates appropriate for discussion of the core–mantle boundary, and starting with an explosive source $M_{ij} = M_{\mathrm{I}}(t)\delta_{ij}$ located at $\mathbf{r}_s$, we note from (9.65)–(9.71) that

$$u_r^{\mathrm{inc}}(r, \Delta_0, \omega) = \frac{-i\omega M_{\mathrm{I}}(\omega) i\omega}{4\pi\rho_s\alpha_s^4}\int_\Gamma \omega^2 p\pi^{(1)}(r_s)[\alpha(r)\xi(r)\pi^{(1)}(r)]Q^{(2)}_{\omega p - \frac{1}{2}}(\cos\Delta_0)\,dp. \tag{9.88}$$

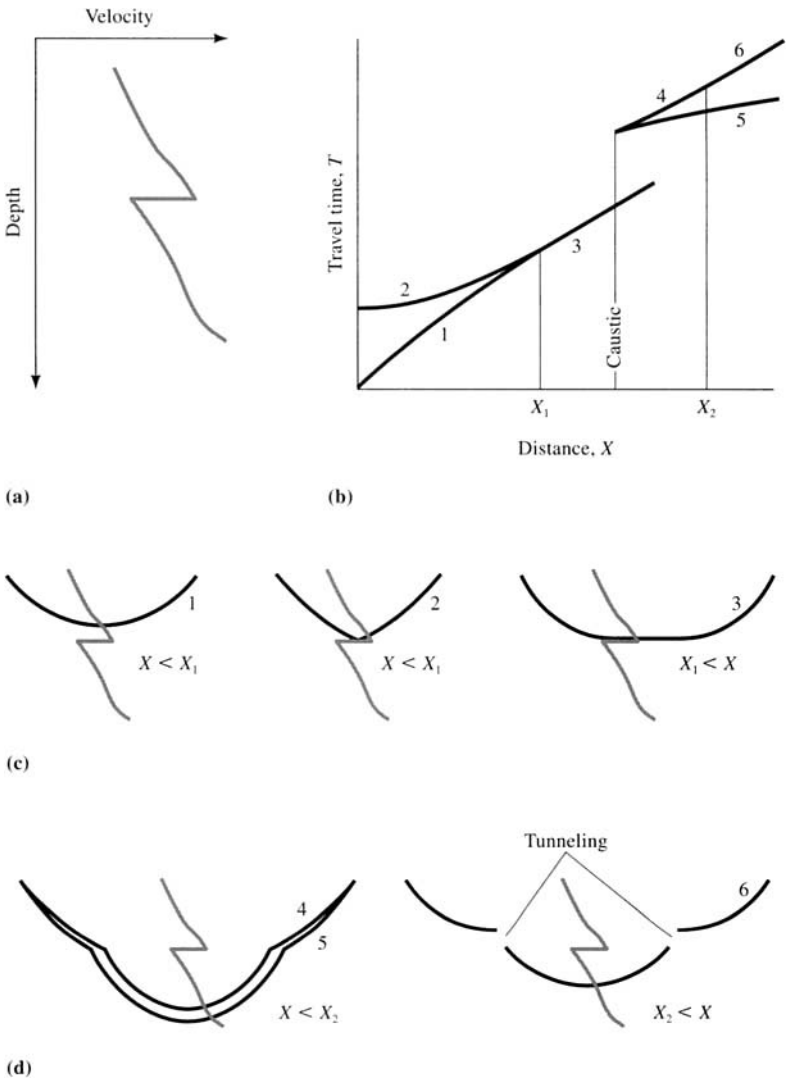

FIGURE **9.34**

Canonical problems of rays and a single interface, when velocity just above the interface is greater than velocity below: (**a**) the profile; (**b**) the travel-time curves, and numbered rays; (**c**) three rays that stay in the upper layer; (**d**) three rays that are transmitted into the lower layer. Grazing incidence is associated with rays that emerge near the distances X_1 and X_2. The critical ray parameter is the slope of curves 1, 2, 3, 4, 6 at $X = X_1$ and at $X = X_2$. There is a caustic between these two distances, where rays 4 and 5 merge. Ray 3 is diffracted along the upper side of the interface. Ray 6 entails "tunneling" through the high velocities at the bottom of the upper layer. From Richards (1988). If the interface is the core–mantle boundary and these are P-waves, then rays 1, 2, and 3 are respectively P, PcP, and P_{diff}, and distance X_1 is the shadow boundary of the Earth's core, at around 95°; rays 4 and 5 are PKP waves, merging in a caustic at around 144°.

This is just the direct wave, departing downward from $\mathbf{r}_s$ to $\mathbf{r}$ at (r, Δ_0), shown in Figure 9.28. For present purposes, we assume smoothly varying profiles for ρ and α, all the way down from source and receiver depths to the core-mantle boundary. It is this profile that is used to define wavefunctions $\pi^{(1)}$, and to distinguish core profiles and mantle profiles we shall use subscripts c and m where necessary. We refer to (9.88) as u_r^{inc}, because it is an incident wave of precisely this type that interacts with the core-mantle boundary. Note that the r-dependence in (9.88) is due entirely to the integrand factor $[\alpha(r)\dot{\xi}(r)\pi^{(1)}(r)]$. Just this term appears as an entry in the expected row and column of $\mathbf{F}$ (radial displacement component of an upward-arriving P-wave at r). This illustrates the satisfactory bookkeeping qualities of our new notation for vertical wave functions. It also confirms the fact that the reflection/transmission coefficients developed in Box 9.9 for columns of $\mathbf{F}$ are directly applicable to the integrand in (9.88).

The generalized reflection at the core–mantle boundary is obtained in full by introducing the factor $\grave{P}\acute{P}$ into (9.88):

$$u_r^{P+PcP}(r, \Delta_0, \omega) = \frac{-i\omega M_I(\omega) i\omega}{4\pi\rho_s\alpha_s^4} \times \int_\Gamma \omega^2 p \pi^{(1)}(r_s)\grave{P}\acute{P}[\alpha(r)\dot{\xi}(r)\pi^{(1)}(r)]Q^{(2)}_{\omega p-\frac{1}{2}}(\cos\Delta_0)\,dp, \tag{9.89}$$

where path Γ and associated features of the complex ray-parameter plane are shown in Figure 9.35. $\grave{P}\acute{P}$ is given in Box 9.9, with core and mantle taken as layers 1 and 2, respectively. Although a rigorous derivation of (9.89) is intricate (Nussenzveig, 1965, describes a related canonical problem), the result makes sense when simple properties of this integrand are identified and understood. Thus, at distances Δ_0 such that P and PcP are received (Figure 9.35a), the integrand has two saddle points. That for the direct P-wave has ray parameter p, greater than p_d, where $p_d = r_{CMB}/\alpha_m(r_{CMB})$ is appropriate for a ray just touching the core–mantle boundary. Subscript m refers to a property of the mantle. If $p > p_d$, then $\grave{\xi}_m \sim \acute{\xi}_m$, and it is readily shown that $\grave{P}\acute{P} \sim 1$. The saddle for direct P in (9.89) is then just the same as that we examined earlier in (9.66). If $p < p_d$, the *phase* of the integrand in (9.89) is derived from factors

$$\pi_m^{(1)}(r_s)[\pi_m^{(2)}(r_{CMB})/\pi_m^{(1)}(r_{CMB})]\pi_m^{(1)}(r)\,Q^{(2)}_{\omega p-\frac{1}{2}}(\cos\Delta_0).$$

WKBJ theory for this phase turns out to give $\exp[i\omega(p\Delta_0 + T - p\Delta)]$, where $T(p)$ and $\Delta(p)$ are appropriate to the PcP ray. We have previously described how such phase factors give saddle points. In this case $\partial\Delta/\partial p$ is positive, giving the saddle orientation shown in Figure 9.35c. Furthermore, using WKBJ theory in the range $p < p_d$, the *amplitude* of $\grave{P}\acute{P}$ turns out to be equal to the plane-wave reflection coefficient (still a function of p). Going on to make the saddle-point approximation for the integral over this PcP saddle (Box 6.3), we should merely recover classical ray theory for this phase (i.e., geometrical spreading together with a plane-wave reflection coefficient to describe the scattering at the core–mantle boundary).

This preliminary discussion of PcP brings out a special example of a general rule: if a real ray is present between source and receiver, then a combination of two approximations

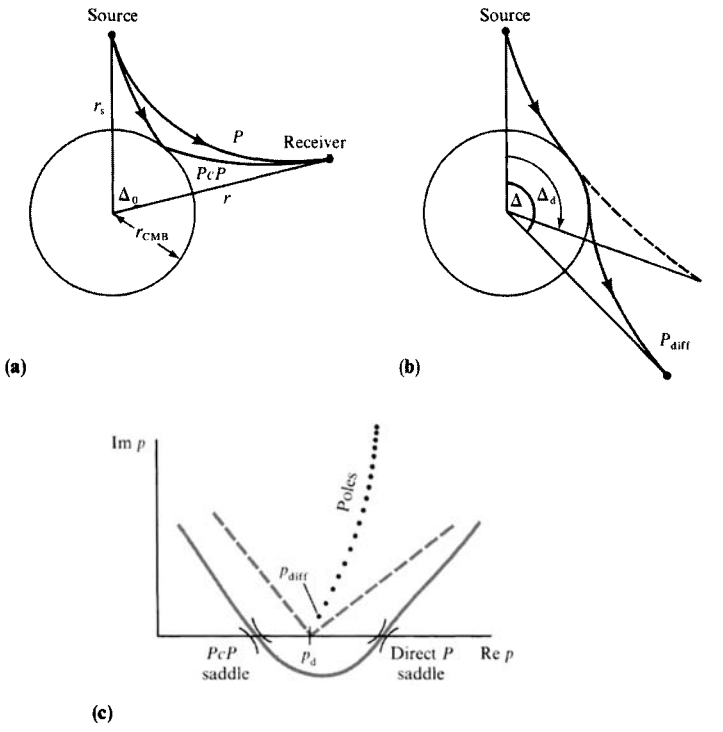

FIGURE **9.35**
(a) Rays for direct P and PcP. **(b)** Beyond Δ_d lies a shadow zone into which P-waves are diffracted. **(c)** The associated complex p-plane. For distances $\Delta_0 < \Delta_d$, two saddles are present. Diffraction poles stringing upward from p_d are always present, but we can always evaluate (9.89) by integrating along a contour such as the broken line, rather than making saddle-point approximations or evaluating individual residues. Pole locations are described in Box 9.11. Note that one path is adequate for a range of distances Δ_0 on either side of Δ_d. Compare with the path shown in Figure 6.22e.

(WKBJ theory and saddle-point approximation) applied to the integral representation for the generalized ray (cf. (9.89)) will merely yield geometrical ray theory. We first obtained a result of this nature in our derivation of (6.19) for homogeneous media. Seckler and Keller (1959) gave many examples for inhomogeneous media. Of course, our interest is in improving upon classical ray theory. We shall give several examples of the improvement that results when neither the WKBJ approximations nor the saddle-point approximation is used.

Returning to Figure 9.35, observe that, as Δ_0 increases, rays for direct P and PcP move closer together until they merge at the special distance Δ_d. Taking a phrase from optics, it is natural to call Δ_d the *shadow boundary*, because it marks the edge of a region $\Delta_d < \Delta_0$ within which neither direct P nor PcP can arrive. As shown in Figure 9.35b, rays arriving within the shadow must creep around the base of the mantle. This arrival is often observed, and is known as a *diffracted P-wave* (written P_{diff}). It is similar in geometry

to the diffraction of radio waves over the Earth's curved surface, a problem for which Watson originally developed the transformation that now bears his name. At $\Delta_0 = \Delta_d$, the two saddles have merged at $p = p_d$. Within the shadow, the line integral (9.89) can be evaluated as a rapidly converging series of residues from a string of poles (zeros of the denominator of $\grave{P}\acute{P}$, described in Box 9.11) that stretches up into the first quadrant from the first pole just above p_d. If the receiver is well into the shadow, so that Δ_0 is considerably greater than Δ_d, only the first residue is significant. It is located at p_{diff}, close to p_d, in that $p_{diff} = p_d + \lambda e^{i\pi/3}\omega^{-2/3}$, where λ is a positive constant having a magnitude of the same order as $p_d^{1/3}$. Well into the shadow, it follows that the amplitude of the diffracted wave P_{diff} is proportional to

$$\exp\left[-\omega^{1/3}\lambda \sin(\pi/3)(\Delta_0 - \Delta_d)\right].$$

Amplitudes in P_{diff} are thus more attenuated at higher frequencies and at greater distances into the shadow.

All these properties of (9.89) were described by Scholte (1956). Phinney and Cathles (1969) pointed out that a numerical evaluation of the line integral (9.89) has many advantages. A suitable path is the two broken line segments shown in Figure 9.35c, and the result of an integration at two different frequencies is shown in Figure 9.36.

In the remainder of this section, we shall be describing the results of numerical integration along paths consisting of straight-line segments in the complex ray-parameter plane.

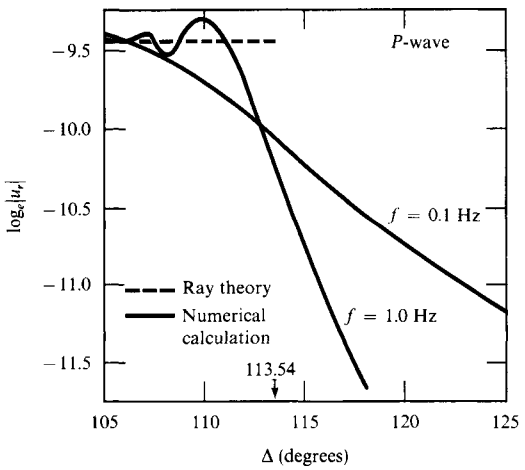

FIGURE **9.36**

Vertical component of P-wave displacement amplitude due to an explosive source for which $M_I(t)$ is a step function. Computation is via (9.89) at two different frequencies, and the path of integration (linear segments) is shown in the previous figure. The shadow boundary Δ_d is at 113.54° in this crude Earth model. For $\Delta_0 < \Delta_d$ there is interference of P and PcP. The broken line gives ray theory for direct P only. Although there is no sharp shadow boundary, the amplitudes at 1 Hz do decay quite rapidly with distance in the vicinity of Δ_d. The longer-period waves would be observable far into the shadow.

But one new element is needed in the theory. We find there is frequently the need to evaluate wavefunctions like $\pi_m^{(1)}(r_{CMB}, p, \omega)$ as p varies near values for which the radial argument is a turning point. Such is the case, for example, near p_d in Figure 9.35c, and note that almost all the energy in P_{diff} has this ray parameter. The problem is that WKBJ approximations break down in precisely this turning-point region, as described in Box 9.6. (The computation in Figure 9.36 presented no problem, because "mantle" and "core" were homogeneous, so that vertical wavefunctions $\pi^{(j)}$ and $\sigma^{(j)}$ were exactly given by spherical Hankel functions.) Fortunately, for many cases of radial inhomogeneity, there *is* a uniformly asymptotic approximation for $\pi^{(j)}$ and $\sigma^{(j)}$ that is satisfactory. A brief review is given in Box 9.10, and we state results here as the Langer approximation

$$\overset{(1)}{\pi}{}^{(2)}(r, p, \omega) \sim \sqrt{\frac{\pi\rho_s\alpha_s}{2\rho\alpha}} \cdot \frac{\alpha_s e^{\pm i\pi/6}}{\omega r} \cdot \sqrt{\frac{\omega\tau}{\alpha\xi}} \cdot \overset{(1)}{H}{}^{(2)}_{1/3}(\omega\tau), \tag{9.90}$$

where $\tau = T - p\Delta = \int_{r_p}^{r} \xi(r')\, dr'$ and $\xi = \xi(r) = \sqrt{1/\alpha^2(r) - p^2/r^2}$. The associated vertical slownesses are

$$\grave{\xi} \sim \sqrt{\frac{1}{\alpha^2} - \frac{p^2}{r^2}} \cdot e^{-i\pi/6} \frac{H^{(2)}_{2/3}(\omega\tau)}{H^{(2)}_{1/3}(\omega\tau)} \quad \text{and} \quad \acute{\xi} \sim \sqrt{\frac{1}{\alpha^2} - \frac{p^2}{r^2}} \cdot e^{i\pi/6} \frac{H^{(1)}_{2/3}(\omega\tau)}{H^{(1)}_{1/3}(\omega\tau)}. \tag{9.91}$$

Analogous expressions for $\sigma^{(j)}$, $\grave{\eta}$, and $\acute{\eta}$ are based on $\beta(r)$ and the shear-wave turning point.

In the remainder of this section, we shall draw upon examples of body waves in seismology having properties that are readily quantified by using line integrals like (9.89) in the complex ray-parameter plane, but with the Langer approximation for the vertical wavefunctions.

Thus for our second canonical problem in this section we look now at P-waves that have been transmitted into the Earth's fluid core, these being an excellent example of what can happen when waves interact with a discontinuity in which the slower medium (in this case, the fluid core) lies below the interface. Specializing to the example of $P4KP$ (see Fig. 9.37a), which has been observed following large nuclear explosions (Adams, 1972, Buchbinder, 1972) and deep earthquakes, our theory allows us to write down the radial displacement at distance Δ_0 as

$$u_r^{P4KP}(r, \Delta_0, \omega) = \frac{-i\omega M_I(\omega) i\omega}{4\pi\rho_s\alpha_s^4} \times \int_\Gamma \omega^2 p \pi^{(1)}(r_s) \grave{P}\grave{K} \cdot (\acute{K}\grave{K})^3 \cdot (\acute{K}\acute{P})[\alpha(r)\acute{\xi}(r)\pi^{(1)}(r)] Q^{(2)}_{\omega p - \frac{1}{2}}(\cos\Delta_0)\, dp. \tag{9.92}$$

We are here using K as the P-wave in the fluid core, so that $\grave{P}\grave{K}$ is a transmission coefficient (readily obtained from the general $\grave{P}\grave{P}$ given in Box 9.9), $\acute{K}\grave{K}$ is the internal reflection, and $\acute{K}\acute{P}$ is another transmission coefficient. The ray-theoretical travel-time curve for $P4KP$ is shown in Figure 9.37b, and it is curious that observations of the phase (which are plentiful at short-period, so that the frequency content is high enough for one to expect classical

BOX 9.10

A uniformly asymptotic approximation for vertical wavefunctions

In our early discussions of vertical wavefunctions ($g^{(1)}, g^{(2)}, f, \pi^{(1)}, \pi^{(2)}, \sigma^{(1)}, \sigma^{(2)}$), the main emphasis was on the equations of motion that these functions satisfy, hence we regarded them principally as functions of r. But to evaluate the waves set up by a point source, we usually work with vertical wavefunctions at fixed r (a source or receiver position or a level on which some boundary condition is imposed) and varying p and ω.

After an appropriate normalization has been determined, the WKBJ approximation (9.60)–(9.61), (9.85) is often suitable, evaluating wavefunctions as p and ω vary for large ω. However, this is a nonuniform approximation, being poor or grossly wrong for p-values near that particular p-value p_r which makes the radial argument r a turning point. To obtain a uniform approximation, we shall again revert to the equation of motion.

In what follows, we shall study $g^{(1)}$ and $g^{(2)}$, introduced as the outgoing and ingoing solutions of

$$\frac{d^2}{dr^2}[ra(r,l)] + \omega^2\left[\frac{1}{\alpha^2(r)} - \frac{l(l+1)}{\omega^2 r^2}\right] ra(r,l) = 0. \tag{1}$$

Early attempts to solve (1) as r varies near r_p hinged on developing a Taylor series expansion for the coefficient of the term $ra(r,l)$, i.e., expanding this term as a series in powers of $r - r_p$. In the turning-point region itself, this leads to Airy-function solutions with argument proportional to $(r - r_p)$ (e.g., see the derivation of equation (5), Box 9.6). However, this again is a nonuniform approximation, because it works *only* in the turning-point region.

The uniformly asymptotic solution we shall use is based on work of Langer (1951) and Olver (1954a,b). Effectively, the method uses a new depth variable, derived from r and $\alpha(r)$, in terms of which the equation (1) is close to being an Airy equation at *all* depths, including the turning-point level. We shall merely state the results, referring the reader to Richards (1976b) for more details.

Thus, working from $\tau = \tau(r,p) = \int_{r_p}^{r} \xi\, dr$ as defined for the WKBJ approximation, we introduce the new depth variable $\zeta = (\frac{3}{2}\omega\tau)^{2/3}$. It is assumed here that the velocity profile is an analytic function of radius, so that r_p is an analytic function of p. It follows that ξ, τ, and ζ are analytic functions of p, and so are $g^{(1)}$ and $g^{(2)}$. If the velocity profile is *not* analytic (e.g., it might be made up from many layers, in each of which the velocity is given by ar^b with a and b constant—such a dependence on radius is known as a Mohorovičić layer), then r_p is not an analytic function of p, and neither are $g^{(1)}$ and $g^{(2)}$. See Frazer (1983). Even so, $g^{(1)}$ and $g^{(2)}$ may vary sufficiently smoothly with p so as to be treated for our purposes as analytic functions in the complex plane.

In terms of ζ, (1) can be written in the form

$$\frac{d^2}{d\zeta^2}\left[r\sqrt{\frac{d\zeta}{dr}}\, a(r,l)\right] + \zeta\left[r\sqrt{\frac{d\zeta}{dr}}\, a(r,l)\right] = \text{terms two orders lower in frequency.} \tag{2}$$

For large ω, the right-hand side is uniformly negligible (i.e., for *all* depths). It follows that $r\sqrt{d\zeta/dr}\, a(r,l)$ has solutions made up from a linear combination of Airy functions

$$\mathrm{Ai}(-\zeta),\ \mathrm{Ai}(-e^{2i\pi/3}\zeta),\ \mathrm{Ai}(-e^{-2i\pi/3}\zeta). \tag{3}$$

(continued)

BOX **9.10** *(continued)*

We have now obtained the desired uniformly asymptotic solutions for $a(r, l)$, and it remains only to identify the particular linear combination of (3) for each of the special solutions $g^{(1)}$ (outgoing) and $g^{(2)}$ (ingoing). This is most easily done by comparing the WKBJ approximations for the three functions in (3) with WKBJ approximations for $g^{(1)}$ and $g^{(2)}$. The comparison tells us that

$$g^{(1)}_{(2)} \sim \frac{2}{\omega r}\sqrt{\frac{\pi\alpha_s}{\xi}}\,\zeta^{1/4}\,e^{\mp i\pi/3}\,\mathrm{Ai}(-e^{\pm 2i\pi/3}\zeta). \tag{4}$$

WKBJ theory was used only to obtain the normalization above, and (4) gives the uniformly asymptotic approximations we require. They are little more difficult to evaluate than WKBJ approximations. Both require $\tau = \tau(r, p)$, and then (4) works with Airy functions, whereas WKBJ approximations use exponentials.

The Langer approximations quoted in the text (9.90) are based upon (4) above, (9.85), and standard formulas relating Airy functions to Hankel functions of order $\frac{1}{3}$. Various branch cuts needed for individual factors in (4) and (9.90) are chosen so that the product of factors, the Langer approximation itself, is an entire function (single valued and analytic), bounded everywhere in the p-plane for finite p. Zeros of $g^{(1)}$ lie in the first and third quadrants of this plane, and zeros of $g^{(2)}$ lie in the second and fourth quadrants (see Box 9.11).

ray theory to apply) are associated only with the later branch. Even more curious, the observations are predominantly at distances beyond the "end" of this later branch, i.e., beyond the cut-off point A, so that although they are short-period, they are seen at distances "forbidden" by ray theory. The explanation of these observations can best be appreciated by examining $\grave{P}\grave{K} \cdot (\acute{K}\grave{K})^3 \cdot \acute{K}\acute{P}$ at values of p in the vicinity of saddle points corresponding to the two ray arrivals (i.e., travel-time branches) shown in Figure 9.37b. This product of coefficients is plotted in Figure 9.37c for frequencies $\frac{1}{2}$ Hz, 2 Hz, and for the limiting case as frequency tends to infinity. A critical ray-parameter value at 254.6 s is apparent, beyond which the amplitude is zero in the limiting case. The critical value is the parameter p_d for a mantle ray that just grazes the core. However, at finite frequencies, energy *can* be transmitted along this generalized ray, even for $p > p_d$. This phenomenon is known as *tunneling* (after a phenomenon in quantum mechanics for which there is a similar theory), and is described further in Figure 9.37d. In terms of the canonical problems illustrated in Figure 9.34 we are discussing the transition between rays 4 and 6, in the distance range near $X = X_2$. In the present example of waves tunneling into the fluid core, $\grave{P}\grave{K}$ becomes small as p increases beyond p_d because of the factor $(\dot{\xi}_m + \dot{\xi}_m)\pi_m^{(2)}(r_{CMB})$. Using (9.87) and the Wronskian for $(\pi^{(1)}, \pi^{(2)})$, this factor is of order $[\pi_m^{(1)}(r_{CMB})]^{-1}$. Both $\pi^{(1)}$ and $\pi^{(2)}$ *grow* exponentially below the turning point, so that the factor we are examining must decay exponentially. Numerically, $\acute{K}\acute{P}$ also behaves like $[\pi_m^{(1)}(r_{CMB})]^{-1}$. However, $\acute{K}\grave{K}$ is of order 1. It just happens that, for this case of the core–mantle boundary, $\acute{K}\grave{K}$ has a zero very near to $p = 240$ s (i.e., to the left of p_d), and $\acute{K}\grave{K}$ grows rapidly from zero as p increases near p_d. It is the cube of this reflection coefficient that we must evaluate in the case of $P4KP$, and the rapid growth of $(\acute{K}\grave{K})^3$ outweighs the decay in $\grave{P}\grave{K} \cdot \acute{K}\acute{P}$ for a short part

of the range $p_d < p$, giving the broken and gray curves in Figure 9.37c, which actually have their maxima in the tunneling region. The choice of Γ for a computation of (9.92) can be taken as shown in Figure 9.37e. More simply, it can be taken as the real axis from $p \sim 240$ s to $p \sim 265$ s (because the zero in $\acute{K}\grave{K}$ gives a natural tapering on the left, and there is exponential tapering to the right, as shown in Figure 9.37c). Finally, shown in Figure 9.37f is the result of evaluating our line integral (9.92) for $P4KP$ at different distances. Indeed, this does show that the strongest arrivals, in the period range $\frac{1}{2} - 2$ s, do lie beyond the ray-theoretical cutoff point A. The effect is not small, because arrivals are seen, and are explained by the theory, at distances 20° (i.e., around 2000 km) into the "forbidden" region. Fuchs and Schulz (1976) have shown that tunneling also can be significant for body waves in crustal structures within which there is a high-velocity layer.

We next examine the wave *SKS*, and related multiples *SKKS*, *SKKKS*, etc., denoted in brief as *SmKS* for various integers m. These SV-waves are an excellent example of the third canonical problem, namely, what can happen when waves interact with a discontinuity in which the faster medium lies below the interface. (The S-wave speed at the base of the mantle is less than the P-wave speed at the top of the core.) Choy (1977) has used the Langer approximation for these phases, integrating over complex p and also over real ω to give synthetic seismograms in the time domain. The travel-time curves for this problem are illustrated generically by rays 1, 2, and 3 of Figure 9.38. These rays provide the standard "triplication" associated with this type of discontinuity, but our interest now is in the distance ranges near X_1 and X_2 where one or more of the rays is at a near-grazing angle to the interface, and also in the possibility of multiple underside reflections and the interference between them.

For SV-waves, we must first look at a source other than the isotropic P-wave source we have so far considered in this chapter. A useful source for which to obtain explicit results is the shear dislocation with strike ϕ_s, rake λ, dip δ, and strength (i.e., moment) $\mu A\bar{u} = M_0(\omega)$. We obtained the radiation pattern for such a source, as well as the geometrical spreading formula, in (4.85) and (4.89). Our present goal is therefore to improve upon that approximation, for which the horizontal component is

$$u_\Delta^{SV}(r, \Delta_0, \phi, \omega) \sim \frac{\mathcal{F}^{SV}(-i\omega M_0(\omega))(-\cos\ j)\exp(i\omega T^S)}{4\pi\sqrt{\rho_s\rho(r)\beta_s^5\beta(r)}\,\mathcal{R}^S(\mathbf{r}, \mathbf{r}_s)}. \tag{9.93}$$

(A factor $-\cos j(r)$ appears here, because (4.89) gives amplitude in the $\hat{\mathbf{p}}$-direction and we want the horizontal component in the direction of Δ increasing.) From our previous experience with P-waves, we know that

$$\frac{i\omega}{\alpha_s^4}\int_\Gamma \omega^2 p\pi^{(1)}(r_s)[\alpha(r)\acute{\xi}(r)\pi^{(1)}(r)]Q^{(2)}_{\omega p-\frac{1}{2}}(\cos\Delta_0)\,dp$$

$$\sim \sqrt{\frac{\rho_s}{\rho(r)\alpha_s^5\alpha(r)}}\,\frac{\cos\ i}{\mathcal{R}^P(\mathbf{r}, \mathbf{r}_s)}\exp(i\omega T^P).$$

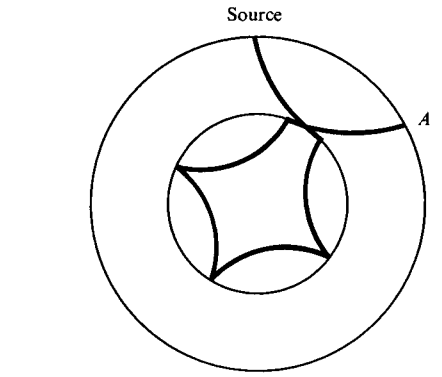
Source
A

(a)

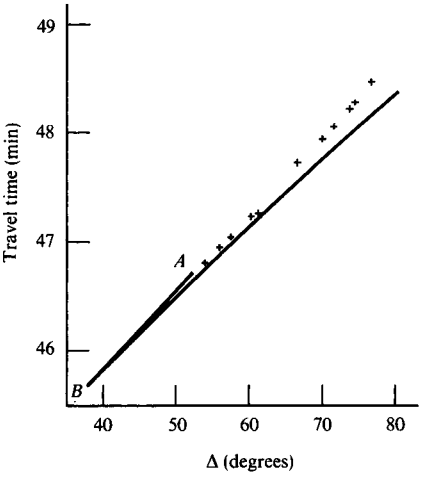
Travel time (min)
49
48
47
46
A
B
40
50
60
70
80
Δ (degrees)

(b)

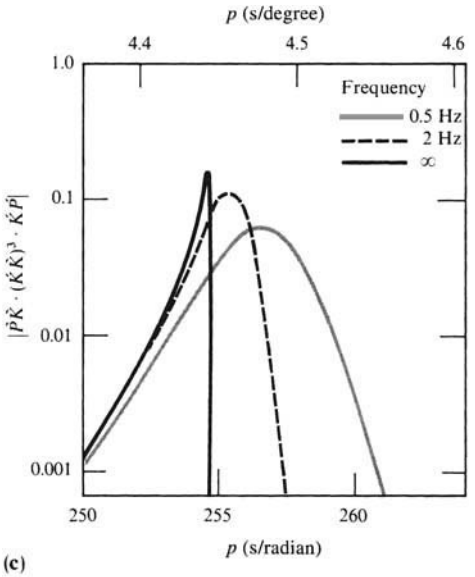
p (s/degree)
4.4
4.5
4.6
1.0
0.1
0.01
0.001
Frequency
0.5 Hz
2 Hz
∞
250
255
260
p (s/radian)

(c)

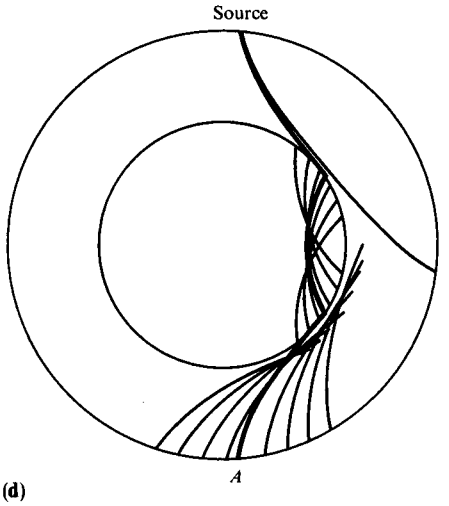
Source
A

(d)

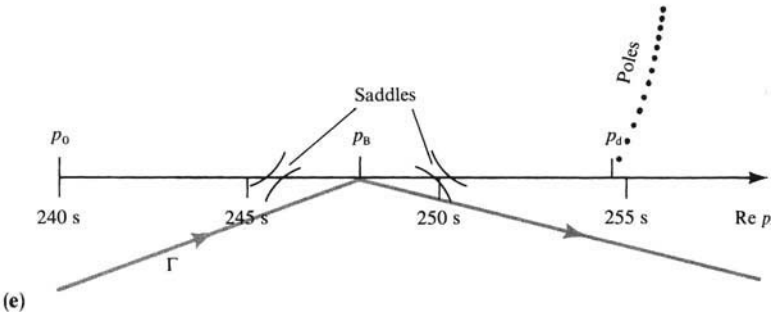
Poles
Saddles
p_0
p_B
p_d
240 s
245 s
250 s
255 s
Re p
Γ

(e)

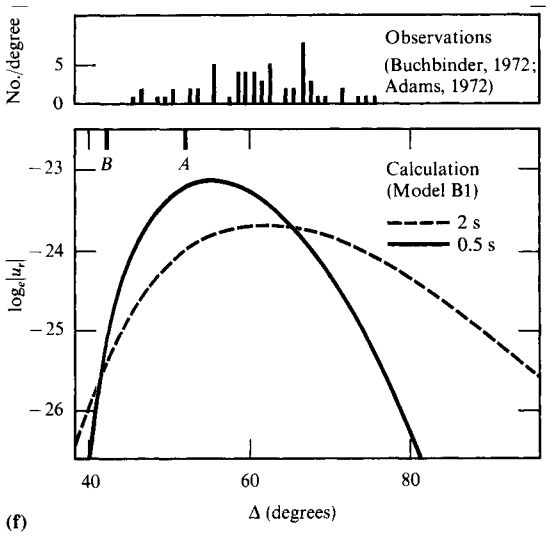

FIGURE **9.37**

Waves that travel as P in the mantle, and which have been internally reflected below the Earth's core–mantle boundary, are known as $PmKP$, with m an integer specifying the number of legs within the fluid core. **(a)** The ray path for $P4KP$. The ray parameter shown is exactly the core-grazing ray parameter p_d. For this special ray parameter, the point of emergence of $P4KP$ at the Earth's surface is designated as A. On the basis of classical ray theory, it may be expected that $P4KP$ is observed only for ray parameters less than or equal to p_d. Such, however, is not the case. **(b)** The travel-time curve for $P4KP$ in the Jeffreys–Bullen Earth model is shown as a solid line. From the maximum ray parameter at A, where the curve begins, there is a decrease to a minimum (in $\Delta = \Delta(p)$) at B where there is a caustic. Continued decrease of ray parameter is then on a branch for which $\partial\Delta/\partial p > 0$. Shown as crosses are some travel times observed for nuclear explosions in Novaya Zemlya, recorded at North American stations. **(c)** The product of reflection and transmission coefficients relevant to $P4KP$ is shown against ray parameter for two finite frequencies. The limiting case, as frequency tends to infinity, is also shown (it is zero for $p_d < p$, and is merely a product of plane-wave coefficients (5.40) for $p < p_d$). [After Richards, 1973a.] **(d)** The ray drawn heaviest is the core-grazing ray, emerging at A. There is exponential decay of energy below a turning point. Thus, for a ray with ray parameter slightly greater than p_d, the core–mantle boundary has energy leaking down from above. Below the boundary, energy can propagate along real rays. The high-velocity region just below the turning point therefore acts as a barrier, through which, at finite frequencies, some energy can pass into the low-velocity zone (the core in this case). For clarity, we here show only PKP, but this tunneling phenomenon occurs for all $PmKP$. Energy can also tunnel back out into the mantle. Tunneling will spread energy over a range of distances, and this range extends well beyond the point A. **(e)** Features in the complex p-plane, for the integrand in (9.92). Saddles on either side of $p = p_B$ behave similarly to those shown in Figure 9.30b,c. At $p = p_0$, there is a zero of $\acute{K}\grave{K}$. **(f)** The amplitudes of $P4KP$ at two frequencies are shown against distance, as computed from (9.92) using the Earth model B1 of Jordan and Anderson (1974). Points A and B for this model are marked, and note that the maximum amplitudes occur beyond the point A. $P4KP$ is observed typically with period about 1 s, and in the top half of the figure is shown a histogram based on observations reported by Buchbinder (1972) and Adams (1972). Maxima in the computed curves do occur at distances where observations are relatively plentiful.

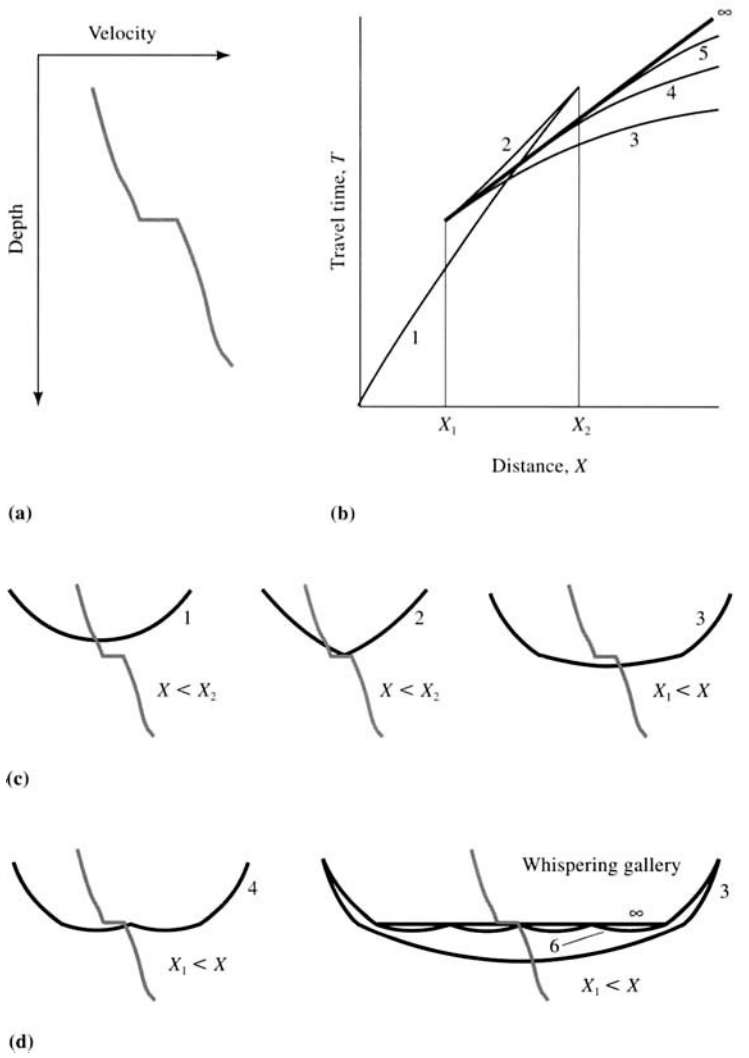

FIGURE **9.38**

The canonical problem of rays and a single interface, when velocity just above is slower than velocity just below: (**a**) the profile; (**b**) the travel-time curves, and numbered rays; (**c**) the most important three rays, which together form a "triplication," i.e., they are all three present between distances X_1 and X_2 (ray 2, shown here as a wide-angle reflection, also exists as a narrow-angle reflection all the way back to $X = 0$); (**d**) examples of rays that are reflected back downward below the interface. The sequence of rays 3, 4, 5, . . . all merge to the same ray as distance X tends down to X_1 from above. From Richards (1988). If the interface is the core–mantle boundary and rays above/below the interface are for S-waves/P-waves, then rays 1 to 4 are S, ScS, SKS, and $SKKS$. If the interface is the outer core/inner core boundary and these are all P-waves, then rays 1 to 4 are PKP, $PKiKP$, $PKIKP$, and $PKIIKP$.

Therefore, the corresponding result for SV allows us to write

$$u_{\Delta}^{\text{inc}SV}(r, \Delta_0, \phi, \omega) = \frac{i\omega M_0(\omega) i\omega}{4\pi\rho_s\beta_s^4} \times \int_{\Gamma} \omega^2 p \mathcal{F}^{SV} \sigma^{(1)}(r_s)[\beta(r)\dot{\eta}(r)\sigma^{(1)}(r)] Q^{(2)}_{\omega p - \frac{1}{2}}(\cos\Delta_0)\, dp. \tag{9.94}$$

This represents an SV-wave that is downgoing at the source and is received at (r, Δ_0) as an upgoing SV-wave. From this description alone, we could have written down most of the integrand factors in (9.94). The remaining factors simply give the normalization, and for this we can use classical ray theory since the turning point radius is far below the source depth. Thus $\mathcal{F}^{SV}$ in (9.94) is given as a function of (p, ϕ) from (4.85):

$$\mathcal{F}^{SV}(p, \phi) \sim [\sin\lambda \cos 2\delta \sin(\phi - \phi_s) - \cos\lambda \cos\delta \cos(\phi - \phi_s)](1 - 2\beta_s^2 p^2 / r_s^2) + [\cos\lambda \sin\delta \sin 2(\phi - \phi_s) - \sin\lambda \sin 2\delta (1 + \sin^2(\phi - \phi_s))] \frac{\beta_s^2 p}{r_s} \sqrt{\frac{1}{\beta_s^2} - \frac{p^2}{r_s^2}}. \tag{9.95}$$

Since (9.95) originates from ray theory, it is only approximate. However, it is highly accurate for body waves when the turning point for the ray is well below the source level, and this of course is always the case for the core phases. Although (9.95) substituted into (9.94) gives two different integrands, $\mathcal{F}^{SV}(p, \phi)$ may vary so slowly with p along those parts of Γ from which there is a numerically significant integrand that $\mathcal{F}^{SV}$ is effectively constant and can be taken outside the integration (see also Box 9.12).

If the wavelength of waves radiated from the source is not very much greater than the spatial dimensions of the rupture surface of the fault, then the finite extent of faulting can have a significant effect on seismic waves in the far field. This subject is covered in Chapter 10, and the necessary correction to our present theory is given in Box 10.2.

In (9.94), we have obtained the representation of the "incident wave" from which *SmKS* waves are derived. Thus, for *SKS*,

$$u_{\Delta}^{SKS}(r, \Delta_0, \phi, \omega) = \frac{i\omega M_0(\omega) i\omega}{4\pi\rho_s\beta_s^4} \times \int_{\Gamma} \omega^2 p \mathcal{F}^{SV} \sigma^{(1)}(r_s) \grave{S}\grave{K} \cdot \acute{K}\acute{S} \left[\beta(r)\dot{\eta}(r)\sigma^{(1)}(r)\right] Q^{(2)}_{\omega p - \frac{1}{2}}(\cos\Delta_0)\, dp, \tag{9.96}$$

where Γ is shown in Figure 9.39b. Choy (1977) studied (9.96) using the Earth model 1066B of Gilbert and Dziewonski (1975). For large enough Δ_0, the saddle point on the real p-axis, corresponding to *SKS*, can move to the left of the line of diffraction poles emanating from $p = p_d$. The effect of integrating along Γ is then to pick up the contribution from diffraction poles, as well as from the saddle. Thus (9.96) automatically contains the phase $SP_{\text{diff}}KS$ described in Figure 9.39a. Choy also carried out the ω-integration of (9.96), and some of his results are shown in Figure 9.39c. Clearly, the diffraction as P along the base of the mantle (contained within *SKS*) can be significant, as recorded by short-period and long-period seismometers. Garnero and Helmberger (1996) studied such signals for paths

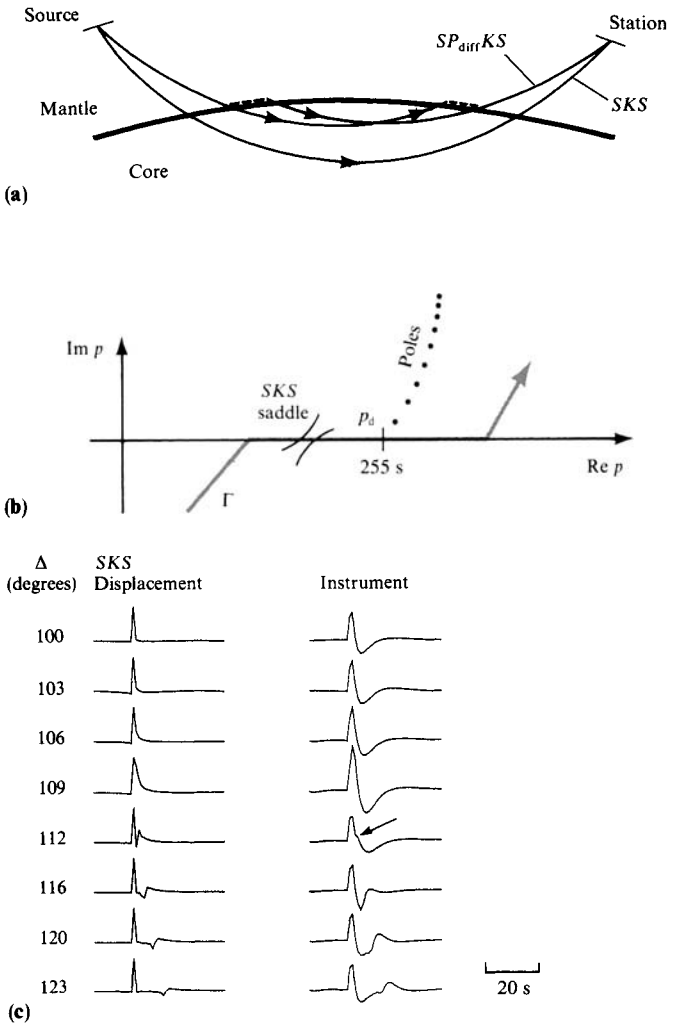

FIGURE **9.39**

If *SKS* is observed at distances beyond 100° then the ray is incident upon the core–mantle boundary with a slowness that allows some coupling to a *P*-wave diffracted around the base of the mantle. We label this phase as $SP_{diff}KS$, shown in **(a)**. The diffracted part of the path can occur at either end of the *K*-leg. In **(b)** is shown the path of integration for (9.96), and the effect of $SP_{diff}KS$ will be apparent whenever the saddle for *SKS* lies to the left of diffraction poles emanating from p_d. **(c)** *Left.* The impulse response computed from (9.96) in Earth model 1066B of Gilbert and Dziewonski (1975). *Right.* The impulse response, after convolution with a long-period WWSSN instrument (15–100) (T_s = 15 s, T_g = 100 s; see Section 12.3.3). An arrow marks the emergence of $SP_{diff}KS$, and a strong effect of this phase can be seen in the coda of *SKS* beyond 112°. [After Choy, 1977.]

BOX **9.11**

Poles of scattering coefficients

The sixteen P-SV coefficients obtained in Box 9.9 all share the same factor $(1/\mathsf{D})$, where

$$\mathsf{D} = (b\grave{\xi}_1 + c\acute{\xi}_2)(b\grave{\eta}_1 + c\acute{\eta}_2) + (a - d\grave{\xi}_1\acute{\eta}_2)(a - d\acute{\xi}_2\grave{\eta}_1)p^2/r_1^2.$$

Zeros of D (as p varies) are then poles of the scattering coefficients, and must receive special consideration when paths Γ are deformed in the complex p-plane.

In fact, D^{-1} has Stoneley poles on the real p-axis, just as we found for plane-wave theory (see discussion following (5.57)). More important, D^{-1} has strings of poles that have properties similar to the branch cuts we encountered in solving Lamb's problem. Fortunately, the locations of pole strings for D^{-1} are about the same as the locations of pole strings for the four quantities $\grave{\xi}_1, \acute{\xi}_2, \grave{\eta}_1, \acute{\eta}_2$ that appear in D. Our notation has been chosen to emphasize the similarity of these four quantities to the vertical slownesses $\xi = \alpha^{-1}\cos i$ and $\eta = \beta^{-1}\cos j$ that appear in plane-wave theory for homogeneous media. (The appearance of $\alpha^{-1}\cos i$ and $\beta^{-1}\cos i$ in plane-wave scattering coefficients (5.40) was due to vertical differentiation of wave functions $e^{\pm i\omega\xi z}$ and $e^{\pm i\omega\eta z}$. In (9.87) we have generalized this for waves with turning points, finding that downgoing and upgoing vertical slownesses must be distinguished.)

For real values of the ray parameter, $\grave{\xi}$ and $\acute{\xi}$ are complex conjugates. If $p < r/\alpha$, then WKBJ theory applied to (9.87) gives $\grave{\xi} \sim \sqrt{1/\alpha^2 - p^2/r^2} \sim \acute{\xi}$. As p approaches r/α, Langer approximation (9.91) for $\grave{\xi}$ and $\acute{\xi}$ is necessary. For $r/\alpha < p$, $\pi^{(1)}$ and $\pi^{(2)}$ are exponentially large but $\pi^{(1)} + \pi^{(2)}$ is exponentially small. It follows that $\pi^{(1)} \sim -\pi^{(2)}$ and $\grave{\xi} \sim -\acute{\xi} \sim -i\sqrt{p^2/r^2 - 1/\alpha^2}$.

More generally, it may be shown that $\grave{\xi}$ and $\acute{\xi}$ are analytic functions of p, with singularities located as shown in Figures A and B. The strings depart from the real p-axis near $r/\alpha(r)$. The poles of $\acute{\xi}$ are the zeros of $H_{1/3}^{(1)}(\omega\tau)$ (see (9.91)), and they lie near lines (called Stokes' lines) given by requiring $\tau = \tau(r, p)$ to be real. Away from the singularities, $\acute{\xi} \sim \sqrt{1/\alpha^2 - p^2/r^2}$. For example, this approximation would be accurate for lines such as AB shown in the figure below. As a line of singularities is approached, the approximation fails—and fails radically if BC lies on or very close to one of the poles in the string. After crossing the line of singularities, then $\acute{\xi} \sim -\sqrt{1/\alpha^2 - p^2/r^2}$ and a sign change is found to have occurred, giving the appearance of having crossed a branch cut for the square root. Since $ABCD$ does not cross a line of singularities for $\grave{\xi}, \acute{\xi} \sim \sqrt{1/\alpha^2 - p^2/r^2}$ is accurate for the whole path, and does not undergo a jump between B and C.

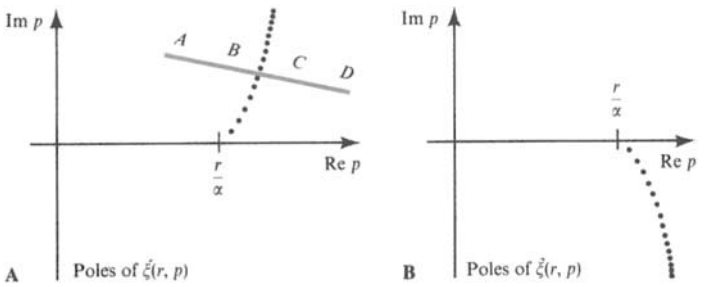

(continued)

BOX **9.11** *(continued)*

There are also poles for $\acute{\xi}$ in the third quadrant, and poles for $\grave{\xi}$ in the second quadrant, obtained from those shown here by reflection in the origin ($\acute{\xi}$ and $\grave{\xi}$ are even in p).

Interlaced with the first-quadrant poles of $\acute{\xi}$ are zeros of $\acute{\xi}$. Because both zeros and poles of $\acute{\xi}$ lie along the same general line, $\acute{\xi}$ undergoes a rapid variation in amplitude along this line. A rational function of $\acute{\xi}$ will therefore also have poles and zeros along the same line in the first quadrant. Scattering coefficients in seismology are typically rational functions of several vertical slownesses, each based on a different velocity profile ($\grave{\xi}$, $\acute{\eta}$, etc.).

For the core–mantle boundary, $\alpha_m = \alpha_2 > \alpha_c = \alpha_1 > \beta_m = \beta_2$ and $\beta_1 = 0$. Then the denominator D becomes $b^2\grave{\xi}_c + bc\acute{\xi}_m - d(a - d\grave{\xi}_c\acute{\eta}_m)\acute{\xi}_m p^2/r_{CMB}^2$. Poles of D^{-1} are located near poles of $\grave{\xi}_c$, $\acute{\xi}_m$, and $\acute{\eta}_m$, as shown in Figure C.

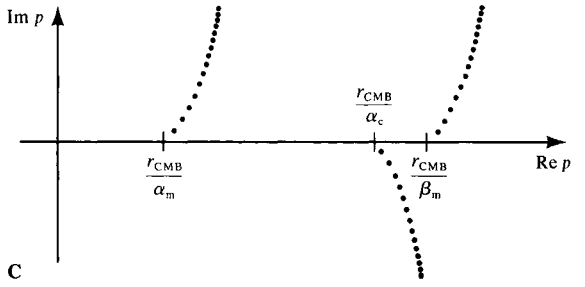

Poles for the scattering coefficients $P\grave{K}$, $\acute{K}\grave{K}$, $S\grave{K}$, etc., associated with the core–mantle boundary. Since D is even in p, there are also poles in the second and third quadrants, which are obtained from those shown here by reflection in the origin.

in the South Pacific and concluded for part of such paths that the P-wave velocity at the base of the mantle is anomalously low.

The representation for $SmKS$ ($m = 2, 3, \ldots$) is modified from (9.96) merely by the insertion of $(\acute{K}\grave{K})^{m-1}$ to account for the $(m - 1)$ internal reflections. Shown in Figure 9.40 are several such rays and an appropriate path of integration. A problem is apparent, in that $S(m + 1)KS$ arrives in the coda of $SmKS$, hence the pulse shape observed on a seismogram is composed on many superimposed multiples. Choy (1977) found that the convergence of $SKKS + SKKKS + SKKKKS + \cdots$ is very slow, even at distances several thousand kilometers beyond the critical distance ($\sim 62°$) at which SKS originates. It is, however, an important system of multiples to study, since it is sensitive to velocities in the outermost fluid core. Choy found that the velocities of 1066B required some slight modification in this region, and Figure 9.41 shows his comparison between observations and synthetic seismograms for an Earth model like 1066B, but with an adiabatic velocity gradient in the outermost 200 km of the core.

The problem of a slowly converging series of multiples, like $SmKS$, will always arise when a faster medium lies below a discontinuity (provided the velocity does not decrease with depth so fast that turning points are absent in the lower medium). This is very often

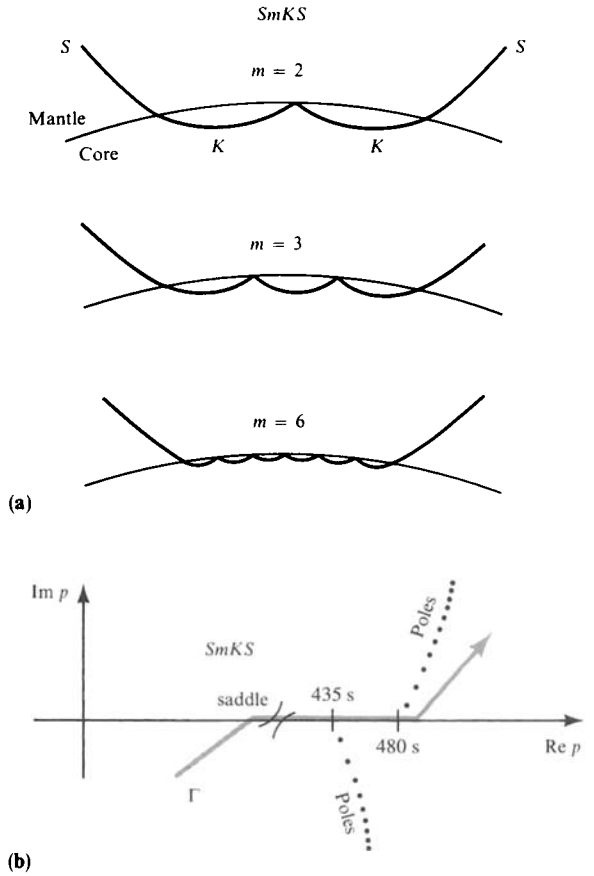

FIGURE **9.40**
In the coda of *SKS* lie *SKKS*, *SKKKS*, etc. (**a**) Note that such multiples have ever higher turning points as the number of K-legs is increased. By inserting a factor $(\acute{K}\grave{K})^{m-1}$ in (9.96), the representation of *SmKS* is obtained. (**b**) The integration path shown is affected by poles stringing down from about $p =$ 435 s (associated with a P-wave turning point at the top of the fluid core) and by poles stringing up from about $p = 480$ s (the S-wave turning point at the base of the mantle).

the case for interfaces within the Earth, and the wave composed of all the multiples taken together is known as the *interference head wave* (Červeńy and Ravindra, 1971). The ray system is shown in Figure 9.42, and examples abound in oceanic sediments, in crustal layering (Hill, 1971a,b), possibly in the upper mantle, and certainly in core phases. A medium that supports such rays is known classically as a *whispering gallery* (Rayleigh, 1910). Convergence of the system of multiples can be particularly poor if the receiver position is taken close to the critical distance.

Cormier and Richards (1977) have shown that a good way to avoid the difficulty is to work directly with an expression that accounts for *all* the multiples taken together. The geophysical problem they studied was actually that of P-waves that have traversed both the outer fluid core and the inner solid core of the Earth, and the interference head wave here arises at the inner-core/outer-core interface (having radius r_1). In Figure 9.43a is shown the travel-time curve for *PKP*, also with branch *CD* for *PKiKP* (the reflection from r_1); branch *DF* for *PKIKP* (with a single transmission leg below r_1); and a branch for *PKIIKP*. A natural notation for the reflection coefficient in *PKiKP* is $\grave{K}\acute{K}$, with similar notation

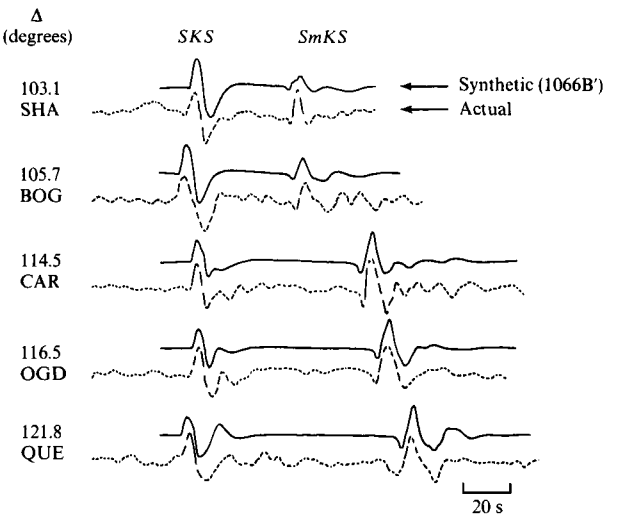

FIGURE **9.41**
Comparison between synthetic seismograms (computed in model 1066B, but modified by replacing the outermost 200 km of the fluid core with the velocity given by Jeffreys) and observed seismograms for a deep Fijian earthquake on July 21 1973. Note the change of *SKS* pulse shape with distance, due (presumably) to $SP_{diff}KS$. Note too the satisfactory agreement between synthetics and observation for the interfering multiples in *SmKS*. Choy summed from $m = 2$ to $m = 15$ to obtain these synthetics, and found that an adiabatic outer core (like that of Jeffreys) was required by the *SmKS* data. [From Choy, 1977.]

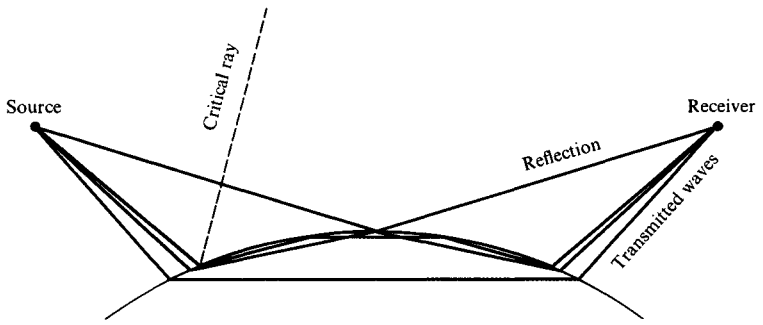

FIGURE **9.42**
An interface between two media, with the faster medium lying below. At a receiver placed beyond the critical ray, an infinity of ray paths connect the source and receiver. The wave set up by this family of multiples is the interference head wave. The reflected ray is also shown. As the receiver is moved toward the critical ray, travel times for all ray paths will tend to a common limit. We have shown here a curved interface and straight rays. However, an interference head wave can be set up at the interface between inhomogeneous media (with curved rays), e.g., by superimposing rays shown in Figure 9.40a. The uppermost part of the faster medium is here acting as a wave guide, and the effect is similar to that found in a "whispering gallery."

BOX **9.12**

The moment tensor and generalized rays

For a seismic point source described objectively by a second-order moment tensor, we have given specific formulas ((7.148) to (7.151) and (8.38)) showing how the surface waves and normal modes of the Earth will be excited. We give here the corresponding excitation formulas for body waves.

We made a preliminary attempt at finding the body-wave excitation when we obtained the radiation patterns in (4.96) based on geometrical ray theory. In terms of the take-off angle, either i_ξ (for P-waves) or j_ξ (for S-waves), the key factors for P-, SV-, and SH-waves can be written out as

$$(P) \quad \boldsymbol{\gamma}\cdot\dot{\mathbf{M}}\cdot\boldsymbol{\gamma} = \sin^2 i_\xi[\cos^2\phi\dot{M}_{xx} + \sin 2\phi\dot{M}_{xy} + \sin^2\phi\dot{M}_{yy} - \dot{M}_{zz}] + 2\sin i_\xi\cos i_\xi[\cos\phi\dot{M}_{xz} + \sin\phi\dot{M}_{yz}] + [\dot{M}_{zz}], \tag{1}$$

$$(SV) \quad \hat{\mathbf{p}}\cdot\dot{\mathbf{M}}\cdot\boldsymbol{\gamma} = \sin j_\xi\cos j_\xi[\cos^2\phi\dot{M}_{xx} + \sin 2\phi\dot{M}_{xy} + \sin^2\phi\dot{M}_{yy} - \dot{M}_{zz}] + (1 - 2\sin^2 j_\xi)[\cos\phi\dot{M}_{xz} + \sin\phi\dot{M}_{yz}], \tag{2}$$

$$(SH) \quad \hat{\boldsymbol{\phi}}\cdot\dot{\mathbf{M}}\cdot\boldsymbol{\gamma} = \sin j_\xi[\tfrac{1}{2}\sin 2\phi(\dot{M}_{yy} - \dot{M}_{xx}) + \cos 2\phi\dot{M}_{xy}] + \cos j_\xi[\cos\phi\dot{M}_{yz} - \sin\phi\dot{M}_{xz}]. \tag{3}$$

These formulas use the notation of Chapter 4, and they have been arranged here to display the dependence on certain combinations of moment-tensor elements. When setting up a theory for generalized rays in which the body-wave solution associated with a particular ray path is given by an integral over ray parameter, then one of the expressions (1), (2), or (3) will enter as a factor in the integrand. This will be true for the Cagniard method, for the reflectivity method as given in Section 9.2, for the WKBJ seismogram, and also (with possible modifications, described below) for the full-wave-theory methods described in Section 9.7. Common to each of these methods is a decision about whether the ray path of interest is one that departs upward or downward from the source. To illustrate the procedure for general $\mathbf{M}$, we shall use a full-wave theory for SH and look at $S + ScS$ waves (becoming S_{diff} in the shadow of the Earth's core). Thus, in the frequency domain, we can write

$$u_\phi^{S+ScS}(r, \Delta_0, \phi, \omega) = \frac{-i\omega\cdot i\omega}{4\pi\rho_s\beta_s^4}\int_\Gamma \omega^2 p(\hat{\boldsymbol{\phi}}\cdot\mathbf{M}\cdot\gamma)\sigma^{(1)}(r_s)\grave{S}\acute{S}\sigma^{(1)}(r)Q^{(2)}_{\omega p-\frac{1}{2}}(\cos\Delta_0)\,dp. \tag{4}$$

This expression can be written down with an eye on (9.89) or (9.94). $\grave{S}\acute{S}$ is the ScS reflection coefficient (for SH), and Γ is a path very similar to that shown in Figure 9.35c. Our interest here is in the source-dependent factor in (4), and to obtain its dependence on ray parameter we note that (1)–(3) can be written as

$$(P) \quad \boldsymbol{\gamma}\cdot\dot{\mathbf{M}}\cdot\boldsymbol{\gamma} = [\dot{M}_{zz}] + (p\alpha_s/r_s)^2[\cos^2\phi\dot{M}_{xx} + \sin 2\phi\dot{M}_{xy} + \sin^2\phi\dot{M}_{yy} - \dot{M}_{zz}] + 2(p\alpha_s^2/r_s)\varepsilon\xi_s[\cos\phi\dot{M}_{xz} + \sin\phi\dot{M}_{yz}], \tag{5}$$

$$(SV) \quad \hat{\mathbf{p}}\cdot\dot{\mathbf{M}}\cdot\boldsymbol{\gamma} = (p\beta_s^2/r_s)\varepsilon\eta_s[\cos^2\phi\dot{M}_{xx} + \sin 2\phi\dot{M}_{xy} + \sin^2\phi\dot{M}_{yy} - \dot{M}_{zz}] + (1 - 2\beta_s^2p^2/r_s^2)[\cos\phi\dot{M}_{xz} + \sin\phi\dot{M}_{yz}], \tag{6}$$

$$(SH) \quad \hat{\boldsymbol{\phi}}\cdot\dot{\mathbf{M}}\cdot\boldsymbol{\gamma} = (p\beta_s/r_s)[\tfrac{1}{2}\sin 2\phi(\dot{M}_{yy} - \dot{M}_{xx}) + \cos 2\phi\dot{M}_{xy}] + \beta_s\varepsilon\eta_s[\cos\phi\dot{M}_{yz} - \sin\phi\dot{M}_{xz}]. \tag{7}$$

(continued)

BOX **9.12** *(continued)*

The symbols ξ_s, η_s denote vertical slowness (e.g., $\xi = \alpha^{-1}\cos i = \sqrt{\alpha^{-2} - p^2/r^2}$) evaluated at the source, and ε is $+1$ or -1 according as the ray is downgoing or upgoing at the source. Substituting from (7) into (4), we find that the following scheme is convenient for computation:

Compute and store two fundamental solutions,

$$SH_1(\Delta_0, \omega) = \int_\Gamma \sin j_\xi f(p, \omega)\, dp,$$
$$SH_2(\Delta_0, \omega) = \int_\Gamma \cos j_\xi f(p, \omega)\, dp, \tag{8}$$

where for our present problem $f(p, \omega) = i\omega(4\pi\rho_s\beta_s^4)^{-1}\omega^2 p\sigma^{(1)}(r_s)\dot{S}\dot{S}\sigma^{(1)}(r)\times Q^{(2)}_{\omega p - \frac{1}{2}}(\cos\Delta_0)$, $\sin j_\xi = p\beta_s/r_s$, and $\cos j_\xi = \beta_s\eta_s$. To generate the record section, given any moment rate tensor $\dot{\mathbf{M}}$, we can multiply the spectrum of $[\frac{1}{2}\sin 2\phi(\dot{M}_{yy} - \dot{M}_{xx}) + \cos 2\phi\dot{M}_{xy}]$ by $SH_1(\Delta_0, \omega)$, and the spectrum of $[\cos\rho\dot{M}_{yz} - \sin\phi\dot{M}_{xz}]$ by $SH_2(\Delta_0, \omega)$, add, and invert to the time domain by integrating over real frequencies. This exercise can be done very quickly. We can set up an even simpler numerical procedure if we decide in advance that $\dot{\mathbf{M}}$ is appropriate for a shear dislocation with a certain strike, dip, and rake, and a certain time function for $M_0(t) = \mu A\bar{u}$. In this case we form $\dot{M}_0(t) * SH_1(\Delta_0, t)$ and $\dot{M}_0(t) * SH_2(\Delta_0, t)$. These two record sections are shown below after a recursive filter has been applied to give the effect of a typical long-period seismometer. The virtue of this approach is that the seismogram for a given distance (Δ_0) is given for any source mechanism (and any azimuth) in terms a linear sum of the two seismograms for a given distance in the figure. Coefficients in the linear sum are a function of strike, dip, rake, and azimuth (ϕ) from source to receiver, so that it is easy to test for the effect of a variety of fault-plane solutions. The two coefficients are given in detail by $[\frac{1}{2}\sin 2\phi(M_{yy} - M_{xx}) + \cos 2\phi M_{xy}]/M_0$ and $[\cos\phi M_{yz} - \sin\phi M_{xz}]/M_0$, with components for $\mathbf{M}$ as in Box 4.4.

If, instead of SH, we consider a P-wave departing from the source, then it is necessary to store three fundamental types of solution:

$$P_1(\Delta_0, \omega) = \int_\Gamma f(p, \omega)\, dp,$$
$$P_2(\Delta_0, \omega) = \int_\Gamma \sin^2 i_\xi f(p, \omega)\, dp,$$
$$P_3(\Delta_0, \omega) = \int_\Gamma 2\sin i_\xi \cos i_\xi f(p, \omega)\, dp,$$

If the source is an explosion, only the P_1 solution is needed. For an SV-wave leaving the source, we must in general work with two fundamental solutions,

$$SV_1(\Delta_0, \omega) = \int_\Gamma \sin j_\xi \cos j_\xi f(p, \omega)\, dp,$$
$$SV_2(\Delta_0, \omega) = \int_\Gamma (1 - 2\sin^2 j_\xi) f(p, \omega)\, dp.$$

Underlying the discussion we have just given is the implicit assumption that WKBJ approximations are accurate for vertical wavefunctions evaluated at the source level, r_s. This assumption would have been plain if, for example, we had given a formal derivation

(continued)

BOX **9.12** *(continued)*

of (4). This would entail the usual procedure of writing the source equivalent to **M** in terms of a discontinuity in displacement and traction components (J. A. Hudson, 1969a) and evaluating the excitation of radiated waves via transforms over frequency, horizontal distance, and azimuth (Section 7.4). Where vertical differentiation is necessary at r_s, the result in the transform plane will (if WKBJ methods apply) be like multiplication by plus or minus $i\omega\xi_s$ for P and $i\omega\eta_s$ for S. This arises because vertical wavefunctions have phase factors such as $\exp(\pm i\omega \int \xi\, dr)$. Clearly, then, we took a major shortcut when we avoided the rigorous derivation of (4) and instead wrote this expression using the form that WKBJ theory would give us if it also were to reproduce the radiation patterns we derived in Chapter 4.

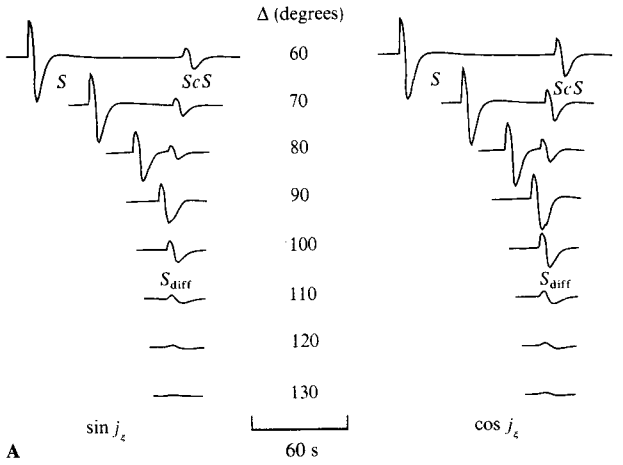

Two record sections for $S + ScS$ waves (polarized as SH). Computation is for the PEM-C Earth model (Dziewonski *et al.*, 1975), with allowance for a 15–100 long-period seismometer and a moment M_0 acting as a linear ramp of 4-s duration. The record section at the left uses a dependence on $\sin j_\xi$ for the integrand; on the right the dependence is on $\cos j_\xi$. Note that the ScS/S amplitude ratio is larger for $\cos j_\xi$ dependence than for $\sin j_\xi$. The reason for this is that the saddle for ScS occurs at a significantly lower ray parameter than does the saddle for S. Though $\cos j_\xi$ is quite insensitive to saddle-point position (note that j_ξ is a small angle for both rays), $\sin j_\xi$ is proportional to p and will be significantly different at the two saddle-point positions.

Although WKBJ theory will be accurate for waves departing steeply downward or upward from the source, it is necessary to use a more accurate method for rays departing nearly horizontally. For such rays, two different problems are present together. First, the WKBJ approximation for $\varepsilon\xi_s$ (or $\varepsilon\eta_s$) in (5)–(7) may be inaccurate. Second, the choice of integration path in the complex p-plane is complicated by the need to consider wavefunctions for both upward- and downward-departing rays. The first problem is easily solved by using a uniformly asymptotic approximation such as (9.91). (Note that downgoing rays require $\varepsilon\xi_s = \check{\xi}_s$, since $\check{\xi}_s$ has a phase that increases if r_s is increased above the turning point, and upgoing rays require $\varepsilon\xi_s = -\check{\xi}_s$.) For the second problem, the solution is to break up the computation into three different line integrals in a way that is very similar to that used in solving the whispering-gallery problem (see Fig. 9.43b,c,d). The critical ray

(continued)

BOX **9.12** *(continued)*

parameter, at which the source level itself is the turning point, is $p_s = r_s/\alpha_s$. To the left of this point in the complex ray-parameter plane, as shown in the figure below, we compute downward-departing waves via a path Γ_2 with $\xi_s = \check{\xi}_s \pi_s^{(1)}$ in the integrand, and use Γ_1 (with $\xi_s = -\check{\xi}_s \pi_s^{(2)}$) for upward-departing waves. Both integrands are combined at a point near p_s. Then, to the right, on Γ_3, the integrand decays exponentially, quantifying the effect of energy tunneling upward from the source level r_s to the turning-point level in the source layer, from which level it can further propagate upward, but with relatively small loss.

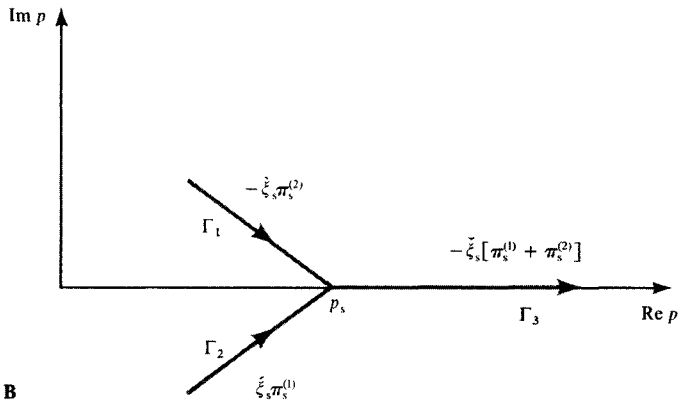

The complex ray-parameter plane, with path Γ_1 for the ray departing upward from the source, path Γ_2 for the ray departing downward, and path Γ_3 for the combined integrand, quantifying tunneling upward from the source depth. Associated with each path is shown the appropriate wavefunction and generalized vertical slowness for the source level r_s.

Finally, we note that just five different linear combinations of $\dot{M}_{ij}$ components are needed in the representation of body waves set up by a system of couples. (From (1) and (2), we see that just three different combinations of moment-tensor elements are needed for *P* and *SV*, and two further combinations are apparent in (3) for *SH*.) The far-field surface-wave formulas we obtained in Chapter 7, (7.148)–(7.151), can also be written in terms of these same five linear combinations of $\dot{M}_{ij}$. Therefore, at each azimuth from the source, one can hope at best to obtain (from far-field data) only five linear constraints on the six independent components of **M**.

FIGURE **9.43**
Generalized *PKP*. (**a**) The travel-time curve for *PKP* and associated reflections and transmissions at the inner-core/outer-core boundary. The numerical integration in (9.102) is handled by separating the *PKiKP* contribution from a single term describing the interference wave. Thus, $\grave{K}(\check{I})\acute{K}$ in (9.102) is broken into two terms via (9.101). (**b**) With $\grave{K}\acute{K}$ in (9.102), the integration is conducted over the path Γ_1. (**c**) With $(\grave{K}\grave{I} \cdot \acute{I}\acute{K})/(1 - \acute{I}\grave{I})$ in (9.102), the integration is conducted over Γ_2. In each case, there are poles trending down into the fourth quadrant (p_c is the critical ray parameter, corresponding to rays with turning point at the top of the solid core; p_g is the ray parameter for the grazing ray, with turning point at the bottom of the fluid core). (**d**) For the remainder of the path, the two integrands are combined together into one term proportional to $\grave{K}(\check{I})\acute{K}$. Poles associated with $\check{\xi}_1$ have been replaced by poles associated with ξ_1. To the right of p_c, $\grave{K}(\check{I})\acute{K}$ tends to +1, hence (9.102) quantifies the *AB* and *BC* branches of *PKP*.

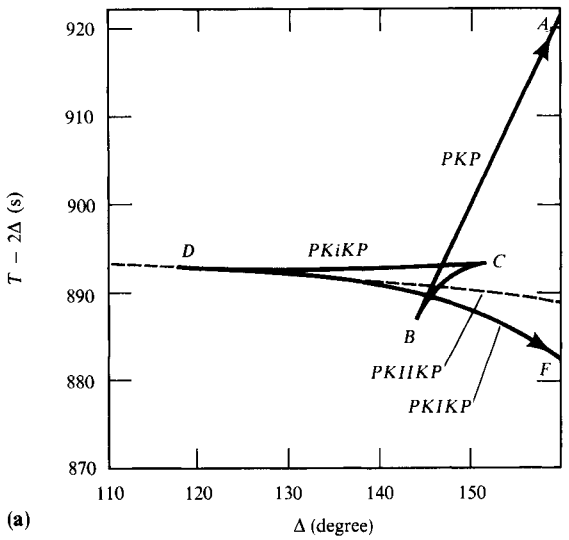
920
910
900
890
880
870
110
120
130
140
150
T − 2Δ (s)
Δ (degree)
A
PKP
D
PKiKP
C
B
PKIIKP
F
PKIKP

(a)

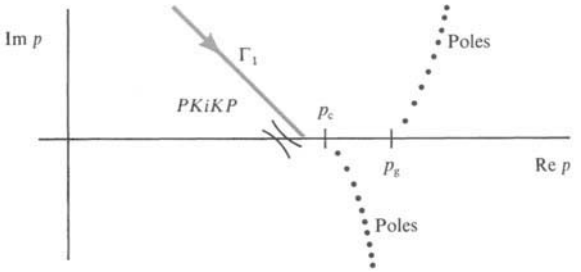
Im p
Γ1
PKiKP
pc
Poles
pg
Re p
Poles

(b)

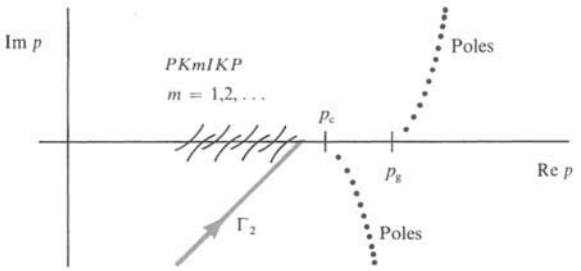
Im p
PKmIKP
m = 1,2, . . .
Poles
pc
pg
Re p
Γ2
Poles

(c)

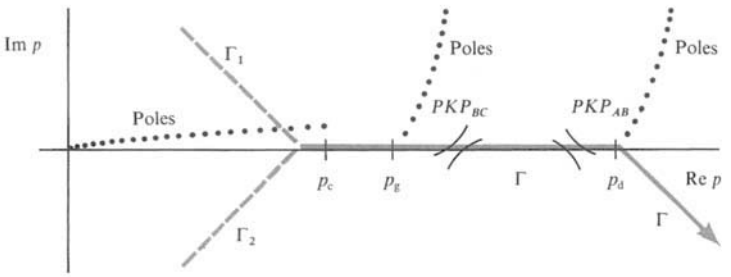
Im p
Γ1
Poles
Poles
Poles
PKPBC
PKPAB
pc
pg
Γ
pd
Re p
Γ
Γ2

(d)

for transmissions across r_1. The whole family of rays shown in Figure 9.42 is therefore described by

$$\grave{K}\acute{K} + \grave{K}\grave{I}\cdot\acute{I}\acute{K} + \grave{K}\grave{I}\cdot\acute{I}\grave{I}\cdot\acute{I}\acute{K} + \grave{K}\grave{I}\cdot(\acute{I}\grave{I})^2\cdot\acute{I}\acute{K} + \cdots = \grave{K}\acute{K} + \frac{\grave{K}\grave{I}\cdot\acute{I}\acute{K}}{1-\acute{I}\grave{I}}. \quad (9.97)$$

The summation of this geometric series is similar to a problem of multiples we described earlier in plane-wave theory, (9.18)–(9.19).

In the derivation of each of $\grave{K}\acute{K}$, $\grave{K}\grave{I}$, $\acute{I}\acute{K}$, $\acute{I}\grave{I}$, it has been assumed that the energy scattered into the lower medium is only downgoing energy. In fact, from Box 9.9 with a liquid layer 2 above solid layer 1,

$$\grave{K}\acute{K} = \frac{\left[\rho_1(1-2\beta_1^2p^2/r_1^2)^2\grave{\xi}_2 - \rho_2\grave{\xi}_1 + 4\rho_1\beta_1^4(p^2/r_1^2)\grave{\xi}_2\grave{\eta}_1\grave{\xi}_1\right]\pi_2^{(2)}}{\left[\rho_1(1-2\beta_1^2p^2/r_1^2)^2\acute{\xi}_2 + \rho_2\grave{\xi}_1 + 4\rho_1\beta_1^4(p^2/r_1^2)\acute{\xi}_2\grave{\eta}_1\grave{\xi}_1\right]\pi_2^{(1)}}. \quad (9.98)$$

The P-wave wavefunctions for the solid inner core appear here only via $\grave{\xi}_1$, and indeed this *is* the appropriate vertical slowness for a downgoing wave. But, as can be seen in Figure 9.42, this downgoing wave ($\pi_1^{(2)}$) is soon turned around to an upgoing wave ($\pi^{(1)}$), because the turning point is not far below the interface. Therefore, for a P-wave incident downward from the fluid core, it is appropriate instead to use $\pi_1^{(1)} + \pi_1^{(2)}$ for the wavefunction in the lower medium, since this is the wavefunction that correctly describes amplitudes throughout the solid core. The reflection coefficient $\grave{K}\acute{K}$ is modified if this new wavefunction in the solid core is used, and a natural notation is $\grave{K}(\check{I})\acute{K}$. Satisfying boundary conditions at the interface, we find

$$\grave{K}(\check{I})\acute{K} = \frac{\left[\rho_1(1-2\beta_1^2p^2/r_1^2)^2\grave{\xi}_2 - \rho_2\check{\xi}_1 + 4\rho_1\beta_1^4(p^2/r_1^2)\grave{\xi}_2\grave{\eta}_1\check{\xi}_1\right]\pi_2^{(2)}}{\left[\rho_1(1-2\beta_1^2p^2/r_1^2)^2\acute{\xi}_2 + \rho_2\check{\xi}_1 + 4\rho_1\beta_1^4(p^2/r_1^2)\acute{\xi}_2\grave{\eta}_1\check{\xi}_1\right]\pi_2^{(1)}}, \quad (9.99)$$

where

$$\check{\xi}_1 \equiv \frac{1}{-i\omega(\pi_1^{(1)} + \pi_1^{(2)})}\frac{d}{dr}(\pi_1^{(1)} + \pi_1^{(2)}). \quad (9.100)$$

Our new reflection coefficient, $\grave{K}(\check{I})\acute{K}$, has two important properties. First, it can be shown after some algebra that

$$\grave{K}(\check{I})\acute{K} = \grave{K}\acute{K} + \frac{\grave{K}\grave{I}\cdot\acute{I}\acute{K}}{1-\acute{I}\grave{I}}, \quad (9.101)$$

and hence this single coefficient accounts for all the rays present in Figure 9.42. The expansion of $\grave{K}(\check{I})\acute{K}$ into the left-hand terms of (9.97) is an example of the *rainbow expansion* (sometimes called the *Debye expansion*), so named because of a similar expansion arising in the theory of the rainbow. (The refractive index of water in air is similar to that of the core relative to the mantle, and the seismological analog of the primary rainbow is the caustic in *PKKP*.) It is usually appropriate to make the rainbow expansion when the medium below the

interface is slower than that above, because the multiples then set up in the lower medium will not interfere with each other. An example is that of $PcP + PKP + PKKP + \cdots$, and each of the transmitted waves can be studied separately. However, it is often inappropriate to make the expansion when the medium below is faster, because the multiples can interfere with each other, and we need to account for all of them in combination.

The second important property of $\grave{K}(\check{I})\acute{K}$ concerns the position of poles in the complex p-plane. Previously, for $\grave{K}\acute{K}$, there was a system of poles associated with $\check{\xi}_1$, and therefore trending down into the fourth quadrant (Box 9.11). But the new ratio defining $\check{\xi}_1$ has poles and zeros stringing just above the real p-axis, between 0 and $r_1/\alpha_1(r_1)$, and it is here that poles of $\grave{K}(\check{I})\acute{K}$ are found.

The representation of P-waves originating from a point shear dislocation with moment $M_0(\omega)$ and transmitted through the inner core can now be written as

$$u_r^{PKP}(r, \Delta_0, \phi, \omega) = \frac{-i\omega M_0(\omega) i\omega}{4\pi\rho_s\alpha_s^4} \times \int_\Gamma \omega^2 p \mathcal{F}^P \pi^{(1)}(r_s)\grave{P}\grave{K} \cdot \grave{K}(\check{I})\acute{K} \cdot \acute{K}\acute{P}\left[\alpha(r)\check{\xi}(r)\pi^{(1)}(r)\right] Q^{(2)}_{\omega p - \frac{1}{2}}(\cos\Delta_0)\, dp. \tag{9.102}$$

The radiation pattern here is derived from (4.89), and $\mathcal{F}^P$ depends upon the strike ϕ_s, dip δ, and rake λ via

$$\begin{aligned}\mathcal{F}^P = {} & \sin\lambda \sin 2\delta + [\cos\lambda \sin\delta \sin 2(\phi - \phi_s) - \sin\lambda \sin 2\delta(1 + \sin^2(\phi - \phi_s))]\alpha_s^2 p^2/r_s^2 \\ & + 2[\sin\lambda \cos 2\delta \sin(\phi - \phi_s) - \cos\lambda \cos\delta \cos(\phi - \phi_s)]\frac{\alpha_s^2 p}{r_s}\sqrt{\frac{1}{\alpha_s^2} - \frac{p^2}{r_s^2}}.\end{aligned} \tag{9.103}$$

It is correct to designate (9.102) as the generalized *PKP*-wave, because it accounts for *all* the compressional phases generated by a P-wave transmitted downward once and upward once at the core–mantle interface. For p such that the wave has a turning point well above the inner core, the factor $\grave{K}(\check{I})\acute{K}$ in (9.102) is approximately $+1$, and the effect of the inner core is negligible. Even the caustic in *PKP* near 142° is accounted for. At lower values of p, the interference head wave is correctly quantified, provided the integrand is broken up into two parts and integrated along separate paths, as shown in Figure 9.43b,c,d.

Using a representation equivalent to (9.102), Cormier and Richards (1977) have computed *PKP* in the parameterized Earth model of Dziewonski *et al.* (1975). Their results are shown in Figure 9.44 and compared with observations in Figure 9.45.

It is clear that integrands like (9.102) can be built up for more and more complicated body waves. Even the effect of crustal and upper mantle layering can be accounted for, because the propagator matrix corresponding to (9.83)–(9.84) can be written in closed form. In this way, it is possible to compute leaking modes, together with other phases that arrive within the same time window. Consider, for example, what happens when an SV-wave is incident from below upon the crust–mantle interface at a ray parameter in the vicinity of 770 s/radian. This is near the critical value at which P is propagating horizontally just beneath the Moho, and a variety of possible ray arrivals for a receiver on the surface

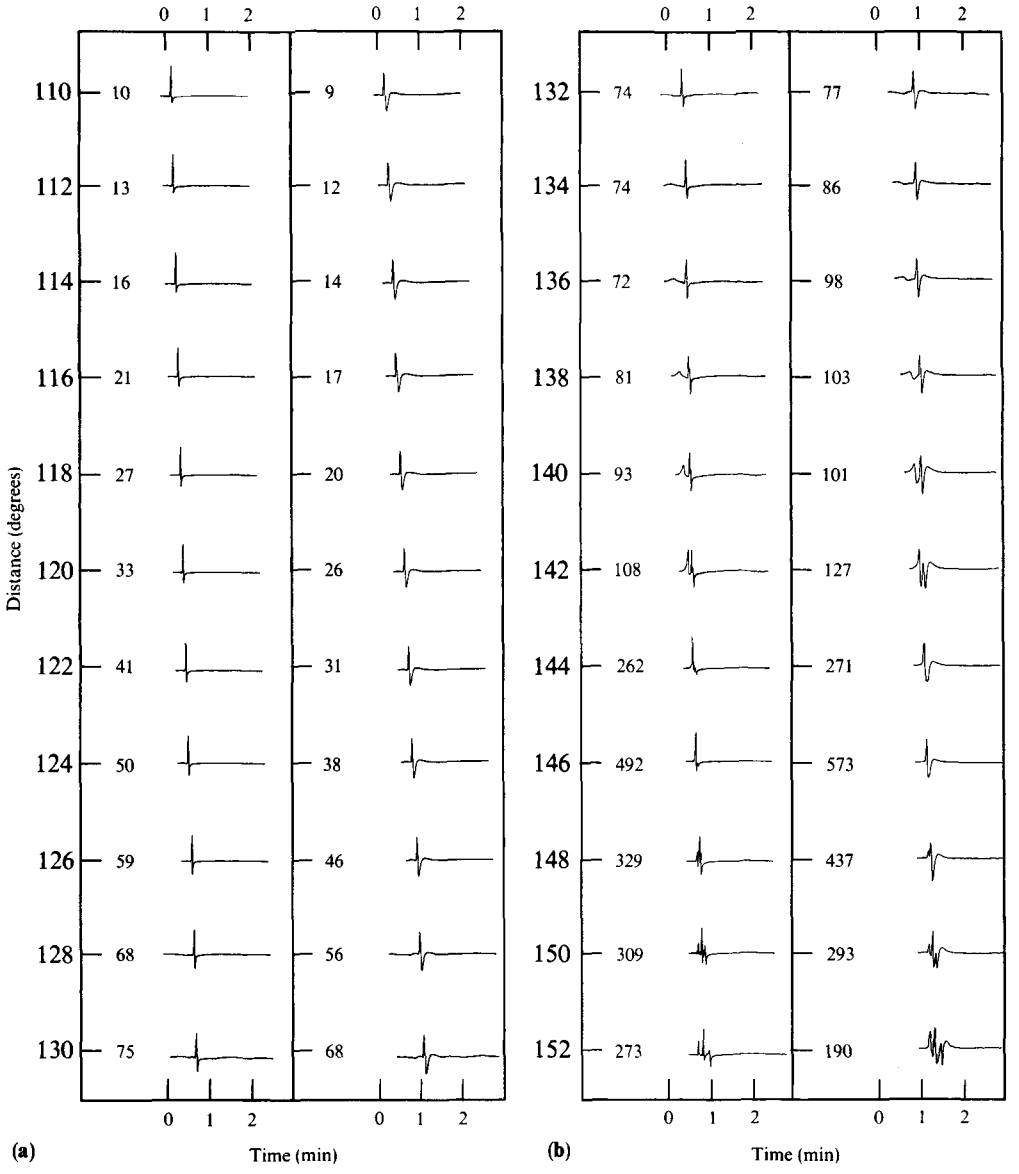

FIGURE **9.44**

Left in (**a**) and (**b**). Impulse response for *PKP*, computed via (9.102) in the parameterized Earth model (PEM) of Dziewonski *et al.* (1975). *Right* in (**a**) and (**b**). Impulse response convolved with the response of a 15–100 (long-period) WWSSN vertical instrument. Numbers at the left of responses indicate relative amplitude in a sequence of increasing distances. Note that the waveform does not change across the critical point near 120°. The position of the critical point merely affects amplitudes. A long-period precursive phase is apparent in 134–140°, and is associated with the caustic in *PKP* (point *B*, Fig. 9.43a) at 143°. This phase lies on the side of the caustic for which ray theory predicts no arrivals. The complicated pulses in 138–152° are a result of interference between all the arrivals shown in Figure 9.43a. [After Cormier and Richards, 1977.]

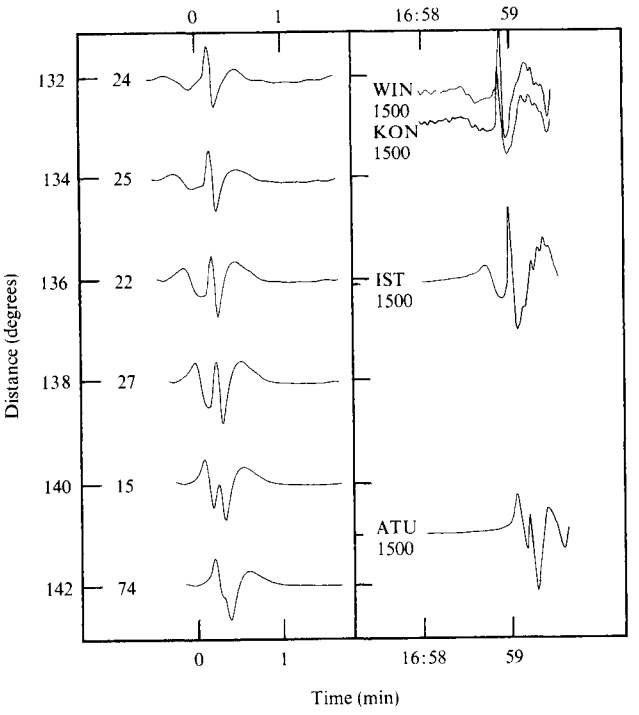

FIGURE **9.45**
Comparison between synthetic seismograms (shown at left), and observed (shown at right) for an earthquake on 1964 July 9. [After Cormier and Richards, 1977.]

are shown in Figure 9.46, including a whispering-gallery effect. It is also known that the crust can support leaking modes, called *PL*-modes, in which the *P*-wave energy below the Moho decays exponentially with depth but *SV*-wave energy is radiated downward. The corresponding phase slowness (ray parameter) of the fundamental is only slightly greater than that of SP_{diff} (see Fig. 9.46e), so that this leaking mode can also be excited by the incident *SV*-wave of Figure 9.46. It has been labeled as shear-coupled *PL* by Oliver (1961), and prominent examples of this phase, together with a discussion of how it may be excited efficiently, are given by Chander *et al.* (1968) and Poupinet and Wright (1972). Frazer (1977) has shown how a single integrand can be developed to describe all the phases of Figure 9.46, plus multiples in the crust and shear-coupled *PL*-waves, and he has integrated over real p and real ω to obtain synthetic record sections, such as the one given in Figure 9.47. To handle the waves scattered into the mantle from a boundary condition imposed at the Moho, he used the wavefunction $\sigma^{(2)}$ for downgoing *SV*, but $\pi^{(1)} + \pi^{(2)}$ for *P*. This is similar to the way in which a whispering gallery phenomenon was handled in Figures 9.42–9.45. He allowed for reverberations in the crust by using the propagator matrix between Moho and surface, and imposed free surface boundary conditions. Frazer was able to show that prominent shear-coupled *PL*-waves require a favorably oriented source and a mantle with anomalously high shear-velocity gradient near 650 km depth.

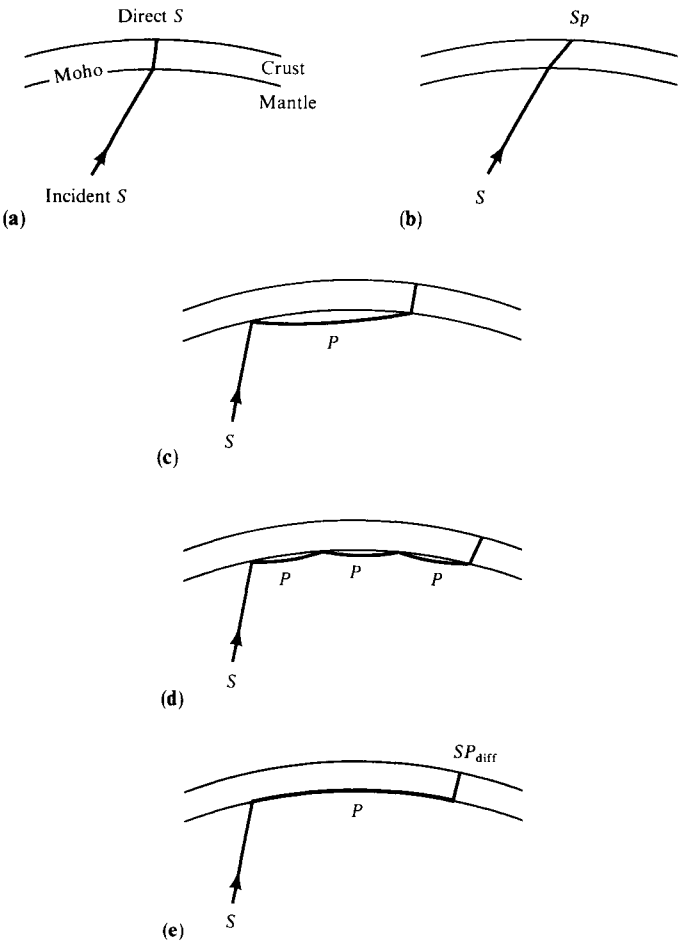

FIGURE **9.46**

Ray paths associated with SV incident upon the Moho at an angle close to that which generates horizontally propagating P at the top of the mantle. (**a**) The direct S-wave (SV in the crust). (**b**) Traveling as P in the crust, this arrival is denoted by Sp. It arrives a little earlier than the direct S-wave, and has been described in detail by Jordan and Frazer (1975). (**c**) A single leg as P in the mantle is included (the crustal path could be P or S). (**d**) Three mantle P-wave legs. (**e**) The number of mantle P-wave legs can be increased indefinitely, until in the limit (at a critical value of ray parameter) the ray path is horizontal. Frazer (1977) labels the associated arrival at the surface SP_{diff}. It contains superposed P- and S-rays through the crust, and, in practice, includes the whole family of rays such as (c) and (d), forming an interference head wave. For a given point source and a given receiver, all the ray paths (a)–(e) may be present together with reverberations in the crust, though each particular ray will in general have a slightly different ray parameter.

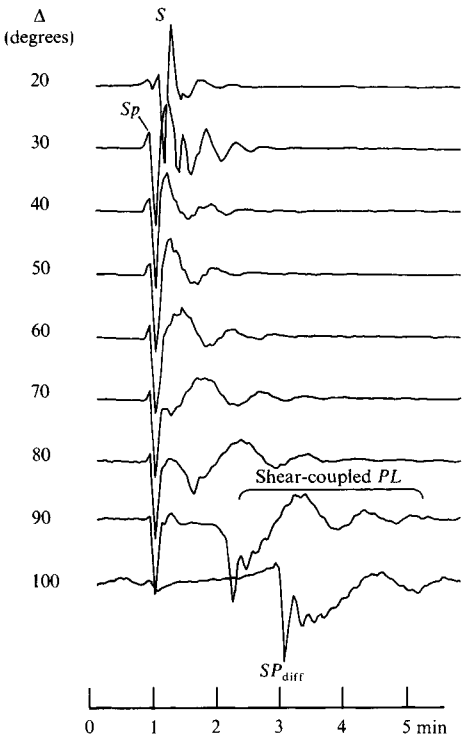

FIGURE **9.47**
A record section showing component phases that make up the complex SV-arrival for a receiver on the free upper surface of a crustal layer. The main SV-path in the mantle has a single turning point between source and receiver. The P-velocity is taken as constant just below the Moho, generating a very effective whispering gallery, as seen by the large SP_{diff} arrival. It is the horizontal component of motion that is computed here, and the traces at different distances Δ have been time-shifted to align the first arrival. [After Frazer, 1977.]

9.7 Comparison between Different Methods

It is only since the late 1960s that the effort to compute accurate body-wave pulse shapes in realistic structures has been more successful in practice than classical ray theory. We have found it convenient to distinguish three computational methods: (i) Cagniard inversion of generalized rays that do not have turning points, (ii) double integration (over real slowness and real frequency) retaining all multiples, and (iii) double integration (over real or complex slowness and real frequency) for generalized rays (possibly with turning points) in inhomogeneous layers. The second method includes the so-called "reflectivity" approach of Section 9.2 originated by Fuchs, and the "Direct Solution Method" discussed in Section 7.4. From the third method we have derived the WKBJ seismogram, which in practice shares some of the features of Cagniard inversion. Where this third method improves upon WKBJ approximations, it is sometimes referred to as a "full-wave theory." These methods can all be compared with (iv) the direct sum of normal modes (as described in Chapter 8).

First, we note that the methods of Cagniard and Fuchs have been developed for plane homogeneous layers. Their application in a spherical Earth requires some preliminary discussion, given in Box 9.2. A trade-off must be addressed in the way that a given inhomogeneous Earth model is approximated by a layered model. Coarser layering can substantially decrease computation costs, but at the expense of accuracy. The decision here, of what layer thickness is appropriate, will of course depend upon the frequency range for which accurate results are required.

For broad-band pulse shapes, Cagniard's method and the WKBJ seismogram have inherent advantages because the response (apart from convolutions) is calculated in the time domain. When the pulse amplitude is rapidly changing with time, details of this change can easily be studied by sampling along the Cagniard path at points that are closely spaced.

If pulse shapes are to be computed at many distances, then methods (ii) through (iv) have an inherent advantage, since the same range of integration or summation can serve for many distances, whereas the Cagniard path (and the equivalent path for the WKBJ seismogram) must be newly determined for each distance. It should be recognized that, by "Cagniard's method" we are referring to a technique that has benefitted from the contributions of many individuals. Computational details are given, for example, by Wiggins and Helmberger (1974). Fuch's reflectivity method also has been extended from its original formulation. For example, Kind (1978) modified the method to allow it to handle reverberations in layers both above and below the source. He was also able to incorporate the effects of attenuation, and surface waves and leaking modes. By using the solution (9.83) and Box 9.9, it is possible to extend Fuch's method further to handle all multiples within *inhomogeneous* layers. By "full-wave theory" we are loosely referring to the whole range of methods summarized in Section 9.6, based on *complex* ray-parameter and real-frequency integration.

If attenuation is strong, in the sense that $Q \gg 1$ but waves are attenuated by propagating over many wavelengths, then the theory for methods (ii) and (iii) is virtually unchanged. The velocity profile itself is defined to be complex (see (5.94)). However, Cagniard's method and the WKBJ seismogram cannot readily accommodate causal attenuation, except by *ad hoc* methods based on classical ray theory.

The various methods differ most strongly in their treatment of problems in which the wave to be synthesized has been influenced by Earth structure in the vicinity of a turning point. Just this kind of body wave can be of great geophysical interest, because anomalous features in a velocity profile are likely to have their strongest effect on body waves with ray paths that bottom near the anomalous structure. To put this another way: the waves that contain maximum information about some velocity anomaly are the waves that spend the longest time in the vicinity of the anomaly. They will therefore be the waves that travel horizontally at the depth of the anomaly (i.e., have their turning point there). Cagniard's and Fuchs' methods differ for these problems, because the first is based on generalized rays (and it is impractical to retain more than a few hundred), whereas the second contains all multiples within a prescribed range of depths and within a prescribed range of slowness ($dT/d\Delta$). These methods are compared in Figure 9.9.

With full-wave theory, turning-point computations are treated no differently from problems of narrow-angle reflection. However, it is important to be able to compute vertical wavefunctions accurately. It is this fact that renders the WKBJ seismogram inaccurate for problems on grazing incidence. Whether the Langer approximation is used or a numerical integration of the equations of motion, the precise way in which velocities are interpolated (in the Earth model) must have some influence on the computed pulse shapes. Earth models are most commonly tabulated as values of density and P- and S-wave speeds at different depths, and geophysicists have no convention about how to obtain values at intermediate levels. Linear interpolation is common, but so are various types of splines. The Earth-flattening transformation, together with the stack of homogeneous plane layers used in Cagniard's and Fuchs' methods, is another form of interpolation (see the figure in

Box 9.2). It will probably be impossible to decide which of the methods of computing body-wave seismograms is most appropriate for a particular problem until the effect of different interpolation laws in the underlying Earth model is thoroughly quantified.

Because the Earth is such a complicated medium (even when assumed to be spherically symmetric), it is necessary in practice to make approximations in all of the different solution methods we have described. It is therefore fortunate that there *are* several methods, since it often appears that the accuracy of any one method (and, more important, the geophysical conclusions that may be drawn from its application) can be verified only by a comparison against other methods. The different methods have some unique and some overlapping areas of applicability.

Suggestions for Further Reading

Ammon, C. J. The isolation of receiver effects from teleseismic *P* waveforms. *Bulletin of the Seismological Society of America*, **81**, 2504–2510, 1991.

Bouchon, M. A simple method to calculate Green's functions for elastic layered media. *Bulletin of the Seismological Society of America*, **71**, 959–971, 1981.

Budden, K. G. *The Propagation of Radio Waves: The Theory of Radio Waves of Low Power in the Ionosphere and Magnetosphere*. Cambridge University Press, 1988.

Bullen, K. E. and B. A. Bolt. *An Introduction to the Theory of Seismology*. 4th ed. (Chaps. 7 and 8 for ray theory). Cambridge University Press, 1985.

Červený, V. *Seismic Ray Theory*, Cambridge: Cambridge University Press, 2001.

Chapman, C. H., and R. A. Phinney. Diffracted seismic signals and their numerical solution. In *Seismology: Body Waves and Sources*, edited by B. A. Bolt. Methods of Computational Physics, Vol. 12. New York: Academic Press, 1972.

Chapman, C. H., and J. A. Orcutt. The computation of body wave synthetic seismograms in laterally homogeneous media. *Reviews of Geophysics*, **23**, 105–163, 1985.

Coddington, E. A., and R. Carlson. *Linear Ordinary Differential Equations*. Society for Industrial and Applied Mathematics, 1997.

Cormier, V. F., and P. G. Richards. Spectral synthesis of body waves in earth models specified by vertically varying layers. In *Seismological Algorithms*, edited by D. Doornbos, 3–45. Academic Press, 1988.

Dey-Sarkar, S. K., and C. H. Chapman. A simple method for the computation of body-wave seismograms. *Bulletin of the Seismological Society of America*, **68**, 1577–1593, 1978.

Emery, V., V. Maupin, and H.-C. Nataf. Scattering of *S* waves diffracted at the core-mantle boundary: Forward modelling. *Geophysical Journal International*, **139**, 325–344, 1999.

Fuchs, K. The reflection of spherical waves from transition zones with arbitrary depth-dependent elastic moduli and density. *Journal of the Physics of the Earth*, **16**, special issue, 27–41, 1968.

Fuchs, K., and G. Müller. Computation of synthetic seismograms with the reflectivity method and comparison of observations. *Geophysical Journal of the Royal Astronomical Society*, **23**, 417–433, 1971.

Helmberger, D. V., and S. D. Malone. Modeling local earthquakes as shear dislocations in a layered half-space. *Journal of Geophysical Research*, **80**, 4881–4888, 1975.

Müller, G. The reflectivity method: A tutorial. *Journal of Geophysics*, **58**, 153–174, 1985.

Nussenzveig, H. M. High-frequency scattering by an impenetrable sphere. *Annals of Physics (New York)*, **34**, 23–95, 1965.

Okal, E. A. A student's guide to teleseismic body wave amplitudes. *Seismological Research Letters*, **63**, 169–179, 1992.

Virieux, J. Seismic ray tracing. In *Seismic Modelling of Earth Structure*, edited by E. Boschi, G. Ekström, and A. Morelli. Istituto Nazionale di Geofisica, Editrice Compositori, 223–304, 1996.

Wasow, W. *Asymptotic Expansions for Ordinary Differential Equations.* Pure and Applied Mathematics, vol. 14. New York: Interscience, 1965.

Wiggins, R. A., and D. V. Helmberger. Synthetic seismogram computation by expansion in generalized rays. *Geophysical Journal of the Royal Astronomical Society*, **37**, 73–90, 1974.

Problems

9.1 Given the generalized ray described in Figures 9.1 and 9.2 and the Cagniard path $p = p(t')$ that solves (9.5),

a) show that the distance L traveled by the head wave in layer $(n + 1)$ is

$$L + \left.\frac{dt'}{dp}\right|_{p=1/\alpha_{n+1}}.$$

b) Show that, for points on the Cagniard path near and to the right of $p = 1/\alpha_{n+1}$,

$$\xi_{n+1} = -i\sqrt{\frac{2}{L\alpha_{n+1}}(t' - t_h)},$$

where t_h is the head-wave arrival time,

$$t_h = \frac{r}{\alpha_{n+1}} + \text{SUM}\left(\frac{1}{\alpha_{n+1}}\right).$$

From (5.39) and (5.40), it can be shown that

$$\grave{P}\acute{P}_n = \frac{A - \xi_{n+1}B}{A' + \xi_{n+1}B'},$$

where

$$A = A(p) = bF\xi_n - a(a + d\xi_n\eta_{n+1})p^2,$$

$$B = cF - d\eta_n(a + d\xi_n\eta_{n+1})p^2,$$

$$A' = bF\xi_n + aGp^2,$$

$$B' = cF - d\eta_n Gp^2,$$

and a, b, c, d, F, G are taken from (5.39) with subscripts n and $n+1$ now used for quantities evaluated just above and just below the boundary, respectively. Note that A, B, A', B' are real for p on the Cagniard path near $1/\alpha_{n+1}$.

c) Obtain the function $\psi(t)$ (see (9.7)) near $t = t_h$. Then use

$$\frac{2}{\pi\sqrt{t}} * \left[\sqrt{t - t_h}H(t - t_h)\right] = (t - t_h)H(t - t_h)$$

(a ramp function) to show that the head-wave pressure response for a source that is a unit step in pressure at distance R_s is approximately

$$\sqrt{\frac{1}{rL^3}}\frac{R_s}{\alpha_{n+1}}\left[(\grave{P}\hat{P})_1 \cdots (\grave{P}\hat{P})_{n-1}\frac{AB' + A'B}{\xi_1 A'^2}(\acute{P}\hat{P})_{n-1} \cdots (\acute{P}\hat{P})_1\right]_{p=1/\alpha_{n+1}}$$
$$\times (t - t_h)H(t - t_h).$$

This is an asymptotic result, valid as $t \to t_h$, and is an example of the first term of a wavefront expansion. The onset of the head wave here has the typical pulse shape we should expect from Chapter 6, i.e., it is the time integral of the pulse radiated from the source.

9.2 For a particular ray path in a stratified medium, two functions of ray parameter that are often useful for evaluating pulse shapes associated with the ray are TIME(p) and DISTANCE(p). We define TIME(p) as the travel time taken along the ray from source to receiver as the receiver position varies (but with fixed depth), and DISTANCE(p) is simply the distance measured horizontally between source and receiver (i.e., the horizontal range for plane stratification; and angle Δ for spherical geometry). Thus, for the wide-angle reflection in Figure 9.1b,

$$\text{TIME}(p) = \frac{Th_1 - d_1}{\alpha_1 \cos i_1} + \frac{2Th_2}{\alpha_2 \cos i_2} + \cdots + \frac{2Th_n}{\alpha_n \cos i_n} + \frac{Th_1 - d_2}{\alpha_1 \cos i_1}$$

and

$$\text{DISTANCE}(p) =$$
$$(Th_1 - d_1)\tan i_1 + 2Th_2 \tan i_2 + \cdots + 2Th_n \tan i_n + (Th_1 - d_2)\tan i_1.$$

a) As the receiver position is varied (at fixed depth), show that

$$p = \frac{d(\text{TIME})}{d(\text{DISTANCE})}$$

(i.e., ray parameter is the gradient of the travel-time curve).

b) Show that the Cagniard path (9.5) is given by

$$t' = pr + \text{TIME}(p) - p\ \text{DISTANCE}(p).$$

We next ask some questions about an approximate evaluation of the wide-angle reflection and about associated features in the ray parameter plane:

c) Show that $dt'/dp = r - \text{DISTANCE}(p)$.
Note then that $dt'/dp = 0$ for ray parameter p_0, provided this is the value for the actual ray that connects source and receiver (i.e., the solution of $\text{DISTANCE}(p) = r$).

d) Show that $d^2t'/dp^2 = -d(\text{DISTANCE}(p))/dp$, and hence that d^2t'/dp^2 is always negative for primary reflections in plane-stratified media.

e) From

$$t' = t_{\text{refl}} + (p - p_0)\frac{dt'}{dp} + \frac{(p - p_0)^2}{2}\frac{d^2t'}{dp^2} + \cdots,$$

where t_{refl} is the ray-arrival time of the wide-angle reflection, show that indeed the Cagniard path $p = p(t')$ *must* leave the real p-axis at right angles at $p = p_0$ as real t' increases through t_{refl}.

f) For times near t_{refl}, show that

$$\frac{dp}{dt'} \sim \frac{1}{\sqrt{t_{\text{refl}} - t'}} \frac{1}{\sqrt{2\dfrac{d}{dp}\text{DISTANCE}}} \qquad t' < t_{\text{refl}},$$

$$\sim \frac{i}{\sqrt{t' - t_{\text{refl}}}} \frac{1}{\sqrt{2\dfrac{d}{dp}\text{DISTANCE}}} \qquad t' > t_{\text{refl}}.$$

g) In an approximate evaluation of the step response $(2/\pi)\int_0^t \psi(t')/\sqrt{t - t'}\, dt'$ (see (9.7)) for times near t_{refl}, it is sufficient to replace all slowly varying factors of $\psi(t')$ by their values *at* $t' = t_{\text{refl}}$, and to convolve $1/\sqrt{t}$ with the only rapidly varying factor, which is dp/dt'.

It follows from (f) that $1/\sqrt{t} * dp/dt$, for times near t_{refl}, is

$$\sqrt{\frac{1}{2\dfrac{d}{dp}\text{DISTANCE}}} \left[i\pi H(t - t_{\text{refl}}) - \log\left(\frac{|t - t_{\text{refl}}|}{t_{\text{refl}}}\right)\right].$$

Use this result to obtain the step-function response for the wide-angle reflection as

$$R_s \left[\frac{1}{\xi_1} \sqrt{\frac{p}{r \frac{d}{dp}\text{DISTANCE}}} (\grave{P}\grave{P}_1) \cdots (\grave{P}\grave{P})_{n-1} (\acute{P}\acute{P})_{n-1} \cdots (\acute{P}\acute{P})_1 \right]_{p=p_0}$$

$$\times \left[\text{Re}(\grave{P}\acute{P}_n) H(t - t_{\text{refl}}) - \frac{\text{Im}(\grave{P}\acute{P}_n)}{\pi} \log \left(\frac{|t - t_{\text{refl}}|}{t_{\text{refl}}} \right) \right].$$

(Recall that R_s is the distance at which the incident wave from the source is a unit step in pressure. It is presumed that R_s is not large enough to place the calibrating receiver outside layer one.)

h) The geometrical ray theory of Chapter 5 would indicate that the unit step-function response is given by

$$\frac{R_s}{\mathcal{R}(\mathbf{x}, \boldsymbol{\xi})} H(t - T(\mathbf{x}, \boldsymbol{\xi})) \times \text{factor to account for loss of energy at interfaces,}$$

where $T(\mathbf{x}, \boldsymbol{\xi})$ is the travel time between source at $\boldsymbol{\xi}$ and receiver at $\mathbf{x}$ and $\mathcal{R}(\mathbf{x}, \boldsymbol{\xi})$ is the geometrical spreading function. Clearly, $T(\mathbf{x}, \boldsymbol{\xi}) = t_{\text{refl}}$. Use the method of Problem 4.4 to show that

$$\mathcal{R}(\mathbf{x}, \boldsymbol{\xi}) = \xi_1 \sqrt{\frac{r}{p} \frac{d}{dp}\text{DISTANCE}}.$$

(*Note:* Source and receiver are both in layer one.)

i) Since transmission coefficients for our generalized ray are real, and only $\grave{P}\acute{P}_n$ is complex, use the results of (h) and of Problem 5.17 to give an alternative derivation of the approximate step-function response, which we obtained in (g) by approximation of Cagniard's method.

9.3 Show that the entries in the propagator matrix $\mathbf{P}(z_m, z_n)$ (for SH-waves, or for P-SV, in a medium composed of homogeneous plane layers, with z_m and z_n possibly being separated by several different layers) do not have branch cuts in ξ_m, η_m, or in any other vertical slowness.

Outline, in the form (9.16), an exact expression for the Fourier transform of the total pressure at point $(r, z_0 + d_2)$ shown in Figure 9.1b (that is, with *all* multiples included and with the source (9.1)). Show that the only branch cuts of the integrand in the p-plane are those associated with ξ_{n+1}, η_{n+1}, and $J_0(\omega p r)$. (This result greatly facilitates a discussion of path deformation. Note that the corresponding integrand for the generalized primary Moho reflection alone, given by (9.2) for the Laplace transform, has many more branch cuts.)

9.4 This problem addresses a difficulty with the standard geometrical spreading formula.

a) For a deep source in a spherically symmetric medium, show that the ray departing horizontally is the ray with maximum ray parameter. Show that this ray corresponds to an inflection on the travel-time curve $T = T(\Delta)$, and hence corresponds to a zero value for $dp/d\Delta$, so that the usual expression for geometrical spreading (9.69) cannot be used.

b) Consider a point source S at radius r_s in a spherically symmetric Earth model with velocity profile $\alpha(r)$. Suppose that a ray departing horizontally from S is received at P (radius r, distance Δ from S). Show in this case that the geometrical spreading at P is given by

$$\mathcal{R}(P, S) = r\sqrt{\frac{\sin\Delta\cos i(r)}{[1-\zeta(r_s)]}},$$

where $\zeta(r)$ is the normalized velocity gradient, $r/\alpha(r)(d\alpha/dr)$. (*Hints:* What is $\mathcal{R}^2(S, P)$ in terms of $\delta r_s/\delta i(r)$? How can $r_s/\alpha(r_s) = p$ give $\delta r_s/\delta i(r)$?)

9.5 The phase of a vertical wavefunction is given, in WKBJ theory, by identifying $\omega\alpha^{-1}\cos i$ as the vertical wavenumber and integrating this quantity over the vertical distance traveled from some reference depth. In this context, interpret the sum of waves $g_n^{(1)}(r) + g_n^{(2)}(r)$ at a level $r > r_p$ in terms of an incident wave $g_n^{(2)}$ and reflected wave $g_n^{(1)}$, and show that a $\pi/2$ phase advance occurs in the "reflection" from the turning point.

9.6 If WKBJ approximations are used for

$$P(\mathbf{r}, \omega) = g^{(1)}_{\omega p-\frac{1}{2}}(r)\,Q^{(2)}_{\omega p-\frac{1}{2}}(\cos\Delta)$$

in the depth range $r > r_p$, show that the phase of P varies most rapidly along paths on which $r(\sin i)/\alpha(r) = p$.

9.7 In association with the WKBJ approximation for $\mathbf{R}_l^0$ and $\mathbf{S}_l^0$, show that $\pi^{(j)}$ and $\sigma^{(j)}$ approximated by (9.85) and (9.86) have the property of conserving the flux rate of energy across horizontal levels in cones with solid angle $\sin\Delta\,\delta\Delta\,\delta\phi$ at the center of the Earth.

9.8 Suppose that the ray path between two points A and B is known in a medium with velocity $c = c(\mathbf{x})$. Suppose now that a slight velocity perturbation $\delta c(\mathbf{x})$ is introduced into the medium. Then the original travel time between A and B,

$$T = \int_A^B \frac{ds}{c(\mathbf{x})} \qquad \text{(where } ds \text{ is an element of path length)}$$

is affected in two ways. One, the integrand becomes $1/(c + \delta c)$; two, the ray path itself is slightly changed. Give a statement of Fermat's principle, and show that the effect of the velocity perturbation on T is given to first order by

$$\delta T = -\int_A^B \frac{\delta c \, ds}{c^2},$$

where the path of integration is the *original* ray path, so that no new ray tracing is needed to evaluate δT. [This result is key to the application of most tomographic methods. It can also be used to obtain travel-time corrections for the Earth's ellipticity of figure and other departures from spherical symmetry. Concise results are given by Dziewonski and Gilbert, 1976; and Kennett and Gudmundsson, 1996.]

9.9 Show that the group velocity for body waves with travel time T at distance Δ on a spherical Earth is Δ / T. Show that, as $\Delta \to 0$ for the body-wave reflection *ScS*, the group velocity tends to zero but the phase velocity ($d\Delta/dT$) tends to infinity.

9.10 In general terms, what are likely to be the typical frequency-dependent and distance-dependent properties of seismic waves near a caustic?

CHAPTER 10

The Seismic Source: Kinematics

In Section 2.5 and Chapter 3, we studied seismic sources so that we could begin to determine what aspects of the theory of wave propagation are needed in seismology. Having completed a study of wave propagation in Chapters 4–9, we return here to a more thorough examination of seismic sources. Of all the various types of source that can generate seismic waves (explosions, rapid phase transformations, etc.), the principal source we shall study is that involving a surface (the fault plane) across which shearing motions develop. In Section 3.1, we showed that if the displacement discontinuity across a fault surface is a known function of time and position on the fault, then motions throughout the medium are completely determined. This result provides the basis of the present chapter, in which we shall characterize what may be learned from far-field and near-field observations about the kinematics of motion at an earthquake source.

To understand the physical processes actually occurring in the source region, one must study stress-dependent material properties such as the way in which material failure nucleates and spreads (e.g., over a fault plane), rapidly relieving stresses that had slowly risen (due to long-term tectonic processes) to exceed the strength of material in the source region. This is a dynamic problem, and a very difficult one, which we take up in the next chapter. As we develop now the simpler problem of fault kinematics, we are guided to some extent by the constraint that faulting is a process of failure in shear.

Our starting point is the representation theorem (equation (3.2)) of Chapter 3. Neglecting body forces and stress discontinuities, recall that the elastic displacement $\mathbf{u}$ caused by a displacement discontinuity $[\mathbf{u}(\xi, \tau)]$ across an internal surface Σ has the components

$$u_i(\mathbf{x}, t) = \int_{-\infty}^{\infty} d\tau \iint_{\Sigma} [u_j(\xi, \tau)] c_{jkpq} G_{ip,q}(\mathbf{x}, t; \xi, \tau) \nu_k \, d\Sigma(\xi), \tag{10.1}$$

where c_{jkpq} are the elastic moduli defined in equation (2.18); $G_{ip}(\mathbf{x}, t : \xi, \tau)$ is the Green function defined in Section 2.4; ν is the normal to Σ as shown in Figure 3.1; and $G_{ip,q}(\mathbf{x}, t : \xi, \tau)$ is the derivative of G_{ip} with respect to ξ_q. In a homogeneous, isotropic, unbounded

medium, the Green function can be stated explicitly. Thus, using (2.37) and (4.23), with body force taken as a unit impulse, it follows that

$$\begin{aligned} G_{ip}(\mathbf{x},t;\boldsymbol{\xi},\tau) = {} & \frac{1}{4\pi\rho}(3\gamma_i\gamma_p - \delta_{ip})\frac{1}{r^3}\int_{r/\alpha}^{r/\beta} t'\,\delta(t-\tau-t')\,dt' \\ & + \frac{1}{4\pi\rho\alpha^2}\gamma_i\gamma_p\frac{1}{r}\delta\left(t-\tau-\frac{r}{\alpha}\right) \\ & - \frac{1}{4\pi\rho\beta^2}(\gamma_i\gamma_p - \delta_{ip})\frac{1}{r}\delta\left(t-\tau-\frac{r}{\beta}\right), \end{aligned} \tag{10.2}$$

where $\boldsymbol{\gamma}$ is the unit vector from the source point $\boldsymbol{\xi}$ to the receiver point $\mathbf{x}$, and $r = |\mathbf{x} - \boldsymbol{\xi}|$ is the distance between those two points.

10.1 Kinematics of an Earthquake as Seen at Far Field

We shall obtain formulas for the displacement waveforms of P- and S-waves in the far field for faulting in a homogeneous medium. After outlining some general properties of these waveforms, we shall look in particular at their low-frequency component. Specializing next to the case of unidirectional propagation, we shall study waveforms due to a source characterized by five parameters: the fault length; the fault width; the rupture velocity; the final offset; and the "rise time," which characterizes the time taken for the offset, at a particular point on the fault, to reach its final value. This simple five-parameter characterization is often adequate to interpret the waves leaving a finite source. Where a more detailed description of the fault motions is required, we can separately study different stages of the faulting process such as nucleation of motion, the spreading of rupture, and the stopping of motion. We describe several examples of these stages and conclude the analysis of far-field waveforms with an examination of their intermediate-frequency and high-frequency content.

10.1.1 FAR-FIELD DISPLACEMENT WAVEFORMS OBSERVED IN A HOMOGENEOUS, ISOTROPIC, UNBOUNDED MEDIUM

We choose to work with a homogeneous, isotropic, unbounded medium in order to minimize the complication of path effects.

If the receiver position $\mathbf{x}$ is sufficiently far from all points $\boldsymbol{\xi}$ on the fault surface Σ, then only the far-field terms in the Green function (10.2) are significant. From (10.1), after carrying out the integral with respect to τ, we obtain the far-field displacement

$$\begin{aligned} u_i(\mathbf{x},t) = {} & -\frac{1}{4\pi\rho\alpha^2}\frac{\partial}{\partial x_q}\iint_\Sigma c_{jkpq}\frac{\gamma_i\gamma_p}{r}\left[u_j\left(\boldsymbol{\xi},t-\frac{r}{\alpha}\right)\right]\nu_k\,d\Sigma \\ & + \frac{1}{4\pi\rho\beta^2}\frac{\partial}{\partial x_q}\iint_\Sigma c_{jkpq}\left(\frac{\gamma_i\gamma_p - \delta_{ip}}{r}\right)\left[u_j\left(\boldsymbol{\xi},t-\frac{r}{\beta}\right)\right]\nu_k\,d\Sigma, \end{aligned} \tag{10.3}$$

in which we have used the relation $\partial/\partial\xi_q = -\partial/\partial x_q$, valid for operations on quantities such as γ and r, which are dependent only on the difference between $\mathbf{x}$ and ξ. Carrying out the differentiation with respect to x_q, noting that $\partial r/\partial x_q$ is merely γ_q, and ignoring all terms that attenuate with distance more rapidly than r^{-1}, we obtain

$$\begin{aligned}\text{far-field of } u_i(\mathbf{x},t) = &\iint_\Sigma \frac{c_{jkpq}}{4\pi\rho\alpha^3 r}\gamma_i\gamma_p\left[\dot{u}_j\left(\xi, t-\frac{r}{\alpha}\right)\right]\gamma_q\nu_k\, d\Sigma \\ &-\iint_\Sigma \frac{c_{jkpq}}{4\pi\rho\beta^3 r}(\gamma_i\gamma_p-\delta_{ip})\left[\dot{u}_j\left(\xi, t-\frac{r}{\beta}\right)\right]\gamma_q\nu_k\, d\Sigma.\end{aligned} \tag{10.4}$$

Obviously, the first term corresponds to P-waves and the second to S-waves.

If the station is far enough away, as compared to the linear dimension of fault surface Σ, we can safely assume that the distance r and direction cosine γ_i are approximately constant, independent of ξ, and that such slowly varying factors can be taken outside the integral. For simplicity, we shall further assume that the fault surface Σ is a plane and that the direction of the displacement discontinuity is the same everywhere on the fault. We write

$$[u_j(\xi,t)] = n_j \cdot \Delta u(\xi,t), \tag{10.5}$$

where Δu is a scalar function, which we shall call the "source function," or the "slip function" in the case of a shear fault. Under these assumptions, equation (10.4) reduces to

$$\begin{aligned}\text{far-field of } u_i(\mathbf{x},t) = &\frac{\gamma_i}{4\pi\rho\alpha^3 r_0}\cdot c_{jkpq}\gamma_p\gamma_q\nu_k n_j \cdot \iint_\Sigma \Delta\dot{u}\left(\xi, t-\frac{r}{\alpha}\right) d\Sigma \\ &+\frac{\delta_{ip}-\gamma_i\gamma_p}{4\pi\rho\beta^3 r_0}\cdot c_{jkpq}\gamma_q\nu_k n_j \cdot \iint_\Sigma \Delta\dot{u}\left(\xi, t-\frac{r}{\beta}\right) d\Sigma.\end{aligned} \tag{10.6}$$

In general, $\Delta\dot{u}$ can vary rapidly with time and space—so the retarded times in the integrands of (10.6) must include the variation of r with ξ. The overall amplitude factor r_0^{-1} is based on the distance r_0 to the receiver from a reference point on the fault.

The above equation permits a remarkably simple exposition of far-field displacement due to P- and S-waves from an earthquake source. Since $\gamma_i\gamma_i = 1$ and $\gamma_i(\delta_{ip} - \gamma_i\gamma_p) = 0$, we see immediately that the particle motion of P-waves is parallel to γ, and that of S-waves is perpendicular to γ. Wave amplitudes attenuate with distance as r_0^{-1}, and are inversely proportional to the cube of their propagation velocities. Since other factors are comparable between them, the S-wave amplitude is roughly α^3/β^3 (~ 5) times larger than the P-wave amplitude.

The factor $(c_{jkpq}\gamma_p\gamma_q\nu_k n_j)$ represents the radiation pattern of P-waves, determined by the orientation of the fault plane (ν_k), the direction of the displacement discontinuity (n_j), and the direction to the station (γ_p) from the fault. Similarly, taking γ' and γ'' as orthogonal unit vectors in the plane perpendicular to γ, the radiation of S-waves is described by their amplitude $(c_{jkpq}\gamma'_p\gamma_q\nu_k n_j)$ in the γ'-direction and $(c_{jkpq}\gamma''_p\gamma_q\nu_k n_j)$ in the γ''-direction.

Relative amplitudes between the two directions determine the polarization angle for S-waves, which is sometimes used (in addition to the first motion for P-waves) for determining fault-plane solutions.

Finally, the shapes of the displacement waveforms of P- and S-waves in equation (10.6) are described by the only terms exhibiting a time dependence. These waveform shapes are therefore simple integrals of the form

$$\Omega(\mathbf{x}, t) = \iint_{\Sigma} \Delta\dot{u}\left(\xi, t - \frac{|\mathbf{x} - \xi|}{c}\right) d\Sigma(\xi), \tag{10.7}$$

where c is the velocity of wave propagation (either α or β).

10.1.2 FAR-FIELD DISPLACEMENT WAVEFORMS FOR INHOMOGENEOUS ISOTROPIC MEDIA, USING THE GEOMETRICAL-SPREADING APPROXIMATION

In Chapter 4, equations (4.84)–(4.86), we obtained the far-field displacement at $\mathbf{x}$ under the assumption that the whole fault (with area A) was acting effectively as a point source. This is the case when wavelengths of interest are much longer than the fault dimensions, but are much shorter than the distance from source region to receiver. But throughout all of this Section 10.1 we are interested in the more general case in which wavelengths may be comparable with (and possibly less than) the fault dimensions, so that there can be interference between waves radiated from different parts of the fault surface. Making an analogy with electromagnetic wave generation, we are thinking here of the waves from a finite antenna, whose linear dimensions may be longer than the radiated wavelength.

Note that an alternative way to obtain the far-field displacement waveform (10.4) is to integrate the effect of each area element $d\Sigma$ regarded as a point source, using (4.84) for the P-waves and (4.85) for S-waves, but making allowance for different travel times to $\mathbf{x}$ from different parts of the fault surface. For example, for P-waves, using $[\dot{\mathbf{u}}]\,d\Sigma$ now instead of $\bar{\dot{\mathbf{u}}}A$, we find from (4.84) that

$$\text{far-field } P\text{-wave of } u_i(\mathbf{x}, t) = \frac{1}{4\pi\rho\alpha^3} \iint_{\Sigma} 2\mu \frac{\gamma_i \gamma_j}{r} \left[\dot{u}_j\left(\xi, t - \frac{|\mathbf{x} - \xi|}{\alpha}\right)\right] \gamma_k \nu_k \, d\Sigma(\xi), \tag{10.8}$$

which is just the same as the P-wave component in (10.4), since $c_{jkpq}[\dot{u}_j]\gamma_q \nu_k = 2\mu\gamma_j[\dot{u}_j]\gamma_k\nu_k$ for slip in isotropic media.

The virtue of this latter approach is that it can so easily be extended to inhomogeneous media, since in Chapter 4 we identified the far-field approximation with the geometrical-spreading approximation, and in equations (4.93)–(4.95) we gave what can be regarded as

the integrand of the integral we now need for a finite fault surface. For inhomogeneous media, then, the equation that generalizes the P-wave component of (10.6) is

$$\text{far-field } P\text{-wave of } \mathbf{u}(\mathbf{x}, t)$$
$$= \frac{\mathcal{F}^P \mu(\xi_0)\,\mathbf{l}}{4\pi\sqrt{\rho(\xi_0)\rho(\mathbf{x})\alpha(\xi_0)\alpha(\mathbf{x})}\;\alpha^2(\xi_0)\mathcal{R}^P(\mathbf{x}, \xi_0)} \iint_\Sigma \Delta\dot{u}(\xi, t - T^P(\mathbf{x}, \xi))\, d\Sigma, \tag{10.9}$$

in which $\mathbf{l}$ (the direction at $\mathbf{x}$ of the ray from the fault), $\mathcal{F}^P$ (the radiation pattern), and $\mathcal{R}^P$ (the geometrical spreading factor) are evaluated for some reference point ξ_0 on Σ. Formulas similar to (10.9) but for the waveforms of SV and SH can immediately be written down from (4.94) and (4.95).

10.1.3 GENERAL PROPERTIES OF DISPLACEMENT WAVEFORMS IN THE FAR FIELD

For convenience in presentation, we shall continue to use homogenous media for development of the theory, giving in Box 10.2 an example of how our source theory can be merged with wave-propagation theory for realistic media.

Taking the origin of coordinates at a reference point on the fault, the distance r between the surface element $d\Sigma$ and the receiver point $\mathbf{x}$ can be written as

$$\begin{aligned} r = |\mathbf{x} - \xi| &= r_0\sqrt{1 + \frac{|\xi|^2}{r_0^2} - \frac{2(\xi \cdot \gamma)}{r_0}} \\ &= r_0\left\{1 + \frac{1}{2}\left[\frac{|\xi|^2}{r_0^2} - \frac{2(\xi \cdot \gamma)}{r_0}\right] - \frac{1}{8}\left[\quad\right]^2 \cdots\right\} \\ &= r_0 - (\xi \cdot \gamma) + \frac{1}{2}\frac{|\xi|^2}{r_0} - \frac{(\xi \cdot \gamma)^2}{2r_0} + \cdots, \end{aligned} \tag{10.10}$$

where r_0 is the distance to the receiver from the origin, $r_0 = |\mathbf{x}|$, γ is the unit vector pointing to the receiver, and ξ is the location vector of $d\Sigma$ measured from the origin (Fig. 10.1).

For r_0 large compared with the linear dimension of Σ, we may approximate equation (10.10) by

$$r \sim r_0 - (\xi \cdot \gamma). \tag{10.11}$$

The error δr in path length due to this approximation may be estimated by the largest terms neglected in the series expansion in equation (10.10):

$$\delta r = \frac{1}{2r_0}[|\xi|^2 - (\xi \cdot \gamma)^2].$$

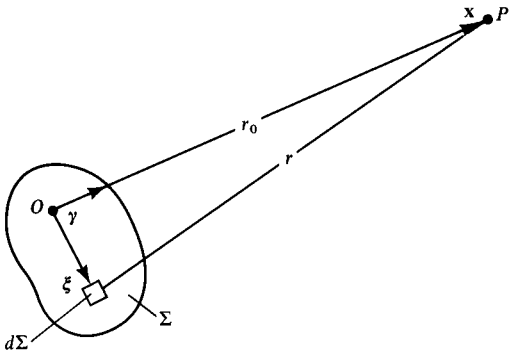

FIGURE **10.1**
The origin of coordinates is taken on a finite fault surface.

If this error is equal to or greater than a quarter wavelength, $\lambda/4$, a serious error will be introduced in the result of integration. Therefore, the approximation by equation (10.11) is justified only for

$$\frac{1}{2r_0}\left[|\xi|^2 - (\xi \cdot \gamma)^2\right] \ll \frac{\lambda}{4}$$

or, conservatively,

$$L^2 \ll \tfrac{1}{2}\lambda r_0, \tag{10.12}$$

where L is the maximum of $|\xi|$ on Σ. This is the same as the condition to be satisfied for the region of Fraunhofer diffraction in optics. For comparison, note that the condition we assumed in Chapter 4, in which the whole fault was regarded as a point source, amounted to $L \ll \lambda$, which is a much more restrictive condition on the applicable frequency range than (10.12). Under condition (10.12), we can rewrite the displacement waveform given in equation (10.7) as

$$\Omega(\mathbf{x}, t) = \Omega(\gamma, t) = \iint_{\Sigma} \Delta\dot{u}\left[\xi, t - \frac{r_0 - (\xi \cdot \gamma)}{c}\right] d\Sigma. \tag{10.13}$$

Note that the far-field pulse shape depends more directly on γ than on $\mathbf{x}$, since it is position on the focal sphere which governs this pulse shape, and many positions $\mathbf{x}$ have the same value of γ.

Taking the Fourier transform of the above equation with respect to t, we get

$$\begin{aligned}\Omega(\mathbf{x}, \omega) = \Omega(\gamma, \omega) &= \iint_{\Sigma} \Delta\dot{u}(\xi, \omega)\ \exp\left\{\frac{i\omega\left[r_0 - (\xi \cdot \gamma)\right]}{c}\right\} d\Sigma \\ &= \exp\left(\frac{i\omega r_0}{c}\right) \iint_{\Sigma} \Delta\dot{u}(\xi, \omega)\ \exp\left[\frac{-i\omega(\xi \cdot \gamma)}{c}\right] d\Sigma\end{aligned} \tag{10.14}$$

This shows that the Fourier transform $\Omega(\boldsymbol{\gamma}, \omega)$ of the observed displacement waveform with phase correction for the delay $\omega r_0/c$ due to propagation can be expressed as a superposition of plane waves of the type $\exp[-i\omega(\boldsymbol{\xi} \cdot \boldsymbol{\gamma})/c]$. Specifically,

$$\Omega(\boldsymbol{\gamma}, \omega) e^{-i\omega r_0/c} = \iint_{\Sigma} \Delta\dot{u}(\boldsymbol{\xi}, \omega) \exp\left[-i\omega(\boldsymbol{\xi} \cdot \boldsymbol{\gamma})/c\right] d\Sigma. \tag{10.15}$$

This right-hand side has the form of a double Fourier transform in space. It is given by $\iint_{\Sigma} \Delta\dot{u}(\boldsymbol{\xi}, \omega) \exp[-i(\boldsymbol{\xi} \cdot \mathbf{k})]\, d\Sigma = f(\mathbf{k})$. If the transform were known for all $\mathbf{k}$ in wavenumber space, we could invert the double integral and determine $\Delta\dot{u}(\boldsymbol{\xi}, \omega)$ completely, as a function of $\boldsymbol{\xi}$, from far-field observations. Unfortunately, (10.15) shows that the two-dimensional transform is known not for all $\mathbf{k}$, but only for the projection of $\omega\boldsymbol{\gamma}/c$ on Σ (we are assuming that Σ is flat, so that $\boldsymbol{\xi}$ lies in the plane of Σ). The range of $\mathbf{k}$ we can recover from far-field observations is therefore restricted to $\mathbf{k}$ parallel to Σ, and, since $\boldsymbol{\gamma}$ is a unit vector, $|\mathbf{k}| \leq \omega/c$. It follows that we cannot find details of the seismic source with scale lengths shorter than the shortest wavelength observed. The phase velocity along the plane Σ of the plane waves in (10.15) is $\omega/|\mathbf{k}|$, and $c \leq \omega/|\mathbf{k}|$. So the underlying reason for not being able to elucidate short wavelength features of the source is that the only waves which can radiate to the far field are those whose phase velocity (along the plane Σ) is greater than the medium velocity c. The waves with phase velocity smaller than c are inhomogeneous waves trapped near Σ, and we investigate them further in Sections 10.2.3 and 10.2.4. Here, we note that for a complete recovery of the source function $\Delta u(\boldsymbol{\xi}, t)$, we need observations at near field.

10.1.4 BEHAVIOR OF THE SEISMIC SPECTRUM AT LOW FREQUENCIES

As the frequency ω approaches zero, the Fourier transform $\Omega(\mathbf{x}, \omega)$ of the far-field displacement waveform, given in (10.14), approaches a constant value:

$$\Omega(\mathbf{x}, \omega \to 0) = \iint_{\Sigma} \Delta\dot{u}(\boldsymbol{\xi}, \omega \to 0)\, d\Sigma.$$

Since

$$\Delta\dot{u}(\boldsymbol{\xi}, \omega) = \int \Delta\dot{u}(\boldsymbol{\xi}, t) \exp(i\omega t)\, dt$$

and also

$$\Delta\dot{u}(\boldsymbol{\xi}, \omega \to 0) = \int \Delta\dot{u}(\boldsymbol{\xi}, t)\, dt = \Delta u(\boldsymbol{\xi}, t \to \infty),$$

we have

$$\Omega(\mathbf{x}, \omega \to 0) = \iint_{\Sigma} \Delta u(\boldsymbol{\xi}, t \to \infty)\, d\Sigma. \tag{10.16}$$

Thus $\Omega(\mathbf{x}, \omega \to 0)$ in the limit is the integral of the final slip over the fault area—which is independent of γ, since the effect of the radiation pattern has been accounted for in a separate factor (see (10.6)). In other words, the spectrum (absolute value of Fourier transform) of the far-field displacement waveform tends to a constant at low frequencies, whose height is proportional to the seismic moment defined in equation (3.16). We leave it as Problem 10.5 to show that the spectrum is flat at the origin. This result is true for any $\Delta u(\xi, t)$ provided the final offset is the same, and the spectrum at low frequencies is independent of details of the process by which the final offset is acquired on the fault plane.

If we make an additional assumption that the fault-slip velocity never reverses its direction (i.e., that $\Delta \dot{u}$ does not change sign during an earthquake—a reasonable assumption if there is significant friction still operating on the fault plane at the time when $\Delta \dot{u}$ returns to zero, so that no further slip takes place), then, from equation (10.13), we find that $\Omega(\mathbf{x}, t)$ will have the same sign for all t. In that case, the Fourier transform $\Omega(\mathbf{x}, \omega)$ is not only flat but takes its maximum value at $\omega = 0$, and we say the source spectrum has no overshoot. This result, which is again independent of the details of faulting, has been pointed out by Savage (1972), Molnar, Jacob, and McCamy (1973), and Randall (1973) in a controversy triggered by Archambeau (1968) on the low-frequency behavior of the seismic spectrum of earthquake faulting. In contrast, the source spectrum of an explosion can have a prominent overshoot.

If the area of fault surface Σ is infinitesimally small and if the slip $\Delta u(\xi, t)$ varies as a step function in time, then we find from (10.13) or (4.84) that the far-field waveform is a delta function and hence that the spectrum is flat for the whole frequency range. Therefore, we may say that for low frequencies where the spectrum is flat, the seismic source is equivalent to a point source with a step-function slip. This simple source has been extensively used in the single-station method of determining phase velocities for Love and Rayleigh waves from relatively small earthquakes. Weidner (1972) compared the results obtained by the single-station method with those by the two-station method for North Atlantic paths and found that the step-function assumption was correct within a phase error of less than about 0.02–0.1 cycle for periods of 20–80 s and for earthquakes with magnitude 6 or less. The same assumption was also used successfully in the determination of the focal depth of earthquakes with magnitude less than about 6, using the amplitude (Tsai and Aki, 1971) and the phase (Weidner and Aki, 1973) of Rayleigh waves. The step-function assumption using free-oscillation data in the period range 150–1200 s is supported by Mendiguren (1972) and Russakof *et al.* (1997) for a deep earthquake in 1970 in Colombia. A summary of measurements on seismic moment and fault area was given by Kanamori and Anderson (1975) for many earthquakes of various magnitudes.

10.1.5 A FAULT MODEL WITH UNIDIRECTIONAL PROPAGATION

As shown in the preceding section, observed waveforms in the far field alone cannot uniquely determine the source function $\Delta u(\xi, t)$. It is therefore useful to establish a minimum set of source parameters that can adequately describe the source function. Limited observations in the far field can then be effectively used to determine these parameters.

Let us first describe the fault plane as a rectangle with length L and width W. The rupture initiates at one end of the fault and propagates along the length L with velocity v.

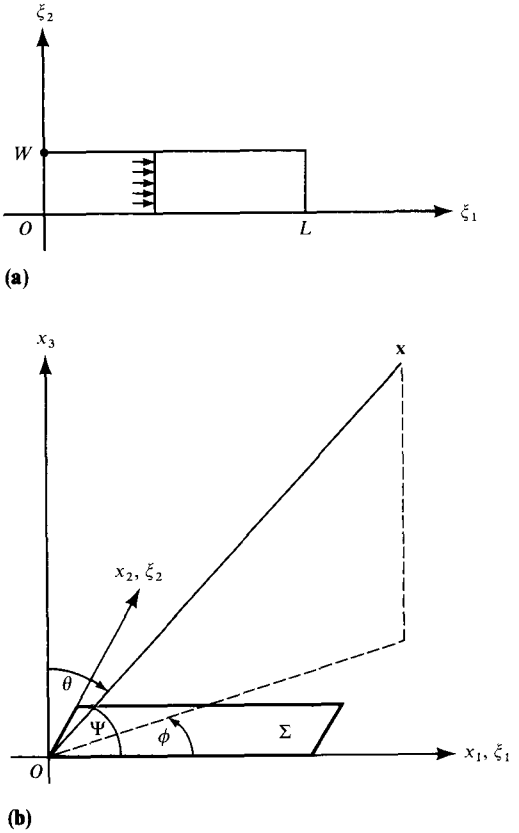

FIGURE **10.2**
Unidirectional faulting on a rectangular fault. (**a**) The fault plane. (**b**) Direction $\theta = 0$ is normal to the fault plane, and $\Psi = 0$ is the direction of rupture propagation.

Setting the coordinate system (ξ_1, ξ_2) parallel to the length and width of the fault plane as shown in Figure 10.2, we specify the rupture propagation by

$$\begin{aligned} \Delta u(\boldsymbol{\xi}, t) &= f(t - \xi_1/v) \qquad \text{if } 0 < \xi_1 < L \quad \text{and} \quad 0 < \xi_2 < W, \\ &= 0 \qquad\qquad\quad \text{if } \xi_1 < 0 \text{ or } \xi_1 > L, \quad \text{or} \quad \xi_2 < 0 \text{ or } \xi_2 > W. \end{aligned} \tag{10.17}$$

Putting this into equation (10.13), we get

$$\Omega(\mathbf{x}, t) = \int_0^W \int_0^L \dot{f}\left(t - \frac{r_0}{c} - \frac{\xi_1}{v} + \frac{\xi_1\gamma_1 + \xi_2\gamma_2}{c}\right) d\xi_1\, d\xi_2. \tag{10.18}$$

Assuming that W and $\xi_2\gamma_2$ are small, and taking Ψ as the angle between the direction to the receiver and the direction of rupture propagation, we can rewrite equation (10.18) as

$$\Omega(\mathbf{x}, t) = W \int_0^L \dot{f}\left[t - \frac{r_0}{c} - \xi_1\left(\frac{1}{v} - \frac{\cos\Psi}{c}\right)\right] d\xi_1. \tag{10.19}$$

Since this integrand ranges from $\dot{f}(t - r_0/c)$ to $\dot{f}(t - r_0/c - L[1/v - (\cos\Psi)/c])$, $\Omega(\mathbf{x}, t)$ given by (10.19) is proportional to a moving average of $\dot{f}(t - r_0/c)$ taken over a time interval

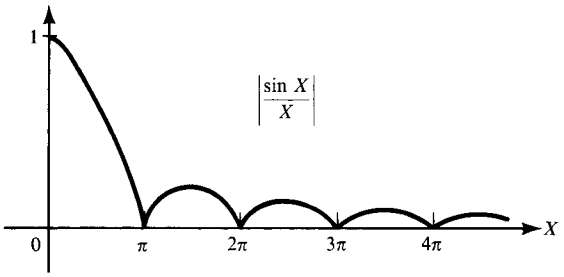

FIGURE **10.3**
The factor $|X^{-1} \sin X|$ in the spectrum of an observed pulse shape can be thought of in the time domain as convolution with a box function of temporal duration $L(1/v - c^{-1} \cos \Psi) = L[1/v - c^{-1}(\sin \theta \cos \phi)]$. This is the *apparent* duration of rupture, as detected by receivers along the direction (θ, ϕ), for rupture speed v and wave-propagation speed c.

with duration $L[1/v - (\cos \Psi)/c]$. Noting that $\dot{f}(t - r_0/c)$ is the far-field displacement waveform expected for an infinitesimally small fault, we see that rupture propagation over a finite fault length has a smoothing effect on the waveform.

To find this effect on the spectrum, we take the Fourier transform of (10.7). Writing the Fourier transform of $f(t)$ as $f(\omega)$, we get

$$\begin{aligned} \Omega(\mathbf{x}, \omega) &= -i\omega W f(\omega) e^{i\omega r_0/c} \int_0^L \exp\left[i\omega\xi_1 \left(\frac{1}{v} - \frac{\cos \Psi}{c}\right)\right] d\xi_1 \\ &= \omega f(\omega) W L \frac{\sin X}{X} \exp\left[i\left(\frac{\omega r_0}{c} - \frac{\pi}{2} + X\right)\right], \end{aligned} \tag{10.20}$$

where $X = (\omega L/2)[1/v - (\cos \Psi)/c]$. The effect of the finiteness of the fault on the amplitude spectrum is expressed by $X^{-1} \sin X$, which is depicted in Figure 10.3. This effect, first discussed by Ben-Menahem (1961), produces nodes at $X = \pi, 2\pi, \ldots$. The first node corresponds to the period $2\pi/\omega = L[1/v - (\cos \Psi)/c]$. An example of observed spectral nodes is shown in Figure 10.4 for Love waves from the Parkfield earthquake of 1966 June, observed at Berkeley, California (Filson and McEvilly, 1967). The first node at $T = 22.5$ s is explained by the rupture velocity of 2.2 km/s, the fault length of about 30 km, and $\cos \Psi$ of about 1.

For higher frequencies, the envelope of $X^{-1} \sin X$ is proportional to ω^{-1}. This smoothing effect is weakest in the direction of rupture propagation ($\Psi = 0$) and strongest in the opposite direction ($\Psi = \pi$). As a result, we observe more high-frequency waves at $\Psi = 0$ than at $\Psi = \pi$.

Two additional source parameters are needed to complete the unidirectional rectangular fault model. They are the final slip D and the rise time T characterizing the slip function $f(t)$. Haskell (1964) used a ramp function

$$\begin{aligned} f(t) &= 0 \qquad && t < 0, \\ &= Dt/T \qquad && 0 < t < T, \\ &= D \qquad && T < t, \end{aligned} \tag{10.21}$$

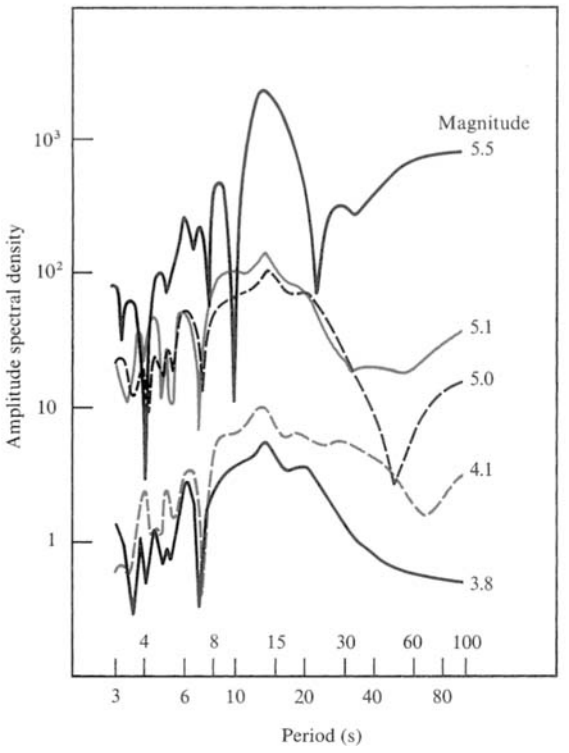

FIGURE **10.4**
Amplitude spectra of Love waves from a series of earthquakes in Parkfield, California, recorded at Berkeley, California, at a distance of 270 km. The main shock, with local magnitude 5.5 ($M_s = 6.4$), shows nodes at 22.5, 9.8, and 7.6 s. The last node is probably a path effect, because it shows up for all earthquakes, independent of magnitude. [From Filson and McEvilly, 1967.]

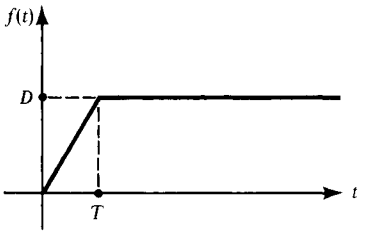

FIGURE **10.5**
Definition of rise time T.

as shown in Figure 10.5. Taking the Fourier transform of $\dot{f}(t)$ and putting it into (10.20), we obtain

$$|\Omega(\mathbf{x}, \omega)| = WLD\frac{\sin X}{X}\left|\frac{1 - e^{i\omega T}}{\omega T}\right|. \tag{10.22}$$

The effect of a finite rise time T therefore introduces additional smoothing of the waveform: for high frequencies, it attenuates the spectrum proportional to ω^{-1}. Thus the finite length of the fault over which the rupture is propagated, together with the finite time needed to complete the slip at a point on the fault, make the spectrum attenuate as ω^{-2} at high frequencies.

So far, we have introduced the following five source parameters:

(i) Fault length L.

(ii) Fault width W.

(iii) Rupture velocity v.

(iv) Permanent slip D.

(v) Rise time T.

The corresponding far-field displacement spectrum is given by (10.22). The spectrum is flat near $\omega = 0$, and the height of the flat part is proportional to DWL, or seismic moment. For frequencies higher than the reciprocals of apparent rupture time $L[1/v - (\cos \Psi)/c]$ and rise time T, the spectrum decays with frequency as ω^{-2}. If the effect of finite width is also taken into account, as done by Hirasawa and Stauder (1965), a spectral decay of ω^{-3} should be expected. Another extension of the model often used in practice is to assume that the rupture propagates from a point in the fault plane to positive and negative directions along its length. This is called bilateral faulting and the corresponding seismic spectrum can be easily obtained by appropriately superposing the results for two unilateral fault motions propagating in opposite directions.

The seismic energy, spectral density, and near-field effects of the above five-parameter model were studied in detail by Haskell (1964, 1966, 1969), and it is often called Haskell's model. For many earthquakes, reliable estimates of the product of L, W, and D have been made—and hence of the seismic moment (by assuming a value of the rigidity). The measurement of L is easier than that of W or D, because its effect can be studied using longer waves, which suffer less from complex path effects. The reliable estimation of D and T require near-field data, which are usually difficult to obtain. Types of fault slip more general than those of the Haskell model are considered in Problem 10.7, showing that the far field spectrum can still be regarded as the product of two factors, the first being associated with an equivalent point source (and having spectral decay due to the finite rise time), the second being due to the finiteness of faulting (and having spectral decay due to spatial interference).

Once the fault area and fault slip are determined, one can make a rough estimate of stress drop associated with the faulting, by referring to a crack problem of similar geometry. With some exceptions we can summarize results roughly as the statement that for most earthquakes the stress drop lies in the range from 10 to 100 bars, independent of magnitude. The slip velocity (D/T) across the fault also appears to lie in a limited range: from 10 to 100 cm/s. According to Abe's (1975) summary, the stress drop $\Delta\sigma$ and the slip velocity (D/T) appear to be related via $\Delta\sigma = \beta\rho(D/T)$, where the coefficient of proportionality, $\beta\rho$ (= shear wave speed $\times$ density), is just the impedance for plane shear waves (see Box 5.4 with angle $j = 0$).

Equations such as (10.7), (10.16), (10.22) and extensions of them such as discussed in Problem 10.7 provide the kinematic framework for interpretation of earthquake phenomena across a range of different geometries and stress drops. Thus, equation (10.7) indicates that if the slip velocity is constant, then the seismic radiation scales directly with the size of the rupture. The simplest scaling is one in which slip velocity is constant; and fault width, rise time, and final offset are all proportional to fault length. The stress drop is then constant, independent of moment, and $M_0 \propto L^3$. Abercrombie and Leary (1993) reported low-magnitude seismic data from a deep borehole in Southern California, and data from several other regions, in support of such a simple scaling law across a moment range spanning 20 orders of magnitude. Other seismologists who have drawn upon data

across a smaller but still significant magnitude range, for events all from the same region, have in some cases reported a different result, namely that stress drop appears to increase monotonically with increasing moment for events below a critical size, becoming constant for events larger than critical (e.g., Shi *et al.*, 1998). Heaton (1990) pointed out numerous earthquakes with fault length much greater than width, for which the rise time was likely to be independent of fault length, resulting in a different scaling law.

An extensive study of source parameters of major earthquakes in and near Japan was made by Kanamori and his colleagues using the Haskell model. The result, as summarized by Kanamori (1973), showed that the amount of slip and the extent of the fault area obtained by the seismic method are in good agreement with those obtained by a static method, using geodetic measurements for earthquakes caused by "brittle elastic" rebound. On the other hand, for earthquakes attributed to "visco-elastic" rebound, the slip and fault area were found to be significantly greater by the static method than by the seismic method, indicating that the seismic event does not totally represent tectonic processes associated with an earthquake. The completion of the Global Positioning Satellite system in the 1990s permits subcentimeter determination of absolute locations of points nearly anywhere on Earth, and Heki *et al.* (1997) made such a measurement of ground displacements at 16 stations in the vicinity of a magnitude 7.8 subduction zone earthquake that occurred on 1994 December 28, off the Sanriku coast of northeastern Japan. During the ensuing 12 months, the displacement of 15 of these sites grew to exceed the displacement that had occurred at the time of the earthquake at these same sites. These authors and DeMets (1997) interpreted the observations as evidence for afterslip, somewhere on the fault plane that ruptured in the main shock, rather than as an effect of viscosity in a lower layer. The motion between tectonic plates is apparently accommodated by a continuum of processes, including slow-rupture earthquakes, aseismic creep, and afterslip, as well as by more conventional earthquakes.

10.1.6 NUCLEATION, SPREADING, AND STOPPING OF RUPTURE

The unidirectional propagation of rupture in Haskell's source model is an oversimplification of faulting when we look closer at the nucleation of the rupture process. To make the model more realistic, it is desirable to allow rupture to initiate at a point (rather than simultaneously everywhere along a line segment) and then spread out radially (rather than propagate in a single direction), until it covers an arbitrary two-dimensional surface on the fault plane. Far-field waveforms from this type of source model, using a uniform rupture velocity, were first studied by Savage (1966) using equation (10.13).

As shown in Figure 10.6, we shall place the fault in the plane $x_3 = 0$ and assume that rupture propagates from the origin in all directions with uniform velocity v and stops at the perimeter of the fault plane Σ. Initially the rupture front is a circle described by $\rho = vt$, but the final fault will have a perimeter given by $\rho = \rho_b(\phi')$, where (ρ, ϕ') are cylindrical coordinates in the fault plane.

Savage (1966) assumed the displacement discontinuity was a step function in time with final value $\Delta U(\rho, \phi')$. In our notation and using Heaviside step functions, the model can be expressed as

$$\Delta u(\xi, t) = \Delta U(\rho, \phi') H(t - \rho/v)[1 - H(\rho - \rho_b)]. \tag{10.23}$$

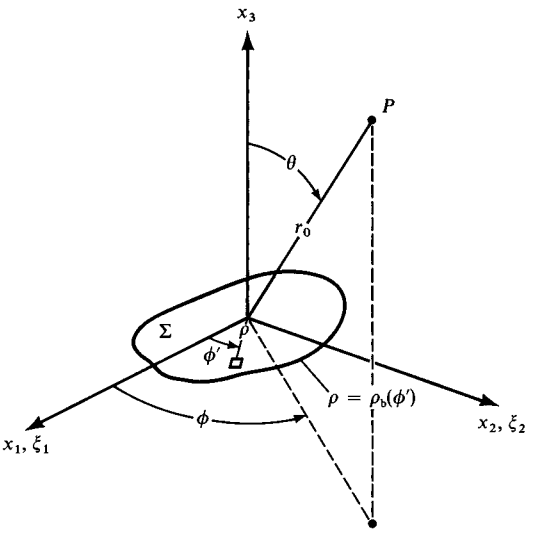

FIGURE **10.6**
The rupture starts from the origin and spreads in the x_1x_2-plane with a constant velocity v. Initially, the rupture front is a circle $\rho = vt$, but the final fault plane has a perimeter given by $\rho = \rho_b(\phi')$. P is the observation point, and an element $d\Sigma$ of the fault is shown at (ρ, ϕ').

Putting this into (10.13), we find

$$\begin{aligned}\Omega(\mathbf{x}, t) &= \iint_\Sigma \Delta\dot{u}\left(\xi, t - \frac{r_0 - (\xi \cdot \gamma)}{c}\right) d\Sigma(\xi) \\ &= \iint \delta\left(t - \frac{r_0}{c} + \frac{\rho \sin\theta \cos(\phi - \phi')}{c} - \frac{\rho}{v}\right) \Delta U(\rho, \phi') \\ &\quad \times [1 - H(\rho - \rho_b)]\rho \, d\rho \, d\phi',\end{aligned} \tag{10.24}$$

where we used the spherical coordinates shown in Figure 10.6 for expressing $(\xi \cdot \gamma)$. Since $\int f(x)\, \delta(ax - b)\, dx = f(b/a)/a$, the integration with respect to ρ gives

$$\begin{aligned}&\int \delta\left(t - \frac{r_0}{c} - \frac{\rho q_c}{v}\right) \Delta U(\rho, \phi')[1 - H(\rho - \rho_b)]\rho \, d\rho \\ &\qquad = \left(t - \frac{r_0}{c}\right) \Delta U\left(\frac{t - \frac{r_0}{c}}{q_c/v}, \phi'\right) \frac{v^2}{q_c^2} \qquad \text{for } 0 < \frac{t - \frac{r_0}{c}}{q_c/v} < \rho_b \\ &\qquad = 0 \qquad \text{for } \rho_b < \frac{t - \frac{r_0}{c}}{q_c/v},\end{aligned}$$

where $q_c = 1 - (v/c)\sin\theta\cos(\phi - \phi')$ is assumed positive everywhere; in other words, $v < c$ and the rupture is subsonic. [If $v > c$, waves would arrive before r_0/c in the directions (θ, ϕ) for which q_c is negative, because $\Delta U[(t - r_0/c)/(q_c/v), \phi']$ will be nonvanishing for $t < r_0/c$.]

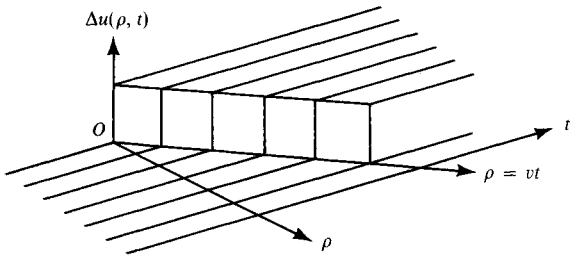

FIGURE **10.7**
Slip function for a circular fault with uniform slip.

For subsonic rupture propagation, (10.24) can be written as

$$\Omega(\mathbf{x},t) = v^2\left(t-\frac{r_0}{c}\right)H\left(t-\frac{r_0}{c}\right)\int \frac{\Delta U\left(\dfrac{t-r_0/c}{q_c/v},\phi'\right)}{q_c^2}d\phi', \qquad (10.25)$$

where the integral is taken over the range of ϕ' for which $[(t-r_0/c)/(q_c/v)v] < \rho_b$.

Suppose that the final slip ΔU is uniform except near the fault perimeter, and suppose that we look at the beginning of the far-field displacement waveform, when $t - r_0/c$ is small and the range of integration for ϕ' covers 0 to 2π. In that case, we see from (10.25) that the displacement waveform is a linear function of time (a ramp function). The linearity will hold until the rupture front reaches the perimeter of the prescribed fault surface.

Thus a subsonically spreading rupture with a uniform step-function slip generates a far-field displacement waveform $(t - r_0/c)H(t - r_0/c)$ until the stopping signal arrives from the perimeter of the fault. The corresponding particle-velocity waveform due to this type of nucleation is a step function with a discontinuity at $t = r_0/c$. The acceleration is a δ-function, reaching infinity at $t = r_0/c$. The spectral density of acceleration, velocity, and displacement are therefore constant, and proportional to ω^{-1} and ω^{-2}, respectively.

In order to see what happens when the rupture stops propagating, let us consider the case of a circular fault with uniform slip, in which $\rho_b = \rho_0$ (constant), $\Delta U(\rho,\phi') = \Delta U_0$ (constant). Then $\Delta u(\xi,t)$ is a function of ρ and t, as shown in Figure 10.7. The simplest result is obtained in the direction normal to the fault plane. For $\theta = 0$, $q_c = 1$ and equation (10.25) shows that the integral with respect to ϕ' is constant for $v(t - r_0/c) < \rho_0$ and vanishes for $v(t - r_0/c) > \rho_0$. In other words, the far-field displacement waveform $\Omega(\mathbf{x},t)$ for $\theta = 0$, which grows like a ramp function beginning at $t = r_0/c$, subsequently has a jump discontinuity at $t = r_0/c + \rho_0/v$, when $\Omega(\mathbf{x},t)$ suddenly becomes zero. This jump discontinuity gives infinite particle velocity and acceleration. The spectral density of displacement, in the high-frequency limit, will decay in proportion to ω^{-1}. A seismic signal associated with the stopping of rupture was named a "stopping phase" by Savage.

For $\theta \neq 0$, $q_c = 1 - (v/c)\sin\theta\cos(\phi - \phi')$ is a function of ϕ', taking its minimum value in the azimuth $\phi' = \phi$ to the station and its maximum in the opposite azimuth $\phi' = \phi + \pi$. Since $\Delta U(\rho,\phi')$ is constant and q_c is a smooth function, the integral in equation (10.25) is proportional to the range of ϕ' for which $[v(t - r_0/c)]/q_c < \rho_0$. As long as the locus of $\rho = [v(t - r_0/c)]/q_c$ is contained inside the circle $\rho = \rho_0$, the integration range of ϕ' is 2π.

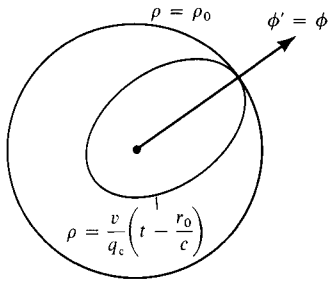

FIGURE **10.8**

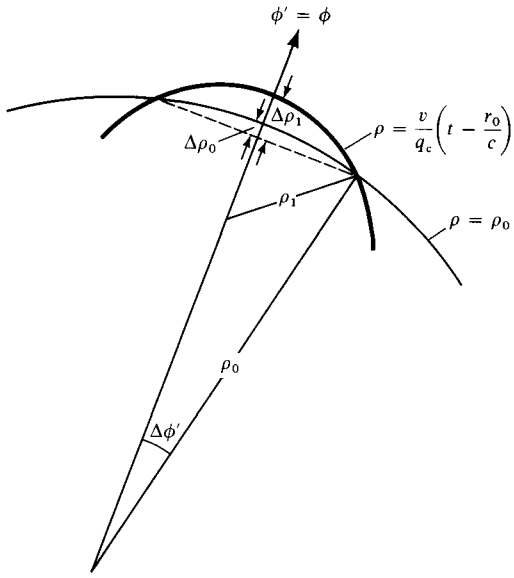

FIGURE **10.9**

Since the minimum of q_c is at $\phi' = \phi$, the locus of $\rho = [v(t - r_0/c)]/q_c$ will touch the circle $\rho = \rho_0$ first at $\phi' = \phi$, as shown in Figure 10.8. The growth $\Delta\phi'$ of the portion of ϕ' for which $[v(t - r_0/c)]/q_c > \rho_0$ can be found from the geometry shown in Figure 10.9.

Expressing ρ_1 as the radius of curvature of $\rho = [v(t - r_0/c)]/q_c$ at the point of contact, and taking into account the relation

$$\Delta\rho_0 = \rho_0 - \sqrt{\rho_0^2 - (\rho_0 \Delta\phi')^2} \sim (\rho_0/2)(\Delta\phi')^2$$

and a similar relation for $\Delta\rho_1$, we get

$$\Delta\rho = \Delta\rho_1 - \Delta\rho_0 \sim \left(\frac{\rho_0^2}{2\rho_1} - \frac{\rho_0}{2}\right)(\Delta\phi')^2.$$

Since $\Delta\rho$ is proportional to the time Δt after the two curves make contact, the integration range $\Delta\phi'$ will be proportional to $\sqrt{\Delta t}$, and the far-field displacement $\Omega(\mathbf{x}, t)$ will

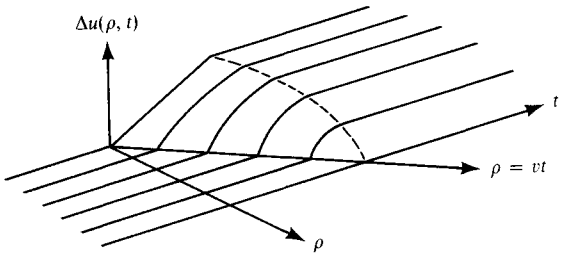

FIGURE **10.10**
Slip function for a circular fault on which the shear stress is constant.

therefore have a sudden change proportional to $\sqrt{\Delta t}$. The corresponding spectral density for displacement will have a high-frequency asymptotic limit decaying as $\omega^{-3/2}$. Both the particle velocity and acceleration will be infinite at the arrival of this stopping phase. Thus the stopping phase ($\propto \omega^{-3/2}$) dominates the nucleation phase ($\propto \omega^{-2}$) at high frequencies in this model. For the special direction $\theta = 0$ the stopping phase is even stronger ($\propto \omega^{-1}$), as would be expected since the stopping of rupture becomes apparent, in retarded time, at the same instant from all points on the perimeter of this circular fault as rupture ceases.

As can be seen from the derivation given above, the $\omega^{-3/2}$ frequency dependence (for $\theta \neq 0$) applies not only to the stopping of a circular crack front but to that of any smoothly curved crack front.

There are some unrealistic aspects about the above model as an example of shear fracture. First, the slip is not consistent with the known static solution; and second, the stopping of slip in the interior of the fault occurs everywhere instantaneously and therefore has no causal relationship with the stopping of the rupture front. The first point was partially taken into account by Savage (1966) but was more fully considered by Sato and Hirasawa (1973), who assumed the following slip function:

$$\begin{aligned} \Delta u(\rho, t) &= K\sqrt{(vt)^2 - \rho^2}\, H(t - \rho/v)[1 - H(\rho - \rho_0)] && \text{for } vt < \rho_0 \\ &= K\sqrt{\rho_0^2 - \rho^2}\, [1 - H(\rho - \rho_0)] && \text{for } vt > \rho_0, \end{aligned} \tag{10.26}$$

where

$$K = \left(\frac{24}{7\pi}\right)\left(\frac{\Delta\sigma}{\mu}\right).$$

This model is constructed by assuming that Eshelby's (1957) static solution holds at every successive instant of rupture formation for a circular crack under uniform shear stress (see Fig. 10.10). Putting equation (10.26) into equation (10.13) it is possible to carry out the integration exactly, and Sato and Hirasawa obtained the following compact result:

$$\begin{aligned} \Omega(\mathbf{x}, t) &= 2K v\rho_0^2[\pi/(1-k^2)^2]x^2 && \text{for } 0 < x < 1 - k \\ &= 2K v\rho_0^2(\pi/4)[1/k - (x^2/k)(1+k)^{-2}] && \text{for } 1 - k < x < 1 + k, \end{aligned} \tag{10.27}$$

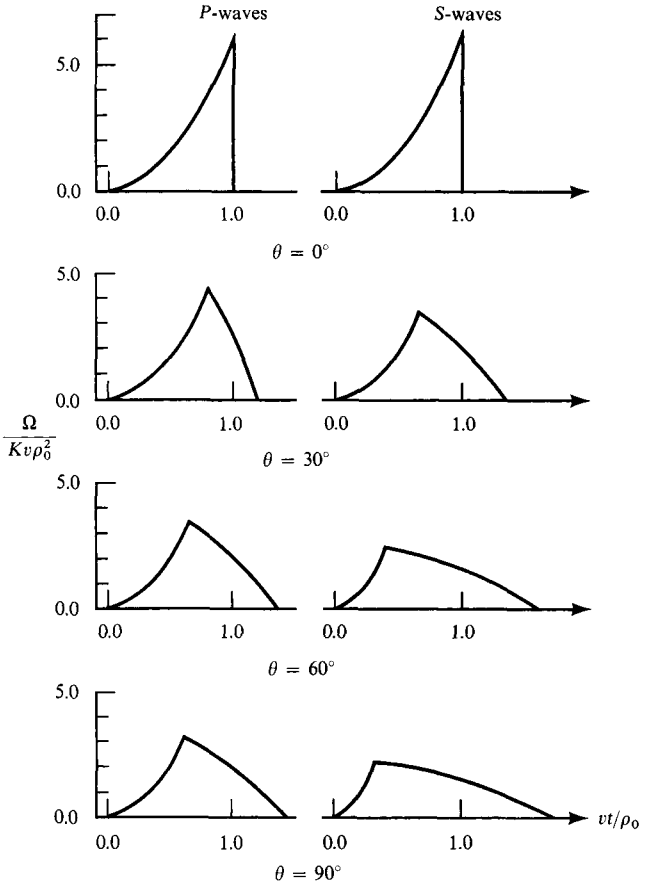

FIGURE **10.11**
Far-field wave forms according to equation (10.27); θ is defined in Figure 10.6. [From Sato and Hirasawa, 1973.]

where $k = (v/c)\sin\theta$ and $x = v(t - r_0/c)/\rho_0$. An example of $\Omega(\mathbf{x}, t)$ is shown in Figure 10.11. The initial rise of the far-field displacement is now proportional to $(t - r_0/c)^2$ instead of $(t - r_0/c)$ as in the previous case of uniform step-function slip. The spectral density corresponding to this rising part will have high-frequency asymptotic decay proportional to ω^{-3}. The spectral density for the total waveform, however, shows a high-frequency asymptotic decay of ω^{-2}, indicating once again that the stopping phase dominates the nucleation phase at high frequencies. The ω^{-2} decay is expected for this case because of an additional $\omega^{-1/2}$ due to the square root dependence of the slip function on distance from the crack tip, as compared with the uniform-slip case in which we obtained the $\omega^{-3/2}$ decay.

A defect of Sato and Hirasawa's model is that particle motions cease at the same instant, everywhere over the fault plane. Let us now look at another kinematic model of circular rupture, proposed by Molnar, Tucker, and Brune (1973). The slip-velocity function for this model is given by

$$\Delta\dot{u}(\rho, t) = \Delta V \left[H\left(t - \frac{\rho}{v} + \frac{\rho_0}{v}\right) - H\left(t + \frac{\rho}{v} - \frac{\rho_0}{v}\right) \right] H(\rho_0 - \rho), \quad (10.28)$$

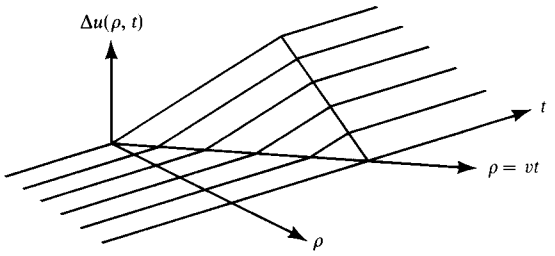

FIGURE **10.12**
Slip function for a circular fault on which a "healing front" (bringing motions to a stop) propagates inward after the fault has reached its final size.

where ρ_0 is the radius of a circular ruptured area and ΔV is the relative particle velocity (assumed to be constant over the area). The rupture nucleates at the center, grows radially in all directions at a constant velocity v to the radius ρ_0, and then contracts back to the center at the same velocity. This is a crude kinematic model of the spontaneous rupture process in which slip starts with the arrival of the rupture front and continues until information from the edges of the fault is radiated back to each point of the interior. The slip function of this model is shown in Figure 10.12.

Putting the Fourier transform of (10.28) into (10.15) and evaluating the integral, Molnar *et al.* obtained the high-frequency asymptotic decay as ω^{-2} to ω^{-3} depending on θ. The $\omega^{-5/2}$ decay is expected for a stopping phase in this case because of an additional ω^{-1} due to the linear dependence of the slip function on distance from the crack tip, as compared with the uniform-slip case in which we obtained the $\omega^{-3/2}$ decay.

As far as the initial part is concerned, this slip function is simply a time integral of the one for the uniform step-function case (equation (10.23)). Therefore, the initial rise of far-field displacement is the time-integral of linear increase. It is thus a parabolic increase, in common with the model of Sato and Hirasawa.

Dahlen (1974) extended the analysis of rupture kinematics to an elliptical crack that keeps on growing with the same shape. He used the following slip function, obtained by Burridge and Willis (1969) as an exact solution of the self-similar problem of an expanding elliptical crack:

$$\Delta u(\xi, t) = \Delta V \sqrt{t^2 - \frac{\xi_1^2}{u^2} - \frac{\xi_2^2}{v^2}}\, H\left[t - \sqrt{\frac{\xi_1^2}{u^2} + \frac{\xi_2^2}{v^2}}\right], \tag{10.29}$$

where ΔV is the relative velocity across the center of the crack, and u and v are rupture-propagation velocities in the ξ_1- and ξ_2-directions, respectively. As we shall see in Section 11.1.4, the slip function (10.29) leads to a uniform stress drop on the fracture surface, and thus is a solution of the crack problem as long as the crack continues to grow self-similarly (see Box 10.1). If $u = v$, the above equation reduces to (10.26) for the circular crack considered by Sato and Hirasawa for $t < \rho_0/v$. The initial rise of far-field displacement is again parabolic, and the corresponding high-frequency asymptotic decay is proportional to ω^{-3}. Unlike the models discussed earlier, Dahlen's model considers the rupture as being slowly brought to a halt as the crack edge propagates into regions of either increasing

BOX 10.1
On the concept of "self-similarity"

A self-similar wave-propagation phenomenon is one for which there is no intrinsic length scale or time scale, so that the phenomenon appears the same at all scales of space and time. Commonly, there is a resulting simplicity in the space–time dependence of the propagating wave that can allow an exact solution of the displacements and stresses, for all $(\mathbf{x}, t)$.

For example, the solution to Lamb's problem (the waves set up throughout a homogeneous elastic half-space by an impulse applied to its surface) is self-similar. If distances from the source are doubled in a fixed direction from the source, the shape of the exact waveform at the second distance—the complete waveform in this case is made up from the P-wave, S-wave, and Rayleigh wave—is derived from the first waveform by doubling the time scale. But if the impulse is applied at a fixed depth rather than at the surface, this depth provides a scale length and the resulting wave solution is not self-similar.

The waves set up in an elastic whole space by the slip function given in (10.29) are self-similar, as is apparent from inspection of the solution for this problem presented in Section 11.1.4. Note that we can write this slip function in terms of a dimensionless time coordinate $t' = t/T$ and dimensionless space coordinates $\xi_i' = \xi_i/L_i$ $(i = 1 \text{ or } 2)$, for our choice of constants T, L_1, L_2. The resulting expression is

$$\Delta u(\xi, t) = \Delta V \cdot T \sqrt{t'^2 - \frac{\xi_1'^2}{u'^2} - \frac{\xi_2'^2}{v'^2}}\; H\left[t' - \sqrt{\frac{\xi_1'^2}{u'^2} + \frac{\xi_2'^2}{v'^2}}\right],$$

where $u' = (T/L_1)u$ and $v' = (T/L_2)v$ are dimensionless parameters related to rupture velocities. The ability to represent key variables in dimensionless form is another feature of self-similar solutions.

friction or decreasing tectonic stress. For such a slow stopping process he concluded that the nucleation phase would dominate the stopping phase at high frequencies.

If we neglect the contribution from the stopping phase, the high-frequency limits of the far-field spectrum can be obtained by putting the Fourier transform of (10.29) into equation (10.15). The result is given by

$$|\Omega(\mathbf{x}, \omega)| = \frac{4\pi u v\, \Delta V \omega^{-3}}{\left(1 - \frac{u^2}{c^2} \sin^2\theta \cos^2\phi - \frac{v^2}{c^2} \sin^2\theta \sin^2\phi\right)^2}, \tag{10.30}$$

where θ and ϕ are defined in Figure 11.7. Since (10.30) does not contain parameters involving the final size of the crack, this model predicts a high-frequency behavior that is independent of earthquake size. On the other hand, if the stopping phase dominates at high frequencies, the size of the earthquake will be a factor, and the high-frequency values of $|\Omega|$ for larger earthquakes will be larger than for small ones. We shall come back to this point later in the discussion of scaling laws for seismic spectra.

10.1.7 CORNER FREQUENCY AND THE HIGH-FREQUENCY ASYMPTOTE

As shown in preceding sections, the far-field displacement due to any reasonable kinematic model of an earthquake is expected to have a spectrum with a constant value at low frequencies and proportional to a negative power of frequency at high frequencies. Following Brune (1970), we shall define a corner frequency as the frequency at the intersection of the low- and high-frequency asymptotes in the spectrum. The far-field spectrum is then roughly characterized by three parameters: (i) the low-frequency level, which is proportional to seismic moment; (ii) the corner frequency; and (iii) the power of the high-frequency asymptote.

Let us find the corner frequency as a function of source parameters for some of the kinematic models discussed earlier. We shall find that a major disagreement arises among various models concerning the relative magnitude of the P-wave and S-wave corner frequencies.

Savage (1972) calculated the corner frequencies for P- and S-waves assuming bilateral faulting with rupture velocity v and final fault length L:

$$\begin{aligned} \Delta u(\xi, t) &= D_0 G(t - \xi_1/v) && 0 \le \xi_1 < L/2 \\ &= D_0 G(t + \xi_1/v) && -L/2 < \xi_1 < 0 \\ &= 0 && \text{otherwise,} \end{aligned} \tag{10.31}$$

where

$$\begin{aligned} G(t) &= 0 && t < 0 \\ &= 1 - \exp(-t/T) && 0 \le t. \end{aligned}$$

Assuming that the rise time T is equal to the travel time of the rupture front over half a fault width, i.e., $T = W/2v$, Savage obtained the corner frequency as a geometric mean of two corner frequencies associated with the finite rupture propagation and the rise time. In this case, the high-frequency asymptote is proportional to ω^{-2}. Assuming further that $v = 0.9\beta$, the corner frequency averaged over all directions is obtained as

$$2\pi \langle f_P \rangle = \sqrt{2.9} \cdot \alpha / \sqrt{LW} \tag{10.32}$$

for P-waves and

$$2\pi \langle f_S \rangle = \sqrt{14.8} \cdot \beta / \sqrt{LW} \tag{10.33}$$

for S-waves. For a normal Poisson's ratio, the above formula shows for this model of fault slip that the P-wave corner frequency is lower than the S-wave corner frequency.

However, Furuya (1969) observed that the predominant period of S-waves is 1.3 to 1.5 times greater than that of P-waves for a given magnitude, implying that $\langle f_P \rangle$ is higher than $\langle f_S \rangle$, and he pointed out that the simple propagating fault model cannot explain such observations. The majority of subsequent observational studies of corner frequency support $\langle f_P \rangle > \langle f_S \rangle$.

The circular-crack model of Sato and Hirasawa also gives an asymptote like ω^{-2}, as discussed in the preceding section, but predicts higher corner frequency for P-waves than

TABLE **10.1**
Table of C_P and C_S values appearing in (10.34) and (10.35)

v/β	C_P	C_S
0.5	1.11	1.53
0.6	1.25	1.70
0.7	1.32	1.72
0.8	1.43	1.76
0.9	1.53	1.85

for S-waves, in accordance with observations. Their corner frequencies averaged over all directions are

$$2\pi\langle f_P\rangle = C_P\alpha/R \tag{10.34}$$

for P-waves and

$$2\pi\langle f_S\rangle = C_S\beta/R \tag{10.35}$$

for S-waves, where R is the radius of the crack and C_P and C_S are functions of rupture velocity, as shown in Table 10.1.

In this case, $\langle f_P\rangle$ is higher than $\langle f_S\rangle$, and their ratio varies from 1.26 to 1.43 as v/β increases from 0.5 to 0.9. Sato and Hirasawa attribute the inadequacy of fault models of the type considered by Haskell to the restrictive form of $\Delta u(\xi, t)$ given in (10.17) or (10.31), where the time-dependence is assumed to be common to all the points on the fault. This assumption may be approximately valid for a long thin fault in which the slip function is determined by the width alone, but it is poor for an equidimensional fault in which the rupture nucleates at a point and spreads out to all directions on the fault plane. Both their model and the model of Molnar *et al.* (described in Section 10.1.6), which also predicts $\langle f_P\rangle > \langle f_S\rangle$, are free from this restriction. As we shall discuss in Section 11.1.5, some of the important features of the solution to a dynamic problem of finite circular crack formation are contained in the models of Sato and Hirasawa, and of Molnar *et al.*

On the other hand, formula (10.30) for a self-similar elliptical crack predicts lower corner-frequency for P-waves than for S-waves. The formula is based on the assumption that the nucleation phase dominates the stopping phase at high frequencies. The high-frequency asymptote given in (10.30) is determined by the rupture velocities and the particle velocity. Since the rupture velocities are given as material constants and the particle velocity is determined by rupture velocities and the initial stress, the asymptote in this case is determined independent of the size of the final ruptured area: at a given travel distance the far-field seismic waves would have the same absolute spectrum for frequencies higher than

the corner frequency, independent of earthquake magnitude, if formula (10.30) is correct. This result appears to contradict observations on the scale effect on seismic spectra, as discussed below.

An observed seismic spectrum is a function of source, path, and receiver. The simplest way of eliminating the path and receiver effects is to compare seismograms obtained by the same seismograph at the same station from two earthquakes with the same epicenter. Berckhemer (1962) was able to collect six such earthquake pairs recorded at the Stuttgart station for the period 1931–1951, and found a strong frequency dependence of amplitude ratios between the pair. These data were interpreted by Aki (1967) using two kinematic models: the ω-square and ω-cube models. The ω-cube model is a special case of the earthquake model suggested by Haskell (1966) and has the exact property described in the previous paragraph (a high-frequency spectrum that is independent of earthquake size). The far-field displacement spectrum for the ω-cube model is expressed as

$$S(\omega) = \frac{S(0)}{[1 + (\omega/\omega_0)^2]^{3/2}}, \tag{10.36}$$

where $S(0)$ is proportional to seismic moment. The value of ω_0 is effectively the corner frequency, though in practice it may differ somewhat from the definition given previously in terms of the intersection between high- and low-frequency asymptotes (see Shi *et al.*, 1998). As discussed in Section 10.1.5, if we assume similarity between large and small earthquakes the seismic moment will be proportional to L^3. The corner frequency will be proportional to L^{-1}, so we have

$$S(0) = \text{const.} \times \omega_0^{-3}. \tag{10.37}$$

Once the above constant is fixed, a family of spectral curves is determined that will describe the scaling law of seismic spectra. Neighboring curves shown in Figure 10.13 are separated by a constant factor at frequency 0.05 Hz, so that the curves are designated by a uniform scale of M_s defined by Gutenberg and Richter (Appendix 2) using the amplitude of surface waves at a period of 20 s. If the M_s of one curve is fixed, then M_s is determined for the rest. One can then find the amplitude ratio between two earthquakes of any magnitude as a function of frequency. By trial and error, Aki (1967) found the family of spectral curves, shown in Figure 10.13, which best fit Berckhemer's observed amplitude ratio. These spectral curves share the same high-frequency asymptote in the absolute sense, independent of earthquake magnitude. This feature is expected when the nucleation is responsible for the high-frequency asymptote as in Dahlen's model: the effect may be observed for the initial portion of the seismogram in which the effect of stopping has not appeared. In fact, the body-wave magnitude m_b (Appendix 2), defined by the amplitude of short-period (about 1 s) P-waves in the first 5 s, reaches a maximum value at around $m_b = 6$ and does *not* increase with earthquake size (Geller, 1976). This is in agreement with the spectral curves of Figure 10.13, which show that the spectral density at frequencies of 1 Hz and higher is the same for all M_s greater than 5.5.

BOX 10.2

Allowance for finite faulting in calculating far-field body waves within depth-dependent structures

In all our chapters on wave propagation in heterogeneous media, we have used very simple sources, usually a point source. But to explain seismic data it is necessary to merge the theories of wave propagation with the source theory we are developing in this chapter and the next. Provided we can make the Fraunhofer approximation, based on (10.12), all that is needed for purposes of computing the radiation from finite faulting is to know the slip function $[\mathbf{u}(\xi, \tau)]$ over the fault Σ, and the Green function $\mathbf{G}(\mathbf{x}, t; \xi, \tau)$.

Thus, in the far-field it is often adequate to make the approximation

$$\mathbf{G}(\mathbf{x}, t; \xi, \tau) \sim \mathbf{G}\left(\mathbf{x}, t; \mathbf{0}, \tau - \frac{\xi \cdot \gamma}{c}\right) \tag{1}$$

for that part of the wave field at $\mathbf{x}$ associated with waves having velocity $c(\xi)$ in the source region. Here γ is a unit vector at the origin of coordinates (taken on Σ); and γ is in the direction of waves departing from Σ.

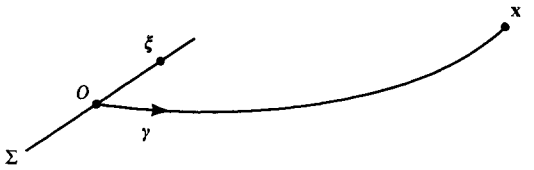

The approximation (1) above is equivalent to approximation (10.11), which was used in deriving (10.13). When the Green function is integrated over Σ, we need only make an allowance for the far-field phase correction (i.e., the travel-time difference) between ξ and O. This is appropriate for far-field body waves and surface waves in depth-varying and laterally-varying media.

For example, in Chapter 9 we obtained integrals over ray parameter p that gave far-field body-wave pulse shapes in depth-varying media. Point sources were used, and often the source was characterized by $M_0(\omega)$, together with some strike, dip, and rake (see, e.g., (9.96) and (9.102)). To generalize these results in order to allow for finite faulting, it is clear that one must replace

$$M_0(\omega) \quad \text{by} \quad \iint_\Sigma \mu \, \Delta u(\xi, \omega) \exp\left[-\frac{i\omega(\xi \cdot \gamma)}{c(\xi)}\right] d\Sigma \tag{2}$$

(assuming slip in the same direction everywhere over Σ).

Note that γ itself is dependent on ray parameter, so that the expression (2) should appear within the integration over p which characterized much of our numerical work in Chapter 9. However, for many practical purposes it is adequate to evaluate (2) at one representative value of γ for each $\mathbf{x}$.

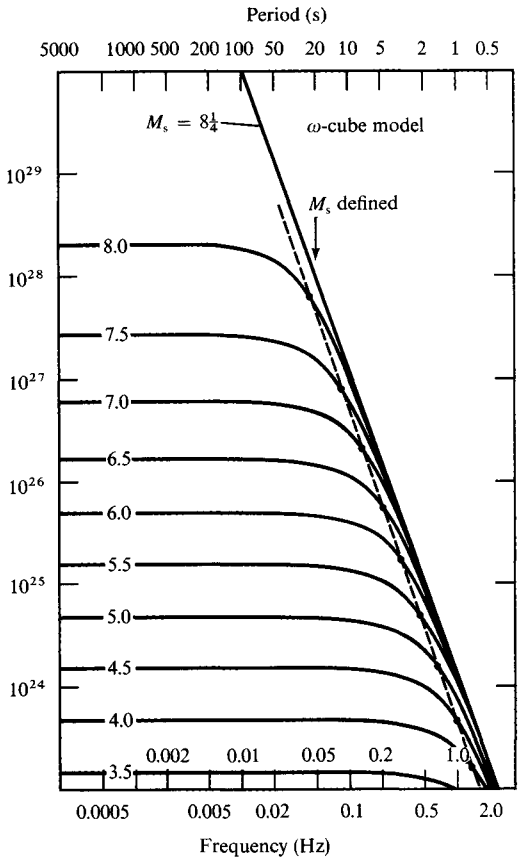

FIGURE **10.13**
Spectra of far-field body-wave displacement observed at a fixed distance from earthquakes with different M_s. The vertical coordinate shows the corresponding seismic moment. All curves share the common shape of equation (10.36), and similarity between large and small earthquakes is assumed. The broken line is the locus of the corner frequency ω_0. [From Aki, 1967; copyright by the American Geophysical Union.]

The curves in Figure 10.13, however, do not seem to apply to the total seismogram. The duration of seismic signal is longer for larger earthquakes, so if the spectral density is independent of magnitude, it follows that larger earthquakes should show smaller amplitudes for frequencies higher than 1 Hz. This clearly contradicts the observation on peak accelerations for $6 < M < 8$, as shown later in Figure 12.13. Peak accelerations observed at short distances are at frequencies higher than 1 Hz, and they are greater for larger earthquakes at a given distance.

Fortunately, Aki's ω-square model gives more satisfactory results. This model has the far-field spectrum given by

$$S(\omega) = \frac{S(0)}{[1 + (\omega/\omega_0)^2]}. \tag{10.38}$$

The corresponding family of spectral curves fitting the Berckhemer data is shown in Figure 10.14. In this case, the spectral amplitude increases with magnitude M_s for all frequencies, in agreement with observation.

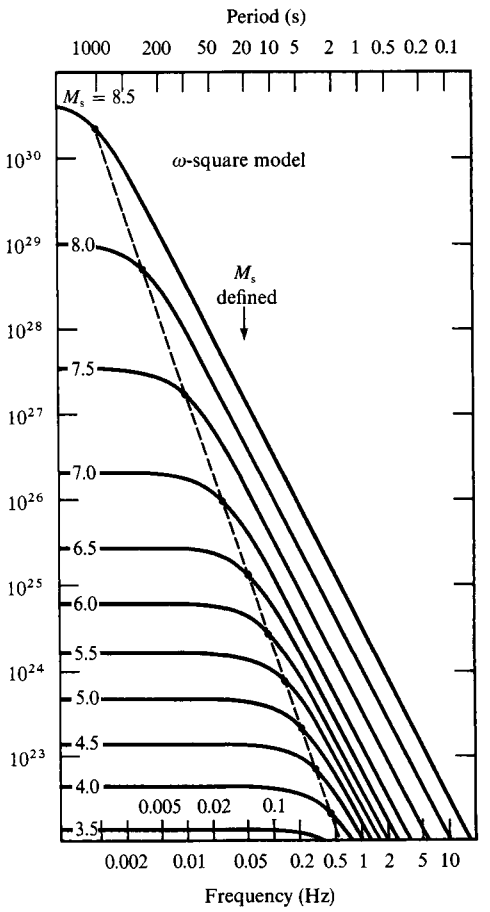

FIGURE **10.14**
Same as Figure 10.13 except that the spectra share the common shape of equation (10.38). The broken line is the locus of ω_0. [From Aki, 1967; copyright by the American Geophysical Union.]

That the high-frequency spectrum for the ω-square model should increase with magnitude without ceiling was expected because the ω^{-2} asymptote indicates the dominance of a stopping phase at high frequencies, and the number of stopping points (or the length of stopping loop) increases with the ruptured area. There was a ceiling for the ω-cube model, because the nucleation point is a single point for any earthquake.

10.2 Kinematics of an Earthquake as Seen at Near Field

In the preceding section, we studied seismic waves observed in the far field, for which a simple relation (10.13) exists between the waveform and the fault slip function. There are, however, two major drawbacks to the study of seismic sources from far-field observation. First, as shown by (10.15), the far-field waves carry information about the source function only for that part of the space-time spectrum for which $|\omega/k| > c$, where ω is the frequency, k is the wavenumber component in the fault plane, and c is the wave-propagation velocity. A complete determination of the slip function requires observation near the seismic source. Second, the waves recorded in the far field had to travel a long distance from the source.

During the propagation, waves will suffer from attenuation, scattering, spreading, focusing, multipath interference, and other complex path effects. One way of minimizing the path effects is to make observations at a short distance from the seismic source, again leaning upon the near-field data for more complete study of the source mechanism.

Ideally, we wish to measure the slip function $\Delta u(\xi, t)$ at various points ξ directly on the fault plane. Since such a measurement is almost impossible in practice, we must find out how the seismic motion close to but at some distance from the fault is related to the slip on the fault. This relation is complicated because the seismograms at short distances are composed of far-field and near-field terms of P- and S-waves coming from each element of the fault, as discussed in Section 4.2. These different terms cannot be isolated on the records, and therefore the total seismogram must be computed for comparison with observations. Such a computation is useful also for predicting seismic effects at the site of an engineering structure, due to a nearby earthquake fault on which the kinematic motions have been prescribed.

10.2.1 SYNTHESIS OF NEAR-FIELD SEISMOGRAMS FOR A FINITE DISLOCATION

The near-field seismic motion for a finite dislocation source buried in a homogeneous, isotropic, unbounded medium can be calculated by integrating the solution obtained in Section 4.2 for seismic displacement due to an infinitesimal fault $d\Sigma$ across which the slip is given as $[\mathbf{u}(\xi, t)]$. The solution for an arbitrary slip function over a finite fault surface $\Sigma(\xi)$ can be obtained using equation (4.30), or equations (10.1) and (10.2), as

$$
\begin{aligned}
u_i(\mathbf{x}, t) = \iint_{\Sigma} \mu \Bigg[& \left(\frac{30\gamma_i n_p \gamma_p \gamma_q \nu_q - 6\nu_i n_p \gamma_p - 6n_i \gamma_q \nu_q}{4\pi\rho r^4} \right) \\
& \times \left(F\left(t - \frac{r}{\alpha}\right) - F\left(t - \frac{r}{\beta}\right) + \frac{r}{\alpha}\dot{F}\left(t - \frac{r}{\alpha}\right) - \frac{r}{\beta}\dot{F}\left(t - \frac{r}{\beta}\right) \right) \\
& + \left(\frac{12\gamma_i n_p \gamma_p \gamma_q \nu_q - 2\nu_i n_p \gamma_p - 2n_i \gamma_q \nu_q}{4\pi\rho\alpha^2 r^2} \right) \Delta u\left(\xi, t - \frac{r}{\alpha}\right) \\
& - \left(\frac{12\gamma_i n_p \gamma_p \gamma_q \nu_q - 3\nu_i n_p \gamma_p - 3n_i \gamma_q \nu_q}{4\pi\rho\beta^2 r^2} \right) \Delta u\left(\xi, t - \frac{r}{\beta}\right) \\
& + \frac{2\gamma_i n_p \gamma_p \gamma_q \nu_q}{4\pi\rho\alpha^3 r} \Delta \dot{u}\left(\xi, t - \frac{r}{\alpha}\right) \\
& - \left(\frac{2\gamma_i n_p \gamma_p \gamma_q \nu_q - \nu_i n_p \gamma_p - n_i \gamma_q \nu_q}{4\pi\rho\beta^3 r} \right) \Delta \dot{u}\left(\xi, t - \frac{r}{\beta}\right) \Bigg] \, d\Sigma(\xi),
\end{aligned}
\tag{10.39}
$$

where $F(t) = \int_0^t dt' \int_0^{t'} \Delta u(\xi, t'')\, dt''$, $\mathbf{n}\, \Delta u(\xi, t) = [\mathbf{u}]$, ν is the fault normal, $r = |\mathbf{x} - \xi|$, and $\gamma = (\mathbf{x} - \xi)/r$. Each of the terms under the surface integral has a simple form identifiable as waves propagating either as P or S, attenuating as a certain negative power

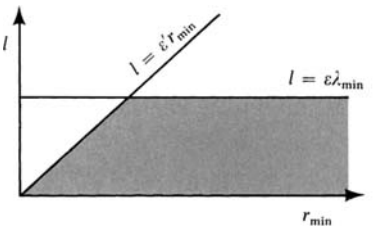

FIGURE **10.15**

of distance from the source. The waveform of each term can be easily calculated for a given slip function $\Delta u(\xi, t)$. It is difficult, however, to make a general statement on the total displacement because, at short distances, those terms arrive almost simultaneously, often canceling each other because they are of comparable size, so that the behavior of the sum of all the terms is quite unpredictable from separate consideration of individual terms. This is especially true for motion close to the fault, because each term tends to infinity as $r \to 0$, although physically we expect the sum of all the terms to be finite (see Problem 4.1).

Early work on evaluating the near field of finite faulting was based mostly on the direct numerical integration of (10.39) with respect to ξ. For a numerical integration of (10.39), we replace the integral by a summation over grid points, assuming that the integrand varies smoothly in the grid interval. Each term of the integrand in (10.39) contains two distinct factors: one is a negative power of $r = |\mathbf{x} - \xi|$, and the other is a function directly derivable from $\Delta u(\xi, t - r/c)$, where c is the wave velocity. Subsequent work on the evaluation of (10.39) has entailed making an efficient choice of grid size, and associated approximations, as we next discuss.

For r^{-n} to be smooth over $(r_0, r_0 + l)$, nl/r_0 must be negligible as compared to 1. Therefore, the grid interval l must be taken to be much smaller than r_{min}/n, where r_{min} is the minimum distance from the observation point $\mathbf{x}$ to the fault plane $\Sigma(\xi)$.

The smoothness of the other factor is determined by the slip-time function. Since $\Delta u(\xi, t - r/c)$ contains $t - r/c$ in place of the time variable of the slip function, it varies rapidly as a function of ξ over a distance l if the slip function varies rapidly over a time interval l/c. For this factor to be smooth over the grid interval l, l/c must be much smaller than the minimum period T_{min} contained in the slip function. For example, if the slip function is characterized by the rise time T, then l must be much smaller than cT. The choice of l is restricted by the above two conditions to the shaded region of Figure 10.15, where λ_{min} is the wavelength corresponding to T_{min}, and ε and ε' are small fractions.

For a relatively large r_{min}, we can relax the above restriction on l to some degree by the same approximate method used for the far-field calculation in Section 10.1.3. If l^2 is much less than $r_{min} \cdot \lambda_{min}$, then from (10.11) applied to each grid interval we can put

$$r = r_0 - (\gamma \cdot \xi),$$

where γ is the unit vector directed from a grid point to the observation point. Then we can get a compact result for the integral over each grid interval, assuming that the factor r^{-n} is constant. For example, if we set the time dependence of $\Delta u(\xi, t)$ as $\exp(-i\omega t)$, the integral

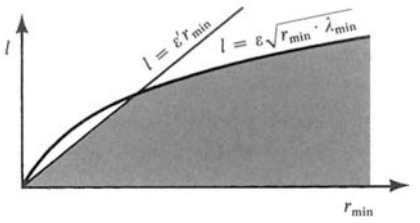

FIGURE **10.16**

over the grid interval will have a factor $(x^{-1} \sin x)e^{ix}$, where $x = \omega l/2(1/v - c^{-1} \cos \Psi)$, as defined in Section 10.1.5. We can then sum these integrated terms over all the grid points. The time-domain solution for a given slip function can be synthesized for the solutions for various ω. The appropriate choice of l for this method will be in the shaded region of Figure 10.16, which allows a coarser grid (larger l) for much of the spatial region than is the case in Figure 10.15.

Both methods have been used in interpreting the records of strong-motion (or low-magnification) seismographs located at short distances from earthquakes, and several interesting results have been obtained from comparison with observations. For example, for a Haskell-type moving dislocation (10.21) with slip motion parallel to the direction of rupture propagation, it was predicted that the displacement near the fault in the direction perpendicular to the fault plane should have an impulsive form with amplitude being a significant fraction of the amount of slip and with width being nearly equal to the rise time. Such an impulsive displacement with the expected sense of motion was actually observed by a strong-motion seismograph located only 80 meters from the San Andreas fault during the Parkfield earthquake of 1966 June 28. Figure 10.17 shows the perpendicular component of the acceleration, velocity, and displacement. A slightly different displacement record was published by Housner and Trifunac (1967), who used an integration technique different from the one used to obtain Figure 10.17. Figure 10.18 shows the theoretical displacement seismogram synthesized for a unilaterally propagating fault. The rise time and slip for the models that fit the observation are about 0.4–0.9 s and 60–100 cm, respectively. Although these estimates of source parameters had to be revised by later work of Bouchon (1979), who also included the effect of a low-velocity sedimentary layer, the successful comparison between the theoretical and experimental results encouraged seismologists to pursue further the synthesis of strong motion near an earthquake fault.

Numerical integration methods were also used by Anderson and Richards (1975) in a comparative study of the near-field motion for Haskell's model with that calculated for several different kinematic models of faulting. They found that it is often difficult in practice to determine the slip function from kinematic modeling, even when several records of ground motion are available within one fault length from the source region.

In order to simulate ground motion in Southern California associated with a hypothetical large earthquake on the San Andreas fault, Olsen *et al.* (1995) modeled a strike slip source kinematically with $\Delta\dot{u}$ taken to have a gaussian shape, moving along strike with a rupture velocity equal to 85% of the local S-wave speed. They used finite differencing to solve for the wave propagation in an inhomogeneous crustal structure described by a

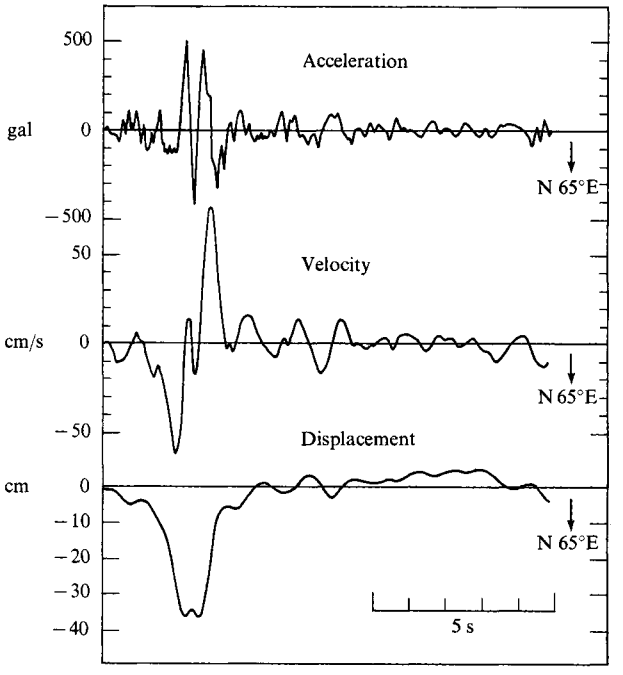

FIGURE **10.17**
Acceleration, velocity, and displacement observed at 80 meters from the San Andreas fault in the direction perpendicular to the fault trace during the 1966 Parkfield earthquake. [From Aki, 1968; copyright by the American Geophysical Union.]

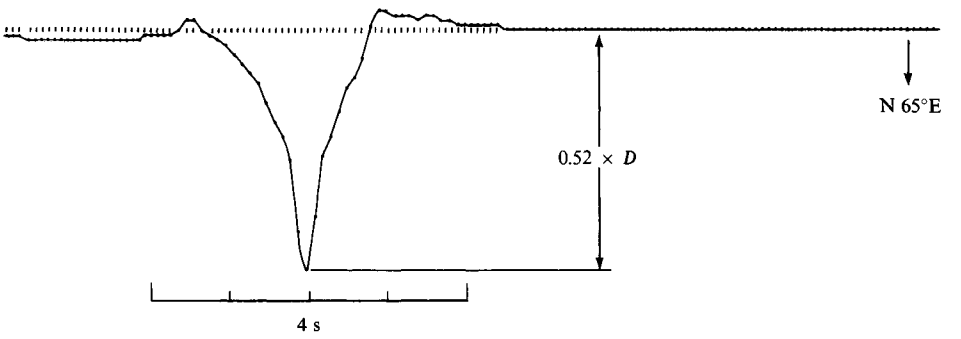

FIGURE **10.18**
Synthetic displacement corresponding to the observation shown in Figure 10.17 for a right-lateral strike slip fault propagating with rupture velocity 2.2 km/s. [From Aki, 1968; copyright by the American Geophysical Union.]

three-dimensional grid with 576 points along strike, 352 points perpendicular to strike, and 116 points in the depth direction. Body waves and surface waves were included, and the finite difference solution was integrated for points on the gridded fault surface, and over the source duration. The simulation of ground motion over about 20,000 km^2 of crustal surface for a duration of two minutes took about 24 hours on a machine with 512 processors. They found that the ground motion is amplified by a factor of about 2.5 at some locations, over that for a uniform layered model with overall similar properties.

Such numerical-integration methods described above can be very useful and are entirely appropriate when crustal structure is well known, but they are time-consuming and do not always give good physical insight. Thus one cannot generalize the behavior of seismic motion. It must be calculated for each specific case. This limitation is especially severe for high-frequency waves.

To overcome this limitation, compact, exact analytic solutions have been sought for simplified source models. For example, Boatwright and Boore (1975) and Sato (1975) showed that analytic solutions may be obtained for Haskell's model in the case when the fault width W becomes zero. The other extreme model is the case when W becomes infinity, reducing the problem to two dimensions. This reduction may be justified for frequencies higher than a certain critical frequency f_c determined by the minimum distance r_{min} to the fault from the station and by the width W of the fault plane: if the station is close to the fault plane, the seismic motion will be independent of W for frequencies higher than f_c. For two-dimensional problems, we can find compact and exact solutions more easily, as shown in Sections 10.2.3 and 10.2.4. The result will be useful for understanding the high-frequency motions—especially the nature of ground accelerations near the fault, which could not effectively be studied by the numerical method described above.

10.2.2 HIGH-FREQUENCY MOTIONS NEAR A PROPAGATING FAULT

To gain physical insight into the near field of a propagating fault, we shall consider greatly simplified models and obtain analytical solutions for the resulting motions. Let us put the fault in the zx-plane, with its rupture front parallel to the z-axis and propagating in the x-direction, as shown in Figure 10.19. For a nearby observation point on the xy-plane, the effect of the width of the fault on high-frequency motions may be neglected and we can use the solution for two-dimensional problems in which the fault width is set equal to infinity. This simplifies the analysis greatly, because every quantity becomes independent of z.

We shall consider two basic types of propagating faults: anti-plane and in-plane. For the anti-plane type with rupture propagation in the x-direction, the slip is in the z-direction as shown in Figure 10.19, and the resulting displacement has a component only in the z-direction. In crystal-dislocation theory, this is called a *screw dislocation*, in which the slip direction (Burger's vector) is parallel to the dislocation line. If the fault plane is horizontal, the resulting motions are composed solely of SH-waves. For the in-plane type, the slip is in

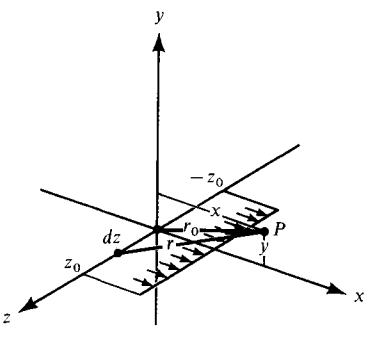

FIGURE **10.19**

the x-direction, and the resulting displacement has x- and y-components, associated with both P- and SV-waves. In crystal-dislocation theory, this is called an *edge dislocation*, in which the slip direction is perpendicular to the dislocation line. When the edge-dislocation line moves in the direction parallel to the slip, the movement is called *gliding*.

10.2.3 ANTI-PLANE PROBLEMS

As the simplest anti-plane problem, we shall consider the case in which phenomena appear to be stationary if looked at in coordinates

$$x' = x - vt, \qquad y' = y, \qquad t' = t,$$

which move with a constant velocity v. Such a case is possible for a semi-infinite fault plane propagating with velocity v from the time $-\infty$. The condition on the discontinuity in the displacement $w(x, y, t)$ across the fault plane is given by

$$w(x, +0, t) - w(x, -0, t) = \Delta w H(-x'), \tag{10.40}$$

where $H(x)$ is the unit step function. The stress is assumed to be continuous, so that

$$\mu \frac{\partial w}{\partial y}(x, +0, t) = \mu \frac{\partial w}{\partial y}(x, -0, t). \tag{10.41}$$

The equation of motion for an isotropic homogeneous body reduces to a wave equation for w:

$$\frac{1}{\beta^2} \frac{\partial^2 w}{\partial t^2} = \frac{\partial^2 w}{\partial x^2} + \frac{\partial^2 w}{\partial y^2}. \tag{10.42}$$

Using the new coordinates, and applying the stationarity condition $\partial/\partial t' = 0$, i.e.,

$$\frac{\partial}{\partial t} = \frac{\partial}{\partial t'} - v\frac{\partial}{\partial x'} = -v\frac{\partial}{\partial x'}, \qquad \frac{\partial}{\partial x} = \frac{\partial}{\partial x'}, \qquad \frac{\partial}{\partial y} = \frac{\partial}{\partial y'},$$

equation (10.42) can be rewritten as

$$\left(1 - \frac{v^2}{\beta^2}\right) \frac{\partial^2 w}{\partial x'^2} + \frac{\partial^2 w}{\partial y'^2} = 0. \tag{10.43}$$

For $v = 0$, this reduces to the Laplace equation and its solution for boundary conditions (10.40) and (10.41) is based on properties of $\log(x' + iy')$ and is well known. We use the fact that the imaginary part of $\log(x' + iy')$ satisfies the Laplace equation, so the solution of (10.43) when $v = 0$, that is discontinuous (but with continuous derivative) across $y = 0$ is

$$w(x', y') = A \tan^{-1} \frac{y'}{x'} \qquad \text{for some constant } A.$$

The function $\tan^{-1}$ here is taken to lie in the range $(-\pi, \pi)$. Since $w(x', y')$ is a solution of the Laplace equation, $w(x'/\sqrt{1 - v^2/\beta^2}, y')$ will be a solution of (10.43). Here we have assumed subsonic rupture propagation, $v < \beta$. Our solution of (10.42) is therefore given by

$$w(x, y, t) = \frac{\Delta w}{2\pi} \tan^{-1} \frac{y\sqrt{1 - v^2/\beta^2}}{x - vt} \tag{10.44}$$

where the constant A has been assigned the value $\Delta w/(2\pi)$. This satisfies the boundary conditions (10.40), requiring the continuity of w everywhere except at $y = 0$, $x < vt$, because (10.44) does correctly give

$$\begin{aligned} w(x, y, t) &= 0 && \text{at } y = 0, x > vt \\ &= \frac{\Delta w}{2} && \text{at } y = +0, x < vt \\ &= -\frac{\Delta w}{2} && \text{at } y = -0, x < vt. \end{aligned}$$

Since the stress components are

$$\begin{aligned} \tau_{xz} &= -\frac{\mu\, \Delta w}{2\pi} \frac{\sqrt{1 - v^2/\beta^2} \cdot y}{(x - vt)^2 + (1 - v^2/\beta^2)y^2}, \\ \tau_{yz} &= \frac{\mu\, \Delta w}{2\pi} \frac{\sqrt{1 - v^2/\beta^2}\,(x - vt)}{(x - vt)^2 + (1 - v^2/\beta^2)y^2}, \end{aligned} \tag{10.45}$$

τ_{xz} vanishes at $y = 0$, and the condition (10.41) is satisfied at $y = 0$, where

$$\tau_{yz} = \mu \frac{\partial w}{\partial y} = \mu \frac{\Delta w}{2\pi} \frac{\sqrt{1 - v^2/\beta^2}}{x - vt}. \tag{10.46}$$

The stress τ_{yz} on the plane $y = 0$ is an odd function of $x - vt$, and becomes $-\infty$ behind the tip and $+\infty$ ahead of the tip. Note that τ_{yz} vanishes when the rupture velocity is β. Equation (10.44) was obtained by Frank (1949), Liebfried and Dietze (1949), and Eshelby (1949).

The particle velocity is obtained from (10.44) as

$$\frac{\partial w}{\partial t} = \frac{\Delta w}{2\pi} \frac{yv\sqrt{1 - v^2/\beta^2}}{(x - vt)^2 + y^2(1 - v^2/\beta^2)}. \tag{10.47}$$

The peak velocity occurs at $x = vt$, and the peak value is $(\Delta w/2\pi) \cdot [v/(y\sqrt{1 - v^2/\beta^2})]$. The peak value tends to infinity as the rupture velocity approaches β for this semi-infinite crack. It decays as the inverse of distance from the fault.

The acceleration can be obtained from (10.47) as

$$\frac{\partial^2 w}{\partial t^2} = \frac{\Delta w}{2\pi} \cdot \frac{2y(x - vt)v^2\sqrt{1 - v^2/\beta^2}}{[(x - vt)^2 + y^2(1 - v^2/\beta^2)]^2}.$$

The peak acceleration occurs at $x - vt = (y/\sqrt{3})\sqrt{1 - v^2/\beta^2}$, and is

$$\frac{\Delta w}{2\pi} \frac{9}{8\sqrt{3}} \frac{v^2}{y^2(1 - v^2/\beta^2)}.$$

The peak acceleration also tends to infinity as the rupture velocity approaches β. It decays as the inverse square of distance from the fault.

The nature of motions in the near field of a propagating dislocation may be better interpreted from their spectrum. The Fourier transform of $\partial w/\partial t$ at $x = 0$ can be obtained by residue evaluation at poles $t = \pm iy\sqrt{1 - v^2/\beta^2}/v$, and is equal to

$$\frac{\Delta w}{2} \exp\left(-|y| \cdot |\omega| \cdot \frac{\sqrt{1 - v^2/\beta^2}}{v}\right).$$

This shows an exponential decay with both y and ω, indicating that they are composed of inhomogeneous plane waves trapped near the fault plane. Thus, for a subsonic rupture propagation with uniform velocity that starts at time $-\infty$ and continues to time $+\infty$, the near-field motion decays quickly with the distance y from the fault plane; the peak velocity decays as y^{-1}, and the peak acceleration as y^{-2}. The spectrum decays exponentially with increasing frequency, as expected for inhomogeneous plane waves.

Next let us introduce simple models of starting and stopping in the fault propagation, and see what will happen in the near field. To study the effect of starting, we shall replace (10.40) with the following boundary condition:

$$w(x, +0, t) - w(x, -0, t) = \Delta w \cdot H\left(t - \frac{x}{v}\right) H(x), \tag{10.48}$$

which corresponds to a step-function slip starting from $x = 0$ at $t = 0$ and propagating in the $+x$-direction with velocity v, as shown in Figure 10.19. Since the motion is not stationary in the moving coordinates, equation (10.43) no longer applies. Expressing the Laplace transform of $w(x, y, t)$ as

$$w(x, y, s) = \int_0^\infty w(x, y, t) e^{-st}\, dt,$$

we rewrite the equation of motion (10.42) as

$$\frac{s^2}{\beta^2} w = \frac{\partial^2 w}{\partial x^2} + \frac{\partial^2 w}{\partial y^2}. \tag{10.49}$$

Taking the Laplace transform of the boundary condition (10.48), we have

$$w(x, +0, s) - w(x, -0, s) = \frac{\Delta w \cdot e^{-sx/v}}{s} H(x). \tag{10.50}$$

Since

$$e^{-sx/v} H(x) = \frac{1}{2\pi} \int_{-\infty}^{\infty} \frac{e^{ikx}}{i(k - is/v)} dk,$$

which can be obtained easily by residue evaluation of the pole at $k = is/v$, the boundary condition (10.50) can be rewritten as

$$w(x, +0, s) = -w(x, -0, s) = \frac{\Delta w}{4\pi s} \int_{-\infty}^{\infty} \frac{e^{ikx}}{i(k - is/v)} dk, \tag{10.51}$$

where we have used the antisymmetry with respect to y: $w(x, -y, t) = -w(x, y, t)$.

To meet the above boundary condition, we assume the solution of (10.49) has the form

$$w(x, y, s) = \int_{-\infty}^{\infty} Q(k) e^{ikx - vy}\, dk,$$

where $v^2 = k^2 + s^2/\beta^2$. $Q(k)$ is determined by putting $y = \pm 0$ and comparing with (10.51). The result is

$$\begin{aligned} w(x, y, s) &= \frac{\Delta w}{4\pi s} \int_{-\infty}^{\infty} \frac{e^{ikx - vy}}{i(k - is/v)} dk, \qquad y > 0 \\ &= -\frac{\Delta w}{4\pi s} \int_{-\infty}^{\infty} \frac{e^{ikx + vy}}{i(k - is/v)} dk, \qquad y < 0. \end{aligned} \tag{10.52}$$

The stress $\mu(\partial w/\partial y)$ is continuous at $y = 0$.

Equation (10.52) has a familiar form to which the Cagniard method is applicable (Mitra, 1966; Boore and Zoback, 1974). Transforming the variable k to τ by the relation

$$-s\tau = ikx - \sqrt{k^2 + s^2/\beta^2}\, y,$$

(10.52) is reduced to

$$\begin{aligned} w(x, y, s) = &-\frac{\Delta w}{2\pi} \int_0^{\infty} \mathrm{Re} \frac{\sqrt{\tau^2 - r^2/\beta^2} \cos\theta - i\tau \sin\theta}{\sqrt{\tau^2 - r^2/\beta^2} \sin\theta + i(\tau \cos\theta - r/v)} \\ &\times \frac{H(\tau - r/\beta)}{\sqrt{\tau^2 - r^2/\beta^2}} \frac{e^{-s\tau}}{s} d\tau, \end{aligned}$$

where $x = r\cos\theta$ and $y = r\sin\theta$. Since the above equation now has the form of the Laplace transform for $sw(x, y, s)$, the corresponding time-domain solution $\partial w(x, y, t)/\partial t$ can be identified as

$$\begin{aligned} \frac{\partial w(x, y, t)}{\partial t} = &\frac{\Delta w}{2\pi} \frac{(t^2 - r^2/\beta^2) \sin\theta \cos\theta - t \sin\theta (t\cos\theta - r/v)}{(t^2 - r^2/\beta^2) \sin^2\theta + (t\cos\theta - r/v)^2} \\ &\times \frac{H(t - r/\beta)}{\sqrt{t^2 - r^2/\beta^2}}. \end{aligned} \tag{10.53}$$

This equation reduces to (10.47) for the dislocation propagating from $t = -\infty$ if we make θ small and $x \to vt$. In other words, the near-field motion at the time of arrival of a rupture front is approximately explained by the simple solution given in equation (10.47).

The new solution, however, contains an additional sharp waveform originating from the starting points at $t = 0$ and propagating with the velocity of shear waves. The particle velocity is unbounded at $t = r/\beta$, where it has a square-root singularity. Near $t = r/\beta$, (10.53) becomes approximately

$$\frac{\partial w}{\partial t} = \frac{\Delta w}{2\pi} \frac{\sin\theta}{(\beta/v - \cos\theta)} \frac{1}{\sqrt{2r/\beta}} \frac{H(t - r/\beta)}{\sqrt{t - r/\beta}}. \tag{10.54}$$

This wave attenuates with distance as $1/\sqrt{r}$, representing a cylindrical wave that originates at the starting point of the fault propagation, and shows a radiation pattern given by $\sin\theta/(\beta/v - \cos\theta)$. For example, the x-direction along which the fault is propagating is a node. The spectrum of particle velocity $\partial w/\partial t$ given in (10.54) has a high-frequency asymptote of $1/\sqrt{\omega}$.

The acceleration associated with this "starting phase" has a singularity of the form $(t - r/\beta)^{-3/2} H(t - r/\beta)$ near the shear-wave arrival, and the corresponding spectrum has a high-frequency asymptote of $\sqrt{\omega}$.

If the slip function is a ramp function (equation (10.21)) instead of a step function, the peak particle velocity will be finite, but the peak acceleration will have a square-root singularity at $t = r/\beta$.

The effect of stopping can be studied by superposition of another moving dislocation starting at, say, $x = L$ at $t = L/v$, propagating with the same velocity v, but with opposite sign of slip. This will annihilate the fault ahead of $x = L$, and gives the solution for a finite fault that started at $x = 0$ and stopped at $x = L$. We then obtain another singularity propagating from the stopping point as cylindrical waves. The nature of this "stopping" phase is nothing but the "starting" phase of the superposed second fault. The equivalence here of stopping and starting is due to the unidirectional nature of fault propagation. If the rupture starts from a point and grows over an expanding area, the two effects will be quite different, as discussed in Section 10.1.6 for the far field.

Note that all the two-dimensional anti-plane faults in this section generate SH-waves alone.

10.2.4 IN-PLANE PROBLEMS

The simplest in-plane problem (Fig. 10.19) is the semi-infinite fault plane moving with a constant velocity v from time $-\infty$, and it generates both P-waves and SV-waves. We shall consider the case of a step-function slip, in which the boundary condition is written as

$$u(x, +0, t) - u(x, -0, t) = \Delta u \cdot H(-x'), \tag{10.55}$$

where $x' = x - vt$. The y-component of displacement, $v(x, y, t)$, and the traction on the fault plane, are continuous across $y = 0$.

The displacement components that satisfy the equation of motion in the in-plane problem can be written in terms of two scalar potentials as

$$u(x, y, t) = \frac{\partial \phi}{\partial x} - \frac{\partial \psi}{\partial y}, \qquad v(x, y, t) = \frac{\partial \phi}{\partial y} + \frac{\partial \psi}{\partial x} \tag{10.56}$$

(see Section 5.1 for development of two scalar potentials for two-dimensional $P-SV$ problems). The potentials ϕ and ψ satisfy the following wave equations:

$$\frac{1}{\alpha^2}\frac{\partial^2\phi}{\partial t^2}=\frac{\partial^2\phi}{\partial x^2}+\frac{\partial^2\phi}{\partial y^2}, \qquad \frac{1}{\beta^2}\frac{\partial^2\psi}{\partial t^2}=\frac{\partial^2\psi}{\partial x^2}+\frac{\partial^2\psi}{\partial y^2},$$

where $\alpha=\sqrt{(\lambda+2\mu)/\rho}$ and $\beta=\sqrt{\mu/\rho}$ are P and S velocities, respectively. Using the moving-coordinate system (compare with the development of (10.43)), the wave equations can be rewritten as

$$\left(1-\frac{v^2}{\alpha^2}\right)\frac{\partial^2\phi}{\partial x'^2}+\frac{\partial^2\phi}{\partial y^2}=0, \qquad \left(1-\frac{v^2}{\beta^2}\right)\frac{\partial^2\psi}{\partial x'^2}+\frac{\partial^2\psi}{\partial y^2}=0.$$

We consider here only subsonic motion, i.e., $v<\alpha$ and $v<\beta$.

The above equations have solutions of the form

$$\exp(ikx'\pm\sqrt{1-v^2/\alpha^2}\,ky) \text{ for } \phi, \qquad \text{and} \qquad \exp(ikx'\pm\sqrt{1-v^2/\beta^2}\,ky) \text{ for } \psi.$$

Since there are no sources of waves at infinity, we require that ϕ and ψ propagate away from $y=0$. For $y>0$, then, we introduce coefficients $\acute{\phi}$ and $\acute{\psi}$ in terms of which

$$\phi=\acute{\phi}\exp(ikx'-\sqrt{1-v^2/\alpha^2}\,|k|y), \qquad \psi=\acute{\psi}\exp(ikx'-\sqrt{1-v^2/\beta^2}\,|k|y), \quad (10.57)$$

and similarly for $y<0$,

$$\phi=\grave{\phi}\exp(ikx'+\sqrt{1-v^2/\alpha^2}\,|k|y), \qquad \psi=\grave{\psi}\exp(ikx'+\sqrt{1-v^2/\beta^2}\,|k|y),$$

As usual, we express the displacement u, v in terms of $\acute{\phi}$, $\acute{\psi}$, $\grave{\phi}$, and $\grave{\psi}$ using (10.56). The stress components τ_{xy} and τ_{yy} are related to displacement by

$$\tau_{yy}=\lambda\left(\frac{\partial u}{\partial x}+\frac{\partial v}{\partial y}\right)+2\mu\frac{\partial v}{\partial y}, \qquad \tau_{xy}=\mu\left(\frac{\partial u}{\partial y}+\frac{\partial v}{\partial x}\right). \quad (10.58)$$

The condition of discontinuity for u (see (10.55)) and the condition of continuity for v, τ_{xy}, τ_{yy} give four equations to determine four unknowns $\acute{\phi}$, $\acute{\psi}$, $\grave{\phi}$, and $\grave{\psi}$. The continuity of v and τ_{xy} imposes the following constraint on $(\acute{\phi}+\grave{\phi})$ and $(\acute{\psi}-\grave{\psi})$:

$$-\sqrt{1-v^2/\alpha^2}(\acute{\phi}+\grave{\phi})+i(\acute{\psi}-\grave{\psi})=0,$$

$$2i\sqrt{1-v^2/\alpha^2}(\acute{\phi}+\grave{\phi})+(2-v^2/\beta^2)(\acute{\psi}-\grave{\psi})=0.$$

The determinant of coefficients here is

$$\begin{vmatrix} -\sqrt{1-v^2/\alpha^2} & i \\ 2ik\sqrt{1-v^2/\alpha^2} & 2-v^2/\beta^2 \end{vmatrix}=-\sqrt{1-v^2/\alpha^2}\cdot v^2/\beta^2,$$

and it does not vanish as long as $v \neq \alpha$, so we must have

$$\acute{\phi} + \grave{\phi} = 0, \qquad \acute{\psi} - \grave{\psi} = 0.$$

From this, we find that $u(x, y, t)$ and $\tau_{yy}(x, y, t)$ are odd functions of y, and $v(x, y, t)$ and $\tau_{xy}(x, y, t)$ are even functions of y. Since the function τ_{yy} must be continuous at $y = 0$, it must vanish at $y = 0$:

$$\tau_{yy} = 0 \qquad \text{at } y = 0. \tag{10.59}$$

Since u is an odd function, the discontinuity condition (10.55) can be rewritten as

$$u(x, +0, t) = -u(x, -0, t) = \frac{\Delta u}{2} H(-x') = -\frac{\Delta u}{4\pi} \int_{-\infty+i\varepsilon}^{\infty+i\varepsilon} \frac{e^{ikx'}}{ik} dk, \tag{10.60}$$

where ε is a small positive number.

From the conditions (10.59) and (10.60), we can determine $\acute{\phi}$ and $\acute{\psi}$ for each k and express u and v as an integral of (10.57) with respect to k. The result for $y > 0$ is

$$\begin{aligned} u(x, y, t) = & -\frac{\Delta u}{2\pi} \int_{-\infty+i\varepsilon}^{+\infty+i\varepsilon} \left[\frac{\beta^2}{v^2} \exp\left(-\sqrt{1 - v^2/\alpha^2}\, |k| y\right) \right. \\ & \left. - \frac{(\beta^2 - v^2/2)}{v^2} \exp\left(-\sqrt{1 - v^2/\beta^2}\, |k| y\right) \right] e^{ikx'} \cdot \frac{dk}{ik}, \\ v(x, y, t) = & -\frac{\Delta u}{2\pi} \int_{-\infty+i\varepsilon}^{+\infty+i\varepsilon} \left[\frac{\beta^2}{v^2} \sqrt{1 - v^2/\alpha^2} \exp\left(-\sqrt{1 - v^2/\alpha^2}\, |k| y\right) \right. \\ & \left. - \frac{(\beta^2 - v^2/2)}{v^2 \sqrt{1 - v^2/\beta^2}} \exp\left(-\sqrt{1 - v^2/\beta^2}\, |k| y\right) \right] i \operatorname{sign}(\operatorname{Re} k) \cdot e^{ikx'} \frac{dk}{ik}, \end{aligned}$$

where sign(Re k) means the sign of the real part of k. Putting $y = 0^+$, we get the desired value $u(x, 0, t) = (\Delta u/2) \cdot H(-x')$. The integrand decays exponentially with k and y, showing that they are superpositions of inhomogeneous plane waves, as in the anti-plane case. We expect, therefore, that they are trapped near the fault plane and attenuate quickly with distance from the fault. Both components show a similar amplitude spectrum, but there is a $\pi/2$ phase shift between the two components indicated by the factor i in the integrand for $v(x, y, t)$. If $u(x, y, t)$ is antisymmetric with respect to $x' = 0$, then $v(x, y, t)$ will be symmetric. We shall see shortly that for the step-function slip, the transverse component displacement $v(x, y, t)$ shows an impulsive form with a logarithmic singularity at $x' = 0$.

To avoid the singularity at $k = 0$, we shall first evaluate the particle velocities $\partial u/\partial t$ and $\partial v/\partial t$. Since $\partial/\partial t$ introduces a factor $-ikv$ in the integrand that removes the singularity,

we can put $\varepsilon = 0$. Then the integrals will be either of the form

$$\begin{aligned}
&\int_{-\infty}^{\infty} \exp\left(ikx' - \sqrt{1 - v^2/\alpha^2}\,|k|y\right) dk \\
&\quad = \int_0^{\infty} \exp\left(ikx' - \sqrt{1 - v^2/\alpha^2}\,ky\right) dk + \int_{-\infty}^{0} \exp\left(ikx' + \sqrt{1 - v^2/\alpha^2}\,ky\right) dk \\
&\quad = \frac{2\sqrt{1 - v^2/\alpha^2}\,y}{x'^2 + (1 - v^2/\alpha^2)y^2}
\end{aligned} \tag{10.61}$$

or of the form

$$\begin{aligned}
&\int_{-\infty}^{\infty} i\,\mathrm{sign}(k) \exp\left(ikx' - \sqrt{1 - v^2/\alpha^2}\,|k|y\right) dk \\
&= \int_0^{\infty} i \exp\left(ikx' - \sqrt{1 - v^2/\alpha^2}\,ky\right) dk - \int_{-\infty}^{0} i \exp\left(ikx' + \sqrt{1 - v^2/\alpha^2}\,ky\right) dk \\
&= \frac{-2x'}{x'^2 + (1 - v^2/\alpha^2)y^2}.
\end{aligned} \tag{10.62}$$

We can also recognize that (10.61) is the derivative of $-2\tan^{-1}\left(\sqrt{1 - v^2/\alpha^2}\,y/x'\right)$ and that (10.62) is the derivative of $\log[x'^2 + (1 - v^2/\alpha^2)y^2]$ with respect to x'. Using these relations, we obtain the particle velocity for $y > 0$ as

$$\begin{aligned}
\frac{\partial u(x,y,t)}{\partial t} = -v\frac{\partial u(x,y,t)}{\partial x'} = \frac{v\,\Delta u}{\pi}\Bigg[&\frac{\beta^2}{v^2}\frac{\sqrt{1 - v^2/\alpha^2}\cdot y}{x'^2 + (1 - v^2/\alpha^2)y^2} \\
&- \frac{(\beta^2 - v^2/2)}{v^2}\frac{\sqrt{1 - v^2/\beta^2}\cdot y}{x'^2 + (1 - v^2/\beta^2)y^2}\Bigg], \\
\frac{\partial v(x,y,t)}{\partial t} = -v\frac{\partial v(x,y,t)}{\partial x'} = -\frac{v\,\Delta u}{\pi}\Bigg[&\frac{\beta^2}{v^2}\sqrt{1 - v^2/\alpha^2}\frac{x'}{x'^2 + (1 - v^2/\alpha^2)y^2} \\
&- \frac{(\beta^2 - v^2/2)}{v^2\sqrt{1 - v^2/\beta^2}}\frac{x'}{x'^2 + (1 - v^2/\beta^2)y^2}\Bigg]
\end{aligned} \tag{10.63}$$

and the displacement for $y > 0$ as

$$\begin{aligned}
u(x,y,t) &= \frac{\Delta u}{\pi}\left[\frac{\beta^2}{v^2}\tan^{-1}\frac{\sqrt{1 - v^2/\alpha^2}\cdot y}{x'} - \frac{(\beta^2 - v^2/2)}{v^2}\tan^{-1}\frac{\sqrt{1 - v^2/\beta^2}\cdot y}{x'}\right], \\
v(x,y,t) &= \frac{\Delta u}{2\pi}\left\{\frac{\beta^2}{v^2}\sqrt{1 - v^2/\alpha^2}\log\left(x'^2 + (1 - v^2/\alpha^2)y^2\right)\right. \\
&\qquad \left. - \frac{(\beta^2 - v^2/2)}{v^2\sqrt{1 - v^2/\beta^2}}\log\left(x'^2 + (1 - v^2/\beta^2)y^2\right)\right\}.
\end{aligned} \tag{10.64}$$

The above formula was first obtained by Eshelby (1949), and turns out to be valid for $y < 0$ as well as for $y > 0$. Values of $\tan^{-1}$ lie in the range $(-\pi, \pi)$, so that there is a step discontinuity in u of amount Δu across $y = 0$ for $x' < 0$. This is the fault plane, and (10.64) correctly reproduces the discontinuity (10.60). The transverse component $v(x, y, t)$ shows an impulsive symmetric form with a logarithmic singularity $\log |x'|$ at $x' = 0$ or $x = vt$. This result qualitatively agrees with the result of the numerical solution discussed in Section 10.2.1 in relation to the record of the Parkfield earthquake.

The stress components may be obtained from (10.63) and (10.57) as

$$\tau_{xx} = \frac{2\mu\ \Delta u \beta^2}{\pi v^2} \left[\frac{(v^2/\alpha^2 - v^2/2\beta^2)\sqrt{1 - v^2/\alpha^2}\, y}{x'^2 + (1 - v^2/\alpha^2)y^2} + \frac{(1 - v^2/2\beta^2)\sqrt{1 - v^2/\beta^2}\, y}{x'^2 + (1 - v^2/\beta^2)y^2} \right],$$

$$\tau_{yy} = \frac{2\mu\ \Delta u \beta^2}{\pi v^2} \left[\frac{(1 - v^2/2\beta^2)\sqrt{1 - v^2/\alpha^2}\, y}{x'^2 + (1 - v^2/\alpha^2)y^2} - \frac{(1 - v^2/2\beta^2)\sqrt{1 - v^2/\beta^2}\, y}{x'^2 + (1 - v^2/\beta^2)y^2} \right],$$

$$\tau_{xy} = \frac{2\mu\ \Delta u \beta^2}{\pi v^2} \left[\frac{\sqrt{1 - v^2/\alpha^2}\, x'}{x'^2 + (1 - v^2/\alpha^2)y^2} - \frac{(1 - v^2/\beta^2)^2 x'}{\sqrt{1 - v^2/\beta^2}\,[x'^2 + (1 - v^2/\beta^2)y^2]} \right].$$

As imposed by the boundary condition (10.59), $\tau_{yy} = 0$ on the fault plane $y = 0$, and τ_{xy} is continuous across $y = 0$, where

$$\tau_{xy} = \frac{2\mu\ \Delta u \beta^2}{\pi v^2 x'} \left[\sqrt{1 - v^2/\alpha^2} - (1 - v^2/2\beta^2)^2 / \sqrt{1 - v^2/\beta^2} \right]. \tag{10.65}$$

Thus, τ_{xy} has an $(x')^{-1}$ singularity at the crack tip, reaching $-\infty$ behind the tip and $+\infty$ ahead of the tip. Comparing the bracket [ ] of (10.65) with the expression given in equation (5.56) for determining the phase velocity of Rayleigh waves in a homogeneous half-space, we see that the in-plane shear stress across the fault plane vanishes when the crack tip propagates with the Rayleigh wave velocity.

For the particle velocity, the spectral contents and attenuation with distance are quite similar to those obtained earlier for the anti-plane problem. For example, the peak velocity decays inversely in proportion to the distance from the fault for both components. On the fault, the particle velocity is a δ-function for the parallel component and proportional to $(x - vt)^{-1}$ for the transverse component. Both functions have the same constant spectral density, but they differ by $\pi/2$ in phase for all frequencies. Off the fault, the high-frequency asymptote has an exponential decay, as expected for inhomogeneous plane waves.

Let us now consider the effect of a sudden start to the in-plane faulting, by solving a problem similar to the one studied in the anti-plane case (equation (10.48)). The faulting starts at $x = 0$ and propagates in the x-direction with velocity v. The boundary conditions are

$$u(x, +0, t) - u(x, -0, t) = \Delta u \cdot H(t - x/v)H(x), \tag{10.66}$$

with continuity for v, τ_{xy}, and τ_{yy} as before. Again u and τ_{yy} are odd functions of y, and v and τ_{xy} are even functions. It then follows that τ_{yy} must vanish at $y = 0$, as in the case of the fault propagated from $t = -\infty$ (see Problem 14.2, for a general result in three dimensions).

Working with potentials (10.56) and the Laplace transform, e.g., $\phi(x, y, s) = \int \phi(x, y, t)e^{-st}\, dt$, the equation of motion is satisfied if the potentials satisfy the following wave equations:

$$\frac{\partial^2\phi}{\partial x^2} + \frac{\partial^2\phi}{\partial y^2} = \frac{s^2}{\alpha^2}\phi, \qquad \frac{\partial^2\psi}{\partial x^2} + \frac{\partial^2\psi}{\partial y^2} = \frac{s^2}{\beta^2}\psi.$$

The solutions of these equations are of the forms $e^{ikx\pm\gamma y}$ and $e^{ikx\pm\nu y}$, where

$$\gamma^2 = k^2 + s^2/\alpha^2, \qquad \text{and} \qquad \nu^2 = k^2 + s^2/\beta^2.$$

The boundary condition for $u(x, +0, s)$ can be obtained by taking the Laplace transform of (10.66):

$$u(x, +0, s) = -u(x, -0, s) = \frac{\Delta u}{2}\frac{e^{-sx/v}}{s}H(x) = \frac{\Delta u}{4\pi s}\int_{-\infty}^{\infty}\frac{e^{ikx}\, dk}{i(k - is/v)}. \tag{10.67}$$

This condition and the vanishing τ_{yy} at $y = 0$ determine the solution for $y > 0$ as

$$u(x, y, s) = -\frac{\Delta u}{2\pi}\int_{-\infty}^{\infty}\left(\frac{\beta^2k^2}{s^2}e^{-\gamma y} - \frac{2\beta^2k^2 + s^2}{2s^2}e^{-\nu y}\right)\frac{e^{ikx}\, dk}{i(k - is/v)}$$

$$v(x, y, s) = -\frac{\Delta u}{2\pi}\int_{-\infty}^{\infty}\left[\frac{\beta^2}{s^2}ik\gamma e^{-\gamma y} - \frac{(2\beta^2k^2 + s^2)}{2\nu s^2}ike^{-\nu y}\right]\frac{e^{ikx}\, dk}{i(k - is/v)}.$$

To each term of the above integral, we can apply Cagniard's method. By transforming the variable k to either

$$\tau = \frac{1}{s}(-ikx + \gamma y) \qquad \text{or} \qquad \tau = \frac{1}{s}(-ikx + \nu y)$$

and identifying the resulting integral as a Laplace transform, we obtain

$$\frac{\partial u(x, y, t)}{\partial t} = \frac{\beta^2\,\Delta u}{\pi}\left\{\mathrm{Im}\left[\frac{p_1^2\left(t\sin\theta + i\cos\theta\sqrt{t^2 - r^2/\alpha^2}\right)}{i/v - p_1}\right]\frac{H(t - r/\alpha)}{r\sqrt{t^2 - r^2/\alpha^2}}\right.$$

$$\left. -\mathrm{Im}\left[\frac{(p_2^2 + 1/2\beta^2)\left(t\sin\theta + i\cos\theta\sqrt{t^2 - r^2/\beta^2}\right)}{i/v - p_2}\right]\frac{H(t - r/\beta)}{r\sqrt{t^2 - r^2/\beta^2}}\right\} \tag{10.68}$$

$$\frac{\partial v(x, y, t)}{\partial t} = \frac{\beta^2\,\Delta u}{\pi}\left\{\mathrm{Re}\left[\frac{(p_1^2 + 1/\alpha^2)\,p_1}{i/v - p_1}\right]\frac{H(t - r/\alpha)}{\sqrt{t^2 - r^2/\alpha^2}}\right.$$

$$\left. -\mathrm{Re}\left[\frac{(p_2^2 + 1/2\beta^2)\,p_2}{i/v - p_2}\right]\frac{H(t - r/\beta)}{\sqrt{t^2 - r^2/\beta^2}}\right\},$$

where $(x, y) = r(\cos\theta, \sin\theta)$, and

$$p_1 = \frac{1}{r}\sqrt{t^2 - \frac{r^2}{\alpha^2}}\ \sin\theta + i\frac{t}{r}\cos\theta, \qquad p_2 = \frac{1}{r}\sqrt{t^2 - \frac{r^2}{\beta^2}}\ \sin\theta + i\frac{t}{r}\cos\theta.$$

The above formulas were obtained by Ang and Williams (1959) and were used by Boore and Zoback (1974) in the interpretation of accelerograms recorded at Pacoima Dam during the San Fernando earthquake of 1971 February 9.

For points that are distant from where the faulting originates, the motion near the fault should look like the one obtained earlier in equations (10.63). Actually, if we make both y/r $(= \sin\theta)$ and $r - vt$ small, equations (10.68) reduce to (10.63). That is, the near-field motion at the time of arrival of the rupture front is approximately explained by the simple forms given in (10.63).

Equation (10.68) contains additional arrivals propagating as P- and S-waves from the starting point of rupture. Making $t - r/\alpha$ small, we find P-waves of the form

$$\begin{matrix}\frac{\partial u}{\partial t} \\ \frac{\partial v}{\partial t}\end{matrix} = \begin{matrix}\cos\theta \\ \sin\theta\end{matrix} \times \frac{\Delta u}{\pi}\frac{\beta^2}{\alpha^2}\frac{\sin 2\theta}{2(\alpha/v - \cos\theta)}\frac{H(t - r/\alpha)}{\sqrt{t - r/\alpha}\sqrt{2r/\alpha}}, \tag{10.69}$$

and making $t - r/\beta$ small, we find S-waves of the form

$$\begin{matrix}\frac{\partial u}{\partial t} \\ \frac{\partial v}{\partial t}\end{matrix} = \begin{matrix}-\sin\theta \\ \cos\theta\end{matrix} \times \frac{\Delta u}{\pi}\frac{\cos 2\theta}{2(\beta/v - \cos\theta)}\frac{H(t - r/\beta)}{\sqrt{t - r/\beta}\sqrt{2r/\beta}}. \tag{10.70}$$

As shown schematically in Figure 10.20, the radiation patterns of these waves have a double-couple symmetry modified by the factor $(\alpha/v - \cos\theta)^{-1}$ for P and $(\beta/v - \cos\theta)^{-1}$ for S. They are cylindrical waves, attenuating as $1/\sqrt{r}$. As in the case of the anti-plane solution, the particle velocity has a square-root singularity at the onset. The accelerations associated with these "starting phases" are also unbounded at the onset, where they have 3/2 power singularities. If the slip function is a ramp function, the peak particle velocity will be finite, but the peak acceleration will have a square-root singularity at the onset.

As discussed in the preceding section, the effect from stopping of the fault propagation can be obtained by superposing another moving dislocation. The stopping phases are similar to the starting phases in the case of unidirectional fault propagation.

For the Haskell model with a uniform slip function over a rectangular fault, Madariaga (1978) obtained an exact analytic solution for motions at any point in an unbounded, elastic, homogeneous medium. The solution consists of (i) cylindrical waves from the suddenly appearing initial dislocation line of length W and from the sudden arrest of rupture, and (ii) spherical waves radiated from the corners of the rectangular fault. The cylindrical waves dominate in the regions of a slab normal to the dislocation line containing the fault plane, and have the same characteristics as the cylindrical waves from the moving dislocation line given in equations (10.54), (10.69), and (10.70).

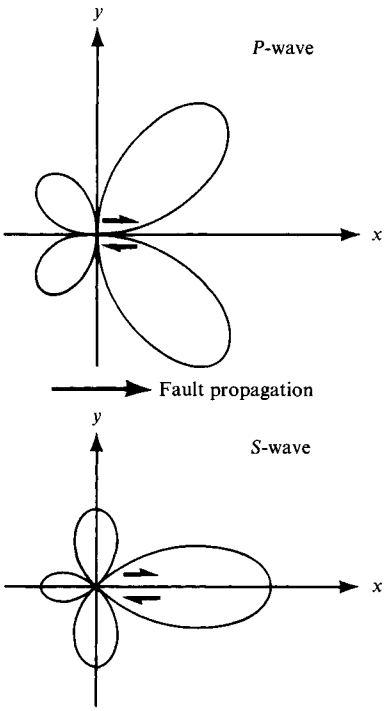

FIGURE **10.20**
Radiation patterns for the body waves radiating from the point of nucleation of a propagating in-plane shear fault. Compare with the usual double-couple radiation patterns (Figs. 4.5a and 4.6b).

Suggestions for Further Reading

Aki, K. Earthquake mechanism. *Tectonophysics*, **13**, 423–446, 1972.

Boatwright, J. The seismic radiation from composite models of faulting. *Bulletin of the Seismological Society of America*, **78**, 489–508, 1988.

Brune, J. N. Seismic source dynamics. *Reviews of Geophysics, Supplement*, **29**, 688–699, 1991.

Haskell, N. Total energy and energy spectral density of elastic wave radiation from propagating faults. *Bulletin of the Seismological Society of America*, **54**, 1811–1842, 1964; **56**, 125–140, 1966.

Heaton, T. H. Evidence for and implications of self-healing pulses of slip in earthquake rupture. *Physics of the Earth and Planetary Interiors*, **64**, 1–20, 1990.

Honda, H. Earthquake mechanism and seismic waves. *Journal of Physics of the Earth*, **10**, 1–98, 1962.

Jeffreys, H. On the mechanics of faulting. *Geological Magazine*, **79**, 291–295, 1942.

Kanamori, H. Great earthquakes at island arcs and the lithosphere. *Tectonophysics*, **12**, 187–198, 1971.

Kanamori, H. Mechanics of earthquakes. *Annual Reviews of Earth and Planetary Sciences*, **22**, 207–237, 1994.

Kanamori, H., and D. L. Anderson. Theoretical basis of some empirical relations in seismology. *Bulletin of the Seismological Society of America*, **65**, 1073–1095, 1975.

Mansinha, L., D. E. Smylie, and A. E. Beck, eds. *Earthquake Displacement Fields and the Rotation of the Earth*. New York: Springer-Verlag, 1970.

Olsen, K. B., and R. J. Archuleta. Three-dimensional simulation of earthquakes on the Los Angeles fault system. *Bulletin of the Seismological Society of America*, **86**, 575–596, 1996.

Savage, J. C. Corner frequency and fault dimensions. *Journal of Geophysical Research*, **77**, 3788–3795, 1972.

Scholz, C. H. *The Mechanics of Earthquakes and Faulting*. Cambridge University Press, 1990.

Sato, T. Seismic radiation from circular cracks growing at variable rupture velocity. *Bulletin of the Seismological Society of America*, **84**, 1199–1215, 1994.

Stevens, J. L., and S. M. Day. The physical basis of m_b: M_s and variable frequency magnitude methods for earthquake/explosion discrimination. *Journal of Geophysical Research*, **90**, 3009–3020, 1985.

Trifunac, M. D. A three-dimensional dislocation model for the San Fernando, California, earthquake of February 9, 1971. *Bulletin of the Seismological Society of America*, **64**, 149–172, 1974.

Weertman, J. Dislocations in uniform motion on slip or climb planes having periodic force laws. In *Mathematical Theory of Dislocations*, edited by T. Mura. New York: American Society of Mechanical Engineers, 1969.

Problems

10.1 One of the most powerful methods for discriminating an underground nuclear explosion from an earthquake is based on the excitation of short-period P-waves relative to long-period surface waves. If we take an explosion and a shallow earthquake that generate comparable P-waves with period around 1 s, it is observed that the Rayleigh waves generated by the explosion are an order of magnitude smaller (with period around 20 s) than those generated by the earthquake. Assume a double-couple point source for the earthquake and a point source with isotropic moment tensor for the explosion, both buried in a homogeneous half-space. Find out if the difference in source type and focal depth (the depth of an explosion cannot be greater than a few kilometers) can cause an order of magnitude difference in Rayleigh vs. P-wave excitation. If not, what other effects can account for this observation?

10.2 Some important symmetry properties for the radiation from general shear faulting on a plane surface within an infinite, homogeneous, isotropic medium can be inferred from (10.39). For shear faulting in the plane $x_3 = 0$, show that displacement components *parallel* to the fault plane are *odd* functions of distance x_3 from the fault and that the displacement *normal* to the fault is an *even* function of x_3. Hence, for traction on planes parallel to Σ at distance x_3, show that the normal component is an odd function of x_3 and that the shear components are even. Finally, show that the normal component of traction on a planar fault (in an infinite, homogeneous, isotropic medium) cannot be changed by any shearing event on the fault.

10.3 Equation (10.41) amounts to a dynamic boundary condition for tractions on the fault plane. Where do we take this condition into account in setting up a representation of the solution, such as (10.39)? Verify that this representation of the radiated field does indeed have continuity of shear stress across the fault (use results of Problem 10.2).

10.4 The opening of a crack may be represented by a displacement discontinuity $[\mathbf{u}]$ that is parallel to ν, the fault normal. Obtain the equivalent body force in an isotropic elastic body, and find the far-field body waves (P and S) in an infinite homogeneous medium (cf. equation (10.6)).

10.5 Show that the source spectrum for a faulting episode, derived from the far-field displacement as discussed in Section 10.1.4 in the limit of low frequencies, is flat at the origin ($\omega = 0$). (This result is true, whether the spectrum has a maximum at the origin, or whether there is overshoot.)

10.6 Under the assumptions of shear faulting on a plane, and slip everywhere in the same direction, we have seen that the far-field pulse shape is given by (10.13) provided fault length L, wavelength λ, and source–receiver distance r_0 satisfy the constraint $L^2 \ll \frac{1}{2}\lambda r_0$. Far-field pulse shapes for P-waves and S-waves radiate out to every direction on the focal sphere. Suppose that the pulse shape $\Omega(t)$ is radiated as a P-wave in some direction $\boldsymbol{\gamma}^P$.

a) Show that it is always possible to find a direction $\boldsymbol{\gamma}^S$ in which this same pulse shape $\Omega(t)$ is radiated as an S-wave (though the arrival time will be different, and note that we are neglecting the effects of different attenuation between P- and S-waves).

b) Show that the relationship between $\boldsymbol{\gamma}^P$ and $\boldsymbol{\gamma}^S$ is similar to Snell's law (5.20) governing the angles i and j of P- and S-waves coupled at a plane surface.

c) Given an S-wave pulse shape observed in direction $\boldsymbol{\gamma}^S$, show that it is *not* always possible to find a direction in which this same pulse shape is observed as a P-wave.

10.7 The "finiteness factor" $X^{-1} \sin X$ that appears in equations (10.20)–(10.22) is very simple, because (i) the rupture is unilateral (i.e., it proceeds from one end of the fault to the other); (ii) it has constant rupture velocity; (iii) the fault width W is very small; and (iv) the slip function at each point of the fault plane is the same, apart from a delay due to the time taken for rupture to initiate.

a) Suppose that we drop assumptions (i), (ii), and (iii), but retain (iv). Show that the far-field pulse shape is then given by

$$\Omega(\mathbf{x}, \omega) = \Omega_0(\mathbf{x}, \omega) F(\boldsymbol{\gamma}, \omega),$$

where $\Omega_0(\mathbf{x}, \omega)$ is the pulse shape radiated by a point shear dislocation of strength $A \times \Delta u(\omega)$, and the finiteness factor in this more general case is

$$F(\boldsymbol{\gamma}, \omega) = \frac{1}{A} \iint_{\Sigma} \exp\, i\omega \left[\tau(\xi) - \frac{\xi \cdot \boldsymbol{\gamma}}{c} \right] d\Sigma.$$

Here A is the fault area, $\tau(\boldsymbol{\xi})$ is the time taken for the rupture to reach $\boldsymbol{\xi}$ on the fault plane, and $\boldsymbol{\gamma}$ is the ray direction from source to receiver.

b) In the time domain, show that $\Omega(\mathbf{x}, t)$ is given by convolving $\Omega_0(\mathbf{x}, t)$ with a pulse shape having unit "area," i.e., show that $\int_{-\infty}^{\infty} F(\boldsymbol{\gamma}, t)\, dt = 1$.

c) Now drop assumption (iv) also, and show that the corresponding finiteness factor is

$$F(\boldsymbol{\gamma}, \omega) = \frac{1}{M_0(\omega)} \iint_{\Sigma} \mu(\boldsymbol{\xi})\, \Delta u(\boldsymbol{\xi}, \omega) \exp i\omega \left[\frac{-\boldsymbol{\xi} \cdot \boldsymbol{\gamma}}{c}\right] d\Sigma,$$

where $M_0(\omega) = \iint \mu(\boldsymbol{\xi}) \Delta u(\boldsymbol{\xi}, \omega)\, d\Sigma$. Show that this more general finiteness factor also has unit area in the time domain.

CHAPTER 11

The Seismic Source: Dynamics

Seismic waves propagate in ways that are largely governed by the relationship $\rho \ddot{u}_i = \tau_{ji,j}$ between acceleration and stress gradient, and by the relationship between stress and strain known as Hooke's law (2.18). But in the source region of a particular earthquake, Hooke's law fails. If we are to reach a quantitative understanding of the ground motions that result from that earthquake, we need to replace Hooke's law by some other relationship that accurately determines stress as a function of the deformation of materials within the source region—or, that determines deformation as a function of stress.

So far we have suppressed the difficulties of this problem, because to interpret the seismograms from one particular earthquake in detail, within the framework of Green functions weighted by a displacement discontinuity across a fault surface, we saw in Section 2.5 and Chapter 3 that we all we need to know is the fault slip as a function of space and time on the fault. See equation (3.2), with which we started Chapter 10 on source kinematics, allowing us to study the seismic motion at near and far field for a propagating dislocation in cases where the slip function has already been specified—or at least parameterized in a particular way. The form of the slip function was adopted intuitively to simulate geologic faulting with the least number of parameters, preferably ones that could be determined from analysis of the resulting seismic radiation. But unfortunately, some of the slip functions analyzed in Chapter 10 turn out to have consequences that are physically unacceptable.

Take the simplest case of an anti-plane problem in which a semi-infinite fault is propagating with uniform velocity (Section 10.2.3). When the slip occurs as a step function, the shear stress acting on the fault plane is given by equation (10.46),

$$\tau_{yz} = \mu \frac{\Delta w}{2\pi} \frac{\sqrt{1 - v^2/\beta^2}}{x'} \qquad (\text{putting } x' = x - vt). \tag{11.1}$$

We expect that the fault plane, once ruptured, cannot sustain stress greater than the frictional stress. But according to (11.1), the shear stress has nonzero values inside the fault plane ($x' < 0$), becoming larger and larger without limit on the fault plane as the crack tip is approached (i.e., as $x' \to 0$ from below). Obviously, then, the assumption of step-function slip leads to a gross violation of physical expectation. In this chapter we shall develop a

variety of better alternatives to step-function slip, with the principal aim of finding fault motions that not only are kinematically satisfactory for shear failure, but are also associated with plausible stresses on the fault plane.

In considering the failure of Hooke's law for a particular earthquake, we can regard the fault plane—which will eventually rupture—as a surface of weakness. For example, as stress slowly rises in the source region due to tectonic processes, we may assume that the capacity of frictional stress to resist the growing shearing stress is eventually exceeded. It is the pre-existing fault surface that fails rather than another surface, precisely because the fault is relatively weak. But how does the failure actually take place? As stress rises during the tectonic loading process over a period of perhaps decades, does strain generally stay proportional to stress, or is there a tendency for some ductility (in which strain rate would be nonzero at fixed high stress, even if the stress were constant)? Even if there is no ductility, does strain stay proportional to stress right up to the instant of failure, or do materials in the source region exhibit a nucleation process in which strain departs slightly from the linearity predicted by Hooke's law, just prior to failure? If there is a nucleation process, then what is its time scale and its dependence on stress relative to a critical stress? If failure occurs and stress levels on the fault surface drop from their static frictional values as fault slip begins, then how quickly do they drop, what is the value of frictional resistance during the actual process of fault slip, and how do stress levels continue to change as fault slip comes to a halt?

These questions on material properties have long been the subject of laboratory experiment. Many observations are summarized by Coulomb's law of friction, stating that frictional resistance to one object sliding over another is proportional to the net force bringing the two objects into contact. The expression of Coulomb's law in seismology is that the frictional shearing stress between the two faces of a fault surface is proportional to the normal stress. As reviewed by Scholz (1998), in the standard model of stick-slip friction it is assumed that sliding begins when the ratio of shear stress to normal stress reaches a value μ_s, called the static friction coefficient. Once sliding begins, frictional resistance falls to a lower value so that the coefficient of dynamic friction, μ_d, is less than μ_s. An instability can result, leading to slip propagation and all the phenomena of fault rupture and associated radiation of seismic waves.

It has been found experimentally that μ_s is greater the longer the fault surfaces have been in contact without sliding. Furthermore, the value of μ_d depends on the relative velocity with which the fault surface slides. The general subject of fault constitutive laws has been developed extensively by Dieterich and others (see Dieterich, 1981; Ruina, 1983; Sleep, 1987, Marone, 1998; and Dieterich and Kilgore, 1996). As we shall see in considering particular examples, there is often a question as to whether the details of some particular relationship between fault slip and fault stress can be inferred from properties of the resulting seismic waves, or whether these details entail time scales and length scales too short to measure from the radiated signals. In the latter case, progress will more likely come from extrapolation of phenomena measured in the laboratory—over scales on the order of a meter or much less—up to scales on the order of a kilometer or much more, as needed in application to earthquakes of significant size.

This chapter studies simple models of dynamic faulting in two main sections, followed by a shorter section that outline features of more complicated models. Thus in Section 11.1 we shall suppose that the rupture velocity has been prescribed (usually, we shall assume

it has some constant value). We obtain a simple relation between slip and shear stress on a fault plane for anti-plane problems. Then we describe the energy balance at the rupture front for anti-plane and in-plane faulting, and introduce the concept of cohesive force. As a useful illustration of rupture propagation that originates from a point (and therefore involves both anti-plane and in-plane motions), we look at the case of a growing elliptical fault, for which the radiated motions are known in detail. As an example of a fault that grows steadily (from a point) and then suddenly stops, we describe a growing circular fault with known final radius and use an important numerical procedure to obtain the far-field motions. In the second main section, we recognize that shear failure is a spontaneous process and that the velocity of rupture is itself an unknown and probably varying quantity, to be determined as part of the solution to the problem in hand. The rupture-velocity history is known for a variety of anti-plane problems and for certain in-plane problems. Our intent in these Sections 11.1 and 11.2 is to develop analytical methods that provide ways to explore a variety of relationships between fault stress and fault slip or slip velocity.

In consideration of the dynamics of a particular earthquake, it is vastly simplifying to restrict attention to situations in which normal stress is unchanged by the faulting process. But as we point out in Section 11.3, there are a number of important situations in which normal stress is itself changed by faulting.

11.1 Dynamics of a Crack Propagating with Prescribed Velocity

11.1.1 RELATIONS BETWEEN STRESS AND SLIP FOR A PROPAGATING CRACK

In order to find an appropriate slip function for a crack propagating with a constant velocity v, we shall first find a relationship between the stress and slip on the fault plane for a propagating anti-plane dislocation.

Let the slip function $\Delta w(x')$ be an arbitrary function. We shall express $\Delta w(x')$ by a superposition of step functions, as shown in Figure 11.1. An arbitrary $\Delta w(x')$ can be written as

$$\Delta w(x') = -\int_{x'}^{0} \frac{\partial\, \Delta w}{\partial \xi}\, d\xi = -\int_{-\infty}^{0} \frac{\partial\, \Delta w}{\partial \xi} H(\xi - x')\, d\xi. \tag{11.2}$$

The step-function slip $H(\xi - x')$ with tip at $x' = \xi$ will generate a stress component τ_{yz} according to equation (11.1) given by

$$\tau_{yz}(x', \xi) = \frac{\mu}{2\pi} \cdot \frac{\sqrt{1 - v^2/\beta^2}}{x' - \xi}.$$

Multiplying by the step height $-(\partial\, \Delta w/\partial \xi)\, d\xi$ and integrating over ξ from $-\infty$ to 0, we find that the stress due to the slip function $\Delta w(x')$ is

$$\tau_{yz}(x') = -\frac{\mu}{2\pi}\sqrt{1 - v^2/\beta^2} \int_{-\infty}^{0} \frac{\partial\, \Delta w/\partial \xi}{x' - \xi}\, d\xi = -\frac{\mu}{2\pi} \frac{\sqrt{1 - v^2/\beta^2}}{v} \int_{-\infty}^{0} \frac{\Delta \dot{w}}{\xi - x'}\, d\xi, \tag{11.3}$$

where $\Delta \dot{w}$ is the slip velocity.

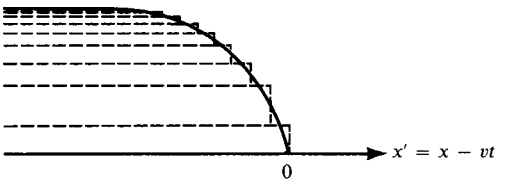

FIGURE **11.1**
Approximating an arbitrary slip function $\Delta w(x')$ by a superposition of step functions.

For the in-plane problem, a similar relation is found between the shear stress τ_{xy} on the fault plane and slip velocity $\Delta\dot{w}$. Applying the same superposition to equation (10.65), we get

$$\tau_{xy}(x') = -\frac{2\mu\beta^2}{\pi v^3}\left[\sqrt{1-v^2/\alpha^2} - \frac{(1-v^2/2\beta^2)^2}{\sqrt{1-v^2/\beta^2}}\right]\int_{-\infty}^{0}\frac{\Delta\dot{u}}{\xi - x'}d\xi. \qquad (11.4)$$

In both (11.3) and (11.4), we see that the shear stress on the fault plane is a constant times the Hilbert transform of slip velocity.

A function and its Hilbert transform are very closely related. From Box 5.6, we see that if $g(x)$ is the Hilbert transform of a function $f(x)$, then these two function share a common amplitude spectral density, and their spectral phases differ by $\pi/2$.

Thus the shear stress and the slip velocity on the plane $y = 0$ must share a common amplitude spectral density apart from a constant factor, with a phase difference of $\pi/2$. Furthermore, the slip velocity must be zero outside the crack (because no slip occurs there yet), and the shear stress must be zero inside the crack (assuming no frictional stress for simplicity). In other words, we want to find a pair of functions $f(x)$ and $g(x)$ that satisfy

$$f(x) = 0 \text{ if } x > 0, \qquad g(x) = 0 \text{ if } x < 0, \qquad \text{and} \qquad g(x) = \frac{1}{\pi}\int_{-\infty}^{\infty}\frac{f(\xi)}{\xi - x}d\xi. \qquad (11.5)$$

From tables of Hilbert transforms, we find that the following choices of $f(x)$ and $g(x)$ satisfy these three conditions:

$$f(x) = \frac{H(-x)}{\sqrt{-x}} \qquad \text{and} \qquad g(x) = \frac{-H(x)}{\sqrt{x}}.$$

It is easy to show that they satisfy the integral in equation (11.5) by extending ξ to a complex plane and making a branch cut along the negative real axis (Fig. 11.2). The integral along AO will be equal to the one along OB because of the opposite signs of $\sqrt{-\xi}$ on the two paths. For $x > 0$, the residue evaluation of $\xi = x$ gives $g(x) = 1/\sqrt{x}$, and for $x < 0$ the integral vanishes because the pole is outside the contour.

Thus we find for our mechanics problem that the boundary conditions for a moving crack are satisfied by a square-root singularity in stress ahead of the crack tip, and another square-root singularity in slip velocity behind the crack tip. The square-root singularity in stress is well known for a static crack.

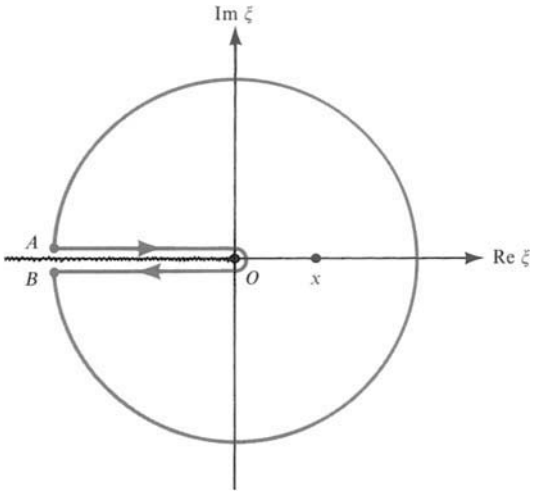

FIGURE **11.2**
Integration path for (11.5) when $f(\xi) = H(-\xi)\sqrt{-\xi}$.

By integrating the slip velocity, we find that the slip itself is proportional to $\sqrt{-x'}$ for $x' < 0$. We can now summarize results for the anti-plane case as

$$\Delta w = A\sqrt{-x'}H(-x'), \qquad \Delta \dot{w} = \frac{Av}{2\sqrt{-x'}}H(-x'), \qquad \text{and} \qquad \tau_{yz} = \frac{K}{\sqrt{2\pi x'}}H(x'), \tag{11.6}$$

where

$$K = \sqrt{2\pi}\,\frac{\mu A\sqrt{1 - v^2/\beta^2}}{4},$$

and the in-plane case as

$$\Delta u = A'\sqrt{-x'}H(-x'), \qquad \Delta \dot{u} = \frac{A'v}{2\sqrt{-x'}}H(-x'), \qquad \text{and} \qquad \tau_{xy} = \frac{K'}{\sqrt{2\pi x'}}H(x'), \tag{11.7}$$

where

$$K' = \sqrt{2\pi}\,\frac{\mu A'\beta^2\left[\sqrt{1 - v^2/\alpha^2} - (1 - v^2/2\beta^2)^2/\sqrt{1 - v^2/\beta^2}\right]}{v^2}.$$

The coefficients K and K' are called *stress-intensity factors* in fracture mechanics.

Note that K is zero for $v = \beta$. And since

$$K' = -\tfrac{1}{4}\sqrt{2\pi}\mu A'\beta^2 v^2 \mathsf{R}(1/v)/\sqrt{1 - v^2\beta^2},$$

where R is the Rayleigh function introduced in (5.56), we find that the stress singularity ahead of the in-plane crack is zero for rupture speed $v = c_R$, the Rayleigh wave speed.

In the preceding chapter, we studied seismic motion from a propagating dislocation with step-function slip. Now that we have found a more appropriate slip function for the

BOX 11.1

Stress singularities for static, in-plane, and anti-plane shear cracks of finite width 2a.

The equilibrium equation for the anti-plane displacement $w(x, y)$ is given by

$$\frac{\partial^2 w}{\partial x^2} + \frac{\partial^2 w}{\partial y^2} = 0. \tag{1}$$

For a crack plane defined by $|x| < a$, $y = 0$, and a uniform stress τ_∞ acting at $x \to \infty$ and $y \to \infty$, the boundary conditions for a stress-free crack are

$$\frac{\partial w}{\partial y} = 0 \qquad |x| < a, y = 0, \tag{2}$$

and

$$w \to \frac{\tau_\infty}{\mu} y \qquad \text{as } x, y \to \infty. \tag{3}$$

(The reference state for displacement is here taken as the stress-free state, in contrast with many of the dynamic solutions in this chapter and the previous one, where the reference state is the static strained state just prior to crack growth.)

Equation (1) can be satisfied by the real or imaginary part of an analytic function of $z = x + iy$. It is easy to show that the imaginary part of

$$f(x + iy) = \frac{\tau_\infty}{\mu}\sqrt{(x + iy)^2 - a^2} \tag{4}$$

satisfies equations (1), (2), and (3). So

$$\begin{aligned} w &= \text{Im } f(x + iy) \\ &= \frac{\tau_\infty}{\mu}\text{Im}\{[(x^2 - y^2 - a^2)^2 + 4x^2y^2]^{1/4} e^{i\theta/2}\}, \end{aligned} \tag{5}$$

where $\sin\theta = 2xy \Big/ \sqrt{(x^2 - y^2 - a^2)^2 + 4x^2y^2}$. We then have

$$\begin{aligned} w &= \frac{\tau_\infty}{\mu}\sqrt{a^2 - x^2} \qquad y = +0, |x| < a \\ &= -\frac{\tau_\infty}{\mu}\sqrt{a^2 - x^2} \qquad y = -0, |x| < a. \end{aligned} \tag{6}$$

The stress on the plane $y = 0$, but outside of the crack, is

$$\mu \frac{\partial w}{\partial y}\bigg|_{y=0} = \tau_\infty \frac{x}{\sqrt{x^2 - a^2}} \qquad |x| > a. \tag{7}$$

Here we find the square-root singularity of stress at both ends of the crack $x = a$. The stress intensity factor is $\tau_\infty\sqrt{\pi a}$, and grows in proportion to the square root of the crack

(continued)

BOX **11.1** *(continued)*

length a. The above solution was given by Knopoff (1958). A solution for an in-plane shear crack was given by Starr (1928), with the following results:

$$\begin{aligned} u &= \frac{\tau_\infty}{2}\frac{\lambda+2\mu}{\mu(\lambda+\mu)}\sqrt{a^2-x^2} \qquad y=+0,\ |x|<a \\ &= -\frac{\tau_\infty}{2}\frac{\lambda+2\mu}{\mu(\lambda+\mu)}\sqrt{a^2-x^2} \qquad y=-0,\ |x|<a \end{aligned} \tag{8}$$

and

$$\tau_{xy} = \tau_\infty \frac{x}{\sqrt{x^2-a^2}} \qquad y=0,\ |x|>a. \tag{9}$$

crack in the form $\sqrt{-x'}\,H(-x')$ (instead of $H(-x')$), we shall re-examine the motion in the vicinity of the fault. Using equation (11.2), we can express the slip function for the moving crack as a superposition of step functions:

$$A\sqrt{-x'}H(-x') = \frac{A}{2}\int_{-\infty}^{0}\frac{1}{\sqrt{-\xi}}H(\xi-x')\,d\xi.$$

Since our system is linear, if the seismic motion corresponding to unit step-function slip $H(-x')$ was $f(x', y)$, then the motion $g(x', y)$ for the moving crack will be

$$g(x', y) = \frac{A}{2}\int_{-\infty}^{0}\frac{1}{\sqrt{-\xi}}f(x'-\xi, y)\,d\xi. \tag{11.8}$$

Using this relation, we can obtain the motion and stress around the tip of the anti-plane crack from the results previously obtained for a step-function dislocation. Putting equations (10.47) and (10.45) into $f(x', y)$ of equation (11.8), the particle velocity $\dot{w}$ and stress component τ_{yz} for the moving crack can be written as

$$\dot{w} = \frac{Av}{4\pi}\int_{-\infty}^{0}\frac{1}{\sqrt{-\xi}}\frac{\gamma y\,d\xi}{(x'-\xi)^2+\gamma^2y^2} \quad \text{and} \quad \tau_{yz} = \frac{A\mu}{4\pi}\int_{-\infty}^{0}\frac{1}{\sqrt{-\xi}}\frac{\gamma(x'-\xi)\,d\xi}{(x'-\xi)^2+\gamma^2y^2}$$

where $\gamma = \sqrt{1-v^2/\beta^2}$. Both integrals can be evaluated easily by using the contour shown in Figure 11.2. Now poles are located at $\xi = x' \pm i\gamma y$, and the evaluation of residues at these poles gives

$$\dot{w} = \frac{Av}{4}\left(\frac{1}{2i\sqrt{x'-i\gamma y}} - \frac{1}{2i\sqrt{x'+i\gamma y}}\right) = \frac{Av}{4\sqrt{2}}\frac{\sqrt{\sqrt{x'^2+\gamma^2y^2}-x'}}{\sqrt{x'^2+\gamma^2y^2}}, \tag{11.9}$$

$$\tau_{yz} = \frac{A\mu\gamma}{4}\left(\frac{1}{2\sqrt{x'+i\gamma y}} + \frac{1}{2\sqrt{x'-i\gamma y}}\right) = \frac{A\mu\gamma}{4\sqrt{2}}\frac{\sqrt{\sqrt{x'^2+\gamma^2y^2}+x'}}{\sqrt{x'^2+\gamma^2y^2}}. \tag{11.10}$$

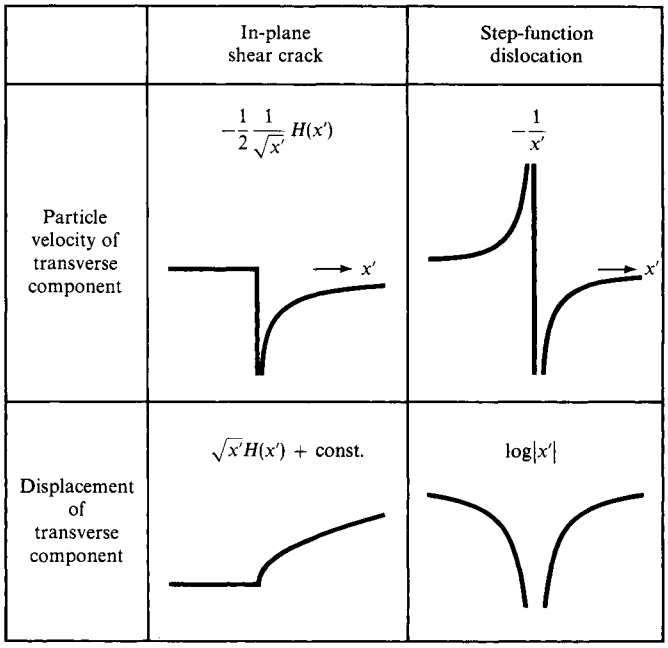

FIGURE **11.3**
Particle velocity and displacement normal to the fault plane for a shear crack and for a step-function shear dislocation.

In contrast to the case of a step-function dislocation, the peak amplitude of particle velocity decays with distance from the fault as $1/\sqrt{y}$. The motion for the crack is smoother than for a dislocation. Before discussing the difference in their spectra, we shall point out a drastic difference in the transverse component of particle motion between the in-plane crack and the in-plane step-function dislocation ("transverse" here means "perpendicular to the fault plane").

The transverse component of particle velocity for the in-plane step-function dislocation (corresponding to $\dot{v}(x,0,t)$ in (10.63)) is of the form $f(x',y) = 1/x'$ along $y = 0$. Using (11.8), the corresponding solution for the crack is (see Fig. 11.3)

$$g(x',0) = \frac{1}{2}\int_{-\infty}^{0} \frac{1}{\sqrt{-\xi}}\frac{d\xi}{x'-\xi} = -\frac{1}{2}\frac{1}{\sqrt{x'}} \qquad x' > 0$$
$$= 0 \qquad x' < 0,$$

which has the same form as the shear stress τ_{xy} of the in-plane crack obtained earlier. Remarkably, the transverse component of particle velocity is zero inside the crack. The corresponding displacement will then be constant inside the crack, and of the form $\sqrt{x'}$ ahead of the crack. In the case of step-function slip, the transverse component of displacement shows a symmetric impulsive form ($\sim \log|x'|$), as can be seen in Figure 11.3, which qualitatively agrees with the observed form for the Parkfield earthquake, as discussed in Section 10.2.1. The solution for the crack, on the other hand, does not show the symmetric impulsive form, but an asymmetric step-like form, $\sqrt{x'}\,H(x')$ + constant, as shown in Figure 11.3.

Equation (11.8) shows that $g(x, y)$ is the convolution of $f(x, y)$ with $\frac{1}{2}H(-x)/\sqrt{-x}$. For $k = \omega p > 0$, the Fourier transform of the latter function can be obtained as

$$\begin{aligned}
\frac{1}{2}\int_{-\infty}^{0} \frac{1}{\sqrt{-x}} e^{-ikx}\, dx &= \frac{1}{2}\int_{-i\infty}^{0} \frac{1}{\sqrt{-x}} e^{-ikx}\, dx && \text{(changing the path to the negative imaginary } x\text{-axis)} \\
&= \tfrac{1}{2} e^{i\pi/4} \int_0^{\infty} \frac{1}{\sqrt{y}} e^{-ky}\, dy && \text{(putting } x = -iy\text{)} \\
&= e^{i\pi/4} \int_0^{\infty} e^{-kz^2}\, dz && \text{(putting } y = z^2\text{)} \\
&= \frac{1}{2}\sqrt{\frac{\pi}{k}}\, e^{i\pi/4} = \frac{1}{2}\sqrt{\frac{\pi}{\omega p}}\, e^{i\pi/4}.
\end{aligned}$$

In the frequency domain, therefore, $g(x, y)$ (the seismic motion caused by a propagating semi-infinite crack) has an amplitude spectrum proportional to $1/\sqrt{\omega}$ times the spectrum of $f(x, y)$ (the seismic motion caused by a propagating dislocation with step-function slip), and the phase is shifted by $\pi/4$. This phase shift in the x-coordinate corresponds to a delay of $\pi/4$ in the time axis. Because the $1/\sqrt{\omega}$ factor will attenuate higher frequencies, the motion caused by the propagating crack is smoother than the motion caused by the propagating dislocation with step-function slip.

11.1.2 ENERGETICS AT THE CRACK TIP

As the crack tip propagates, slip occurs across the fault plane. Neglecting friction, the traction on the fault plane is zero over the part where slip is occurring. It seems, therefore, that there is no work done on a crack except for the work against friction. A closer look, however, reveals that a finite amount of work is indeed done at the crack tip per unit distance of its propagation. Since the crack tip is moving, it is not obvious how to calculate this work. Let us first derive a general formula for two-dimensional cracks following Freund (1972). To obtain compact equations we shall use x_i $(i = 1, 2, 3)$ coordinates, put the crack plane at $x_2 = 0$, and let its tip propagate toward the $+x_1$-direction with velocity v. As shown in Figure 11.4, we consider an external surface S_e fixed to the solid body, with the crack surface S_c already formed and an internal surface S_t enclosing and traveling with the crack tip.

In the volume V bounded by these three surfaces, the body obeys the equation of motion, Hooke's law, and strain–displacement relations:

$$\rho \ddot{u}_i = \tau_{ij,j}, \qquad \tau_{ij} = c_{ijkl} e_{kl}, \tag{11.11}$$

$$e_{ij} = \tfrac{1}{2}(u_{i,j} + u_{j,i}), \tag{11.12}$$

where c_{ijkl}, τ_{ij}, e_{ij}, and u_i are the elastic moduli and components of stress, strain, and displacement. We assume that body forces are absent.

On the surfaces S_e and S_t, traction T_i is given as $T_i = \tau_{ij} n_j$, where n_j is the outward normal of the surface of V.

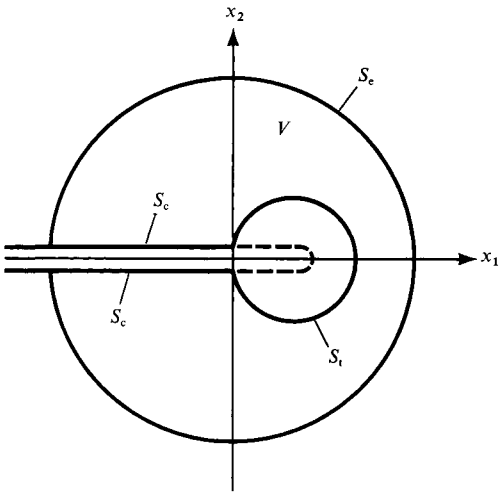

FIGURE **11.4**

The rate of work of the tractions on S_e, and the rates of increase of kinetic energy and strain energy in V, are, respectively,

$$\dot{W} = \int_{S_e} T_i \dot{u}_i \, dS, \qquad \dot{K} = \frac{d}{dt} \int_V \tfrac{1}{2} \rho \dot{u}_i \dot{u}_i \, dV, \qquad \dot{U} = \frac{d}{dt} \int_V \tfrac{1}{2} \tau_{ij} e_{ij} \, dV. \quad (11.13)$$

The energy flow g into the crack tip can now be obtained as a limit of the flow into the inside of S_t:

$$g = \dot{W} - \lim_{S_t \to 0} [\dot{K} + \dot{U}].$$

Since S_t is moving along with the crack tip, the region V in equation (11.13) is time-dependent. Thus both $\dot{K}$ and $\dot{U}$ consist of the change in energy occurring inside V and the flux of energy through the boundary S_t. These contributions are

$$\dot{K} = \int_V \rho \dot{u}_i \ddot{u}_i \, dV + \int_{S_t} \tfrac{1}{2} \rho \dot{u}_i \dot{u}_i v_n \, dS,$$

$$\dot{U} = \int_V \tau_{ij} \dot{u}_{i,j} \, dV + \int_{S_t} \tfrac{1}{2} \tau_{ij} u_{i,j} v_n \, dS \qquad (\text{using } \tau_{ij} = \tau_{ji}),$$

where v_n is the normal component of velocity of a point on S_t. Replacing the first integrand for $\dot{U}$ by $(\tau_{ij}\dot{u}_i)_{,j} - \tau_{ij,j}\dot{u}_i$ and applying the divergence theorem to $\int_V (\tau_{ij}\dot{u}_i)_{,j} \, dV$, we find

$$\begin{aligned} g = & \int_{S_e} T_i \dot{u}_i \, dS - \lim_{S_t \to 0} \left[\int_V (\rho \dot{u}_i \ddot{u}_i - \tau_{ij,j} \dot{u}_i) \, dV + \int_{S_e + S_c} \tau_{ij} n_j \dot{u}_i \, dS \right. \\ & \left. + \int_{S_t} \left(\tau_{ij} n_j \dot{u}_i + \tfrac{1}{2} \tau_{ij} u_{i,j} v_n + \tfrac{1}{2} \rho \dot{u}_i \dot{u}_i v_n \right) dS \right] \qquad (11.14) \\ = & - \lim_{S_t \to 0} \int_{S_t} \left(\tau_{ij} n_j \dot{u}_i + \tfrac{1}{2} \tau_{ij} \dot{u}_{i,j} v_n + \tfrac{1}{2} \rho \dot{u}_i \dot{u}_i v_n \right) dS, \end{aligned}$$

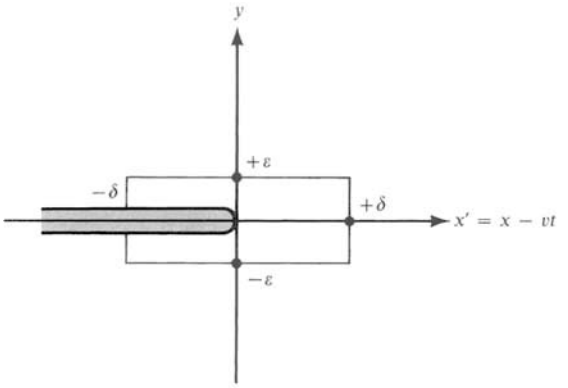

FIGURE **11.5**

where we used (11.11) and (11.12). The contribution from S_c is zero because $v_n = 0$ and because the crack surface is traction-free. (As mentioned in the beginning of this section, we chose to neglect the effect of friction here.)

Now, coming back to the coordinate frame (x', y) moving with the tip, we shall choose a rectangular surface shown in Figure 11.5 as S_t. The side lengths of the rectangle are 2δ in the x-direction and 2ε in the y-direction. If we shrink the width ε to zero, the contribution from the sides $x = \pm\delta$ is zero. Since v_n is zero on the sides $y = \pm\varepsilon$, equation (11.14) is simplified to

$$g = \lim_{\delta \to 0} \int_{-\delta}^{\delta} \mathbf{T}(x', 0) \cdot \left[\dot{\mathbf{u}}(x', +0) - \dot{\mathbf{u}}(x', -0)\right] dx'.$$

Thus, by putting equation (11.6) into the above integral, the rate of work for the anti-plane case is obtained as

$$g = \frac{AvK}{2\sqrt{2\pi}} \lim_{\delta \to 0} \int_{-\delta}^{\delta} \frac{H(-x')}{\sqrt{-x'}} \frac{H(x')}{\sqrt{x'}} dx'$$

and, using equation (11.7) for the in-plane case, as

$$g = \frac{A'vK'}{2\sqrt{2\pi}} \lim_{\delta \to 0} \int_{-\delta}^{\delta} \frac{H(-x')}{\sqrt{-x'}} \frac{H(x')}{\sqrt{x'}} dx'.$$

The integrand in the above formulas is zero except at $x' = 0$, yet the integration gives a finite result because the integrand behaves like a Dirac delta function. To show this, let us consider the following integral:

$$\int_{-\infty}^{\infty} \frac{H(x')H(x - x')}{\sqrt{x'}\sqrt{x - x'}} dx' = \int_{0}^{x} \frac{dx'}{\sqrt{x'}\sqrt{x - x'}} = \pi H(x) \qquad \text{(see Box 9.3).}$$

It then follows that

$$\int_{-\infty}^{\infty} \frac{H(x')}{\sqrt{x'}} \frac{H(-x')}{\sqrt{-x'}} dx' = \pi H(0) = \frac{\pi}{2}.$$

Thus, for the anti-plane crack, the rate of work done at the crack tip is

$$g = \sqrt{\frac{\pi}{2}}\frac{AvK}{4} = \frac{vK^2}{2\mu}\Big/\sqrt{1-\frac{v^2}{\beta^2}}, \tag{11.15}$$

and for the in-plane crack

$$g = \frac{v}{8}\frac{v^2K'^2}{\mu\beta^2}\left[\sqrt{1-\frac{v^2}{\alpha^2}} - \left(1-\frac{v^2}{2\beta^2}\right)^2\Big/\sqrt{1-\frac{v^2}{\beta^2}}\right]^{-1}. \tag{11.16}$$

The above result may be obtained without using a value of $H(x)$ at $x = 0$. From equations (11.9) and (11.12) for stress and particle velocity of the anti-plane crack, the first term of the integrand of (11.14) is given by

$$2\tau_{yz}(x', y)\dot{w}(x', y) = \frac{vK^2y}{2\pi\mu(x'^2 + \gamma^2y^2)},$$

where K is the stress-intensity factor defined earlier and $\gamma = \sqrt{1 - v^2/\beta^2}$. Putting $y = \pm\varepsilon$ into the above formula and integrating from $x' = -\delta$ to $x' = +\delta$, we get

$$g = \lim_{\varepsilon\to 0}\lim_{\delta\to 0}\frac{vK^2}{\pi\mu\gamma}\tan^{-1}\left(\frac{\varepsilon}{\delta\gamma}\right) = \frac{vK^2}{2\mu\gamma}, \tag{11.17}$$

which confirms the result given in (11.15).

In the case of the anti-plane crack, the energy flow at the tip is zero when $K = 0$, i.e., when the rupture velocity is equal to the shear velocity. In the case of the in-plane crack, it is zero when the rupture velocity is equal to the Rayleigh-wave velocity. Thus, at these velocities, energy needed for creating new surfaces of the crack cannot be supplied to the crack tip. In this sense, they are the terminal velocities of crack propagation. Equation (11.16) shows that if the rupture velocity exceeds the Rayleigh-wave velocity, g becomes negative. In other words, the crack tip becomes a source of energy flow instead of a sink. This is physically unacceptable, and it appears that the speed of the in-plane shear crack cannot exceed the Rayleigh-wave velocity. This conclusion, however, will be modified in Section 11.2.3, where we discuss rupture propagation in a medium with finite cohesive force.

11.1.3 COHESIVE FORCE

The solutions for stress and particle velocity around the propagating crack tip obtained in Section 11.1.1 are still not realistic, because they both become infinite at the crack tip. All materials have a finite strength and cannot withstand stress beyond some limit. The way to eliminate the singularities is found by using the concept of *cohesive force*, introduced by Barenblatt (1959). This force is distributed inside the crack near the tip, and it opposes the external stress.

BOX **11.2**
Fracture criteria

Since most materials fracture when stressed beyond some critical level, it is natural to describe the condition for fracture by a critical applied stress, or strength of material. It practice, however, it has long been known that the fracture strength of a given material varies greatly. The theories built around the concept of strength as a material constant were for a long time incapable of accounting for observed diversity in fracture behavior.

A breakthrough was made by A.A. Griffith in 1920. He assumed the existence of flaws in material in the form of cracks. Creating new crack surfaces requires an increase of the free surface energy. This energy must be supplied from the surrounding medium for the crack to extend. Griffith's fracture criterion is based on the balance of consumed surface energy and the supply of mechanical energy for an infinitesimal virtual increase in crack length. In this section, we have just calculated the rate of supply of mechanical energy to the crack tip when the crack tip moves at a constant speed ((11.15) and (11.16)). In Section 11.2.1, we shall use the Griffith concept of energy balance in deriving the equation of motion for a crack tip, equation (11.34).

An alternative approach to fracture mechanics was formulated around the concept of stress-intensity factor by G. R. Irwin and his associates in about 1950. It was found that the Griffith fracture criterion is equivalent to the existence of a critical stress-intensity factor. If the stress-intensity factor exceeds the critical value, the crack will extend. We shall call this the Irwin criterion.

In equation (11.15) and (11.16), we have shown that the energy flow into the crack tip is determined by the stress-intensity factor K or K', and the rupture-propagation velocity v. Therefore, at the initiation of crack extension, when $v = 0$, the energy flow and stress-intensity factor are uniquely related, demonstrating the equivalence of Griffith and Irwin criteria. The equivalence relation is shown explicitly in (11.22), setting $v = 0$ there for an anti-plane crack and also in (11.82) for an in-plane crack.

For a finite rupture velocity v, both the Griffith surface energy and the critical stress-intensity factor may depend on v. In Sections 11.2.2 and 11.2.3, we shall consider two fracture criteria. In the Griffith criterion, we assume that the surface energy does not depend on v; in the Irwin criterion, we assume that the critical stress intensity factor is independent of v. Figure 11.21 compares the motion of the crack tip obtained by the two criteria.

Let us consider the case of an anti-plane crack, and put the total traction on the ruptured surface ($x' \leq 0$) as

$$\sigma_{yz}(x', 0) = \sigma_{yz}^{\mathrm{d}} + \sigma_{\mathrm{c}}(x'). \tag{11.18}$$

Here σ_{yz}^{d} is due to dynamic friction and acts all over the crack, but the cohesive force (per unit area) $\sigma_{\mathrm{c}}(x')$ is nonzero only in $-d < x' \leq 0$, where d is the length of the end region, as shown in Figure 11.6. The distribution of the cohesive force will generate a concentration of τ_{yz} ahead of the crack tip, with the stress-intensity factor given by

$$-\sqrt{\frac{2}{\pi}} \int_{-d}^{0} \frac{\sigma_{\mathrm{c}}(\xi)}{\sqrt{-\xi}}\, d\xi. \tag{11.19}$$

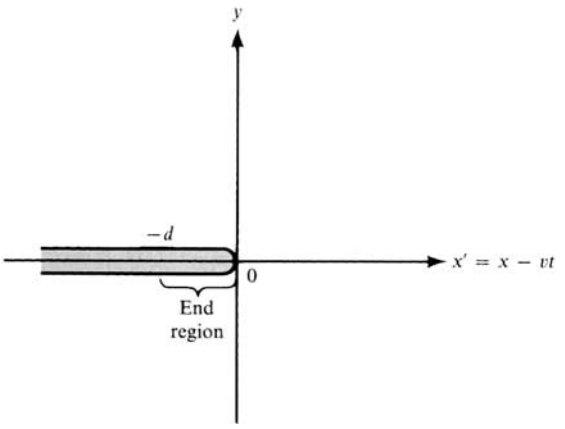

FIGURE **11.6**

This result is derived later in Box 11.3, in a discussion of equation (11.55). The original stress singularity due to the external stress may be eliminated if we choose the cohesive force $\sigma_c(\xi)$ that satisfies the condition

$$K = \sqrt{\frac{2}{\pi}} \int_{-d}^{0} \frac{\sigma_c(\xi)}{\sqrt{-\xi}}\, d\xi. \tag{11.20}$$

With this choice of $\sigma_c(\xi)$, the stress component $\sigma_{yz}(x', 0)$ will be finite and continuous at the crack tip. Since the slip velocity $\Delta\dot{w}$ is the Hilbert transform of the shear stress times a constant, as shown in equation (11.3), the singularity of $\Delta\dot{w}$ is also removed if the shear stress becomes continuous there.

If d is small, the elastic field due to the cohesive force is limited near the crack tip and does not affect the field outside the immediate vicinity of the crack tip. Then the energy flow into the crack tip through the external surface will be the same as given in (11.15) for the case of no cohesive force. This energy flow is absorbed to create a new surface of the crack. Expressing the surface energy per unit area as G, we have

$$g = 2Gv, \tag{11.21}$$

where the factor 2 accounts for both faces of the crack. From (11.15) and (11.21), we find

$$G = \frac{K^2}{4\mu} \Big/ \sqrt{1 - \frac{v^2}{\beta^2}} \tag{11.22}$$

(A similar relation may be obtained for an in-plane shear crack using (11.16).)

In order to get a rough estimate of the highest frequencies involved in seismic motion caused by propagation of a crack, we shall assume that the cohesive force is uniformly distributed over the end region. The corresponding stress-intensity factor is

$$K = \sqrt{\frac{2}{\pi}} \int_{-d}^{0} \frac{\sigma_c}{\sqrt{-\xi}}\, d\xi = \frac{2\sigma_c}{\sqrt{\pi}} \sqrt{2d}, \tag{11.23}$$

where σ_c is the cohesive force per unit area. Putting (11.23) into (11.22), we find

$$G = \frac{2\sigma_c^2 d}{\mu\pi} \Big/ \sqrt{1 - \frac{v^2}{\beta^2}}. \tag{11.24}$$

This is a relationship between important quantities that determine the seismic motion around the crack tip, about which we know very little. In general, G, σ_c, and d may depend on the rupture velocity.

Since d is the measure of distance over which slip is resisted, the larger d is, the slower the slip at the initial stage of faulting. Contrarily, we expect higher slip velocity and acceleration as d gets shorter. The characteristic time constant t_d may be given by d/v:

$$t_d = d/v = \frac{\pi\mu G\sqrt{1 - (v^2/\beta^2)}}{2\sigma_c^2 v}. \tag{11.25}$$

t_d is the time constant that controls the high end of the seismic spectrum. Static experiments on rock samples in the laboratory give G on the order of 10^3 erg/cm^2 and σ_c on the order of 10^9 dyn/cm^2. For a rough estimate, we shall assume that their order of magnitude remains the same in the dynamic case, so that for $\beta = 3.5$ km/s, $v = 3$ km/s, and $\mu = 3 \times 10^{11}$ dyn/cm^2, we get

$$t_d = 10^{-9}\text{s}.$$

Thus we expect radiation of seismic waves with frequency up to a gigahertz if the laboratory values are applicable.

In the actual field situation, G may increase with crack length. The stress around the crack tip increases as the crack length increases. (As shown in Box 11.1, the static stress-intensity factor increases for larger cracks.) Consequently, the volume of the region of microcracks and plastic deformation will increase. This region will absorb energy, making the apparent value of G greater for larger earthquakes.

The highest frequency contained in usual earthquake records is on the order of 100 Hz. Assuming that the cohesive stress σ_c in the actual fault gouge is on the order of 10^8 dyn/cm^2, the value of G corresponding to $t_d = 0.01$ s will be around 10^8 erg/cm^2 from (11.25), which is many orders of magnitude greater than the laboratory values.

The physical meaning of cohesive force becomes clearer if we write it, instead of equation (11.18), in the form of constitutive equations, such as

$$\sigma_{yz}(x', 0) = \sigma_{yz}^{\text{d}} + \sigma_c[\Delta w(x')] \qquad x' \le 0 \tag{11.26}$$

or

$$\sigma_{yz}(x', 0) = \sigma_{yz}^{\text{d}} + \sigma_c[\varepsilon(x')] \qquad x' \le 0, \tag{11.27}$$

where ε is the plastic strain in the fault gouge and Δw is the equivalent slip between the fault surfaces corresponding to the plastic strain. If the thickness of the fault gouge is b, we may take $\Delta w = b\varepsilon$. The specific surface energy G can be expressed as $G = \frac{1}{2}\int_0^\infty \sigma_c(D)\, dD$,

where the factor $\frac{1}{2}$ accounts for the two surfaces of the crack. Relation (11.27) may be determined by laboratory experiments on the stress–strain relation of rock samples and field studies of gouge thickness, and it may be appropriate to allow σ_c to depend on $\Delta\dot{w}$ as well as on Δw. Once the relation is known, the slip function can be calculated by an iterative method. We start with an initial guess of the slip function $\Delta w(x')$ and obtain the corresponding cohesive force from (11.26) or (11.27). Then we can calculate the stress-intensity factor K from (11.20). At a distance sufficiently far from the tip compared with the scale of the end region, the cohesive force no longer governs the slip function, which is determined instead by macroscopic crack parameters such as the shape, length, and stress drop. Knowing σ_{yz} for $-\infty < x' < \infty$, the slip velocity can be obtained by the Hilbert transform (see equation (11.3)). The resulting slip function can be used as the second trial function for revising the cohesive force. The iteration proceeds until the slip function converges to a final solution. Ida (1972, 1973) used this method to calculate the slip function and its time derivatives for various cases of the cohesive force diagram (σ_c as a function of slip $[\Delta w]$), assuming a semi-infinite crack with constant stress drop as the macroscopic model, and discussed the maximum acceleration and velocity in terms of this material property. Andrews (1976) extended Ida's work and incorporated the cohesive force in a finite-difference calculation of crack propagation (discussed in Section 11.2.3 and Fig. 11.26), combining numerical analysis of rupture propagation with laboratory results on rock mechanics.

11.1.4 NEAR FIELD OF A GROWING ELLIPTICAL CRACK

In Section 10.1.6, we studied the far-field body waves from an elliptical crack growing with constant velocity and keeping the same shape. Neglecting the stopping phase, we found that the initial rise of far-field displacement grows parabolically, being proportional to the square of time measured from the onset. The corresponding acceleration showed a finite discontinuity at the onset. In this section, we shall consider seismic motion in the near field of the growing elliptical crack, for which a Cagniard solution is available.

Let us assume initially a state of uniform stress $\boldsymbol{\sigma}^0$ and suppose that a plane shear crack nucleates at the origin at time $t = 0$. The fault surface $S(t)$ is defined in Cartesian coordinates by the ellipse

$$S(t) = \left\{x_3 = 0: x_1^2/u^2 + x_2^2/v^2 \le t^2\right\},$$

which (see Figure 11.7)) has axes growing steadily at speeds u and v, each less than (or equal to) the shear-wave speed β. The shear stresses across plane $x_3 = 0$ are influenced by waves emanating from the point of nucleation, but after arrival of the rupture they drop to new values prescribed over $S(t)$.

To describe the problem further, let $\mathbf{u}$ be displacement from the initial (prestressed, static) position, with $\boldsymbol{\tau}$ as the stress tensor due to $\mathbf{u}$ (so that $\boldsymbol{\sigma}^0 + \boldsymbol{\tau}$ is the total stress). Within an infinite homogeneous medium, $\mathbf{u}$ and $\boldsymbol{\tau}$ have certain symmetric properties with respect to the crack plane $x_3 = 0$ (see Problem 10.2): from equation (10.39) or an argument similar to the one used in the in-plane problem (Section 10.2.4), we find that τ_{33}, u_1, and u_2 are odd functions of x_3 when the discontinuity across the crack plane is restricted to

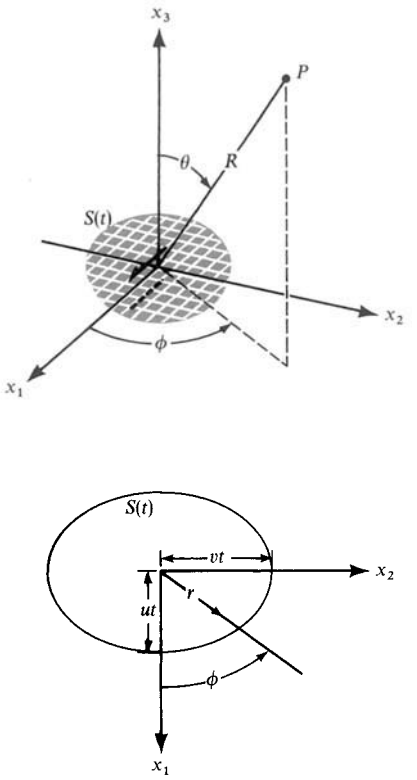

FIGURE **11.7**

shearing. These quantities must therefore be zero at $x_3 = 0$ wherever they are continuous there. Thus we have the following boundary conditions:

$$\tau_{33} = 0 \qquad \text{everywhere on} \quad x_3 = 0 \tag{11.28}$$

and

$$u_1 = u_2 = 0 \qquad \text{on} \quad x_3 = 0 \quad \text{but off } S(t). \tag{11.29}$$

Burridge and Willis (1969) found the following simple solution for the slip function across a growing elliptical shear crack:

$$\begin{aligned} \begin{pmatrix} u_1 \\ u_2 \end{pmatrix} &= \begin{pmatrix} a \\ b \end{pmatrix} \sqrt{t^2 - \frac{x_1^2}{u^2} - \frac{x_2^2}{v^2}} \qquad \text{on } x_3 = +0 \text{ and } S(t) \\ &= \begin{pmatrix} 0 \\ 0 \end{pmatrix} \qquad \text{on } x_3 = +0 \text{ but off } S(t). \end{aligned} \tag{11.30}$$

The elastic field generated by this slip function under the conditions (11.28) and (11.29) indeed gives a shear-stress jump (τ_{13}, τ_{23}) that is constant in time and space on $S(t)$; τ_{13} is proportional to a and τ_{23} is proportional to b, where a and b are particle-velocity components

at the center of the crack, as can be seen from (11.30). For simplicity, we shall take the x_1-axis in the direction of maximum initial shear, so that no drop occurs in the stress component τ_{23}. In this case, $b = 0$ and the slip component u_2 disappears. On the moving part of the fault, τ_{13} is constant, and we can think of the total shear stress $\sigma_{13}^0 + \tau_{13}$ as being proportional to σ_{33}^0 via a dynamic coefficient of friction according to the Coulomb law of friction.

Following Richards (1973b, 1976a), we shall take the following steps for computing the elastic field radiated from the growing crack:

(i) Fourier transformation for x_1 and x_2; Laplace transformation for t:

$$f(x_1, x_2, x_3, t) \rightarrow f(k_1, k_2, k_3, s)$$

where f is any dependent variable (such as a displacement component) of interest. Boundary conditions on $x_3 = 0$ are thus transformed to

$$\tau_{33} = 0, \qquad u_1 = \frac{4\pi auv}{(s^2 + k_1^2 u^2 + k_2^2 v^2)^2}, \qquad u_2 = 0.$$

(ii) Transformation of the wave equation and use of potentials to derive algebraic expressions for $\mathbf{u}(k_1, k_2, x_3, s)$. The double Fourier inverse transform is taken, yielding the forward Laplace transform as an explicit double integral over the whole (k_1, k_2) plane. A rotation and stretch of the (k_1, k_2) plane to variables (w, q) is carried out via the de Hoop transformation

$$k_1 = (s/\alpha)(q \cos\phi - w \sin\phi),$$
$$k_2 = (s/\alpha)(q \sin\phi + w \cos\phi),$$

where α is the P-wave speed. The Laplace-transformed P-wave component of displacement at position $\mathbf{x}$ then has the form

$$\mathbf{u}^P(\mathbf{x}, s) = (1/s^2) \int_0^\infty dw \int_{-\infty}^\infty dq\, \mathbf{F}(q, w, \phi) e^{-st}, \tag{11.31}$$

where $\mathbf{F}$ is known, $t = t(q, w, \theta) \equiv \left[-iq \sin\theta + \sqrt{1 + q^2 + w^2} \cos\theta\right] (R/\alpha)$, and the spherical polars (R, θ, ϕ) for $\mathbf{x}$ are shown in Figure 11.7. It can be shown that only the positive real q-axis is needed for the integration in (11.31). There is a similar expression for the S-wave component.

(iii) Application of Cagniard's method, turning the q-integral into the Laplace transform of the w-integral, so that displacement in the time domain is recognized as a single integral over w. A complication arises because of singularities of the integrand $\mathbf{F}$, as shown in Figure 11.8. This is a diagram of the complex q-plane, and it shows that between the real-axis path of integration needed in (11.31) and the Cagniard path (on which the exponent $t(q, w, \theta)$ in (11.31) is real), the integrand has a pole. It turns

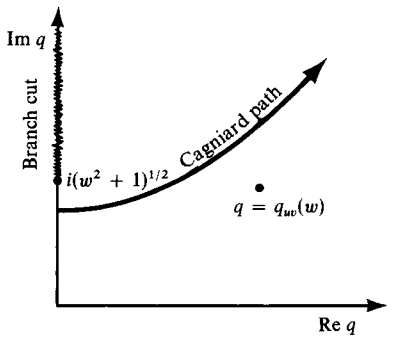

FIGURE **11.8**
There is a pole at q_{uv} near the Cagniard path for evaluating (11.31). [From Richards, 1976a.]

out to be a second-order pole, denoted by q_{uv}, and is due to the moving nature of the source. It is necessary to pick up residues in converting to the Cagniard path, giving the form

$$\mathbf{u}^P(\mathbf{x}, s) = \frac{1}{s^2}\int_0^\infty dw \int_0^\infty dt\, \mathbf{F}(q(t), w, \phi)e^{-st}\frac{dq}{dt} + \int_0^\infty dw\, \mathbf{R}(q_{uv}, w, \phi, s)e^{-st}(q_{uv}, w, \theta), \tag{11.32}$$

From the first term on the right-hand side here, one can invert to the time domain in the usual fashion (i.e., by reversing the order of integration and recognizing the result as a forward Laplace transform), obtaining a single integral over w. The second term on the right-hand side of (11.32) is already in the form suitable for recognition as the Laplace transform of a function of time. This term therefore results in an algebraic closed-form expression. This overall method, an algebraic expression resulting from an integral of residues, was first developed by Gakenheimer and Miklowitz (1969) for solving Lamb's problem with a moving source.

As usual for Cagniard inversion of three-dimensional problems (see Section 6.5), the complete seismogram can be calculated only numerically, an integration being necessary for each point in the time series. Figure 11.9 shows theoretical record sections for x_1- and x_3-components of acceleration near a left-lateral strike-slip fault. The coordinates for the four stations are (1, 1.5, 0.5), (4, 1.5, 0.5), (7, 1.5, 0.5), and (10, 1.5, 0.5). The density of the medium is 2.7 gm/cm^3, the P-wave velocity is 5.2 km/s, and the S-wave velocity is 3 km/s. The rupture speed in the x_1-direction is 90% of the Rayleigh-wave velocity, and that in the x_2-direction is 90% of the S-wave velocity. We see, in this case, small P-waves, sharp step-like S-waves arriving from the nucleation point, and large acceleration associated with the passage of the crack tip. The amplitude of waves from the nucleation point decreases with distance, whereas the acceleration associated with passage of the crack tip increases because the stress-intensity factor increases with increasing crack length.

The corresponding displacement records are shown in Figure 11.10. As discussed in Section 11.1.1, the transverse component shows a step-like waveform rather than a

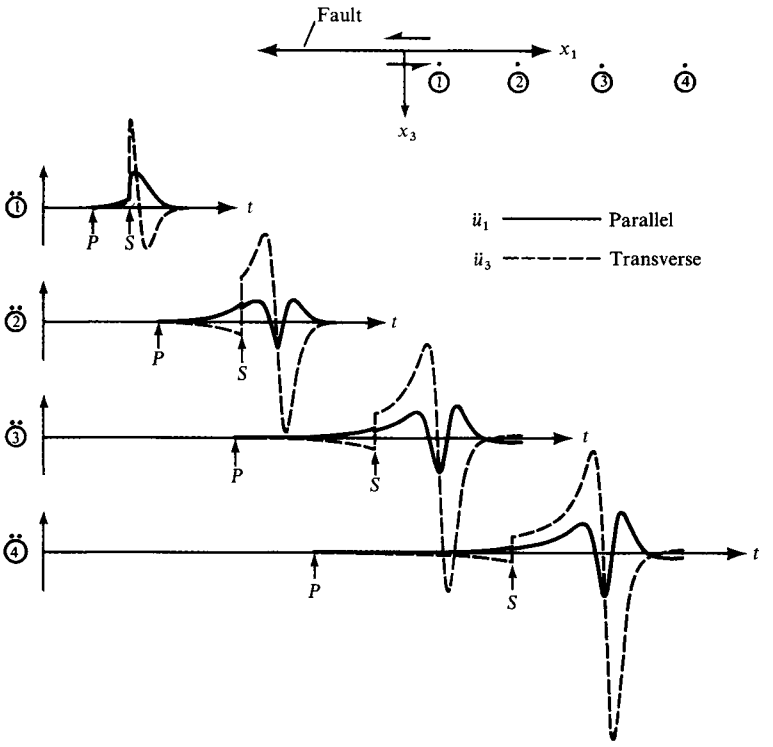

FIGURE **11.9**
Synthetic seismograms for x_1- and x_3-components of acceleration at stations shown at the top. [From Richards, 1976a.]

symmetric, impulsive form. The parallel components show a very slow rise beginning at the arrival of P-waves from the nucleation point, and do not show any clear feature that can be associated with passage of the rupture front. This shows the difficulty of accurately estimating rupture velocity from displacement measurements at points off the crack plane.

Compact formulas can be obtained for approximate waveforms corresponding to the arrivals of P- and S-waves from the nucleation point. At the arrival time $t = R/\alpha$, we find that the acceleration has a jump discontinuity:

$$\ddot{\mathbf{u}}^P = \frac{4uv\beta^2 \cos\theta \sin\theta}{\alpha^3(1 - D\sin^2\theta)^2}\, a\cos\phi\, \frac{H(t - R/\alpha)}{R}\hat{\mathbf{R}},$$

where $D = (u^2\cos^2\phi + v^2\sin^2\phi)/\alpha^2$. (R, θ, ϕ) are the spherical coordinates shown in Figure 11.7. The vector $\ddot{\mathbf{u}}^P$ points to the radial (i.e. longitudinal) direction from the nucleation point, given by the unit vector $\hat{\mathbf{R}}$. The acceleration due to shear waves from the nucleation point shows a jump discontinuity at $t = R/\beta$:

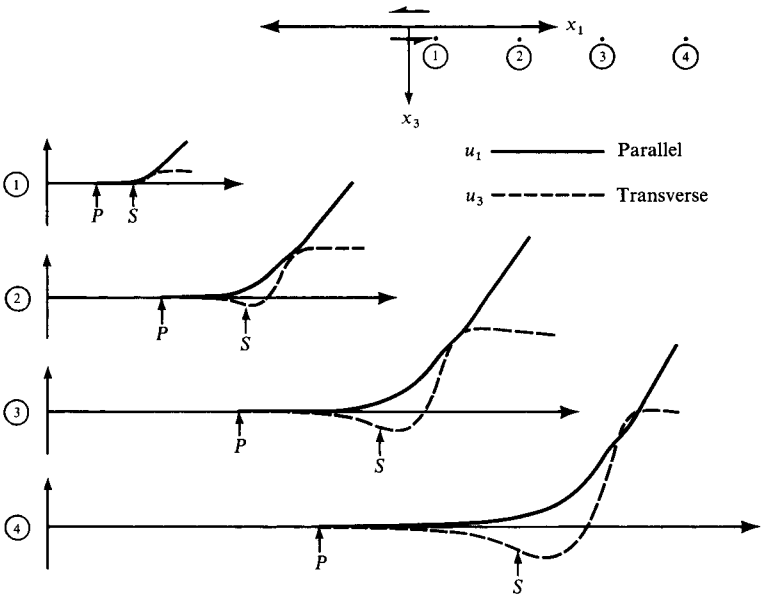

FIGURE **11.10**
Synthetic seismograms for x_1- and x_3-components of displacement at stations shown at the top. [From Richards, 1976a.]

$$[\ddot{u}_1^S, \ddot{u}_2^S, \ddot{u}_3^S] = \frac{2uv}{(1 - D\alpha^2 \sin^2 \theta/\beta^2)^2} \left[\cos\theta\ (a, 0, 0)\right.$$
$$\left. -a \sin\theta \cos\phi\ (\sin 2\theta \cos\phi, \sin 2\theta \sin\phi, \cos 2\theta)\right] \frac{H(t - R/\beta)}{R}.$$

The high-frequency asymptote of the acceleration is therefore proportional to ω^{-1}, and the corresponding displacement spectrum has a high-frequency asymptote like ω^{-3}, in agreement with previous results (equation (10.30)). The radiation pattern of these waves shows a double-couple symmetry modified by the factors $(1 - D \sin^2\theta)^{-2}$ for P-waves and $(1 - D\alpha^2 \sin^2 \theta/\beta^2)^{-2}$ for S-waves.

Another compact form of approximate solution can be obtained for singularities of particle velocity and traction components near the crack tip. Let us denote the arrival time of the crack tip at $(x_1, x_2, 0)$ as t_c, so that

$$t_c = \sqrt{x_1^2/u^2 + x_2^2/v^2}.$$

The particle velocity $\dot{u}_1$ on the plane $x_3 = 0$ is given by boundary conditions (11.29) and (11.30) as

$$\dot{u}_1 \sim a\sqrt{t_c/2}\, H(t - t_c)/\sqrt{t - t_c}. \tag{11.33}$$

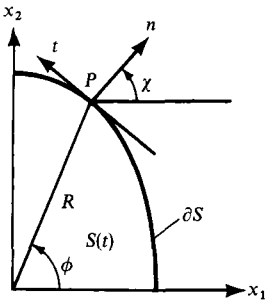

FIGURE **11.11**
Local Cartesian coordinates in the normal (n) and tangent (t) directions. [From Richards, 1976a.]

Singularities in $\dot{u}_2$ and τ_{33} are absent on $x_3 = 0$, since these quantities are zero throughout the plane. Singularities in the remaining velocity and traction components on $x_3 = 0$ are

$$\dot{u}_3 \sim \frac{2\beta^2 V a \cos\phi}{U\alpha^2 B_S}\left[\tfrac{1}{2}\alpha^2/\beta^2 + B_S^2 - B_P B_S\right]\sqrt{\frac{t_c}{2F}}\,\frac{H(t_c - t)}{\sqrt{t_c - t}},$$

$$\tau_{13} \sim \frac{4\mu\beta^2 a}{U^2\alpha^3 F B_S}\left[\left(B_P - B_S\right)B_S V^2\cos^2\phi + \tfrac{1}{4}\left(U^2 B_S^2 F - V^2\cos^2\phi\right)\left(\alpha^2/\beta^2\right)\right] \tag{11.34}$$

$$\times\sqrt{t_c/2}\,H(t_c - t)/\sqrt{t_c - t},$$

$$\tau_{23} \sim \frac{4\mu\beta^2 a\cos\phi\sin\phi}{\alpha^3 F B_S}\left[B_S B_P - B_S^2 - \tfrac{1}{4}\left(\alpha^2/\beta^2\right)\right]\sqrt{\frac{t_c}{2}}\,\frac{H(t_c - t)}{\sqrt{t_c - t}},$$

where μ is the rigidity and all capital letter symbols are dimensionless quantities given by

$$U = u/\alpha, \qquad V = v/\alpha, \qquad F = U^2\sin^2\phi + V^2\cos^2\phi,$$

$$B_P^2 + 1 = B_S^2 + \frac{\alpha^2}{\beta^2} = \frac{U^4\sin^2\phi + V^4\cos^2\phi}{U^2V^2F}.$$

Since the singularities (11.33) and (11.34) describe local properties of the motion at points near the crack tip, it is instructive to work with a coordinate system related naturally to the local geometry. Figure 11.11 shows such a system, using directions of the normal, the tangent, and the binormal (i.e., the x_3-axis). Tensor components are rotated to

$$\tau_{3n} = \tau_{31}\cos\chi + \tau_{23}\sin\chi, \quad \tau_{t3} = -\tau_{31}\sin\chi + \tau_{23}\cos\chi.$$

Letting v_n be the velocity of rupture in direction n, we find that

$$v_n = \frac{uv}{\alpha}\sqrt{\frac{F}{U^4\sin^2\phi + V^4\cos^2\phi}},$$

which is simply related to B_P and B_S.

We can now resolve the local motion into in-plane components (u_n and τ_{zn}) and anti-plane components (u_t and τ_{zt}). Then the singularities for the in-plane components are

$$\dot{u}_n \sim \frac{a v_n V \cos\phi}{\alpha U}\sqrt{\frac{t_c}{2F}}\,\frac{H(t-t_c)}{\sqrt{t-t_c}},$$

$$\tau_{3n} \sim \frac{-a\mu\beta^2 v_n V \mathsf{R}(1/v_n)\cos\phi}{B_S U}\sqrt{\frac{t_c}{2F}}\,\frac{H(t_c-t)}{\sqrt{t_c-t}},$$

where $\mathsf{R}(1/v_n) = [(\alpha^2/\beta^2)(v_n^2/\beta^2) - 4B_S B_P + 4B_S^2]/(\alpha^2 v_n^2)$, so that R is the Rayleigh function of (5.56),

$$\mathsf{R}(p) \equiv \left(\frac{1}{\beta^2} - 2p^2\right)^2 - 4p^2\sqrt{p^2 - \frac{1}{\alpha^2}}\sqrt{p^2 - \frac{1}{\beta^2}}, \tag{11.35}$$

and singularities for the anti-plane components are

$$\dot{u}_t \sim \frac{-a v_n U \sin\phi}{\alpha V}\sqrt{\frac{t_c}{2F}}\,\frac{H(t-t_c)}{\sqrt{t-t_c}},$$

$$\tau_{t3} \sim \frac{-a\mu U v_n B_S \sin\phi}{\alpha^2 V}\sqrt{\frac{t_c}{2F}}\,\frac{H(t_c-t)}{\sqrt{t_c-t}}.$$

In agreement with results obtained in Section 11.1.1, the in-plane stress singularity will vanish wherever the rupture velocity is the Rayleigh-wave velocity, and the anti-plane singularity will be zero wherever the rupture velocity is the shear velocity (then, $B_S = 0$). The energy flow into the crack tip per unit length of rupture front can be obtained in the same way as for the two-dimensional crack. Integrating the work rate over the area enclosing the crack tip and moving with it, we find the rate of energy flow into the crack tip as

$$\begin{aligned} g &= \lim_{\substack{\delta^+\to 0\\ \delta^-\to 0}} \int_{-\delta^-}^{\delta^+} \left(\tau_{3n}\,\Delta\dot{u}_n + \tau_{t3}\,\Delta\dot{u}_t\right) dn \\ &= \frac{\pi\mu\beta^2 v_n}{4\alpha^3 U^2 V^2 B_S F} a^2 t_c \left[B_S^2 \left(v_n/\beta\right)^2 U^4 \sin^2\phi - \mathsf{R}\left(1/v_n\right)\alpha^2 v_n^2 V^4 \cos^2\phi\right]. \end{aligned} \tag{11.36}$$

For v_n less than the Rayleigh-wave speed c_R, $\mathsf{R}(1/v_n)$ is negative and the crack tip is an energy sink of both anti-plane and in-plane motions. But for $v_n > c_R$, $\mathsf{R}(1/v_n)$ is positive and the crack tip becomes the apparent energy source for in-plane motion. This is unrealistic for a pure in-plane crack, but may be possible if the energy flow supplied by the anti-plane component (positive for $v_n < \beta$) can compensate for it (Andrews, 1994). The motion at $\phi = 0$ is purely in-plane, and the terminal velocity of the crack tip will be the Rayleigh-wave velocity c_R. The motion at $\phi = 90°$ is purely anti-plane, with its terminal velocity being the shear-wave velocity β. For arbitrary ϕ, setting $g = 0$ in (11.36) will give the terminal velocity. The resultant terminal crack will be approximately elliptical, with major and minor axes growing at speeds β and c_R.

The above discussion of terminal velocity is based only on the rates of energy balance at the crack tip. In the case of an in-plane shear crack, it is possible that the stress associated with P- and S-waves running ahead of the crack tip can overcome the cohesive force (if finite), and the rupture velocity will exceed the Rayleigh-wave velocity, eventually reaching the P-wave velocity. We shall come back to this point in Section 11.2.3.

11.1.5 THE FAR-FIELD SPECTRUM FOR A CIRCULAR CRACK THAT STOPS

So far we have considered only cases in which the crack grows with a constant velocity. The results gave us some insight into the slip function expected for a shear crack and also some understanding of its elastic near field. But to understand its far field, we must solve a more difficult problem in which the growth of the crack is stopped.

Let us consider a circular crack that nucleates at its center at time $t = 0$, expands with a constant velocity v, and suddenly stops at a radius r_c. Up to the time of stopping, $t = r_c/v$, the problem is self-similar and the slip function given in (11.30) for $u = v$ gives the exact solution. If we freeze the motion at this instant, we get the kinematic model depicted in Figure 10.10, for which the compact far-field solution of Sato and Hirasawa (1973) is given in equation (10.27). This freezing of motion is unrealistic, because it violates causality. At the instant of stopping, the points inside the crack have not yet sensed the termination of crack growth. The slip function of another kinematic model, proposed by Molnar *et al.* (1973) and shown in Figure 10.12, is more plausible; and the ramp-function slip at the crack center is quite appropriate, although the slip function at other points should have a square-root rise, as proposed by Boatwright (1980).

The high-frequency asymptote of the far-field displacement spectrum was determined by the form of the slip function in space near the crack tip, as discussed in Section 10.1.6. For the step-function rise, the asymptote is expected to be $\omega^{-3/2}$, and for the square-root rise, ω^{-2}. As discussed in Section 11.1.3, the cohesive force smooths these singularities over the length of the end region. The rupture velocity divided by this length will give the upper limit of frequency to which the asymptote is applicable.

Because of the difficulty in dealing with multiple diffraction at the edges of the crack, no analytic solution is available for the elastic field of a growing crack that stops. Burridge (1969) used a numerical solution of the integral-equation representation of the problem to solve some finite in-plane and anti-plane cracks. A similar method, originated by Hamano (1974), has been used by Das and Aki (1977a). Finite-difference or finite-element methods have also been used for similar problems by Hanson *et al.* (1971), Dieterich (1973), and Andrews (1975). Here we shall outline the work of Madariaga (1976), who used a finite-difference method to calculate the far-field seismic spectrum from a growing circular crack that stops. As we shall see in his results, the finite mesh size and some smoothing procedures introduce an artificial end region similar to that due to cohesive force.

We shall use the same notation and coordinate system as for the elliptical crack in Section 11.1.4 (Fig 11.7). We shall again assume that the stress drop on the crack occurs only in the τ_{13} component. Similarly, τ_{33} is zero on the plane $x_3 = 0$, and u_1 and u_2 are zero outside the crack on the plane $x_3 = 0$. The boundary conditions on $x_3 = 0$ are therefore

$$\left.\begin{aligned}\tau_{13} &= -p_0 \\ \tau_{23} &= 0\end{aligned}\right\} \quad \text{for } r < \min(vt, r_c),$$
$$u_1 = u_2 = 0 \quad \text{for } r > \min(vt, r_c), \text{ and} \tag{11.37}$$
$$\tau_{33} = 0 \quad \text{for all } r$$

(p_0 is the stress drop, as discussed in more detail in Section 11.2).

The circular shape of the crack, which has a final radius of r_c, suggests cylindrical coordinates (r, ϕ, z) as the most convenient system to study the problem. We can rewrite the boundary conditions (11.37) as

$$\left.\begin{aligned}\tau_{rz} &= -p_0 \cos\phi \\ \tau_{\phi z} &= p_0 \sin\phi\end{aligned}\right\} \quad \text{for } r < \min(vt, r_c),$$
$$u_r = u_\phi = 0 \quad \text{for } r > \min(vt, r_c), \text{ and}$$
$$\tau_{zz} = 0 \quad \text{for all } r.$$

These boundary conditions have a simple sinusoidal azimuthal dependence. Consequently, we find that the ϕ-dependence of displacement components is either $\sin\phi$ or $\cos\phi$. They can be written as

$$u_r = u(r, z, t)\cos\phi, \quad u_\phi = v(r, z, t)\sin\phi, \quad u_z = w(r, z, t)\cos\phi.$$

The corresponding stress components can also be written in the same form:

$$\tau_{rr} = \Sigma_{rr}(r, z, t)\cos\phi, \quad \tau_{\phi\phi} = \Sigma_{\phi\phi}(r, z, t)\cos\phi, \quad \tau_{zz} = \Sigma_{zz}(r, z, t)\cos\phi,$$
$$\tau_{rz} = \Sigma_{rz}(r, z, t)\cos\phi, \quad \tau_{r\phi} = \Sigma_{r\phi}(r, z, t)\sin\phi, \quad \tau_{z\phi} = \Sigma_{z\phi}(r, z, t)\sin\phi.$$

Three components of particle velocity, $\dot{u}, \dot{v}, \dot{w}$, and six stress components make up nine unknowns, for which we have a system of nine first-order differential equations: three equations of motion and six equations from Hooke's law (the stress–strain relation). Denoting partial derivatives by a comma followed by the variable with respect to which the finite difference derivative is taken, the nine equations can be written as

$$\rho\dot{u}_{,t} = \frac{1}{r}(r\Sigma_{rr})_{,r} + \frac{1}{r}(\Sigma_{r\phi} - \Sigma_{\phi\phi}) + \Sigma_{rz,z},$$
$$\rho\dot{v}_{,t} = \frac{1}{r}(r\Sigma_{r\phi})_{,r} + \frac{1}{r}(\Sigma_{r\phi} - \Sigma_{\phi\phi}) + \Sigma_{z\phi,z},$$
$$\rho\dot{w}_{,t} = \frac{1}{r}(r\Sigma_{rz})_{,r} + \frac{1}{r}\Sigma_{z\phi} + \Sigma_{zz,z},$$
$$\Sigma_{rr,t} = (\lambda + 2\mu)\dot{u}_{,r} + \lambda(\dot{u} + \dot{v})/r + \lambda\dot{w}_{,z},$$
$$\Sigma_{zz,t} = \lambda\dot{u}_{,r} + \lambda(\dot{u} + \dot{v})/r + (\lambda + 2\mu)\dot{w}_{,z},$$
$$\Sigma_{\phi\phi,t} = \lambda\dot{u}_{,r} + (\lambda + 2\mu)(\dot{u} + \dot{v})/r + \lambda\dot{w}_{,z},$$
$$\Sigma_{r\phi,t} = \mu\dot{v}_{,r} - \mu(\dot{u} + \dot{v})/r, \qquad \Sigma_{z\phi,t} = \mu\dot{v}_{,z} - \mu\dot{w}/r, \qquad \Sigma_{zr,t} = \mu\dot{w}_{,r} + \mu\dot{u}_{,z},$$

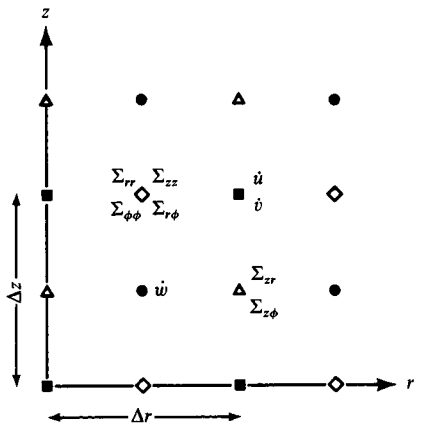

FIGURE **11.12**
Grid-point assignment for each of nine stress/particle-velocity components.

where λ, μ are the Lamé constants and ρ is the density. We have to solve these equations subject to the following boundary conditions on $z = 0$:

$$\Sigma_{rz} = -\Sigma_{\phi z} = -p_0 \qquad \text{for } r < \min(vt, r_c),$$
$$\dot{u} = \dot{v} = 0 \qquad \text{for } r > \min(vt, r_c), \text{ and}$$
$$\Sigma_{zz} = 0 \qquad \text{for all } r.$$

The slip components Δu_1 and Δu_2 in the original coordinates can be written in terms of u and v at $z = 0$:

$$\Delta u_1 = 2u \cos^2 \phi - 2v \sin^2 \phi, \qquad \Delta u_2 = (u + v) \sin 2\phi.$$

In the case of self-similar cracks studied in the preceding section, Δu_2 vanishes. In the present case Δu_2 does not necessarily vanish but is found to be practically negligible; i.e., $u \sim -v$, so that

$$\Delta u_1 = 2u = -2v. \tag{11.38}$$

Interestingly, Δu_1 is independent of ϕ.

Madariaga (1976) solved the above problem by the finite-difference method using a so-called staggered grid in which the velocities are defined at discrete times $k\,\Delta t$ and the stresses at times $(k + \frac{1}{2})\Delta t$, for integer values of k, where Δt is the time-grid interval. The spatial grid-point assignment for each of the nine stress-particle velocity components is shown in Figure 11.12.

Figure 11.13 shows the slip function $\Delta u(r, t) = u(r, +0, t) - u(r, -0, t)$ at several points on the crack. The rupture starts at $t = 0$ and expands with velocity 0.9β, where β is the shear velocity. The slip is measured with $p_0 r_c/\mu$ as the unit. The time t and radial distance r' are normalized to r_c/α and r_c, respectively, where α is the P-velocity. The slip function in time is shown at the center ($r = 0$) and at four other points at intervals of $0.2\,r_c$. At each position for which the slip history is shown, an arrow indicates the time of arrival of P-waves, originating from the perimeter of the crack at the instant the rupture

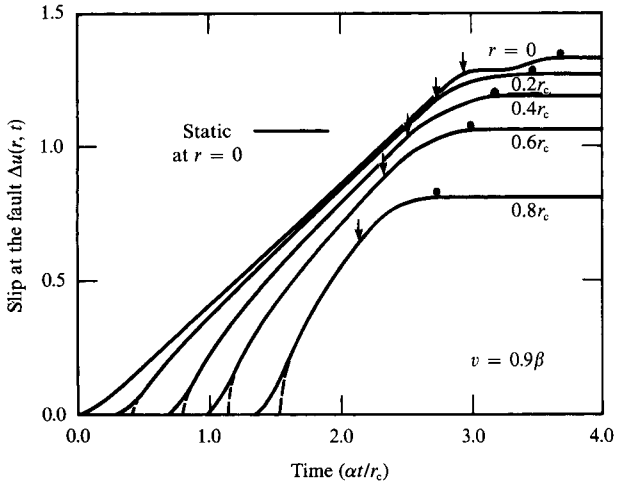

FIGURE **11.13**
Slip function at several distances from the center on the circular crack plotted against time. See text for explanation of symbols. [From Madariaga, 1976.]

stops. Figure 11.13 also shows the static slip expected at the center, $r = 0$. This level is low compared to the dynamic solutions for $r \leq 0.4\, r_c$, indicating a significant overshoot of dynamic slip. When the dynamic slip reaches a maximum and its velocity becomes zero, the slip is held fixed. (This would actually occur if static friction were large enough.) A closed circle indicates the time of slip arrest at each point. The broken curve at the initial rise shows the square-root function expected for the analytic solution. The numerical solution shows a less sharp rise because of the smoothing. This is an example of the effect of the artificially introduced end region discussed earlier.

The far-field displacement waveform corresponding to the slip function Δu_1 was given by equation (10.13), which in our present notation is

$$\Omega(\mathbf{x}, t) = \int_\Sigma \Delta \dot{u}_1 \left(\xi, t - \frac{R - (\xi \cdot \gamma)}{c} \right) d\Sigma,$$

where γ is the unit vector pointing to the receiver, ξ is the position vector of $d\Sigma$, and c is the speed of P- or S-waves. Writing the Fourier transform of $\Delta \dot{u}_1(\xi, t)$ as $\Delta \dot{u}_1(\xi, \omega)$, the far-field displacement spectrum can be obtained from equation (10.15) as

$$\Omega(\mathbf{x}, \omega) = e^{i\omega R/c} \int_\Sigma \Delta \dot{u}_1(\xi, \omega) \exp[-i\omega(\xi \cdot \gamma)/c]\, d\Sigma.$$

In our case, since $d\Sigma = r\, dr\, d\phi$ and Δu_1 is independent of ϕ, as shown in (11.38), we get

$$\Omega(\mathbf{x}, \omega) = e^{i\omega R/c} \int_0^{r_c} r\, dr\, \Delta \dot{u}_1(r, \omega) \int_{-\pi}^{\pi} \exp\left[i \frac{\omega r}{c} \sin\theta \cos(\phi - \phi_0) \right] d\phi,$$

where we have used $\xi \cdot \gamma = r \sin\theta \cos(\phi - \phi_0)$. Using the property of a Bessel function given prior to (6.7), we find

$$\Omega(\mathbf{x}, \omega) = 2\pi e^{i\omega R/c} \int_0^{r_c} r\, dr\, \Delta \dot{u}_1(r, \omega) J_0 \left(r \frac{\omega}{c} \sin\theta \right). \tag{11.39}$$

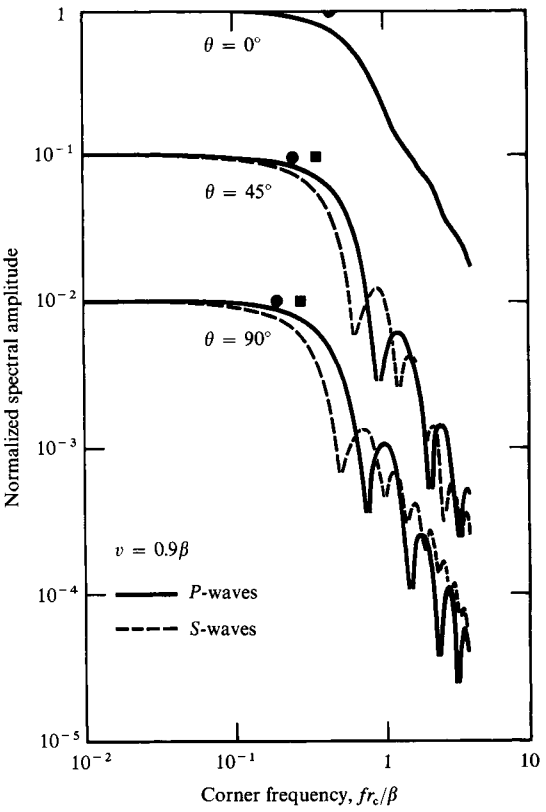

FIGURE **11.14**
Far-field spectra $|\Omega(\mathbf{x}, \omega)|$ for P- and S-waves in the case of rupture velocity $v = 0.9\beta$. [From Madariaga, 1976.]

This equation shows that the far-field displacement spectrum is a Hankel transform of $\Delta\dot{u}_1(r, \omega)$. As discussed for a more general case in Section 10.1.3, the far-field spectrum can recover the slip function only for wavenumbers less than ω/c, because $|\sin\theta| \leq 1$ for real θ.

The numerical solutions for $\Delta\dot{u}_1(r, t)$ are Fourier-transformed in t and Hankel-transformed in r to find the far-field spectrum $\Omega(\mathbf{x}, \omega)$ by (11.39). Figure 11.14 shows the resulting spectra, $|\Omega(\mathbf{x}, \omega)|$ for P- and S-waves at three receiver directions from a circular crack with rupture velocity $v = 0.9\beta$ ($\theta = 0$ corresponds to the normal to the crack plane). The spectra are flat at low frequencies and decay roughly as ω^{-2}. If the nucleation phase determines the high-frequency asymptote, we should have obtained ω^{-3}. We must, therefore, conclude that the stopping phase dominates the high-frequency spectrum, and the power of asymptotic decay is more like 2 (rather than like 3) in the case of a circular crack that suddenly stops.

The corner frequencies of the spectra were determined by the intersection of the low-frequency level and the high-frequency asymptote. They are indicated in Figure 11.14 by a closed circle for S-waves and a square for P-waves. The results for corner frequencies for various directions θ and rupture velocities are summarized in Figure 11.15. The corner frequencies are given in units of β/r_c for rupture velocities 0.6β, 0.7β, and 0.9β. Although the corner frequency increases with the rupture velocity, the variation is not very strong for

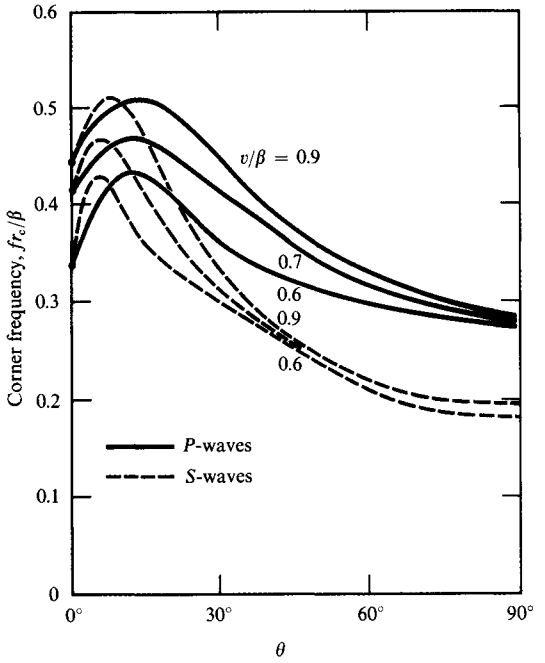

FIGURE **11.15**
Corner frequencies of P- and S-waves plotted against radiation direction for various rupture velocities. [From Madariaga, 1976.]

the range of rupture velocity considered here. The average values of the corner frequencies over all directions, for the case of $v = 0.9\beta$, are given by

$$f_c^P \text{ (in Hz)} = 0.32\beta/r_c \qquad f_c^S \text{ (in Hz)} = 0.21\beta/r_c$$

for P- and S-waves, respectively. The above equations predict considerably lower corner frequencies (by about a factor of 2) than Brune's (1970) formula, which was derived from a simple kinematic approach and which has been widely used in the interpretation of observed seismic spectra. The corner frequency for P-waves is higher than for S-waves, as expected from the earlier result of Molnar *et al.* (1973) for kinematic models with a similar slip function (see Figure 10.12 and Section 10.1.6).

11.2 Dynamics of Spontaneous Planar Rupture Propagation

One of the most challenging problems in seismology is to predict the occurrence of an earthquake and the resultant seismic motion from the study of physical properties of rocks in the epicentral region and the tectonic stress existing in the region. In order to approach this problem, we must go beyond the treatment of rupture propagation in the preceding section, in which the nucleation, propagation, and stopping of a rupture front are arbitrarily prescribed. There are three important lines of work to be carried out before we solve this problem. First, we must study properties of fault-gouge material, such as the specific surface energy, the length of the end region, and the static and dynamic values of friction and their distribution in space. Second, we must determine the tectonic stress acting on the fault

zone. Third, we must be able to predict the entire rupture phenomena from beginning to end solely on the basis of the initial stress condition and material properties of the fault zone. In this section, we shall consider the last aspect of the problem for an idealized case. We shall concentrate on how the stress distribution and the fracture criterion determine the movement of a crack tip, and (consequently) the slip function. For simplicity we shall confine our attention to planar shear cracks in an infinite homogeneous medium (so that the normal stress is unchanged by the rupture process—see Problem 10.2). We start with the case of an anti-plane crack, following the pioneering work of Kostrov (1966).

11.2.1 SPONTANEOUS PROPAGATION OF AN ANTI-PLANE CRACK: GENERAL THEORY

Using the (x, y, z) coordinates shown in Figure 10.19, we define the crack as

$$x_1 < x < x_2, \quad -\infty < z < \infty, \quad \text{and } y = 0.$$

For an anti-plane case (Section 10.2.3), only the z-component of displacement $w(x, y, t)$ is nonzero, and the only nonvanishing elements of the stress tensor are $\tau_{zx} = \mu(\partial w/\partial x)$ and $\tau_{yx} = \mu(\partial w/\partial y)$. The problem is two-dimensional, with no dependence on z. The equation of motion in this case reduces to the wave equation

$$\frac{1}{\beta^2}\frac{\partial^2 w}{\partial t^2} = \frac{\partial^2 w}{\partial x^2} + \frac{\partial^2 w}{\partial y^2}, \tag{11.40}$$

where $\beta = \sqrt{\mu/\rho}$ is the shear velocity.

Suppose that initially the crack is absent and the body is in equilibrium with an initial state of stress $\boldsymbol{\sigma}^0$. We shall take this initial state as the reference state and measure the displacement relative to this state. The total stress is then $\boldsymbol{\sigma} = \boldsymbol{\sigma}^0 + \boldsymbol{\tau}$, where the incremental stress $\boldsymbol{\tau}$ is derived from $\mathbf{u}$ by Hooke's law. Initial conditions are that w and $\partial w/\partial t$ are zero for $t = 0$. When the crack is formed (i.e., when a displacement discontinuity develops across the crack), the traction on the crack drops to the dynamic frictional stress. The only changing component of traction on the crack ($y = 0$) is σ_{yz}, and it changes from its original value σ^0_{yz} to a new value, say σ^{d}_{yz}. We shall equate the stress drop $\sigma^0_{yz}(x, 0) - \sigma^{\mathrm{d}}_{yz}(x, 0, t)$ to $p(x, t)$. The appropriate boundary condition for traction on the crack for the above choice of reference state is then given by

$$\tau_{yz} = -p(x, t) \qquad \text{for } x_1 < x < x_2, \quad y = 0. \tag{11.41}$$

In order to find the boundary condition outside of (x_1, x_2) on $y = 0$, we first need to establish that $w(x, y, t)$ is an odd function of y. This is done by writing the solution of equation (11.40) as

$$w = \iint \hat{w}(\omega, k) \exp(-i\omega t + ikx - \nu y)\, d\omega\, dk \qquad y > 0$$

$$= \iint \hat{w}(\omega, k) \exp(-i\omega t + ikx + \nu y)\, d\omega\, dk \qquad y < 0,$$

where $\nu = \sqrt{k^2 - \omega^2/\beta^2}$ and $\operatorname{Re} \nu \geq 0$ because of the radiation condition. Continuity of traction τ_{yz} across $y = 0$ then gives

$$\hat{w}(\omega, k) = -\hat{w}(\omega, k),$$

so $w(x, y, t)$ must indeed be an odd function of y. Secondly we note that an odd function of y must be zero at $y = 0$ if it is continuous there. Since w is continuous at $y = 0$ outside the crack, it follows that

$$w(x, y, t) = 0 \qquad x < x_1, x_2 < x, y = 0. \tag{11.42}$$

Equations (11.41) and (11.42) together give what is called a mixed boundary condition on $y = 0$. Because of the symmetry, it is sufficient to obtain a solution only in the half-space $y < 0$.

To solve this boundary-value problem, let us start with the representation theorem (2.43), using the Green function that satisfies the stress-free condition on the surface $y = 0$. Since displacements and stresses are independent of z, the relevant form of (2.43) is

$$w(x_0, y_0, t_0) = \int_{-\infty}^{\infty} dt \int_{-\infty}^{\infty} G_{33}^{\text{free}}(x_0, y_0, t_0; x, 0, t)\, T_3(x, 0, t)\, dx \tag{11.43}$$

where G_{33} is the displacement at (x_0, y_0, t_0) in the direction perpendicular to (x_0, y_0) for a line source at $(x, 0, t)$ in the direction perpendicular to (x, y).

Such a Green function, entailing only SH-waves, can be obtained by first finding the Green function G for a full space corresponding to a line body-force impulse located at $(x, 0, t)$:

$$\rho \frac{\partial^2 G}{\partial t_0^2} - \mu \frac{\partial^2 G}{\partial x_0^2} - \mu \frac{\partial^2 G}{\partial y_0^2} = \delta(x_0 - x)\, \delta(y_0)\, \delta(t_0 - t).$$

Apart from differences in notation, this is the equation (6.42) that is solved by (6.43), and for our present purposes we obtain the full space solution as

$$G(x_0, y_0, t_0; x, 0, t) = \frac{H\left[(t_0 - t) - \sqrt{(x_0 - x)^2 + y_0^2}/\beta\right]}{2\pi\mu R},$$

where $R^2 = (t_0 - t)^2 - [(x_0 - x)^2 + y_0^2]/\beta^2$ and $H[\ ]$ is the unit step function. Since the full-space Green function G, with a source on $y = 0$, satisfies the stress-free condition at $y_0 = 0$, the Green function G_{33}^{free} for a source on the free surface $y_0 = 0$ is merely $2G$, where the effect of reflection is taken care of by doubling the amplitude. That is,

$$G_{33}^{\text{free}}(x_0, y_0, t_0; x, 0, t) = 2G(x_0, y_0, t_0; x, 0, t). \tag{11.44}$$

Another way to obtain (11.44) is to use reciprocity and the result given in Problem 5.6 for SH-waves recorded on a free surface.

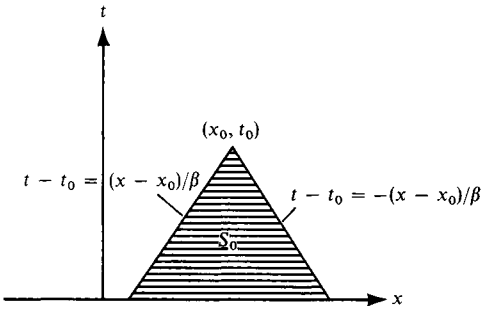

FIGURE **11.16**
All points within S_0 can influence the displacement at (x_0, t_0).

In terms of the traction $T_3 = \tau_{yz} = \tau(x, t)$, say, for all x on $y = 0$, we can write the solution for displacement w by putting $2G(x_0, t_0; x, t)$ into the representation (11.43) as

$$w(x_0, y_0, t_0) = \frac{1}{\pi\mu} \iint_S \frac{\tau(x,t)}{R}\, dx\, dt \qquad y_0 < 0, \tag{11.45}$$

where S is that part of the xt-plane which lies inside the cone

$$\beta^2(t_0 - t)^2 - (x_0 - x)^2 - y_0^2 \geq 0 \qquad 0 \leq t \leq t_0.$$

For $y_0 = 0^-$, we obtain

$$w(x_0, 0^-, t_0) = \frac{1}{\pi\mu} \iint_{S_0} \frac{\tau(x,t)\, dx\, dt}{\sqrt{(t_0 - t)^2 - (x_0 - x)^2/\beta^2}}, \tag{11.46}$$

where S_0, shown as the shaded area in Figure 11.16, is the triangle

$$\beta^2(t_0 - t)^2 - (x_0 - x)^2 \geq 0 \qquad 0 \leq t \leq t_0.$$

Since we do not yet know $\tau(x, t)$ for the whole area of S_0, equation (11.46) does not immediately give the solution. To find τ we can use (11.42), to obtain the following equation for $x_0 < x_1$ and $x_0 > x_2$:

$$\iint_{S_0} \frac{\tau(x,t)\, dx\, dt}{\sqrt{(t_0 - t)^2 - (x_0 - x)^2/\beta^2}} = 0.$$

$\tau(x, t)$ is known in some parts of the above integration region S_0, shown in Figure 11.17, where the loci of crack tips are indicated by $x_1(t)$ and $x_2(t)$. The subregion S_1 lies inside the crack, and $\tau(x, t)$ is known there from (11.41). We also know that $\tau(x, t)$ is zero in the subregion $S_0 - S_1 - S_2$, for which $x > x_2(0) + \beta t$, because any disturbances from the crack have not yet reached this subregion. The value of $\tau(x, t)$ in subregion S_2 is unknown.

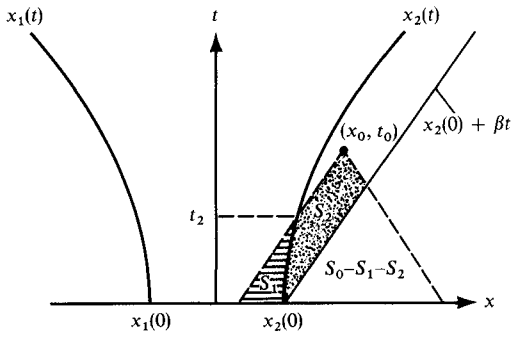

FIGURE **11.17**
$\tau(x,t)$ is known in S_1, but unknown in S_2. It is zero in $S_0 - S_1 - S_2$.

Thus, as long as S_0 does not intersect $x_1(t)$ (when the disturbances from the left crack tip have not yet reached the observation point), for $x_0 < x_1$ and $x_0 > x_2$ we have

$$\iint_{S_2} \frac{\tau(x,t)\,dx\,dt}{\sqrt{(t_0-t)^2-(x_0-x)^2/\beta^2}} = \iint_{S_1} \frac{p(x,t)\,dx\,dt}{\sqrt{(t_0-t)^2-(x_0-x)^2/\beta^2}}. \tag{11.47}$$

To solve this integral equation for $\tau(x,t)$ in S_2, we make the following transformation:

$$\xi = (\beta t - x)/\sqrt{2}, \qquad \eta = (\beta t + x)/\sqrt{2}. \tag{11.48}$$

Then (11.47) can be rewritten as

$$\int_{-x_2(0)/\sqrt{2}}^{\xi_0} \frac{d\xi}{\sqrt{\xi_0-\xi}} \int_{\eta_2(\xi)}^{\eta_0} \frac{\tau(\xi,\eta)\,d\eta}{\sqrt{\eta_0-\eta}} = \int_{-x_2(0)/\sqrt{2}}^{\xi_0} \frac{d\xi}{\sqrt{\xi_0-\xi}} \int_{-\xi}^{\eta_2(\xi)} \frac{p(\xi,\eta)\,d\eta}{\sqrt{\eta_0-\eta}} \tag{11.49}$$

where $\eta_2(\xi)$ is the solution of

$$\eta_2 - \xi = \sqrt{2}x_2\left(\frac{\eta_2+\xi}{\sqrt{2}\beta}\right),$$

which defines the position of the right crack tip in terms of ξ and η. The integration limits for ξ and η can be found from Figure 11.18, and (11.49) will be satisfied if

$$\int_{\eta_2(\xi)}^{\eta_0} \frac{\tau(\xi,\eta)\,d\eta}{\sqrt{\eta_0-\eta}} = \int_{-\xi}^{\eta_2(\xi)} p(\xi,\eta)\frac{d\eta}{\sqrt{\eta_0-\eta}}. \tag{11.50}$$

Equation (11.50) is in the form of Abel's integral equation for $\tau(\xi,\eta)$. The solution is described in Box 9.3, and in our case we find

$$\tau(\xi_0,\eta_0) = \frac{1}{\pi}\frac{d}{d\eta_0}\int_{\eta_2(\xi_0)}^{\eta_0} \frac{d\eta_1}{\sqrt{\eta_0-\eta_1}} \int_{-\xi_0}^{\eta_2(\xi_0)} p(\xi_0,\eta)\frac{d\eta}{\sqrt{\eta_1-\eta}}.$$

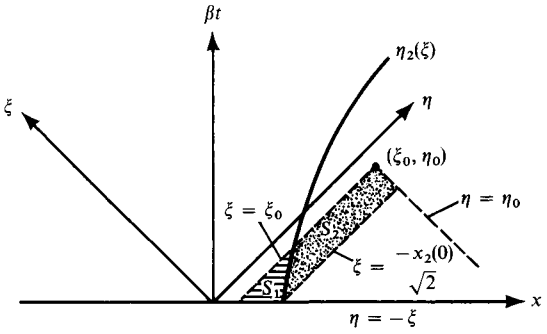

FIGURE **11.18**
Change of integral variables from (x, t) to (ξ, η).

Since

$$\int_{\eta_2}^{\eta_0} \frac{d\eta_1}{\sqrt{\eta_0 - \eta_1}\sqrt{\eta_1 - \eta}} = \sin^{-1}\left(1 + \frac{2(\eta_0 - \eta_1)}{\eta - \eta_0}\right)\Bigg|_{\eta_1=\eta_2}^{\eta_1=\eta_0},$$

the above equation reduces to

$$\tau(\xi_0, \eta_0) = \frac{1}{\pi\sqrt{\eta_0 - \eta_2(\xi_0)}} \int_{-\xi_0}^{\eta_2(\xi_0)} p(\xi_0, \eta) \frac{\sqrt{\eta_2(\xi_0) - \eta}}{\eta_0 - \eta}\, d\eta. \tag{11.51}$$

The path of integration is along $\xi = \xi_0$, which corresponds to the path $t - t_0 = (x - x_0)/\beta$ in xt-coordinates. Transforming back to xt-coordinates, and referring to Figures 11.17 and 11.18, we obtain

$$\tau(x_0, t_0) = \frac{1}{\pi\sqrt{x_0 - x_2(t_2)}} \int_{x_0 - \beta t_0}^{x_2(t_2)} p[x, t_0 + (x - x_0)/\beta] \frac{\sqrt{x_2(t_2) - x}}{x_0 - x}\, dx \tag{11.52}$$

for $x_0 > x_2(t_0)$, where t_2 is the solution of

$$\beta t_0 - x_0 = \beta t_2 - x_2(t_2).$$

In other words, t_2 is the time at which the crack-tip locus $x_2(t)$ intersects the integration path. The above expression is valid for the time interval $0 < t_0 < [x_0 - x_1(0)]/\beta$. A similar result may be obtained for the region $x_0 < x_1$ for the time interval $0 < t_0 < [x_2(0) - x_0]/\beta$. To determine $\tau(x_0, t_0)$ for later periods, additional subregions of S_0 with unknown $\tau(x, t)$ appear, corresponding to repeated diffraction of the waves at the crack boundary.

Equation (11.52) shows that the stress $\tau(x_0, t_0)$ becomes infinite when the crack tip arrives at the receiver, so that $x_0 = x_2(t_0)$. At any given time t_0 prior to arrival, the distance between the crack tip and the receiver is $x_0 - x_2(t_0)$. Using the stress-intensity factor K defined in Section 11.1.1, $\tau(x_0, t_0)$ near and ahead of the crack tip can be written as

$$\tau(x_0, t_0) \sim \frac{K}{\sqrt{2\pi[x_0 - x_2(t_0)]}}. \tag{11.53}$$

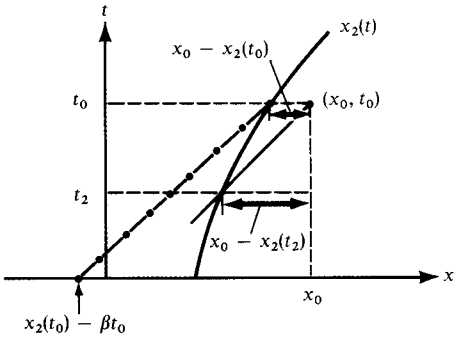

FIGURE **11.19**
Integration path for (11.55).

On the other hand, as can be seen from Figure 11.19,

$$x_0 - x_2(t_2) = \beta(t_0 - t_2),$$
$$x_2(t_0) - x_2(t_2) \sim \dot{x}_2(t_0)(t_0 - t_2),$$

and therefore

$$\frac{x_0 - x_2(t_0)}{x_0 - x_2(t_2)} \sim 1 - \dot{x}_2(t_0)/\beta. \tag{11.54}$$

Comparing (11.52), (11.53), and (11.54), we find that

$$K = \frac{\sqrt{1 - \dot{x}_2(t_0)/\beta}}{\sqrt{\pi/2}} \int_{x_2(t_0)-\beta t_0}^{x_2(t_0)} p\{x, t_0 - [x_2(t_0) - x]/\beta\} \frac{dx}{\sqrt{x_2(t_0) - x}} \tag{11.55}$$

near the crack tip, where $x_0 \sim x_2(t_2) \sim x_2(t_0)$. The integration path is a straight line, shown connecting $[t_0, x_2(t_0)]$ and $[0, x_2(t_0) - \beta t_0]$ in Figure 11.19.

In Section 11.1.2, we showed that the tip of an anti-plane crack moving with a subsonic velocity v absorbs energy at a rate given by

$$g = \frac{vK^2}{2\mu} \Big/ \sqrt{1 - \frac{v^2}{\beta^2}}. \tag{11.15 again}$$

Expressing the surface energy required to create a new unit area as G, we have

$$G = \frac{g}{2v} = \frac{K^2}{4\mu} \Big/ \sqrt{1 - \frac{v^2}{\beta^2}}.$$

Combining this equation with (11.55) (and dropping the subscript 0 from t_0), we obtain

$$K = 2\sqrt{\mu G}(1 - v^2/\beta^2)^{1/4}$$
$$= \sqrt{\frac{2}{\pi}} \sqrt{1 - v/\beta} \int_{x_2-\beta t}^{x_2} p[x, t - (x_2 - x)/\beta] \frac{dx}{\sqrt{x_2 - x}}$$

or

$$\int_{x_2-\beta t}^{x_2} p[x, t-(x_2-x)/\beta]\frac{dx}{\sqrt{x_2-x}} = \sqrt{2\mu\pi G}\left(\frac{1+v/\beta}{1-v/\beta}\right)^{1/4}, \qquad (11.56)$$

where $v = \dot{x}_2(t)$. This equation, first derived by Kostrov (1966), gives the velocity of the crack tip for given $p(x,t)$ and G. Equation (11.56) holds only when

$$\int_{x_2-\beta t}^{x_2} p[x, t-(x_2-x)/\beta]\frac{dx}{\sqrt{x_2-x}} \geq \sqrt{2\mu\pi G}.$$

Otherwise, the crack tip does not move.

Once the locus $x_2(t)$ of the crack tip is determined, $\tau(x_0, t_0)$ can be calculated by equation (11.51). Then we can use (11.45) to determine the displacement at any point. In fact, the displacement inside the crack can be determined using only the stress drop $p(x,t)$ inside the crack. To see this, we transform the variables (x,t) to (ξ,η) by equation (11.48), and rewrite (11.46) as

$$w(\xi_0,\eta_0) = \frac{1}{\pi\mu}\iint \frac{\tau(\xi,\eta)\,d\xi\,d\eta}{\sqrt{2}\sqrt{\xi_0-\xi}\sqrt{\eta_0-\eta}} \qquad \text{on } y=0^-.$$

Next, we divide the area of integration into four parts, as shown in Figure 11.20. In S_1 and S_3, $-\tau(\xi,\eta)$ is given as the stress drop $p(\xi,\eta)$. In S_2, $\tau(\xi,\eta)$ is unknown but is determined by equation (11.51) using $p(\xi,\eta)$. In the remaining parts of S_0, $\tau(\xi,\eta)$ vanishes.

From equation (11.50), for a point (ξ_1,η_1) close to the crack-tip locus but outside the crack, we have

$$\int_{\eta_2(\xi)}^{\eta_1} \frac{\tau(\xi_1,\eta)\,d\eta}{\sqrt{\eta_1-\eta}} - \int_{-\xi_1}^{\eta_2(\xi)} \frac{p(\xi_1,\eta)\,d\eta}{\sqrt{\eta_1-\eta}} = 0.$$

Our integral with respect to η for the areas S_1 and S_2 is exactly of the above form, with $\eta_0 = \eta_1$. Thus the contributions from S_1 and S_2 are zero. The only contribution comes from S_3, so that the displacement on $y = 0^-$ is

$$w(\xi_0,\eta_0) = \frac{-1}{\sqrt{2\pi}\,\mu}\int_{\xi_2(\eta_0)}^{\xi_0}\frac{d\xi}{\sqrt{\xi_0-\xi}}\int_{-\xi}^{\eta_0}\frac{p(\xi,\eta)\,d\eta}{\sqrt{\eta_0-\eta}}, \qquad (11.57)$$

where $\xi = \xi_2(\eta)$ is the locus of the crack tip in the (ξ,η) plane. The above equation, giving the fault slip $(2w)$ as a function of stress drop $p(\xi,\eta)$ and crack-tip location $\xi_2(\eta)$, was used by Ida (1973) in a study of spontaneous rupture propagation that is one of the examples we take up in the next section.

11.2.2 EXAMPLES OF SPONTANEOUS ANTI-PLANE CRACK PROPAGATION

Let us find how the equation of crack tip motion, (11.56), is solved for some simple examples.

BOX 11.3

The stress-intensity factor associated with cohesive force alone

Here we shall show that equation (11.55) can be used to derive (11.19) for the case of a crack tip moving at constant velocity.

Let the coordinate in the x-direction in a frame moving with the crack tip at a velocity v be x'. Then $x' = x - x_2(t)$, where $x_2(t) = \text{constant} + vt$.

We have previously defined p as the stress drop $\sigma_{yz}^0 - \sigma_{yz}^d$. But if a cohesive force is considered, as in (11.18), the stress on the fault plane becomes $\sigma_{yz}^d + \sigma_c$, so that the stress drop is $\sigma_{yz}^0 - \sigma_{yz}^d - \sigma_c$, i.e., it is augmented by an amount $-\sigma_c$. The effect of the cohesive force is therefore to add a stress concentration, with the stress-intensity factor derived from (11.55) by replacing p with $-\sigma_c$. The integration is limited to the region $-d \le x' \le 0$ in which $\sigma_c \neq 0$, and all this range is included in the integration limits of (11.55).

As can easily be seen from the figure,

$$x_2(t_0) - x = \frac{\beta}{v}(-x') \qquad \text{and} \qquad dx = \frac{\beta}{v}\,dx'.$$

Therefore, equation (11.55) is transformed to

$$K = -\sqrt{\frac{2}{\pi}} \int_{-d}^{0} \sigma_c(x') \frac{dx'}{\sqrt{-x'}},$$

which is the result used earlier in (11.19). Note that K is independent of v in this case.

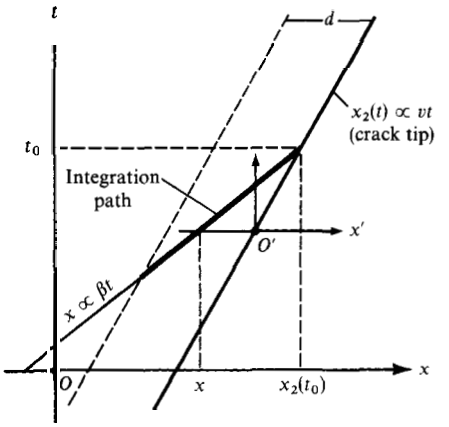

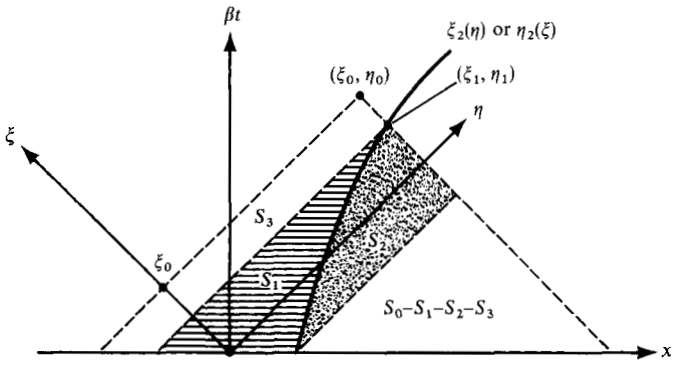

FIGURE **11.20**

A SEMI-INFINITE CRACK

Consider an unbounded body under a uniform shear stress σ_{yz}^0. A crack appears instantaneously at $t = 0$ over the half-plane $y = 0, x < 0$. Assuming that the dynamic friction is zero, a stress drop of σ_{yz}^0 occurs instantaneously for $y = 0, x < 0$. We shall find the position $x_2(t)$ of the crack tip $t > 0$ using the equation of crack-tip motion. Since

$$p(x,t) = \sigma_{yz}^0 \qquad \text{for } x < x_2(t),$$

we have from equation (11.56)

$$\int_{x_2-\beta t}^{x_2} \frac{\sigma_{yz}^0\, dx}{\sqrt{x_2 - x}} = \sqrt{2\mu\pi G}\left(\frac{1+\dot{x}_2/\beta}{1-\dot{x}_2/\beta}\right)^{1/4}. \tag{11.58}$$

The left-hand side here is equal to $2\sigma_{yz}^0\sqrt{\beta t}$. The above equation cannot be satisfied for t smaller than t_c given by

$$2\sigma_{yz}^0\sqrt{\beta t_c} = \sqrt{2\mu\pi G}, \tag{11.59}$$

and the crack tip does not propagate until time t_c. Once this time is passed, the crack-tip motion is governed by equation (11.58), i.e.,

$$\sqrt{\frac{t}{t_c}} = \left(\frac{1+\dot{x}_2/\beta}{1-\dot{x}_2/\beta}\right)^{1/4}.$$

Solving for $\dot{x}_2$ and integrating with respect to t from t_c to t, we find

$$x_2(t) = \beta t - \beta t_c\left[1 + 2\tan^{-1}\left(\frac{t}{t_c}\right) - \frac{\pi}{2}\right].$$

The crack tip starts moving at $t = t_c$ with zero initial velocity, rapidly reaching a terminal velocity β. Figure 11.21 shows the motion of the crack tip for different t_c. The solid lines correspond to the Irwin criterion in which the critical stress-intensity factor is assumed to be a material constant, independent of rupture velocity (see Problem 11.3). The step-like curves are obtained by a numerical method that is discussed later.

A SEMI-INFINITE CRACK THAT STOPS

The above classic example given by Kostrov (1966) was extended by Husseini *et al.* (1975) to include the stopping of crack-tip motion. The crack-tip motion can be stopped by placing a barrier of high surface energy along the fault plane or by limiting the prestressed region to a finite size. In either case, the following condition is imposed on the stress drop $p(x,t)$ over the initial semi-infinite crack:

$$\begin{aligned} p(x,t) &= 0 \qquad \text{for } x < -a \text{ and } t > 0, \\ &= p_0 \qquad \text{for } -a < x < x_2(t) \text{ and } t > 0, \end{aligned}$$

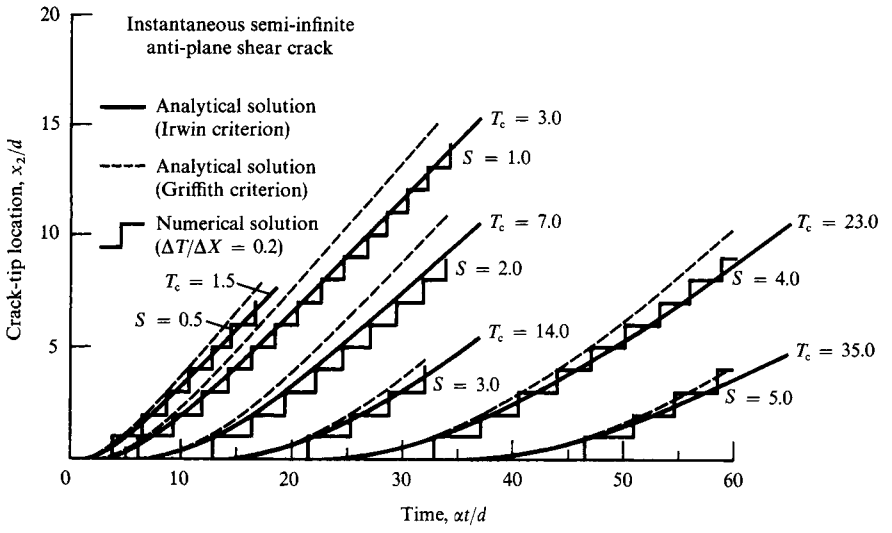

FIGURE **11.21**
The crack-tip location x_2 as a function of time for various values of T_c, where $T_c = \alpha t_c/d$, α is the compressional wave velocity, t_c is the rupture starting time defined in (11.59), and d is the grid length used in the numerical solution described in Section 11.2.3. S is the parameter of a fracture criterion used in the numerical solution, and $1 + S = S_c/(\sigma_{xy}^0 - \sigma_{xy}^d)$, where S_c is the critical stress difference defined in (11.78). Broken curves correspond to the criterion of constant surface energy, and solid curves to the criterion of constant critical stress-intensity factor. [From Das and Aki, 1977a.]

where p_0 is a constant. This is intended to simulate a finite crack without introducing complex multiple diffractions at crack edges. For a given p_0 and specific surface energy G_0 at $x = 0$, a must be greater than βt_c so that the rupture can be initiated. From (11.59), the condition is

$$a > \frac{\mu\pi G_0}{2p_0^2}.$$

The rupture can be stopped by making G increase with x. For example, consider a linearly increasing surface energy

$$G(x) = (1 + mx)G_0.$$

From equation (11.56), we get

$$\begin{aligned} \dot{x}_2(t) &= \beta \frac{t^2 - t_c^2(1 + mx_2)^2}{t^2 + t_c^2(1 + mx_2)^2} && x_2 - \beta t > -a \\ &= \beta \frac{(x_2 + a)^2/\beta^2 - t_c^2(1 + mx_2)^2}{(x_2 + a)^2/\beta^2 + t_c^2(1 + mx_2)^2} && x_2 - \beta t < -a. \end{aligned} \tag{11.60}$$

The stopping position of the crack tip, x_s, may be obtained from the second equation in (11.60) by setting $\dot{x}_2(t) = 0$. Then

$$x_s = \frac{a - \beta t_c}{m\beta t_c - 1}.$$

Since the solution x_s must be positive, the rate m of increase in specific energy must be greater than $(\beta t_c)^{-1}$ for the crack tip to stop. The motion of the crack tip can be obtained by solving the differential equation (11.60).

Another simple case of a barrier is a step-like increase in G:

$$\begin{aligned} G &= G_0 \qquad\qquad 0 \le x < b, \\ G &= G_0 + \Delta G \qquad b < x. \end{aligned}$$

In this case, for $x_2(t) > b$, we have

$$\dot{x}_2 = \frac{(x_2 + a)^2/\beta^2 - t_c^2[1 + (\Delta G/G_0)]^2}{(x_2 + a)^2/\beta^2 + t_c^2[1 + (\Delta G/G_0)]^2}, \tag{11.61}$$

and setting $\dot{x}_2 = 0$ we can solve for the stopping position of the tip,

$$x_s = \beta t_c[1 + (\Delta G/G_0)] - a.$$

Since $x_s \ge b$, an inequality has to be satisfied for the stopping to occur:

$$\beta t_c \left(1 + \frac{\Delta G}{G_0}\right) = \frac{\mu\pi(G_0 + \Delta G)}{2p_0^2} \ge (a + b). \tag{11.62}$$

If we put this condition into equation (11.61), we find $\dot{x}_2$ to be zero or negative. Since $\dot{x}_2$ cannot be negative physically, $\dot{x}_2$ must vanish and the equality holds in (11.62). The equality means that $x_s = b$, or that the crack tip stops immediately at b if condition (11.62) holds. If not, the tip will propagate indefinitely beyond b. For example, if $G_0 = 10^4$ erg/cm^2, $(a + b) = 1$ km, $p_0 = 10$ bar, and $\mu = 3 \times 10^{11}$ dyn/cm^2, then ΔG must be about 10^7 erg/cm^2 or greater for the rupture to stop. Furthermore, the larger the length or the larger the stress drop, the greater ΔG must be to stop the rupture.

An alternative way of stopping a rupture is to limit the size of the prestressed region. For example, consider the case in which, for $t > 0$,

$$\begin{aligned} p(x,t) &= 0 \qquad \text{for } x < -a \\ &= p_0 \qquad -a < x < x_2(t) < b \\ &= 0 \qquad b < x. \end{aligned}$$

The equation of motion (11.56) gives the crack-tip velocity as

$$\dot{x}_2 = \frac{[f(x_2,t)]^4 - \beta^2 t_c^2}{[f(x_2,t)]^4 + \beta^2 t_c^2},$$

where

$$\begin{aligned} f(x_2, t) &= \sqrt{\beta t} && x_2 < b, x_2 - \beta t > -a \\ &= \sqrt{x_2 + a} && x_2 - \beta t < -a \\ &= \sqrt{\beta t} - \sqrt{x_2 - b} && x_2 > b, x_2 - \beta t > -a \\ &= \sqrt{x_2 + a} - \sqrt{x_2 - b} && x_2 - \beta t < -a. \end{aligned}$$

From the final equation, the stopping position may be obtained by setting $\dot{x}_2 = 0$. Then

$$x_s = \frac{(a+b)^2}{4\beta t_c} + \frac{b-a}{2} + \frac{\beta t_c}{4}.$$

For example, if $b \sim a \sim \beta t_c$, then $x_s \sim b(1 + \frac{1}{4})$; but if $b \gg a \sim \beta t_c$, then $x_s \sim b(1 + b/4a)$. Thus, if the length b of the prestressed region is much greater than $\beta t_c = \mu\pi G_0/2p_0^2$, there will be a considerable overshoot of crack extension into the initially unstressed region. For typical values of the surface energy G measured in the laboratory ($\sim 10^4$ ergs/cm^2), and $\tau_0 = 10$ bar, βt_c is only 50 cm. However, as mentioned in Section 11.1.3, the real value of G for earthquakes may be around 10^8 erg/cm^2, which corresponds to values of βt_c around 5 km. Since G is expected to increase with earthquake magnitude because of increase in the zone of microcrack formation and plastic deformation, overshoot may not play a very important role in practice.

Slip-rate-dependent boundary condition on the fault

If there should be any constitutive relation between the stress and slip, or between stress and slip rate, it can be incorporated into our equation of rupture propagation. For example, Ida (1973) assumed that the stress σ_{yz} on the fault is related to the slip rate $\Delta\dot{w}$ by the following equation (see Fig. 11.22):

$$\begin{aligned} \sigma_{yz} &= \gamma\, \Delta\dot{w} && \text{for } \Delta\dot{w} \le v_c \\ &= \sigma_{yz}^{d} && \text{for } \Delta\dot{w} > v_c, \end{aligned} \tag{11.63}$$

where σ_{yz} is *total* stress acting on the fault plane, i.e., the sum of the initial stress σ_{yz}^0 and the stress increment τ_{yz} due to crack formation. The slip rate $\Delta\dot{w}$ is equal to $-2\dot{w}$ for $\dot{w}$ evaluated on $y = 0^-$ (which is the side of the fault for which we have studied displacement; see, e.g., (11.45)). Although the above constitutive relation is not very realistic, it does display a transition from ductile to brittle behavior. This may grossly simulate the behavior of an earthquake fault on which creep and dynamic failure are both occurring.

Suppose we start with an initially unstressed fault. As the tectonic stress increases, slow creep may occur across the fault, and the slip rate may increase in proportion to the stress. When the slip rate reaches a certain yield limit v_c, the stress may suddenly drop to the dynamic friction level σ_{yz}^{d}, creating an earthquake.

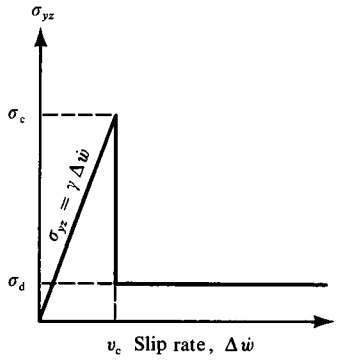

FIGURE **11.22**
Constitutive relation between the stress across the fault plane and slip rate given by (11.63). [From Ida, 1973; copyright by the American Geophysical Union.]

To incorporate the above constitutive relation into the equation of rupture propagation, we make use of

$$w(\xi_0, \eta_0) = \frac{-1}{\sqrt{2}\pi\mu} \int_{\xi_2(\eta_0)}^{\xi_0} \frac{d\xi}{\sqrt{\xi_0 - \xi}} \int_{-\xi}^{\eta_0} \frac{p(\xi, \eta)\, d\eta}{\sqrt{\eta_0 - \eta}}, \qquad \text{(11.57 again)}$$

from which we can find the slip $\Delta w = -2w$ inside the crack in terms of the stress drop p inside the crack.

Let us assume, as before, that a semi-infinite crack suddenly appears for $x < 0$ at $t = 0$. Since, for $t < -x/\beta$ or $\eta < 0$, we expect no disturbance from the crack tip, the slip will be uniform under a uniform initial stress σ_{yz}^0. The slip for $\eta < 0$ can be expressed by equation (11.57) in terms of a uniform stress drop p_0, which is to be determined by the constitutive relation (11.63). Since the integration region is bounded by $t = 0$, $\xi_2(\eta) = -\eta$ for $\eta < 0$. Then equation (11.57) can easily be integrated to give

$$w(\xi_0, \eta_0) = \frac{-1}{\sqrt{2}\pi\mu} \int_{-\eta_0}^{\xi_0} \frac{d\xi}{\sqrt{\xi_0 - \xi}} \int_{-\xi}^{\eta_0} \frac{p_0\, d\eta}{\sqrt{\eta_0 - \eta}} = -\frac{\beta p_0 t}{\mu} \qquad \text{on } y = 0^-,$$

where (11.48) has been used. From equation (11.63), we have

$$\sigma_{yz} = \sigma_{yz}^0 - p_0 = \gamma\, \Delta\dot{w} = -2\gamma\dot{w} = 2\gamma\beta p_0/\mu \qquad \text{for } \beta t < -x. \qquad (11.64)$$

This equation determines the stress drop p_0 occurring for $\beta t < -x$ in terms of the initial stress and the material constants, i.e.,

$$p_0 = \frac{\sigma_{yz}^0}{1 + 2\gamma\beta/\mu}.$$

For $\beta t > -x$ or $\eta > 0$, we can determine the stress drop $p(\xi, \eta)$ in essentially the same way as the above by solving (11.57) and (11.63) simultaneously. We must, however, use numerical methods to solve the integral equation (11.57). Since the integration range is limited to S_3, shown in Figure 11.20, the discretized integral equation can be solved in steps, in each of which the unknowns are $p(\xi_n, \eta_n)$ and $\dot{w}(\xi_n, \eta_n)$ at one discretized point

(n, m). Since $p(\xi_n, \eta_n)$ and $\Delta\dot{w} = -2\dot{w}(\xi_n, \eta_n)$ must be related by equation (11.63), the two equations can determine both p and $\Delta\dot{w}$ at the point.

In solving (11.57), the crack-tip location $\xi_2(\eta)$ must be known. Recognizing that $\xi = [\beta t - x_2(t)]/\sqrt{2}$ and $\eta = [\beta t + x_2(t)]/\sqrt{2}$ on the crack-tip locus, we have

$$\frac{d\xi_2}{d\eta} = \frac{d\xi_2/dt}{d\eta/dt} = \frac{\beta - \dot{x}_2(t)}{\beta + \dot{x}_2(t)}.$$

Then the equation (11.56) for the motion of the crack tip can be rewritten as

$$\frac{d\xi_2}{d\eta} = \frac{(2\pi\mu G)^2}{\left\{\int_{x_2-\beta t}^{x_2} p[x, t - (x_2 - x)/\beta]\dfrac{dx}{\sqrt{x_2 - x}}\right\}^4}. \tag{11.65}$$

The above equation is valid only when

$$\int_{x_2-\beta t}^{x_2} p[x, t - (x_2 - x)/\beta]\frac{dx}{\sqrt{x_2 - x}} \geq \sqrt{2\mu\pi G}, \tag{11.66}$$

otherwise the crack tip does not move and $x_2(t) = 0$. In that case,

$$\frac{d\xi_2}{d\eta} = 1. \tag{11.67}$$

The condition (11.66) can be checked by a numerical integration of discretized $p(\xi_n, \eta_n)$. Then, either (11.65) or (11.67) is used to determine the locus of the crack tip by

$$\xi_2(\eta_{m+1}) = \xi_2(\eta_m) + \frac{d\xi_2}{d\eta}\Delta\eta,$$

where $\Delta\eta$ is the grid spacing in η.

Ida (1973) made numerical calculations for various choices of the parameters v_c, γ, and σ_{yz}^d, and found two distinctly different types of rupture propagation, depending on the parameter values. One type is a smooth rupture propagation in which, once the rupture starts, the crack tip accelerates smoothly and approaches the shear velocity. An example of smooth propagation is shown in Figure 11.23. Here the time t is measured in units of $t_c = \pi\mu G/2\beta p_0^2$. This is the delay time given in (11.59), which corresponds to the stress drop given in (11.64). We discussed the magnitude of t_c in earthquakes in the previous example of a semi-infinite crack that stops. The distance x is measured in units of βt_c, and the numbers in Figure 11.23 represent $\sigma_{yz}(x, t)$ in units of p_0. The parameters are chosen as $\gamma = 2\mu/\beta$, $v_c = 2.1 \times (\beta p_0/\mu)$, and $\sigma_{yz}^d = 0$. In the case of smooth rupture propagation, the cracked region (for which $\sigma_{yz} = 0$ in this case of $\sigma_{yz}^d = 0$) extends in both directions.

For a slightly different choice of parameters, the mode of rupture propagation can be quite different. The result is shown in Figure 11.24 for $\gamma = 2\mu/\beta$, $v_c = 2.6 \times (\beta p_0/\mu)$, and $\sigma_{yz}^d = 0$. The rupture propagation is quite irregular; the crack tip moves for a short distance, then stops, restarts, and repeats the process. The fault, once cracked, can be quickly healed,

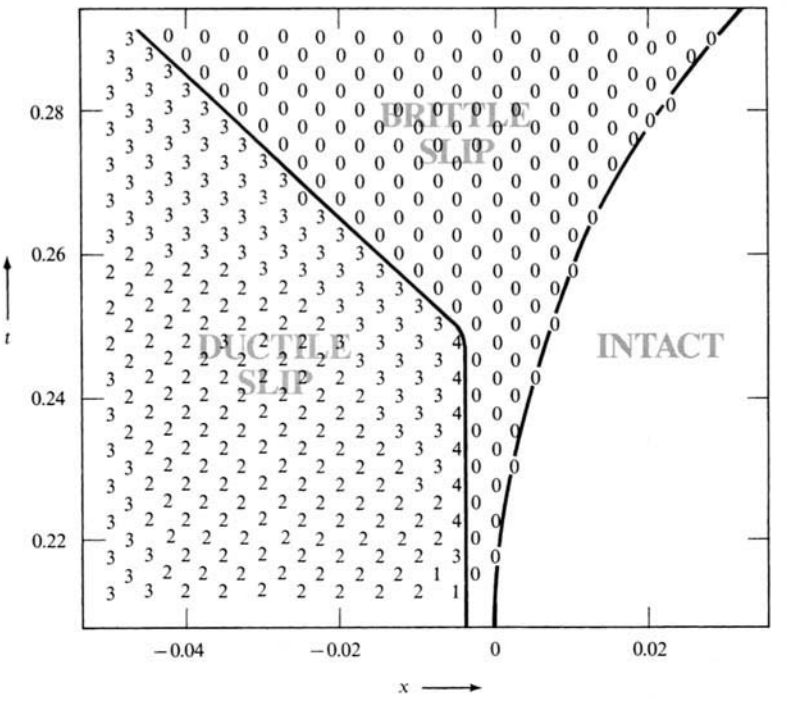

FIGURE **11.23**
Plot of $\sigma_{yz}(x, t)$ in units of p_0. A smooth propagation occurs in this case. [From Ida, 1973; copyright by the American Geophysical Union.]

because the slip rate drops below v_c. Thus the healing front follows the crack tip with a similar speed, making the effective crack length always roughly constant.

As discussed in Chapter 10, the high-frequency spectrum of seismic waves in the far field consists primarily of contributions from rupture nucleation and stopping points. We therefore anticipate a long duration of complex high-frequency waves from an irregular rupture process such as shown in Figure 11.24. On the other hand, a smooth earthquake like the one shown in Figure 11.23 will generate large long-period waves, with distinct short-period phases associated with the initial start and the final stopping points.

Ida's result indicates that the smooth type of rupture occurs when μ/β (the impedance associated with plane shear waves—see Box 5.4) is only a small multiple of p_0/v_c. Thus, roughly speaking, the smooth type of fault propagation occurs when the impedance in the creep region is higher than in the elastic region. For a given value of v_c, the smooth type of rupture occurs at lower frictional stress σ_{yz}^{d}.

Cohesionless crack

Burridge and Halliday (1971) considered an anti-plane crack that nucleates along a line at a constant depth in a homogeneous half-space. The crack propagates vertically both upward and downward. Their fracture criterion is a special case of (11.56), in which the

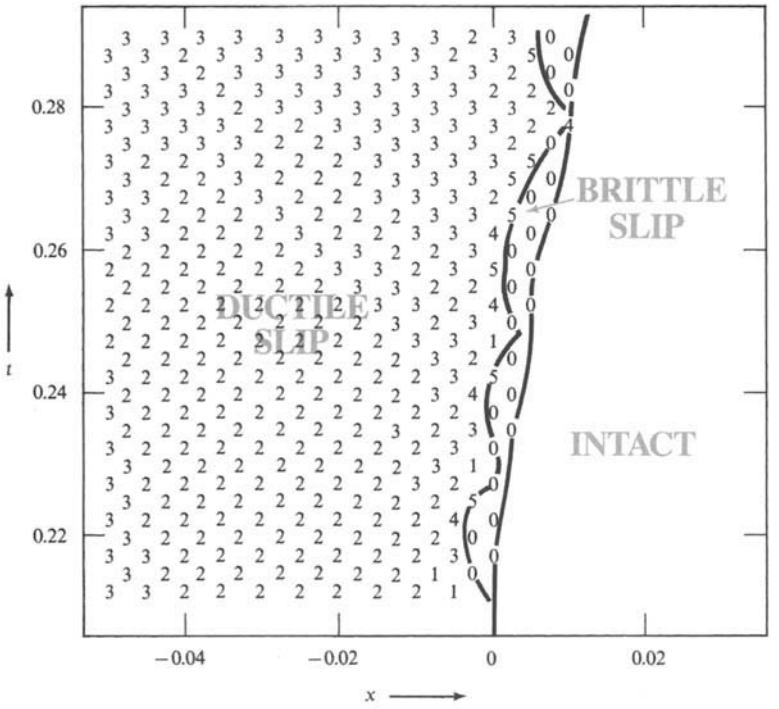

FIGURE **11.24**
Plot of $\sigma_{yz}(x,t)$ in units of p_0. A case of irregular propagation. [From Ida, 1973; copyright by the American Geophysical Union.]

specific surface energy G is set to zero. From (11.56), the condition that $G = 0$ can be met either by

$$v = \beta$$

or by

$$\int_{x_2-\beta t}^{x_2} p[x, t-(x_2-x)/\beta]\frac{dx}{\sqrt{x_2-x}} = 0. \tag{11.68}$$

Equation (11.68) is possible only if $p(x,t)$ changes sign along the above integration path. If (11.68) is not met, the crack tip must propagate with the shear velocity β. To slow down a propagating crack, therefore, one must postulate a negative stress drop. Taking the x-axis vertically downward, Burridge and Halliday considered the stress drop given by

$$p(x,t) = p_0(1 - x^2/b^2), \tag{11.69}$$

where p_0 is a constant. The crack tip propagates downward and past the depth b with the velocity β until the contribution from negative p matches that from positive p to satisfy equation (11.68). Then the crack tip moves deeper with a velocity determined by

equation (11.68). Thus the stress along the fault plane above the depth b drops to a lower value, but that below b jumps to a higher value. We shall come back to the cohesionless fracture in the discussion of in-plane cracks in the next section.

11.2.3 SPONTANEOUS PROPAGATION OF AN IN-PLANE SHEAR CRACK

Let us now consider spontaneous propagation of an in-plane shear crack. As in the anti-plane case, the crack lies on the plane $y = 0$, extending to infinity in the z-direction but confined in the x-direction between $x_1(t)$ and $x_2(t)$ at time t. For the in-plane case, the nonvanishing displacement components are $u(x, y, t)$ and $v(x, y, t)$ (see Section 10.2.4). As in the anti-plane case studied in Section 11.2.1, we assume that initially the crack is absent and that the body is in equilibrium with an initial state of stress $\boldsymbol{\sigma}^0$. We shall take this initial state as the reference state and measure the displacement relative to it. The initial conditions are then given by

$$u = v = 0 \qquad \text{and} \qquad \frac{\partial u}{\partial t} = \frac{\partial v}{\partial t} = 0 \qquad \text{for} \quad t < 0.$$

The total stress is then $\boldsymbol{\sigma} = \boldsymbol{\sigma}^0 + \boldsymbol{\tau}$. When the crack is formed, σ_{xy} on the crack drops from σ^0_{xy} to the dynamic frictional stress σ^{d}_{xy}. Putting the stress drop $\sigma^0_{xy} - \sigma^{\mathrm{d}}_{xy} = p(x, t)$, the boundary condition for incremental stress on the crack appropriate for the above choice of reference state is given by

$$\tau_{xy} = -p(x, t) \qquad x_t(t) < x < x_2(t), y = 0. \tag{11.70}$$

As shown in Section 10.2.4, the continuity of $v(x, y, t)$ and $\tau_{xy}(x, y, t)$ across $y = 0$ leads to symmetries such that $u(x, y, t)$ and $\tau_{yy}(x, y, t)$ are odd functions of y and $v(x, y, t)$ and $\tau_{xy}(x, y, t)$ are even functions of y. Since τ_{yy} is continuous across $y = 0$,

$$\tau_{yy} = 0 \qquad y = 0. \tag{11.71}$$

We need another condition on $y = 0$ outside the crack. This is given by the continuity of u. Since a continuous odd function of y must vanish at $y = 0$, we have

$$u = 0 \qquad x < x_1(t), x_2(t) < x, y = 0. \tag{11.72}$$

(11.70) and (11.72) taken together are a mixed boundary condition on $y = 0$, and (11.71) gives the other boundary condition for all x on $y = 0$. Because of the symmetry, it is sufficient to obtain a solution only in the half-space $y < 0$.

We shall define the two-dimensional Green functions $g_{x\xi}(x, y, t; \xi, y, \tau)$ and $g_{y\xi}(x, y, t; \xi, y, \tau)$, for a homogeneous half-space $y \leq 0$ with free surface at $y = 0$, as the displacement components u and v observed at (x, y, t) due to a line-impulsive force applied at (ξ, y, τ) in the ξ-direction. Then, from the representation theorem (2.43),

since our $g_{x\xi}, g_{y\xi}$ satisfy the stress-free boundary condition, and since $\tau_{yy} = 0$ on $y = 0$, we have

$$u(x, y, t) = \iint_S \tau_{xy}(\xi, \tau) g_{x\xi}(x, y, t; \xi, 0, \tau)\, d\xi\, d\tau,$$
$$v(x, y, t) = \iint_S \tau_{xy}(\xi, \tau) g_{y\xi}(x, y, t; \xi, 0, \tau)\, d\xi\, d\tau.$$

The region of integration S is, from causality, that region of the (ξ, τ) plane for which

$$\alpha^2(t - \tau)^2 - (x - \xi)^2 - y^2 \geq 0 \qquad t \geq \tau \geq 0,$$

where α is the P-wave velocity. The above representation is valid also for displacements on the crack plane $y = 0^-$, in which we are particularly interested. In this case, the region of integration is a triangle S_0 in the (ξ, τ) plane given by

$$\alpha^2(t - \tau)^2 - (x - \xi)^2 \geq 0 \qquad t \geq \tau \geq 0,$$

and we write

$$\begin{aligned} u(x, 0, t) &= \iint_{S_0} \tau_{xy}(\xi, \tau) g_{x\xi}(x - \xi, 0, t - \tau)\, d\xi\, d\tau, \\ v(x, 0, t) &= \iint_{S_0} \tau_{xy}(\xi, \tau) g_{y\xi}(x - \xi, 0, t - \tau)\, d\xi\, d\tau. \end{aligned} \tag{11.73}$$

This notation for the Green function refers to the case of a homogeneous half-space when source (ξ, η, τ) and receiver (x, y, t) are both on the free surface. Explicit formulas for $g_{x\xi}$ and $g_{y\xi}$ are easily derived by Cagniard's method (Section 6.4), and they are particularly simple when $y = \eta = 0$. The result for this case is

$$\begin{aligned} g_{x\xi}(x, 0, t) &= \frac{4\sigma^2}{\pi\mu\beta^2 x} \frac{(\sigma^2 - \beta^{-2})\sqrt{\sigma^2 - \alpha^{-2}}}{\mathsf{R}(\sigma)\mathsf{R}^*(\sigma)} && \frac{1}{\alpha} < \sigma < \frac{1}{\beta} \\ &= \frac{1}{\pi\mu\beta^2 x} \frac{\sqrt{\sigma^2 - \beta^{-2}}}{\mathsf{R}(\sigma)} && \frac{1}{\beta} < \sigma, \\ g_{y\xi}(x, 0, t) &= \frac{K_I}{\mu}\delta\left(t - \frac{x}{c_{\mathrm{R}}}\right) + \frac{2\sigma}{\pi\mu\beta^2 x} \frac{(2\sigma^2 - \beta^{-2})\sqrt{\sigma^2 - \alpha^{-2}}\sqrt{\beta^{-2} - \sigma^2}}{\mathsf{R}(\sigma)\mathsf{R}^*(\sigma)}, \end{aligned} \tag{11.74}$$

where $\sigma = t/x$, β is the velocity of shear waves, R is the Rayleigh function

$$\mathsf{R}(\sigma) = (2\sigma^2 - \beta^{-2})^2 - 4\sigma^2\sqrt{\sigma^2 - \alpha^{-2}}\sqrt{\sigma^2 - \beta^{-2}},$$

R^* and K_I are defined by

$$\mathsf{R}^*(\sigma) = (2\sigma^2 - \beta^{-2})^2 + 4\sigma^2\sqrt{\sigma^2 - \alpha^{-2}}\sqrt{\sigma^2 - \beta^{-2}},$$

$$K_I = \frac{(2\beta^2/c_{\mathrm{R}}^2 - 1)^3}{\dfrac{16\beta^2}{c_{\mathrm{R}}^2}\left[1 - \left(6 - 4\dfrac{\beta^2}{\alpha^2}\right)\dfrac{\beta^2}{c_{\mathrm{R}}^2} + 6\left(1 - \dfrac{\beta^2}{\alpha^2}\right)\dfrac{\beta^4}{c_{\mathrm{R}}^4}\right]},$$

and c_{R} is the velocity of Rayleigh waves ($\mathsf{R}(c_{\mathrm{R}}^{-1}) = 0$). Equation (11.74) was first derived by Lamb (1904).

If $\tau_{xy}(\xi, t)$ were known on the whole x-axis, equation (11.73) would give the solution of the problem. From the boundary condition (11.70), however, the stress component (11.72) is known only on the crack surface. Outside the crack, the boundary condition (11.72) is a constraint on the displacement component u. Separating the region of integration S_0 in (11.73) into a part S_1 inside the crack $[x_1(t) < x < x_2(t)]$, for which τ_{xy} is known by (11.70), and a part S_2, we can rewrite the condition (11.72) as

$$\iint_{S_1} p(\xi, \tau) g_{x\xi}(x - \xi, 0, t - \tau)\, d\xi\, d\tau \tag{11.75}$$

$$= \iint_{S_2} \tau_{xy}(\xi, \tau) g_{x\xi}(x - \xi, 0, t - \tau)\, d\xi\, d\tau \qquad \begin{matrix}\text{for } x < x_1(t) \\ \text{or } x_2(t) < x.\end{matrix}$$

Kostrov (1975) obtained an analytic solution of the above equation. The result, however, is much more involved than in the case of an anti-plane crack. For example, the stress-intensity factor given by only one integration in the anti-plane case (equation (11.55)) now requires five integrations and one differentiation. Besides, the result is valid only for a crack-tip velocity less than the Rayleigh-wave velocity. It therefore appears that a numerical approach may be more satisfactory.

A sophisticated method of discretizing the integral equations (11.73) and (11.75) was described by Burridge (1969). However, a more conventional method, such as the one used by Hamano (1974), reproduces Burridge's result quite closely. In Hamano's method, the x-axis is divided into segments of equal interval d, and each segment is presumed to take the average value of stress and displacement over the segment. Then it is natural to replace the point-to-point Green function $g(x - \xi, 0, t - \tau)$ by a segment-to-segment Green function $\bar{\bar{g}}(x_i - \xi_j, 0, t - \tau)$, which is the averaged displacement over the ith segment due to the force distributed over the jth segment:

$$\bar{\bar{g}}(x_i - \xi_i, 0, t - \tau) = \frac{1}{d^2}\int_{x_i - (d/2)}^{x_i + (d/2)} dx \int_{\xi_j - (d/2)}^{\xi_j + (d/2)} g(x - \xi, 0, t - \tau)\, d\xi. \tag{11.76}$$

For $g_{x\xi}(x, 0, t)$ given in (11.74), $\bar{\bar{g}}_{x\xi}(x, 0, t)$ can be obtained in a compact form, as given in Das and Aki (1977a). Using the averaged Green function, the integral equation (11.75) can be discretized as

$$\sum_{\substack{j \\ \text{in } S_1}} \sum_{l} p(\xi_j, \tau_l)\bar{\bar{g}}_{x\xi}(x_i - \xi_j, t_k - \tau_l) = \sum_{\substack{j \\ \text{in } S_2}} \sum_{l} \tau_{xy}(\xi_j, \tau_l)\bar{\bar{g}}_{x\xi}(x_i - \xi_j, t_k - \tau_l) \quad \begin{matrix} \text{for } x_i < x_1(t_k) \\ \text{or } x_2(t_k) < x_i. \end{matrix} \tag{11.77}$$

The order of solving the above set of equations in Hamano's method can be arranged so that there is only one unknown, $\tau_{xy}(\xi_j, \tau_l)$, when each equation is solved. Once τ_{xy} is determined for the whole region, the displacement can be calculated by the discretized equation (11.73).

So far, we have been proceeding as if the locations of crack tips $x_1(t)$ and $x_2(t)$ were known. But these locations are determined by some fracture criterion. The simplest criterion that can be easily incorporated in the discretized formulation (11.77) is to monitor the stress difference between the neighboring grid points that bracket the position of the crack tip. The total stress at the point inside the crack is known to be σ_{xy}^{d}, and that outside is determined as $\sigma_{xy}^{0} + \tau_{xy}$ by solving (11.77) for the incremental stress τ_{xy}. Thus the excess of stress outside the crack over that inside is $\tau_{xy} + \sigma_{xy}^{0} - \sigma_{xy}^{\mathrm{d}} = \tau_{xy} + p$. As soon as this stress difference exceeds a certain limit S_{c}, i.e.,

$$\tau_{xy} - \sigma_{xy}^{\mathrm{d}} + \sigma_{xy}^{0} \geq S_{\mathrm{c}}, \tag{11.78}$$

we presume that rupture takes place. The crack tip advances beyond the point at which the stress difference had been exceeded, and the stress at the point is set to σ_{xy}^{d}. The stress difference across the crack tip may be considered as a smeared-out stress concentration. We know from equation (11.7) that the stress concentration takes the form

$$\sigma = \frac{K'}{\sqrt{2\pi x'}} H(x'),$$

where $x' = x - vt$ is the distance measured from the crack tip and K' is the stress-intensity factor for in-plane cracks. Suppose that the crack tip lies halfway between two grid points as shown in Figure 11.25. Then the average stress over the grid immediately outside the tip will be

$$\bar{\sigma} = \frac{1}{d}\int_0^d \frac{K'}{\sqrt{2\pi x'}}\, dx' = 2\frac{K'}{\sqrt{2\pi d}}.$$

In Box 11.2, we introduced Irwin's fracture criterion, which is based on the critical intensity factor K_{c}. The critical average stress $\bar{\sigma}$ over the grid immediately outside the tip corresponding to K_{c} may be written as

$$S_{\mathrm{c}} = 2\frac{K_{\mathrm{c}}}{\sqrt{2\pi d}}. \tag{11.79}$$

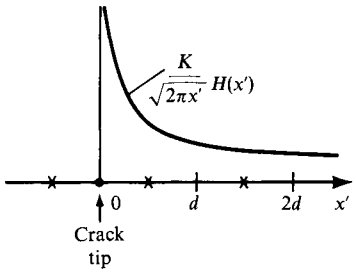

FIGURE **11.25**
Grid points are shown by X symbols.

Das and Aki (1977a) compared a numerical solution based on the criterion for S_c and an analytic solution based on the criterion for K_c for the case of a semi-infinite, anti-plane crack. Figure 11.21 shows the analytic solution as solid curves and the numerical solution as step-like curves. The symbol T_c attached to the analytic solution is the rupture starting time t_c defined in (11.59), normalized to α/d as $T_c = \alpha t_c/d$. For an anti-plane crack the critical stress intensity factor K_c may be obtained by setting $v = 0$ in (11.22), i.e., $K_c^2 = 4\mu G$. Then, from (11.59), we have $\beta t_c = (\pi/2)K_c^2/(2\sigma_{yz}^2)^2$. The parameter S, used to specify the numerical solution, is related to S_c by $1 + S = S_c/(\sigma_{yz}^0 - \sigma_{yz}^d)$. If our assumed relation (11.79) is correct, we should find the relation between T_c and S is $T_c = (\pi/4)^2(\alpha/\beta)(1 + S)^2 \sim 1.07\,(1 + S)^2$, where we take into account the assumption $\sigma_{yz}^d = 0$ made in deriving (11.59). Figure 11.21 shows that equation (11.79) gives a good approximation to the actual value for large S. For small S, the constant factor in (11.79) must be slightly larger than 2. For the range of S from 0.5 to 5, the appropriate value of the constant varies from 2.10 to 2.53. For a given S_c, S can be increased by making the grid length smaller.

Thus the fracture criterion for the critical stress difference S_c may be approximately the same as the fracture criterion for the critical intensity factor, which we called Irwin's criterion in Box 11.2. As discussed in the Box, the Irwin and Griffith criteria are equivalent as far as the initiation of crack extension is concerned. However, for a finite rupture velocity, the two criteria are different, and the fracture criterion by S_c is not exactly the same as the Griffith criterion, resulting in different crack-tip motions as shown in Figure 11.21.

Das (1980) extended Hamano's discretization method to determine the slip function for general three-dimensional motion—that is, for slip in two dimensions on a fault plane within a homogeneous whole space, radiating a mix of anti-plane and in-plane motions into three dimensions. In some respects the problem is simpler than the analysis of shear stress by (11.77), and the subsequent determination of fault slip, because for the three-dimensional problem the basic Green functions corresponding to (11.74) are simpler. These 3D Green functions, the solutions to Lamb's problem for a point source when both source and receiver lie in the surface of a homogeneous half-space, become zero once the Rayleigh waves have passed. This results in a great reduction of the memory needed to store the Green functions, unlike the two-dimensional problem with a line source where the disturbance never ceases. The two-dimensional problem is of course simpler in physical terms because of the reduced number of relationships between stress and strain.

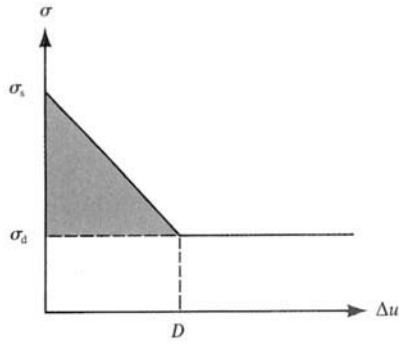

FIGURE **11.26**
Relation between shear stress and slip used by Ida (1972) and Andrews (1976). The static friction is σ_s: at this upper level of friction, instability begins and weakening occurs. For slip greater than D, stress drops to the dynamic friction level, σ_d. The shaded area corresponds to surface energy, i.e., the work done against the cohesive force (see Section 11.1.3). [After Andrews, 1976; copyright by the American Geophysical Union.]

Andrews (1976) used Ida's description of cohesive force to introduce the Griffith criterion (Section 11.1.3) into a finite-difference calculation of the in-plane shear-crack propagation. He assumed that traction across the fault plane is related to the slip Δu by the following formulas (see Figure 11.26):

$$\begin{aligned} \sigma(\Delta u) &= \sigma_s - (\sigma_s - \sigma_d)\,\Delta u/D \qquad && \Delta u < D, \\ \sigma(\Delta u) &= \sigma_d && \Delta u \geq D, \end{aligned} \tag{11.80}$$

where σ_s is the static friction, σ_d is the dynamic friction, and D is the slip required for stress to drop to σ_d. This is an example of what has come to be called a "slip-weakening" law. More specifically, it is a slip-weakening law with a constant weakening rate. The inelastic work done at the rupture front in excess of the work done against the dynamic frictional stress σ_d is identified as the specific surface energy (for each unit surface of newly created crack),

$$G = \tfrac{1}{4}(\sigma_s - \sigma_d)D. \tag{11.81}$$

The boundary condition on the fault plane must next be described. When the crack is not slipping,

$$\frac{\partial\,\Delta u}{\partial t} = 0 \qquad \text{and} \qquad |\sigma^0_{xy} + \tau_{xy}| \leq \sigma(\Delta u);$$

and during slip,

$$\frac{\partial\,\Delta u}{\partial t} \neq 0 \qquad \text{and} \qquad \sigma^0_{xy} + \tau_{xy} = \sigma(\Delta u)\ \text{sign}\left(\frac{\partial\,\Delta u}{\partial t}\right).$$

With this boundary condition, the propagation of a crack expands symmetrically in both the $+x$ and $-x$ directions. The results are discussed in terms of two nondimensional numbers: L_c/L and $(\sigma_s - \sigma_0)/(\sigma_0 - \sigma_d)$, where σ_0 is the initial stress σ^0_{xy} and L_c is the critical half-length of an in-plane Griffith crack, which can be obtained from equation (11.16).

Taking the limit as $v \to 0$, the critical stress intensity factor K_c will satisfy the following equation:

$$\begin{aligned} G &= \frac{g}{2v} \\ &= \frac{1}{16}\frac{K_c^2}{\mu\beta^2}\lim_{v\to 0}\frac{v^2}{\left(1-\frac{v^2}{\alpha^2}\right)^{1/2}-\left(1-\frac{v^2}{2\beta^2}\right)^2\left(1-\frac{v^2}{\beta^2}\right)^{-1/2}} \\ &= \frac{K_c^2}{8\mu}\frac{\lambda+2\mu}{\lambda+\mu}. \end{aligned} \tag{11.82}$$

From equation (9) of Box 11.1, the stress-intensity factor K' is related to the crack half-length L by $K' = (\sigma_0 - \sigma_d)\sqrt{\pi L}$. Therefore, the critical half-length L_c is given by

$$L_c = \frac{8\mu(\lambda+\mu)G}{\pi(\lambda+2\mu)(\sigma_0-\sigma_d)^2}. \tag{11.83}$$

Das and Aki (1977a) solved the same problem using Hamano's method, with the fracture criterion based on S_c, discussed earlier. In their case, L_c can be calculated by putting the value of K_c obtained from (11.79) into $K = (\sigma_0 - \sigma_d)\sqrt{\pi L}$ to find

$$L_c = d\frac{S_c^2}{2(\sigma_0-\sigma_d)^2}. \tag{11.84}$$

The other parameter, $(\sigma_s - \sigma_0)/(\sigma_0 - \sigma_d)$, is nothing but the parameter S used in the discussion of Figure 11.21:

$$S = \frac{S_c}{\sigma_0-\sigma_d} - 1 = \frac{\sigma_s-\sigma_d}{\sigma_0-\sigma_d} - 1 = \frac{\sigma_s-\sigma_0}{\sigma_0-\sigma_d}. \tag{11.85}$$

The results of calculation by the two methods agree in general, and only Andrew's result is reproduced in Figure 11.27. There are two distinct styles of rupture propagation. If the parameter S is greater than about 1.63, the velocity of rupture propagation is always less than the Rayleigh-wave velocity c_R, and the velocity approaches c_R as the crack length increases. On the other hand, if S is less than 1.63, the rupture starts with sub-Rayleigh velocity. But as the crack length exceeds a certain limit (which depends on S), the rupture velocity exceeds the shear velocity and approaches the P-wave velocity as the crack length increases. The critical value of $S = 1.63$ was obtained by Burridge (1973), using the cohesionless fracture criterion discussed in the example of anti-plane crack propagation (see the last part of Section 11.2.2). The cohesionless crack cannot propagate at velocities lower than the Rayleigh-wave velocity because of its inability to sustain any stress singularity. It can propagate with the Rayleigh velocity, at which speed the stress-intensity factor is zero. Burridge, however, showed that even at the Rayleigh velocity, the stress ahead of the crack at the S-wave front may exceed the static friction if S is less than 1.63. In that case, the admissible speed of the crack tip is the P-wave velocity. In Section 11.1.2, we concluded from the study of energetics at the crack tip that the speed of an in-plane crack cannot

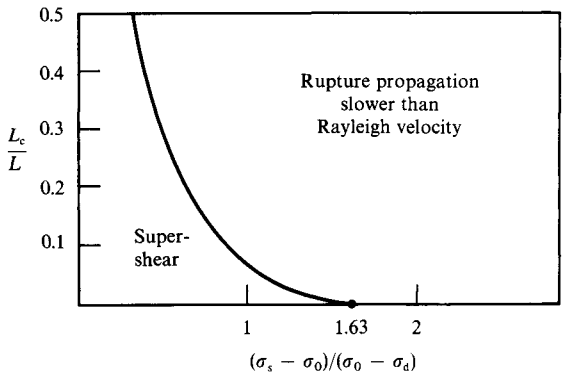

FIGURE **11.27**
Showing separate regions in which rupture propagates with sub-Rayleigh velocity, and with super-shear velocity. [After Andrews, 1976; copyright by the American Geophysical Union.]

exceed the Rayleigh-wave velocity. For a cohesionless crack, the stress-intensity factor is always zero and there is no energy flow through the crack tip. Therefore, the conclusion from the energetics does not apply to a cohesionless crack. A more difficult question is why the numerical solutions, which apparently involve a finite energy flow through the crack tip (as demonstrated by the agreement with analytic solutions for such cases), show rupture-propagation velocities exceeding that of Rayleigh waves. The answer lies in their fracture criterion, in which the initiation of fault slip does not require an infinite stress but only a finite stress, Thus, the stress associated with P- and S-waves propagating ahead of a crack tip can cause the fault slip. Hence we may say that the super-Rayleigh-wave velocity propagation is a consequence of finite cohesive forces.

The finite cohesive force has another important consequence on what happens when the rupture propagates along a fault plane with obstacles or barriers. These barriers may be expressed by a localized high value of S_c defined in (11.78). Das and Aki (1977b) found that three different situations can occur when a crack tip passes such a barrier, depending on the relative magnitude of barrier strength to initial stress:

(i) If the initial stress is relatively high, the barrier is broken immediately.

(ii) If the initial stress is relatively low, the crack tip proceeds beyond the barrier, leaving behind an unbroken barrier.

(iii) If the initial stress is intermediate, the barrier is not broken at the initial passage of the crack tip, but eventually breaks due to a later increase in stress.

If the barrier encounter of type (i) occurs throughout the fault plane, rupture propagation is smooth, generates a simple impulsive seismic signal, and results in a high average stress drop. On the other hand, if the type (ii) encounter occurs at many barriers, rupture propagation becomes rough, generates a long sequence of high-frequency waves, and ends up with a low average stress drop. Type (iii) propagation generates seismograms with ripples superimposed on long-period motion. The seismic radiation becomes less dependent on direction of rupture propagation than others, because the slip on the central part of the crack occurs more or less simultaneously, resulting in an effectively symmetric source. Similar results were obtained by Mikumo and Miyatake (1978), who studied rupture propagation over a fault plane with a two-dimensional nonuniform distribution of static friction.

Thus, a variety of rupture processes can be generated by distributing a number of barriers with different strengths on the fault plane to serve as more complex models of actual earthquakes. The fault model with barriers is particularly important for the study of short-period motions from a large earthquake, because it is associated with strong ground motion in the frequency band that is most damaging to man-made structures.

Our numerical methods of solving for fault slip in this chapter have included both finite difference methods as in Section 11.1.5, in which seismic motions are propagated throughout a volume, and so-called boundary integral methods such as those of the present Section 11.2.3, in which calculations of displacement and stress are confined only to the plane of the fault itself (via (11.73) and (11.75)). Bizzarri *et al.* (2001) have thoroughly studied the slip distribution for two-dimensional in-plane shear rupture governed by the slip-weakening law shown in Figure 11.26, and also by more general rate- and state-dependent friction laws proposed by Dieterich and Ruina. They find the two numerical methods of solving for fault slip lead to identical solutions if care is taken to ensure numerical stability and adequate resolution. Their boundary integral method, developed by Andrews (1985), was faster than their finite difference method.

11.3 Rupture Propagation Associated with Changes in Normal Stress

Many times in the solutions discussed above we have made use of the fact that shear discontinuities on a planar fault surface, in a homogeneous isotropic elastic whole space, cannot change the normal stress on the fault. See Problem 10.2. (This constancy of normal stress does not mean that the original planar fault surface stays flat. In practice it warps during slip in a fashion that keeps the normal stress unchanged.) The constancy of normal stress simplifies the discussion of shearing stresses on the fault plane, since in practice we can relate shearing stress via a coefficient of friction to the normal stress. Because the normal stress cannot change, changes in the coefficient of friction are directly reflected as changes in the shear stress. But this simplification is lost if the fault surface is nonplanar, or if the fault surface is itself a material discontinuity between media with different elastic moduli, or if the fault is shallow. In the latter case, seismic motions will be reflected from the Earth's free surface, back down into the source region. If the reflections reach the fault while it is still in the process of slipping, then the normal stress on the fault will be changed in ways that can influence the process of slip. In this section, we briefly review each of these three possibilities for changing the normal stress.

If the fault surface is bumpy, then resistance to slip may be greater due to the possibilities of indentation of material on one side of the fault into the other. Conceptually such a fault can lock, and a new plane of weakness can develop nearby. Models of such an asperity can be developed in terms of a spatially varying coefficient of friction applied over a planar fault, so that greater shear stress is needed to accomplish slip near the location of the indentation. But such an approach does not reproduce the fact that normal stress across the fault will change as an asperity begins to slip. Bouchon and Streiff (1997) considered a generalized version of the spontaneous rupture model discussed above in Section 11.2. They allowed for nonplanar faulting by assuming that shear stress at the time of nucleation drops from its initial static level to the value given by a dynamic coefficient of friction times the original normal stress. For a fault with a bend, their boundary integral method allows for friction

that varies as the dynamic normal stress changes continuously. But Tada and Yamashita (1996) have pointed out fundamental differences in behavior for in-plane shear cracks that are nonplanar, between cracks that change their orientation smoothly from point to point, and cracks with an abrupt kink (discontinuous change in fault normal). They found that the normal stress along a smoothly curved crack differs from that along a chain of line segments connected at abrupt kinks (the chain being a discrete version of the smooth variation).

Faults that have endured numerous earthquakes over millions of years can accumulate many kilometers of offset, bringing rocks of quite different composition—and different elastic properties—into contact. When a new episode of slip occurs across a surface that is also a material discontinuity, the resulting wavefields are significantly more complicated than the usual P and S body waves. For example, head waves can propagate along the faster side of the interface, delivering energy into the slower (more compliant) medium by refraction at a critical angle. This energy arrives earlier and from a different direction than would be the case if slip occurred only within a homogeneous block of the slower medium. Ben-Zion and Malin (1991) showed for the San Andreas fault, in central California, that such head waves have sometimes been misinterpreted as body waves arriving directly from an earthquake hypocenter, leading to erroneous estimates of the hypocenter location. Weertman (1980) showed that for a dislocation moving along a material interface at constant speed, the change in normal stress increases with increasing dislocation velocity up to the speed of the S-wave in the slower medium. Andrews and Ben-Zion (1997) used a finite difference method for two-dimensional plane strain to study slip between materials that had a 20% contrast in elastic wave speeds, and found features similar to those predicted by Weertman. They showed that a self-sustaining and spatially narrow pulse of slip, associated with a tensile change of normal stress, could propagate at about the velocity of the slower S-wave speed. The direction of propagation is always the same as the direction of slip in the slower medium.

The phenomenon of tensile changes in normal stress has also been found for slip on planar faults in homogenous media. These tensile changes, which can be large enough to cause separation of the two surfaces of the fault, arise in laboratory experiments conducted by Brune and coworkers. They used foam rubber blocks in a geometry that simulated shallow-angle thrust faulting. Mora and Place (1994) modeled the geometry of the foam block experiments using a numerical lattice model, and also found interface waves associated with tensile changes in normal stress that tended to separate the fault surfaces. The reason for such changes in normal stress is presumably the interaction between fault motions on the shallow fault and motions reflected from the free surface, which cause tensile changes on the fault plane. Brune *et al.* (1993) found that the observed particle motions show several features very different from those commonly found for planar dislocations within a whole space. Interface waves associated with fault opening propagate updip along the thrusting fault plane, and temporarily decouple the hanging wall from the foot wall. Seismic energy becomes trapped in the overlying wedge, and consequently the particle motions are asymmetrical, being far greater in the hanging wall than the foot wall. The energy becomes increasingly concentrated toward the tip of the upper wedge—the toe of the hanging wall—leading to what these experimenters call spectacular breakout phases when the rupture reaches the free surface. Their results suggest that the seismic hazard of great subduction zone thrust earthquakes, and continental shallow angle thrust faults, may

be significantly greater than would be predicted by standard dislocation models that do not take into account the interactions of fault rupture with a nearby free surface.

Throughout our chapters on source theory, we have focused on models that apply to individual earthquakes. For each such model we have sought to explain how its associated fault slip and radiated motions can be analyzed. We have avoided the obvious fact that earthquakes occur in the setting provided by previous earthquakes. But each earthquake changes the stress environment in which it was triggered, dropping the stress over length scales comparable to the width and length of the fault-ruptured area. Each new earthquake, whether large or small, occurs in the inhomogeneous initial stress established by all its predecessors, though typically increased by tectonic loading. It is therefore of interest to determine how the balance is maintained between large earthquakes, which presumably tend to reduce stresses over wide regions, and small earthquakes, which introduce short wavelength inhomogeneities into the stress field. These underlying characteristics of the environment in which individual earthquake occur will determine the size of each new earthquake in a sequence. The overall relationship between earthquakes of different sizes may be governed by the principles of self-organized criticality. Earthquakes show properties that we still do not understand. It is a challenge to bring the wide range of observed earthquake phenomena into a complete and satisfactory framework established on basic physical principles.

Suggestions for Further Reading

Achenbach, J. D. On dynamic effects in brittle fracture. In *Mechanics Today*, vol. 1, edited by S. Nemat-Nasser, New York: Pergamon Press, 1974.

Andrews, D. J. Dynamic plane-strain shear rupture with a slip-weakening friction law calculated by a boundary integral method. *Bulletin of the Seismological Society of America*, **75**, 1–21, 1985.

Ben-Zion, Y., and D. J. Andrews. Properties and implications of dynamic rupture along a material interface. *Bulletin of the Seismological Society of America*, **88**, 1085–1094, 1998.

Bizzarri, A., M. Cocco, D. J. Andrews, and E. Boschi. Solving the dynamic rupture problem with different numerical approaches and constitutive laws. *Geophysical Journal International*, **144**, 656–678, 2001.

Bouchon, M., and D. Streiff. Propagation of a shear crack on a non-planar fault: A method of calculation. *Bulletin of the Seismological Society of America*, **87**, 61–66, 1997.

Cochard, A., and R. Madariaga. Dynamic faulting under rate-dependent friction. *Pure and Applied Geophysics*, **142**, 419–445, 1994.

Das, S., J. Boatwright, and C. H. Scholz, eds. *Earthquake Source Mechanics*. Geophysical Monograph 37, Maurice Ewing Series, vol. 6. Washington, D.C.: American Geophysical Union, 1986.

Dieterich, J. H. A model for the nucleation of earthquake slip. In *Earthquake Source Mechanics*, edited by S. Das, J. Boatwright, and C. H. Scholz. Geophysical Monograph 37, Maurice Ewing Series, vol. 6, 37–47. Washington, D.C.: American Geophysical Union, 1986.

Ellsworth, W. L., and G. C. Beroza. Seismic evidence for an earthquake nucleation phase. *Science*, **268**, 851–855, 1995.

Freund, L. B. Crack propagation in an elastic solid subject to general loading. II. Non-uniform rate of extension. *Journal of Mechanics and Physics of Solids*, **20**, 141–152, 1972.

Freund, L. B. The mechanics of dynamic shear crack propagation. *Journal of Geophysical Research*, **84**, 2199–2209, 1979.

Geubelle, P., and J. R. Rice. A spectral method for 3D elastodynamic fracture problems. *Journal of Mechanics and Physics of Solids*, **43**, 1791–1824, 1995.

Liebowitz, H., ed. *A Treatise on Fracture,* vol. 2. New York: Academic Press, 1968.

Kostrov, B. V., and S. Das. *Principles of Earthquake Source Mechanics*. Cambridge University Press, 1988.

Madariaga, R. High frequency radiation from crack (stress drop) models of earthquake faulting. *Geophysical Journal of the Royal Astronomical Society*, **51**, 625–651, 1977.

Marone, C. Laboratory-derived friction laws and their applications to seismic faulting, *Annual Reviews of Earth and Planetary Sciences*, **26**, 634–696, 1998.

Orowan, E. Mechanism of seismic faulting. In *Rock Deformation*, edited by D. Griggs and J. Handin, Ch. 12. Geological Society of America, 1960.

Rice, J. R. A path independent integral and the approximate analysis of strain concentration by cracks and notches. *Journal of Applied Mechanics*, **35**, 379–386, 1968.

Rice, J. R., Y. Ben-Zion, and K. S. Kim. Three-dimensional perturbation solution for a dynamic planar crack moving unsteadily in a model elastic solid. *Journal of Mechanics and Physics of Solids*, **42**, 813–843, 1994.

Scholz, C. H. Earthquakes and friction laws. *Nature*, **391**, 37–42, 1998.

Zheng, G., and J. R. Rice. Conditions under which velocity-weakening friction allows a self-healing versus crack-like mode of rupture. *Bulletin of the Seismological Society of America*, **88**, 1466–1483, 1998.

Problems

11.1 If slip across a fault surface Σ is known as a function of position and time, is this enough to determine completely the motions throughout the medium within which the fault is situated (assuming no other source is active)? If your answer is "yes," then explain why this result is only of limited use in earthquake source theory. If your answer is "no," then describe what else must be known about the source in order to determine the motions that it radiates.

Suppose that, instead of the slip, we know the *traction* at all times on the part of the fault surface that is undergoing slip (i.e., on $\Sigma(t)$). Is this enough to determine the motion radiated away from the fault? Comment on your answer here (yes or no) in the same fashion requested above.

11.2 For the self-similar elliptical crack described in Sections 10.1.6 and 11.1.4, show that

a) the fault area grows like t^2,

b) the average slip grows like t,

c) the seismic moment grows like t^3, and hence that

d) the far-field velocity seismogram is proportional to $(t - t_P)H(t - t_P)$ near the arrival time $t = t_P$.

11.3 For a semi-infinite crack described as an example in Section 11.2.2, the stress-intensity factor K is given by

$$K = \frac{(1 - \dot{x}_2/\beta)^{1/2}}{\sqrt{\pi/2}} \int_{x_2 - \beta t}^{x_2} p(x, t - (x_2 - x)/\beta) \frac{dx}{\sqrt{x_2 - x}}$$

$$= \frac{2(1 - \dot{x}_2/\beta)^{1/2} \tau_0}{\sqrt{\pi/2}} \sqrt{\beta t}.$$

In that example, we derived the crack-tip motion assuming that the surface energy G is independent of rupture velocity. Show that if instead the critical stress intensity factor is constant (i.e., instead of G), then the crack-tip motion is given by

$$x_2(t) = \beta(t - t_c) - \beta t_c \log t/t_c.$$

This curve is shown in Figure 11.21 together with the curves corresponding to constant G.

11.4 For an in-plane tensile crack, the rupture propagation always has velocities lower than the Rayleigh velocity, even in the case of finite cohesive force. Confirm this conclusion by investigating the sense of stress associated with the P- and S-wave part of the Green function appropriate for a tensile crack.

CHAPTER 12

Principles of Seismometry

The data on which seismology depends are records of ground motion. To define ground motion carefully, we begin with a statement of what we mean by ground displacement. Consider a particle within the ground that, at time t_0, is located at $\mathbf{x} = (x, y, z)$ with respect to Cartesian axes that are fixed in an inertial reference frame. At time t, this particle has coordinates $\mathbf{u} + \mathbf{x} = (u + x, v + y, w + z)$ with respect to the same axes. The displacement $\mathbf{u} = \mathbf{u}(\mathbf{x}, t)$ is the *ground displacement.* In Chapter 2 we called this formulation the Lagrangian description of motion. An instrument that is attached at t_0 to the ground at $\mathbf{x}$ and which responds to the time-dependence of $\mathbf{u}$ is a *seismometer.* If the instrument makes a record of the ground motion, we shall often refer to it as a *seismograph.*

It is possible to measure Earth motions by a sensor fixed to an inertial reference frame. An example is the use of the radio signal from a quasar to measure ground motions by long-baseline interferometry; this has become an important tool in geodetic measurement. But all existing seismometers and seismographs are fixed to the Earth, not to an inertial reference frame. The receiver of seismic waves is moving with the object within which the waves are traveling. Furthermore, the reference frame with respect to which most seismic motions are conventionally reported is not, in fact, an inertial frame, but one that rotates steadily once every 24 hours. The fact that the observer is moving with the object during an earthquake makes the experimental aspects of seismometry distinctly different from those of most other branches of physical science.

The challenge with any seismograph is to make recordings that are a linear and time-invariant response to ground motion. Seismic signals and noises cover wide ranges of frequency and amplitude, which for most of the 1900s led to the use of numerous different types of seismographs, typically with analog recording, that faithfully measured ground motion in narrow ranges of frequency and amplitude. For example, special instruments, many of them still in use, were designed with very low sensitivity to record (without going off scale) the strong ground motion found near the epicenter of damaging earthquakes. At the other extreme, highly sensitive seismographs capable of amplifying ground displacement by a factor of about 10^6 at around 1 Hz were used at quiet sites for detecting weak signals from distant earthquakes and explosions. In Section 12.2.5 we shall describe the noise spectrum of ground motion, which includes power in the range 0.07 to 0.4 Hz due to ocean waves that couple their energy into the solid Earth. For several decades it was traditional in seismology

to design most instruments to operate either in the frequency band below this range (so-called "long-period" seismometers, most useful for the study of teleseismic surface waves and normal modes), or in the band above ocean wave noise ("short-period" seismometers, used for studying the arrival times and waveforms of teleseismic body waves, and regional waves such as P_n and L_g). But two major developments changed these traditional practices. First, beginning in the 1960s, digital recording began to replace analog. This had the immediate advantage that more sophisticated data processing became possible. Signals could be automatically detected, and they could be filtered and stacked to enhance signal-to-noise ratios. A later advantage, as sensors and digital recorders improved, was that weak and strong signals could both be faithfully recorded from the same sensor. The second major development, beginning in the 1970s, was the successful construction of sensors that maintained sensitivity across broad bands of frequency, permitting the acquisition, in one seismogram, of all the information that had previously required long-period and short-period instrumentation.

As an example of a modern broadband digital recording, Figure 12.1 shows the vertical ground motion at a station in China from an underground nuclear explosion in Kazakhstan at a distance of about 1000 km. The signal is very different in different frequency bands.

In this chapter we shall describe basic instrumentation (Section 12.1), the frequency and dynamic range of seismic signals and noises (Section 12.2), and the main features of classical and modern seismometers (Section 12.3). We still need to understand the older types of instrumentation, because they provided almost all the recordings we have of earthquakes prior to about 1980, and because they are still operating and acquiring useful data in many locations. As examples of classical or traditional instruments, we have in mind the short-period and long-period seismometers used with analog recording for the World-Wide Standardized Seismographic Network from about 1962 to the late 1980s. These instruments, and many like them in previous decades, featured an inertial sensor with a velocity transducer sending current into a galvanometer, whose output was recorded optically on paper. Modern instruments, as deployed by the Federation of Digital Seismographic Networks, including the IRIS Consortium and the U.S. Geological Survey, feature inertial sensors with feedback to improve linearity and increase bandwidth, and signals recorded digitally after being filtered to achieve a desired response (for example, flat to velocity).

FIGURE **12.1**
Broadband vertical-component seismogram of ground velocity recorded at station WMQ in China, for an underground nuclear explosion on 1989 July 8 in Kazakhstan at a distance of about 955 km, together with the results of filtering the original data with six different pass bands. The time scale begins at the source origin time. The peak signal strength is shown for each trace. Note that different seismic waves (P_n, L_g, surface waves) appear in different frequency bands, which would have required different instruments using traditional seismometry available prior to about 1980. A long period signal (0.01–0.05 Hz) can be clearly seen, about a hundred times smaller than the dominant signal (1–5 Hz). [Figure, courtesy of Won-Young Kim.]

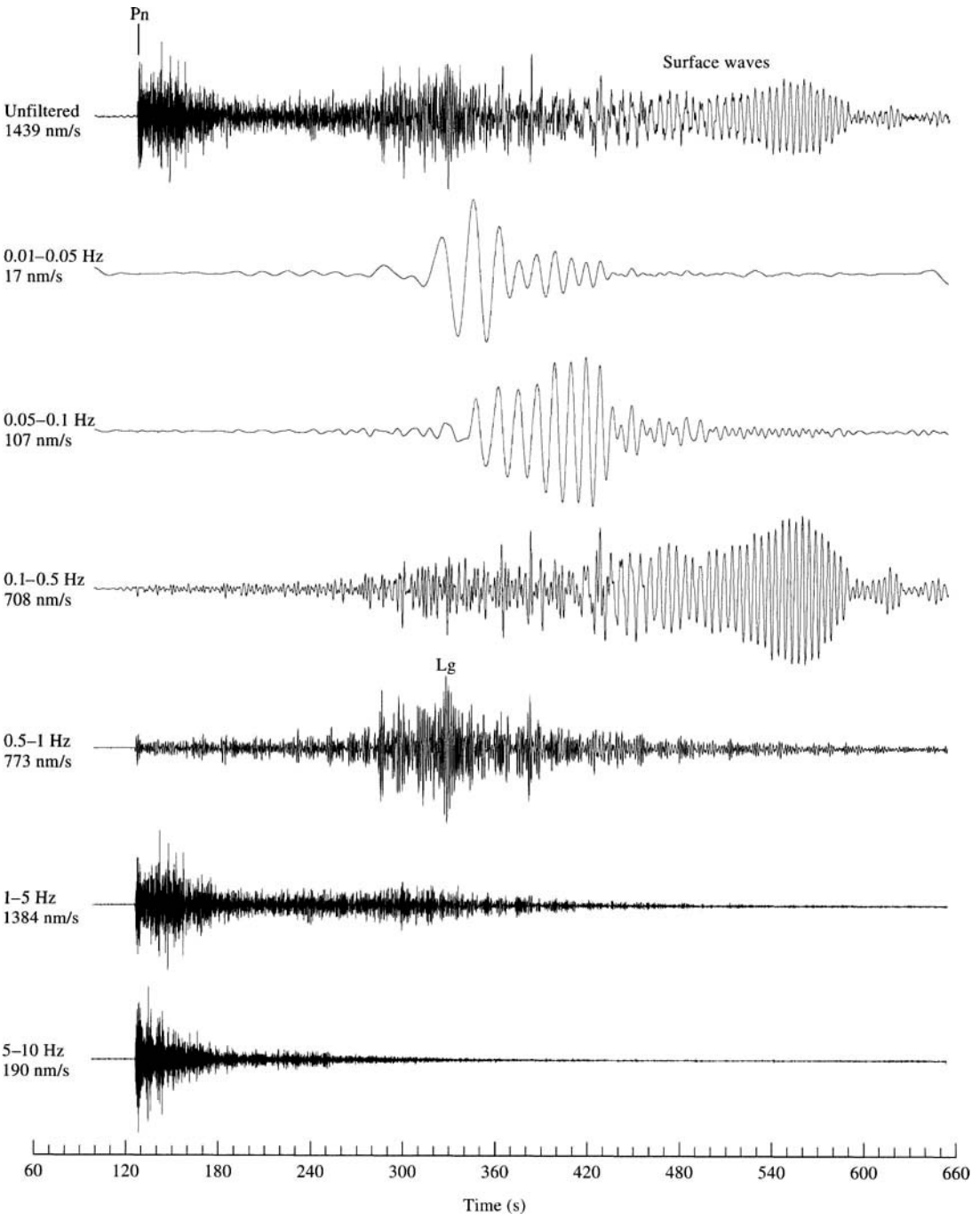
Pn
Surface waves
Unfiltered
1439 nm/s
0.01–0.05 Hz
17 nm/s
0.05–0.1 Hz
107 nm/s
0.1–0.5 Hz
708 nm/s
Lg
0.5–1 Hz
773 nm/s
1–5 Hz
1384 nm/s
5–10 Hz
190 nm/s
60
120
180
240
300
360
420
480
540
600
660
Time (s)

12.1 Basic Instrumentation

There are two basic types of measurement used routinely today to quantify seismic motion. The one most commonly used is based on the principle of inertia, and the *pendulum seismometer* is an example of an inertial sensor. The other type is based on the deformation of a small part of the Earth, and the *strainmeter,* or *strain seismometer,* is the sensor. This chapter is mostly about these two methods of measuring ground motion, and in this section we describe the two basic types of sensor. We shall later describe traditional inertial sensors introduced in the early 1900s, in which the relative velocity of the mass and its supporting frame is detected electromagnetically. We also describe modern inertial sensors, introduced in the 1970s, that incorporate feedback. And we describe a variety of strain sensors. At long period, the techniques of strain and displacement measurement, needed by seismologists, merge with the techniques of geodesy.

In principle a third type of measurement is needed in seismology and geodesy, namely the measurement of rotation, to study changes in Earth rotation associated for example with the Chandler wobble and with tidal friction, and the rotation of tectonic plates as well as the rotation carried by S-waves (Takeo and Ito, 1997). Methods of rotation measurement could be based on the conservation of angular momentum, which can find application in numerous types of sensor. In the absence of external torque, the direction of the angular momentum of a gyroscope would stay the same in an inertial reference frame, allowing the measurement of rotation of the Earth-fixed gimbal system. Another useful property of the gyroscope is its precession under the action of torque, which also could be used for detecting rotation. Such devices are commonly used in inertial navigation and are beginning to be used in geophysics for more complete descriptions of Earth motion. The motions within a torus of superfluid helium are reported by Schwab *et al.* (1997) as a way to measure Earth rotation ($\sim 15°$/hour) with a precision of around two parts in 10^5 after one hour. Their approach differs from one based on conservation of angular momentum in providing an estimate of absolute rotation. Ring laser rotational seismograms are described by McLeod *et al.* (1998), who conclude that although these instruments are far too expensive and bulky for practical field deployments, foreseeable developments may eventually permit practical applications. Pancha *et al.* (2000) report ring laser detection of rotations from teleseismic waves caused by two earthquakes (magnitudes 7.0 and 7.3).

12.1.1 BASIC INERTIAL SEISMOMETER

An inertial seismometer consists of a mass M attached to a point of the Earth through a parallel arrangement of a spring and a dashpot, as shown in Figure 12.2. Assuming that all motion is restricted to the x-direction, we denote the motion of the Earth in the inertial reference frame as $u(t)$ and the motion of mass M relative to the Earth as $\xi(t)$. The spring will exert a force proportional to its elongation $\xi - l_0$ from its zero-tension length l_0, and the dashpot will exert a force proportional to the relative velocity $\dot{\xi}(t)$ between the mass and the Earth. Representing these constants of proportionality as k and D, the equation of motion is given by

$$M\frac{d^2}{dt^2}\left[\xi(t)+u(t)\right]+D\frac{d\xi(t)}{dt}=Mg-k\left[\xi(t)-l_0\right]=-k\left[\xi(t)-\xi_0\right]. \quad (12.1)$$

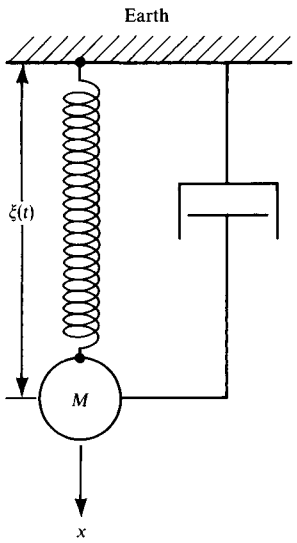

FIGURE **12.2**
A seismometer based on an inertial sensor is essentially a mass suspended by a parallel arrangement of spring and dashpot. If the initial length of the spring (with no tension) is l_0, then the equilibrium length ξ_0 for a vertical sensor is related to the spring modulus (k), to the mass (M), and to the strength of the gravitational field (g) by $k(\xi_0 - l_0) = Mg$ (used to eliminate Mg and l_0 in equation (12.1)).

Rewriting the displacement $\xi(t) - \xi_0$ relative to the equilibrium position ξ_0 as $\xi(t)$, we have

$$\ddot{\xi} + 2\varepsilon\dot{\xi} + \omega_s^2\xi = -\ddot{u} \tag{12.2}$$

where $2\varepsilon = D/M$ and $\omega_s^2 = k/M$.

The inertia sensor responds only to $\ddot{u}$, and equation (12.2) shows that we can reproduce the acceleration of Earth motion by a linear and measurable combination of $\xi(t)$ and its time derivatives. For very rapid Earth motion, the first term of the left-hand side of (12.2) dominates, and $\ddot{\xi}$ becomes nearly equal to $-\ddot{u}$. In other words, the record $\xi(t)$ reproduces the Earth's displacement $-u(t)$ if the movement is rapid. For very low frequency motion, in which the third term dominates, the term $\omega_s^2\xi$ becomes nearly equal to $-\ddot{u}$. It follows that the record $\xi(t)$ reproduces the acceleration $\ddot{u}(t)$ if the motion is slow. The sensitivity in this case is proportional to T_s^2, where $T_s = 2\pi/\omega_s$ is the undamped period of the sensor and ω_s is the corresponding undamped angular frequency.

The response of such a seismometer to sinusoidal ground displacement $u(t) = Ue^{-i\omega t}$ can be written as $UX(\omega)e^{-i\omega t}$ where U is the (constant) amplitude of the input sinusoid. $X(\omega)$ is called the *frequency-response function*, and it completely describes the performance of the sensor. In general, the input spectrum $u(\omega)$ and output spectrum $\xi(\omega)$ are related by $\xi(\omega) = u(\omega)X(\omega)$, and equation (12.2) gives

$$X(\omega) = \frac{-\omega^2}{\omega^2 + 2i\varepsilon\omega - \omega_s^2}. \tag{12.3}$$

Defining the *amplitude response* $|X(\omega)|$ and the *phase delay* $\phi(\omega)$ by

$$X(\omega) = |X(\omega)|e^{i\phi(\omega)},$$

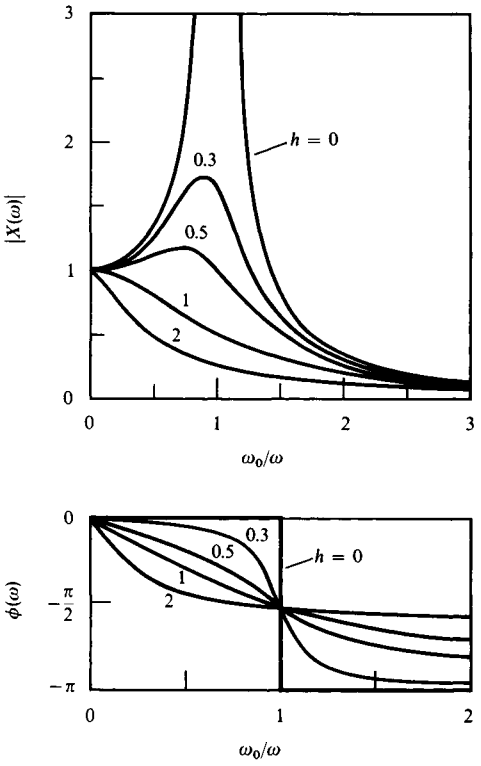

FIGURE **12.3**
Amplitude response $|X(\omega)|$ and phase delay $\phi(\omega)$ of an inertial seismometer according to (12.4). h is the dimensionless damping constant, ε/ω_s.

we find

$$|X(\omega)| = \frac{\omega^2}{\sqrt{(\omega^2 - \omega_s^2)^2 + 4\varepsilon^2\omega^2}} \quad \text{and} \quad \phi(\omega) = -\tan^{-1}\frac{2\varepsilon\omega}{\omega^2 - \omega_s^2} + \pi. \tag{12.4}$$

For $\omega \gg \omega_s$, $|X(\omega)| \to 1$ and $\phi(\omega) \to \pi$. In other words, the sensor displacement ξ records the ground displacement faithfully at low frequencies, but with reversed sign. The sign difference is usually eliminated by indicating the direction of ground motion properly on the record. Figure 12.3 shows $|X(\omega)|$ and $\phi(\omega)$ without the π term in (12.4). The curves are shown with $h = \varepsilon/\omega_s$ as a parameter; h is the *damping constant,* equal to half the reciprocal of the Q-value (the quality factor of a damped oscillator).

The performance of an inertial seismometer can also be completely described by its response $f(t)$ to a unit impulsive acceleration $\ddot{u}(t) = \delta(t)$, the Dirac δ-function. From equation (12.2), $f(t)$ satisfies

$$\ddot{f} + 2\varepsilon\dot{f} + \omega_s^2 f = -\delta(t). \tag{12.5}$$

Taking the Fourier transform of both sides of (12.5) and putting

$$\int_{-\infty}^{\infty} f(t)e^{i\omega t}\,dt = f(\omega), \tag{12.6}$$

we have

$$f(\omega) = \frac{-1}{-\omega^2 - 2i\varepsilon\omega + \omega_s^2}. \tag{12.7}$$

Since $f(\omega) = -X(\omega)/\omega^2$, the frequency-response function can be obtained from the impulse-response function by the Fourier transform, and vice versa. From the inverse transform of (12.6),

$$f(t) = \frac{1}{2\pi}\int_{-\infty}^{\infty} \frac{e^{-i\omega t}\,d\omega}{\omega^2 + 2i\varepsilon\omega - \omega_s^2} = \frac{1}{2\pi}\int_{-\infty}^{\infty} \frac{e^{-i\omega t}\,d\omega}{(\omega - \omega_1 + i\varepsilon)(\omega + \omega_1 + i\varepsilon)}, \tag{12.8}$$

where $\omega_1^2 = \omega_s^2 - \varepsilon^2$. If we extend ω to the complex ω-plane, we find that poles of the integrand always lie in the lower half-plane because $\varepsilon > 0$. Then, for $t < 0$, the integral along the real axis can be replaced by one around the infinite semicircle in the upper half-plane, which vanishes because of the factor $|\exp(-i\omega t)| = \exp(+\mathrm{Im}\{\omega t\})$. Thus

$$f(t) = 0, \qquad t < 0. \tag{12.9}$$

For $t > 0$, the residue contribution from the poles gives, in the case $\omega_s > \varepsilon$,

$$f(t) = \frac{-1}{\omega_1} e^{-\varepsilon t} \sin \omega_1 t, \tag{12.10}$$

and in the case $\omega_s < \varepsilon$,

$$f(t) = \frac{-1}{2\sqrt{\varepsilon^2 - \omega_s^2}} \left\{ \exp\left[-\left(\varepsilon - \sqrt{\varepsilon^2 - \omega_s^2} \right) t \right] - \exp\left[-\left(\varepsilon + \sqrt{\varepsilon^2 - \omega_s^2} \right) t \right] \right\}. \tag{12.11}$$

In the limiting case of $\omega_s = \varepsilon$, both formulas give

$$f(t) = -te^{-\varepsilon t}, \qquad t > 0. \tag{12.12}$$

If the seismometer is underdamped ($\omega_s \gg \varepsilon$), the impulse response will show undesirable ringing. On the other hand, if it is overdamped ($\omega_s \ll \varepsilon$), one of the exponential decay constants in equation (12.11), $\varepsilon - \sqrt{\varepsilon^2 - \omega_s^2}$, is nearly $\frac{1}{2}(\omega_s^2/\varepsilon)$ and hence very small, and the response will be delayed longer for greater damping. For these reasons, the best practical result is usually obtained near the critical damping $\omega_s = \varepsilon$.

The response $\xi(t)$ of the seismometer to an arbitrary ground acceleration $\ddot{u}(t)$ can be obtained by a convolution with the acceleration impulse response $f(t)$:

$$\xi(t) = \int_0^{\infty} \ddot{u}(t - \tau) f(\tau)\,d\tau, \tag{12.13}$$

and this is the general solution of (12.2).

12.1.2 STABLE LONG-PERIOD VERTICAL SUSPENSION

The response of an inertial sensor at low frequency ($\omega \ll \omega_s$) is found from (12.3) to be $X(\omega) \sim \omega^2/\omega_s^2$, which in turn is proportional to the square of the sensor's free period. Therefore, finding a stable, long-period sensor was the most important problem of instrumental seismology for many years, until LaCoste invented the "zero–initial-length" spring in 1935. LaCoste's spring can theoretically achieve an infinite period without instability.

Usually, when a spring is stretched, the applied load F is proportional, via a modulus k, to the elongation $l - l_0$, where l is the actual length and l_0 is known as the initial length. Thus a zero–initial-length spring is one in which the tension is proportional to the actual length. The zero–initial-length spring must be wound with a twist applied to the wire as it is coiled, and it has a residual tension even when no load is applied because of the finite size of the coils. When loaded slightly, the residual tension will keep the spring length unchanged until the load increases to a certain limit. Then the coils begin to separate and the spring length l will increase proportionally with the load, $F = kl$.

An easy but accurate test for checking whether a given spring has zero initial length is as follows: suspend the spring vertically with a load that extends it to some new equilibrium length l. Let it oscillate vertically about this equilibrium position, and measure the period T. We leave it as an exercise (Problem 12.2) to show that $T = 2\pi\sqrt{(l - l_0)/g}$ for any spring that obeys Hooke's law, and from this formula one can obtain $l - l_0$. Then, if $l - l_0$ is equal to the directly measured value of l, the spring has zero initial length.

Figure 12.4 illustrates how the spring is used to measure the vertical component of ground motion. Mass M is fixed to a boom that rotates around a hinge point B. One end of the zero–initial-length spring is connected to a point A through a short flexible wire, and the other end is similarly connected to a point on the boom near mass M. Point A is vertically above point B, and both are fixed to the Earth.

Let us consider the equilibrium of the pendulum under no Earth movement. The torque around point B due to the gravitational force exerted on M is equal to $Mgh_1 \sin\phi$, where h_1 is the boom length and ϕ is the angle between the boom and the vertical. Because of the zero initial length, the torque due to the spring is equal to $klh_2 \sin\theta$, where l is the spring length, k is the spring constant, h_2 is the distance between A and B, and θ is the angle between the spring and vertical. At the equilibrium position, the two torques balance each other:

$$Mgh_1 \sin\phi = klh_2 \sin\theta.$$

But from the sine rule we see that $l \sin\theta = h_1' \sin\phi$, where h_1' is the distance along the boom from B to the point of spring attachment. Therefore, the equilibrium condition is given by $Mgh_1 \sin\phi = kh_1'h_2 \sin\phi$, or

$$Mgh_1 = kh_1'h_2. \tag{12.14}$$

Surprisingly, this balance condition is independent of ϕ. In other words, once the lengths and mass are properly chosen, there is no restoring force. Any mass position is in equilibrium, so the pendulum has an infinite period.

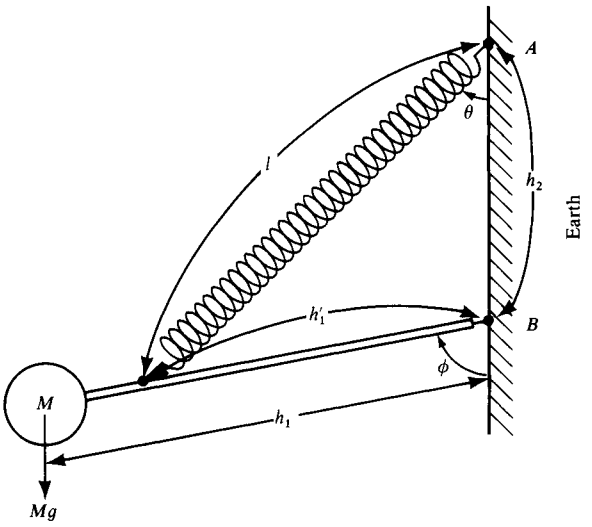

FIGURE **12.4**
Vertical (LaCoste) pendulum, with a zero–initial-length spring. Since the boom will also respond to a change in gravity, this instrument is sometimes called a *gravimeter.*

There are many conceptual ways of suspending mass and spring other than the one shown in Figure 12.4 to achieve an infinite period. In practice infinite period is unattainable, because of inexact spring length, hinge positions at not quite the right locations, finite restoring force of the hinge, variations in spring constant k due to temperature change, variations in gravity, and other disturbances. Traditional long-period seismometers based on the zero–initial-length spring are usually operated at periods of 15 to 30 s, though periods up to 80 s have been attained in routine operation.

As mentioned above, the sensitivity of a sensor to long-period acceleration is proportional to the square of the sensor's free period. From (12.2), for a gradual change in acceleration by an amount $-\Delta a$, we have

$$\xi = \frac{\Delta a}{\omega_s^2} = \frac{\Delta a}{(2\pi)^2} T_s^2.$$

For example, if $T_s \sim 60$ s, $\xi \sim \Delta a \cdot 10^2$ s^2. The pendulum mass will move by 1 mm when the acceleration changes by 1 milligal ($= 10^{-3}$ cm/s^2).

Stable long-period pendulums for a horizontal-component seismometer have been known for more than a hundred years. The long-period horizontal pendulum of the traditional seismograph—for example, for the World Wide Standardized Seismographic Network that dominated global seismology studies from about 1962 to 1982—is shown schematically in Figure 12.5a. The top and bottom wires supporting the mass and boom are kept in tension by the weight. This method of suspension, originally due to Zöllner (1869), eliminated friction at the pivots that hampered earlier horizontal pendulums, which

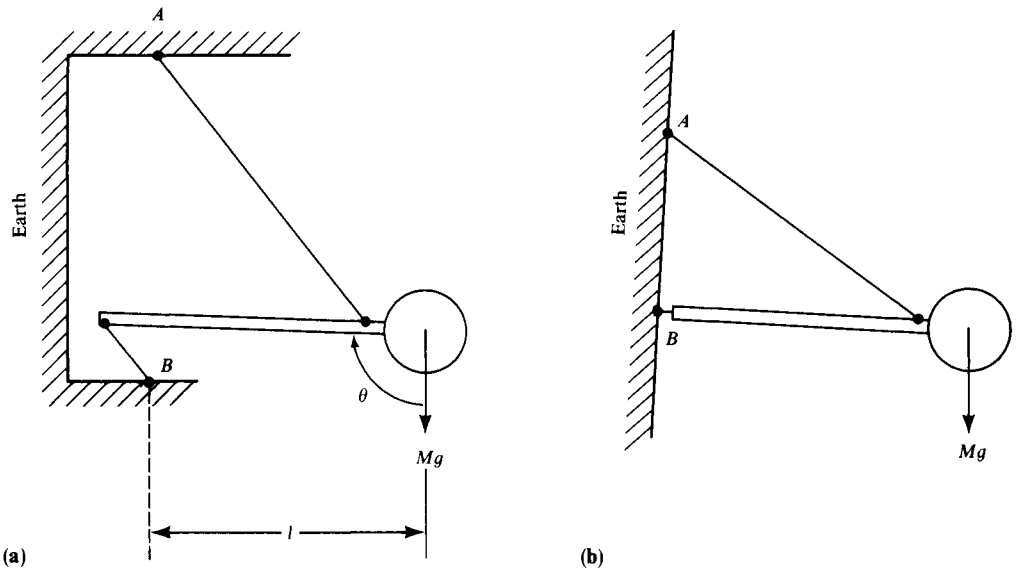

FIGURE **12.5**
Horizontal pendulums. (**a**) The Zöllner suspension. Both wires are kept in tension to avoid buckling instability. (**b**) Often called the "garden gate" suspension. The line AB, fixed to the Earth, is tipped slightly away from the vertical in both (a) and (b). In practice, the pivot at B in (b) and in Figure 12.4 is provided with a hook, so that the pivot is under tension.

were based on the design shown in Figure 12.5b. For small-amplitude oscillations, the pendulum moves in a plane inclined at an angle θ from the vertical plane. The component of gravity in this plane is $g \cos\theta$, so the pendulum period is $2\pi\sqrt{l/(g\cos\theta)}$, where l is the boom length. As the boom direction approaches horizontal ($\theta \to \pi/2$), the oscillation period approaches infinity and becomes unstable. The maximum stable period achieved by a traditional horizontal-component instrument is around 30 s.

12.1.3 MEASUREMENT OF HORIZONTAL ACCELERATION

For all sensors that use local **g** to define the vertical, it is not possible to distinguish between a horizontal acceleration of the ground and a contribution from gravity due to tilt. Figure 12.6 illustrates this situation using a simple pendulum. When the seismometer frame is tilted by an amount $\delta\Psi$, a torque will be exerted around the hinge and will cause pendulum motion relative to the frame. The effect of this torque is the same as that produced by a horizontal acceleration of magnitude $g \sin\delta\Psi$.

A preliminary attempt to separate the effects of tilt and horizontal acceleration was made by Farrell (1969) using gyroscopes, but typically seismologists have been content with the rather arbitrary assumption that either acceleration or tilt dominates a particular signal. The response of the horizontal pendulum (Fig. 12.5) has been analyzed in detail by

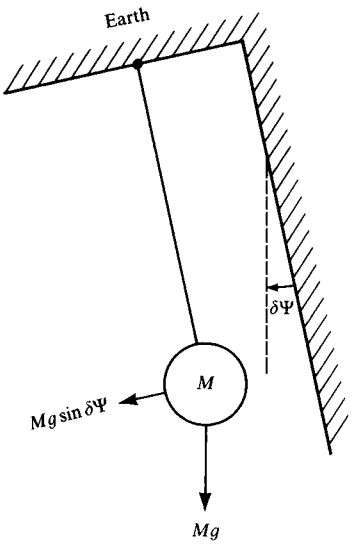

FIGURE **12.6**
Tilt causes apparent horizontal acceleration of a suspended mass.

Rodgers (1968), who described another problem with this design, apart from the ambiguity between tilt and horizontal acceleration. Although the instrument is sensitive primarily to horizontal accelerations (and their tilt equivalent) perpendicular to the boom, its response is affected also by along-the-boom accelerations and by tilt components that change the angle θ (see Fig. 12.5). Rodgers called these "parametric effects," because they act to change the free period of the instrument.

It has been customary to consider the motion of a seismometer pendulum in Cartesian coordinates, where the gravitational force is directed parallel to the z-axis. Actually, the gravitational force is directed to a point, the center of the Earth. A design that takes this into account is the Schuler pendulum, used in inertial navigation. This design is shown in Figure 12.7; the pendulum is hinged at P, and for simplicity in the derivation below, we shall consider a motion restricted to the xy-plane. The equation of pendulum motion is

$$J_p \frac{d^2\theta}{dt^2} = M(\mathbf{h} \times \mathbf{g})_z - M\left(\mathbf{h} \times \frac{d^2\mathbf{r}}{dt^2}\right)_z, \tag{12.15}$$

where J_p is the moment of inertia of the pendulum around P, θ is the rotation of the pendulum measured from the x-axis, M is the mass of the pendulum; $\mathbf{h}$ is the position of the mass relative to P, $\mathbf{g}$ is the gravitational acceleration, and $\mathbf{r}$ is the position of P relative to the center of the Earth.

Let us consider the motion of the pendulum when P moves horizontally, i.e., perpendicular to the direction toward the center of the Earth. In this case, the components of the acceleration vector $d^2\mathbf{r}/dt^2$ are $(-r\ddot{\vartheta} \sin\theta, r\ddot{\vartheta} \cos\theta, 0)$, where ϑ is the angle between

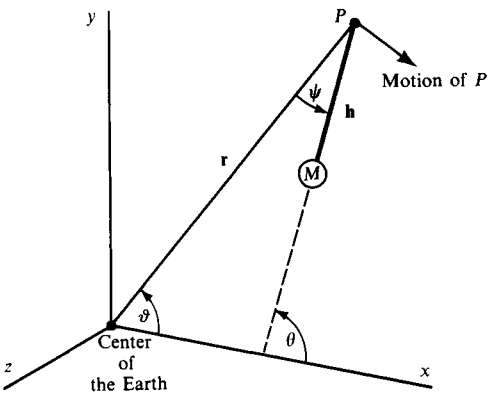

FIGURE **12.7**
The motion of a pendulum subjected to a gravitational force directed toward the center of the Earth. Cartesian axes here have directions fixed in inertial space.

r and the x-axis. The components of other vectors are $\mathbf{h} = (-h\cos\theta, -h\sin\theta, 0)$ and $\mathbf{g} = (-g\cos\vartheta, -g\sin\vartheta, 0)$. Equation (12.15) becomes

$$J_p\frac{d^2\theta}{dt^2} = Mhg\sin(\vartheta - \theta) + Mhr\ddot{\vartheta}. \tag{12.16}$$

Since the angle ψ of deflection of the pendulum from the vertical is equal to $\theta - \vartheta$, we can rewrite the above equation as

$$J_p\left(\frac{d^2\psi}{dt^2} + \frac{d^2\vartheta}{dt^2}\right) + Mgh\sin\psi = Mhr\ddot{\vartheta} \tag{12.17}$$

or

$$J_p\left(\frac{d^2\psi}{dt^2}\right) + Mhg\sin\psi = -(J_p - Mhr)\ddot{\vartheta}. \tag{12.18}$$

The pendulum period T_0 for small ψ, for which $\sin\psi \sim \psi$, is given by

$$\frac{2\pi}{T_0} = \sqrt{\frac{Mgh}{J_p}}. \tag{12.19}$$

The force due to horizontal acceleration vanishes when $J_p = Mhr$. This condition is equivalent to

$$\frac{2\pi}{T_0} = \sqrt{\frac{Mgh}{Mhr}} = \sqrt{\frac{g}{r}}, \tag{12.20}$$

which is the period of a simple pendulum with length equal to the Earth's radius. The corresponding period is 84 min. A pendulum with this period is called a *Schuler pendulum.*

A Schuler pendulum carried by aircraft will always point to the center of the Earth, and will be unaffected by horizontal acceleration. If we mount an accelerometer on the Schuler pendulum, measure the horizontal acceleration during a flight from one point to another on the Earth, and then integrate that acceleration twice with respect to time, we can measure the distance between the two points.

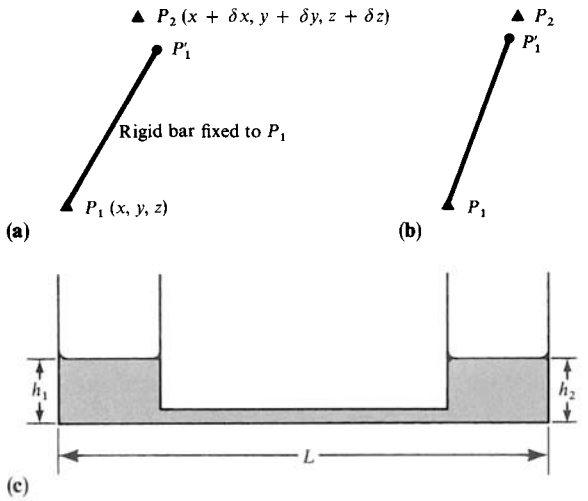

FIGURE **12.8**
Measurement of strain and tilt. (**a**) The bar P_1P_1' is anchored at P_1 and rotates with P_1. (**b**) The bar P_1P_1' is fixed at P_1, but P_1, P_1', P_2 are effectively collinear. This arrangement is achieved either by pivoting the bar at P_1 or by having the sensor of $P_1'P_2$ be a capacitance detector that is insensitive to slight misalignments of P_1, P_1', P_2. (**c**) A tiltmeter consisting of two fluid reservoirs, connected by a tube. Fluid levels h_1 and h_2 are monitored, and temporal changes in the quantity $(h_2 - h_1)/L$ are interpreted as tilt. See Beavan and Bilham (1977) for discussion of temperature effects.

Instruments developed for inertial navigation thus have intrinsic potential for more exact description of Earth movements, such as distinguishing acceleration from tilt.

12.1.4 MEASUREMENT OF STRAIN AND ROTATION

Consider a strain seismometer (or *strainmeter*) that measures the relative displacement of two nearby points in the Earth, in a manner sketched in Figure 12.8a. The movement at P_1 is transmitted to P_1' by a bar fixed at P_1, and the relative position of P_1' and P_2 is measured. Since ground motion in practice has periods very much longer than the natural period of waves in the bar, the strains in the bar itself are negligible and it can be considered rigid.

Initially, P_1 is located at $\mathbf{x}$ and P_2 at $\mathbf{x} + \delta\mathbf{x}$. These points subsequently undergo displacements $\mathbf{u}(\mathbf{x})$ and $\mathbf{u}(\mathbf{x} + \delta\mathbf{x})$, respectively, so that P_2 moves to $\mathbf{u}(\mathbf{x}) + (\delta\mathbf{x} \cdot \nabla)\mathbf{u}$. (We are using a Lagrangian description of the motion: see Section 2.1 and the first paragraph of this chapter.)

The displacement of P_1' is that of P_1 plus an additional term due to rotation $\frac{1}{2}$ curl $\mathbf{u}$ (see equation (2.2)). To first order, the length and the orientation of the bar in its original position are given by the vector $\delta\mathbf{x}$, and the bar then rotates as P_1 rotates, so that the relative displacement of P_2 from P_1' is $\mathbf{u} + (\delta\mathbf{x} \cdot \nabla)\mathbf{u} - \mathbf{u} - \frac{1}{2}(\text{curl } \mathbf{u}) \times \delta\mathbf{x}$. The ith component of this vector is

$$\delta x_j \frac{\partial u_i}{\partial x_j} - \varepsilon_{ijk}\left(\frac{1}{2}\varepsilon_{jlm}\frac{\partial u_m}{\partial x_l}\right)\delta x_k,$$

which can be rewritten as $e_{ij}\,\delta x_j$, with e_{ij} as the Cartesian components of the strain tensor:

$$e_{ij} = \frac{1}{2}\left(\frac{\partial u_i}{\partial x_j} + \frac{\partial u_j}{\partial x_i}\right).$$

This result shows that the strainmeter, based on a bar that is anchored at one end, is indeed sensitive to strain components, but not to the rotation.

But in practice, it is the scalar difference between P_2P_1 and $P_1'P_1$ that is measured, not the vector $e_{ij}\,\delta x_j$, so that P_1 need provide only a pivot for the bar and the "bar" can just as well be a wire. Rotation is not considered, and P_2P_1 and $P_1'P_1$ are aligned as in Figure 12.8b. As shown following equation (2.3), the length $|\delta\mathbf{x} + \delta\mathbf{u}| - |\delta\mathbf{x}|$ of P_2P_1' is $e_{ij}\nu_i\nu_j|\delta\mathbf{x}|$, where $\boldsymbol{\nu}$ is a unit vector along the bar. In order to determine six components of strain, we need in general six different strainmeters, each oriented along a different direction $\boldsymbol{\nu}$. For a measurement made near the Earth's free surface, the condition of zero traction imposes three linear constraints on the stress components, so that only three different strainmeters are needed to determine the strain tensor completely. A variety of site effects can contaminate the local (measured) strain field, making it different from the strain field of geophysical interest. In particular, there can be a significant effect from the cavity within which the instrument is emplaced (Harrison, 1976a; Agnew, 1986) and from topography near the instrument site.

A rotation sensor may be constructed by suspending a mass at its center of mass and coupling it to the Earth through a spring and a dashpot. This approach has been attempted but the sensitivity has been inadequate for producing a useful result. The use of gyroscopes and ring lasers to measure rotation is briefly mentioned near the beginning of Section 12.1. Takeo and Ito (1997) note the utility of measuring rotation near a rupturing fault plane (to improve estimates of the distribution of slip on that fault surface), but as of this writing seismology still awaits a suitable instrument for making such measurements.

As a special case, rotation about a horizontal axis is known in geophysics as *tilt*. Small rotations can be represented vectorially with three components, and tilt is concerned with the two horizontal components. We have remarked already that the principles upon which tiltmeters and horizontal accelerometers are presently designed do not in any way permit a separation of the two effects. Pendulum tiltmeters have been used extensively for measuring solid Earth tides, as described in detail by Melchior (1966). Apart from pendulums, most common in geophysics is the use of two fluid-filled reservoirs connected by a tube (Fig. 12.8c): measurement is made of the differential level in the reservoirs. Spatial fluctuations in temperature within the working fluid can give a spurious signal, which is reduced if the connection between the reservoirs is an open half-filled channel rather than a closed tube. Using a tiltmeter of this design, with 500 feet between reservoirs and with interferometers to measure water height, Michelson and Gale in 1919 were able to measure tidal tilting.

Tilt can be measured over a short baseline via an air bubble that is free to move within the working fluid trapped under a slightly curved horizontal plate (Agnew, 1986). The bubble position is monitored continuously, so that, if tilt occurs, a signal is generated that is proportional to the bubble displacement. Harrison (1976b) has described the operation of a similar instrument, using a bubble trapped under an optical flat. If tilt occurs, the plate is

re-leveled to maintain the bubble position. Using this feedback as the output signal, Harrison was able to measure the M_2 tide to about 0.5% after 3 months of observation. However, short-base tiltmeters are inherently susceptible to very local site effects, which are hard to quantify. If nearby rock units are heterogeneous, then an applied overall strain can cause local tilting, which partly explains why closely spaced short-baseline tiltmeters do not always give the same signal.

12.2 Frequency and Dynamic Range of Seismic Signals and Noise

Most of the signals studied in seismology are transient, i.e., they have in practice a finite duration, such as seismograms from explosions and earthquakes. For such a transient signal $f(t)$, the Fourier transform $f(\omega)$ exists with the definition

$$f(\omega) = \int_{-\infty}^{\infty} f(t)e^{i\omega t}\,dt, \qquad \text{and} \qquad f(t) = \int_{-\infty}^{\infty} f(\omega)e^{-i\omega t}\frac{d\omega}{2\pi}, \tag{12.21}$$

in which t is the time and ω is the angular frequency. We shall define the *amplitude spectral density* as the absolute value of $f(\omega)$, and the *phase-delay spectrum* $\phi(\omega)$, by

$$f(\omega) = |f(\omega)|e^{i\phi(\omega)}. \tag{12.22}$$

Our reason for calling ϕ the phase delay is given in Box 5.5. Since $f(t)$ is real,

$$f^*(\omega) = f(-\omega), \qquad |f(\omega)| = |f(-\omega)|, \qquad \text{and} \qquad \phi(\omega) = -\phi(-\omega), \tag{12.23}$$

where the asterisk indicates the complex conjugate.

The unit of $|f(\omega)|$ is the unit of $f(t)$ divided by the unit of frequency $(\omega/2\pi)$. For example, if $f(t)$ represents the ground displacement in cm, then the unit of $|f(\omega)|$ is cm per Hz—which explains why $|f(\omega)|$ is called the amplitude spectral *density* (though the abbreviation "amplitude spectrum" is common). The most commonly used units of $\phi(\omega)$ are the radian or the circle (i.e., 2π radians).

There are three other distinct types of signal for which the ordinary Fourier transform does not exist. One is the superposition of sinusoidal oscillations with frequencies ω_n, such as the tidal Earth-strain caused by the gravitational attraction of the Sun and the Moon. For this, we define amplitude A_n and phase delay ϕ_n in the following manner:

$$f(t) = \sum_n A_n \exp(-i\omega_n t + i\phi_n), \tag{12.24}$$

where A_n has the same physical dimension as $f(t)$.

Another type of signal we shall consider is the stationary stochastic process, such as ambient seismic ground noise caused by the atmosphere, the oceans, some volcanic processes, industrial activities, and traffic. These signals cannot be expressed either by (12.21) or by (12.24). We first introduce the *autocorrelation function* $P(\tau)$, defined as

$$P(\tau) = \langle f(t)f(t+\tau)\rangle, \tag{12.25}$$

where the symbols $\langle\ \rangle$ indicate averaging over time t. We then introduce the *power spectral density*, $P(\omega)$, which is the Fourier transform of $P(\tau)$:

$$P(\omega) = \int_{-\infty}^{\infty} P(\tau) e^{i\omega\tau} d\tau. \tag{12.26}$$

The unit of $P(\omega)$ is the square of the unit of $f(t)$, divided by the unit of frequency $(\omega/2\pi)$. For displacement $f(t)$ measured in cm, the unit of $P(\omega)$ is cm^2/Hz. Note that $P(\omega)$ does not contain information about the phase.

The final type of signal we consider that lacks an ordinary Fourier transform is nonstationary, nonsinusoidal, and has unknown behavior outside the finite length of our record. We shall refer to signals of this type as "drift." Approximating them as some overall time-dependent change, these signals may be characterized by the total change and the rise time. They may be approximated by a linear trend, in which case the rate of change will be the key parameter.

When a signal has an approximately sinusoidal form with a certain frequency, the amplitude may be measured from the record. If the bandwidth of the signal is known, then one can estimate the amplitude or power spectral density. Likewise, if the spectral densities and the signal bandwidth are known, one can estimate the signal amplitude.

For a rough approximation, the amplitude of a wavelet is the product of amplitude spectral density and bandwidth of the wavelet. For example, if $|f(\omega)| = F$ (a constant) for $-\omega_0 < \omega < \omega_0$, $|f(\omega)| = 0$ otherwise, and $\phi(\omega) = 0$ for all ω, then the corresponding signal $f(t)$ is

$$f(t) = \frac{1}{2\pi} \int_{-\omega_0}^{\omega_0} F e^{-i\omega t}\, d\omega = 2 \cdot F f_0 \cdot \frac{\sin \omega_0 t}{\omega_0 t},$$

where $f_0 = \omega_0/2\pi$. The maximum amplitude is at $t = 0$, and is equal to $F \cdot 2f_0$ (i.e., spectral amplitude $\times$ bandwidth) because $x^{-1} \sin x \to 1$ as $x \to 0$. Likewise, for a band-passed signal with $|f(\omega)| = F$ for $\omega_0 < |\omega| < \omega_1$, $|f(\omega)| = 0$ otherwise, and $\phi(\omega) = 0$, we obtain

$$f(t) = 2Ff_1 \frac{\sin \omega_1 t}{\omega_1 t} - 2Ff_0 \frac{\sin \omega_0 t}{\omega_0 t},$$

where $f_1 = \omega_1/2\pi$. The maximum amplitude occurs at $t = 0$, and is

$$f(t)_{t=0} = F \cdot 2(f_1 - f_0), \tag{12.27}$$

which again is the product of the amplitude spectral density and the bandwidth.

For the power spectral density $P(\omega)$ defined for noise, we obtain

$$P(\tau) = \frac{1}{2\pi} \int_{-\infty}^{\infty} P(\omega) e^{-i\omega\tau}\, d\omega, \tag{12.28}$$

which is the inverse transform of (12.26). Thus

$$P(\tau)\Big|_{\tau=0} = \frac{1}{2\pi} \int_{-\infty}^{\infty} P(\omega)\, d\omega.$$

On the other hand, by definition,

$$P(\tau)\Big|_{\tau=0} = \langle f^2(t)\rangle.$$

Therefore, we have

$$\frac{1}{2\pi}\int_{-\infty}^{\infty} P(\omega)\, d\omega = \langle f^2(t)\rangle. \tag{12.29}$$

For example, if $P(\omega) = P$ for $\omega_0 < |\omega| < \omega_1$, and $P(\omega) = 0$ otherwise, then we have

$$\langle f^2(t)\rangle = P \cdot 2(f_1 - f_0). \tag{12.30}$$

Thus, for a rough approximation, the mean square amplitude of noise in the time domain is equal to the product of the power spectral density and the bandwidth.

By using (12.27) and (12.30), and knowing the bandwidth of the signal, we can approximately relate the amplitude spectral density to the amplitude, and the power spectral density to the mean square amplitude.

With this background we can now make a survey of seismic signals and explore the frequency and dynamic range covered by various observations. In each case, we shall characterize the observations in terms of one of the four types of signal we have considered above.

12.2.1 SURFACE WAVES WITH PERIODS AROUND 20 SECONDS

The most prominent signals recorded by a traditional long-period seismograph for a distant shallow earthquake are surface waves with a period around 20 s. Body waves show smaller amplitude because of stronger geometrical spreading than surface waves. The surface waves with periods less than about 10 or 15 s suffer from scattering due to shallow heterogeneities, and those with periods longer than 25 s begin to lose energy into the asthenosphere. Besides, the magnification of traditional seismographs decreases with periods of more than 20 s. It was quite natural, therefore, that a magnitude scale M_s was introduced by Gutenberg and Richter (1936) based on the surface wave amplitude at a period of 20 s (see Appendix 2).

Figure 12.9 shows the amplitude of surface waves from a shallow earthquake with magnitude $M_s = 3$ as a function of epicentral distance. The curve is obtained from a table given by Richter (1958, p. 346). Sensitive long-period seismometers can detect a distant

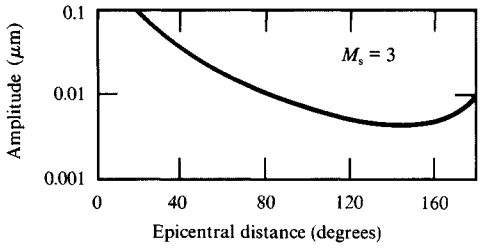

FIGURE **12.9**
Amplitude of surface waves from a shallow earthquake with magnitude $M_s = 3$ as a function of epicentral distance.

BOX 12.1
Terminology associated with large ranges in value

In astronomy, acoustics, seismology, and other physical sciences, and in electrical engineering, there is often the need to measure physical fields whose values range over many orders of magnitude. It is natural to report such values on specialized logarithmic scales, such as those underlying astronomical and seismic magnitudes. But there is also a standard terminology for measurement over large ranges, which is widely applied across all of these different physical subjects.

For example, whether the measurement is pressure, displacement, acceleration, volts or electrical current, the so-called *dynamic range*, R, of the measuring system is commonly taken to be the ratio of the amplitudes of the largest signal to the smallest signal. The limitation at the low end comes from system sensitivity, and at the high end typically comes from requiring system linearity. (Signals that are too big will "clip" or "go off scale.")

The ratio R is commonly reported in decibels (abbreviated as dB), derived from R by the formula $20 \log_{10} R$. For example, if R is a million, the dynamic range would be 120 dB. (The decibel unit is based on a power ratio, and conventionally the squared original signal is referred to as a power signal regardless of whether it is displacement^2 or acceleration^2, or a true physical power signal such as volts$\times$current. The dynamic range in bels is given as $\log_{10} R^2$, which is $2 \log_{10} R$ and hence equal to $20 \log_{10} R$ in decibels.)

It is also common to state the amplitude of a particular measurement, of signal or background noise, in units of decibels above or below a standard signal level. For example, Figure 12.12 shows noise levels in the frequency domain using measurements of power spectral density, which are referenced to the standard levels of 1(m/s)^2 per Hz (Fig 12.12a) and 1(m/s^2)^2 per Hz (Fig 12.12b). Because these reference values and the right-hand vertical axes of Fig 12.12ab are already in power units, their logarithms are in bels and the dB values as shown are simply $10 \log_{10}$(power).

The output of a digital recording system is typically a stream of integer numbers, sometimes called counts, representing a physical signal that has been sampled at different times. The instrument response to various inputs is then in units of "counts per input unit." For example, an instrument designed to be "flat to velocity" between two specified frequencies would respond to input ground velocity with an approximately constant output value of counts per m/s, for input with frequency lying between the two specified frequencies. A common convention is to change this definition slightly so that two specified frequencies are given, say f_{lower} and f_{upper}, such that the signal amplitude is a few dB (often 3 dB) down from its maximum value between f_{lower} and f_{upper}.

Early digitizers used in seismology were applied to sensors that had dynamic ranges of a few hundred or in some cases up to about a thousand. Since $1000 \sim 2^{10}$, and the underlying physical signal could have positive and negative values, only 11 binary bits were needed to record the full range of signals, large and small. Early digitizers were usually 8-bit or 10-bit, though the Soviet Union developed an 11-bit digitizing system used for example at the Borovoye Geophysical Observatory in Northern Kazakhstan, when it began digital seismic recording in 1966. Improved sensors became widely available in the 1970s and 1980s with much larger dynamic range, requiring more bits for faithful recording. Western scientists had access to 12-bit systems at fairly low cost in the mid-1970s, then 16-bit digitizers became standard for a few years, only to be superceded by 24-bit systems, which are appropriate for signals ranging from ± 1 up to ± 8 million (dynamic range of about 140 dB). It should be noted that in practice the bottom few bits are used to record background noise levels. Since the lowest signal level will be comparable to such noise, the number of bits of signal will be less than 24 for a 24-bit recording system, and in this sense the dynamic range will be less than 140 dB.

BOX **12.2**
Recording media

Digital recording is superior to analog recording, both in dynamic range and in ease of processing on computers. For a few decades it had the drawback of relatively low density of information per unit area of recorded medium, which for many years placed inconvenient restrictions on the amount of data that could be recorded in the field. But beginning in the 1970s, VCR technology for increasing the information density on tapes became available, which used helical scanning for analog recording, and which was further developed in the 1980s to solve the practical problem of recording large amounts of easily usable digital information.

Cheap mass storage can preserve the enormous volume of digital data produced by modern instruments, for temporary field deployments as well as for fixed stations. It became common in the mid-1990s to use hard disks in the field with a capacity of 1 Gbyte, backed up on cheap tapes holding several Gbytes each. At data centers, mass storage in the late 1990s was still based largely upon tape rather than optical technology, with tape libraries of a thousand or more cartridges accessed via robot, and methods of helical scanning that place up to 50 Gbytes of data on a single cartridge. It can be expected that major improvements in recording technology will continue, driven largely by the entertainment industry (including digital television).

Note that seismological data centers differ from mass storage systems where data is kept in large blocks, in that seismologists often want access to numerous short time segments of the data, corresponding to the arrival times (at different stations) of particular waveforms, none of which may have long duration.

earthquake with $M_s \sim 3$, which will show an amplitude of 100 nm (10^{-5} cm) at $\Delta = 20°$ and 10 nm at $\Delta = 80°$. On the other hand, the largest earthquake ($M_s = 8\frac{1}{2}$) will show an amplitude of several cm at $\Delta = 20°$ and several mm at 80°. The large dynamic range of these signals (from 10^{-6} cm to 1 cm) imposes heavy demands on seismic instrumentation and recording media (see Box 12.2).

As described in Section 12.1, three different types of sensor are needed in seismology: the inertial sensor, which is sensitive to acceleration; the strainmeter, which measures strain in the Earth beneath it; and various sensors for measuring rotation. It is instructive to give the value of acceleration α, strain ε, and rotation θ associated with the 20-s surface waves from a small earthquake, say $M_s \sim 3$. For plane Rayleigh waves with period 20 s, phase velocity 3.5 km/s, and displacement amplitude 0.1 μm (appropriate for $M_s \sim 3$ at distances of a few tens of degrees), we have

$$\alpha \sim \left(\frac{2\pi}{20}\right)^2 \cdot 10^{-5}\ \text{cm/s}^2 \sim 10^{-6}\ \text{gal} = 10^{-9}\ \text{g},$$

$$\varepsilon \sim \frac{2\pi}{3.5 \times 10^5 \times 20} \cdot 10^{-5} \sim 10^{-11},$$

$$\theta \sim \varepsilon = 10^{-11} \sim 2 \times 10^{-6}\ \text{arc-s}.$$

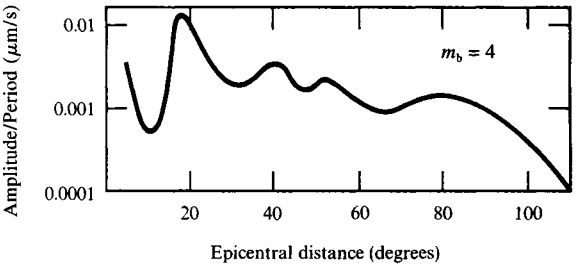

FIGURE **12.10**
The value of A/T (A = amplitude, T = period) for a shallow earthquake with $m_b = 4$, as a function of epicentral distance.

Large explosions, such as an underground nuclear test, generate 20-s surface waves with amplitude approximately proportional to the yield (Marshall *et al.*, 1971). A 1-megaton shot in hard rock roughly corresponds to $M_s \sim 5$, and thus the most sensitive long-period seismometer will detect a distant shot of several kilotons (corresponding to $M_s \sim 3$).

12.2.2 *P*-WAVES FOR $5° < \Delta < 110°$

The signal level of *P*-waves from a distant earthquake may be found from Gutenberg's calibration curve (see Richter, 1958, p. 688) for determining the body-wave magnitude m_b. Figure 12.10 shows the value of A/T as a function of epicentral distance, where A is the amplitude in μm and T is the period in seconds for a shallow earthquake with $m_b = 4$. This curve can be used to find m_b for any shallow earthquake, as

$$m_b = 4 + \log_{10}(A/T)_{obs} - \log_{10}(A/T)_{m_b=4},$$

where $(A/T)_{obs}$ is the observed value of A/T at a certain epicentral distance (which must be known), and $(A/T)_{m_b=4}$ is the value obtained from Figure 12.10 for that distance. For *P*-waves recorded by traditional short-period seismographs at teleseismic distances, T is approximately 1 s, and the amplitude of ground motion for $m_b = 4$ is about 10 nm at $\Delta = 20°$ and 1 nm at $\Delta = 90°$. These signals may be detected by sensitive short-period seismometers provided background noise is small. With an array of instruments in the same general region, signals can be stacked (after a time shift to align the individual arrivals, using the coherence of the signal and the incoherence of the noise), to achieve almost an order of magnitude greater sensitivity (i.e., down to a few tenths of 1 nm). The greatest earthquake ($m_b \sim 8$) will show A/T of 1 mm/s at $\Delta = 20°$. For such large earthquakes, T may be about 10 s, and the amplitude on the order of 1 cm. Again we see a requirement for large dynamic range, from 10^{-7} cm to 1 cm.

The 1 nm (nanometer) displacement at $T = 1$ s corresponds to an acceleration of 4×10^{-9} g, and to rotations and strains of around 10^{-12}.

12.2.3 RANGE OF AMPLITUDE SPECTRAL DENSITIES FOR SURFACE WAVES AND *P*-WAVES

In Figures 12.9 and 12.10, we showed signal amplitudes as a function of distance. Figure 12.11 shows the amplitude spectral density (defined in Section 12.2) as a function of frequency for both surface waves and *P*-waves at $\Delta = 90°$.

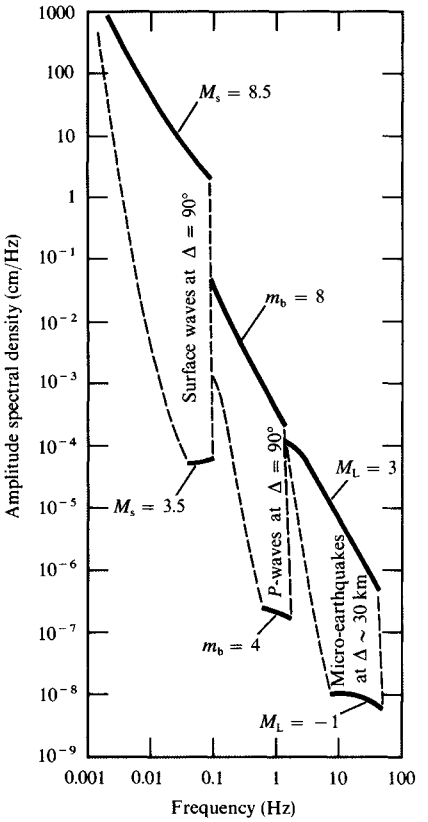

FIGURE **12.11**
The ranges of amplitude spectral density for surface waves at the epicentral distance 90° corresponding to the range of M_s from $3\frac{1}{2}$ to $8\frac{1}{2}$; for P-waves at 90° corresponding to the range of m_b from 4 to 8; and for S-waves from microearthquakes at distance 30 km corresponding to magnitude M_L from -1 to 3.

The solid lines with specified magnitudes represent typical spectral densities for the smallest detectable events and the largest events. They are obtained by interpreting empirical data with the aid of theoretical spectra calculated for a realistic Earth model (Box 7.7) and using a scaling law for earthquake sources (Figure 10.14).

The broken lines indicate the rough limits of the spectral range usually studied for each type of wave. For surface waves studied teleseismically, the high-frequency limit corresponds to a period of about 10 s. Shorter waves are either hidden in the high ambient seismic noise shown later, in Figure 12.12, or are scattered by the strong lateral heterogeneity of the Earth near the surface. The effect is path-dependent: paths in an ocean basin wipe out Rayleigh waves with periods shorter than about 15 s, whereas paths in a shield area transmit short-period surface waves over long distances. The low-frequency limit is determined by the sensitivity of conventional seismometers, and may in some cases be reduced if instruments with greater sensitivity can be operated in quiet sites.

For P-waves, the high-frequency limit is due primarily to attenuation. The low-frequency limit for small events is due to the characteristic response of traditional short-period seismographs, which are designed to suppress the frequency range of high ambient noise, discussed below. For larger events, it is possible to extend the spectral range to longer periods.

12.2.4 MICROEARTHQUAKE WAVES AT SHORT DISTANCE

Figure 12.11 also shows the frequency and dynamic range of S-waves from microearthquakes observed at $\Delta \sim 30$ km. The microearthquake is usually defined as an earth-

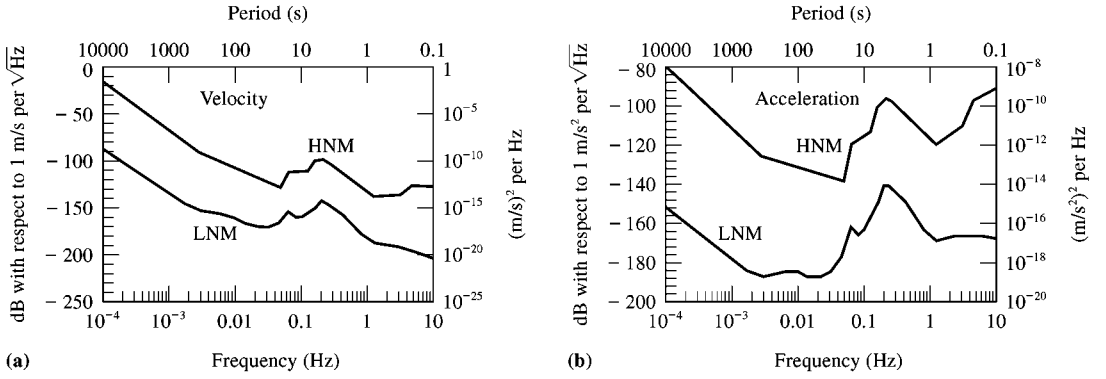

FIGURE **12.12**
(a) Velocity power spectra and **(b)** acceleration power spectra of ambient seismic noise at noisy and quiet conditions. These are respectively the high noise model (HNM) and low noise model (LNM) of Peterson (1993). No single station has these noise curves. Instead, LNM represents the lower envelope of the noise for a series of quiet stations on hard basement rock remote from cultural activities when there is no strong wind in the vicinity of the stations. HNM is the upper envelope, for a series of stations as sited in practice where various sources of noise may be a problem. The typical station will be subject to noise somewhere between the extremes of LNM and HNM.

quake with $M_L < 3$, where M_L is the Richter magnitude originally defined for local earthquakes in southern California. The lower-magnitude limit $M_L \sim -1$ is typical and is determined by the ambient noise. The displacement amplitude for $M_L \sim -1$ at $\Delta = 30$ km is on the order of 10^{-7} cm, with frequencies up to several tens of Hz. The corresponding acceleration ($\sim 10^{-6}$ g) is, however, considerably higher than the thresholds for teleseismic P- and S-waves, so that instrumentation can be less sophisticated. The corresponding strain and rotation are on the order of 10^{-9}. Seismic signals from earthquakes even smaller than $M_L \sim -1$ are sometimes recorded, for example in the context of an aftershock survey to detect "nanoearthquakes," where special field efforts are made so that the distance between source and instrument is only a few km.

12.2.5 AMBIENT SEISMIC NOISE

Figure 12.12 shows the low noise and high noise models of Peterson (1993), who proposed them as lower and upper bounds of the background noise found for stations on hard basement rock, based on many years of making noise surveys in different frequency bands. No station is as quiet as this low noise model across the whole band shown, but the background at a particular site may reach the LNM level for some smaller range of frequency. Another point to bear in mind, when comparing the low noise model of Figure 12.12 with a particular station, is that some stations are quiet because of their location in a region that not only has low noise from local sources (far from towns, railroads, lakes, and seas), but also because of a location where seismic waves regionally are attenuated (for example, because of elevated temperatures in a tectonic region, associated with low seismic Q values). Such attenuation can reduce signal as well as noise, reducing the benefit of low noise when evaluating the signal-to-noise ratio, which is what determines the quality of recordings and in general the

utility of the station. The best stations for global studies are located in regions with low noise from local sources, and with high seismic Q values for waves propagating in both crust and upper mantle.

The main features of the noise spectra commonly found at a particular station are two peaks, usually at about 0.2 Hz and about 0.07 Hz. Both peaks are due to ocean waves. The smaller peak occurs at the primary frequency at which most ocean waves are observed and is considered to be due to the action of ocean waves on coasts, as proposed first by Wiechert in 1904. Part of the main peak was explained by Longuet-Higgins in 1950 as due to the pressure from standing ocean waves, which may be formed by waves traveling in opposite directions in the source region of a storm or near the coast. This mechanism generates seismic waves with a frequency twice that of ocean waves. Hasselman (1963) showed that both theories quantitatively explain seismic and ocean-wave observations. The minimum in noise power beginning at long periods of around 40 s was first reported by Savino *et al.* (1972), who used records of the first global network of so-called high-gain long-period (HGLP) seismographs developed by Pomeroy *et al.* (1969) and installed at eight stations around the world.

The level of noise recorded on vertical-component seismographs housed in an airtight casing on competent rock is independent of local meteorological conditions and of the depth of overburden. On the other hand, horizontal-component long-period seismographs are affected by the noise due to local meteorological conditions if the vault is shallow. This effect attenuates quickly with depth. The noise level in power can be reduced to 10% of the level at the surface by placing the seismograph at a depth of 100 meters. This substantial decay was correctly predicted by Sorrells (1971), who modeled the noise source by a wind-induced pressure field propagating as a plane wave with ground-level wind velocities (see Problem 12.3).

The power spectra in Figure 12.12b are for ground acceleration. Showing the information in these units is preferred for some purposes, because the two curves (LNM, HNM) then span a smaller vertical range than for the velocity spectra.

12.2.6 AMPLITUDE OF FREE OSCILLATIONS

The amplitude of free oscillations excited by an earthquake attenuates with time (see Figure 8.3). The initial amplitude corrected for attenuation was obtained for the great Chilean earthquake of 1960 by Benioff *et al.* (1961). This measurement was made by a strainmeter, and the initial strain amplitudes for the fundamental-mode spheroidal free oscillations, ${}_0S_2$ ($T = 54$ min), ${}_0S_5$ (20 min), and ${}_0S_{19}$ (6 min) were 2×10^{-11}, 8×10^{-11}, and 2×10^{-9} respectively.

Free oscillations from the same earthquake were also observed by the LaCoste–Romberg tidal gravimeter. Power spectral analysis by Ness *et al.* (1961) revealed spectral peaks with amplitude about $0.1 - 1 \times (10^{-9}\ \text{g})^2/\text{cph}$ (cycles per hour) and bandwidth a small fraction of 1 cph. The vertical acceleration amplitude of these oscillations, therefore, was a fraction of 10^{-9} g.

An estimate for the initial displacement amplitude was given by Abe (1970) for the Kurile Islands earthquake of 1963 October 13 ($M_s = 8\frac{1}{4}$, seismic moment $= 7.5 \times 10^{28}$ dyn-cm) and for the great Alaska earthquake of 1964 March 28 ($M_s = 8.3$, seismic moment $= 7.6 \times 10^{29}$ dyn-cm). The initial amplitudes were about 10^{-2} cm for ${}_0S_{10}$ through ${}_0S_{14}$ for the Alaskan earthquake.

Free-oscillation peaks from individual earthquakes as small as $M_s = 6.5$ can now be routinely detected. The signal level of these peaks in the frequency range 10 to 20 cph (25 to 60 mHz) is about 10^{-21} g^2/cph, that is, about 3.5×10^{-16} (m^2/s^4)/Hz.

12.2.7 AMPLITUDES OF SOLID EARTH TIDE, CHANDLER WOBBLE, PLATE MOTION, AND MOONQUAKES

The semi-diurnal and diurnal Earth tides are the largest signals in the frequency range lower than 1 cph. Their acceleration peak-to-peak amplitude is about 3×10^{-7} g, and their strain amplitude is about 10^{-7}.

The variation of latitude due to free nutation was predicted by Euler in 1765, and was named after Chandler, a merchant in Cambridge, Massachusetts, who discovered the wobble period of 428 days. The amplitude of the wobble is about 0.2 arc-s, or 10^{-6} radian.

The fastest relative rotation of lithospheric plates is that of the Pacific plate relative to the Antarctic plate at the rate of 10^{-6} degree/year (Le Pichon, 1968) or 2×10^{-8} radian/year. Plates have relative motion typical amounting to a few cm/year, which can accumulate as strain (eventually relieved by earthquakes) over distances on the order of 100 km near plate boundaries. Faithful measurement of the resulting strain rates (10^{-14} s^{-1}) requires extremely high instrumental stability.

Natural moonquakes (category A, Latham *et al.*, 1971) were recorded with amplitudes in the range $10^{-8} - 10^{-7}$ cm with periods around 1 s. The noise spectra (Fig. 12.12) for the Earth show that they could not be detected teleseismically on the Earth. A challenge in building the seismometers used on the Moon in the 1960s and 1970s was that these instruments had to be designed to operate in an environment quieter than anywhere on Earth.

12.2.8 SEISMIC MOTION IN THE EPICENTRAL AREA

Figure 12.13a shows the peak horizontal ground acceleration (in units of gravitational acceleration) as a function of distance to the closest surface trace of fault slip for three ranges of earthquake magnitude summarized by Page *et al.* (1975). The largest value is 1.25 g recorded on a rock ridge 3 km from the fault plane during the 1971 San Fernando, California, earthquake (magnitude 6.6). The 1992 Petrolia earthquake and the 1994 Northridge earthquake, both in California, also led to recordings of peak acceleration in excess of 1 g. Figure 12.13b shows Campbell's (1997) summary fit to strong motion data, giving the variation of peak acceleration with distance and magnitude.

A curve for the typical acceleration spectral density is given in Figure 12.14 for a station at a distance of 8 km from the fault break of a medium-sized earthquake (Temblor station record during the Parkfield, California, earthquake 1966 June 28; $M_s = 6.3$, $M_L = 5.5$, seismic moment $= 1.4 \times 10^{25}$ dyn-cm). The curve was obtained from the actual record for periods shorter than 1 s and by an extrapolation for periods longer than 1 s using an appropriate dislocation model.

For a complete description of the source mechanism of an earthquake, it is necessary to obtain a wide spectral range such as that shown in Figure 12.14. This requirement poses a difficult problem in seismic instrumentation. As Figure 12.14 shows, the main signal

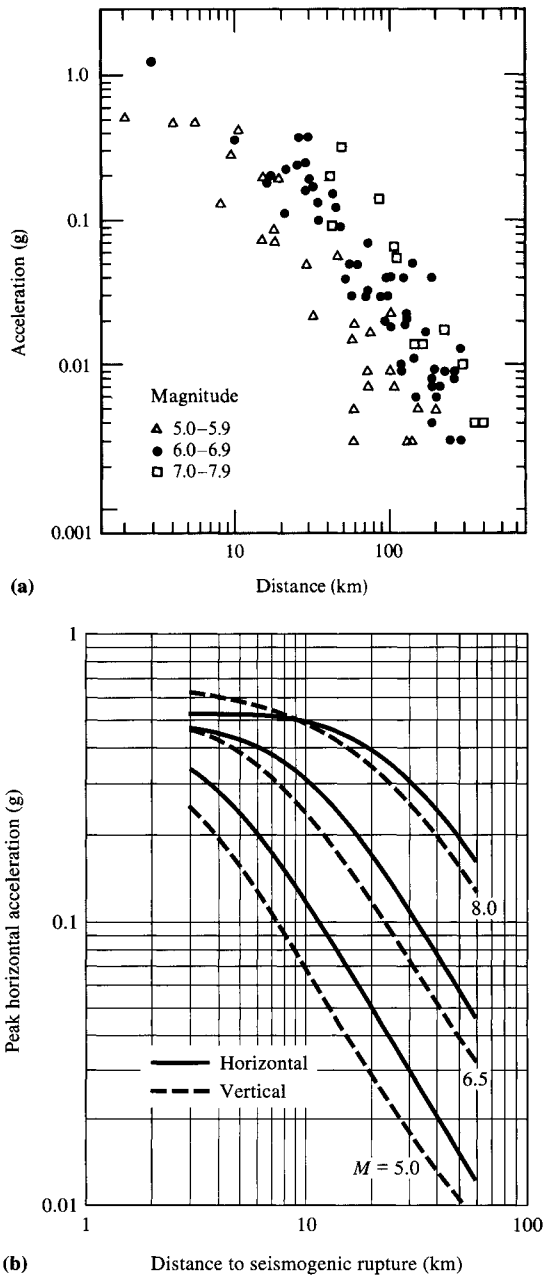

FIGURE **12.13**

(a) Peak horizontal ground acceleration (in units of gravitational acceleration) as a function of distance to the closest surface trace of fault slip. Different symbols are used for different magnitude ranges. [After Page *et al.*, 1975; copyright by the American Association for the Advancement of Science.] **(b)** Scaling of peak acceleration with magnitude and distance, for horizontal and vertical components, obtained as a fit to strong motion data. [From Campbell, 1997; published by the Seismological Society of America.]

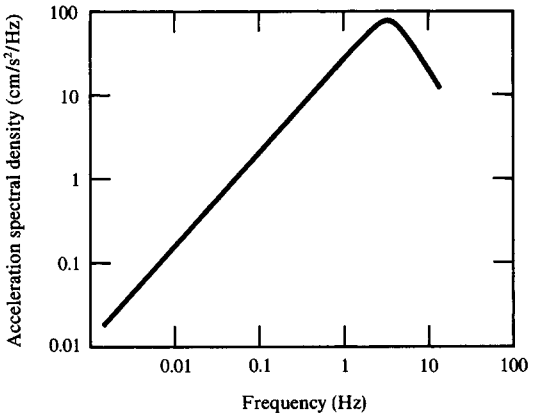

FIGURE **12.14**
An example of acceleration spectral density in the epicentral area of a medium-sized earthquake.

has its peak acceleration spectral density of 100 $(cm/s^2)/Hz$ at 3 Hz, which corresponds to acceleration amplitudes of 0.3 g. On the other hand, the acceleration amplitude of the signal contained in the spectral band around 0.01 Hz is about 10^{-6} g. The problem is to isolate low-frequency signal with amplitude one millionth of that of the coexisting high-frequency signal. Therefore, linearity is a very important requirement for the instrument in wide-band near-field seismic experiments. Since no physical sensor is perfectly linear, a small fraction of high frequency waves will be rectified and show up as a spurious low-frequency motion that will contaminate long-period signals.

12.2.9 STRAIN AMPLITUDES OF GRAVITATIONAL WAVES

Einstein's general relativity theory predicts the existence of gravitational waves as ripples in the fabric of space and time, which will be produced by violent events such as the spiraling together and final collision of two black holes or neutron stars, or by supernova explosions. These gravitational waves potentially are detectable as a squeezing and stretching of matter in directions perpendicular to the direction of wave propagation (Abramovici *et al.*, 1992). On Earth, the outcome of violent sources of gravitational waves within a distance of several tens of millions of light years is predicted to be a strain signal of about 10^{-22} or 10^{-21}, which is several orders of magnitude smaller than the strains we have discussed so far. The gravitational wave strain signal is comparable to the diameter of a hydrogen atom ($\sim 10^{-10}$ m) in the distance of the Earth from the Sun ($\sim 1.5 \times 10^{11}$ m).

The Laser Interferometer Gravitational-Wave Observatory (LIGO) was built in the 1990s at two sites located about 2,000 km apart, and began operations in 2002. One site is at Hanford, Washington, the other near Livingston, Louisiana. Each site contains two 4-km long interferometers arranged in an L shape. The gravitational wave strain signature, about $10^{-12}\mu$m over 4 km, is to be amplified by bouncing laser light many many times between mirrors and measuring to within a thousandth of a fringe. Since Earth strain due to microseismic noise is measured at around 10^{-10} or more at these sites, and acoustic noises from local pipelines, traffic, and aircraft will also impact the installations, isolators must reduce unwanted environmental noise by many orders of magnitude to have a chance of permitting detection of gravitational waves. The isolators, originally conceived

BOX 12.3
Engineering response spectra

The concept of a response spectrum was introduced in Section 12.1.1 as the output spectrum of a seismometer divided by the input spectrum of ground motion. The instrument output is then the product or convolution of the input and the response, depending on whether we are using the frequency domain or the time domain. These are basic ideas in linear filter theory.

In the terminology of engineering seismology, a "response spectrum" means something quite different. Engineers are interested in the response of buildings, rather than seismometers, and we begin this discussion with the equation for displacement $\xi(t)$ of a building mass M that is exposed to ground motion via structure with stiffness k and damping D, so that $M\ddot{\xi} + D\dot{\xi} + k\xi = -M\ddot{u}$. In this way the building is treated as a one-degree-of-freedom system, with an equation that can be rewritten as

$$\ddot{\xi} + 2\varepsilon\dot{\xi} + \omega^2\xi = -\ddot{u}, \tag{1}$$

in which the natural frequency $\omega = \sqrt{k/M}$ and $2\varepsilon = D/M$. Critical damping corresponds to $\varepsilon = \omega$.

Equation (1) here, for motion in a building, is the same as (12.2) for the motion of a pendulum used as a seismic sensor. Following the steps from (12.2) to (12.13), we can show that the solution of (1), if $\omega > \varepsilon$, is the convolution

$$\xi(t, \omega, \varepsilon) = -\ddot{u}(t) * \left(\frac{e^{-\varepsilon t}}{\omega_1} \sin \omega_1 t \right) \qquad \text{where} \quad \omega_1 = \sqrt{\omega^2 - \varepsilon^2}. \tag{2}$$

If $\ddot{u}$ is known, $\xi(t, \omega, \varepsilon)$ can be computed from (2) for different values of (ω, ε). The *engineering response spectrum*, SD, is then defined to be the maximum value of $|\xi(t, \omega, \varepsilon)|$ for all values of t. This definition has three major differences from response spectra of seismometers. First, the engineering response spectrum is based on time-domain motions driven by $\ddot{u}$ and hence is different for every earthquake. Second, it is a function of the natural frequency and damping of the responding objects—which we can think of as a double series of different buildings, rather than a particular seismometer subjected to a series of different frequencies. Third, it is derived from the maximum value of $|\xi(t, \omega, \varepsilon)|$, not from an rms value or a mean, and not from a spectral ratio.

We have defined $\text{SD} = \text{SD}(\omega, \varepsilon)$ as the engineering displacement response spectrum, and in a similar way we could define SV and SA based on maximum values of $|\dot{\xi}(t, \omega, \varepsilon)|$ and $|\ddot{\xi}(t, \omega, \varepsilon)|$ as t varies. But instead it is common to work with the so-called pseudo velocity spectrum PSV and the pseudo acceleration spectrum PSA, defined as $\text{PSV} = \omega\text{SD}$ and $\text{PSA} = \omega^2\text{SD}$. Hudson (1962) showed $\text{SV} \sim \text{PSV}$ and $\text{SA} \sim \text{PSA}$ over most of the usual frequency and damping ranges of relevance in engineering seismology.

(continued)

as alternating layers of rubber and steel, are now more elaborate. Seismic noise is expected to be the dominant noise below about 70 Hz, because vibration isolation systems work less effectively at lower frequencies. The range from about 70 to about 300 Hz appears to be the best detection band for the first operational LIGO system. Detections will be needed at both sites to build confidence that gravitational waves are indeed observed.

BOX **12.3** *(continued)*

An advantage of the two pseudo spectra is that values of SD, PSV, and PSA can all be read off a single figure of the type shown below.

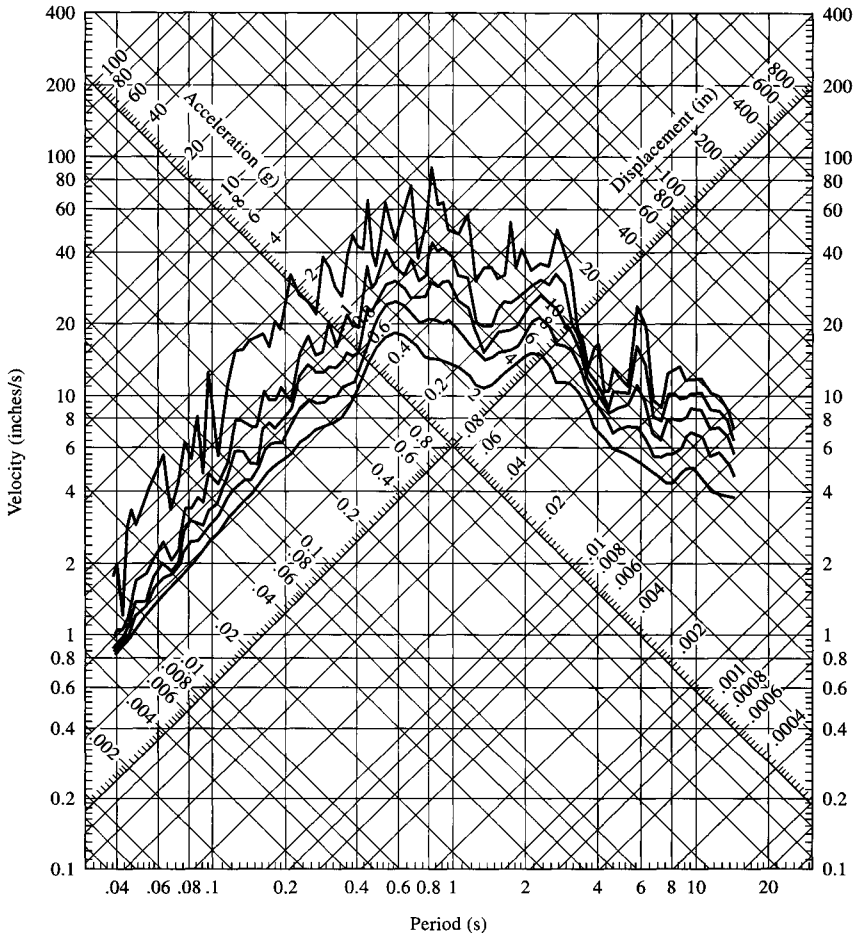

Typical earthquake response spectra, shown as a tripartite logarithmic plot. Damping values are 0, 2, 5, 10, and 20% of critical (the smoothest curve correspond to the greatest damping). These spectra are based on an accelerogram record of ground motion $\ddot{u}$ for the 1940 Imperial Valley, California, earthquake. For 30 years this recording was famous as providing one of the very few examples of near-field strong ground motion. As indicated by Figures 12.13ab, many such near-field records are now available. From D. E. Hudson (1979).

Basically this figure is a plot of log PSV vs. log T where period $T = 2\pi/\omega$, and a factor of 10 has the same length on the vertical and horizontal axes. It follows that values of SD ($= \text{PSV}/\omega$) and PSA ($= \text{PSV} \times \omega$) can be read off axes rotated $\mp 45°$ from the PSV axis.

12.3 Detection of Signal

Now that we have reviewed the frequency and dynamic range of various seismic signals, let us consider more practical aspects of seismic sensors. First, of course, the seismometer must be sensitive enough to detect the signal. The sensitivity of a sensor is ultimately limited by the thermal noise generated in its dissipative elements.

12.3.1 BROWNIAN MOTION OF A SEISMOMETER PENDULUM

A pendulum with one degree of freedom (i.e., with movement restricted to one direction) has mean kinetic energy given by $\frac{1}{2}kT$ (k = Boltzmann's constant) when it is in thermal equilibrium with the surrounding air at the absolute temperature T (degrees Kelvin). If it had more energy, it would warm the air by accelerating the motion of air molecules. If it had less energy, the collision of air molecules would accelerate the pendulum motion.

Referring back to Figure 12.2 and equations (12.1) and (12.2), the motion of the pendulum due to the force $e(t)$ exerted by the collision of air molecules is the solution of the equation

$$M\ddot{\xi} + D\dot{\xi} + k\xi = e(t). \tag{12.31}$$

The solution is given by the convolution of $e(t)$ with the impulse response $f(t)$ obtained earlier in equation (12.10):

$$\xi(t) = \frac{1}{M}\int_{-\infty}^{t} e(t')f(t-t')\,dt'. \tag{12.32}$$

Since the motions of individual molecules are independent and uncorrelated, the autocorrelation of $e(t)$ should have the form

$$\langle e(t)e(t')\rangle = \sigma^2\delta(t-t'), \tag{12.33}$$

where σ^2 is determined by the condition that the mean kinetic energy of the pendulum is equal to $\frac{1}{2}kT$. From (12.32), we have

$$\begin{aligned} M\langle\dot{\xi}^2(t)\rangle &= \frac{1}{M}\int_{-\infty}^{t}\dot{f}(t-t')\,dt'\int_{-\infty}^{t}\langle e(t')e(t'')\rangle\dot{f}(t-t'')\,dt'' \\ &= \frac{\sigma^2}{M}\int_{-\infty}^{t}[\dot{f}(t-t')]^2\,dt' = \frac{\sigma^2}{M}\int_{0}^{\infty}[\dot{f}(\tau)]^2\,d\tau. \end{aligned}$$

Then, using equations (12.9) and (12.10), we have

$$M\langle\dot{\xi}^2(t)\rangle = \frac{\sigma^2}{M}\cdot\frac{1}{4\varepsilon} = kT \tag{12.34}$$

or

$$\sigma^2 = 4M\varepsilon kT.$$

Since the pendulum mass is moving with velocity $\dot{\xi}(t)$ under the force $e(t)$, the power received is

$$\begin{aligned}\langle \dot{\xi}(t)e(t)\rangle &= \frac{1}{M}\int_{-\infty}^{t} \langle e(t)e(t')\rangle \dot{f}(t-t')\,dt' \\ &= \frac{\sigma^2}{M}\dot{f}(0) = 4\varepsilon kT.\end{aligned} \tag{12.35}$$

This shows that there is no thermal noise power if $\varepsilon = 0$. In other words, if there is no lossy element, energy cannot flow into the system, because the outflow and inflow must balance at equilibrium. Only the dashpot can convert its kinetic energy into heat; the mass and spring cannot.

In order to see the noise generation of the dashpot more directly, we can remove the spring and then compute the power:

$$\langle \dot{\xi}(t)e(t)\rangle = \frac{\langle e(t)e(t)\rangle}{2\varepsilon M} = \frac{\sigma^2\,\delta(0)}{2\varepsilon M}. \tag{12.36}$$

The power is infinite! But the power spectral density defined in (12.26) is finite. Since $\delta(t) = 1/(2\pi)\int_{-\infty}^{\infty}\exp(-i\omega t)\,d\omega$, we can write

$$\langle \dot{\xi}(t)e(t)\rangle = \frac{\sigma^2\,\delta(0)}{2\varepsilon M} = \frac{1}{2\pi}\cdot\frac{\sigma^2}{2\varepsilon M}\int_{-\infty}^{\infty} d\omega = \int_0^{\infty} 4kT\,df, \tag{12.37}$$

where $f = \omega/(2\pi)$. In other words, the available thermal power of the dashpot in the frequency band of width Δf is $4kT\Delta f$. This form of thermal power is independent of ε, and is applicable not only to any mechanical dissipative system but also to an electrical dissipative system. For example, the bandwidth of our pendulum system is about ε, and the total noise power is $4\varepsilon kT$ according to equation (12.35), giving the power density $4kT$. The noise power from an electric resistance R may be expressed as $\langle V^2\rangle/R$, where V is voltage. Equating this power to $4kT\Delta f$, we obtain the well-known formula for Johnson noise:

$$\langle V^2\rangle = 4RkT\Delta f. \tag{12.38}$$

Let us now consider the ground acceleration $\alpha(t)$ that would generate pendulum motion equal to its Brownian motion. Since the acceleration produces the force $M\alpha(t)$, the available noise power of the dashpot is

$$M\langle \dot{\xi}(t)\alpha(t)\rangle = \frac{M}{2\varepsilon}\langle \alpha(t)\alpha(t)\rangle = 4kT\Delta f$$

or

$$\langle \alpha^2(t)\rangle = \frac{8\varepsilon kT\Delta f}{M}. \tag{12.39}$$

This gives a ground acceleration equivalent to the Brownian motion of the pendulum. Using $Q^{-1} = 2\varepsilon/\omega_s$, where $2\pi/\omega_s = T_s$ is the undamped pendulum period, (12.39) is rewritten as

$$\frac{\langle \alpha^2(t) \rangle}{\Delta f} = \frac{8\pi kT}{MQT_s}. \tag{12.40}$$

Thus the instrumental acceleration-noise power-density is inversely proportional to the product of mass, instrument Q, and pendulum period.

For comparison with the ground-noise spectra given in Figure 12.12, it is interesting to note that the Low Noise Model ground-noise spectrum is approximately flat in acceleration for frequencies in the range 0.002 to 0.03 Hz, and also for frequencies greater than about 1.5 Hz. In order to estimate the instrument parameters required for the thermal noise to be kept below the ground noise, we can therefore fit (12.40) to the observed LNM ground noise spectra, shown in Figure 12.12b, at long periods and short periods separately. From the figure, we would want

$$\frac{8\pi kT}{MQT_s} < 10^{-17}(\text{m/s})^2/\text{Hz} \qquad \text{at frequencies below 0.03 Hz,}$$

$$< 10^{-19}(\text{m/s})^2/\text{Hz} \qquad \text{at frequencies above 1.5 Hz.}$$

Putting $kT \sim 4 \times 10^{-14}$ erg, we therefore find that the requirement for thermal noise to be below the ground noise is given approximately by

$$MQT_s > 1 \text{ kg-s} \qquad \text{for long periods} \tag{12.41}$$

and

$$MQT_s > 0.01 \text{ kg-s} \qquad \text{for short periods.} \tag{12.42}$$

The traditional long-period seismograph has about a 10-kg mass and a period of 15–30 s, easily satisfying (12.41) with near-critical damping ($Q = \frac{1}{2}$). One of the first instruments to satisfy the long-period requirement (12.41) with much smaller mass was an accelerometer described by Block and Moore (1970). This instrument had M about 10 grams and a relatively short period of 1 s, and it achieved low thermal noise by making the pendulum Q high (200) and using capacitive sensing and electrostatic feedback—techniques we discuss further in Section 12.3.6.

Many simple short-period seismometers still in common use have pendulum periods of 0.1 to 1 s. The mass required to overcome the thermal noise is then only 10 to 100 grams. The pendulum mass traditionally used in the short-period sensor of the Worldwide Standardized Seismographic System is much larger. The sensing device of these instruments (a moving coil in a magnet gap) requires a larger pendulum mass for greater signal power, as shown in the next section.

12.3.2 ELECTROMAGNETIC VELOCITY SENSOR

The motion of a pendulum relative to the seismometer frame was for decades measured most commonly in seismology by the electromagnetic velocity sensor shown schematically

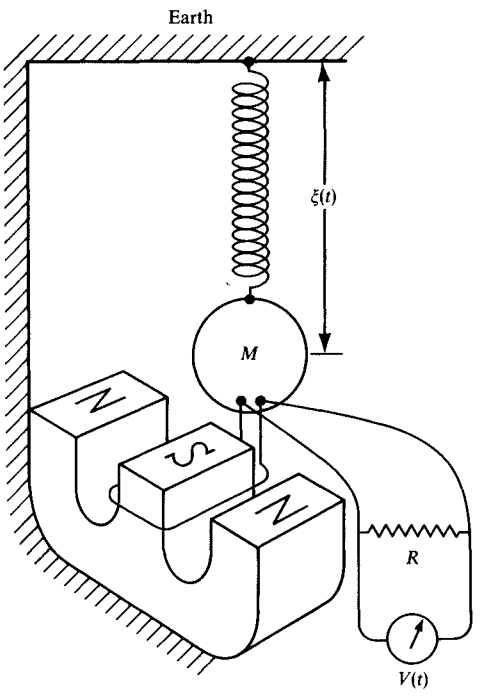

FIGURE **12.15**
When a coil attached to the mass moves through the magnetic field, the voltage across the coil terminals is proportional to the relative velocity between mass and magnet.

in Figure 12.15. A voltage $V(t)$ is generated across the terminals of a coil that is fixed to the mass M and is moving with velocity $\dot{\xi}(t)$ through a magnetic field. The terminal is shunted by resistance R, representing the internal resistance of the recorder. Let l represent the length of coil wire within the magnetic field of flux density B, and assume that the directions of coil movement, magnetic field, and electric current in the coil are perpendicular to each other.

Consider first the mechanical work done by the mass moving through the magnetic field. The force F encountered is, by the Biot–Savart law,

$$F = IlB, \tag{12.43}$$

where I is the current in the coil. The mechanical power consumed is

$$F\dot{\xi} = IlB\dot{\xi}. \tag{12.44}$$

This power must be consumed by the resistance $R + R_0$ (R for the shunt and R_0 for the coil), since these are the only dissipative elements of the system. Thus we have $VI = IlB\dot{\xi}$ or

$$V = lB\dot{\xi}. \tag{12.45}$$

If we write G for lB, we find the interesting result that $V = G\dot{\xi}$ and $F = GI$, which is a special case of Onsager's reciprocal theorem on irreversible thermodynamics.

It follows that

$$I = \frac{G\dot{\xi}}{R_0 + R} \tag{12.46}$$

and

$$F = \frac{G^2\dot{\xi}}{R_0 + R}.$$

With this force F acting on the mass, the equation of motion of the pendulum is

$$\ddot{\xi} + \omega_s^2 \xi = -\ddot{u} - \frac{G^2}{R_0 + R}\frac{\dot{\xi}}{M}. \tag{12.47}$$

Comparing (12.47) with the equation for a pendulum with dashpot (12.2), we find

$$2\varepsilon = \frac{G^2}{(R_0 + R)M}. \tag{12.48}$$

In general, if the pendulum's mechanical attenuation is not zero but ε_0, the total damping is given by

$$\varepsilon = \varepsilon_0 + \frac{G^2}{2(R_0 + R)M}. \tag{12.49}$$

The electric power generated in the shunt resistance by the pendulum motion $\dot{\xi}(t)$ is, from (12.46),

$$\langle VI \rangle = R\langle I^2 \rangle = \frac{RG^2}{(R_0 + R)^2}\langle \dot{\xi}^2(t) \rangle. \tag{12.50}$$

In order to make the sensor powerful, $G^2/(R_0 + R)$ must be large—which, from (12.49), tends to increase the attenuation ε, potentially making the pendulum response insensitive to ground motion. In order to keep ε small, we have to increase M. This is the reason a large mass is needed for a sensitive instrument without an electronic amplifier.

Neglecting ε_0, critical damping is achieved for

$$\frac{\varepsilon}{\omega_s} = \frac{G^2}{2(R_0 + R)M\omega_s} = 1 \tag{12.51}$$

or

$$\frac{G^2}{R_0 + R} = 2M\omega_s. \tag{12.52}$$

Putting (12.52) into (12.50), the power is given by

$$\langle VI \rangle = \frac{R}{R_0 + R} \cdot 2M\omega_s \langle \dot{\xi}^2 \rangle. \tag{12.53}$$

The power is proportional to mass and inversely proportional to pendulum period. The internal resistance of the coil cannot be much larger than the shunt resistance for effective operation. For a traditional seismometer with mass 5 kg and period 1 s, (12.53) gives

$$\langle VI \rangle \sim 5 \times 10^3 \times 2\pi \times \langle \dot{\xi}^2 \rangle.$$

The highest ground-noise level, such as caused by traffic in a city built on soft sediment, may amount to $\sqrt{\langle \dot{\xi}^2 \rangle} \simeq 10^{-2}$ cm/s. Then

$$\langle VI \rangle \sim 1 \text{ erg/s} = 10^{-7} \text{ W},$$

showing the impracticality of generating electricity from traffic noise using a seismometer.

The electromagnetic sensor was introduced to seismology by Galitzin in 1914. He treated seismometry with the exact methods of experimental physics, and cleared up the question of identification of P- and S-waves once and for all for teleseismic events.

Galitzin used a galvanometer to measure the voltage generated by the electromagnetic sensor. A galvanometer is a coil suspended by a thin fiber at its center of mass in a magnetic field, so that electric current passing through the coil will exert a torque around the fiber. A mirror is attached to the coil, and the deflection of the mirror is optically recorded. For several decades this design provided the most common seismographic system at many observatories, and it is still widely in use.

The power sensitivity of such a system is proportional to the pendulum mass, as shown by (12.53). If the mass is large, it is difficult to damp its oscillation electromagnetically as shown in equation (12.48). We need a high G-value to obtain a high-gain seismometer. Before 1939, the quality of magnets was poor and the available magnetic flux B was limited; the only way to increase G was to increase the length l of the coil. Benioff's (1932) variable reluctance seismograph achieved this by using a magnet as the pendulum mass, which moves between two armatures fixed to the seismometer frame and wound with a long wire. He was able to damp critically a pendulum mass of 100 kg at periods of about 1 s. His seismograph supplied valuable data on short-period body waves at teleseismic distances.

Rihn (1969) gives an estimate for the volume V of magnet necessary to provide critical damping for a pendulum with mass M and period T: for the ALNICO V magnet, V (cm^3) $= 50\ M$ (kg)$/T$ (s).

With the improved quality of modern magnets, we no longer need a 100-kg mass to gain the required sensitivity at short periods. Willmore (1960) summarized the later development of electromagnetic sensors and concluded that a pendulum mass of 5 kg is just right for a system directly coupled to a galvanometer. He also showed that, for pendulum periods longer than 1 s, one can minimize the total instrument weight by using the magnet as the pendulum mass.

One can further reduce the mass by using an amplifier or by using a displacement transducer. The Block–Moore accelerometer with a mass of 10 gm can sense a displacement of 1 nm at 5-s periods. Broadband Guralp and Streckeisen feedback instruments introduced in the 1980s have masses of a few tens of grams. The classic pendulum seismograph of Wiechert had to overcome the friction of the pen running over smoked paper. The largest

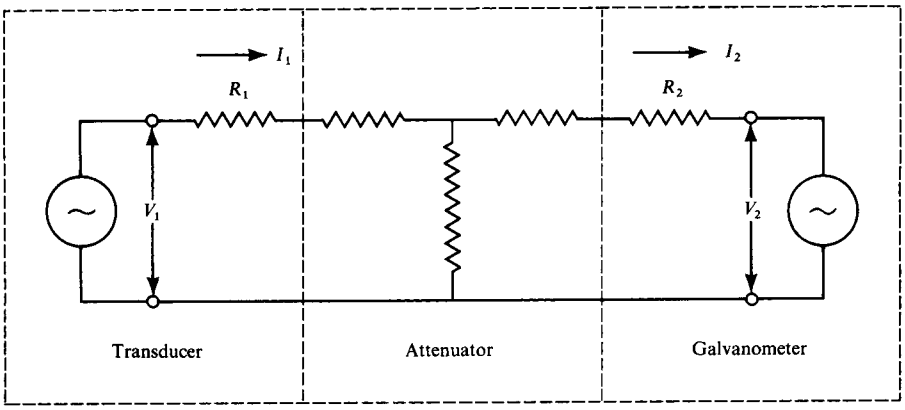

FIGURE **12.16**
Transducer–recorder circuit of a traditional observatory seismograph.

mass of a Wiechert seismograph was 17 tons and achieved a magnification of 10^4, which corresponds to a minimum detectable displacement at a 5-s period of more than 10 nm.

12.3.3 THE RESPONSE CHARACTERISTICS OF TRADITIONAL OBSERVATORY SEISMOGRAPHS

In traditional observatory seismographs, such as those at stations of the World-Wide Standardized Seismographic Network, the output current of the electromagnetic transducer coil is fed into a sensitive galvanometer through an attenuating circuit, such as that shown in Figure 12.16. V_1 is the electromotive force induced in the transducer coil, and V_2 is that in the galvanometer coil. The currents I_1 and I_2 may be expressed in terms of the motions of the two coils. The equation of motion for the coils, on the other hand, includes the force terms due to these currents. The complete description of the galvanometer deflection corresponding to a given ground motion requires the solution of a fourth-order differential equation. A historical summary of the analysis of this problem can be found in Eaton (1957). Here we shall follow Hagiwara (1958), who gave a simple and practical description of the solution. In a later section we shall briefly describe the merits of feedback systems, now common in modern instruments.

The seismometer motion ξ is affected by a restoring force $-G_1 I_1$, where G_1 is the electrodynamical constant of the seismometer (coil and magnet), so that the equation for the relative motion of the moving mass in a traditional instrument is

$$\ddot{\xi} + 2\varepsilon_{0s}\dot{\xi} + \omega_s^2 \xi = -\ddot{u} - \frac{G_1 I_1}{M}. \tag{12.54}$$

Here, ε_{0s} is the mechanical damping of the seismometer, ω_s is the undamped resonant frequency, u is the ground motion, and M is the moving mass of (12.2).

The current I_2 in the galvanometer leads to a couple, $G_2 I_2$, which acts to rotate the galvanometer mirror through an angle Φ. Here, G_2 is the electrodynamical constant of the galvanometer, and

$$\ddot{\Phi} + 2\varepsilon_{0g}\dot{\Phi} + \omega_g^2 \Phi = \frac{G_2 I_2}{K}, \tag{12.55}$$

where ε_{0g} is the mechanical damping of the galvanometer, ω_g is its undamped resonant frequency, and K is the moment of inertia of the galvanometer coil and mirror.

We can regard the current I_1 as the sum of currents due to two separate voltage sources:

$$\begin{aligned} I_1 &= (\text{current through } R_1 \text{ with } V_2 = 0) + (\text{current through } R_1 \text{ with } V_1 = 0) \\ &= I_1\Big|_{V_2=0} + I_1\Big|_{V_1=0}. \end{aligned} \tag{12.56}$$

R_1 here is the resistance of the seismometer coil. V_2 can be maintained at zero if the galvanometer coil is physically restrained from moving; such a coil is said to be *clamped.* Similarly, $I_1|_{V_1=0}$ is given by clamping the seismometer coil. From (12.46) we have

$$I_1\Big|_{V_2=0} = \frac{G_1}{Z_{11}}\dot{\xi},$$

with the impedance Z_{11} here being the ratio of V_1 to I_1 when the galvanometer is clamped. Similarly,

$$I_2\Big|_{V_1=0} = -\frac{G_2}{Z_{22}}\frac{d\Phi}{dt},$$

with Z_{22} as the impedance V_2/I_2 with a clamped seismometer. This last current flows partly through the attenuator circuit and partly through the seismometer coil, so that

$$I_1\Big|_{V_1=0} = -\frac{\mu_2 G_2}{Z_{22}}\frac{d\Phi}{dt},$$

where $\mu_2 = (I_1/I_2)|_{V_1=0}$ is an attenuation factor. From (12.56) we conclude that

$$I_1 = \frac{G_1}{Z_{11}}\dot{\xi} - \frac{\mu_2 G_2}{Z_{22}}\frac{d\Phi}{dt}, \tag{12.57}$$

and similarly

$$I_2 = \frac{\mu_1 G_1}{Z_{11}}\dot{\xi} - \frac{G_2}{Z_{22}}\frac{d\Phi}{dt} \qquad \text{with } \mu_1 = \left(\frac{I_2}{I_1}\right)_{V_2=0}. \tag{12.58}$$

When (12.57) is substituted into the seismometer equation (12.54), we see that an extra damping term is present, and

$$\ddot{\xi} + 2\varepsilon_s\dot{\xi} + \omega_s^2\xi = -\ddot{u} + \frac{\mu_2 G_1 G_2}{Z_{22}M}\frac{d\Phi}{dt}. \tag{12.59}$$

ε_s now is the total seismometer damping, $\varepsilon_{0s} + \frac{1}{2}G_1^2/(Z_{11}M)$ (cf. (12.49)). The reaction of the galvanometer on the seismometer motions is quantified by the last term in (12.59).

When (12.58) is substituted into the galvanometer equation (12.55), we find

$$\ddot{\Phi} + 2\varepsilon_g\dot{\Phi} + \omega_g^2\Phi = \frac{\mu_1 G_1 G_2}{Z_{11}K}\dot{\xi}, \tag{12.60}$$

in which ε_g is the total galvanometer damping, $\varepsilon_{0g} + \frac{1}{2}G_2^2/(Z_{22}K)$.

The seismograph response $\Phi(t)$, for a given input $u(t)$, can be obtained by solving the fourth-order equation that results when $\dot{\xi}$ is eliminated between (12.59) and (12.60). We find that

$$\begin{aligned}\dddot{\Phi} + 2(\varepsilon_s + \varepsilon_g)\ddot{\Phi} + [\omega_s^2 + \omega_g^2 + 4\varepsilon_s\varepsilon_g(1-\sigma^2)]\dot{\Phi} \\ +2(\varepsilon_s\omega_g^2 + \varepsilon_g\omega_s^2)\dot{\Phi} + \omega_s^2\omega_g^2\Phi = -\frac{\mu_1 G_1 G_2}{Z_{11}K}\ddot{u},\end{aligned} \tag{12.61}$$

where

$$\sigma^2 = \frac{\mu_1\mu_2 G_1^2 G_2^2}{4Z_{11}Z_{22}MK\varepsilon_s\varepsilon_g} = \frac{\mu_1\mu_1(\varepsilon_s - \varepsilon_{0s})(\varepsilon_g - \varepsilon_{0g})}{\varepsilon_s\varepsilon_g}.$$

The quantity σ^2 is a dimensionless measure of the *coupling* between seismometer and galvanometer. The coupling is small when the attenuation is strong, and the electromagnetic damping is small relative to the mechanical damping. The effect of coupling on the shape of the seismograph response is strongest when the periods of pendulum and galvanometer are equal. Even then, according to Hagiwara (1958), if we take $\sigma^2 < \frac{1}{4}$, the maximum deviation from the zero-coupling response is about 20% in amplitude and about 15° in phase. If the coupling is neglected ($\sigma^2 = 0$), the reaction term ($\propto d\Phi/dt$) in (12.59) is taken as zero, and the response function of the seismograph can be easily calculated. Taking $u = U\exp(-i\omega t)$, the solution of (12.59) is $\xi = \omega^2 U\exp(-i\omega t)/[-\omega^2 - 2i\varepsilon_s\omega + \omega_s^2]$. From this as input to (12.60) we find

$$\Phi = \frac{\mu_1 G_1 G_2(-i\omega)}{Z_{11}K[-\omega^2 - 2i\varepsilon_g\omega + \omega_g^2]}\frac{\omega^2 U e^{-i\omega t}}{[-\omega^2 - 2i\varepsilon_s\omega + \omega_s^2]}. \tag{12.62}$$

For large ω, we have

$$\Phi \sim \frac{\mu_1 G_1 G_2}{Z_{11}K}\left(\frac{1}{i\omega}\right)Ue^{-i\omega t}. \tag{12.63}$$

For small ω, we have

$$\Phi \sim \frac{\mu_1 G_1 G_2}{Z_{11}K}\left(\frac{\omega^3}{i\omega_s^2\omega_g^2}\right)Ue^{-i\omega t}. \tag{12.64}$$

The above equations show that the amplitude response peaks at frequencies between ω_s and ω_g, decreases with increasing frequency as ω^{-1} for higher frequencies, and decreases with increasing period as T^{-3} for longer periods.

The absolute value of seismograph sensitivity is determined by a product of constants, $\mu_1 G_1 G_2 / Z_{11} K$, which is easily measured. For example, if we put a constant current I_0 through the galvanometer coil, the deflection Φ is given by (12.55) as

$$\Phi = \frac{G_2}{K\omega_g^2} I_0,$$

from which G_2/K can be calculated. Other quantities are discussed earlier.

The phase response can also be calculated easily using (12.62). Putting $\Phi = |\Phi| \exp[-i\omega t + i\phi(\omega)]$, $\phi(\omega)$ represents the instrumental phase delay. A small problem here is the choice of sign in (12.62) or a phase uncertainty by π. The choice depends on how the instrument is calibrated. Suppose we are calibrating a vertical-component seismograph and we apply a downward impulse on the pendulum mass. The galvanometer deflection trace will swing to one direction, which will be marked as "up" because the downward mass movement corresponds to an upward ground movement. For an impulsive movement, the seismograph will respond according to the high-frequency asymptotic characteristics (12.63). With the choice of sign given in (12.62)–(12.64), the response would be like a *negative* step, because this is the time-domain signal corresponding to $(1/i\omega)$ as $\omega \to \infty$. But since we now designate the direction of galvanometer swing as "up" when the ground moves impulsively "up", we change the sign of (12.63) so that

$$\Phi \sim \frac{\mu_1 G_1 G_2}{Z_{11} K} U \cdot \frac{1}{\omega} \exp(-i\omega t + i\pi/2) \qquad \text{as } \omega \to \infty.$$

The signs for (12.62) and (12.64) must also be reversed. The phase delay is $+\pi/2$ for infinite frequency, decreases monotonically with decreasing frequency, and reaches $-3\pi/2$ at zero frequency (see Box 12.4).

The phase values shown in Hagiwara's original figures must be corrected by adding π in order to be consistent with this conventional method of marking the direction of Earth movement on the record. Corrected phase delays as well as the amplitude response curves are shown in Figure 12.17 for various coupling constants σ^2, in the case of $\omega_s/\omega_g = 6$ and $\varepsilon_s/\omega_s = \varepsilon_g/\omega_g = 1$, which roughly apply to the long-period seismographs of WWSSN stations. (Such seismographs are often referred to as "15–100 instruments." The numbers here, 15 and 100, are, respectively, the seismometer free period and the galvanometer free period, both in seconds. Also common are 30–100 instruments. A widely used WWSSN short-period seismograph has the configuration 1–0.75.)

12.3.4 HIGH SENSITIVITY AT LONG PERIODS

The frequency response of the traditional velocity-transducer–galvanometer system attenuates inversely proportional to the cube of period at long periods, as shown in (12.64). By increasing the pendulum period, the highly attenuating range can be pushed further toward longer periods. In Section 12.1 we mentioned LaCoste's pendulum, which operates stably at periods of several tens of seconds.

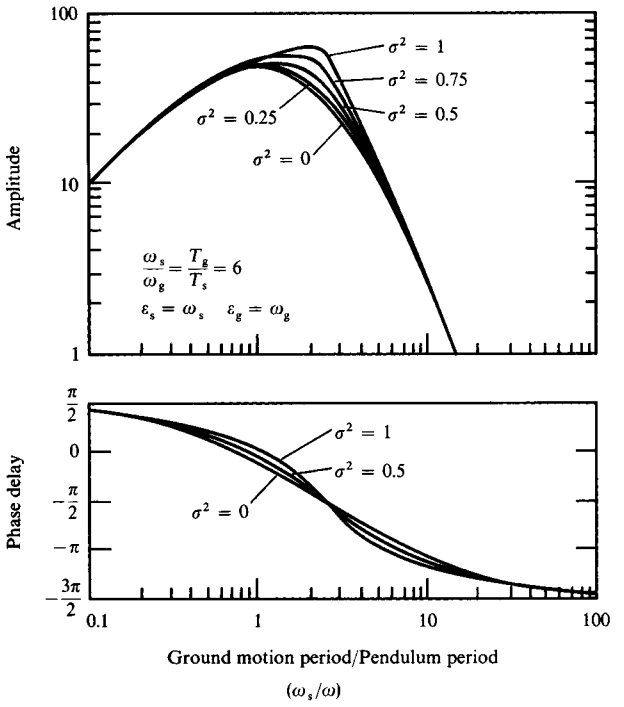

FIGURE **12.17**
Amplitude and phase-delay response for various coupling constants σ^2. [After Hagiwara, 1968.]

Two basically different ways of improving high sensitivity at long periods are the use of (1) a displacement transducer instead of a velocity transducer and (2) a strain sensor instead of an inertial sensor. Either way, the low-frequency response is improved proportionately with the period. Both improvements were combined in Benioff's extensometer (1959), which successfully recorded the Earth's free oscillations during the great Chilean earthquake of 1960.

The displacement transducer developed by Benioff used a capacitor plate attached to the moving part of the seismometer and sandwiched between two plates fixed to the frame. But the circuitry had inherent nonlinearities for large displacement. Later displacement transducers use a different circuitry, though also based on capacitors. For the circuit shown in Figure 12.18, a fixed-frequency oscillator (16 kHz in Block and Moore, 1966; 3 kHz in Stacey *et al.*, 1969; and 500 kHz in Buck *et al.*, 1971) supplies equal and opposite voltage

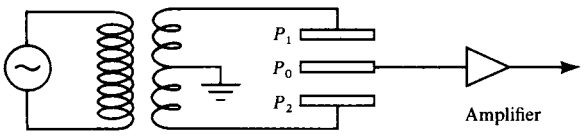

FIGURE **12.18**
Displacement transducer. The plate P_0 is attached to the moving part of the seismometer, and the other two plates are attached to the frame. With this design, response is linear over a wide range of input ground motions.

BOX 12.4

General features of the response of a traditional electromagnetic seismograph

We have seen how an instrument that records seismic motions can usefully be thought of in terms of several components. It is informative to look at the frequency response of each component, using an approximate theory if necessary to get a simple result. We shall find responses that are proportional to different powers of frequency, so that graphical display is best done with log–log plots.

As examples of the basic inertial sensor, we have considered masses on both springs and pendulums. For these devices, the output ξ (Fig. 12.2) has an amplitude response $|X(\omega)|$ given by (12.4). $|X(\omega)|$ is just the ratio between output and input amplitude spectra, $|\xi(\omega)|/|u(\omega)|$. It tends to a constant at high frequencies, and is proportional to ω^2 at low frequencies, so that the behavior is roughly as shown in Figure A below.

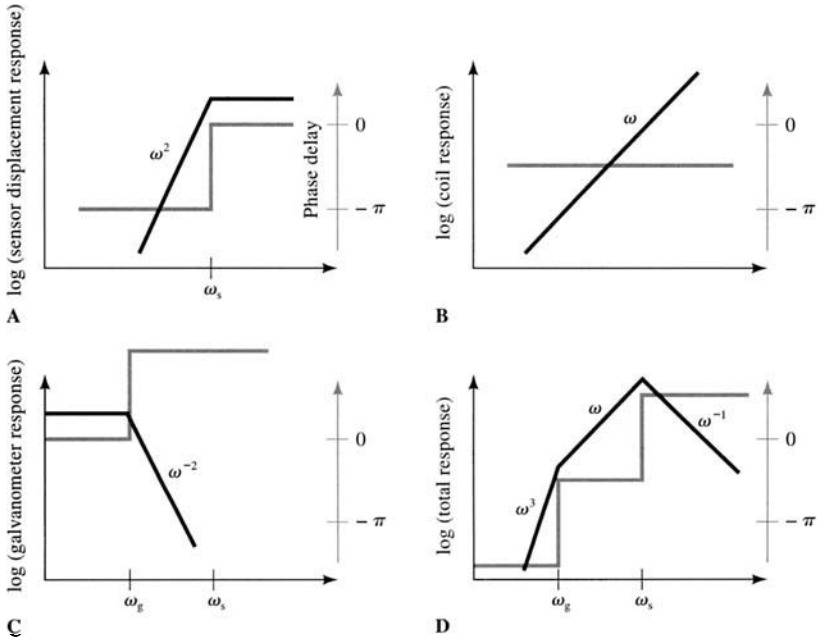

The main features of the sensor's displacement response are its constant amplitude at frequencies above ω_s and its rapid falloff (12 db per octave) below ω_s. In Figure B, the coil response is proportional to frequency at all frequencies. In Figure C, the galvanometer response is constant below its natural frequency (ω_g) and falls off rapidly at higher frequencies. Summing the first three log (response) curves, in the case $\omega_g < \omega_s$, we see in Figure D an extremely rapid falloff at low frequencies. If, instead, $\omega_s < \omega_g$, the shape of the total response is unchanged. Note that double differentiation to get acceleration response (i.e., response to ground acceleration) corresponds to multiplying (a) by ω^{-2}, so that it will be flat below ω_s and decay according to ω^{-2} at higher frequencies.

(continued)

BOX **12.4** *(continued)*

The next component may be a coil, for which $\xi(\omega)$ is the input and current $I(\omega)$ is the output. From (12.46) we see that the amplitude-response spectrum of this component is proportional to ω (Figure B), because $\dot{\xi}(\omega) = -i\omega\xi(\omega)$.

The final component may be a galvanometer, for which $I(\omega)$ is the input and the mirror angle $\Phi(\omega)$, perhaps multiplied by some frequency-independent constant, is the output. We have made the simplifying assumptions that the current in the galvanometer is directly related (proportional) to the current in the seismometer coil and that neither current has a feedback effect (coupling) on the pendulum motion. From (12.55), it follows that the galvanometer response, $\Phi(\omega)/I(\omega)$, has an amplitude that is constant at low frequencies and behaves like ω^{-2} at high frequencies (Figure C).

The total response is a product of the component responses, becoming a summation when studied with log (response) plots. Typically, one finds for the so-called "velocity pickup" (i.e., the coil), that the total response is as shown in Figure D. If the inertial sensor has its displacement output (instead of its velocity output) directly converted to an electrical signal, then the final response is merely the sum of Figures A and C. In modern instruments, the seismometer output (inertial sensor plus coil) may become the input to a variety of electronic amplifiers with different frequency characteristics, in which case curves in Figures A and B must be added to the amplifier response.

The phase-delay spectrum is approximated, for the inertial sensor, by a step jump from $-\pi$ to 0 as ω increases through ω_s. (It is assumed that the direction of ground motion has been properly marked, as discussed following equation (12.4).) For the coil, the phase delay is constant at $-\pi/2$, and for the galvanometer the phase delay is a step jump from 0 to π as ω increases through ω_g. These delays are shown in gray in the figures.

on the capacitor plates P_1 and P_2 by use of a transformer with a split secondary. The center tap of the secondary is grounded. When the plate P_0 is in the mid position, the voltage of P_0 relative to the ground is zero. Since the capacitance of a pair of parallel plates is inversely proportional to the distance between the plates, the voltage of P_0 is directly proportional to the displacement of P_0 from the midpoint. This voltage can be measured very precisely by the tuned amplifier—either a lock-in amplifier or a synchronous detector—because the signal frequency is precisely known. An important point about the lock-in method used with a capacitive sensor is that the the signal is being measured at a high frequency, thus lowering the noise (since most electronic devices have much increased noise at a few Hz and below).

The strain seismometer has a certain advantage over the inertial seismometer as a sensor of long-period waves. Consider a simple harmonic wave with velocity c propagating in the x-direction. Let the displacement u in the x-direction be

$$u = Ue^{-i\omega(t-x/c)}.$$

Then the extensional strain in the x-direction is

$$\frac{\partial u}{\partial x} = \frac{i\omega}{c} Ue^{-i\omega(t-x/c)}.$$

If a displacement transducer is used, the output voltage will be proportional to $\omega U/c$. On the other hand, the sensor displacement, at periods longer than the pendulum period, will be proportional to $\omega^2 U$ (see (12.3) for $\omega \ll \omega_s$). In other words, as mentioned earlier, the strain sensor's frequency response is better than that of the pendulum, the improvement increasing proportionately with the period at long periods.

Another advantage of the strainmeter is that it can record secular strain changes, whereas the pendulum seismometer cannot respond to zero frequency signals except for those produced by tilt and by changes in the gravity field.

A disadvantage of the strainmeter, however, is its use of the Earth as a part of the instrument. The presence of cracks, joints, loose rocks, water, and other weak material having unpredictable mechanical behavior tends to introduce undesirable noise and makes the system more nonlinear and even nonstationary.

12.3.5 THE NONLINEARITY OF THE SEISMIC SENSOR

The response of any physical system is nonlinear unless the magnitude of the input is very small. The seismograph is no exception. Let us start with the nonlinearity of the traditional seismograph described in Section 12.3.3. Berckhemer and Schneider (1964) made a careful study of ground displacement by solving the fourth-order differential equation of the Galitzin–Wilip seismograph (T_s (seismometer pendulum period) = 12 s, T_g (galvanometer period) = 12 and 50 s) and the Press–Ewing seismograph ($T_s = 30$ s, $T_g = 100$ s), on an analog computer at the Stuttgart Institute of Technology.

The records of earthquakes at long distances indicated the ground displacement coming back to the initial position after the passage of seismic waves. On the other hand, the waveforms from nearby earthquakes indicated a residual displacement, or more precisely a parabolic increase in displacement corresponding to a permanent change in acceleration. A typical record of such a long-period transient waveform is shown in Figure 12.19. In order to explain these records, it was required that an earthquake of magnitude 5 produce a permanent change in acceleration of the order of 10^{-7} to 10^{-8} g at a distance of about 100 km. This means a change of gravity by 0.01–0.1 milligal for the vertical component, and a tilt of 10^{-7}–10^{-8} radian for the horizontal component. Press (1965) suspected instrumental hysteresis as the cause, inasmuch as the observed tilt was three to four orders of magnitude larger than the value he calculated for that size earthquake using a simple dislocation model. We know since the mid-1960s that dislocation models work quite well, but Berckhemer and Schneider (1964) instead took the tilt to be a real phenomenon, and rejected the reality of

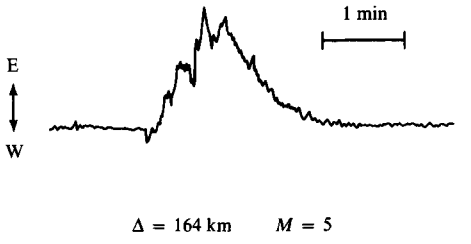

FIGURE **12.19**
Typical record of a near earthquake by a traditional long-period seismograph.

BOX 12.5
Poles and zeros

A succinct convention has been developed in many fields of physical science for quantifying the response function of a causal linear time-invariant system such as a seismometer. The response is simply given by specifying the location of poles and zeros of the transformed impulse response. This could be done using the Fourier transform—for example by specifying the poles and zeros of expressions such as (12.3) and (12.7)—but conventionally for decades the specification has been based on the Laplace transform, $f(s) = \int_0^\infty f(t)e^{-st}dt$, rather than the Fourier transform.

Linearity means that the principle of superposition applies. If the inputs $u_1(t)$ and $u_2(t)$ separately produce outputs $\xi_1(t)$ and $\xi_2(t)$ respectively, then for any constants A and B the input $Au_1(t) + Bu_2(t)$ produces the response $A\xi_1(t) + B\xi_2(t)$. Time invariance means that the response does not change with time—for example, because of changes in temperature, or aging of materials. The response of any linear time-invariant system to the steady-state unit input $e^{-i\omega t}$ contains only the same steady-state variation $e^{-i\omega t}$, multiplied by a frequency-dependent factor $f(\omega)$ which we have called the frequency response. Because the input $u(t)$ is the sum of its frequency components, linearity tells us that the output is $\xi(t) = \frac{1}{2\pi}\int_{-\infty}^{\infty} u(\omega)f(\omega)e^{-i\omega t}d\omega = u(t) * f(t)$.

All the sensors of seismic motion described in this chapter have idealized outputs that satisfy ordinary differential equations with constant coefficients. This is true for the simplest pendulums as well as for compound instruments involving various magnets, coils, capacitors, electronic filters, and feedback loops. Such instruments have a relationship between input ground motion $u(t)$ and output $\xi(t)$ in the form

$$a_n\frac{d^n\xi}{dt^n} + a_{n-1}\frac{d^{n-1}\xi}{dt^{n-1}} + \cdots + a_0\xi = b_m\frac{d^m u}{dt^m} + b_{m-1}\frac{d^{m-1}u}{dt^{m-1}} + \cdots + b_0 u. \qquad (1)$$

See, for example, the relationship (12.61) for the traditional seismograph.

An input $u(t)$ that first becomes nonzero at time $t = 0$ has an output $\xi(t)$ that also is zero prior to $t = 0$, and by Laplace-transforming (1) we obtain the response

$$f(s) \equiv \frac{\xi(s)}{u(s)} = \frac{b_m s^m + b_{m-1}s^{m-1} + \cdots + b_0}{a_n s^n + a_{n-1}s^{n-1} + \cdots + a_0}. \qquad (2)$$

Since the numerator and denominator here are both polynomials, we can factor them and express (2) in terms of their roots:

$$f(s) = K\frac{\prod_{i=1}^{m}(s - z_i)}{\prod_{j=1}^{n}(s - p_j)}, \qquad (3)$$

where $K = b_m/a_n$. The roots of the numerator, $z_1, z_2, \ldots z_m$, are called the *zeros* and those of the denominator, $p_1, p_2, \ldots p_n$, are called the *poles* of the response. Since the two polynomials in (2) have real coefficients, the poles and zeros are themselves either real, or else occur in complex conjugate pairs. Since the response is causal, the singularities of (3) must all lie in the left half-plane (i.e., $\mathrm{Re}(p_j) \leq 0$). The traditional seismograph response, derived from (12.61), has three zeros and four poles. The instrument used in the Global Seismographic Network, operated by the IRIS Consortium and the U.S. Geological Survey, has a response described in detail by Fels and Berger (1994). It has five zeros, all of them real, and 14 poles, four of them real and ten that occur as five pairs of conjugate complex values.

The response f is easily obtained in the time domain by expressing (3) as a sum of partial fractions and inverting them one by one.

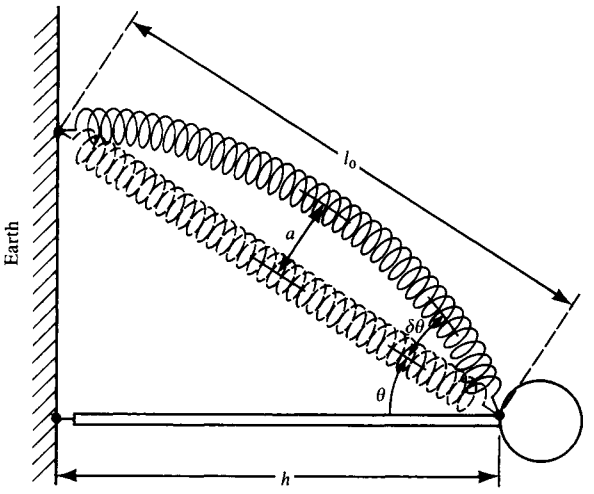

FIGURE **12.20**
Bow-stringing of a helical spring.

gravity change. They attributed it to a nonlinearity of the vertical-component seismograph, which they were able to explain in a qualitative way.

The nonlinearity they considered is due to the bow-stringing effect of a helical spring. A strong earthquake at a short distance will shake the seismograph strongly and may cause an oscillation of the spring, as depicted in Figure 12.20. Assuming a sinusoidal fundamental mode of oscillation with the amplitude a at the center, the spring length will be

$$l = \int_0^{l_0} \sqrt{1 + \left(\frac{dy}{dx}\right)^2}\, dx \qquad \text{where} \qquad y = a \sin\left(\frac{\pi x}{l_0}\right).$$

For small values of (a/l_0) this gives

$$l \sim l_0 \left[1 + \frac{1}{4}\left(\frac{a\pi}{l_0}\right)^2\right].$$

The angle $\delta\theta$ will be

$$\delta\theta = \left.\frac{dy}{dx}\right|_{x=0} = \frac{a\pi}{l_0}.$$

The torque exerted by the spring is

$$(T + \delta T)\, h \sin(\theta + \delta\theta) \sim Th \sin\theta + \delta T\, h \sin\theta + Th \cos\theta\, \delta\theta - Th \sin\theta \frac{(\delta\theta)^2}{2},$$

where T is the tensional force exerted by the spring to maintain itself at length l_0, and δT is the change in T due to the bow-stringing effect.

For the zero–initial-length spring with spring constant k, we can go on to find that

$$T = kl_0 \qquad \text{and} \qquad \delta T = k\frac{l_0}{4}\left(\frac{a\pi}{l_0}\right)^2.$$

Then the torque exerted by the spring is

$$(T + \delta T)\, h \sin(\theta + \delta\theta) = Th \sin\theta \left[1 - \frac{1}{4}\left(\frac{a\pi}{l_0}\right)^2\right] + Th \cos\theta\, \delta\theta.$$

Since $\delta\theta$ is a rapidly oscillating term due to bow-stringing, it vanishes on the average. Thus the effect of bow-stringing averaged over time is always to reduce the torque in the spring and hence to lower the mass position. This effect transforms a high-frequency disturbance into a low-frequency spurious signal. For the LaCoste-type vertical seismometer, this effect will always look like a step increase of gravity.

Nonlinearity was also a serious problem for early designs of strain seismometer. Sacks *et al.* (1971) specifically designed a strainmeter free from the effects of nonlinearity and hysteresis, and installed three of them at Matsushiro, Japan, close to a quartz-tube strainmeter. Their instrument consists of a liquid-filled resilient tube, which is buried in a borehole and held in tight contact with the rock wall. The coupling between the wall and the tube is made by the use of expanding cement. The tube is designed to follow the minute distortion of the borehole down to 10^{-6} μm. The instrument measures only the dilatational strain. Their principal observation was that a number of strain changes associated with near earthquakes had been recorded by the quartz extensometer, but not by the borehole strainmeter. Their result suggests that many strain changes observed by the quartz extensometer may be spurious and probably due to nonlinearity. Ágústsson *et al.* (1999) describe volumetric strain changes measured with the borehole instrument, which are reliably associated with an earthquake in Iceland that was possibly triggered by magmatic intrusion.

12.3.6 FEEDBACK SEISMOMETERS

We have seen that a traditional seismometer is based upon measurement of ground motion against an inertial reference, such as a pendulum or a mass on a spring. The best modern seismometers sense ground motion using the same inertial principle, but add an additional electromagnetic or electrostatic restoring force in a direction such that the inertial mass closely follows the motion of the ground. Such a system provides *negative feedback*. Because relative motion between the mass and its surroundings (moving with the ground) is greatly reduced, this type of system can avoid the parametric effects mentioned in Section 12.1.3, and the nonlinearities associated with excursions from what (without the feedback) would be the equilibrium position. The electric voltage or current that generates the restoring force is nearly proportional to ground acceleration, and is used as the output signal. Such an approach, based on an electronic network without moving elements, can have linearity and dynamic range that are greatly superior to those of mechanical systems

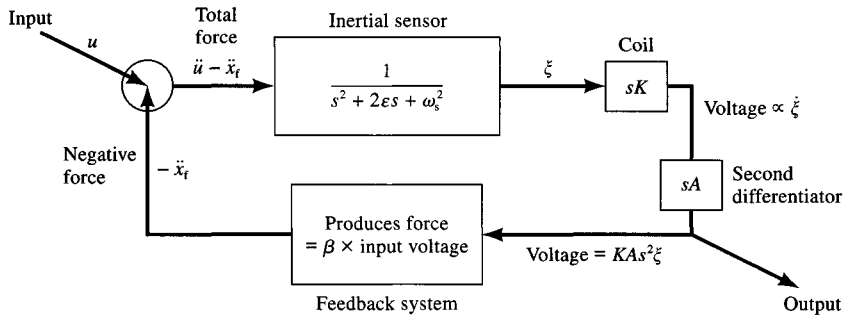

FIGURE **12.21**
Schematic for an acceleration feedback seismometer. The seismometer mass is made to appear very large. Adapted from Usher *et al.* (1979).

with relative motion between their components. Because feedback affects signal and ground noise equally, it does not affect detection capability.

As an example of a simple acceleration feedback system, we follow Usher *et al.* (1979) and show ground motion $\ddot{u}$ in Figure 12.21 as an input to the inertial sensor with free period $\omega_s = \sqrt{k/M}$ and damping $\varepsilon = D/M$. The sensor output is detected by a coil, which in the traditional instrument delivers current to a galvanometer. But in Figure 12.21 the coil output goes to a second differentiator with output voltage $V(s) = KAs^2\xi(s)$. A feedback system then delivers an acceleration $\ddot{x}_f(s)$, proportional to V, which is applied as a negative acceleration to the inertial sensor.

The equations governing this system are

$$\ddot{x}_{\text{total}} = \ddot{u} - \ddot{x}_f, \qquad V = \frac{KA\,s^2}{s^2 + 2\varepsilon s + \omega_s^2}\,\ddot{x}_{\text{total}}, \qquad \ddot{x}_f = \beta V$$

so that the overall response is

$$\frac{V}{\ddot{u}} = \frac{KA\,s^2}{s^2(1 + KA\beta) + 2\varepsilon s + \omega_s^2}. \tag{12.65}$$

In effect, the original mass M has been increased to $M(1 + KA\beta)$, and the natural frequency has been decreased to $\omega_s/\sqrt{1 + KA\beta}$.

A simple displacement feedback system is shown in Figure 12.22. Here, the inertial sensor is monitored with a displacement transducer, which is then amplified to provide an output voltage $V(s) = rA\xi(s)$. In this case the feedback system delivers an acceleration $rA\beta V$, applied in the negative direction to the inertial sensor. The governing equations are

$$\ddot{x}_{\text{total}} = \ddot{u} - \ddot{x}_f, \qquad V = \frac{rA}{s^2 + 2\varepsilon s + \omega_s^2}\,\ddot{x}_{\text{total}}, \qquad \ddot{x}_f = rA\beta V$$

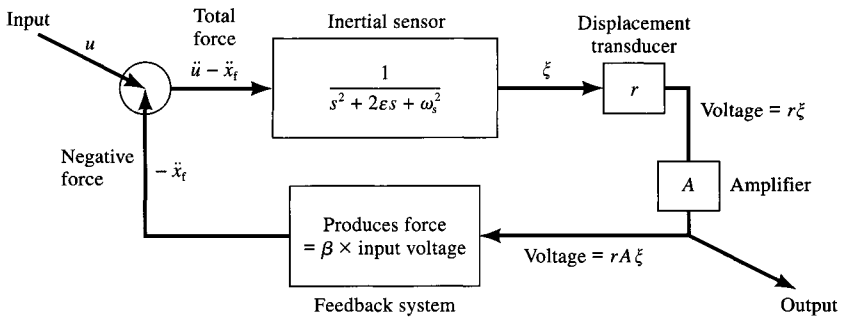

FIGURE **12.22**
Schematic for a displacement feedback seismometer. The seismometer spring is effectively made to appear very stiff. Adapted from Usher *et al.* (1979).

and the overall response is

$$\frac{V}{\ddot{u}} = \frac{rA}{s^2 + 2\varepsilon s + (\omega_s^2 + rA\beta)}. \tag{12.66}$$

Here, the original stiffness of the sensor has effectively been increased. The response is flat to acceleration from low frequencies up to near the new natural frequency, $\sqrt{\omega_s^2 + rA\beta}$.

We saw in (12.41) and (12.42) that the requirement for thermal noise to lie below ground noise can be met with instruments of low mass (a few tens of grams) and period around 1 s, provided the instrument Q is large enough (on the order of 100). An advantage of seismometers with low values of M and T_s is that, unlike traditional electromagnetic seismographs, they can be made small enough for borehole deployments. A borehole can provide a temperature-stable environment, as well as the ground-noise reduction needed for good recordings of weak horizontal-component seismic signals.

The importance of operating sensitive long-period and broadband seismometers under rigid environmental control is recognized as a key step in the series of improvements that lie between Galitzin's instruments of the early 1900s, and the modern observatory instrument. The high-gain long-period system of Pomeroy *et al.* (1969) was the first to place seismometers in an airtight chamber with controls to maintain near-constant temperature. (Slight temperature changes of air at normal pressure would change the buoyancy force acting on the inertial mass.) Wielandt and Streckeisen (1982) describe a compact feedback instrument that is placed in a chamber with air evacuated down to a pressure around 10 mbar. With careful attention to the design of springs and circuit elements, such broadband instruments are operated with internal noise less than ground noise over a band ranging at least from 0.3 to 300 s period and typically from 0.1 to 3000 s, and have a dynamic range of 140 dB. The key to the compact design is replacement of the traditional zero–initial-length spring with a leaf spring, made of a rectangular piece of metal. Wielandt achieved details of the design shown in Figure 12.23 by trial and error with the help of computer simulation, and it can be constructed with a long natural period of oscillation. Wielandt and Steim (1986) describe a modification to the feedback circuit of these instruments, giving

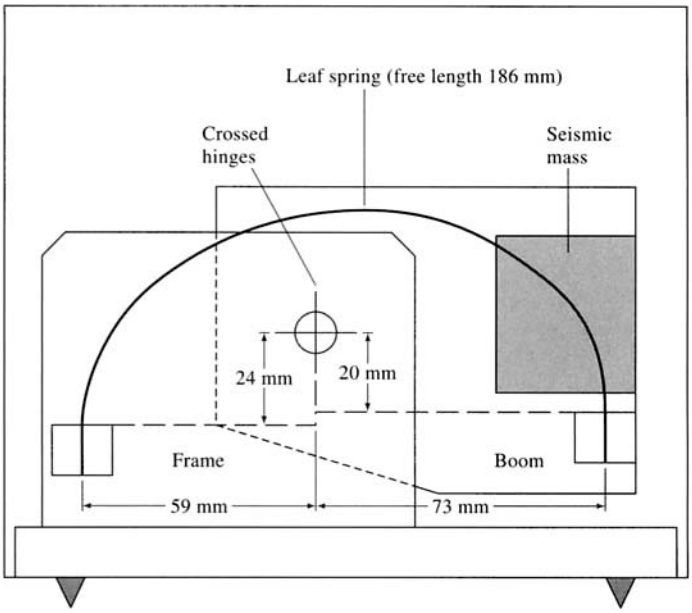

FIGURE **12.23**
Spring geometry of a vertical component seismometer, in which the inertial mass is supported by a leaf spring. The spring is bent over into an arch, with its left-hand end fixed to the frame. The right-hand end is fixed to the boom to which the inertial mass is attached. This type of spring is stiff compared to the traditional spring (which can bow-string as shown in Figure 12.20), and its lowest resonance is at 80 Hz. Adapted from Wielandt and Streckeisen (1982).

them an output flat to ground velocity from 0.2 to 360 s period. This wide band is well suited to the study of normal modes, surface waves, and most teleseismic body waves, but it does not extend sufficiently far at the short period end to record the information carried by regional waves such as P_g, P_n, S_n and L_g, which may include ground motion at frequencies above 20 Hz. Short-period signals are particularly important in discriminating between earthquakes and explosions. For such work, the instrument used for the records in Figure 12.1 is more suitable.

We conclude by noting that much progress has been made to develop seismometers capable of recording across wide bands of frequency and amplitude. But for the great variety of signals to be observed, it is still not possible to record ground motions faithfully by use of a single instrument.

Suggestions for Further Reading

Agnew, D. C. Strainmeters and tiltmeters. *Reviews of Geophysics*, **24**, 579–624, 1986.

Beauchamp, K. G., ed. *Exploitation of Seismograph Networks*. Leiden, Noordhoff: International Publishing, 1975.

Fels, J.-F., and J. Berger. Parametric analysis and calibration of the STS-1 seismometer of the IRIS/IDA seismographic network. *Bulletin of the Seismological Society of America*, **84**, 1580–1592, 1994.

Kanamori, H. Importance of historical seismograms for geophysical research. In *Historical Seismograms and Earthquakes of the World*, edited by W. H. K. Lee, H. Meyers, and K. Shimazaki, 16–33. 1988.

LaCoste, L. C. Measurement of gravity at sea and in the air. *Reviews of Geophysics*, **5**, 477–526, 1967.

McLeod, D. P., G. E. Stedman, T. H. Webb, and U. Schreiber. Comparison of standard and ring laser rotational seismograms. *Bulletin of the Seismological Society of America*, **88**, 1495–1503, 1998.

Melton, B. S. The sensitivity and dynamic range of inertial seismographs. *Reviews of Geophysics and Space Physics*, **14**, 93–116, 1976.

Murphy, A., J. Savino, J. Rynn, G. Choy, and K. McCamy. Observations of long-period (10 s–100 s) seismic noise at several worldwide locations. *Journal of Geophysical Research*, **77**, 5042–5049, 1972.

Riedesel, M. A., R. D. Moore, and J. A. Orcutt. Limits of sensitivity of inertial seismometers with velocity transducers and electronic amplifiers. *Bulletin of the Seismological Society of America*, **80**, 1725–1752, 1990.

Rodgers, P. W. The response of the horizontal pendulum seismometer to Rayleigh and Love waves, tilt, and free oscillations of the earth. *Bulletin of the Seismological Society of America*, **58**, 1384–1406, 1968.

Sax, L. R. Stationarity of seismic noise. *Geophysics*, **33**, 668–674, 1968.

Scales, J. A., and R. Snieder. What is noise? *Geophysics*, **63**, 1122–1124, 1998.

Scherbaum, F. *Of Poles and Zeroes: Fundamentals of Digital Seismology*. Hingham, Mass.: Kluwer Academic Publishers, 1996.

Usher, M. J., R. F. Burch, and C. Guralp. Wide-band feedback seismometers. *Physics of the Earth and Planetary Interiors*, **18**, 38–50, 1979.

Wielandt, E., and G. Streckeisen. The leaf-spring seismometer: Design and performance. *Bulletin of the Seismological Society of America*, **72**, 2349–2367, 1982.

Wielandt, E., and J. Steim. A digital very-broad-band seismograph. *Annales Geophysicae*, Series B, **4**, 227–232, 1986.

Problems

12.1 Show that the convolution (12.13) can also be written in the form

$$\xi(t) = \int_0^\infty u(t-\tau)\ddot{f}(\tau)\,d\tau.$$

12.2 Show that the period T of a mass suspended vertically by a spring is equal to $T = 2\pi\sqrt{(l-l_0)/g}$, where l is the equilibrium length of the spring (under its gravitational load) and l_0 is the initial length (under no tension).

12.3 This problem is motivated by the need to know how much ground motion is caused by atmospheric disturbances, and how much this motion (which is noise, for most studies) can be reduced by burying seismometers at some depth (Sorrells, 1971).

Consider a homogeneous half-space with its surface at $z = 0$. Suppose that a moving pressure is applied to the surface, and is modeled by boundary conditions $\tau_{zx} = \tau_{yz} = 0, \tau_{zz} = -P \exp[i\omega(x/c - t)]$.

a) Show that *P–SV* motion in the half-space is given by the motion-stress vector $\mathbf{f} = \mathbf{F}\mathbf{w}$, where $\mathbf{f}$ and $\mathbf{F}$ are given by (5.60) and (5.65), and

$$\mathbf{w} = \frac{iP}{\omega\rho\beta^2 \mathsf{R}(p)} \begin{pmatrix} \left(\frac{1}{\beta^2} - 2p^2\right)\frac{1}{\alpha} \\ \frac{-2p\xi}{\beta} \\ 0 \\ 0 \end{pmatrix}$$

where $p = c^{-1}$, $\mathsf{R}(p)$ is the Rayleigh function (5.54), and $\xi = \sqrt{1/\alpha^2 - p^2}$.

b) If $c \ll \beta$ and $\omega z c/2\beta^2 \ll 1$ show that the horizontal and vertical components of displacement are, respectively,

$$u_x = \frac{icP}{\omega\rho\beta^2}\left[\frac{\beta^2}{\alpha^2 - \beta^2} - \frac{\omega z}{c}\right] e^{i\omega z/c} \exp\left[-\omega\left(\frac{x}{c} - t\right)\right]$$

and

$$u_z = \frac{cP}{\omega\rho\beta^2}\left[\frac{\alpha^2}{\alpha^2 - \beta^2} + \frac{\omega z}{c}\right] e^{-\omega z/c} \exp\left[i\omega\left(\frac{x}{c} - t\right)\right].$$

c) If P is a few millibars, and ω is a frequency corresponding to periods of a few minutes, how deeply should long-period seismometers be buried, according to the above equations, to ensure that seismic noise due to atmospheric disturbances is at most a few nanometers?

12.4 Show that the coil response, in part (b) of the figure in Box 12.4, can be characterized as "rising at 6 dB per octave." (*Note:* An octave represents a factor of 2 in frequency.) What is the corresponding number of dB per octave for the low frequency response ($\omega < \omega_g$) in part (d) of the same figure?

12.5 From the outputs of a pendulum and a strainmeter at the same site, how could you obtain the surface-wave dispersion? (That is, how could you study the frequency dependence of phase velocity $c(\omega)$, where c is given in terms of frequency and horizontal wavenumber by $c = \omega/k$?)

12.6 Give a schematic (similar to Figures 12.21 and 12.22) for a velocity feedback seismometer, and show that with an appropriate choice of parameters it can make the damping very high.

12.7 With reference to Box 12.3, suppose that a building (treated as a one-degree-of-freedom system) is subjected to ground acceleration $\ddot{u}(t) = A \sin \Omega t H(t)$. If $\varepsilon = 0$ (no damping), show that the resulting building displacement is

$$\xi(t) = \frac{A}{2\omega}\left[\frac{\sin(\Delta\omega t)}{\Delta\omega}\cos(\omega + \Delta\omega)t - \frac{\sin(\omega + \Delta\omega t)}{\omega + \Delta\omega}\cos(\Delta\omega t)\right]$$

where $\Delta\omega = \frac{1}{2}(\Omega - \omega)$. In the limit as $\Omega \to \omega$, show that

$$\xi = \frac{A}{2\omega^2}(\omega t \cos \omega t - \sin \omega t).$$

[These two solutions indicate that displacements can grow with time to large and thus hazardous values, if a building is subjected to ground motion close to, or at, its resonant frequency. The growth continues indefinitely in this case, because the input shaking has no end.]

If the ground motion has finite duration at a fixed frequency, so that $\ddot{u} = A \sin \Omega t H(t) H(T - t)$, show that the undamped engineering displacement response spectrum $\mathrm{SD}(\omega, \varepsilon)|_{\varepsilon=0}$ is approximately $AT/(2\omega)$ if $|(\Omega - \omega)T| \ll 1$ and $\omega T \gg 1$. [This result makes clear the importance of the *duration* of shaking at frequencies close to resonance, since the undamped response spectrum near these frequencies has amplitude proportional to T.]

A modern form of Stokes' solution, giving the component of displacement in the x_n direction due to the force $\mathbf{F}(t)$ applied at position $\boldsymbol{\xi}$, is

$$\begin{aligned} u_n(\mathbf{x},t) = F_p * G_{np} = \frac{1}{4\pi\rho}(3\gamma_n\gamma_p - \delta_{np})\frac{1}{r^3}\int_{r/\alpha}^{r/\beta} \tau F_p(t-\tau)\,d\tau \\ + \frac{1}{4\pi\rho\alpha^2}\gamma_n\gamma_p\frac{1}{r}F_p\left(t-\frac{r}{\alpha}\right) \\ - \frac{1}{4\pi\rho\beta^2}(\gamma_n\gamma_p - \delta_{np})\frac{1}{r}F_p\left(t-\frac{r}{\beta}\right). \end{aligned} \tag{4.27}$$

The far-field displacement due to a point source dislocation of strength $M_0(t)$ is

$$\mathbf{u}(\mathbf{x},t) = \frac{1}{4\pi\rho\alpha^3}\mathbf{A}^{FP}\frac{1}{r}\dot{M}_0\left(t-\frac{r}{\alpha}\right) + \frac{1}{4\pi\rho\beta^3}\mathbf{A}^{FS}\frac{1}{r}\dot{M}_0\left(t-\frac{r}{\beta}\right), \tag{4.32}$$

where the far-field radiation patterns are given by

$$\mathbf{A}^{FP} = \sin 2\theta\cos\phi\,\hat{\mathbf{r}} \qquad \text{and} \qquad \mathbf{A}^{FS} = \cos 2\theta\cos\phi\,\hat{\boldsymbol{\theta}} - \cos\theta\sin\phi\,\hat{\boldsymbol{\phi}}. \tag{4.33}$$

The definition of geometric spreading along a ray tube is

$$\mathcal{R}(\mathbf{x},\boldsymbol{\xi}) = \sqrt{\frac{dA}{d\Omega}}. \tag{4.61}$$

Generalization of far-field displacement (4.32), for a point-source moment tensor, to give P, SV, and SH components in a spherically symmetric Earth according to geometric ray theory:

$$\begin{aligned} \mathbf{u}^P(\mathbf{x},t) &= \left(\frac{\boldsymbol{\gamma}\cdot\dot{\mathbf{M}}\left(t-T^P\right)\cdot\boldsymbol{\gamma}}{4\pi\sqrt{\rho(\xi)\,\rho(\mathbf{x})\,\alpha(\xi)\,\alpha(\mathbf{x})\,\alpha^2(\xi)\,\mathcal{R}^P(\mathbf{x},\xi)}}\right)\mathbf{l}, \\ \mathbf{u}^{SV}(\mathbf{x},t) &= \left(\frac{\hat{\mathbf{p}}(\xi)\cdot\dot{\mathbf{M}}\left(t-T^S\right)\cdot\boldsymbol{\gamma}}{4\pi\sqrt{\rho(\xi)\,\rho(\mathbf{x})\,\beta(\xi)\,\beta(\mathbf{x})\,\beta^2(\xi)\,\mathcal{R}^S(\mathbf{x},\xi)}}\right)\hat{\mathbf{p}}(\mathbf{x}), \\ \mathbf{u}^{SH}(\mathbf{x},t) &= \left(\frac{\hat{\boldsymbol{\phi}}(\xi)\cdot\dot{\mathbf{M}}\left(t-T^S\right)\cdot\boldsymbol{\gamma}}{4\pi\sqrt{\rho(\xi)\,\rho(\mathbf{x})\,\beta(\xi)\,\beta(\mathbf{x})\,\beta^2(\xi)\,\mathcal{R}^S(\mathbf{x},\xi)}}\right)\hat{\boldsymbol{\phi}}(\mathbf{x}). \end{aligned} \tag{4.97}$$

The Rayleigh function $\mathsf{R}(p)$, which is zero for $p = 1/c_{\mathrm{R}}$, is defined as

$$\mathsf{R}(p) \equiv \left(\frac{1}{\beta^2} - 2p^2\right)^2 - 4p^2\sqrt{p^2 - \frac{1}{\alpha^2}}\sqrt{p^2 - \frac{1}{\beta^2}}. \tag{5.56}$$

Sections (5.4) and (7.2.2) cover the motion–stress vector equation

$$\frac{d\mathbf{f}(z)}{dz} = \mathbf{A}(z)\mathbf{f}(z), \quad \text{solved by } \mathbf{f} = \mathbf{F}\mathbf{w} = \mathbf{E}\boldsymbol{\Lambda}\mathbf{w}.$$

Continued on rear endpaper

Key Formulas

Formulas for the quality factor, Q, used to characterize attenuation:

$$\frac{1}{Q(\omega)} = -\frac{\Delta E}{2\pi E} = -\frac{\mathrm{Im}M(\omega)}{\mathrm{Re}M(\omega)}. \qquad \text{(Box 5.7 and (5.86))}$$

The excitation of Love waves by a point-source moment tensor is

$$\mathbf{u}^{\mathrm{LOVE}}(\mathbf{x},\omega) = \sum_n \frac{l_1(z)}{8cUI_1}\sqrt{\frac{2}{\pi k_n r}}\exp\left[i\left(k_n r + \frac{\pi}{4}\right)\right] \qquad \text{((7.149) and (7.148))}$$

$$\times \left\{ ik_n l_1(h)[M_{xx}\sin\phi\cos\phi - M_{yx}\cos^2\phi + M_{xy}\sin^2\phi \right.$$

$$\left. - M_{yy}\sin\phi\cos\phi] - \left.\frac{dl_1}{dz}\right|_h [M_{xz}\sin\phi - M_{yz}\cos\phi] \right\} \hat{\boldsymbol{\phi}}.$$

The excitation of Rayleigh waves by a point-source moment tensor has vertical component given by

$$u_z^{\mathrm{RAYLEIGH}} = \sum_n \frac{r_2(z)}{8cUI_1}\sqrt{\frac{2}{\pi k_n r}}\exp\left[i\left(k_n r + \frac{\pi}{4}\right)\right] \times \left\{ k_n r_1(h)[M_{xx}\cos^2\phi \right.$$

$$\left. + (M_{xy} + M_{yx})\sin\phi\cos\phi + M_{yy}\sin^2\phi] + i\left.\frac{dr_1}{dz}\right|_h [M_{xz}\cos\phi \right. \qquad (7.150)$$

$$\left. + M_{yz}\sin\phi] - ik_n r_2(h)[M_{zx}\cos\phi + M_{zy}\sin\phi] + \left.\frac{dr_2}{dz}\right|_h M_{zz} \right\}.$$

Seismic displacement as an explicit sum of normal modes excited by a point-source moment tensor is given by:

$$\mathbf{u}(\mathbf{x},t) = \sum_i [{}_i e^*_{pq}(\mathbf{x}_s)\dot{M}_{pq}(t)] * {}_i\mathbf{u}(\mathbf{x}) \left(\frac{1 - \exp(-\omega_i t/2Q_i)\cos\omega_i t}{\omega_i^2} \right). \qquad (8.39)$$

The ray parameter is used in Chapters 4, 5, 6, 8, and 9 in several ways, sometimes as a constant (along a ray), sometimes as a real or a complex variable (to specify different rays or the angle of incidence at an interface), and also for integration (to evaluate the total field radiated by a particular source):

$$\text{ray parameter} = \text{horizontal slowness} = p = \frac{r\sin i}{v} = \frac{r_p}{v(r_p)} = \frac{dT}{d\Delta} = \frac{l+\frac{1}{2}}{\omega}.$$

A general Cagniard path for a ray that may cross numerous layers is given by solving for $p = p(t)$ where

$$t = p \times \text{horizontal distance} + \int_{\text{ray path}} (\text{vertical slowness})\, dz. \qquad \text{((9.4) and (9.5))}$$

APPENDIX 1

Glossary of Waves

Air waves Audible sounds are sometimes generated by earthquakes; a local earthquake may sound like distant thunder. Instrumental measurements show that these sounds arrive simultaneously with the first *P*-waves (Hill *et al.*, 1976). Long-period (minutes to hours) acoustic-gravity waves are also excited by great earthquakes, as well as by volcanic explosions, meteorite falls, and nuclear blasts in the atmosphere (Harkrider, 1964a).

Air-coupled surface waves Despite the great density contrast between air and ground, atmospheric pressure disturbances traveling over the Earth's surface can amplify surface waves if the phase velocity is equal to the acoustic velocity in the air. Such a coupling with air has been observed for flexural waves in ice sheets floating on the ocean and for Rayleigh waves in ground with low-velocity surface layers (Press *et al.*, 1951). A simultaneous arrival of air waves and tidal disturbances was observed after the famous explosion of the volcano Krakatoa in 1883.

Airy phase Portions of dispersed wavetrains associated with the maxima or minima of the group velocity (as a function of frequency). The stationary phase approximation blows up for them, but the method we describe in Problem 7.8 is still accurate. Alternatively, an Airy function can be used for an approximate calculation of the waveform (Savage, 1969b). Examples are continental Rayleigh waves at periods around 15 s and mantle Rayleigh waves at periods of 200 to 250 s.

Body waves Waves that propagate through an unbounded continuum are called body waves, as opposed to surface waves, which propagate along the boundary surface.

c This symbol is used to indicate the reflection at the core-mantle boundary for waves incident from the mantle. For example, incident *S*-waves are designated *ScS*. A major study of *PcP* is described by Frasier and Chowdury (1974).

Coda waves of a local earthquake The seismograms of a local earthquake usually show some vibrations long after the passage of body waves and surface waves. This portion of the seismogram to its end is called the coda. They are believed to be back-scattering waves due to lateral inhomogeneity distributed throughout the Earth's crust and upper mantle (Aki and Chouet, 1975). Coda has been successfully used to obtain source spectra (Rautian and Khalturin, 1978), and can be made the basis of a regional magnitude scale that has excellent properties of stability and precision.

Converted waves Conversion of P to S and S to P occurs at a discontinuity for non-normal incidence. These converted waves sometimes show distinct arrivals on the seismogram between the P and S arrivals, and may be used to determine the location of the discontinuity.

Crary waves Crary waves are a train of sinusoidal waves with nearly constant frequency observed on a floating ice sheet. They are multi-reflected SV-waves with horizontal phase velocity near the speed of compressional waves in ice.

Depth phases (pP, pS, sP, sS) The symbol pP has been used for P-waves propagated upward from the hypocenter, turned into downward propagating P-waves by reflection at the free surface, and observed at teleseismic distances. sS, sP, and pS have analogous meanings. For example, sP corresponds to a phase that ascends from the focus to the surface as S-waves and then, after reflection, travels as P-waves to the recording station. These phases are useful for an accurate determination of focal depth. See Figure 9.15 for sS.

Diffracted P The P-wave ray path from a surface focus that grazes the Earth's core emerges at an epicentral distance of about 100°. Although geometrical optics predicts no direct arrivals of P-waves in the shadow zone beyond this distance, we continue to observe P-waves, especially of long period, up to distances of at least 130°. They are diffracted around the core boundary. See Figure 9.35b.

Flexural waves A normal mode in an infinite plate in vacuum with motion antisymmetric with respect to the median plane of the plate. Examples in nature are the waves in floating ice. (For short waves, the period equation for a normal mode reduces to that for flexural waves in a plate modified slightly by the presence of water. For long waves, however, the gravity term in the period equation dominates, and the mode approaches that of gravity waves in water.)

Frozen waves In the epicentral area of a great earthquake, walls, embankments, and the like are sometimes left in the form of a wave. These "frozen waves" are attributed to cracking open of the ground at the crests of the waves, sometimes with the emission of sand and water. Frozen waves are also seen on the surface of the Moon, concentric with very large impact craters.

Gravity waves Normal modes in a surface layer with very low shear velocity, such as unconsolidated sediments, may be affected significantly by gravity at long periods (Gilbert, 1967). Waves similar to the gravity waves in a fluid layer are possible in addition to the shortening of wavelength of normal modes by gravity. So-called "visible waves" with large amplitude and relatively long periods observed in the epicentral area of a great earthquake have been suggested to be gravity waves (Lomnitz, 1970).

Ground roll A term used in exploration seismology to refer to surface waves generated from explosions. They are characterized by low velocity, low frequency, and high amplitude, and are observed in regions where the near-surface-layering consists of poorly consolidated, low-velocity sediments overlying more competent beds with higher velocity. Thus ground roll usually consists of Rayleigh waves.

Guided waves Guided waves are trapped in a waveguide by total reflections or bending of rays at the top and bottom boundaries. An outstanding example is the acoustic waves in the SOFAR channel, a low-velocity channel in the ocean. Since the absorption coefficient for sound in seawater is quite small for frequencies on the order of a few hundred cycles per second, transoceanic transmission is easily achieved. If

we consider the Earth's surface as the top of a waveguide, surface waves, such as Rayleigh, Love, and their higher modes, are guided waves. The waves associated with a low-velocity channel in the crust or mantle may be interpreted as normal modes with concentration of energy in the channel. Where they can exist, guided waves may propagate to considerable distances, because they are effectively spreading in only two spatial dimensions.

***G*-waves (*Gn*)** Another name for long-period Love waves. Because the group velocity of Love waves in the Earth is nearly constant (4.4 km/s) over the period range from about 40 to 300 s, their waveform is rather impulsive, and they have received this additional name. They are called *G*-waves after Gutenberg. It takes about $2\frac{1}{2}$ hours for *G*-waves to make a round trip of the Earth. After a large earthquake, a sequence of *G*-waves may be observed. They are named $G1, G2, \ldots, Gn$, according to the arrival time. The odd numbers refer to *G*-waves traveling in the direction from epicenter to station, and the even numbers to those leaving the epicenter in the opposite direction and approaching the station from the antipode of the epicenter. See Problem 7.9 and Figure 8.5.

Head waves Head waves are observed in a half-space that is in welded contact with another half-space with higher velocity when the seismic source is located in the lower-velocity medium. The ray path of head waves is along the interface, and the wavefront in the lower-velocity half-space is a part of the surface of an expanding cone. For this reason, head waves are sometimes called "conical waves."

I, i The symbol *I* is used to indicate that part of a ray path has traversed the Earth's inner core as a *P*-wave. For example, *PKIKP* refers to *P*-waves that have penetrated to the interior of the inner core and returned to the surface without conversion to *S*-waves throughout the entire path. On the other hand, *i* is used to indicate reflection at the boundary between outer and inner core (for example, *PKiKP*) in the same manner that *c* is used for reflection at the core-mantle boundary.

Inhomogenous plane waves Plane waves with amplitudes varying in a direction different from the direction of propagation. The velocity of propagation is lower than that of the regular plane waves. They are also called "evanescent waves."

J The symbol *J* is used to indicate that part of a ray path has traversed the Earth's inner core as an *S*-wave. Unambiguous observations of waves such as *PKJKP* and *SKJKP* have not yet been achieved, but they may be possible with suitable sources and instrument responses.

K *P*-waves in the outer core are designated as *K* (the German word for core is Kern). For example, *S*-waves traveling steeply downward in the mantle, converted to *P*-waves at the core boundary, propagated through the outer core as *P*-waves, and converted back to *S*-waves at re-entry to the mantle are designated as *SKS*. Just as *PP*, *PPP*, etc. are used to designate surface reflections, *KK*, *KKK*, etc. are used for *P*-waves in the core reflected at the core-mantle interface from below.

***L* (*LQ*, *LR*)** The symbol *L* is used to designate long-period surface waves. When the type of surface wave is known, *LQ* and *LR* are used for Love and Rayleigh waves, respectively.

Leaking modes Normal modes in a layered half-space, in general, have cutoff frequencies below which the phase velocity exceeds the *P*- and/or *S*-velocities of the half-space,

and the energy leaks through the half-space as body waves. Because of the leakage, the amplitude of leaky modes attenuates exponentially with distance.

***Lg*-waves** Short-period (1–6 s) large amplitude arrivals with predominantly transverse motion (Press and Ewing, 1952). *Lg*-waves propagate along the surface with velocities close to the average shear velocity in the upper part of the continental crust (Herrin and Richmond, 1960). The waves are observed only when the wave path is entirely continental. As little as 2° of intervening ocean is sufficient to eliminate the waves. When *Lg*-waves arrive in two distinct groups, they are called *Lg*1 and *Lg*2.

***Li*-waves** These are similar to *Lg*-waves, but their existence is not as widely accepted as that of *Lg*. The velocity of *Li*-waves is 3.8 km/s (as compared to 3.5 km/s for *Lg*) and may be associated with the lower continental crust (Båth, 1954, 1957).

Longitudinal waves Displacement associated with far-field *P*-waves in a homogeneous isotropic solid is parallel to the direction of propagation. For this reason, *P*-waves are also called "longitudinal waves."

Love waves *SH*-waves having their largest amplitudes confined near the surface of an elastic body. Their existence was first predicted (by A. E. H. Love) for a homogeneous layer overlying a homogeneous half-space with an *S*-wave velocity greater than that of the layer. They can exist, in general, in a vertically heterogeneous medium. They cannot, however, exist in a homogeneous half-space as long as the surface is plane.

Mantle Rayleigh waves Just as long-period Love waves are given another name, "*G*-waves," long-period Rayleigh waves are sometimes called mantle Rayleigh waves.

Microseisms Continuous ground motion constituting background noise for any seismic experiment. Microseisms with frequencies higher than about 1 Hz are usually caused by artificial sources, such as traffic and machinery, and are sometimes called microtremors, to be distinguished from longer-period microseisms due to natural disturbances. At a typical station in the interior of a continent, the microseisms have predominant periods of about 6 s. They are caused by the pressure from standing ocean waves, which may be formed by waves traveling in opposite directions in the source region of a storm or near the coast (Longuet-Higgins, 1950).

Normal modes Normal modes were originally defined as free vibrations of a system with a finite number of degrees of freedom, such as a finite number of particles connected by a massless spring. Each mode is a simple harmonic vibration at a certain frequency called an eigenfrequency. There are as many independent modes as the number of degrees of freedom. An arbitrary motion of the system can be expressed as a superposition of normal modes. Free vibrations of a finite continuum body, such as the Earth, are also called normal modes. In this case, there are an infinite number of normal modes, and an arbitrary motion of the body can be expressed by their superposition. The concept of normal modes has been extended to waveguides in which free waves with a certain phase velocity can exist without external force. Examples are Rayleigh waves in a half-space and Love waves in a layered half-space. In these cases, however, one cannot express an arbitrary motion by superposing normal modes.

P* Designates *P*-waves refracted through an intermediate layer in the Earth's crust with a velocity near 6.5 km/s. The upper boundary of this layer has been called the Conrad discontinuity. See Box 6.4.

P′ Another symbol for *PKP*.

***P* coda** The portion of P-waves after the arrival of the primary waves. They may be due to P to S conversions at interfaces or to multiple reflections in layers or to scattering by three-dimensional inhomogeneities.

P_dP* or *PdP This wave is like the surface reflection PP, except that the reflection occurs at an interface at depth d (expressed in kilometers, e.g., $P_{600}P$) instead of at the surface.

P_d*, *P_u*, *P_r The travel time for P-waves near $\Delta = 20°$ shows a triplication due to a sharp velocity increase in the upper mantle below the low-velocity layer. Three branches are designated in the order of decreasing $dt/d\Delta$ as P_d (direct), P_u (upper), and P_r (refracted).

Plate waves The period equation for normal modes in an infinite plate in a vacuum can be split into two. One of the equations governs the mode with motion symmetric with respect to the median of the plate, and the other governs the mode with antisymmetric motion. The former is sometimes called the $M1$-wave, and the latter $M2$. For example, $M11$ and $M12$ are the fundamental and first higher modes of the $M1$ wave, respectively. For very short waves, both $M11$ and $M21$ approach Rayleigh waves in an elastic half-space made of the plate material. For wavelengths that are long compared with plate thickness, $M21$ are called flexural waves. They are dispersive, with phase velocities decreasing to zero with increasing wavelength (Satô, 1951).

***PL*-waves** A train of long-period waves (30 to 50 s) observed in the interval between P- and S-waves for distances less than about 30°. They show normal dispersion (longer periods arriving earlier). They are explained as a leaking mode of the crust-mantle waveguide (Oliver and Major, 1960; Su and Dorman, 1965).

P_n* or *Pn Beyond a certain critical distance, generally in the range from 100 to 200 km, the first arrival from seismic sources in the crust corresponds to waves refracted from the top of the mantle. Called P_n, these waves are relatively small, with long-period motion followed by larger and sharper waves of shorter period called $\overline{P}$, which are propagated through the crust. The P_n-wave has long been interpreted as a head (conical) wave along the interface of two homogeneous media—namely, crust and mantle. The observed amplitude, however, is usually greater than that predicted for head waves, implying that the velocity change is not exactly step-like but has a finite gradient at or below the transition zone. The designation P_n has been applied to short-period P-waves that propagate over considerable distances (even up to 20°) with horizontal phase velocities in the range 7.8–8.3 km/s. Thus Herrin (1969) defines P_n as "the first arrival of seismic energy in the range from a few degrees to a distance where the travel-time function begins to show appreciable curvature." An interpretation in terms of head waves at the Moho is here unsatisfactory (although the horizontal velocity and travel times would be explained), because head waves must decay rapidly with distance. More likely is an explanation in terms of guided waves, within a high-Q layer several tens of kilometers in thickness at the top of the mantle. See description of the related wave S_n.

***$\overline{P}$* (*Pg*)** Travel-time curves at short distances (up to a few hundred km) for seismic sources in the Earth's crust usually consist of two intersecting straight lines: one with velocity about 6 km/s at shorter distances and the other about 8 km/s at greater distances. The former is attributed to direct P-waves propagating through the crust and is designated as $\overline{P}$ or Pg, which stands for granitic layer. The latter is Pn.

***P*-waves** Compressional elastic waves are called P-waves in seismology, P standing for "primary." In a homogeneous isotropic body, the velocity of P-waves is equal to $\sqrt{(\kappa + \frac{4}{3}\mu)/\rho}$, where κ, μ, and ρ are bulk modulus, rigidity, and density, respectively. The particle displacement associated with P-waves is often parallel to the direction of wave propagation. For this reason, P-waves are sometimes called longitudinal waves.

Rayleigh waves The most fundamental of the surface waves, with strongest amplitudes in the neighborhood of the free surface of a planar elastic body. For the case of a homogeneous body, the velocity of propagation is 0.88 to 0.95 times the shear velocity, depending on Poisson's ratio. Rayleigh waves in a vertically heterogeneous half-space have frequency-dependent phase and group velocities. Higher modes can exist in the vertically heterogeneous half-space.

Rg Short-period, fundamental-mode Rayleigh waves (in the range 8 to 12 s) observed for continental paths are sometimes designated as Rg (Press and Ewing, 1952).

***S*-waves** Elastic shear waves are called S-waves in seismology, S standing for "secondary." In a homogeneous isotropic body, the velocity of S-waves is equal to $\sqrt{\mu/\rho}$, where μ and ρ are rigidity and density, respectively. The particle displacement associated with S-waves is perpendicular to the direction of wave propagation if the medium is isotropic. For this reason, S-waves are sometimes called transverse waves.

***$\overline{S}$* (*Sg*)** S-waves propagating through the crust like $\overline{P}$ or Pg. These waves are seen with simple impulsive onsets at short distances (up to a few tens of km). At greater distances, onset may not be impulsive (due to multiple paths all trapped in the crust) and Sg then is an alternate name for the wave also called Lg.

***Sa*-waves** Sa-waves typically have periods of 10 to 30 s and a group velocity of 4.4 to 4.5 km/s measured along the surface. They can have both SV- and SH-components of motion. Their waveforms are usually complex and vary from station to station in an irregular manner (Brune, 1965).

Seiche A free oscillation (resonance) of the surface of an enclosed body of water, such as a lake, pond, or bay with a narrow entrance. They are sometimes excited by earthquakes and by tsunamis. The period of oscillation ranges from a few minutes to a few hours, and the oscillation may last for several hours to one or two days.

Shear-coupled *PL*-waves This is a long-period wavetrain that follows S for distances up to about 80°. It has been explained as being due to the coupling of S-waves with a leaking mode of the crust-mantle waveguide, i.e., PL-waves. The coupling of PL-waves with SS and SSS has also been observed (Chander *et al.*, 1968; Poupinet and Wright, 1972).

***SH*-wave** S-waves with displacement only in the horizontal direction. For a vertically heterogeneous medium, SH-waves do not interact with P-waves and are simpler than SV-waves.

S_n* or *Sn Early use of the designation S_n was in reference to short-period S-waves that were presumed to propagate as head waves along the top of the mantle. Quite commonly, the term is also now applied to a prominent arrival of short-period shear waves that may be observed (with a straight-line travel-time curve) at epicentral distances as great as 40° (Molnar and Oliver, 1969). Stephens and Isacks (1977) suggest that these waves travel in a waveguide at the top of the mantle. Propagation for shorter periods is more efficient, because longer-period waves have a substantial fraction of their energy

within lower-Q material, at greater depth, and hence are filtered out. Examples of S_n at great distances are given by Walker *et al.* (1978).

Stoneley waves These are interface waves with the largest amplitudes confined to the neighborhood of a plane interface of two elastic media. They are always possible at a solid–fluid interface, but can exist at a solid–solid interface only in restrictive cases where the shear-wave velocities in the two media are nearly equal.

Surface *P*-waves The ray path of surface P consists of two segments: an S-wave path from the source to the free surface with an apparent horizontal velocity equal to the P-wave velocity, and a P-wave path along the free surface to the receiver. The surface P-waves appear at the critical distance and can be a sharper arrival than the direct S-waves, although they attenuate very rapidly with distance. In some respects they behave like head waves.

Surface reflections (*PP*, *SS*, *SP*, *PS*, *PPP*, *SSS*) P-waves that have undergone one reflection at the surface before arriving at the recording station are denoted as *PP* if the wave initially left the hypocenter in the downward direction (in contrast to *pP*, which leaves in an upward direction). Those reflected twice at the surface are denoted as *PPP*. Likewise, *PS* is a once-reflected wave arriving at the station as an S-wave after conversion by reflection from P-waves. See Figure 9.15.

***SV*-wave** For an isotropic homogeneous body, the displacement associated with far-field S-waves is restricted to a plane perpendicular to the direction of the propagating ray. The particle motion in the plane can be described by two orthogonal vectors, one in the horizontal direction and the other perpendicular to it. The latter component is the SV-wave. SV-waves interact with P-waves in a vertically heterogeneous medium.

***T*-phase, *T*-waves** The letter T here stands for tertiary, following the interpretation of P as primary and S as secondary. T-waves are late-arriving phases with period less than 1 s, observed at stations on islands or in coastal regions for earthquakes in which the path of propagation is mostly oceanic. T-waves travel the oceanic part of the path within the ocean itself, in the SOFAR channel (SOund Fixing And Ranging). They arrive late compared to P and S, because the speed of sound in water is so slow compared to the speed of longitudinal and transverse waves in rocks (Linehan, 1940; Ewing *et al.*, 1952).

Tsunami, or "tidal wave" Gravity waves set up on the surface of the sea by disturbances in the sea bed. This disturbance may be an upheaval or subsidence due to a submarine earthquake, submarine landslide, or volcanic explosion. Because their wavelength (hundreds of km) is so much greater than ocean depths, their behavior is governed by the theory of waves in shallow water.

Tube waves in a borehole In an empty cylindrical hole, a kind of surface wave can propagate along the axis of the hole with energy confined to the vicinity of the hole. Such waves exhibit dispersion with phase velocity increasing with the wavelength. At wavelengths much shorter than the hole radius, they approach Rayleigh waves. The phase velocity reaches the shear velocity at wavelengths of about three times the radius. Beyond this cutoff wavelength, they attenuate quickly by radiating S-waves. In a fluid-filled cylindrical hole, in addition to a series of multi-reflected conical waves propagating in the fluid, tube waves exist without a cutoff for the entire period range. At short wavelengths, they approach Stoneley waves for the plane liquid-solid interface. For wavelengths longer than about 10 times the hole radius, the velocity of tube waves becomes constant, given in terms of the bulk modulus κ of the fluid and

the rigidity μ of the solid, by $v = c/\sqrt{1 + \kappa/\mu}$, where c is the acoustic velocity in the fluid (Biot, 1952; White, 1965).

Visible earthquake waves Slow waves with long period and short wavelengths reported by eyewitnesses in the epicentral area of a great earthquake (Lomnitz, 1970).

Volcanic tremor The seismic signals generated by volcanic activity are quite variable in character, ranging from those indistinguishable from tectonic earthquakes to continuous vibrations with sharply peaked spectra. The continuous vibrations are known as volcanic, or harmonic, tremor (Minakami, 1974; Aki *et al.*, 1977).

APPENDIX 2

Definition of Magnitudes

An earthquake magnitude was originally defined by Richter (1935) as the logarithm (to the base 10) of maximum amplitude measured in microns on the record of a standard torsion seismograph with a pendulum period of 0.8 s, magnification of 2800, and dampling factor 0.8, located at a distance of 100 km from the epicenter. This standard instrument, known after its designers as the Wood-Anderson seismometer, consists of a small copper cylinder (with mass less than 1 gram and with its axis vertical) attached to a vertical metal fiber. The restoring force is supplied by tension in the fiber. The instrument as a whole is sensitive to horizontal motions, which are detected via light reflected from a small mirror in the cylinder. A calibration curve was constructed to reduce the amplitude observed at an arbitrary epicentral distance to that expected at 100 km. This magnitude scale is now referred to as local magnitude M_L. In practice the scale requires different calibration curves for regions such as stable continental interiors, as compared to the Southern California region for which the scale was originally defined, because the attenuation of seismic waves with distance is very different for different geological/geophysical provinces. A local magnitude scale for Eastern North America is described by Kim (1998).

A magnitude scale based on teleseismic surface waves was described by Gutenberg and Richter (1936) and developed more extensively by Gutenberg (1945). For shallow earthquakes at distances $15° < \Delta < 130°$, he found the formula

$$M_s = \log A + 1.656 \log \Delta + 1.818, \tag{A.1}$$

where A is the horizontal component of the maximum ground displacement (in microns) due to surface waves with periods of 20 s.

Many formulas for M_s have been proposed since that of Gutenberg. They were summarized by Vaněk *et al.* (1962), who proposed the formula

$$M_s = \log(A/T)_{max} + 1.66 \log \Delta + 3.3 \tag{A.2}$$

which has been adopted officially by the International Association for Seismology and Physics of the Earth's Interior (IASPEI). In equation (A.2), $(A/T)_{max}$ is the maximum of all

A/T (amplitude/period) values of the wave groups on a record. For $T = 20$ s, equation (A.2) becomes nearly identical to (A.1).

Another important magnitude scale is the one based on the amplitude of teleseismic body waves. It is defined by the formula

$$m_b = \log(A/T) + Q(\Delta, h), \tag{A.3}$$

where Q is a function of epicentral distance Δ and focal depth h, empirically determined by Gutenberg and Richter (1956) for eliminating the path effect from observed amplitude (see Figure 12.10). A/T is the maximum in the wave group of either P, PP, or SH, with separate tables and charts of Q for each phase. Vaněk *et al.* (1962) also summarized later formulas for m_b and proposed a revised calibration function for Q.

The practice of m_b determination used by the U.S. Geological Survey is, however, significantly different from what was used by Gutenberg and Richter. The most important difference is in the instrument characteristics used for the determination. Gutenberg and Richter used broadband instruments that register relatively long-period P-waves (4–10 s) for major events, but for most of the 1970s and 1980s the U.S. Geological Survey measurements typically were made using short-period instruments such as those of the WWSSN, which show P-waves with period nearly always about 1 s. With the gradual replacement of analog recording (of short-period or long-period sensors) by digital recording of broadband instruments, beginning in the 1980s and becoming dominant in the 1990s, practical details of how A and T are measured (for application of equations (A.1)–(A.3)) have changed again. It is common to pass the broadband signal through filters that more-or-less represent classical short-period or long-period responses, as appropriate for a particular magnitude scale, and then to measure A and T.

In practice there are many different magnitude scales, associated with the slightly different measurement practices of different agencies as well as with choices of the frequency band in which ground motion is filtered before being measured. With one exception, these scales are all empirical. The exception is the moment magnitude scale, discussed briefly in Section 3.2. The moment magnitude has the great merit of being based on a physical model. The more traditional empirical scales, with all their defects (the same earthquake can result in a sometimes bewildering set of different magnitude values), are still widely used. Perhaps this is because the empirical scales are all based on measurements of A (albeit with corrections for distance and source depth), and so they are more directly related to what for many people is the most important characteristic of a particular earthquake, namely, "How strongly did the ground shake?"

The fact that a seismic event may have different magnitudes on different scales (for example, m_b and M_s), is in practice the basis for methods of identifying the event (perhaps as an earthquake, or an explosion). Thus, rather than seeing different magnitude scales as an inconvenience, they can be viewed as a useful means for characterizing the great variety of different sources of seismic signals.

Bibliography

Abe, K. Determination of seismic moment and energy from the Earth's free oscillation. *Physics of the Earth and Planetary Interiors*, **4**, 49–61, 1970.

———. Static and dynamic fault parameters of the Saitama earthquake of July 1, 1968. *Tectonophysics*, **27**, 223–238, 1975.

Abercrombie, R., and P. Leary. Source parameters of small earthquakes recorded at 2.5 km depth, Cajon Pass, Southern California: Implications for earthquake scaling. *Geophysical Research Letters*, **20**, 1511–1514, 1993.

Abramovici, A., and 13 co-authors. LIGO: The Laser Interferometer Gravitational-Wave Observatory, *Science*, **256**, 323–333, 1992.

Abramowitz, M., and I. A. Stegun. *Handbook of Mathematical Functions*, U.S. National Bureau of Standards, 1964.

Adams, R. D. Multiple inner core reflections from a Novaya Zemlya explosion. *Bulletin of the Seismological Society of America*, **62**, 1063–1071, 1972.

Agnew, D. C. Strainmeters and tiltmeters. *Reviews of Geophysics*, **24**, 579–624, 1986.

Agnew, D., J. Berger, R. Buland, W. Farrell, and F. Gilbert. International deployment of accelerometers: A network for very long period seismology. *EOS, Transactions of the American Geophysical Union*, **51**, 180–188, 1976.

Ágústsson, K., A. T. Linde, R. Stefánsson and S. Sacks. Strain changes for the 1987 Vatnafjöll earthquake in south Iceland and possible magmatic triggering. *Journal of Geophysical Research*, **104**, 1151–1161, 1999.

Aki, K. Crustal structure in Japan from the phase velocity of Rayleigh waves. *Bulletin of the Earthquake Research Institute, Tokyo University*, **39**, 255–283, 1961.

———. Generation and propagation of *G* waves from the Niigata earthquake of June 16, 1964. 2. Estimation of earthquake movement, released energy, and stress-strain drop from *G* wave spectrum. *Bulletin of the Earthquake Research Institute, Tokyo University*, **44**, 23–88, 1966.

———. Scaling law of seismic spectrum. *Journal of Geophysical Research*, **72**, 1217–1231, 1967.

———. Seismic displacements near a fault. *Journal of Geophysical Research*, **73**, 5359–5376, 1968.

———. Scale dependence in earthquake phenomena and its relevance to earthquake prediction. *Proceedings of the National Academy of Sciences, USA*, **93**, 3740–3747, 1996.

Aki, K., and L. B. Chouet. Origin and coda waves: Source, attenuation, and scattering effects. *Journal of Geophysical Research*, **80**, 3322–3342, 1975.

Aki, K., M. Fehler, and S. Das. Source mechanism of volcanic tremor; fluid-driven crack models and their application to the 1973 Kilauea eruption. *Journal of Vocanology and Geothermal Research*, **2**, 259–287, 1977.

Alekseyev, A. S., and B. G. Mikhaylenko. Solution of Lamb's problem for a vertically inhomogeneous elastic half space. *Izvestiya, Physics of the Solid Earth*, 11–25, 1976.

Alsop, L. E., G. H. Sutton, and M. Ewing. Free oscillations of the Earth observed on strain and pendulum seismographs. *Journal of Geophysical Research*, **66**, 631–641, 1961a.

———. Measurement of Q for very long period free oscillations. *Journal of Geophysical Research*, **66**, 2911–2915, 1961b.

Alterman, Z., H. Jarosch, and C. L. Pekeris. Oscillations of the Earth. *Proceedings of the Royal Society of London*, **A252**, 80–95, 1959.

Anderson, D. L., and C. B. Archambeau. The anelasticity of the Earth. *Journal of Geophysical Research*, **69**, 2071–2084, 1964.

Anderson, D. L., A. Ben-Menahmen, and C. B. Archambeau. Attenuation of seismic energy in the upper mantle. *Journal of Geophysical Research*, **70**, 1441–1448, 1965.

Anderson, J. G., and P. G. Richards. Comparison of strong ground motion from several dislocation models. *Geophysical Journal of the Royal Astronomical Society*, **42**, 347–373, 1975.

Andrews, D. J. From anti-moment to moment: Plane strain models of earthquakes that stop. *Bulletin of the Seismological Society of America*, **65**, 163–182, 1975.

———. Rupture velocity of plane-strain shear cracks. *Journal of Geophysical Research*, **81**, 5679–5687, 1976.

———. Dynamic plane-strain shear rupture with a slip-weakening friction law calculated by a boundary integral method. *Bulletin of the Seismological Society of America*, **75**, 1–21, 1985.

———. Dynamic growth of mixed-mode shear cracks. *Bulletin of the Seismological Society of America*, **84**, 1184–1198, 1994.

Andrews, D. J., and Y. Ben-Zion. Wrinkle-like slip pulse on a fault between different materials. *Journal of Geophysical Research*, **102**, 553–571, 1997.

Andrianova, Z. S., V. I. Keilis-Borok, A. L. Levshin, and M. G. Neiganz. *Seismic Love Waves*. New York: Consultants Bureau, 1967.

Ang, D. D., and M. L. Williams. The dynamic stress field due to an extensional dislocation. *Proceedings of the Fourth Midwestern Conference on Solid Mechanics*. Austin: University of Texas Press, 1959.

Ansell, J. H. On the scattering of *SH* waves from a point source by a sphere. *Geophysical Journal of the Royal Astronomical Society*, **54**, 359–387, 1978.

Archambeau, C. B. General theory of elasto-dynamic source fields. *Reviews of Geophysics*, **16**, 241–288, 1968.

Archambeau, C. B., E. A. Flinn, and D. G. Lambert. Fine structure of the upper mantle. *Journal of Geophysical Research*, **74**, 5825–5865, 1969.

Arons, A. B., and D. R. Yennie. Phase distortion of acoustic pulses obliquely reflected from a medium of higher sound velocity. *Journal of the Acoustical Society of America*, **22**, 231–327, 1950.

Auld, B. A. *Acoustic Fields and Waves in Solids*, 2 vols., 2nd. ed. Malabon, Florida: Krieger Publishing Co., 1990.

Azimi, Sh. A., A. V. Kalinin, V. V. Kalinin, and B. L. Pivovarov. Impulse and transient characteristics of media with linear and quadratic absorption laws. *Izvestiya, Physics of the Solid Earth*, 88–93, 1968.

Backus, G. A class of self-sustaining dissipative spherical dynamos. *Annals of Physics (N.Y.)*, **4**, 372–447, 1958.

———. Possible forms of seismic anisotropy in the uppermost mantle under oceans. *Journal of Geophysical Research*, **70**, 3429–3439, 1965.

Backus, G., and F. Gilbert. The rotational splitting of the free oscillations of the Earth. *Proceedings of the National Academy of Sciences*, **47**, 362–371, 1961.

———. Numerical applications of a formalism for geophysical inverse problems. *Geophysical Journal of the Royal Astronomical Society*, **13**, 247–276, 1967.

———. The resolving power of gross Earth data. *Geophysical Journal of the Royal Astronomical Society*, **16**, 169–205, 1968.

———. Uniqueness in the inversion of inaccurate gross Earth data. *Philosophical Transactions of the Royal Society of London*, **A266**, 123–192, 1970.

Backus, G., and M. Mulcahy. Moment tensors and other phenomenological descriptions of seismic sources. I. Continuous displacements. *Geophysical Journal of the Royal Astronomical Society*, **46**, 341–361, 1976a.

———. Moment tensors and other phenomenological descriptions of seismic sources. II. Discontinious displacements. *Geophysical Journal of the Royal Astronomical Society*, **47**, 301–329, 1976b.

Barenblatt, G. I. The formation of equilibrium cracks during brittle fracture. General ideas and hypotheses. *Journal of Applied Mathematics and Mechanics*, **23**, 622–636, 1959.

Båth, M. The elastic waves *Lg* and *Rg* along Eurasiatic paths. *Arkiv Geophysik*, **2**, 295–342, 1954.

———. A continental channel wave guided by the intermediate layer in the crust. *Geofisica pura e applicata*, **38**, 19–31, 1957.

Beavan, J., and R. Bilham. Thermally induced errors in fluid tube tiltmeters. *Journal of Geophysical Research*, **82**, 5699–6704, 1977.

Benioff, H. A new vertical seismograph. *Bulletin of the Seismological Society of America*, **22**, 155–169, 1932.

———. Long waves observed in the Kamchatka earthquake November 4, 1952. *Journal of Geophysical Research*, **63**, 589–593, 1958.

———. Fused-quartz extensometer for secular, tidal, and seismic strain. *Bulletin of the Geological Society of America*, **70**, 1019–1032, 1959.

Benioff, H., B. Gutenberg, and C. F. Richter. Progress report, *Transactions of the American Geophysical Union*, **35**, 979–987, 1954.

Benioff, H., F. Press, and S. W. Smith. Excitation of the free oscillations of the Earth by earthquakes. *Journal of Geophysical Research*, **66**, 605–620,1961.

Ben-Menahem, A. Radiation of seismic surface waves from finite moving sources. *Bulletin of the Seismological Society of America*, **51**, 401–435, 1961.

Ben-Menahem, A., M. Rosenman, and D. G. Harkrider. Fast evaluation of source parameters from isolated surface-wave signals. I. Universal tables. *Bulletin of the Seismological Society of America* , **60**, 1337–1387, 1970.

Ben-Menahem, A., S. W. Smith, and T.-L. Teng. A procedure for source studies from spectrums of long-period seismic body waves. *Bulletin of the Seismological Society of America*, **55**, 203–235, 1965.

Ben-Menahem, A., and M. N. Toksöz. Source mechanism from spectra of long period surface waves. *Journal of Geophysical Research*, **68**, 5207–5222, 1963.

Ben-Zion, Y. On quantification of the earthquake source. *Seismological Research Letters*, **72**, 151–152, 2001.

Ben-Zion, Y., and P. Malin. San Andreas fault zone head waves near Parkfield, California. *Science*, **251**, 1592–1594, 1991.

Berckhemer, H. Die Ausdehnung der Bruchfläche im Erdbeben Herd und ihr Einfluss auf das seismische Wellen Spektrum. *Gerlands. Beitr. Geophys.*, **71**, 5–26, 1962.

Berckhemer, H., and G. Schneider. Near earthquakes recorded with long-period seismographs. *Bulletin of the Seismological Society of America*, **54**, 973–985, 1964.

Berry, M. J., and G. G. West. Reflected and head wave amplitudes in a medium of several layers. In *The Earth Beneath Continents*, Geophysical Monograph 10. Washington, D.C.: American Geophysical Union, 1966.

Bessonova, E. N., V. M. Fishman, V. Z. Ryaboy, and G. A. Sitnakova. The tau method for inversion of travel times. I. Deep seismic sounding data. *Geophysical Journal of the Royal Astronomical Society*, **36**, 377–398, 1974.

Bessonova, E. N., V. M. Fishman, M. G. Shnirman, G. A. Sitnikova, and L. R. Johnson. The tau method for inversion of travel times. II. Earthquake data. *Geophysical Journal of the Royal Astronomical Society*, **46**, 87–108, 1976.

Biot, M. A. Propagation of elastic waves in a cylindrical bore containing a fluid. *Journal of Applied Physics*, **23**, 997–1005, 1952.

Biswas, N. N., and L. Knopoff. Exact earth-flattening calculation for Love waves. *Bulletin of the Seismological Society of America*, **60**, 1123–1137, 1970.

Bizzarri, A., M. Cocco, D. J. Andrews, and E. Boschi. Solving the dynamic rupture problem with different numerical approaches and constitutive laws. *Geophysical Journal International*, **144**, 656–678, 2001.

Block, B., J. Dratler, and R. D. Moore. Earth and normal modes from a 6.5 magnitude earthquake. *Nature*, **226**, 343–344, 1970.

Block, B., and R. D. Moore. Measurements in the earth mode frequency range by an electrostatic sensing and feedback gravimeter. *Journal of Geophysical Research*, **71**, 4361–4375, 1966.

———. Tidal to seismic frequency investigations with a quartz accelerometer of new geometry. *Journal of Geophysical Research*, **75**, 1493–1506, 1970.

Boatwright, J. A spectral theory for circular seismic sources; simple estimates of source dimension, dynamic stress drop, and radiated seismic energy. *Bulletin of the Seismological Society of America*, **70**, 1–27, 1980.

Boatwright, J., and D. M. Boore. A simplification in the calculation of motions near a propagating dislocation. *Bulletin of the Seismological Society of America*, **65**, 133–138, 1975.

Bôcher, M. *An Introduction to the Study of Integral Equations*. Cambridge: Cambridge University Press, p. 9, 1909.

Bolt, B. A. Gutenberg's early *PKP* observations. *Nature*, **196**, 122–124, 1962.

———. The velocity of seismic waves near the Earth's center. *Bulletin of the Seismological Society of America*, **67**, 43–67, 1964.

Boore, D. M., and M. D. Zoback. Near-field motions from kinematic models of propagating faults. *Bulletin of the Seismological Society of America*, **64**, 321–342, 1974.

Borcherdt, R. D. Energy and plane waves in linear viscoelastic media. *Journal of Geophysical Research*, **78**, 2442–2453, 1973.

———. Reflection and refraction of type-II *S* waves in elastic and anelastic media. *Bulletin of the Seismological Society of America*, **67**, 43–67, 1977.

Bortfeld, R. Approximation to the reflection and transmission coefficients of plane longitudinal and transverse waves. *Geophysical Prospecting*, **9**, 485–502, 1961.

Bouchon, M. Predictability of ground displacement and velocity near an earthquake fault; an example, the Parkfield earthquake of 1966. *Journal of Geophysical Research*, **84**, 6149–6156, 1979.

Bouchon, M., and K. Aki. Discrete wave-number representation of seismic-source wave fields. *Bulletin of the Seismological Society of America*, **67**, 259–277, 1977.

Bouchon, M., and D. Streiff. Propagation of a shear crack on a nonplanar fault: A method of calculation. *Bulletin of the Seismological Society of America*, **77**, 61–66, 1997.

Bracewell, R. B. *The Fourier Transform and Its Applications*. New York: McGraw-Hill, 1965.

Brekhovskikh, L. M. *Waves in Layered Media*, Chapter 4. New York: Academic Press, 1960.

Bromwich, T. J. I'A. On the influence of gravity on elastic waves, and, in particular, on the vibrations of an elastic globe. *Proceedings of the London Mathematical Society*, vol. 30, 1898.

Brune, J. N. Attenuation of dispersed wave trains. *Bulletin of the Seismological Society of America*, **52**, 109–112, 1962.

———. The *Sa* phase from the Hindu Kush earthquake of July 6, 1962. *Pure and Applied Geophysics*, **62**, 81–95, 1965.

———. Seismic moment, seismicity, and rate of slip along major fault zones. *Journal of Geophysical Research*, **73**, 777–784, 1968.

———. Tectonic stress and the spectra of seismic shear waves from earthquakes. *Journal of Geophysical Research*, **75**, 4997–5009, 1970.

Brune, J. N., and J. Dorman. Seismic waves and Earth structure in the Canadian Shield. *Bulletin of the Seismological Society of America*, **53**, 167–210, 1963.

Brune, J. N., J. E. Nafe, and L. E. Alsop. The polar phase shift of surface waves on a sphere. *Bulletin of the Seismological Society of America*, **51**, 247–257, 1961.

Brune, J. N., J. E. Nafe, and J. Oliver. A simplified method for the analysis and synthesis of dispersed wave trains. *Journal of Geophysical Research*, **65**, 287–304, 1960.

Brune, J. N., S. Brown, and P. A. Johnson. Rupture mechanism and interface separation in foam rubber model of earthquakes: A possible solution to the heat flow paradox and the paradox of large overthrusts. *Tectonophysics*, **218**, 59–67, 1993.

Buchbinder, G. G. R. Travel times and velocities in the outer core from *PmKP*. *Earth and Planetary Science Letters*, **14**, 161–168, 1972.

Buchen, P. W. Plane waves in linear viscoelastic media. *Geophysical Journal of the Royal Astronomical Society*, **23**, 531–542, 1971.

Buck, S. W., F. Press, D. Shepard, M. N. Toksöz, and H. Trantham. Development of a mercury tiltmeter for seismic recording. Final Technical Report to the Advanced Research Projects Agency on Contract No. F44620–69-C-0126, Massachusetts Institute of Technology, 1971.

Buland, R. P., and F. Gilbert. The theoretical basis for the rapid and accurate computation of normal mode eigenfrequencies and eigenfunctions. In *Retrieving the Seismic Moment Tensor*, Ph.D. thesis of R. P. Buland, University of California, San Diego, 1976.

———. Computation of free oscillations of the Earth. *Journal of Computational Physics*, **54**, 95–114, 1984.

Bullen, K. E. The ellipticity correction to travel-times of *P* and *S* earthquake waves. *Monthly Notices of the Royal Astronomical Society*, Geophysical Supplement, **4**, 143–157, 1937.

———. Notes on cusps in seismic travel-times. *Geophysical Journal of the Royal Astronomical Society*, **3**, 354–359, 1960.

Burridge, R. The numerical solution of certain integral equations with non-integrable kernels arising in the theory of crack propagation and elastic wave diffraction. *Philosophical Transactions of the Royal Society of London*, **A265**, 353–381, 1969.

———. Admissible speeds for plane-strain self-similar shear cracks with friction but lacking cohesion. *Geophysical Journal of the Royal Astronomical Society*, **35**, 439–456, 1973.

Burridge, R., and G. S. Halliday. Dynamic shear cracks with friction as models for shallow focus earthquakes. *Geophysical Journal of the Royal Astronomical Society*, **25**, 261–283, 1971.

Burridge, R., and L. Knopoff. Body force equivalents for seismic dislocations. *Bulletin of the Seismological Society of America*, **54**, 1875–1888, 1964.

Burridge, R., and J. Willis. The self-similar problem of the expanding elliptical crack in an anisotropic solid. *Proceedings of the Cambridge Philosophical Society*, **66**, 261–283, 1969.

Byrne, C. J. Instrument noise in seismometers. *Bulletin of the Seismological Society of America*, **51**, 69–84, 1961.

Cagniard, L. *Reflection and Refraction of Progressive Seismic Waves*. Trans. by E. A. Flinn and C. H. Dix. New York: McGraw-Hill, 1962.

Campbell, K. W. Empirical near-source attenuation relationships for horizontal and vertical components of peak ground acceleration, peak ground velocity, and pseudo-absolute acceleration response spectra, *Seismological Research Letters*, **68**, 154–179, 1997.

Červený, V. Seismic rays and ray intensities in inhomogeneous anisotropic media. *Geophysical Journal of the Royal Astronomical Society*, **29**, 1–13, 1972.

———. Reflection and transmission coefficients for transition layers. *Studia Geophysica et Geodetica*, **18**, 59–68, 1974.

———. *Seismic Ray Theory*. Cambridge, New York: Cambridge University Press, 2001.

Červený, V., and R. Ravindra. *Theory of Seismic Head Waves*. University of Toronto Press, 1971.

Chaisri, S., and E. S. Krebes. Exact and approximate formulas for *P–SV* reflection and transmission coefficients for a nonwelded contact interface. *Journal of Geophysical Research*, **105**, 28045–28054, 2000.

Chander, R., L. E. Alsop, and J. Oliver. On the synthesis of shear-coupled *PL* waves. *Bulletin of the Seismological Society of America*, **58**, 1849–1877, 1968.

Chao, B. F., and R. S. Gross. Changes in the Earth's rotational energy induced by earthquakes. *Geophysical Journal International*, **122**, 776–783, 1995.

Chao, B. F., R. S. Gross, and D.-N. Dong. Changes in global gravitational energy induced by earthquakes. *Geophysical Journal International*, **122**, 784–789, 1995.

Chapman, C. H. On the computation of seismic ray travel times and amplitudes. *Bulletin of the Seismological Society of America*, **61**, 1267–1274, 1971.

———. Lamb's problem and comments on the paper, "On Leaking Modes" by Usha Gupta. *Pure and Applied Geophysics*, **94**, 23–247, 1972.

———. The Earth flattening transformation in body wave theory. *Geophysical Journal of the Royal Astronomical Society*, **35**, 55–70, 1973.

———. The turning point of elastodynamic waves. *Geophysical Journal of the Royal Astronomical Society*, **39**, 613–621, 1974.

———. Exact and approximated generalized ray theory in vertically inhomogeneous media. *Geophysical Journal of the Royal Astronomical Society*, **46**, 201–233, 1976a.

———. A first motion alternative to geometrical ray theory. *Geophysical Research Letters*, **3**, 153–156, 1976b.

———. A new method for computing seismograms. *Geophysical Journal of the Royal Astronomical Society*, **54**, 481–518, 1978a.

———. Body waves in seismology. In *Modern Problems in Elastic Wave Propagation*, edited by J. Miklowitz and J. D. Achenbach, 477–498, New York: Wiley, 1978b.

Chapman, C. H., and J. A. Orcutt. The computation of body wave synthetic seismograms in laterally homogeneous media. *Reviews of Geophysics*, **23**, 105–163, 1985.

Chapman, C. H., and R. A. Phinney. Diffracted seismic signals and their numerical solution. In *Seismology: Body Waves and Sources*, edited by B. A. Bolt, *Methods in Computational Physics*, vol.12. New York: Academic Press, 1972.

Chernov, L. A. *Wave Propagation in a Random Medium*. New York: McGraw-Hill, 1960.

Choy, G. L. Theoretical seismograms of core phases calculated by a frequency-dependent full wave theory, and their interpretation. *Geophysical Journal of the Royal Astronomical Society*, **51**, 275–311, 1977.

Choy, G. L. , and P. G. Richards. Pulse distortion and Hilbert transformation in multiply reflected and refracted body waves. *Bulletin of the Seismological Society of America*, **65**, 55–70, 1975.

Cisternas, A., O. Betancourt, and A. Leiva. Body waves in a "real Earth." Part I. *Bulletin of the Seismological Society of America*, **63**, 145–156, 1973.

Coddington, E. A., and N. Levinson. *Theory of Ordinary Differential Equations*. New York: McGraw-Hill, 1955.

Cormier, V., and P. G. Richards. Full-wave theory applied to a discontinuous velocity increase: The inner core boundary. *Journal of Geophysical Research*, **43**, 3–31, 1977.

Cormier, V. F. The polarization of *S* waves in a heterogeneous isotropic Earth model. *Journal of Geophysics*, **56**, 20–23, 1984.

Crampin, S. The dispersion of surface waves in multi-layered anisotropic media. *Geophysical Journal of the Royal Astronomical Society*, **21**, 387–402, 1970.

———. The propagation of surface waves in anisotropic media. *Geophysical Journal of the Royal Astronomical Society*, **25**, 71–87, 1971.

———. Distinctive particle motion of surface waves as a diagnostic of anisotropic layering. *Geophysical Journal of the Royal Astronomical Society*, **40**, 177–186, 1975.

———. A review of the effects of anisotropic layering on the propagation of seismic waves. *Geophysical Journal of the Royal Astronomical Society*, **49**, 9–27, 1977.

Crampin, S., and D. Bamford. Inversion of *P*-wave anisotropy. *Geophysical Journal of the Royal Astronomical Society*, **49**, 123–132, 1977.

Crampin, S., and D. W. King. Evidence for anisotropy in the upper mantle beneath Eurasia from the polarization of higher mode surface waves. *Geophysical Journal of the Royal Astronomical Society*, **49**, 59–85, 1977.

Crossley, D. J., and D. Gubbins. Static deformation of the Earth's liquid core. *Geophysical Research Letters*, **2**, 1–4, 1975.

Cummins, P. R., R. J. Geller, T. Hatori, and N. Takeuchi. DSM complete synthetic seismograms; *SH*, spherically symmetric, case. *Geophysical Research Letters*, **21**, 533–536, 1994a.

Cummins, P. R., R. J. Geller, and N. Takeuchi. DSM complete synthetic seismograms; *P–SV*, spherically symmetric, case. *Geophysical Research Letters*, **21**, 1633–1666, 1994b.

Currie, R. G. Period and *Q* of the Chandler wobble. *Geophysical Journal of the Royal Astronomical Society*, **38**, 179–185, 1974.

Dahlen, F. A. The normal modes of a rotating elliptical Earth. *Geophysical Journal of the Royal Astronomical Society*, **16**, 329–467, 1968.

———. The normal modes of a rotating elliptical Earth. II. Near-resonance multiplet coupling. *Geophysical Journal of the Royal Astronomical Society*, **18**, 397–436, 1969.

———. Elastic dislocation for a self-gravitating elastic configuration with an initial static stress field. *Geophysical Journal of the Royal Astronomical Society*, **28**, 357–383, 1972.

———. Elastic dislocation theory for a self-gravitating elastic configuration with an initial static stress field. II. Energy release. *Geophysical Journal of the Royal Astronomical Society*, **31**, 469–484, 1973.

———. On the ratio of *P*-wave to *S*-wave corner frequencies for shallow earthquake sources. *Bulletin of the Seismological Society of America*, **64**, 1159–1180, 1974.

———. Seismic faulting in the presence of a large compressive stress. *Geophysical Research Letters*, **3**, 245–248, 1976a. (Correction, p. 506.)

———. The passive influence of the oceans upon the rotation of the Earth. *Geophysical Journal of the Royal Astronomical Society*, **46**, 363–406, 1976b.

———. The balance of energy in earthquake faulting. *Geophysical Journal of the Royal Astronomical Society*, **48**, 239–261, 1977.

Dahlen, F. A., and M. L. Smith. The influence of rotation on the free oscillations of the Earth. *Philosophical Transactions of the Royal Society of London*, **A279**, 583–629, 1975.

Dahlen, F. A., and J. Tromp. *Theoretical Global Seismology*. Princeton, New Jersey: Princeton University Press, 1998.

Das, S., and K. Aki. A numerical study of two-dimensional spontaneous rupture propagation. *Geophysical Journal of the Royal Astronomical Society*, **50**, 643–668, 1977a.

———. Fault plane with barriers: A versatile earthquake model. *Journal of Geophysical Research*, **82**, 5658–5670, 1977b.

Davies, D., and D. P. McKenzie. Seismic travel-time residuals and plates. *Geophysical Journal of the Royal Astronomical Society*, **18**, 51–63, 1969.

de Hoop, A. T. Representation theorems for the displacement in an elastic solid and their applications to elastodynamic diffraction theory. D.Sc. Thesis, Technische Hogeschool, Delft, 1958.

———. A modification of Cagniard's method for solving seismic pulse problems. *Applied Science Research*, **B8**, 349–356, 1960.

DeMets, C. Afterslip no longer an afterthought. *Nature*, **386**, 549, 1997.

Dewey, J., and P. Byerly. The early history of seismometry (to 1900). *Bulletin of the Seismological Society of America*, **18**, 51–63, 1969.

Dieterich, J. H. A deterministic near-field source model. *Proceedings of the 5th World Conference of Earthquake Engineers*, Rome, 1973.

———. Constitutive properties of faults with simulated gouge. In *Mechanical Behavior of Crustal Rocks*, edited by N. L. Carter, M. Friedman, J. M. Logan, and D. W. Stearns, Geophysical Monograph 24, 103–120, Washington, D.C.: American Geophysical Union, 1986.

Dieterich, J. H., and B. Kilgore. Implications of fault constitutive properties for earthquake prediction. *Proceedings of the National Academy of Sciences, U.S.A.*, **93**, 3787–3794, 1996.

Doornbos, D. J., and E. S. Husebye. Array analysis of *PKP* phases and their precursors. *Physics of the Earth and Planetary Interiors*, **5**, 387–399, 1972.

Dorman, J., and M. Ewing. Numerical inversion of seismic surface wave dispersion data and crust mantle structure in the New York–Pennsylvania area. *Journal of Geophysical Research*, **67**, 5227–5241, 1962.

Dunkin, J. W. Computation of modal solutions in layered, elastic media at high frequencies. *Bulletin of the Seismological Society of America*, **55**, 335–358, 1965.

Dziewonski, A. M. Mapping the lower mantle: Determination of lateral heterogeneity in *P* velocity up to degree and order 6. *Journal of Geophysical Research*, **89**, 5929–5952, 1984.

Dziewonski, A. M., T.-A. Chou, and J. H. Woodhouse. Determination of earthquake source parameters from waveform data for studies of global and regional seismicity. *Journal of Geophysical Research*, **86**, 2825–2852, 1981.

Dziewonski, A. M., and F. Gilbert. The effect of small aspherical perturbations on travel-times and a re-examination of the corrections for ellipticity. *Geophysical Journal of the Royal Astronomical Society*, **44**, 7–17, 1976.

Dziewonski, A. M., A. L. Hales, and E. R. Lapwood. Parametrically simple Earth models consistent with geophysical data. *Physics of the Earth and Planetary Interiors*, **10**, 12–48, 1975.

Dziewonski, A. M., and J. H. Woodhouse. An experiment in systematic study of global seismicity: Centroid-moment tensor solutions for 201 moderate and large earthquakes of 1981. *Journal of Geophysical Research*, **88**, 3247–3271, 1983.

Eaton, J. P. Theory of the electromagnetic seismograph. *Bulletin of the Seismological Society of America*, **74**, 37–75, 1957.

Edmonds, A. R. *Angular Momentum in Quantum Mechanics*. Princeton, New Jersey: Princeton University Press, 1960.

Eshelby, J. D. Uniformly moving dislocations. *Proceedings of the Physical Society*, **A62**, 307–314, 1949.

———. The determination of the elastic field of an ellipsoidal inclusion, and related problems. *Proceedings of the Royal Society of London*, **A241**, 376–396, 1957.

Ewing, M., W. Jardetzky, and F. Press. *Elastic Waves in Layered Media*. New York: McGraw-Hill, 1957.

Ewing, M., F. Press, and J. L. Worzel. Further study of the *T*-phase. *Bulletin of the Seismological Society of America*, **42**, 37–51, 1952.

Ewing, M., and J. L. Worzel. *Long-range Sound Transmission*. Geological Society of America Memoir 27, 1948.

Farrell, W. E. A gyroscopic seismometer: Measurements during the Borrego earthquake. *Bulletin of the Seismological Society of America*, **59**, 1239–1246, 1969.

Fels, J.-F., and J. Berger. Parametric analysis and calibration of the STS-1 seismometer of the IRIS/IDA seismographic network, *Bulletin of the Seismological Society of America*, **84**, 1580–1592, 1994.

Filson, J., and T. V. McEvilly. Love wave spectra and the mechanism of the 1966 Parkfield sequence. *Bulletin of the Seismological Society of America*, **57**, 1245–1259, 1967.

Forsyth, D. W. The early structural evolution and anisotropy of the oceanic upper mantle. *Geophysical Journal of the Royal Astronomical Society*, **43**, 103–162, 1975.

Frank, F. C. On the equations of motion of crustal dislocations. *Proceedings of the Physical Society*, **A62**, 131–134, 1949.

Frasier, C. W. Discrete time solution of plane *P–SV* waves in a plane layered medium. *Geophysics*, **35**, 197–219, 1970.

Frasier, C. W., and D. K. Chowdury. Effect of scattering on *PcP/P* amplitude ratios at LASA from 40° to 84° distance. *Journal of Geophysical Research*, **79**, 5469–5477, 1974.

Frazer, L. N. Synthesis of shear-coupled *PL*. Ph.D. thesis, Princeton University, 1977.

———. Two problems in WKBJ theory: The interpolation of sampled velocity profiles and the use of frequency-dependent, complex velocities. *Geophysical Journal of the Royal Astronomical Society*, **72**, 193–211, 1983.

Freund, L. B. Energy flux into the tip of an extending crack in an elastic solid. *Journal of Elasticity*, **2**, 341–348, 1972.

Friedman, B. Propagation in a non-homogeneous atmosphere. *Communications of Pure and Applied Mathematics*, **4**, 317–350, 1951.

Fuchs, K. The reflection of spherical waves from transition zones with arbitrary depth-dependent elastic moduli and density. *Journal of Physics of the Earth*, Special Issue, **16**, 27–41, 1968.

———. On the determination of velocity depth distributions of elastic waves from the dynamic characteristics of the reflected wave field. *Zeitschrift für Geophysik*, **36**, 531–548, 1970.

———. The method of stationary phase applied to the reflection of spherical waves from transition zones with arbitrary depth-dependent elastic moduli and density. *Zeitschrift für Geophysik*, **37**, 89–117, 1971.

Fuchs, K, and G. Müller. Computation of synthetic seismograms with the reflectivity method and comparison of observations. *Geophysical Journal of the Royal Astronomical Society*, **23**, 417–433, 1971.

Fuchs, K, and K. Schulz. Tunneling of low-frequency waves through the subcrustal lithosphere. *Journal of Geophysics*, **42**, 175–190, 1976.

Furuya, I. Predominant period and magnitude. *Journal of Physics of the Earth*, **17**, 119–126, 1969.

Futterman, W. I. Dispersive body waves. *Journal of Geophysical Research*, **67**, 5279–5291, 1962.

Gakenheimer, D. C., and J. Miklowitz. Transient excitation of an elastic half-space by a point load travelling on the surface. *Journal of Applied Mechanics (Trans. ASME, Ser. E)*, **36**, 505–515, 1969.

Galitzin, B. *Vorlesungen über Seismometrie*. Leipzig: Teubner, 1914.

Gantmacher, R. R. *Theory of Matrices* (2 vols). New York: Chelsea Publishing Co., 1959.

Garnero, E. J., and D. V. Helmberger. Seismic detection of a thin laterally varying boundary layer at the base of the mantle beneath the central-Pacific. *Geophysical Review Letters*, **23**, 977–980, 1996.

Geller, R. J. Scaling relations for earthquake source parameters and magnitudes. *Bulletin of the Seismological Society of America*, **66**, 1501–1523, 1976.

Geller, R., T. Hara, and S. Tsuboi. On the equivalence of two methods for computing partial derivatives of seismic waveforms. *Geophysical Journal International*, **100**, 153–156, 1990a.

———. On the equivalence of two methods for computing partial derivatives of seismic waveforms—II. Laterally homogeneous initial model. *Geophysical Journal International*, **102**, 499–502, 1990b.

Gerver, M., and V. Markushevich. Determination of a seismic wave velocity from the travel time curve. *Geophysical Journal of the Royal Astronomical Society*, **11**, 165–173, 1966.

———. On the characteristic properties of travel time curves. *Geophysical Journal of the Royal Astronomical Society*, **13**, 241–246, 1967.

Gilbert, F. Gravitationally perturbed elastic waves. *Bulletin of the Seismological Society of America*, **57**, 783–784, 1967.

———. Excitation of the normal modes of the Earth by earthquake sources. *Geophysical Journal of the Royal Astronomical Society*, **22**, 223–226, 1971.

———. The representation of seismic displacements in terms of travelling waves. *Geophysical Journal of the Royal Astronomical Society*, **44**, 275–280, 1976.

———. Elastic waves in a transitional solid with arbitrarily small rigidity. *Geophysical Journal International*, **133**, 230–232, 1998.

Gilbert, F., and G. Backus. Propagator matrices in elastic wave and vibration problems. *Geophysics*, **31**, 326–332, 1966.

Gilbert, F., and A. M. Dziewonski. Application of normal mode theory to the retrieval of structural parameters and source mechanisms from seismic spectra. *Philosophical Transactions of the Royal Society of London*, **A278**, 187–269, 1975.

Gilbert, F., and D. V. Helmberger. Generalized ray theory for a layered sphere. *Geophysical Journal of the Royal Astronomical Society*, **2**, 57–80, 1972.

Gilbert, F., and S. J. Laster. Experimental investigation of *PL* modes in a single layer. *Bulletin of the Seismological Society of America*, **52**, 59–66, 1962.

Gilbert, F., S. J. Laster, M. M. Backus, and R. Schell. Observations of pulses on an interface. *Bulletin of the Seismological Society of America*, **52**, 847–868, 1962.

Gladwin, M. T., and F. D. Stacey. Anelastic degradation of acoustic pulses in rock. *Physics of the Earth Planetary Interiors*, **8**, 332–336, 1974.

Green, G. On the laws of reflexion and refraction of light. *Transactions of the Cambridge Philosophical Society*, vol. 7, 1839. (Reprinted in Mathematical Papers of George Green, pp. 245–269, London, 1871).

Griffith, A. A. The phenomena of rupture and flow in solids. *Philosophical Transactions of the Royal Society of London*, **A221**, 163–198, 1920.

Gutenberg, B. Über die Konstitution des Erdinnern, erschlossen aus Erdbebenbeobachtungen. *Zeitschrift für Geophysik*, **14**, 1217–1218, 1913.

Gutenberg, B., and C. F. Richter. Magnitude and energy of earthquakes, *Science*, **83**, 183–185, 1936.

———. Amplitudes of surface waves and magnitudes of shallow earthquakes. *Bulletin of the Seismological Society of America,* **35**, 3–12, 1945.

———. Earthquake magnitude, intensity, energy, and acceleration. *Bulletin of the Seismological Society of America*, **46**, 105–145, 1956.

Haddon, R. A. W. Corrugations on the mantle-core boundary or transition layers between inner and outer cores? *EOS, Transactions of the American Geophysical Union*, **53**, 600, 1972.

———. Computation of synthetic seismograms in layered Earth models using leaking modes. *Bulletin of the Seismological Society of America*, **74**, 1225–1248, 1984.

Hagiwara, T. A note on the theory of the electromagnetic seismograph. *Bulletin of the Earthquake Research Institute, Tokyo University*, **36**, 139–164, 1958.

Hales, A. L., and J. L. Roberts. The Zoeppritz amplitude equations: More errors. *Bulletin of the Seismological Society of America*, **64**, 285, 1974.

Hamano, Y. Dependence of rupture-time history on the heterogeneous distribution of stress and strength on the fault plane. *EOS, Transactions of the American Geophysical Union*, **55**, 362, 1974.

Hanson, M. E., A. R. Sanford, and R. J. Shaffer. A source function for a dynamic bilateral brittle shear failure. *Journal of Geophysical Research*, **76**, 3375–3383, 1971.

Hara, T., S. Tsuboi, and R. J. Geller. Inversion for laterally heterogeneous earth structure using a laterally heterogeneous starting model: Preliminary results. *Geophysical Journal International*, **104**, 523–540, 1991.

Harkrider, D. G. Theoretical and observed acoustic-gravity waves from explosive sources in the atmosphere, *Journal of Geophysical Research*, **69**, 5295–5321, 1964a.

———. Surface waves in multilayered elastic media, I. Rayleigh and Love waves from buried sources in a multilayered elastic half-space. *Bulletin of the Seismological Society of America*, **54**, 627–679, 1964b.

Harkrider, D. G., and D. L. Anderson. Surface wave energy from point sources in plane layered Earth models. *Journal of Geophysical Research*, **71**, 2967–2980, 1966.

Harrison, J. C. Cavity and topographic effects in tilt and strain measurements. *Journal of Geophysical Research*, **81**, 319–328, 1976a.

———. Tilt observations in the Poorman Mine near Boulder, Colorado. *Journal of Geophysical Research*, **81**, 329–336, 1976b.

Haskell, N. A. The dispersion of surface waves in multilayered media. *Bulletin of the Seismological Society of America*, **43**, 17–34, 1953.

———. Crustal reflections of plane *SH* waves. *Journal of Geophysical Research*, **65**, 4147–4150, 1960.

———. Crustal reflection of plane *P* and *SV* waves. *Journal of Geophysical Research*, **67**, 4751–4767, 1962.

———. Radiation pattern of surface waves from point sources in a multi-layered medium. *Bulletin of the Seismological Society of America*, **54**, 377–394, 1964.

———. Total energy and energy spectral density of elastic wave radiation from propagating faults. II. *Bulletin of the Seismological Society of America*, **56**, 125–140, 1966.

———. Elastic displacements in the near-field of a propagating fault. *Bulletin of the Seismological Society of America*, **59**, 865–908, 1969.

Hasselman, K. A statistical analysis of the generation of microseisms. *Reviews of Geophysics*, **1**, 177–210, 1963.

Haubrich, R. A. Microseisms. In *International Dictionary of Geophysics*, edited by S. K. Runcorn. London: Pergamon Press, 1967.

He, W., G. Guerin, R. N. Anderson, and U. T. Mello. Time-dependent reservoir characterization of the LF sand in the South Eugene Island 330 Field, Gulf of Mexico. *The Leading Edge*, **17**, 1434–1437, 1998.

Healy, J. H. Crustal structure along the coast of California from seismic-refraction measurements. *Journal of Geophysical Research*, **68**, 5777–5787, 1963.

Heaton, T. H. Evidence for and implications of self-healing pulses of slip in earthquake rupture. *Physics of the Earth and Planetary Interiors*, **64**, 1–20, 1990.

Heaton, T. H., and R. E. Heaton. Static deformation from point forces and force couples located in welded elastic Poissonian half-spaces: Implications for seismic moment tensors. *Bulletin of the Seismological Society of America*, **79**, 813–841, 1989.

Heaton, T. H., and D. V. Helmberger. A study of the strong ground motion of the Borrego Mt., California, earthquake. *Bulletin of the Seismological Society of America*, **57**, 315–330, 1977.

Heki, K., S. Miyazaki, and H. Tsuji. Silent fault slip following an interplate thrust earthquake at the Japan Trench. *Nature*, **386**, 595–598, 1997.

Helmberger, D. V. The crust-mantle transition in the Bering Sea. *Bulletin of the Seismological Society of America*, **58**, 179–214, 1968.

Helmberger, D. V., and D. A. Harkrider. Modeling earthquakes with generalized ray theory. In *Modern Problems in Elastic Wave Propagation*, edited by J. Miklowitz and J. D. Achenbach, 499–518. New York: Wiley–Interscience, 1978.

Helmberger, D. V., and S. D. Malone. Modeling local earthquakes as shear dislocations in a layered half space. *Journal of Geophysical Research*, **80**, 4881–4888, 1975.

Herglotz, G. Über das Benndorfsche Problem der Fortpflanzungsgeschwindigkeit der Erdbebenstrahlen. *Zeitschrift für Geophysik*, **8**, 145–147, 1907.

Herrera, D. V. A perturbation method for elastic wave propagation. I. Non-parallel boundaries. *Journal of Geophysical Research*, **69**, 3845–3851, 1964.

Herrin, E. Regional variation of *P*-wave velocity in the upper mantle beneath North America. In *The Earth's Crust and Upper Mantle,* edited by P. J. Hart, Geophysical Monograph 13, 242–246. Washington, D.C.: American Geophysical Union, 1969.

Herrin, E., and J. Richmond. On the propagation of the *Lg* phase. *Bulletin of the Seismological Society of America*, **50**, 197–210, 1960.

Hess, H. Seismic anisotropy of the uppermost mantle under oceans. *Nature*, **203**, 629–631, 1964.

Hildebrand, F. B. *Methods of Applied Mathematics*, 2nd. ed., Englewood Cliffs, New Jersey: Prentice-Hall, 1952.

Hill, D. P. Velocity gradients and anelasticity from crustal body wave amplitudes. *Journal of Geophysical Research*, **76**, 3309–3325, 1971a.

———. Velocity gradients in the Earth's crust from head-wave amplitudes. In *The Structure and Physical Properties of the Earth's Crust*, edited by J. G. Heacock, Geophysical Monograph 14, 71–75. Washington, D.C.: American Geophysical Union, 1971b.

Hill, D. P., F. G. Fischer, K. M. Lahr, and J. M. Coakley. Earthquake sounds generated by body-wave ground motion. *Bulletin of the Seismological Society of America*, **66**, 1159–1172, 1976.

Hirasawa, T., and W. Stauder. On the seismic body waves from a finite moving source. *Bulletin of the Seismological Society of America*, **55**, 1811–1842, 1965.

Hobson, E. W. *The Theory of Spherical and Ellipsoidal Harmonics*. New York: Chelsea Publishing Co., 1955.

House, L., and J. Boatwright. Investigation of two high stress drop earthquakes in the Shumagin seismic gap, Alaska. *Journal of Geophysical Research*, **85**, 7151–7165, 1980.

Housner, G. W., and M. D. Trifunac. Analysis of accelerograms—Parkfield earthquake. *Bulletin of the Seismological Society of America*, **57**, 1193–1220, 1967.

Hron, F. Criteria for selection of phases in synthetic seismograms for layered media. *Bulletin of the Seismological Society of America*, **61**, 765–779, 1971.

———. Numerical methods of ray generation in multilayered media. In *Seismology: Body, Waves and Sources*, edited by B. A. Bolt. *Methods in Computational Physics*, vol. 12. New York: Academic Press, 1972.

Hudson, D. E. Some problems in the application of spectrum techniques to strong-motion earthquake analyses. *Bulletin of the Seismological Society of America*, **52**, 417–430, 1962.

———. *Reading and Interpreting Strong Motion Accelerograms*, monograph, Berkeley, California: Earthquake Engineering Research Institute, 1979.

Hudson, J. A. The total internal reflection of *SH* waves. *Geophysical Journal of the Royal Astronomical Society*, **6**, 509–531, 1962.

———. A quantitative evaluation of seismic signals at teleseismic distances. I. Radiation from seismic sources. *Geophysical Journal of the Royal Astronomical Society*, **18**, 233–249, 1969a.

———. A quantitative evaluation of seismic signals at teleseismic distances. II. Body waves and surface waves from an extended source, *Geophysical Journal of the Royal Astronomical Society*, **18**, 353–370, 1969b.

Husseini, M. I., D. B. Jovanovich, M. J. Randall, and L. B. Freund. The fracture energy of earthquakes. *Geophysical Journal of the Royal Astronomical Society*, **43**, 367–385, 1975.

Ida, Y. Cohesive force across the tip of a longitudinal shear crack and Griffith's specific surface energy. *Journal of Geophysical Research*, **77**, 3796–3805, 1972.

———. Stress concentration and unsteady propagation of longitudinal shear cracks. *Journal of Geophysical Research*, **78**, 3418–3429, 1973.

Isacks, B., J. Oliver, and L. R. Sykes. Seismology and the new global tectonics. *Journal of Geophysical Research*, **73**, 5855–5899, 1968.

Jackson, D. D., and D. L. Anderson. Physical mechanisms of seismic-wave attenuation. *Review of Geophysics and Space Physics*, **8**, 1–63, 1970.

Jeffreys, H. On compressional waves in two superposed layers. *Proceedings of the Cambridge Philosophical Society*, **23**, 472–481, 1926.

———. On the cause of oscillatory movement in seismograms. *Monthly Notices of the Royal Astronomical Society, Geophysical Supplement*, **2**, 407–416, 1931.

———. Rock creep, tidal frictions and the Moon's ellipticities. *Monthly Notices of the Royal Astronomical Society*, **118**, 14–17, 1958.

———. Small correction in the theory of surface waves. *Geophysical Journal of the Royal Astronomical Society*, **6**, 115–117, 1961.

———. *Cartesian Tensors*. Cambridge University Press, 1965.

Jeffreys, H., and B. S. Jeffreys. *Methods of Mathematical Physics*, 3rd. ed., Cambridge: Cambridge University Press, 1972.

Johnson, L. E., and F. Gilbert. Inversion and inference for teleseismic ray data. In *Seismology: Body Waves and Sources*, edited by B. A. Bolt. *Methods in Computational Physics,* vol. 12. New York: Academic Press, 1972.

Jordan, T. H., and D. L. Anderson. Earth structure from free oscillations and travel times. *Geophysical Journal of the Royal Astronomical Society*, **26**, 411–459, 1974.

Jordan, T. H., and L. N. Frazer. Crustal and upper mantle structure from *Sp* phases. *Journal of Geophysical Research*, **80**, 1504–1518, 1975.

Julian, B. R., and D. L. Anderson. Travel times, apparent velocities and amplitudes of body waves. *Bulletin of the Seismological Society of America*, **58**, 339–366, 1968.

Julian, B. R., A. D. Miller, and G. R. Foulger. Non-double-couple earthquakes 1. Theory. *Reviews of Geophysics*, **36**, 525–549, 1998.

Julian, B. R., and M. K. Sengupta. Seismic travel time evidence for lateral inhomogeneity in the deep mantle. *Nature*, **242**, 443–447, 1973.

Kanamori, H. Mode of strain release associated with major earthquakes in Japan. *Annual Review of Earth and Planetary Sciences*, **1**, 213–239, 1973.

———. Re-examination of the Earth's free oscillations excited by the Kamchatka earthquake of November 4, 1952. *Physics of the Earth and Planetary Interiors*, **11**, 216–226, 1976.

———. The energy release in great earthquakes. *Journal of Geophysical Research*, **82**, 2981–2987, 1977.

Kanamori, H., and D. L. Anderson. Theoretical basis of some empirical relations in seismology. *Bulletin of the Seismological Society of America*, **65**, 1073–1095, 1975.

Karal, F. C., and J. B. Keller. Elastic wave propagation in homogeneous and inhomogeneous media. *Journal of the Acoustical Society of America*, **31**, 694–705, 1959.

Keilis-Borok, V. I., and T. B. Yanovskaya. Dependence of the spectrum of surface waves on the depth of the focus within the Earth's crust. *Bulletin of the Academy of Sciences, U.S.S.R.*, Geophysics Series (English translation), **11**, 1532–1539, 1962.

Keith, C., and S. Crampin. Seismic body waves in anisotropic media; reflection and refraction at a plane interface. *Geophysical Journal of the Royal Astronomical Society*, **49**, 181–208, 1977.

Kennett, B. L. N. The removal of free surface interactions from three-component seismograms. *Geophysical Journal of the Royal Astronomical Society*, **52**, 215–229, 1991.

Kennett, B. L. N., and E. R. Engdahl. Travel times for global earthquake location and phase association. *Geophysical Journal International*, **105**, 429–465, 1991.

Kennett, B. L. N., and O. Gudmundsson. Ellipticity corrections for seismic phases. *Geophysical Journal International*, **127**, 40–48, 1996.

Kennett, B. L. N., N. J. Kerry, and J. H. Woodhouse. Symmetries in the reflection and transmission of elastic waves. *Geophysical Journal of the Royal Astronomical Society*, **104**, 153–163, 1978.

Kim, W.-Y. The M_L scale in Eastern North America, *Bulletin of the Seismological Society of America*, **88**, 935–951, 1998.

Kim, W.-Y., V. Aharonian, A. L. Lerner-Lam, and P. G. Richards. Discrimination of earthquakes and explosions in Southern Russia using regional high-frequency three-component data from the IRIS/JSP Caucasus Network. *Bulletin of the Seismological Society of America*, **87**, 569–588, 1997.

Kind, R. Computation of reflection coefficients for layered media. *Journal of Geophysics*, **42**, 191–200, 1976.

———. The reflectivity method for a buried source. *Journal of Geophysics*, **44**, 603–612, 1978.

Kiselev, S. G., A. N. Kuznetsov, and V. M. Markushevich. The Earth flattening problem: Genesis, exact solving methods, and expansion into series, *Computational Seismology*, **29**, 28–43 (in Russian), 1997.

Knopoff, L. Diffraction of elastic waves. *Journal of the Acoustical Society of America*, **28**, 217–229, 1956.

———. Energy release in earthquakes. *Geophysical Journal of the Royal Astronomical Society*, **1**, 44–52, 1958.

———. *Q*. *Reviews of Geophysics*, **2**, 625–660, 1964a.

———. A matrix method for elastic wave problems. *Bulletin of the Seismological Society of America*, **54**, 431–438, 1964b.

Knopoff, L., M. J. Berry, and F .A. Schwab. Tripartite phase velocity observations in laterally heterogeneous regions. *Journal of Geophysical Research*, **72**, 2595–2601, 1967.

Knott, C. G. Reflection and refraction of elastic waves with seismological applications. *Philosophical Magazine*, Series 5, **48**, 64–97, 1899.

Kosarev, G. L., L. I. Makeyeva, Ye. F. Savarensky, and Ye. M. Chesnokov. Influence of anisotropy under a seismograph station on the records of body waves, *Izvestiya, Physics of the Solid Earth*, translated by the American Geophysical Union, **15**, 102–110, 1979.

Kosarev, G. L., L. I. Makeyeva, and L. P. Vinnik. Anisotropy of the mantle inferred from observations of *P* to *S* converted waves. *Geophysical Journal of the Royal Astronomical Society*, **76**, 209–220, 1984.

Kostrov, B. V. Unsteady propagation of longitudinal shear cracks. *Journal of Applied Mathematics and Mechanics*, **30**, 1241– 1248, 1966.

———. Seismic moment and energy of earthquakes, and seismic flow of rock. *Izvestiya, Physics of the Solid Earth*, **10**, 13–21, 1974.

———. On the crack propagation with variable velocity. *International Journal of Fracture*, **11**, 47–56, 1975.

LaCoste, L. J. C. A simplification in the conditions for the zero-length-spring seismograph. *Bulletin of the Seismological Society of America*, **25**, 176–179, 1935.

Lamb, H. On the propagation of tremors over the surface of an elastic solid. *Philosophical Transactions of the Royal Society of London*, **A203**, 1–42, 1904.

Landisman, M., T. Usami, Y. Sato, and R. Massé. Contributions of theoretical seismograms to the study of modes, rays, and the Earth. *Review of Geophysics and Space Physics*, **8**, 533–589, 1970.

Langer, R. E. Asymptotic solutions of a differential equation in the theory of microwave propagation. *Communications of Pure and Applied Mathematics*, **3**, 427–438, 1951.

Langston, C. A., and D. V. Helmberger. A procedure for modelling shallow dislocation sources. *Geophysical Journal of the Royal Astronomical Society*, **42**, 117–130, 1975.

Lapwood, E. R. The disturbance to a line source in a semi-infinite elastic medium. *Philosophical Transactions of the Royal Society of London*, **A242**, 63–100, 1949.

Latham, G., M. Ewing, J. Dorman, D. Lammlein, F. Press, N. Toksöz, G. Sutton, F. Duennebier, and Y. Nakamura. Moonquakes. *Science*, **174**, 687–692, 1971.

LePichon, X. Sea-floor spreading and continental drift. *Journal of Geophysical Research*, **73**, 3661–3697, 1968.

Liebfried, G., and H. D. Dietze. Zur Theorie der Schraufenversetzung. *Zeitschrift für Geophysik*, **126**, 790–808, 1949.

Linehan, D. Earthquakes in the West Indian region. *Transactions of the American Geophysical Union*, **21**, 229–232, 1940.

Liu, H.-P., D. L. Anderson, and H. Kanamori. Velocity dispersion due to anelasticity; implications for seismology and mantle composition. *Geophysical Journal of the Royal Astronomical Society*, **47**, 41–58, 1976.

Lomnitz, C. Creep measurements in igneous rocks. *Journal of Geology*, **64**, 473–479, 1956.

———. Linear dissipation in solids. *Journal of Applied Physics*, **28**, 201–205, 1957.

———. Some observations of gravity waves in the 1960 Chile earthquake. *Bulletin of the Seismological Society of America*, **60**, 669–670, 1970.

Longman, I. M. A Green's function for determining the deformation of the Earth under surface mass loads. 2. Computations and numerical results. *Journal of Geophysical Research*, **68**, 485–496, 1963.

Longuet-Higgins, M. S. A theory of the origin of microseisms. *Philosophical Transactions of the Royal Society of London*, **A243**, 1–35, 1950.

Love, A. E. H. *Some Problems of Geodynamics*. Cambridge: Cambridge University Press, 1911 (reprinted, New York: Dover Publications, 1967).

———. *A Treatise on the Mathematical Theory of Elasticity*. Cambridge: Cambridge University Press, 1892 (reprinted, New York: Dover Publications, 1944).

Luh, P. C. Free oscillations of the laterally inhomogeneous Earth: Quasi-degenerate multiplet coupling. *Geophysical Journal of the Royal Astronomical Society*, **32**, 203–218, 1973.

Luh, P. C., and A. M. Dziewonski. Theoretical seismograms for the Colombian earthquake of 1970 July 31. *Geophysical Journal of the Royal Astronomical Society*, **43**, 579–695, 1975.

Madariaga, R. Toroidal free oscillations of the laterally heterogeneous Earth, *Geophysical Journal of the Royal Astronomical Society*, **27**, 81–100, 1972.

———. Dynamics of an expanding circular fault. *Bulletin of the Seismological Society of America*, **66**, 639–666, 1976.

———. The dynamic field of Haskell's rectangular dislocation fault model. *Bulletin of the Seismological Society of America*, **68**, 869–888, 1978.

Major, M. W., G. Sutton, J. E. Oliver, and P. Metsger. On elastic strain of the Earth in the period range 5 seconds to 100 hours. *Bulletin of the Seismological Society of America*, **54**, 295–346, 1964.

Malvern, L. E. *Introduction to the Mechanics of a Continuous Medium*. Englewood Cliffs, New Jersey: Prentice-Hall, 1969.

Mantovani, E., F. Schwab, and L. Knopoff. Generation of complete theoretical seismograms for *SH*–II. *Geophysical Journal of the Royal Astronomical Society*, **48**, 531–536, 1977.

Marone, C. Laboratory-derived friction laws and their application to seismic faulting. *Annual Reviews of Earth and Planetary Sciences*, **26**, 634–696, 1998.

Marshall, P. D., A. Douglas, and J. A. Hudson. Surface waves from underground explosions. *Nature*, **234**, 8–9, 1971.

Maruyama, T. On the force equivalents of dynamic elastic dislocations with reference to the earthquake mechanism. *Bulletin of the Earthquake Research Institute, Tokyo University*, **41**, 467–486, 1963.

Mason, W. P. *Physical Acoustics and the Properties of Solids*. London: D. Van Nostrand, 1958.

Masters, G., and K. Richards-Dinger. On the efficient calculation of ordinary and generalized spherical harmonics. *Geophysical Journal International*, **135**, 307–309, 1998.

McLeod, D. P., G. E. Stedman, T. H. Webb, and U. Schreiber. Comparison of standard and ring laser rotational seismograms. *Bulletin of the Seismological Society of America*, **88**, 1495–1503, 1998.

McHugh, S., and M. J. S. Johnston. Short-period nonseismic tilt perturbations and their relation to episodic slip. *Journal of Geophysical Research*, **81**, 6341–6346, 1976.

McKenzie, D. P. The relation between fault plane solutions for earthquakes and the directions of the principal stresses. *Bulletin of the Seismological Society of America*, **59**, 295–346, 1969.

Melchior, P. *The Earth Tides*. London: Pergamon Press, 1966.

Mellman, G. R., and D. V. Helmberger. High-frequency attenuation by a thin high-velocity layer. *Bulletin of the Seismological Society of America*, **64**, 1383–1388, 1974.

Mendiguren, J. Identification of free oscillation spectral peaks for 1970 July 31, Colombian deep shock using the excitation criterion. *Geophysical Journal of the Royal Astronomical Society*, **33**, 281–321, 1973a.

———. High resolution spectroscopy of the Earth's free oscillations, knowing the earthquake source mechanism. *Science*, **179**, 179–180, 1973b.

Menke, W. *Geophysical Data Analysis: Discrete Inverse Theory*, New York: Academic Press, 1984.

Michelson, A. A., and H. G. Gale. The rigidity of the Earth. *Astrophysical Journal*, **50**, 330–345, 1919.

Mikumo, T., and T. Miyatake. Dynamic rupture process on a three-dimensional fault with non-uniform frictions and near-field seismic waves. *Geophysical Journal of the Royal Astronomical Society*, **54**, 417–438, 1978.

Minakami, T. Seismology of volcanoes in Japan. In *Physical Volcanology,* edited by L. Civetta, P. Jasparini, G. Luongo, and A. Rapolla. Amsterdam: Elsevier, 1974.

Mitra, M. Surface displacement produced by an underground fracture. *Geophysical Journal of the Royal Astronomical Society*, **31**, 204–213, 1966.

Molnar, P., K. H. Jacob, and K. McCamy. Implications of Archambeau's earthquake source theory for slip on faults. *Bulletin of the Seismological Society of America*, **63**, 101–104, 1973.

Molnar, P., and J. Oliver. Lateral variations of attenuation in the upper mantle and discontinuities in the lithosphere. *Journal of Geophysical Research*, **74**, 2648–2682, 1969.

Molnar, P., B. E. Tucker, and J. N. Brune. Corner frequencies of *P* and *S* waves and models of earthquake sources. *Bulletin of the Seismological Society of America*, **63**, 2091–2104, 1973.

Mora, P., and D. Place. Simulation of the frictional stick-slip instability. *Pure and Applied Geophysics*, **143**, 61–87, 1994.

Müller, G. Amplitude studies of core phases. *Journal of Geophysical Research*, **78**, 3469–3490, 1973a.

———. Correction. *Journal of Geophysical Research*, **82**, 2541–2542, 1977.

———. Seismic moment and long-period radiation of underground nuclear explosions. *Bulletin of the Seismological Society of America*, **63**, 847–857, 1973b.

———. Volume change of seismic sources from moment tensors. *Bulletin of the Seismological Society of America*, **91**, 880–884, 2001.

Müller, G., and R. Kind. Observed and computed seismogram sections for the whole Earth. *Geophysical Journal of the Royal Astronomical Society*, **44**, 699–716, 1976.

Musgrave, M. J. P. *Crystal Acoustics*. San Francisco: Holden-Day, 1970.

Nafe, J. E. Reflection and transmission coefficients at a solid-solid interface of high velocity contrast. *Bulletin of the Seismological Society of America*, **47**, 205–219, 1957.

Nakanishi, K., F. Schwab, and L. Knopoff. Generation of complete theoretical seismograms for *SH*-I. *Geophysical Journal of the Royal Astronomical Society*, **48**, 525–530, 1977.

Ness, N. F., J. C. Harrison, and L. B. Slichter. Observations of the free oscillations of the Earth. *Journal of Geophysical Research*, **66**, 621–629, 1961.

Niazy, A. Elastic displacements caused by a propagating crack in an infinite medium: An exact solution. *Bulletin of the Seismological Society of America*, **63**, 357–379, 1973.

———. An exact solution for a finite, two-dimensional moving dislocation in an elastic half-space with application to the San Francisco earthquake of 1971. *Bulletin of the Seismological Society of America*, **65**, 1797–1826, 1975.

Nowick, A. S., and B. S. Berry. *Anelastic Relaxation in Crystalline Solids*. New York: Academic Press, 1972.

Nussenzveig, H. M. High-frequency scattering by an impenetrable sphere. *Annals of Physics (N.Y.)*, **34**, 23–95, 1965.

———. *Causality and Dispersion Relations*, Mathematics in Science and Engineering, vol. 95, edited by R. Bellman, New York: Academic Press, 1972.

O'Connell, R. J., and B. Budiansky. Measures of dissipation in viscoelastic media. *Geophysical Research Letters*, **5**, 5–8, 1978.

Okal, E. A. A student's guide to teleseismic body wave amplitudes. *Seismological Research Letters*, **63**, 169–180, 1992.

Oliver, J. On the long-period character of shear waves. *Bulletin of the Seismological Society of America*, **51**, 1–12, 1961.

Oliver, J., and M. Major. Leaking modes and the *PL* phase. *Bulletin of the Seismological Society of America*, **50**, 165–180, 1960.

Olsen, K. B., R. J. Archuleta, and J. R. Matarese. Three-dimensional simulation of a magnitude 7.75 earthquake on the San Andreas Fault. *Science*, **270**, 1628–1632, 1995.

Olver, F. W. J. The asymptotic solution of linear differential equations of the second order for large values of a parameter. *Philosophical Transactions of the Royal Society of London*, **A247**, 307–327, 1954a.

———. The asymptotic expansion of Bessel functions of large order. *Philosophical Transactions of the Royal Society of London*, **A247**, 328–368, 1954b.

Orcutt, J. A., B. L. N. Kennett, and L. M. Dorman. Structure of the East Pacific Rise from an ocean bottom seismometer survey. *Geophysical Journal of the Royal Astronomical Society*, **45**, 305–320, 1976.

Page, R. A., J. A. Blume, and W. B. Joyner. Earthquake shaking and damage to buildings. *Science*, **189**, 601–608, 1975.

Pancha, A., T. H. Webb, G. E. Stedman, D. P. McLeod, and K. U. Schreiber. *Geophysical Research Letters*, **27**, 3553–3556, 2000.

Parker, R. L. *Geophysical Inverse Theory*. Princeton, New Jersey: Princeton University Press, 1994.

Pekeris, C. L. *Theory of Propagation of Explosive Sound in Shallow Water*. Geological Society of America Memoir 27, 1948.

Pekeris, C. L., and Y. Accad. Dynamics of the liquid core of the Earth. *Philosophical Transactions of the Royal Society of London*, **A273**, 237–260, 1972.

Pekeris, C. L., Z. Alterman, and H. Jarosch. Rotational multiplets in the spectrum of the Earth. *Physics Review*, **122**, 1692–1700, 1961.

Peterson, J. Observations and modeling of seismic background noise. *U.S. Geological Survey Open-File Report*, 93-322, 95 pages, 1993.

Peterson, J., H. M. Butler, L. G. Holcomb, and C. R. Hutt. The seismic research observatory. *Bulletin of the Seismological Society of America*, **66**, 2049–2068, 1976.

Phinney, R. A. Leaking modes in the crustal wave-guide. 1. The oceanic *PL* wave. *Journal of Geophysical Research*, **66**, 1445–1469, 1961.

Phinney, R. A., and S. Alexander. *P* wave diffraction theory and the structure of the core mantle boundary. *Journal of Geophysical Research*, **71**, 5943–5958, 1966.

Phinney, R. A., and L. M. Cathles. Diffraction of *P* by the core: A study of long-period amplitudes near the edge of the shadow. *Journal of Geophysical Research*, **74**, 1556–1574, 1969.

Pomeroy, P. W., G. Hade, J. Savino, and R. Chander. Preliminary results from high-gain wide-band long-period electromagnetic seismograph systems. *Journal of Geophysical Research*, **74**, 3295–3298, 1969.

Poupinet, G., and C. Wright. The generation and propagation of shear-coupled *PL* waves. *Bulletin of the Seismological Society of America*, **62**, 1699–1710, 1972.

Press, F. Determination of crustal structure from phase velocity of Rayleigh waves. Part 1. Southern California. *Bulletin of the Seismological Society of America*, **67**, 1647–1658, 1956.

———. Displacements, strains, and tilts at teleseismic distances. *Journal of Geophysical Research*, **70**, 2395–2412, 1965.

Press, F., A. P. Crary, J. Oliver, and S. Katz. Air-coupled flexural waves in floating ice. *Transactions of the American Geophysical Union*, **32**, 166–172, 1951.

Press, F., and M. Ewing. Two slow surface waves across North America. *Bulletin of the Seismological Society of America,* **42**, 219–228, 1952.

Ramos, A. C. B., and J. P. Castagna. Useful approximations for converted-wave AVO. *Geophysics*, **66**, 1721–1734, 2001.

Randall, M. J. Spectral peaks and earthquake source dimensions. *Journal of Geophysical Research*, **78**, 2609–2611, 1973.

Rautian, T. G., and V. I. Khalturin. The use of coda for determination of the earthquake source spectrum, *Bulletin of the Seismological Society of America,* **68**, 923–948. 1978.

Rayleigh, J. W. S. On waves propagated along the plane surface of an elastic solid. *Proceedings of the London Mathematical Society*, **17**, 4–11, 1887.

———. The problem of the whispering gallery. *Philosophical Magazine*, **20**, 1001–1004, 1910.

———. On the propagation of waves through a stratified medium, with special reference to the question of reflection. *Proceedings of the Royal Society of London*, **A86**, 207–226, 1912.

———. *The Theory of Sound*, 2 vols. New York: Dover Publications, 1945.

Richards, P. G. An elasticity theorem for heterogeneous media, with an example of body wave dispersion in the Earth. *Geophysical Journal of the Royal Astronomical Society*, **22**, 453–472, 1971.

———. Calculation of body waves, for caustics and tunnelling in core phases. *Geophysical Journal of the Royal Astronomical Society*, **35**, 243–264, 1973a.

———. The dynamic field of a growing plane elliptical shear crack. *International Journal of Solids and Structures*, **9**, 843–861, 1973b.

———. Weakly coupled potentials for high-frequency elastic waves in continuously stratified media. *Bulletin of the Seismological Society of America*, **64**, 1575–1588, 1974.

———. Dynamic motions near an earthquake fault: A three-dimensional solution. *Bulletin of the Seismological Society of America*, **66**, 1–31, 1976a.

———. On the adequacy of plane-wave reflection/transmission coefficients in the analysis of seismic body waves. *Bulletin of the Seismological Society of America*, **66**, 701–717, 1976b.

———. On wavefronts and interfaces in anelastic media. *Bulletin of the Seismological Society of America*, **74**, 2157–2165, 1984.

———. A short course on theoretical seismology. In *Oceanographic and Geophysical Tomography*, edited by Y. Desaubies, A. Tarantola, and J. Zinn-Justin, Session L, NATO ASI, North-Holland: Amsterdam, 1988.

———. Earth's inner core—Discoveries and conjectures. *Astronomy & Geophysics, The Journal of the Royal Astronomical Society*, **41**, 20–24, 2000.

Richards, P. G., and C. W. Frasier. Scattering of elastic waves from depth-dependent inhomogeneities. *Geophysics*, **41**, 441–458, 1976.

Richards, P. G., D. Witte and G. Ekström. Generalized ray theory for seismic waves in structures with planar non-parallel interfaces. *Bulletin of the Seismological Society of America*, **81**, 1309–1331, 1991.

Richter, C. F. An instrumental earthquake magnitude scale. *Bulletin of the Seismological Society of America*, **25**, 1–32, 1935.

———. *Elementary Seismology*. San Francisco: W. H. Freeman and Company, 1958.

Rihn, W. J. The design of electromagnetic damping circuits. *Bulletin of the Seismological Society of America*, **59**, 967–972, 1969.

Robin, L. *Fonctions Sphériques de Legendre et Fonctions Sphéroidales*, 3 vols. Paris: Gautier-Villars, 1957.

Rodgers, P. W. The response of the horizontal pendulum seismometer to Rayleigh and Love waves, tilt and free oscillations of the Earth. *Bulletin of the Seismological Society of America*, **58**, 1384–1406, 1968.

Rodi, W. L., P. Glover, T. M. C. Li, and S. S. Alexander. A fast, accurate method for computing group-velocity partial derivatives for Rayleigh and Love modes. *Bulletin of the Seismological Society of America*, **65**, 1105–1114, 1975.

Rosenbaum, J. H. The long-time response of a layered elastic medium to explosive sound. *Journal of Geophysical Research*, **65**, 1577–1613, 1960.

Ruina, A. Slip instability and state variable friction laws. *Journal of Geophysical Research*, **88**, 10359–10370, 1983.

Russakof, D., G. Ekström, and J. Tromp. A new analysis of the great 1970 Colombia earthquake and its isotropic component. *Journal of Geophysical Research*, **102**, 20423–20434, 1997.

Russell, B. (editor). Introduction to AVO, *Leading Edge*, **12**, 161–208 and 230–233, 1993.

Sacks, I. S., S. Suyehiro, and D. W. Evertson. Sacks-Evertson strainmeter, its installation in Japan and some preliminary results concerning strain steps. *Proceedings of the Japanese Academy*, **47**, 707–712, 1971.

Saito, M. Excitation of free oscillations and surface waves by a point source in a vertically heterogeneous Earth. *Journal of Geophysical Research*, **72**, 3689–3699, 1967.

———. Synthesis of rotational and dilatational seismograms. *Journal of Physics of the Earth*, **16**, 53–62, 1968.

Sato, R. Fast computation of theoretical seismograms for an infinite medium. Part I. Rectangular fault. *Journal of Physics of the Earth*, **23**, 323–331, 1975.

Sato, T., and T. Hirasawa. Body wave spectra from propagating shear cracks. *Journal of Physics of the Earth*, **21**, 415–431, 1973.

Satô, Y. Study on surface waves. II. Velocity of surface waves propagated upon elastic plates. *Bulletin of the Earthquake Research Institute, Tokyo University*, **29**, 223–261, 1951.

———. Numerical integration of the equations of motion for surface waves in a medium with arbitrary variation of material constants. *Bulletin of the Seismological Society of America*, **49**, 57–77, 1959.

Satô, Y., T. Usami, and M. Ewing. Basic study on the oscillation of a homogeneous elastic sphere. IV. *The Geophysical Magazine*, **31**, 237–242, 1962.

Savage, J. C. Radiation from a realistic model of faulting. *Bulletin of the Seismological Society of America*, **56**, 577–592, 1966.

———. Steketee's paradox. *Bulletin of the Seismological Society of America*, **59**, 381–384, 1969a.

———. A new method of analyzing the dispersion of oceanic Rayleigh waves. *Journal of Geophysical Research*, **74**, 2608–2617, 1969b.

———. Relation of corner frequency to fault dimensions. *Journal of Geophysical Research*, **27**, 3788–3795, 1972.

———. Anelastic degradation of acoustic pulses in rock—comments. *Physics of the Earth and Planetary Interiors*, **11**, 284–285, 1976.

Savage, J. C., and M. E. O'Neill. The relation between the Lomnitz and Futterman theories of internal friction. *Journal of Geophysical Research*, **80**, 249–251, 1975.

Savino, J., K. McCamy, and G. Hade. Structures in Earth noise beyond twenty seconds—A window for earthquakes. *Bulletin of the Seismological Society of America*, **62**, 141–176, 1972.

Schaff, D. 4D high resolution seismology: Repeating events and large scale relocation, Ph. D. Thesis, Stanford University, California, 2001.

Scholte, J. G. J. The range of existence of Rayleigh and Stoneley waves. *Monthly Notices of the Royal Astronomical Society, Geophysical Supplement*, **5**, 120–126, 1947.

———. On seismic waves in a spherical Earth. *Koninkl. Ned. Meteorol. Inst. Publ. 102–65*, 1–55, 1956.

Scholz, C. H. Earthquakes and friction laws. *Nature*, **391**, 37–42, 1998.

Schwab, F., and L. Knopoff. Surface wave dispersion computations. *Bulletin of the Seismological Society of America*, **60**, 321–344, 1970.

Schwab, K., R. Bruckner, and R. E. Packard. Detection of the Earth's rotation using superfluid phase coherence. *Nature*, **386**, 585–587, 1997.

Seckler, B. D., and J. B. Keller. Asymptotic theory of diffraction in inhomogeneous media. *Journal of the Acoustical Society of America*, **31**, 206–216, 1959.

Shi, J., W.-Y. Kim, and P. G. Richards. The corner frequencies and stress drops of intraplate earthquakes in the Northeastern United States. *Bulletin of the Seismological Society of America*, **88**, 531–542, 1998.

Shimshoni, M., and A. Ben-Menahem. Computation of the divergence coefficient for seismic phases. *Geophysical Journal of the Royal Astronomical Society*, **21**, 285–294, 1970.

Shuey, R.T. A simplification of the Zoeppritz equations. *Geophysics,* **50**, 609–614, 1985.

Silver, P. G., and W. W. Chan. Shear wave splitting and subcontinental mantle deformation. *Journal of Geophysical Research*, **96**, 16429–16454, 1991.

Sleep, N. H. Application of a unified rate and state friction theory to the mechanics of fault zones with strain localization. *Journal of Geophysical Research*, **102**, 2875–2895, 1987.

Slichter, L. B. The theory of the interpretation of seismic travel time curves in horizontal structures. *Physics*, **3**, 273–295, 1932.

Smith, M. L. Wobble and nutation of the Earth, *Geophysical Journal of the Royal Astronomical Society*, **50**, 103–140, 1977.

Smith, M. L., and F. A. Dahlen. The azimuthal dependence of Love and Rayleigh wave propagation in a slightly anisotropic medium. *Geophysical Journal of the Royal Astronomical Society*, **78**, 3321–3333, 1973.

———. The period and Q of the Chandler wobble. *Geophysical Journal of the Royal Astronomical Society*, **64**, 223–281, 1981.

Smith, W. D. A non-reflecting plane boundary for wave propagation problems. *Journal of Computational Physics*, **15**, 492–503, 1974.

———. The application of finite element analysis to body wave propagation problems. *Geophysical Journal of the Royal Astronomical Society*, **42**, 747–768, 1975.

Solomon, S. C. Seismic-wave attenuation and partial melting in the upper mantle of North America. *Journal of Geophysical Research*, **77**, 1483–1502, 1972.

———. Shear wave attenuation and melting beneath the Mid-Atlantic Ridge. *Journal of Geophysical Research*, **78**, 6044–6059, 1973.

Song, X. Joint inversion for inner core rotation, inner core anisotropy, and mantle heterogeneity. *Journal of Geophysical Research*, **105**, 7931–7943, 2000.

Sorrells, G. G. A preliminary investigation into the relationship between long-period seismic noise and local fluctuations in the atmospheric pressure field. *Geophysical Journal of the Royal Astronomical Society*, **26**, 71–82, 1971.

Spencer, T. W. Long-time response predicted by exact elastic ray theory. *Geophysics*, **25**, 625–641, 1960.

———. The method of generalized reflection and transmission coefficients. *Geophysics*, **30**, 363–368, 1965.

Spudich, P. K. P., and D. V. Helmberger. Synthetic seismograms from model ocean bottoms. *Journal of Geophysical Research*, **84**, 189–204, 1979.

Stacey, F. D., M. T. Gladwin, B. McKavanagh, A. T. Linde, and L. M. Hastie, Anelastic damping of acoustic and seismic pulses. *Geophysical Survey*, **2**, 133–157, 1975.

Stacey, F. D., J. M. Rynn, E. C. Little, and C. Croskell. Displacement and tilt transducers of 140 db range. *Journal of Scientific Instrumentation (Journal of Physics, E)*, Series 2, **2**, 945–949, 1969.

Starr, A. T. Slip on a crystal and rupture in a solid due to shear. *Proceedings of the Cambridge Philosophical Society*, **24**, 489–500, 1928.

Stauder, W. Mechanism of the Rat Island earthquake sequence of February 4, 1965, with relation to island arcs and sea-floor spreading. *Journal of Geophysical Research*, **73**, 3847–3853, 1968.

Stein, S., and R. J. Geller. Time domain observation and synthesis of split spheroidal and torsional free oscillations of the 1960 Chilean earthquake: Preliminary results. *Bulletin of the Seismological Society of America*, **68**, 325–332, 1978.

Stephens, C., and B. L. Isacks. Toward an understanding of S_n: Normal modes of Love waves in an oceanic structure. *Bulletin of the Seismological Society of America,* **67**, 69–78, 1977.

Stolt, R. H., and A. B. Weglein. Migration and inversion of seismic data. *Geophysics*, **50**, 2458–2472, 1985.

Strick, E. Propagation of elastic wave motion from an impulsive source along a fluid/solid interface. II. Theoretical pressure pulse. *Philosophical Transactions of the Royal Society of London*, **A251**, 465–523, 1959.

———. A predicted pedestal effect for pulse propagation in constant-Q solids. *Geophysics*, **35**, 387–403, 1970.

Su, S. S., and J. Dorman. The use of leaking modes in seismogram interpretation and in studies of crust-mantle structure. *Bulletin of the Seismological Society of America*, **55**, 989–1021.

Su, S. S., and J. Dorman. The use of leaking modes in seismogram interpretation and in studies of crust-mantle structure. *Bulletin of the Seismological Society of America,* **55**, 989–1021, 1967.

Swanger, H. J., and D. M. Boore. Simulation of strong-motion displacements using surface-wave modal superposition. *Bulletin of the Seismological Society of America*, **68**, 907–922, 1978.

Sykes, L. R. Mechanism of earthquakes and nature of faulting on the mid-oceanic ridges. *Journal of Geophysical Research,* **72**, 2131–2153, 1967.

Tada, T., and T. Yamashita. The paradox of smooth and abrupt bends in two-dimensional in-plane shear-crack mechanics. *Geophysical Journal International*, **127**, 795–800, 1996.

Takeo, M., and H. M. Ito. What can be learned from rotational motions excited by earthquakes? *Geophysical Journal International*, **129**, 319–329, 1997.

Takeuchi, H., and N. Kobayashi. Surface waves propagating along a free surface of a semi-infinite elastic medium of variable density and elasticity. Part I. *Journal of the Seismological Society of Japan*, Series 2, **12**, 115–121, 1959.

Takeuchi, H., and M. Saito. Seismic surface waves, In *Seismology: Surface Waves and Earth Oscillations*, edited by B. A. Bolt. *Methods in Computational Physics,* vol. 11, 217–295. New York: Academic Press, 1972.

Tarantola, A. *Inverse Problem Theory: Methods for Fitting and Model Parameter Estimation.* New York: Elsevier, 1987.

Thomson, W. T. Transmission of elastic waves through a stratified solid. *Journal of Applied Physics*, **21**, 89–93, 1950.

Titchmarsh, E. C. Conjugate trigonometrical integrals. *Proceedings of the London Mathematical Society*, Series 2, **24**, 109–130, 1926.

———. *The Theory of Functions*, 2nd. ed. London: Oxford University Press, 1939.

Tsai, Y. B., and K. Aki. Amplitude spectra of surface waves from small earthquakes and underground nuclear explosions. *Journal of Geophysical Research*, **76**, 3440–3452, 1971.

Usher, M. J., R. F. Burch, and C. Guralp. Wide-band feedback seismometers. *Physics of the Earth and Planetary Interiors*, **18**, 38–50, 1979.

van der Hilst, R. D., S. Widiyantoro, and E. R. Engdahl. Evidence for deep mantle circulation from global tomography. *Nature*, **386**, 578–584, 1997.

van der Hilst, R. D., S. Widiyantoro, K. C. Creager, T. J. McSweeney. Deep subduction and aspherical variations in *P*-wavespeed at the base of Earth's mantle. In *The Core-mantle Boundary Region*, edited by M. Gurnis, M. Wysession, E. Knittle, and B. A. Buffett, Geodynamics Series 28, 5–20. Washington, D.C.: American Geophysical Union, 1998.

Vaněk, J., A. Zapotek, V. Karnik, N. V. Kondorskaya, Yu. V. Rizmichenko, E. F. Saverensky, S. L. Solov'yov, and N. V. Shebalin. Standardization of magnitude scales. *Izvestiya Akad. Nauk S. S. S. R.*, Ser. Geofiz., **2**, 153–158, 1962.

Vared, M., and A. Ben-Menahem. Application of synthetic seismograms to study of low-magnitude earthquakes and crustal structure in the northern Red Sea region. *Bulletin of the Seismological Society of America*, **64**, 1221–1237, 1974.

Vavryčuk, V., and I. Pšenčík. *PP*-wave reflection coefficients in weakly anisotropic elastic media. *Geophysics*, **63**, 2129–2141, 1998.

Verweij, M. D., and A. T. de Hoop. Determination of seismic wavefields in arbitrarily continuously layered media using the modified Cagniard method. *Geophysical Journal International*, **108**, 731–754, 1990.

Vidale, J. E., S. Goes, and P. G. Richards. Near-field deformation seen on distant broadband seismograms. *Geophysical Research Letters*, **22**, 1–4, 1995.

Vinnik, L. P., R. Kind, G. L. Kosarev, and L. I. Makeyeva. Azimuthal anisotropy in the lithosphere from observations of long-period *S*-waves. *Geophysical Journal International*, **99**, 549–559, 1989.

Vinnik, L. P., and J.-P. Montagner. Shear wave splitting in the mantle *Ps* phases. *Geophysical Research Letters*, **23**, 2449–2452, 1996.

Vlaar, N. J. The field from an *SH*-point source in a continuously layered inhomogeneous medium. 1. The field in a layer of a finite depth. *Bulletin of the Seismological Society of America*, **56**, 715–724, 1966.

———. Ray theory for an anisotropic inhomogeneous elastic medium. *Bulletin of the Seismological Society of America*, **58**, 2053–2072, 1968.

Vvedenskaya, A. V. The determination of displacement fields by means of dislocation theory. *Izvestiya Akad. Nauk. S.S.S.R.*, Ser. Geofiz., 227–284, 1956.

Walker, D. A., C. C. McCreely, G. H. Sutton, and F. K. Dunnebier. Spectral analyses of high frequency *Pn* and *Sn* phases observed at great distances in the western Pacific. *Science*, **199**, 1333–1335, 1978.

Weertman, J. Unstable slippage across a fault that separates elastic media of different elastic constants. *Journal of Geophysical research*, **85**, 1455–1461, 1980.

Weidner, D. J. Rayleigh waves from mid-ocean ridge earthquakes: Source and path effects. Ph. D. thesis, Massachusetts Institute of Technology, 1972.

———. Rayleigh wave phase velocities in the Atlantic Ocean. *Geophysical Journal of the Royal Astronomical Society*, **36**, 105–139, 1974.

Weidner, D. J., and K. Aki. Focal depth and mechanism of mid-ocean ridge earthquakes. *Journal of Geophysical Research*,**78**, 1818–1831, 1973.

Wesson, R. L. A time integration method for computation of the intensities of seismic rays. *Bulletin of the Seismological Society of America*, **60**, 307–316, 1970.

White, J. E. *Seismic Waves*. New York: McGraw Hill, 1965.

Wideman, C. J., and M. W. Major. Strain steps associated with earthquakes. *Bulletin of the Seismological Society of America*, **57**, 1429–1444, 1967.

Wiechert, E. Ein astatische Pendel höher Empfindlichkeit zur mechanischen Registrierung von Erdbeben. *Beitr. Geophys.*, **6**, 435–450, 1904.

———. Bestimmung des Weges der Erdbebenwellen im Erdinnern. I. Theoretisches. *Phys. Z.*, **11**, 294–304, 1910.

Wielandt, E., and J. M. Steim. A digital very-broad-band seismograph. In *Symposium on Broad-band and Long-period Seismology in Europe*, edited by R. Madariaga and B. Romanowicz, Annales Geophysicae, Series B: Terrestrial and Planetary Physics, vol. 4, 227–232, 1986.

Wielandt, E., and G. Streckeisen. The leaf-spring seismometer: Design and performance. *Bulletin of the Seismological Society of America*, **72**, 2349–2367, 1982.

Wiggins, R. A. Body wave amplitude calculations. II. *Geophysical Journal of the Royal Astronomical Society*, **46**, 1–10, 1976a.

———. A fast, new computational algorithm for free oscillations and surface waves. *Geophysical Journal of the Royal Astronomical Society*, **47**, 135–150, 1976b.

Wiggins, R. A. and D. V. Helmberger. Synthetic seismogram computation by expansion in generalized rays. *Geophysical Journal of the Royal Astronomical Society*, **37**, 73–90, 1974.

Wiggins, R. A., and M. Saito. Evaluation of computational algorithms for the associated Legendre polynomials by internal analysis. *Bulletin of the Seismological Society of America*, **61**, 375–381, 1971.

Willmore, P. L. The detection of Earth movement. In *Methods and Techniques in Geophysics*, edited by S. K. Runcorn, 230–276. New York: Interscience, 1960.

Woodhouse, J. H. On Rayleigh's principle. *Geophysical Journal of the Royal Astronomical Society*, **46**, 11–22, 1976.

———. Asymptotic results for elastodynamic propagator matrices in plane stratified and spherically stratified Earth models. *Geophysical Journal of the Royal Astronomical Society*, **54**, 263–280, 1978.

Woodhouse, J. H., and A. M. Dziewonski. Mapping the upper mantle: Three-dimensional modeling of Earth structure by inversion of seismic waveforms, *Journal of Geophysical Research*, **89**, 5953–5986, 1984.

Wyss, M., and J. N. Brune. Seismic moment, stress and source dimensions for earthquakes in the California-Nevada region. *Journal of Geophysical Research*, **73**, 4681–4694, 1968.

———. Regional variations of source properties in Southern California estimated from the ratio of short- to long-period amplitudes. *Bulletin of the Seismological Society of America*, **61**, 1153–1167, 1971.

Young, G. B., and L. W. Braile. A computer program for the application of Zoeppritz's amplitude equations and Knott's energy equations. *Bulletin of the Seismological Society of America*, **66**, 1881–1885, 1976.

Zener, C. M. *Elasticity and Anelasticity of Metals*. Chicago: The University of Chicago Press, 1948.

Zeng, Y., and J. G. Anderson. A method for direct computation of the differential seismogram with respect to the velocity change in a layered elastic solid. *Bulletin of the Seismological Society of America*, **85**, 300–307, 1995.

Zhao, L., and F. A. Dahlen. Asymptotic eigenfrequencies of the Earth's normal modes. *Geophysical Journal International*, **115**, 729–758, 1993.

———. Asymptotic normal modes of the Earth—Part II. Eigenfunctions. *Geophysical Journal International*, **121**, 585–626, 1995a.

———. Asymptotic normal modes of the Earth—Part III. Fréchet kernel and group velocity. *Geophysical Journal International*, **122**, 299–325, 1995b.

Zöllner, F. Über eine neue Methode zur Messung anziehender und abstossender Kräfte. *Ber. sächs. Akad. Wis. Math.-nat. Klasse*, **21**, 280–284, 1869.

INDEX

C

F

G

H

N

O

Q

Y

Z